Tubular carbonate concretions from North Island, New Zealand: Evidence for hydrocarbon migration and the subsurface plumbing system of cold seeps

Stephanie Leigh Nyman

THE UNIVERSITY OF WAIKATO

HAMILTON, NEW ZEALAND

2009

Tubular carbonate concretions from North Island, New Zealand: evidence for hydrocarbon migration and the subsurface plumbing system of cold seeps

Volume 1

THE UNIVERSITY OF
WAIKATO
Te Whare Wānanga o Waikato

Stephanie Leigh Nyman

THE UNIVERSITY OF WAIKATO

HAMILTON, NEW ZEALAND

2009

ABSTRACT

Among the cold seep research community, it is now appreciated that tubular carbonate concretions are important indicators of hydrocarbon migration in the subsurface. In the last few years, several publications have documented tubular concretions and interpreted a subsurface seep origin. However, the nature, timing, and relative importance of tubular concretions as records of fluid flux and chemistry over time is yet to be fully appreciated.

In North Island, New Zealand, tubular concretions are geographically widespread but occur in localised clusters in several Cenozoic (especially Miocene) sedimentary formations of the East Coast Basin (Hikurangi Margin) and Taranaki Basin. They formed by precipitation of micritic dolomite and calcite cement within host siliciclastic mudstone and contain 50 to 85% carbonate (dolomite dominated), indicating precipitation in shallow burial (0 to 300 m). Several concretion morphologies occur, especially pipe, bulbous, doughnut, corkscrew, and conical shapes, and they include some of the largest examples known worldwide, ranging up to 10 m or more in length (limited only by exposure) and 0.1 to 1 m in diameter. The concretions typically support near-central conduits, from 1 to 40 cm in diameter, which may be open or variably filled with sediment and/or late cements.

As well as diverse morphologic types, the tubular concretions also show, within limits, variable mineralogic, petrographic, and geochemical characteristics. Additionally, some examples display association with slope instability, fault control on fluid migration, and stratigraphic placement directly below ancient seafloor seep carbonates.

$\delta^{13}C$ values of the cement forming the concretions range from –52 to +13‰ PDB and are interpreted to reflect carbonate precipitation from the onset of methane migration to the end of a major fluid migration event. A trend from strongly negative to strongly positive $\delta^{13}C$ values reflects either a mixing of methane and methanogenic CO_2 and/or the extensive anaerobic oxidation of methane (AOM) as supported by lipid biomarkers. $\delta^{18}O$ values range from −3 to +5‰ PDB

suggesting an evolved fluid source influenced by cycles of methane hydrate formation and dissociation.

The tubular carbonate concretions are interpreted to represent the subsurface plumbing pathways of methane expulsion in ancient hydrocarbon seep systems in North Island. Additionally, they suggest that gas hydrates may have been forming and dissociating along the Hikurangi Margin off eastern North Island for the past 23 Ma. The diverse geologic characteristics of the tubular concretions provide a unique opportunity to construct a comprehensive 4-D model of the subsurface development of such a system. The resulting schematic model of tubular concretion formation is an analogue for the subsurface fluid migration system of hydrocarbon seeps along the modern Hikurangi Margin, and possibly for many modern and ancient hydrocarbon seep systems in general.

ACKNOWLEDGEMENTS

First and foremost I want to thank my supervisor Professor Campbell Nelson. There are innumerable things to thank Cam for, firstly, his decision to accept me as his student and bring me to New Zealand. He has given me strong guidance, yet given me the encouragement and freedom to explore and test my own ideas. It is because of his support that I have become confident in my abilities and the scientist I am now. I am also grateful for his critical reviews and edits of draft versions of the thesis. I give humble thanks to Cam as it has been an honour and pleasure to work with him.

I also thank my second supervisor, Associate Professor Kathleen Campbell. Kathy has given me great encouragement and helpful criticism throughout my studies. I have enjoyed discussing new ideas with Kathy and am grateful for her ability to help me visualise the broader implications of the new ideas presented in this study to the wider seep community. I have been very fortunate to work with Kathy, it has been a delight.

To both Cam and Kathy: thank you for giving me this project. I have thoroughly enjoyed working with both of you. I will miss working with you, and hope there will be cause to do so in the future.

I also thank the Department of Earth and Ocean Sciences, Department Chairs Dave Campbell and Megan Balks, and Cam Nelson for the initial assistant lectureship position, the effort it took to bring me to New Zealand, and all the support while here. I also thank Sydney Wright for all of her helpful assistance over the years.

As well as Cam, many people assisted me with field work, and they all made the trips so enjoyable that they felt like holidays. I have many wonderful memories thanks to Kat Robertson, Sarah Ewen, Alison Graettinger, Chris McKinnon, Kris Saether, Debra Stokes, Ronald Nalin, Todd Snyder, Susan Nyman, Scotty Fraser, and Steve Hood. I also thank all the land owners who so graciously allowed me access to their properties and gave me assistance. A very special thanks goes to Dave Francis who helped me locate many of the tubular concretion sites.

Many thanks for the technical and laboratory assistance from Annette Rodgers, Chris McKinnon, Helen Turner (SEM), Steve Hood (CL), Ganqing Xu (XRD and sample preparation), Steve Cooke (stable isotopes), Neil Ogle (stable isotopes; Queen's University, Belfast), Jacinta Parenzee, and Steve Cameron (ICPMS).

I also am very grateful for all the collaborative discussions and intellectual advice from Jens Greinert, Julie Rowland, Jöern Peckmann, Michael Pearson, Peter King, Greg Browne, Peter Kamp, Chris Hendy, Sarah Ewen, Graham Logan, Dave Francis, Penny Cooke, and Steve Hood.

For financial support, I gratefully acknowledge the Royal Society of New Zealand Marsden Fund to University of Auckland (06-UOA-082) and University of Waikato (V083), and other logistical support from the Department of Earth and Ocean Sciences, University of Waikato.

I would also like to give a special thanks to my family and friends. My father, Douglas Nyman, and mother Susan Nyman for their encouragement, advice, and constant support which has taught me so much and given me the strength to reach my goals. My brother Joel Nyman, just for being my brother; miss you. Margaret Nelson, a beautiful lady who has been so wonderful to me; huge hugs and many thanks. My New Zealand friends, I already miss you. The American in Kiwiland will never be the same, I will always be a little bit Kiwi because of ya'll (I will never give up the ya'll). Thank you all for such wonderful memories.

And a compulsion to shout out to: Kat – beware the tides of March; Sarah and Alison – all the people that we meet, recon and serpentinite; Alison – a Mexican Christmas and digging up doughnuts; Cam – did you know the only thing rocks are good for is jewellery?; Steve, Sarah, and Kris – HAWKE; Bradley – keep grinning; Fiona – someone else who is sane, chĭlds; Debs – careful of those anti-inflam creams with cayenne pepper in the label, somewhat contradictory don't you think?; Sarah and Rob – what will I do without Sunday?; Rob – my brother, OK, brother-in-law; Sarah – because I cannot express it in words, so, coke in a can little sis, this isn't goodbye ☺.

TABLE OF CONTENTS

Volume 1

Volume 2

Appendicies

LIST OF TABLES

LIST OF FIGURES

Chapter 1 – Introduction

Chapter 2 – Background: hydrocarbon migration and tubular concretions in the subsurface seep system

Chapter 3 – The role of tubular concretions in hydrocarbon cold seep systems: Late Miocene Urenui Formation, Taranaki Basin, New Zealand

Chapter 4 – Miocene tubular concretions in the East Coast Basin, New Zealand: Analogue for the subsurface plumbing of cold seeps

Chapter 5 – Fault control on the distribution of concretionary subsurface seep carbonates, East Cape, North Island, New Zealand

Chapter 7 – Overview synthesis of New Zealand tubular concretions and schematic subsurface hydrocarbon seep model

CHAPTER 1

Introduction

1. Hydrocarbon seep systems

Hydrocarbon seep systems are sourced from the subsurface migration of methane rich fluids upwards to the seafloor (Roberts and Aharon, 1994; Peckmann et al., 2001; Campbell et al., 2002). Associated with this migration, the fluids may leave behind some characteristic morphologic, textural, and geochemical signatures of their ascent in the rock archive. The seafloor expression of such methane rich fluids are cold seep carbonate deposits that have been widely documented worldwide in both modern and ancient continental margin settings (Fig. 1) (Campbell, 2006; Judd and Hovland, 2007). However, any subsurface expression of the plumbing system of these cold seeps is presently poorly understood, being logistically difficult to investigate in the modern subsurface.

Hydrocarbon seep systems (Fig. 2) are initiated by the onset of fluid migration along pathways of enhanced permeability within a sedimentary pile, such as along micro-fissures, joints, faults, and stratigraphic discontinuities and boundaries. The ascending methane rich fluids eventually encounter an appropriately shallower burial environment where conditions are conducive to carbonate precipitation, typically one involving increased alkalinity, lower pressures, and lower temperatures (Boggs, 1992). In the subsurface, carbonate precipitation likely occurs preferentially along the pathways of focused fluid migration. Once the methane rich fluids reach the shallow burial environment in the sulphate reducing zone, anaerobic oxidation of methane (AOM) occurs via methanogenic Archaea and sulphate reducing Bacteria which convert methane and sulphate to water, bicarbonate, and sulphide (Reitner et al., 2005). Today, AOM and sulphate reduction occurring at the seafloor in seep provinces provide the appropriate habitat for colonisation by chemosymbiotic biota, including tube worms and lucinid and vesicomyid bivalves (Campbell, 2006; Judd and Hovland, 2007).

CHAPTER 2

Background: hydrocarbon migration and tubular concretions in the subsurface seep system

1. Seabed fluid flow

Seabed fluid flow involves subsurface fluids migrating upwards toward the surface, sourced from shallow to deep burial depths, in places escaping at the seafloor into the water column. The term fluid refers to both liquids and gases of any composition derived from within the Earth's crust (Judd and Hovland, 2007). Seabed fluid flow can be categorised into three types: 1) vents – involves hot fluids of hydro– or geothermal sources; 2) springs – encompasses terrestrial or meteoric fluids escaping at the seafloor; and 3) seeps – involves 'cold' fluids sourced from diagenetic reactions and/or hydrocarbons (Judd and Hovland, 2007). 'Cold' refers to ambient seawater temperatures or slightly elevated from relatively shallow burial.

This discussion focuses on hydrocarbon derived seeps and the term seabed fluid flow will be used in this context unless otherwise specified. Additionally, this Chapter is limited in its scope because hydrocarbon seep research is multidisciplinary involving the fields of geophysics, tectonics and structural geology, oceanography, microbiology, biogeochemistry, fluid-rock geochemistry, petroleum systems, fluid migration, sedimentology, and petrology. Consequently, this Chapter will be selective and review mainly some aspects of hydrocarbon sources, fluid migration, and the controls on carbonate cementation. Judd and Hovland (2007) have published the most comprehensive book to date on seabed fluid flow. Much of the information discussed in this Chapter (Sections 2 to 7) has come from Judd and Hovland (2007) which will not be repeatedly referred to throughout the text unless specific clarification is required. Section 9 is a

selective literature review of some key papers that discuss the occurrence of tubular concretions in various, mainly overseas examples.

2. General settings

Cold seeps have been documented from both passive and tectonically active continental margins and occur in marine sediments in continental slope and rise environments and in polar regions beneath permafrost (Fig. 1). New Zealand modern seep settings are prominent along the convergent Hikurangi Subduction Margin off eastern North Island (Lewis and Marshall, 1996; Greinert et al., in review). In such convergent settings, fluids are expelled along tectonic structures in the subduction zones (Fig. 2). In particular, sediments trapped along the plate margin of the accretionary wedge are compressed and contorted, forcing trapped fluids out of the sediment (Lewis and Marshall, 1996; Sibson and Rowland, 2003). Safer and Bekins (1998) determined that in the convergent margin Nankai Trough, 71% of the sediment porewater was expelled by diffuse flow at the seabed, <5% through focused flow expulsion, and about 1% was subducted. Fluid loss along the Hikurangi Margin is estimated to be more than 2×10^6 m^3 per year over a 100 km length (Townend, 1997). This indicates that fluid expulsion from sediments can be significant. Moreover, faulting within such structurally complex zones also provides major pathways for fluid migration, the fluid migration and escape at the seabed decreasing with distance from the deformation zone (Kukowski and Pecher 1999).

Other settings where cold seeps occur include fore-arc basins, subducting seamounts, and transform plate boundaries. Evidence of seepage at the seafloor is present in fore-arc basins along depressions between the island arc and subduction zone. Subducting seamounts cut a furrow in the overlying plate, affecting fluid flow pathways (cf. Rock Garden, modern hydrocarbon seep, Hikurangi Margin, New Zealand; Barnes et al., in press). Transform plate boundaries consist of intensive zones of roughly parallel faults, including severely shattered rock. These provide fluid migration pathways and if the fault movement is not exactly opposed then compression of the sediments will result in fluid expulsion.

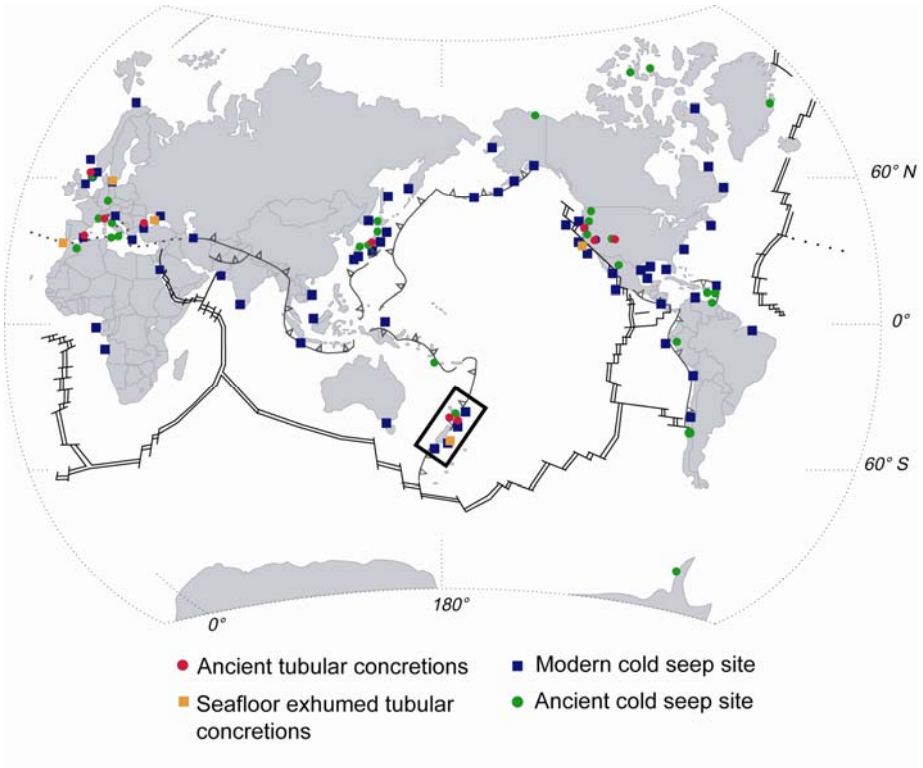

Figure 1. Map of global occurrences of reported ancient tubular concretions, exhumed tubular concretions on the modern seafloor (most near active seep sites), ancient seafloor cold seeps, and modern seafloor colds seeps (modified from Campbell, 2006). The black box outlines New Zealand.

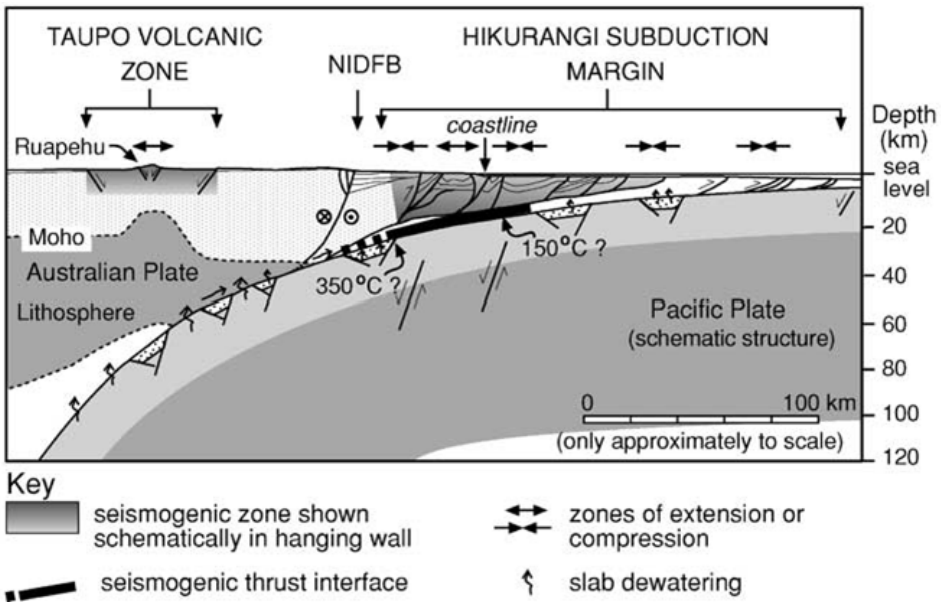

Figure 2. NW–SE cross section across central eastern North Island (See Chapter 1, Fig. 3) from the Taupo Volcanic Zone to the Hikurangi Margin illustrating subduction of the Pacific Plate underneath the Australian Plate, faulting style and depths of crustal seismogenic zones, and dewatering of the Pacific Plate (from Sibson and Rowland, 2003).

3. Significance of cold seeps and seabed fluid flow

Cold seeps and their plumbing systems have a significant impact on ocean water composition, the global carbon cycle, and ecological communities. Studies of modern seepage at the seafloor reveals that volumetrically significant quantities of hydrocarbons are released into the water column (Judd, 2004). These hydrocarbons can be oxidised and therefore removed from the water column, remain in the oceans, or escape into the atmosphere. Methane reaching the seabed and hydrosphere can be oxidised and then utilised by biological communities dependent on chemosynthesis.

Fluid seeps can have various benefits, including as natural resources, exploration tools, and industrial uses. Gas hydrates can be closely associated with seep systems and potentially offer an abundant future energy source (Grauls, 2001; Milkov and Sassen, 2002; Milkov et al., 2004). Many biota from chemosymbiotic communities contain microbes not found elsewhere that are already being used to process industrial sulphide wastes, and to produce bioproteins (Judd and Hovland, 2007) and other bioactive compounds for agricultural, environmental, pharmaceutical, and medical uses (Querellou, 2003). Moreover, chemosymbiotic communities introduce microbes and nutrients into the water column, which create a favourable environment for fish life and subsequently as fishing grounds.

Fluid flow upwards into the shallow burial environment and escape at the seafloor can result in marine geohazards, either natural or human induced, with the potential for significant casualties and/or financial losses. Common natural phenomenona associated with seabed fluid flow include slope destabilisation, catastrophic fluid escape, earthquakes, and tsunamis. On the other hand, slope destabilisation and earthquakes are known to induce higher seepage rates or activate intermittent seeps, where the influx of fluids near the seabed has also been hypothesised to act as triggers. Such events may lead to blowouts and tsunamis.

Marine operations may be risky or cumbersome near seep fields, with human made marine structures such as cables, pipelines, and platforms being at particular risk from seep related hazards. For example, seafloor trenching operations can be

very time consuming and expensive if methane derived authigenic carbonate (MDAC) is encountered. Gassy sediments can result in foundation problems. The integrity of pipelines can be compromised when crossing pockmarks or areas of active MDAC formation. And there is the potential for gas induced buoyancy loss of surface vessels during the sudden escape of large amounts of gas from beneath the seabed.

Human induced hazards associated with gas escape are high risk for drilling operations. In particular, careful assessment of potential overpressured gas zones is crucial during offshore drilling operations as gas blowouts may cause explosions and fires, mechanical damage, and loss of buoyancy. Some of the more dangerous situations arise from underground blowouts which have been known to catastrophically disrupt the seabed and destroy an entire drilling rig. Careful assessment of the presence and activity of seep fields and the potential associated hazards is pertinent when developing any seabed structures.

Despite the significance of fluid migration and expulsion into the water column, cold seep research remains in its infancy. This is as much due to the fact that seep systems were virtually unknown up to a couple of decades ago when technology for studying deep ocean systems (e.g., side scan sonar and deep sea drilling) became more routinely available. Moreover, the study of cold seeps is complex as it requires a multi-disciplinary approach, being linked to, and influenced by, all of the geo-, bio-, and hydro-spheres. Most studies to date have naturally focused on the accessible modern seafloor seep system and its carbonate deposits, with any subsurface interpretations relying mainly on remote geophysical techniques. Fewer studies have investigated possible subsurface cold seep carbonates (Aiello et al., 2001; Díaz-del-Río et al., 2003; Clari et al., 2004; De Boever et al., 2006a,b). To date, any geological features marking the ascent pathways of fluids in the shallow subsurface are poorly understood, yet study of subsurface seep systems provides unique insights into the factors that govern fluid migration and seep development, as well as their evolution over time. One such feature archived in the stratigraphic record that may mark the pathways of focused fluid flow is tubular carbonate concretions. Moreover, unlike the modern occurrences, the potential exists for ancient surface and subsurface seep deposits to provide a

unique view of the three-dimensional subsurface geometry of entire seep fields (Nelson et al., 2004).

4. Fluid origins

Hydrocarbon rich fluids are volumetrically relatively common in sedimentary basins and the primary fluids involved in seep systems are methane rich. Methane in marine sediments is sourced mainly from microbial and/or thermogenic processes. Microbial methane is sometimes referred to as biogenic methane, but the term microbial is preferred because thermogenic methane also has an organic source and so is itself also 'biogenic'.

4.1 Microbial methane

Microbial methane is generated by methanogenic Archaea in the shallow subsurface, from ~2 m to 1 km burial, and likely even deeper (Rice, 1992), This process is termed methanogenesis. Methanogenic Archaea (methanogens) thrive in anoxic environments with a high concentration of organic material and inhabit temperature ranges from 4 to 55^{o}C or more, with one species even up to 97^{o}C (Wiese and Kvenvolden, 1993). Methanogenic Archaea can produce hydrocarbons from a limited number of substrates, and most commonly from carbon dioxide via the formula:

$$CO_2 + 4H_2 \rightarrow CH_4 + 2H_2O \qquad (1)$$

Microbial methanogenesis occurs in anoxic environments with low sulphate concentration, low temperatures (optimum 35 to 45^{o}C), and abundant organic matter (in excess of 0.5% TOC) (Rice, 1992). Methanogenesis is also dependent on the type of organic matter and the state in which it has already been degraded, since methanogens require other microbes to breakdown complex organic compounds to a degree before they are capable of utilising it (Rice, 1992). Optimal conditions for methanogenesis also depend on sedimentation rate. If sedimentation rates are too high, organic rich sediments will move through the zone of methanogenesis too quickly, lessening the amount of methane produced. Alternatively, low sedimentation rates will keep sediments in the sulphate

reduction zone too long so that organic matter present will be oxidised, thereby becoming unavailable for later methane generation (Rice, 1992). According to Clayton (1992), optimal sedimentation rates for microbial methane generation are from about 200 to 1000 m/my^{-1} (depending on geothermal gradient).

Clayton (1992) suggested that under optimal conditions, about 10% of the total organic carbon (TOC) present can be converted to methane. He also proposed that at typical methane generation depths, 0.2% of carbon converted to methane will result in methane saturation of pore waters, and thus 10% conversion would result in the formation of a free microbial gas phase. As sediments compact, the water soluble and gassy by-products of microbial activity are expelled, while any remaining organic material that is insoluble and resistant to degradation forms condensed polymers ("geopolymers") and eventually kerogen.

4.2 Thermogenic methane

In general, sedimentary rocks retaining more than about 2% TOC in the form of kerogen (organic carbon remaining after methanogenesis) are called source rocks. The kerogen retained in the rocks has the same characteristics as the original organic matter − known as insoluble amorphous organic remains. Thermogenic methane is produced from the thermal 'cracking' of kerogen during late catagenesis to early metagenesis (temperatures > 90ºC; burial depths > 2km).

4.3 Gas hydrates

Gas trapped in sediments beneath the seafloor is a widespread occurrence and methane sequestered as methane hydrate is important as a potential hydrocarbon resource, as a geohazard, and its potential influence on climate. Gas hydrates are a possible future energy resource and these hydrocarbon 'holding tanks' could be considered reservoirs from an exploration viewpoint where the hydrate structure is the actual hydrocarbon trap. Upon dissociation, hydrocarbons again migrate and eventually expel into the water column. As the formation of gas hydrates is an intermediate stop for some migrating hydrocarbons, and their formation and dissociation influence water compositions, they are further addressed in this section.

Gas hydrates are ice-like crystalline compounds of gas molecules trapped within cages of water molecules bonded by hydrogen (Fig. 3). The gas hydrate structure is referred to as a clathrate molecule. Gas hydrates are most commonly methane, but may be composed of ethane, butane, and non-hydrocarbon gases such as CO_2 and H_2S. Gas hydrates can be present in marine bottom sediments at water depths below 300 m as well as in polar regions where temperatures are low. Hydrates present at and below the seafloor have a limited temperature and pressure range in which the clathrate molecule is stable (Fig. 4). This is a function of water temperature, geothermal gradient, pressure, pore water salinity, and other present gases. Methane hydrate forms when ascending thermogenic or microbial methane encounters the gas hydrate stability zone (GHSZ, Fig. 4). Free gas exists below the GHSZ. The boundary marking the phase change between solid hydrate and free gas can be imaged using seismic reflection and is referred to as a bottom simulating reflector (BSR) (Fig. 5). Although hydrate stability is more common beneath the seafloor, under the right conditions hydrates can also occur at and above the seabed.

Hydrates may be present in several morphologies. They can be massive, forming in coarse-grained sediments and acting like a reservoir, or they can be veined in a host rock, occurring usually in fractures. They can be lenticular-bedded, porphyraceous, or even fill more area than the host grains themselves (hydrate-rock). When hydrates fill all available pore spaces within a sediment they act as a seal, prohibiting further fluid migration.

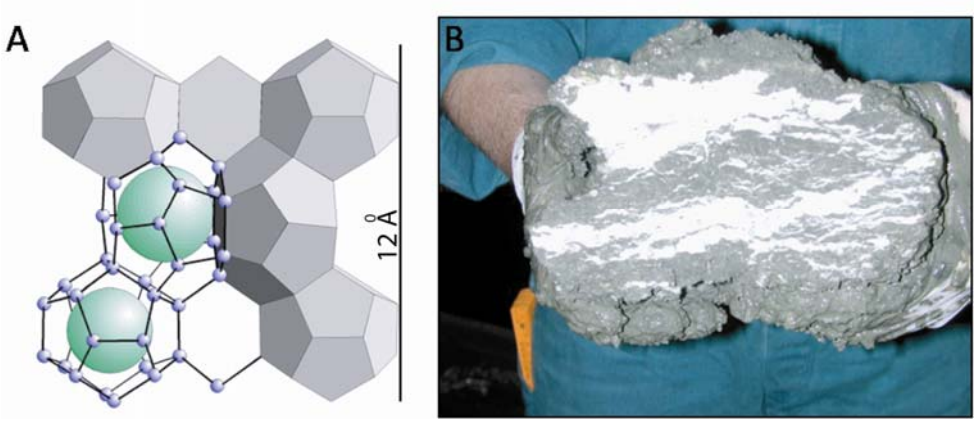

Figure 3. (A) Diagram of the gas hydrate molecule. Gas molecules (e.g., methane) trapped between cubic and hexagonal water cages. (B) Photograph of lenticular-bedded gas hydrate in marine sediments. Courtesy of Jens Greinert (IFM-GEOMAR, Kiel, Germany; now at NIOZ, Texel, The Netherlands).

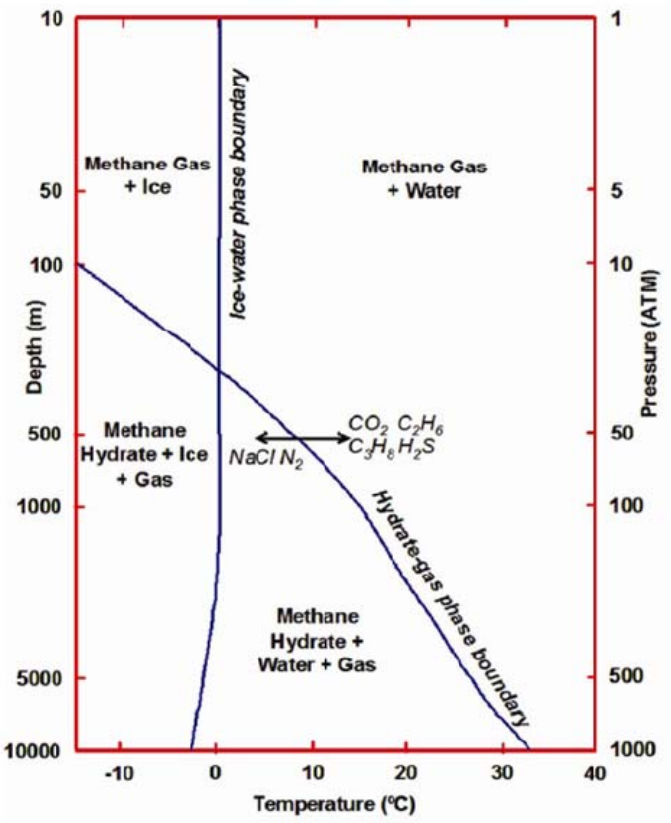

Figure 4. Phase diagram of gas hydrate stability zone (GHSZ) which are defined by temperature and pressure. The GHSZ is beneath the hydrate-gas phase boundary (from Judd and Hovland, 2007).

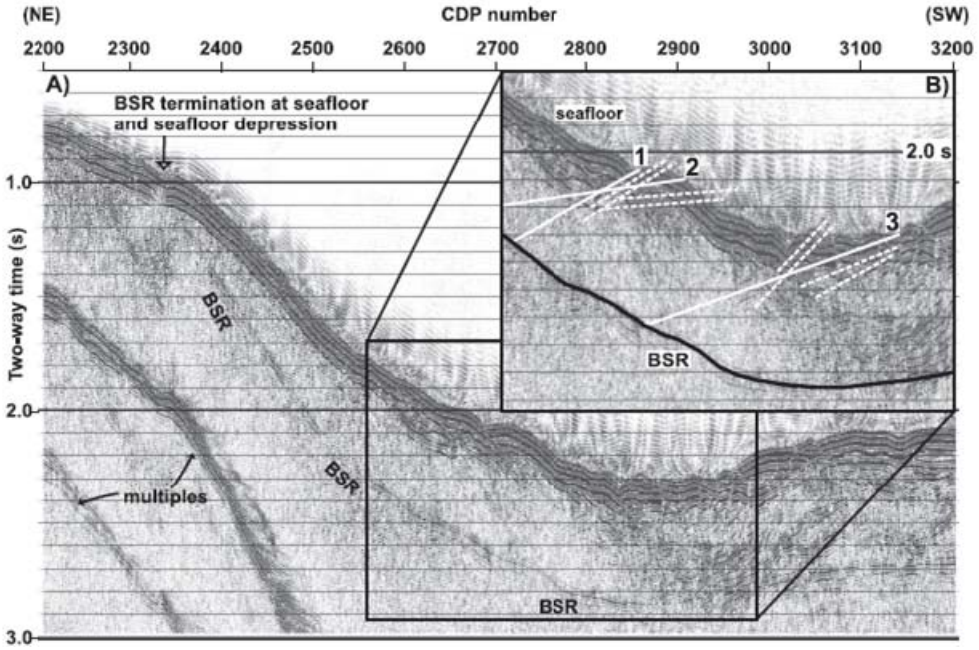

Figure 5. Example of a bottom simulating reflector (BSR) in a seismic line. (A) The BSR terminates at the seafloor in the left side of the diagram. (B) Interpretation of slope failure propagating from the BSR to the seafloor (solid and broken white lines). From Crutchley et al. (2007). The seismic line is 250 m long.

Gas hydrates may form by two processes: 1) if gas is dissolved in solution then hydrate can be precipitated out of pore waters, similar to the process of mineral precipitation; 2) if free gas is present, then the water for the hydrate molecule must be extracted from the sediment, a processes referred to as segregation. The formation of gas hydrates utilises large amounts of water, which results in dewatering of the sediments, which in turn may show signs of shrinkage. Salt is excluded from the hydrate molecule, so as hydrate formation continues the residual waters become more saline. Additionally, during hydrate formation, the heavier oxygen isotope is preferentially incorporated into the hydrate molecule, resulting in anomalously ^{18}O-depleted remaining porewaters. Upon hydrate dissociation, the enriched oxygen from the hydrate molecule is released into the pore waters resulting in anomalously ^{18}O-enriched porewaters by up to 3‰ (Davidson et al., 1983; Ussler and Paul, 1995). This process is invoked in this study to help explain the positive oxygen isotope values recorded in several of the New Zealand tubular concretions.

Gas hydrates will dissociate (return to gas phase) with increased temperatures or decreased pressures. The volume of gas released is approximately 172 times that of the volume of hydrate (Sloan, 1988). This increase in volume can completely change the sediments, often resulting in their liquefaction. The sudden release of large volumes of gas hydrates can lead to catastrophic effects, such as the formation of seabed pockmarks, slope instability, and damage to human made marine structures.

5. Driving forces of fluid migration

The cold seep system is initiated with the onset of fluid migration. The resultant effects of upward migration depend on the environment at the origin of the migrating fluids, the ratio of solids to fluids, triggers, and available migration pathways. Three forces drive the ascent of fluids: overpressure, buoyancy, and gas exsolution and expansion. Overpressure occurs when fluids cannot drain out of the sediments. Situations which may trap fluids are sands between impermeable clay layers, gas generation at greater rates than it can be expelled from the

sediment, and tectonic compression. Where fluids cannot be expelled, the sediments cannot be compacted, resulting in reduced to no grain contacts. Since the grains are not in contact, the fluids are supporting a higher proportion of the overlying sediments than normal, resulting in under-consolidation of the sediment. Additionally, shear strength, tensile strength, and lithification are inhibited and any water in the fluids retains heat. As a consequence, the energy retained in overpressured sediments plays a major role in driving fluid ascent.

The second driving force is buoyancy. For fluids to become buoyant and ascend, a density inversion must occur where the sediments below are less dense than those above. Factors reducing density and so increasing buoyancy are higher amounts of fluids, less dense sediments or fluids, higher temperatures, higher amounts of gas, and lowered pressures.

Conditions which favour overpressure and buoyancy inversions are: higher fluid volumes, methane generation, compressional tectonic regimes, and increased burial. Migration will begin along pathways of relatively greater permeability, which may be micro-fissures, minor fractures, major faults, or topographic highs. Once migration starts, the third driving force comes into play, namely gas exsolution and expansion (Fig. 6). As fluids rise they are under less pressure. As pressure decreases, gas can then come out of solution in the form of bubbles (gas exsolution). Any free gas bubbles will increase in size (expansion). Exsolution and expansion reduce bulk density, thereby increasing buoyancy. Lowering of density and increasing buoyancy leads to further fluid ascent which reduces pressure, so starting the cycle over again (Judd and Hovland, 2007).

The frequency and duration of fluid flow depend on migration pathways and fluid supply. More direct pathways over shorter distances and along faults lead to more constant fluid flows. Longer and more tortuous pathways may result in intermittent fluid supply. Additionally, fluid flow may be triggered by sudden or other events such as: earthquakes, enhanced sediment accumulation or removal, changes in sea level, atmospheric pressure changes, waves or tides, and human intervention. Seabed fluid flow can lead to: 1) fluid escape at the sea floor with no affect on the sediment; 2) fluid escape at the sea floor that disrupts the sediment; 3) fluidised sediments which become mobilised; and, 4) mobile

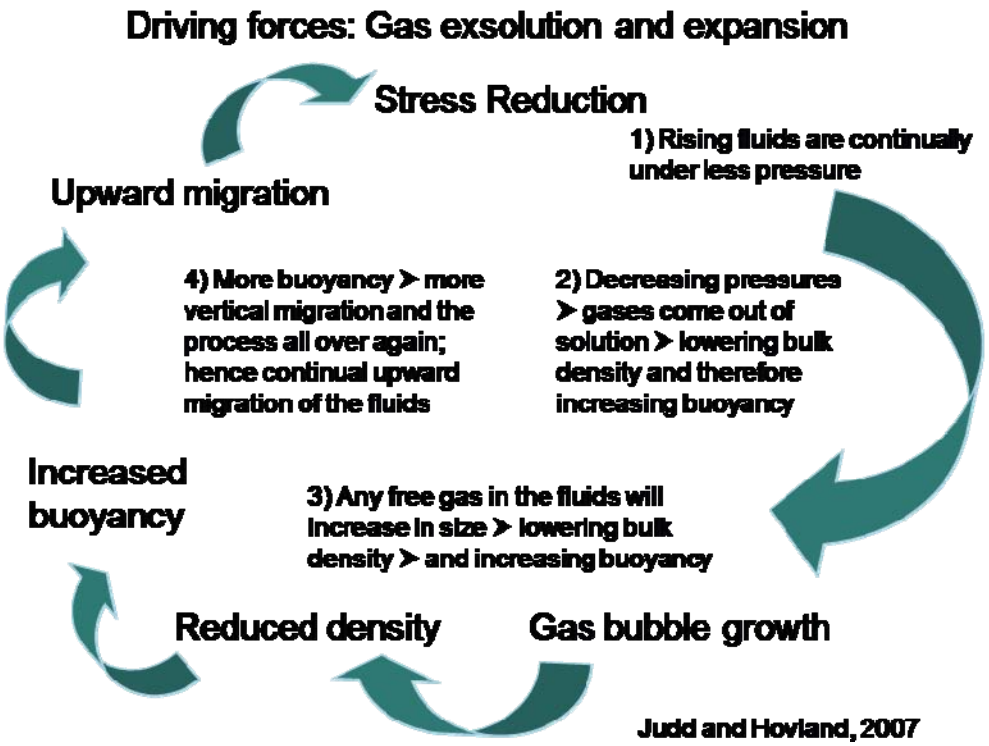

Figure 6. The process of gas exsolution and expansion driving upward fluid migration (modified from Judd and Hovland, 2007).

sediments that are not fluidised. Features and processes of seabed fluid flow are interconnected, each process affecting another, which makes classification of seep systems difficult. However, features resulting from seabed fluid flow record the influences which governed the development of the system. As such they can provide insight into the history and evolution of the system in question.

6. Chemistry of hydrocarbon seeps and mineral precipitation

6.1 Life without photosynthesis

The first benthic communities discovered at hydrothermal vents came from 2600 m water depth on the Galapagos Rift (Corliss et al., 1979). The deep water biota included siboglinid tubeworms, giant bivalves, serpulids, crabs, lobsters, sea anemones, barnacles, limpets, sea cucumbers, and fish, amongst others. These benthic communities were at water depths far beneath the zone of photosynthesis and it was suggested that these communities were somehow deriving energy from the venting fluids. Since their discovery more than 350 species have been identified in the Atlantic, Pacific, and Indian oceans; 93% of these species are new discoveries (Judd and Hovland, 2007).

The first hydrocarbon (cold) seep community was discovered by Mahlon Kennicut and colleagues in 1985 along the Louisiana continental slope. Their investigations (Kennicut et al., 1985) found bivalves, gastropods, tubeworms, fish, crabs, shrimps, and bacterial mats. Further studies documented similar biological communities at hydrocarbon seeps in other marine settings, such as subduction zones and accretionary wedges, mud volcanoes, trenches, and brine filled pockmarks (Kulm et al., 1986; Mayer et al., 1988; MacDonald et al., 1990; Olu et al., 1997).

Organisms living at vents and seeps are supported by chemosynthesis. During the mid-1980s, research focused on microbes in the marine environment that could produce energy to drive the food chain. It was not until the late 1990s that an anaerobic microbial consortium was discovered.

6.2 Anaerobic oxidation of methane via microbes

Organic material in sediments at the seabed is degraded by sulphate reducing bacteria and methanotrophic Archaea, occurring in the sulphate-methane transition zone (SMTZ). Iversen and Jørgensen (1985) suggested that methane was being oxidised in the SMTZ via the anaerobic oxidation of methane (AOM), as represented by the following equation:

$$CH_4 + SO_4^{2-} \rightarrow HCO^-_3 + HS^- + H_2O \qquad (2)$$

Sulphate is depleted where there is an excess of methane, resulting in increased bicarbonate, reduced sulphur, and lower pH in the pore waters. Any excess bicarbonate will result in carbonate precipitation. Any addition of iron will combine with the reduced sulphur to precipitate pyrite and an excess of sulphur not incorporated into pyrite will form hydrogen sulphide which can be used by sulphide oxidising bacteria.

It was previously thought that methanogenic Archaea need oxic environments, while sulphate reducing bacteria require anoxic environments. However, Boetius et al. (2000) discovered a microbial consortium that was able to anaerobically oxidise methane. The microbes are believed to work via reverse processes compared with the previously recognised methanotropic Archaea and are referred to as anaerobic oxidisers of methane. They were discovered along the Cascadia accretionary wedge at Hydrate Ridge underneath *Beggiatoa* bacterial mats. The microbes are framboidal in shape, and surround carbonate precipitates (Fig. 7) (Boetius and Suess, 2004). Carbon isotope analysis of the microbial cells yielded $\delta^{13}C$ values of –96.2‰ PDB, indicating the cell's utilisation of methane. Since the discovery of anaerobic oxidisers of methane, similar microbes have been found worldwide in seep environments.

The anaerobic Archaea play an important role as energy suppliers to the food chain at cold seeps. Organisms that that live in symbiosis with AOMS include

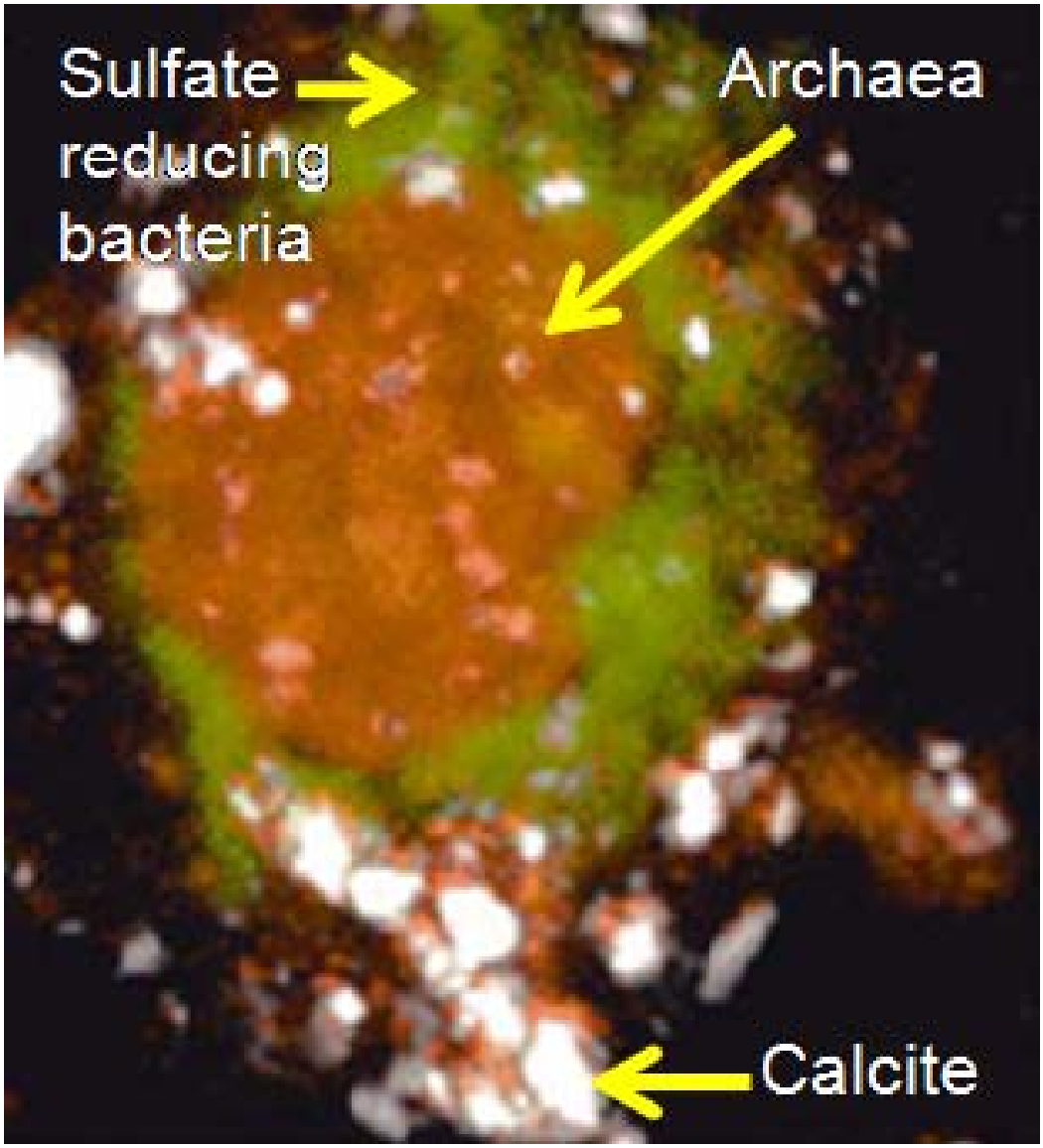

Figure 7. Microphotograph of an aggregate of methanotrophic Archaea (red), sulphate reducing bacteria (green), and calcite precipitates (white). Modified from Boetius and Suess (2004); photograph courtesy of T. Neu. Scale not provided, aggregate approximately <5 μm across.

bacterial mats (*Beggiatoa*, *Thirthrix*, and *Thioploca*), tube worms (Perviata, Monilifera, and Vestimenifera), bivalves (Vesicomyidae, *Bathymodiolus*, *Solemya*, *Acharax*, Thyasiridae, and Lucinidae), and carnivorous sponges (*Cladorhiza*) (Fig. 8). Additionally, organisms that are non-symbiotic can also survive in seep environments by feeding off those that do live in symbiosis with the anaerobic oxidisers. Non-symbiotic biota include gastropods, starfish, octopi, shrimps, crabs, lobsters, echinoids, and fish.

6.3 Role of anaerobic oxidation of methane in carbonate precipitation

Mineralogically, hydrocarbon seeps are characterised by carbonate precipitation where the carbon incorporated into the carbonate lattice is derived from methane. In general, mineral precipitation reflects a balance among three variables: temperature, pressure, and solute concentration, where a decrease in temperature or pressure and/or an increase in concentration leads to mineral precipitation.

Figure 8. Examples of seep organisms. (A) Modern bacterial mats (white) from Hydrate Ridge, Cascadia convergent margin. From Boetius and Suess (2004); photograph from GEOMAR, Kiel. (B) Fossilised bacterial mats (thrombolites, brown) from an ancient seep limestone, Rocky Knob, eastern North Island, New Zealand. See Chapter 1, Fig. 3 for location. (C) Modern tubeworms at East Wall hydrothermal vent, East Pacific Rise (From Campbell, 2006; courtesy of C.L. Van Dover). (D) Cross sectional slab of fossilised worm tubes from an ancient seep limestone, Rocky Knob, eastern North Island, New Zealand (courtesy of Kathy Campbell). (E) Modern (upper) Vesicomyid from an active hydrocarbon seep on the Hikurangi convergent margin, Richie Bank, East Coast Basin, North Island, New Zealand (from Campbell et al., 2008; sample courtesy of B.A. Marshall). Vesicomyid fossil (lower) from an ancient seep complex, Rocky Knob, East Coast Basin, North Island, New Zealand (from Campbell et al., 2008). (F) Ancient *Bathymodiolus* from Rocky Knob, East Coast Basin, North Island, New Zealand (courtesy of Kathy Campbell). (G) Ancient *Solemya* from the Upper Jurassic seep carbonate, Paskenta, Great Valley Group, California (from Vokes, 1955; Campbell, 2006). (H) Lucinid bivalve from a Miocene seep complex, Italian Appenines (from Campbell, 2006). (I) Thin section photograph of ancient Thyasirid in glauconite/detrital-rich micrite, Eocene Keasey Formation, Vernonia–Timber seep, NW Oregon, U.S.A. (from Campbell, 2006).

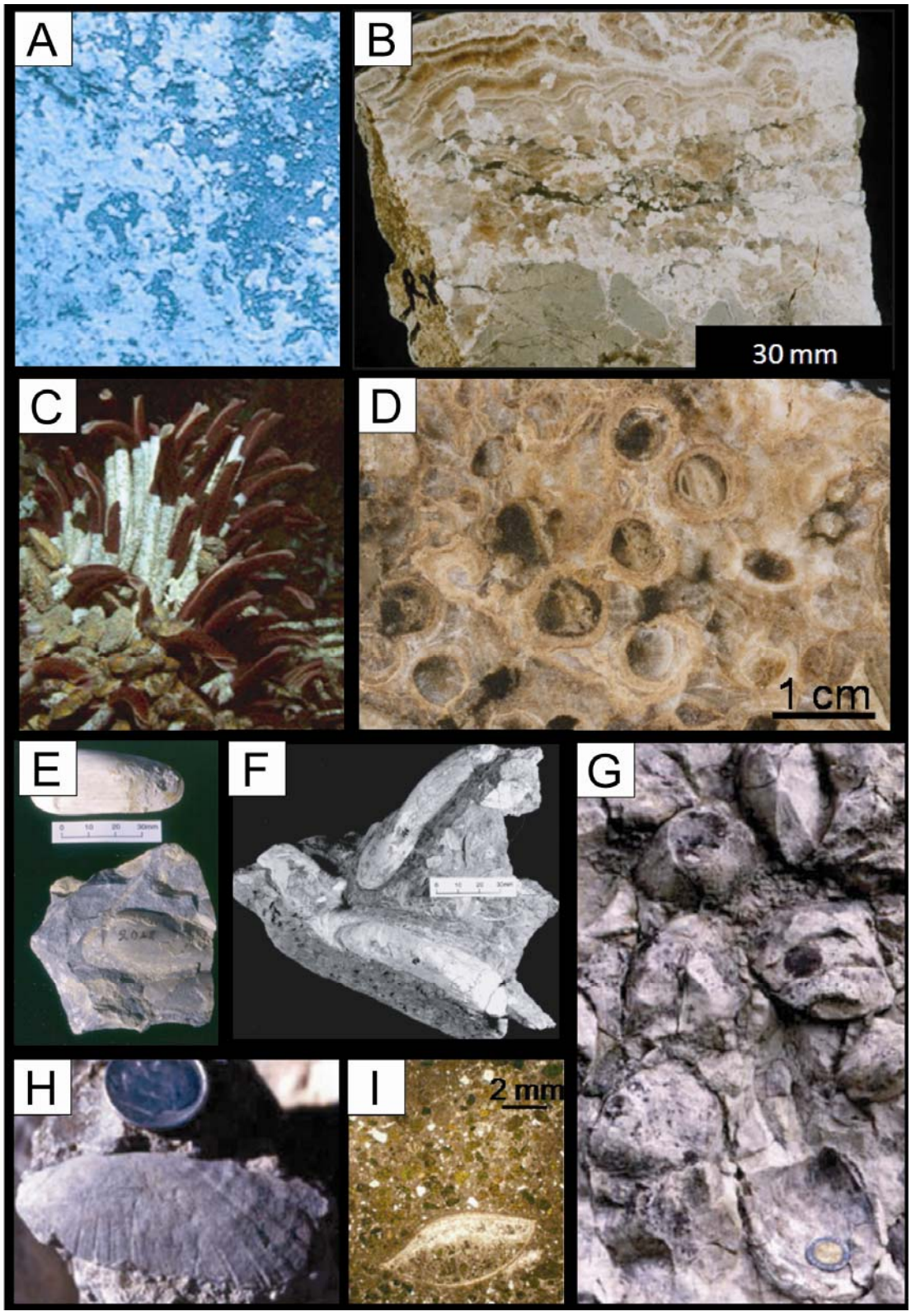
A
B
30 mm
C
D
1 cm
E
F
G
H
I
2 mm

In the seep environment, carbonate precipitation is driven by the anaerobic oxidation of methane (AOM) via sulphate reducing bacteria and methanogenic Archaea. Sulphate reducing bacteria form a layer around the methanogenic Archaea which appear to be in an organic matrix acting as a nucleus for the precipitation of calcite or aragonite, confirming the relationship between the microbes and carbonate precipitation (Boetius and Suess, 2004) (Fig. 7). In addition, bacteria and biofilms characteristic of bacteria have been found in seep environments entombed or fossilised in seep carbonate (Belenkaia, 2000). Moreover, Thiel et al. (2001) found biomarkers (PMI, ether-bound biphytane, cyclic C40-isoprenoids, and others) that are related to the anaerobic oxidation of methane.

The process of anaerobic oxidation of methane was previously mentioned (Section 6.2, equation 2) where AOM occurs via reverse working methanogenic Archaea and sulphate reducing bacteria which convert methane and sulphate to water, bicarbonate, and sulphide (Reitner et al., 2005). Along with introducing free bicarbonate into the system, the introduction of HS^- also increases alkalinity, thereby driving carbonate precipitation (Cavagna et al., 1999; Hinrichs et al., 1999; Orphan et al., 2001), as expressed by the formula:

$$X^{2+} + 2HCO_3^- \rightarrow XCO_3 + H_2O + CO_2 \qquad (5)$$

(X = Ca, Mg, and/or Fe)

6.4 Carbonate precipitates

Calcite and aragonite precipitate via the formula:

$$Ca^{2+} + 2HCO^-_3 \rightarrow CaCO_3 + H_2O + CO_2 \qquad (6)$$

Depending on availability, magnesium can be substituted into the carbonate lattice for calcium where carbonates with greater than 4 mol% are named high magnesium calcite (HMC). This study recognizes an intermediate Mg Calcite (4 – 12% mol% MgCO3) (e.g., Nelson et al., 2003) In general, HMC is favoured over aragonite in cooler temperature, high phosphate, low sulphate waters (Tucker and Wright, 1990; Jørgensen, 1992; Peckmann et al., 2001). In addition, a high

rate of supply of CO_3^{2-} and well oxygenated conditions also are preferential for aragonite. Aragonite probably represents an early carbonate phase in seep environments. As the sulphate reducing bacteria deplete sulphate concentrations then carbonate precipitation turns to calcite. Additionally, aragonite will be favoured nearer to the seafloor and in oxygenated pore water.

Although calcite and aragonite are the dominant cement mineralogies found in cold seeps, dolomite can sometimes also be common. The formation mechanism for dolomite precipitation is poorly understood, although usually dolomite is found as replacing a precursor carbonate phase via the reaction

$$2CaCO_3 + Mg^{2+} \rightarrow CaMg(CO_3)_2 + Ca^{2+} \quad (7)$$

However, in conditions of seawater evaporation or dilution, increased temperature, increased phosphate concentrations, lowered sulphate concentrations, and/or anoxic conditions, dolomite can precipitate directly from seawater (Tucker and Wright, 1990; Jørgensen, 1992). In cold seep environments, continued precipitation of aragonite and/or calcite decrease the Ca/Mg ratio and microbial activity consumes sulphate, and increases alkalinity, making the environment more conducive to dolomite precipitation. Moreover, as the sediments are buried, the increase in temperature makes these fluids even more favourable for dolomite formation in the subsurface.

6.5 Associated minerals

Pyrite, gypsum, and barite can be common mineral precipitates in cold seep environments, but much less so than carbonate. AOM produces HS^- via equation 2 which leads to hydrogen sulphide formation (H_2S). H_2S can then be used by microbes and sulphide oxidising bacteria hosted by symbiotic organisms. Additionally, in the presence of reduced iron, H_2S reacts with available iron to precipitate iron monosulphide (Fe_3S_4) followed almost immediately by conversion to pyrite (FeS_2) (Wilkin and Barnes, 1997) via the equations:

$$Fe_3S_4 + 2H_2S \rightarrow 3FeS_2 + 4H^+ + 4e^- \quad (8)$$

$$4H^+ + 4e^- + 2S^0 \leftrightarrow 2H_2S \quad (9)$$

$$Fe_3S_4 + 2S^0 \leftrightarrow 3FeS_2 \quad (10)$$

Pyrite precipitates as framboids encased in MDAC or filling shell material. Gypsum concretions have been documented with MDACs in the Kattegat, Denmark (Jørgensen, 1980). Barite ($BaSO_4$) has also been found as concretions and crusts in association with seeping methane fluids and seep related communities (Lonsdale and Becker, 1985; Fu et al., 1994; Torres et al., 1996).

7. MDAC formation

The oxidation of methane in seabed sediments may result in carbonate precipitation in the pore spaces between sediment grains as cement. In the more recent literature this cement is referred to as methane derived authigenic carbonate, or MDAC. Carbonate precipitated as cement most commonly exhibits acicular, fibrous, botryoidal, or microcrystalline fabrics.

7.1 Isotope signatures

As MDAC is derived from methane, its carbon isotope signature is distinctive and reflects this origin. MDAC carbon isotope values typically range from –60 to –20‰ PDB. Within this range of values, the parent methane may be discerned. Carbon isotope values between –90 and –50‰ suggest a source of microbial methane, while those from –50 to –20‰ imply a thermogenic methane source (Irwin et al., 1977; Roberts and Aharon, 1994). Additionally, carbon isotope values between +5 and +20‰ PDB indicates methanogenesis, specifically, carbon sourced from the residual CO_2 remaining after microbial methane production (Irwin et al., 1977; Roberts and Aharon, 1994). As methane is oxidised, the remaining pool becomes more enriched in ^{13}C (Coleman et al., 1981; Whiticar, 1999; Pancost et al., 2000; Cowen et al., 2002). Oxidation of 80 to 90% of a methane pool can enrich the $\delta^{13}C$ value by up to 60‰ PDB (Whiticar, 1999). Mixing of any of these carbon sources and/or processes can further influence the carbon isotope values of carbonate precipitates, further complicating any interpretations.

Oxygen isotope values reflect the water composition at the time of carbonate precipitation (Longstaff, 1987). In general, seawater has a $\delta^{18}O$ composition near 0‰ SMOW (with slight variations dependent on geologic age and latitude). More depleted $\delta^{18}O$ values indicate increased temperatures (e.g., diagenetic fluids) or influences from meteoric waters. Enriched $\delta^{18}O$ suggests influences from colder waters, evaporation, clay transformation, and/or gas hydrate formation/dissociation (Davidson et al., 1983; Ussler and Paul, 1995). However, seeps involve migrating fluids from either shallow or deep methane reservoirs. As such, oxygen isotope values may be difficult to interpret due to the mixing of fluids and/or exposure of the fluids to different processes during migration.

7.2 MDAC features

Continued carbonate precipitation combined with entombment of characteristic seep biota result in distinctive MDAC deposits at and near the seafloor. MDACs have been documented worldwide, and a variety of morphologies have been described, including mounds, build-ups, slabs, blebs, chimneys, and tubular concretions (Fig. 9) (e.g., Aloisi et al., 2002; Aiello et al., 2001; Peckmann et al., 2001; Clari et al., 2004; Conti et al., 2004; Conti and Fontana, 2005; Hovland et al., 2005; Campbell, 2006; De Boever et al., 2006). The morphology of MDACs typically reflects their precipitation position within the seep system (surface vs sub-seafloor or subsurface) and the fluid flow rates. Common features of MDACs include multiple phases and textures of carbonate cement, disseminated pyrite, open or filled conduits which can be millimetres to tens of centimetres in diameter, brecciated clasts, and hydrofracturing.

While MDAC has become the more common term, sea floor carbonate precipitation at seep sites also has been described as seep carbonates, concretions, and seep limestones. However, in all cases, except for possible carbonate precipitation into the water column, carbonate is precipitated within clastic marine sediments and/or between shell fragments. The term limestone may be inappropriate, since it can be shown that MDAC is often a carbonate cemented siliciclastic sediment and so, by definition, would be a clastic deposit. On the other hand, if carbonate content is greater than 50%, then by definition the MDAC

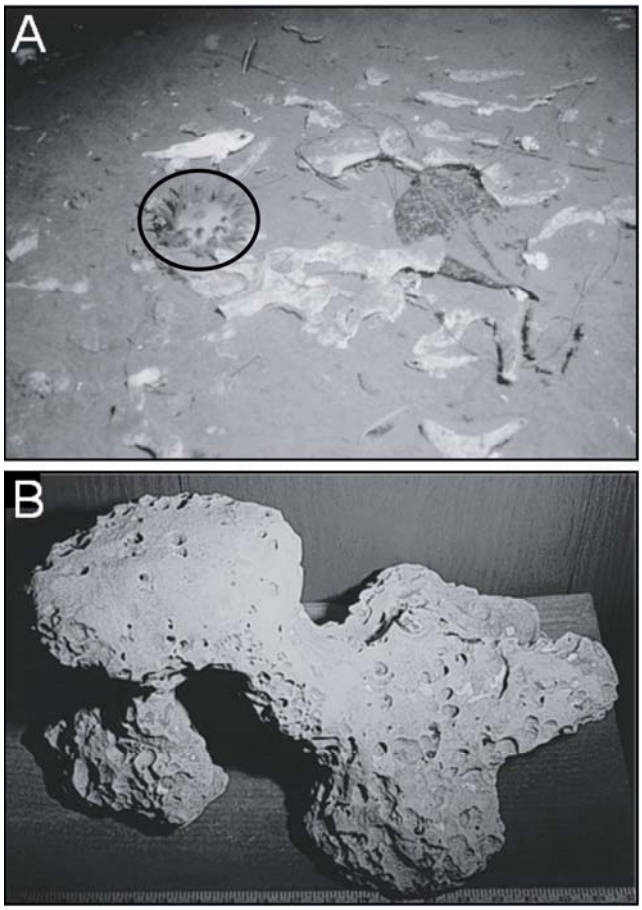

Figure 9. Examples of carbonates forming on the modern seafloor. (A) Common appearance of seep carbonate crusts. Sea anemone (circled) is 10 cm across. (B) A 45 cm long knobby carbonate concretion from the seafloor. Monterey Bay, California (from Stakes et al., 1999).

Figure 10. Examples of tubular concretions from New Zealand. (A) A common example of tubular concretions, and others illustrating an open (B) and cement filled (C) central conduit. The concretion in (B) is 40 cm across.

would be a carbonate rock. However, limestones have a classification scheme, textures, and morphologies much their own (Folk, 1962; Dunham, 1962). If MDAC is referred to as a limestone, the terminology conjures up certain preordained ideas of what these rocks should look like, behave like, and the rules governing their formation. From previous discussions, it is evident that most MDACs do not resemble 'normal' carbonate rocks except for their moderately high content of carbonate and so use of the name limestone potentially leads to some confusion for those not familiar with cold seeps. In fact, historically, there have been occurrences of 'limestones' reported in the literature that were 'strange' that have, with more recent work, become appreciated to be MDACs. This is the situation for several ancient occurrences in New Zealand (cf. Kamp and Nelson, 1988; Campbell and Bottjer, 1993; Campbell et al., 2008). For the purpose of this study the term MDAC or seep carbonate will be used to refer to any carbonate precipitated authigenically from methane.

8. Tubular concretions

A tubular concretion is a well-cemented body of rock within an otherwise less cemented host rock, typically siliciclastic mudstone. Tubular concretions are mainly cylindrical, tubular, or pipe-like in shape (Fig. 10A), and often include a conspicuous central hole or conduit that runs the length of the concretion (Fig. 10B). Conduits range from millimetres to decimetres in diameter. They may be empty (Fig. 10B) or filled with later generation cements and/or foreign sediments (Fig. 10C). Some tubular concretions have multiple conduits, while others appear to lack a well-defined conduit, except for slight concentric variations in colour depending on cement composition or abundance.

Tubular concretions typically have a relatively high carbonate content (35 to 85%) compared to the host mudstone (<10%), which is due to precipitation of microcrystalline carbonate or microsparite carbonate cement within the host sediment beneath the seafloor. By definition, concretions form by mineral precipitation within the pore spaces of sediment (Gautier and Claypool, 1984; McBride et al., 1995), which therefore implies subsurface formation. This subsurface origin is important because tubular concretionary structures can often

Figure 11. Tubular carbonate concretions exhumed on the seabed off Otago, South Island, New Zealand. The taller of the two is 50 cm high. Additional carbonate concretionary debris litters the surrounding seabed around the concretions. From Orpin, 1997.

be found lying or protruding upwards from the modern seafloor near seep sites (Fig. 11) (e.g., Orpin, 1997; Díaz-del-Río et al., 2003). However, if the tubular concretions formed above the seafloor and into the water column, their compositions should be almost entirely carbonate precipitate with little to no siliciclastic component.

In the literature, tubular shaped carbonate structures have been referred to as tubular, pipe-like, and cylindrical concretions, doughnuts and chimneys, and variations of these names. The term chimney is misleading as it is used in relation to a 'seismic' chimney identifying the upward migration of fluids in the sediment column (e.g., Gay et al., 2006). The term is also used for hydrothermal chimneys which form from mineral precipitation above the seafloor in the water column. Additionally, there may be examples of tubular structures related to cold seeps that actually do form above the seafloor (similar to the hydrothermal chimney counterparts) (e.g., Peckmann et al., 2001). As such, this study advocates that the term tubular concretion should be used for any seep related tubular structure with a centralised conduit, where carbonate minerals have cemented host sediment and a subsurface origin has been determined. Additional terminology can be used when appropriate to further describe variations in morphology and mineralogy (e.g., pipe, bulbous, calcitic pipe, etc).

9. Previous studies of tubular concretions

The study of seep systems is a very broad topic with extensive literature in which most articles focus on some one main feature, such as biota, biogeochemistry, seabed features, or MDAC origin. Only in the past twenty years that tubular concretions begun to be recognised as being part of the cold seep system, mainly from the discrete occurrences of tubular concretions, often toppled, exposed/exhumed at the seafloor near modern active seep sites. Most studies only mention the tubular concretions in passing because of other research objectives. The following sections briefly overview aspects of some important recent studies, focusing primarily on tubular concretions where a subsurface origin has been determined.

9.1 Sandstone pillars on the modern seafloor, Kattegat, Denmark

Jensen et al. (1992) reported the first known occurrence of tubular concretions at a modern methane seepage site from Kattegat, offshore Denmark (Fig. 12). The study location is a NW-SE extensional basin with scattered occurrences of carbonate pillars (pipes and slabs) on the seafloor. Gas seepage currently occurs nearby and the tubular concretions are cemented by high-Mg calcite, dolomite, and aragonite. The isotope values of the carbonate indicate the cement precipitated from oxidised methane and seawater. The sandstone pillars were interpreted to have formed within the subsurface and then to have been exhumed on the seafloor.

9.2 Miocene tubular concretions exposed on the seabed, Otago, New Zealand

Orpin (1997) described tubular concretions exhumed at the seafloor in Miocene sediments on a small part of the Otago continental margin, South Island, New Zealand. The tubular concretions are carbonate cemented siltstone (37–53% carbonate) and range in size from 10–90 cm long and 10–25 cm in diameter (Figs. 11 and 13). The tubular concretions were interpreted to have formed in the subsurface on the inner to mid shelf. Carbon isotope values suggested the carbon sourced from the degradation of organic matter. Oxygen isotope values were interpreted to be either marine in composition or aquifer-forced meteoric fluids.

9.3 Tubular concretions protruding from the modern seafloor, Monterey Bay, California

In the active transform margin of Monterey Bay, in central California, Stakes et al. (1999) reported a variety of cold seep features. The seeps are located around the presently active San Gregorio and Monterey Bay fault zones. Along the faults, cold seeps with chemoautotrophic organisms, MDAC, and active mud volcanoes are present in isolated occurrences. MDAC features include interconnected pavements, circular or pipe-like ‘chimneys’, rings, doughnuts, and slabs. The MDAC is high-Mg calcite or dolomite that has cemented organic rich

Figure 12. An artists interpretation of the carbonate sandstone pillars on the seafloor of Kattegat, Denmark. The 'bubbling reefs' are 10 to 12 m high. From Jensen et al., 1992; Artwork by Wiirgler Hansen.

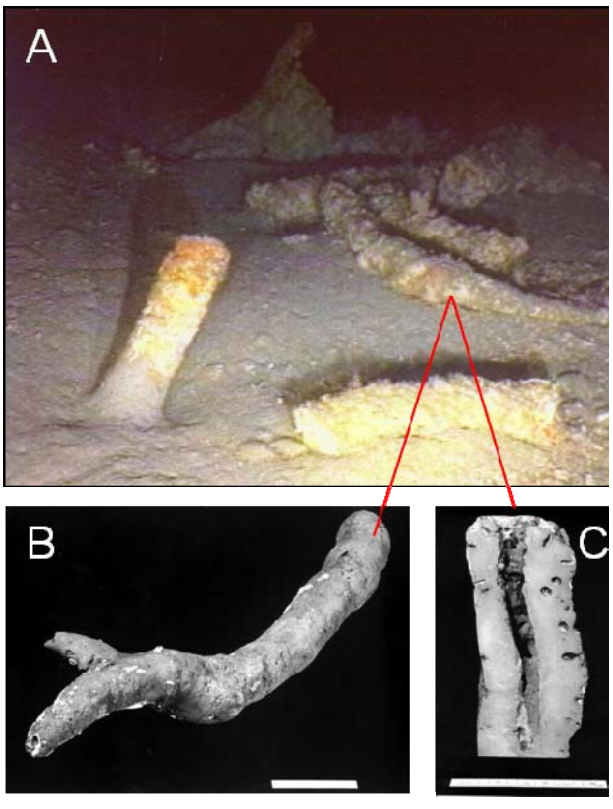

Figure 13. Exhumed tubular concretions from the Otago shelf seabed, North Island, New Zealand. (A) In place and toppled tubular concretions. The inclined sample in the foreground is 50 cm long. (B) Close up (B) and longitudinally cut section (C) of toppled tubular concretion in (A). The scale bar in B and C is 150 mm long. From Orpin, 1997.

fine grained marine siliciclastic sediments. The tubular concretions occur at the base of a submarine scarp, some standing upright and others toppled over on the seafloor (Fig. 14). The tubular concretions were interpreted to have formed within the sediment (dolomite cementing the sediment grains) and to have subsequently been exhumed at the seafloor. Presently, there is no fluid venting out of the tubular concretions, but their morphology suggests that fluid escape was formerly vigorous and/or extremely focused. On the basis of their morphology and isotope values, the tubular concretions were suggested to have originated from fluids that were sourced from depths of bacterial fermentation, and potentially sequestered as gas hydrates, which subsequently migrated towards the seafloor. Additionally, the San Gregorio Fault Zone probably acted as focused migration pathways for the hydrocarbons.

9.4 Miocene tubular concretions in opal-CT porcelanites, Monterey Bay, California

Aiello et al. (1999, 2001) and Aiello (2005) reported cylindrical calcite tubes in Miocene opal-CT porcelanites interbedded with mudstones in the Santa Cruz Mudstone Formation, Monterey Bay, California. The carbonate tubes resemble modern tube structures related to cold seeps. The cylindrical tubes are up to 40 cm long and elongated at high angles to bedding with central conduits (Fig. 15). Many are aligned with fracture sets. The tubes are calcite cemented mudstones with cement both in interparticle spaces and partially replacing grains. The presence of foraminifera and well-preserved diatoms in the tubes, but their absence in the opal-CT layers, indicates the concretions formed before the silica transformation phase. Carbonate cement between the interparticle spaces of siliciclastic grains and the absence of seep biota indicate the tubes formed within the sediment below the seafloor. Oxygen isotope values ($\delta^{18}O$ from –2 to –1‰ PDB) indicate precipitation at low temperatures. Although the carbon isotope values are only slightly depleted ($\delta^{13}C$ from –4 to –9‰ PDB), the authors favoured a source for carbon from microbial activity in the zone of sulphate reduction or methanogenesis.

Aiello et al. (1999, 2001) suggested that early fracturing of opal-A bearing sediments provided the migration pathways for fluids. As fluids moved through

Figure 14. Tubular concretion exhumed on the seabed, Monterey Bay, California. From Stakes et al., 1999. Top of scale bar is in inches.

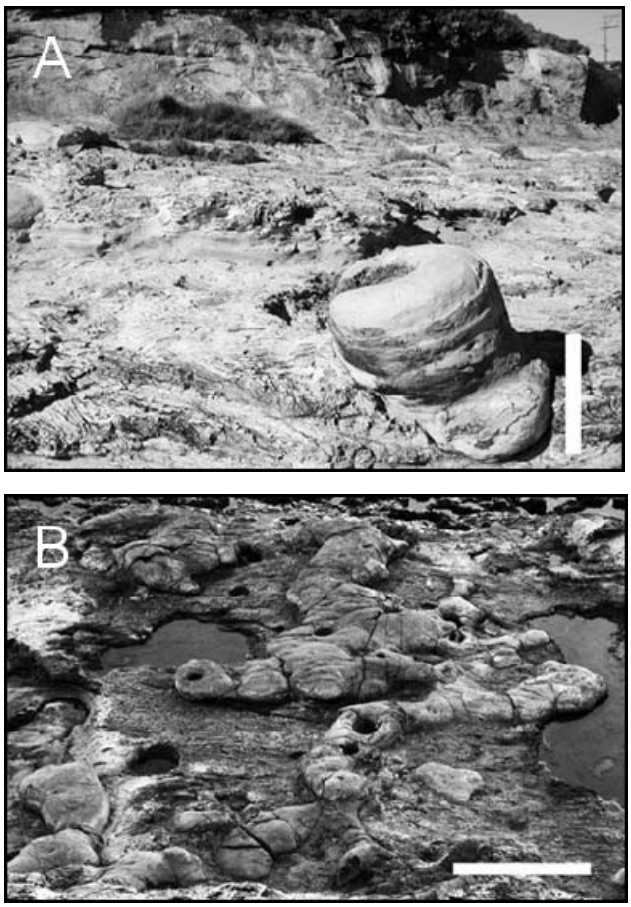

Figure 15. Tubular concretions from the Santa Cruz Mudstone Formation, Santa Cruz. A) The large tubular concretion in the foreground protrudes from an opal-CT porcelanite layer. The tubular concretion is not vertical, but dips southwest. Scale bar is 50 cm. (B) Carbonate slabs parallel to bedding with open conduits. Finger-like projections are parallel to fractures. From Aiello, 2005. Scale bar is 50 cm.

the fractures, calcite precipitated in shallow burial conditions forming the cylindrical tubes. Upon further burial, opal-A was transformed to opal-CT followed later by uplift and exhumation. The carbonate structures are interpreted to represent the structurally controlled sub-seafloor seepage of formation fluids.

9.5 Carbonate chimneys protruding from the modern seafloor, Gulf of Cádiz, Portugal

Pockmarks, mud volcanoes, gas hydrates, and authigenic carbonate crusts have been reported in the Gulf of Cádiz, Portugal (Díaz-del-Río et al., 2003). These reveal active hydrocarbon seepage along the shelf break and continental slope, where fluid seepage is relatively high in comparison to other extensive seep fields. The study location is a NW-SE convergent margin and consists of Jurassic to Middle Miocene units of the olistostrome/accretionary wedge of the Gibraltar arc.

The tubular concretions occur in 500 to 1200 m water depth nearby active seepage and associated with mud volcanoes and mud/salt diapirism. Hydrocarbons, brines, and fluidised sediments have migrated to the seafloor from overpressures beneath wedges of salt/shale units. Tubular concretions are lying on the seafloor, some protruding from the sediment in high densities with 10 to 15 cm thick carbonate slabs at their base.

Tubular concretions were found in four different locations. Field 1 involves Early to Middle Miocene marls located near the front of the olistostrome/accretionary wedge between 850 and 1100 m water depth. 76 tubular concretions were sampled along a mud ridge. Field 2 comprises active fluid seepage, crater-like collapse structures, and a mud volcano in 750 to 900 m water depth. The mud volcano is 3 km in diameter and 150 m in height, and sits atop a mud diapir with six cones and tubular concretions along its flanks. Field 3 consists of a Diapir Zone in the olistostrome/accretionary complex with extensive mud volcanism and ‘mushroom’ pipe-like tubular concretions. Field 4 includes salt diapirs along the frontal thrust wedges of the accretionary complex where a small piece of tubular concretion was found. At times, local fissures and alignments of tubular concretions were present, indicating a relationship between faulting and tubular concretion alignment. The tubular concretions were up to 2 m in length and

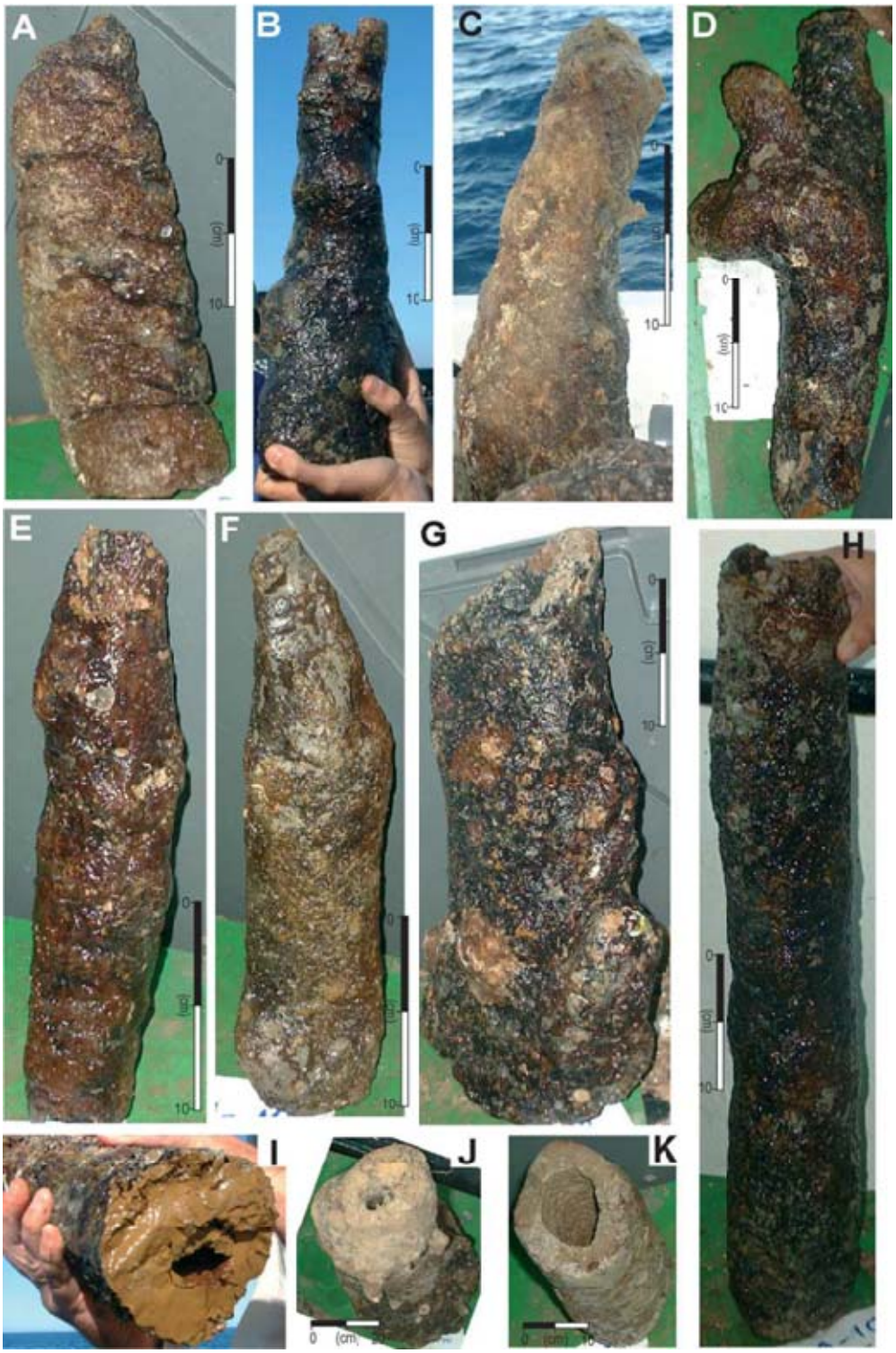

Figure 16. Examples of tubular concretions collected from the seafloor in the Gulf of Cádiz classified as (A) helical, (B) conical, (C) mounded, (D) bifurcated cylindrical, (E) cylindrical, (F) bullet terminated cylindrical, (G) cylindrical with basal protuberances, and (H) cylindrical. (I) Open conduit of a cylindrical pipe, (J) open conduit of a mounded chimney, and (K) large open conduit with thin concretion walls. From Díaz-del-Rio et al., 2003.

showed a wide range of morphologies, including spiral, cylindrical, conical, mushroom-like, and mounded (Fig. 16). Often nodules and protuberances were present along the outside of the tubular concretions. Authigenic ankerite, Fe-dolomite, and calcite make up the carbonate cements in the tubular concretions, while pyrite is also a common mineral phase. The tubular concretions can be grouped into three categories based on morphology, pipe types, and fluid channels. Morphologically the tubular concretions form cylindrical pipes which are equant in diameter through their length, usually with a tapered termination (1A). Cylindrical 1B types have a mushroom shaped termination. Conical morphologies (2A) appear to taper inwards towards the middle of their lengths, while type 2B has a bifurcated termination. Mounded tubular concretions (3A) taper upwards (smaller diameters) while type 3B has mushroom terminations. Pipe types can be straight, curved, or helical, and fluid channels may have nodule protuberances, secondary vent orifices on their sides, or bifurcate.

The Gulf of Cádiz carbonate tubular concretions are interpreted to have formed in the subsurface, but near the seafloor. Based on carbon isotope values, the carbonates were interpreted to have been sourced from thermogenic methane, while those having more depleted values ($\delta^{13}C \sim -40‰$ PDB) were suggested to be sourced from microbial methane. The enriched oxygen isotope values ($\delta^{18}O$ from +4 to +6‰ PDB) were interpreted to arise from the dissociation of methane hydrates.

9.6 Miocene-Pliocene tubular concretions from Cape Turnagain, New Zealand

Lédesert et al. (2003) reported tubular concretions from Cape Turnagain, North Island, New Zealand (Fig. 17). The concretions occur in Miocene-Pliocene age, middle to upper slope marine mudstones from an accretionary wedge. They are cemented by calcite and dolomite. The concretions were interpreted to have formed from fluid expulsion along the Hikurangi subduction margin and overpressures created during the compressive event. The study determined a positive correlation between size of the concretions and their conduits, and suggested this relationship was a function of the amount of fluid flowing through

Figure 17. Tubular carbonate concretion eroded out from the Miocene Whangaehu Mudstone, Cape Turnagain, North Island, New Zealand. Photo from Nyman et al. (accepted).

the plumbing network. They suggested that the concretions may be 'root' structures to cold seeps and could be analogous to other dewatering tubular concretions reported from offshore New Zealand by Orpin (1997, see Section 9.2). Their studies were based on field observations and measurements and some petrography. No geochemical analyses were undertaken on the samples and consequently they could not confirm a methane source. This topic is expressly addressed for the Cape Turnagain site later in this thesis study (Chapter 4; see also Nyman et al., accepted).

9.7 Small tubular concretions in a core from Gryphon Field, North Sea

Mazzini et al. (2003) analysed a core from late Paleocene to early Eocene Gryphon Field, North Sea, taken from above an oil reservoir. The core is dominantly a mudstone/shale with three intervals of sandstone intrusions. Stratigraphically between the uppermost and middle intrusions are several intervals with concentrated zones of small tubular carbonate concretions up to 3 cm in diameter (Fig. 18). Tubes also are present within sandstone dykes where sand fills fractures and cavities in the tubes, indicating the intrusion occurred after formation of the pipes. Tubular concretions have concentric zones of carbonate cement, where crystal orientation indicates cement growth towards the central conduit. Cement near the central conduit consists mostly of sparry calcite and aragonite, whereas the central conduit is usually open but in places filled with intruded sandstone or oil. The surrounding concretion is a clay-rich micrite cemented mudstone with common framboidal pyrite. Dissolution features were not found, suggesting cement precipitation occurred continuously during the formation of the tubes.

Carbon isotope values of the tubular concretions range from –27 to –18‰ PDB and oxygen from –3 to 0‰ PDB. Isotope compositions of the carbonate within the sandstone injections ($\delta^{13}C$ from –27 to –22‰ PDB and $\delta^{18}O$ from –2.5 to –1‰ PDB) falls within the range for tubular concretions, supporting a genetic relationship between the fluids responsible for carbonate precipitation and the source from the microbial oxidation of methane. The tubular concretions were suggested to have formed in the subsurface, based on petrographic characteristics, isotope values, and the absence of chemosynthetic fossils. However, they

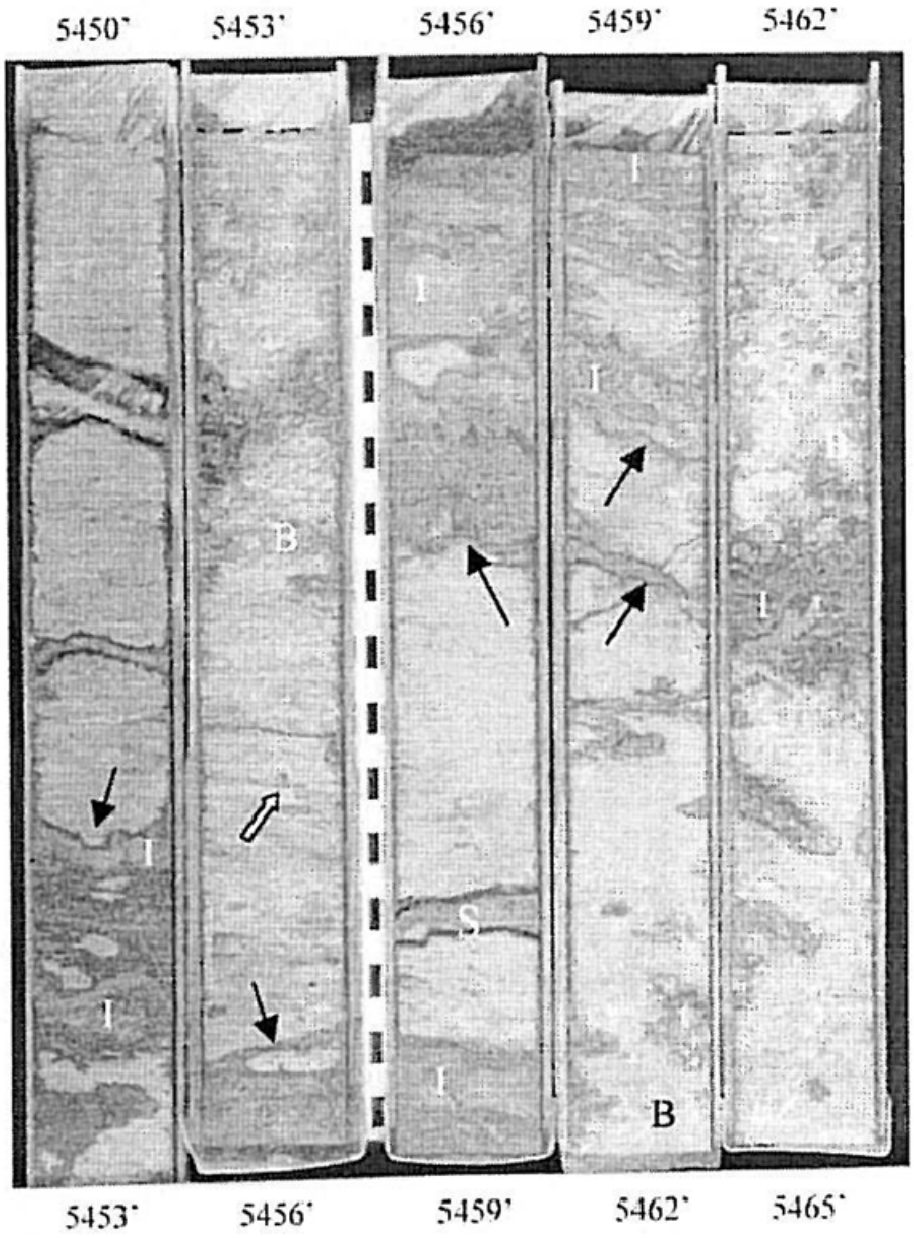

Figure 18. Photograph of a core with centimetre sized tubular concretions in mudstone. Closed arrows show the margins of sandstone dykes and open arrow indicate the small tubular concretion, 'B' indicates discrete levels of tubular concretions. 'I' denotes oil saturated injected sandstones, 'S' denotes a sandstone sill. Numbers are core depths in feet (core in photograph is 15 feet long). From Mazzini et al. (2003).

suggested that precipitation took place near the seafloor due to the local occurrence of aragonite, which requires higher sulphate concentrations to precipitate. Formation was associated with a first phase of fluid migration into the shallow (sub)seafloor environment. Later, re-mobilised sand from the underlying Balder Sandstone reservoir migrated upward as dykes and sills, which crosscut the shales during tubular concretion formation.

9.8 Cenozoic cold seep carbonates and sandstone intrusions, Panoche Hills, California

Schwartz et al. (2003) reported sandstone dykes and seep carbonates from the western margin of the San Joaquin Valley, California, in a late Jurassic to Oligocene forearc basin. The Panoche Formation consists of a 6.5 km thick section of submarine fan deposits. The Moreno Formation conformably overlies the Panoche Formation and consists of shale and concretionary sandstone. The youngest member (Dos Palos member, Paleocene) of the Moreno Formation is shale and contains the ancient seep carbonates.

The sandstone dykes are sourced from the Panoche Formation and cut through the Moreno shales at high angles. Sills also occur, branching out and rejoining dykes to form a complex network of intrusions. Localised carbonate bodies and seep limestones crop out over 45 m of section in the uppermost shale member and 5 km laterally. These contain tubeworms, with less abundant lucinid bivalves, solemyid bivalves, seep related gastropods, corals, and distinctive textures resembling microbial mats.

The carbonate bodies occur mainly as cements, veins, and replacement material in the sandstone and siltstone forming: 1) fossil rich mounds containing vugs and fluid conduits up to 0.5 to 6 m tall and 0.5 to 5 m wide (Fig. 19); 2) carbonate slabs and pavements containing fossils which are up to 1–5 m thick and up to tens of metres long; and 3) spherical concretions, centimetres to 3 m in diameter. Carbonate pavements occur near the upper boundary of the sequence while other carbonate bodies occur throughout.

Figure 19. An ancient seep carbonate mound (bird's eye view) interpreted to have formed around tubeworms. Tubes (yellow dashed circles) and open relict conduits (arrows) in tube centres crop out at the surface. From Schwartz et al. (2003).

The cement and veins are dominated by Mg-calcite with lesser amounts of calcite and dolomite. Cement phases begin with the earliest micrite to sparry Mg-calcite (rarely dolomite) that coats clastic grains. This phase dominates the seep carbonate, comprising more than 80% of the deposit. Veins and pipes post-date the micrite/spar. Veins range from millimetres to centimetres in width, with several generations of fibrous and micritic cement, including crack-seal textures. The micrite usually is present as an infill and is, in places, associated with brecciation and dissolution. Pipe features are tubular in shape and are up to 2 cm in diameter and several centimetres long. Pipes are cemented by fibrous Mg-calcite growing towards their centres. The cement is banded due to inclusions, insoluble material, pyrite, and hydrocarbons. Carbon isotope values range from $\delta^{13}C$ –42.6 to +0.6‰ PDB and oxygen values from $\delta^{18}O$ –5.7 to +7.3‰ PDB.

The main cement phase was interpreted to reflect an early stage of diffuse fluid flow which progressed to focused flow later in seep development. In contrast, the pipes were interpreted to have formed from matrix cementation, dissolution, and advective focused flow. The carbonate pipes formed around tube worms. Isotope values were suggested to indicate a carbon source from a combination of microbial and/or thermogenic methane mixed with seawater bicarbonate, with the authors favouring microbial methane over a thermogenic source.

The sandstone intrusions provided the main permeable pathways for fluid flow in the overlying shales, as the main seep deposits are situated just above the stratigraphic top of the sandstone dykes. Although there are faults near the deposits, they post-date the seeps and intrusions and so did not act as fluid migration pathways.

The driving forces for fluid migration through the section were suggested to have been caused by overpressuring from a thickness imbalance of impermeable shales over permeable sandstones (thicker towards the centre of the basin). Hydrofracturing of the shale seal and fluid migration probably initiated by seismic and tectonic changes, depositional overburden, and hydrocarbon generation.

9.9 Miocene mud volcano and its plumbing system, Monferrato Italy

Clari et al. (2004) investigated an ancient (Miocene) mud volcano and associated plumbing in Monferrato, Italy. Monferrato is located at the junction of the Alpine and Apennine mountain chains. To the west of the study is a major wrench-fault zone, while to the east there are thrusts along the frontal Apenninic belt. The Monferrato area consists of Oligocene to Miocene age, coarse to fine grained siliciclastic sediments unconformably overlying Mesozoic units. The region has numerous faults in a complex network that have strongly deformed the sediments with compressional deformation, resulting in anticlinal folds and larger shallow synclines. Clari et al. (2004) refer to the seep deposit as a 'chaotic complex' which is a large, chaotic, diapiric structure of varying ages that reaches the surface and is surrounded by the terrigenous sediments of Eocene hemipelagic slope marls and Pliocene fossil rich inner shelf silts and calcarenites.

The chaotic complex has a maximum thickness of 50 m, of which 30 m was studied in detail. Within the intrusion structure are silty clays, mud breccias, sheared mud breccias, cemented mud breccias and brecciated marly limestones, silts and clay, coquinoid limestones, softground and hardground burrows, glauconite encrusted and bored limestones, lucinid bivalves, and cylindrical (tubular) concretions (Fig. 20). Three types of carbonates occur in the complex: 1) a strongly carbonate cemented, mud matrix supported breccia of various clasts, shells, muti-generational cemented veins, and lucinid bivalves; 2) blocks of microcrystalline limestones with diffuse boundaries and interconnected fractures, giving the appearance of brecciation; and 3) cylindrical concretions (tubular concretions) hosted in the mud breccias and interlayered clays. Additionally, breccias with sheared clasts that are not cemented occur, cross-cutting the mud breccias at high angles. The tubular concretions have been grouped into two categories. Group A is from the lower part of the section and group B is from the middle.

Group A concretions range from 8 to 15 cm in diameter and more than 1 m in length. They are hosted in homogeneous clays with local burrowing and are at high angles to bedding. The concretions have sharp boundaries with rounded and smooth edges and are described as marly limestones. The tubes comprise host

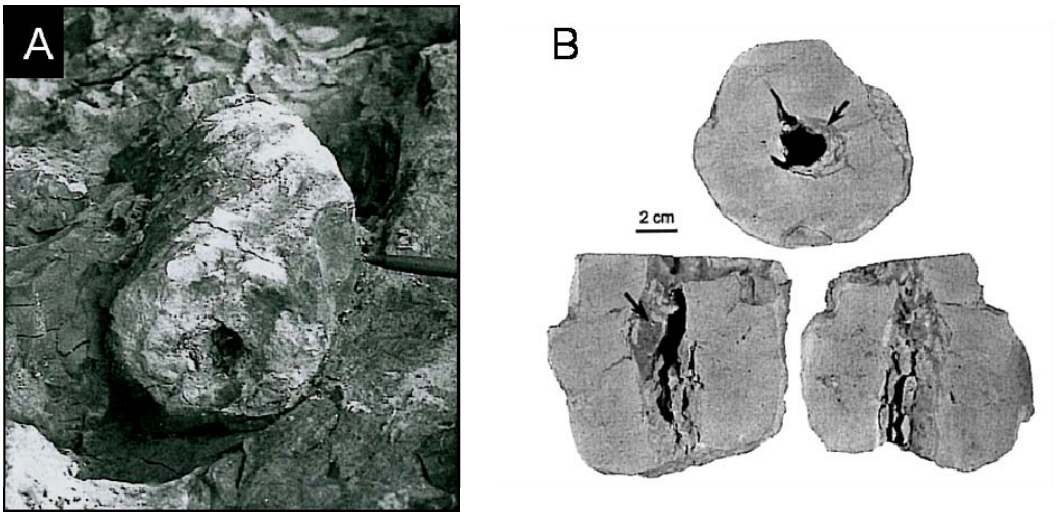

Figure 20. (A) Tubular concretion (10 cm in diameter) weathering out of mud breccias and silty marls of Miocene age, Monferrato, Italy. (B) Sections through type A1 tubular concretion from Monferrato with calcite spar partially filling the central conduit and septarian-like fractures. From Clari et al., 2004.

sediments cemented by dolomite. Cement content is consistent within individual concretions, but may vary between them. Type A concretions have four conduit varieties. A1 conduits are empty but have irregular shaped walls with septarian-like fractures radiating outwards. A2 conduits are filled with sediment of different origin from the host that also includes scattered clasts. Dolomite cement is similar to that in A1 conduits, but has concentric zoning. A3 conduits do not have a clearly defined central hole, but rather have a complex network of fractures a few millimetres wide and in the direction of concretion length. Some fractures have small lateral branches up to 2 cm long. The fractures are filled with blocky calcite spar. A4 conduits appear to be a combination of A2 and A3 with irregular walls, brecciation, and fractures filled with blocky calcite spar. Some fractures are larger and filled with sediment. All conduits except for A1 have a white ring around the outer conduit.

Group B concretions are smaller (<5 cm diameter) than group A and comprise cemented, matrix supported breccias. They display more diffuse boundaries with the host sediments than group A and have no clear conduit apart from central zones differentiated by their lighter colour, lesser cementation, and clasts elongated in the direction of concretion length.

The carbon isotope values of all the Italian concretions are interpreted to be sourced from methane ($\delta^{13}C$ from –10 to –25‰ PDB) and the positive oxygen isotope values ($\delta^{18}O$ from +4 to +8‰ PDB) from gas hydrate dissociation. The stratigraphic placement of the tubular concretions with respect to the chaotic complex, their isotope values, resemblance to modern ‘chimneys’ and pipes from active cold seeps, and subsurface formation have been interpreted by Clari et al. (2004) to represent the direct geological record of a mud volcano plumbing system. They envisaged, without elaboration, the concretions to have formed from their outer margins first, with cement precipitation continuing towards their centres. Differences in fluid flow influenced the type of concretion formed. The open conduits of A1, A2, and B concretions are interpreted to have formed from vigorous fluid flow which pushed sediment out of the pathway and kept the conduit open. A2 concretions were also influenced by foreign sediments moving through the pathway, often carrying larger clasts which filled and choked the conduit. A3 concretions formed from lesser rates of fluid flow resulting in a

branching network of central fractures. A4 concretions resulted from intermediate flows that were able to enlarge some central fractures.

9.10 Eocene tubular concretions from Varna, Bulgaria

De Boever et al. (2006a,b) reported on carbonate tubular concretions from Bulgaria up to 8 m high and 1.5 m in diameter that are cemented by calcite, often with decreasing cementation towards their conduits (Fig. 21). The tubular concretions are suggested to have formed in the subsurface near the seafloor. The tubular concretions occur in Lower Eocene sandstones of the Dikilatash Member near Varna, Bulgaria. The system is characterised by normal and reverse faulting in an east-west orientation, and a north-south oriented normal and strike-slip system. Carbon isotope values range from $\delta^{13}C$ –10 to –45‰ PDB and have been interpreted to reflect a mixture of the degradation of organic matter and methane rich fluids. Concretions show more depleted $\delta^{13}C$ values towards their conduits, suggesting strong variations in fluid compositions and characteristics. Oxygen isotope values range from $\delta^{18}O$ –9‰ PDB to just below 0‰ PDB and are interpreted to record burial temperature fluids. They suggested the relatively depleted oxygen isotope values record higher fluid flow rates in which hotter burial fluids ascended quickly and did not have enough time to re-equilibriate with surrounding pore waters. As such, the oxygen isotopes nearer to 0‰ PDB were interpreted to indicate slower or diffuse fluid flows, allowing for the warm ascending fluids to cool and record oxygen isotope values near marine compositions.

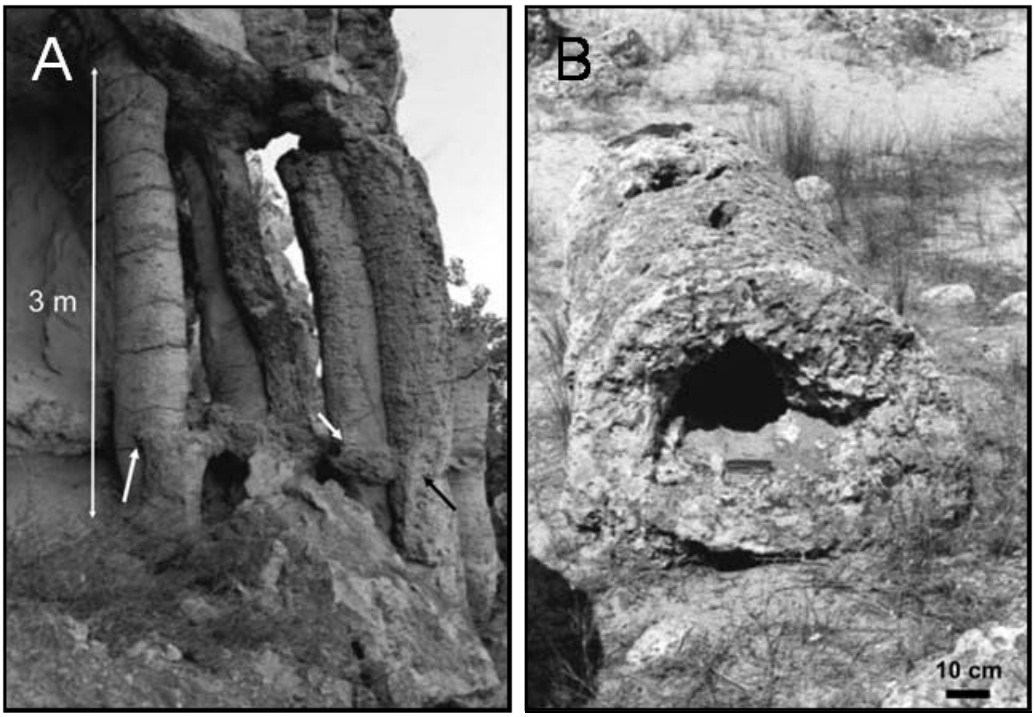

Figure 21. (A) Unusually large carbonate sandstone tubular concretions from Varna, Bulgaria. (B) Cross-sectional view of a tubular concretion from Varna with an open central conduit. From De Boever et al. (2006).

10. References

Aiello, I.W., Stakes, D.S., Kastner, M., Garrison, R.E., 1999. Carbonate vent structures in the Upper Miocene Santa Cruz Mudstone at Santa Cruz, California. In: Garrison, R.E., Aiello, I.W., Moore, J.C. (Eds.), Late Cenozoic Fluid Seeps and Tectonics Along the San Gregorio Fault Zone in the Monterey Bay Region, California. Pacific Section AAPG, v. GB-76, pp. 35-52.

Aiello, I.W., Garrison, R.E., Moore, J.C., Kastner, M., Stokes, D.S., 2001. Anatomy and origin of carbonate structures in a Miocene cold-seep field. Geology 29, 1111-1114.

Aiello, I.W., 2005. Fossil seep structures of the Monterey Bay region and tectonic/structural controls on fluid flow in an active transform margin. Palaeogeography, Palaeoclimatology, Palaeoecology, 227, 124-142.

Aloisi, G., Pierre, C., Rouchy, J., Faugères, J., 2002. Isotopic evidence of methane-related diagenesis in the mud volcanic sediments of the Barbados Accretionary Prism. Continental Shelf Research, 22, 2355-2372.

Barnes, P.M., Lamarche, G., Bialas, J., Henrys, S., Pecher, I. Netzeband, G.L., Greinert, J., Mountjoy, J.J., pedley, K., Crutchley, G., accepted. Tectonic and geological framework for gas hydrates and cold seeps on the Hikurangi subduction Margin, New Zealand. Submitted to Marine Geology, special publication, methane seeps.

Belenkaia, I., 2000. Gas-derived carbonates: reviews in morphology, mineralogy, chemistry and isotopes (data collected during the TTR programme cruises during 1993-1999). In Abstracts of the Sixth International Conference on Gas in Marine Sediments. St. Petersburg, VNIOkeangeologia, pp. 9-10 (abstract).

Boetius, A., Ravenschlag, K., Schubert, C.J., Rickert, D., Widdel, F., Giesecke, A., Amann, R., Joergensen, B.B., Witte, U., Pfannkuche, O., 2000. A marine microbial consortium apparently mediating anaerobic oxidation of methane. Nature, 407, 623-626.

Boetius, A., Suess, E., 2004. Hydrate Ridge: a natural laboratory for the study of microbial life fuelled by methane from near-surface gas hydrates. Chemical Geology, 205, 291-310.

Campbell, K.A., Bottjer, D.J., 1993. Fossil cold seeps (Jurassic-Pliocene) along the convergent margin of western North America. National Geographic Research and Exploration, 9, 326-343.

Campbell, K.A., 2006. Hydrocarbon seep and hydrothermal vent paleoenvironments and paleontology: Past developments and future research directions. Palaeogeography, Palaeoclimatology, Palaeoecology, 232, 362-407.

Campbell, K.A., Francis, D.A., Collins, M., Gregory, M.R., Nelson, C.S., Greinert, J., Aharon, P., 2008. Hydrocarbon seep-carbonates of a Miocene forearc (East Coast Basin), North Island, New Zealand. Sedimentary Geology, 204, 83-105.

Cavagna, S., Clari, P., Martire, I., 1999. The role of bacteria in the formation of cold seep carbonates: geological evidence from Monferrato (Tertiary, NW Italy). Sedimentary Geology, 126, 253-270.

Clari, P., S. Cavagna, Martire, L., Hunziker, J., 2004. A Miocene mud volcano and its plumbing system: A chaotic complex revisited (Monferrato, MW Italy). Journal of Sedimentary Research, 74, 662-676.

Clayton, C., 1992. Source volumetrics of biogenic gas generation. In Vially, R. (Ed.), Bacterial Gas. Paris, Editions Technip, pp. 191-204.

Coleman, D.D., Risatti, J.B., Schoell, M., 1981. Fractionation of carbon and hydrogen isotopes by methane-oxidising bacteria. Geochimica et. Cosmochimicha Acta, 45, 1033-1037.

Conti, S., Fontana, D., Gubertini, A., Sighinolfi, G., Tateo, F., Fioroni, C., Fregni, P., 2004. A multidisciplinary study of middle Miocene seep-carbonates from the northern Apennine foredeep (Italy). Sedimentary Geology, 169, 1-19.

Conti, S., and Fontana, D., 2005. Anatomy of seep-carbonates: Ancient examples from the Miocene of the northern Apennines (Italy). Palaeogeography, Palaeoclimatology, Palaeoecology, 227, 156-175.

Corliss, J.B., Dymond, J.R., Gordon, L.I. et al., 1979. Submarine thermal springs on the Galapagos Rift. Science, 203, 1073-1083.

Cowen, J.P., Wen, X., Popp, B.N., 2002. Methane in aging hydrothermal plumes. Geochimica et. Cosmochimicha Acta, 66, 3563-3571.

Crutchley, G.J., Gorman, A.R., Fohrmann, M., 2007. Investigation of the role of gas hydrates in continental slope stability west of Fiordland, New Zealand. New Zealand Journal of Geology and Geophysics, 50, 357-364.

Davidson, D. W., Leaist, D.J., Hesse, R., 1983. Oxygen-18 enrichment in water of a clathrate hydrate. Geochimica et. Cosmochimicha Acta, 47, 2293-2295.

De Boever, E., Swennen, R., Dimitrov, L., 2006a. Lower Eocene carbonate cemented chimneys (Varna, NE Bulgaria): Formation mechanisms and the (a)biological mediation of chimney growth? Sedimentary Geology, 185, 159-173.

De Boever, E., Swennen, R., Dimitrov, L., 2006b. Lower Eocene carbonate-cemented 'chimney' structures (Varna, Bulgaria) – Control of seepage rates on their formation and stable isotopic signature. Journal of Geochemical Exploration, 89, 78-82.

Díaz-del-Río, V., Somoza, L., Martínez-Frias, J., Mata, M.P., Delgado, A., Hernandez-Molina, F.J., Lunar, R., Martín-Rubí, J.A., Maestro, A., Fernández-Puga, M.C., León, R., Llave, E., Medialdea, T., Vázquez, J.T., 2003. Vast fields of hydrocarbon-derived carbonate chimneys related to the accretionary wedge/olistostrome of the Gulf of Cádiz. Marine Geology, 195, 177-200.

Dunham, R.J., 1962. Classification of carbonate rocks according to depositional texture. Ham, W.E., (Ed.), Classification of carbonate rocks. American Association of Petroleum Geologists Memoir, 1, pp. 108-121.

Folk, R. L., 1962. Spectral subdivision of limestone types. Ham, W.E., (Ed.), Classification of carbonate rocks. American Association of Petroleum Geologists Memoir, 1, pp. 108-121.

Fu, B., Aharon, P., Byerly, G.R., Roberts, H.H., 1994. Barite chimneys on the Gulf of Mexico slope: initial report on their petrography and geochemistry. Geo-Marine Letters, 14, 81-7.

Gay, A., Lopez, M., Cochonat, P., Séranne, M., Levaché, D., Sermondadaz, G., 2006. Isolated seafloor pockmarks linked to BSRs, fluid chimneys, polygonal faults and stacked Oligocene-Miocene turbiditic palaeochannels in the Lower Congo Basin. Marine Geology, 226, 25-40.

Gautier D.L. and Claypool, G.E., 1984. Interpretation of methanic diagenesis in ancient sediments by analogy with processes in modern diagenetic environments. In: McDonald, D.A., Surdam, R.C. (Eds.), Clastic Diagenesis. American Association of Petroleum Geologist Memoirs, 37, pp. 111-123.

Grauls, D. 2001. Gas hydrates: importance and applications in petroleum exploration. Marine and Petroleum Geology 18: 519-523.

Greinert, J., Bialas, J., Lewis, K., Suess, E., in review. Methane seeps and gas hydrates offshore New Zealand's North Island: Compiling results from three cruises in 2006 and 2007. Submitted to Marine Geology, special publication, methane seeps.

Hinrichs, K. U., Hayes, J.M., Sylva, S.P., Brewer, P.G., DeLong, E.F., 1999. Methane-consuming archaebacteria in marine sediments. Nature, 398, 802-805.

Hovland, M., Svensen, H., Forsberg, C.F., Johansen, H., Fichler, C., Fosså, J.H., Jonsson, R., Rueslåtten, H., 2005. Complex pockmarks with carbonate-ridges off mid-Norway: Products of sediment degassing. Marine Geology, 218, 191-206.

Irwin, H., Curtis, C., Coleman, M., 1977. Isotopic evidence for source of diagenetic carbonates formed during burial of organic-rich sediments. Nature, 269, 209-213.

Iversen, N., Jørgensen, B.B., 1985. Anaerobic methane oxidation rates at the sulphate-methane transition in marine sediments from Kattegat and Skagerrak (Denmark). Limnology and Oceanography, 30, 944-955.

Jensen, P., Aagaard, I., Burke Jr. R.A., Dando, P.R., Jørgensen, N.O., Kuijpers, A., Laier, T., O'Hara, M.O., Schmaljohann, R., 1992. 'Bubbling reefs' in the Kattegat: submarine landscapes of carbonate-cemented rocks support a diverse ecosystem at methane seeps. Marine Ecology Progress Series, 83, 103-112.

Jørgensen, N.O., 1992. Methane-derived carbonate cementation of marine sediments from the Kattegat, Denmark: Geochemical and geological evidence. Marine Geology, 103, 1-13.

Judd, A.G., 2004. Natural seabed gas seeps as sources of atmospheric methane. Environmental Geology, 46, 988-996.

Judd, A.G., Hovland, M., 2007. Seabed Fluid Flow: The Impact on Geology, Biology and the Marine Environment. Cambridge University Press, Cambridge. 475 pp.

Kamp, P.J.J., Nelson, C.S., 1988. Nature and occurrence of modern and Neogene active margin limestones in New Zealand. New Zealand Journal of Geology and Geophysics, 31, 1–20.

Kennicut, M.C., Brooks, J.M., Bidigare, R.R., et al., 1985. Vent type taxa in a hydrocarbon seep region on the Louisiana Slope. Nature, 317, 351-353.

Kukowski, N., Pecher, I., 1999. Thermo-hydraulics of the Peruvian accretionary complex at 12˚ S. Geodynamics, 27, 373-402.

Kulm, L.D., Suess, E., Moore, J.C., et al., 1986. Oregon subduction zone: venting fauna, and carbonates. Science, 231, 561-566.

Lédesert, B., Buret, C., Chanier, F., Fèrriere, J., Recourt, P., 2003. Tubular structures of northern Wairarapa (New Zealand) as possible examples of ancient fluid expulsion in an accretionary prism: evidence from field and petrographical observations. Geological Society of London, Special Publication, 216, 95-107.

Lewis, K.B., Marshall, B.A., 1996. Seep faunas and other indicators of methane-rich dewatering on New Zealand convergent margins. New Zealand Journal of Geology and Geophysics, 39,181-200.

Longstaffe, F.J., 1987. Stable isotope studies of diagenetic processes. In Kyser, T. (Ed) Short Course in Stable Isotope Geochemistry of Low Temperature Processesions Mineralogical Society of Canada, Saskatoon, SK, pp. 187-257.

Lonsdale, P. Becker, K., 1985. Hydrothermal plumes, hot springs, and conductive heat flow in the Southern Trough of Guaymas Basin. Earth and Planetary Science Letters, 73, 211-225.

MacDonald, I.R., Reilly, J.F., Guinasso, N.L., Jr., et al., 1990. Chemosynthetic mussels at a brine-filled pockmark in the northern Gulf of Mexico. Science, 248, 1096-1099.

Mayer, L.A., Shor, A.N., Hughes Clark, J., Piper, D.J.W., 1988. Dense biological communities at 3850 m on the Laurentian Fan and their relationship to the deposits of the 1929 Grand Banks earthquake. Deep-Sea Research, 35, 1235-1246.

Mazzini, A., Duranti, D., Jonk, R., Parnell, J., Cronin, B.T., Hurst, A., Quine, M., 2003. Palaeo-carbonate seep structures above an oil reservoir, Gryphon Field, Tertiary, North Sea. Geo-Marine Letters, 23, 323-339.

McBride E.F., Milliken K.L., Cavazza W., Cibin U., Fontana D., Picard M.D. Zuffa G.G., 1995. Heterogeneous distribution of calcite cement at the outcrop scale in Tertiary sandstones, northern Apennines, Italy. American Association of Petroleum Geologists Bulletin, 79, 1044-1063.

Milkov, A.V., Sassen, R., 2002. Economic geology of offshore gas hydrate accumulations and provinces. Marine and Petroleum Geology, 19, 1-11.

Milkov, A.V., Vogt, P.R., Crane, K., Lein, A.Y., Sassen, R., and Cherkashev, G.A. 2004. Geological, geochemical, and microbial processes at the hydrate-bearing Hakon Mosby mud volcano: a review. Chemical Geology 205, 347-366.

Nelson, C., Schellenberg, F., King, P., Ricketts, B., Kamp, P., Browne, G., Campbell, K., 2004. Note on paramoudra-like concretions in the Urenui Formation, North Taranaki: possible plumbing system for a Late Miocene methane seep field. 2004 New Zealand Petroleum Conference Proceedings, Auckland, 7-10 March 2004. 5 pp. [http://crownminerals.med.govt.nz/petroleum/publications/nzpconf/nzpconf-2004.html]

Nyman, S.L., Nelson, C.S., Campbell, K.A., accepted. Possible late Miocene analogue for the subsurface plumbing of modern Hikurangi Margin cold seeps: Evidence from tubular concretions in southern Hawke's Bay. Submitted to Marine Geology special publication: methane seeps.

Orphan, V. J., Hinrichs, K.U., Ussler, III, W., Paull, C.K., Taylor, L.T., Sylva, S.P., Hayes, J.M., DeLong, E.F., 2001. Comparative analysis of methane-oxidizing archaea and sulphate-reducing bacteria in anoxic marine sediments. Applied and Environmental Microbiology, 67, 1922-1934.

Olu, K., Lance, S., Sibuet, M., et al., 1997. Cold seep communities as indicators of fluid expulsion patterns through mud volcanoes seaward of the Barbados Accretionary Prism. Deep-Sea Research, 44, 811-841.

Orpin, A. R., 1997. Dolomite chimneys as possible evidence of coastal fluid expulsion, uppermost Otago continental slope, southern New Zealand. Marine Geology, 138, 51-67.

Pancost, R.D., Damasté, J.S., De Lint, S., Van Der Maarel, M.J.E.C., Gottschal, J.C., Medinaut Shipboard Scientific Party, 2000. Biomarker evidence for widespread anaerobic methane oxidation in Mediterranean sediments by a consortium of methanogenic archaea and bacteria. Applied Environmental Microbiology, 66, 1126-1132.

Peckmann, J., Reimer, A., Luth, U., Luth, C., Hansen, B.T., Heinicke, C., Hoefs, J., Reitner, J., 2001. Methane-derived carbonates and authigenic pyrite from the northwestern Black Sea. Marine Geology, 177, 129-150.

Querellou, J., 2003. Biotechnology of marine extremophiles. Gook of Abstracts, International Conference on the sustainable development of the Mediterranean and Black Sea environment, Thessaloniki, Greece, 28 May – 1 June (extended abstract).

Reitner, J., Peckmann, J., Blumenberg, M., Michaelis, W., Reimer, A., Thiel, V., 2005. Concretionary methane-seep carbonates and associated microbial communities in Black Sea sediments. Palaeogeography, Palaeoclimatology, Palaeoclimatology, 227, 18-30.

Rice, D.D., 1992. Controls, habitat, and resource potential of ancient bacterial gas. In: Vially, R. (Ed.), Bacterial Gas. Paris, Editions Technip, 91-118.

Roberts, H.H., Aharon, P., 1994. Hydrocarbon-derived carbonate buildups of the northern Gulf of Mexico continental slope: A review of submersible investigations. Geo-Marine Letters, 14, 135-148.

Safer, D.M., Bekins, B.A., 1998. Episodic fluid flow in the Nankai accretionary complex: timescale, geochemistry, flow rates, and fluid budget. Journal of Geophysical Research, 103, 30351-30370.

Schwartz, H., Sample, J., Weberling, K.D., Minisini, D., Moore, J.C., 2003. An ancient linked fluid migration system: cold-seep deposits and sandstone intrusions in the Panoche Hills, California, USA. Geo-Marine Letters, 23, 340-350.

Sibson, R.H., Rowland, J.V., 2003. Stress, fluid pressure, and structural permeability in seismogenic crust, North Island, New Zealand. Geophysical Journal International, 154, 584-594.

Sloan, E.D., 1988. Clathrate Hydrates of Natural Gas, 2nd Edn. New York, NY, Marcel Dekker.

Stakes, D., Orange, D., Paduan, J.B., Salamy, K.A., Maher, N., 1999. Cold-seeps and authigenic carbonate formation in Monterey Bay, California. Marine Geology, 159, 93-109.

Thiel, V., Peckmann, J., Richnow, H.-H., et al., 2001. Molecular signals for anaerobic methane oxidation in Black Sea seep carbonates and a microbial mat. Marine Chemistry, 73, 97-112.

Torres, M.E., Bohramann, G., Suess, E., 1996. Authigenic barites and fluxes of barium associated with fluid seeps in the Peru subduction zone. Earth and Planetary Science Letters, 144, 469-481.

Townend, J., 1997. Subducting a sponge: minimum estimates of the fluid budget of the Hikurangi Margin accretionary prism. Geological Society of New Zealand Newsletter, 112, 14-16.

Tucker, M.E. and Wright, V.P., 1990. Carbonate Sedimentology. Oxford, Blackwell Scientific. 482 pp.

Ussler III, W., Paull, C.K., 1995. Effects of ion exclusion and isotopic fractionation on pore water geochemistry during gas hydrate formation and decomposition. Geo-Marine Letters, 15, 37-44.

Vokes, H.E., 1955. Notes on Tertiary and Recent Solemyacidae. Journal of Paleontology, 29, 534-535.

Whiticar, M.J., 1999. Carbon and hydrogen isotope systematics of bacterial formation and oxidation of methane. Chemical Geology, 161, 291-314.

Wiese, K., Kvenvolden, K.A., 1993. Introduction to microbial and thermal methane. In Howell, D.G. (Ed.), The Future of Energy Gases. United States Geological Survey Professional Paper, 1570, 13-20.

Wilkin, R.T., Barnes, H.L., 1997. Formation processes of framboidal pyrite. Geochimica et Cosmochimica Acta, 61, 323-339.

CHAPTER 3

The role of tubular concretions in hydrocarbon cold seep systems: Late Miocene Urenui Formation, Taranaki Basin, New Zealand

Abstract

The late Miocene Urenui Formation, North Island, New Zealand, is dominated by siliciclastic slope mudstone (<5% carbonate) and includes a wide variety of tubular carbonate concretions. Most of these support a central conduit that may be empty or filled with sediment or multiple generations of later carbonate cements. Pipe and bulbous tubular concretions formed within the subsurface in a hydrocarbon seep system; however, they are unique not only because of their exceptionally large size (up to at least 10 m long and 70 cm diameter), but also the lack of associated seafloor related cold seep features (e.g., paleoseep carbonates and chemosynthesis based biotic communities).

The tubular concretions comprise micritic calcite and dolomite cement within the interparticle spaces of siliciclastic mudstone. Carbonate content ranges from 50 to 85% indicating the concretions formed in the subsurface near the seafloor before any significant compaction of the sediments.

Strongly depleted $\delta^{13}C$ values of the calcite cements (−40 to −25‰ PDB) indicate carbon was sourced from oxidised methane. In contrast, enriched $\delta^{13}C$ values of dolomite cements (−10 to +11‰ PDB) indicate their carbon was sourced from methanogenic CO_2 and/or extensive methane oxidation. $\delta^{18}O$ values recorded in the carbonates (between −2 and +5‰ PDB) indicate precipitation from fluids both depleted and enriched with respect to New Zealand Miocene marine waters. The depleted and enriched $\delta^{18}O$ values are interpreted to reflect episodes of gas hydrate formation and dissociation, respectively.

It is hypothesised that he tubular concretions formed by cement precipitation initiating at their outer margins and proceeding inwards towards their central conduits. At times cement precipitation continued to partially or completely fill the conduit, all the while creating an impervious crust encasing the fluid flow passageway.

The Taranaki Fault was potentially a major pathway and instigator of fluid migration within this system. The tubular concretions probably underwent cyclic intervals of exhumation and burial caused by slope failure due to greater slope instability from injected fluids and gases. Slope failure deposits resulted in associated conglomeratic channel fill, which includes dislodged and mass emplaced tubular concretions.

1. Introduction

Cold seeps are sites of hydrocarbon escape at the seafloor that are commonly marked by a variety of morphological, geological, and biological features, including pockmarks, mud volcanoes, methane derived authigenic carbonate (MDAC) deposits, and distinctive assemblages of chemosymbiotic invertebrates (e.g., Barry et al., 1996; Lewis and Marshall, 1996; Greinert et al., 2001; Judd and Hovland, 2007). They are widely reported in the modern offshore, from both passive and active continental margins (Fig. 1) (Judd, 2003; Campbell, 2006), where the origin of the ascending hydrocarbons may be from the degradation of shallow buried organic matter, the thermal maturation of deeply buried kerogen, or the dissociation of clathrate hydrates (e.g., Roberts and Aharon, 1994). MDAC forming as the seafloor expression of cold seeps is typically patchily distributed but morphologically extremely diverse, ranging from concreted nodules, slabs, and chimneys, to small biogenic mounds, to much larger biogenic build ups (e.g., Roberts and Aharon, 1994; Diaz-del-Río et al., 2003; Gay et al., 2006; Judd and Hovland, 2007).

Many ancient examples of these seafloor cold seep carbonate structures have been discovered in the geological record (e.g., see review by Campbell, 2006). The occurrence of chemosynthesis based fossil assemblages and carbon stable isotope signatures of carbonates indicating anaerobic oxidation of methane are especially

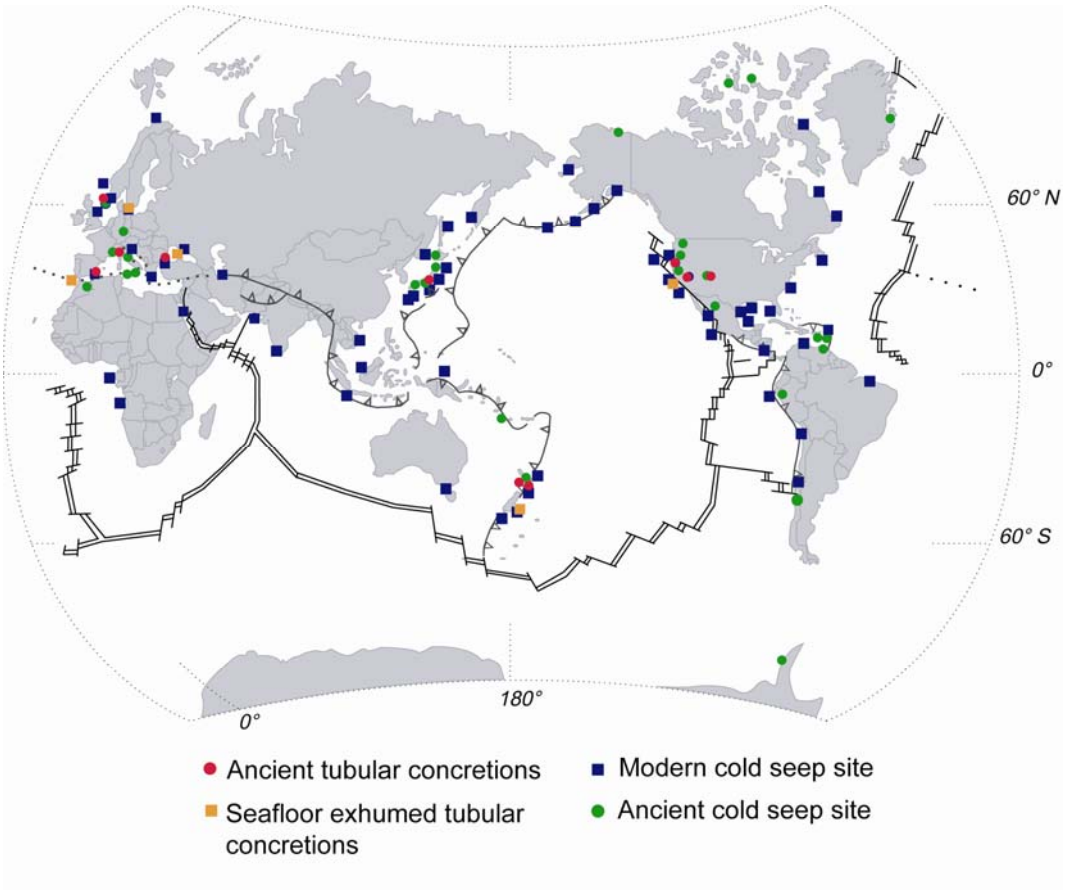

Figure 1. Map of global occurrences of reported ancient tubular concretions, exhumed tubular concretions on the modern seafloor (most near active seep sites), ancient seafloor cold seeps, and modern seafloor colds seeps (modified from Campbell, 2006).

diagnostic features. However, certainly for modern, and also many ancient seep carbonates, much less is known about the nature of the subsurface plumbing systems that provided the pathways for the ascent of hydrocarbon fluids to the seabed. Regionally, seismic reflection imaging can reveal “opaque” zones of acoustic turbidity purported to delineate possible ascent regions of hydrocarbon fluids (e.g., Gay et al., 2006; Judd and Hovland, 2007), but at outcrop scale, it is unclear whether particular geological features might enable the field recognition of such fluid escape.

Here the field and petrological aspects of a variety of tubular carbonate concretionary structures are described from coastal exposures of Miocene mudrock in north Taranaki, North Island, New Zealand. The tubular concretions may delineate sub-seafloor pathways of focused methane infused fluid escape from below. If so, such concretionary features afford some three-dimensional perspective on the shallow subsurface geometry of seep fields. Moreover, in this particular case they could have relevance for active petroleum system evolution in the adjoining Taranaki Basin, currently the only commercially exploited hydrocarbon basin in New Zealand (Townsend et al., 2008).

2. Geological setting

Taranaki Basin covers approximately 100,000 km^2 off the west coast of central North Island (Fig. 2 inset) and contains a late Cretaceous to Quaternary sedimentary fill up to 9 km thick, as described by King and Thrasher (1996) (Fig. 3). The Cretaceous to Oligocene deposits are principally terrestrial, marginal marine, and shallow marine siliciclastics with minor carbonates associated with the rifting, drifting, and thermal relaxation of the New Zealand subcontinent following its separation from eastern Gondwanaland about 80 Ma and formation of the Tasman Sea (Laird, 1994). Near basal coal measures are part of this broadly transgressive fill and constitute the main source beds for the commercially exploited oil and gas in Taranaki Basin (Fig. 3) (King and Thrasher, 1996). Propagation of the present Pacific-Australian convergent plate boundary through New Zealand (Fig. 1) at the close of the Oligocene heralded strongly differential uplift and subsidence throughout the country, and widespread deposition of deep

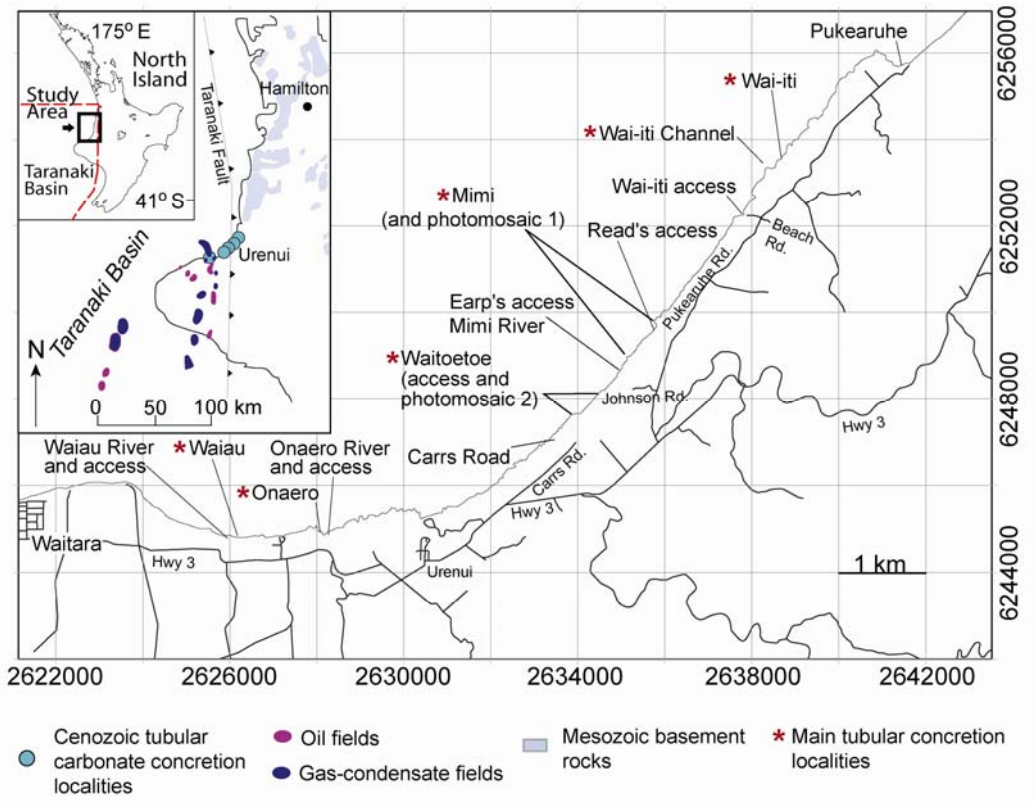

Figure 2. Locality map of tubular concretion sites along the north Taranaki coastline. The main tubular concretion locations are at Mimi and Wai-iti. Minor locations include Waiau, Onaero, and Waitoetoe. Map grid coordinates from NZ Map Series 260, 1:50000 scale, sheets Q19 and Q18 (GPS Easting 2626000 - 2639000). Tubular concretion locality information is derived mainly from personal observations, Nelson et al. (2004), Schellenberg (2002), and Peter King (pers. comm., GNS Science). Producing oil and gas locations from Crown Minerals: http://www.crownminerals. govt.nz/petroleum/index.asp.

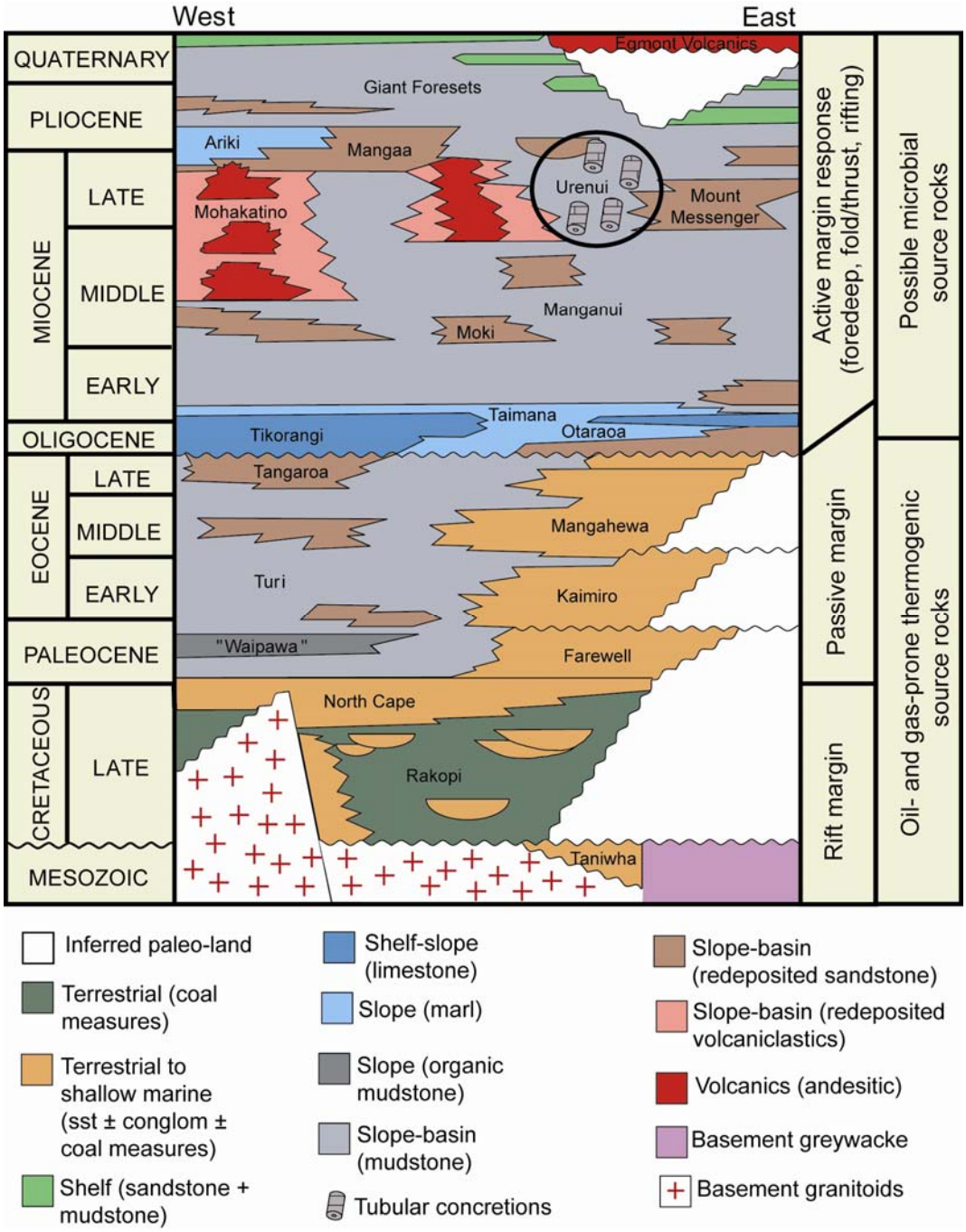

Figure 3. Generalised stratigraphic column and some formation names of the late Cretaceous to Quaternary fill of Taranaki Basin, highlighting the position of the late Miocene Urenui Formation and its contained tubular concretions (adapted from Crown Minerals: http://www.crownminerals.govt.nz).

water mass emplaced facies (Fig. 3) (Kamp, 1986; Kamp et al., 2002; Kamp et al., 2004). In the early Miocene (New Zealand Otaian Stage; see Appendix 8 for time scale) continuing to the late Miocene, a complex fold-thrust belt developed (King and Thrasher, 1996). Basement overthrusting into Taranaki Basin instigated loading and pronounced subsidence with development of a major foreland basin. Throughout the Neogene (Miocene to Recent) this basin has filled with about a 3 km thick, overall regressive succession of predominantly basin floor, submarine fan, and especially slope siliciclastic facies, including the late Miocene Urenui Formation under discussion in this study (Figs. 3, 4) (King and Thrasher, 1996). Despite being mud dominated, the Neogene succession includes several sandstone intervals that form potential reservoirs for hydrocarbons (King and Thrasher, 1996), such as the Mount Messenger Formation, a deeper water facies associated with the Urenui Formation, and several of the channel fill sandstones within the Urenui Formation itself (Figs. 3−5) (King et al., 2007). Uplift along the eastern margin of Taranaki Basin has exposed an onland strip of some of this Neogene succession, especially well exposed in coastal cliffs (King et al., 1993) (Fig. 2), which includes the Urenui Formation that hosts the tubular concretions described herein (Fig. 3).

The Urenui Formation is one of four coeval stratigraphic units building a shelf-to-basin continental margin in the late Miocene eastern Taranaki Basin (Fig. 4). It consists of up to 900 m of mid to upper slope mudstone with occasional channel fills of fine sandstone, mudstone, and conglomerate (Falconbridge, 1994; King and Thrasher, 1996; King et al., 2007). The Urenui Formation accumulated during a period of a million years or so within the New Zealand Tongaporutuan Stage (Fig. 5; see time scale in Appendix 8), with sedimentation rates averaging 750 m/m.y. (not decompacted) (King et al., 2007). However, biostratigraphy indicates sedimentation rates were higher over short intervals (King et al., 2007). Its shallower water correlative is the Matemateaonga Formation which comprises cyclothemic shelf sandstone, mudstone, and shell beds, and the outer shelf to upper slope Kiore Formation, which comprises sandstone, sandy siltstone, and bedded siltstone with thin sand lenses. The contiguous deep water Mount Messenger Formation represents base-of-slope and basin floor fan deposits of

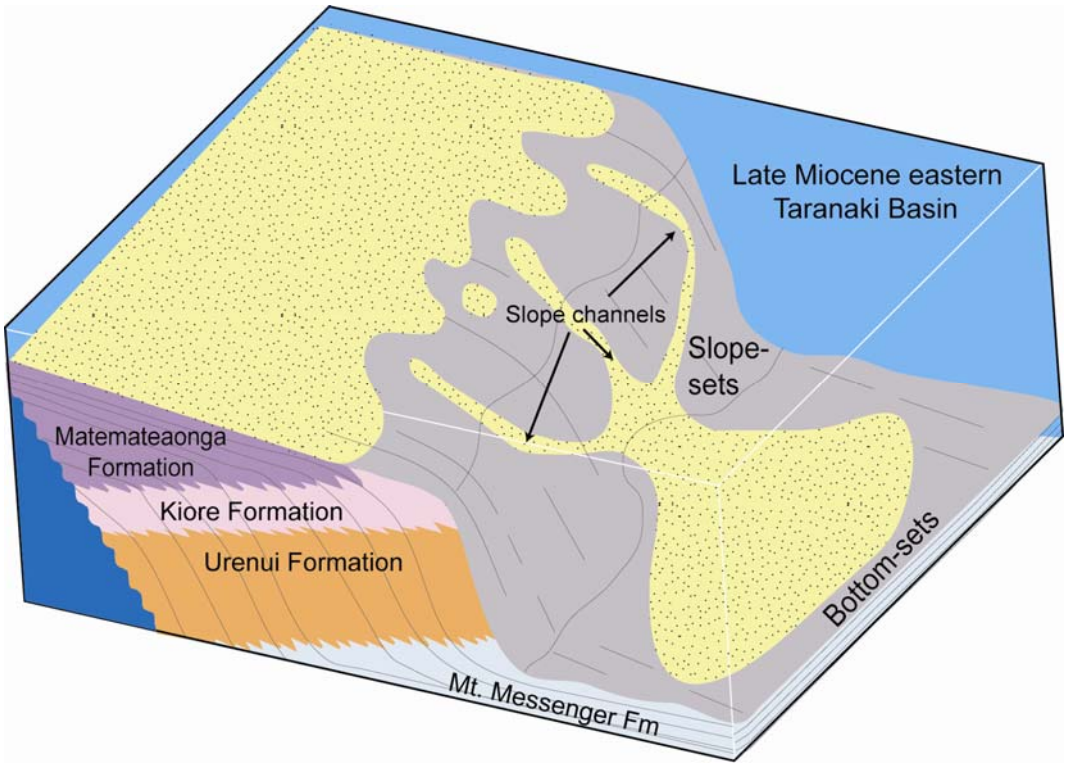

Figure 4. Simplified pictorial representation of the contiguous stratigraphic units building the shelf-to-basin continental margin of eastern Taranaki Basin in the late Miocene (modified from Kamp et al., 2004.)

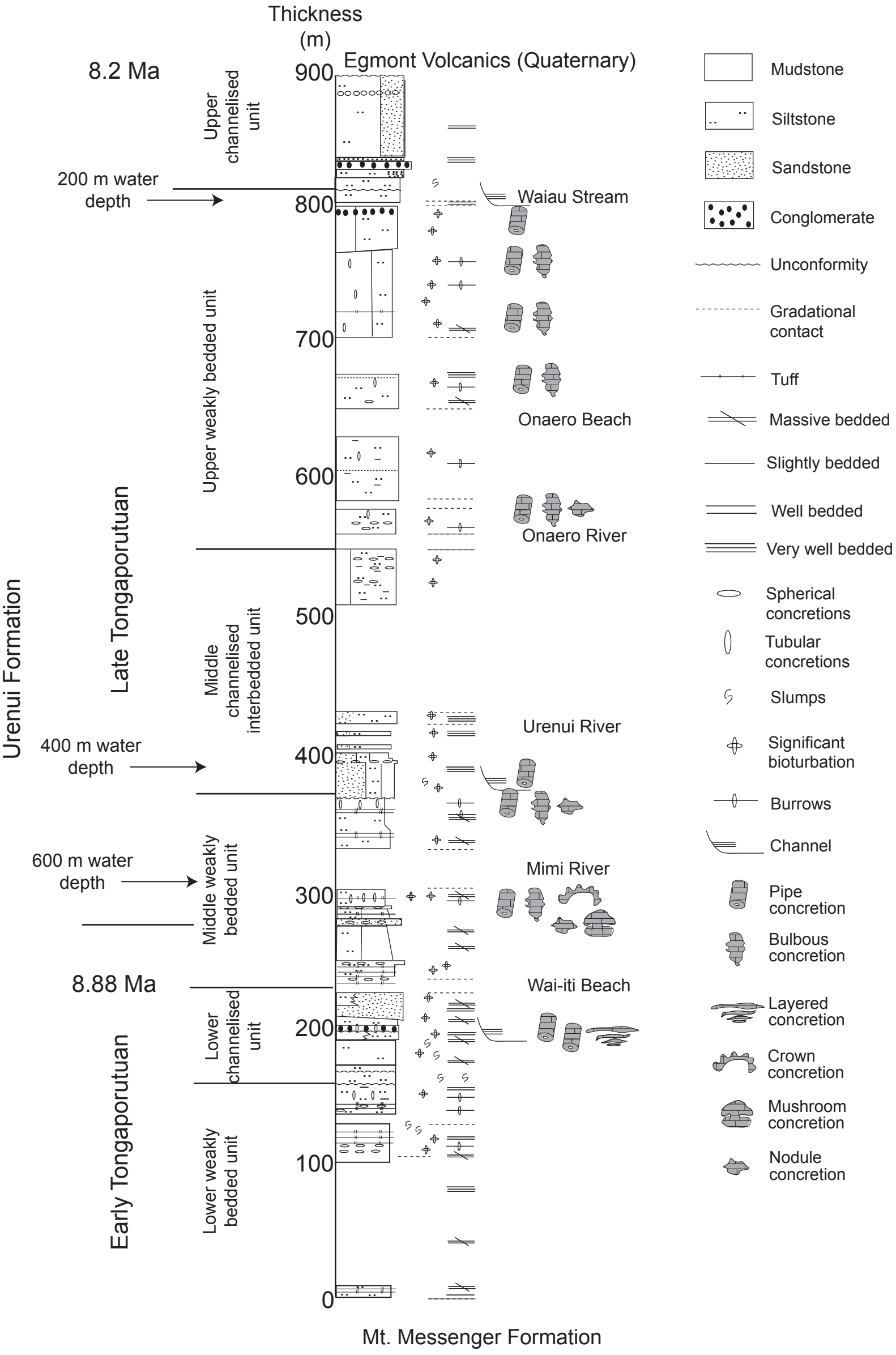

Figure 5. Detailed stratigraphic and sedimentologic column of the Urenui Formation in coastal north Taranaki (modified from King et al., 1993) showing the general distribution of the main tubular concretion occurrences. Locality names identified in Fig. 2.

mudstone and redeposited sandstone (Fig. 4) (Kamp et al., 2002, 2004; King and Browne, 2002; Townsend et al., 2008).

The Urenui Formation is typified by a predominantly grey mudstone facies that is massive to vaguely bedded, bioturbated, and slightly calcareous (<5% carbonate) (Fig. 5). It dips a few degrees towards the SW. Scattered carbonate concretions are common and include mainly subspherical types, up to a few tens of cm across, but also a variety of other concretionary structures, including pipes, bulbs, slabs, and rings. All these other varieties are grouped under the general name 'tubular concretions' because in most cases they contain a central conduit, which remains empty or is sediment/cement filled. The tubular concretions are well exposed along portions of the coastal cliff and platform south of Pukearuhe Beach to almost as far as Waitara, especially in the vicinity of Wai-iti and Mimi Beaches (Fig. 2). These Taranaki occurrences were first noted by Grange (1927) and again by King et al. (1993), without further discussion or interpretation, and also in a poster by the Taranaki GSNZ (1994) that mentioned the paramoudra-like nature of the tubular concretions and an implied association with trace fossil activity (cf. Bromley et al., 1975).

3. Methods

Tubular concretions are exposed on the shore platform and in cliff outcrops over a distance of 16 km along the North Taranaki coast. Along this stretch of coastline the concretions tend to occur in clusters spanning a few hundred metres in the smallest occurrence to 2 km in extent at the main outcrop at Mimi Beach. The study focused on five coastal sections (Wai-iti, Wai-iti Channel, Mimi, Waitoetoe, Onaero, and Waiau) where tubular concretions are present (Fig. 2). The two most prominent sections occur at Mimi Beach (NZ Map Series 260, 1:50000 scale, grid reference Q19, Eastings 2635549−2634948) and Wai-iti Beach (Q18, Eastings 2638853−2638353), which are accessible only at low tide during fair weather conditions (Fig. 2). Following stratigraphic logging and photographic imaging of these coastal sections, field work focused on descriptions of the distribution, morphology, size, and stratigraphic position of the concretions. Full records of this field information are contained in Appendix 1.

Where possible, *in situ* oriented samples were collected using a chisel and heavy duty rock hammer; samples were also collected from fallen blocks lying on the intertidal platform. Sawn slabs were related to their photographic and sketched positions in the sampled concretions. In several cases, small subsamples were then cut and extracted to provide representative rock material along transects from the centre to the periphery of the tubular concretions.

Laboratory analytical work included routine thin section petrography and cathodoluminescence (CL) of resin impregnated samples. Scanning electron microscopy (SEM) aided in viewing the microstructure of the micritic carbonate, following the procedure of Munnecke and Samtleben (1996). X-ray diffraction (XRD) determined the mineralogy of samples and the $MgCO_3$ content of calcite (e.g., Goldsmith et al., 1961). Stable isotope mass spectrometry was used to derive the $\delta^{18}O$ and $\delta^{13}C$ composition of the carbonate phases (e.g., McCrea, 1950; Nelson and Smith, 1996). In samples of mixed calcite and dolomite composition, the carbonate fractions are difficult to physically separate for stable isotope analysis. In this study, a variation of the differential phosphoric acid extraction method (Al-Aasm et al., 1990; Kyser et al., 2002) was used to derive values for calcite-CO_2 and dolomite-CO_2. Calcite-CO_2 and dolomite-CO_2 were determined in two separate reactions, for 10 minutes and 2 hours, respectively, due to restrictions on gas transfer rates induced by the geometry of the mass spectrometer inlet system. Isotope results are reported as per mille $\delta^{18}O$ and $\delta^{13}C$ relative to VPDB, and have an analytical precision of better than ±0.10‰. Lipid analyses are available for a few samples and have been previously reported by Pearson and Nelson (2005) in a wider study of mainly New Zealand septarian concretions, and by Pearson et al. (2008) in a more focused study of some tubular concretions from several North Island locations, including Taranaki.

Details of field and laboratory techniques and instruments are available in Appendix 7.

4. Tubular concretions

4.1 Morphology

The tubular concretions are typically oriented at high angles to bedding and range in length from 0.5 to 10+ m (limited only by height of the coastal cliff exposure) and in diameter from about 5 to 70 cm. They can be straight, sinuous or tortuous, may branch, anastomose and coalesce, and can taper upward or downward or bend over to produce slabs (Fig. 6).

A morphological classification of the concretions is developed in Figure 7, of which the pipe and bulbous varieties overwhelmingly dominate at the Taranaki localities. Pipe concretions are visibly up to 2 to 3 m long and from 5 to 20 cm across, with the diameter remaining more or less constant throughout their length (Fig. 6A-C). They are mainly straight to slightly sinuous structures. Bulbous concretions are overall much larger and more irregular than the pipe concretions, in places extending the full height (10 m) of coastal cliff exposures in a meandering fashion (Fig. 6H). They range up to 50 cm or more across and can be variable in width along their length as a consequence of prominent annulated or pinch-and-swell external shapes (Fig. 6D-F). Both these varieties of tubular concretions support a conspicuous hole or conduit, up to several cm across, running the length of the structures at or near their centre (Fig. 8). Rarely the central conduit is replaced by many central tubelets, each a few mm across. The conduits are often (now) empty (Fig. 8A,B), but may be filled with later generation cements or by host or foreign sediments (Fig. 8E). Occasionally a central conduit is not evident, or is cryptic and marked only by subtle concentric colour changes in cross sectional views of the tubular concretions (Fig. 8D).

A notable feature of many of the bulbous concretions in particular is the occurrence of internal brecciation about their conduits (Fig. 8F). The fractures can be complexly arranged but often show either a roughly radial or concentric pattern that tends to disappear towards the outer margins of the concretions (Fig. 8F). They are healed by one or more of the same cements that precipitated within the

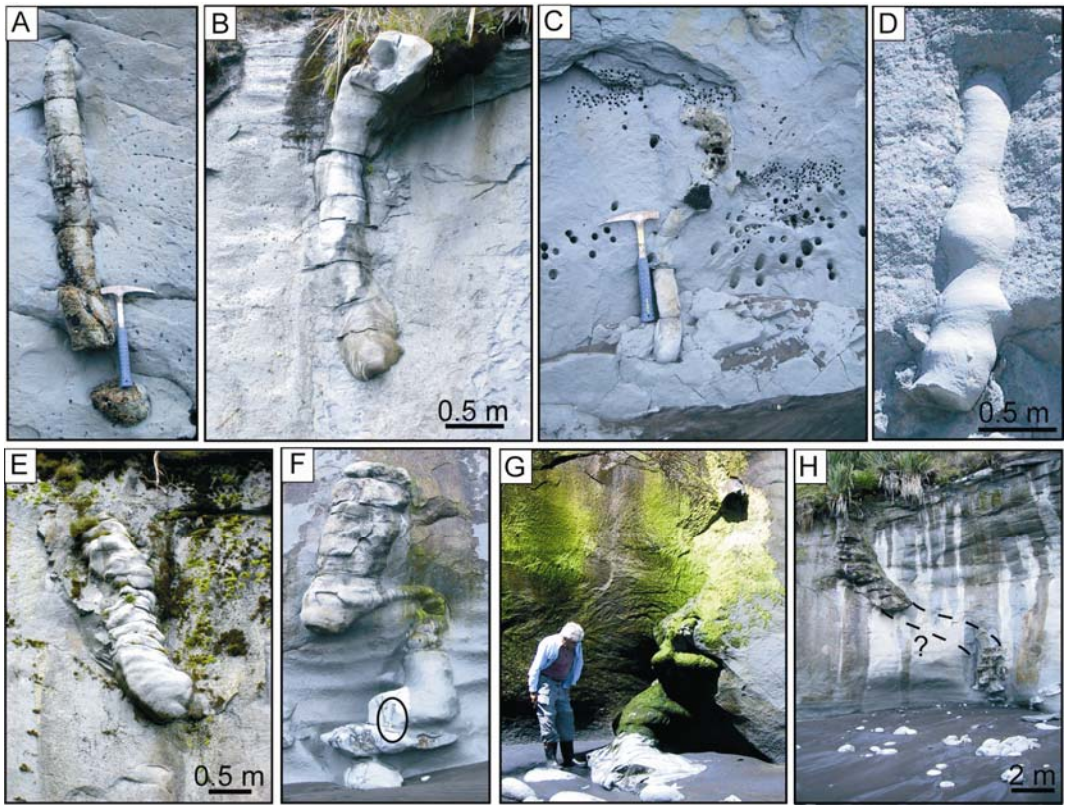

Figure 6. Examples of tubular concretions in Urenui slope mudstone at Mimi, north Taranaki coastline. (A-C) Pipe concretions and (D-H) bulbous concretions exposed in cliff outcrops.

Morphology		Description
Pipes		W: 0.1-1 m L: up to many metres
Bulbous		W: up to 0.5 m L: 0.1-10 m
Layered		W: up to 2 m L: up to 2 m
Crowns		W: av. 0.5 m L: up to 0.5 m D: 4 m
Mushrooms		D = 3 m
Nodules		D: av. < 0.5 m

Figure 7. Morphologic classification of tubular concretions on the north Taranaki coastline in eastern Taranaki Basin. Pipe and bulbous varieties dominate in outcrop. L = Length of (exposed) tubular concretion; D = diameter; W = width.

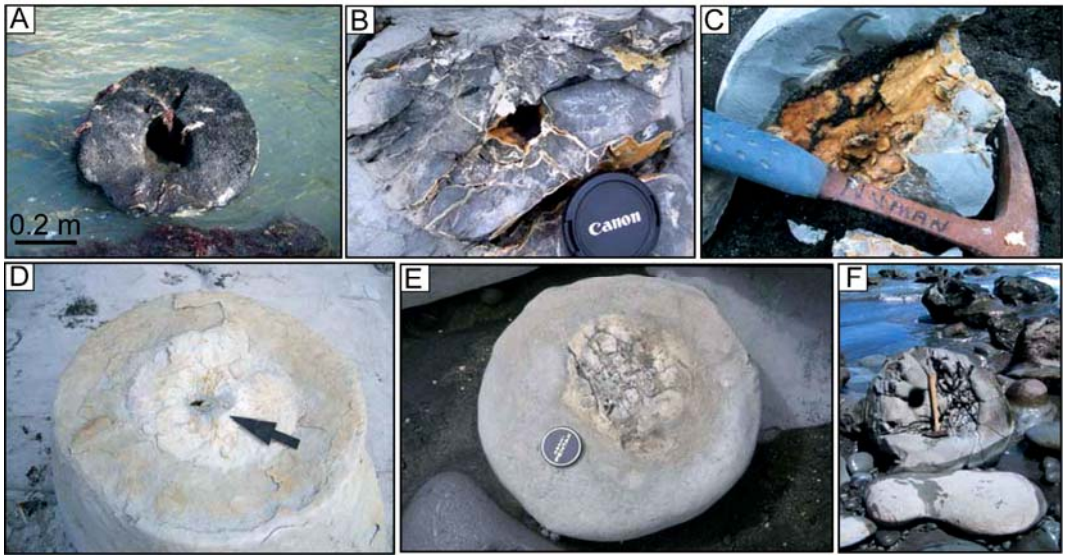

Figure 8. Examples of different varieties of conduits within the Urenui tubular concretions. (A) Large open conduit in tubular pipe concretion; (B) open conduit supporting a rim of calcite spar crystals in bulbous tubular concretion that has been radially fractured and healed by later calcite vein cements; (C) split tubular concretion with yellow (iron stained) crystalline calcite lining the conduit; (D) pipe concretion with pin hole conduit and colour zonation (arrowed); (E) pipe concretion with brecciated, sediment filled conduit; (F) tubular concretion with crude radial and some concentric fractures and brecciation. Lens cap is 5 cm in diameter and arrow is 7 cm long.

central conduits. Petrographic relationships demonstrate that multiple generations of fracturing and cement precipitation characterise many of the central conduit-associated areas of the tubular concretions.

In some localities, other concretionary structures can be associated with the pipe and bulbous types. These include layered, crown, mushroom, and irregular nodule morphologies (Figs. 7, 9). The layered varieties are associated with interbeds of slightly more permeable, silt-rich mudstones and comprise a zone of stacked concretionary slabs up to 2.5 m high by 1-3 m across. Sometimes, pipe or bulbous concretions feed into the bottom and exit the top of stacks of layered concretions (Fig. 9A). At low tide along the Mimi section (Fig. 2), conspicuous (semi-circular) ring concretions, up to 4 m in diameter, stand proud in the plane of bedding towards the outer margin of the shore platform (Fig. 9B). The concreted rings are c. 0.5 m wide at their top and taper gently downwards into the platform substrate. Rare scattered mushroom-like slabs and irregular carbonate bodies or nodules complete the spectrum of concretionary types (Figs. 7, 9C-I).

Spherical concretions are relatively common throughout the Urenui Formation and are typically 25 to 50 cm in diameter. They tend to occur closely spaced in clusters (see photomosaic in Appendix 1).

4.2 Petrography and mineralogy

Mineralogically, the Urenui Formation mudstone hosting the concretions is dominated by illite and chlorite clays, subangular silt to fine sand sized grains of quartz and sodic plagioclase feldspar, scattered quantities of skeletal remains (predominantly foraminifera), and accessory amounts of hornblende, epidote, and authigenic framboidal pyrite (Nelson and Hume, 1977). The host mudstone carbonate content is <5%, comprising exclusively low-Mg calcite.

The pipe and bulbous concretions have similar bulk mineralogy to the host mudstone, but their carbonate contents are significantly higher, ranging from 50 to 85%. There is no obvious sedimentological, textural, or grain size variation

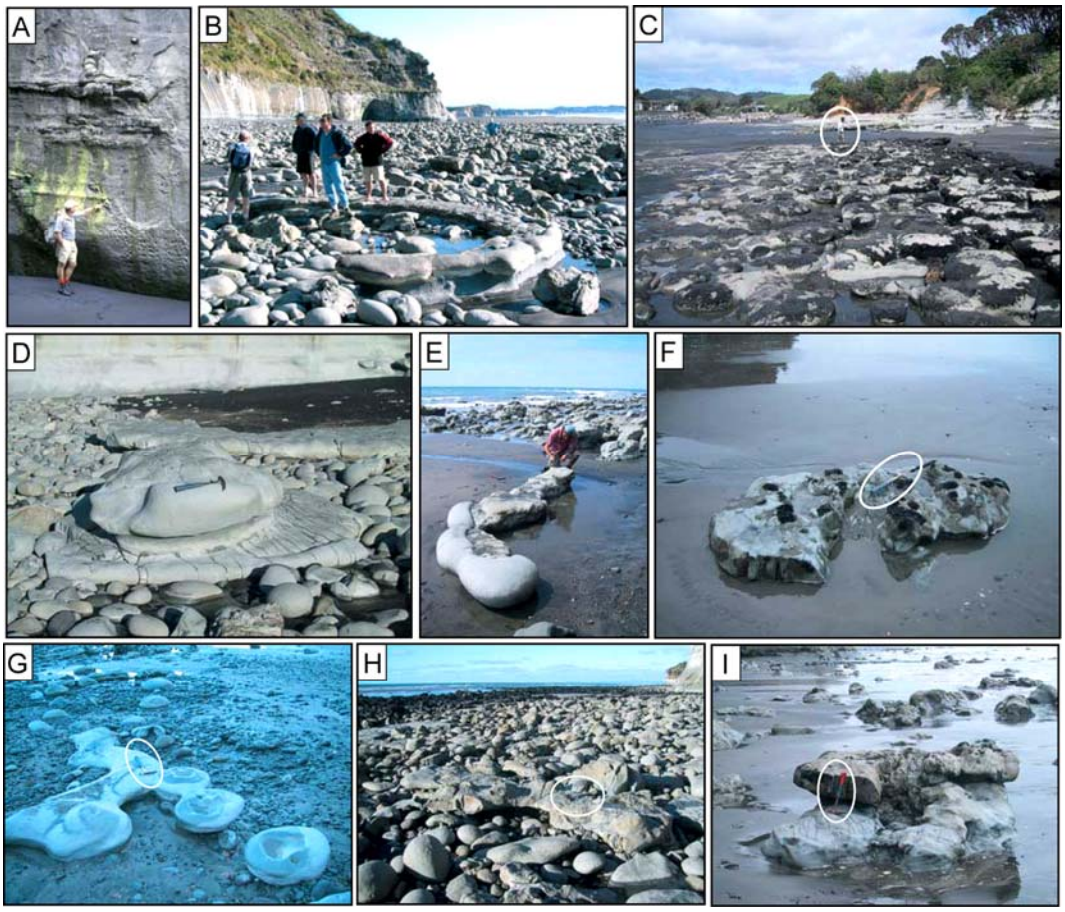

Figure 9. Some examples of additional concretionary morphologies in Urenui slope mudstone in coastal north Taranaki. (A) Layered (stratiform) concretions linked by associated pipe concretion below and above; (B) large concretionary rings standing proud in the shore platform amongst much tubular concretion litter; (C) nodular slabs exposed at Wai-iti Beach are similar to those also exposed at the northern end of Mimi section; (D) mushroom shaped concretion exposed on the shore platform at Mimi section, site adjacent to a concreted ring; (E-I) nodular concretions exposed on the shore platform at Mimi. The concretions shown here (E-I) do not have conduits. Scales provided by people or standard rock hammer (sometimes circled).

between the pipe and bulbous concretions. The carbonate cement consists of a tightly interlocking mosaic of calcite or dolomite micritic and microsparitic cement, leaving little residual porosity (Fig. 10A-D). These cement crystals are typically 2-10 μm in size, xenomorphic and inclusion rich, and under SEM display a heterogeneous crimpy surface texture (Fig. 10A). A feature in thin sections of the concretions is the presence of scattered to common, oval to bean shaped peloidal masses, individually 250−1500 μm in size and often aggregated, which are darker and more homogeneous than the surrounding sediment due to a reduced content of terrigenous silt grains and possibly a higher organic content (Fig. 10B). The peloids are inferred to be of biological origin, defining pre-concreted mudstone burrow traces and/or faecal pellets.

Slow scan XRD indicates the pipe and bulbous varieties of tubular concretions have contrasting cement mineralogies. Pipe concretions are almost always low-Mg calcite (<4 mol% $MgCO_3$), rarely with some intermediate-Mg calcite (4−12 mol% $MgCO_3$). Bulbous concretions are mainly (proto)dolomitic (c. 40−48 mol% $MgCO_3$), but may include also some high-Mg calcite (>12 mol% $MgCO_3$). Full records of XRD data are contained in Appendix 1.

Figure 10 (on page 90). Petrographic images of tubular concretions. (A) SEM image of tubular concretion with micritic carbonate cement; (B) thin section image (PPL) of tubular concretion with peloids (1) and quartzofeldspathic silt and irresolvable clay minerals in micritic carbonate cement; (C,D) thin section image pair (PPL and CL, respectively) of mudstone with micritic, orange luminescing calcite cement; (E,F) thin section image pair (PPL and CL, respectively) of multi-generational cements. The first phase (1) is micritic dolomite cement between siliciclastic silt and clay grains, the second phase (2) is coarse crystalline dolomite lining vugs and conduit, and the third phase (3) is a dolomitic micrite lining the conduit. (G,H) thin section image pair (PPL and CL, respectively) of a calcite vein cross cutting concretion interior as a later precipitation phase than the interstitial sediment pore filling micritic dolomite; (I,J) thin section image pair (PPL and CL, respectively) of crystalline calcite cement (2) growing into an open vug after earlier precipitation of interstitial pore filling micrite (1). PPL = plane polarised light; CL = cathodoluminescent light.

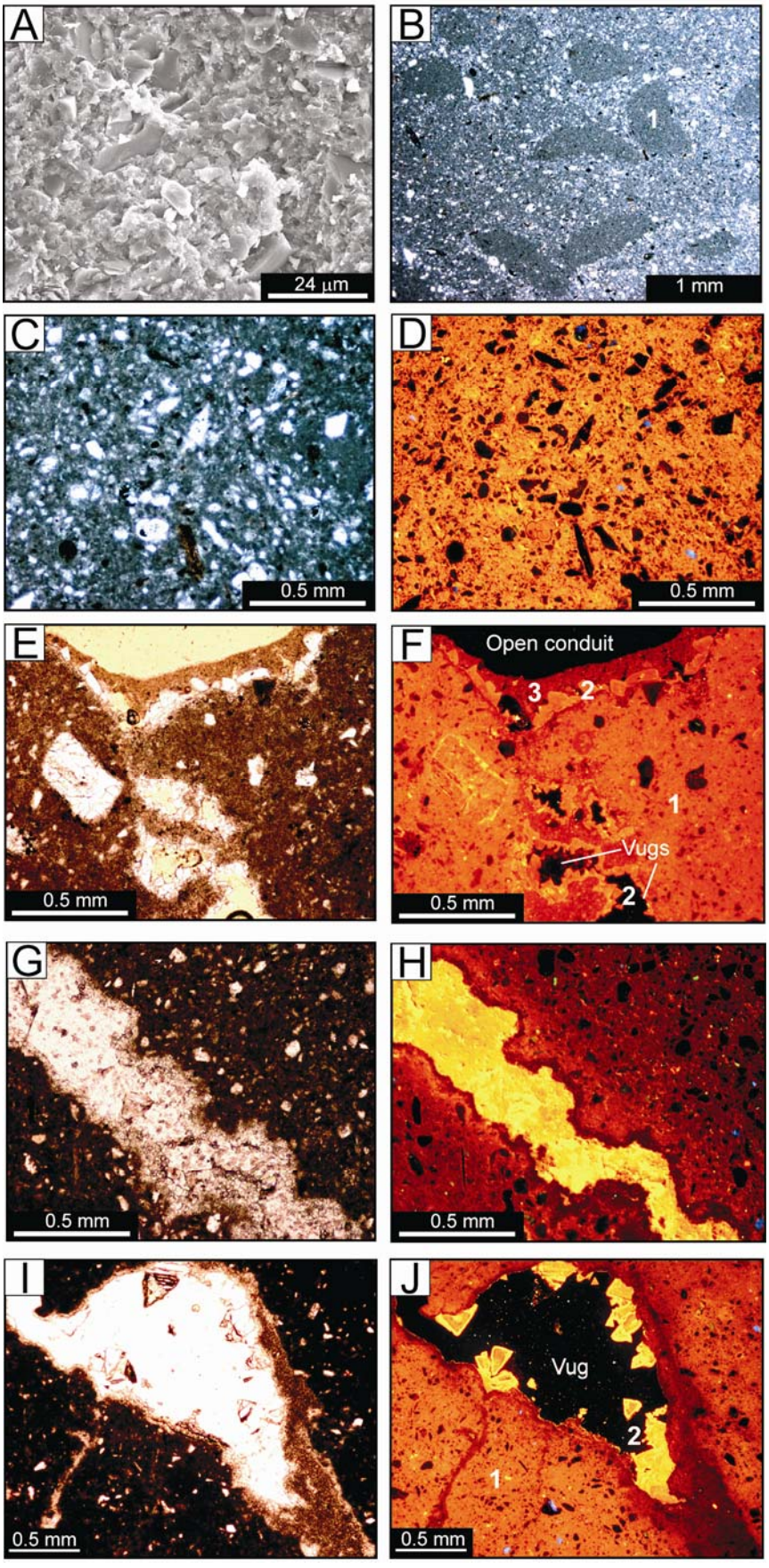
A
24 μm
B
1
1 mm
C
0.5 mm
D
0.5 mm
E
0.5 mm
F
Open conduit
3
2
1
Vugs
2
0.5 mm
G
0.5 mm
H
0.5 mm
I
0.5 mm
J
Vug
2
1
0.5 mm

The conduits and fractures within the tubular concretions are sharply bordered and truncate any stratigraphic or sedimentologic features in the concretions and host sediments, as well as any older precipitated cement (Fig. 10E-H). Sediment fill in the conduits consists primarily of mudstone clasts probably derived from erosion of the conduit walls of the host concretion. Clast abundance varies from few to many. Clast size ranges widely, from less than a millimetre to several centimetres, and also in shape, from angular to well rounded. Some examples show mudstone clasts partially broken away from the conduit wall, while others exhibit a first generation of cement detached from the conduit wall, and examples of clast breakup after precipitation of the first conduit cement (Fig. 10I-J).

Up to three generations of cement can fill the conduits and fractures in the tubular concretions. First generation cements comprise an isopachous rim, up to 100 μm thick, of micrite or stubby calcite lining the substrate walls and about mudstone clasts (Fig. 11). Pyrite is commonly included in this cement phase. Second generation cements mainly have fibrous (Fig. 11A) or bladed (Fig. 11B) habits, in places are inclusion rich, and form isopachous rinds upon first-formed cements or original substrates, and locally may fill pore spaces. Granular calcite is the final generation cement, commonly filling the central portion of conduits and fractures (Fig. 11A). Nonetheless, most conduits of the tubular concretions are only partially filled by cement and/or cemented siliciclastic sediment, or remain completely empty in the present day outcrop.

4.3 Stable isotope composition

Carbon and oxygen isotope signatures aid in identification of the fluid compositions responsible for precipitation of carbonate cement (e.g., Roberts and Aharon, 1994; Nelson and Smith, 1996). The carbonates in the various tubular concretionary features fall within relatively distinct clusters or groups on a $\delta^{13}C$ – $\delta^{18}O$ cross plot, especially the pipe concretions, the bulbous concretions, and the conduit or fracture cement fills (Table 1, Fig. 12).

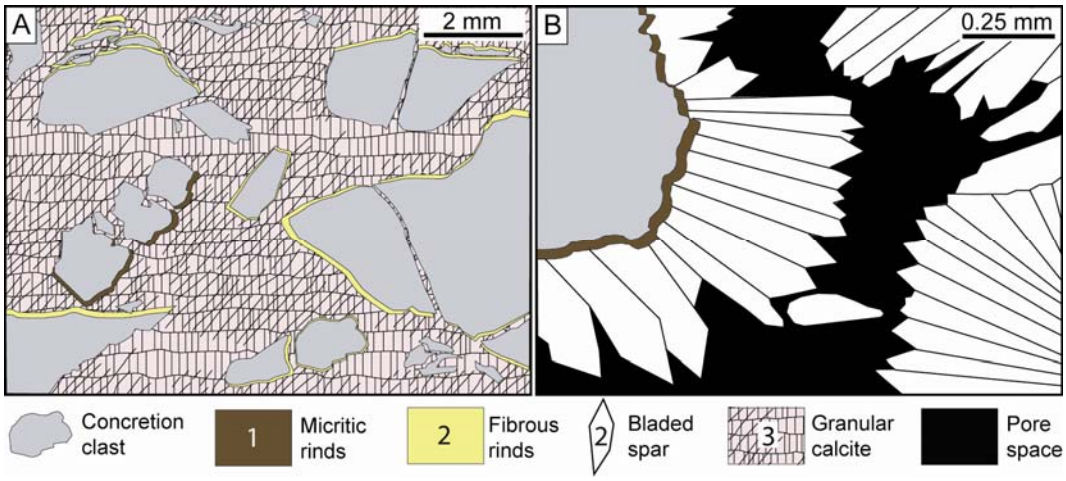

Figure 11. Schematic sketches of pipe concretion conduits from Mimi section with brecciated tubular concretion clasts drawn from thin section images. (A) jigsaw-like breccia clasts of micrite cemented tubular concretions with a fibrous calcite rind cemented by granular calcite, and (B) micrite cemented tubular concretion clast with a micritic carbonate rind and bladed calcite growing into a void. Numbers in key indicate order of cement generation in the conduit after main tubular concretion formation (i.e., concretion clast consists of micritic calcite or dolomite precipitated during the main cementation phase from methane rich fluids).

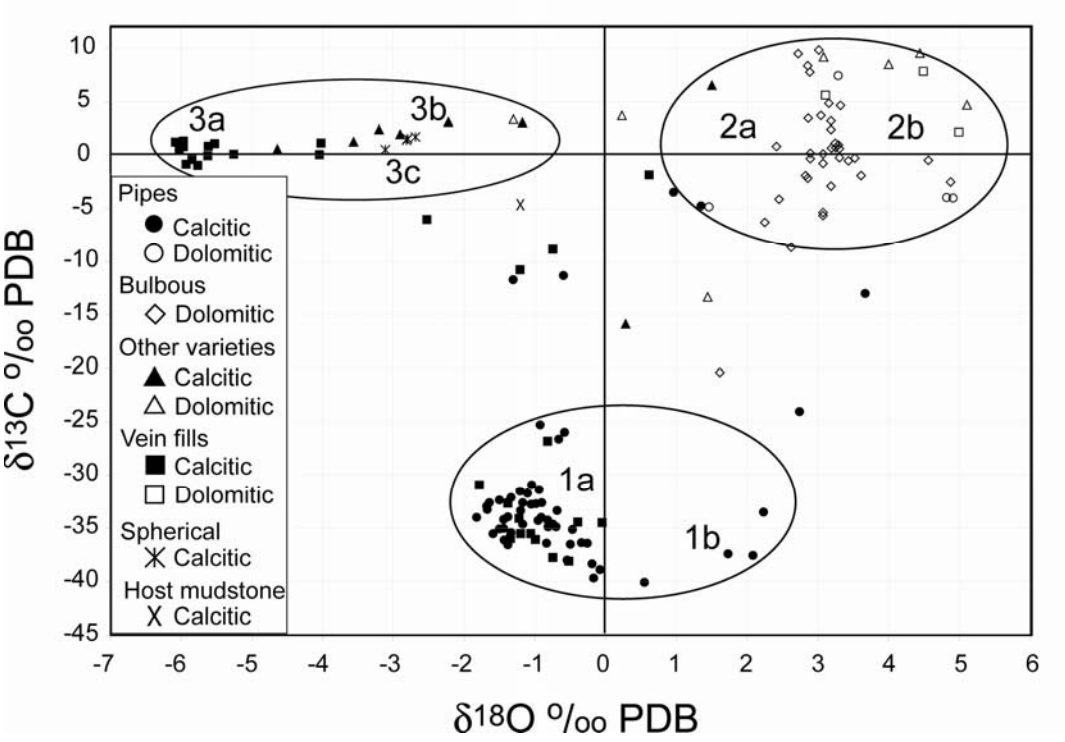

Figure 12. Stable oxygen and carbon isotope values for tubular (pipe and bulbous) concretions, vein fills in tubular concretions, other concretions (layered, crown, mushroom, and nodules), spherical concretions, and the host Urenui mudstone from onshore Taranaki Basin (extended from Nelson et al., 2004). Note clustering of the data within three areas of the plot. Group 1 consists of calcitic pipe concretions, group 2 is predominately dolomitic bulbous concretions, and group 3 involves mainly vein fills, spherical concretions, and host mudstone. Table 1 lists details of samples and stable isotope values.

Table 1. Table of stable isotope data for Urenui samples. Concretion sample denotes main concretion, sub-sample denotes samples through a transect of the main concretion. All stable isotope values are reported in ‰ PDB. Data from Schellenberg (2002)*.

Concretion sample	Sub-sample	$\delta^{13}C$ ‰ PDB calcite	$\delta^{18}O$ ‰ PDB calcite	$\delta^{13}C$ ‰ PDB dolomite	$\delta^{18}O$ ‰ PDB dolomite	% calcite, dolomite
Pipe morphology						
TMc1	TMc1-1	-36.41	-0.26			100, 0
	TMc1-2	-34.88	-0.70			100, 0
	TMc1-3	-34.64	-1.17			100, 0
TMf2	TMf2-1			-4.03	+4.91	0, 100
	TMf2-2			-3.96	+4.82	0, 100
	TMf2-3			+2.17	+4.99	0, 100
TWAf1	TWAf1-1	-4.74	+1.35	-4.84	+1.46	78, 22
	TWAf1-2	-3.48	+0.96	+7.43	+3.29	79, 21
	TWAf1-3	-1.83	+0.62	+5.59	+3.11	81, 19
***TMcP7** 1st transect	TMcP71-1	-13.03	+3.67			100, 0
	TMcP71-2	-24.01	+2.74			100, 0
	TMcP71-3	-33.49	+2.23			100, 0
	TMcP71-4	-37.56	+2.08			100, 0
	TMcP71-5	-37.43	+1.73			100, 0
	TMcP71-6	-40.11	+0.55			100, 0
	TMcP71-z1	-0.05	-5.62			100, 0
	TMcP71-z2	-0.41	-5.84			100, 0
	TMcP71-z3	-0.94	-5.76			100, 0
***TMcP7** 2nd transect	TMcP72-1	-33.34	-0.68			100, 0
	TMcP72-2	-35.14	-0.47			100, 0
	TMcP72-3	-36.4	-0.34			100, 0
	TMcP72-4	-30.91	-1.04			100, 0
	TMcP72-5	-32.75	-1.05			100, 0
	TMcP72-z1	+0.8	-5.96			100, 0
	TMcP72-z2	+0.61	-6.02			100, 0
	TMcP72-z3	+1.11	-5.52			100, 0
***TMcP7** 3rd transect	TMcP73-1	-36.52	-0.5			100, 0
	TMcP73-2	-31.54	-1.21			100, 0
	TMcP73-3	-31.71	-1.1			100, 0
	TMcP73-4	-32.61	-0.9			100, 0
	TMcP73-3b	-34.29	-0.95			100, 0
	TMcP73-2b	-34.63	-0.74			100, 0
	TMcP73-1b	-38.36	-0.19			100, 0
	TMcP73-z1	-6.06	-2.52			100, 0
	TMcP73-z2	+0.12	-5.25			100, 0

Table 1 continued.

Concretion sample	Sub-sample	$\delta^{13}C$ ‰ PDB calcite	$\delta^{18}O$ ‰ PDB calcite	$\delta^{13}C$ ‰ PDB dolomite	$\delta^{18}O$ ‰ PDB dolomite	% calcite, dolomite
	Pipe morphology					
***TMcP81**	TMcP81-2	-39.7	-0.17			100, 0
	TMcP81-3	-36.15	-1.43			100, 0
	TMcP81-4	-36.43	-0.83			100, 0
	TMcP81-z1	-34.5	-0.05			100, 0
	TMcP81-z2	-34.45	-0.39			100, 0
	TMcP81-z3	-30.94	-1.78			100, 0
	TMcP81-z4	-32.68	-1.38			100, 0
	TMcP81-z5	-26.82	-0.82			100, 0
	TMcP81-5b	-35.55	-1.59			100, 0
	TMcP81-3b	-38.01	-0.54			100, 0
	TMcP81-2b	-38.89	-0.08			100, 0
	TMcP81-1b	-32.69	-0.98			100, 0
***TMcP83**	TMcP83_1	-32.94	-1.68			100, 0
	TMcP83_2	-36.58	-1.38			100, 0
	TMcP83_3	-35.41	-1.33			100, 0
	TMcP83_4	-35.03	-1.44			100, 0
	TMcP83_5	-35.1	-1.5			100, 0
	TMcP83_6	-33.96	-1.38			100, 0
	TMcP83_7	-34.02	-1.82			100, 0
	TMcP83_8	-34.19	-1.44			100, 0
	TMcP83_9	-33.24	-1.67			100, 0
	TMcP83_z1	-0.85	-5.92			100, 0
	TMcP83_z2	-10.79	-1.21			100, 0
	TMcP83_z3	-8.88	-0.74			100, 0
***TMcP9**	TMcP9-1	-32.61	-1.64			100, 0
	TMcP9-2	-11.37	-0.59			100, 0
	TMcP9-3	-25.99	-0.58			100, 0
	TMcP9-4	-11.72	-1.3			100, 0
	TMcP9-5	-25.28	-0.92			100, 0
	TMcP9-6	-26.6	-0.66			100, 0
	TMcP9-7z	-35.99	-1.34			100, 0
	TMcP9-z1	-34.08	-1.22			100, 0
	TMcP9-z2	-37.78	-0.74			100, 0
	TMcP9-z3	-38.11	-0.52			100, 0
	TMcP9-z4	-36.09	-0.99			100, 0
	TMcP9-z5	-35.53	-1.06			100, 0
	TMcP9-z6	-35.54	-1.2			100, 0
***TMcP10**	TMcP10-1	-34.87	-0.81			100, 0
	TMcP10-2	-34	-0.91			100, 0
	TMcP10-3	-33.33	-1.2			100, 0
	TMcP10-4	-32.58	-1.38			100, 0
	TMcP10-5	-32.09	-1.33			100, 0
	TMcP10-5b	-32.38	-1.5			100, 0
	TMcP10-3b	-32.6	-1.17			100, 0
	TMcP10-1b	-34.22	-0.82			100, 0

Table 1 continued.

Concretion sample	Sub-sample	$\delta^{13}C$ ‰ PDB calcite	$\delta^{18}O$ ‰ PDB calcite	$\delta^{13}C$ ‰ PDB dolomite	$\delta^{18}O$ ‰ PDB dolomite	% calcite, dolomite
	Bulbous morphology					
TMf1	TMf1-1			-2.48	+4.87	0, 100
	TMf1-2			-0.43	+4.56	0, 100
	TMf1-3			+7.84	+4.49	0, 100
	TMcP1-1			-1.9	+3.61	0, 100
***TMcP1**	TMcP1-2			-0.27	+2.89	0, 100
	TMcP1-3			-2.89	+3.18	0, 100
	TMcP1-4			-5.36	+3.07	0, 100
	TMcP1-5			-6.28	+2.25	0, 100
	TMcP1-6			-4.12	+2.45	0, 100
	TMcP1-7			+0.16	+3.07	0, 100
	TMcP1-z1			+0.84	-5.61	0, 100
	TMcP1-z2			+1.26	-6.07	0, 100
	TMcP1-z3			+1.36	-5.96	0, 100
***TMcP3**	TMcP3-1			+3.73	+3.04	0, 100
	TMcP3-2			+0.18	+2.89	0, 100
	TMcP3-3			-2.11	+2.85	0, 100
	TMcP3-4			-1.86	+2.82	0, 100
	TMcP3-5			+3.47	+2.86	0, 100
	TMcP3-6			+7.77	+2.88	0, 100
	TMcP3-7			+8.39	+2.85	0, 100
	TMcP3-9			+9.87	+3.01	0, 100
	TMcP3-10			+9.52	+2.72	0, 100
	TMcP3-11			+4.64	+3.32	0, 100
***TMcP5**	TMcP5-1			-0.73	+3.07	0, 100
	TMcP5-2			-5.63	+3.07	0, 100
	TMcP5-3			-8.68	+2.62	0, 100
	TMcP5-4			-20.39	+1.61	0, 100
	TMcP5-z1			+0.03	-4.04	0, 100
	TMcP5-z2			+1.13	-4.02	0, 100
***TMcP6**	TMcP6-1			+2.42	+3.18	0, 100
	TMcP6-2			+1.15	+3.24	0, 100
	TMcP6-3			+1	+3.29	0, 100
	TMcP6-4			+0.63	+3.3	0, 100
	TMcP6-5			-0.22	+3.52	0, 100
	TMcP6-6			-0.51	+3.43	0, 100
	TMcP6-7			-0.2	+3.3	0, 100
	TMcP6-8			+0.76	+3.25	0, 100
	TMcP6-4b			+0.83	+2.41	0, 100
	TMcP6-3b			+0.72	+3.19	0, 100
	TMcP6-2b			+3.24	+3.18	0, 100
	TMcP6-1b			+4.85	+3.15	0, 100

Table 1 continued.

Concretion sample	Sub-sample	$\delta^{13}C$ ‰ PDB calcite	$\delta^{18}O$ ‰ PDB calcite	$\delta^{13}C$ ‰ PDB dolomite	$\delta^{18}O$ ‰ PDB dolomite	% calcite, dolomite
	Irregular morphology					
TOf1	TOf1-1	+5.66	-0.37			100, 0
	TOf1-2	+5.1	-3.66			100, 0
T1	T1	+2.43	-3.2			100, 0
T2	T2	+1.29	-3.56			100, 0
T3	T3	+3.11	-2.22	+3.36	-1.3	62, 38
T4	T4			+9.21	+3.08	0, 100
T5	T5			+4.69	+5.1	0, 100
T6	T6	+6.54	+1.5	+8.52	+4	32, 68
T7	T7			+9.58	+4.44	0, 100
T8	T8	+0.62	-4.64	-	-	100, 0
T9	T9	+1.99	-2.9	-	-	100, 0
T10	T10	+3.08	-1.18	+3.72	+0.23	42, 58
T11	T11	-15.87	+0.28	-13.35	+1.44	63, 37
	Spherical morphology					
Tmcs	Tmcs1-1v	+0.53	-3.11			100, 0
	Tmcs1-2v	+1.43	-2.81			100, 0
	Tmcs1-2h3h	+1.6	-2.8			100, 0
	Tmcs1-3c	+1.73	-2.69			100, 0
Host mud	**Host mudstone**					
	Tm-host	-4.79	-1.23			100, 0

Figure 13 (on pages 98-99). Stable carbon and oxygen isotope transects for two calcitic pipe concretions and two dolomitic bulbous concretions from Mimi section. (A) A calcitic pipe concretion with no apparent conduit in which the sampled transect crosses the full diameter of the tube, with position 4-5 situated near the central portion of the concretion. There is little to no variation in stable isotope compositions through the transect. (B) A calcitic pipe concretion with an open conduit. Sample positions 10−12 of the transect are along the boundary of the open conduit. Stable isotope values are relatively constant throughout the transect, except that $\delta^{13}C$ shifts by 25 to 35‰ PDB in the cements lining the conduit (positions 10−12). (C) A dolomitic bulbous concretion with a 1 cm diameter open conduit in which sample positions 8−10 are along the boundary of the conduit. Overall there are some small variations only in $\delta^{13}C$ values, while $\delta^{18}O$ remains constant through the concretion, but shifts by −9‰ PDB in the cements lining the conduit. (D) A dolomitic bulbous concretion with no apparent conduit. The sample transect crosses the full diameter of the tube where positions 6−7 approximate the central portion of the concretion. There is no variation in $\delta^{18}O$ along the transect, but $\delta^{13}C$ varies by up to +11‰ PDB.

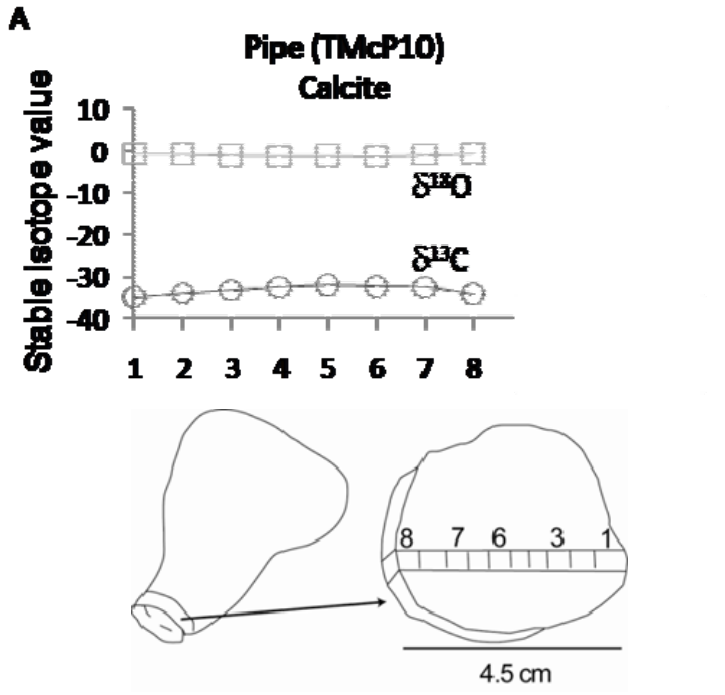
A
Pipe (TMcP10)
Calcite
Stable Isotope value
10
0
-10
-20
-30
-40
δ18O
δ13C
1 2 3 4 5 6 7 8
8 7 6 3 1
4.5 cm

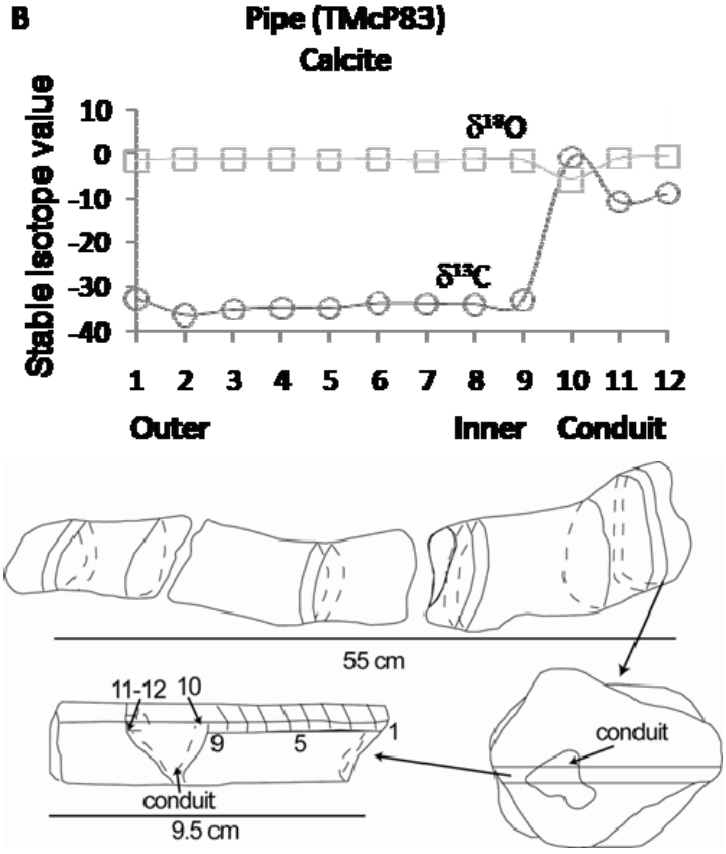
B
Pipe (TMcP83)
Calcite
Stable Isotope value
10
0
-10
-20
-30
-40
δ18O
δ13C
1 2 3 4 5 6 7 8 9 10 11 12
Outer
Inner
Conduit
55 cm
11-12 10
9
5
1
conduit
9.5 cm
conduit

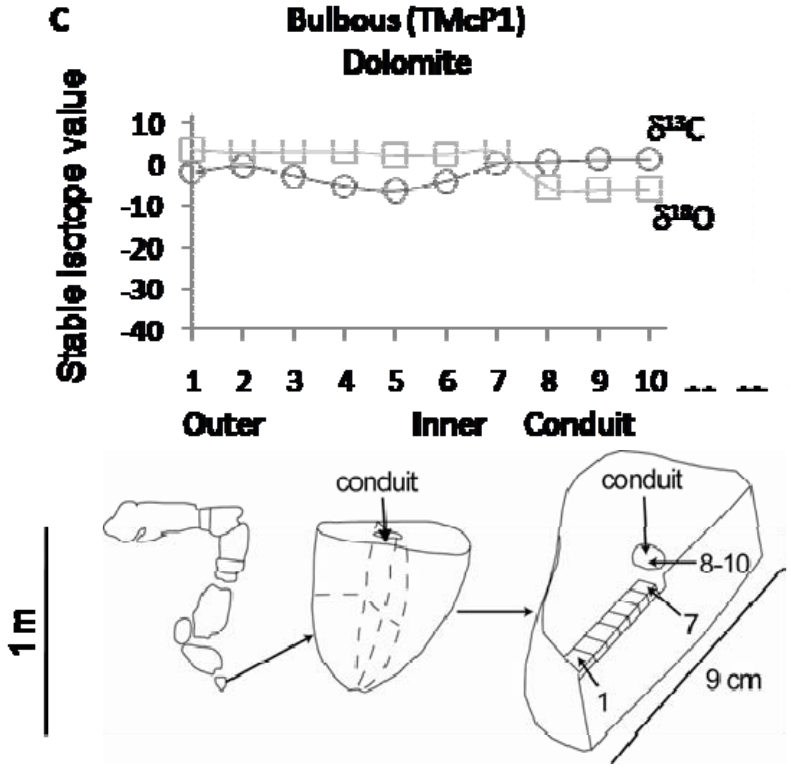
C
Bulbous (TMcP1)
Dolomite
Stable Isotope value
10
0
-10
-20
-30
-40
δ13C
δ18O
1 2 3 4 5 6 7 8 9 10
Outer
Inner
Conduit
1 m
conduit
conduit
8-10
7
1
9 cm

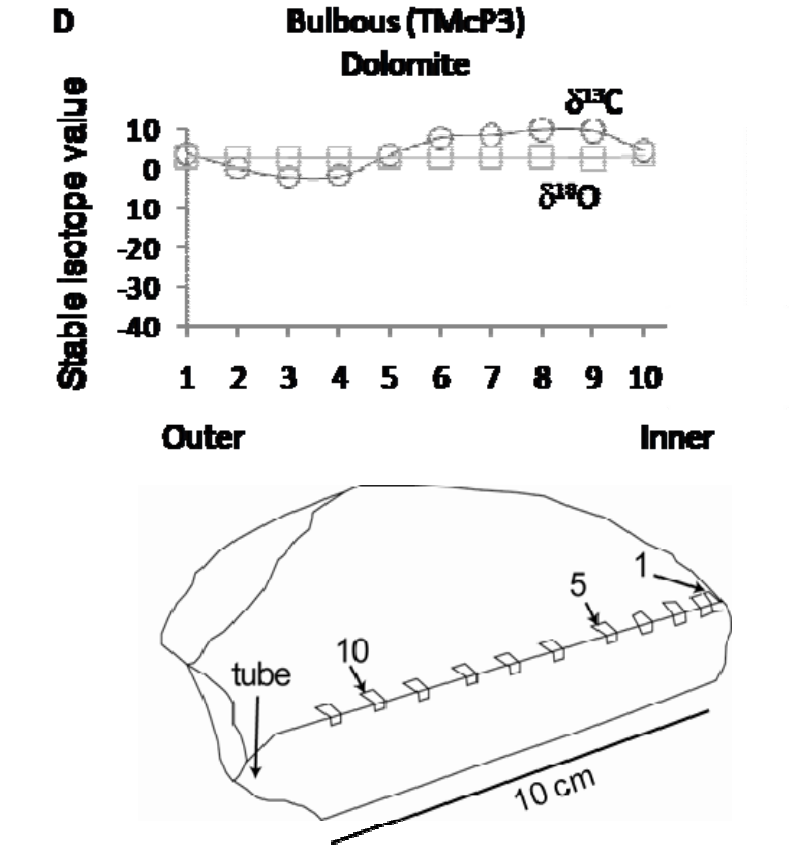
D
Bulbous (TMcP3)
Dolomite
Stable Isotope value
10
0
10
-20
-30
-40
δ13C
δ18O
1 2 3 4 5 6 7 8 9 10
Outer
Inner
1
5
10
tube
10 cm

Group 1a is associated with pipe concretions and involves strongly negative carbon and slightly negative oxygen values ($\delta^{13}C$ –40 to –26‰ PDB, $\delta^{18}O$ –2 to 0‰ PDB). Group 1b is also associated with calcitic pipe concretions with similar carbon isotope values to group 1a; however, their oxygen isotope values are more enriched than that of group 1a and $\delta^{18}O$ ranges from 0.5 to +3‰ PDB.

Group 2a corresponds to the bulbous concretions with slightly negative to mainly moderately positive carbon values ($\delta^{13}C$ between –10 and +11‰ PDB) and small positive oxygen values ($\delta^{18}O$ between +0.8 and +3‰ PDB). Group 2b is also associated with dolomitic bulbous concretions with similar carbon isotope values to group 2a; however, their oxygen isotope values are more enriched than that of group 2a and $\delta^{18}O$ ranges from +3 to +5‰ PDB.

Lastly, group 3 constitutes the conduit and fracture late cement fills of tubular concretions, as well as the concretionary carbonate from typical subspherical concretions within the same stratigraphy as the associated tubular concretions. This cluster records carbon isotope values near zero and moderately negative oxygen values ($\delta^{13}C$ from –1 to +5‰ PDB, $\delta^{18}O$ from –6.3 to –1‰ PDB).

To investigate whether there are any systematic changes in the stable isotope compositions of the carbonate cements within the tubular concretions, closely spaced samples were subsampled along transects extending from their outer margins to their central conduits. In total, 15 transects were analysed, each involving typically 3−10 subsamples. Results of four transects, two from pipe and two from bulbous concretion examples, are illustrated in Figure 13; the others are shown in Appendix 1. Generalising, despite mainly small differences in the isotope values among transects from tubular concretions of the same type (i.e. pipe vs. bulbous), in most transects the $\delta^{13}C$ and $\delta^{18}O$ values from the outside rim to the central conduit either remain quite similar for any one concretion, or become slightly more negative (lighter) by a few per mille. Where conduit cements occur, their $\delta^{13}C$ values are always far more positive (heavier) than the immediately adjacent concretionary carbonate, while $\delta^{18}O$ values are typically more negative (lighter) or similar.

5. Discussion

5.1 Fluid composition

5.1.1 Carbon

Carbon isotope values recorded in authigenic carbonate reflect the source of carbon incorporated into the carbonate lattice. Carbon sources include marine shell material, decomposition of organic matter, oxidised microbial or thermogenic methane, and residual carbon as a by-product of microbial methanogenesis (Irwin et al., 1977; Curtis, 1978, 1986; Roberts and Aharon, 1994). Table 2 illustrates the relationship between burial diagenetic zones and the range in $\delta^{13}C$ of authigenic carbonates precipitated. The strongly depleted carbon isotopes recorded in the group 1a and 1b pipe concretions (Fig. 12; $\delta^{13}C$ = –40 to –25‰ PDB) are consistent with these concretions forming from oxidised thermogenic methane, although other possibilities exist.

Conventionally, enriched carbon signatures such as those recorded by the Urenui bulbous concretions in group 2 (Fig. 12; $\delta^{13}C$ –10 to +10‰ PDB) have been interpreted as sourced from reduced CO_2 produced as a by-product of methanogenesis (Greinert et al., 2001; Pierre et al., 2002; Peckmann et al., 2002; Pierre and Rouchy, 2004; Gieskes et al., 2005). Carbon isotope signatures have a large fractionation during microbial methane production, producing $\delta^{13}C$ values between –110 and –50‰ PDB (Table 2) (Gautier and Claypool, 1984; Whiticar, 1999). As a result, the carbon dioxide produced during fermentation reactions utilises the remaining carbon which is very heavy ($\delta^{13}C$ from –10 to +15‰ PDB) (Curtis, 1978, 1986; Roberts and Aharon, 1994). Conditions conducive to microbial methanogenesis occur between 10s of metres to 1 km below the seabed (Irwin et al., 1977). As such, the enriched $\delta^{13}C$ values in the Urenui bulbous concretions could be interpreted as derived from the CO_2 left over from the microbial production of methane during shallow burial (10s of m to 1 km) of the sediment pile.

Table 2. Carbon isotope values of carbonate cement in relation to carbon source, burial diagenetic zone, subsurface depth, and chemical reactions at the time of precipitation. Modified from Irwin et al. (1977) and Roberts and Aharon (1994).

Zone	Processes	Depth beneath seafloor (m)	Carbon source	$\delta^{13}C$ ‰ PDB of precipitated carbonate
Sulphate reducing	Anaerobic oxidation of methane via methanotrophic Archaea and sulphate-reducing Bacteria $CH_4 + SO_4^{2-} \Rightarrow HCO_3^- + H_2O + HS^-$	0.01 - 10	Microbial methane	-80 to -50
			Thermogenic methane	-50 to -25
Methanogenic zone	Anaerobic bacterial methanogenesis $2CH_2O \Rightarrow CH_4 + CO_2$	10 - 1000	CO_2 byproduct of methane production	-10 to +15

Alternatively, intensive methane oxidation may also result in enriched carbon isotope values. Microbial methane has $\delta^{13}C$ values from –110 to –50‰ PDB and thermogenic methane from –50 to –20‰ PDB (Whiticar, 1999). As methane is oxidised, the residual methane pool becomes more enriched in $\delta^{13}C$ due to isotope fractionation (Coleman et al., 1981; Whiticar, 1999; Pancost et al., 2000; Cowen et al., 2002). Oxidation of 80% of the methane pool can enrich the residual methane pool by 10–30‰, while oxidation of 99% of the pool would do so by 20–60‰ PDB (Whiticar, 1999). Therefore, oxidation of 80% of a thermogenic methane pool ($\delta^{13}C$ –50 to –20‰ PDB) can result in the residual methane having a $\delta^{13}C$ signature between –40 and +10‰. Additionally, the oxidation of microbial methane can result in $\delta^{13}C$ signatures of the residual methane pool identical to that of thermogenic methane. Such processes may naturally cause difficulty in accurately identifying the source of methane (Coleman et al., 1981).

Biomarker compounds in the Urenui pipe concretions include pentamethyl icosane (PMI) and archeol indicative of anaerobic oxidation of methane (AOM) consortia, and C33 dialkyl glycerol diether (DGD) and macrocyclic diether (MD) indicative of sulphate reducing bacteria in AOM consortia (Pearson et al., 2008). In comparison, the host mudstone does not contain PMI or MD and only traces of archaeol and DGD. Although the $\delta^{13}C$ values of carbonate are dominantly positive, the AOM markers are all very ^{13}C-depleted and confirm that AOM by methanotropic Archaea and sulphate reducing Bacteria was occurring in the

sediments (Pearson et al., 2008). Unfortunately, the Urenui bulbous concretions had very low lipid recovery and it was not possible to determine if they too were influenced by AOM.

5.1.2 Oxygen

Oxygen isotope values recorded in authigenic carbonate relate mainly to the fluid composition at the time of carbonate precipitation and the temperature of precipitation (Longstaffe, 1987), unless recrystallised. Based on the volume of carbonate cement in the Urenui tubular concretions (50-85%), precipitation likely occurred at < 300 m of burial, with higher volumes nearer to the seafloor (Boggs, 1992; Bjørlykke, 1998). However, a majority of the concretions have minus cement porosities >70% and therefore probably formed very near the seafloor in highly permeable and relatively uncompacted, loose sediments, probably <100 m.

Fluid compositions at the time of carbonate precipitation can be constrained in terms of their formation temperature and source based on the equations from Friedman and O'Neil (1977) for calcite (Fig. 14A) and from Fritz and Smith (1970) for dolomite (Fig. 14B). If upper slope bottom water temperatures were in the range of 5–10˚C (Ridgway, 1969), and precipitation occurred near the seafloor (assuming <100 m burial), then temperatures during carbonate precipitation ranged between 5 and 13˚C assuming a geothermal gradient of 30˚C/km (King and Thrasher, 1996). For the purpose of this discussion, a temperature of 10˚C will be used as an average and to account for slightly elevated temperatures below the surface. Feary et al. (1991) suggested that Miocene marine water in New Zealand had an average $\delta^{18}O$ of –0.7‰ SMOW. The $\delta^{18}O$ values of the Urenui tubular concretions are slightly depleted to significantly enriched ($\delta^{18}O$ from –2 to +5‰ PDB) compared to New Zealand marine waters in the late Miocene (Fig. 14). Based on these conditions, carbonate precipitated in equilibrium with New Zealand Miocene seawater at 10˚C would have $\delta^{18}O_{calcite}$ values near 0‰ PDB, and $\delta^{18}O_{dolomite}$ values near +3‰ PDB. Therefore, calcite and dolomite samples near these values can be interpreted as forming from normal marine fluids.

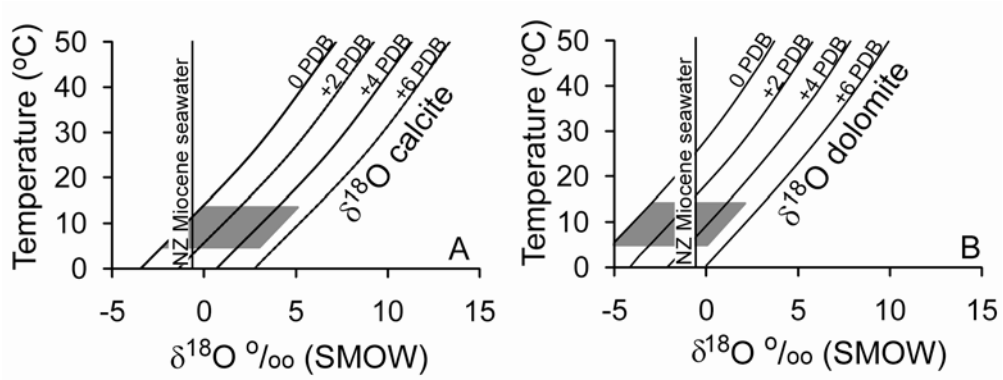

Figure 14. Possible water compositions (SMOW) responsible for carbonate precipitation in the Urenui mudstone. The grey polygons mark the range of water composition responsible for the formation of (A) calcitic pipes and (B) bulbous dolomitic concretions in the subsurface from 0 to 100 m burial and 5–13˚C. Calcite equilibrium calculation from Friedman and O'Neil (1977) and dolomite equilibrium calculation from Fritz and Smith (1970).

However, calcite and dolomite samples with $\delta^{18}O$ values less than 0 and +3‰ PDB for calcite and dolomite, respectively, are depleted, while those with higher values are enriched with respect to seawater.

The slightly depleted oxygen values (groups 1a and 2a) could be explained by carbonate precipitation associated with higher temperatures. Elevated temperatures could have been encountered nearer to the seafloor if burial fluids quickly ascended and did not have time to cool to temperatures of the surrounding environment before carbonate precipitation occurred, an explanation invoked elsewhere by De Boever et al. (2006). Therefore, rapid ascent of warmer fluids could explain the pipe concretions with lower $\delta^{18}O$ values which have been interpreted to have formed in <100 m burial. An alternative interpretation for the depleted $\delta^{18}O$ values in the tubular concretions could be due to gas hydrate formation. During gas hydrate formation, the heavier oxygen molecule is preferentially accepted into the clathrate molecule, thereby leaving the remaining fluids anomalously depleted in $\delta^{18}O$ (Davidson et al., 1983; Ussler and Paull, 1995).

The slightly enriched oxygen values (groups 1b and 2b) could be explained by carbonate precipitation associated with (1) lower temperatures; (2) evaporation; (3) clay dehydration; or (4) gas hydrate dissociation. The most enriched dolomite sample (near +4.5‰ PDB) could have precipitated at about 4˚C, however these temperatures are almost too low for upper slope conditions. Additionally, temperatures near 0˚C are necessary to account for the most enriched calcite samples, which are probably unreasonable. Evaporative conditions in the subsurface environment are unlikely, and any burial transformation of clays is unlikely to have occurred before the shallow burial precipitation of carbonate in the Urenui concretions. Moreover, clay dehydration as a source of enriched oxygen is also unlikely as Nelson and Hume (1977) determined that the illite and smectite in the Urenui mudstone were detrital and not diagenetically formed. It is possible that enriched oxygen from clay transformation could have been introduced into the pore waters of the Urenui mudstone from deeper ascending fluids. However, if the source fluids for carbonate precipitation were enriched in

oxygen due to clay transformation, then it is difficult to envisage why the calcitic pipe concretions do not record similarly enriched $\delta^{18}O$ values. Based on these arguments, clay transformation is a difficult mechanism to support for the $\delta^{18}O$ enrichment in the bulbous concretions. Consequently, the favoured explanation for enriched $\delta^{18}O$ values in the concretionary carbonates is the dissociation of gas hydrates. During gas hydrate formation, heavy oxygen is preferentially accepted into the hydrate molecule, and upon dissociation of large volumes of gas hydrates, it is released into sediment pore fluids (Davidson et al., 1983; Ussler and Paull, 1995).

5.1.3 $\delta^{13}C$ vs $\delta^{18}O$ groupings

When plotted on a $\delta^{13}C$ vs. $\delta^{18}O$ diagram, the isotope signatures of the Taranaki tubular concretions fall into three main groupings (groups 1, 2, and 3; Fig. 12). Each group represents carbonate precipitation under different fluid compositions and carbon sources. Their interpretations are summarised here based on the discussions in Sections 5.1.1 and 5.1.2.

The carbon and oxygen isotope compositions of group 1a display strongly depleted $\delta^{13}C$ values and slightly depleted $\delta^{18}O$ values. Group 1a values coincide with calcitic pipes (Fig. 12). The carbon isotope signatures are indicative of oxidised methane (Table 2) (Roberts and Aharon, 1994) which is supported by the lipid biomarker evidence (PMI and archeol) for AOM from the pipe concretions. The fluid compositions were influenced either from hotter ascending fluids from depth mixing with seawater or gas hydrate formation in fluids of marine composition. As group 1b and group 2b concretions are enriched in oxygen isotope values supporting gas hydrate dissociation (see below), it is more likely that group 1a concretions precipitated from fluids influenced by the formation of gas hydrates.

Group 1b consists of a few calcitic pipe concretions with similar carbon isotope signatures as group 1a ($\delta^{13}C$ –45 to –25‰ PDB), and thus the same carbon source. However, the oxygen isotope signatures of group 1b are enriched ($\delta^{18}O$

+0.5 to +3‰ PDB) compared with group 1a. Based on calcite equilibrium calculations, the oxygen isotope values for group 1b nearer to 0‰ PDB reflect carbonate precipitated from marine waters (Fig. 14A). The more enriched oxygen isotope values (up to +2.5‰ PDB) indicate ^{18}O-enriched fluids due to gas hydrate dissociation.

The group 2a carbon and oxygen isotope category has ^{13}C-enriched (–10 to +11‰ PDB) and ^{18}O-depleted (+0.2 to +3‰ PDB, with respect to marine water) isotope values (Fig. 12). The concretions are primarily bulbous in morphology and dolomitic in composition, with several having irregular morphologies, and a few encompassing calcitic pipes which are slightly depleted in carbon with respect to the bulbous concretions. The carbon incorporated into the carbonate cement is interpreted to be sourced either from residual CO_2 produced as a by-product of methanogenesis or extensive methane oxidation. The depleted oxygen isotope values indicate group 2a concretions formed from fluids influenced by gas hydrate formation as in group 1a (Fig. 14B).

Group 2b tubular concretions have the same morphology, mineralogy, and carbon isotope values as group 2a and thus the same carbon interpretation. However, group 2b concretions have ^{18}O-enriched (+3 to +5‰ PDB) isotope values (Fig. 12). The enriched oxygen isotope values are consistent with group 2b concretions forming from fluids influenced by gas hydrate dissociation (Fig. 14B). Formation scenarios are discussed in Sections 6.2 and 6.3.

The isotope compositions of group 3 carbonates comprise calcitic fracture and conduit fills of tubular concretions (3a), calcitic irregular morphologies (3b), and spherical concretions (3c, Fig. 12). Group 3a carbonate cements have carbon isotope values near 0 ($\delta^{13}C$ –0.5 to +1.1‰ PDB) and depleted oxygen isotope values ($\delta^{18}O$ –6.0 to –5.3‰ PDB). They are interpreted to have precipitated following cessation of methane migration from dissolved marine shell material in diagenetic pore waters at burial temperatures near 40^{o}C (approximately 1km burial depth) (Fig. 14A).

Group 3b carbonate cements have $\delta^{13}C$ values from +0.6 to +3.1‰ PDB and depleted $\delta^{18}O$ values from –4.6 to –1.8‰ PDB, and are interpreted to have precipitated from carbon contributed from methanogenesis and relatively warmer fluids (Fig. 14A). Whether they formed at depth or near the seafloor is unclear; however, their calcitic composition suggests a closer affiliation to the seafloor than that of group 2 carbonates. Depleted oxygen isotope values indicate fluid temperatures between 20 and 30^{o}C (Fig. 14A). These temperatures may support formation either at burial depths of approximately 500 to 750 m (Fig. 14A), or nearer to the seafloor from fast ascending burial fluids which did not have time to fully re-equilibrate to surrounding temperatures (cf. De Boever et al., 2006).

Group 3c carbonate cements have similar isotope signatures to group 3b, although their carbon isotope values are slightly less positive ($\delta^{13}C$ = +0.5 to +1.7‰ PDB cf. +0.6 to +3.1‰ PDB). Thus, they are interpreted to have precipitated under similar conditions as group 3b but with less influence from methanogenic carbon and more carbon sourced from dissolved marine shell material. Fluid composition at the time of carbonate precipitation was likely derived from burial fluids near 25^{o}C at depths near 600 m (Fig. 14A) or under shallower burial conditions from ascending warmer fluids re-equilibrating with surrounding pore fluids.

The few concretions falling outside the main groups are interpreted to reflect a degree of mixing of the end member groups (Fig. 12). Those falling to the right side of the diagram between groups 1 and 2 suggest mixing of residual methanogenic carbon with oxidised methane and enriched fluids. Those falling to the left side of the diagram are situated between groups 1 and 3 and suggest mixing of multiple carbon sources (oxidised methane, marine shell material, and methanogenic carbon) from slightly warmer fluids. These mixing zones reflect a dynamic system which was changing over time.

5.2 Plumbing system of a hydrocarbon seep field

Recent literature has described irregular concretionary bodies in mudstones interpreted to be associated with cold seeps. The concretionary bodies have been variously referred to as tubular concretions, pipes, chimneys, doughnuts, circular-pipe-like cavities, cylindrical concretions, and other names, all having a central hole or conduit running the length of the concretions, which may be filled with sediment or cements (e.g., Kulm and Suess, 1990; Jensen et al., 1992; Orpin, 1997; Aiello et al., 1999, 2001; Lédesert et al., 2003; Mazzini et al., 2003; Clari et al., 2004; Conti et al., 2004; Conti and Fontana, 2005; De Boever et al., 2006; Campbell et al., 2008). In the majority of cases, the size of these concretionary bodies is measured in centimetres to a few tens of centimetres, exceptions being examples from Kattegat, Denmark (Jensen et al., 1992), Gulf of Cadiz, Portugal (Díaz-del-Río et al., 2003), Bulgaria (De Boever et al., 2006), and New Zealand (Lédesert et al., 2003; Nyman et al., 2006), where the tubular features are unusually large (up to 10 m or more in length and 4 m in diameter).

5.2.1 Tubular concretions versus chimneys

The Urenui Formation hosting the tubular concretions is a slightly calcareous (<5%) siliciclastic mudstone whose carbonate content is derived primarily from contained microfossils. In comparison, the tubular concretions differ only in their much higher content of carbonate (50−85%) derived from the precipitation of micrite or microsparite cement between the siliciclastic grains (Fig. 10A-D). The presence of micrite cementing siliciclastic grains in the tubular concretions confirms that they developed within sediments in the subsurface.

In the literature, similar tubular shaped carbonate structures most commonly have been referred to as chimneys (e.g., Orpin, 1997; Peckman et al., 2001; Díaz-del-Río et al., 2003; De Boever et al., 2006) or tubular concretions (e.g., Clari et al., 2004). The term chimney can be confusing as the name is associated with hydrothermal vents and seismic lines. In hydrothermal settings, a chimney is used to describe mineral precipitation (e.g., anhydrite, iron, manganese hydroxides,

silica, sulphides, pyrite, barite, calcite, and others) above the seafloor in the water column around the venting fluids (Judd and Hovland, 2007). Seismic chimney is a term used to describe the identification of upward migration of fluids in the sediment column in a seismic line (e.g., Gay et al., 2006).

As such, the term chimney can be misleading and a clearer definition is warranted in the seep carbonate literature. By definition, concretions form by mineral precipitation within the pore spaces of sediment in the subsurface (Gautier and Claypool, 1984; McBride et al., 1995). As such, it is recommended that any tubular structure including a centralised conduit that has formed by carbonate precipitation within host sediment should be referred to as a tubular concretion. Where appropriate, morphological varieties can be further defined (e.g., Fig. 7).

5.2.2 Tubular concretions as subsurface markers of fluid migration

The morphologies, position in outcrop, presence of central conduits, and stable carbon and oxygen isotope compositions of the Taranaki tubular concretions suggest that they formed from cement precipitation around focused migration pathways of methane rich fluids in marine pore waters influenced by episodes of gas hydrate formation and dissociation. As these fluids migrated towards the surface and encountered appropriate chemical environments, carbonate precipitation occurred along the boundaries of these pathways. Consequently, the tubular concretions are interpreted to reflect a shallow sub-seafloor plumbing network of a Taranaki cold seep system where methane rich fluids/gases migrated upwards along directed pathways toward the Urenui seabed in the late Miocene. Thus they provide a unique opportunity to examine the subsurface fluid migration development of an ancient cold seep system.

6. Late Miocene Taranaki cold seep system

6.1 Controlling factors of fluid migration

Methane migration begins with a source for hydrocarbons and conditions conducive to upward fluid migration. In Taranaki Basin, sources for microbial methane were likely organic rich sediments beneath the Urenui mudstone which had not yet reached thermal maturity. Thermogenic methane may have been sourced from deeper formations, such as the late Cretaceous Rakopi and Paleocene Waipawa deposits (Fig. 3) within the zone of thermal cracking of oil to gas.

Hydrocarbon generation, seismic activity, and/or changes in stress fields due to tectonic activity were likely conditions in Taranaki Basin during the late Miocene (King and Thrasher, 1996). Such conditions generally result in overpressured sediments which leads to density inversion initiating the upward migration of fluids (Judd and Hovland, 2007). The fluids may then preferentially migrate along more permeable pathways such as faults, joints, and permeable sediment layers. In addition, if the overpressured sediments exceed their confining pressures, microfissures will be produced. The fissures then become preferential focused pathways for migrating fluids through otherwise impermeable sediments.

Many examples of tubular concretions have been documented adjacent to major fault zones (Kulm and Suess, 1990; Jensen et al., 1992; Peckmann et al., 2002; Diaz-del-Rio et al., 2003; Schwartz et al., 2003; Conti et al., 2005; De Boever et al., 2006). In areas of the East Coast Basin of New Zealand, tubular concretions are situated along the strike of, and within, linear fractures, demonstrating that faulting and jointing play a significant role in preferential fluid migration pathways (see Chapter 5) (Nyman et al., 2006). The Taranaki Fault is a major thrust fault in the region, oriented north-south and bordering the eastern margin of the basin (Fig. 2). Although it has no surface rupture, interestingly it strikes directly below the Urenui tubular concretion occurrences (Fig. 2), which may indicate a positive genetic link between the Taranaki Fault system and focused

fluid migration associated with a late Miocene cold seep system and formation of the tubular concretions. While movement along the northern sector of the Taranaki Fault (north of the Taranaki Peninsula) had ceased by the middle Tongaporutuan, a rejuvenated phase of movement occurred in the upper Tongaporutuan in the onshore and southern sectors of the fault that was associated with broad scale regional uplift (Vonk and Kamp, 2008). This uplift phase post-dated deposition of the Urenui Formation. Such conditions would likely have been conducive to dewatering of fluid rich marine sediments and subsequent upward migration of fluids. During the late Miocene (late Tongaporutuan), the uplift continued, resulting in a localised regression and influx of sediment which may have influenced gas hydrate dissociation. This regional inversion event (SCTIP; the late Miocene Southern and Central Taranaki Inversion Phase of Vonk and Kamp, 2008) within the Taranaki Basin during the Tongaporutuan may have provided the appropriate structural regime for the Taranaki Fault and other minor faults within the region to serve as potential migration pathways for escaping fluids.

Following initiation of fluid migration, ascending methane rich fluids would have eventually reached the shallow subsurface (less than 500 m). The Urenui tubular concretions are hypothesised to have formed from ascending microbial and/or thermogenic methane via a scenario discussed in some detail in Section 6.3.

6.2 Role of gas hydrate dissociation

It is well documented in the literature that the dissociation of gas hydrates releases enriched oxygen into pore waters, because heavy oxygen is preferentially accepted into the hydrate molecule (Davidson et al., 1983; Ussler and Paull, 1995). Seep carbonates precipitating under such influences may record these events in their oxygen isotope signatures (Greinert et al., 2001; Aloisi et al., 2002; Clari et al., 2004; Pierre and Fouquet, 2007). However, most previous studies documenting enriched $\delta^{18}O$ values in such carbonate precipitates have done so in association with strongly negative $\delta^{13}C$ values reflecting oxidised microbial or thermogenic methane sources. To my knowledge, only one other study has

suggested that enriched $\delta^{13}C$ values and enriched $\delta^{18}O$ values can also result from methanogenic conditions and hydrate dissociation. That study reported dolomitic seep related carbonates (layers, nodules with conduits, and chimney structures) from the Lorca Basin, Mediterranean with $\delta^{13}C$ and $\delta^{18}O$ isotope values mainly above zero (Pierre et al., 2002; Pierre and Rouchy, 2004). However, these authors did not provide a mechanism to explain how carbonate precipitation utilising residual reduced CO_2 from methanogenesis and heavy oxygen from the hydrate molecule fails to incorporate the light carbon of the CH_4 from the former hydrate molecule. A possible mechanism is suggested in the following Section 6.3.

6.3 Tubular concretion formation scenario

The main tubular concretion formation scenario presented here is based on utilising residual CO_2 from methanogenesis as the source for the dolomitic bulbous concretions and methane oxidation as the source for the calcitic pipe concretions (Fig. 15, for reader convenience occurs as a foldout on pg. 139). In this scenario, microbial methane is used. However, an alternative which also discusses thermogenic methane, is presented in Section 6.3.5. The fluid compositions were influenced by episodes of gas hydrate formation and dissociation.

6.3.1 Stage 1 (Fig. 15A, pg. 139)

Following the initiation of fluid migration, microbial methane and the by-products of methanogenesis (CO_2) eventually reach temperature and pressure regimes conducive to gas hydrate formation, ca. < 500 m burial (Fig. 15A). Methane hydrate formation initiates at the base of the hydrate stability zone (HSZ) where light methane and water (utilising heavy oxygen, Fig. 15E) are incorporated into the hydrate molecule. However some methane will pass through the HSZ and continue to ascend. Remaining in the pore water is the residual CO_2 from methanogenesis (heavy carbon), pore waters that are anomalously ^{18}O-depleted with respect to the burial environment, and additional methane (light carbon) that

did not form hydrates. Near the seafloor, methane is oxidised via AOM which increases alkalinity and induces carbonate precipitation.

During the onset of fluid migration in stage 1, high fluid pressures and buoyancy result in focused, straight migration pathways. Additionally, the near seafloor environment should have high sulphate concentrations and Ca/Mg ratios. As AOM begins, calcitic pipes develop, reflecting the high Ca/Mg ratios and high fluid pressures. $\delta^{13}C$ values between −40 and −25‰ PDB reflect microbial methane oxidation mixed with residual methanogenic CO_2 and depleted $\delta^{18}O$ values reflect pore waters influenced from hydrate formation (isotope group 1a).

6.3.2 Stage 2 (Fig. 15B, pg. 139)

Continued AOM lowers the methane and sulphate concentrations. Lowered methane concentrations in the fluids reduce pressure and in turn buoyancy, resulting in more tortuous fluid migration pathways. Additionally, the Ca/Mg ratio is lowering due to continued calcite precipitation which eventually leads to dolomite precipitation being favoured over calcite. These late stage conditions within the system form dolomitic tubular concretions with morphologies ranging from pipes to more sinuous and tortuous bulbous concretions. Tubular concretions formed during this stage will record increasingly enriched carbon isotope values as methane is no longer available and only methanogenic CO_2 remains. The oxygen isotope values remain depleted reflecting continued hydrate formation (isotope group 2a).

6.3.3 Stage 3 (Fig. 15C, pg. 139)

At some later stage, relative seabed uplift (probably slope failure as indicated by the truncated tubular concretions along channel margins and tubular concretions present in basal channel fills; see Section 6.5) shifts the HSZ so that hydrate which is no longer within this zone begins to dissociate. Pore fluids become enriched due to heavy oxygen released from the clathrate molecule. Fluid pressure and buoyancy increase due to the injection of methane released from the

hydrate. Methane and ^{18}O-rich fluids ascend towards the seafloor. As in stage 1, methane is oxidised and due to high fluid pressures, and increased sulphate concentrations and Ca/Mg ratios (due to sediment removal and contact with seawater), calcitic pipe concretions form. However, unlike stage 1, the oxygen isotopes recorded in the pipe concretions are slightly enriched as a result of hydrate dissociation (group 1b, Fig. 12). If slope failure occurred, some pipe concretions could have been transported down slope and deposited in channel-axis conglomerate. Although it cannot be determined whether slope failure was caused by tectonic uplift, sediment deposition increasing the angle of the slope, fluid injection into shallow sediments, or gas hydrate dissociation, their interrelationships suggest they may all be related to some extent.

6.3.4 Stage 4 (Fig. 15D, pg. 139)

As in stage 2, continued AOM lowers methane and sulphate concentrations, and continued carbonate precipitation lowers the Ca/Mg ratio leading eventually to dolomite precipitation being favoured over calcite precipitation. Lowered methane concentrations in the fluids reduce pressure and in turn buoyancy, resulting in more tortuous fluid migration pathways. These late stage conditions within the system form dolomitic tubular concretions with both enriched carbon and oxygen isotope values (isotope group 2b) and morphologies ranging from pipes to more sinuous and tortuous bulbous concretions.

6.3.5 Alternative scenario

An alternative to the hypothesised scenario discussed in Sections 6.3.1 through 6.3.4 is that extensive oxidation of methane could have resulted in similar carbon isotope trends to that involving mixing of microbial methane and residual methanogenic CO_2. Also, if methane concentrations were lowering due to hydrate formation and methane oxidation, then theoretically extensive oxidation should take place. If extensive oxidation was the cause of carbon isotope enrichment, then methane was more likely to have been of thermogenic origin as less oxidation would need to have occurred to account for the large shift in carbon

isotope values (e.g., Table 2). Of course, extensive oxidation coupled with methanogenic CO_2 (which was likely present if the methane source was microbial) could also account for the large isotope shift.

6.4 Concretion growth patterns

The relatively high content of carbonate in the tubular concretions (50−85%) compared to the host mudstone (<5%) is present as micrite or microsparite carbonate cement that was precipitated within interparticle spaces of the muddy sediment beneath the paleo−seafloor. Unlike widely known (sub)spherical concretions in which cement precipitation initiates about some nucleation site such as decaying organic matter or shell fragments, and thereafter continues to precipitate in a concentric, centre-to-margin growth pattern (e.g., McBride et al., 1995), there is no “solid” nucleation centre in the Urenui tubular concretions; rather they mainly support open conduits. It appears that the nucleation site was about that “core” of sediment subjected to focused fluid flow, so that the initial precipitation of carbonate formed a jacket or pipe containing this flow (Fig. 16A,B). Additionally, the methane rich fluids need a source of oxygen for the methane to be oxidised, which is supplied from the pore waters. As the methane rich fluids are migrating along focused pathways, the first fluids in contact with oxygenated waters will be on the outer boundaries of the migrating fluids. Consequently, it is proposed that cement precipitation began at the outer margins of a tubular concretion and then continued to precipitate inwards towards the central conduit (Fig. 16A-D), potentially leaving an empty conduit if flushed of sediment (Fig. 16E). Following concretion formation, later generation cements or sediment may partially to completely fill the conduit void space (Fig. 16F-H). This kind of scenario involving “outside to inside” precipitation to form tubular concretions is also how Clari et al. (2004) interpreted similar kinds of concretionary features inside an Italian Miocene mud volcano.

The pattern of tubular concretion growth is regarded as similar for both pipe and bulbous concretions, with cement precipitation beginning towards the outer boundaries of the migrating fluid (Fig. 16A,B). Assuming a more or less constant

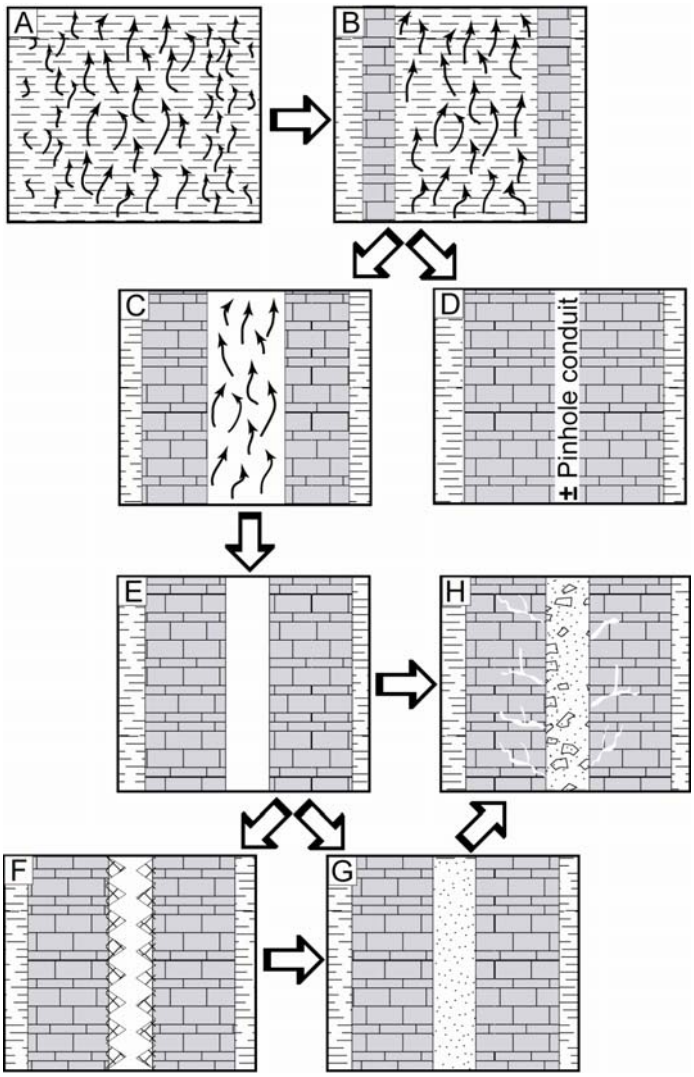

Figure 16. Postulated growth patterns for tubular concretions. (A, B) During stages A and B of pipe concretion formation, focused fluid 'plumes' ascend through the sediment and carbonate precipitation begins towards the outer margins of this flow. (C) Over time, fluid migration could eventually evacuate sediment from the increasingly restricted conduit. (D) Alternatively, if fluid pressures are not high enough, sediment may not be ejected and carbonate precipitation may continue inward leaving no apparent conduit or only a pinhole conduit. Phases A, B, and D also apply to bulbous concretion formation, in which case, during the final stages of D the pinhole conduit may close, leaving a fine network of unconnected open vugs in the vicinity of the central axis of the concretion. (E) Represents cessation of methane migration and (F) subsequent lining of the conduit with crystalline calcite precipitating from later (e.g., burial) diagenetic fluids. (G) Additionally, after the fluid source becomes cut off, or exhausted, sediments from above may infill the conduit. (H) If fluid was re-established, then the conduit could also become infilled with foreign sediments from below. Continued fluid migration with sediment and/or cement infilling of the conduit would restrict flowage and potentially result in hydrofracturing and/or brecciation of the conduit material.

volume of fluid is passing through the sediments, then flow rates would increase with continued precipitation due to increased pore pressures (Fig. 16B,C). As the flow rates increases, sediment may be mobilised and evacuated from the central migration pathway, creating an open conduit (Fig. 16C). If, however, fluid flow rates are insufficient to expel sediment, cement may continue to precipitate inwards leaving a largely cemented (concreted) sediment conduit instead of an open hole, or perhaps only a "pinhole" (Fig. 16D). Nonetheless, if sediment is evacuated from the central flow pathway (Fig. 16C,E) then the resulting conduit may subsequently become variably filled by different mechanisms: (1) Cement may precipitate from solution along the conduit walls (Fig. 16F) and could eventually fill the conduit. The cements may be sourced from either methane rich fluids or later diagenetic burial fluids. (2) Fluids may transport sediment from below into the migration pathway, essentially obstructing the conduit, or sediments from above may collapse into the conduit if fluid rates/volumes are reduced (Fig. 16G). (3) As conduits become closed off due to cementation or sediment infill then, assuming continued flow rates, pressures in the conduit system will increase resulting in hydrofracturing and breccia clasts (Figs. 8E,F, 11A).

6.4.1 Hydrofracturing

Carbonate cemented veins radiating from the central conduit outward into the concretion body indicate progressive cement precipitation closing off fluid diffusion pathways within the tubular concreted body (Fig. 10F-H). Breccia clasts within conduits vary in size, often displaying a jig-saw-like pattern, indicating that the broken clasts were once entire. Multiple jig-saw clasts, clasts broken away from the conduit wall, and multi-generational cements surrounding the clasts indicate hydrofracturing caused by increasing pressure regimes in the conduit as the fluid diffusion pathways were sealed by previous cement precipitation (Fig. 11). Hydrofracturing of the central conduit or concretionary material may also reflect a sudden release of fluids under high pressures, such as the blow out pipes described by Judd and Hovland (2007). Previous studies have also linked breccia

clasts to gas hydrate dissociation (Bohrmann et al., 1998; Suess et al., 1999; Greinert et al., 2001).

6.5 Continental margin instability

6.5.1 Slope channels

King et al. (2007) described the deep-water clastic successions of the Mount Messenger and Urenui Formations exposed along the coastline in northern Taranaki Basin. Within that study, the three channel units of the Urenui Formation were described in detail, as summarised herein (Figs. 5, 18A). The Urenui Formation includes at least three large seismic scale channels cut within its background hemipelagic mudstone facies (Figs. 4, 5, 17, 18). They are located north of Wai-iti, south of Waitoetoe (referred to as the Mimi channel in King et al., 2007), and at Waiau (Fig. 2). In outcrop, channel thickness is 30−65 m, but they are inferred to have a total thickness up to 100 m as their base or top is not exposed (King et al., 2007). The channels are slope channels, through which more proximal sediments were transported to the basin, and then became backfilled.

Wai-iti channel is the oldest and depositionally deepest of the channels in the Urenui sequence, located along the late Miocene mid- to upper slope at about 800 m water depth (Fig. 5, 18, 19). *In situ* tubular concretions in the slope mudstone are cut off by the channel. The lowest part of this channel fill comprises a 5 m thick conglomerate that thins laterally and pinches out along the northern margin of the west flowing channel and interfingers with channel sandstones (Fig. 17). The conglomerate is a pebble to cobble deposit that is fossil rich and contains mass transported tubular pipe concretions. It is interpreted to represent the lag deposits from an initial slope failure event (King et al., 2007). Above the conglomerate, the main channel fill comprises thick bedded sandstone with thin beds of siltstone interpreted to have backfilled the channel during later deposition (King et al., 2007).

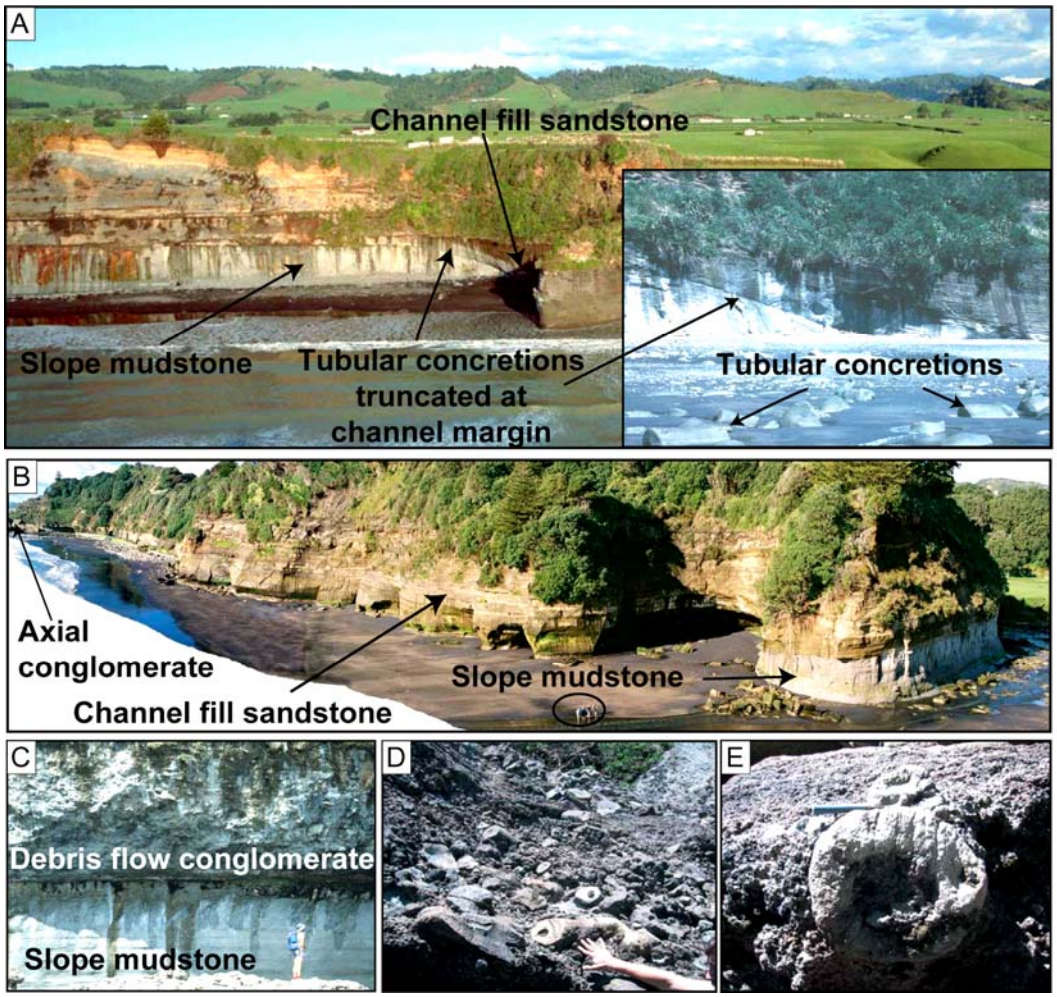

Figure 17. Waiau and Wai-iti channels and channel facies in the Urenui Formation. (A) The Waiau channel fill sandstone truncating tubular concretions in the Urenui slope mudstone. (B) The channel fill sandstone of the Wai-iti channel. The incised slope mudstone can be seen on the far right side of the photograph, and the Whakarewa Conglomerate fill (King et al., 2007) occurs in the distant left, marked axial conglomerate. (C) Contact between the Whakarewa Conglomerate and slope mudstone, and (D-E) close-up view showing reworked, mass emplaced pipe concretions as part of the axial fill of the Whakarewa Conglomerate. Photographs A, B, and C kindly supplied by Peter King, GNS Science.

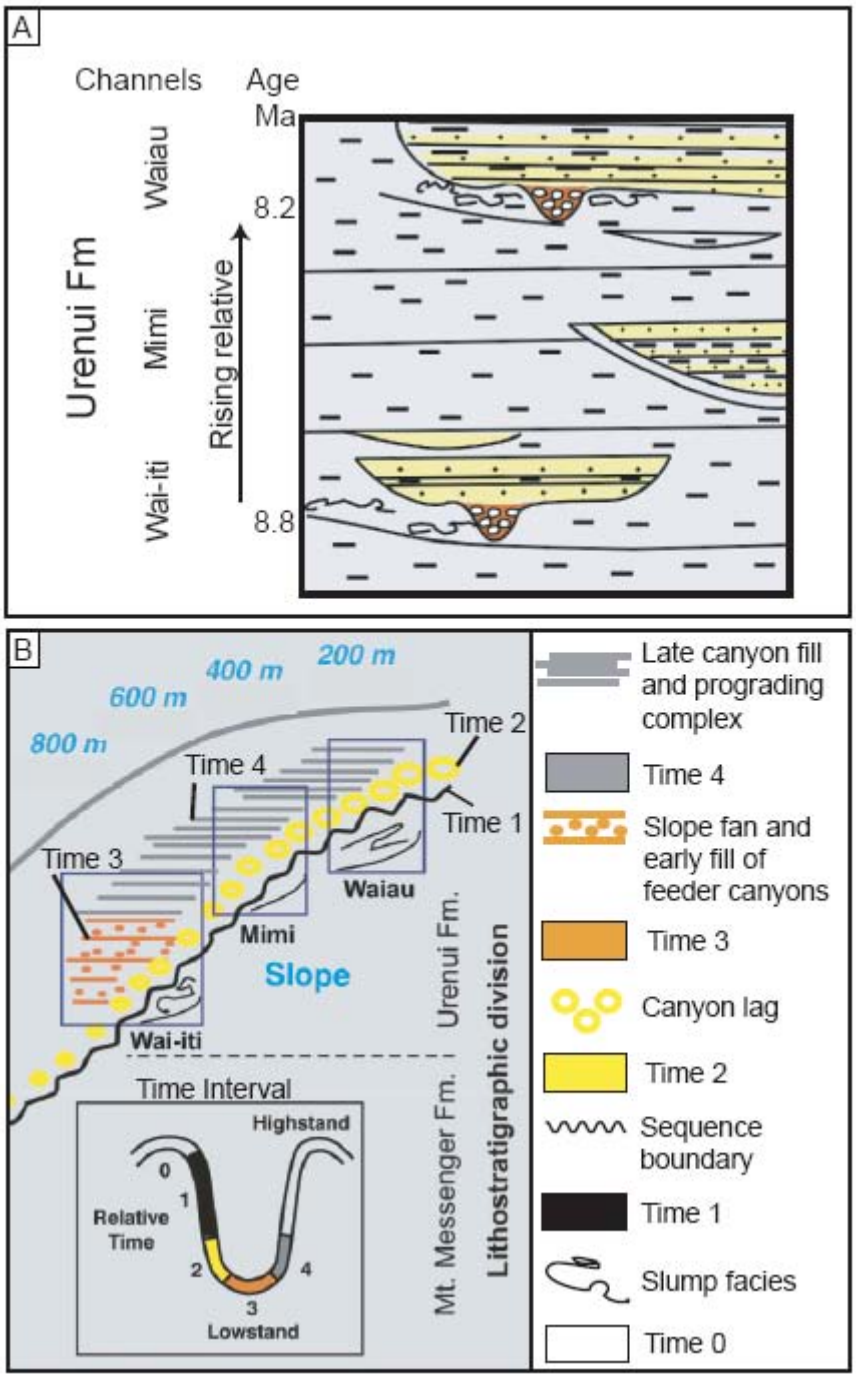

Figure 18. Schematic diagram of the three channel units in the Urenui Formation (see also Fig. 5). Time 0 represents the initiation of slope failure and the slump facies during a sea-level highstand. Time 1 represents a sequence boundary and regression. Time 2 follows with canyon lag, and time 3 with fill of the canyons during a sea level lowstand. Time 4 represents late canyon fill and progradation during transgression. See Section 6.5 for explanation (modified from King et al., 2007).

The Waitoetoe channel (Mimi channel of King et al., 2007) developed along the upper slope in approximately 400 m paleo-water depth and is located stratigraphically above the main occurrence of tubular concretions at the Mimi section. Unlike the Wai-iti channel, the Mimi channel is not filled with slump or conglomerate deposits. The Mimi channel deposits comprise thin bedded, parallel, wavy and ripple laminated sandstones that pinch out or onlap the channel margin (Figs. 17, 18). In the siltstone directly beneath the channel are *in situ* tubular pipe concretions truncated by the channel margin (Fig. 17A).

The Waiau channel is situated along the shelf break in approximately 200 m paleo-water depth and is the most proximal of the Urenui channels (Fig. 18). It is similar to the Wai-iti channel as it comprises a mass transported complex within slope mudstone containing tubular concretions, followed by a conglomeratic fill from the base of the channel, overlain by interbedded sandstone and siltstone.

6.5.2 Channels and slope failure

The three slope channels in the Urenui Formation have distinct similarities. Stratigraphically below each channel are *in situ* tubular concretions which represent subsurface fluid migration pathways. At the base of the Wa-iti and Waiau channels are slump intervals indicating slope instability and mass transport of sediments downslope. Additionally, the basal conglomerates in these two channels include mass transported tubular concretions. These associations strongly suggest there is a connection between subsurface fluid migration and slope instability. High sedimentation rates (750 m/m.y.) during the Miocene along a steep slope could have increased instability. Fluid migration into these sediments also would have increased instability as pore fluid pressure increased (King et al., 2007). The occurrence of tubular concretions throughout the section, below, between, and mass emplaced within two of the Urenui channels, suggests ongoing fluid migration, and periodic slope failure throughout the depositional history of this interval of Urenui sedimentation.

6.5.3 Influence of gas hydrates and slope instability

The isotope evidence recorded in the tubular concretions (Fig. 12, Sections 4.3 and 5.1) and the association of reworked tubular concretions in the conglomerate channel fills of the Urenui Formation (Figs. 17, 18) are compatible with slope instability along the northern Taranaki margin in the late Miocene being influenced by gas hydrate dissociation. Hydrate dissociation in the Urenui Formation would have resulted in overpressuring due to the volume expansion from solid to gas phases, and potentially could have caused or triggered slope failure events. Rising pore fluid pressure resulting from gas hydrate dissociation can increase shelf margin/slope instability because of an associated decrease in the shear strength of the sediment (Crutchley et al., 2007).

Several studies have linked slope failure events with the presence of gas hydrates, for example, the Cape Fear slide, North Carolina (Popenoe et al., 1993), the Humboldt slide, northern California (Field and Barber, 1993), the Storegga slide, Norway (Bouriak et al., 2000), and more recently submarine slope failures on the Hikurangi Margin, New Zealand (Faure et al., 2006) and near Fiordland, New Zealand (Crutchley et al., 2007). Other examples are known (e.g., Paul et al., 1991; Suess et al., 1999; Locat, 2001; Pratson, 2001; Conti and Fontana, 2005; Conti et al., 2004). It is still unclear whether gas hydrate dissociation is a singular cause of slope failure or a trigger, but certainly it has a significant influence on slope destabilisation. The tubular concretions within the Urenui channel conglomerates are perhaps another example linking gas hydrate dissociation and slope instability.

6.6 Lack of paleoseep carbonates

A characteristic feature of Jurassic and younger cold seeps at the seafloor is the presence of chemosynthesis based fossil assemblages, including microbial fabrics, siboglinid tube worms, and solemyid, vesicomyid, lucinid, thyasirid, and bathymodiolin bivalves (Campbell, 2006). The shells of these biota, together with

precipitation of AOM derived authigenic carbonate cementing them into carbonate buildups, are often prominent sedimentary facies of cold seep systems.

In the case of the Urenui Formation, seafloor seep carbonate deposits are absent. This could be due to the fact that: (1) the migrating methane rich fluids never reached the seafloor; (2) the fluids reached the seafloor, but were short lived; (3) any developed seafloor seep carbonates were subsequently eroded; (4) seafloor seep carbonates remain to be found or exposed.

Consequently, at this stage it is impossible to rule out the possibility that seafloor seep carbonate deposits exist in the Urenui Formation. Certainly the evidence of slope failures, canyon cutting, and conglomerate channel fills containing tubular concretions all support that the ascending methane fluids likely reached the seabed, or nearly so.

7. Conclusions

1) Tubular carbonate concretions in late Miocene slope mudstones of the Urenui Formation in Taranaki Basin formed from shallow burial (<300 m) precipitation of micritic dolomite and calcite within siliciclastic mud.

2) The tubular concretions mainly exhibit pipe and bulbous morphologies, range widely in size (0.5 to 10+ m in length and 5 to 70 cm in diameter), and support a central open or sediment/crystalline spar filled conduit.

3) The Urenui tubular concretions demarcate shallow subsurface pathways of focused methane fluid ascent associated with a cold seep system on the late Miocene Taranaki continental margin.

4) As the tubular concretion occurrences in eastern Taranaki Basin are situated directly above the major Taranaki Fault, the fault is interpreted to be a major fluid escape pathway.

5) Stable carbon and oxygen isotope values for the carbonate cements in the tubular concretions plot in two distinct groups on a $\delta^{13}C$ vs $\delta^{18}O$ cross plot.

Group 1 consists of calcitic pipe concretions with $\delta^{13}C$ values from –40 to –26‰ PDB and $\delta^{18}O$ values from −2 to +3‰ PDB. Group 2 consists of dolomitic bulbous concretions with $\delta^{13}C$ values from –10 to +11‰ PDB and $\delta^{18}O$ values from +1 to +5‰ PDB.

6) The carbon isotope values in group 1 pipe concretions suggest that the carbon was derived from anaerobically oxidised methane, as supported by lipid biomarkers. The strongly enriched carbon isotope values in group 2 bulbous concretions indicate that carbon was sourced from either residual CO_2 from methanogenesis and/or from extensive oxidised methane where >80% of the methane had been oxidised by the time the bulbous concretions formed.

7) Oxygen isotope values in group 1 pipe concretions ($\delta^{18}O$ –2 to +3‰) are interpreted to have resulted from either variable temperatures of marine fluids or the $\delta^{18}O$ composition of the water being influenced by cycles of formation and dissociation of gas hydrates. Gas hydrate formation is favoured for group 1a and 2a concretions. Oxygen isotope values in group 1b and 2b concretions are interpreted to have resulted from gas hydrate dissociation. Tubular concretion samples near marine compositions precipitated from marine fluids between episodes of hydrate formation and dissociation.

8) The isotope signatures of the conduit cement fills within the tubular concretions ($\delta^{13}C$ –4 to +2‰ PDB, $\delta^{18}O$ –6 to –2‰ PDB) are most compatible with a post-methane origin from subsurface burial fluids, indicating there were changes in fluid composition during evolution of the cold seep system.

9) Calcitic pipe concretions are interpreted to have formed in the early stages of AOM methane oxidation where sulphate and Ca^{2+} concentrations, and fluid pressures, were high. Dolomitic bulbous and irregular concretions are interpreted to have formed in the late stages of AOM when sulphate concentrations and Ca^{2+} concentrations, and fluid pressures, had decreased.

10) The tubular concretions are inferred to have formed by precipitation initiating at their outer margins, with continued precipitation of cement towards their central conduit, rather than outwards from some central nucleus as is the case for most ‘normal’ spherical concretions. At times, cement precipitation may have continued into, and partially to completely filled, the conduit. In this model, cement precipitation at the outer margins first would have created an impervious crust encasing the dominant fluid flow passages.

11) Truncated tubular concretions along channel margins and tubular concretions within basal channel fills suggest that slope failure in the Urenui Formation may have been caused by slope instability from injected fluids and gases.

12) Prominent seafloor features of many paleoseeps, such as chemosynthesis based biotic communities and paleoseep carbonates, appear to be lacking in the Urenui mudstone. It is probable that the cold seep system in the Taranaki Basin did at one time reach the seabed, but that any surface evidence remains buried, has been eroded, or has not yet been found.

13) The tubular concretionary plumbing features in the Urenui Formation afford a conceptual model for envisaging subsurface fluid migration pathways beneath other modern and ancient seep systems.

8. References

Aiello, I.W., Stakes, D.S., Kastner, M., Garrison, R.E., 1999. Carbonate vent structures in the Upper Miocene Santa Cruz Mudstone at Santa Cruz, California. In: Garrison, R.E., Aiello, I.W., Moore, J.C. (Eds.), Late Cenozoic Fluid Seeps and Tectonics Along the San Gregorio Fault Zone in the Monterey Bay Region, California. Pacific Section AAPG, v. GB-76, pp. 35-52.

Aiello, I.W., Garrison, R.E., Moore, J.C., Kastner, M., Stokes, D.S., 2001. Anatomy and origin of carbonate structures in a Miocene cold-seep field. Geology, 29, 1111-1114.

Al-Aasm, I.S., Taylor, B.E., South, B., 1990. Selective stable isotope analysis of multiple carbonate samples using selective acid extraction. Chemical Geology, Isotope Geoscience Section, 80, 119-125.

Aloisi, G., Pierre, C., Rouchy, J., Faugères, J., 2002. Isotopic evidence of methane-related diagenesis in the mud volcanic sediments of the Barbados Accretionary Prism. Continental Shelf Research, 22, 2355-2372.

Barry, J.P., Greene, H.G., Ornage, D.L, Baxter, C.H., Robison, B.H., Kochevar, R.E., Nybakken, J.W., Reed, D.L., McHugh, C.M., 1996. Biologic and geologic characteristics of cold seeps in Monterey Bay, California. Deep Sea Research, 45, 1739-1762.

Bjørlykke, K., 1998. Clay mineral diagenesis in sedimentary basins – a key to the prediction of rock properties. Examples from the North Sea Basin. Clay Minerals, 33, 15-34.

Boggs, S., 1992. McConnin, R.A., (Ed.), Petrology of Sedimentary Rocks. Macmillian Publishing Company, New York. 707 pp.

Bohrmann, G., Greinert, J., Suess, E., Torres, M., 1998. Authigenic carbonates from the Cascadia subduction zone and their relation to gas hydrate stability. Geology, 26, 647-650.

Bouriak, S., Vanneste, M., Saoutkine, A., 2000. Inferred gas hydrates and clay diapirs near the Storegga Slide on the southern edge of the Vøring Plateau, offshore Norway. Marine Geology, 163, 125-148.

Bromley, R.G., Curran, H.A., Frey, R.W., Gutscheck, R.G., Suttner, L.J., 1975. Problems in interpreting unusually large burrows. In: Frey, R.W. (Ed.), The Study of Tracefossils. Springer-Verlag, New York., Pp. 351-376.

Campbell, K.A., 2006. Hydrocarbon seep and hydrothermal vent paleoenvironments and paleontology: Past developments and future research directions. Palaeogeography, Palaeoclimatology, Palaeoecology, 232, 362-407.

Campbell, K.A., Francis, D.A., Collins, M., Gregory, M.R., Nelson, C.S., Greinert, J., Aharon, P., 2008. Hydrocarbon seep-carbonates of a Miocene forearc (East Coast Basin), North Island, New Zealand. Sedimentary Geology, 204, 83-105.

Clari, P., S. Cavagna, Martire, L., Hunziker, J., 2004. A Miocene mud volcano and its plumbing system: A chaotic complex revisited (Monferrato, MW Italy). Journal of Sedimentary Research, 74, 662-676.

Coleman, D.D., Risatti, J.B., 1981. Fractionation of carbon and hydrogen isotopes by methane-oxidising bacteria. Geochimica et Cosmochimica Acta, 45, 1033-1037.

Conti, S., Fontana, D., Gubertini, A., Sighinolfi, G., Tateo, F., Fioroni, C., Fregni, P., 2004. A multidisciplinary study of middle Miocene seep-carbonates from the northern Apennine foredeep (Italy). Sedimentary Geology, 169, 1-19.

Conti, S., Fontana, D., 2005. Anatomy of seep-carbonates: Ancient examples from the Miocene of the northern Apennines (Italy). Palaeogeography, Palaeoclimatology, Palaeoecology, 227, 156-175.

Cowen, J.P., Wen, X., Popp, B.N., 2002. Methane in aging hydrothermal plumes. Geochimica et Cosmochimica Acta, 66, 3563-3571.

Crutchley, G.J., Gorman, A.R., Fohrmann, M., 2007. Investigation of the role of gas hydrates in continental slope stability west of Fiordland, New Zealand. New Zealand Journal of Geology and Geophysics, 50, 357-364.

Curtis, C.D., 1978. Possible links between sandstone diagenesis and depth related geochemical reactions occurring in enclosing mudstones: Geological Society of London Journal, 135, 107-177.

Curtis, C.D., 1986. Mineralogic consequences of organic matter degradation in sediments: inorganic/organic diagenesis. In: Leggett, J.K., Zuffa, G.G., (Eds.), Marine Clastic Sedimentology. London, Graham and Trotman. Pp. 108-123.

Davidson, D. W., Leaist, D.J., Hesse, R., 1983. Oxygen-18 enrichment in water of a clathrate hydrate. Geochimica et Cosmochhimica Acta, 47, 2293-2295.

De Boever, E., Swennen, R., Dimitrov, L., 2006. Lower Eocene carbonate cemented chimneys (Varna, NE Bulgaria): Formation mechanisms and the (a)biological mediation of chimney growth? Sedimentary Geology, 185, 159-173.

Díaz-del-Río, V., Somoza, L., Martínez-Frias, J., Mata, M.P., Delgado, A., Hernandez-Molina, F.J., Lunar, R., Martín-Rubí, J.A., Maestro, A., Fernández-Puga, M.C., León, R., Llave, E., Medialdea, T., Vázquez, J.T., 2003. Vast fields of hydrocarbon-derived carbonate chimneys related to the accretionary wedge/olistostrome of the Gulf of Cádiz. Marine Geology, 195, 177-200.

Falconbridge, J., 1994. Sedimentology, paleontology and petrology of the Urenui Formation, North Taranaki. Unpublished MSc Thesis, University of Auckland, New Zealand.

Faure, K., Greinert, J., Pecher, I.A., Graham, I.J., Massoth, G.J., De Ronde, C.E.J., Wright, I.C., Baker, E.T., Olson, E.J., 2006. Methane seepage and its relation to slumping and gas hydrate at the Hikurangi margin, New Zealand. New Zealand Journal of Geology and Geophysics, 49, 503-516.

Feary, D.A., Davies, P.J., Pigram, C.J., Symonds, P.A., 1991. Climatic evolution and control on carbonate deposition in northeast Australia. Palaeogeography, Palaeoclimatology, Palaeoecology, 89, 341-361.

Field, M.E., Barber, J.H.J., 1993. A submarine landslide associated with shallow seafloor gas and gas hydrates off Northern California. In: Schwab, W.C., Lee, H.J., Twichell, D.C. (Eds.), Submarine Landslides: Selected Studies in the U.S. Exclusive Economic Zone. U.S. Geological Survey Bulletin, 2002, 151-157.

Friedman, I., O'Neil, J.R., 1977. Compilation of stable isotope fractionation factors of geochemical interest, In Fleisher, M., (Ed.), U.S. Geological Survey Professional Paper, 440-kk.

Fritz, P., Smith, D.G.W., 1970. The isotopic composition of secondary dolomite. Geochimica et Cosmochimica Acta, 34, 1161-1173.

Gautier D.L., Claypool, G.E. 1984. Interpretation of methanic diagenesis in ancient sediments by analogy with processes in modern diagenetic environments. In: McDonald, D.A., Surdam, R.C. (Eds.), Clastic Diagenesis. American Association of Petroleum Geologist Memoirs, 37, 111-123.

Gay, A., Lopez, M., Ondreas, H., Charlou, J-L., Sermondadaz, G., Cochonat, P., 2006. Seafloor facies related to upward methane flux within a Giant Pockmark of the Lower Congo Basin. Marine Geology, 226, 81-95.

Gieskes, J., Mahn, C., Day, S., Martin, J.B., Greinert, J., Rathburn, T., McAdoo, B., 2005. A study of the chemistry of pore fluids and authigenic carbonates in methane seep environments: Kodiak Trench, Hydrate Ridge, Monterey Bay, and Eel River Basin. Chemical Geology, 220, 329-345.

Goldsmith, J.R., Graf, D.L., Heard, H.C., 1961. Lattice constants of the calcium-magnesium carbonate. The American Mineralogist, 46, 453-457.

Grange, L.I., 1927. The geology of the Tongaporutu-Ohura subdivision, Taranki division. New Zealand Geological Survey Bulletin 31. Government Printer, Wellington.

Greinert, J., Bohrmann, G., Suess, E., 2001. Gas hydrate-associated carbonates and methane-venting at Hydrate Ridge: Classification, distribution, and origin of authigenic lithologies. In: Parnell, C.K., Dillon, K.P. (Eds.), Natural Gas Hydrates: Occurrence, Distribution and Detection. Geophysical Monograph, 124, 99-113.

Irwin, H., Curtis, C., Coleman, M., 1977. Isotopic evidence for source of diagenetic carbonates formed during burial of organic-rich sediments. Nature, 269, 209-213.

Jensen, P., Aagaard, I., Burke Jr. R.A., Dando, P.R., Jørgensen, N.O., Kuijpers, A., Laier, T., O'Hara, M.O., Schmaljohann, R., 1992. 'Bubbling reefs' in the Kattegat: submarine landscapes of carbonate-cemented rocks support a diverse ecosystem at methane seeps. Marine Ecology Progress Series, 83, 103-112.

Judd, A.G. 2003. The global importance and context of methane escape from the seabed. Geo-Marine Letters, 23,147-154.

Judd, A.G., Hovland, M., 2007. Seabed fluid flow: The impact on geology, biology and the marine environment. Cambridge University Press, Cambridge, 475 pp.

Kamp, P.J.J., 1986. The mid-Cenozoic Challenger Rift system of western New Zealand and its implications for age of the Alpine Fault inception. Geological Society of America Bulletin, 97, 255-281.

Kamp, P.J.J., Vonk, A.J., Bland, K.J., Griffin, A.G., Hayton, S., Hendy, A.J.W., McIntyre, A.P., Nelson, C.S., Naish, T., 2002. Measequence architecture of Taranaki, Wanganui, and King Country basins and Neogene progradation of two continental margin wedges across western New Zealand. 2002 New Zealand Petroleum Conference Proceedings, pp. 464-481.

Kamp, P.J.J, Vonk, A.J., Bland, K.J., Hansen, R.J., Hendy, A.J.W., McIntyre, A.P., Ngatai, M., Cartwright, S.J., Hayton, S., Nelson, C.S., 2004. Neogene stratigraphic architecture and tectonic evolution of Wanganui, King Country, and eastern Taranaki Basins, New Zealand. New Zealand. New Zealand Journal of Geology and Geophysics, 47, 625-644.

King, P.R., Scott, G.H., Robinson, P.H., 1993. Description, correlation and depositional history of Miocene sediments outcropping along North Taranaki coast. Institute of Geological and Nuclear Sciences Monograph 5. Institute of Geological and Nuclear Sciences Ltd, Lower Hutt.

King, P.R., Thrasher, G.P., 1996. Cretaceous-Cenozoic geology and petroleum systems of the Taranaki Basin, New Zealand. Institute of Geological and Nuclear Sciences Monograph 13. Institute of Geological and Nuclear Sciences Ltd, Lower Hutt.

King, P., Browne, G., 2002. Miocene slope to basin-floor sequences exposed in North Taranaki, New Zealand. 2002 New Zealand Petroleum Conference Proceedings, pp. 482-481.

King, P.R., Browne, G.H., Arnot, M.J., Crundwell, M.P., 2007. A 2-D oblique – dip outcrop transect through a third-order, progradational, deep-water clastic succession, Urenui-Mount Messenger Formations, New Zealand. In: Nilsen, T.H., Shew, R.D., Steffens, G.S., Studlick, J.R.J., (Eds.), Atlas of deep-water outcrops: AAPG Studies in Geology 56, CD-ROM, 42 pp.

Kulm, L.D., Suess, E. 1990. Relationship between carbonate deposits and fluid venting: Oregon accretionary prism. Journal of Geophysical Research, 95, 8899-8915.

Kyser, T.K., James, N.P., Bone Y., 2002. Shallow burial dolomitization and dedolomitization of Cenozoic cool-water limestones, southern Australia: geochemistry and origin. Journal of Sedimentary Research, 72, 146-157.

Laird, M.G., 1994. Geological aspects of the opening of the Tasman Sea. In: van der Lingen, G.J., Swanson, K.M., Muir, R.J. (Eds.). Evolution of the Tasman Sea Basin. A.A. Balkenma, Rotterdam. Pp. 1-17.

Lédesert, B., Buret, C., Chanier, F., Fèrriere, J., Recourt, P., 2003. Tubular structures of northern Wairarapa (New Zealand) as possible examples of ancient fluid expulsion in an accretionary prism: evidence from field and petrographical observations. Geological Society of London, Special Publication, 216, 95-107.

Lewis, K.B., Marshall, B.A., 1996. Seep faunas and other indicators of methane-rich dewatering on New Zealand convergent margins. New Zealand Journal of Geology and Geophysics, 39, 181-200.

Locat, J., 2001. Instabilities along ocean marine: a geomorphological and geotechnical perspective. Marine and Petroleum Geology, 18, 503-512.

Longstaffe, F.J., 1987. Stable isotope studies of diagenetic processes. In Kyser, T. (Ed.) Short Course in Stable Isotope Geochemistry of Low Temperature Processes. Mineralogical Society of Canada, Saskatoon, SK, pp. 187-257.

Mazzini, A., Duranti, D., Jonk, R., Parnell, J., Cronin, B.T., Hurst, A., Quine, M., 2003. Palaeo-carbonate seep structures above an oil reservoir, Gryphon Field, Tertiary, North Sea. Geo-Marine Letters, 23, 323-339.

McBride E.F., Milliken K.L., Cavazza W., Cibin U., Fontana D., Picard M.D., Zuffa G.G., 1995. Heterogeneous distribution of calcite cement at the outcrop

scale in Tertiary sandstones, northern Apennines, Italy. American Association of Petroleum Geologists Bulletin, 79, 1044-1063.

McCrea, J.M., 1950. On the isotopic chemistry of carbonates and a paleotemperature scale. The Journal of Chemical Physics, 18, 849-857.

Munnecke, A., Samtleben, C., 1996. The formation of micritic limestones and the development of limestone-marl alternations in the Silurian of Gotland, Sweden. Facies, 34, 159-176.

Nelson, C.S., Hume, T.M., 1977. Relative intensity of tectonic events revealed by the Tertiary sedimentary record in the North Wanganui Basin and adjacent areas, New Zealand. New Zealand Journal of Geology and Geophysics, 20, 369-392.

Nelson, C.S., Smith, A.M., 1996. Stable oxygen and carbon isotope compositional fields for skeletal and diagenetic components in New Zealand Cenozoic nontropical carbonate sediments and limestones: a synthesis and review. New Zealand Journal of Geology and Geophysics, 39, 93-107.

Nelson, C., Schellenberg, F., King, P., Ricketts, B., Kamp, P., Browne, G., Campbell, K., 2004. Note on paramoudra-like concretions in the Urenui Formation, North Taranaki: possible plumbing system for a Late Miocene methane seep field. 2004 New Zealand Petroleum Conference Proceedings, Auckland, 7-10 March 2004. 5 pp. [http://crownminerals.med.govt.nz/petroleum/publications/nzpconf/nzpconf-2004.html]

Nyman, S.L., Nelson, C.S., Campbell, K.A., Schellenberg, F., Pearson, M.J., Kamp, P.J.J., Browne, G.H., King, P.R., 2006. Tubular carbonate concretions as hydrocarbon migration pathways? Examples from North Island New Zealand. 2006 New Zealand Petroleum Conference Proceedings, Auckland, 6-8 March 2006. 10 pp. [http://www.crownminerals.govt.nz/petroleum/conference/papers/Poster_papers_21.pdf]

Orpin, A. R., 1997. Dolomite chimneys as possible evidence of coastal fluid expulsion, uppermost Otago continental slope, southern New Zealand. Marine Geology, 138, 51-67.

Pancost, R.D., Damasté, J.S., De Lint, S., Van Der Maarel, M., Gottschal, J.C., Medinaut Shipboard Scientific Party, 2000. Biomarker evidence for widespread anaerobic methane oxidation in Mediterranean sediments by a consortium of methanogenic archaea and bacteria. Applied Environmental Microbiology, 66, 1126-1132.

Paull, C.K., Ussler, W., Dillon, W.P., 1991. Is the extent of glaciation limited by marine gas-hydrates? Geophysical Research Letters, 18, 432-434.

Pearson, M.J., Nelson, C.S., 2005. Organic geochemistry and stable isotope composition of New Zealand carbonate concretions and calcite fracture fills. New Zealand Journal of Geology and Geophysics, 48, 395-414.

Pearson, M.J., Grosjean, E., Nyman, S.L., Logan, G.A., Nelson, C.S., Hood, S.D., Campbell, K.A., 2008. Tubular concretions in New Zealand petroliferous basins: Lipid evidence for mineralization around proposed Miocene hydrocarbon seep conduits. 2008 New Zealand Petroleum Conference Proceedings, Auckland, 10-12 March 2008. 6 pp.

Peckmann, J., Reimer, A., Luth, U., Luth, C., Hansen, B.T., Heinicke, C., Heofs, J., Reitner, J., 2001. Methane-derived carbonates and authigenic pyrite from the northwestern Black Sea. Marine Geology, 177, 129-150.

Peckmann, J., Goedert, J.L., Thiel, V., Michaelis, W., Reitners, J., 2002. A comprehensive approach to the study of methane-seep deposits from the Lincoln Creek Formation, western Washington State, USA. Sedimentology, 49, 855-873.

Pierre, C., Rouchy, J.-M., Blanc-Valleron, M.-M., 2002. Gas hydrate dissociation in the Lorca Basin (SE Spain) during the Mediterranean Messinian salinity crisis. Sedimentary Geology, 147, 247-252.

Pierre, C., Rouchy, J.-M., 2004. Isotopic compositions of diagenetic dolomites in the Tortonian marls of the western Mediterranean margins: evidence of past gas hydrate formation and dissociation. Chemical Geology, 205, 469-484.

Pierre, C. Foquat, Y., 2007. Authigenic carbonates from methane seeps of the Congo deep-sea fan. Geo-Marine Letters, 27, 249-257.

Popenoe, P., Schmuck, E.A., Dillon, W.P., 1993. The Cape Fear Landslide: slope failure associated with salt diapirism and gas hydrate decomposition. In: Schwab, W.C., Lee, H.J., Twichell, D.C. (Eds.), Submarine Landslides: Selected Studies in the U.S. Exclusive Economic Zone. U.S. Geological Survey Bulletin 2002, 40-53.

Pratson, L.F., 2001. A perspective on what is known and not known about seafloor instability in the context of continental margin evolution. Marine and Petroleum Geology, 18, 449-501.

Roberts, H.H., Aharon, P., 1994. Hydrocarbon-derived carbonate buildups of the northern Gulf of Mexico continental slope: A review of submersible investigations. Geo-Marine Letters, 14, 135-148.

Ridgway, N.M., 1969. Temperature and salinity of sea water at the ocean floor in the New Zealand region. New Zealand Journal of Marine Freshwater Research, 3, 57-72.

Schellenberg, F., 2002. The paramoudra concretions within the Urenui Formation, Taranaki Basin, West Coast of New Zealand: Fossil fluid conduits or giant trace fossils? Institute of Geology and Palaeontology, University of Tübingen, unpublished MSc Thesis.

Schwartz, H., Sample, J., Weberling, K.D., Minisini, D., Moore, J.C., 2003. An ancient linked fluid migration system: cold-seep deposits and sandstone intrusions in the Panoche Hills, California, USA. Geo-Marine Letters, 23, 340-350.

Suess, E., Torres, M.E., Bohrmann, G., Collier, R.W., Greinert, J., Linke, P., Rehder, G., Trehu, A., Wallmann, K., Winckler, G., Zueger, E., 1999. Gas hydrate destabilization: enhanced dewatering, benthic material turnover and large methane plumes at the Cascadia convergent margin. Earth and Planetary Science Letters, 170, 1-15.

Taranaki GSNZ, 1994. *Paramoudra/Zoophycos* trace fossil association in the Miocene of the North Taranaki coast. Geological Society of New Zealand Miscellaneous Publication, 80A, 175.

Townsend, D., Vonk, A., Kamp, P.J.J., (compilers) 2008. Geology of the Taranaki area. Institute of Geological and Nuclear Sciences 1:250 000 geological map 7. 1 sheet + 79 p. Lower Hutt, New Zealand. GNS Science Limited, Lower Hutt, New Zealand, Department of Earth and Ocean Sciences, University of Waikato, Hamilton 2008.

Ussler III, W., Paull, C.K., 1995. Effects of ion exclusion and isotopic fractionation on pore water geochemistry during gas hydrate formation and decomposition. Geo-Marine Letters, 15, 37-44.

Vonk, A.J., Kamp, P.J.J., 2008. The Late Miocene southern and central Taranaki inversion phase (SCTIP) and related sequence stratigraphy and paleogeography. 2008 New Zealand Petroleum Conference Proceedings, Auckland, 10-12 March 2008, 17 pp.

Whiticar, M.J., 1999. Carbon and hydrogen isotope systematics of bacterial formation and oxidation of methane. Chemical Geology, 161, 291-314.

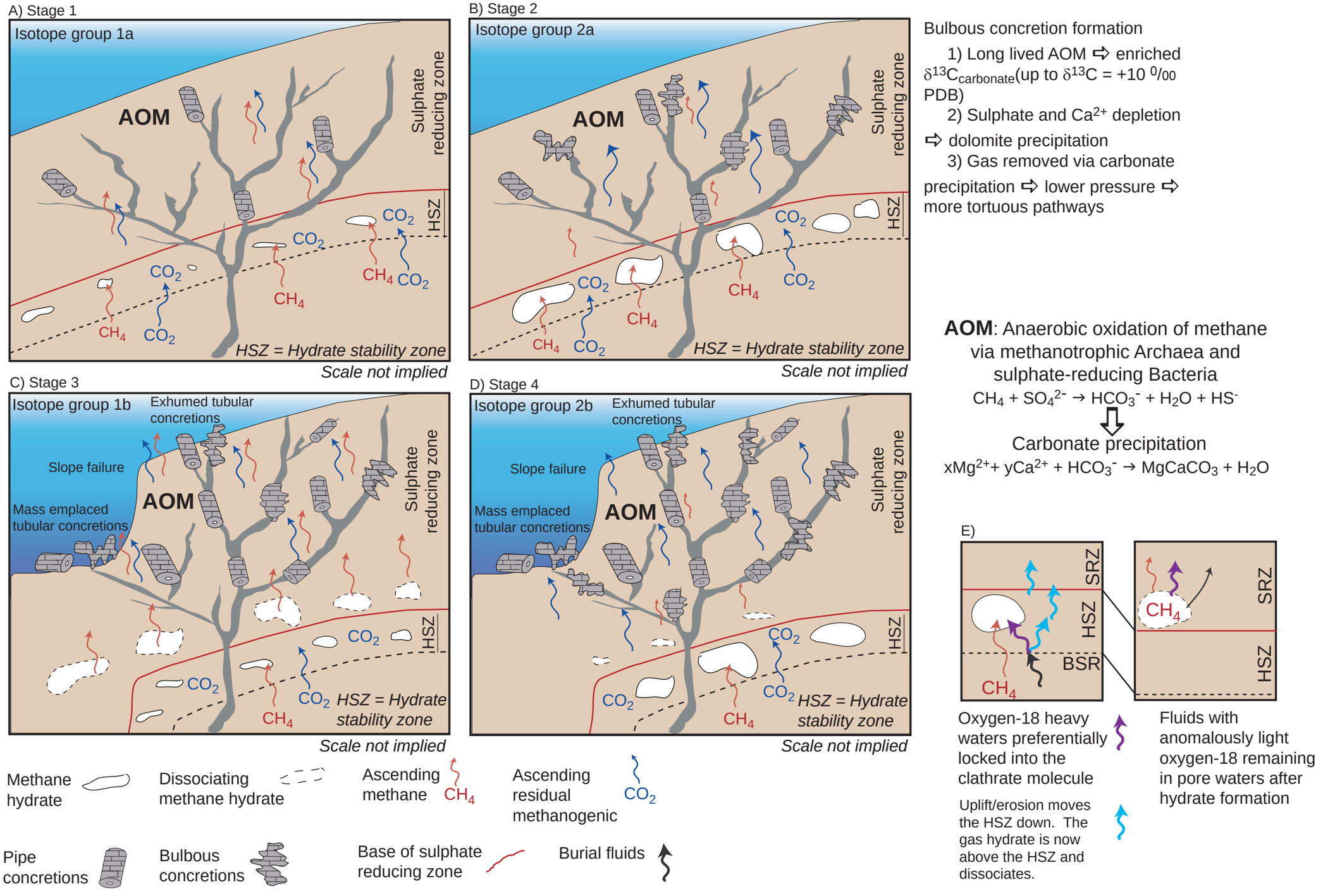

Bulbous concretion formation

1) Long lived AOM ⇨ enriched $\delta^{13}C_{carbonate}$ (up to $\delta^{13}C$ = +10 $^{0}/_{00}$ PDB)

2) Sulphate and Ca^{2+} depletion ⇨ dolomite precipitation

3) Gas removed via carbonate precipitation ⇨ lower pressure ⇨ more tortuous pathways

AOM: Anaerobic oxidation of methane via methanotrophic Archaea and sulphate-reducing Bacteria

$CH_4 + SO_4^{2-} \rightarrow HCO_3^- + H_2O + HS^-$

⇩

Carbonate precipitation

$xMg^{2+} + yCa^{2+} + HCO_3^- \rightarrow MgCaCO_3 + H_2O$

Figure 15. Schematic representation of the hypothesised scenario for the development of tubular concretions in the subsurface of a Taranaki cold seep system in the context of a progradational shelf-slope continental margin. See Section 6.3 for further explanation. A-D corresponds to stages 1-4 in the model, and each stage is associated with one or other of the isotope groups 1a, 1b, 2a, 2b noted in Fig. 12. E illustrates the incorporation of heavy oxygen into the hydrate molecule during formation and subsequent release into the pore fluids upon dissociation.

CHAPTER 4

Miocene tubular concretions in East Coast Basin, New Zealand: Analogue for the subsurface plumbing of cold seeps

Abstract

The uplifted accretionary prism of East Coast Basin in Hikurangi Margin, North Island, New Zealand, exposes late Miocene slope mudrocks (Whangaehu Mudstone, <10% carbonate) in coastal cliffs north of Cape Turnagain that contain conspicuous tubular carbonate concretions (50−85% carbonate) supporting near-central conduits. Pipe and bulbous morphologies dominate, ranging in exposed length up to 5 m and up to 1 m in diameter. The concretions formed by the precipitation of micritic dolomite (and some calcite) cement within the host mudstone at shallow burial depths (probably <100 m). $\delta^{13}C$ values of the cement range from –22 to +13‰ PDB and are interpreted to reflect carbonate precipitation from either the extensive anaerobic oxidation of methane (AOM) and/or mixing of microbial methane and methanogenic CO_2. AOM is confirmed by lipid biomarker evidence indicating methane oxidation occurred in the sediments at the time of carbonate precipitation. The mixed dolomite/calcite mineralogies and the trend of $\delta^{13}C$ in the tubular concretions from strongly negative to strongly positive values are interpreted to reflect methane oxidation from the onset of ascent through to the end of a migration event. Depleted and enriched $\delta^{18}O$ values suggest an evolved fluid source influenced by the dissociation of gas hydrates. Collectively, our results indicate that the tubular concretions within the upper slope mudstones delineate parts of the subsurface plumbing network of a cold seep system on the late Miocene paleo-Hikurangi Margin in which the fluids were sourced from ascending methane. The intermediate location of the Whangaehu concretions between older (early Miocene) seep carbonates to the west and modern ones offshore to the east

indicates a progressive eastwards shift with time of a long-lived, if only periodically active, seep system. The concretionary plumbing features at Whangaehu provide a conceptual model for subsurface fluid pathways and seep-related processes beneath the modern Hikurangi Margin seabed, and possibly also for other modern and ancient cold seep carbonate systems.

1. Introduction

Modern cold seep research reveals valuable information about the processes and products of fluid flow at the seabed, but it is logistically difficult to study the subsurface realm of the seep system. While ancient and modern cold seeps have been documented worldwide (Fig. 1), the emphasis has been on their seafloor expressions and carbonate deposits (e.g., Campbell et al., 2002; Peckmann et al., 2002; Mazzini et al., 2003; Schwartz et al., 2003; Conti et al., 2004, Conti and Fontana, 2005; Hovland et al., 2005; Gay et al., 2006a,b; Campbell et al., 2008) rather than their subsurface features (Aiello et al., 2001; Clari et al., 2004; De Boever et al., 2006). Several Tertiary mudrock sequences in New Zealand contain tubular concretions that may provide a window into the subsurface plumbing system beneath paleoseeps.

The focus of this study is the Whangaehu Mudstone cropping out on the coast immediately north of Cape Turnagain, North Island, New Zealand (Fig. 2). These upper slope deposits (Moore, 1981) include a variety of tubular concretions that are hypothesised to document subsurface seep activity in the region during the late Miocene. The concretions range up to a metre in diameter and several metres in exposed length, are locally abundant in outcrop, and exhibit an extremely diverse range of morphologic types.

The tubular concretions in this study were first noted by Moore (1981), but their origin was not mentioned. Tubular concretions nearby the study area were later suggested to have formed about animal burrows (Neef, 1984). More recently, Lédesert et al. (2003) described some of the concretions at Whangaehu and suggested they were fossil fluid expulsion chimneys based on their morphologic similarity to exhumed chimneys on the seabed off southeastern New Zealand and on petrographic evidence. They also suggested that the migrating fluids were not

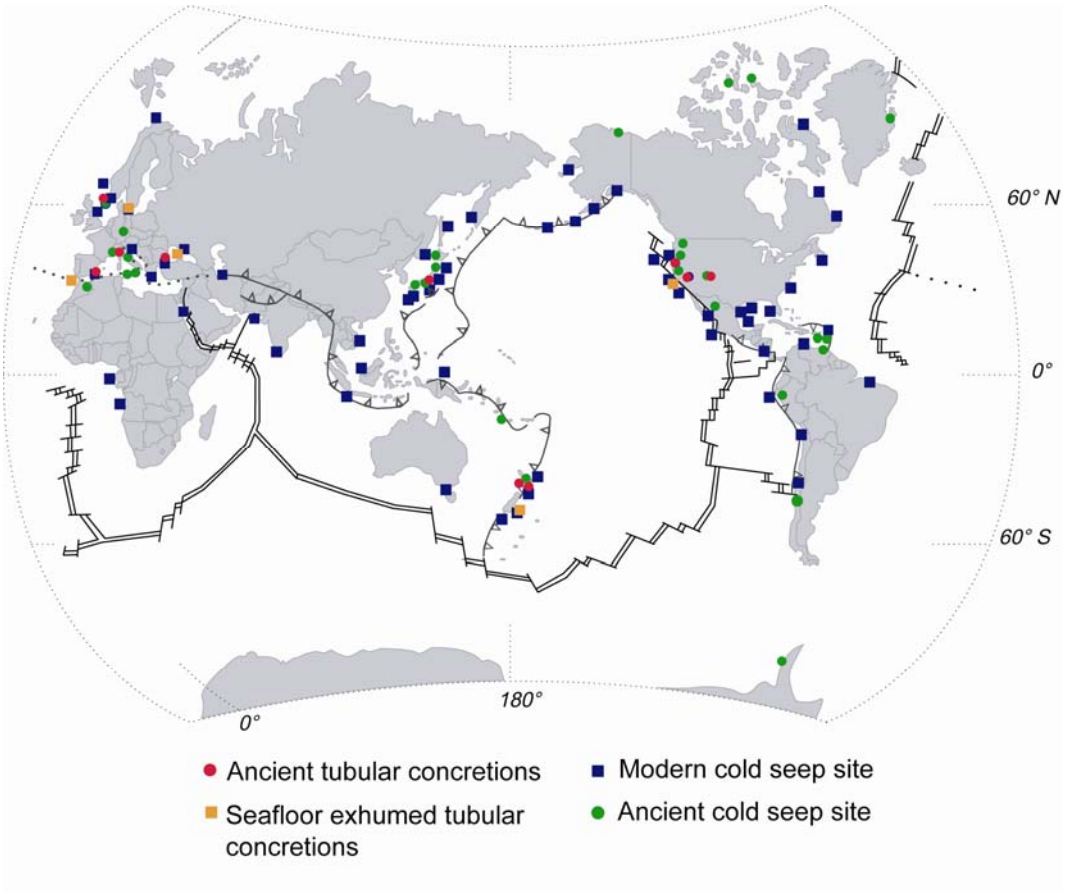

Figure 1. Global occurrences of reported ancient tubular concretions, exhumed tubular concretions on the seafloor (most near active seep sites), ancient cold seeps, and modern colds seeps (adapted and extended from Campbell, 2006).

methane rich, as typical seep fauna were absent, although supporting geochemical data were not presented. The current study is the first to confirm geochemically that the concretions mark the subsurface plumbing system of a late Miocene cold seep in which the fluids were likely sourced from the dissociation of gas hydrates formed from ascending methane. Additionally, this study potentially links the Whangaehu seep system to some inland occurrences of paleoseep carbonates and provides a possible ancient analogue for subsurface fluid migration processes beneath the modern Hikurangi Margin seeps off eastern North Island (Fig. 2A).

2. Geologic setting

The study area is located along the coastline between Whangaehu Beach and Cape Turnagain in southern Hawke's Bay, East Coast Basin, North Island, within the wider Hikurangi Margin (Fig. 2). Cape Turnagain is approximately 100 km northwest of the modern Australian/Pacific Plate subduction boundary marked by the Hikurangi Trough (Figs. 2A, 3). Subduction of the Pacific Plate southwest underneath the Australian Plate was initiated in the early Miocene (~23 Ma), the leading edge of the Pacific Plate reaching the position of Cape Turnagain at ~10 Ma (Fig. 3) (Kamp and Furlong, 2006). Presently, the Pacific Plate is subducting at about 40 mm per year (DeMets et al., 1994).

Onshore, within the forearc basin, deformed Cretaceous to Paleogene sedimentary rocks deposited in a passive margin prior to subduction, are overlain by relatively less deformed Neogene marine sediments deposited after the onset of subduction (Fig. 4), both of which have been thrust faulted and back tilted during subduction (Figs. 2B, 3) (Lewis and Pettinga, 1993). The Cretaceous and Paleocene sediments contain known hydrocarbon source rocks, in particular the Whangai Formation and Waipawa Formation (Fig. 4), both of which source onshore active oil and gas seeps (Rogers et al., 1999; Francis et al., 2004; Hollis and Manzano-Kareah, 2005). Neogene slope sediments lie offshore and landward of the active accretionary wedge (Lewis and Pettinga, 1993; Lee and Begg, 2002). Thrust faulting and back tilting during subduction characterise the strata east of the axial ranges (Fig. 3) (Lewis and Pettinga, 1993; Field et al., 1997; Lee and Begg, 2002).

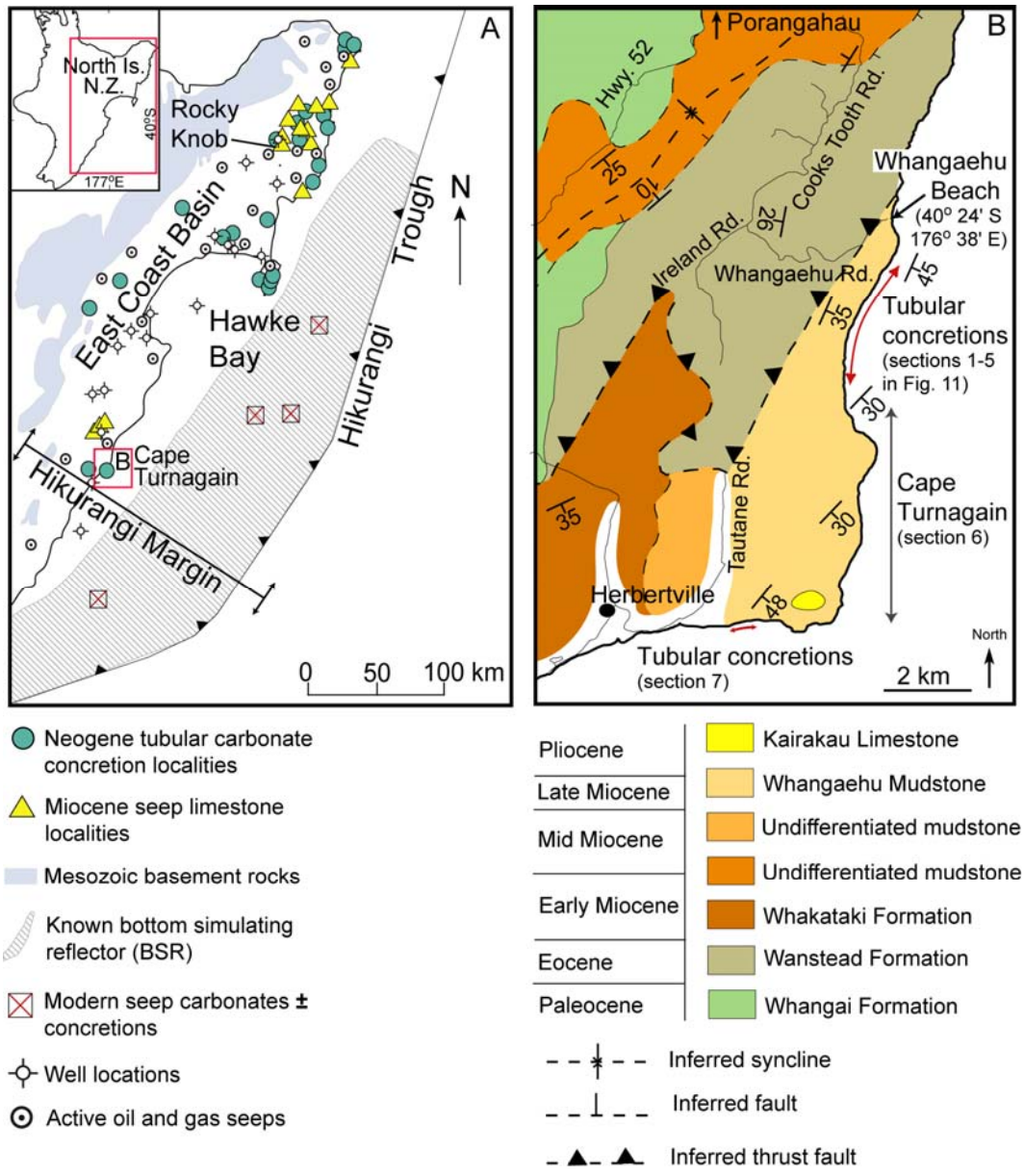

Figure 2. (A) Locality map of Hikurangi Margin (including East Coast Basin), North Island, New Zealand and study location near Cape Turnagain. The map broadly identifies some sites of tubular concretions, Miocene seep limestones, modern active seeps, onshore modern oil/gas seeps and well locations, and offshore modern bottom simulating reflector (BSR) region indicative of gas hydrates. Based on information in Francis (1997), Lewis and Marshall (1996), from personal communication with Dave Francis (Geological Research Ltd, Lower Hutt), and personal observations. (B) Geological map of the Cape Turnagain and Whangaehu Beach area including the general distribution (coastline arrows) of main occurrences of tubular concretions in outcrop (Lee and Begg, 2002).

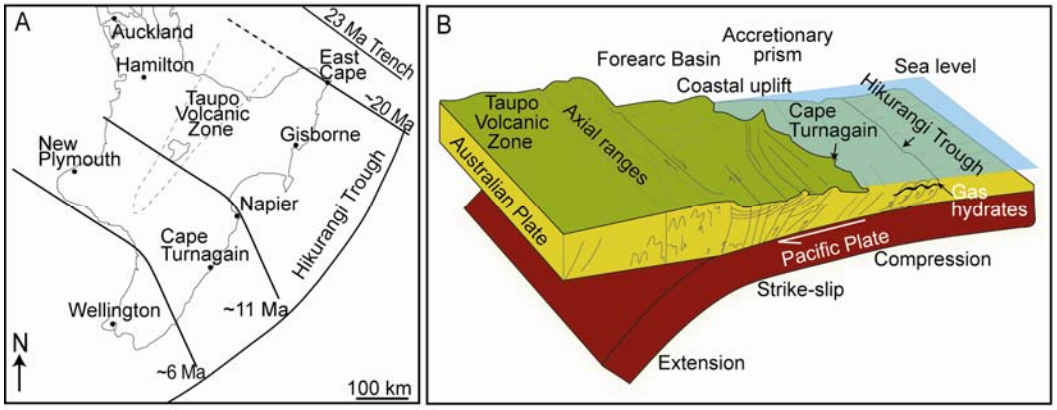

Figure 3. Subduction margin along the New Zealand Pacific-Australian Plate boundary. (A) Location of leading edge of the subducting Pacific Plate from 23 to 6 Ma in reference to present day geography (modified from Kamp and Furlong, 2006). (B) Schematic cross section of the present day East Coast Basin subduction margin; note the location of Cape Turnagain (modified from Lewis and Marshall, 1996; Lee and Begg, 2002).

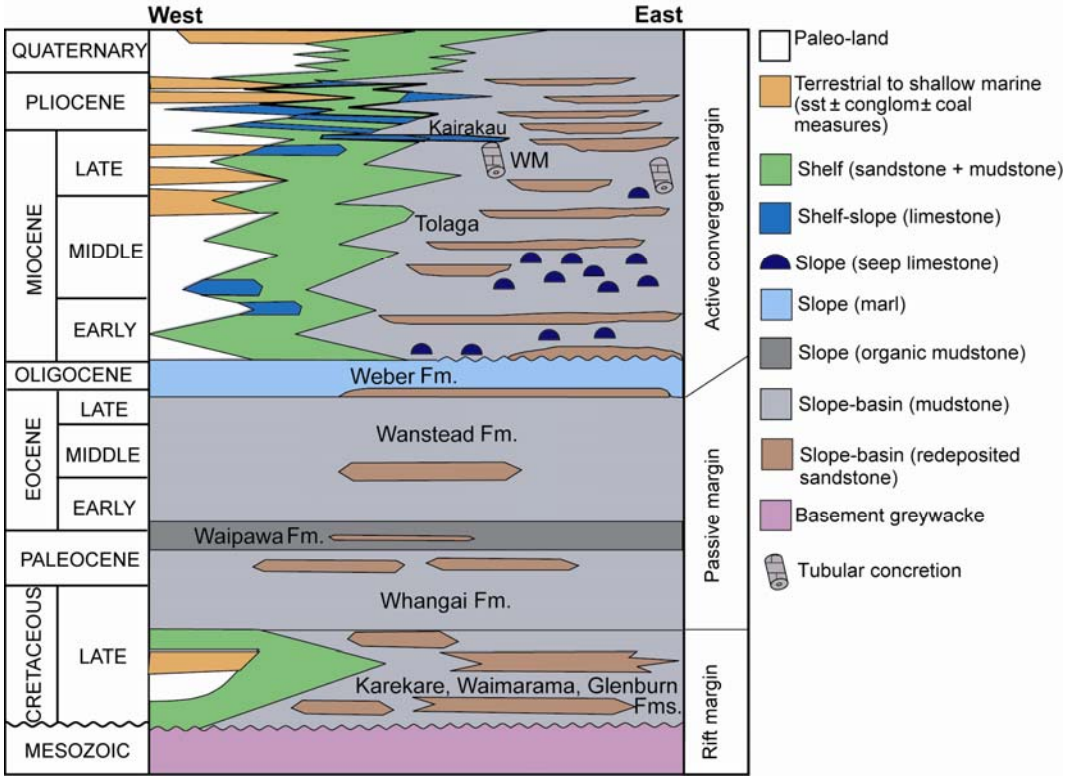

Figure 4. Generalised stratigraphy and depositional paleoenvironments for the East Coast Basin sedimentary fill (modified from Francis, 2004). WM marks approximate stratigraphic position of the Whangaehu Mudstone containing the tubular concretions described in this study. Vertical time axis not to scale.

The Whangaehu Mudstone crops out upon the frontal ridge axis seaward of the forearc basin (Figs. 2, 3) (Field et al., 1997). It is late Miocene to early Pliocene in age, up to 1000−1300 m thick, and conformably overlies undifferentiated middle Miocene marine mudstone (Moore, 1981; Field et al., 1997) (Fig. 2B). The Whangaehu Mudstone is blue-grey, bioturbated, typically massive to sometimes vaguely bedded, and slightly calcareous (<10% $CaCO_3$). Conspicuous tubular and spherical carbonate concretions and carbonate cemented beds are present in varying abundance and size along the coastal section (Fig. 5). The formation dips seawards between about 30 and 45° ESE (Fig. 2B). Little faulting is directly evident in this coastal section aside from some jointing, however a major thrust fault parallels the outcrop a few kilometres inland and marks the contact between the older Wanstead Formation and younger Whangaehu Mudstone (Fig. 2B). Foraminifera support deposition of the mudstone at mainly upper slope depths, and it shallows upwards across an unconformity into the inner shelf early Pliocene Kairakau Limestone that caps Cape Turnagain itself (Moore, 1981; Nelson et al., 2003; Beu, 1995).

3. Methods

Tubular concretions crop out mainly from just south of Whangaehu Beach along the shore platform and coastal cliffs towards Cape Turnagain for a distance of about 3 km, and also along a 500 m section on the south side of the Cape (Fig. 2B, 5). The coastline is safely accessible from the Whangaehu Beach end only at mid to low tide during fair weather conditions. The rapidly eroding mudstone cliffs, along with longshore sand transport, result in continual changes to the shoreline outcrop, both destroying or concealing previously noted concretions and exposing new examples. Along this stretch of coastline, the concretions are not uniformly distributed, but tend to occur in clusters, each spanning a few to several hundred metres of the platform section (Fig. 6).

Following stratigraphic logging and photographic imaging of the coastal section during the austral summer of 2004/5, field work focused on descriptions of the distribution, morphology, size, and stratigraphic position of the main concretion occurrences. This information is presented full in Appendix 2.

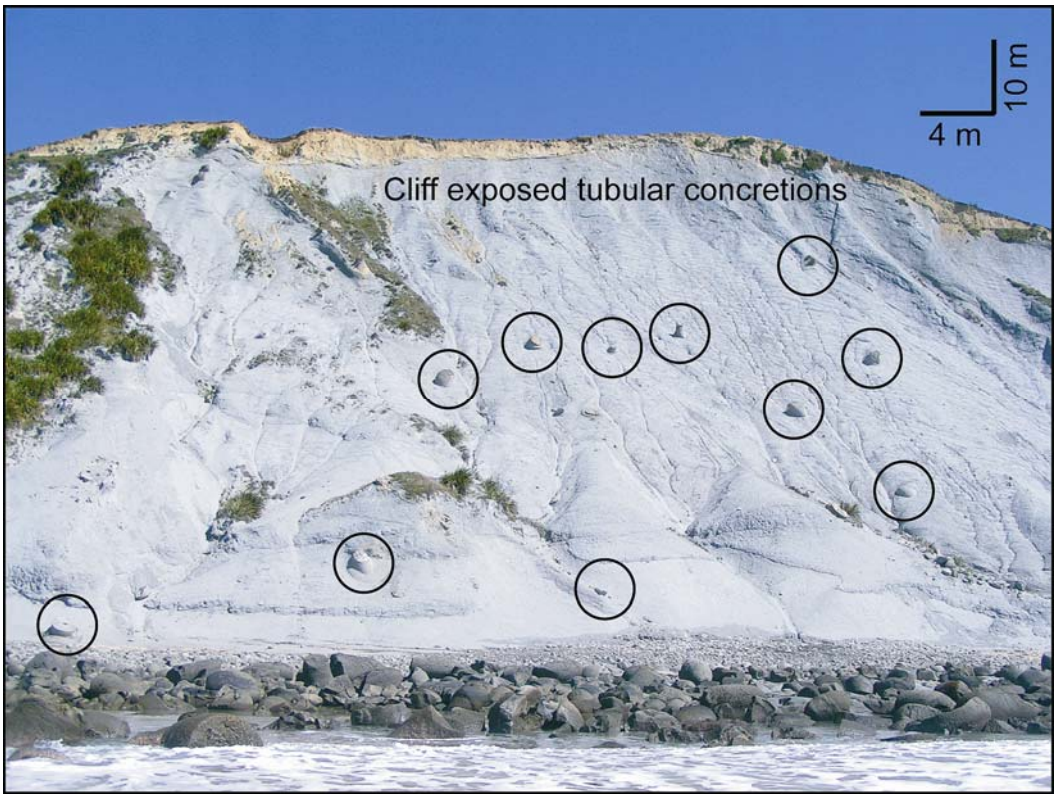

Figure 5. Example of tubular concretions in outcrop. Circles indicate tubular concretions large enough to be visible from the shoreline. The rocks exposed on the shoreface are composed primarily of tubular concretions, both *in situ* and transported. Photograph is within section 2 (see Fig. 11) of the logged coastline.

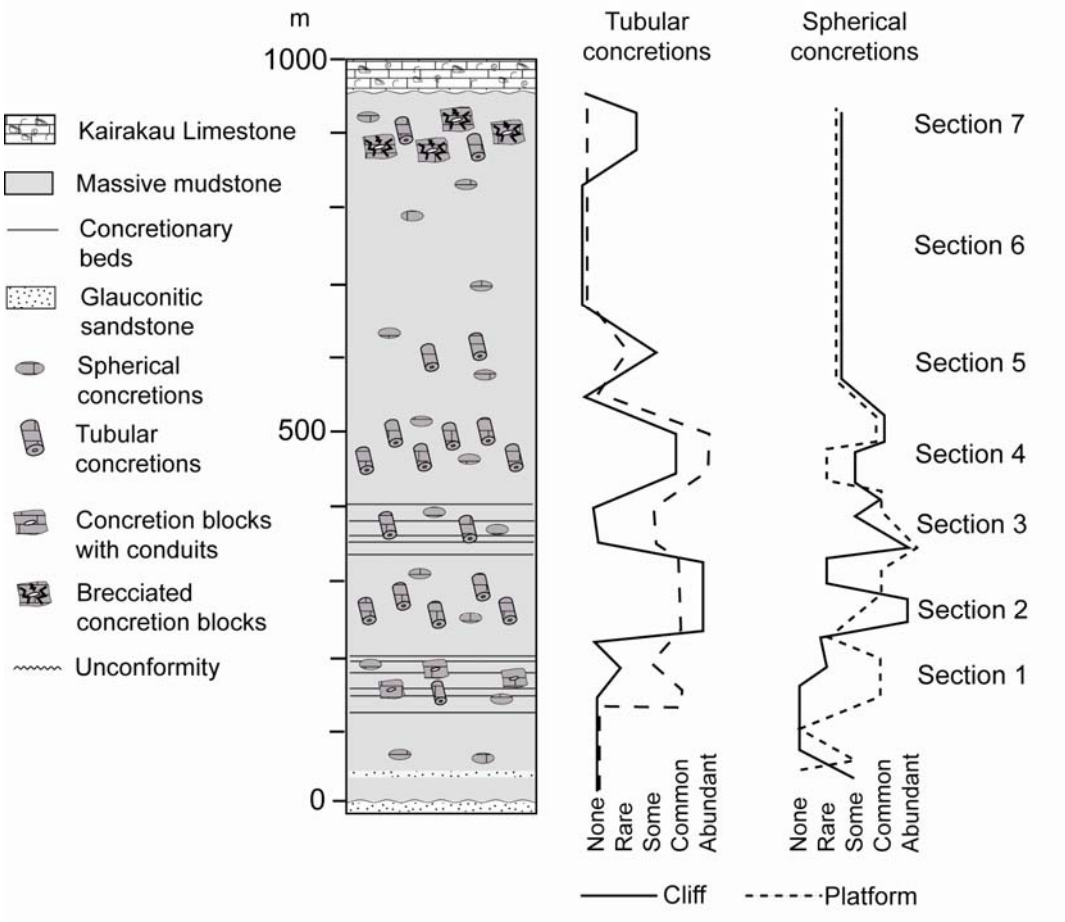

Figure 6. Schematic stratigraphic column of the Whangaehu Mudstone from Whangaehu Beach in the north (base of column) to Cape Turnagain in the south (Fig. 2B) showing approximate stratigraphic placement of concretionary features and their corresponding morphologies. Graphs adjacent to column indicate the relative abundance of *in situ* tubular and spherical concretions in the coastal cliff and in the shore platform. See Fig. 11 for definition of section numbers.

Where possible, *in situ* oriented samples from concretions were collected using a chisel and heavy duty rock hammer, but collections also were made from fallen blocks lying on the shore platform. Sawn slabs were related to their photographed and sketched positions in the sampled concretions, and in several cases small subsamples were then cut and extracted to provide representative rock material along transects from the centre to the periphery of the tubular concretions. Some representative samples of the mudstone hosting the concretions were also collected.

Laboratory analytical work included standard thin section petrography of resin impregnated samples, cathodoluminescence (CL) petrography, scanning electron microscopy (SEM) to view the ultrastructure of the micritic carbonate following the procedure of Munnecke and Samtleben (1996), X-ray diffraction (XRD) to determine the mineralogy of samples and the $MgCO_3$ content of calcite and dolomite (e.g., Goldsmith et al., 1961), and stable isotope mass spectrometry to derive the $\delta^{18}O$ and $\delta^{13}C$ composition of the carbonate phases (e.g., McCrea 1950; Nelson and Smith 1996). In samples of mixed calcite and dolomite composition, the carbonate fractions are difficult to physically separate for stable isotope analysis. In this study, a variation of the differential phosphoric acid extraction method (Al-Aasm et al., 1990; Kyser et al., 2002) was used to derive values for calcite-CO_2 and dolomite-CO_2. Calcite-CO_2 and dolomite-CO_2 were determined in two separate reactions, for 10 minutes and 2 hours, respectively, due to restrictions on gas transfer rates induced by the geometry of the mass spectrometer inlet system. Isotope results are reported as per mille $\delta^{18}O$ and $\delta^{13}C$ relative to VPDB, and have an analytical precision of better than ±0.10‰.

Full records of field and laboratory data from Whangaehu are available in Appendix 2. Details of methodology and instruments are available in Appendix 7.

4. Tubular concretions

4.1 Morphology

The tubular concretions represent cemented host mudstone and are generally cylindrical or pipe-like in shape (Figs. 7, 8). Typically a conspicuous central hole or conduit, ranging from several mm to 40 cm in diameter, runs along the exposed length of concretions (Fig. 8A-C). Conduits may be empty or filled with later generations of cement and/or sediment. Some concretions have multiple conduits, while a few appear to lack a conduit, and instead may preserve a vague concentric colour banding related to subtle compositional and/or weathering differences (Fig. 8D). Some filled conduits are strongly brecciated, and may extend out into the surrounding concretion (Fig. 8E). The tubular concretions are typically oriented at high angles (70−90˚) to sedimentary bedding, and they can be straight, tortuous, or sinuous in length, and may branch, anastomose, or coalesce within the mudstone. Spherical concretions from 5 cm to 1 m in diameter are also present in various abundances along the coastline (Fig. 6). Additionally, 14 concretionary beds, 2 to 50 cm thick, crop out along the coastal section. The concretionary beds appear to be discontinuously cemented zones associated with subtle stratification and textural contrasts within restricted stratigraphic intervals (Fig. 6).

The tubular concretions have several different morphologies, not seemingly related to any grain size variations in the massive host mudstone (Figs. 7, 8). *Pipe* concretions are strongly cylindrical, straight, and more or less equal in diameter throughout their length (0.5 to 1 m exposed length; 0.1 to 0.4 m diameter) (Fig. 8A-C). *Sinuous* concretions are similar to the pipes, with equal diameter throughout, but they are highly tortuous and twist through stratigraphy (av. 1 m exposed length, 5 cm diameter) (Fig. 8F-G). *Conical* concretions taper upwards through the mudstone up to 1.5 m high with their widest diameter at the base (1 m av.) and least diameter at the top (0.5 m av.) (Fig. 8H). Conduits of conical concretions typically can only be discerned by large scale fractures in the concretion centre. *Bulbous* concretions remain elongated (0.1 to 5 m exposed length) but display an irregular external morphology that pinches and swells to

Morphology		Size	Morphology		Size
Pipe		L: 0.5 - 1 m D: 10 - 40 cm	Spherical		D: 0.5 - 2 m
Bulbous		L: 0.1 - 5 m D: up to 0.5 m	Blocks		D: 1 m (av)
Sinuous		L: 1 m (av) D: 5 cm (av)	Brecciated blocks		D: 0.5 - 2 m (av)
Conical		L: 1 - 1.5 m D: 1 m (av)	Concretionary beds		L: 10s m W: 5 cm - 1 m

Figure 7. Morphologic classification adopted for the tubular and other concretions at Whangaehu. L = length of tubular concretion, D = diameter, W = width.

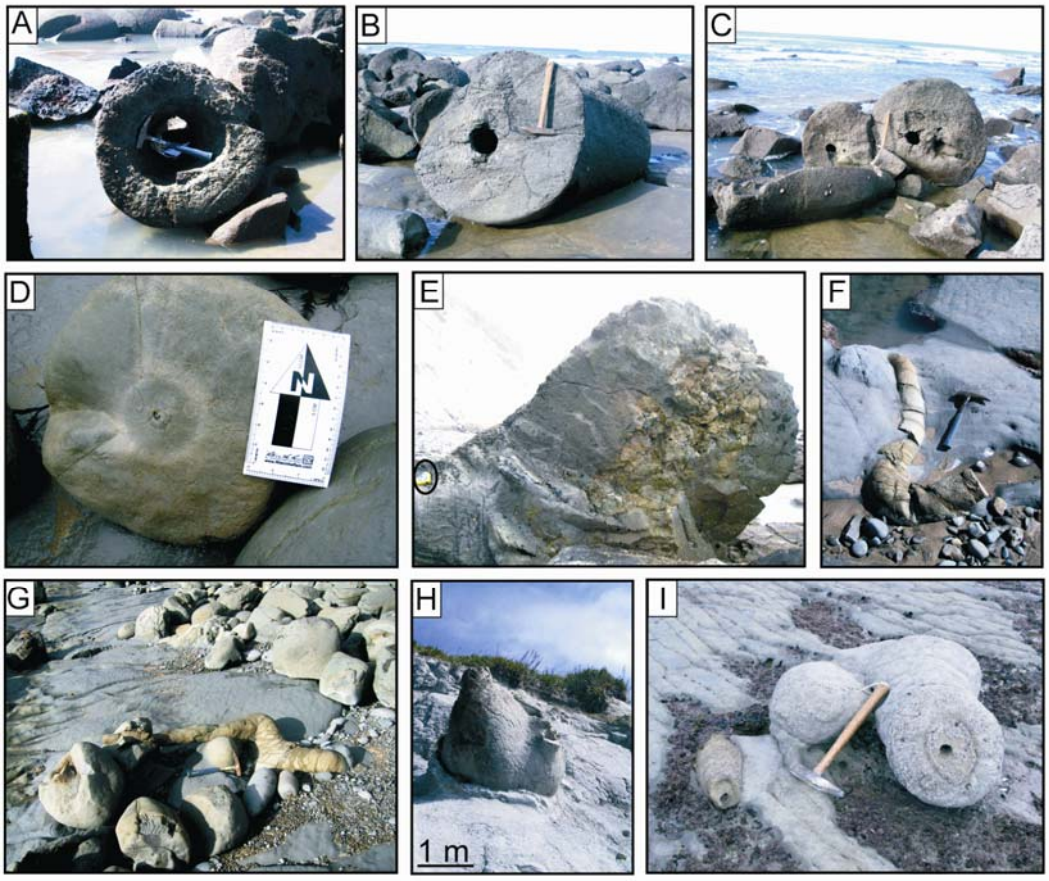

Figure 8. Examples of tubular concretions at Whangaehu. (A) Pipe concretion with a large open conduit and thin surrounding concretion; (B) pipe concretion with conduit and thick surrounding concretion; (C) a branching pipe concretion with multiple conduits; (D) pipe concretion with a pinhole conduit and colour zonation; (E) large pipe concretion with brecciated interior (tape measure for scale); (F) sinuous concretion; (G) tortuous and branching sinuous concretion; (H) conical concretion with fractured conduits; (I) tortuous bulbous concretion with small open conduit.

give variable concretion diameters (from 0.01 to 0.5 m) along their tortuous pathway through the host mudstone. Conduits in the bulbous concretions tend to be obscure or very small (up to a few centimetres) (Fig. 8I). Strongly brecciated concreted blocks averaging 1.5 m in size contain multiple small conduits and are especially abundant on the south side of Cape Turnagain (Fig. 9).

In an earlier study of tubular concretions along parts of the Whangaehu coastline, Lédesert et al. (2003) suggested that a direct relationship existed between concretion and conduit sizes – the larger the concretion the larger the conduit. The relationship was further explored in this study based on casual observations as well as direct measurements of the well-preserved tubular concretions spread across the various morphological types represented (Fig. 10). Results suggest that a weak relationship (R^2 = +0.49) exists between tubular concretion size and conduit size, most evident for concretions over 1 m in diameter.

4.2 Distribution

The logged Whangaehu coastline begins at the prominent headland at the south end of Whangaehu Beach (40˚ 24’ S, 176˚ 38’ E) and continues southwards towards Cape Turnagain (40˚ 29’ S, 176˚ 37’ E) for about 3 km (Fig. 2B). A further 7 km south, continuing around Cape Turnagain, was visited but not logged in any detail due to an apparent lack of tubular concretions, except for a short section south of the Cape (Fig. 2B). Tubular and spherical concretions, along with laterally continuous concretionary beds, are exposed in variable abundance in the mudstone that forms the shore platform and backing cliffs (Fig. 6). The presence of vegetation over many parts of the cliff exposures undoubtedly obscures some concretions. The coastline outcrop from Whangaehu Beach to Herbertville has been divided into seven sections reflecting the abundance and morphology of the concretions therein (Figs. 2B,11).

Section 1 (700 m long) is positioned within the lower part of the Whangaehu Mudstone stratigraphy (Fig. 2B, 6, 11). The main feature of this section is the occurrence of up to six concretionary beds (labelled A-F in Fig. 11) that dip 40˚ ESE. The concretionary beds are spaced 10 to 30 m apart, are 0.5 m thick, and

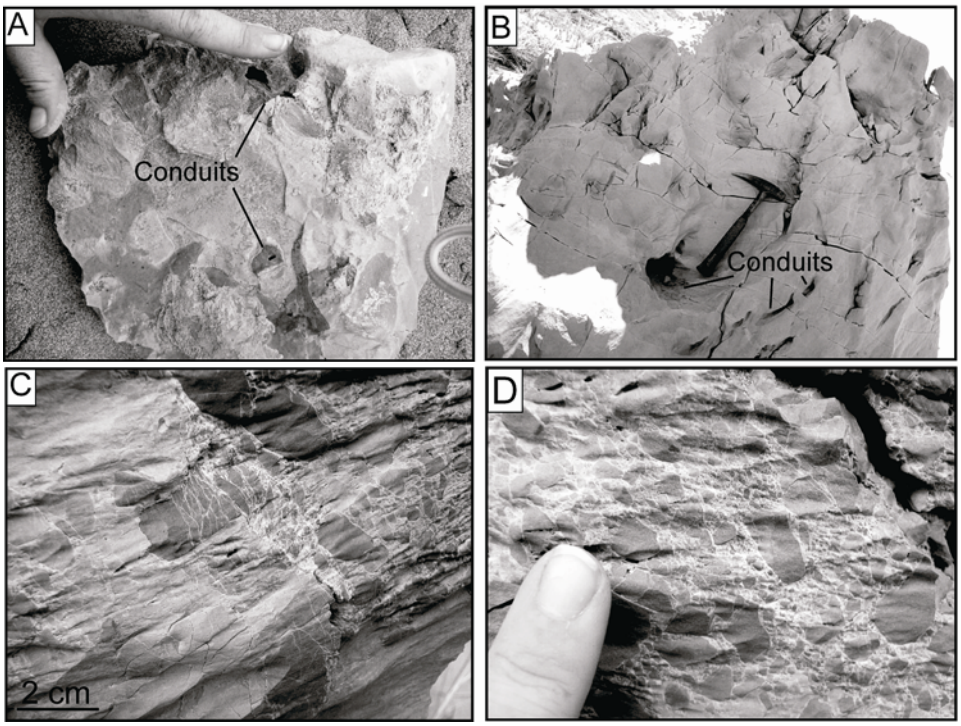

Figure 9. Brecciated concreted blocks from the Herbertville outcrop, south of Cape Turnagain (Fig. 2B). (A) Concreted block with three small open conduits; (B) concreted block with conduits, thin curved fractures, and 'zipper' like seams; (C,D) strongly brecciated concreted block without conduits. Brecciated zone is nearby a thin fracture. Clasts appear to be similar to surrounding concreted mudstone and 'float' in a white carbonate matrix.

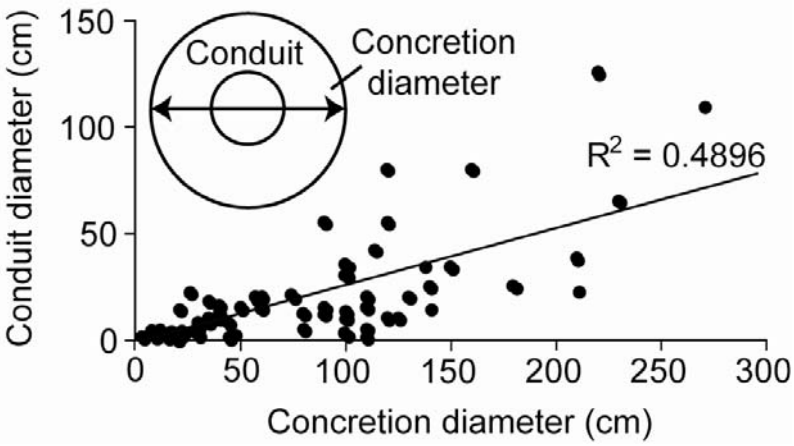

Figure 10. Diameter of concretion conduits plotted against the diameter of the tubular concretion (whole, including conduit). The data show a weak relationship between concretion size and conduit size (R^2 = 0.49), which is stronger for concretions > 1 m in diameter. Conduits for 73 concretions are plotted in the graph.

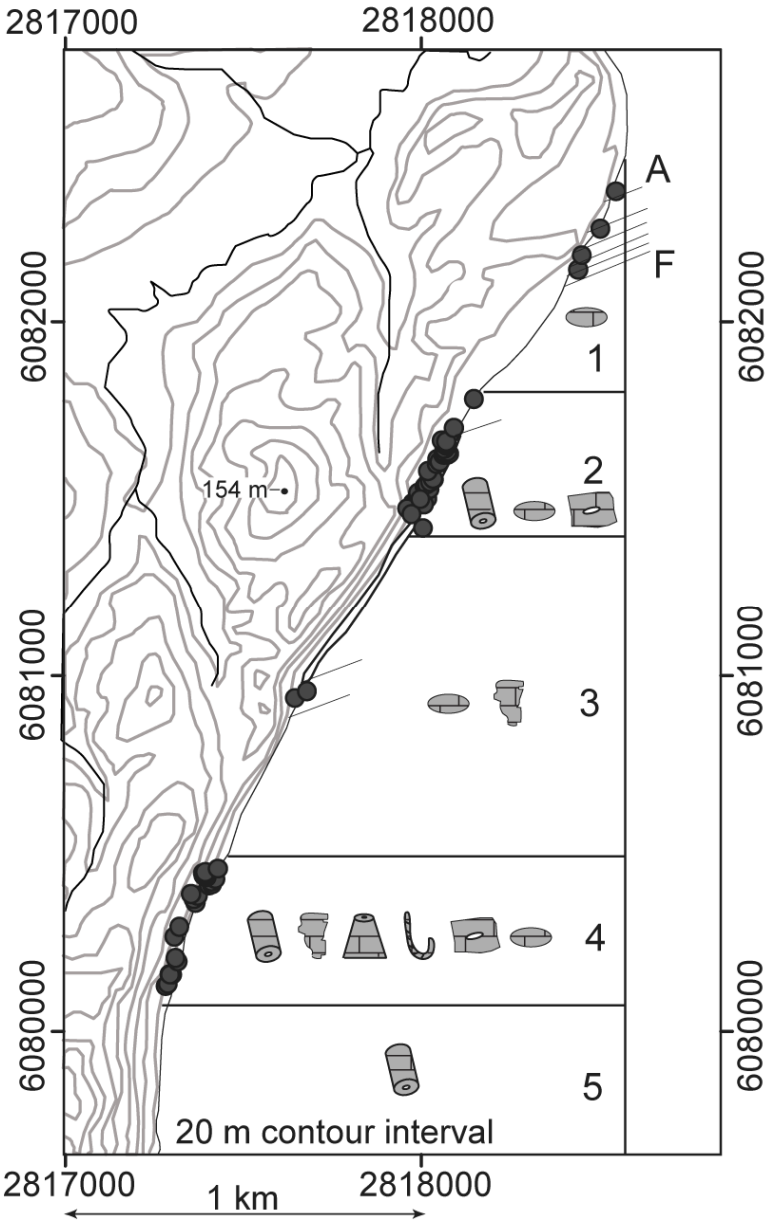

Figure 11. Map of tubular concretion distribution south of the headland at south end of Whangaehu Beach (Fig. 2B) showing coastal sections 1−5 (described in text). Samples and detailed mapping were done only for these sections; sections 6 and 7, not shown here, are labelled in Fig. 2B. Filled circles represent GPS locations of collected measurements and are not inclusive of all tubular concretions present along the coastline. Several GPS locations had multiple samples collected. See Fig. 7 for tubular concretion symbols and Fig. 6 for stratigraphic placement of sections. Diagonal lines at the coast correspond to locations of some concretionary beds. The map coordinates correspond to the New Zealand Map Grid coordinate system and locations may be found on NZ Map Series 260, 1:50,000 scale, sheet V24.

discontinuously raised ~ 0.5 m above the shore platform. Near bed D, pipe-like tubular concretionary debris is common. Between beds D through F, concretionary blocks with conduits are present, but their eroded state does not allow a clear distinction as to source from the concretionary beds or other concretion morphologies. Occasional spherical concretions are exposed. Joint intersections produce small siltstone blocks a few to several cm in size. The joints are gently sinuous with their main orientations bearing 320˚, 270˚, 220˚, or 180˚.

The northern boundary of section 2 (500 m long) marks the first occurrence of distinctive tubular concretions (Fig. 11). These range up to 2 m in diameter (typically 0.5 to 1 m) and at least a couple of metres in length, the latter measurement being governed by degree of exposure in outcrop. Tubes are primarily found *in situ* on the shore platform, but a large cluster of approximately 30 tubes is exposed in the cliff face near the southern end of the section (Figs. 5, 11). Tubular concretions increase in number towards the southern end of this section. The morphologies are predominantly large pipes over 1 m in diameter. Many pipes coalesce and in places have double and triple conduits (Fig. 8C). Conduits are mainly open, and those that are filled are cemented with similar material to that of the concretion, or are filled with dark grey micrite sometimes preceded by a rim of yellow crystalline calcite. Spherical concretions are common along section 2, but generally less so than the tubular concretions (Fig. 6). Three 5 cm thick concretionary beds are present (Figs. 6, 11). Three clusters of concretionary beach rubble comprising small tubes, spheres, and larger blocks occur between about the middle and the southern end of section 2.

Tubular concretions are present in section 3 (1 km long) as tortuous bulbous concretions up to 1 m in diameter and at least 2 m in length on the shore platform, generally oriented along joints, and small pipe concretions are present in isolated deposits of beach rubble (Fig. 11). In places, the bulbous concretions change morphology to more pipe-like tubes. Joint orientations strike 040˚ and 110˚. Five concretionary beds are present and are discontinuously raised ~ 5 cm above the shore platform, spaced about 15 m apart. The beds dip 30˚ ESE. Overall, this section is dominated by small to medium sized (5 to 50 cm) spherical concretions scattered along the shore platform and cliff exposure (Fig. 6). A significant

portion of this cliff section is covered by vegetation, and so the presence of tubular concretions in the cliff face is difficult to fully evaluate.

Section 4 (500 m long) includes the most prominent outcrop of tubular concretions (Figs. 8E-H, 11). Large (up to 3 m diameter and at least 2 m exposed length) tubular concretions are present high in the cliff face. Towards the northern end of section 4, both large (up to 3 m diameter, and 2 m exposed length) and small (0.3 m diameter, and 0.5 m exposed length) tubular concretions crop out. On the shore platform, tubes of various sizes are present, including all morphologies except brecciated blocks and concretionary beds. Small tubes on the platform are commonly straight; others are sinuous and even tortuous. The sinuous pipes are typically small (10−20 cm diameter) and twist across the shore platform to disappear and reappear in different places. Many tubes (both large and small) have narrow open conduits, or filled and fractured conduits. One large tube (2 m high and 1 m wide) has a strongly fractured and brecciated central zone which obscures the conduit boundaries (Fig. 8E). Up to five conduits have been noted in one concretion. A few of the tubular concretions have relatively thin (10–15 cm) concretionary bodies about rather large open conduits (up to 40 cm) (Fig. 8A). Spherical concretions up to 0.5 m in size are common (Fig. 6). Large cemented blocks (not brecciated) with conduits are present on parts of the shore platform. Beach rubble with small tubes is abundant. The host mudstone in this section is highly bioturbated and dips 30˚ SSE.

Section 5 (500 m long) contains small clusters of tubular concretions over a distance of ~ 1 km whose sizes are similar to those in the previous sections, but they consist only of very straight pipe morphologies (Fig. 11). Again, the host mudstone dips ~ 30˚ SSE.

Section 6 (7 km long) lies south beyond section 5 and continues around Cape Turnagain where the mudstone dips ~ 48˚ SE (Fig. 2B) (Moore, 1981). Spherical concretions characterise parts of this section, but tubular concretions have not been recorded and so the section has not been logged in detail.

Tubular concretions reappear in section 7 on the south side of Cape Turnagain where they crop out over 500 m distance in mudstone, dipping ~ 50˚ SE (Fig. 2B)

(Moore, 1981). Here the shore platform is covered by thick deposits of modern dune sand and the tubes are only exposed in the backing cliff face. In comparison to previous sections, the tubes are small (av. 10 cm diameter). In addition, large concretionary blocks with conduits are present, as previously recorded in section 1. In this case, however, the blocks contain multiple small (0.1 to 0.5 cm) conduits (up to five; Fig. 9A,B), many crescent-shaped fractures which appear suture-like (Fig. 9B), and strongly brecciated zones with millimetre to centimetre sized clasts and fine grained sedimentary infill composed of the same material as in the blocks (Fig. 9C,D). The tubular concretions and brecciated blocks are aligned along bedding (dip 50˚ SE). The linear trends appear to follow stratigraphy, with tubes elongated at high angles with respect to bedding.

4.3 Petrography

4.3.1 Concretions

The tubular concretions are composed of silt sized siliciclastic sediments comprising mainly quartz and plagioclase feldspar "floating" in micritic carbonate cement which occludes all pore spaces (Fig. 12A-C). The micritic cement is a mixture of dolomite (strictly protodolomite because Mg content from XRD ranges typically from 44 to 48 mol %) and calcite in varying amounts (Table 1). The carbonate content of concretions ranges from 50–85%, the higher values tending to be closer to their conduits (cf. <10% in the host sediment siltstone). Typically, dolomite is volumetrically the more abundant cement, comprising 50–100% of the total carbonate fraction. Tubular concretions involving calcite cement have trends of increasing calcite content towards the conduit, reaching values of 30–60% (of total carbonate fraction). Little variation in cement fabric is evident within the concretions.

4.3.2 Conduits

Conduits may be open or partially to completely filled. Conduit fills have carbonate contents typically >70%, and involve calcite and/or dolomite cement and cemented sediment. The latter may incorporate veinlets, cement lined vugs,

and/or brecciated clasts (Fig. 12D-H). Conduit fills can be grouped into four types. Type 1 consists of white to yellow, pure calcite cement crystals lining the conduit walls (Fig. 12D, 13A). Uncommonly, this precipitate completely infills the conduits (Fig. 13A). Type 2 conduits are filled with similar material to their concretion, and can be more or less cemented than the concretion (Fig. 13B). Sometimes in this case two conduit zones are distinguishable; an outer portion which is less cemented than the concretion, and a narrow (<1 cm diameter) inner portion which is equally or more strongly cemented than the concretion. Those without this zonation usually have a 'pinhole' conduit a few mm in diameter (Fig. 13B). Type 3 conduits are distinguished by brecciated or veined conduits (Fig. 13C). Typically their outer portion is light grey to rusty yellow-brown micritic siltstone, while their central region is light to dark grey micritic siltstone. Type 4 conduits have yellow to white calcite spar in places and a dark grey micritic fill in the centre (Fig. 13D). Gradations exist amongst the above four conduit types.

Figure 12 (on pg. 161). Petrographic images from tubular concretions. (A,B) Thin section pair (PPL and CL respectively) of tubular concretion showing silt sized clastic material mainly composed of quartz and feldspars and pore filling micritic dolomite cement (orange CL in B); (C) SEM image of mudstone with micritic carbonate cement; (D) SEM image of blocky calcite cement showing crystal formation within an open space; (E) thin section image (PPL) and (F) CL image of a conduit with at least three phases of cement precipitation (1) micritic dolomite (red) cement (2) cement filled veins and vugs (brown/yellow CL, calcite) radiating away from the conduit and (3) calcite cement (bright yellow CL) lining conduits and veins; (G) Thin section image and (H) CL images (lower magnification of E and F) of multi-generational cements. Cement generations (1, 2, and 3) are the same as E and F. Additionally, a sugared/clotted micrite texture can be seen on the left side of the image (yellow CL - calcite). Twelve small conduits with small amounts of detrital material indicate a complex pattern of fluid movement through the mudstone. Typical CL operating conditions: current ~450 μA; voltage ~16 to 20 kV.

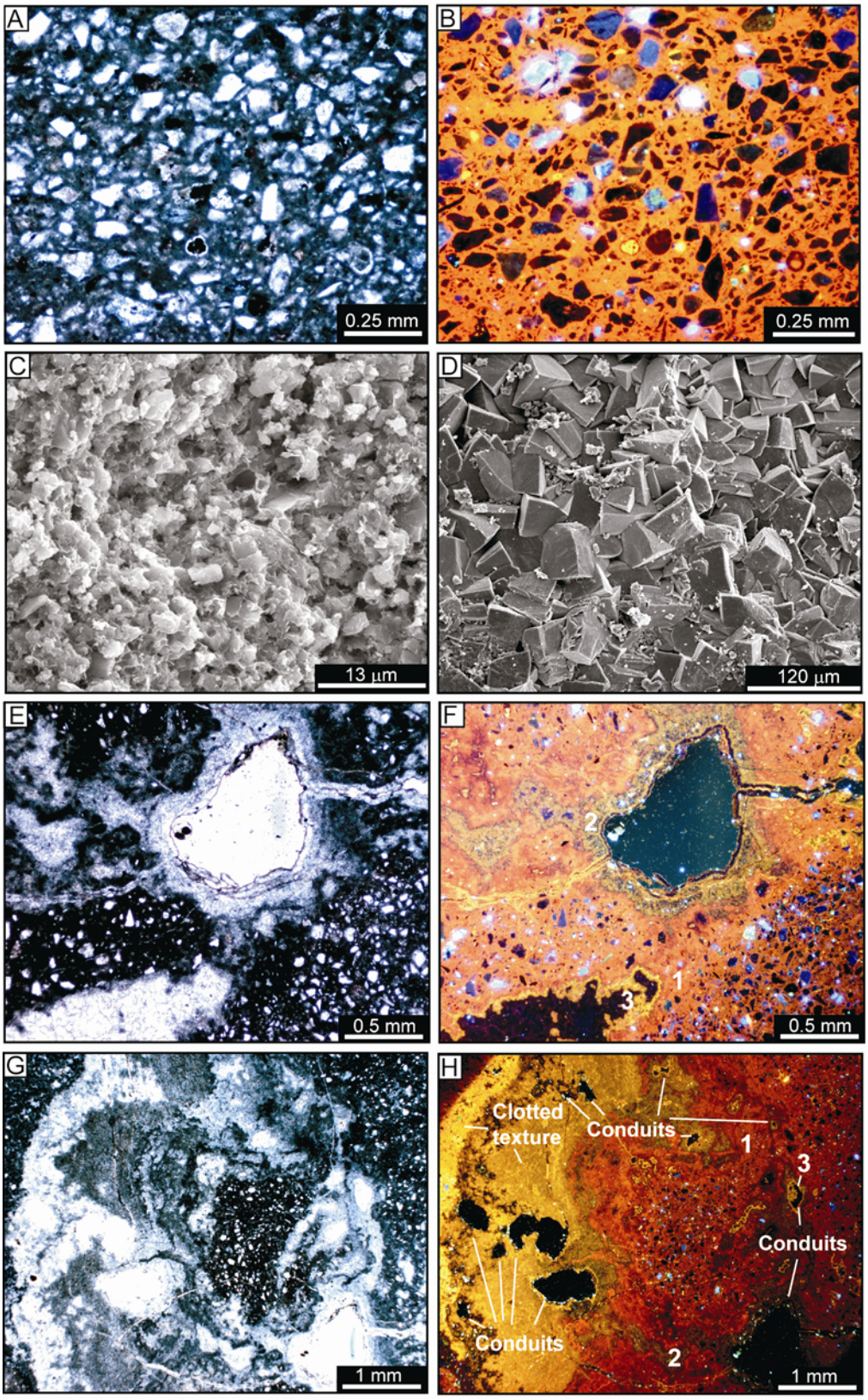
A
0.25 mm
B
0.25 mm
C
13 μm
D
120 μm
E
0.5 mm
F
2
1
3
0.5 mm
G
1 mm
H
Clotted texture
Conduits
1
3
Conduits
Conduits
2
1 mm

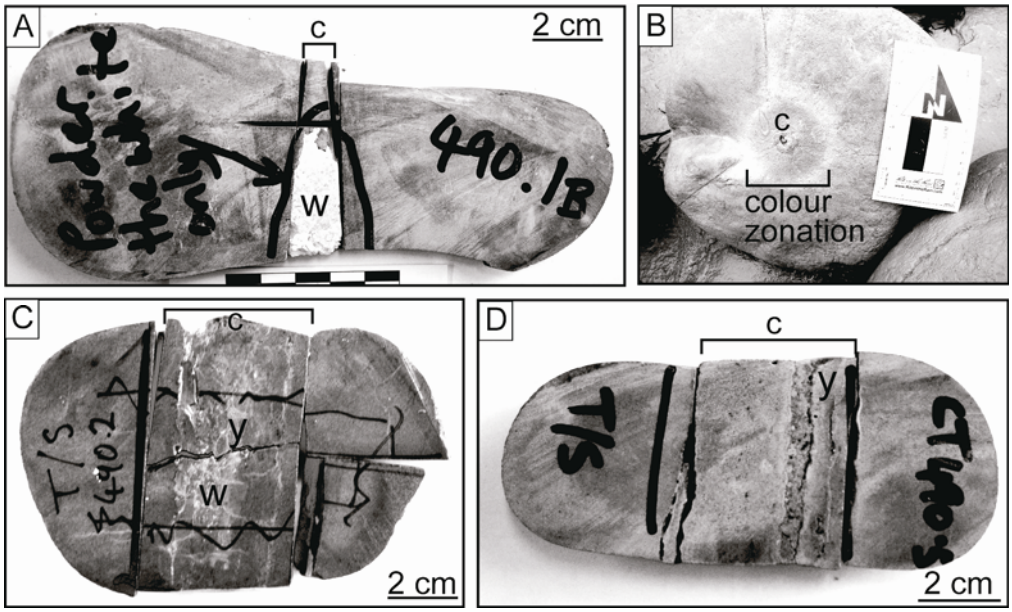

Figure 13. Examples of Whangaehu tubular concretions showing different varieties of conduit fills or fabrics. (A) Coarse crystalline white calcite conduit fill (w); (B) pinhole conduit with two colour zonations suggestive of an earlier outer conduit; (C) white (w) and yellow (y) micritic dolomite with a strongly carbonate brecciated central conduit; and (D) conduit lined with yellow (y) carbonate and micritic (dolomite) cemented mudstone infill.

Two different cement fabrics occur in the conduits: (1) a micritic texture similar to that in the concretions; and (2) a clotted micritic fabric (Fig. 12E,F). CL petrography distinguishes up to five cement types characterised by brownish yellow, greenish-yellow, bright yellow, light orange, and dark reddish-orange CL colours. The yellow end of this CL spectrum reflects more calcitic compositions and the reddish end dolomitic (Fig. 12E-H). The yellow CL also supports a suboxic diagenetic setting. In general, the bright yellow (calcitic) phase lines vugs, and is followed by the greenish-yellow, and then by either the orange phases or the brownish-yellow and then bright yellow, clotted textures. Veins and some vugs are filled or lined with bright yellow calcite and/or a red-brown dolomite. Scattered framboidal pyrite often lines veins.

4.4 Stable isotope composition

Carbon and oxygen isotope signatures can help determine the fluid compositions and carbon sources responsible for carbonate precipitation (e.g., Roberts and Aharon 1994; Nelson and Smith 1996). Carbon and oxygen isotopes were analysed for a variety of concretion types, including transects across tubular concretions, fracture and conduit fills, and host mudstones (Fig. 14). Samples with mixed calcite/dolomite mineralogies were analysed for isotopes in separate reactions (see Section 3) and results for each sample can be compared in Table 1.

The stable isotope values of the tubular concretions group in two overlapping areas on a $\delta^{13}C$ vs $\delta^{18}O$ diagram based on their carbonate mineralogy (Fig. 14). Additionally, the host mudstone, spherical concretions, and conduit/fracture fills also plot in separate regions of the $\delta^{13}C$ vs $\delta^{18}O$ diagram (Fig. 14). Overall, four groups can be distinguished.

Group 1 is associated with calcitic tubular concretions and has $\delta^{13}C$ values ranging from –21 to +12‰ PDB, and $\delta^{18}O$ values from –1 to +5‰ PDB. Twelve samples make up group 1 which are all calcite cement in tubular concretions of mixed mineralogies. Dolomite from the same samples plots in group 2 (Table 1). Three calcite samples from tubular concretions fall outside group 1 (one sample actually plots in group 2, the other two samples lie outside any group). $\delta^{13}C$ values of these three samples are consistent with end member group 1, indicating

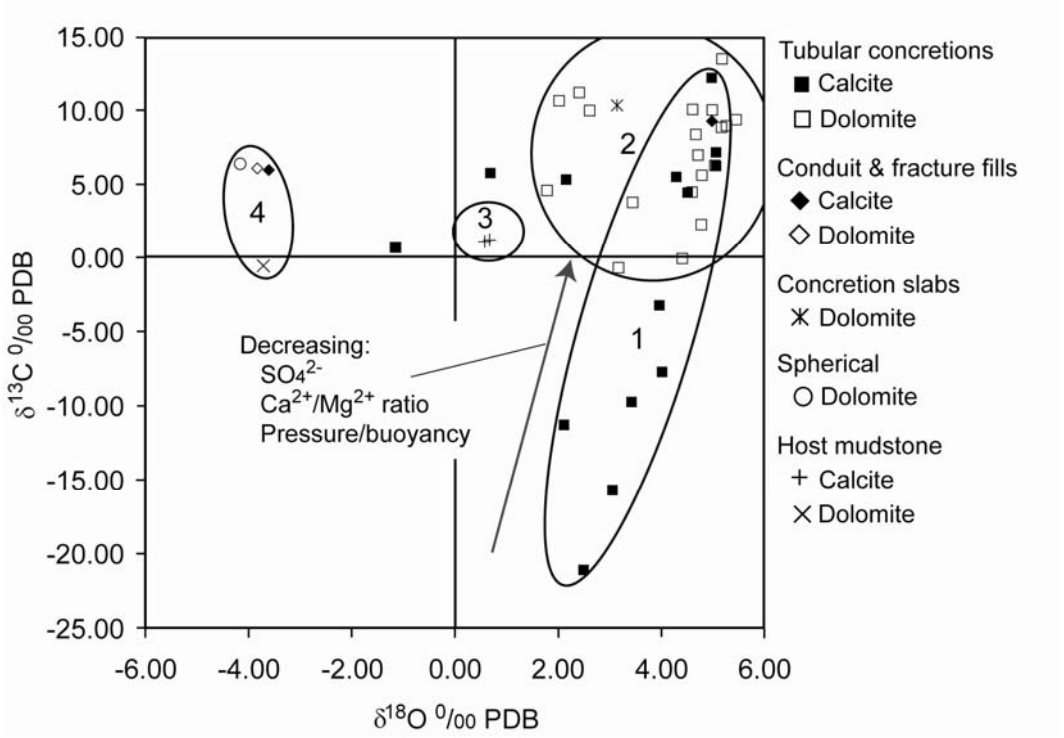

Figure 14. Stable oxygen and carbon isotope plot for tubular concretions from Whangaehu. Note the tendency for dolomite samples to cluster within the upper right quadrant (positive $\delta^{13}C$ and $\delta^{18}O$, group 2), while calcitic samples may do likewise or trend towards moderately negative $\delta^{13}C$ values (group 1). Samples were analysed for dolomite and calcite separately, based on separate digestion reactions (see Section 3). Table 1 identifies paired calcite and dolomite samples. Note the suggested change in diagenetic conditions moving from group 1 into 2 (see Section 5.3).

the same carbon sources. However, $\delta^{18}O$ values are more depleted, suggesting different fluid compositions.

Group 2 is more clustered and corresponds to the dolomitic tubular concretions (11 samples) with $\delta^{13}C$ values from −0.5 to +13‰ PDB and $\delta^{18}O$ from +1.8 to +5.5‰ PDB.

Group 3 corresponds to calcite in the host mudstones (<10% $CaCO_3$), mainly due to foraminifera. The two samples plot near zero with $\delta^{13}C$ of +1‰ and $\delta^{18}O$ of +0.5‰ PDB.

Group 4 consists of two conduit and fracture fills of tubular concretions (dolomite and calcite), a spherical concretion (dolomite), and a dolomite cemented zone surrounding a large concretion. Slightly negative to positive carbon and negative oxygen values characterise these samples ($\delta^{13}C$ –0.5 to +6‰, and $\delta^{18}O$ –4 to −3.7‰ PDB).

To investigate whether there are any systematic changes in the stable isotope composition of the carbonate cement within the tubular concretions, spaced samples were taken along transects extending from their outer margins to the central conduits. Transects were analysed from five tubular concretions, and two representative transects of the five are illustrated in Figure 15 (others in Appendix 2). Each plot is for one tubular concretion and shows the variation in carbon and oxygen for calcite and dolomite along a cross-section of the sample. Three of the five tubular concretions show a depletion trend for both carbon and oxygen toward their conduits. Two display an enrichment trend in carbon isotope values, while their oxygen values remain relatively constant. Systematic variations between tubular concretions are not discernible. Consequently, the variation in isotope values with position in the tubular concretions are interpreted to reflect cement precipitation from different fluid compositions over time.

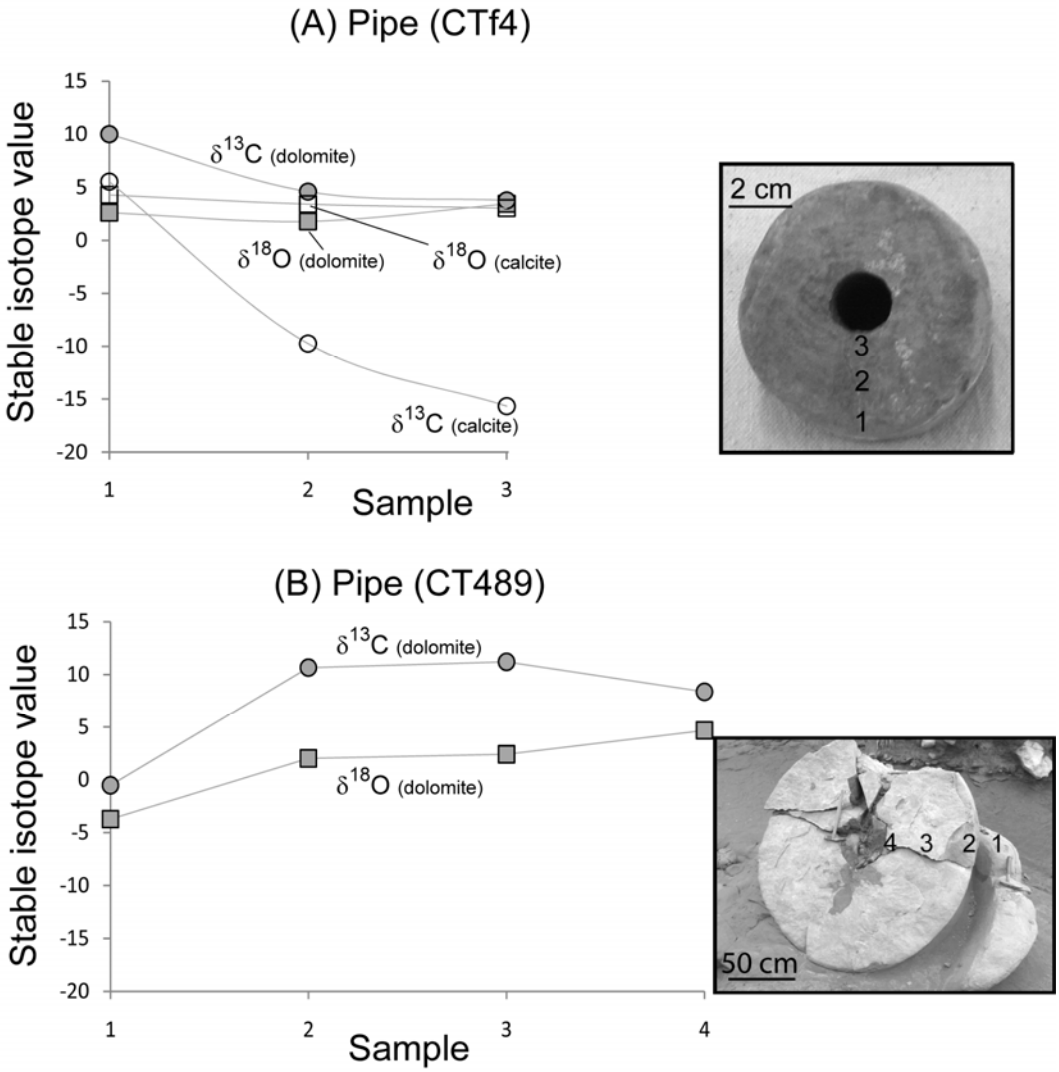

Figure 15. Carbon and oxygen isotope transects through two pipe concretions. (A) In CTf4, a mixed dolomite-calcite sample, the isotope values are relatively constant along the transect except that the $\delta^{13}C$ values, for calcite in particular, become more depleted toward the conduit. (B) In CT489, a solely dolomite sample, the isotope values remain similar, but note the more depleted values in the outermost margin of the concretion. Samples come from coastal section 4 (Fig. 11).

Table 1. Stable carbon and oxygen isotope values of carbonate in the tubular concretions from Whangaehu, along with their percentages of calcite versus dolomite (out of 100% carbonate).

Concretion sample	Sub sample	Sample description	$\delta^{13}C$ ‰ PDB calcite	$\delta^{18}O$ ‰ PDB calcite	Isotope group	$\delta^{13}C$ ‰ PDB dolomite	$\delta^{18}O$ ‰ PDB dolomite	Isotope group	% Calcite	% Dolomite
CTc1	CTc1-1	Outer	+6.3	+5.1	1	+9.4	+5.5	2	5	95
	CTc1-2	Middle	-7.7	+4	1	+6.3	+5.0	2	25	75
	CTc1-3	Conduit fill	-21.1	+2.5	1	-0.1	+4.4	2	59	41
CTc2	CTc2-1	Outer	-3.2	+4.0	1	+5.6	+4.8	2	32	68
	CTc2-2	Middle	+4.5	+4.5	1	+4.5	+4.6	2	48	52
	CTc2-3	Conduit fill	+9.3	+5.0	1	+9.3	+5.0	2	39	61
CTf3	CTf3-1	Outer	+7.2	+5.1	1	+8.9	+5.2	2	11	89
	CTf3-2	Middle				+9.0	+5.3	2	0	100
	CTf3-3	Conduit fill	+12.3	+5.0	1	+13.5	+5.2	2	10	90
CTf4	CTf4-1	Outer	+5.5	+4.3	1	+10.0	+2.6	2	20	80
	CTf4-2	Middle	-9.70	+3.4	1	+4.6	+1.8	2	50	50
	CTf4-3	Pipe conduit rim	-15.70	+3.0	1	+3.8	+3.4	2	63	37
209.1	209.10	Concretion layer				+10.4	+3.1	2	0	100
682.1a	682.1a	Small tube				+7.0	+4.7	2	0	100
682.1b	682.1b	Small tube	+5.8	+0.7	X	+10.1	+4.6	2	12	88
682.2a	682.2a	Small tube	+5.3	+2.1	X	+10.0	+5.0	2	17	83
682.2c	682.2c	Small tube	+6.0	-3.6	4	+6.1	-3.8	4	11	89
841.1	841.1a	Small tube	-11.3	+2.1	1	-0.7	+3.2	2	58	42
	841.1b	Small tube	+0.7	-1.2	X				100	0
489	489.10	Conduit				+8.4	+4.7	2	0	100
	489.20	Middle				+11.2	+2.4	2	0	100
	489.30	Outer				+10.7	+2.0	2	0	100
	489.40	Cemented host mud surrounding 489				-0.5	-3.7	4	0	100
530.1	530.10	Spherical				+6.4	-4.2	4	0	100
372.10	372.10	Host mud, section 5	+1.1	+0.6	3				100	0
352.10	352.10	Host mud near site entry	+1.2	+0.7	3				100	0
490.1	490.1	Small tube				+2.3	+4.8	2	0	18

5. Discussion

5.1 Fluid composition

5.1.1 Carbon

Carbon isotope values recorded in authigenic carbonate reflect the source of carbon incorporated into the carbonate lattice. Carbon sources include marine shell material, decomposition of organic matter, oxidised microbial or thermogenic methane, and residual CO_2 as a by-product of microbial methanogenesis (Irwin et al., 1977; Curtis, 1978, 1986; Roberts and Aharon, 1994).

Conventionally, enriched carbon signatures such as those recorded by most of the Whangaehu concretions (Fig. 14; $\delta^{13}C$ from +4 to +13‰ PDB) have been interpreted as being sourced from reduced CO_2 produced as a by-product of methanogenesis (Greinert et al., 2001; Pierre et al., 2002; Peckmann et al., 2002; Pierre and Rouchy 2004; Gieskes et al., 2005). As such, the enriched ^{13}C values in the Whangaehu concretions could be interpreted as derived from the microbial production of methane during shallow burial (up to 1 km) of the sediment pile.

Alternatively, intensive methane oxidation may also result in enriched carbon isotope values. Microbial methane has $\delta^{13}C$ values from –110 to –50‰ PDB and thermogenic methane from –50 to –20‰ PDB (Whiticar, 1999). As methane is oxidised, the residual methane pool becomes more enriched in $\delta^{13}C$ due to isotope fractionation (Coleman et al., 1981; Whiticar, 1999; Pancost et al., 2000; Cowen et al., 2002). Oxidation of 80% of the methane pool can enrich the residual methane pool by 10–30‰, while oxidation of 99% of the pool would do so by 20–60‰ PDB (Whiticar, 1999). Therefore, 80 to 99% oxidation of a thermogenic or microbial methane pool can result in the residual methane having a strongly positive $\delta^{13}C$. Interestingly, Cowen et al. (2002) reported both strongly negative and positive $\delta^{13}C$ isotope values of methane ($\delta^{13}C_{methane}$ from –50 to +10‰ PDB) from hydrothermal plumes along the Juan de Fuca Ridge. The $\delta^{13}C$ values became increasingly enriched with distance from the main methane expulsion site,

a relationship interpreted to have been caused by extensive methane oxidation. Additionally, the oxidation of microbial methane can result in $\delta^{13}C$ signatures of the residual methane pool identical to that for thermogenic methane. Such processes may obviously cause difficulty in positively identifying the source of methane (Coleman et al., 1981).

Calcite with low $\delta^{13}C$ values corresponds to dolomite with high $\delta^{13}C$ values within the same tubular concretion sample (Table 1, Fig. 15A). This indicates that fluids evolved over the time of tubular concretion formation, whether from extensive oxidation or microbial methane oxidation and methanogenic CO_2. If extensive oxidation caused the variation in $\delta^{13}C$ values, the calcite would have precipitated before dolomite. Alternatively, if carbon sources were mixed microbial methane and residual CO_2 from methanogenesis, then calcite would have precipitated during AOM whereas dolomite would have precipitated at times when AOM was not occurring in the sediments.

Carbonate cement from a tubular concretion with mixed calcite/dolomite composition (sample CTf3; Table 1) has been analysed for lipid biomarkers. Biomarker compounds in the sample include pentamethyl icosane (PMI) and archeol, indicative of anaerobic oxidation of methane (AOM) consortia, and C33 dialkyl glycerol diether (DGD) and macrocyclic diether (MD), indicative of sulphate reducing bacteria and AOM consortia (Pearson et al., 2008). In comparison, the host mudstone does not contain PMI or MD, and only traces of archaeol and DGD. The $\delta^{13}C$ values of both calcite and dolomite are not characteristic of oxidised methane (< −50‰) but instead are enriched (+7 to +13‰, Table 1). However, the AOM markers are all very ^{13}C-depleted and confirm that AOM by methanotropic Archaea and sulphate reducing Bacteria was occurring in the sediments (Pearson et al., 2008).

Extensive methane oxidation could explain lipid biomarkers indicative of AOM in the ^{13}C-enriched carbonate samples. Alternatively, the positive $\delta^{13}C$ values of the carbonate cement could reflect residual CO_2 from methanogenesis. In such a case, calcite with low $\delta^{13}C$ values would have precipitated first from AOM. Then, ^{13}C-enriched carbonates could have formed after AOM ceased, and potentially incorporated residual biomarker signals into the cement precipitates.

5.1.2 Oxygen

Oxygen isotope values recorded in authigenic carbonate relate mainly to the fluid composition at the time of carbonate precipitation and the temperature of precipitation (Longstaffe, 1987). Based on minus cement porosities in the Whangaehu concretions (50−85% carbonate) and porosity vs burial depth relationships, precipitation occurred at shallow burial depths, likely < 100 m and no deeper than 300 m (e.g., Boggs, 1992; Bjørlykke, 1998). If upper slope bottom water temperatures were in the range 5–10˚C (Ridgway, 1969), then maximum burial temperatures during carbonate precipitation would probably have been between 12 and 17˚C with a geothermal gradient of 23˚C/km (Field et al., 1997).

Fluid compositions at the time of carbonate precipitation can be constrained in terms of their burial and source based on the equation from Friedman and O'Neil (1977) for calcite (Fig. 16A) and from Fritz and Smith (1970) for protodolomite (Fig. 16B). Although there are several equilibrium equations for dolomite precipitation, many relate to high temperature conditions (> 350˚C). The derived equation used for interpretation of this data set is based on experiments by Fritz and Smith (1970) for protodolomite (40−50% Mg) at low temperatures (25˚C) since this best reflects the dolomite composition and temperature conditions for this study.

Feary et al. (1991) suggested that Miocene marine water in New Zealand had an average $\delta^{18}O$ of –0.7‰ SMOW. Based on equilibrium calculations, calcite precipitation from seawater should have $\delta^{18}O$ values from +0.5 to +1.5‰ PDB and dolomite from +3 to +4.5‰ PDB (Fig. 16). If the Whangaehu tubular concretions formed near the seafloor (within ~50 m) then the carbonate is enriched by up to +4.5‰ for calcite and +2.5‰ for dolomite at temperatures between 5 and 10˚C. A few dolomitic tubular concretion samples are slightly depleted from marine waters which may reflect higher temperatures or , as discussed below, periods of gas hydrate formation.

The enriched oxygen isotope values could be explained by: (1) evaporation; (2) clay dehydration; or (3) gas hydrate dissociation. Evaporative conditions in the

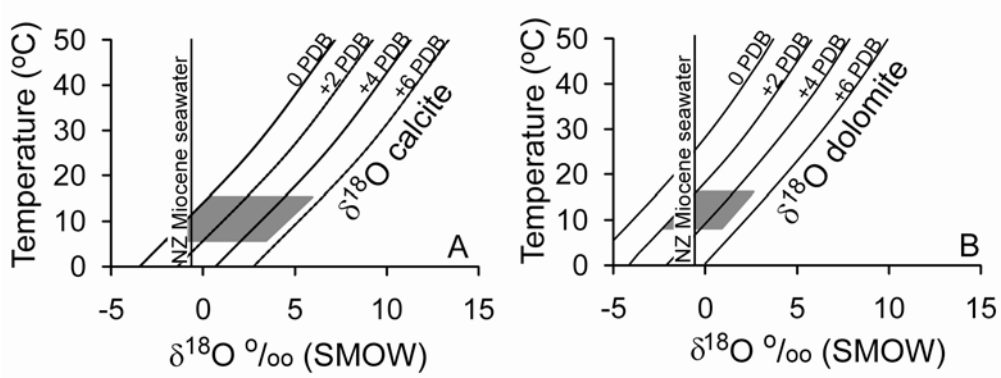

Figure 16. Possible water isotope compositions (SMOW) responsible for carbonate precipitation in the Whangaehu concretions. The grey polygons highlight the possible water compositions responsible for the positive oxygen isotope values in the tubular concretions. (A) Calcite equilibrium calculation from Friedman and O'Neil (1977); (B) dolomite equilibrium calculation from Fritz and Smith (1970). New Zealand Miocene seawater composition from Feary et al. (1991).

subsurface environment are unlikely, and any burial transformation of clays would not have occurred before the shallow burial precipitation (< 100 m) of carbonate in the Whangaehu concretions. Moreover, the persistence of common to abundant smectite in the clay fraction of many of the older East Coast Basin formations (e.g., Pearce et al., 1981; Fergusson, 1985) effectively negates clay mineral alteration as a burial source of ^{18}O-enriched fluids. Consequently, we suggest the most likely explanation for enriched $\delta^{18}O$ values in the concretionary carbonate is the dissociation of gas hydrates. During gas hydrate formation heavy oxygen is preferentially accepted into the clathrate water molecule, and upon dissociation of large volumes of gas hydrates, heavy oxygen can be released into sediment pore fluids (Davidson et al., 1983; Ussler and Paull, 1995). If gas hydrates are the most likely cause of enriched oxygen isotope values in the tubular concretions, then the depleted oxygen isotope values were probably due to gas hydrate formation.

5.2 Plumbing system of a hydrocarbon seep field

Recent literature has described irregular concretionary bodies in mudstones interpreted to be associated with cold seeps. The concretionary bodies have been referred to as tubular concretions, pipes, chimneys, doughnuts, circular-pipe-like cavities, cylindrical concretions, and variations of these names, all having a central hole or conduit running the length of the concretions, which may be filled with sediment or cements (e.g., Kulm and Suess, 1990; Jensen et al., 1992; Orpin, 1997; Aiello et al., 1999, 2001; Lédesert et al., 2003; Mazzini et al., 2003; Clari et al., 2004; Conti et al., 2004; Conti and Fontana, 2005; Hovland et al., 2005; De Boever et al., 2006). In the majority of cases, the size of these concretions is measured in centimetres to a few tens of centimetres, exceptions being examples from Kattegat, Denmark (Jensen et al., 1992), Gulf of Cadiz, Portugal (Díaz-del-Río et al., 2003), Bulgaria (De Boever et al., 2006), and New Zealand (Lédesert et al., 2003; Nyman et al., 2006), where the tubular features are unusually large (up to 10 m or more in length and 4 m in diameter).

The Whangaehu tubular concretions display a wide range of sizes and morphologies which provide an opportunity to further investigate the variable conditions within a subsurface seep system. Previously, Lédesert et al. (2003)

suggested the tubular concretions at Whangaehu represented fluid expulsion structures which were not sourced by methane rich fluids based on the lack of seep related fauna. However, the present study now provides the isotope evidence to confirm that the fluids responsible for carbonate precipitation in the tubular concretions were likely sourced from methane. As a consequence, the tubular concretions are interpreted herein to reflect a shallow sub-seafloor plumbing network of a late Miocene cold seep system where methane rich fluids migrated upwards along directed pathways toward the seabed. No clear fault control on the distribution of the tubular concretions at the outcrop scale is evident within the Whangaehu coastal section. However, at the regional scale, roughly coastline parallel thrust faults are a conspicuous feature of this sector of the Hikurangi Margin (Figs. 2B, 3B) and likely afforded the principal pathways for focused fluid ascent (cf. Lewis and Marshall, 1996; Sibson and Rowland, 2003).

5.2.1 Implicating methane hydrates

Additionally, the oxygen isotope values of the carbonate indicate gas hydrate dissociation influenced the water composition at the time of carbonate precipitation. Carbonates with isotopically light carbon and heavy oxygen are reported in the literature as derived from the dissociation of microbial or thermogenic methane hydrate (Greinert et al., 2001; Aloisi et al., 2000; Clari et al., 2004; Pierre and Fouquet, 2007). To my knowledge, only two other studies, involving dolomite concretions in late Miocene marls from the Mediterranean (Pierre et al., 2002; Pierre and Rouchy, 2004), have interpreted the co-occurrence of isotopically heavy carbon and heavy oxygen to be a result of methane hydrate dissociation. In those studies, the authors interpreted the heavy carbon to have been sourced from residual CO_2 from methanogenesis.

The geochemical processes that result in carbonate precipitation utilising residual reduced CO_2 from methanogenesis and heavy oxygen from the hydrate molecule, but not incorporating the light carbon in the CH_4 from the former hydrate molecule, have not been previously discussed. Geochemically it is difficult to envisage how isotopically heavy carbon can be incorporated into the carbonate lattice but excluding light CH_4 carbon. Therefore any explanation must rely on

separation of the constituents during carbonate precipitation or when AOM is not occurring. Such conditions could occur if the fluids were a mix of microbial methane and residual CO_2 from methanogenesis. If microbial methane migrates into the gas hydrate stability zone, methane hydrate will form trapping the methane molecule in the clathrate while the CO_2 remains in the pore spaces. Theoretically, the pore spaces would be anomalously ^{18}O-depleted as the hydrate molecule preferentially incorporates the heavier oxygen. However, over time, mixing with seawater or continued fluid ascent would minimise such an effect. Subsequently, when hydrate dissociation occurs, heavier water and methane are released back into the pore fluids. During AOM, carbon from both microbial methane (strongly depleted) and residual CO_2 (strongly enriched) precipitated calcite with moderately depleted $\delta^{13}C$ values and enriched $\delta^{18}O$ values. If AOM is later inhibited (either due to diminished sulphate or methane supply) then calcite and dolomite with increasingly enriched carbon isotope values will precipitate.

An alternative explanation considers extensive AOM resulted in strongly positive carbon isotope values. The most enriched $\delta^{13}C$ values in the tubular concretions (+12‰ PDB) could be accounted for by oxidation of 80% of a thermogenic methane pool or 99% of a microbial methane pool. However, if microbial methane was the carbon source, then it is probable that residual CO_2 was also present and incorporated into the carbonate. Therefore a microbial methane pool with methanogenic CO_2 would require much less extensive oxidation.

Moreover, as the methane pool becomes depleted, the sulphate concentration reduces and continued carbonate precipitation lowers the Ca/Mg ratio leading eventually to dolomite precipitation being favoured over calcite precipitation.

Consequently, we suggest that a combination of anaerobic methane oxidation (AOM) and gas hydrate dissociation is the most likely hypothesis for the positive $\delta^{18}O$ and $\delta^{13}C$ values in the Whangaehu tubular concretions. Carbon sources were most likely microbial methane and residual CO_2 from methanogenesis, however, thermogenic methane cannot be ruled out. A three stage scenario is described for tubular concretion formation in the subsurface seep system in Section 5.3 (and Fig. 17 inserted on page 195) based on microbial methane and CO_2. Extensive

AOM could also be operating within such a system, thereby requiring less CO_2 to account for the enriched $\delta^{13}C$ values. Additionally, thermogenic methane can be substituted via the explanation of extensive methane oxidation. The hypothesised scenario may be applicable in other cold seep studies where heavy carbon isotopes are associated with heavy oxygen isotopes in their authigenic carbonate cements. Moreover, the tubular concretions and hypothesised scenario may also provide a conceptual model for the subsurface fluid pathways and seep-related processes occurring today beneath the modern Hikurangi Margin seabed.

5.3 Subsurface seep plumbing model

5.3.1 Stage 1 (Fig. 17A, pg. 195)

Following initiation of upward fluid migration, methane rich fluids eventually reach the shallow subsurface (less than 300 m). Major fluid migration pathways were probably along thrust faults in the Hikurangi Margin subduction complex (Fig. 3B) (Lewis and Marshall, 1996; Sibson and Rowland, 2003). As methane enters the gas hydrate stability zone (HSZ), gas hydrate forms if methane concentrations are at or higher than saturation (Fig. 17A). Methane and heavy water is then trapped in the hydate molecule. CO_2 and anomalously light porewaters continue to migrate upwards. During stage 1 and transition into stage 2, methane and CO_2 are still being supplied from below, replenishing the porewaters with buried marine fluids.

5.3.2 Stage 2 (Fig. 17B, pg. 195)

Later, sediment burial or relative seabed uplift shifts the HSZ so that hydrate no longer within this zone begins to dissociate (Fig. 17B). In the case of the Whangaehu Mudstone, we suggest relative seabed uplift (or sea level fall) caused hydrate destabilisation. The Pliocene Kairakau Limestone sitting stratigraphically above the Whangaehu Mudstone (Fig. 6) indicates a progression from slope to shelf paleodepths over time. Additionally, sea level oscillations during the late Miocene are prevalent, in particular sea level fall in the Messinian (New Zealand Kapitean Stage) (e.g., Hodell et al., 1986; Cooke et al., 2008).

Upon hydrate dissociation, $\delta^{18}O$ values of pore fluids become enriched due to the release of ^{18}O-rich water from gas hydrates. Methane and ^{18}O-rich fluids ascend towards the seafloor. Once the fluids encounter sediments containing methanotrophic Archaea and sulphate reducing Bacteria, the methane can be oxidised. AOM processes increase alkalinity and induce carbonate precipitation. The first carbonate precipitates should reflect the beginning of methane oxidation and have more negative carbon isotope signatures (–50 to –20‰ PDB). The Whangaehu concretions do not record such values; therefore, the tubular concretions with more depleted $\delta^{13}C$ values (–21‰ PDB) and positive $\delta^{18}O$ values are consistent with oxidised methane mixed with residual CO_2 (or extensive AOM) and hydrate dissociation (Table 1, Figs. 14, 17B).

5.3.3 Stage 3 (Fig. 17C, pg. 195)

During Stage 3, AOM is restricted due to the removal of sulphate and/or methane. In this scenario, it is hypothesised that methane concentrations lowered as methane hydrate dissociation returned to conditions of formation (i.e., hydrate that had moved out of the stability zone upon uplift was now all dissociated, but hydrate is still forming below). Lower volumes of methane will reduce gas concentrations, which in turn reduces fluid pressures and buoyancy, resulting in more tortuous fluid migration pathways (Judd and Hovland, 2007). Calcite continues to precipitate but with more enriched $\delta^{13}C$ values. Eventually, Ca/Mg ratios decrease and dolomite is favoured over calcite. These late-stage conditions within the system form dolomitic tubular concretions with both heavy carbon and oxygen isotope values and morphologies ranging from pipes to more sinuous and bulbous concretions (Fig. 17C). As fluids become increasingly influenced by hydrate formation, $\delta^{18}O$ values become slightly depleted.

Alternatively, extensive oxidation of methane could also result in the trend from strongly depleted to strongly enriched carbon isotope values via the same scenario in Stages 2 and 3. This process could be operating in a system sourced from microbial methane and residual methanogenic CO_2 which would explain why such a large number of samples have positive carbon isotope values. Additionally, if the methane source was thermogenic, extensive oxidation can

explain the enriched carbon. Consequently, based on the hypothesised model and the ^{13}C-enriched methane from the Juan de Fuca Ridge hydrothermal vents interpreted as being due to methane oxidation by Cowen et al. (2002), it is suggested that extensive oxidation of methane in seep systems may play a significant role resulting in carbon isotope enrichment, particularly in ephemeral seep systems. This concept requires further assessment.

5.4 Concretion growth patterns

The relatively high content of carbonate in the tubular concretions (50−85%) compared to the host mudstone (<10%) is present as micrite or microsparite carbonate cement that was precipitated within interparticle spaces of the muddy sediment beneath the paleo-seafloor (Fig. 12A-C). Unlike widely known spherical concretions in which cement precipitation initiates about some nucleation site such as decaying organic matter or shell fragments, and thereafter continues to precipitate in a concentric, centre-to-margin growth pattern (McBride et al., 1995), there is no "solid" nucleation centre in the Whangaehu tubular concretions; rather they mainly support open conduits. Consequently, we hypothesise that the nucleation site was about that "core" of sediment subjected to focused fluid flow and that cement precipitation began at the outer margins of a tubular concretion and continued to precipitate inwards towards the central conduit (Fig. 18A-D). This kind of scenario involving "outside to inside" precipitation to form tubular concretions is also how Clari et al. (2004) interpreted similar kinds of concretionary features inside an Italian Miocene mud volcano. Apart from the Italian study, other explanations about the growth direction of tubular concretions have not been addressed in the literature. We cannot conclusively explain the growth pattern, however we find it difficult to imagine cement precipitation beginning at the conduit and continuing outward. The following discussion postulates a potential geochemical mechanism that may control the tubular concretion growth pattern via cement precipitation from the outer margins towards the conduit, although it is acknowledged there may well be a degree of overlap in precipitation across such a transect.

For carbonate precipitation to occur, a source of oxygen needs to be available for methane oxidation. In this case, oxygen is supplied from sulphate in the adjacent

pore water. The migrating fluids will create advection currents effectively drawing in the adjacent sulphate rich pore waters, along with sulphate reducing Bacteria and methanotrophic Archaea. Additionally, as the adjacent pore fluids are being drawn inwards, they are also directed upwards as they mix with the ascending methane-rich fluids. Methane is then oxidised by AOM resulting in tubular concretion formation via carbonate precipitation from the outer margins of the flow path inward, as well as upward (Fig. 18B).

As carbonate precipitation continues, flow rates through the conduit increase due to increased pore pressures in the concretion, assuming no change in the volume of fluid passing through the sediments (Fig. 18B,C). As flow rates increase, sediment may be mobilised and evacuated from the central migration pathway, creating an open conduit (Fig. 18C). If, however, fluid flow rates are insufficient to expel sediment, cement may continue to precipitate inwards leaving a largely cemented (concreted) sediment conduit instead of an open hole (Fig. 18D).

If sediment is evacuated from the central flow pathway (Fig. 18C,E) then the resulting conduit may subsequently become variably filled by different mechanisms: (1) Cement may precipitate from solution along the conduit walls (Fig. 18F) and could eventually fill the conduit. The cements could be sourced from either methane-rich fluids or later diagenetic burial fluids. (2) Fluids may transport sediment from below into the migration pathway, essentially obstructing the conduit, or sediments from above may collapse into the conduit if fluid rates/volumes are reduced (Fig. 18G). (3) As conduits become closed off due to cementation or sediment infill then, assuming continued flow rates, pressures in the conduit system will increase. Constriction of the pathway and associated pressure increase can result in hydrofracturing of the central conduit or concretionary material to produce breccias (angular clasts of host concretion, foreign material, or conduit cement fill) in a finer-grained sediment matrix (Fig. 18H). Brecciated conduits may also reflect a sudden increase in the volume of fluids migrating through the system, a feature in previous studies that has been linked to gas hydrate dissociation (Suess et al., 1999; Greinert et al., 2001).

The size of the tubular concretions at Whangaehu bears a very general direct relationship ($R^2 = +0.5$) to the size of their conduits (Fig. 10). However, the trend

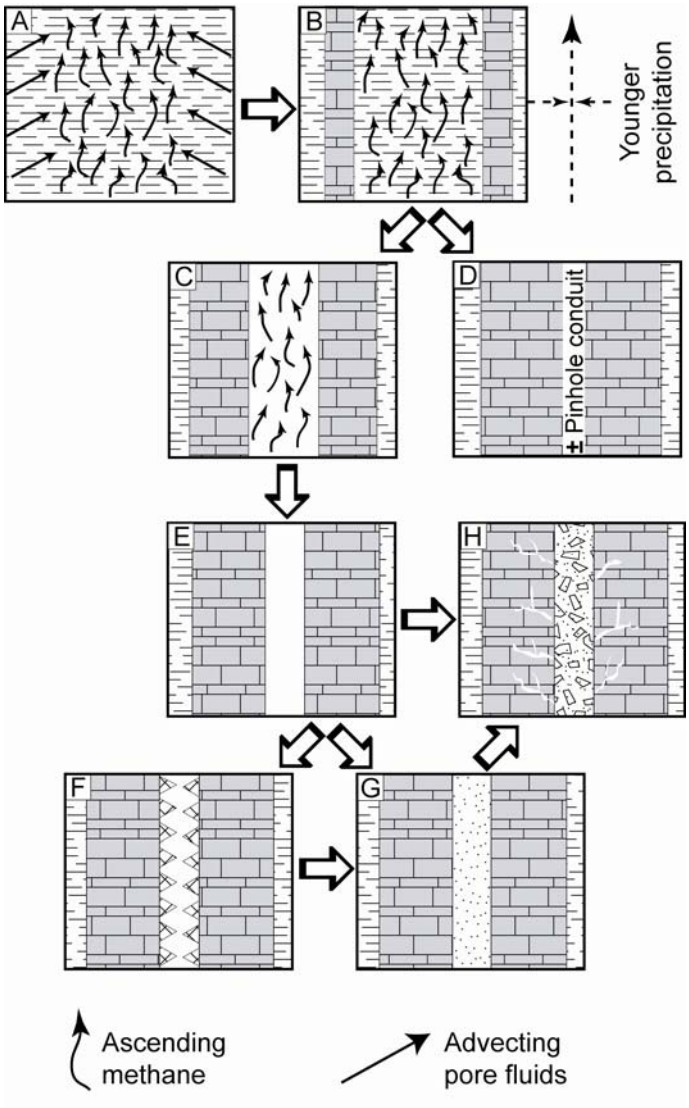

Figure 18. Hypothesised growth patterns for tubular concretions. (A,B) Focused fluid migration through the sediment is accompanied by carbonate precipitation towards the outer margins. (C) Over time, fluid movement may eventually evacuate sediment from the conduit. (D) Alternatively, if fluid pressures are insufficiently high, sediment may not be ejected and carbonate precipitation may continue inward leaving no apparent conduit or only a pinhole conduit. (E) Represents the cessation of methane migration and (F) a subsequent lining of the conduit with crystalline calcite precipitated from later burial fluids. (G) Additionally, after the fluid source is cut off or volumes/pressures reduced, sediments from above may infill the conduit. (H) If fluid migration continues or re-initiates, then the restricted passageway results in brecciation and fracturing of the conduit material. Concretion growth patterns can progress from E to H (skipping F and G). In such cases, sediment infill may also be supplied from below if fluid flow regimes are not reduced.

is poor for tubular concretions smaller than about 1 m in diameter. Observations in outcrop reveal that large tubular concretions may have large or small conduits, concretions larger than 1 m in diameter tend to have conduits 25−50% larger than concretions less than this. Moreover, many of the larger tubular concretions often have multiple conduits (e.g., Fig. 8C), up to as many as five. The above relationships suggest that conduit versus concretion size likely reflects a complicated history of changing fluid volumes, pressures, sediment strength of fluid passageways, velocity of fluid movement, and duration of migration events (cf. Mörz et al., 2007).

5.5 Longevity of cold seep system

The Hikurangi subduction margin off eastern North Island was initiated in the early Miocene (Fig. 3) (van der Lingen and Pettinga, 1980; Field et al., 1997; Nicol et al., 2002; Kamp and Furlong, 2006). Fluid ascent from overpressured sediments at depth occurs today throughout the Hikurangi Margin due to compaction and compressional tectonics (Lewis and Marshall, 1996; Sibson and Rowland, 2003) and results in modern seepage both onshore and offshore the East Coast Basin (Fig. 2A) (Rogers et al., 1999; Francis et al., 2004). We infer the same driving forces of upward fluid migration were acting in the accretionary prism during the late Miocene, resulting in localised fluid migration through the Whangaehu Mudstone. Subduction related faulting (Lewis and Pettinga, 1993; Field et al., 1997; Lee and Begg, 2002) probably provided the major fluid migration pathways for seepage at the seafloor within the region.

5.5.1 Seafloor fluid expulsion

Paleo-seep limestones and chemosymbiotic fossils are lacking in the Whangaehu Mudstone, so there is no direct evidence for fluid expulsion at the seafloor in these deposits. Within section 4 of the coastal outcrop (Fig. 11), the tortuosity, branching, and coalescing of many small tubular concretions is similar to that exhibited by tubular concretions occurring just below the Rocky Knob seep limestone in northern Hawke's Bay (Fig. 2A; Campbell et al., 2008; topic addressed in Chapter 6), and so may reflect fluid migration close below a paleo-

seafloor. The wide variety of concretion morphologies and isotope values in coastal section 4 may reflect variations in fluid flow volumes through time, with the more pipe-like morphologies and ^{13}C-depleted isotope values associated with higher fluid flux and the more tortuous and bulbous morphologies and ^{13}C-enriched isotope values with lower fluid flux. In section 7 on the south side of Cape Turnagain (Fig. 2B), the highly brecciated blocks (Fig. 9) may represent zones near the seafloor where fluids were less confined, so that fluid migration could move laterally away from the more focused pathways. Ongoing cementation potentially blocked fluid movement, leading to increased pressures and hydrofracturing to form fissures and zones of intensely brecciated clasts. The concretionary beds (Fig. 6) may have also developed in more permeable sediment horizons nearer the seafloor, likely reflecting subtle sedimentary stratification in the host siliciclastic muds.

Early Miocene seafloor seep limestones with chemosynthetic fossils occur in at least five separate localities some 20 km inland to the NW of Whangaehu Beach (Fig. 2A) (Nelson et al., 2007; Campbell et al., 2008). The occurrences clearly record fluid migration to the seafloor prior to deposition of the Whangaehu Mudstone. As the inboard portion of the accretionary margin was progressively upthrusted during the Miocene, and the sea regressed, ascending fluids presumably found alternative migration routes and expelled through sediments accumulating further eastwards along the contemporary margin of the time, including within the Whangaehu muds. In the modern, recent research cruises along the Hikurangi Margin (Lewis and Marshall, 1996; Pecher et al., 2007; Greinert et al., in review**)** have documented active cold seeps on the seafloor (Fig. 2A) that include many features similar to those seen in the onshore paleo-seep limestones. The age progression of cold seep related features from inland (early Miocene) to Whangaehu (late Miocene) to modern offshore indicates that fluid seepage associated with subduction along the Hikurangi Margin has been a long lived, if intermittent phenomenon throughout the Neogene.

6. Conclusions

1. Tubular carbonate concretions in late Miocene slope mudstones (Whangaehu Mudstone) of the uplifted accretionary prism of East Coast Basin in the Hikurangi Margin of North Island formed from shallow burial (<100 m) precipitation of micritic dolomite (and calcite) within siliciclastic mud.

2. The tubular concretions mainly exhibit pipe and bulbous morphologies, range widely in size (up to 5 m or more in length and over 1 m in diameter), and support a central open or sediment/cement filled conduit. A weak correlation between concretion and conduit diameters suggests that fluid flow rates and volumes may influence conduit size, particularly in concretions >1 m in diameter. The morphology of the tubular concretions is interpreted to reflect variations in fluid pressures, volumes, and buoyancy.

3. It is proposed that growth of the tubular concretions was inwards away from their margins towards the conduit, rather than outwards from some central nucleus as is the case for most standard spherical concretions.

4. Carbon isotope values ($\delta^{13}C$ from −20 to +5‰) suggest that the carbon for carbonate precipitation in the tubular concretions was derived either from anaerobically oxidised microbial methane and residual methanogenic CO_2 and/or extensively oxidised methane. The results of this study suggest extensive oxidation may play a significant role in hydrocarbon seeps, a concept that requires further study and testing in both modern and ancient seep systems.

5. Heavy oxygen isotope values ($\delta^{18}O$ from +1 to +5‰) in the cement of the tubular concretions indicate the $\delta^{18}O$ composition of the precipitating fluid was influenced by the dissociation of gas hydrates.

6. The Whangaehu tubular concretions likely demarcate shallow subsurface pathways of focused methane fluid ascent associated with a cold seep system on the late Miocene continental margin. The occurrence of older (early Miocene) seep limestones inland from Whangaehu and of modern offshore cold seeps on the

Hikurangi Margin, demonstrates the existence of long-lived, if intermittent, methane seepage in the region throughout the Neogene.

7. The tubular concretionary plumbing features at Whangaehu afford a conceptual model for envisaging subsurface fluid migration pathways beneath the modern Hikurangi Margin seabed, and potentially in other modern and ancient seep systems.

7. References

Aiello, I.W., Stakes, D.S., Kastner, M., Garrison, R.E., 1999. Carbonate vent structures in the Upper Miocene Santa Cruz Mudstone at Santa Cruz, California. In: Garrison, R.E., Aiello, I.W., Moore, J.C. (Eds.), Late Cenozoic Fluid Seeps and Tectonics Along the San Gregorio Fault Zone in the Monterey Bay Region, California. Pacific Section AAPG, v. GB-76, pp. 35-52.

Aiello, I.W., Garrison, R.E., Moore, J.C., Kastner, M., Stokes, D.S., 2001. Anatomy and origin of carbonate structures in a Miocene cold-seep field. Geology, 29, 1111-1114.

Al-Aasm, I.S., Taylor, B.E., South B., 1990. Selective stable isotope analysis of multiple carbonate samples using selective acid extraction. Chemical Geology, Isotope Geoscience Section, 80, 119-125.

Aloisi, G., Pierre, C., Rouchy, J.M., Foucher, J.P., Woodside, J., MEDINAUT Scientific Party, 2000. Methane-related authigenic carbonates of eastern Mediterranean Sea mud volcanoes and their possible relation to gas hydrate destabilisation. Earth and Planetary Science Letters, 184, 321-338.

Beu, A. G., 1995. Pliocene limestones and their scallops: lithostratigraphy, pectinid biostratigraphy and paleogeography of Eastern North Island late Neogene limestone. Institute of Geological and Nuclear Sciences monograph, 10, 243 pp.

Bjørlykke, K., 1998. Clay mineral diagenesis in sedimentary basins – a key to the prediction of rock properties. Examples from the North Sea Basin. Clay Mineralogy, 33, 15-34.

Boggs, S., 1992. McConnin, R.A., (Ed.), Petrology of Sedimentary Rocks; Macmillian Publishing Company, New York. Pp. 707.

Campbell, K.A., Farmer, J.D., Des Marais, D., 2002. Ancient hydrocarbon seeps from the Mesozoic convergent margin of California: carbonate geochemistry, fluids and palaeoenvironments. Geofluids, 2, 63-94.

Campbell, K.A., 2006. Hydrocarbon seep and hydrothermal vent paleoenvironments and paleontology: Past developments and future research directions. Palaeogeography, Palaeoclimatolog, Palaeoecolology, 232, 362-407.

Campbell, K.A., Francis, D.A., Collins, M., Gregory, M.R., Nelson, C.S., Greinert, J., Aharon, P., 2008. Hydrocarbon seep-carbonates of a Miocene forearc (East Coast Basin), North Island, New Zealand. Sedimentary Geology, 204, 83-105.

Clari, P., S. Cavagna, Martire, L., Hunziker, J., 2004. A Miocene mud volcano and its plumbing system: A chaotic complex revisited (Monferrato, MW Italy). Journal of Sedimentary Research, 74, 662-676.

Coleman, D.D., Risatti, J.B., Schoell, M., 1981. Fractionation of carbon and hydrogen isotopes by methane-oxidising bacteria. Geochimica et. Cosmochimicha Acta, 45, 1033-1037.

Conti, S., Fontana, D., Gubertini, A., Sighinolfi, G., Tateo, F., Fioroni, C., Fregni, P., 2004. A multidisciplinary study of middle Miocene seep-carbonates from the northern Apennine foredeep (Italy). Sedimentary Geology, 169, 1-19.

Conti, S., Fontana, D., 2005. Anatomy of seep-carbonates: Ancient examples from the Miocene of the northern Apennines (Italy). Palaeogeography, Palaeoclimatolog, Palaeoecolology, 227, 156-175.

Cooke, P.J., Nelson, C.S., Crundwell, M.P., 2008. Miocene isotope zones, paleotemperatures, and carbon maxima events at intermediate water-depth, Site 593, Southwest Pacific. New Zealand Journal of Geology and Geophysics, 51, 1-22.

Cowen, J.P., Wen, X., Popp, B.N., 2002. Methane in aging hydrothermal plumes. Geochimica et. Cosmochimicha Acta, 66, 3563-3571.

Curtis, C.D., 1978. Possible links between sandstone diagenesis and depth related geochemical reactions occurring in enclosing mudstones: Geological Society of London Journal, 135, 107-177.

Curtis, C.D., 1986. Mineralogic consequences of organic matter degradation in sediments: inorganic/organic diagenesis. In: Leggett, J.K., Zuffa, G.G., (Eds.), Marine Clastic Sediments, London, Graham & Trotman. Pp. 108-123.

Davidson, D. W., Leaist, D.J., Hesse, R., 1983. Oxygen-18 enrichment in water of a clathrate hydrate. Geochimica et Cosmochimicha Acta, 47, 2293-2295.

De Boever, E., Swennen, R., Dimitrov, L., 2006. Lower Eocene carbonate cemented chimneys (Varna, NE Bulgaria): Formation mechanisms and the (a)biological mediation of chimney growth? Sedimentary Geology, 185, 159-173.

DeMets, C., Gordon, R.G., Argus, D.F., Stein, S., 1994. Effect of recent revisions to the geomagnetic reversal time scale on estimates of current plate motions. Geophysical Research Letters, 21, 2191-2194.

Díaz-del-Río, V., Somoza, L., Martínez-Frias, J., Mata, M.P., Delgado, A., Hernandez-Molina, F.J., Lunar, R., Martín-Rubí, J.A., Maestro, A., Fernández-Puga, M.C., León, R., Llave, E., Medialdea, T., Vázquez, J.T., 2003. Vast fields of hydrocarbon-derived carbonate chimneys related to the accretionary wedge/olistostrome of the Gulf of Cádiz. Marine Geology, 195, 177-200.

Feary, D.A., Davies, P.J., Pigram, C.J., Symonds, P.A., 1991. Climatic evolution and control on carbonate deposition in northeast Australia. Palaeogeography, Palaeoclimatology, Palaeoecolology, 89, 341-361.

Fergusson, L., 1985. The mineralogy, geochemistry and origin of lower Tertiary smectite-mudstones, East Coast Deformed Belt, New Zealand. Unpublished MSc thesis, University of Canterbury, Christchurch, New Zealand.

Field, B.D., Uruski, C.I., and others, 1997. Cretaceous-Cenozoic geology and petroleum systems of the East Coast Region, New Zealand. Institute of Geological and Nuclear Sciences monograph, 19, 301 pp.

Francis, D.F., 1997. Oil and Gas Generation in the East Coast Basin – an update. Petroleum Exploration in New Zealand News, volume 51, October 1997.

Francis, D., Bennett, D., Courteney, S., 2004. Advances in understanding of onshore East Coast Basin structure, stratigraphic thickness and hydrocarbon generation. 2004 New Zealand Petroleum Conference Proceedings, Auckland, 7-10 March 2004. 20 pp.

Friedman, I., O'Neil, J.R., 1977. Compilation of stable isotope fractionation factors of geochemical interest, In Fleisher, M., (Ed.), U.S. Geolological Survey Professional Paper, 440-kk.

Fritz, P., Smith, D.G.W., 1970. The isotopic composition of secondary dolomite. Geochimica et. Cosmochimicha Acta, 34, 1161-1173.

Gay, A., Lopez, M., Cochonat, P., Séranne, M., Levaché, D., Sermondadaz, G., 2006a. Isolated seafloor pockmarks linked to BSRs, fluid chimneys, polygonal faults and stacked Oligocene-Miocene turbiditic palaeochannels in the Lower Congo Basin. Marine Geology, 226, 25-40.

Gay, A., Lopez, M., Ondreas, H., Charlou, J-L., Sermondadaz, G., Cochonat, P., 2006b. Seafloor facies related to upward methane flux within a Giant Pockmark of the Lower Congo Basin. Marine Geology, 226, 81-95.

Gieskes, J., Mahn, C., Day, S., Martin, J.B., Greinert, J., Rathburn, T., McAdoo, B., 2005. A study of the chemistry of pore fluids and authigenic carbonates in methane seep environments: Kodiak Trench, Hydrate Ridge, Monterey Bay, and Eel River Basin. Chemical Geology, 220, 329-345.

Goldsmith, J.R., Graf, D.L., Heard, H.C., 1961. Lattice constants of the calcium-magnesium carbonate. American Mineralogist, 46, 453-457.

Greinert, J., Bohrmann, G., Suess, E., 2001. Gas hydrate-associated carbonates and methane-venting at Hydrate Ridge: Classification, distribution, and origin of authigenic lithologies. In: Parnell, C.K., Dillon, K.P. (Eds.), Natural Gas Hydrates: Occurrence, Distribution and Detection. Geophysical Monograph, 124, 99-113.

Greinert, J., Bialas, J., Lewis, K., Suess, E., in review. Methane seeps and gas hydrates offshore New Zealand's North Island: Compiling results from three cruises in 2006 and 2007. Submitted to Marine Geology, special publication, methane seeps.

Hodell, D.A., Elmstrom, K.M., Kennett, J.P., 1986. Latest Miocene benthic $\delta^{18}O$ changes, global ice volume, sea level and the 'Messinian salinity crisis'. Nature, 320, 411-414.

Hollis, C., Manzano-Kareah, K., 2005. Source rock potential of the East Coast Basin. Open-file petroleum report 3179, Crown Minerals, Ministry of Commerce, Wellington.

Hovland, M., Svensen, H., Forsberg, C.F., Johansen, H., Fichler, C., Fosså, J.H., Jonsson, R., Rueslåtten, H., 2005. Complex pockmarks with carbonate-ridges off mid-Norway: Products of sediment degassing. Marine Geology, 218, 191-206.

Irwin, H., Curtis, C., Coleman, M., 1977. Isotopic evidence for source of diagenetic carbonates formed during burial of organic-rich sediments. Nature, 269, 209-213.

Jensen, P., Aagaard, I., Burke Jr. R.A., Dando, P.R., Jørgensen, N.O., Kuijpers, A., Laier, T., O'Hara, M.O., Schmaljohann, R., 1992. 'Bubbling reefs' in the Kattegat: submarine landscapes of carbonate-cemented rocks support a diverse ecosystem at methane seeps. Marine Ecology Progress Series, 83, 103-112.

Judd, A.G., Hovland, M., 2007. Seabed Fluid Flow: The Impact on Geology, Biology and the Marine Environment. Cambridge University Press, Cambridge. 475 pp.

Kamp, P.J.J., Furlong, K.P., 2006. Neogene plate tectonic reconstructions and geodynamics of North Island sedimentary basins: Implications for the petroleum systems. 2006 New Zealand Petroleum Conference Proceedings, Auckland, 6-8 March 2006. 16 pp.

Kulm, L.D., Suess, E. 1990. Relationship between carbonate deposits and fluid venting: Oregon accretionary prism. Journal of Geophysical Research, 95, 8899-8915.

Kyser, T.K., James, N.P., Bone, Y., 2002. Shallow burial dolomitization and dedolomitization of Cenozoic cool-water limestones, southern Australia: geochemistry and origin. Journal of Sedimentary Research, 72, 146-157.

Lédesert, B., Buret, C., Chanier, F., Fèrriere, J., Recourt, P., 2003. Tubular structures of northern Wairarapa (New Zealand) as possible examples of ancient fluid expulsion in an accretionary prism: evidence from field and petrographical observations. Geological Society of London Special Publication, 216, 95-107.

Lee, J.M., Begg, J.G., compilers, 2002. Geology of the Wairarapa Area. Institute of Geological and Nuclear Sciences Limited, Lower Hutt, N. Z., 66 pp.

Lewis, K.B., Pettinga, J.R., 1993. The emerging imbricate forntal wedge of the Hikurangi Margin. In: South Pacific Sedimentary Basins of the World, 2. Ballance, P.F. (Ed.), Elsevier Science Publishers B.V. Amsterdam. Pp. 225-250.

Lewis, K.B., Marshall, B.A., 1996. Seep faunas and other indicators of methane-rich dewatering on New Zealand convergent margins. New Zealand Journal of Geology and Geophysics, 39,181-200.

Longstaffe, F.J., 1987. Stable isotope studies of diagenetic processes. In: Kyser, T. (Ed.), Short Course in Stable Isotope Geochemistry of Low Temperature Processesions Mineralogical Society of Canada, Saskatoon, SK, pp. 187-257.

Mazzini, A., Duranti, D., Jonk, R., Parnell, J., Cronin, B.T., Hurst, A., Quine, M., 2003. Palaeo-carbonate seep structures above an oil reservoir, Gryphon Field, Tertiary, North Sea. Geo-Marine Letters, 23, 323-339.

McBride, E.F., Milliken, K.L., Cavazza, W., Cibin, U., Fontana, D., Picard, M.D., Zuffa, G.G., 1995. Heterogeneous distribution of calcite cement at the outcrop scale in Tertiary sandstones, northern Apennines, Italy. AAPG Bulletin, 79, 1044-1063.

McCrea, J.M., 1950. On the isotopic chemistry of carbonates and a paleotemperature scale. Journal of Chemical Physics, 18, 849-857.

Moore, J.C., 1981. Geology of the Late Tertiary section at Cape Turnagain. Journal of the Royal Society of New Zealand, 11, 223-230.

Mörz, T., Karlik, E.A., Kreiter, S., Kopf, A., 2007. An experimental setup for fluid venting in unconsolidated sediments: New insights to fluid mechanics and structures. Sedimentary Geology, 196, 251-267.

Munnecke, A., Samtleben, C., 1996. The formation of micritic limestones and the development of limestone-marl alternations in the Silurian of Gotland, Sweden. Facies, 34, 159-176.

Neef, G., 1984. Late Cenozoic and Early Quaternary stratigraphy of the Eketahuna District (N153), New Zealand Geological Survey Bulletin, 96, 101 pp.

Nelson, C.S., Smith, A.M., 1996. Stable oxygen and carbon isotope compositional fields for skeletal and diagenetic components in New Zealand Cenozoic nontropical carbonate sediments and limestones: a synthesis and review. New Zealand Journal of Geology and Geophysics, 39, 93-107.

Nelson, C.S., Winefield, P.R., Hood, S.D., Caron, V., Pallentin, A., Kamp, P.J.J., 2003. Pliocene Te Aute limestones, New Zealand: expanding concepts for cool-water shelf carbonates. New Zealand Journal of Geology and Geophysics, 46, 407-424.

Nelson, C.S., Campbell, K.A., Nyman, S.L., Francis, D.A., Hood, S.D., Collins, M., Gregory, M.R., Greinert, J., Peckmann, J. Pearson, M.J., 2007. Miocene hydrocarbon seep-carbonate systems in North Island, New Zealand. 2007 GSA Denver Annual Meeting (28-31 October 2007), Geological Society of America, Abstracts with Programs, Vol. 39, No. 6, p. 147.

Nicol, A., Van Dissen, R., Vella, P., Alloway, B., Melhuish, A., 2002. Growth of contractional structures during the last 10 Ma, Hikurangi forearc, New Zealand. New Zealand Journal of Geology and Geophysics, 45, 365-385.

Nyman, S.L., Nelson, C.S., Campbell, K.A., Schellenberg, F., Pearson, M.J., Kamp, P.J.J., Browne, G.H., King, P.R., 2006. Tubular carbonate concretions as hydrocarbon migration pathways? Examples from North Island New Zealand. 2006 New Zealand Petroleum Conference Proceedings, Auckland, 6-8 March 2006. 10 pp.

Orpin, A.R., 1997. Dolomite chimneys as possible evidence of coastal fluid expulsion, uppermost Otago continental slope, southern New Zealand. Marine Geology, 138, 51-67.

Pancost, R.D., Damasté, J.S., De Lint, S., Van Der Maarel, M.J.E.C., Gottschal, J.C., Medinaut Shipboard Scientific Party, 2000. Biomarker evidence for widespread anaerobic methane oxidation in Mediterranean sediments by a consortium of methanogenic archaea and bacteria. Applied Environmental Microbiology, 66, 1126-1132.

Pearce, A.R., Black, R.D., Nelson, C.S., 1981. Lithologic and weathering influences on slope form and process, eastern Raukumara Range, New Zealand. International Association of Hydrologic Science, 132, 95-122.

Pearson, M.J., Grosjean, E., Nyman, S.L., Logan, G.A., Nelson, C.S., Hood, S.D., Campbell, K.A., 2008. Tubular concretions in New Zealand petroliferous basins: Lipid evidence for mineralization around proposed Miocene hydrocarbon seep conduits. 2008 New Zealand Petroleum Conference Proceedings, Auckland, 10-12 March 2008. 6 pp.

Pecher, I., Coffin, R., Henrys, S., et al., 2007. Tangaroa TAN0607 cruise report: gas hydrate exploration on the East Coast, North Island, New Zealand. Institute of Geological and Nuclear Sciences Ltd, Lower Hutt, New Zealand. GNS Science Report 2007/2. 112 pp.

Peckmann, J., Goedert, J.L., Thiel, V., Michaelis, W., Reitners, J., 2002. A comprehensive approach to the study of methane-seep deposits from the Lincoln Creek Formation, western Washington State, USA. Sedimentology, 49, 855-873.

Pierre, C., Rouchy, J.-M., Blanc-Valleron, M.-M., 2002. Gas hydrate dissociation in the Lorca Basin (SE Spain) during the Mediterranean Messinian salinity crisis. Sedimentary Geology, 147, 247-252.

Pierre, C., Rouchy, J.-M., 2004. Isotopic compositions of diagenetic dolomites in the Tortonian marls of the western Mediterranean margins: evidence of past gas hydrate formation and dissociation. Chemical Geology, 205: 469-484.

Pierre, C. Foquat, Y., 2007. Authigenic carbonates from methane seeps of the Congo deep-sea fan. Geo-Marine Letters, 27, 249-257.

Ridgway, N.M., 1969. Temperature and salinity of sea water at the ocean floor in the New Zealand region. New Zealand Journal of Marine and Freshwater Research, 3, 57-72.

Roberts, H.H., Aharon, P., 1994. Hydrocarbon-derived carbonate buildups of the northern Gulf of Mexico continental slope: A review of submersible investigations. Geo-Marine Letters, 14, 135-148.

Rogers, K.M., Collen, J.D., Johnston, J.H., Elgar, N.E., 1999. A geochemical appraisal of oil seeps from East Coast Basin, New Zealand. Organic Geochemistry, 30, 593-605.

Schwartz, H., Sample, J., Weberling, K.D., Minisini, D., Moore, J.C., 2003. An ancient linked fluid migration system: cold-seep deposits and sandstone intrusions in the Panoche Hills, California, USA. Geo-Marine Letters, 23, 340-350.

Sibson, R.H., Rowland, J.V., 2003. Stress, fluid pressure, and structural permeability in seismogenic crust, North Island, New Zealand. Geophysical Journal International, 154, 584-594.

Suess, E., Torres, M.E., Bohrmann, G., Collier, R.W., Greinert, J., Linke, P., Rehder, G., Trehu, A., Wallmann, K., Winckler, G., Zueger, E., 1999. Gas hydrate destabilization: enhanced dewatering, benthic material turnover and large methane plumes at the Cascadia convergent margin. Earth and Planetary Science Letters, 170, 1-15.

Ussler III, W., Paull, C.K., 1995. Effects of ion exclusion and isotopic fractionation on pore water geochemistry during gas hydrate formation and decomposition. Geo-Marine Letters, 15, 37-44.

van der Lingen, G.J., Pettinga, J.R., 1980. The Makara Basin: a Miocene slope-basin along the New Zealand sector of the Australian-Pacific obliquely convergent plate boundary. In: Ballance, P.F., Reading, H.G. (Eds.), Sedimentation in Oblique Strike-slip Mobile Zones. Special Publication of the International Association of Sedimentologists, 191-215.

Whiticar, M.J., 1999. Carbon and hydrogen isotope systematics of bacterial formation and oxidation of methane. Chemical Geology, 161, 291-314.

Figure 17. Schematic staged diagram (no scale implied) for the development of tubular concretions in the subsurface of a Whangaehu cold seep system along a subduction margin. (A) Stage 1: microbial methane and residual methanogenic CO_2 ascend into the gas hydrate stability zone (HSZ). Gas hydrate forms, trapping methane and heavy water into the clathrate molecule. CO_2 and pore waters continue to migrate upward. (B) Stage 2: Regional (or sea level lowering) uplift begins resulting in a relative downward shift of the HSZ. Previously formed hydrates begin to dissociate releasing methane and heavy water into the pore fluids. During Stages 1 and 2, methane and CO_2 are being supplied from below and result in hydrate formation in the 'new' HSZ. When AOM begins, carbonate precipitation occurs and calcitic tubular concretions with low $\delta^{13}C$ and high $\delta^{18}O$ values form. The tubular concretions incorporate the oxidised methane, residual CO_2, and heavy water from hydrate dissociation. (C) Stage 3: As methane released from hydrate dissociation diminishes, AOM ceases and fluid pressure/buoyancy lowers. Dolomite is favoured over calcite as Ca/Mg ratios are reduced due to calcite precipitation in earlier Stages. Carbon isotope values in carbonate precipitated during Stage 3 will reflect bicarbonate from residual methanogenic CO_2 and/or extensive methane oxidation (more enriched $\delta^{13}C$). Oxygen isotopes will reflect the transition from hydrate dissociation to hydrate formation (shift from slightly enriched to slightly depleted $\delta^{18}O$). The resulting tubular concretions are more sinuous to bulbous dolomitic varieties. See Section 5.3 for further explanation. SRZ = Sulphate reduction zone; BSR = bottom simulating reflector.

Stage 1

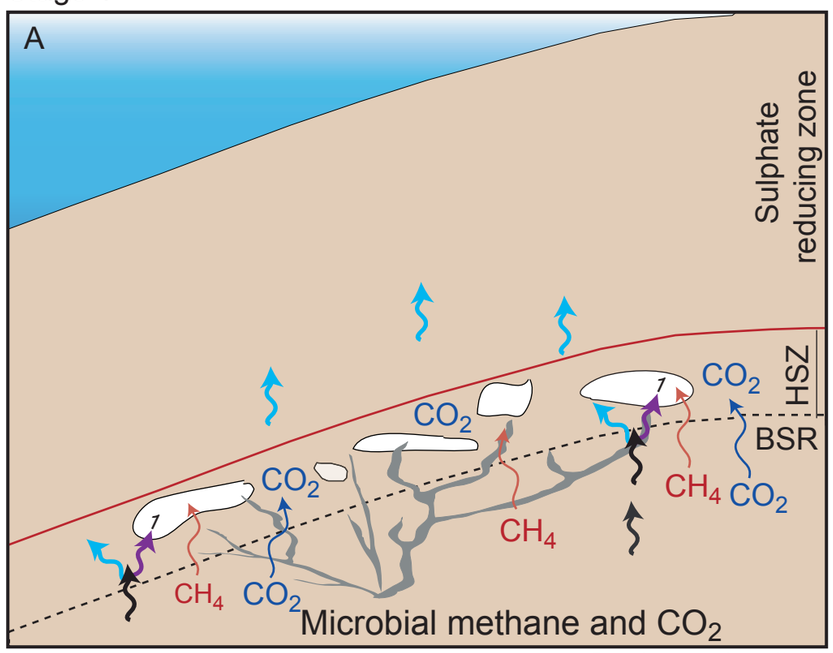

Scale not implied

Stage 2

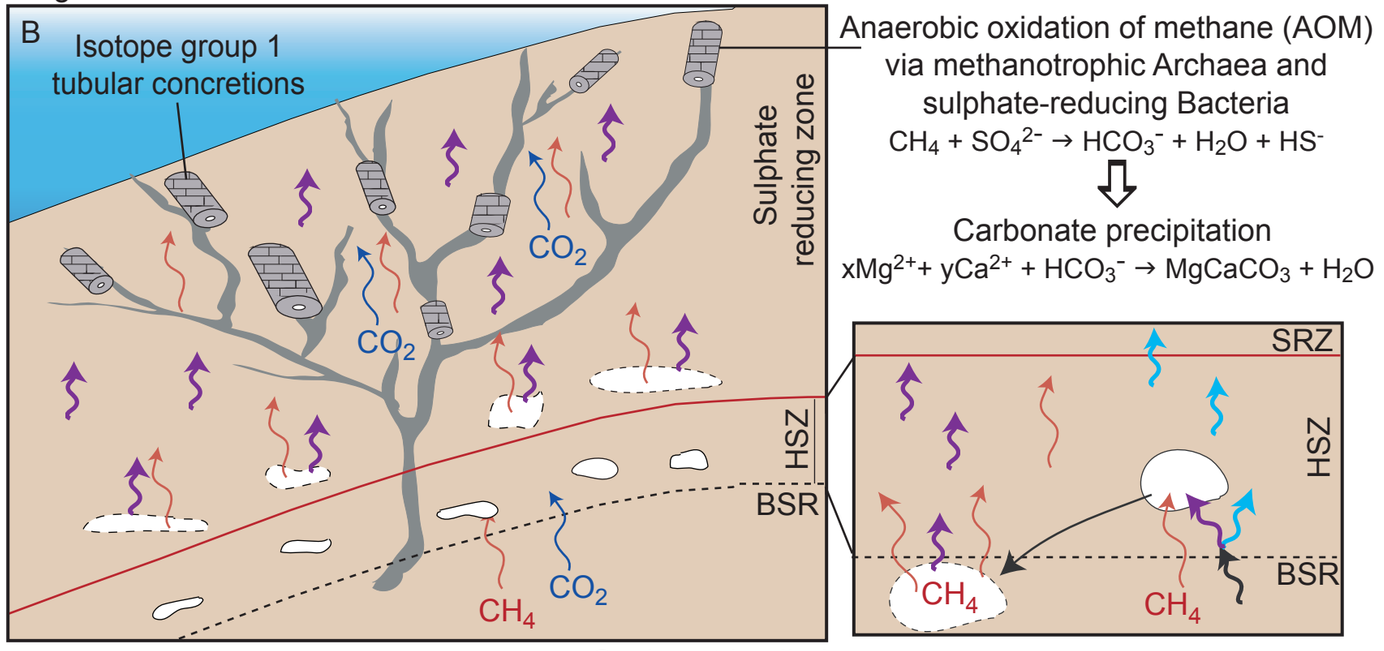

Scale not implied

Anaerobic oxidation of methane (AOM) via methanotrophic Archaea and sulphate-reducing Bacteria

$CH_4 + SO_4^{2-} \rightarrow HCO_3^- + H_2O + HS^-$

⇩

Carbonate precipitation

$xMg^{2+} + yCa^{2+} + HCO_3^- \rightarrow MgCaCO_3 + H_2O$

Stage 3

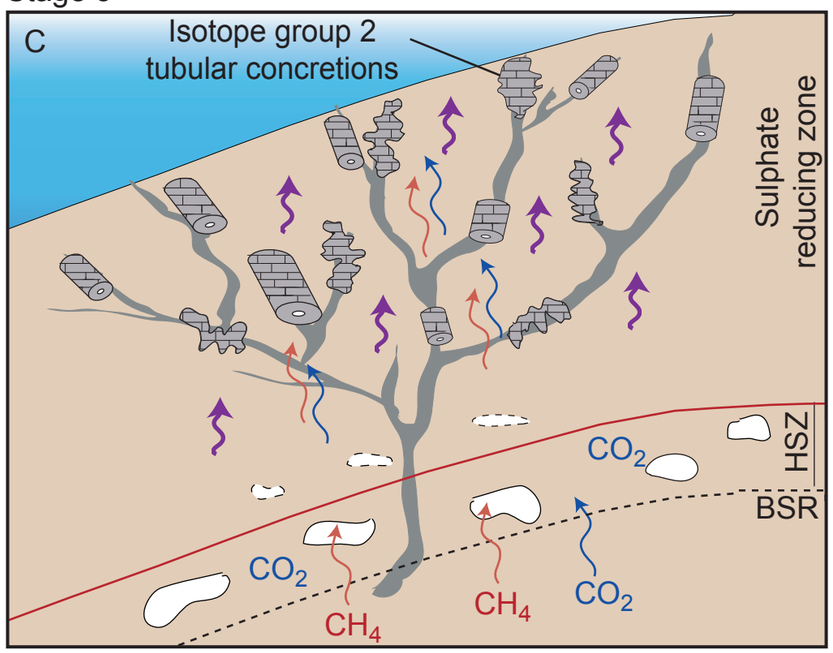

Scale not implied

Bulbous concretion formation

1) Long lived AOM ⇨ enriched $\delta^{13}C_{carbonate}$ (up to $\delta^{13}C$ = +10 $^{0}/_{00}$ PDB)

2) Sulphate and Ca^{2+} depletion ⇨ dolomite precipitation

3) Gas removed via carbonate precipitation ⇨ lower pressure ⇨ more tortuous pathways

Methane hydrate

Dissociating methane hydrate

Ascending porewater

Ascending methane CH_4

Ascending residual methanogic CO_2

Base of sulphate reducing zone

Oxygen-18 heavy waters preferentially locked into the clathrate molecule

Pipe concretions

Fluids with anomalously light oxygen-18 remaining in pore waters after hydrate formation

Sinuous, bulbous, and conical concretions

CHAPTER 5

Fault control on the distribution of concretionary subsurface seep carbonates, East Cape, North Island, New Zealand

Abstract

The late Miocene Pohutu Formation, Horoera Point, East Cape, North Island, New Zealand, is dominated by slope deposits which contain tubular carbonate concretions. Most of these support a near central conduit which is either open or filled with cemented sediment. The tubular concretions consist of dolomicrite cement between fine grained siliciclastic sediment and are present as pipe, conical, and doughnut morphologies. Minus cement porosities between 62 and 80% indicate precipitation occurred near the seafloor.

The tubular concretions have the largest diameters of examples known worldwide. The doughnut concretions are the most abundant morphology and range in size from 3 to 8 m across (avg. 4 m). Pipe concretions range from 0.5 to 1 m in length (exposed) and 0.1 to 0.75 m in diameter, and conical concretions from 0.5 to 1 m in diameter and up to 1.5 m tall.

Stable carbon and oxygen isotope values of the carbonate cement in the tubular concretions range between $\delta^{13}C$ −17.2 and +9.3‰ PDB and $\delta^{18}O$ +1.9 and +5.8‰ PDB. Lipid biomarkers confirm anaerobic oxidation of methane was occurring in the sediments at the time of carbonate precipitation. The carbon in carbonate cement is interpreted to have been sourced from either extensive methane oxidation (greater than 80% oxidation of methane pool) based on the carbon isotope values and lipid biomarkers, or microbial methane and methanogenic CO_2. Dolomite $\delta^{18}O$ values vary; those from +3 to +3.5‰ PDB precipitated in equilibrium with seawater at bottom water temperatures of 8 to 10ºC. $\delta^{18}O$ values from +1 to +3‰

PDB may indicate elevated fluid temperatures from rapidly ascending fluids and/or methane hydrate formation; more positive $\delta^{18}O$ values from +3.5 to +5.8‰ PDB likely indicate methane hydrate dissociation.

NE−SW and ESE−WNW trending faults dominate the outcrop at Horoera Point with mutual cross-cutting relationships. The NE−SW oriented faults are right lateral, and the ESE−WNW oriented faults are left lateral, both with some vertical displacement (normal/extensional). The faults intersect at angles of ~46° producing conjugate fault sets. The tubular concretions are commonly located along or bisecting the faults, and in places they are equally spaced, and can be deformed, broken, or displaced. These relationships suggest that faulting controlled fluid migration and the concretions formed contemporaneously over a period of multiple fault ruptures.

The tubular concretions at Horoera Point are interpreted to mark the subsurface migration of hydrocarbon rich fluids towards the seafloor where faulting resulted in intermittent fluid ascent, hypothesised to have been caused by a fault-valve mechanism. The relationship between these concretions and structural deformation may help to determine how the subsurface cold seep system develops and evolves through time. The concretionary plumbing network exposed at Horoera Point may provide a conceptual model for the subsurface fluid migration system of the offshore seeps along the modern Hikurangi Margin, and potentially also as an analogue for other cold seep plumbing systems.

1. Introduction

Modern cold seeps have been documented worldwide and have been the focus of numerous studies (Fig. 1, see Judd and Hovland, 2007 and references therein). In comparison, ancient seeps have received much less attention (e.g., Campbell et al., 2002 and references therein, 2008; Peckmann et al., 2002; Schwartz et al., 2003; Conti et al., 2004; Conti and Fontana, 2005). Cold seeps are commonly a result of hydrocarbon migration sourced from either microbial methane, thermogenic oil and gas, or gas hydrate disassociation (Greinert et al., 2001; Clari et al., 2004; Conti et al., 2004; Judd and Hovland, 2007). As such, cold seeps can provide key

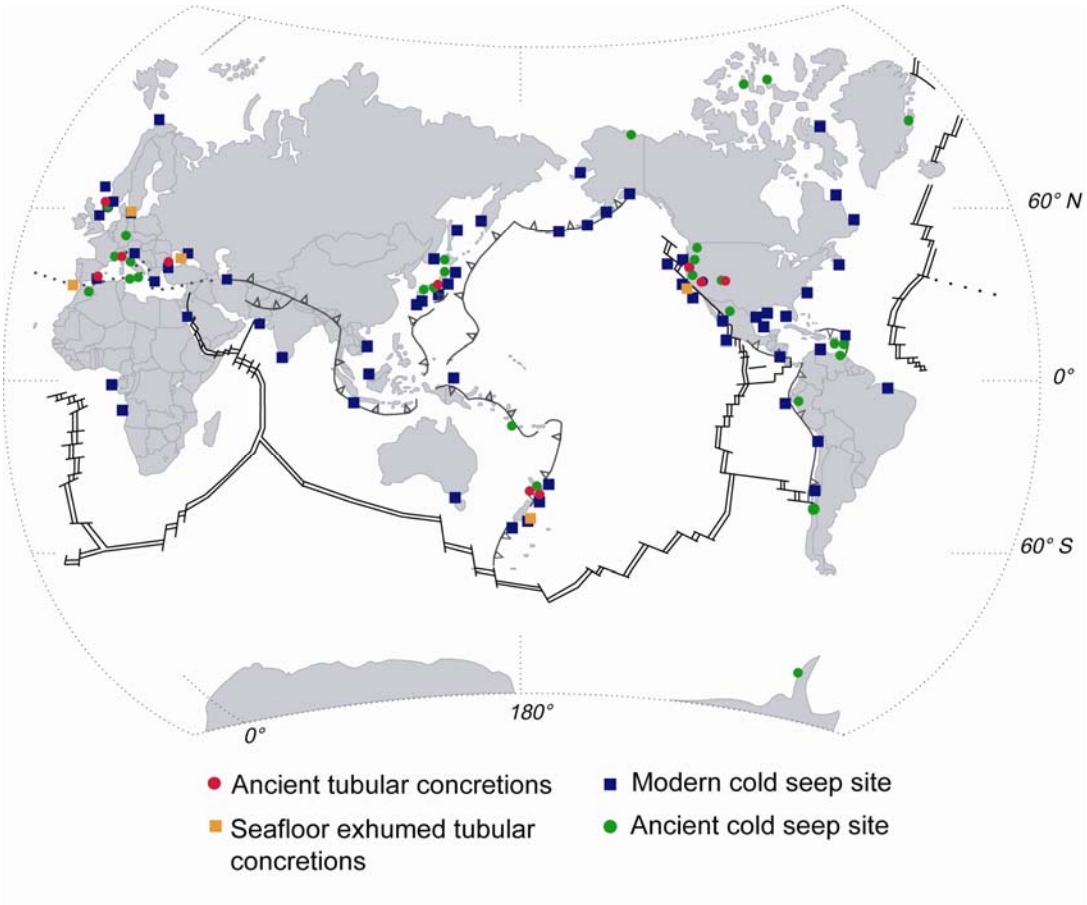

Figure 1. Global occurrences of reported ancient tubular concretions, exhumed tubular concretions on the seafloor (most near active seep sites), ancient cold seeps, and modern colds seeps (adapted and extended from Campbell, 2006).

information on the factors that control hydrocarbon migration and hazards associated with trapped gases, as well as elements that control gas hydrate formation and their potential as a future energy source (Grauls, 2001; Milkov and Sassen, 2002; Milkov et al., 2004). Studies of modern cold seeps reveal valuable information on the development and evolution of these systems, but it is logistically difficult to study the subsurface seep system. Some ancient New Zealand examples provide a window into the strata below paleo-seep deposits and so provide a unique opportunity to study aspects of the subsurface plumbing system feeding such seeps.

The New Zealand examples document subsurface seep activity in the form of tubular carbonate concretions. Tubular shaped concretionary structures have been documented in association with ancient seeps worldwide (Fig. 1) (Aiello et al., 2001; Clari et al., 2004; De Boever et al., 2006). These concretions formed below the surface through carbonate cement precipitation within the pore spaces of sediments. To date, known examples of tubular concretions are mainly on the scale of centimetres (a few at the decimetre scale) and they are primarily found in mudstones. Notable exceptions are examples from the Kattegat, Denmark (Jensen et al., 1992), the Gulf of Cadíz, Portugal (Diaz-del-Rio et al., 2003), Bulgaria (De Boever et al., 2006), and New Zealand (Lédesert et al., 2003; Nyman et al., 2006) where the tubular features can be unusually large (up to 10 m in height and 4 m in diameter) and locally abundant in outcrop.

This study focuses on the tubular concretions at Horoera Point near East Cape, North Island, New Zealand (Fig. 2) and their significance as markers of the plumbing system of ancient cold seeps during the late Miocene. These tubular concretions are unique not only because of their unusual size but also their intimate association with faults and their stable isotope values, which may help illuminate the dynamics of the subsurface seep system.

2. Geologic setting

East Cape is located in the East Coast Allochthon (ECA) in the northern Raukumara Peninsula of North Island. It is approximately 50 km west of the

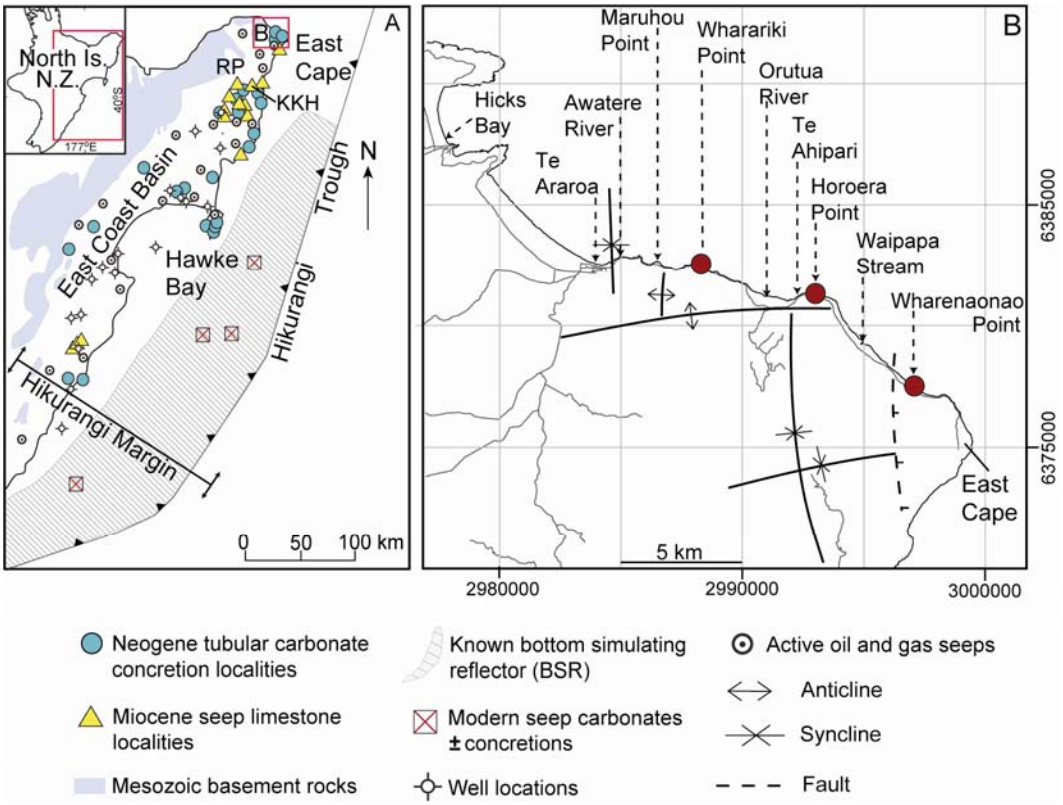

Figure 2. Map of study location near East Cape, North Island, New Zealand. (A) Map of East Coast Basin with locations of tubular concretions, ancient and modern seep sites, onshore modern oil/gas seeps and well locations, and offshore bottom simulating reflector (BSR) indicating gas hydrates. KKH indicates location of Karikarihuata, a Miocene seafloor seep carbonate (see Fig. 22). (B) Locality map of tubular concretion sites near East Cape. The map coordinates correspond to the New Zealand Map Grid system and locations may be found on NZ Map Series 260, 1:50000 scale, sheet Z14. Locality information comes mainly from personal observation, as well as from Francis (1997), Lewis and Marshall (1996), Tonkin (2003), and from personal communication with Dave Francis (Geological Research Ltd, Lower Hutt, New Zealand). RP = Raukumara Peninsula. Red dots in B are main locations of tubular concretions.

modern Australian/Pacific plate subduction boundary marked by the Hikurangi Trough (Figs. 2A, 3A) (Field et al., 1997). The ECA was emplaced during the late Oligocene and earliest Miocene. Thrust faults mark the onset of subduction along the Hikurangi Margin (Fig. 3) (Cole and Lewis, 1981; Kenny, 1984; Rait et al., 1991). Subduction of the Pacific Plate southwest underneath the Australian Plate was initiated in the early Miocene (~23 Ma), the leading edge of the Pacific Plate reaching the position of East Cape ~20 Ma (Kamp and Furlong, 2006). Presently, the Pacific Plate is subducting at about 40 mm per year (DeMets et al., 1994).

In the East Coast Basin (ECB), Cretaceous to Paleogene sedimentary rocks were deposited in a passive margin, and are overlain by Neogene marine sediments after the initiation of subduction (Fig. 4). The Cretaceous and Paleocene sedimentary succession includes known source rocks (especially Whangai and Waipawa Formations; Field et al., 1997) that have reached maturity and expelled hydrocarbons since late Miocene time (Fig. 4). After emplacement of the earliest Miocene ECA, the onset of subduction saw sediments deposited along the slope trench, between thrust ridges of the ECB (van der Lingen and Pettinga, 1980; Cole and Lewis, 1981; Lewis and Pettinga, 1993; Ballance, 1993). During the early Miocene, deposition of the Whakai limestone occurred near East Cape, followed by deep water siliciclastics (Chaproniere, 1969; Chapman-Smith and Grant-Mackie, 1971). A period of non-deposition, uplift, tilting, and erosion of the Whakai Formation occurred during the middle Miocene, and was followed by deposition of siliciclastic sediments in the late Miocene (Chaproniere, 1969; Chapman-Smith and Grant-Mackie, 1971), including the Pohutu and Paeoneone Formations (Fig. 5) which gradually infilled the basin and unconformably overlie the ECA.

Structurally, the regional dip is northwest (Martin, 1986) and is characterised by broad, gentle, and open anticlines and synclines (Fig. 2B) (Martin, 1986; Mazengarb et al., 1991). Major folds include: Te Araroa Syncline (NNW/SSE trending), Whararikí Anticline (N/S trending), Orutua Syncline (NNE/SSW trending), Hautai Anticline (NE/SW trending), Te Wharenaonao Syncline (NE/SW trending), and East Cape Anticline (N/S trending) (Martin, 1986). Faults usually parallel the adjacent fold axes. Faults are mainly located from the Orutua

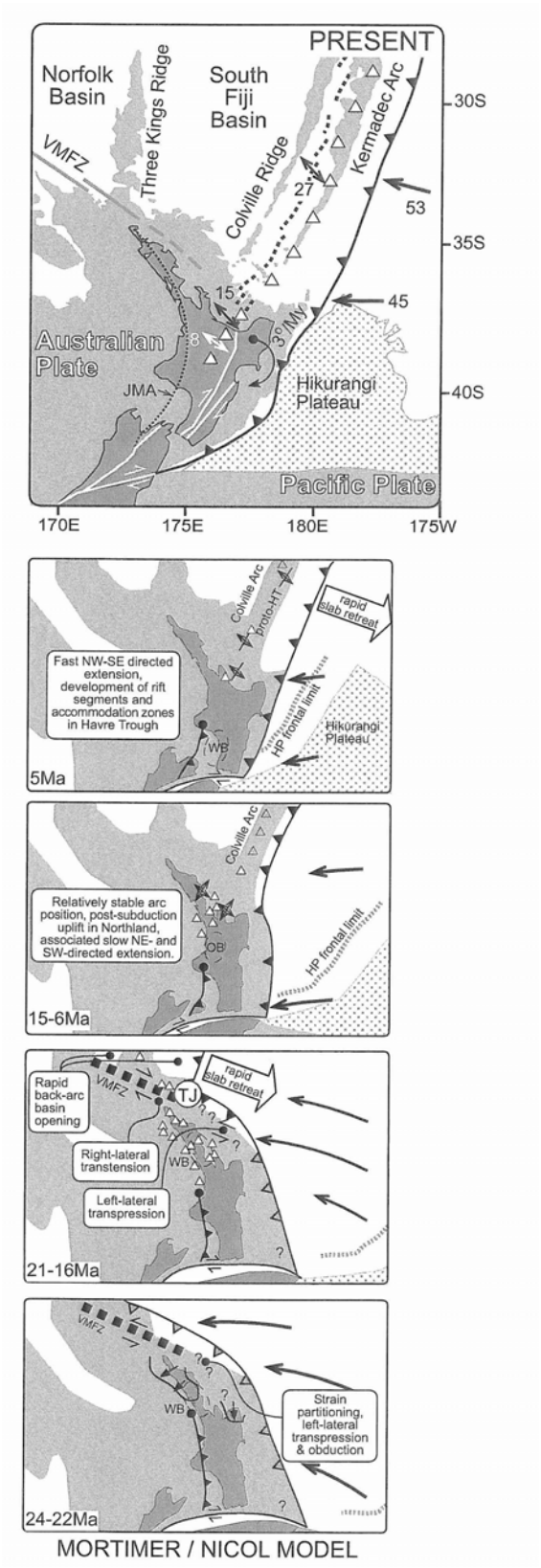

Figure 3. The New Zealand Pacific-Australian plate boundary. New Zealand tectonic setting from 24 Ma to the present (modified from Mortimer et al., 2007; Nicol et al., 2007; Stagpoole and Nicol, 2008).

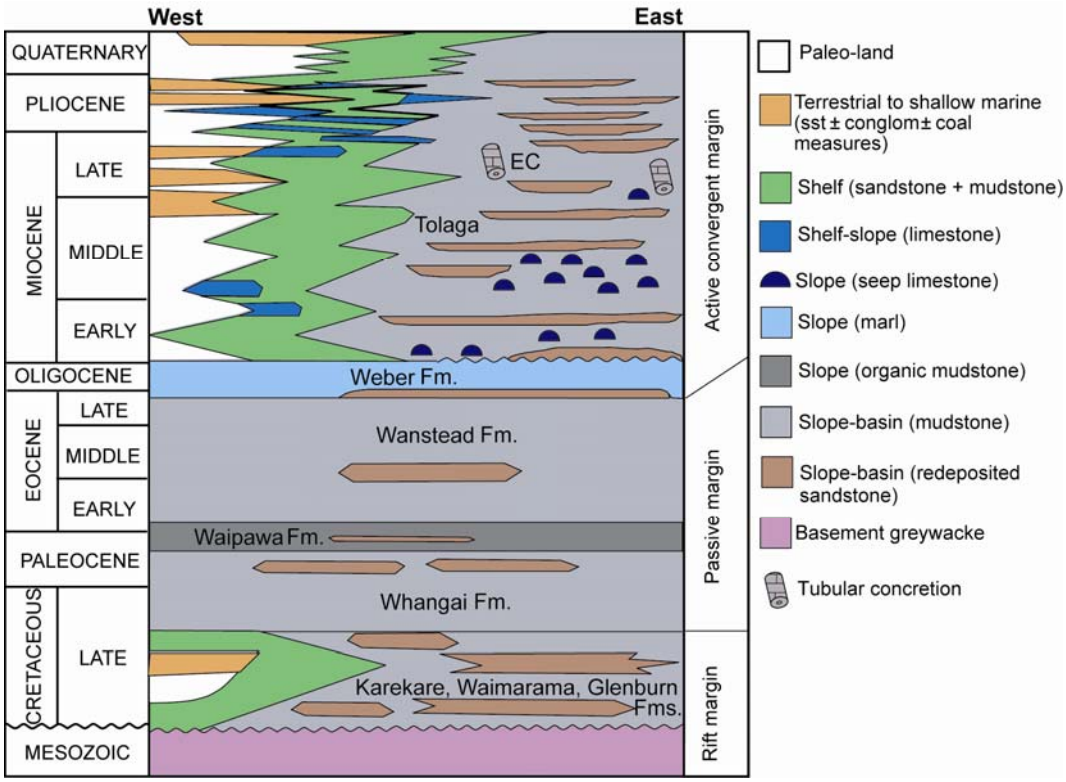

Figure 4. Generalised stratigraphic column for the East Coast Basin with respect to depositional paleoenvironments (modified from Francis et al., 2004). EC marks approximate stratigraphic position of the tubular concretions from the Pohutu Formation at East Cape, described in this study.

River mouth to the East Cape, with intense small scale faulting (1−1.5 m throw) on the shore platform at Horoera Point (Tonkin, 2003).

The Pohutu (Upper Tongaporutuan to Kapitean) and Paeoneone (Kapitean; see Appendix 8 for New Zealand time scale) Formations are a shelf/slope, coarsening upward (Fig. 5), forearc sequence which has undergone slight folding and faulting and shallow burial (Chaproniere, 1969; Martin, 1986; Ballance, 1993). These sediments are exposed along the shore platform and marine terraces from East Cape to Te Araroa. The Pohutu Formation crops out from East Cape to Maruhou Point (Fig. 2B) and was deposited on the mid- to upper slope. The sediments are light grey to white, calcareous, very fine sandy mudstones and muddy sandstones approximately 200 – 300 m thick (Ballance et al., 1984). Fossils are rare in the lower Pohutu Formation but allochthonous shelf derived *Cuccullaea* valves do occur within olistostrome units (Fig. 5). However, fossils become more common up-section, indicating a shallowing upward sequence. In the mid- to upper Pohutu Formation *Nemocardium quinarium* appears, and *Cuccullaea* appears (autochthonous) in the upper Pohutu Formation at the gradational contact with the Paeoneone Formation (Ballance et al., 1984).

Evidence of slope failure is present in olistostrome units (Wharenaonao Point), turbidites (Wharenaonao Point, Horoera Point), slumps (Wharenaonao and Te Ahipari), and grain flows (Te Ahipari and Whararíki Point) (Figs. 2B, 5). All are variably bioturbated, have erosional bases, and include a rhyolitic volcanogenic provenance (Tonkin, 2003).

Thick tephra horizons occur in the sequence, one at Horoera Point, one at Whararíki Point, and six between Wharenaonao Point and Waipapa Stream (Figs. 2B, 5). Numerous thin volcanic ash horizons also occur throughout the section, increasing in occurrence up-section (Ballance et al., 1984).

The contact between the Pohutu and Paeoneone Formations is gradational. The Paeoneone Formation comprises about 300 m of light grey, massive to bedded, fine muddy sandstones deposited on the outer shelf, and is exposed from Maruhou Point to the west bank of the Awatere River (Fig. 2B) (Chaproniere, 1969; Ballance et al., 1984; Martin, 1986). Grain size increases up-section, becoming

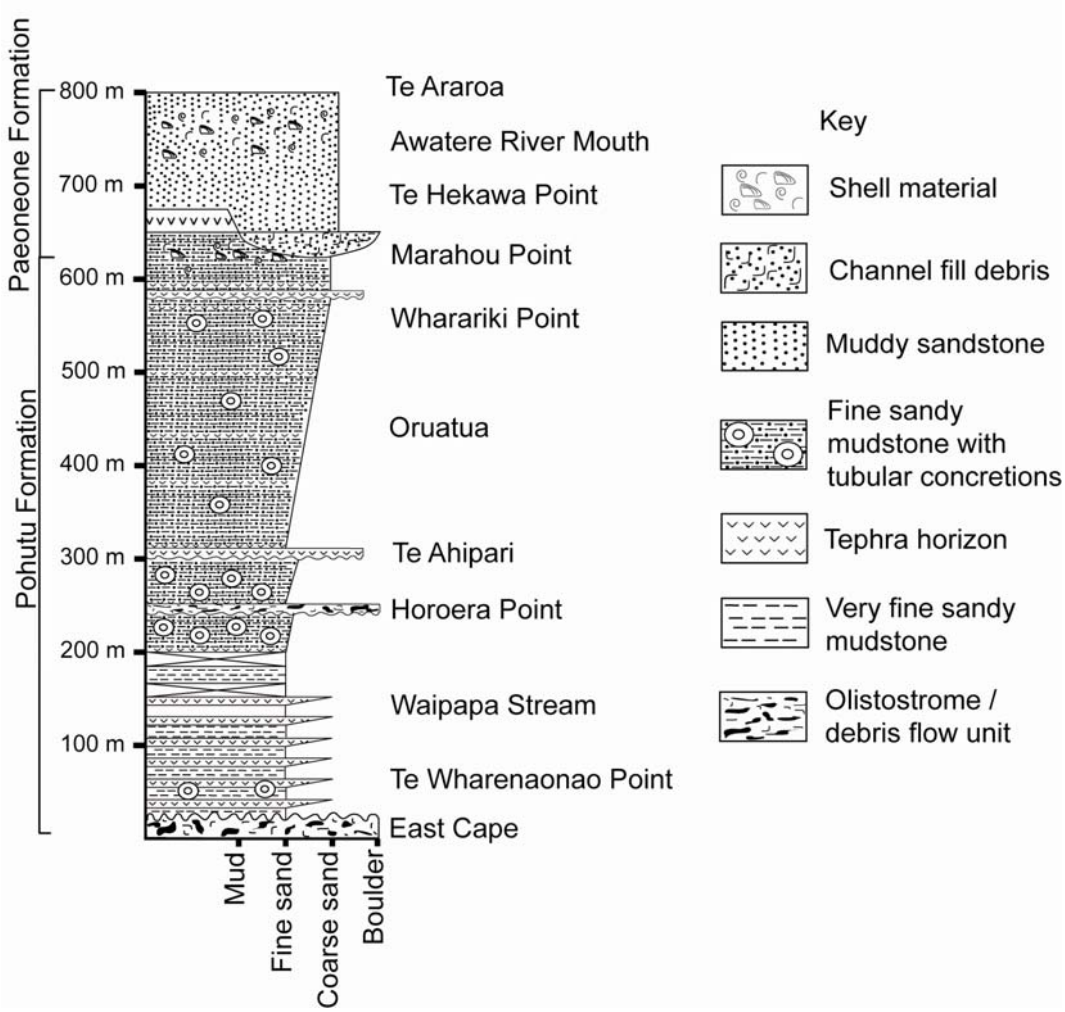

Figure 5. Schematic stratigraphic column of the Pohutu and Paeoneone Formation from East Cape to Te Araroa (Fig. 2B) showing approximate stratigraphic positions of tubular concretions (adapted from Tonkin, 2003).

sandier, and increases in fossil content and bioturbation supporting a shallowing upward sequence (Tonkin, 2003). Fossils occur throughout the Paeoneone Formation as shell hash, in lags, bands, and pockets, and include pectinids, ostreids, *Cucullaea*, scleractinian corals (Tonkin, 2003), and carbonised plant fragments (Martin, 1986). A channel fill deposit is present at Maruhou Point (Figs. 2B, 5), which is 20 m thick, 12.5 m wide, and 32 or more m long. The channel has an erosional base and is filled by poorly sorted, blue-grey volcanic breccia, basic igneous material, volcanic grit, sand, and macrofossils. Sedimentary dykes compositionally similar to the channel fill also are present, probably formed from compaction and dewatering of volcanic breccia channel fill (Tonkin, 2003).

Tubular concretions are present within the East Cape – Te Araroa sequence (Fig. 2B, 4). They are concentrated at three main locations: 1) Te Wharenaonao Point (lower Pohutu); 2) Horoera Point (middle to upper Pohutu); and 3) Whararikí Point (Upper Pohutu). The focus of this study is the Pohutu Formation at Horoera Point (Figs. 2B, 5) which has the highest density of tubular concretions exposed on the shore platform. The lower Pohutu (Te Wharenaonao Point) contains mostly spherical concretions, but does include a few examples reminiscent of tubular concretions. The Upper Pohuto (Whararikí Point) also has spherical and tubular concretions, but to a much lesser extent than at Horoera Point. The Paeoneone Formation contains only spherical concretions.

3. Methods

Tubular concretions are exposed on the shore platform in three main locations over a distance of 10 km along the coast northwest of East Cape. The most pristine outcrop, and the focus of this study, is located near Horoera Point (Fig. 2B). Within this stretch of coastline, concretions occur over a distance of 1 km in two main clusters, each spanning approximately 350 m. Concretions are accessible primarily at low tide during fair weather conditions. Following stratigraphic logging and photographic imaging of these coastal sections, field work focused on descriptions of the distribution, morphology, size, and stratigraphic position of the concretions (see details in Appendix 3). Oriented, *in*

situ samples were collected using a chisel and heavy duty rock hammer, but also from fallen blocks lying on the intertidal platform. Detailed mapping aided by GPS on the ground, and aerial photography from helicopter, was used to document concretion distribution, sample collection, and fault occurrence. In most cases, subsamples were also collected to provide representative rock material along transects from the centre to the periphery of the tubular concretions. Aerial photographs and structural data were collected to investigate the relationship of concretion formation and faulting. Full records of this field information are contained in Appendix 3.

Laboratory analytical work included standard thin section petrography of resin impregnated samples, scanning electron microscopy (SEM) to view the ultrastructure of the micritic carbonate following the procedure of Munnecke and Samtleben (1996), X-ray diffraction (XRD) to determine the mineralogy of samples and the $MgCO_3$ content of calcite (e.g., Goldsmith et al., 1961), and stable isotope mass spectrometry to derive the $\delta^{18}O$ and $\delta^{13}C$ composition of the carbonate phases (e.g., McCrea, 1950; Nelson and Smith, 1996). Isotope results are reported as per mille $\delta^{18}O$ and $\delta^{13}C$ relative to VPDB and have an analytical precision of better than about ±0.10‰.

Appendix 7 details laboratory methodology and instruments.

4. Tubular concretions

4.1 Morphology

The East Cape tubular concretions occur in three main morphologies (Fig. 6): 1) doughnuts; 2) conical; and 3) pipe (Fig. 7). Doughnut concretions superficially appear like "standard" spherical concretions, but the occurrence of a clear central conduit indicates otherwise (Fig. 7A,B). Doughnut concretions on average are 4 m across and 1.5 m thick, with a conduit diameter up to 0.6 m. In general, the doughnut concretions are equant in diameter to slightly elongate in the direction of dip by up to a metre (Fig. 8). Most doughnuts are slightly elongated and dip in the same direction and angle as bedding (Table 1). Conical concretions taper downwards in the stratigraphy, and show highly fractured conduit fills; fracturing

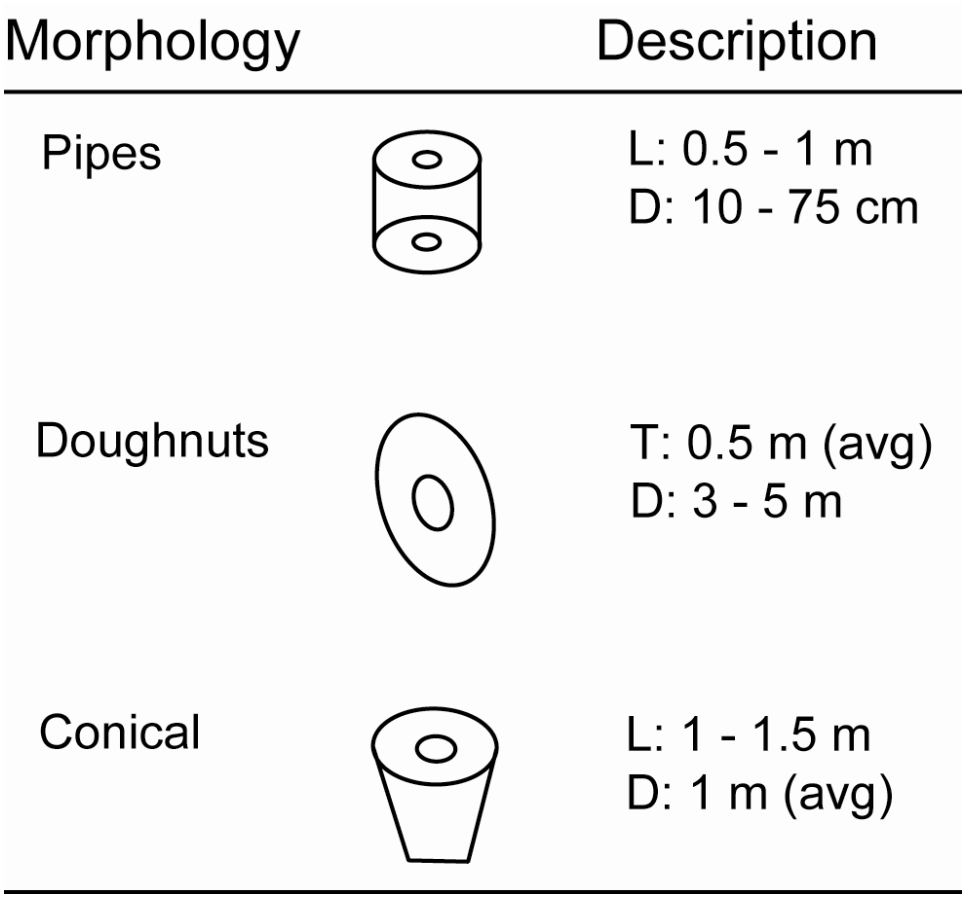

Figure 6. Morphologic classification of tubular concretions at Horoera Point. L = length of tubular concretion, D = diameter, T = thickness.

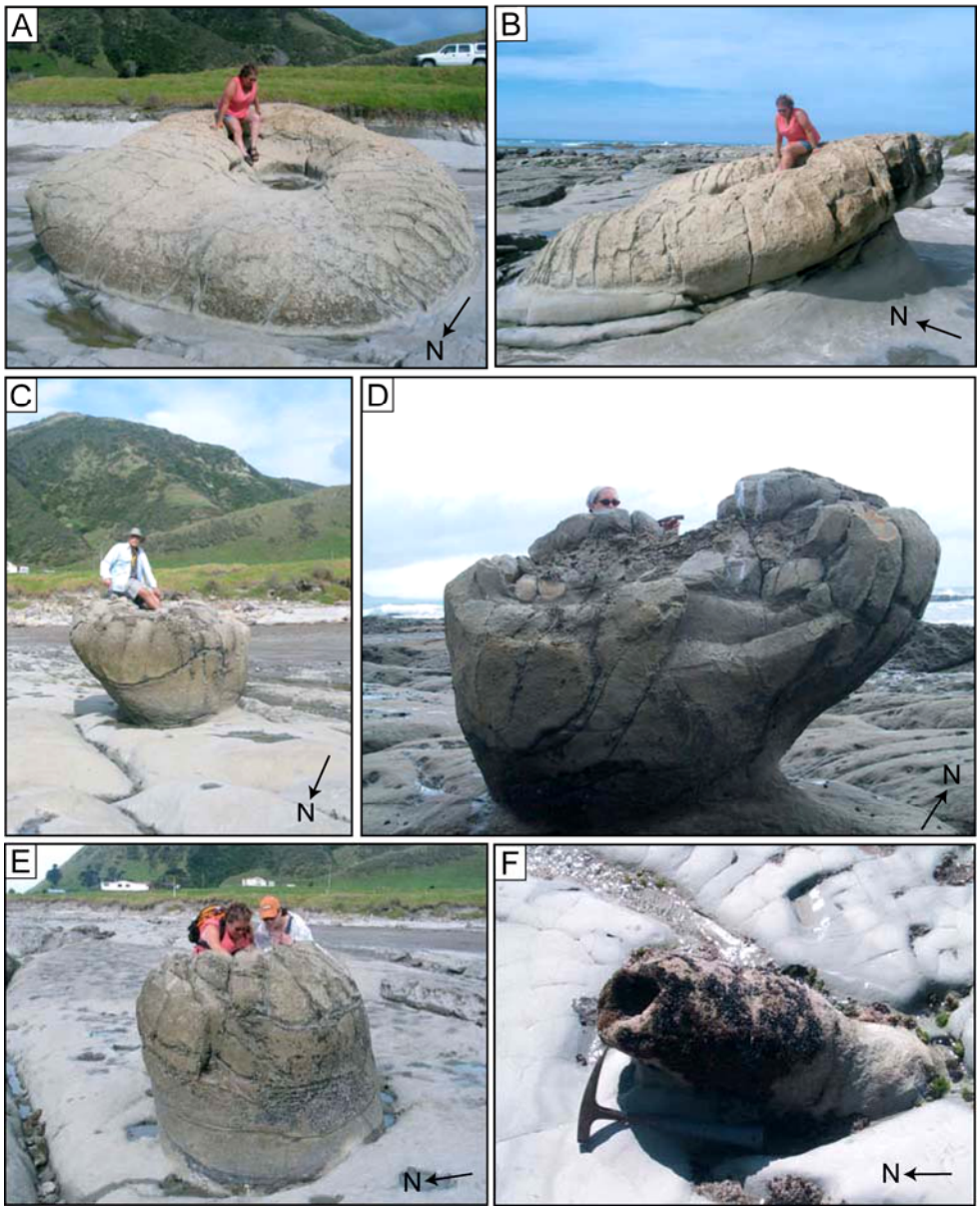

Figure 7. Examples of tubular concretions at Horoera Point. (A) Doughnut concretion with cemented sediment filled conduit dipping gently seaward. (B) Side view of A. (C) Conical concretion that tapers downward. (D) Close up view of C showing the internal brecciated conduit and fractures extending out into the wall of the concretion itself. (E) Large pipe concretion with a brecciated internal conduit fill. (F) Small pipe concretion with an open conduit. Samples 2361 (A,B); 2208 (C,D); 2188 (E); and EC3 (F).

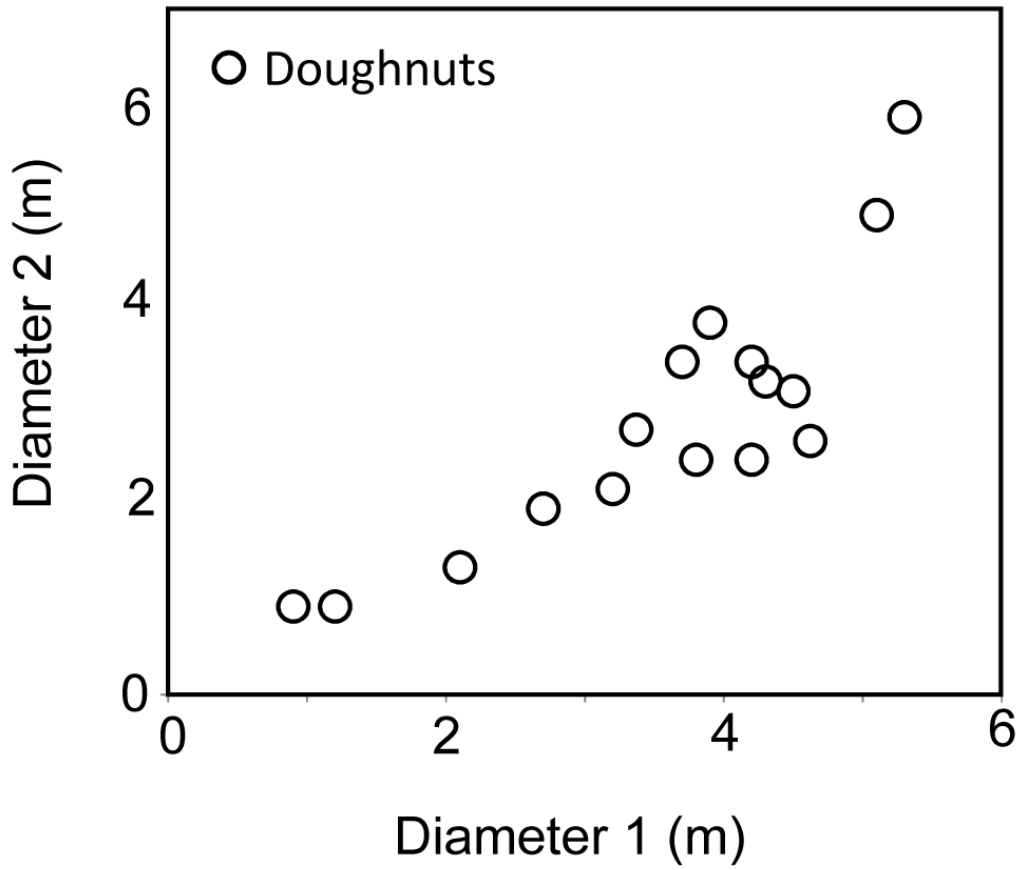

Figure 8. Graph of doughnut concretion aspect ratios, diameter 1 vs. diameter 2 of the doughnut. Diameter 1 is the longer axis of the doughnut concretions and is almost always in a perpendicular direction to bedding strike. Diameter 2 is at right angles to diameter 1, across the centre (conduit) of the concretion.

Table 1. Structural field data collected during detailed GPS mapping of the tubular concretions on the shore platform at Horoera Poing. Sample numbers correspond to GPS numbers. GPS locations are shown in Figure 10. Photographs of each sample location can be found in Appendix 3 and on the accompanied DVD (Appendix\EastCape\GIS). JPG numbers in the far right column correspond to the photograph file name on the DVD and in Appendix 3.

Easting / Sample number	Northing	Morphology	Notes	Dip (concretion)	Dip direction (concretion)	Fracture orientations (concretion)	Fault orientations	Dip (bedding)	Dip direction (bedding)	Photo JPG #
2992074	6381198	Doughnut	Landward side broken by fault	042	020	080, 105	050, 103			2225-2229
2992108	6381214	Doughnut	Broken in half by fault	040	008	050	050			2223-2224
2992112	6381213	Pipe	Two pipes, thick concretionary walls, open conduit							
2992122	6381219	Doughnut	Broken along joint, seaward side	038	360	058, 210	058, 210			2218-2219
2992141	6381223	Doughnut	Broken along joint, landward side	040	360	058	058		70	2214-2217
2992157	6381170	Doughnut	Newly exposed							
2992159	6381171	Doughnut		038	320					2276-2277
2992172	6381149	Doughnut	Newly exposed	038	347					2275
2992174	6381223	Doughnut	Small, joint diverts around concretion	035	293	058, 378	058, 378			2210-2213
2992179	6381216	Doughnut	No conduit discernable, egg shaped	042	010					2230
2992180	6381151	Doughnut	Newly exposed	038	360					2273-2274
2992184	6381152	Doughnut	Newly exposed	038	080					2272
2992188	6381211	Conical	Seaward, many fractures, lots of spurs from main joints	092	103	103, 060	103, 060			2231-2239
2992208	6381195	Conical	Landward, many fractures			103, 060	103, 060			2240-2248
2992222	6381214	Doughnut	Near flower pots, joints divert around concretion	040	350	103, 060	103, 060			2249-2250

Table 1 continued

Easting / Sample number	Northing	Morphology	Notes	Dip (concretion)	Dip direction (concretion)	Fracture orientations (concretion)	Fault orientations	Dip (bedding)	Dip direction (bedding)	Photo JPG #
2992241	6381251	Doughnut	Large doughnut broken in middle along fault			052	052			2203-2209
2992243	6381261	Rubble								
2992280	6381280	Pipe	Horizontal to bed, multi-conduits, ends in doughnut			082, 228	082, 228			2193-2195
2992301	6381278	Doughnut	Small doughnut at end of long pipe							2197-2202
2992301(b)	6381269	Doughnut	Joints divert around concretion	040	020	051, 078	051, 078			2251-2253
2992321	6381300	Conical	Small seaward	055	312	226, 269	226, 269			2186-2190
2992327	6381290	Doughnut	No clear conduit, egg shaped	040	015	072	072			2257-2260
2992329	6381311	Doughnut	Small, broken along fault	038	328	226, 269	226, 269			2191-2192
2992347	6381297	Doughnut	Half doughnut	037	320	070	045, 100			2172-2173
2992361	6381279	Doughnut	Largest fully exposed	030	356	035, 356	050, 095		50	2169-2171
2992371	6381310	Doughnut	Half doughnut?, possibly not *in situ*	020						2179-2181
2992376	6381318	Doughnut	Half doughnut, broken along fault	045	322				50	2182-2185
2992409	6381415	West turbidite								
2992418	6381420	West turbidite								
2992423	6381439	West turbidite								
2992467	6381319	West turbidite						20	320	
2992476	6381324	West turbidite						20	380	

Table 1 continued

Easting / Sample number	Northing	Morphology	Notes	Dip (concretion)	Dip direction (concretion)	Fracture orientations (concretion)	Fault orientations	Dip (bedding)	Dip direction (bedding)	Photo JPG #
2992481	6381343	West turbidite						20	380	
2992621	6381363	East turbidite						18	276	
2992631	6381379	East turbidite						18	276	
2992639	6381389	East turbidite						18	276	2319-2320
2992649	6381392	Unknown	Weathered concretionary body							2321-2323
2992657	6381413	Unknown	Weathered concretionary material along fault			078	078			2324-2329
2992702	6381387	Doughnut	Strongly weathered							2313-2318
2992702	6381387	Unknown	Weathered concretionary material along fault							
2992753	6381389	Pipe	Partially buried, concretionary body							2308-2312
2992754	6381366	Unknown	Partially buried, concretionary body							2301-2307
2992755	6381361	Conical								2294-2300
2992756	6381366	Doughnut	Radial fracture pattern in concretion							2291-2293
2992760	6381471	Pipe	Along fault			065, 115	065, 115			2330-2332
2992767	6381409	Unknown	Concretionary material along fault							2333-2334
2992773	6381419	Doughnut	Half doughnut, broken along fault, lower displaced on fault			040	040		170	2235-2237
2992785	6381390	Doughnut	No clear conduit							2345-2346
2992785(b)	6381378	Rubble	Concretionary rubble							2347
2992790	6381408	Doughnut	Small doughnuts in fault							2338

Table 1 continued

Easting / Sample number	Northing	Morphology	Notes	Dip (concretion)	Dip direction (concretion)	Fracture orientations (concretion)	Fault orientations	Dip (bedding)	Dip direction (bedding)	Photo JPG #
2992794	6381390	Conical	Joints divert around concretion (but do not reconnect)			210, 235	210, 235		190	2339-2344
2992820	6381327	Unknown	Partially buried, concretionary body							2290
2992835	6381357	Doughnut		038	340					2348-2349
2992836	6381394	Conical	Adjacent to fault	040	330	045	045			2367-2371
2992841	6381361	Conical					078, 050			2350-2356
2992862	6381330	Doughnut	Largest doughnut, partially buried in sand	040	310					2281-2289
2992880	6381335	Unknown	Small concretionary material							2390
2992881	6381360	Unknown	Small concretionary material, highly weathered							2358
2992884	6381334	Unknown	Small concretionary material							2389
2992886	6381351	Unknown	Small concretionary material, highly weathered							2360
2992890	6381350	Unknown	Small concretionary material, highly weathered							2361
2992895	6381358	Unknown	Small concretionary material, highly weathered							2359
2992951	6381363	Conical		040	320					2362-2366
2992967	6381345	Concretionary layer	Possibly connected to same layer							2388

Table 1 continued

Easting / Sample number	Northing	Morphology	Notes	Dip (concretion)	Dip direction (concretion)	Fracture orientations (concretion)	Fault orientations	Dip (bedding)	Dip direction (bedding)	Photo JPG #
2992978	6381374	Unknown	Small concretionary material							
2992983	6381374	Concretionary layer	Possibly connected to same layer							2387
2992994	6381380	Concretionary layer		040	308					2386
2992997	6381391	Concretionary layer		040	308					2386
2993002	6381410	Concretionary layer		040	308					2386
2993007	6381422	Concretionary layer		040	308					2386
2993008	6381475	Unknown	Weathered, seaward concretionary material	035	330	110	110			2375
2993009	6381465	Unknown	Weathered, seaward concretionary material			110	110			2376
2993011	6381462	Doughnut	Possibly allochthonous							2377
2993015	6381374	Unknown	Small concretionary material							
2993025	6381439	Doughnut								2378-2380
2993038	6381374	Conical		030	300					2384-2385
2993041	6381415	Doughnut		040	290					2383
2993042	6381424	Pipe	Pipe-like in fault							2381-2382

also characterises the walls of the uppermost portion of these concretions (Fig. 7C,D). Their widest point averages 1 m in diameter (horizontal), tapering to about 0.5 m, and they stand up to 1.5 m tall above the shore platform. Pipe concretions generally have a straight or cylindrical morphology with their long axis perpendicular to bedding (Fig. 7E,F). The length of exposed pipe examples ranges from 0.5 to 1 m. Their diameter ranges from 10 to 75 cm, the value remaining more or less constant throughout the length of any one pipe concretion.

4.2 Concretion distribution

The main occurrence of tubular concretions is at Horoera Point, where they crop out over about 1 km along the shore platform (Fig. 2B, 9). The best preserved exposure is towards the west side of the location (i.e., youngest part of sequence). Here, about 30 doughnuts, along with a few pipes and conical concretions, are exposed in linear trends (Fig. 10). The centre of the platform extends over a distance of 300 m that is void of concretions. Two prominent turbidite beds are located within this section of the shore platform (Fig. 10). The east side of the platform (i.e., oldest part of sequence) extends across 350 m. Approximately 15 doughnuts and a few conical concretions are exposed here on the shore platform. Abundant concretionary debris and concretions that are too weathered to determine morphology are scattered along the entire platform (Fig. 10).

4.3 Petrography

The tubular concretion matrix contains angular to subangular silt size grains of quartz and feldspar, among other siliciclastic material (Fig. 11A,B). Carbonate cement in the tubular concretions is protodolomite to dolomite (44–51 mol% Mg) comprising beige to grey micrite/microsparite (Fig. 11A-C), whereas two samples are high-Mg calcite (pipe concretions). Minus cement porosities range from 60−80%. Conduits are often filled with cement and/or sediment distinctly different from that of the concretion matrix (Fig. 11D-F). Conduits often contain moderate amounts of planktic and benthic foraminifera, echinoderm spines, and bioturbation, whereas skeletal material is minor to absent in the outer concretion (Fig. 11D-F). Framboidal pyrite is present filling shells in conduits as well as in the muddy matrix of concretions (Fig. 11G-I).

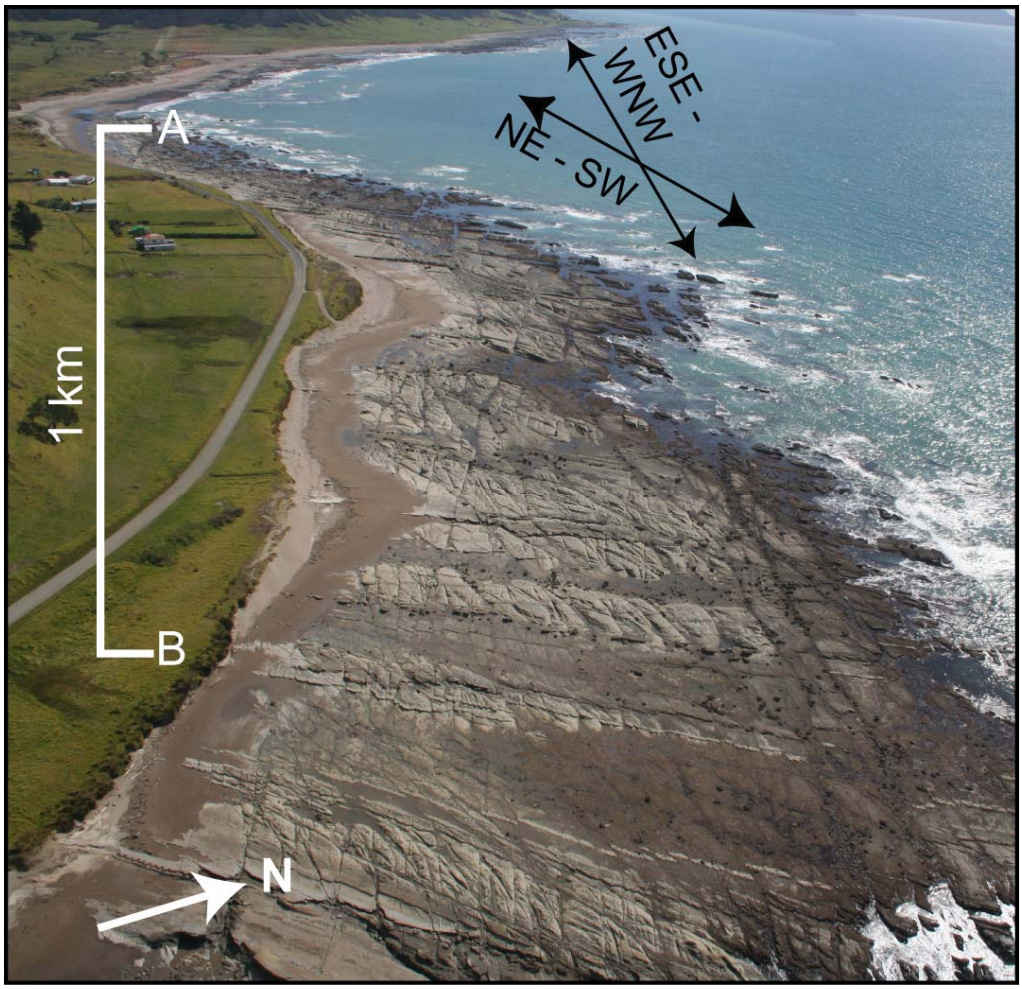

Figure 9. Aerial photograph of the shore platform outcrop at low tide at Horoera Point. Black arrows indicate the general directions of major faults in the outcrop. A and B identify the corresponding locations on the distribution map of Figure 10. The distance from point A to B on the photograph is approximately 1 km, however the appearance is distorted due to the oblique angle the photograph was taken from.

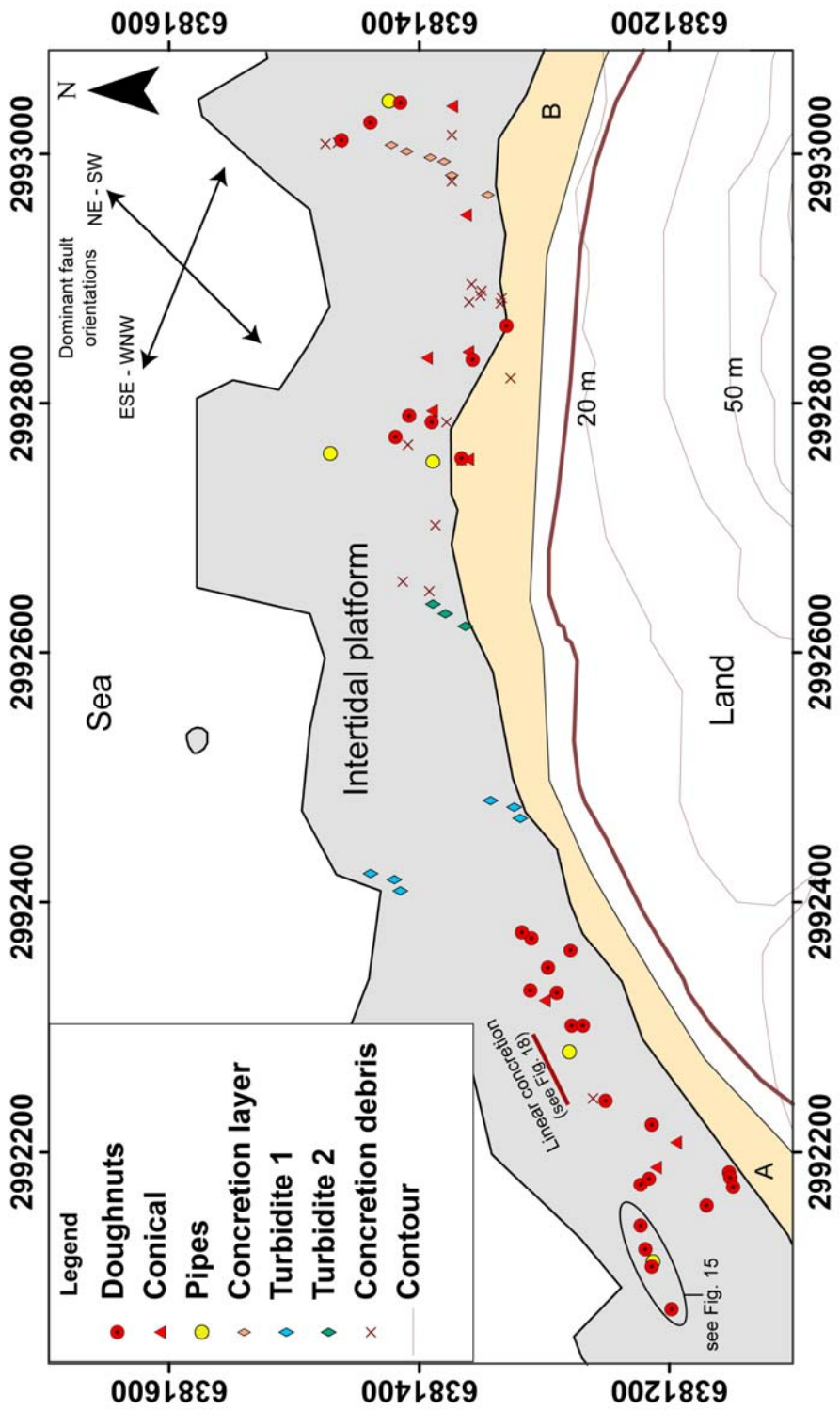

Figure 10. Distribution map of tubular concretions at Horoera Point. A and B identify the corresponding locations in Figure 9. Detailed field data are in Table 1 where sample number corresponds to GPS location. The map coordinates correspond to the New Zealand Map Grid coordinate system and locations may be found on NZ Map Series 260, 1:50,000 scale, sheet Z14.

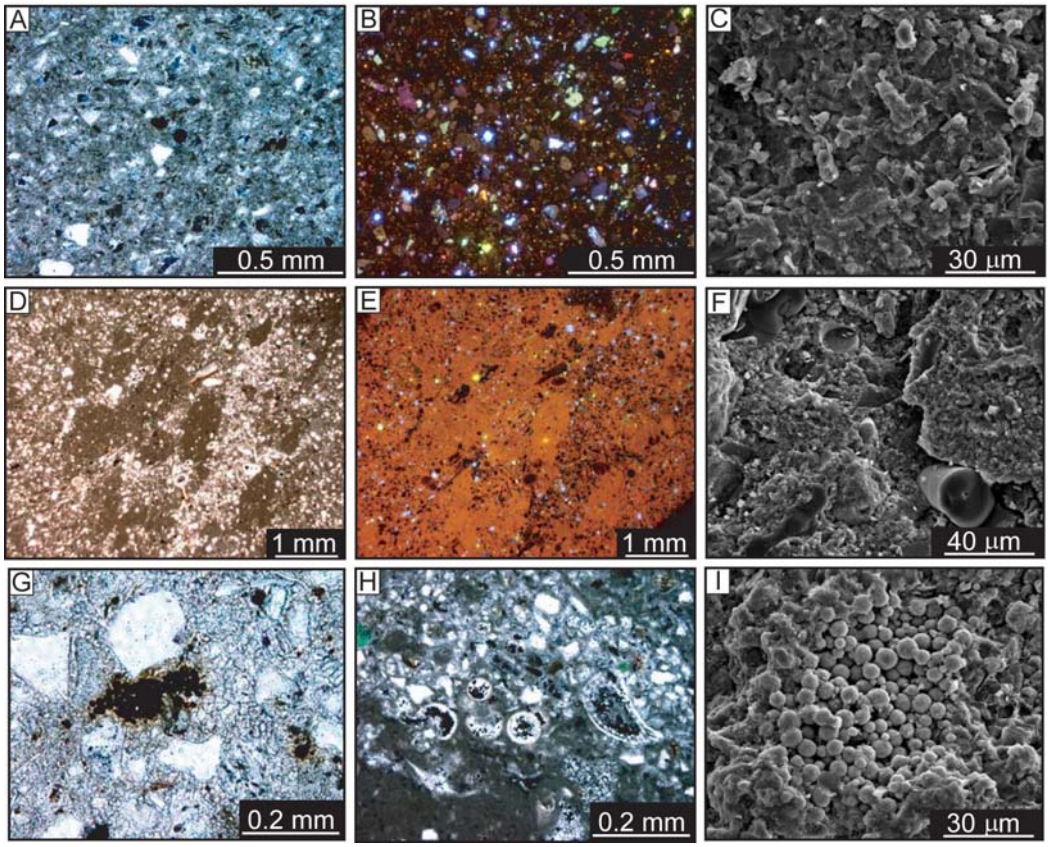

Figure 11. Petrographic images from doughnut concretions. (A,B) Thin section pair (PPL and CL respectively) of tubular concretion showing silt sized clastic material, mainly composed of quartz and feldspar, and pore filling micritic dolomite cement (orange CL in B). (C) SEM image of mudstone with micritic carbonate cement. (D,E) Thin section pair (PPL and CL respectively) of doughnut concretion conduit with bioturbation and micritic dolomite cement (orange-red CL). (F) SEM image of doughnut concretion with dolomite cement and sponge spicules. (G,H) Thin section (PPL) and (I) SEM images of framboidal pyrite in intergranular spaces (G,I) and filling benthic forams (H). Samples 2361 (A,B,C); 2361 conduit (D,E,F); and 2208 (G,H,I); see Tables 1 and 2.

4.4 Isotope composition

Carbon and oxygen isotopes were analysed from 8 concretions, including 4 doughnuts, 2 conical, and 2 pipes (Table 2). Concretion isotope values for $\delta^{13}C$ range from −17 to +9‰ PDB and for $\delta^{18}O$ from +2 to +6‰ PDB (Table 2, Fig. 12). Concretions were subsampled along a horizontal transect from their outer margin to the concretion conduit wall; one doughnut was also sampled along a vertical transect. Carbon and oxygen isotope values remain relatively similar along the concretion transects, although some concretions record a compositional variation between the concretion and the conduit (Fig. 13).

4.5 Faults

Many faults dissect the shore platform. Two main orientations are present: 1) NE–SW trends; and 2) ESE−WNW trends (Table 1, Fig. 14). The NE−SW orientation predominately has a right lateral sense of shear; whereas, the ESE−WNW predominately has a left lateral sense of shear (Fig. 14). In places, both fault orientations have some vertical displacement. Most faults have centimetre to a few metres displacement, whereas some of the major faults may have a much larger displacement. The faults intersect repeatedly along the platform, often one being displaced by the other. In places the repetitive fault intersections create rhomb-like features in the strata.

4.6 Concretion distribution with respect to faults

Doughnut concretions are mainly aligned along the two main fault orientations or their bisection (Fig. 14). Several linear trends occur, whereby four or more doughnuts are more or less aligned, about equally spaced, along a fault or its bisect (Fig. 15). In this example, the doughnuts become more progressively fractured by faulting from west to east. In other locations, doughnuts are dissected by faults (Fig. 16A) and have centimetre-scale displacement (Fig. 16B). Other doughnuts are cut in half, with the second half either completely broken into debris or entirely missing (Fig. 16C,D). In places, fault shear zones can be seen crossing the doughnut concretions (Fig. 16D). Additionally, some doughnuts

are deformed and offset (Fig. 17). In some cases a fault or joint diverts around a concretion and rejoins on the other side.

Along an ESE−WNW trending fault, an elongate concretion with at least 18 open conduits is exposed (Fig. 18). The concretion is discontinuous over 50 m and averages 1 m in width. In places, the concretion is wider and strays from the fault. On the east end of the elongate concretion, a small doughnut is present (Fig. 18), which extends approximately 3 m southward from the fault. On the west end within the fault, the elongate concretion curves to an end, adjacent to another doughnut (Fig. 18).

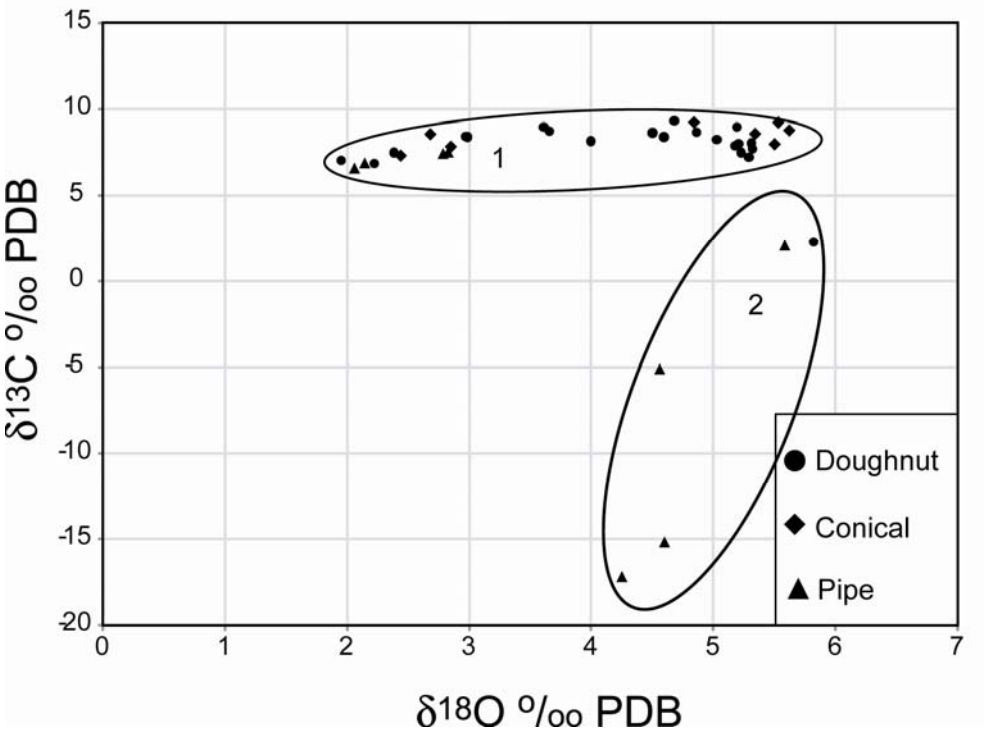

Figure 12. Stable oxygen and carbon isotope cross plot for tubular concretions at Horoera Point. Note that the tubular concretions mainly group together (1) except for several pipe concretions (2), which trend down towards more negative carbon values.

Table 2. Stable carbon and oxygen isotope values from tubular concretions at East Cape.

Sample number	Morphology	$\delta^{13}C$ ‰ PDB	$\delta^{18}O$ ‰ PDB
2361_1	Doughnut - outer	+8.7	+3.7
2361_2	Doughnut - middle	+9.3	+4.7
2361_3	Doughnut - middle	+8.5	+3.0
2361_4	Doughnut - conduit rim	+9.0	+3.6
2361_5	Doughnut - conduit rim	+8.4	+3.0
2361_6	Doughnut - conduit fill	+2.3	+5.8
2208-1	Conical - outer	+8.6	+2.7
2208-2	Conical - middle	+8.6	+5.3
2208-3	Conical - centre	+8.8	+5.6
2208-4	Conical - centre	+8.0	+5.5
2208-5	Conical - middle	+9.3	+5.5
2208-6	Conical - outer	+9.3	+4.8
EC3-1c	Pipe - outer (no GPS)	-5.1	+4.6
EC3-2c	Pipe - middle (no GPS)	-15.2	+4.6
EC3-3c	Pipe - conduit rim (no GPS)	-17.2	+4.3
2280-1	Linear concretion, see Fig. 18	+2.1	+5.6
2280-2	Linear concretion, see Fig. 18	+7.5	+2.8
2280-3	Linear concretion, see Fig. 18	+6.9	+2.1
2280-4	Linear concretion, see Fig. 18	+6.6	+2.1
2280-5	Linear concretion, see Fig. 18	+7.4	+2.8
2301-2	Doughnut at ESE end of 2280, see Fig. 18	+6.9	+2.2
2301-3	Doughnut at ESE end of 2280, see Fig. 18	+7.1	+2.0
2347-1	Half doughnut, see Fig. 13	+8.67	+4.5
2347-2	Half doughnut, see Fig. 13	+8.1	+5.2
2347-3	Half doughnut, see Fig. 13	+7.5	+5.2
2347-4	Half doughnut, see Fig. 13	+7.2	+5.3
2347-5	Half doughnut, see Fig. 13	+7.9	+5.2
2347-6	Half doughnut, see Fig. 13	+9.0	+5.2
2347-7	Half doughnut, see Fig. 13	+7.7	+5.3
2347-8	Half doughnut, see Fig. 13	+8.1	+5.3
2347-9	Half doughnut, see Fig. 13	+7.5	+2.4
2862-1	Doughnut - outer	+8.2	+4.0
2862-2	Doughnut - middle	+8.7	+4.9
2862-3	Doughnut - conduit	+8.3	+5.0
2862-4	Doughnut - middle	+8.4	+4.6
2862-5	Doughnut - outer	+7.6	+4.7
2836-1	Conical - outer	+7.4	+2.4
2836-2	Conical - centre	+7.9	+2.8

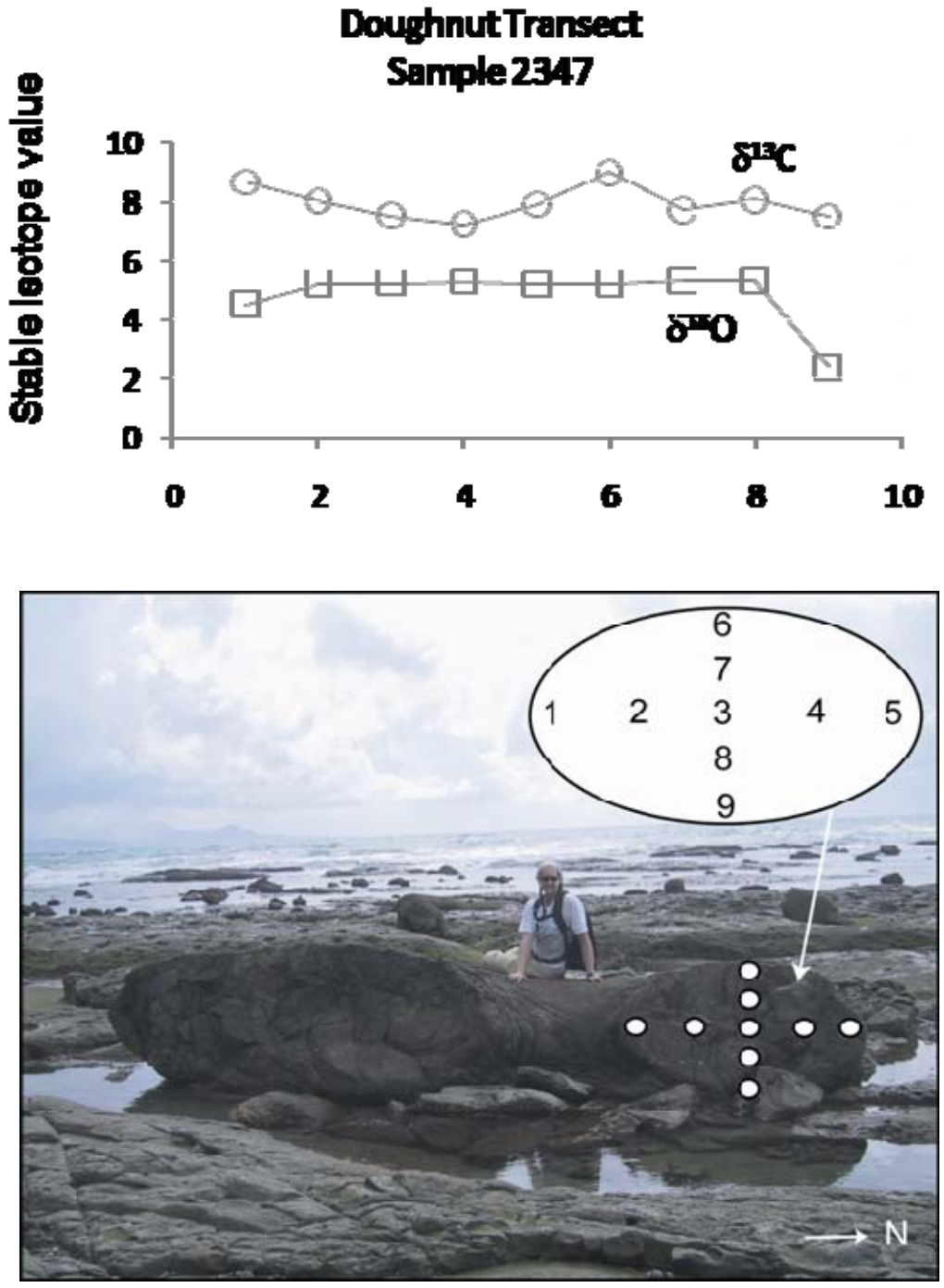

Figure 13. Carbon and oxygen isotope transects through a doughnut concretion. The isotope values are relatively constant, varying by only 2‰ PDB (carbon and oxygen). Transect positions (x-axis) correspond to sample numbers in lower photograph (Sample 2347, see Tables 1 and 2).

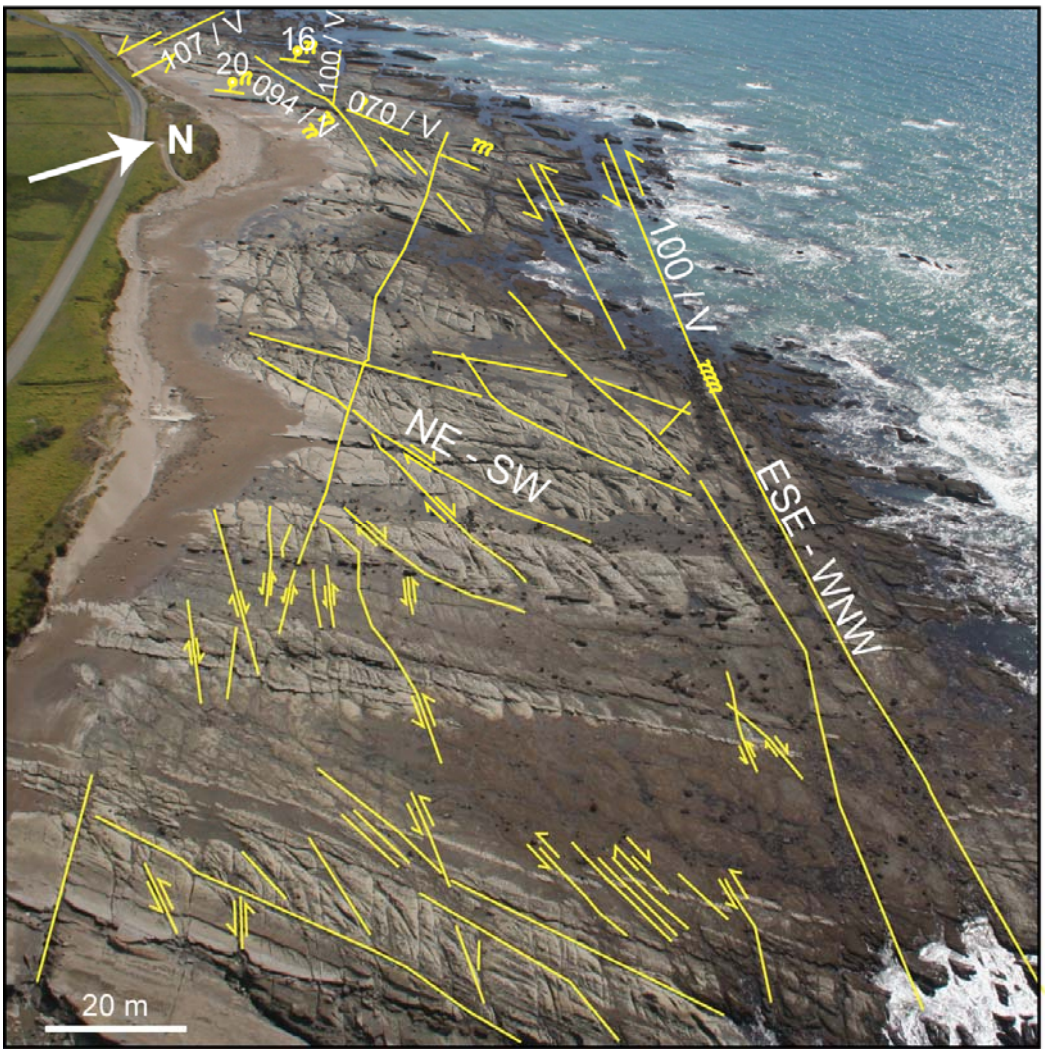

Figure 14. Aerial photograph (from helicopter) of Horoera Point with some superimposed structural data. The main fault orientations are NE– W and ESE–WNW. Detailed structural data are in Table 1. The faults have a lateral sense of shear, however, a few also have some vertical displacement (V).

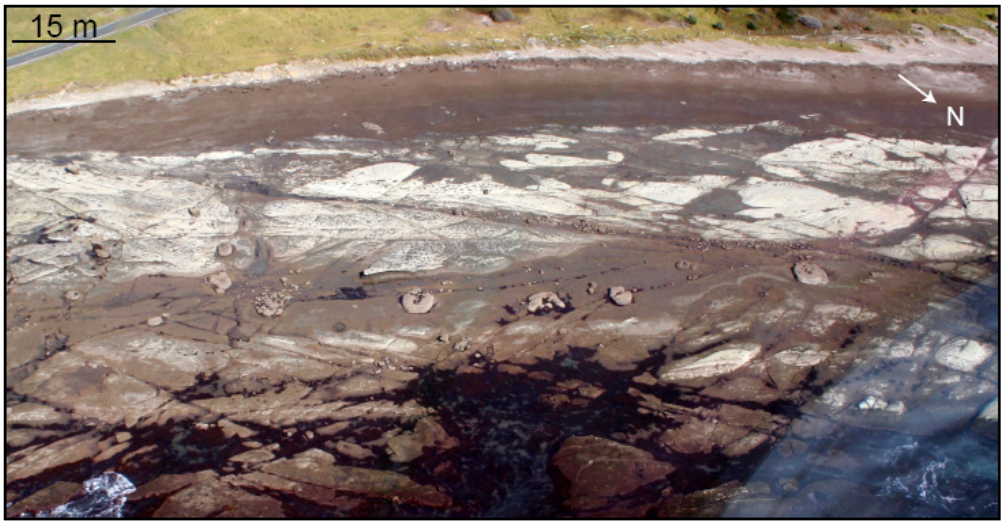

Figure 15. Aerial photograph (from helicopter) of doughnuts aligned on an ESE–WNW trending fault. Note doughnuts are progressively more broken to the left (SE) of the photograph. Samples 2122, 2112, 2108, 2074 (left to right), details of samples are in Table 1.

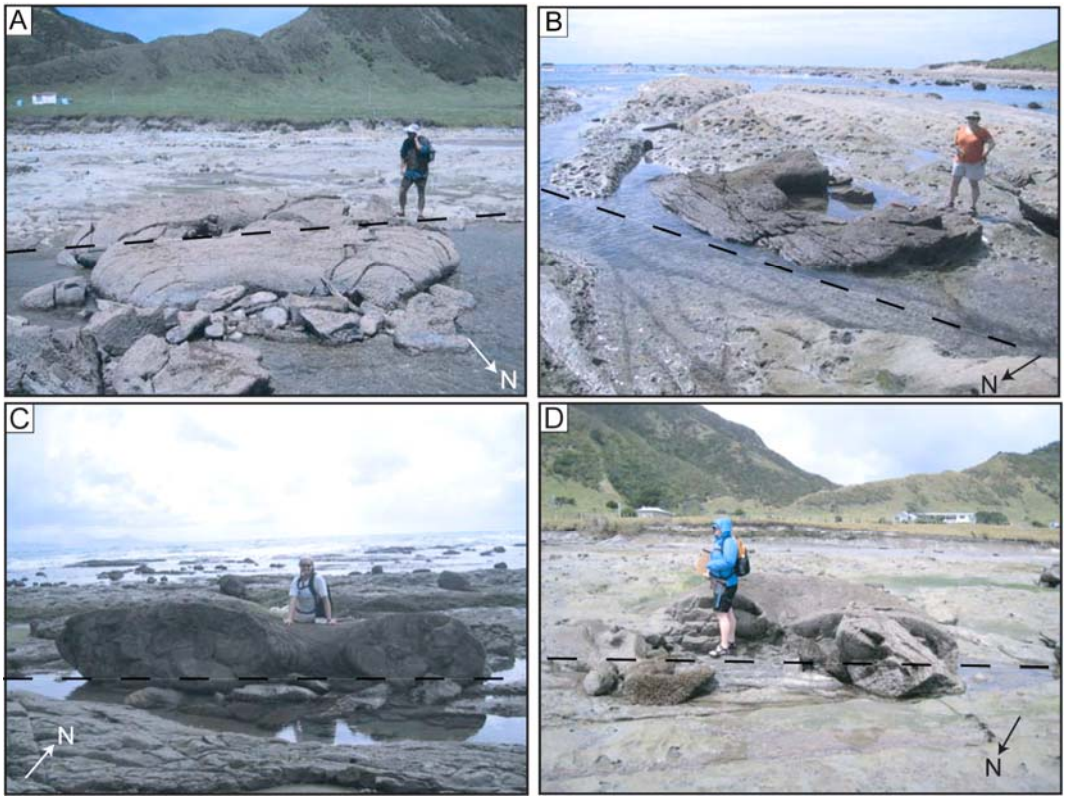

Figure 16. Photographs of doughnut concretions along and adjacent to faults. (A) Doughnut dissected by fault (sample 2241). (B) Doughnut along fault with cm displacement (sample 2773). (C) Half a doughnut situated on a fault (sample 2347). (D) Doughnut bisected by a fault, fault shear zone visible.

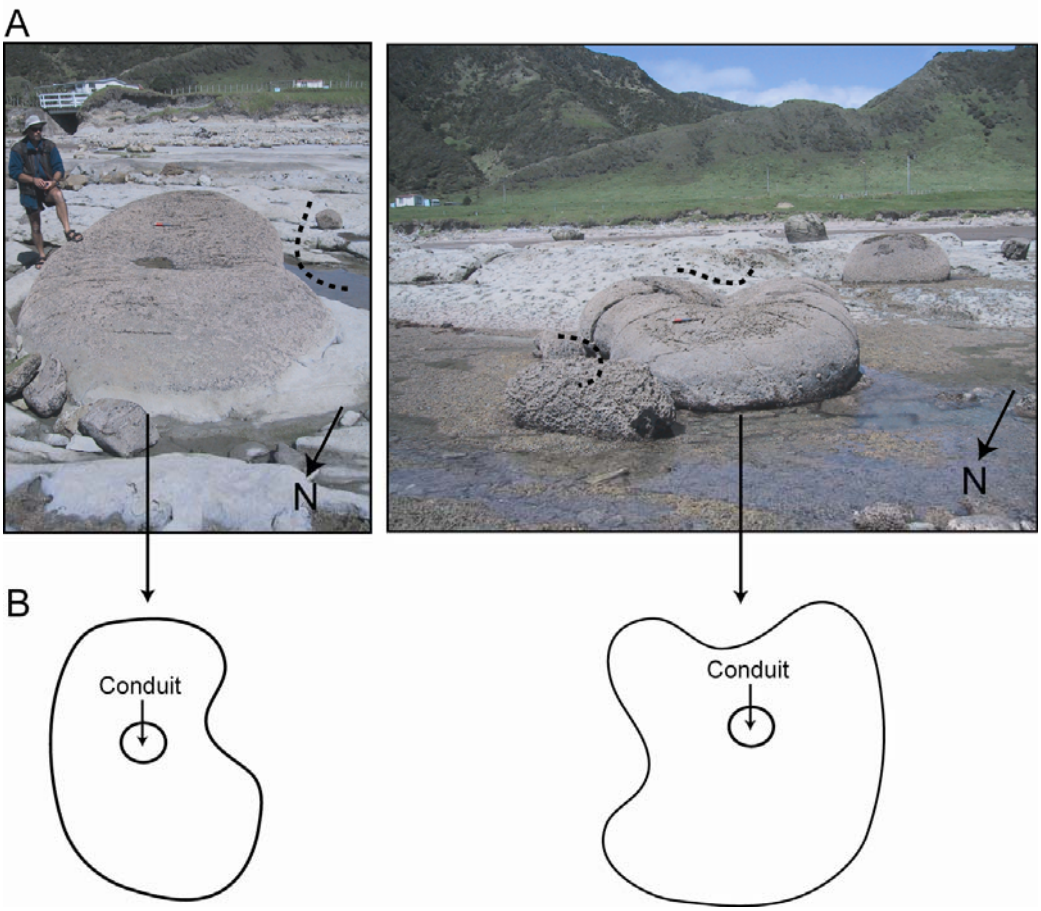

Figure 17. (A) Photographs of two doughnut concretions that are deformed (bean shaped) and displaced along a fault. (B) Diagrams of the photographs (in A) to illustrate the concretion shapes and displacements.

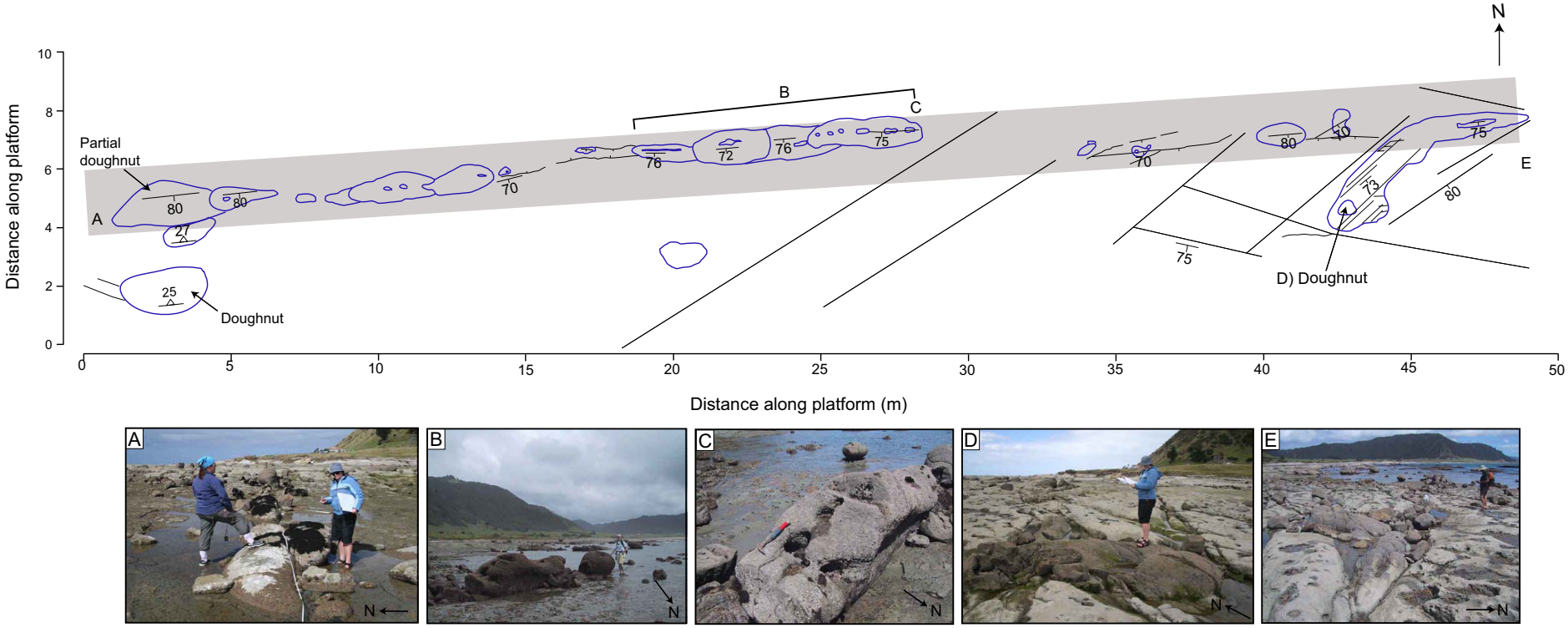

Figure 18. Sketch of a linear concretionary body from bird's eye view, with at least 18 open conduits. The concretion is situated on an ESE-WNW oriented fault. The concretion is discontinuous over 50 m and cross-cut by a NE-SW oriented fault. At the ESE end (right side of sketch), the concretion deviates southward into a doughnut concretion. At the WNW end, the concretion appears to curve slightly southward. A half doughnut is situated 1 m away from the WSW end and may have once been joined to the linear concretion. Photographs A-E correspond with locations on sketch. Grey shaded area represents the fault. See Tables 1, 2, sample 2280.

5. Discussion

5.1 Fluid composition

5.1.1 Carbon isotopes

Carbon isotope values recorded in authigenic carbonate reflect the source of carbon incorporated into the carbonate lattice. Potential carbon sources include marine shell material, decomposition of organic matter, oxidised microbial or thermogenic methane, and residual carbon as a by product of microbial methanogenesis (Irwin et al., 1977; Curtis, 1978; Roberts and Aharon, 1994). Table 3 illustrates the relationship between burial diagenetic zones, the chemical processes, depth ranges, and carbon source of the authigenic carbonates precipitated. Carbon isotope values of the tubular concretions show little variation between concretions or along concretion transects. Typically, strongly positive carbon signatures such as those recorded by most of the East Cape concretions (Fig. 12; $\delta^{13}C$ from +6 to +9‰ PDB) have been interpreted as sourced from reduced CO_2 produced as a by-product of methanogenesis (Table 3) (Greinert et al., 2001; Pierre et al., 2002; Peckmann et al., 2002; Pierre and Rouchy, 2004; Gieskes et al., 2005). As such, carbon for the East Cape concretions could have been derived from the microbial production of methane during shallow burial of the sediment pile (10s m to 1 km).

Alternatively, extensive oxidation of thermogenic methane can fractionate the carbon isotope values enough to account for strongly positive $\delta^{13}C$ values of the East Cape concretions. Continual methane oxidation results in enrichment of $\delta^{13}C$ values in the residual methane pool due to isotope fractionation (Coleman et al., 1981; Whiticar, 1999; Pancost et al., 2000; Cowen et al., 2002). Oxidation of 80% of a thermogenic methane pool ($\delta^{13}C$ –50 to –20‰ PDB) can enrich the residual methane up to 30‰, whereas 99% oxidation can enrich it up to 60‰. The resulting $\delta^{13}C$ signature of the residual methane and any carbonate

Table 3. Chemical reactions of methane oxidation and methane production during diagenesis, depth of occurrence, source of carbon, and observed carbon isotope signatures of authigenic carbonate (modified from Irwin et al., 1977; Roberts and Aharon, 1994).

Zone	Processes	Depth beneath seafloor (m)	Carbon source	$\delta^{13}C$ ‰ PDB of precipitated carbonate
Sulphate reducing	Anaerobic oxidation of methane via methanotrophic Archaea and sulphate reducing Bacteria $CH_4 + SO_4^{2-} \Rightarrow HCO_3^- + H_2O + HS^-$	0.01 - 10	Microbial methane	-90 to -50
			Thermogenic methane	-50 to -25
Methanogenic zone	Anaerobic bacterial methanogenesis $2CH_2O \Rightarrow CH_4 + CO_2$	10 - 1000	CO_2 byproduct of methane production	-10 to +15

precipitates after oxidation can therefore reach positive values during the end stages of methane oxidation. Additionally, extensive oxidation of microbial methane can result in $\delta^{13}C$ values identical to that of thermogenic methane. For example, microbial methane with $\delta^{13}C$ of −90‰ and a +60‰ shift due to extensive oxidation could result in $\delta^{13}C$ values of −30‰, which is otherwise indicative of thermogenic methane. As such, it may be difficult to distinguish between microbial and thermogenic methane sources (Coleman et al., 1981). Interestingly, Cowen et al. (2002) reported wide variations in the $\delta^{13}C$ values of methane fluids from active hydrothermal plumes along the Juan de Fuca Ridge. The $\delta^{13}C_{methane}$ values are strongly negative at the main vent but become increasingly positive (up to +10‰ PDB) with distance from the main expulsion site. Their measurements clearly illustrate the phenomenon of extensive methane oxidation at the seafloor, one which needs to be more fully evaluated with respect to hydrocarbon seep fluids.

Biomarker compounds in the East Cape concretions include pentamethyl icosane (PMI) and archeol indicative of anaerobic oxidation of methane (AOM) consortia, and C33 dialkyl glycerol diether (DGD) and macrocyclic diether (MD) indicative of sulphate reducing Bacteria in AOM consortia (Pearson et al., 2008). However, the AOM markers are more dominant in the concretion conduit fills than in the primary concretions. In comparison, the host mudstone does not contain PMI or MD and only traces of archaeol and DGD. The AOM markers confirm that AOM

by methanotropic Archaea and sulphate reducing Bacteria was occurring in the sediments (Pearson et al., 2008), even though the $\delta^{13}C$ values of the carbonate are dominantly positive. Consequently, we favour that the positive $\delta^{13}C$ values of the carbonate cement in the East Cape concretions result from extensive ongoing oxidation of either microbial methane mixed with methanogenic CO_2 or extensive oxidation of thermogenic methane.

5.1.2 Oxygen isotopes

Oxygen isotope values of authigenic carbonate can indicate the composition and temperature of the fluid at the time of carbonate precipitation (Longstaffe, 1987). Based on the volume of carbonate cement in the East Cape concretions (62−80%), precipitation likely occurred near below the seafloor under depositional to shallowest burial conditions (Boggs, 1992; Bjørlykke, 1998). Fluid compositions at the time of carbonate precipitation can be constrained based on the equation from Fritz and Smith (1970) for protodolomite (Fig. 19). Dolomite precipitated in equilibrium with New Zealand Miocene marine waters (estimated $\delta^{18}O$ between –0.7 and –0.5‰ SMOW; Feary et al., 1991) at upper slope bottom water temperatures from 5–10˚C (Ridgway, 1969) would have a $\delta^{18}O$ value between +3.2 and +4.2‰ PDB (Fig. 19). Only four samples fall within the region of dolomite precipitation in marine waters (Fig. 12). The majority of samples are slightly depleted or rather enriched with respect to marine water compositions.

Dolomite samples with $\delta^{18}O$ values from +2 to +3‰ PDB (Fig. 19) are depleted from normal marine waters (dashed line) by up to 2.2‰. Interestingly, most of these samples are from the elongated concretion located on a fault (see Section 4.6; Fig. 18). The depleted $\delta^{18}O$ values could be due to an increase in temperature from 10–15ºC (Fig. 19). Raised fluid temperatures may suggest either dolomite precipitation at depth (up to 450 m with a geothermal gradient of 23 ºC/km and bottom water temperatures between 5 and 10ºC) or rapid ascent of warmer fluids. Ascending warmer fluids could have been sourced from much greater depths, yet precipitated dolomite near the seafloor (within a few metres) with $\delta^{18}O$ values suggestive of temperatures between 10 and 15ºC and burial depths 70 to 240 m, so long as they ascended rapidly so as not to have time to completely cool with

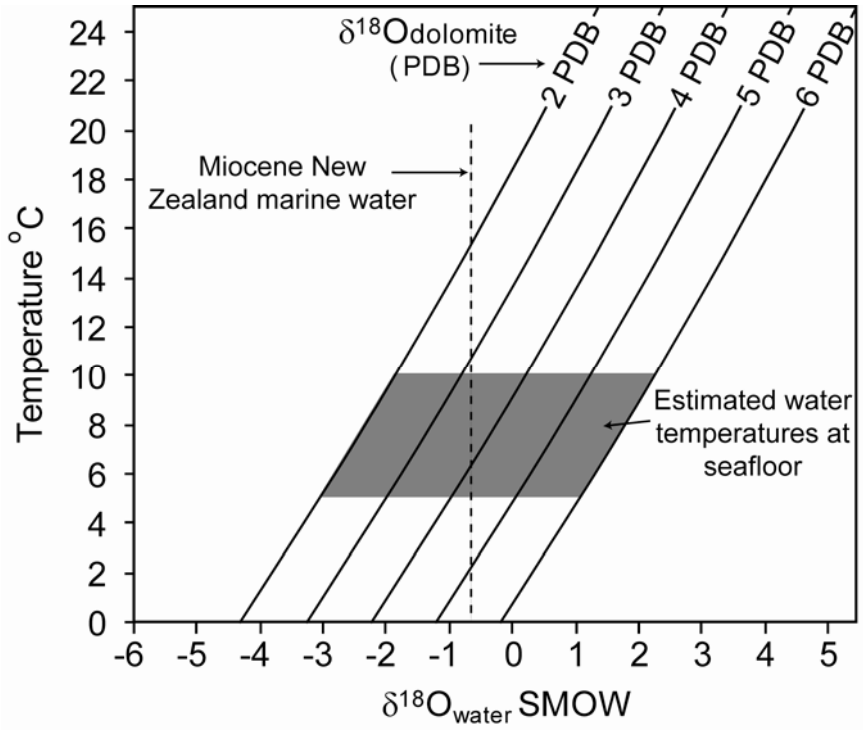

Figure 19. Possible water compositions (SMOW) responsible for carbonate precipitation in the Pohutu Formation. The grey highlighted region marks the possible water compositions at the time of carbonate precipitation (near seafloor at approximately 5 to 10 ºC). Curves crossing 5 to 10 ºC (grey rectangle) to the left of dashed line (Miocene New Zealand marine water composition; Feary et al., 1991) are depleted with respect to marine seawater by up to 2.5‰ PDB and indicate precipitation from fluids at higher temperatures or gas hydrate formation. Curves crossing 5 to 10 ºC to the right of dashed line are enriched with respect to marine seawater by up to 2‰ PDB and indicate precipitation from fluids influenced by gas hydrate dissociation. See text for explanation. Dolomite equilibrium calculations from Fritz and Smith (1970).

respect to the surrounding environment. Alternatively, $\delta^{18}O$ values slightly depleted from marine water compositions could have been caused by gas hydrate formation as the heavier oxygen is preferentially accepted into the clathrate water molecule (Davidson et al., 1983; Ussler and Paull, 1995).

Dolomite samples with $\delta^{18}O$ values from +4.2 to +5.8‰ PDB (Fig. 19) are +1.6 to +3 enriched from normal marine waters at 5–10 ºC (by +3 to +4‰ if 10–15 ºC) (Fig. 19). Evaporation, clay dehydration, or gas hydrate dissociation could explain the ^{18}O-enriched isotopes in the East Cape concretions. However, it is unlikely evaporative conditions were met in the subsurface environment. Additionally, clay transformation would not have begun at such shallow depths as that at which the concretions are inferred to have formed. Moreover, the persistence of common to abundant smectite in the clay fraction of many of the older East Coast Basin formations (e.g., Pearce et al., 1981; Fergusson, 1985) effectively negates clay mineral alteration as a burial source of ^{18}O-enriched fluids. Therefore, it is unlikely that ^{18}O-enriched fluids resulting from clay transformation at depth migrated through the Pohutu Formation during the time of concretion formation.

Gas hydrate dissociation may also cause $\delta^{18}O$ enrichment in pore waters. As methane hydrate forms, the clathrate molecule preferentially accepts the heavy oxygen. During dissociation, the heavy oxygen is released back into the sediment pore fluids resulting in anomalously enriched pore fluids (Davidson et al., 1983; Ussler and Paull, 1995). Consequently, it is surmised that the most likely explanation for enriched $\delta^{18}O$ values in the concretionary carbonate is the dissociation of gas hydrates. Certainly, methane hydrates are known to be widespread today beneath the offshore Hikurangi Margin (Fig. 2A).

5.2 Plumbing system of a cold seep

Based on their morphologies, presence of central conduits, stable carbon and oxygen isotope values, pore filling micritic cement, and a lack of seafloor MDAC features and chemosymbiotic fossils, the tubular concretions in the Pohutu Formation are interpreted to have formed from cement precipitation beneath the seafloor as a result of ascending methane rich fluids. Based on this evidence, and

previous studies linking similar characteristics and concretionary bodies to cold seeps (Aiello et al., 1999, 2001; Lédesert et al., 2003; Mazzini et al., 2003; Clari et al., 2004; Conti et al., 2004, Conti and Fontana, 2005; Hovland et al., 2005; De Boever et al., 2006), the East Cape concretions are interpreted to mark the ancient subsurface plumbing system of cold seep development in the East Coast Basin during the late Miocene. While the tubular pipe concretions mark the fluid ascent pathways, the doughnut concretions may reflect stages of fluid entrapment during ascent. Section 5.4 discusses the evidence for doughnut formation and potential temporal and spatial placement within the seep system. Based on the isotope evidence and lipid biomarkers, the ascending fluids were methane. Lipids confirm AOM was occurring in the sediments and therefore the strongly positive $\delta^{13}C$ values are interpreted to have been associated with extensive methane oxidation and potentially methanogenic CO_2. The positive $\delta^{18}O$ values in the tubular concretions are interpreted to be a result of methane hydrate dissociation.

Previously, positive $\delta^{18}O$ values coupled with strongly negative $\delta^{13}C$ values in carbonate precipitates have been interpreted to have formed from methane hydrate dissociation and subsequent anaerobic methane oxidation (Greinert et al., 2001; Aloisi et al., 2000; Clari et al., 2004; Pierre and Fouquet, 2007). On the other hand, only two other studies (Pierre et al., 2002; Pierre and Rouchy, 2004) have interpreted the co-occurrence of isotopically heavy carbon and heavy oxygen to be a result of methane hydrate dissociation. In these latter studies, the authors interpreted late Miocene dolomite concretions form Mediterranean marls to have been sourced from heavy residual CO_2 from methanogenesis and methane hydrate dissociation. However, the geochemical processes that link residual methanogenic CO_2 and hydrate released oxygen (positive $\delta^{13}C$ and positive $\delta^{18}O$) as a source for carbonate constituents, but not incorporating CH_4 released during hydrate dissociation (negative $\delta^{13}C$), has not been previously explained. Any explanation must rely on the inability for CH_4 to oxidise at the time of carbonate precipitation, otherwise the light carbon would be utilised. A geochemical explanation is difficult to envisage and an alternative hypothesis is proposed here based on the interpretation of the East Cape concretion carbon source from extensive methane oxidation. Geochemically more simple, dissociation of methane (thermogenic or microbial) hydrate would enrich the pore fluids by up to

+3‰ while subsequent extensive oxidation of (thermogenic or microbial) methane driven by AOM processes induces carbonate precipitation resulting in dolomite cement with strongly positive carbon and oxygen isotope values. Additionally, $\delta^{18}O$ values below +3‰ PDB may record episodes of methane hydrate formation. Moreover, the $\delta^{18}O$ values of dolomitic doughnuts are notably separated on Figure 12 with samples plotting between +1 and +2‰ to the left and right (depleted and enriched) of marine waters. The division indicates pore fluid evolution over the time during which the concretions formed, and the paucity of samples (only four) that plot near marine compositions together may also support a methane hydrate formation/dissociation hypothesis.

5.3 Hypothesised East Cape subsurface seep plumbing model

5.3.1 Hydrocarbon sources

Isotope values of East Cape tubular concretions (Fig. 12) cannot differentiate whether methane sources were microbial methane and methanogenic CO_2 or thermogenic methane. However, lipid biomarkers confirm AOM was occurring in the sediments at the time of precipitation. Therefore, the positive carbon isotopes must reflect either bicarbonate sourced from methanogenic CO_2 after CH_4 in the system was exhausted, or extensively oxidised methane. Regardless of the methane source, both explanations require extensive methane oxidation. Additionally, it is entirely plausible that methane was mixed microbial/ thermogenic in origin. Microbial methane may have been sourced from sediments just below the Pohutu Formation buried deeply enough to undergo methanogenesis.

Source rocks for thermogenic methane were potentially from slope to basin sediments of the Cretaceous Karekare, Waimarama, and Glenburn Formations, late Cretaceous to Paleocene deep water mudstones of the Whangai Formation, or the Paleocene Waipawa Black Shale (Fig. 4). The Cretaceous sediments reached maturity and expelled hydrocarbons from the early Miocene and the late Cretaceous and younger sediments expelled hydrocarbons from the Pliocene onwards (Francis et al., 2004). Deposition of sediments containing tubular

concretions primarily occurred in the late Miocene to early Pliocene, with concretion formation sometime after burial. Currently, modern onshore oil and gas seeps occurring throughout the East Coast Basin (Francis et al., 2004) predominately expel thermogenic methane (Francis, 1997) sourced from the late Cretaceous Whangai Formation (Rogers et al., 1999). On this basis, we tentatively suggest that the methane rich fluids migrating through the Pohutu Formation during the late Miocene to early Pliocene; if of thermogenic origin, may have been sourced (or partially sourced) from the Cretaceous rift margin related sediments of the East Coast Basin (Fig. 4).

5.3.2 Initiation of fluid migration

Tubular concretions have been documented in subduction margins with accretionary wedges and nearby to major fault zones (Kulm and Suess, 1990; Jensen et al., 1992; Peckmann et al., 2002; Diaz-del-Rio et al., 2003; Schwartz et al., 2003; Conti et al., 2005; De Boever et al., 2006). The East Coast Basin is located along the Hikurangi convergent margin which began subducting in the early Miocene, with major uplift and compressional events during the late Miocene (Fig. 3) (van der Lingen and Pettinga, 1980; Field et al., 1997; Nicol et al., 2002). Overpressured sediments along the Hikurangi Margin are a result of dewatering of the accretionary wedge, low permeability mudstones in the accretionary wedge, and the subducting sedimentary pile riding on the Pacific Plate (Moore and Vrolijk, 1992; Lewis and Marshall, 1996; Sibson and Rowland, 2003). The resulting fluid loss along the Hikurangi Margin is estimated to be more than 2×10^6 m^3 per year over 100 km (Townend, 1997). Close to East Cape, but further inland in the Raukumara Peninsula, several examples of ancient seafloor seep carbonates occur of Miocene age (Campbell et al., 2008). This suggests that the compressional regime along the Hikurangi Margin, where overpressured sediments and compressional faulting were the driving forces of fluid migration, resulted in fluid migration at East Cape, aided by further local lateral fault movement. Inland ancient seep sites likely had the same tectonosedimentary driving forces, and also delineate sites where fluids actually reached the seafloor.

5.3.3 Fluid ascent through the Pohutu Formation

The preferential distribution of doughnut concretions along or adjacent to faults indicates an intimate relationship between faulting and fluid migration (Figs. 15−18). Concretions aligned along fault planes, fault intersections, and the planar, pipe-like concretionary feature suggest faulting has influenced the release of fluids and their migration pathways (Figs. 15−18). Fractured concretions indicate faulting continued during and/or after concretion formation (Fig. 16), whereas deformed concretions suggest some concretions continued forming through multiple fault ruptures (Fig. 17).

The mutual cross-cutting relationships between the two major fault orientations (NE−SW and ESE−WNW), sense of shear on the concretionary structures, pattern of faulting, and slip vector for the doughnuts and linear concretion indicate the faults at Horoera Point are conjugate fault sets (Fig. 20). Additionally, the angle between the fault sets is about 46°, less than the 60° which is what would be expected for perfect conjugates assuming typical rock friction (μ = ~0.7), a value which is reasonable for siltstones. To accommodate the lateral movement along the conjugate fault sets, an extensional component was probably also operating. This would be conducive to creating pathways for fluid flow from source to surface.

A working hypothesis for structural control on doughnut formation is considered here, although it is emphasised that further detailed structural analysis of the region is required. The hypothesis considers fluid convection and a valve-like mechanism of fault movement and fluid ascent. The behaviour of the fault valve mechanism is based on Sibson (1992). Overpressured environments are conducive for fault-valve action (Sibson, 1992). The valve action depends on high permeability along the fault, created during fault rupture. After rupture the fault seals, resulting in low permeability (Fig. 21A) (Sibson, 1992). With respect to the East Cape concretions, the fault-valve scenario can be described by a four stage cycle.

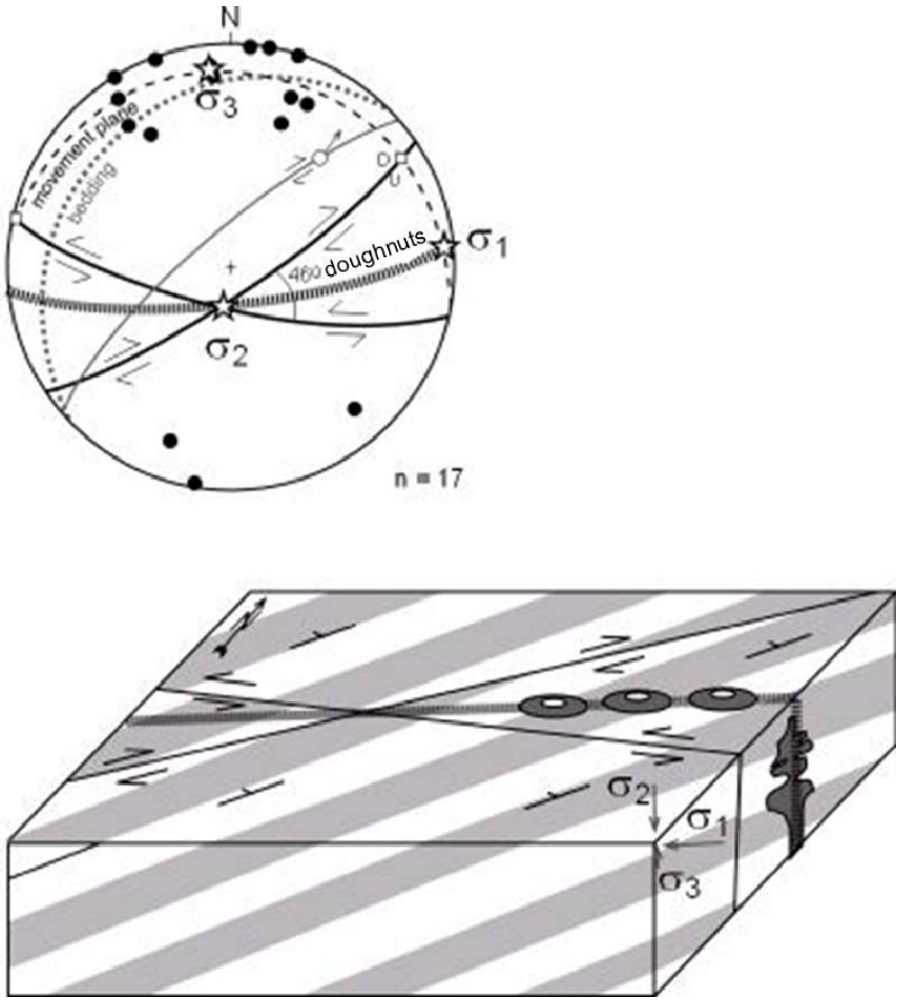

Figure 20. Summarised structural aspects at Horoera Point. (A) Lower hemisphere equal area stereonet showing the structural relationships on the shore platform in the vicinity of the aligned doughnuts shown in Fig. 18, annotated with data from elsewhere on the shore platform. Two main fault sets trend NE−SW and ESE−WNW, form a conjugate pair (opening angle = 46°), and accommodate right-lateral and left-lateral slip, respectively. The alignment of doughnuts bisects the acute angle between the faults. Predicted slip vectors based on a conjugate fault analysis are shown (squares), together with expected sense of strike-slip and dip-slip movement; D = down, U = up. The principal directions of compressive stress inferred to operate at the time of conjugate fault development are annotated (stars) and labelled (s1 > s2 > s3). Poles to fault planes recorded elsewhere on the shore platform are shown by black dots. A fault plane and slip vector are shown for a structure that exhibited well-developed fault striae. Bedding orientation is shown by the representative grey great circle. (B) Block model illustrating the structural context for the development of doughnuts, which are here inferred to occur on pure extension or hybrid extensional shear fractures in the acute angle between conjugate strike-slip faults. A subhorizontal greatest principal stress trends ESE−WNW, and the least principal stress is directed N−S. Intersections between faults and other fractures active in this tectonic regime favour vertical permeability.

In stage 1, fluid ascent ceases due to a structural (fault) trap (Fig. 21A, B Stage 1). Fluid injection continues, supplied from below, which then results in an overpressured system.

Stage 2 is characterised by increasing fluid pressure which decreases frictional strength, thereby exceeding the fault strength and causing rupture of the fault (Fig. 21A, B Stage 2). Permeability is created along the fault plane and fluid ascends upwards (Fig. 21B). As fluid is discharged, fluid pressures decrease (Fig. 21B).

In stage 3, fluid pressures continue to decrease. Migrating methane is anaerobically oxidised leading to carbonate precipitation (via the reaction in Table 3) along the fault pathways (Fig. 21A, B Stage 3). Doughnut concretions dissected and/or offset by faults (Fig. 16) indicate these concretions were formed (as rigid structures) before further fault rupture. A few doughnuts that are deformed (Fig. 17) indicate that at least in some cases, concretions were not fully formed before additional fault rupturing and indicate that carbonate precipitation may have continued over a long period of time.

During stage 4, the fault seals due to decreasing fluid pressures and cement precipitation increasing frictional strength, which destroys permeability along the fault plane, effectively trapping fluids again (Fig. 21A, B Stage 4). Any upward migrating fluids below the fault will again become trapped, leading to fluid pressure increase and a repeating cycle.

5.4 Concretion growth patterns

Previously, tubular concretion formation was determined to have occurred in the subsurface from cement precipitation originating at the outer margins of the concretion and continuing to precipitate towards the central conduit (Chapter 3, Section 6.4; Chapter 4, Section 5.4). The same growth pattern interpretation probably also holds for the East Cape pipe concretions; however, the doughnut concretions remain in question. A hypothesised growth pattern for the doughnuts is described below in Section 5.4.1.

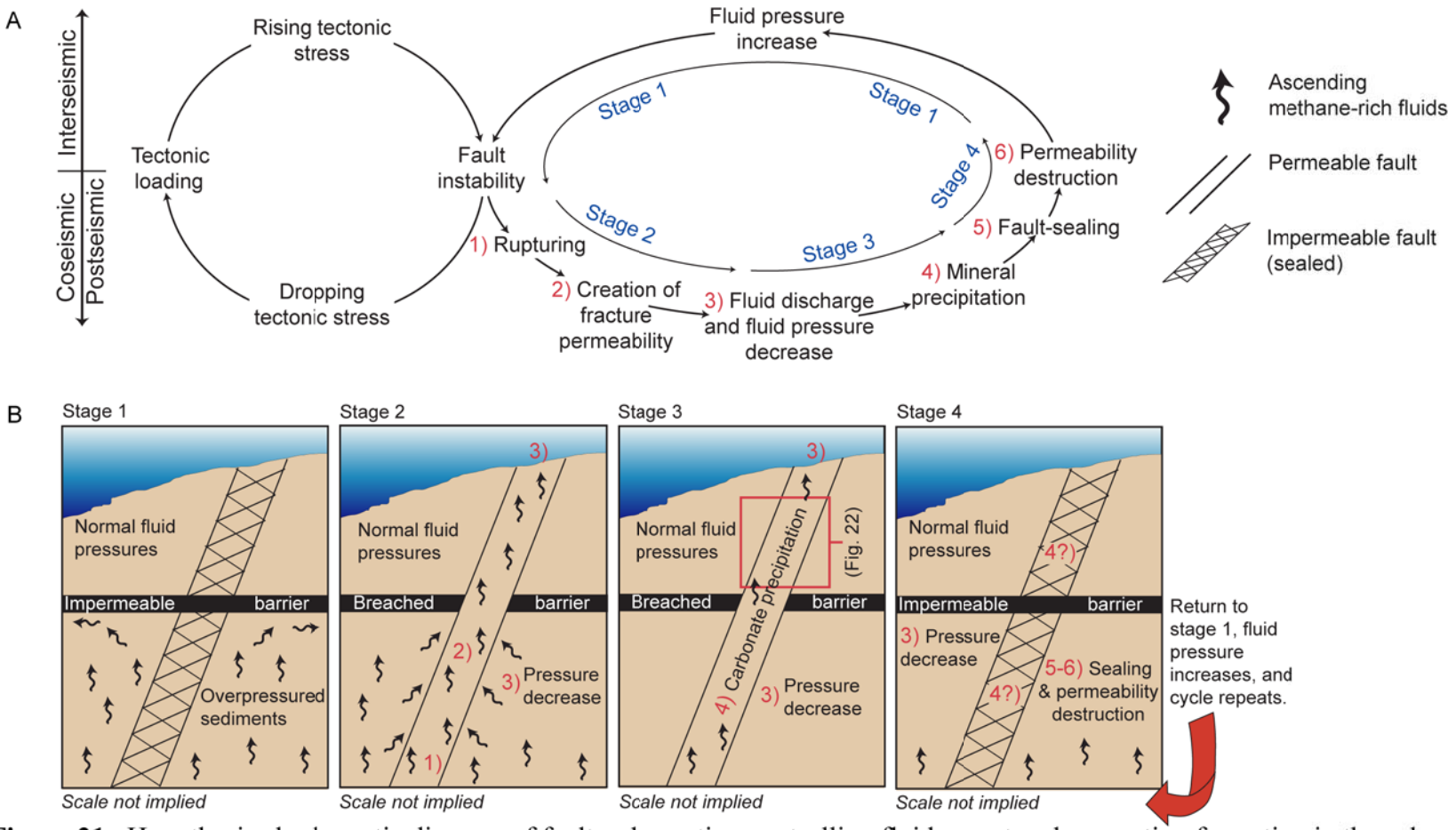

Figure 21. Hypothesised schematic diagram of fault-valve action controlling fluid ascent and concretion formation in the subsurface of an East Cape cold seep system along the Hikurangi subduction margin. Diagram showing the relationship between (A) fluid pressure build up and fault valve activity (modified and adapted from Sibson, 1992) with respect to (B) East Cape doughnut concretion formation subsurface. See Section 5.3.3 for text explanation. Stage numbers in A correspond to B.

5.4.1 Doughnut formation

Only horizontal sections of doughnut concretions are exposed at the East Cape location which raises the question as to what these concretions look like in three dimensions. Further inland, near locations of seep carbonates, are a few occurrences of concretionary features that appear morphologically like stacked doughnuts (Fig. 22A). In between each concretionary doughnut is a thin interbed of finer grained mudstone than that hosting the concretion. If these concretions represent the East Cape doughnuts in 3D, then they may indicate intermittent fluid ascent where fluid becomes trapped by a thin stratigraphic layer.

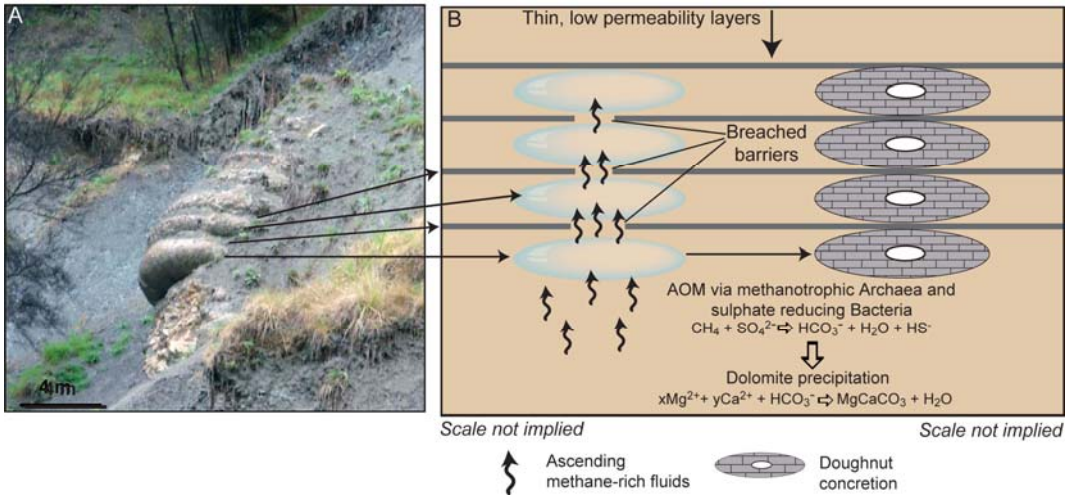

Figure 22. Hypothesised model for doughnut concretion formation. (A) Photograph of a tubular concretion, at the nearby early Miocene seafloor seep deposit at Karikarihuata (see Fig. 2, KKH) (cf., Campbell et al., 2008). These stacked(?) doughnuts may be analogous to the Hororera doughnut concretions in 3D. (B) Hypothesised growth model for doughnut concretions; see Section 5.4.1 for explanation. Doughnut formation occurs along a fault, above the breached impermeable barrier (see red box in Fig. 21, stage 3).

Doughnuts with closed conduits are strongly bioturbated and filled with sediments different to that of the host concretion (Fig. 11D,E). This suggests the conduits became filled from the collapse of overlying sediments after fluid expulsion or filled later by normal sedimentation over longer time intervals. Isotope values of the conduit fills are consistent with those for the outer concretions, indicating the conduits were filled during methane rich fluid ascent and AOM, and not later

(e.g., modern infilling after surface exposure). Additionally, undeformed bioturbation structures in the conduit fill sediments preserved by cementation suggest precipitation was occurring near the seafloor, further supported by the high minus cement porosities (60–80 %).

Considering the potential stacked doughnut morphology in 3D, the different sediments that fill the doughnut conduits (with respect to the outer concretion), and the fault-valve action described in Section 5.3.3, doughnut formation may have proceeded during stage 3 of fluid ascent, at times continuing through stages 4 back into 1 (Fig. 21). During fluid ascent through alternating thin layers of higher (relatively coarser grained) and lower (relatively finer grained) permeability sediments, fluids may become congested and build up in the coarser grained intervals before the lower permeability sediments are punctured (Fig. 22B). A 'bubble-like' pocket of fluid is created in the coarser grained sediment and remains trapped there as fluids continue to ascend through the main conduit. As fluid pressure drops, carbonate precipitation begins in the 'fluid bubble'. As fluid pressure lowers and the fault seals, overlying sediments may then infill the conduits. Continued AOM results in carbonate cementation of the conduit.

5.5 Gas hydrates

Isotope evidence suggests that dissociation of gas hydrates may have been responsible for the oxygen enrichment recorded in the doughnut concretions (Fig. 12, 19). Faults may have provided a migration pathway for deeper fluids. As the fluids migrated upwards, they entered the gas hydrate stability zone and formed methane hydrate. During subsequent fault rupture, methane hydrate dissociated and methane-rich fluids migrated upwards, eventually encountering a small stratigraphic trap and then forming a doughnut concretion.

Based on isotope interpretations (Section 5.1), the fault-valve hypothesis (Section 5.3.3), and doughnut formation (Section 5.4), any methane hydrate formed would have probably occurred above the faults trapping methane rich fluids. In some earlier episode of fault rupture and fluid ascent, methane that did not escape to the seafloor (or oxidise to form carbonates) may have become trapped in hydrate

form. As the fault sealed, fluids became trapped below until enough fluid pressure built up to cause the next fault rupture (Section 5.3.3, Fig. 21).

At the next rupture, the hotter fluids ascended, methane was oxidised, and carbonate precipitated. The resulting carbonate precipitation formed pipe concretions (including the elongated concretion in Fig. 18) with morphologies indicative of more focused flow at higher flux rates and $\delta^{18}O$ values suggestive of warmer fluids. Concurrently, methane hydrate began to dissociate, but the release of methane would have been at much slower rates than the fluids trapped beneath the fault. Over time, methane from the hydrates was gradually added to the sediment pore fluids and ascended towards the seafloor. As pressures dropped, fluids would not have enough buoyancy to continue upward migration and may have become trapped in the bubble-like pockets, subsequently forming doughnut concretions as described in Section 5.4.1. The doughnuts formed would have $\delta^{18}O$ values approximately 3‰ more enriched than those that formed the pipe concretions, which is consistent with the data set (Fig. 12).

Other triggers of hydrate dissociation also are possible such as: a temperature increase or pressure decrease, potentially caused by increased fluid pressure with resultant slope failure; warmer fluids circulating through the system; or shallowing of the water column. These triggers cannot be discounted, particularly with the turbidite deposits in the Pohutu Formation, and therefore may have played a role in hydrate dissociation.

5.6 Seafloor expulsion

Paleoseep carbonates and chemosymbiotic fossils are lacking in the Pohutu Formation which suggests that fluid expulsion at the seafloor did not occur. However, just inland to the southwest (~50 km) are 11 known locations of ancient seep carbonate outcrops of early Miocene age (Fig. 2A) (Campbell et al., 2008), which could be genetically related to forerunner fluid migration events. Hence, seep development at the seafloor may have occurred before fluids migrated through the Pohutu Formation. As the region was uplifted, fluids may have found alternative migration routes and expelled in sediments further eastward. Today, research cruises along the modern Hikurangi Margin (Lewis and Marshall, 1996;

Pecher et al., 2007; Campbell et al., in review; Greinert et al., in review) have documented active cold seeps on the seafloor with features similar to those of the onshore paleoseep carbonates and tubular concretions (Fig. 2A). In addition, modern onshore oil and gas seepage and mud volcanoes occur within the region (Fig. 2A) (Francis, 1997). This suggests that fluid seepage along the Hikurangi Margin began in the early Miocene with the onset of subduction of the Pacific Plate under the Australian Plate and has continued, even if intermittently, to the present day.

6. Conclusions

1. The East Cape tubular concretions in late Miocene slope mudstones (Pohutu Formation) of the East Coast Basin accretionary prism developed within shallow burial (<300 m) conditions from the precipitation of micritic dolomite cement within the interparticle spaces of siliciclastic mud.

2. The tubular concretions are predominantly doughnut morphologies, average 4 m in diameter, and support a central conduit. Most conduits are filled by sediment of different composition from the outer concretion, but are cemented by similar phases of micritic dolomite.

3. Carbon isotope values ($\delta^{13}C$ −17 to +9‰) and lipid biomarkers suggest that the carbon for carbonate precipitation in the tubular concretions was derived from extensive anaerobic oxidation of methane, potentially with an addition of methanogenic CO_2, as supported by lipid biomarkers. The strongly enriched carbon isotope values indicate >80% of the methane had been oxidised by the time the East Cape doughnut concretions formed.

4. $\delta^{18}O$ values of the dolomite in the East Cape dolomite concretions (+2 to +6‰) suggest the $\delta^{18}O$ composition of the pore waters at the time of carbonate precipitation was warmer marine fluids ascending from burial or gas hydrate formation, and that these were subsequently influenced also by the dissociation of gas hydrates.

5. The East Cape tubular concretions mark the shallow subsurface plumbing system of a late Miocene cold seep. The concretions formed along focused fluid migration pathways as methane ascended towards the paleo-seafloor.

6. Faulting controlled the release and subsequent ascent of fluids which continued throughout concretion formation. The faults acted as a valve-like mechanism, rupturing as enough fluid pressure built up, exceeding fault strength. Fault rupture created permeability allowing for fluid ascent. After mineral precipitation and fluid pressure decrease, faults sealed, further trapping fluids and repeating the cycle. Tubular concretions began forming after fault rupture, and may have continued over long periods of time and multiple ruptures.

7. Early Miocene seep carbonates in the Raukumara Peninsula, near the East Cape tubular concretion occurrence, confirm the continuation of long-lived, if episodic, methane seepage in the region throughout the Neogene.

8. The results of this study indicate that tubular concretions can help to differentiate and delineate the development and evolution of methane rich fluids ascending towards the seafloor. The East Cape plumbing concretions may provide a conceptual model linking to the active seepage along the modern Hikurangi Margin, as well as in other modern and ancient seep systems.

7. References

Aiello, I.W., Stakes, D.S., Kastner, M., Garrison, R.E., 1999. Carbonate vent structures in the Upper Miocene Santa Cruz Mudstone at Santa Cruz, California. In: Garrison, R.E., Aiello, I.W., Moore, J.C. (Eds.), Late Cenozoic Fluid Seeps and Tectonics Along the San Gregorio Fault Zone in the Monterey Bay Region, California. Pacific Section AAPG, v. GB-76, pp. 35-52.

Aiello, I.W., Garrison, R.E., Moore, J.C., Kastner, M., Stakes, D.S., 2001. Anatomy and origin of carbonate structures in a Miocene cold-seep field. Geology, 29, 1111-1114.

Aloisi, G., Pierre, C., Rouchy, J.M., Foucher, J.P., Woodside, J., MEDINAUT Scientific Party, 2000. Methane-related authigenic carbonates of eastern Mediterranean Sea mud volcanoes and their possible relation to gas hydrate destabilisation. Earth and Planetary Science Letters, 184, 321-338.

Ballance, P.F., Gregory, M.R., Gibson, G.W., Chaproniere, G.C.H., Kadar, A., Sameshima, T., 1984. A late Miocene to early Pliocene upper slope to shelf sequence in calcareous fine sediment from the Pacific margin of New Zealand. In: stow, D.A.V., Piper, D.J.P., (Eds.), Fine sediments: Deep Water Processes and Facies. Geological Society, London. Pp. 331-342.

Ballance, P.F., 1993. The New Zealand Neogene forearc basins. In: Ballance, P.F. (Ed.), South Pacific Sedimentary Basins: Sedimentary Basins of the World, 2. Amsterdam, Elsevier Publishers B.V. Pp. 93-110.

Bjørlykke, K., 1998. Clay mineral diagenesis in sedimentary basins – a key to the prediction of rock properties. Examples from the North Sea Basin. Clay Minerals, 33, 15-34.

Boggs, S., 1992. McConnin, R.A., (Ed.), Petrology of Sedimentary Rocks; Macmillian Publishing Company, New York. 707pp.

Campbell, K.A., Farmer, J.D., Des Marais, D., 2002. Ancient hydrocarbon seeps from the Mesozoic convergent margin of California: carbonate geochemistry, fluids and palaeoenvironments. Geofluids, 2, 63-94.

Campbell, K.A., 2006. Hydrocarbon seep and hydrothermal vent paleoenvironments and paleontology: Past developments and future research directions. Palaeogeography, Palaeoclimatology, Palaeoecology, 232, 362-407.

Campbell, K.A., Francis, D.A., Collins, M., Gregory, M.R., Nelson, C.S., Greinert, J., Aharon, P., 2008. Hydrocarbon seep-carbonates of a Miocene forearc (East Coast Basin), North Island, New Zealand. Sedimentary Geology, 204, 83-105.

Campbell, K.A., Nelson, C.S., Alfaro, A.C., Boyd, S., Greinert, J., Nyman, S., Grosjean, E., Logan, G.A., Gregory, M.R., Cooke, S., Linke, P., Milloy, S., Wallis, I., in review. Geological imprint of methane seepage on the seabed and biota of the convergent Hikurangi Margin, New Zealand: initial results from core and grab carbonates. Submitted to Marine Geology.

Chapman-Smith, M., Grant-Mackie, J.A., 1971. Geology of the Whangaparaoa area, eastern Bay of Plenty. New Zealand Journal of Geology and Geophysics, 14, 3-38.

Chaproniere, G.C.H., 1969. Geology of the Te Araroa area East Cape. Unpublished MSc. Thesis, University of Auckland.

Clari, P., Cavagna, S., Martire, L., Hunziker, J., 2004. A Miocene mud volcano and its plumbing system: A chaotic complex revisited (Monferrato, MW Italy). Journal of Sedimentary Research, 74, 662-676.

Cole, J.W., Lewis, K.B., 1981. Evolution of the Taupo-Hikurangi subduction system. Tectonophysics, 72, 1-21.

Coleman, D.D., Risatti, J.B., Schoell, M., 1981. Fractionation of carbon and hydrogen isotopes by methane-oxidising bacteria. Geochimica et Cosmochimica Acta, 45, 1033-1037.

Conti, S., Fontana, D., Gubertini, A., Sighinolfi, G., Tateo, F., Fioroni, C., Fregni, P., 2004. A multidisciplinary study of middle Miocene seep-carbonates from the northern Apennine foredeep (Italy). Sedimentary Geology, 169, 1-19.

Conti, S., Fontana, D., 2005. Anatomy of seep-carbonates: Ancient examples from the Miocene of the northern Apennines (Italy). Palaeogeography, Palaeoclimatology, Palaeoecology, 227, 156-175.

Cowen, J.P., Wen, X., Popp, B.N., 2002. Methane in aging hydrothermal plumes. Geochimica et Cosmochimica Acta, 66, 3563-3571.

Curtis, C.D., 1978. Possible links between sandstone diagenesis and depth related geochemical reactions occurring in enclosing mudstones: Geological Society of London Journal, 135, 107-177.

Davidson, D.W., Leaist, D.J., Hesse, R., 1983. Oxygen-18 enrichment in water of a clathrate hydrate. Geochimica et Cosmochimica Acta, 47, 2293-2295.

De Boever, E., Swennen, R., Dimitrov, L., 2006. Lower Eocene carbonate cemented chimneys (Varna, NE Bulgaria): Formation mechanisms and the (a)biological mediation of chimney growth? Sedimentary Geology, 185, 159-173.

DeMets, C., Gordon, R.G., Argus, D.F., Stein, S., 1994. Effect of recent revisions to the geomagnetic reversal time scale on estimates of current plate motions. Geophysical Research Letters, 21, 2191-2194.

Díaz-del-Río, V., Somoza, L., Martínez-Frias, J., Mata, M.P., Delgado, A., Hernandez-Molina, F.J., Lunar, R., Martín-Rubí, J.A., Maestro, A., Fernández-Puga, M.C., León, R., Llave, E., Medialdea, T., Vázquez, J.T., 2003. Vast fields of hydrocarbon-derived carbonate chimneys related to the accretionary wedge/olistostrome of the Gulf of Cádiz. Marine Geology, 195, 177-200.

Feary, D.A., Davies, P.J., Pigram, C.J., Symonds, P.A., 1991. Climatic evolution and control on carbonate deposition in northeast Australia. Palaeogeography, Palaeoclimatology, Palaeoecology, 89, 341-361.

Fergusson, L., 1985. The mineralogy, geochemistry and origin of lower Tertiary smectite-mudstones, East Coast Deformed Belt, New Zealand. Unpublished MSc thesis, University of Canterbury, Christchurch, New Zealand.

Field, B.D., Uruski, C.I., and others, 1997. Cretaceous-Cenozoic geology and petroleum systems of the East Coast Region, New Zealand. Institute of Geological and Nuclear Sciences Monograph, 19, 301 p.

Francis, D.F., 1997. Oil and Gas Generation in the East Coast Basin – an update. Petroleum Exploration in New Zealand News, volume 51, October 1997.

Francis, D.F., Bennett, D., Courteney, S., 2004. Advances in understanding of onshore East Coast Basin structure, stratigraphic thickness and hydrocarbon generation. 2004 New Zealand Petroleum Conference Proceedings, Auckland, 7-10 March 2004. 20pp. http://www.crownminerals.govt.nz/cms/pdf-library/petroleum-conferences-1/2004/papers/Petroleum-23-04NZPC-Paper-ECBStructure.pdf.

Fritz, P., Smith, D.G.W., 1970. The isotopic composition of secondary dolomite. Geochimica et Cosmochimica Acta, 34, 1161-1173.

Gieskes, J., Mahn, C., Day, S., Martin, J.B., Greinert, J., Rathburn, T., McAdoo, B., 2005. A study of the chemistry of pore fluids and authigenic carbonates in methane seep environments: Kodiak Trench, Hydrate Ridge, Monterey Bay, and Eel River Basin. Chemical Geology, 220, 329-345.

Goldsmith, J.R., Graf, D.L., Heard, H.C., 1961. Lattice constants of the calcium-magnesium carbonate. The American Mineralogist, 46,453-457.

Grauls, D., 2001. Gas hydrates: importance and applications in petroleum exploration. Marine and Petroleum Geology, 18, 519-523.

Greinert, J., Bohrmann, G., Suess, E., 2001. Gas hydrate-associated carbonates and methane-venting at Hydrate Ridge: Classification, distribution, and origin of authigenic lithologies. In: Parnell, C.K., Dillon, K.P. (Eds.), Natural Gas Hydrates: Occurrence, Distribution and Detection. Geophysical Monograph, 124, 99-113.

Greinert, J., Bialas, J., Lewis, K., Suess, E., in review. Methane seeps and gas hydrates offshore New Zealand's North Island: Compiling results from three cruises in 2006 and 2007. Submitted to Marine Geology.

Hovland, M., Svensen, H., Forsberg, C.F., Johansen, H., Fichler, C., Fosså, J.H., Jonsson, R., Rueslåtten, H., 2005. Complex pockmarks with carbonate-ridges off mid-Norway: Products of sediment degassing. Marine Geology, 218, 191-206.

Irwin, H., Curtis, C., Coleman, M., 1977. Isotopic evidence for source of diagenetic carbonates formed during burial of organic-rich sediments. Nature, 269, 209-213.

Jensen, P., Aagaard, I., Burke Jr. R.A., Dando, P.R., Jørgensen, N.O., Kuijpers, A., Laier, T., O'Hara, M.O., Schmaljohann, R., 1992. 'Bubbling reefs' in the Kattegat: submarine landscapes of carbonate-cemented rocks support a diverse ecosystem at methane seeps. Marine Ecology Progress Series, 83, 103-112.

Judd, A.G., Hovland, M., 2007. Seabed fluid flow: The impact on geology, biology and the marine environment. Cambridge University Press, Cambridge, 475 pp.

Kamp, P.J.J., Furlong, K.P., 2006. Neogene plate tectonic reconstructions and geodynamics of North Island sedimentary basins: Implications for the petroleum systems. 2006 New Zealand Petroleum Conference Proceedings, Auckland, 6-8 March 2006, 16 pp..

Kenny, J.A., 1984. Stratigraphy, Sedimentology and structure of the Ihungia decollement, Raukumara Peninsula, North Island, New Zealand. New Zealand Journal of Geology and Geophysics, 27, 1-19.

Kulm, L.D., Suess, E., 1990. Relationship between carbonate deposits and fluid venting: Oregon accretionary prism. Journal of Geophysical Research, 95, 8899-8915.

Lédesert, B., Buret, C., Chanier, F., Fèrriere, J., Recourt, P., 2003. Tubular structures of northern Wairarapa (New Zealand) as possible examples of ancient fluid expulsion in an accretionary prism: evidence from field and petrographical observations. Geological Society of London, Special Publication, 216, 95-107.

Lewis, K.B., Pettinga, J.R., 1993. The emerging, imbricate frontal wedge of the Hikurangi margin. In Balance, P.F. (Ed), South Pacific Basins: Sedimentary Basins of the World, 2. Amsterdam, Elsevier Science Publishers. Pp. 225-250.

Lewis, K.B., Marshall, B.A., 1996. Seep faunas and other indicators of methane-rich dewatering on New Zealand convergent margins. New Zealand Journal of Geology and Geophysics, 39,181-200.

Longstaffe, F.J., 1987. Stable isotope studies of diagenetic processes. In: Kyser, T. (Ed.) Short Course in Stable Isotope Geochemistry of Low Temperature Processions of Mineralogical Society of Canada, Saskatoon, SK. Pp. 187-257.

Martin, J.S., 1986. Paleoecology of East Cape upper Miocene strata. Unpublished MSc. Thesis, University of Auckland.

Mazengarb, C., Francis, D.A., Moore, P.R., 1991. Geologicalmap of New Zealand, 1:50,000, Sheet Y16, Geology of the Tauwhareparae area. New Zealand Geological Survey, Wellington, New Zealand.

Mazzini, A., Duranti, D., Jonk, R., Parnell, J., Cronin, B.T., Hurst, A., Quine, M., 2003. Palaeo-carbonate seep structures above an oil reservoir, Gryphon Field, Tertiary, North Sea. Geo-Marine Letters, 23, 323-339.

McCrea, J.M., 1950. On the isotopic chemistry of carbonates and a paleotemperature scale. The Journal of Chemical Physics, 18, 849-857.

Milkov, A.V., Sassen, R., 2002. Economic geology of offshore gas hydrate accumulations and provinces. Marine and Petroleum Geology, 19, 1-11.

Milkov, A.V., Vogt, P.R., Crane, K., Lein, A.Y., Sassen, R., Cherkashev, G.A., 2004. Geological, geochemical, and microbial processes at the hydrate-bearing Hakon Mosby mud volcano: a review. Chemical Geology, 205, 347-366.

Moore, J.C., Vrolijk, P., 1992. Fluid in accretionary prisms. Reviews in Geophysics, 30, 113-135.

Mortimer, N., Herzer, R.H., Gans, P.B., Laporte-Magoni, C., Calvert, A.T., Bosch, D., 2007. Oligocene-Miocene tectonic evolution of the South Fiji basin and Northland Plateau, SW Pacific Ocean: evidence from petrology and dating of dredged rocks. Marine Geology, 237, 1-24.

Munnecke, A., Samtleben, C., 1996. The formation of micritic limestones and the development of limestone-marl alternations in the Silurian of Gotland, Sweden. Facies, 34, 159-176.

Nelson, C.S., Smith, A.M., 1996. Stable oxygen and carbon isotope compositional fields for skeletal and diagenetic components in New Zealand Cenozoic nontropical carbonate sediments and limestones: a synthesis and review. New Zealand Journal of Geology and Geophysics, 39, 93-107.

Nicol, A., Van Dissen, R., Vella, P., Alloway, B., Melhuish, A., 2002. Growth of contractional structures during the last 10 Ma, Hikurangi forearc, New Zealand. New Zealand Journal of Geology and Geophysics, 45, 365-385.

Nicol, A., Mazengarb, C., Chanier, F., Rait, G., Uruski, C., and Wallace, L., 2007, Tectonic evolution of the active Hikurangi subduction margin, New Zealand, since the Oligocene: Tectonics, 26, TC4002, doi:10.1029/ 2006TC002090.

Nyman, S.L., Nelson, C.S., Campbell, K.A., Schellenberg, F., Pearson, M.J., Kamp, P.J.J., Browne, G.H., King, P.R., 2006. Tubular carbonate concretions as hydrocarbon migration pathways? Examples from North

Island New Zealand. 2006 New Zealand Petroleum Conference Proceedings, Auckland, 6-8 March 2006, 10pp. http://www.crownminerals.govt.nz/petroleum/conference/papers/Poster_papers_21.pdf.

Pancost, R.D., Damasté, J.S., de Lint, S., van der Maarel, M.J.E.C., Gottschal, J.C., Medinaut Shipboard Scientific Party, 2000. Biomarker evidence for widespread anaerobic methane oxidation in Mediterranean sediments by a consortium of methanogenic archaea and bacteria. Applied Environmental Microbiology, 66, 1126-1132.

Pearce, A.R., Black, R.D., Nelson, C.S., 1981. Lithologic and weathering influences on slope form and process, eastern Raukumara Range, New Zealand. International Assocociation of Hydrology Science, 132, 95-122.

Pearson, M.J., Grosjean, E., Nyman, S.L., Logan, G.A., Nelson, C.S., Hood, S.D., Campbell, K.A., 2008. Tubular concretions in New Zealand petroliferous basins: Lipid evidence for mineralization around proposed Miocene hydrocarbon seep conduits. 2008 New Zealand Petroleum Conference Proceedings, Auckland, 10-12 March 2008. 6 pp.

Pecher, I., Coffin, R., Henrys, S., et al., 2007. Tangaroa TAN0607 cruise report: gas hydrate exploration on the East Coast, North Island, New Zealand. Institute of Geological and Nuclear Sciences Ltd, Lower Hutt, New Zealand. GNS Science Report 2007/2. 112 pp.

Peckmann, J., Goedert, J.L., Thiel, V., Michaelis, W., Reitners, J., 2002. A comprehensive approach to the study of methane-seep deposits from the Lincoln Creek Formation, western Washington State, USA. Sedimentology, 49, 855-873.

Pierre, C., Rouchy, J.-M., Blanc-Valleron, M.-M., 2002. Gas hydrate dissociation in the Lorca Basin (SE Spain) during the Mediterranean Messinian salinity crisis. Sedimentary Geology, 147, 247-252.

Pierre, C., Rouchy, J.-M., 2004. Isotopic compositions of diagenetic dolomites in the Tortonian marls of the western Mediterranean margins: evidence of past gas hydrate formation and dissociation. Chemical Geology, 205, 469-484.

Pierre, C., Foquat, Y., 2007. Authigenic carbonates from methane seeps of the Congo deep-sea fan. Geo-Marine Letters, 27, 249-257.

Rait, G., Chanier, F., Waters, D.W., 1991. Landward- and seaward-directed thrusting accompanying the onset of subduction beneath New Zealand. Geology, 19, 230-233.

Ridgway, N.M., 1969. Temperature and salinity of sea water at the ocean floor in the New Zealand region. New Zealand Journal of Marine and Freshwater Research, 3, 57-72.

Roberts, H.H., Aharon, P., 1994. Hydrocarbon-derived carbonate buildups of the northern Gulf of Mexico continental slope: A review of submersible investigations. Geo-Marine Letters, 14, 135-148.

Rogers, K.M., Collen, J.D., Johnston, J.H., Elgar, N.E., 1999. A geochemical appraisal of oil seeps from East Coast Basin, New Zealand. Organic Geochemistry, 30, 593-605.

Schwartz, H., Sample, J., Weberling, K.D., Minisini, D., Moore, J.C., 2003. An ancient linked fluid migration system: cold-seep deposits and sandstone intrusions in the Panoche Hills, California, USA. Geo-Marine Letters, 23, 340-350.

Sibson, R.H., 1992. Implications of fault-valve behaviour for rupture nucleation and recurrence. Tectonophysics, 211, 283-293.

Sibson, R.H., Rowland, J.V., 2003. Stress, fluid pressure, and structural permeability in seismogenic crust, North Island, New Zealand. Geophysical Journal International, 154, 584-594.

Stagpoole, V., Nicol, A., 2008. Regional structure and kinematic history of a large subduction back thrust: Taranaki Fault, New Zealand. Journal of Geophysical Research, 113, B01403, doi:10.1029/2007JB005170.

Tonkin, N., 2003. Application of ichnofabric analysis and event stratigraphy to paleoenvironmental reconstruction in Late Miocene strata, East Cape – Te Araroa, New Zealand. Unpublished MSc thesis, University of Auckland.

Townend, J., 1997. Subducting a sponge: minimum estimates of the fluid budget of the Hikurangi Margin accretionary prism. Geological Society of New Zealand Newsletter, 112, 14-16.

Ussler III, W., Paull, C.K., 1995. Effects of ion exclusion and isotopic fractionation on pore water geochemistry during gas hydrate formation and decomposition. Geo-Marine Letters, 15, 37-44.

van der Lingen, G.J., Pettinga, J.R., 1980. The Makara Basin: a Miocene slope-basin along the New Zealand sector of the Australian-Pacific obliquely convergent plate boundary. In: Balance, P.F., Reading, H.G. (Eds.) Sedimentation in Oblique Strike-slip Mobile Zones. Special Publication of the International Association of Sedimentologists, 191-215.

Whiticar, M.J., 1999. Carbon and hydrogen isotope systematics of bacterial formation and oxidation of methane. Chemical Geology, 161, 291-314.

CHAPTER 6

Tubular concretions beneath an ancient seep carbonate, Rocky Knob, New Zealand: A genetic link between cold seeps and their plumbing systems

Abstract

The Rocky Knob seep complex occurs in Miocene age deep water mudstones of the East Coast Basin, and is composed of seep carbonates and tubular concretions. The carbonates developed along the convergent Hikurangi Margin continental slope from localised sites of methane expulsion into the water column during the middle Miocene.

The seep carbonates are a few to two hundred metres across and up to 60 m thick, occurring as scattered pods and lenses. They contain chemosynthesis-based fossil taxa, micritic (calcite) fabrics, thrombolites, and fibrous aragonite. The seep carbonates vary in texture and composition from massive micrite deposits with or without rare mussel shells; brecciated micrite with aragonite veins; coarse grained allochthonous breccia with lucinid bivalves and brachiopods; and fossiliferous carbonate with mussels, worm tubes, gastropods, and brachiopods.

The tubular concretions are present in the host mudstone directly below the seep carbonate and comprise micrite (calcite) cement between the interparticle spaces of siliciclastic mud. They are generally tubular in shape and have central conduits that may be either empty or (partly) filled by sediment and/or multiple generations of cement. Conduit cements include fibrous aragonite, micrite, bladed and blocky calcite, and a dark grey micrite containing peloids. The tubular concretions are morphologically variable and range in size from 5 to 12 cm in diameter and approximately 50 cm in exposed length.

Carbon isotopes in the seep carbonates and tubular concretions are moderately to strongly depleted ($\delta^{13}C$ = –52 to –5‰ PDB), indicating methane oxidation was a primary process during carbonate precipitation. Oxygen isotopes in the seep carbonates and tubular concretions range from $\delta^{18}O$ = –6 to +4‰ PDB, supporting pore fluid evolution associated with gas hydrate formation and dissociation events and/or temperature increases with burial.

Cement components and stable carbon and oxygen isotope values indicate carbonate precipitation took place under varying fluid compositions. However, isotope values of the different cement components are the same between the tubular concretions and seep carbonates, indicating that each component precipitated from the same fluids, albeit in different parts of the seep complex.

1. Introduction

In the East Coast Basin, North Island, New Zealand, 16 known ancient seep carbonates (Appendix 4) occur in isolated pods or lenses within thick sequences of early to late Miocene deep water mudstones (Fig. 1A). The peculiarity of these locally constrained carbonate deposits has been long documented (McKay, 1877; Adams, 1910; Henderson and Ongley, 1920; Kamp and Nelson, 1988; Beu and Maxwell, 1990). Currently, an international team of researchers from New Zealand and Germany are collaborating in a joint effort to systematically investigate the 16 onshore ancient seafloor seep occurrences, 21 onland subsurface plumbing occurrences, and more than 4 offshore modern seep sites (32 more found during the recent New Vents research cruise, Greinert et al., in review) (Fig. 1A).

The best known example of an ancient seep carbonate deposit in New Zealand is the middle Miocene (upper Lillburnian; see timescale in Appendix 8) Rocky Knob complex, located ~40 km north of Gisborne in Moonlight Forest (Fig. 1B). Rocky Knob is the largest occurrence of an ancient seep complex (Fig. 2) (outcrop is 60 m thick and at least 200 m across) in New Zealand with several facets of cold seep

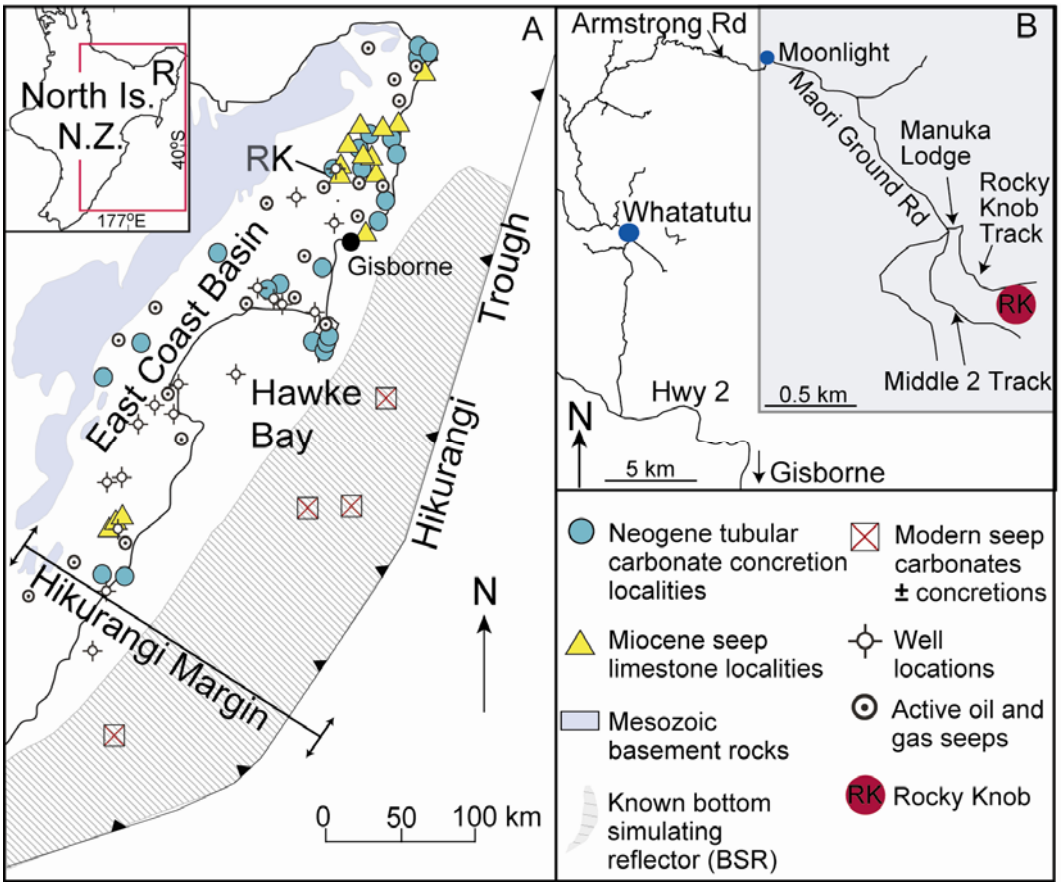

Figure 1. Locality maps. (A) Map of East Coast Basin in North Island, New Zealand, showing tubular concretion localities, ancient and some modern seep sites, some onshore modern oil/gas seeps and well locations, and the general distribution of offshore bottom simulating reflectors (BSRs) indicating subsurface gas hydrates. RK is location of Rocky Knob, R (in inset) = Raukumara Peninsula. (B) Enlarged location map for Rocky Knob. The Rocky Knob location can be found on NZ Map Series 260, 1:50000 scale, sheet Y17, GIS 2941510, 6310525, which correspond to the New Zealand Map Grid coordinate system. Locality information comes from personal observations, Francis (1997), Lewis and Marshall (1996), and personal communication with Dave Francis (Geological Research Ltd, Lower Hutt).

Figure 2. Photograph of the main exposure of Rocky Knob taken in 1997 (courtesy of Kathy Campbell). Seep carbonates crop out above the grass covered surrounding mudstone. Person for scale within the red circle. Today (2008) the outcrop is within a dense pine forest.

systems exposed, including seep carbonates, chemosynthetic fossils, and tubular and nodular carbonate concretions. This paper focuses on the tubular concretions present in the mudstone directly beneath the Rocky Knob seep carbonate.

2. Geologic setting

Rocky Knob is located on Raukumara Peninsula in the East Coast Basin, North Island, New Zealand (Fig. 1A), c. 100 km inboard of the modern Australian/Pacific Plate subduction boundary marked by the Hikurangi Trough (Figs. 1A, 2A) (Field et al., 1997). Subduction of the Pacific Plate southwest under the Australian Plate began in the early Miocene (~23 Ma), with the leading edge of the Pacific Plate reaching the position of East Cape ~20 Ma and Napier approximately 11 Ma (Fig. 3B) (Kamp and Furlong, 2006). Presently, the Pacific Plate is subducting at about 40 mm per year (DeMets et al., 1994). A schematic section illustrating the main morphotectonic elements is shown in Figure 3A. Rocky Knob is located within the forearc basin sector.

Onshore within the forearc basin, deformed Cretaceous to Paleogene sedimentary rocks deposited in a passive margin prior to subduction, are overlain by relatively less deformed Neogene marine sediments deposited after onset of subduction (Fig. 4), all of which have been thrust faulted and back tilted during subduction (Fig. 3A) (Lewis and Pettinga, 1993). Within the accretionary prism, known source rocks within the East Coast Basin are late Cretaceous and Paleocene sediments, in particular the Paleocene Whangai Formation and Waipawa Formation (Fig. 4), which presently source onshore modern oil and gas seeps (Rogers et al., 1999; Francis et al., 2004).

2.1 Historical references

The study site seep carbonates were informally named the “Moonlight limestone” after a nearby sheep station by Kamp and Nelson (1988); however, currently the location is referred to as Rocky Knob after a forestry track which accesses the site

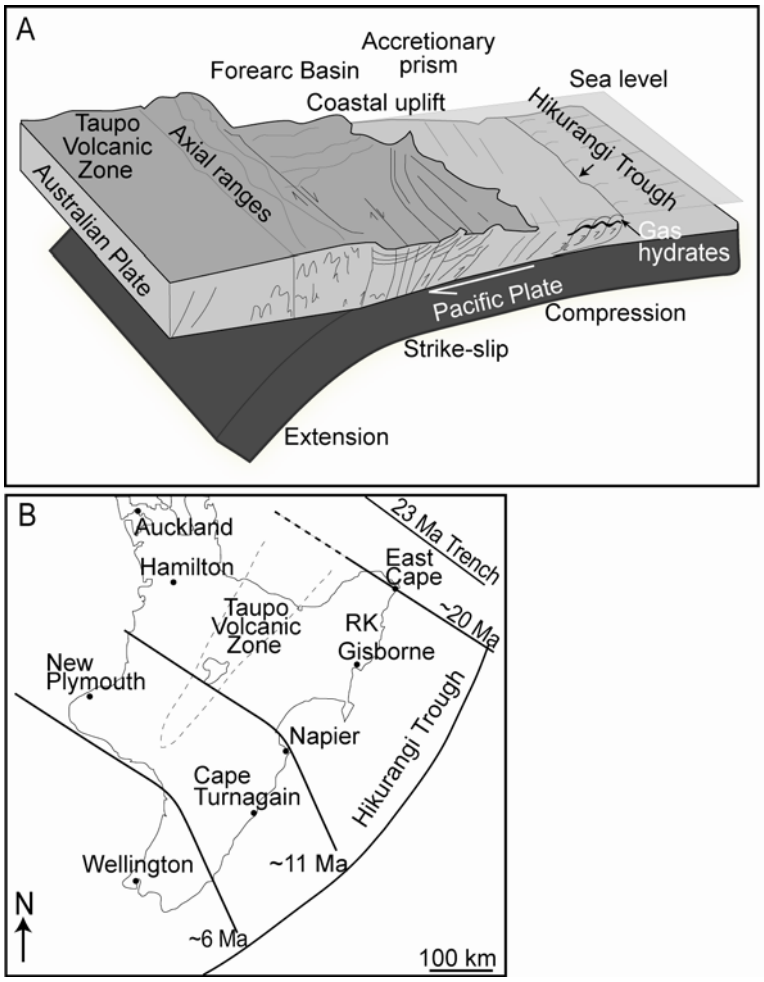

Figure 3. Subduction margin along the New Zealand Pacific/Australian Plate boundary. (A) Location of leading edge of the subducting Pacific Plate at times during the Miocene in reference to present day geography (modified from Kamp and Furlong, 2006). (B) Schematic cross section of the present day East Coast Basin subduction margin showing some morpho-tectonic elements and other features. The Miocene seep carbonates occur within the forearc basin stratigraphy. The location of Rocky Knob is denoted by RK. Modified from Lewis and Marshall, (1996); Lee and Begg, (2002).

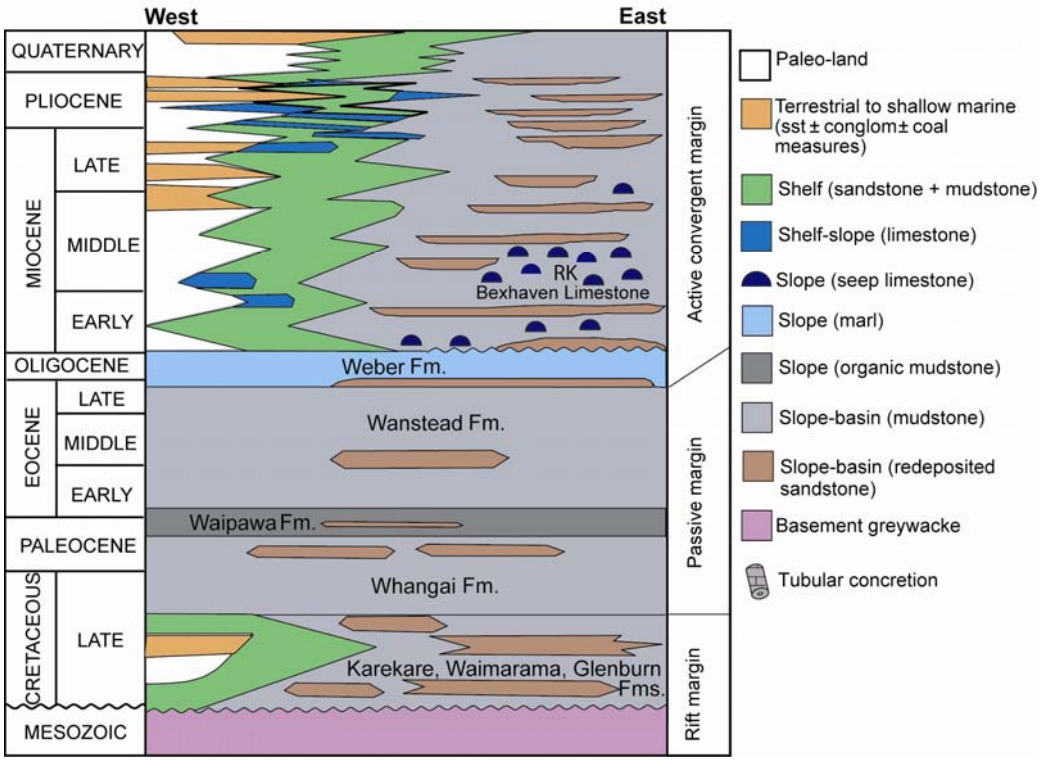

Figure 4. Generalised stratigraphy and depositional paleoenvironments for the East Coast Basin (modified from Francis et al., 2004). RK marks approximate stratigraphic position of the Rocky Knob seep complex described in this study.

(Fig. 1B). The Rocky Knob carbonates are easily distinguishable from the shallow marine, barnacle rich Pliocene Te Aute limestones that are widely distributed in the East Coast Basin (Beu, 1995; Nelson et al., 2003) due to their yellow colour, distinctive fossils (mytilids, lucinid bivalves, trochid gastropods, and lepetellid limpets), and pod like outcrops (Campbell et al., 2008). Rocky Knob and other middle Miocene age limestones previously described as 'unusual' carbonate deposits were collectively termed Bexhaven Limestone in the 1:50,000 geologic map of the area by Mazengarb et al. (1991).

Collins (1999) described the chemosymbiotic bathymodioline mussels at Rock Knob and Campbell et al. (2008) presented some reconnaissance information about the stratigraphy, lithology, paleontology, and petrology of several of the East Coast Basin seep carbonates, including especially Rocky Knob. Currently, more detailed analysis of the carbonates and paleontology at Rocky Knob is being undertaken by the Cold Seeps Research Group at the University of Auckland and University of Waikato.

3. Methods

Tubular concretions are exposed in trackside cliff outcrops stratigraphically immediately below the Rocky Knob seep carbonate. The best section is located in Moonlight Forest, grid reference Y17, GPS 2941510, 6310525 (NZ Map Series 260, 1:50000 scale), and is accessible only with prior permission from PF Olsen Forestry in Gisborne. Field work focused on descriptions of the distribution, morphology, size, and stratigraphic position of the concretions. Full records of this field information are contained in Appendix 4.

Where possible, *in situ* oriented samples were collected using a chisel and heavy duty rock hammer. Subsamples were micro-drilled for isotope analysis. Laboratory analytical work included routine thin section petrography and cathodoluminescence (CL) of resin impregnated samples. Scanning electron microscopy (SEM) aided in viewing the microstructure of the micritic carbonate following the procedure of Munnecke and Samtleben (1996). X-ray diffraction

(XRD) determined the mineralogy of samples and the $MgCO_3$ content of calcite (e.g., Goldsmith et al., 1961). Stable isotope mass spectrometry was used to derive the $\delta^{18}O$ and $\delta^{13}C$ composition of the carbonate phases (e.g., McCrea, 1950; Nelson and Smith, 1996). Isotope results are reported as per mille $\delta^{18}O$ and $\delta^{13}C$ relative to VPDB, and have an analytical precision of better than ±0.10‰. Lipid analyses are available for a few samples and have been previously reported by Pearson et al. (2008).

Details of methodology, laboratory procedures, and instruments is available in Appendix 7.

4. Characteristics of Rocky Knob carbonates

The Rocky Knob carbonates occur in middle Miocene slope mudstones (1500 to 3000 m paleo-water depths) and crop out as small pods of yellow, crystalline carbonates containing distinctive assemblages of chemosynthetic fossils (mytilids, lucinid bivalves, worm tubes, thrombolites, and lepetellid limpets; Collins, 1999; Campbell et al., 2008) (Fig. 5). Tubular carbonate structures are commonly present in the massive thick mudstone sequences that encase the carbonates (Fig. 6). The Rocky Knob carbonate outcrop includes seven facies characteristic of seep carbonates (Fig. 7) (Campbell et al., 2008).

Facies 1: Massive calcareous grey mudstone with microfossils.

Facies 2: Massive mudstone with tubular carbonate concretions and micritic carbonate nodules.

Facies 3: Massive micritic carbonate deposits with rare disarticulated mussel shells.

Facies 4: Brecciated micritic carbonate with aragonite veins 1−2 mm thick. Brecciated clasts of micrite are angular.

Facies 5: Fossiliferous carbonate with mussels, worm tubes, gastropods, and brachiopods.

Facies 6: Coarse grained breccia, allocthonous clasts up to 4 cm, and lucinid bivalves and brachiopods.

Facies 7: Fine grained breccia, involving up to 3 mm micrite clasts, that includes lucinid bivalves and some small gastropods. The gastropods are found in finer grained breccia than the lucinids.

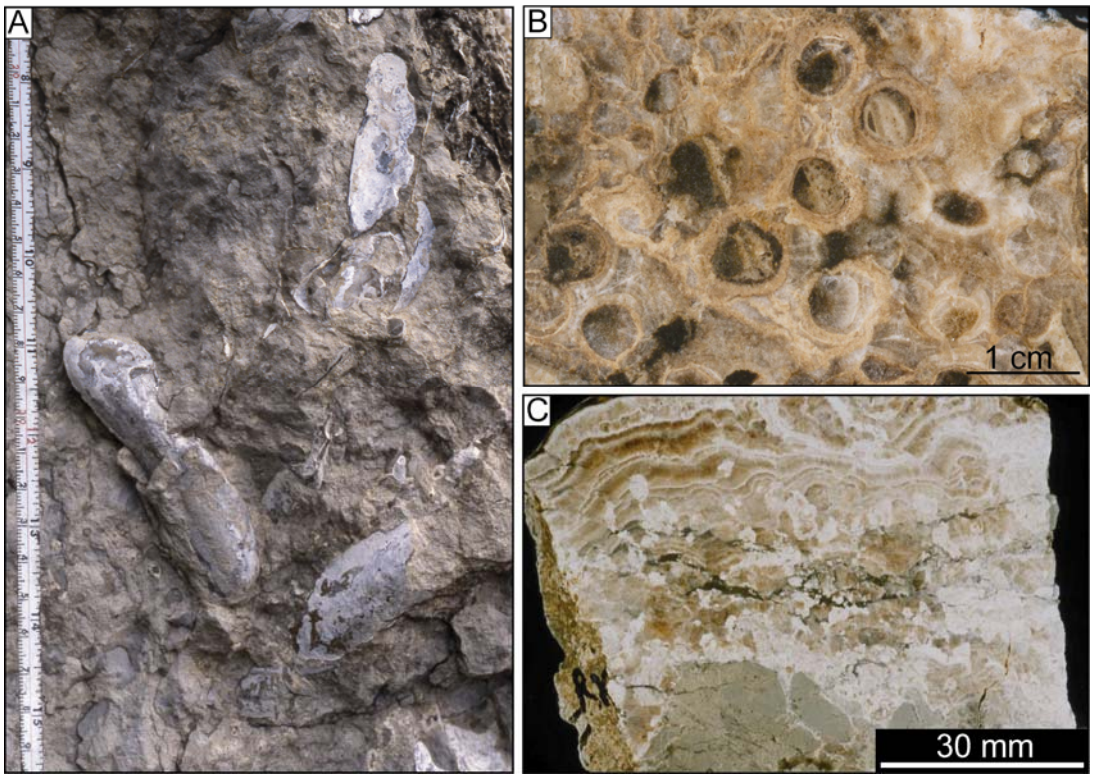

Figure 5. Photographs of seep-related fossils in the Rocky Knob seep carbonate. (A) Large elongate bathymodioline mussels in light grey micrite. (B) Worm tube cross-sections. (C) Micritic digitate thrombolites encased in fibrous aragonite. Photographs courtesy of K.A. Campbell (University of Auckland).

Figure 6. Photograph of a typical tubular carbonate concretion in the slope mudstones underlying the Rocky Knob seep carbonate deposit, showing longitudinal (L) and cross-sectional (X) views. The tubular concretions are pipe-like in shape, often tortuous in direction, and have open or filled central conduits (C).

4.1 Outcrop stratigraphy

The seep carbonates crop out of the host mudstone in seven main pods (a-g in Fig. 7A). The tubular concretions are present in the thick massive mudstone beneath four of these pods (Fig. 6; Tc in Fig. 7A).

Above the tubular concretion containing mudstone is 7 m of hard grey to cream micrite which is typically brecciated (pods c, f, and g in Fig. 7A). In places, stylobedding is present and healed by aragonite precipitates in the fractures (especially f in Fig. 7A).

This stratigraphic interval is overlain by 5 to 10 m thick of micritic seep carbonate (a, b, d, e, f, g in Fig. 7A). Some material appears to be flank deposits of the seep complex (especially a in Fig. 7A). Pod d (in Fig. 7A) is a 5 m thick interval of fossiliferous seep carbonate, possibly with more tubular concretions present in the surrounding mudstone. Some calcareous worm tubes in cement are present at the tops of pods c, d, e, and g (Fig. 7A). Figure 7B is a simplified stratigraphic column for each pod which depicts a generalised progression of tubular concretions, seep facies, and fossils within the Rocky Knob seep complex.

4.2 Tubular concretions

4.2.1 Morphology of tubular and nodular concretions

The concretionary features consist of tubular concretions (Fig. 6), ranging between 5 and 12 cm in diameter and 50 cm in exposed length, many of which contain filled conduits (Fig. 8). Their morphology is pipe-like, although they are strongly tortuous. In many places, the tubular concretions branch, anastomose, and coalesce, forming a complex network of concreted zones within the host mudstone.

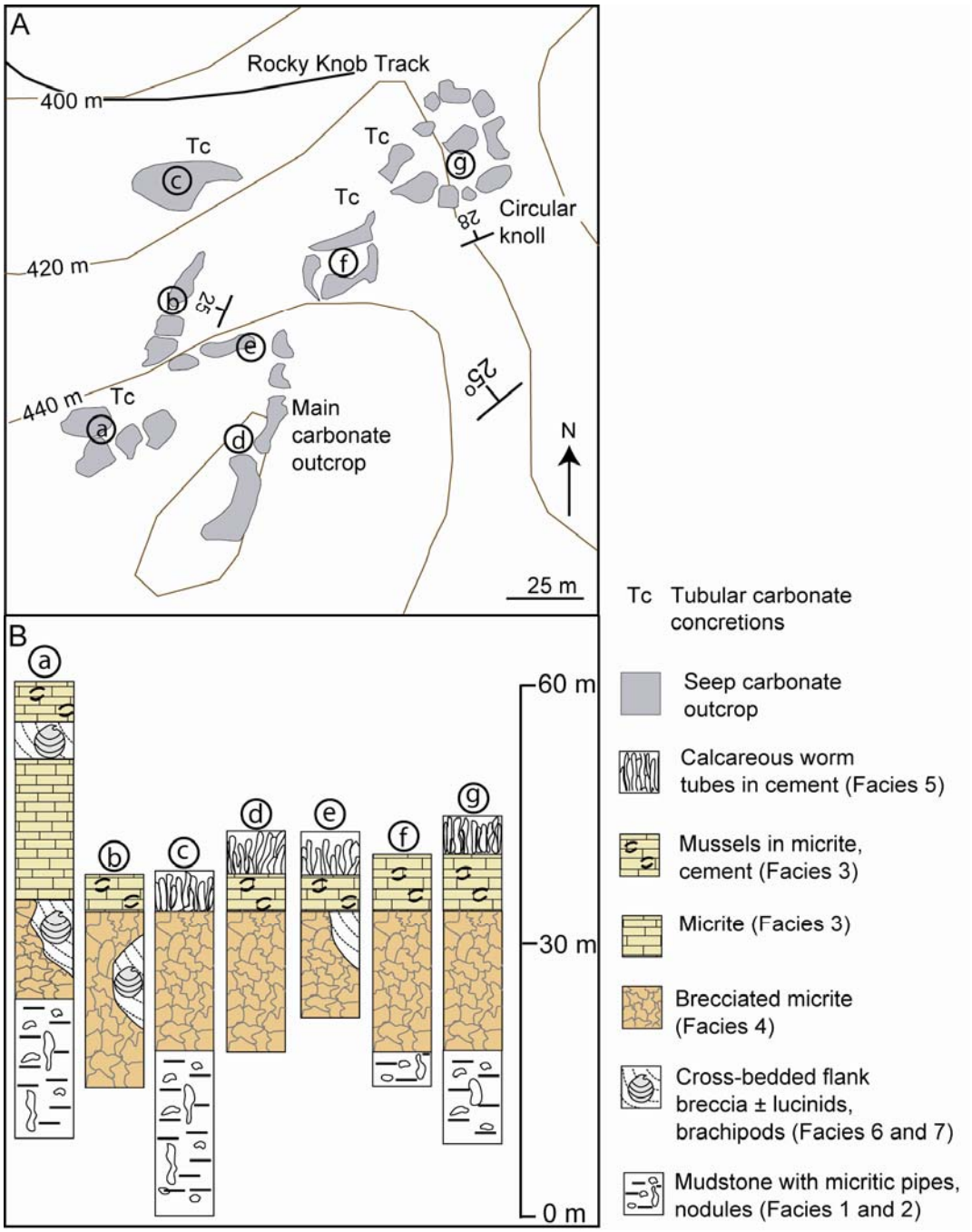

Figure 7. (A) Sketch map of seep limestone outcrops at the Rocky Knob locality in Fig. 1B. (B) Simplified stratigraphic columns at Rocky Knob showing gross lithologic progression from basal mudstone including tubular concretions to seafloor seep carbonate. Modified from Campbell et al. (2008).

The tubular concretions display a distinct central conduit, generally less than 2 cm in diameter (Figs. 6, 8). Up to three conduits have been noted in a tubular concretion (Fig. 8A). The conduits are filled with various cement generations that are different to the micritic cement forming the surrounding concretion. Some conduits contain breccia clasts, veins, and vugs (Fig. 8B). A few are distinguishable by a slight colour variation (Fig. 8C) or may display an open 'pinhole' conduit less than 1 cm in diameter (Fig. 8D), rarely reaching 2 cm in diameter (Fig. 6). Conduit fills can be grouped into four types, with types 1 and 2 the most common.

Type 1 conduits: Lined by white fibrous aragonite followed by a central fill of dark grey peloidal micrite (Fig. 8A).

Type 2 conduits: Light grey, strongly brecciated micrite with light grey calcite veins and crystal lined vugs (Fig. 8B).

Type 3 conduits: Micritic fill only distinguished by slight colour changes from light grey to dark grey in the central conduit (Fig. 8C).

Type 4 conduits: Brownish-yellow argillaceous micrite zonation (~4 cm diameter) around an open 'pinhole' conduit (Fig. 8D).

4.2.2 Petrography of tubular concretions

The host sediments are light grey, fine grained, massive mudstones primarily composed of quartz, plagioclase feldspar, clay minerals, and planktic and benthic foraminifera whose tests are commonly infilled with pyrite framboids (Fig. 9A-D). The tubular concretions derive from the precipitation of micrite (calcite) cement within the interparticle spaces of the host mudstone. The micrite is light grey in plane polarised light (PPL) and is yellow to light orange under cathodoluminescence light (CL). Carbonate content in the concretions ranges from 65 to 87%, suggesting precipitation occurred near seafloor/depositional conditions before any significant compaction.

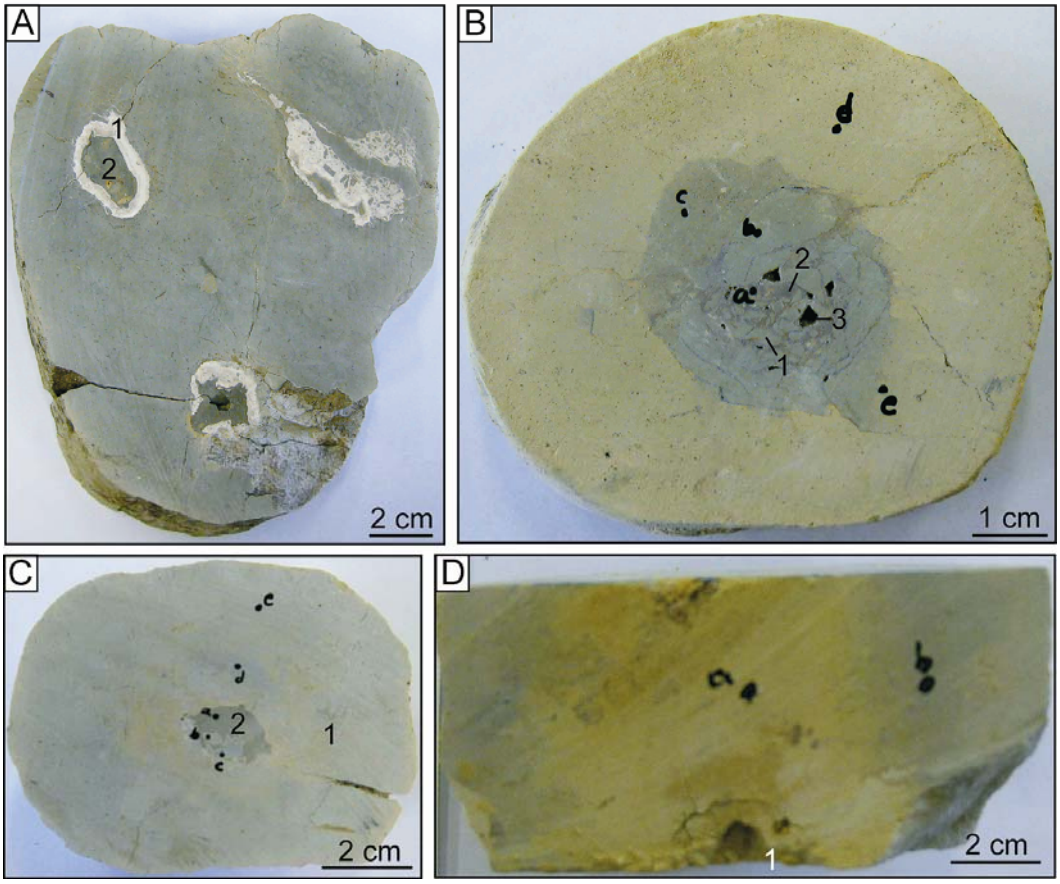

Figure 8. Photographs of cross-section slabs through tubular concretions from the Rocky Knob site. (A) Type 1 conduits with an aragonite lining (1) and dark grey sediment fill (2) (sample RK65). (B) Type 2 conduits with concretion breccia clasts (1), calcite lined vugs (2), and clear grey calcite veins (3) (sample RK60). (C) Type 3 conduits are discernible only by a slight colour zonation, in this case from light grey to cream in the concretion (1) to dark grey in the conduit (2) (sample SN63). (D) Type 4 conduits with one pinhole conduit (1) (sample RK54).

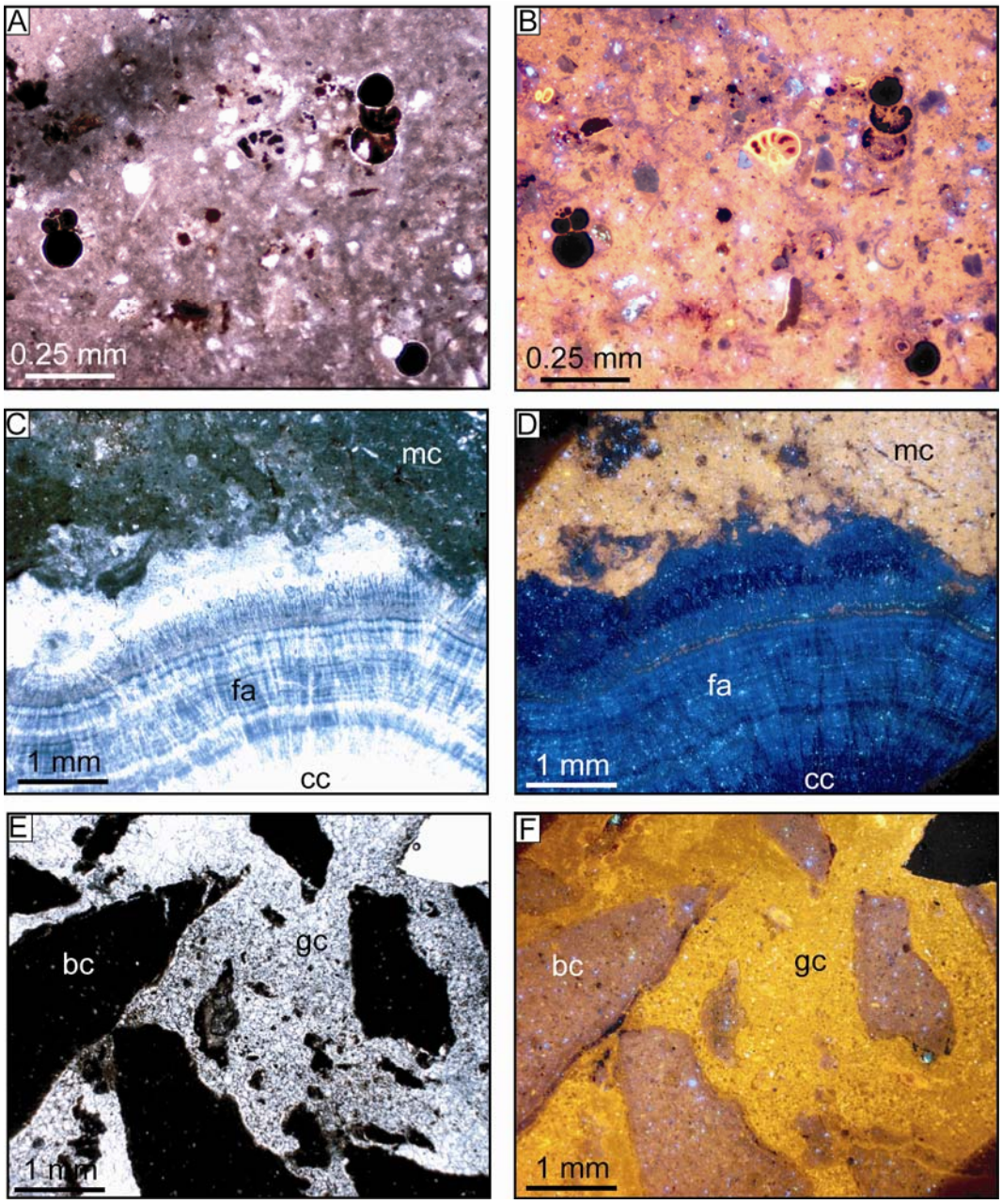

Figure 9. Petrographic images from tubular concretions. (A, B) Thin section pair (PPL and CL, respectively) of the main concretionary part of a tubular concretion showing silt-sized clastic material mainly composed of quartz and feldspars, benthic and planktic foraminifera, pyrite and pore-filling micritic cement (orange to yellow CL in B) (sample RK65); (C, D) thin section pair (PPL and CL, respectively) at concretion-conduit boundary showing micrite in outer concretion (mc) and fibrous aragonite (fa) lining the conduit, with multiple growth bands and fibres pointing toward the conduit centre (cc) (RK65); (E, F) thin section pair (PPL and CL, respectively) of angular breccia clasts (bc) of host concretion 'floating' in granular calcite cement (gc) within a conduit (sample RK60).

The tubular concretions support a central conduit which in most cases is filled with multiple phases of cement and/or sediment (Fig. 8). Carbonate content in the concretion conduits ranges from 80 to 95% and comprises calcite and/or aragonite (Fig. 9C-F).

Aragonite is light grey in PPL, blue in CL, and is always fibrous (Fig. 9C,D) (conduit types 1 and 3). Growth bands in the fibrous aragonite are suggestive of multiple generations of cementation (Fig. 9C,D).

Calcite fabrics can be micritic, granular to clotted, blocky, or bladed. The micrite within conduits is mainly restricted to the breccia clasts (Fig. 9E,F) (predominately type 2 and some type 1 conduits), effectively representing fragments of the concreted mudstone. In places, a clear grey calcite (PPL; yellow CL) is present in concretions that display a high degree of internal brecciation within the conduit fill (Figs. 8B, 9E,F), occupying the spaces between brecciated blocks.

A second micritic carbonate phase is present in some conduits and constitutes dark grey, rounded, peloidal masses (Fig. 10A,B) (type 1 and 3 conduits). Where present, these peloids occupy the more central portions of conduits.

Granular to clotted fabrics are commonly present filling conduits and surrounding breccia clasts. These fabrics are light grey to white in PPL and dull to bright yellow in CL (Figs. 9E,F, 10C,D) (all conduit types). Granular textures also exist lining vugs (Fig. 10E,F).

Bladed and blocky calcite is clear to white in PPL and bright yellow in CL (conduit types 1, 2, and 3). These calcite fabrics occur lining and growing into the vugs, becoming more coarsely crystalline (blocky) toward open spaces (Fig. 10E,F).

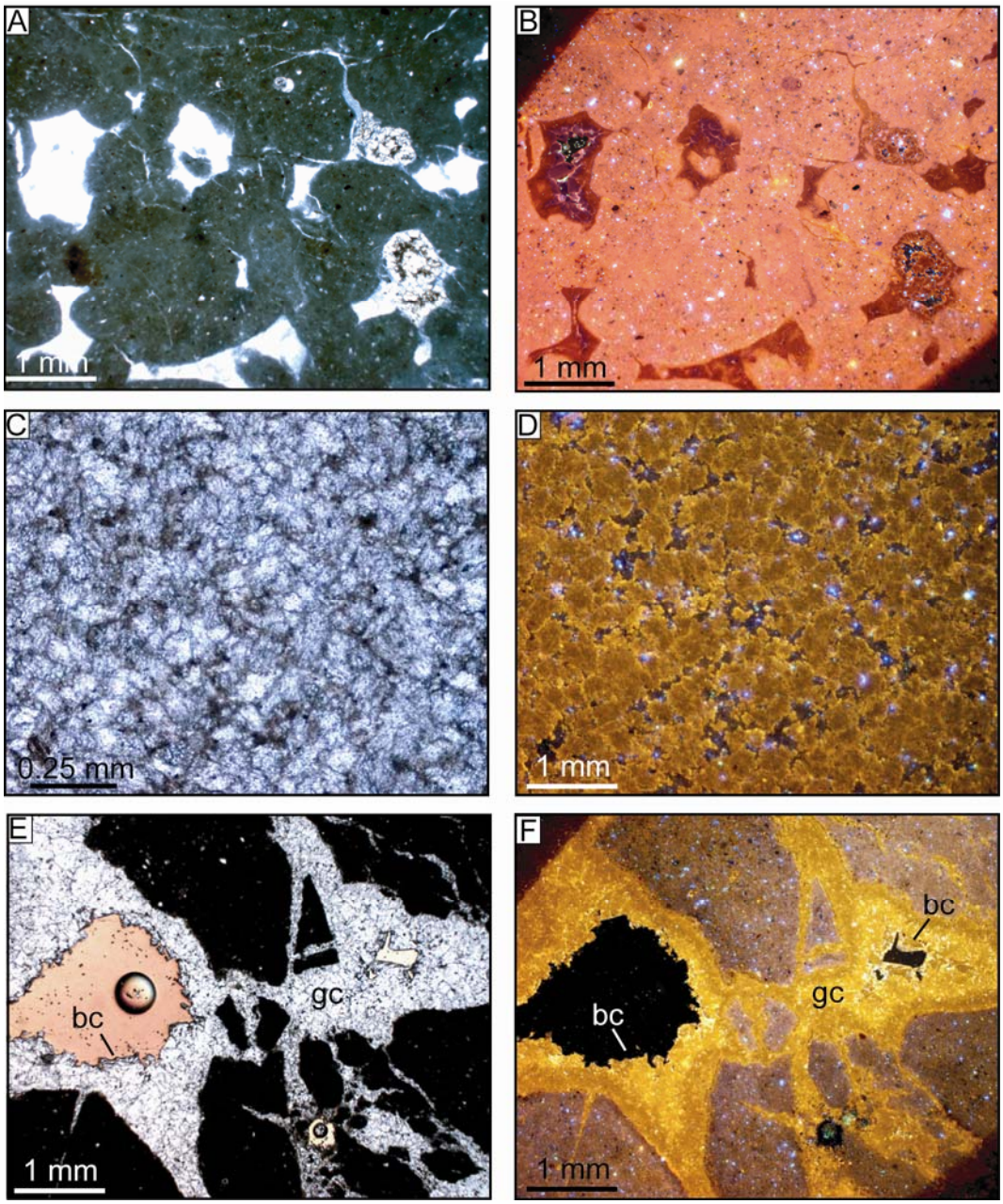

Figure 10. Petrographic images from tubular concretions. (A, B) Thin section pair (PPL and CL, respectively) of peloids of dark grey micrite filling the centre of a conduit (sample RK65). (C, D) Thin section pair (PPL and CL, respectively) of clotted calcite texture in a conduit fill (sample RK64). (E, F) Thin section pair (PPL and CL, respectively) of granular calcite (gc) between breccia fragments. Blocky calcite (bc) lines open vugs encased in granular calcite (sample RK60).

4.2.3 Stable isotope composition of tubular concretions

Carbon and oxygen isotope signatures may help constrain fluid compositions at the time of carbonate cement precipitation (e.g., Roberts and Aharon, 1994; Nelson and Smith, 1996). The Rocky Knob tubular concretion isotope values range from $\delta^{13}C$ of –52.3 to –5.1‰ PDB and $\delta^{18}O$ of –5.3 to +3‰ PDB (Table 1, Fig. 11A). The tubular concretions group in four main regions on a carbon vs oxygen cross plot (Table 2, Fig. 11A), and the host mudstone defines a fifth region.

Concretion group 1 corresponds to the white fibrous aragonite conduit rims associated with type 1 conduits. Their $\delta^{13}C$ values range from –52.3 to –41.8‰ PDB and $\delta^{18}O$ values from +1.1 to +2.7‰ PDB.

Concretion group 2 is associated with the predominant light grey micrite filling the pore spaces of the concretion sediment, and granular/clotted calcite in the conduits. These cements have $\delta^{13}C$ values from –44.2 to –20.0‰ PDB and $\delta^{18}O$ values between –3.9 and +1.3‰ PDB.

Concretion group 3 includes a sample of blocky yellow calcite lining an open vug and the dark grey central fill of type 1 and type 3 conduits. Isotope values range from $\delta^{13}C$ –33.6 to –5.2‰ and $\delta^{18}O$ –5.3 to +2.8‰ PDB.

Concretion group 4 includes two nodular concretion samples which have similar carbon isotope values to concretion group 2, but have more positive oxygen isotope values. The isotope values range from $\delta^{13}C$ –28 to –23‰ PDB and $\delta^{18}O$ +3.2 to +4.2‰ PDB.

Group 5 comprises the mudstone hosting the tubular concretions at the Rocky Knob locality. The carbon and oxygen isotope values differ dramatically from those in the tubular concretions (and also the seep carbonate deposit itself) (Fig. 11). Carbon isotope values range from $\delta^{13}C$ –2.5 to –2.4‰ PDB and $\delta^{18}O$ from –0.3 to +0.7‰ PDB.

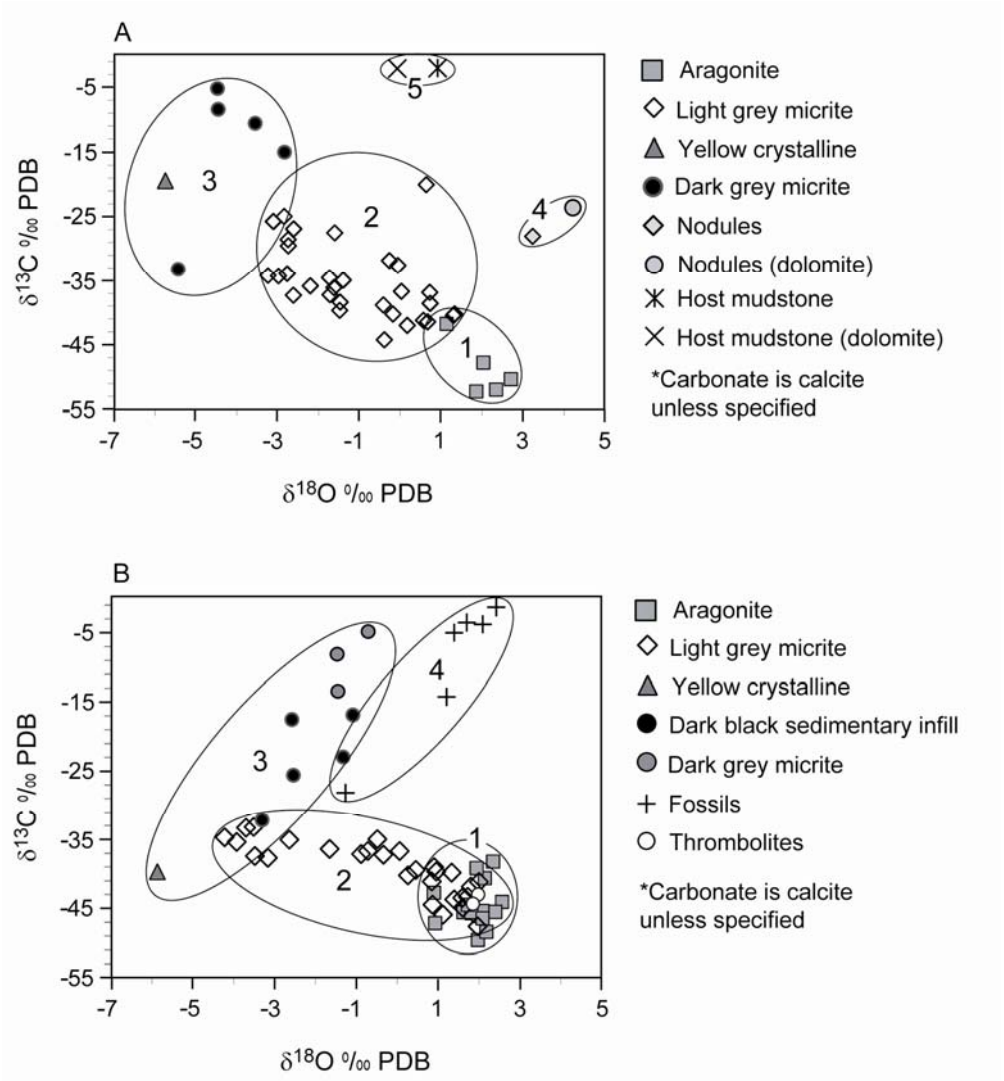

Figure 11. Stable oxygen vs carbon isotope plot for Rocky Knob samples. (A) Samples from tubular (and a couple of nodular) concretions and host mudstone. Circles with numbers correspond to tubular concretion isotope groups defined in the text. (B) Samples from seep carbonates, including fossils and thrombolites. Circles with numbers correspond to seep carbonate isotope groups defined in the text.

Table 1. Stable carbon and oxygen isotope values for Rocky Knob seep carbonates, tubular concretions, fossils, thrombolites, and host mudstone. Sample descriptions are included. Most of the concretionary seep carbonate analyses derive from this study, while much of the seep carbonate, fossil, and thrombolite data were kindly made available by Jens Greinert (unpublished data; Royal Netherlands Institute for Sea Research).

Sample	Sample description	$\delta^{13}C$ ‰ PDB calcite	$\delta^{18}O$ ‰ PDB calcite
Tubular concretions (this study)			
RK48-a	Host mudstone; calcite	-2.4	+0.7
RK48-b	Host mudstone; dolomite	-2.5	-0.3
RK49-a	Nodular concretion; calcite	-28.0	+3.2
RK49-b	Nodular concretion; dolomite	-23.6	+4.2
RK54-a	Conduit; brown/yellow micrite	-20.0	+0.6
RK54-b	Concretion; light blue/grey micrite	-32.6	-0.1
RK60-a	Inner conduit; clear/grey coarse crystalline	-28.5	-2.7
RK60-b	Inner conduit; blue/grey micrite	-36.7	0.0
RK60-c	Outer conduit; brown/grey micrite	-31.8	-0.3
RK60-d	Concretion/conduit contact; brown micrite	-40.5	+1.3
RK60-e	Concretion; brown micrite	-40.2	+1.3
RK60-f	Vug fill; yellow calcite coarse crystalline calcite	-19.4	-5.7
RK62-a	Conduit; dark grey micrite	-5.2	-4.5
RK62-b	Concretion (near conduit); light blue/grey micrite	-44.2	-0.4
RK62-c	Concretion; light blue/grey micrite	-41.2	+0.6
RK63-a	Conduit; dark grey micrite	-10.6	-3.5
RK63-b	Conduit; light blue/grey micrite	-35.8	-2.2
RK63-c	Conduit; light blue/grey micrite	-35.0	-1.4
RK63-d	Concretion (middle); light blue/grey micrite	-34.6	-1.7
RK63-e	Concretion (outer); light blue/grey micrite	-38.8	-0.4
RK64-a	Conduit fill; dark grey/blue micrite	-8.4	-4.5
RK64-b	Conduit rim; white aragonite	-52.3	+1.9
RK64-c	Concretion; light blue/grey micrite	-37.2	-1.7
RK65-1a	Conduit; dark grey micrite	-15.0	-2.8
RK65-1b	Conduit lining; white aragonite	-52.0	+2.3
RK65-1c	Concretion; light blue/grey micrite	-36.1	-1.6
RK65-2a	Conduit; dark grey micrite	-27.5	-1.6
RK65-2b	Conduit lining; white aragonite	-47.8	+2.0
RK65-2c	Concretion; light blue/grey micrite	-33.9	-2.8
RK65-3b	Conduit lining; white aragonite	-50.4	+2.7
RK65-3c	Concretion; light blue/grey micrite	-39.7	-1.5
RK65-4a	Conduit; dark grey micrite	-33.6	-5.3
RK65-4b	Conduit lining; white/brown aragonite	-41.8	+1.1
RK65-4c	Concretion; light blue/grey micrite	-26.9	-2.6
RK65-5a	Conduit; dark blue/grey micrite	-29.5	-2.7
RK65-5c	Concretion; light blue/grey micrite	-40.2	-0.2
RK65-6a	Conduit; dark grey micrite	-25.7	-3.1

Table 1 continued

Sample	Sample description	$\delta^{13}C$ ‰ PDB calcite	$\delta^{18}O$ ‰ PDB calcite
Seep carbonates (this study)			
RK65-6c	Concretion; light blue/grey micrite	-41.5	+0.7
RK1-1	Outer concretion; light blue/grey micrite	-42.0	+0.2
RK1-2	Middle concretion; light blue/grey micrite	-38.4	-1.5
RK1-3	Conduit; light blue/grey micrite	-34.3	-3.0
RK2-1	Outer concretion; light blue/grey micrite	-36.9	+0.7
RK2-2	Middle concretion; light blue/grey micrite	-38.6	+0.7
RK2-3	Conduit; light blue/grey micrite	-25.0	-2.8
RK61-a	Pink aragonite	-45.5	+1.6
RK61-b	Pink aragonite	-42.7	+0.9
RK61-c	Light blue/grey micrite	-35.3	-3.9
RK61-d	Light blue/grey micrite	-33.3	-3.7
RK57-a	Dark grey micrite	-4.8	-0.7
RK57-b	Dark grey micrite	-13.4	-1.5
RK57-c	Dark grey micrite	-8.1	-1.5
RK57-d	Light blue/grey micrite	-37.2	-0.3
RK57-e	Light blue/grey micrite	-41.1	+0.8
RK3	Bulk seep carbonate	-43.3	+1.7
RK59-a	Mussel	-14.2	+1.2
RK59-b	Mussel	-28.1	-1.3
**********			
Seep carbonate samples from Greinert et al., unpublished data			
RK-4-5	Grey-green micrite	-44.5	+0.9
RK-0-4	Grey-green micrite	-36.4	-1.7
RK-1-5	Grey-green micrite inside concretion surrouding (16)	-35.0	-2.6
RK-17A-3	Greenish micrite	-36.7	+0.1
RK-5E-6	Brown-green micrite surrounding tube worms	-44.9	+1.6
RK-9D-4	Grey infill into ?burrow	-34.7	-4.2
RK-15A-5	Grey-green micrite with web texture from ?deep underground	-39.6	+1.0
RK-1-3	Grey-green micrite inside concretion	-37.3	-2.6
RK-1-2	Grey-green micrite inside ?Paramoudra (?concretion)	-34.2	-3.2
RK-41B	Grey micrite	-41.8	+1.8
RK-30B	Green to grey-green micrite	-34.9	-0.5
RK-21A	Green micrite	-39.0	+0.9
RK-43A	Grey-greenish micrite	-39.8	+1.3
RK-64A	Grey-green micrite	-47.6	+1.9
RK-11	Grey-green micrite	-43.5	+1.6
RK-7A	Grey-green micrite	-40.2	+0.3
RK-10A	Grey micrite. Sample has brecciated appearance	-37.4	-3.5
RK-7D	Yellow micrite	-39.4	+0.5

Table 1 continued

Sample	Sample description	$\delta^{13}C$ ‰ PDB calcite	$\delta^{18}O$ ‰ PDB calcite
RK-1-5	Yellow micrite inside concretion surrounding grey-green micrite	-36.7	-0.7
RK	Blue micrite	-45.9	+1.1
RK-1-5	Blue micrite inside concretion (in centre)	-37.7	-3.2
RK-1-2	Blue micrite inside ?Paramoudra (?concretion)	-33.2	-3.5
RK-21A	Blue micrite	-37.1	-0.9
RK-44B	Blue micrite	-41.2	+2.0
RK-11	Blue micrite	-43.7	+1.4
RK-7-4	Botryoidal pink-brown aragonite	-40.6	+2.1
RK-4-1	Pink-brown aragonite vein infill	-49.6	+2.0
RK-8C	Brown-pink aragonite surrounding tube worms	-45.7	+1.8
RK-0-15	Brownish aragonite surrounding tube worms	-39.1	+1.9
RK-17A-3	Brown aragonite vein	-38.2	+2.3
RK-15A-1	Brown ?aragonite laminae below (65)	-46.1	+2.0
RK-9D-1	Brown ?aragonite inside shell	-44.0	+2.6
RK-21B	"Pure" piece of brown aragonite around tube worms	-45.5	+2.4
RK-23B	Brown botryoidal aragonite laminae	-45.4	+2.1
RK-11	Laminae of pink -white botryoidal aragonite surrounding (176)	-48.4	+2.20
RK-15B	Pink aragonite surrounding tube worms	-45.6	+1.8
RK-10A	Brown aragonite inside bivalve shell. Whole rock sample has brecciated appearance	-47.1	+0.9
RK-15A-1	Peloid-?aragonite mixture	-44.5	+1.7
RK-65C-5	"Pure" botryoidal aragonite	-46.4	+2.1
RK-4-3	Dark grey to black sedimentary infill	-16.8	-1.1
RK-0-15	Dark grey to black sedimentary infill	-25.6	-2.5
RK-64A	Black-grey sedimentary infill into vug	-32.2	-3.3
RK-11	Black-grey sedimentary infill into vug	-17.5	-2.6
RK-21B	Black-brown infill into vugs	-22.9	-1.3
RK-19A	Yellow calcite	-39.7	-5.9
RK-9D-1	Large sparitic vein (in shape of a lizard)	-41.9	+1.8
RK-61B-1	Representative powder of matrix	-40.9	+1.6
RK-47D-1	Thrombolites	-43.0	+2.0
RK-15A-1	Clotted ?thrombolitic material	-44.3	+1.8
RK-7E	Bivalve shell	-3.8	+2.1
RK-8A	Bivalve shell	-1.3	+2.4
RK-61B-1	Shell material	-3.5	+1.7
RK-8E-1	Shell material	-5.0	+1.4

Table 2. Maximum and minimum values of stable carbon and oxygen isotope groups for Rocky Knob seep carbonates, tubular concretions, fossils, thrombolites, and host mudstone. Light grey micrite includes all of the grey-green micrite, blue-grey micrite, brown micrite, and light grey micrite samples recorded in Table 1. The micrites were not differentiated because the tubular concretions are composed of the blue-grey micrite only, the focus of this study.

Isotope group	**Description**	**$\delta^{13}C$ ‰ PDB calcite**	**$\delta^{13}C$ ‰ PDB calcite**	**$\delta^{18}O$ ‰ PDB calcite**	**$\delta^{18}O$ ‰ PDB calcite**
		Min	**Max**	**Min**	**Max**
Concretion group 1	Aragonite	-52.3	-41.8	+1.1	+2.7
Concretion group 2	Light grey micrite, granular and clotted calcite	-44.2	-20.0	-3.9	+1.3
Concretion group 3	Yellow calcite crystals and dark black/greymicrite and sedimentary infll	-33.6	-5.2	-5.7	-2.8
Concretion group 4	Nodules	-28.0	-23.6	+3.2	+4.2
Group 5	Host mudstone	-2.5	-2.4	-0.3	+0.7
Seep Carbonate group 1	Aragonite and thrombolites	-49.6	-38.2	+0.9	+2.7
Seep Carbonate group 2	Light grey micrite	-47.6	-33.2	-4.2	+2.0
Seep Carbonate group 3	Yellow calcite crystals and dark black/greymicrite and sedimentary infll	-39.7	-4.8	-5.9	-0.7
Seep Carbonate group 4	Fossils	-28.1	-1.3	-1.3	+2.4

4.3 Seep carbonates

The Rocky Knob seep carbonates sitting stratigraphically directly above the analysed tubular concretions have remarkably similar petrographic and stable isotope characteristics. Because of the focus in this study on tubular concretions only a few seep carbonate samples were collected and analysed for comparison, but unpublished isotope data from Rocky Knob kindly supplied by Jens Greinert have been incorporated to strengthen the comparison (Table 1).

4.3.1 General petrography of seep carbonates

The seep carbonate is composed of siliciclastic grains (primarily quartz, feldspar, and clay minerals), macro- and microfossils, and carbonate cement. The carbonate comprises calcite and aragonite and averages 70% of the seep carbonate composition. The seep carbonate is dominated by a light grey argillaceous micrite, sometimes blue-grey to green-grey in colour (Fig. 12A,B). In some samples, pink to brown aragonite veins cross-cut the deposit (Fig. 12A), appearing white to grey in PPL and blue in CL (Fig. 12 C,D). Rare thrombolites are present as clotted fabrics of microbial micrite and aragonite. In places, small (a few mm in thickness) lenses of dark grey micrite cemented mudstone is present (Fig. 12B). Hand samples and petrography indicate that the carbonate phases present in the seep carbonate are much the same as those in the tubular concretions. Macrofossils are common to abundant in facies 3, 5, and 6 (Figs. 5, 12C,D).

4.3.2 Stable isotope composition of seep carbonates

The Rocky Knob seep carbonate isotope values range from $\delta^{13}C$ –49.6 to –1.3‰ PDB and $\delta^{18}O$ –5.9 to +2.6‰ PDB (Table 1, Fig. 11B). The seep carbonates group in four main regions on a carbon vs oxygen cross plot (Table 2, Fig. 11B) while fossils occupy a distinctly different region. In particular note that these group numbers correspond closely to those assigned to the tubular and nodular concretions (Fig. 11A) being composed of similar mineralogies and cement fabrics and having similar carbon and oxygen isotope values (Table 2, Fig. 13).

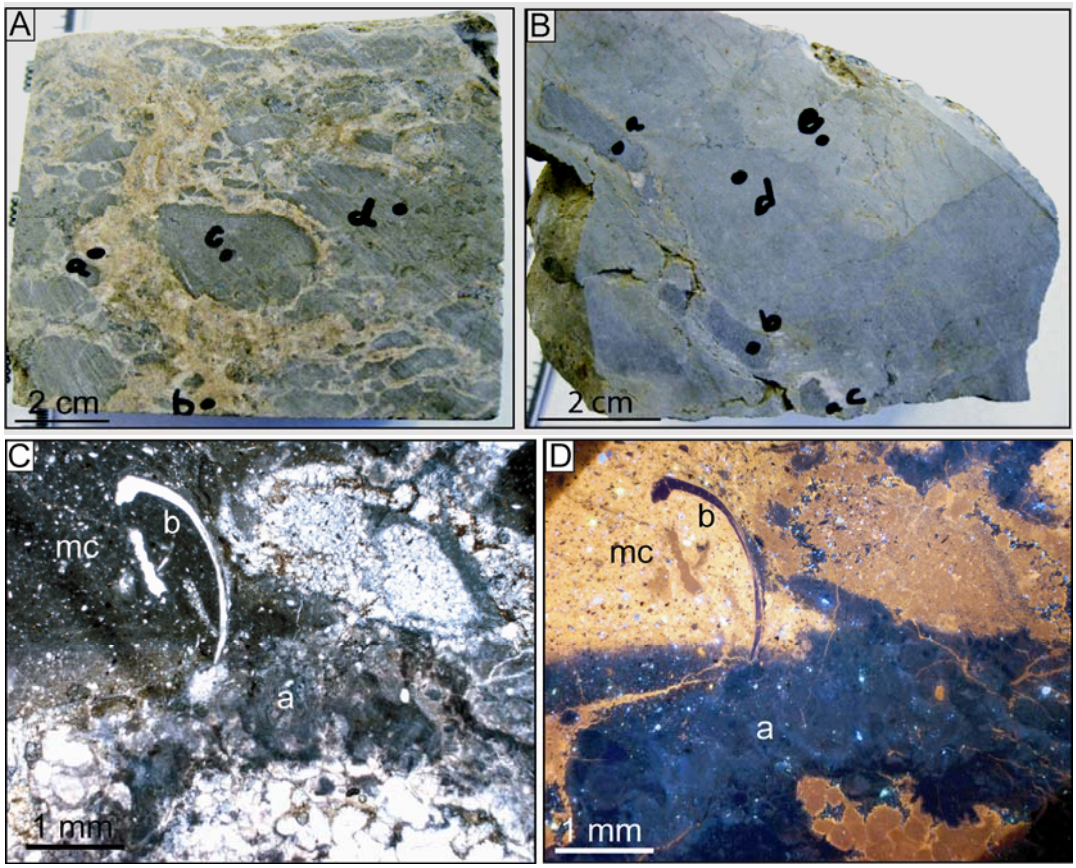

Figure 12. Photographs of seep carbonate slabs and thin sections. (A) Seep carbonate sample (RK61) consists of a profusion of pink aragonite veins (a, b) cross-cutting light grey micrite cemented siliciclastic material (c, d); a-d indicate location of isotope samples in Table 1. (B) Seep carbonate sample RK57 consists of light grey micrite cemented siliciclastic material and dark grey micrite; a-e correspond to location of isotope samples in Table 1. (C, D) Thin section pair (PPL and CL, respectively) of RK61 with aragonite vein (a) cross-cutting light grey micrite (mc) and a disarticulated bivalve (b).

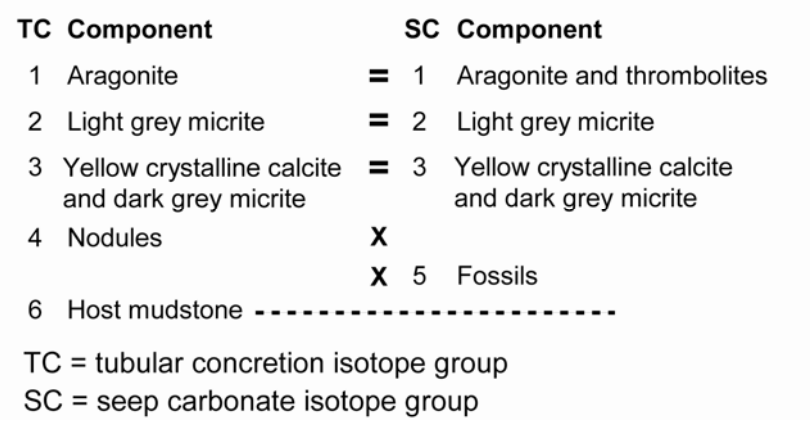

Figure 13. Comparative cement components between the tubular concretions and seep carbonates. = indicates the components have similar isotope values and the same cement fabrics and therefore precipitated from the same fluids. X indicates there is no equivalent component. The host mudstone surrounds both the tubular concretions and seep carbonates (i.e. no correlative component).

Additionally, the corresponding groups plot in similar regions of the carbon vs oxygen isotope cross plot (Fig. 11B), except for group 4.

Seep carbonate group 1 corresponds to the pink-brown aragonite veins that cross-cut light grey micrite and thrombolites. Their $\delta^{13}C$ values range from –49.6 to –38.2‰ PDB and $\delta^{18}O$ values from +0.9 to +2.6‰ PDB.

Seep carbonate group 2 is associated with the light grey micrite cement within the interparticle spaces of siliciclastic material of which the seep carbonate is primarily composed. These cements record strongly negative carbon values ($\delta^{13}C$ –47.6 to –33.2‰ PDB) and oxygen values between $\delta^{18}O$ –4.2 and +2.0‰ PDB.

Seep carbonate group 3 includes a sample of blocky yellow calcite lining an open vug and the dark grey central fill of type 1 and type 3 conduits. Isotope values range from $\delta^{13}C$ –39.7 to –4.8‰ PDB and $\delta^{18}O$ –5.9‰ to −0.7‰ PDB.

Seep carbonate group 4 consists of fossils from the Rocky Knob seep carbonate, which differ dramatically from seep carbonate values. Carbon isotope values range from $\delta^{13}C$ –28.1 to –1.3‰ PDB and $\delta^{18}O$ –1.3 to +2.4‰ PDB.

5. Discussion

5.1 Fluid composition

5.1.1 Carbon

$\delta^{13}C$ values recorded in authigenic carbonate of the tubular concretions (excluding the dark grey central micrite conduit fills) range from $\delta^{13}C$ of –52 to –20‰ PDB and are indicative of carbonate precipitation induced from the anaerobic oxidation of methane (AOM) coupled with microbial sulphate reduction (Roberts and Aharon, 1994). Moreover, these $\delta^{13}C$ values are similar to those recorded in the associated seep carbonates (Fig. 11B) which contain chemosynthesis-based fossils, so confirming AOM processes (Campbell et al., 2008). Further support comes from lipid biomarker analysis of two samples (tubular concretion RK2, seep carbonate RK3) from the Rocky Knob carbonates (Pearson et al., 2008). The lipids extracted were primarily saturated hydrocarbons. Pentamethyl icosane (PMI), indicative of AOM processes was present in both samples. However, archeol, C_{33} dialkyl glycerol diether (DGD), and macrocyclic diether (MD) are absent.

5.1.2 Oxygen

Oxygen isotope signatures of the concretions range from $\delta^{18}O$ –5.7 to +4.2‰ PDB (Fig. 11A). Middle Miocene marine waters in New Zealand have been suggested to have $\delta^{18}O$ values of about –1.1 to –0.7‰ (PDB) (Feary et al., 1991). If upper slope bottom water temperatures were in the range 5 to 10˚C (Ridgway, 1969), then carbonate precipitated near the seafloor (seep carbonate and tubular concretions) should have a $\delta^{18}O$ value between 0 to +1‰ PDB based on the equilibrium equation from Friedman and O'Neil (1977) for calcite (Fig. 14).

Excluding the outliers (nodular concretions, dark grey micrite conduit fills, and blocky crystalline vug and vein fills), the $\delta^{18}O$ values of the seep carbonate and tubular concretions are in the range of –4.2 to +2.7‰ PDB. Carbonates with $\delta^{18}O$

values near –4‰ PDB would have to have precipitated from marine fluids at approximately 25˚C and 500 − 650 m of burial (with geothermal gradient of 23˚C/km; Field et al., 1997) (Fig. 14). Such elevated precipitation temperatures are unlikely to have been met unless (1) fluids ascended extremely quickly and carbonate was precipitated before the fluids re-equilibriated with the surrounding environment or (2) if the carbonate cement recrystallised at higher temperatures later in burial.

Carbonates with $\delta^{18}O$ values near +3‰ PDB would have to have precipitated from marine fluids below 0˚C, which are unrealistic bottom water temperatures. Therefore, carbonates with $\delta^{18}O$ values near +3‰ PDB are enriched from middle Miocene New Zealand marine waters by +2 to +3‰ PDB (assuming bottom water temperatures of 5 to 10˚C) (Fig. 14). Oxygen enrichment may be caused by three mechanisms: 1) evaporation, 2) clay dehydration, and 3) gas hydrate dissociation.

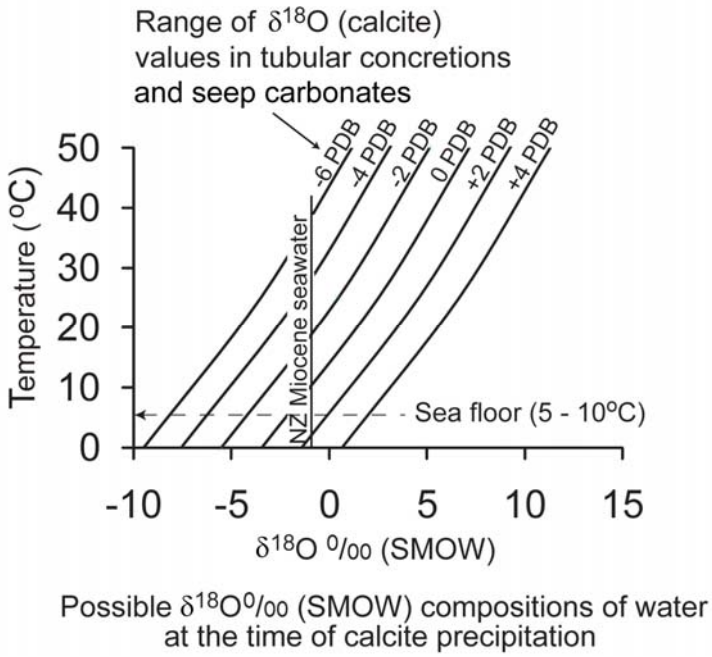

Figure 14. Possible water compositions (SMOW) responsible for carbonate precipitation in the Rocky Knob carbonates. With inferred bottom water temperatures in the range of 5 to 10˚C (Ridgway, 1969), New Zealand Miocene marine water would have precipitated carbonate with a $\delta^{18}O$ = 0 to +1‰ PDB (Feary et al., 1991). Calcite equilibrium calculation from Friedman and O'Neil (1977).

Evaporative conditions in the subsurface environment are unlikely, and any burial transformation of clays is also unlikely to have occurred before the shallow burial precipitation of carbonate in the Rocky Knob carbonates. Moreover, the persistence of common to abundant smectite in the clay fraction of many of the older East Coast Basin formations (e.g., Pearce et al., 1981; Fergusson, 1985) effectively negates clay mineral alteration as a burial source of ^{18}O-enriched fluids. Consequently, the most likely explanation for enriched $\delta^{18}O$ values in the concretionary carbonate is the dissociation of gas hydrates. During gas hydrate formation, heavy oxygen is preferentially accepted into the hydrate molecule, and upon dissociation of large volumes of gas hydrates, heavy oxygen can be released into sediment pore fluids, thereby increasing $\delta^{18}O$ values by up to 3‰ PDB (Davidson et al., 1983; Ussler and Paull, 1995). Moreover, during hydrate formation, when heavy oxygen is accepted into the hydrate molecule, the remaining fluids become 'anomalously' depleted in ^{18}O.

The variation in $\delta^{18}O$ in the Rocky Knob seep carbonates and tubular concretions by –3‰ depleted and +3‰ enriched from middle Miocene New Zealand seawater (measured values range between –4.2 and +2.7‰) PDB also supports a methane hydrate hypothesis. During hydrate formation, carbonate precipitates with lower $\delta^{18}O$ values, while during hydrate dissociation carbonates with higher $\delta^{18}O$ values precipitate. Furthermore, the linear trend (R^2 = 0.52) of carbon isotope enrichment with oxygen isotope depletion (Fig. 15A) may also support a methane hydrate hypothesis. Methane hydrate formation removes methane from the fluids, leaving less methane to be oxidised. During methane oxidation, the residual methane pool becomes more enriched in $\delta^{13}C$ due to fractionation effects (Coleman et al., 1981; Whiticar, 1999; Pancost et al., 2000; Cowen et al., 2002). Without replenishing the methane pool, the residual methane will become more enriched in ^{13}C, which may explain the shift from $\delta^{13}C$ of –52 to –20‰ PDB recorded in the Rocky Knob carbonates during a hydrate forming event. Consequently, the Rocky Knob seep carbonates and tubular concretions are interpreted to have formed from fluctuating cycles of methane hydrate formation and dissociation (Fig. 15B).

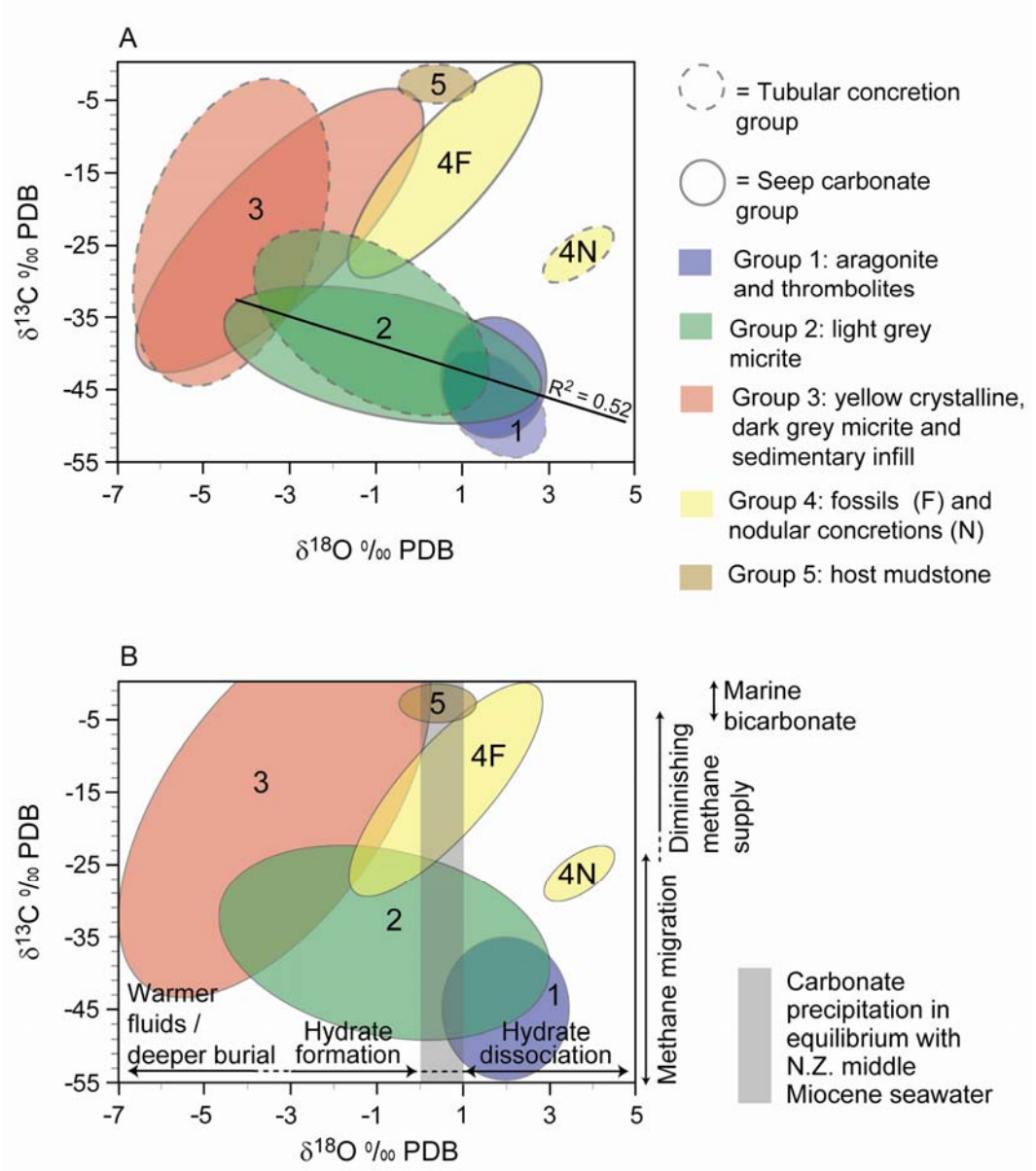

Figure 15. (A) Stable oxygen vs carbon isotope plot of both tubular concretions (dashed lined circles) and seep carbonates (solid lined circles). Note the tendency for the different components from seep carbonates and tubular concretions to plot in similar regions of the graph. Group 1 and 2 carbonates have a linear trend (R^2 = 0.52) and increase in $\delta^{18}O$ with a decrease in $\delta^{13}C$, suggestive of a transition between hydrate formation and dissociation. (B) Rocky Knob samples with superimposed interpretation of isotope groups. Circles correspond to combined fields for isotope groups from the associated tubular concretions and seep carbonates (see Table 2). Grey rectangle highlights the area of the $\delta^{18}O$ values of carbonates precipitated in equilibrium with New Zealand middle Miocene seawater (see Fig. 14).

5.2 Markers of the Rocky Knob seep plumbing system

The carbon and oxygen isotope values in the tubular concretions confirm that cement precipitation resulted from methane rich fluids of marine composition influenced probably by the formation and dissociation of gas hydrates rather than temperature fluctuations. The tubular morphology and presence of central conduits indicate that the tubular concretions formed around focused fluid migration pathways. The stratigraphic position of the tubular concretions directly beneath the Rocky Knob seep carbonate (Fig. 7), and their similar carbon and oxygen isotope values, indicate concurrent formation of tubular concretions deeper in the sediment pile (Table 2, Fig. 13). Consequently, the tubular concretions are interpreted to reflect a shallow sub-seafloor plumbing network of the Rocky Knob cold seep system, where methane rich fluids migrated upwards along directed pathways toward the seabed in the middle Miocene.

5.3 Formation of tubular concretions and conduits

5.3.1 Formation of Rocky Knob tubular concretions

Carbonate mineral phases are remarkably similar geochemically and petrographically between the Rocky Knob seep carbonate and tubular concretions (Table 2, Figs. 9, 10, 12, 13). As such, the corresponding mineral phases are interpreted to have precipitated from the same fluid event/compositions. The cement phases in the seep carbonates are chaotic and complex (Fig. 12), whereas the cement phases in the tubular concretions display more of a ‘zoned’ pattern (Fig. 8). This difference is interpreted to reflect the environment of carbonate precipitation. The seep carbonates formed at or near the surface and represent fluid expulsion at the seafloor. In contrast, the tubular concretions formed in more restricted sediment below the seafloor around focused fluid pathways. The tortuous morphology of the tubular concretions is interpreted to reflect the lowering of fluid pressures as fluids approached the seafloor, the less confining pressures allowing for multiple migration pathways. Additionally, as tubular concretion conduits close, migration pathways became cut off and redirected.

5.3.2 Paragenetic sequence of carbonate precipitation in tubular concretions

In all cases, the tubular concretions comprise fine grained siliciclastic material cemented only by micrite. Only the conduits display multiple cement generations and coarser carbonate cement fabrics. The single phase fine grained carbonate in the concretions vs multiple and coarser cement phases in the conduits suggests that precipitation within conduits occurred in open spaces over a potentially longer fluid-burial history. Furthermore, the multiple phases are suggestive of changing fluid compositions and volumes.

The geometric relationships among carbonate phases in the tubular concretions and conduits provide evidence for the relative timing of each paragenetic event (Fig. 16). Paragenetic event 1 consists of the interparticle micrite cement in the tubular concretions. Event 2 carbonates, where present, consist of fibrous aragonite lining conduit/concretion borders (Figs. 8A, 9C,D). In addition to their location, the aragonite needles point inwards toward the centre of the conduit, suggestive of growth into an open space. Event 3 marks the emplacement of the concretionary breccia clasts in the conduits, followed by event 4 which cemented the breccia clasts in a matrix of granular/clotted calcite fabrics (Fig. 9E,F). Event 5 is marked by blocky and bladed calcite crystals in the open spaces of the granular calcite (Fig. 10E,F). Dark grey micrite-cemented peloids present in the centre of conduits suggest they were emplaced during final event 6 of conduit fill.

5.3.3 Isotope evidence for fluid evolution through time

The correlative carbonate components in Rocky Knob tubular concretions and seep carbonates have similar isotope values; however, the value range varies slightly (Table 2, Fig. 15A). The shift in $\delta^{13}C$ and $\delta^{18}O$ among components present within a sample reflects fluid evolution through time. Five distinctive isotope groups (Table 2, Fig. 15A) are interpreted to record the onset of hydrocarbon migration and expulsion at the seafloor influenced by methane hydrate formation and dissociation (Fig. 15B). Both tubular concretions and seep carbonates also record lowering methane concentration (or extensive oxidation),

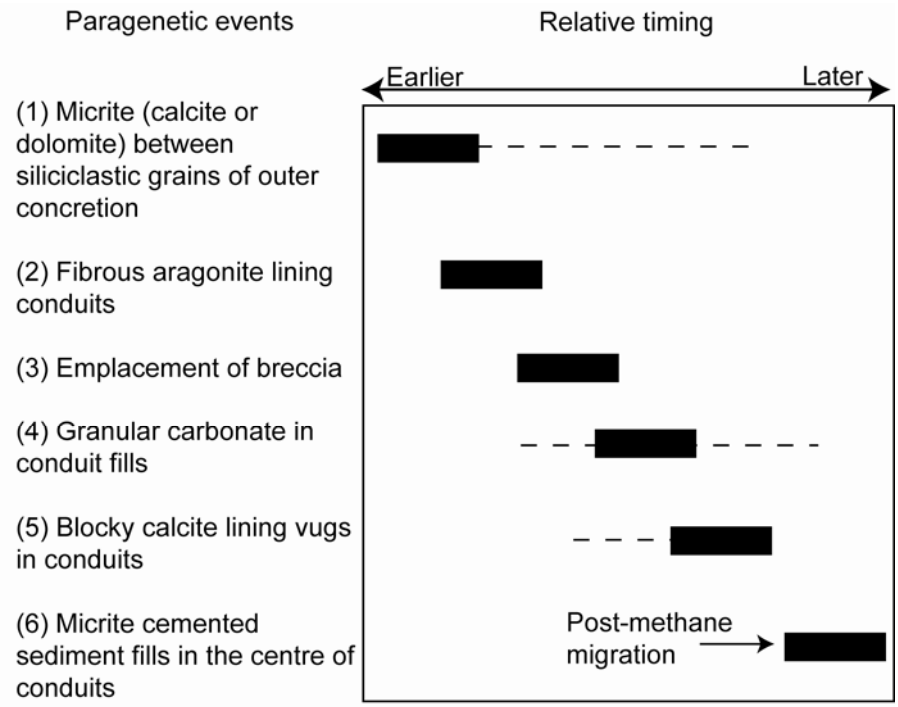

Figure 16. Relative timing relationships of the 6 paragenetic events recorded in the tubular concretions, conduits, and seep carbonates from Rocky Knob. Solid rectangles indicate relative duration and timing; dashed lines suggest possible maximum extent of event.

and/or the incorporation of marine bicarbonate, and, later, non-methane fluid migration through the system during deeper burial.

Tubular concretion and seep carbonate samples (groups 1, 2, and 4) that plot to the left of the marine water line on Figure 15B are interpreted to reflect formation of gas hydrates, as discussed in Section 5.1.2. Samples that plot to the right of the marine water line on Figure 15B are interpreted to have developed during hydrate dissociation events. Group 3 carbonates consist of blocky calcite vug fills and the dark grey micrite central conduit fills are interpreted to have precipitated during late stages in deeper burial, as methane supply was diminishing (Fig. 15B). Temperatures of precipitation for tubular concretion group 3 would have been between 20 and 30ºC (burial depths from 300 to 800 m) and for seep carbonates the temperatures would be from 15 to 20ºC (burial depths between 150 and 300 m) (Fig. 14). The dark grey, carbonate-cemented sediment fill in type 1 and 3 conduits and seep carbonates comprise isotope group 4 and also formed in late stages at burial depths from 400−800 m and diminishing methane supply (Fig. 15B). Carbonates precipitated in groups 6 and 7 probably were sourced from marine carbon and marine fluids near the seafloor. Marine fluid compositions may have been influenced from episodes of hydrate formation and dissociation. Thrombolites (seep carbonate group 1) formed under similar conditions as isotope group 1 (aragonite), and therefore are interpreted as developing during early stages of fluid migration (Fig. 15A,B).

5.4 Comparisons to ancient examples in California and Italy

The Rocky Knob tubular concretions and seep carbonates display many similarities to ancient seep complexes of late Cretaceous to Oligocene age in Panoche Hills, California (Schwartz et al., 2003), and of Miocene age in an, Italian ancient mud volcano including seep carbonates and tubular concretions at Monferrato (Clari et al., 2004) (Table 3). In both cases, the tubular concretions have been interpreted to represent the subsurface plumbing network of an ancient seafloor seep. Moreover, both the seep carbonates and tubular concretions display similar paragenetic sequences and stable carbon and oxygen isotope values.

These include similar orientations and relative timing of the micritic cement between siliciclastic grains, fibrous aragonite within conduits, brecciated concretion clasts in conduits, and blocky calcite lining veins and vugs.

Stable carbon and oxygen isotope values also are similar between the examples: $\delta^{13}C$ from –42.6 to +5‰ PDB and $\delta^{18}O$ from –5.7 to +4‰ PDB for the California carbonates, and $\delta^{13}C$ from –25 to –5‰ PDB and $\delta^{18}O$ from –7 to +8‰ PDB for the Italian carbonates. Both examples were interpreted to have been sourced from ascending methane. Also, the Italian examples were also interpreted to have been derived from dissociating methane hydrate.

The Italian, Californian, and now New Zealand sites contain some of the few examples that document ancient seep complexes and their associated plumbing systems, two of which infer a gas hydrate influence. Together these examples provide insight into the dynamic development of cold seep systems through time.

6. Conclusions

1) The Rocky Knob seep carbonate complex developed within middle Miocene deepwater mudstones. The tubular concretions immediately below the seep complex formed in the subsurface from precipitation of micrite within siliciclastic mud and aragonite and/or micrite within their conduits.

2) The tubular concretions mainly exhibit pipe morphologies, range in diameter from 5 to 12 cm and have exposed lengths up to 50 cm. The tubes support a central open or sediment/crystalline spar-filled conduit. Fill material includes fibrous aragonite, granular, blocky, and bladed calcite, and dark grey micrite. Conduits commonly contain breccia clasts of concretion material, very well-rounded peloids, and vugs.

3) Concretion and conduit development comprised six paragenetic events: (1) micritic carbonate in the (outer) concretion, (2) fibrous aragonite, (3) emplacement of breccia clasts, (4) granular to clotted calcite, (5) bladed and blocky calcite, and (6) dark grey, micrite-cemented peloids.

Table 3. Description of two ancient seep carbonate complexes (seep carbonate and tubular concretions) that are compared to Rocky Knob in Section 5.4

Location / Age	Tubular concretions	Seep carbonate	Isotope interpretation
Panoche Hills, California (Schwartz et al., 2003) / Paleocene	Pipe shaped, up to 2 cm in diameter and several cm long, siliciclastic mud cemented by Mg-calcite (micrite in concretion to fibrous in conduit), circular to irregular in cross-section, located directly beneath the paleo-seep carbonate, authors comment that the pipes are similar to those found in New Zealand	Fossiliferous mounds (0.5 to 6 m tall, 0.5 to 5 m wide) with vugs and fluid conduits, slabs and pavements (1 to 5 m thick and up to 10 m long); fossils include worm tubes, lucinid, and solemyid bivalves, gastropods, corals; cements are mostly Mg-calcite, dolomite and calcite are also present; micritic to sparry Mg-calcite and some dolomite precipitated first around siliciclastic grains followed by cement in veins (micritic and fibrous), brecciation, dissolution, and pipes	$\delta^{13}C$ ‰ PDB from -42.6 to +5; $\delta^{18}O$ ‰ PDB from -5.7 to +4; Mixing between thermogenic and microbial methane oxidation and seawater bicarbonate in normal marine conditions (does not include sandstone intrusions)
Monferrato, Italy (Clari et al., 2004) / Miocene	Dolomite pipes, two morphologies: 1) pipe shaped, light coloured, marly limestone in silty clays, 8 to 15 cm diameter, 1 m long, conduits can be open with prismatic fractures and/or calcite spar; conduits filled with sediment and undifferentiated conduit only discerned by a complex network of branching fractures along the axial portion of the tube; 2) pipe shaped, 5 cm diameter, dark grey cemented concretion with breccia clasts, conduit is only discernible by a lighter coloured zone along the central axial portion	Lithified breccia clasts in muddy matrix (both of the same composition as the surrounding mudstone) with veins filled with carbonate cement and sediments, disarticulated *Lucina* bivalves; light coloured microcrystalline limestone intensely fractured, some fractures are filled by sparry calcite	$\delta^{13}C$ ‰ PDB from -25 to -5; $\delta^{18}O$ ‰ PDB from -7 to +8; Mixing between AOM and marine bicarbonate; methane from hydrate dissociation

4) The tubular concretions, seep carbonates, and the surrounding host mudstone group into five main regions on a carbon vs oxygen cross plot. For both the tubular concretions and seep carbonates, group 1 corresponds to fibrous aragonite (and thrombolites in seep carbonates); group 2 is associated with light grey micrite, and granular and clotted calcite; and group 3 consists of dark grey micrite and blocky calcite. Tubular concretion group 4 consists of nodules whereas in the seep carbonates group 4 consists of fossils. The isotope values between these two components (nodules and fossils) are not correlative. Group 5 consists of the host mudstone and have isotope values distinctly different from that of the tubular concretions and seep carbonates contained within.

5) Carbon isotope values for isotope groups 1, 2, and 4 ($\delta^{13}C$ from –52.2 to –20‰ PDB) suggest that the carbon for carbonate precipitation in both the seep carbonates and tubular concretions was derived from anaerobically oxidised methane, as supported by lipid biomarkers. Isotope groups 3 and 4 ($\delta^{13}C$ –39.7 to 0‰ PDB) reflect a diminishing methane supply and influence from marine bicarbonate.

6) Oxygen isotope values for isotope groups 1, 2, and 5 ($\delta^{18}O$ –4.2 to +4.2‰) indicate that marine fluids were influenced by the formation and dissociation of methane hydrates during carbonate precipitation. Isotope group 3 ($\delta^{18}O$ from –5.9 to –5.7‰) reflects precipitation at burial depths for seep carbonates between 150 and 300 m and for tubular concretions from 300 to 800 m.

7) The tubular concretions at Rocky Knob demarcate part of the plumbing system of the overlying main carbonate seep complex which expelled methane onto the seafloor along the middle Miocene Hikurangi continental margin.

7. References

Adams, J.H., 1910. The geology of the Whatatutu subdivision, Raukumara division, Poverty Bay. New Zealand Geological Survey Branch Bulletin 9 (new series), 1–48.

Beu, A.G., Maxwell, P.A., 1990. Cenozoic mollusca of New Zealand. New Zealand Geological Survey Paleontological Bulletin, 58, 1–518.

Beu, A.G., 1995. Pliocene limestones and their scallops: lithostratigraphy, pectinid biostratigraphy and paleogeography of eastern North Island Late Neogene limestone. Lower Hutt: Institute of Geological and Nuclear Sciences. Institute of Geological and Nuclear Sciences Monograph, 10, 243 pp.

Campbell, K.A., Francis, D.A., Collins, M., Gregory, M.R., Nelson, C.S., Greinert, J., Aharon, P., 2008. Hydrocarbon seep-carbonates of a Miocene forearc (East Coast Basin), North Island, New Zealand. Sedimentary Geology, 204, 83-105.

Clari, P.,S. Cavagna, Martire, L., Hunziker, J., 2004. A Miocene mud volcano and its plumbing system: A chaotic complex revisited (Monferrato, MW Italy). Journal of Sedimentary Research, 74, 662-676.

Coleman, D.D., Risatti, J.B., Schoell, M., 1981. Fractionation of carbon and hydrogen isotopes by methane-oxidising bacteria. Geochimica et Cosmochimicha Acta, 45, 1033-1037.

Collins, M., 1999. A biometric and taxonomic study of Miocene-age, hydrocarbon seep mussels from the East Coast of the North Island, New Zealand. MSc thesis, University of Auckland, Auckland, 67 pp.

Cowen, J.P., Wen, X., Popp, B.N., 2002. Methane in aging hydrothermal plumes. Geochimica et Cosmochimicha Acta, 66, 3563-3571.

Davidson, D.W., Leaist, D.J., Hesse, R., 1983. Oxygen-18 enrichment in water of a clathrate hydrate. Geochimicha et Cosmochimica Acta, 47, 2293-2295.

DeMets, C., Gordon, R.G., Argus, D.F., Stein, S., 1994. Effect of recent revisions to the geomagnetic reversal time scale on estimates of current plate motions. Geophysical Research Letters, 21, 2191-2194.

Feary, D.A., Davies, P.J., Pigram, C.J., Symonds, P.A., 1991. Climatic evolution and control on carbonate deposition in northeast Australia. Palaeogeography, Palaeoclimatology, Palaeoecology, 89, 341-361.

Fergusson, L., 1985. The mineralogy, geochemistry and origin of lower Tertiary smectite-mudstones, East Coast Deformed Belt, New Zealand. Unpublished MSc thesis, University of Canterbury, Christchurch, New Zealand.

Field, B.D., Uruski, C.I., and others, 1997. Cretaceous-Cenozoic geology and petroleum systems of the East Coast Region, New Zealand. Institute of Geological and Nuclear Sciences Monograph, 19, 301 pp.

Francis, D.F., 1997. Oil and Gas Generation in the East Coast Basin – an update. Petroleum Exploration in New Zealand News, volume 51, October 1997.

Francis, D., Bennett, D., Courteney, S., 2004. Advances in understanding of onshore East Coast Basin structure, stratigraphic thickness and hydrocarbon generation. 2004 New Zealand Petroleum Conference Proceedings, Auckland, 7-10 March 2004. 20 pp.

Friedman, I., O'Neil, J.R., 1977. Compilation of stable isotope fractionation factors of geochemical interest. In: Fleisher, M., (Ed.), U.S. Geological Survey Professional Paper, 440-kk.

Goldsmith, J.R., Graf, D.L., Heard, H.C., 1961. Lattice constants of the calcium-magnesium carbonate. The American Mineralogist, 46, 453-457.

Greinert, J., Bialas, J., Lewis, K., Suess, E., in review. Methane seeps and gas hydrates offshore New Zealand's North Island: Compiling results from three

cruises in 2006 and 2007. Submitted to Marine Geology, methane seeps special publication.

Henderson, J., Ongley, M., 1920. The geology of the Gisborne and Whatatutu Subdivisions, Raukumara Division. New Zealand Geological Survey Bulletin, 21, 1–88.

Kamp, P.J.J., Nelson, C.S., 1988. Nature and occurrence of modern and Neogene active margin limestones in New Zealand. New Zealand Journal of Geology and Geophysics, 31, 1–20.

Kamp, P.J.J., Furlong, K.P., 2006. Neogene plate tectonic reconstructions and geodynamics of North Island sedimentary basins: Implications for the petroleum systems. 2006 New Zealand Petroleum Conference Proceedings, Auckland, 6-8 March 2006, 16 pp.

Lee, J.M., Begg, J.G., compilers, 2002. Geology of the Wairarapa Area. Institute of Geological and Nuclear Sciences Limited, Lower Hutt, N. Z., 66 pp.

Lewis, K.B., Pettinga, J.R., 1993. The emerging imbricate frontal wedge of the Hikurangi Margin. In: South Pacific Sedimentary Basins of the World, 2. Ballance, P.F. (Ed.), Elsevier Science Publishers B.V. Amsterdam. Pp. 225-250.

Lewis, K.B., Marshall, B.A., 1996. Seep faunas and other indicators of methane-rich dewatering on New Zealand convergent margins. New Zealand Journal of Geology and Geophysics, 39, 181-200.

Mazengarb, C., Francis, D.A., Moore, P.R., 1991. Geological map of New Zealand, 1:50,000, Sheet Y16, Geology of the Tauwhareparae area. New Zealand Geological Survey, Wellington, New Zealand.

McCrea, J.M., 1950. On the isotopic chemistry of carbonates and a paleotemperature scale. The Journal of Chemical Physics, 18, 849-857.

McKay, A., 1877. On the geology of east Auckland and the northern district of Hawke's Bay. New Zealand Geological Survey, Reports of Geological Explorations during 1886–1887 (No. 18), pp. 183–219.

Munnecke, A., Samtleben, C., 1996. The formation of micritic limestones and the development of limestone-marl alternations in the Silurian of Gotland, Sweden. Facies, 34, 159-176.

Nelson, C.S., Smith, A.M., 1996. Stable oxygen and carbon isotope compositional fields for skeletal and diagenetic components in New Zealand Cenozoic nontropical carbonate sediments and limestones: a synthesis and review. New Zealand Journal of Geology and Geophysics, 39, 93-107.

Nelson, C.S., Winefield, P.R., Hood, S.D., Caron, V., Pallentin, A., Kamp, P.J.J., 2003. Pliocene Te Aute limestones, New Zealand: expanding concepts for cool-water shelf carbonates. New Zealand Journal of Geology and Geophysics, 46, 407-424.

Pancost, R.D., Damasté, J.S., De Lint, S., Van Der Maarel, M.J.E.C., Gottschal, J.C., Medinaut Shipboard Scientific Party, 2000. Biomarker evidence for widespread anaerobic methane oxidation in Mediterranean sediments by a consortium of methanogenic archaea and bacteria. Applied Environmental Microbioliology, 66, 1126-1132.

Pearce, A.R., Black, R.D., Nelson, C.S., 1981. Lithologic and weathering influences on slope form and process, eastern Raukumara Range, New Zealand. International Association of Hydrology Science, 132, 95-122.

Pearson, M.J., Grosjean, E., Nyman, S.L., Logan, G.A., Nelson, C.S., Hood, S.D., Campbell, K.A., 2008. Tubular concretions in New Zealand petroliferous basins: Lipid evidence for mineralization around proposed Miocene hydrocarbon seep conduits. 2008 New Zealand Petroleum Conference Proceedings, Auckland, 10-12 March 2008, 6 pp.

Ridgway, N.M., 1969. Temperature and salinity of sea water at the ocean floor in the New Zealand region. New Zealand Journal of Marine and Freshwater Research, 3, 57-72.

Roberts, H.H., Aharon, P., 1994. Hydrocarbon-derived carbonate buildups of the northern Gulf of Mexico continental slope: A review of submersible investigations. Geo-Marine Letters, 14, 135-148.

Rogers, K.M., Collen, J.D., Johnston, J.H., Elgar, N.E., 1999. A geochemical appraisal of oil seeps from East Coast Basin, New Zealand. Organic Geochemistry, 30, 593-605.

Schwartz, H., Sample, J., Weberling, K.D., Minisini, D., Moore, J.C., 2003. An ancient linked fluid migration system: cold-seep deposits and sandstone intrusions in the Panoche Hills, California, USA. Geo-Marine Letters, 23, 340-350.

Ussler III, W., Paull, C.K., 1995. Effects of ion exclusion and isotopic fractionation on pore water geochemistry during gas hydrate formation and decomposition. Geo-Marine Letters, 15, 37-44.

Whiticar, M.J., 1999. Carbon and hydrogen isotope systematics of bacterial formation and oxidation of methane. Chemical Geology, 161, 291-314.

CHAPTER 7

Overview synthesis of New Zealand tubular concretions and schematic subsurface hydrocarbon seep model

1. Introduction

Tubular concretions have been described in association with hydrocarbon seeps worldwide (Fig. 1) (Judd and Hovland, 2007). They have been interpreted to form in the subsurface and delineate subsurface plumbing systems beneath the seafloor expression of seepage. However, to date these subsurface systems of cold seeps have received relatively little attention. Some exceptions include the studies noted in Table 1.

Previous studies have investigated tubular concretions exposed on the modern seabed both near active seepage sites (Jensen et al., 1992; Stakes et al., 1999; Díaz-del-Río et al., 2003) and without evidence of active seepage (Orpin, 1997) (Table 1, Fig. 1). These examples have provided evidence of tubular concretions forming within the overall time frame of seepage in the region and/or concurrent with modern MDACs. Díaz-del-Río et al. (2003) noted the wide variety of tubular concretions littering the seabed in the Gulf of Cadiz and established a classification scheme based on their morphology: pipes with bifurcations, branches, bends, tapers, protuberances, etc. Additionally, seafloor tubular concretions have been interpreted to record focused (high volume) fluid migration with variable flow rates and compositions over time (Stakes et al., 1999; Díaz-del-Río et al., 2003).

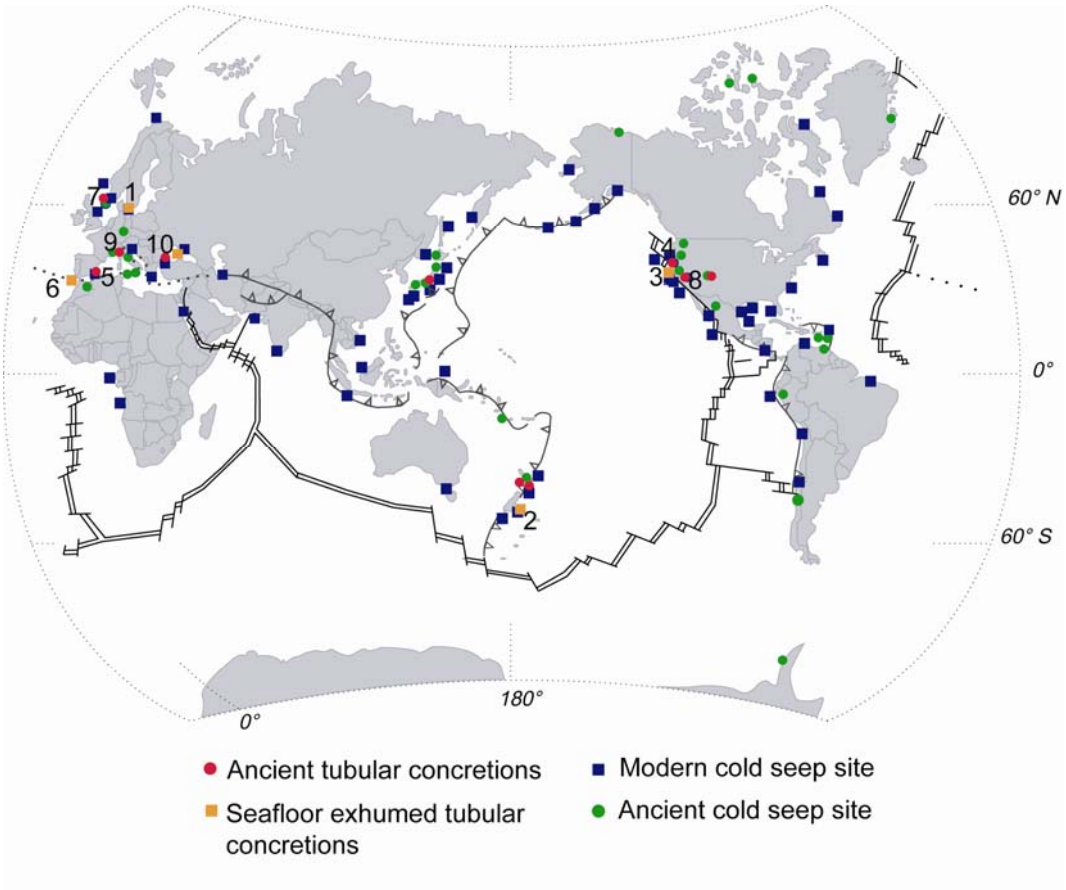

Figure 1. Global occurrences of reported ancient tubular concretions, exhumed tubular concretions on the seafloor (most near active seep sites), ancient cold seep carbonates, and modern cold seep carbonates (adapted and extended from Campbell, 2006). Numbers 1 to 10 correspond to tubular concretion examples described in Table 1.

Ancient examples of tubular concretions exposed beneath or nearby seafloor MDACs (Schwartz et al., 2003; Clari et al., 2004), or without evidence of associated seafloor MDACs (Aiello et al., 1999, 2001; Lédesert et al., 2003; De Boever et al., 2006), have provided further evidence that the tubular concretions afford records of evolving seep systems (Table 1, Fig. 1). Unlike the exhumed seafloor tubular concretions, the ancient examples more clearly demonstrate their spatial and temporal placement and 3D geometry within the seep system and help constrain the factors governing seep development.

In general, both seafloor exposed (i.e. exhumed) and ancient tubular concretions have been interpreted to have developed within the seabed from the ascent of either microbial or thermogenic methane, mainly based on their stable carbon and oxygen isotope values (Table 1). Some tubular concretions have been inferred to have formed from methane hydrate dissociation (e.g., Pierre et al., 2002, Pierre and Rouchy, 2004; Gieskes et al., 2005; Clari et al., 2004; Díaz-del-Río et al., 2003). Table 1 summarises several different properties of the overseas tubular concretions, along with the reported interpretations of their fluid sources (see Chapter 2, section 11 for further comments). A $\delta^{13}C$ – $\delta^{18}O$ cross plot for the isotope data reported in these global examples is shown in Figure 2.

2. New insights from New Zealand tubular concretions

Overall, the North Island, New Zealand tubular concretions are the most geographically, morphologically, and geochemically diverse examples known to date. They are sporadically present across a large geographic region (North Island's Taranaki and East Coast Basins, ~114,000 km^2), in over 25 confirmed locations and, in places, occur nearby or directly beneath ancient seep carbonates (Fig. 3). Additionally, many of the tubular concretions are situated in the East Coast Basin where onshore oil/gas seeps, off- and onshore mud volcanoes, and offshore hydrocarbon seeps are currently active (Lewis and Marshall, 1996; Francis, 1997; Greinert et al., in review). Thus, this study is the first location in the world where tubular concretions have been studied in such a diversity of geologic settings and in clear geographic proximity to either modern or ancient

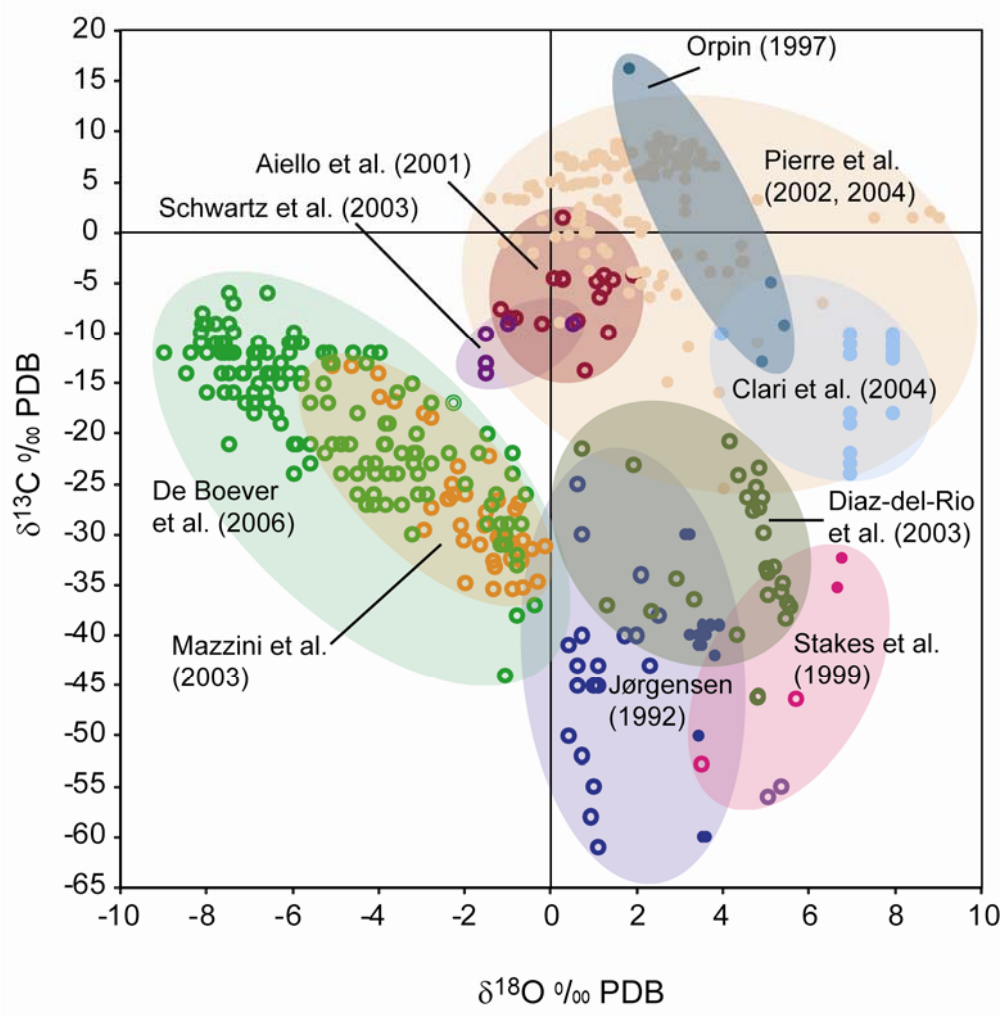

Figure 2. Stable oxygen and carbon isotope plot for global examples of tubular concretions recorded in Table 1. Note the tendency for tubular concretions to plot in the lower left portion and right half of the diagram. In particular, dolomite samples (solid circles) tend to cluster towards the upper right side of the graph (typically positive $\delta^{13}C$ and $\delta^{18}O$), while calcitic samples (open circles) trend more towards moderately to strongly negative $\delta^{13}C$ values.

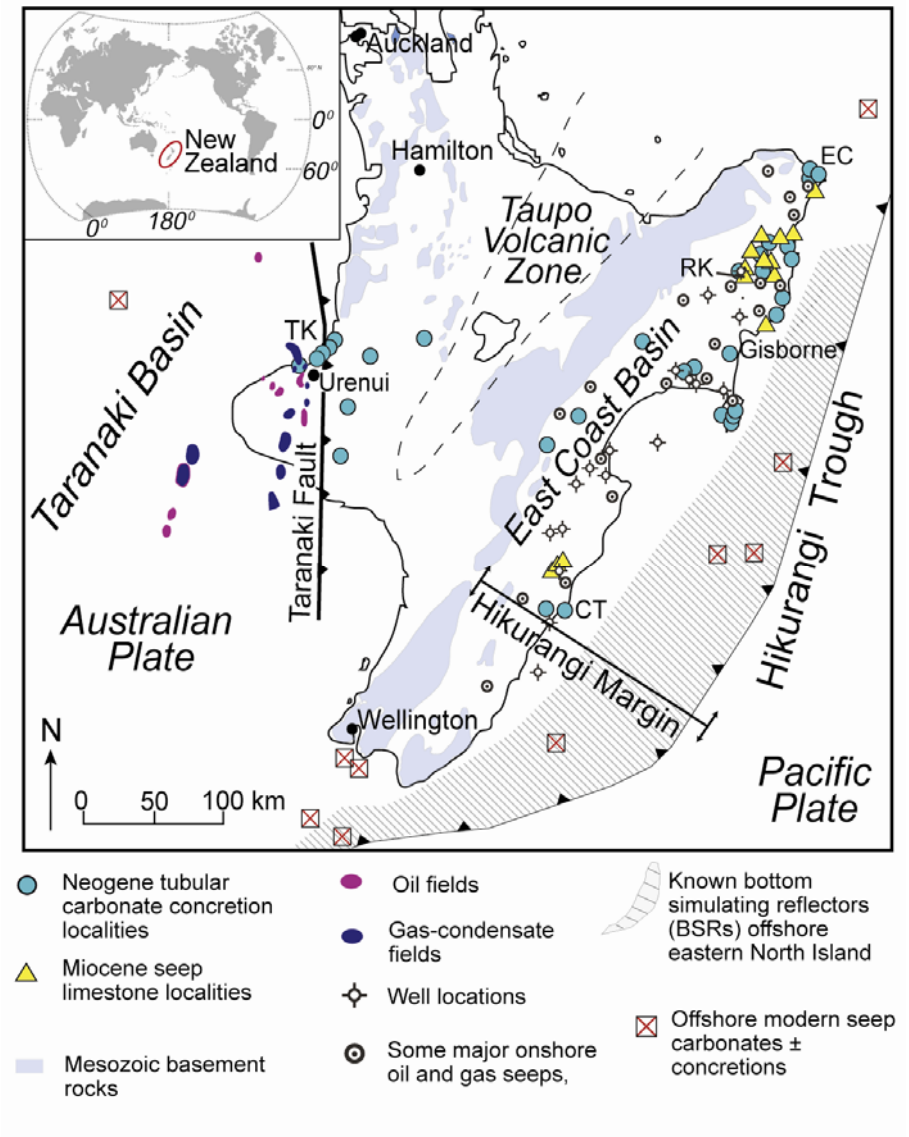

Figure 3. Generalised locality map of some tubular concretion sites in Neogene rocks of North Island, New Zealand. The two main study regions in this research are onshore eastern Taranaki Basin and onshore East Coast Basin. Main study locations are Taranaki (TK), Cape Turnagain (CT), East Cape (EC), and Rocky Knob (RK). Also shown are the locations of some Miocene paleoseep limestones, offshore modern seep carbonates, the area of offshore known bottom simulating reflectors (due to gas hydrate), and some oil and gas fields, well locations in East Coast Basin, and major onshore oil and gas seeps in East Coast Basin. Based on information in Francis (1997), Lewis and Marshall (1996), Nelson et al. (2004), Shellenberg (2002), Peter King (GNS Science), and from personal communication with Dave Francis (Geological Research Ltd, Lower Hutt) and personal observations. Tubular concretion locality information is derived mainly from personal observations. Producing oil and gas locations from Crown Minerals: http://www.crownminerals.govt.nz/petroleum/index.asp.

Figure 4. Stable carbon and oxygen isotope cross-plot for (A) New Zealand and (B) global tubular concretions (Table 1). Plots do not include late stage cement fills (i.e., burial diagenetic cements) in vugs, or conduit fills of the tubular concretions. (A) New Zealand tubular concretion classes (grey ovals; see Section 3.7) and some possible environmental controls on their formation. The carbon source for the tubular carbonate concretions is from the anaerobic oxidation of methane (AOM). Samples in the lower part of the diagram (Class 1) formed during either abundant methane supply and/or near a main methane migration pathway. The trend of all samples from the lower half of the plot towards the upper right side (red arrow) is related to a diminishing methane supply and/or distance from the main methane migration pathway. A diminishing methane supply also equates to decreases in SO_4^{2-} concentration, Ca/Mg ratio, and fluid pressure/buoyancy, resulting ultimately in dolomitic bulbous concretions with strongly positive carbon isotope values. The East Cape doughnut concretions also follow this trend but, unlike the bulbous concretions, they are oval in shape with a central conduit. This is interpreted to reflect fault valve action releasing finite amounts of methane which get trapped as a 'bubble' once buoyancy is lost. Tubular concretions towards the left side of the plot are interpreted to have formed during times of methane hydrate formation (Classes 1A and 2A), while those towards the right side are interpreted to be more associated with phases of methane hydrate dissociation (Classes 1B, 2B, and 3). Samples between the extremes (rectangle indicating Miocene New Zealand marine fluid composition; blue = calcite, green = dolomite) may have formed in normal marine fluids and/or mixing of fluids evolved from hydrate formation/dissociation. Samples are plotted by location and main morphology (pipe, bulbous, doughnut). Open symbols are calcitic tubular concretions, closed symbols are dolomitic tubular concretions, and the plus symbols are aragonite samples (Rocky Knob conduits only). Stages correspond to Figure 6 and illustrate the development of the subsurface seep system overtime from the onset of methane migration (stage 1), methane hydrate formation and dissociation (stage 1 to 2), through to extensively oxidised methane and diminished methane supply (stage 2 to 3). (B) New Zealand tubular concretion classes (grey ovals) superimposed on isotope fields of global examples. Colours for global examples correspond to those in Figure 2. Some previous interpretations of the global examples could be re-evaluated based on the new information from the New Zealand tubular concretions (Table 1).

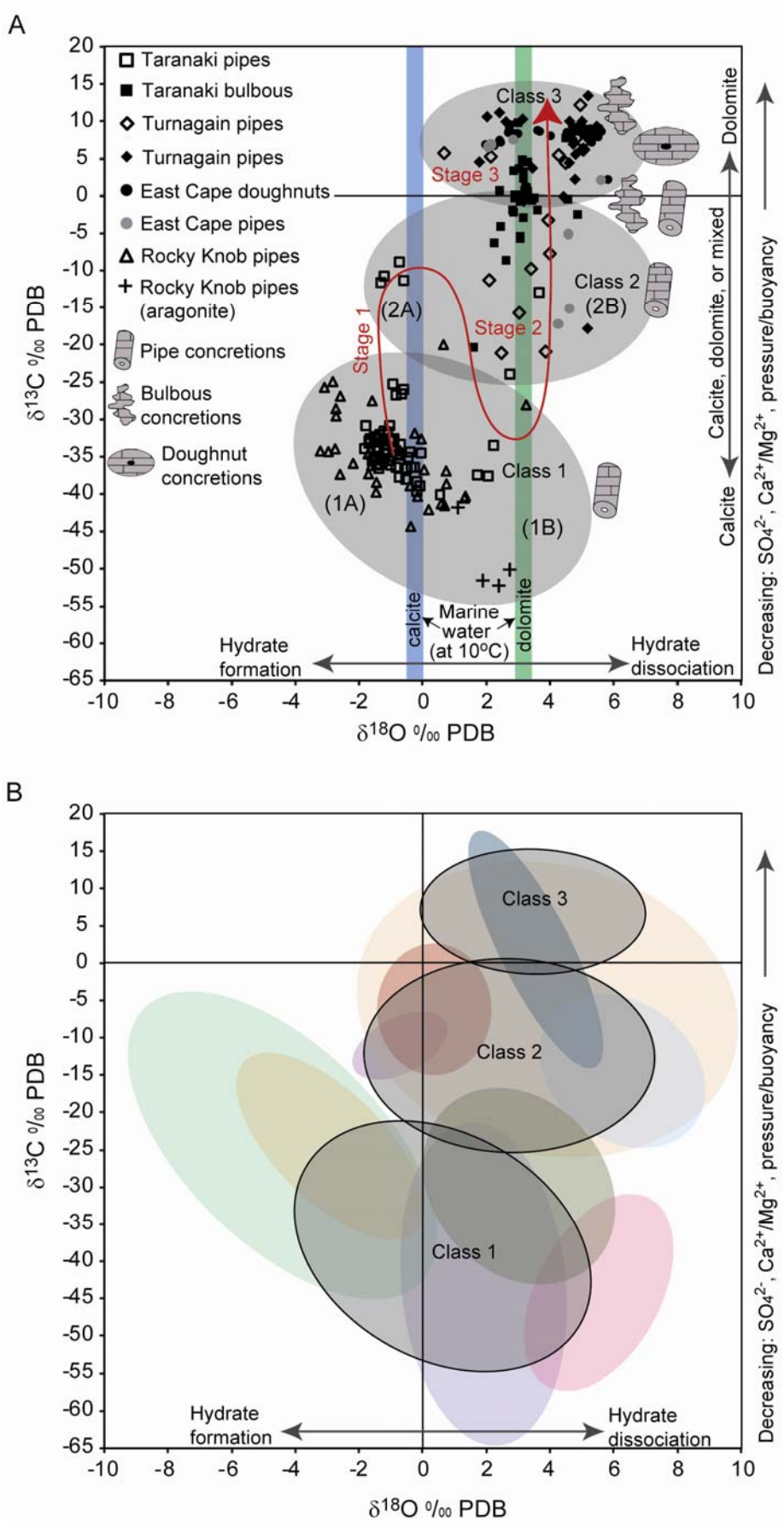
A
Taranaki pipes
Taranaki bulbous
Turnagain pipes
Turnagain pipes
East Cape doughnuts
East Cape pipes
Rocky Knob pipes
Rocky Knob pipes (aragonite)
Pipe concretions
Bulbous concretions
Doughnut concretions
Class 3
Stage 3
Class 2
(2B)
(2A)
Stage 2
Stage 1
Class 1
(1A)
(1B)
calcite
dolomite
Marine water (at 10°C)
Hydrate formation
Hydrate dissociation
Dolomite
Calcite, dolomite, or mixed
Calcite
Decreasing: SO_4^{2-}, Ca^{2+}/Mg^{2+}, pressure/buoyancy
$\delta^{13}C$ ‰ PDB
$\delta^{18}O$ ‰ PDB
B
Class 3
Class 2
Class 1
Hydrate formation
Hydrate dissociation
Decreasing: SO_4^{2-}, Ca^{2+}/Mg^{2+}, pressure/buoyancy
$\delta^{13}C$ ‰ PDB
$\delta^{18}O$ ‰ PDB

seepage. This investigation confirms that the diverse types of tubular concretions delineate the near-seabed portions of subsurface plumbing systems for ascending hydrocarbon rich fluids, that they are genetically related to seafloor seep carbonates, sediment instability and erosion, and/or possibly sea level change. Moreover, the study records the potential role of gas hydrate formation and dissociation within the subsurface plumbing system, and of fault control on fluid flow and intermittent fluid ascent.

The great variations in mineralogy and isotope geochemistry of the New Zealand tubular concretions span the spectrum of ranges previously reported for cold seep associated carbonates (Table 1, Figs. 2, 4). Although their characteristics vary considerably, trends associated with formation conditions are clearly discernible (Section 3). The diverse nature of the New Zealand tubular concretions has resulted in the opportunity to develop schematic models for their site-specific formation (Chapters 3 – 5). Here, the formation mechanisms are combined to produce a comprehensive model of tubular concretion formation in New Zealand, one which has direct implications for interpretations of the subsurface hydrocarbon seep system. Moreover, this integrated subsurface model is combined with information on the development of ancient New Zealand seafloor seep carbonates to produce the first comprehensive schematic hydrocarbon seep model (Section 4). Importantly, such a model may be used as an ancient analogue for the modern Hikurangi Margin cold seeps offshore eastern North Island (Greinert et al., in review).

3. Summary of New Zealand tubular concretions

The tubular carbonate concretions from Miocene [and Pliocene] outer shelf and upper slope marine mudrocks in the North Island of New Zealand are located in the presently tectonically passive eastern margin of Taranaki Basin, along the coastline near Urenui and inland, and throughout the tectonically active East Coast Basin from East Cape in the north to Cape Turnagain (Fig. 3). East Coast Basin examples are located nearby ancient seep carbonates and modern hydrocarbon seeps (Campbell et al., 2008). Modern seepage in the basin occurs

Table 1. Examples of tubular concretions from the literature and their interpreted origins based mainly on stable carbon and oxygen isotope compositions. Plots of the latter are shown in Figure 2.

Author	Location	Age	Mineralogy	$\delta^{13}C$ ‰ PDB (range)	Carbon isotope interpretation	$\delta^{18}O$ ‰ PDB (range)	Oxygen isotope interpretation	Possible New Zealand tubular concretion class (see Fig. 4)
1. Jørgensen et al. (1992)	Kattegat, Denmark	Exposed on modern seafloor	Dolomite	-61 to -34	AOM	+3.2 to +4.1	N/A	Class 1B
			Calcite and aragonite	-57 to -26	AOM	+0.4 to +2.8	Normal marine conditions	Class 1*
2. Orpin (1997)	New Zealand, Otago Shelf	Exposed on modern seafloor in Miocene sediments	Dolomite	-12.8 to -4.9	Degradation of organic matter	+4.9 to +5.4	Normal marine conditions	Class 2B
			Dolomite	+16.3	Residual carbon from methanogenesis	+1.8	Normal marine conditions	Class 3
3. Stakes et al. (1999)	Monterey Bay, Santa Cruz, California	Exposed on modern seafloor	Dolomite; Calcite	-56.0 to -46.4; -35.3 to -32.4	AOM	+3.48 to +5.68; +6.6 to +6.7	N/A	Class 1B
4. Aiello et al. (2001)	Monterey Bay, Santa Cruz, California	Miocene	Low-Mg calcite	-9 to -4	AOM or residual carbon from methanogenesis	-1.2 to +1.9	Normal marine conditions, low temperature fluids	Class 2*
5. Pierre et al. (2002, 2004)	Lorca Basin, Mediterranean	Late Miocene	Dolomite	-26 to +10	Residual carbon from methanogenesis (majority of samples have $\delta^{13}C$ ‰ PDB > 0	-2 to +5	Hydrate dissociation	Class 3
6. Díaz del Río et al. (2003)	Gulf of Cadiz, Portugal	Exposed on modern seafloor	Fe-dolomite, ankerite, calcite	-40 to -20	AOM	+0.5 to +6	Episodic hydrate dissociation (lower values not during dissociation)	Class 1B
7. Mazzini et al. (2003)	Gryphon Field, North Sea	Tertiary	Calcite	-35.5 to -18	AOM	-2.9 to -0.1	Shallow burial of mixed marine/meteoric fluids	Class 1A
8. Schwartz et al. (2003)	Panoche Hills, California	Cretaceous to Paleocene (seep carbonate in Paleocene only)	Mostly Mg calcite; some dolomite and calcite	-14 to -9	Mixing between thermogenic and microbial methane oxidation and seawater bicarbonate	-1.5 to +0.5	Normal marine conditions	Class 2A
9. Clari et al. (2004)	Monferrato, Italy	Miocene	Dolomite	-25 to -10	Mixing between AOM and marine bicarbonate	+4 to +8	Hydrate dissociation	Class 1B and 2B
10. De Boever et al. (2006)	Varna, Bulgaria	Lower Eocene	Calcite	-43 to -8	Methane derived carbon. Samples with less negative $\delta^{13}C$ values were possibly sourced from mixing of methane with marine bicarbonate and/or residual carbon from methanogenesis	-8 to -1	Marine fluids (higher values) to elevated temperatures (lower values). Lower values are suggested to have resulted from higher fluid flow rates	Class 1A

* Class 1 or 2 concretions with $\delta^{18}0$ near 0 ‰ PDB are probably due to normal marine conditons (not hydrates)

AOM = anaerobic oxidation of methane

N/A = interpretation was not discussed in paper

both onshore and offshore, and includes mud volcanoes (Greinert et al., in review; Francis, 1997; Dave Francis, personal communication, 2006). Additionally, gas hydrates are forming along the modern Hikurangi Margin (Lewis and Marshall, 1996; Barnes et al., accepted; Greinert et al., in review). The tubular concretions in Taranaki Basin are located within an active oil and gas producing region (King and Thrasher, 1996). The morphology of all the tubular concretions varies from pipe to bulbous, sinuous pipe, doughnut, and conical. The tubular concretions have been interpreted to have formed from the anaerobic oxidation of microbial (and potentially thermogenic) methane based on stable carbon isotope values and lipid biomarkers (Chapters 3-6). Oxygen isotopes suggest that some concretions formed from waters of marine composition while others are inferred to have formed from the cyclic formation and dissociation of gas hydrates. Sections 3.1 to 3.4 summarise the characteristics and interpretations of the New Zealand tubular concretions at the four main study sites, as gleaned from Chapters 3 to 6.

3.1 Taranaki tubular concretions

The Taranaki tubular carbonate concretions in late Miocene slope mudstones of the Urenui Formation in eastern Taranaki Basin (Fig. 3) exhibit pipe and bulbous morphologies, range widely in size (0.5 to 10 m in length and 5 to 70 cm in diameter), and support a central open or sediment/crystalline spar filled conduit. They formed from shallow burial (<300 m) precipitation of micritic calcite (pipe) and dolomite (bulbous) within siliciclastic mud (Table 2).

Taranaki calcitic pipe concretions have $\delta^{13}C$ values from –40 to –26‰ PDB and $\delta^{18}O$ values from –2 to +3‰ PDB (Table 2, Fig. 4A). The carbon for calcite precipitation in the pipe concretions is interpreted to have been sourced from anaerobically oxidised methane, as supported by lipid biomarkers, especially pentamethyl icosane, C33 dialkyl glycerol diether, and macrocyclic diether (Pearson et al., 2008). The $\delta^{18}O$ values of the calcitic pipe concretions plot in two distinct regions on a $\delta^{13}C$ vs $\delta^{18}O$ graph (Table 2, Fig. 4A) and reflect either variable temperatures of marine fluids and/or marine fluids influenced by cycles of formation and dissociation of gas hydrates. However, elevated temperatures

Table 2. Class descriptions for New Zealand tubular concretions. Location abbreviations: Taranaki Basin (TB), Cape Turnagain (CT), East Cape (EC), and Rocky Knob (RK).

Class	Morphology	Mineralogy	δ^{13}C ‰ PDB (range)	δ^{18}O ‰ PDB (range)	Interpretation
Class 1A / TB	Pipe	Calcite	-44.2 to -25.3	-3.2 to 0.0	Carbonate precipitation from AOM* in marine fluids influenced by gas hydrate formation
Class 1B / TB, RK	Pipe; sinuous pipe	Aragonite; (calcite)	-52.3 to -28	0.0 to +2.7	Carbonate precipitation from AOM* in marine fluids influenced by gas hydrate dissociation
Class 2A / TB	Sinuous pipe	Calcite	-11.7 to+ 8.9	-1.3 to 0.0	Carbonate precipitation from extensive AOM* (~40% of methane pool has been oxidised) in marine fluids influenced by gas hydrate formation
Class 2B / TB, CT, EC	Sinuous pipe; (bulbous)	Calcite (dolomite; EC dolomite only)	-24.0 to 0.0	0.0 to +5.2	Carbonate precipitation from extensive AOM* (~40% of methane pool has been oxidised) in marine fluids influenced by gas hydrate dissociation
Class 3 / TB, CT, EC	Bulbous and doughnuts	Dolomite; (calcite)	0.0 to +13.5	+0.7 to +5.8	Carbonate precipitation from extensive AOM* (~80% of methane pool has been oxidised) in marine fluids influenced by gas hydrate dissociation

*AOM = anaerobic oxidation of methane

cannot explain the positive $\delta^{18}O$ values, therefore cycles of hydrate formation and dissociation is the favoured mechanism to explain the slightly depleted and enriched (with respect to marine waters) $\delta^{18}O$ values with respect to marine water compositions.

Taranaki dolomitic bulbous concretions have $\delta^{13}C$ values from –10 to +11‰ PDB and $\delta^{18}O$ values from +1 to +5‰ PDB (Table 2, Fig. 4A). The strongly enriched carbon isotope values in the bulbous concretions reflect carbon sourced from extensively oxidised methane where >80% of the methane had been oxidised by the time the bulbous concretions formed. Oxygen isotope values of the bulbous concretions are interpreted to have resulted from gas hydrate formation and dissociation based on the discussion in Chapter 3, Section 5.1.2.

Calcitic pipe concretions formed in the early stages of AOM methane oxidation when sulphate and Ca^{2+} concentrations, and fluid pressures, were high. In comparison, the dolomitic bulbous and irregular concretions are suggested to have formed during late stages of AOM when sulphate concentrations, Ca^{2+} concentrations, and fluid pressures had all decreased.

The presence of reworked tubular concretions in channel fills within the Urenui Formation suggest that slope instability and subsequent channel excision may have resulted from injection of the hydrocarbon fluids into slope margin muds. Prominent seafloor features of hydrocarbon seep systems, such as paleo-seafloor seep carbonates and chemosynthesis based communities, appear to be lacking in the Urenui mudstone. However, based on the evidence of AOM (isotope values and lipid biomarkers) and extensive channelised units in the Urenui Formation, it is probable that the late Miocene hydrocarbon seep system in Taranaki Basin did at that time reach the seabed.

3.2 Cape Turnagain tubular concretions

Tubular carbonate concretions of the late Miocene Whangaehu Mudstone at Cape Turnagain (Fig. 3) formed from shallow burial (<300 m) precipitation of micritic dolomite (and some calcite) within upper slope siliciclastic mud. The concretions

mainly exhibit pipe, sinuous (corkscrew), conical, and bulbous morphologies, range widely in size (0.1 to 5 m in length and 0.1 to 1 m in diameter), and support a central open or sediment/crystalline spar filled conduit (Table 2).

Carbon isotope values ($\delta^{13}C$ –20 to +12‰) suggest that the carbon for carbonate precipitation in the tubular concretions was derived from anaerobically oxidised methane (cf., Chapter 4, Section 5.1.1), as supported by lipid biomarkers (pentamethyl icosane, C33 dialkyl glycerol diether, and macrocyclic diether; Pearson et al., 2008) (Table 2). The strongly enriched carbon isotope values require >80% of the methane to have been oxidised by the time the Whangaehu tubular concretions formed. Heavy oxygen isotope values ($\delta^{18}O$ +1 to +5‰) in the cement of the tubular concretions indicate the $\delta^{18}O$ composition of the water was influenced by the dissociation of gas hydrates (Table 2, Fig. 4A).

There is no clear evidence in the Whangaehu Mudstone whether the fluids reached the seafloor; however, indirect evidence suggests that seafloor fluid expulsion was likely. Minus cement porosities (50-85%) indicate the tubular concretions formed between syn-depositional conditions and < 300 m burial. The sinuous morphology, branching, and coalescing of many small tubular concretions is similar to that of tubular concretions found just below a paleo-seafloor seep carbonate in the East Coast Basin (i.e., Rocky Knob, Chapter 6). Strongly brecciated blocks may suggest near seafloor carbonate precipitation in zones of higher permeability (i.e., depositional permeability) where fluids were able to move laterally and were not restricted to focused flow pathways. High cementation and fluid flow rates may have resulted in hydrofracturing to form fissures and zones of intensely brecciated clasts. Additionally, the age progression of seep related features from inland (early Miocene) to coastal (late Miocene) to offshore on the Hikurangi Margin (modern) suggest that seafloor seepage along the East Coast Basin has been long lived, if intermittent, through the Neogene.

3.3 East Cape tubular concretions

The East Cape tubular concretions in late Miocene slope mudstones of the Pohutu Formation, East Coast Basin (Fig. 3), are predominantly doughnut morphologies, average 4 m in diameter, and support a central conduit. Most conduits are filled by sediment of differing composition from the surrounding concretion, but are cemented by the same phase of micritic dolomite. The doughnut concretions formed within the shallow burial zone (<300 m) from the precipitation of micritic dolomite cement within the interparticle spaces of siliciclastic mud (Table 2).

The carbon and oxygen isotope values for the precipitated carbonate in the East Cape tubular concretions ($\delta^{13}C$ from +6 to +9‰ PDB and $\delta^{18}O$ values from +2 to +6‰ PDB) suggest that the carbon was derived from extensive anaerobic oxidation of methane (cf., Chapter 5, Section 5.1.1), as supported by lipid biomarkers (pentamethyl icosane, C33 dialkyl glycerol diether, and macrocyclic diether; Pearson et al., 2008) and from gas hydrate dissociation (Table 2, Fig. 4A).

Fluid ascent is interpreted to have resulted from periodic repeated faulting in which faults afforded a valve-like mechanism, rupturing whenever fault strength was exceeded by fluid pressure built up (cf., Sibson, 1992). Fault rupture created a permeability pathway for fluid ascent, but after mineral precipitation and fluid pressures decreased, the fault sealed, trapping fluids. Cyclic fluid ascent and trapping was repeated as fluids continued to be supplied from deeper sources. Tubular concretion formation occurred after fault rupture and in many cases continued through subsequent fault ruptures.

3.4 Rocky Knob tubular concretions

Tubular carbonate concretions of the Rocky Knob seep complex (Fig. 3), in middle Miocene deep water mudstones, are the only example in this study where tubular concretions are exposed directly below ancient seafloor seep carbonates. The tubular concretions mainly exhibit pipe (sinuous, branching, and coalescing) morphologies, range from 5–12 cm in diameter (length unknown due to outcrop limitations), and support a central open or sediment/crystalline spar filled conduit

(Table 2). They formed from carbonate precipitation within siliciclastic mud in the subsurface. Concretion and conduit development comprises (1) micritic carbonate in the outer concretion; (2) fibrous aragonite which lines the boundary between the main concretion and conduit; (3) emplacement of breccia clasts in the conduit; (4) granular to clotted calcite filling the conduit; (5) bladed and blocky calcite lining vugs in the conduits; and (6) in some conduits, dark grey micrite cemented rounded peloids present in the centre of the conduit fill. This paragenetic sequence is mirrored in the associated paleo-seafloor seep carbonate deposits. Carbon isotope values for the tubular concretions ($\delta^{13}C$ from –52.2 to –20‰ PDB) suggest that carbon was sourced from anaerobically oxidised methane, and oxygen isotope values ($\delta^{18}O$ from –4.2 to +4.2‰ PDB) indicate marine fluid compositions were influenced from the formation and dissociation of methane hydrates (Table 2, Fig. 4A).

3.5 Unique attributes of the four main study sites

Tubular concretions from North Island, New Zealand, are interpreted to represent the 'fossilised' fluid conduits of focused methane escape towards the paleo-seafloor. Characteristics of the tubular concretions (e.g., morphology, mineralogy, isotope geochemistry) record the compositions of the fluids that migrated through the sediments, fluid flow rates, and variations of these components over time. Additionally, each of the four main study locations offers a unique insight into subsurface seep systems (e.g., faulting, slope instability, and spatial and temporal variations) which provides further information regarding controls on the system development.

The Taranaki late Miocene concretions record both the early and late phases of methane migration. They are associated with slope instability. They are located directly above a major fault (Taranaki Fault). They display carbonate structures suggestive of sudden and catastrophic fluid expulsion (e.g., carbonate semi-circular rings).

The Whangaehu late Miocene tubular concretions record either waning methane migration through the Whangaehu slope mudstone, or fluid migration further from

the main methane migration pathways. The locality includes the widest range of tubular concretion morphologies, interpreted to reflect differences between fluid flow rates, focused vs less focused migration pathways, and relative depth differences beneath the seafloor as the subsurface seep system developed.

At East Cape, the late Miocene concretions are principally doughnut shaped with some pipe concretions. These concretions are intimately related to fault patterns within shore platform exposures and are interpreted to reflect upwards fluid migration along fault planes and subsequent 'bubble' like pockets of fluid forming whenever fluids became trapped during their ascent.

The Rocky Knob tubular concretions are the smallest in size of the studied New Zealand examples, and occur directly beneath a middle Miocene seafloor seep carbonate. These concretions likely represent an increasing array of fluid migration pathways as the fluids reached the paleo-seafloor.

3.6 Regional trends

Despite several specific differences amongst the New Zealand tubular concretion examples, there remain some remarkable similarities amongst concretion properties. Common trends amongst locations include: (1) cement mineralogy vs morphology; (2) mineralogy vs isotope values; (3) similarities and patterns amongst isotope values; and (4) isotope values vs paragenesis (within tubular concretions and compared with seep carbonates).

3.6.1 Cement mineralogy vs morphology

Most New Zealand tubular concretions are cemented by dolomite which records strongly positive carbon and oxygen isotope values that are interpreted to have formed during diminishing methane supply (Fig. 4A). These tubular concretions have predominately bulbous and doughnut morphologies, but a few pipe varieties also exhibit dolomitic cements (Table 2). Pipe tubular concretions, primarily from Taranaki and Rocky Knob localities, are generally cemented by calcite which

records strongly negative carbon isotope values and varying oxygen isotope values (Table 2, Fig. 4A).

3.6.2 Cement mineralogy vs carbon isotope values

In general, the New Zealand tubular concretions cemented by calcite display strongly negative carbon isotope values (Table 2, Fig. 4A). The dolomitic tubular concretions typically record strongly positive carbon isotope values. Additionally, the dolomitic tubular concretions usually correspond to strongly positive oxygen isotope values.

3.6.3 Isotope patterns

Carbon and oxygen isotope values for the tubular concretions (excluding any late stage cement or sediment fills in conduits) tend to plot in three distinct areas on a $\delta^{13}C$ vs $\delta\ ^{18}O$ diagram (Fig. 4A) with small overlap. These may reflect events of: (1) methane migration; (2) gas hydrate formation and therefore diminishing methane supply; (3) gas hydrate dissociation (with replenishing methane supply) and methane migration; and (4) diminishing methane supply. Transition between events may be gradational and tubular concretions may form during any of these events. Trends from the lower left to the upper right portions of the $\delta^{13}C$ vs $\delta\ ^{18}O$ plot in Figure 4A may record evolution of a seep system. The main methane migration event, and samples that were in close proximity to the main methane migration pathways, are represented by values in the lower left quadrant. The upper right quadrant represents samples formed during diminishing methane supply or further distance from the main methane migration pathways. Samples plotting on the left side of the $\delta^{13}C$ vs $\delta\ ^{18}O$ diagram represent periods of gas hydrate formation; whereas, the right side samples indicate periods of gas hydrate dissociation.

Interestingly, Cowen et al. (2002) reported strongly positive $\delta^{13}C$ isotope values of methane fluids from hydrothermal plumes along the Juan de Fuca Ridge. The $\delta^{13}C$ values of methane measurements became increasingly positive with distance from the main methane expulsion site. The trend in carbon isotope enrichment

with distance was interpreted to reflect extensive oxidation of the remaining methane, as discussed previously in Chapters 3 to 5. This trend could result in conditions where methane supply is exhausted due to: (1) gas hydrate formation; (2) distance from the main methane migration pathways (less methane to oxidise); (3) blockage and change of migration pathways; or (4) methane supply runs out.

3.6.4 Isotope values vs paragenesis

The general paragenetic sequence of carbonate cementation (Fig. 5) is (1) micritic carbonate in the concretion itself; (2) fibrous aragonite lining vugs in conduits; (3) granular carbonate fabrics in conduits; (4) blocky cements lining vugs in conduits; (5) micrite lining the blocky carbonate in vugs; or (6) micrite cemented sediment fills in the central conduit zone. The cementation sequence of micrite (in concretion proper), granular carbonate, and blocky carbonate occurs in all locations except East Cape, although not all cement fabrics are necessarily present in each sample. Micrite lining vugs only occur in some Taranaki samples and micrite cemented sediment fills occur only in some Rocky Knob samples.

The different cement fabrics imply varying fluid conditions during carbonate precipitation. Micrite (calcite or dolomite) between siliciclastic grains of the concretion indicates cementation within main fluid pathways where sediment evacuation and conduit development has not occurred. Granular fabrics precipitated in open (or partially open) conduits, commonly with breccia inclusions (clasts of surrounding concretion that have been broken off and incorporated into the conduit fill). Fibrous aragonite lines some conduits (Rocky Knob only) and precipitated in high fluid flux rates. Blocky carbonate precipitated in open spaces (e.g., lining vugs), and probably represents lower methane flux rates (exclusive of samples with $\delta^{13}C$ values near 0‰ PDB which formed in later burial).

In some samples, blocky carbonate precipitated from burial fluids post-methane migration. The dark-coloured micrite cemented sediment fills in central conduits (in some Rocky Knob samples) represent late stage carbonate precipitation from post-methane migration of burial fluids.

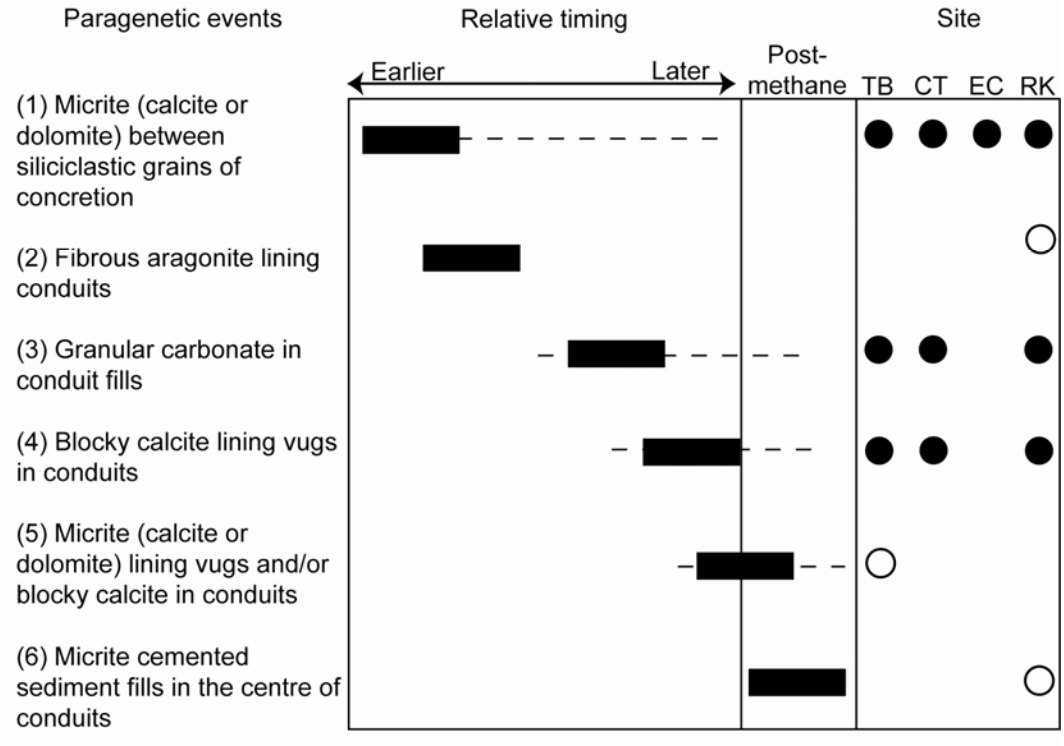

Figure 5. Relative timing relationships of the six paragenetic events recorded in the tubular concretions and conduits from this study. Division between methane migration and post-methane migration is shown. Solid rectangles indicate relative duration and timing; dashed lines suggest possible maximum extent of event. Distribution of each event at the four study sites (TB = Taranaki Basin; CT = Cape Turnagain; EC = East Cape; RK = Rocky Knob) shown on right, with filled circles indicating major occurrence and open circles representing minor occurrence.

3.7 Subsurface seep carbonate classes and formation model

The unique attributes and recurring trends amongst study locations afford an opportunity not only to aid in interpretation of the New Zealand tubular concretions, but also to develop classes that may be used to interpret global examples (Tables 1, 2, Figs. 4, 6 - available as foldout on page 337). Classes are mainly based on stable carbon and oxygen isotope values, but they are further developed based on mineralogy and morphology.

Isotope values can vary throughout a concretion. Therefore, any given concretion may belong to multiple classes. The classes are interpretations which define

development stages of the subsurface seep system. The following sections utilise the term subsurface seep carbonates (SSCs) which refers to carbonate cement within individual subsamples of the tubular concretions or conduits. Only conduit samples which record methane migration are included in the SSC classes. Collectively the characteristics of the SSCs (isotope values, mineralogy, and morphology of the larger tubular concretion in which the subsample is located) can constrain the conditions in which carbonate precipitation occurred. Carbonate precipitation conditions can be used to define the stage of subsurface seep development (e.g., high or low volumes of methane, early or extensive oxidation, hydrate formation, or hydrate dissociation).

3.7.1 Class 1 (Fig. 6, pg. 337)

Class 1 comprises SSCs which plot in the lower area of the $\delta^{13}C$ vs $\delta^{18}O$ diagram and can be subdivided into Class 1A and 1B, differentiated by oxygen isotope values. Class 1A SSCs sit in the lower left quadrant of the $\delta^{13}C$ vs $\delta^{18}O$ plot (Fig. 4A). These SSCs represent formation from anaerobically oxidised methane in normal marine waters or marine waters influenced by gas hydrate formation (more depleted oxygen-18 values). Fluid compositions involved high Ca/Mg ratios and SO_4^{2-} concentrations, and large volumes of fluids and/or fast fluid rates under high pressures. These conditions characterise stage 1 of the subsurface seep system development. The resulting tubular concretions are calcitic pipes that are usually relatively straight (Figs. 4A and 6A). However, in the case of the Rocky Knob occurrence, the pipe concretions are quite tortuous. The tortuosity may reflect formation nearer to the seafloor where cementation rates are high and seafloor sediments relatively permeable. High cementation rates effectively cut off migration routes whereas permeable sediments provide more migration pathways. Combined, these conditions result in strongly tortuous concretions which may branch, anastomose, or coalesce.

Class 1B formed under similar conditions as class 1A; however, these concretions formed during periods of gas hydrate dissociation (Figs. 4A, 6B). Class 1B characterises stage 2 of the subsurface system development.

3.7.2 Class 2 (Fig. 6, pg. 337)

Class 2 comprises SSC samples which plot in the area between Classes 1 and 3 on the $\delta^{13}C$ vs $\delta^{18}O$ diagram and can be subdivided into Class 2A and 2B, differentiated again by oxygen isotope values, as in Class 1A and 1B. Like Class 1, these SSCs represent formation from anaerobically oxidised methane in either normal marine waters or marine waters influenced from gas hydrate formation (2A) and dissociation (2B). However, during their growth the Ca/Mg ratios and SO_4^{2-} concentration of fluids, along with fluid volumes/rates/pressures, were all decreasing (Fig. 4A). Class 2A marks the onset of stage 2, which heralds a shift in subsurface seep system development from hydrate formation to hydrate dissociation and the release of additional methane into the subsurface; whereas Class 2B represents the main phase of methane migration during stage 2. The resulting tubular concretions are predominately calcitic pipes that meander slightly. Some formation of dolomitic pipe, bulbous, and doughnut concretions occurs (Figs. 4A, 6B). The development of Class 2 SSCs indicates extensive methane oxidation and therefore suggests either (1) the end of a methane migration event, (2) distance from the main methane migration pathways, or (3) change of migration pathways (see Section 3.6.3).

3.7.3 Class 3 (Fig. 6, pg. 337)

Class 3 tubular concretions plot in the upper right quadrant of the $\delta^{13}C$ vs $\delta^{18}O$ diagram (Fig. 4A). These SSCs represent formation from anaerobically oxidised methane influenced by gas hydrate dissociation (Figs. 4A, 6C). However, during formation of these concretions, Ca/Mg ratios, SO_4^{2-} concentrations, and fluid volumes/rates/pressures had lowered significantly and >80% of the methane had been oxidised. Class 3 tubular concretions characterise stage 3, which corresponds to the end of methane migration, or the end of a period of intermittent migration. The resulting tubular concretions are predominately dolomitic bulbous and doughnut concretions (Figs. 4A, 6C). Some calcitic and dolomitic pipes occur in this field. These pipes are generally cemented by mixed calcite/dolomite and the pipes meander or are very tortuous. The formation of Class 3 SSCs

indicates extensive methane oxidation and exhaustion of methane in the system. As in Class 2, the formation of Class 3 SSCs suggests either (1) the end of a methane migration event, (2) increased distance from the main methane migration pathways, or (3) change of migration pathways. However, Class 3 represents the end of such a phase.

3.7.4 Implicating gas hydrates

The most likely explanation for enriched $\delta^{18}O$ values in the SSCs is the dissociation of gas hydrates, based on discussions in Chapters 3 to 5. Moreover, the pattern of oxygen isotope values in New Zealand SSCs varies between 3‰ PDB more depleted and 3‰ PDB more enriched than New Zealand Miocene marine waters (-0.7 to -0.5 PDB; Feary et al., 1991). These SSC oxygen isotope signatures also are a strong indication these systems underwent periods of gas hydrate formation and dissociation (Fig. 4A).

3.8 Implications for global examples and previous interpretations

This study has provided a unique opportunity to investigate a wide range of tubular concretions in a variety of geologic settings, and in particular their stable carbon and oxygen isotope values. The three main tubular concretion classes described in Section 3.7 were derived mainly from their isotope values, but also from consideration of their mineralogy, morphology, minus cement porosity, and lipid biomarkers. Collectively, patterns have emerged which enable new insights and interpretations about SSCs. Although some of these interpretations are unconventional with respect to recent seep literature, they are supported by the integrated data. The interpretations may have implications for previous and future research of tubular concretions, and possibly seafloor seep carbonates as well. Table 1 outlines several previous studies of tubular concretions and includes their stable carbon and oxygen isotope values and their reported interpretations. Figure 4B highlights areas of the $\delta^{13}C$ vs $\delta^{18}O$ plot where samples from these previous studies fall. All the data at least partially overlap with the New Zealand tubular concretion classes, and possible correlative New Zealand classes are presented in Table 1. Based on the findings of this study, previous studies with samples that

plot in the middle to upper right side of the diagram may need re-evaluation (e.g., Orpin, 1997; Stakes et al., 1999; Aiello et al., 2001; Pierre et al., 2002, Pierre and Rouchy, 2004, Table 1, Fig. 4B).

4. Proposed model for New Zealand cold seep systems from source to seafloor seep

4.1 Hydrocarbon sources

Isotope signatures of North Island seafloor seep carbonates and subsurface seep carbonates indicate the source of carbon was oxidised methane. Major source rocks for onshore modern hydrocarbon seepage in eastern North Island are the late Cretaceous to early Eocene Whangai and Waipawa (black shale) Formations (Francis, 1997; Rogers et al., 1999) which reached maturity and began expelling hydrocarbons since the Pliocene (Field, 1997; Francis et al., 2004). However, for the Miocene seafloor and subsurface seep carbonates in the East Coast Basin, source rocks were probably the Cretaceous slope to basinal mudstones of the Karekare, Waimarama, and Glenburn Formations, which generated and began expelling hydrocarbons in early to mid Miocene times (Fig. 7A) (Francis et al., 2004). The addition of microbial methane generated below the seep sites may also have occurred. In Taranaki Basin, thermogenic methane was probably sourced from the Cretaceous Rakopi Coal Measures and Paleocene Waipawa (black shale) deposits, potentially with a microbial methane influence from more deeply buried Urenui, Mount Messenger, and Manganui sediments (Figure 7B).

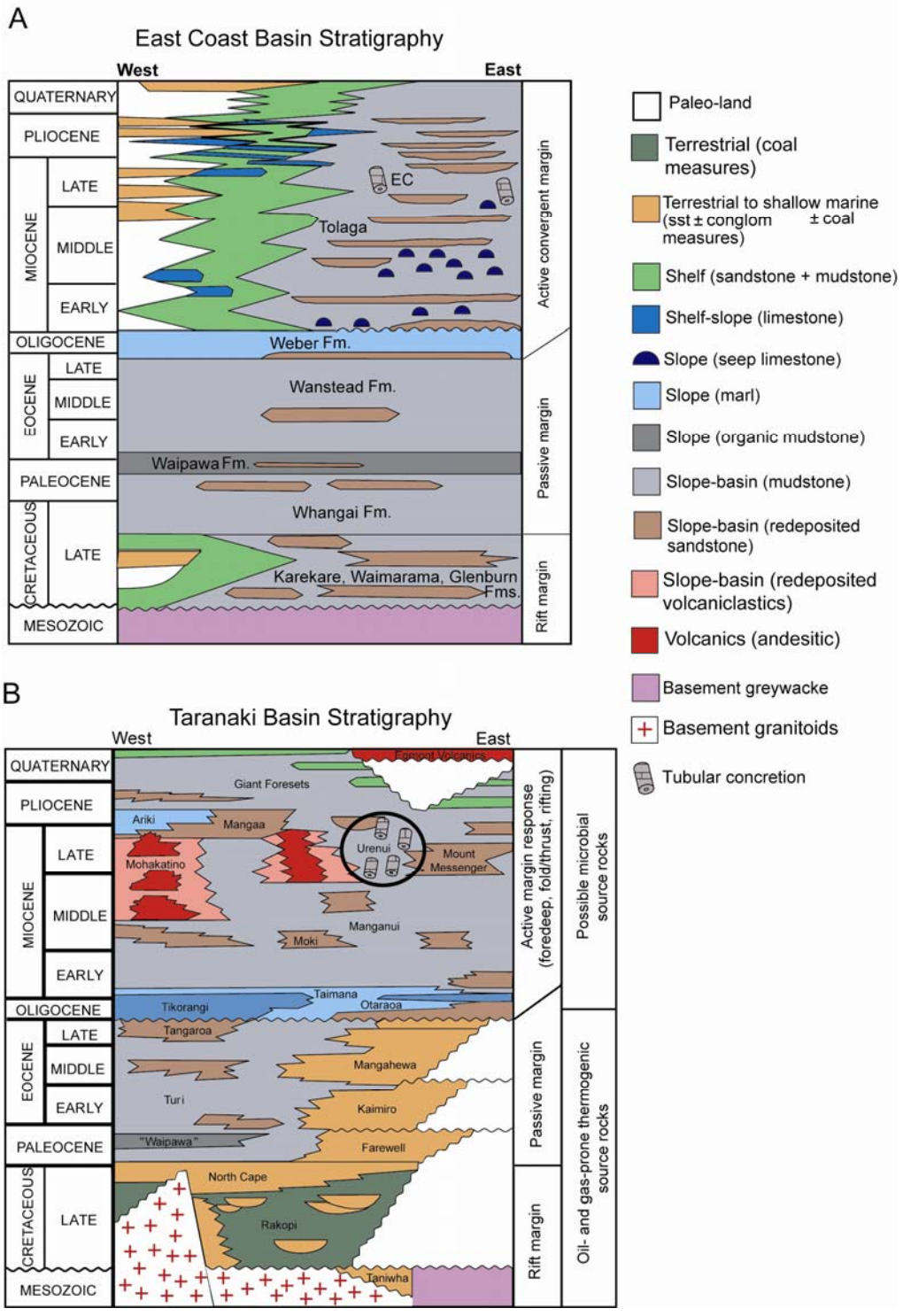

Figure 7. (A) Generalised stratigraphy and depositional paleoenvironments for the East Coast Basin (modified from Francis, 2004). Approximate stratigraphic position of the Cape Turnagain (CT), East Cape (EC), and Rocky Knoby (RK) tubular concretions are denoted. (B) Generalised stratigraphic column of the late Cretaceous to Recent fill in Taranaki Basin, highlighting the position of the late Miocene Urenui Formation and its contained tubular concretions (adapted from Crown Minerals: http://www.crownminerals.govt.nz).

4.2 Initiation of fluid migration

The onset of the Hikurangi subduction margin occurred during early Miocene times and has continued to the present (van der Lingen and Pettinga, 1980; Field et al., 1997; Nicol et al., 2002). As a consequence, overpressured sediments and faulting along the Hikurangi Margin may result in fluid ascent (Lewis and Marshall, 1996; Barnes et al., accepted). As such, fluid migration and hydrocarbon seepage in the East Coast Basin during the Miocene to present probably began as a result of the dewatering of crustal sediments during subduction of the Pacific plate under the Australian plate. In the Taranaki Basin, hydrocarbon generation, seismic activity, and/or changes in stress fields due to tectonic activity were likely causes of upward fluid migration during the late Miocene (King and Thrasher, 1996). A rejuvenated phase of movement along Taranaki Fault and regional inversion in the late Miocene (Vonk and Kamp, 2008) may have provided fluid migration pathways into the Urenui Mudstone.

4.3 Generalised fluid seep model

Figure 8 (as foldout on page 339) illustrates an integrated but highly generalised model for hydrocarbon seep development in North Island based on characteristics of the New Zealand ancient seep carbonates and tubular concretions.

The smaller calcitic pipe concretions with straighter morphologies formed in the subsurface during early methane migration and the dolomitic, tortuous morphologies formed after extensive methane oxidiation (Figs. 4, 8.9, 8.10). Sinuous pipes and nodules like those present beneath the Rocky Knob seep complex characterise the near seafloor expulsion site (Figs. 8.7, 8.8). The doughnut concretions formed from intermittent fluid ascent as a result of fault-valve action (Fig. 8.11). Fluid pressures/volumes were low, and fluids became trapped in ‘bubble-like’ pockets with subsequent carbonate precipitation leading to the doughnut morphology.

When the fluids reached the seafloor, seep carbonates developed within the upper few centimetres of sediment, along with a chemosynthesis-based biota (Figs. 8.4, 8.5). Pipe concretions in Taranaki Basin are observed within a conglomeratic channel fill, suggesting an intimate relationship between fluid injection into the shelf/slope setting and slope instability (Figs. 8.1, 8.2). Slope failures also may partially exhume tubular concretions, leading to pipes protruding upwards into the water column near seep sites, fallen over onto the sea bed nearby seep sites, or transported down slope (e.g., Jensen et al., 1992; Orpin, 1997; Díaz-del-Río et al., 2003). Carbonate ring structures in the Taranaki examples may indicate pockmark formation at the seafloor (Fig. 8.6).

Fluid sources are from deep thermogenic methane and/or more shallow microbial methane, potentially influenced by gas hydrate formation and dissociation (Fig. 8). Catastrophic fluid release may be recorded in the slope failures, pockmarks, and intense brecciation of concretions, whereas intermittent fluid escape may be recorded by the doughnut concretions (Fig. 8).

4.4 Miocene seep development

Early to late Miocene fluid migration and seafloor expulsion is evidenced in scattered pods of seafloor seep carbonates throughout the East Coast Basin (Fig. 3) (Campbell et al., 2008). Late Miocene tubular concretions scattered throughout the North Island also record this fluid migration through the subsurface (Fig. 3). Three ancient seep carbonate occurrences expose small tubular concretions in the underlying strata (Rocky Knob, Karikarihuata Stream, Moonlight North; K. Campbell, pers. comm. 2008). Such features are anticipated in the underlying stratigraphy beneath the other dozen known seafloor seep deposits, but are presently not exposed. Conversely, prominent surface seep features such as paleo-seafloor seep carbonates and chemosynthesis-based paleocommunities appear to be lacking at the main tubular concretion study sites, which could reflect: (1) migrating fluids never reached the surface; (2) lack of exposure of such features (i.e. they remain buried and not yet uplifted); or (3) the features may have been eroded. Although seafloor seep features are not present at three of the main

study sites, evidence suggests that many of the tubular concretions formed at shallow burial depths (e.g., minus cement porosities from 45 to 85% suggest formation conditions at burial depths of <300 m). As such, the fluids responsible for tubular concretion formation in the late Miocene sediments probably reached the sea floor.

5. Future perspectives

This study has developed some new insights into the evolution of subsurface seep systems and the formation of tubular concretions in New Zealand. The findings have both direct and indirect influence to worldwide studies of modern and ancient seep systems. In addition to furthering the understanding of subsurface seep systems, this study has also raised questions and highlighted areas in which future seep research should be directed.

In the light of this research, it is recommended that the following studies could be conducted in the future.

(1) Detailed organic and inorganic geochemical studies of tubular concretions, and their host sediments. The study would best be conducted at a field site that included seafloor seep carbonates, along with geochemical analyses for comparison.

(2) This study has highlighted problems and some alternative interpretations of stable carbon and oxygen isotope values for seep carbonates. Future research should focus on isotope trends in seep carbonates from a geochemical perspective, in particular the seep carbonates with positive carbon and positive oxygen isotope values.

(3) An integrated study of tubular concretions exposed at the seafloor nearby active seeps should be considered. The study should include analysis of both tubular concretions and seafloor seep carbonates (similar in approach to this study). The results should then be integrated with organic/inorganic geochemistry of the sediments, pore fluids, and water column fluids.

Moreover, a control site nearby the active seep site should also have geochemical studies made on the pore and water column fluids. It is imperative to know what the normal marine conditions near the seep site are in order to interpret if, and by how much, the seep conditions vary.

(4) A complete structural analysis of the East Cape region should be conducted and then integrated with the results of Chapter 5 in this study. The structural history of the region will help test and improve the fault-valve mechanism hypothesis presented in Chapter 5.

(5) High resolution seismic studies of the tubular concretion sites, integrated with the results of this study, may help to identify subsurface seep systems and carbonate precipitation in the subsurface in modern offshore settings.

(6) Ideally, a 500 m core and associated drilling data taken from a modern offshore seep site on Hikurangi Margin would provide significant information to integrate with previous seep research.

6. References

Aiello, I.W., Stakes, D.S., Kastner, M., Garrison, R.E., 1999. Carbonate vent structures in the Upper Miocene Santa Cruz Mudstone at Santa Cruz, California. In: Garrison, R.E., Aiello, I.W., Moore, J.C. (Eds.), Late Cenozoic Fluid Seeps and Tectonics Along the San Gregorio Fault Zone in the Monterey Bay Region, California. Pacific Section AAPG, v. GB-76, pp. 35-52.

Aiello, I.W., Garrison, R.E., Moore, J.C., Kastner, M., Stokes, D.S., 2001. Anatomy and origin of carbonate structures in a Miocene cold-seep field. Geology 29, 1111-1114.

Barnes, P.M., Lamarche, G., Bialas, J., Henrys, S., Pecher, I., Netzeband, G.L., Greinert, J., Mountjoy, J.J., Pedley, K., Crutchley, G., accepted. Tectonic and geological framework for gas hydrates and cold seeps in the Hikurangi Subduction Margin, New Zealand. Submitted to Marine Geology.

Campbell, K.A., 2006. Hydrocarbon seep and hydrothermal vent paleoenvironments and paleontology: Past developments and future research directions. Palaeogeography, Palaeoclimatology, Palaeoecology, 232, 362-407.

Campbell, K.A., Francis, D.A., Collins, M., Gregory, M.R., Nelson, C.S., Greinert, J., Aharon, P., 2008. Hydrocarbon seep-carbonates of a Miocene forearc (East Coast Basin), North Island, New Zealand. Sedimentary Geology, 204, 83-105.

Clari, P., Cavagna, S., Martire, L., Hunziker, J., 2004. A Miocene mud volcano and its plumbing system: A chaotic complex revisited (Monferrato, MW Italy). Journal of Sedimentary Research, 74, 662-676.

Cowen, J.P., Wen, X., Popp, B.N., 2002. Methane in aging hydrothermal plumes. Geochimica et Cosmochimica Acta, 66, 3563-3571.

De Boever, E., Swennen, R., Dimitrov, L., 2006. Lower Eocene carbonate cemented chimneys (Varna, NE Bulgaria): Formation mechanisms and the

(a)biological mediation of chimney growth? Sedimentary Geology, 185, 159-173.

Díaz-del-Río, V., Somoza, L., Martínez-Frias, J., Mata, M.P., Delgado, A., Hernandez-Molina, F.J., Lunar, R., Martín-Rubí, J.A., Maestro, A., Fernández-Puga, M.C., León, R., Llave, E., Medialdea, T., Vázquez, J.T., 2003. Vast fields of hydrocarbon-derived carbonate chimneys related to the accretionary wedge/olistostrome of the Gulf of Cádiz. Marine Geology, 195, 177-200.

Feary, D.A., Davies, P.J., Pigram, C.J., Symonds, P.A., 1991. Climatic evolution and control on carbonate deposition in northeast Australia. Palaeogeography, Palaeoclimatology, Palaeoecology, 89, 341-361.

Field, B.D., Uruski, C.I., and others, 1997. Cretaceous-Cenozoic geology and petroleum systems of the East Coast Region, New Zealand. Institute of Geological and Nuclear Sciences monograph, 19, 301 pp.

Francis, D.F., 1997. Oil and Gas Generation in the East Coast Basin – an update. Petroleum Exploration in New Zealand News, volume 51, October 1997.

Francis, D., Bennett, D., Courteney, S., 2004. Advances in understanding of onshore East Coast Basin structure, stratigraphic thickness and hydrocarbon generation. 2004 New Zealand Petroleum Conference Proceedings, Auckland, 7-10 March 2004. 20 pp.

Gieskes, J., Mahn, C., Day, S., Martin, J.B., Greinert, J., Rathburn, T., McAdoo, B., 2005. A study of the chemistry of pore fluids and authigenic carbonates in methane seep environments: Kodiak Trench, Hydrate Ridge, Monterey Bay, and Eel River Basin. Chemical Geology, 220, 329-345.

Greinert, J., Bialas, J., Lewis, K., Suess, E., in review. Methane seeps and gas hydrates offshore New Zealand's North Island: Compiling results from three cruises in 2006 and 2007. Submitted to Marine Geology.

Jensen, P., Aagaard, I., Burke Jr. R.A., Dando, P.R., Jørgensen, N.O., Kuijpers, A., Laier, T., O'Hara, M.O., Schmaljohann, R., 1992. 'Bubbling reefs' in

the Kattegat: submarine landscapes of carbonate-cemented rocks support a diverse ecosystem at methane seeps. Marine Ecology Progress Series, 83, 103-112.

Jørgensen, N.O., 1992. Methane-derived carbonate cementation of marine sediments from the Kattegat, Denmark: Geochemical and geological evidence. Marine Geology, 103, 1-13.

Judd, A.G., Hovland, M., 2007. Seabed Fluid Flow: The Impact on Geology, Biology and the Marine Environment. Cambridge University Press, Cambridge. 475 pp.

King, P.R., Thrasher, G.P., 1996. Cretaceous-Cenozoic geology and petroleum systems of the Taranaki Basin, New Zealand. Institute of Geological and Nuclear Sciences Monograph 13. Institute of Geological and Nuclear Sciences Ltd, Lower Hutt.

Lédesert, B., Buret, C., Chanier, F., Fèrriere, J., Recourt, P., 2003. Tubular structures of northern Wairarapa (New Zealand) as possible examples of ancient fluid expulsion in an accretionary prism: evidence from field and petrographical observations. Geological Society of London, Special Publication, 216, 95-107.

Lewis, K.B., Marshall, B.A., 1996. Seep faunas and other indicators of methane-rich dewatering on New Zealand convergent margins. New Zealand Journal of Geology and Geophysics, 39, 181-200.

Mazzini, A., Duranti, D., Jonk, R., Parnell, J., Cronin, B.T., Hurst, A., Quine, M., 2003. Palaeo-carbonate seep structures above an oil reservoir, Gryphon Field, Tertiary, North Sea. Geo-Marine Letters, 23, 323-339.

Nelson, C., Schellenberg, F., King, P., Ricketts, B., Kamp, P., Browne, G., Campbell, K., 2004. Note on paramoudra-like concretions in the Urenui Formation, North Taranaki: possible plumbing system for a Late Miocene methane seep field. 2004 New Zealand Petroleum Conference Proceedings, Auckland, 7-10 March 2004. 5 pp. [http://crownminerals.med.govt.nz/petroleum/publications/nzpconf/nzpconf-2004.html]

Nicol, A., Van Dissen, R., Vella, P., Alloway, B., Melhuish, A., 2002. Growth of contractional structures during the last 10 Ma, Hikurangi forearc, New Zealand. New Zealand Journal of Geology and Geophysics, 45, 365-385.

Orpin, A. R., 1997. Dolomite chimneys as possible evidence of coastal fluid expulsion, uppermost Otago continental slope, southern New Zealand. Marine Geology, 138, 51-67.

Pearson, M.J., Grosjean, E., Nyman, S.L., Logan, G.A., Nelson, C.S., Hood, S.D., Campbell, K.A., 2008. Tubular concretions in New Zealand petroliferous basins: Lipid evidence for mineralization around proposed Miocene hydrocarbon seep conduits. 2008 New Zealand Petroleum Conference Proceedings, Auckland, 10-12 March 2008. 6 pp.

Pierre, C., Rouchy, J.-M., Blanc-Valleron, M.-M., 2002. Gas hydrate dissociation in the Lorca Basin (SE Spain) during the Mediterranean Messinian salinity crisis. Sedimentary Geology, 147, 247-252.

Pierre, C., Rouchy, J.-M., 2004. Isotopic compositions of diagenetic dolomites in the Tortonian marls of the western Mediterranean margins: evidence of past gas hydrate formation and dissociation. Chemical Geology, 205, 469-484.

Rogers, K.M., Collen, J.D., Johnston, J.H., Elgar, N.E., 1999. A geochemical appraisal of oil seeps from East Coast Basin, New Zealand. Organic Geochemistry, 30, 593-605.

Schellenberg, F., 2002. The paramoudra concretions within the Urenui Formation, Taranaki Basin, West Coast of New Zealand: Fossil fluid conduits or giant trace fossils? Institute of Geology and Palaeontology, University of Tübingen, unpublished MSc Thesis.

Schwartz, H., Sample, J., Weberling, K.D., Minisini, D., Moore, J.C., 2003. An ancient linked fluid migration system: cold-seep deposits and sandstone intrusions in the Panoche Hills, California, USA. Geo-Marine Letters, 23, 340-350.

Sibson, R.H., 1992. Implications of fault-valve behaviour for rupture nucleation and recurrence. Tectonophysics, 211, 283-293.

Stakes, D., Orange, D., Paduan, J.B., Salamy, K.A., Maher, N., 1999. Cold-seeps and authigenic carbonate formation in Monterey Bay, California. Marine Geology, 159, 93-109.

van der Lingen, G.J., Pettinga, J.R., 1980. The Makara Basin: a Miocene slope-basin along the New Zealand sector of the Australian-Pacific obliquely convergent plate boundary. In: Ballance, P.F., Reading, H.G. (Eds.), Sedimentation in Oblique Strike-slip Mobile Zones. Special publication of the International Association of Sedimentologists, 191-215.

Vonk, A.J., Kamp, P.J.J., 2008. The Late Miocene southern and central Taranaki inversion phase (SCTIP) and related sequence stratigraphy and paleogeography. 2008 New Zealand Petroleum Conference Proceedings, Auckland, 10-12 March 2008, 17 pp.

Figure 6. Schematic model for the formation of tubular concretions based on New Zealand examples. (A) Formation of Class 1A tubular concretions from ascending methane and anomalously depleted oxygen isotope values due to methane hydrate formation. Class 2A tubular concretions formed as the methane sources diminish. (B) Class 1B tubular concretions form during episodes of methane hydrate dissociation followed by Class 2B tubular concretions as methane sources diminish. (C) Formation of Class 3 tubular concretions from methane hydrate dissociation, during the final stages of methane migration where >80% of methane has already been oxidised. Doughnut concretions may form as a result of intermittent fluid migration due to the fault valve mechanism discussed in Chapter 5, Section 5.3.3). Mineralogy changes from calcite (Class 1) to mixtures of calcite and dolomite (Class 2) to dolomite (Class 3), reflective of lower Ca/Mg ratios from continued carbonate precipitation.

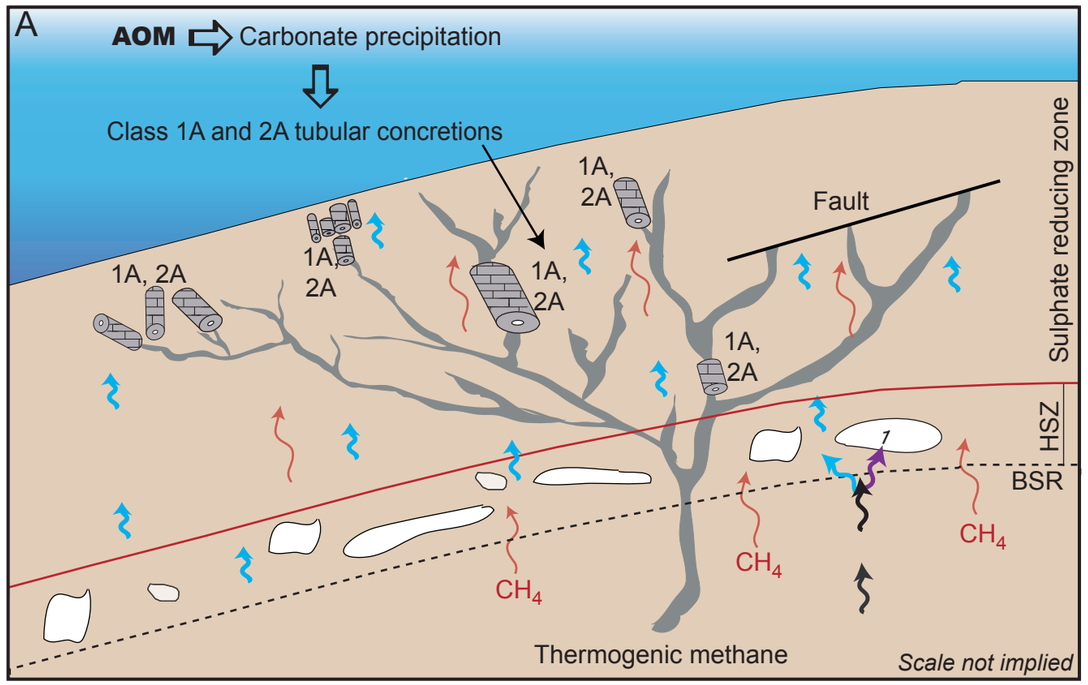

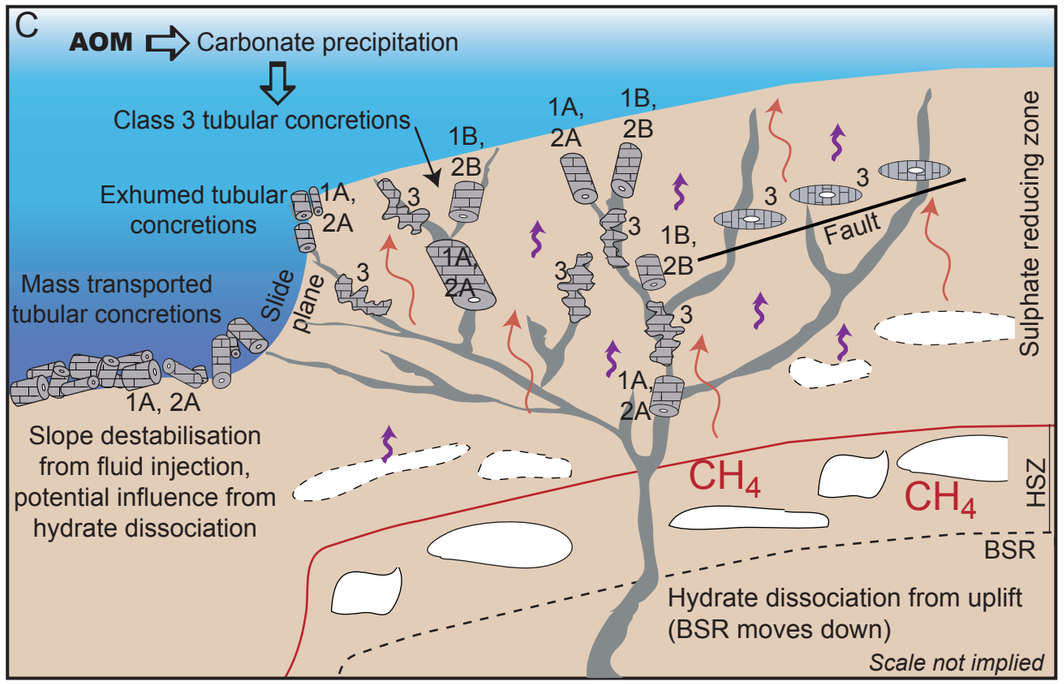

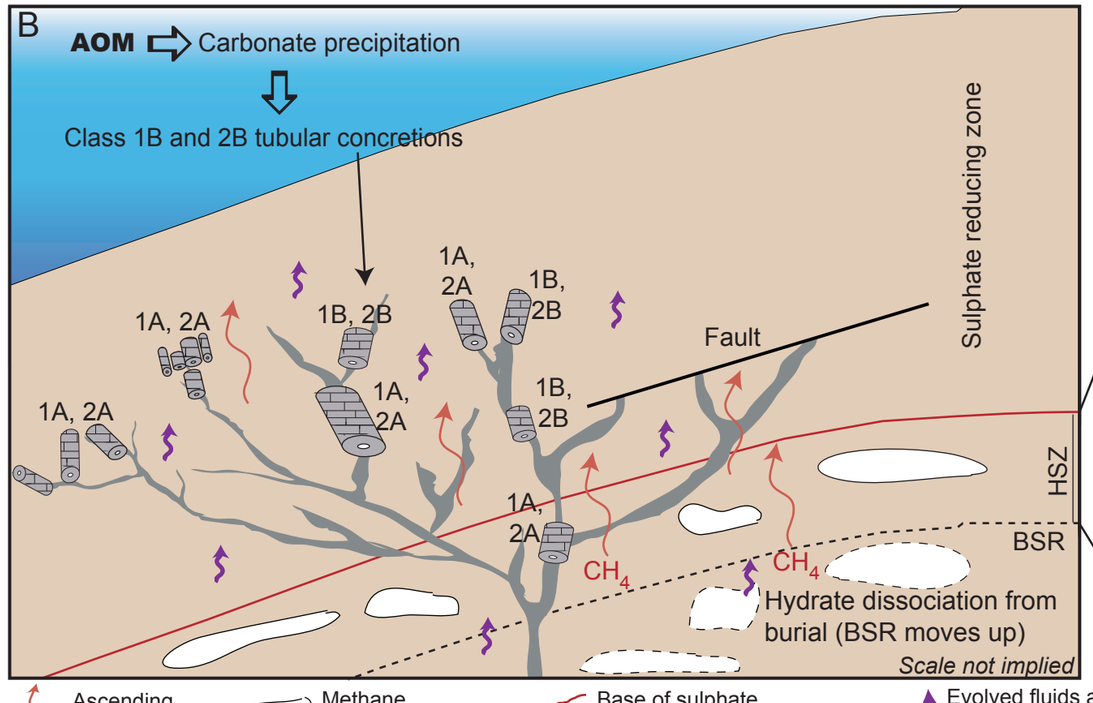

Anaerobic oxidation of methane (**AOM**) via methanotrophic Archaea and sulphate-reducing Bacteria

$CH_4 + SO_4^{2-} \rightarrow HCO_3^- + H_2O + HS^-$

⇩

Carbonate precipitation

$xMg^{2+} + yCa^{2+} + HCO_3^- \rightarrow MgCaCO_3 + H_2O$

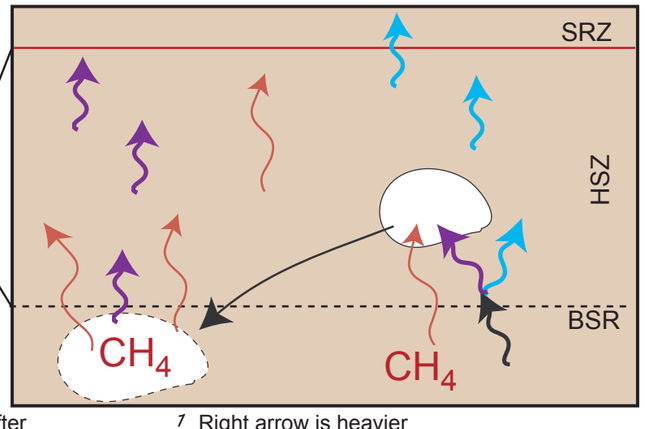

Formation conditions of Class 2 and 3 tubular concretions

1) Long lived AOM ⇨ enriched $\delta^{13}C_{carbonate}$ (up to $\delta^{13}C = +10\ ^{0}/_{00}$ PDB)

2) Sulphate and Ca^{2+} depletion ⇨ dolomite precipitation

3) Gas removed via carbonate precipitation ⇨ lower pressure ⇨ more tortuous pathways

1 + 2 + 3 = Class 2 and 3 tubular

Pipe concretions (Class 1 and 2)

Bulbous concretions (Class 2 and 3)

Doughnut concretions (Class 2)

Ascending methane (CH_4)

Ascending burial fluids

Methane hydrate

Dissociating methane hydrate

Base of sulphate reducing zone

Fluids with anomalously light oxygen-18 remaining in pore waters after hydrate formation

Evolved fluids after second generation of hydrate formation (^{18}O-enriched with respect to burial fluids)

Right arrow is heavier oxygen entering clathrate molecule; left arrow is evolved fluid (lighter) remaining after hydrate formation

SRZ = sulphate reducing zone
HSZ = hydrate stability zone
BSR = bottom simulating reflector (base of HSZ)

Figure 8. A schematic synthesis model for development of a cold seep carbonate system based on interpretation of the New Zealand tubular concretion characteristics and seafloor carbonate and other features. Photographs 1 to 12 show geological field examples of some of the features portrayed in the model. TB = Taranaki Basin; ECB = East Coast Basin.

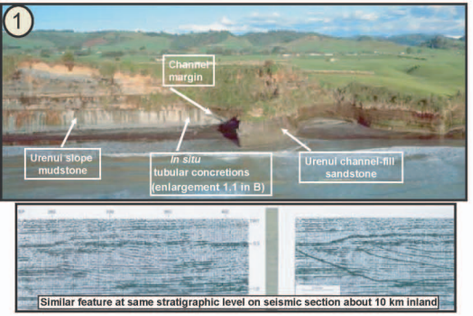

In situ tubular concretions truncated by channelised slope sandstone, Mimi, TB.

Mass-emplaced tubular concretions in axial portion of slope channel fill deposits, Mimi, TB.

Upstanding knolls formed by New Zealand's largest seep limestone, Rocky Knob, ECB.

Worm tubes in seep limestone, Ugly Hill, ECB.

Fossil vesicomyids in seep limestone, Ugly Hill, ECB.

Slabby and nodular micritic carbonate in mudstone below seep limestone, Karikarihuata, ECB.

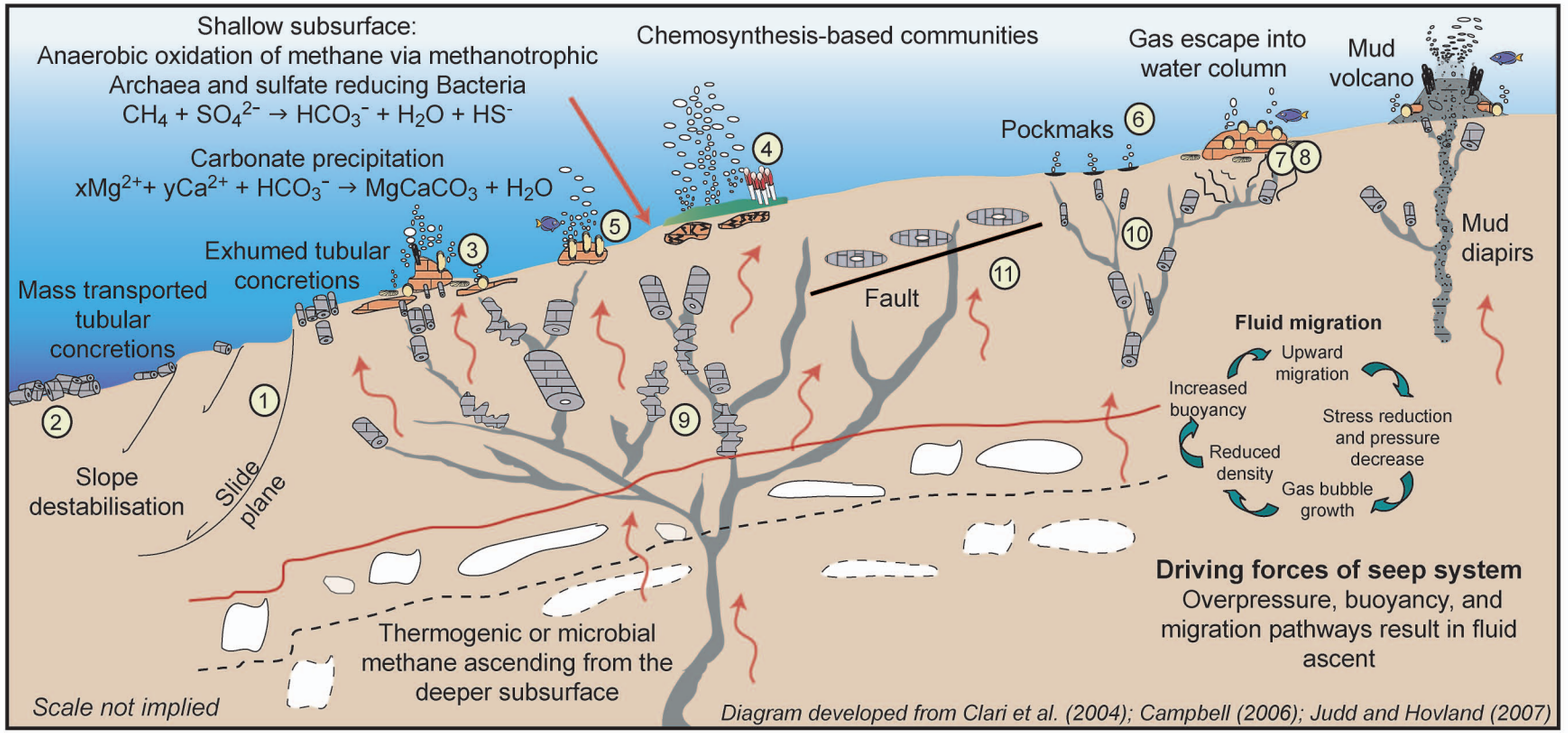

Pipe (left) and bulbous (right) concretions delineate possible fluid ascent pathways (red arrows), Mimi, TB.

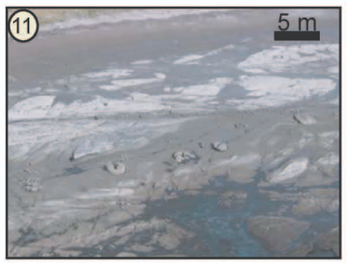

Aerial photograph of doughnut concretions aligned on faults and joints, East Cape, ECB.

Tube worms and bacterial mats commonly associated with higher flow rates

Vesicomyids (e.g., *Calyptogena*) commonly associated with moderate flow rates

Lucinid and Solemyid bivalves commonly associated with diffuse flow rates

Hydro-fracturing

Gas hydrate formation and dissociation

Authigenic carbonate formed at or near sediment-water interface

Mud and brecciated clasts

Base of sulphate reducing zone

Base of the gas hydrate stability zone (HSZ)

Ascending methane rich fluids

Class 1 and 2 tubular concretions

Class 2 and 3 tubular concretions

Class 3 tubular concretions

TB = Taranaki Basin
ECB = East Coast

Combinations or overprinting of features may result due to changes in fluid migration pathways, flow rates, and depositional / burial environment through time

Adjacent images (1) to (11) show some North Island field features and their inferred link to the cold seep system illustrated in above model

Carbonate cemented ring structure, possibly associated with pockmarks, Mimi, TB.

Nodular and pipe-like concretions in mudstone just below the ancient seafloor limestones at Rocky Knob, ECB.

Scattered pipe and bulbous concretions in Urenui Formation, Mimi, TB.

Tubular carbonate concretions from North Island, New Zealand: Evidence for hydrocarbon migration and the subsurface plumbing system of cold seeps

Volume 2

Stephanie Leigh Nyman

THE UNIVERSITY OF WAIKATO

HAMILTON, NEW ZEALAND

2009

Tubular carbonate concretions from North Island, New Zealand: evidence for hydrocarbon migration and the subsurface plumbing system of cold seeps

Volume 2: Appendices

THE UNIVERSITY OF
WAIKATO
Te Whare Wānanga o Waikato

Stephanie Leigh Nyman

THE UNIVERSITY OF WAIKATO

HAMILTON, NEW ZEALAND

2009

Appendix 1

Taranaki

Taranaki table of contents

1. Location

Taranaki field sites are located on coastal sections at Waiau (GPS, E2626178, N6244795) and Wai-iti (GPS E2663825, N6234085) (Figs. A1.1-A1.2). There are also three locations inland from the Taranaki coastal sections (Patea, GPS, E2642650, N6175740; Ohura, E2666166, N6259788; and Whangamomona, E2668005, N6228553) (Fig. A1.1). These latter sites only expose a few tubular concretions and so were not focused on for this study, but are noted here. One sample from Patea has been analysed for isotopes. Table A1.1 lists locations, access details, ownership contacts, outcrop occurrences, credit to colleagues who informed us of location, and tidal information.

1.1 Tides

The coastal outcrops are tide dependent and most can only be accessed 3 hours either side of low tide. There are only a few possible emergency exit points if caught by incoming tides or higher water from unexpected storms. Coastal erosion and deposition along the tidal section is variable. There were notable changes in access ability and outcrop exposure with each visit. The most extreme changes occurred during the 2007 field season when sand had been eroded around points and deposited in coves making access around points difficult to impossible and sand build up on the beach covered most of the best examples of shoreface tubular concretions. Additionally, the Earp's entry point was not accessible due to excessive sand erosion around the first point. Further discussions with locals, Bleu and Shirley Read, pointed out a second entry with access from their property (Table A1.1).

1.2 Outcrop details

1.1.1 Wai-iti

The northernmost occurrence is north of Wai-iti Beach and spans almost 2 km of coastline (Figs. A1.1-A1.2, Table A1.1). Three outcrops are present here. The

first begins approximately 1.5 km north of Wai-iti Stream and contains three morphologies of concretionary material in the cliff outcrop and shoreface (Wai-iti). The second exposure (Wai-iti Channel) is 1 km north of Wai-iti Stream where the Whakerere Conglomerate fills a channel cut into the Urenui mudstone. The conglomerate fill contains numerous mass emplaced tubular concretions (of one morphology) and has the highest density of carbonate cemented features at the Wai-iti location. At the Wai-iti Stream mouth, carbonate cemented material is located on the shoreface spanning a couple of hundred metres.

1.1.2 Mimi Beach

The next exposure involves the Mimi Beach section located 2 km south of Wai-iti, spanning 2.5 km (Figs. A1.1-A1.2, Table A1.1). This stretch of coastline has the highest density of tubular concretions on the Taranaki coast, contains the most diverse morphologies, largest examples, and spans the longest distance. Concretionary material is found in the cliff exposure and along the shoreface.

1.1.3 Waitoetoe Beach

Waitoetoe Beach is 1 km south of the Mimi occurrence and is only a few hundred metres in length (Figs. A1.1-A1.2, Table A1.1). Waitoetoe has a small occurrence of carbonate cemented material of mixed morphologies in both the cliff and shoreface.

1.1.4 Onaero Beach

Onaero Beach is located 6 km south of Waitoetoe and only spans approximately 100 m of coastline (Figs. A1.1-A1.2, Table A1.1). There is concretionary material in the cliff and shoreface, however the concretions are very irregular and vary in morphology.

1.1.5 Waiau Stream

Waiau Stream marks the most southern occurrence and is about 2 km south of Onaero Beach (Figs. A1.1-A1.2, Table A1.1). This outcrop is also small, spanning only a couple of hundred metres and involves only one main concretion morphology.

Table A1.1. Detailed outcrop location

Location	Topo map	GPS	Access and comments	Contacts/Permission	Outcrop	Source Information
1) Pukearuhe	Q18	E2638700, N6253100	End of Pukearuhe Road Beach: White Cliffs Walkway, south entrance.		Site visited, but no tubular concretions found.	Peter King
2) Wai-iti	Q18	E2637800, N6252200	Pukearuhe Road and Beach Road Beach. Attempted access twice, due to tides and sand erosion attempt failed.		Not found, but previously visited by Nelson and colleagues. Tubular concretions found in cliff and on beach. Layered concretions present with tubular features below and above.	Peter King, Cam Nelson, Franziska Schellenberg
3) Wai-iti Channel	Q18	E2638400, N6253400	Pukearuhe Road and Beach Road North end of beach, second point.		Channel fill conglomerate with pipe concretions. Just north of channel fill are concretionary layers on shore platform. Layers also appear on the shore platform at the Wai-iti enterance near river.	Peter King, Cam Nelson, Franziska Schellenberg
4) Mimi	Q19	E2635100, N6248800 to E2635800, N6249800	Mimi River; Pukearuhe Road and Johnson Road Beach. Storms and seasonal variations erode and deposit considerable amounts of sand. The last visit was inaccessable via the Earp's property.	Greg & Karen Earp; 64 Johnson Rd. (06-752-3350, 027-449-5572), Possible accomodation: Robert Blyde (06-752-3769). Alternate enterance from Bleu and Shirley Read (Ph. 06 752 3698). House is first on right after Johnson Rd. Access is up farm track over the coastal cliffs then down a ladder onto the beach. This access enters at the north end of the Mimi section.	Main outcrop of the Taranaki examples. Tubular concretions located in cliff and shore platform. Morphologies include pipe, bulbous, rings, mushrooms, nodules.	Peter King, Cam Nelson, Franziska Schellenberg
5) Waitoetoe	Q19	E2634400, N6248000 to E2633900, N6247700	Waitoetoe Road Beach. Road access from gated entrance is closed off due to slope stability. Proceed with caution down road and scramble down sandy slopes to beach access.		Small occurrence of pipe concretions and bulbous to layered varieties.	Peter King, Cam Nelson, Franziska Schellenberg
6) Carrs Road	Q19	E2633200, N6247000	South of Waitoetoe Road Site not visited. Once had a ladder down cliff to beach, has since been washed away. Access only by boat.		Some concretions truncated by an erosional surface below the channel fill sandstone.	Peter King
7) Onaero	Q19	E2628083, N6244926	Hwy 3; Onaero Motor Camp, south of Urenui. Tubular concretions located south of the river.	Onaero Bay Motor Camp, R.D. 43 Waitara, N. Taranaki; (06-752-3643)	Small occurrence of bulbous to layered concretions.	
8) Waiau	Q19	E2625500, N6244795	Waiau Stream; Hwy 3 and Methanex, south of Urenui and Onaero. North of Waiau Stream. Access through farm and under electric fences and climb down cliff via rope.		Small occurrence of pipe concretions. There is a channel fill (mud) with tubular concretions on shore face and in cliff exposure further north.	Peter King
9) Whanga-momona	R19	E2668005, N6228553	Kohuratahi Road, turn right at road split, turn right at Putikiturna Road On sharp corner is river.	Mark Coppelstone or Rob Low	Tubular concretions reported in river. Attempted to find, but unsuccessful.	Adam Vonk
10) Patea	Q21	E2642650, N6175740	Ball and Maben Road, just before and after large bridge along road cut.		Three pipe concretions found.	Adam Vonk
11) Ohura	R18	E2666166, N6259788	Ahititi-Ohura Road After Kotare Stream, thin massive Otuni mudstone.		One pipe concretion found.	Adam Vonk

1.4 Regional map

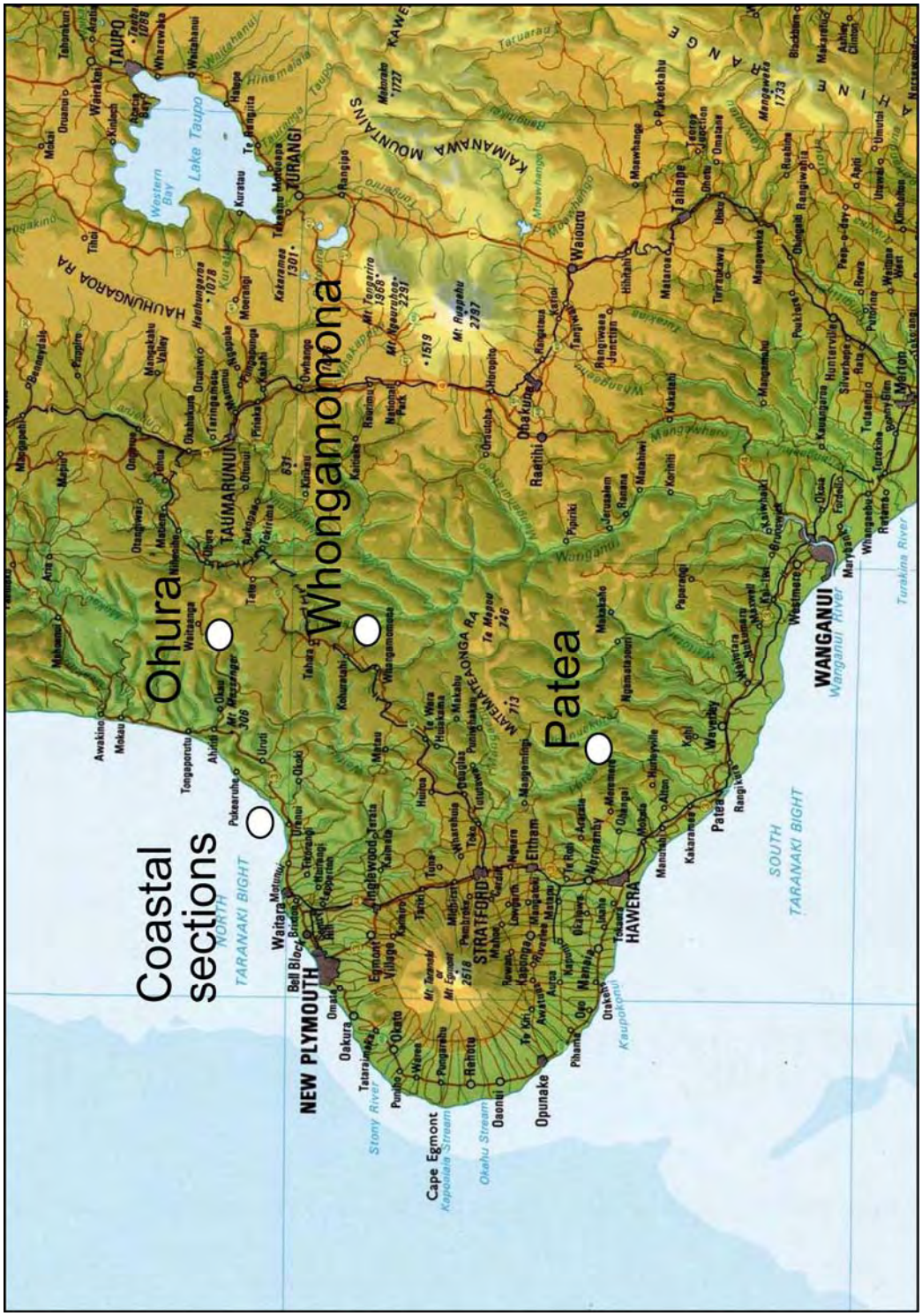

Figure A1.1. Map of Taranaki region. White dots indicate the locations where tubular concretion have been found.

1.5 Map of coastal outcrops

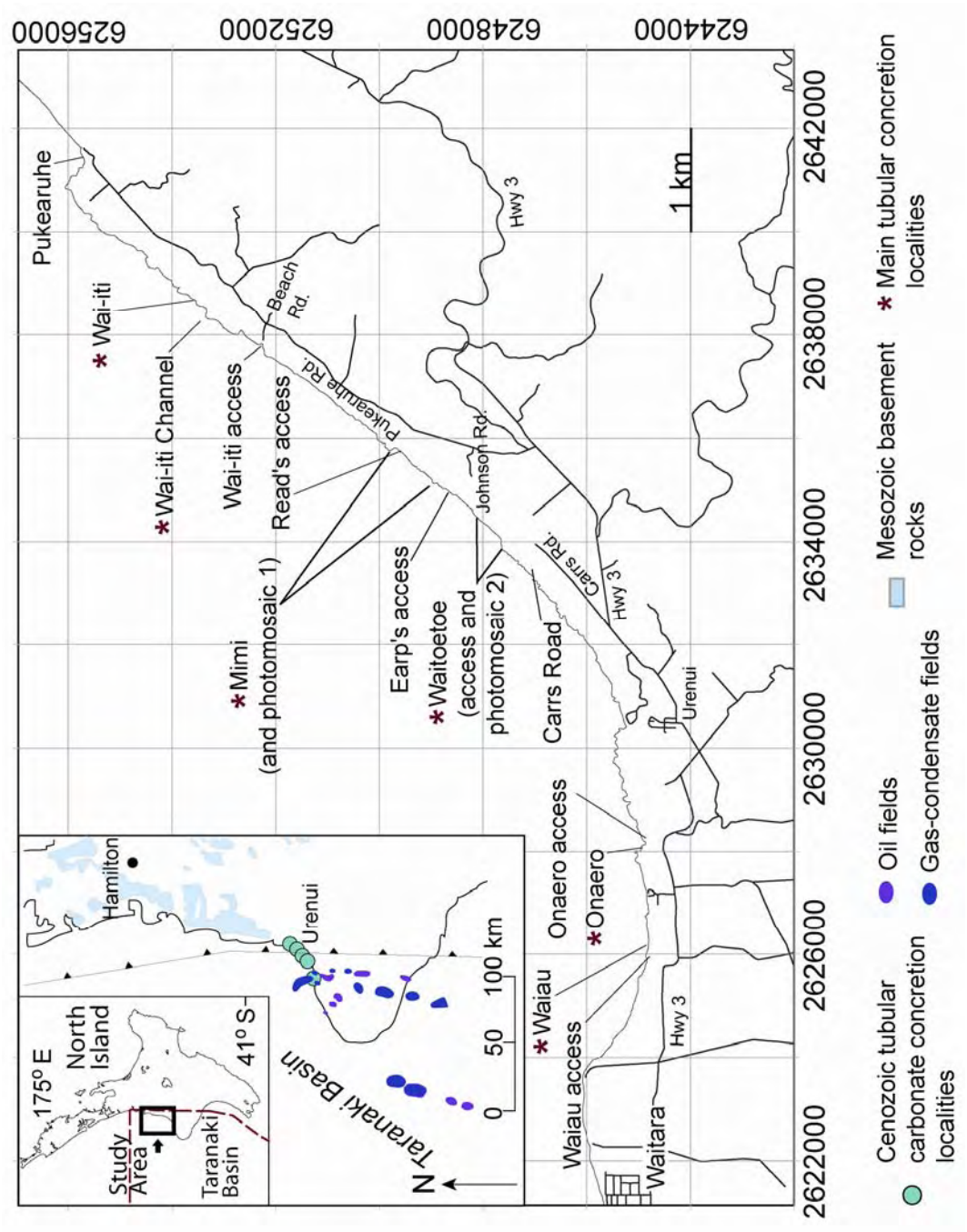

Figure A1.2. Map of coastal outcrops and access, see Table A1.1

2. Photomosaics

Photomosaics were created of Mimi and Waitoetoe sections. The photomosaic is not to scale due to distortion caused by focal length and angle. Scale bars are approximate. Photomosaics were not constructed for the remaining coastal sections because the outcrops did not extend for much of a distance and few tubular concretions were present.

2.1 Photomosaic of Mimi outcrop

Figure A1.3. Photomosaic of the Mimi section.

2.2 Photomosaic of Waitoetoe Outcrop

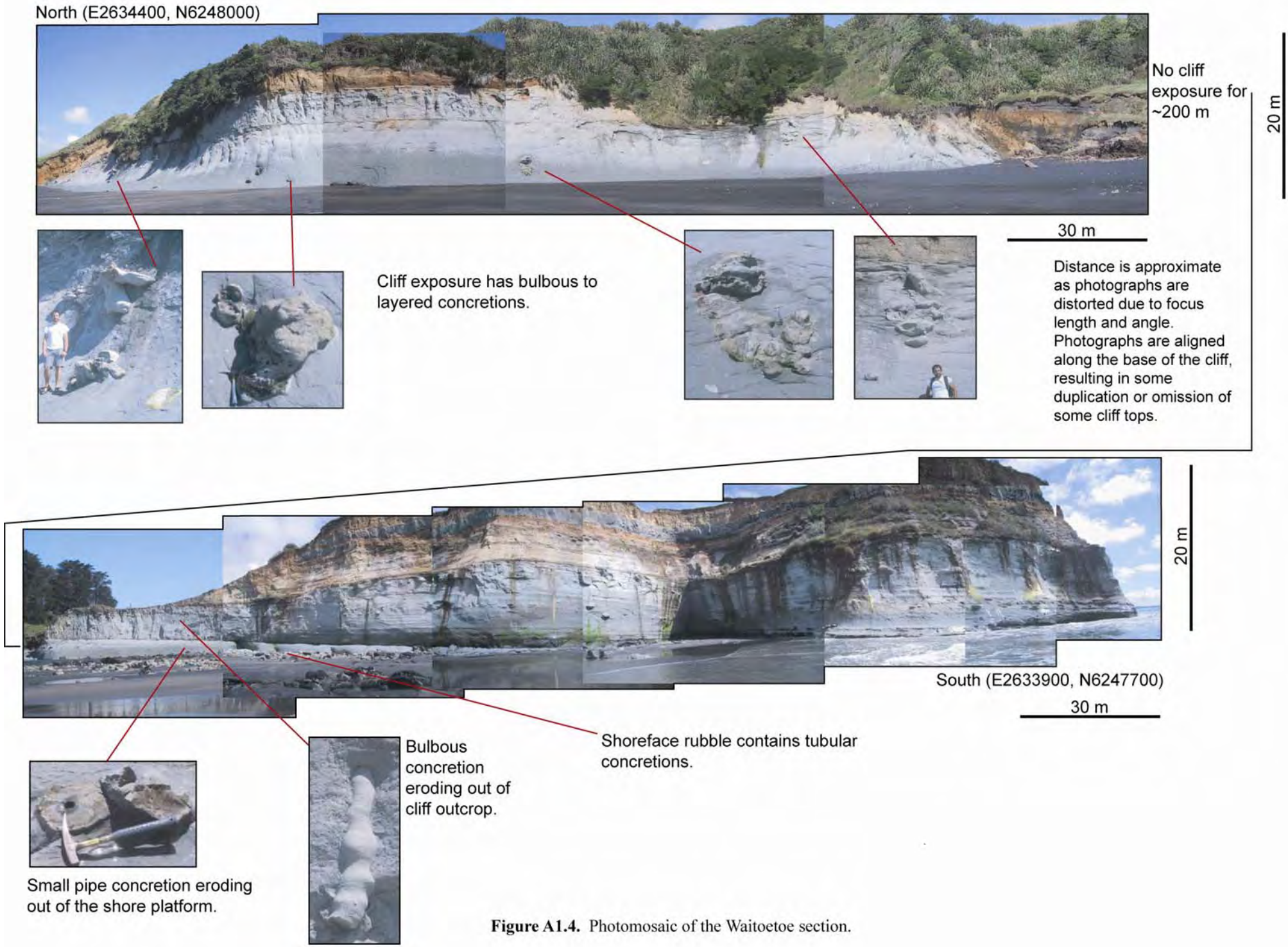

Figure A1.4. Photomosaic of the Waitoetoe section.

3. Field photographs

Photographs of tubular concretions (Figs. A1.5 to A1.8) in the field are presented in this section along with brief descriptions in Tables A1.2-A1.5 (jpg number corresponds to that in Table). A DVD accompanies this volume, where the photographs can be viewed at a larger scale (Appendix\Taranaki\FieldPhotos).

3.1 Pipe concretions

Table A1.2. Photograph descriptions of pipe concretions (see Fig. A1.5).

Photograph jpg no.	Location	Comment
1000	Mimi	Straight, segmented pipe.
1001	Mimi	Meandering pipe.
1002	Mimi	Straight, segmented pipe with nodular-like concretions eroding out of the cliff to the left.
1003	Mimi	Close up of 1002
1004	Mimi	Cross-section of pipe. Conduit has colour zonation and small open pinhole.
1005	Mimi	Meandering, segmented pipe, notice second pipe protruding on the left.
1006	Mimi	Pipe (slightly bulbous) on shore platform with open conduit.
1007	Mimi	Branching pipe concretion.
1008	Mimi	Branching and anastomosing pipe.
1009	Waitoetoe	Close up of pipe that is truncated by an erosional surface.
1010	Wai-iti channel	Pipe concretion weathering out of the Wai-iti Channel conglomerate.
1011	Mimi	Pipe concretion weathering out of the Wai-iti Channel conglomerate.
1012	Mimi	Slabby concretion in the Wai-iti Channel conglomerate.
1013	Mimi	Close up of 1012, also shows a pipe concretion.
1014	Wai-iti Channel	Graded bedding of Wai-iti Conglomerate with pipe concretion cross-sections protruding.
1015	Wai-iti Channel	Cross-sections of pipes protruding fromf Wai-iti Conglomerate, notice the conduits have been filled with the same material (shell hash) as that in the conglomerate matrix.
1016	Wai-iti Channel	Pipe with open conduit (Wai-iti Conglomerate)
1017	Wai-iti Channel	Pipe in Wai-iti Conglomerate. Conduit filled with shell hash of conglomerate matrix.

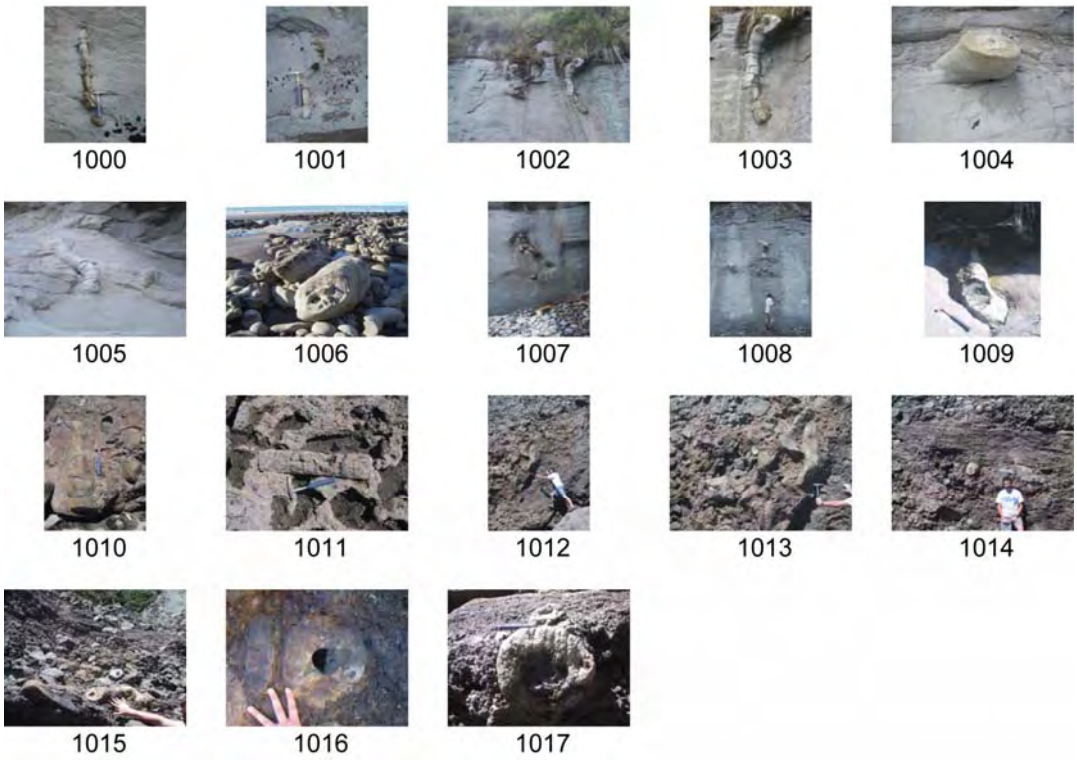

Figure A1.5. Photographs of pipe concretions. See Table A1.2 for descriptions.

3.2 Bulbous concretions

Table A1.3. Photograph descriptions of bulbous concretions (see Fig. A1.6).

Photograph jpg no.	Location	Comment
1018	Mimi	Bulbous concretion, note deviation to the right where the two halves are connected by a thin concretion margin.
1019	Mimi	Same concretion as in 1018. Photograph taken 2 years later, notice sand build up has covered the lower half of the concretion.
1020	Mimi	Meandering bulbous concretion, which is hypothesised to have once been connected. Height of cliff is ~10 m.
1021	Mimi	Close up of 1020 (upper portion).
1022	Mimi	Tortuous bulbous concretion.
1023	Mimi	Rather straight bulbous concretion.
1024	Waitoetoe	Bulbous concretion eroding out of the cliff. Note in the foreground there are several concretions protruding from the platform. Cross-sections display open and filled conduits (see Waitoetoe photomosaic).
1025	Mimi	Close up of bulbous concretion in cliff (1024).
1026	Mimi	Meadering bulbous concretion.
1027	Mimi	Meadering bulbous concretion.
1028	Mimi	Bulbous concretion with layered-like morphology.
1029	Mimi	Bulbous concretion with layered-like morphology.
1030	Mimi	Bulbous concretion with layered-like morphology.
1031	Mimi	Thin bulbous concretion that meanders up the cliff (right side of photograph).
1032	Mimi	Close up of 1031.
1033	Mimi	Bulbous concretion.
1034	Waitoetoe	Bulbous concretion.
1035	Waitoetoe	Bulbous concretion with layered-like morphology.
1036	Mimi	Bulbous concretion barely discernible in the upper cliff exposure.

Figure A1.6. Photographs of bulbous concretions. See Table A1.3 for descriptions.

3.3 Conduits

Table A1.4. Photograph descriptions of concretion conduits (see Fig. A1.7).

Photograph jpg no.	Location	Comment
1037	Mimi	Large open conduit (0.2 m diameter) in pipe concretion.
1038	Mimi	Open conduit in pipe concretion.
1039	Mimi	Open conduit in pipe concretion with strong fracturing of the outer concretion.
1040	Mimi	Open conduit in small pipe concretion.
1041	Mimi	Open conduit in pipe concretion.
1042	Mimi	Open conduit in pipe concretion.
1043	Mimi	Yellow calcite lining an open conduit.
1044	Mimi	Yellow calcite lining an open conduit of a dissected tubular concretion.
1045	Mimi	Yellow calcite lining an open conduit.
1046	Mimi	Yellow calcite lining an open conduit.
1047	Mimi	Pipe concretion with conduit only distinguishable by colour zonation.
1048	Mimi	Pipe concretion with conduit only distinguishable by colour zonation.
1049	Mimi	Sediment filled conduit of a pipe concretion; note the centre of the conduit appears to have more resistant material.
1050	Mimi	Pipe concretion with a small, pinhole open conduit.

Figure A1.7. Photographs of concretion conduits. See Table A1.4 for descriptions.

3.4 Other concretionary features

Table A1.5. Photograph descriptions of other concretionary features (see Fig. A1.8).

Photograph jpg no.	Location	Comment
1051	Mimi	Semi-circular carbonate ring on shore platform with concretionary debris in the background.
1052	Mimi	Semi-circular carbonate ring on shoreplatform.
1053	Mimi	View of 1052 at low tide; note concretionary debris in background.
1054	Mimi	Smaller semi-circular carbonate ring on shor platform.
1055	Mimi	Mushroom-shaped concretion with a semi-circular ring in background.
1056	Mimi	Remnants of a ring structure and concretionary debris on shore platform. Note bulbous concretion in cliff exposure (see photo 1018)
1057	Mimi	Planar concretionary features (note continuation towards upper left in photo) amongst shorface concretion debris.
1058	Mimi	Concreted mudstone partially surrounding a pipe concretion with an open conduit.
1059	Onaero	Nodular concretions with open pinhole conduits at the centre of each rounded portion and at each end of the elongated portion.
1060	Onaero	View of 1059 at another angle and better light conditions.
1061	Mimi	Potentially a bulbous concretion with large conduit.
1062	Mimi	Highly fractured concretionary debris.
1063	Mimi	Semi-circular concretion with conduit.
1064	Mimi	Highly fractured concretionary debris.
1065	Mimi	Scattered irregurlar concretionary debris on the shore platform.
1066-1083	Various	Irregular concretionary morphologies that may represent varying fluid manifestations.
1084-1089	Patea	One small exposure of tubular concretions was found at Patea.

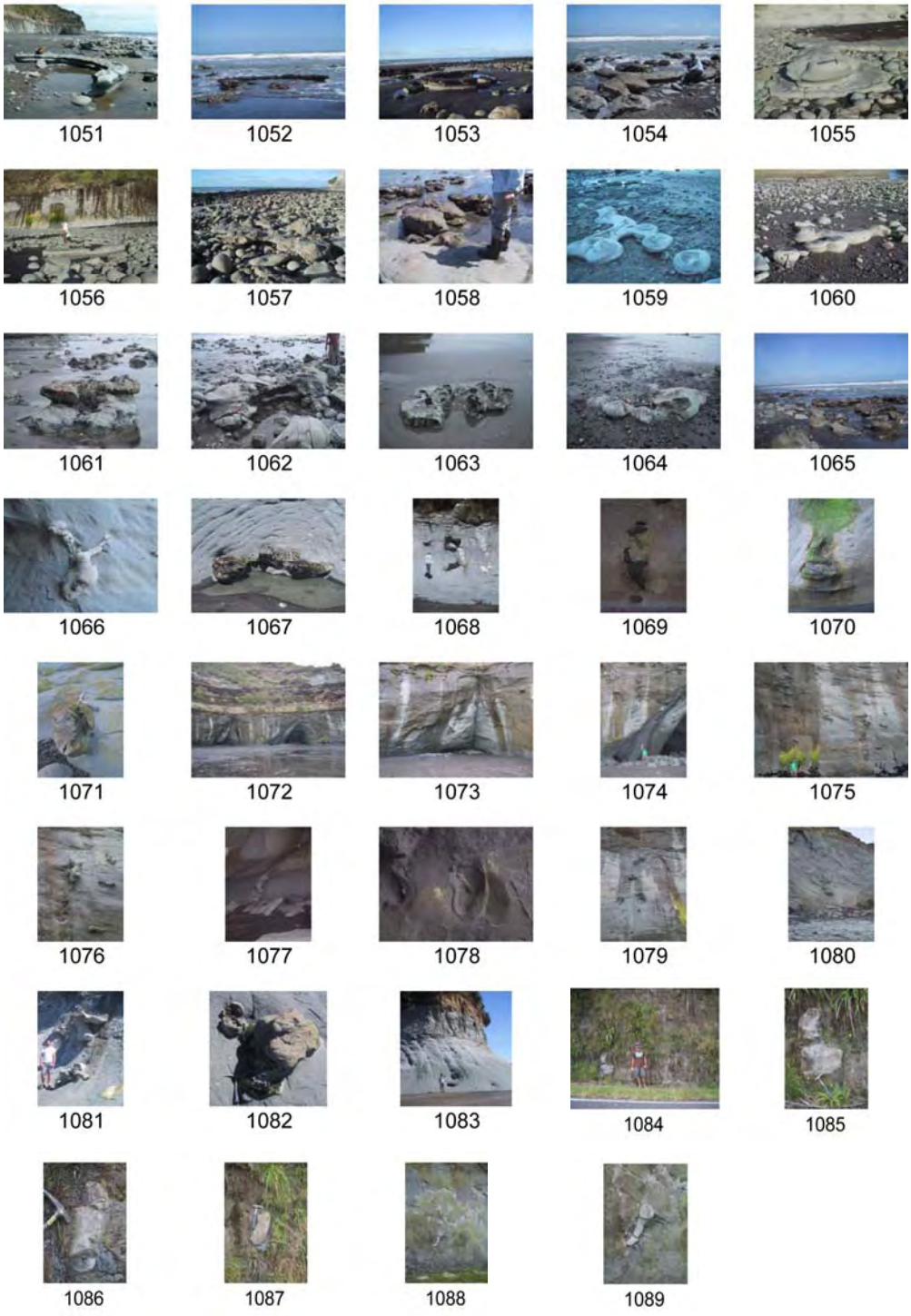

Figure A1.8. Photographs of other concretionary features. See Table A1.5 for descriptions.

4. Samples

Tubular concretion samples are outlined in Table A1.6 and accompanied by photographs (Fig. A1.9, jpg number corresponds to table). Sample names are followed by a hyphen. The number following the hyphen denotes a subsample along a cross-sectional transect (lower number = outer concretion, higher number = conduit/or adjacent to conduit if the conduit is open). The subsamples are treated as individual samples for petrographic and isotopic analyses. Subsample placement along the transect is shown in Section 9 (Isotope transects). A DVD accompanies this volume, where the photographs can be viewed at a larger scale (Appendix\Taranaki\Samples).

Table A1.6. Sample numbers and descriptions.

Waikato no. (UoW)	Sample no.	Comment	Location
20080200	TMc1-1	Pipe outer	Mimi
20080201	TMc1-2	Pipe mid	Mimi
20080202	TMc1-3	Pipe conduit rim	Mimi
20080203	TMf1-1	Bulbous outer	Mimi
20080204	TMf1-2	Bulb mid	Mimi
20080205	TMf1-3	Bulbous conduit	Mimi
20080206	TMf2-1	Pipe outer	Mimi
20080207	TMf2-2	Pipe mid	Mimi
20080208	TMf2-3	Pipe conduit	Mimi
20080209	TWAf1-1	Pipe outer	Waitoetoe
20080210	TWAf1-2	Pipe mid	Waitoetoe
20080211	TWAf1-3	Pipe couduit	Waitoetoe
20080212	TOf1-1	Cannon outer	Onaero
20080213	TOf1-2	Cannon conduit rim	Onaero
20080214	Tmcs1-1v	Sphere outer	Mimi
20080215	Tmcs1-2v	Sphere mid	Mimi
20080216	Tmcs1-2h3h	Sphere mid horz	Mimi
20080217	Tmcs1-3c	Sphere center	Mimi
20080218	T1	Conc. Layer	Mimi
20080219	T2	Waiiti conc layer	Mimi
20080220	T3	Clam crust	Mimi
20080221	T4	Clam inside	Mimi
20080222	T5	Crown	Mimi
20080223	T6	Crown 2	Mimi
20080224	T7	Sub crown inner	Mimi
20080225	T8	Sub crown	Mimi
20080226	T9	Slab 1	Mimi
20080227	T10	Slab 2	Mimi
20080228	T11	Conduit (secondary) fill	Mimi
20080229	Tm-host	Host mudstone	Mimi
20080230	PAc2-1	Outer	Patea Dam
20080231	PAc2-2	Middle	Patea Dam
20080232	PAc2-3	Inner	Patea Dam
20080233	PAc3-1	Outer	Patea Dam
20080234	PAc3-2	Middle	Patea Dam
20080235	PAc3-3	Inner	Patea Dam

Table A1.6 continued

Sample no.	Comment	Location
Legacy data from Franziska Schellenberg (2002)		
TMcP71-z1	Pipe	Mimi
TMcP71-z2	Pipe	Mimi
TMcP71-z3	Pipe	Mimi
TMcP72-4-X	Pipe	Mimi
TMcP72-1	Pipe	Mimi
TMcP72-2	Pipe	Mimi
TMcP72-3	Pipe	Mimi
TMcP72-4	Pipe	Mimi
TMcP72-5	Pipe	Mimi
TMcP72-z1	Pipe	Mimi
TMcP72-z2	Pipe	Mimi
TMcP72-z3	Pipe	Mimi
TMcP73-1	Pipe	Mimi
TMcP73-2	Pipe	Mimi
TMcP73-3	Pipe	Mimi
TMcP73-4	Pipe	Mimi
TMcP73-3b	Pipe	Mimi
TMcP73-2b	Pipe	Mimi
TMcP73-1b	Pipe	Mimi
TMcP73-z1	Pipe	Mimi
TMcP73-z2	Pipe	Mimi
TMcP81-2	Pipe	Mimi
TMcP81-3	Pipe	Mimi
TMcP81-4	Pipe	Mimi
TMcP81-z1	Pipe	Mimi
TMcP81-z2	Pipe	Mimi
TMcP81-z3	Pipe	Mimi
TMcP81-z4	Pipe	Mimi
TMcP81-z5	Pipe	Mimi
TMcP81-5b	Pipe	Mimi
TMcP81-3b	Pipe	Mimi
TMcP81-2b	Pipe	Mimi
TMcP81-1b	Pipe	Mimi
TMcP83_z1	Pipe	Mimi
TMcP83_z2	Pipe	Mimi
TMcP83_z3	Pipe	Mimi
TMcP9-1	Pipe	Mimi
TMcP9-2	Pipe	Mimi
TMcP9-3	Pipe	Mimi
TMcP9-4	Pipe	Mimi
TMcP9-5	Pipe	Mimi
TMcP9-6	Pipe	Mimi

Table A1.6 continued

Sample no.	Comment	Location	Sample no.	Comment	Location
Legacy data from Franziska Schellenberg (2002)					
TMcP71-z1	Pipe	Mimi	TMcP9-7z	Pipe	Mimi
TMcP71-z2	Pipe	Mimi	TMcP9-z1	Pipe	Mimi
TMcP71-z3	Pipe	Mimi	TMcP9-z2	Pipe	Mimi
TMcP72-4-X	Pipe	Mimi	TMcP9-z3	Pipe	Mimi
TMcP72-1	Pipe	Mimi	TMcP9-z4	Pipe	Mimi
TMcP72-2	Pipe	Mimi	TMcP9-z5	Pipe	Mimi
TMcP72-3	Pipe	Mimi	TMcP9-z6	Pipe	Mimi
TMcP72-4	Pipe	Mimi	TMcP10-1	Pipe	Mimi
TMcP72-5	Pipe	Mimi	TMcP10-2	Pipe	Mimi
TMcP72-z1	Pipe	Mimi	TMcP10-3	Pipe	Mimi
TMcP72-z2	Pipe	Mimi	TMcP10-4	Pipe	Mimi
TMcP72-z3	Pipe	Mimi	TMcP10-5	Pipe	Mimi
TMcP73-1	Pipe	Mimi	TMcP10-5b	Pipe	Mimi
TMcP73-2	Pipe	Mimi	TMcP10-3b	Pipe	Mimi
TMcP73-3	Pipe	Mimi	TMcP10-1b	Pipe	Mimi
TMcP73-4	Pipe	Mimi	TMcP1-1	Bulbous	Mimi
TMcP73-3b	Pipe	Mimi	TMcP1-2	Bulbous	Mimi
TMcP73-2b	Pipe	Mimi	TMcP1-3	Bulbous	Mimi
TMcP73-1b	Pipe	Mimi	TMcP1-4	Bulbous	Mimi
TMcP73-z1	Pipe	Mimi	TMcP1-5	Bulbous	Mimi
TMcP73-z2	Pipe	Mimi	TMcP1-6	Bulbous	Mimi
TMcP81-2	Pipe	Mimi	TMcP1-7	Bulbous	Mimi
TMcP81-3	Pipe	Mimi	TMcP1-z1	Bulbous	Mimi
TMcP81-4	Pipe	Mimi	TMcP1-z2	Bulbous	Mimi
TMcP81-z1	Pipe	Mimi	TMcP1-z3	Bulbous	Mimi
TMcP81-z2	Pipe	Mimi	TMcP3-1	Bulbous	Mimi
TMcP81-z3	Pipe	Mimi	TMcP3-2	Bulbous	Mimi
TMcP81-z4	Pipe	Mimi	TMcP3-3	Bulbous	Mimi
TMcP81-z5	Pipe	Mimi	TMcP3-4	Bulbous	Mimi
TMcP81-5b	Pipe	Mimi	TMcP3-5	Bulbous	Mimi
TMcP81-3b	Pipe	Mimi	TMcP3-6	Bulbous	Mimi
TMcP81-2b	Pipe	Mimi	TMcP3-7	Bulbous	Mimi
TMcP81-1b	Pipe	Mimi	TMcP3-9	Bulbous	Mimi
TMcP83 z1	Pipe	Mimi	TMcP3-10	Bulbous	Mimi
TMcP83 z2	Pipe	Mimi	TMcP3-11	Bulbous	Mimi
TMcP83 z3	Pipe	Mimi	TMcP5-1	Bulbous	Mimi
TMcP9-1	Pipe	Mimi	TMcP5-2	Bulbous	Mimi
TMcP9-2	Pipe	Mimi	TMcP5-3	Bulbous	Mimi
TMcP9-3	Pipe	Mimi	TMcP5-4	Bulbous	Mimi
TMcP9-4	Pipe	Mimi	TMcP5-z1	Bulbous	Mimi
TMcP9-5	Pipe	Mimi	TMcP5-z2	Bulbous	Mimi
TMcP9-6	Pipe	Mimi	TMcP6-1	Bulbous	Mimi
			TMcP6-2	Bulbous	Mimi
			TMcP6-3	Bulbous	Mimi
			TMcP6-4	Bulbous	Mimi
			TMcP6-5	Bulbous	Mimi
			TMcP6-6	Bulbous	Mimi
			TMcP6-7	Bulbous	Mimi
			TMcP6-8	Bulbous	Mimi
			TMcP6-4b	Bulbous	Mimi

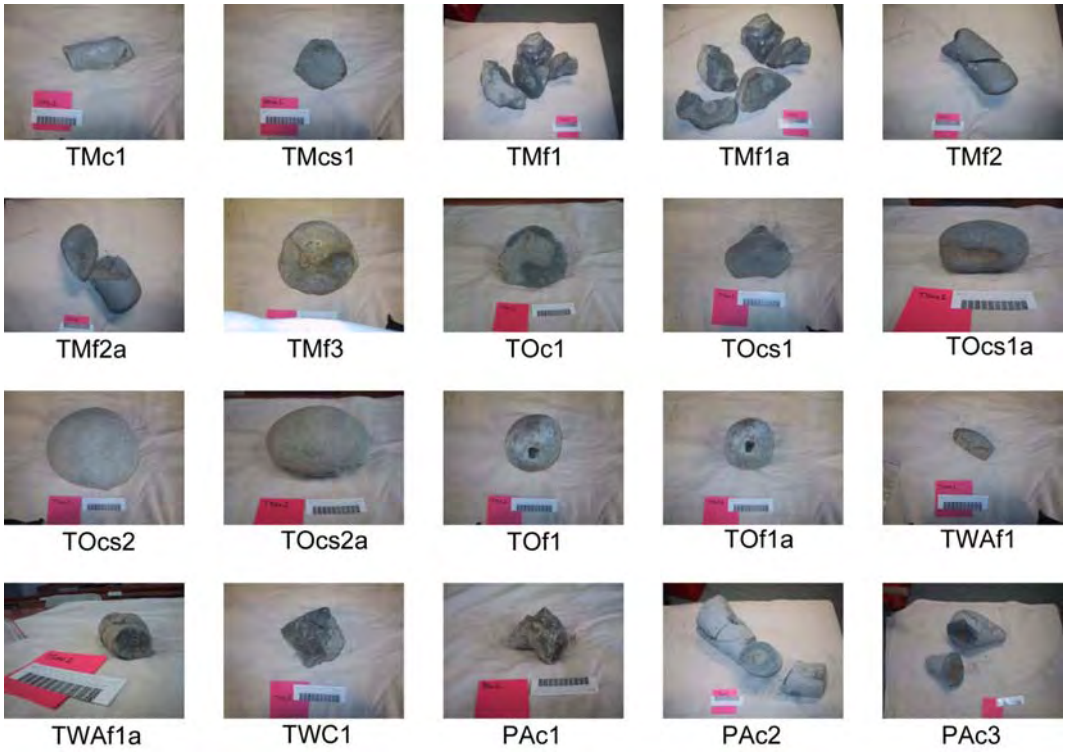

Figure A1.9. Photographs of samples. See Table A1.6 for descriptions.

5. Photomicrographs

Photomicrographs of tubular concretions are presented in Figure A1.10 with brief descriptions in Table A1.7 (jpg number corresponds to table). A DVD accompanies this volume, where the photomicrographs can be viewed at a larger scale (Appendix\Taranaki\Petrography). A selection of subsamples were cut and mounted on glass slides for standard thin section analysis. No staining or impregnation was done on the thin sections. Further thin sections were not produced as the Taranaki samples were predominately micritic carbonate within fine grained siliciclastics.

Table A1.7. Descriptions of photomicrographs.

Sample	Photomicro-graph jpg no.	Comment
TMf2-1	1090	Outer concretion body; siliciclastic mudstone composed mainly of quartz and feldspars cemented by micrite (PPL)
TMf2-1	1091	CL of 1090
TMf2-1	1092	Outer concretion body; siliciclastic mudstone cemented by micritic dolomite (PPL)
TMf2-1	1093	CL of 1092
TMc1-1	1094	Outer concretion body with a benthic foram.
TMc1-1	1095	Outer concretion body with a planktic foram filled with pyrite framboids.
TMc1-1	1096	Gastropod filled with pyrite framboids (PPL).
TMc1-1	1097	Peloids in the concretion (PPL).
TMc1-3	1098	Sample of concretion located adjacent to the conduit; note the higher content of carbonate cement (PPL).
TMc1-3	1099	CL of 1098
TMc1-3	1100	Conduit filled mainly by micrite and blocky calcite lining vugs. A third phase of carbonate (micrite) is present lining the main open conduit. Note the low amount of siliciclastics (PPL).
TMc1-3	1101	CL of 1100
TMc1-3	1102	Higher magnification of 1100 (PPL).
TMc1-3	1103	Higher magnification of 1101 (CL).
TMc1-3	1104	Micrite surrounding pyrite framboid and blocky calcite lining vugs (PPL).
TMc1-3	1105	CL of 1104
TMf1-3	1106	Calcite filled vein (PPL).
TMf1-3	1107	CL of 1106
TMf1-3	1108	Veins through concretion filled with second phase of micrite (PPL).
TMf1-3	1109	CL of 1108
TMf1-3	1110	Veins through concretion filled with second phase of micrite (PPL).
TMf1-3	1111	CL of 1111
TMF2-3	1112	Veins in concretion adjacent to conduit (PPL).
TMF2-3	1113	CL of 1112
TMF2-3	1114	Blocky calcite in vug (PPL).
TMF2-3	1115	CL of 1114
TMF2-3	1116	Blocky calcite in vug (PPL).
TMF2-3	1117	CL of 1116
TMF2-3	1118	Veins in concretion adjacent to conduit (PPL).
TMF2-3	1119	CL of 1117
TMF2-3	1120	Blocky calcite in vug (PPL).
TMF2-3	1121	CL of 1117
TMF2-3	1122	Vugs lined with calcite and small veins extending from vugs through the concretion micrite (PPL).
TMF2-3	1123	CL of 1122

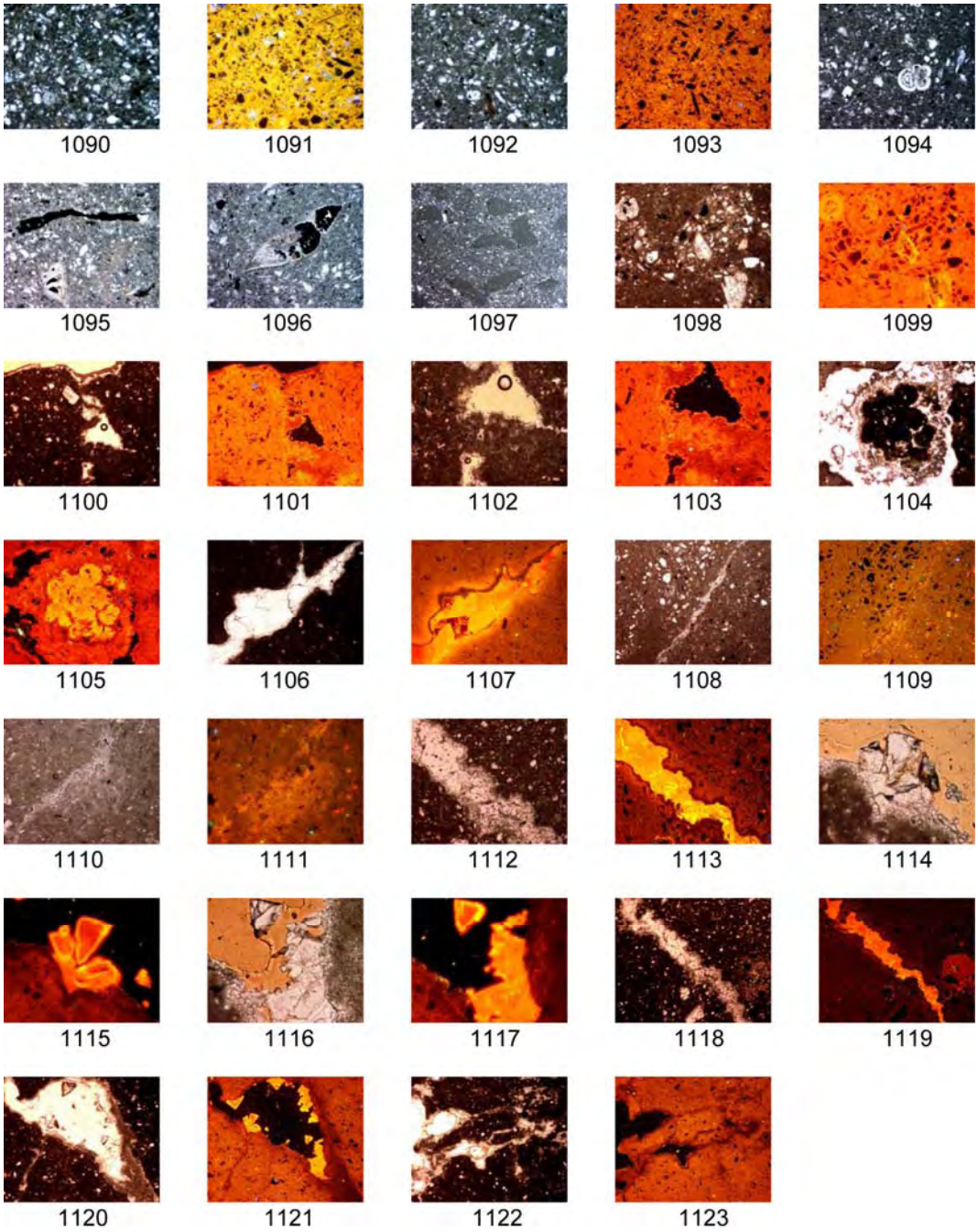

Figure A1.10. Photomicrographs of tubular concretions and conduits. See Table A1.7 for descriptions.

6. XRD graphs

Appendix Section 6 contains XRD graphs that are characteristic of pipe and bulbous concretions. Sample name is in the upper left hand corner of the XRD graph.

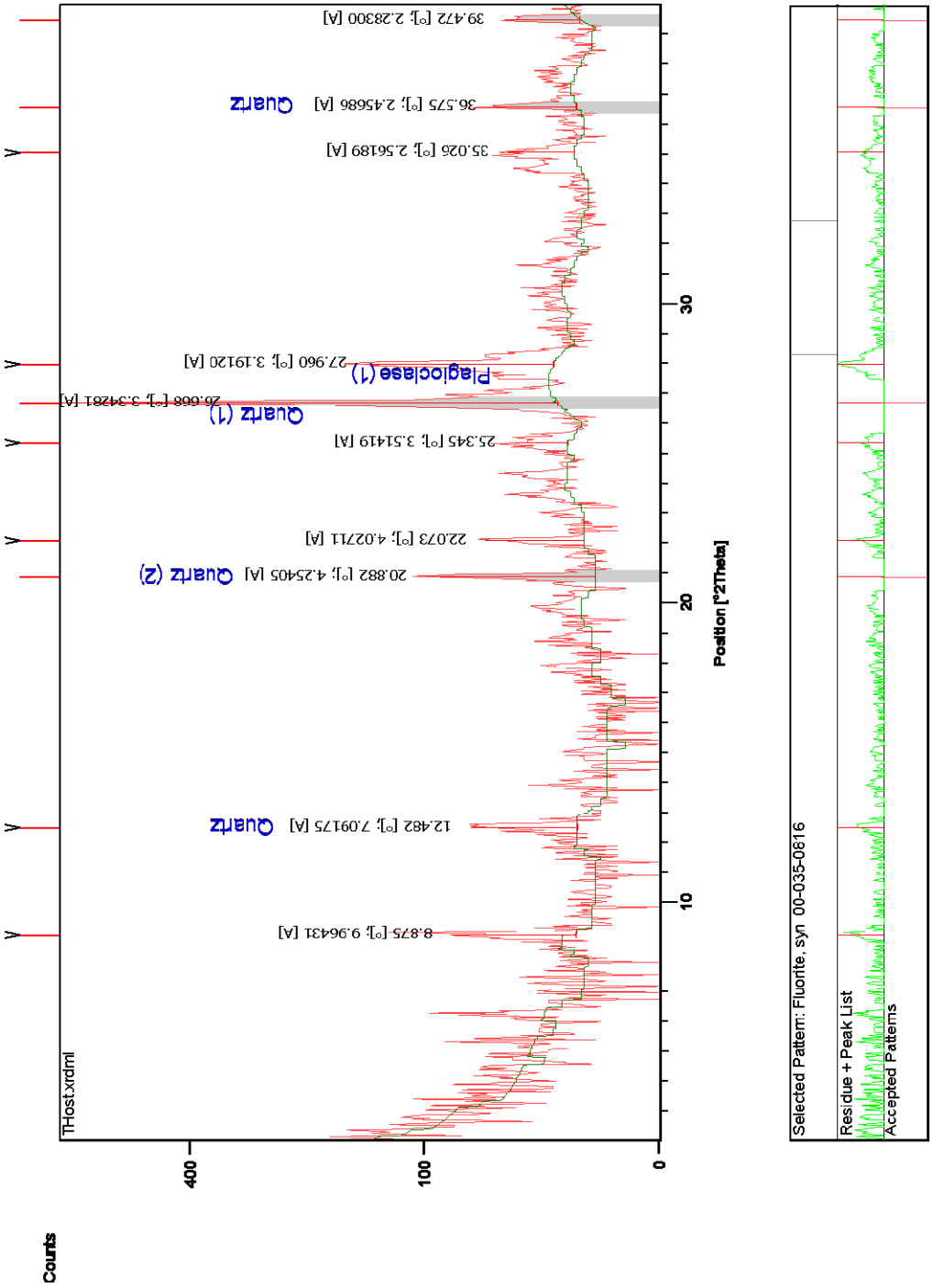
Counts
400
100
0
10
20
30
Position [°2Theta]
THost.xrdml
8.875 [°]; 9.96431 [Å]
Quartz
12.482 [°]; 7.09175 [Å]
Quartz (2)
20.882 [°]; 4.25405 [Å]
22.073 [°]; 4.02711 [Å]
25.345 [°]; 3.51419 [Å]
Quartz (1)
26.668 [°]; 3.34281 [Å]
Plagioclase (1)
27.960 [°]; 3.19120 [Å]
35.026 [°]; 2.56189 [Å]
Quartz
36.575 [°]; 2.45686 [Å]
39.472 [°]; 2.28300 [Å]
Selected Pattern: Fluorite, syn 00-035-0616
Residue + Peak List
Accepted Patterns

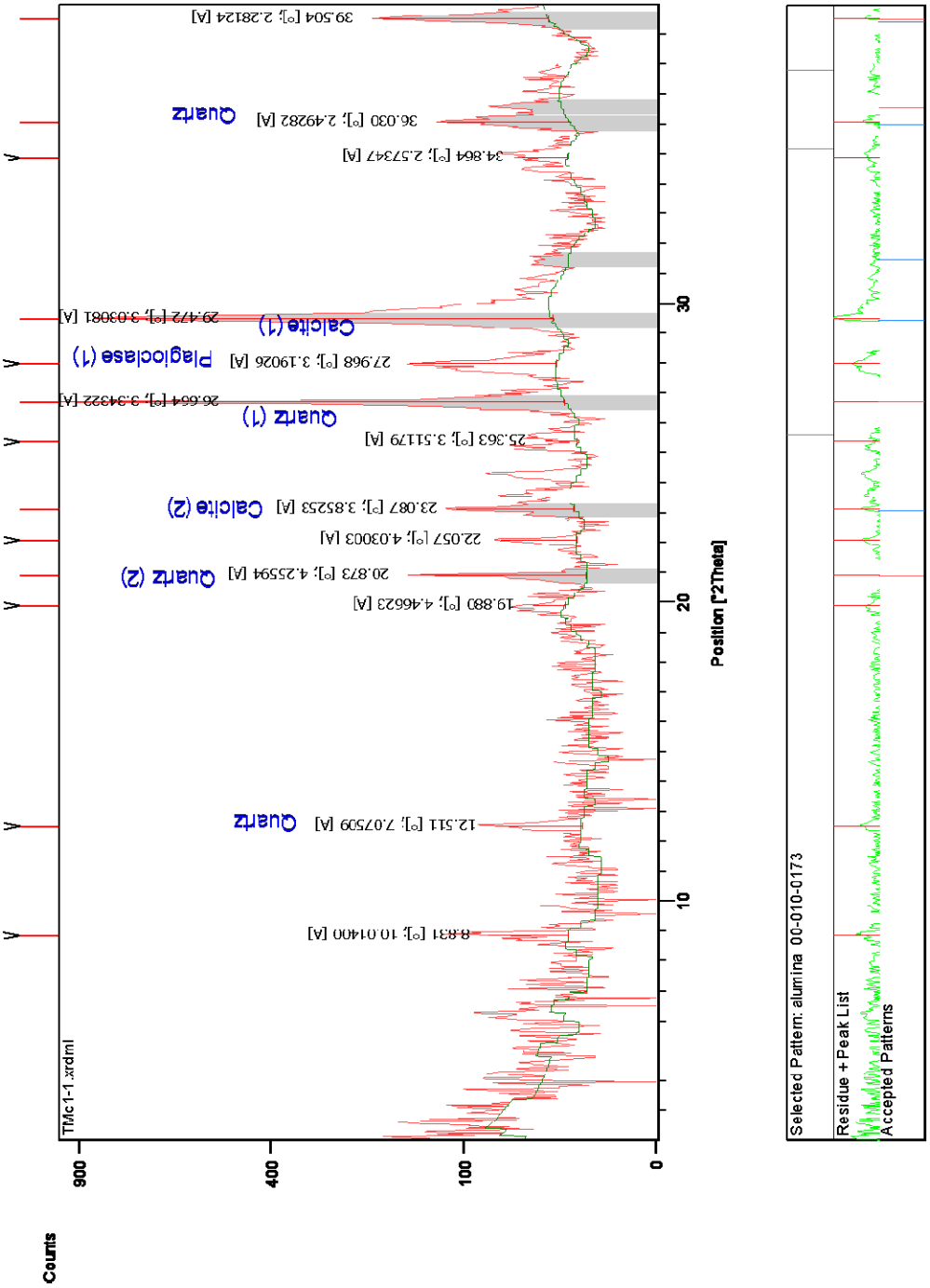
Counts
900
400
100
0
TMc1-1.xrdml
8.831 [°]; 10.01400 [A]
12.511 [°]; 7.07509 [A] Quartz
19.880 [°]; 4.46623 [A]
20.873 [°]; 4.25594 [A] Quartz (2)
22.057 [°]; 4.03003 [A]
23.087 [°]; 3.85253 [A] Calcite (2)
25.363 [°]; 3.51179 [A]
26.664 [°]; 3.34322 [A] Quartz (1)
27.968 [°]; 3.19026 [A] Plagioclase (1)
29.472 [°]; 3.03081 [A] Calcite (1)
34.864 [°]; 2.57347 [A]
36.030 [°]; 2.49282 [A] Quartz
39.504 [°]; 2.28124 [A]
10
20
30
Position [°2Theta]
Selected Pattern: alumina 00-010-0173
Residue + Peak List
Accepted Patterns

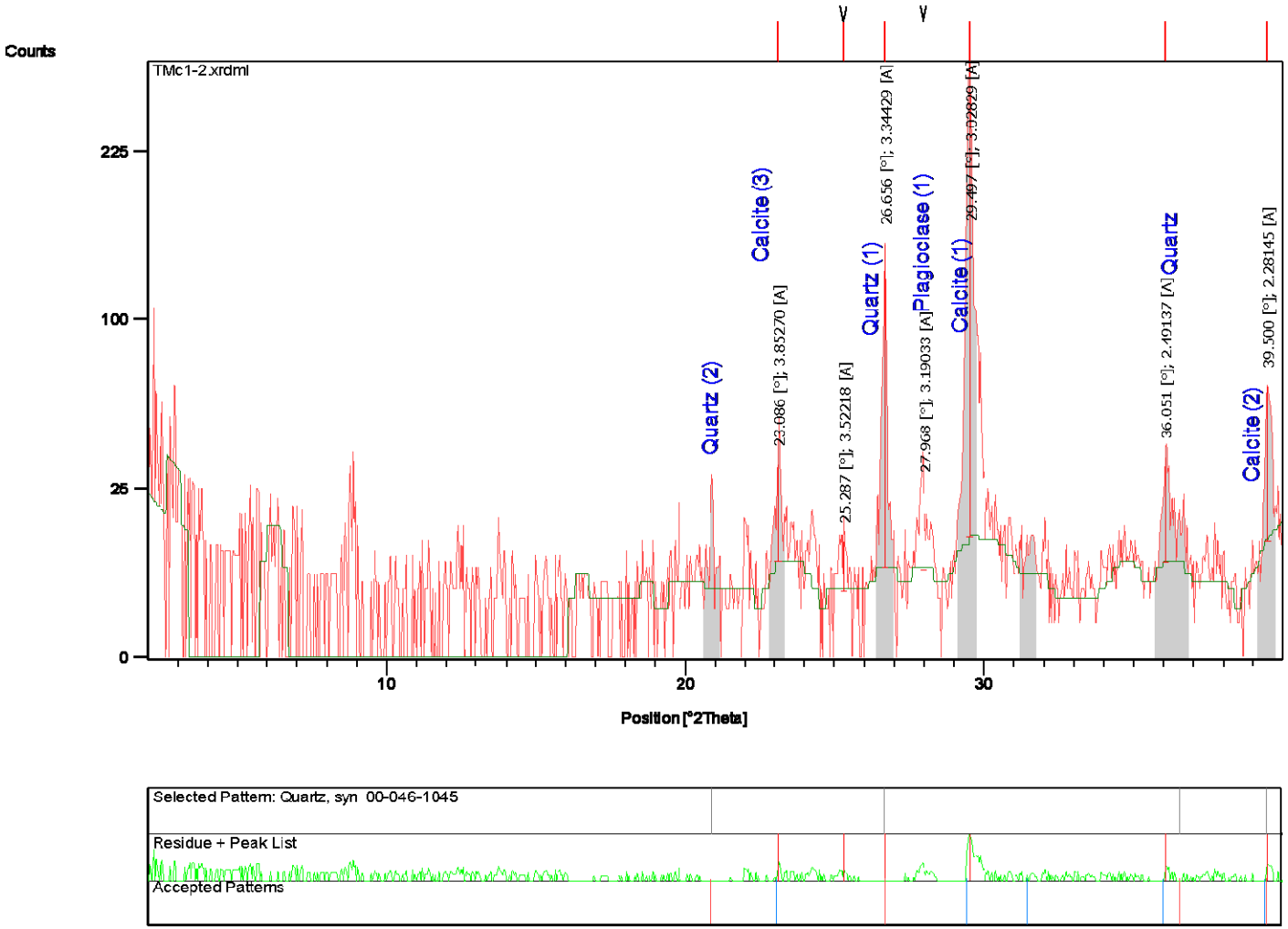
Counts
TMc1-2.xrdml
225
100
25
0
10
20
30
Position [°2Theta]
Quartz (2)
Calcite (3)
23.086 [°]; 3.85270 [A]
25.287 [°]; 3.52218 [A]
Quartz (1)
26.656 [°]; 3.34429 [A]
27.968 [°]; 3.19033 [A]
Plagioclase (1)
Calcite (1)
29.497 [°]; 3.02829 [A]
36.051 [°]; 2.49137 [A]
Quartz
Calcite (2)
39.500 [°]; 2.28145 [A]
Selected Pattern: Quartz, syn 00-046-1045
Residue + Peak List
Accepted Patterns

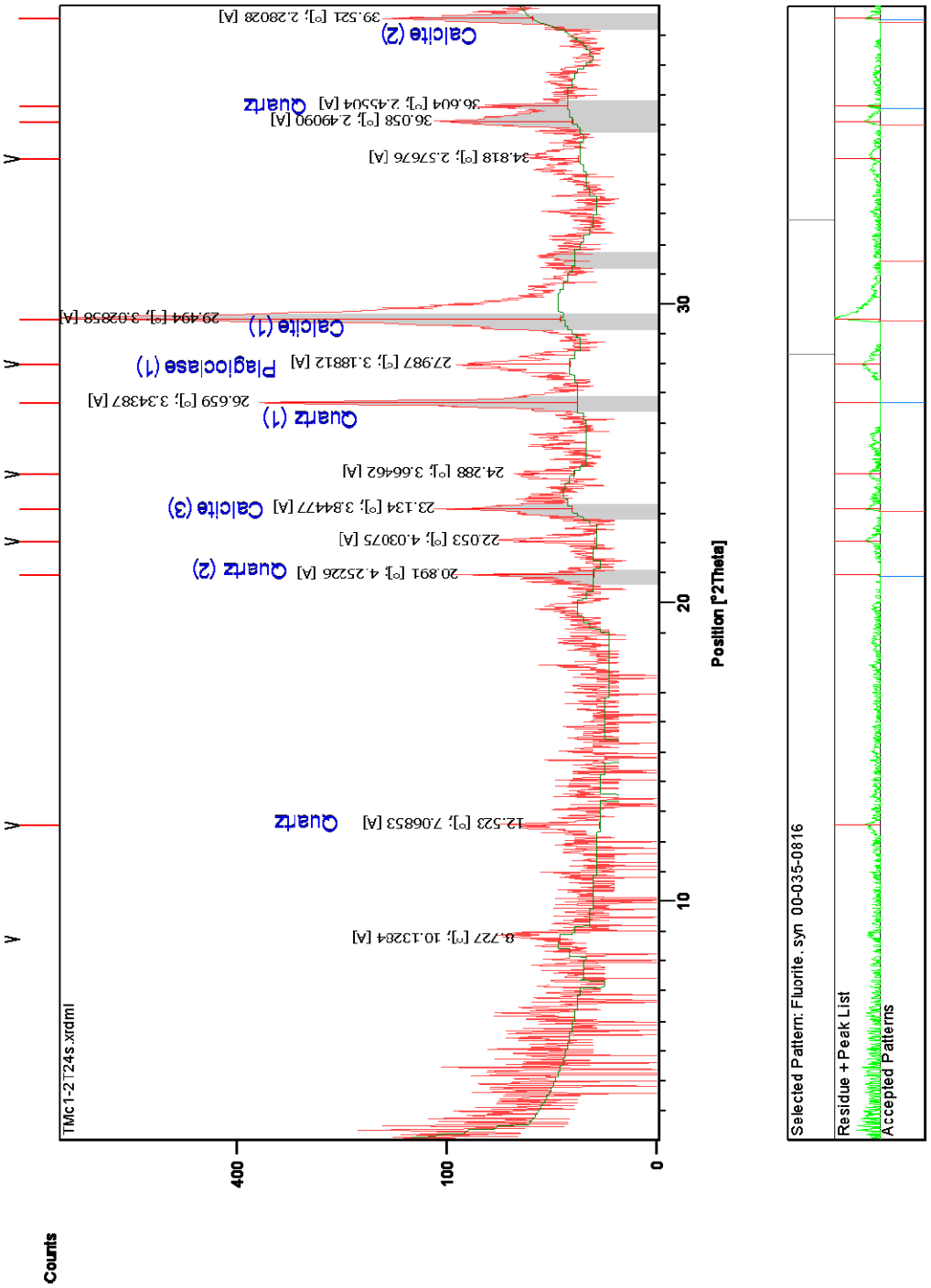
Counts
0
100
400
10
20
30
Position [°2Theta]
TMc1-2T24s.xrdml
8.727 [°]; 10.13284 [A]
12.523 [°]; 7.06853 [A] Quartz
20.891 [°]; 4.25226 [A] Quartz (2)
22.053 [°]; 4.03075 [A]
23.134 [°]; 3.84477 [A] Calcite (3)
24.288 [°]; 3.66462 [A]
26.659 [°]; 3.34387 [A] Quartz (1)
27.987 [°]; 3.18812 [A] Plagioclase (1)
29.494 [°]; 3.02858 [A] Calcite (1)
34.818 [°]; 2.57676 [A]
36.058 [°]; 2.49090 [A]
36.604 [°]; 2.45504 [A] Quartz
39.521 [°]; 2.28028 [A] Calcite (2)
Selected Pattern: Fluorite, syn 00-035-0816
Residue + Peak List
Accepted Patterns

Counts
900
400
100
0
TMc1-2T31s.xrdml
Position [°2Theta]
10
20
30
3.826 [°]; 10.01957 [A]
Quartz
12.483 [°]; 7.09104 [A]
19.838 [°]; 4.47564 [A]
Quartz (2)
20.912 [°]; 4.24810 [A]
22.060 [°]; 4.02944 [A]
Calcite (3)
23.127 [°]; 3.84589 [A]
24.290 [°]; 3.66442 [A]
Quartz (1)
25.394 [°]; 3.50748 [A]
26.662 [°]; 3.34348 [A]
Plagioclasa (1)
27.961 [°]; 3.19107 [A]
Calcite (1)
29.480 [°]; 3.03004 [A]
34.842 [°]; 2.57502 [A]
Quartz
36.068 [°]; 2.49024 [A]
36.575 [°]; 2.45692 [A]
Calcite (2)
39.520 [°]; 2.28032 [A]
Selected Pattern: Fluorite. syn 00-035-0816
Resicue + Peak List
Accepted Patterns

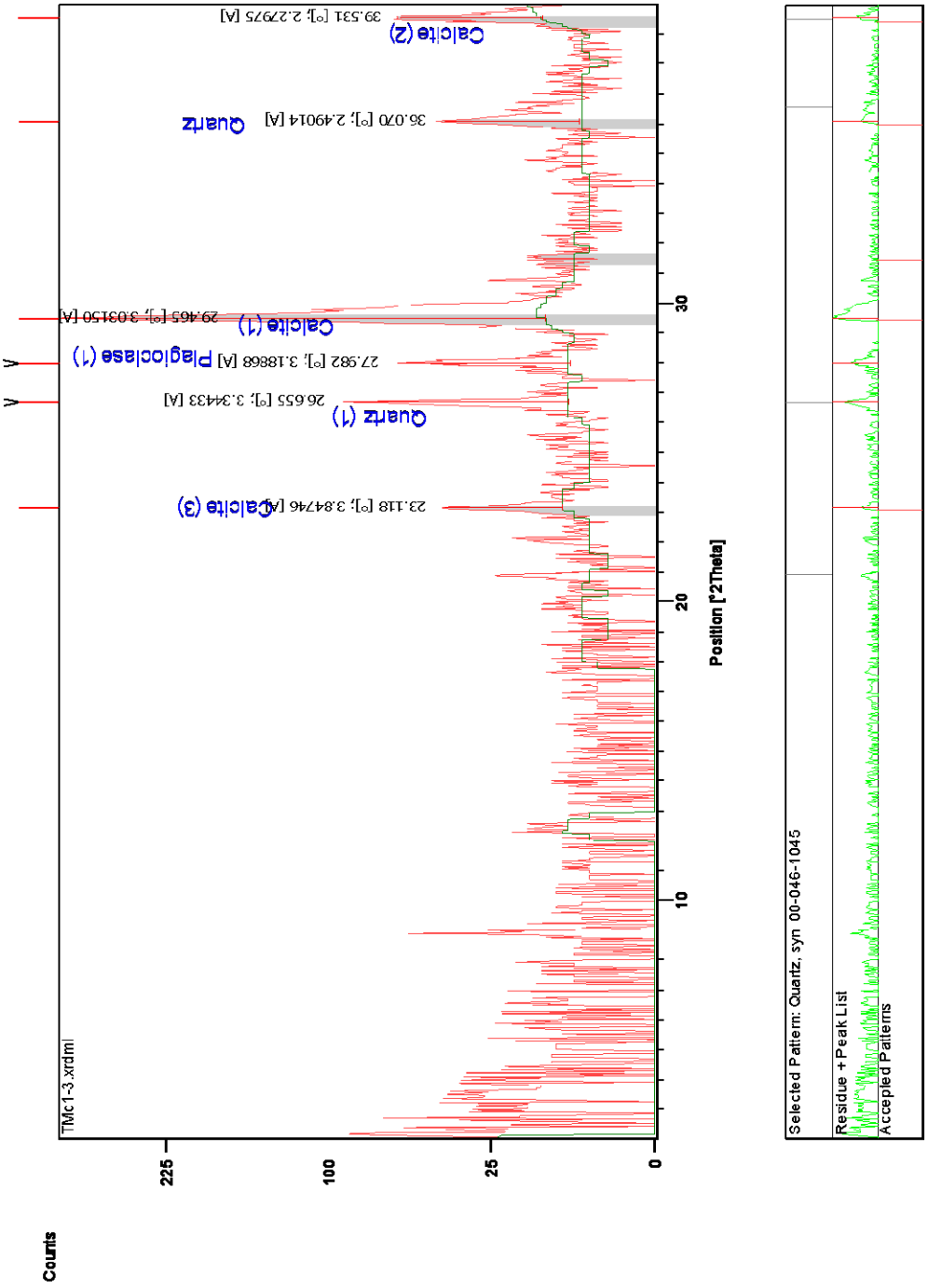
Counts
225
100
25
0
TMc1-3.xrdml
10
20
30
Position [°2Theta]
Calcite (3)
23.118 [°]; 3.84746 [A]
Quartz (1)
26.655 [°]; 3.34433 [A]
Plagioclase (1)
27.982 [°]; 3.18868 [A]
Calcite (1)
29.465 [°]; 3.03150 [A]
Quartz
36.070 [°]; 2.49014 [A]
Calcite (2)
39.531 [°]; 2.27975 [A]
Selected Pattern: Quartz, syn 00-046-1045
Residue + Peak List
Accepted Patterns

Counts
900
400
100
0
TMc1-3A.xrdml
10
20
30
Position [°2Theta]
20.899 [°]; 4.25057 [A] Quartz (2)
22.053 [°]; 4.03076 [A]
23.142 [°]; 3.84343 [A] Calcite (3)
26.673 [°]; 3.34218 [A] Quartz (1)
27.975 [°]; 3.18949 [A] Plagioclase (1)
29.502 [°]; 3.02778 [A] Calcite (1)
34.992 [°]; 2.56431 [A]
36.083 [°]; 2.48926 [A] Quartz
39.545 [°]; 2.27893 [A] Calcite (2)
Selected Pattern: burnt ochre 00-033-0664
Residue + Peak List
Accepted Patterns

Counts
225
100
25
0
TMcs1_1v.xrdml
8.816 [°]; 10.03079 [A]
12.460 [°]; 7.10395 [A]
Quartz
20.837 [°]; 4.26318 [A]
Quartz (2)
22.039 [°]; 4.03323 [A]
25.453 [°]; 3.49951 [A]
Quartz (1)
26.626 [°]; 3.34794 [A]
27.943 [°]; 3.19307 [A]
Plagioclase (1)
29.692 [°]; 3.00888 [A]
Calcite (1)
34.807 [°]; 2.57751 [A]
36.362 [°]; 2.47083 [A]
Quartz
Calcite (2)
10
20
30
Position [°2Theta]
Selected Pattern: Calcite, syn 00-005-0586
Residue + Peak List
Accepted Patterns

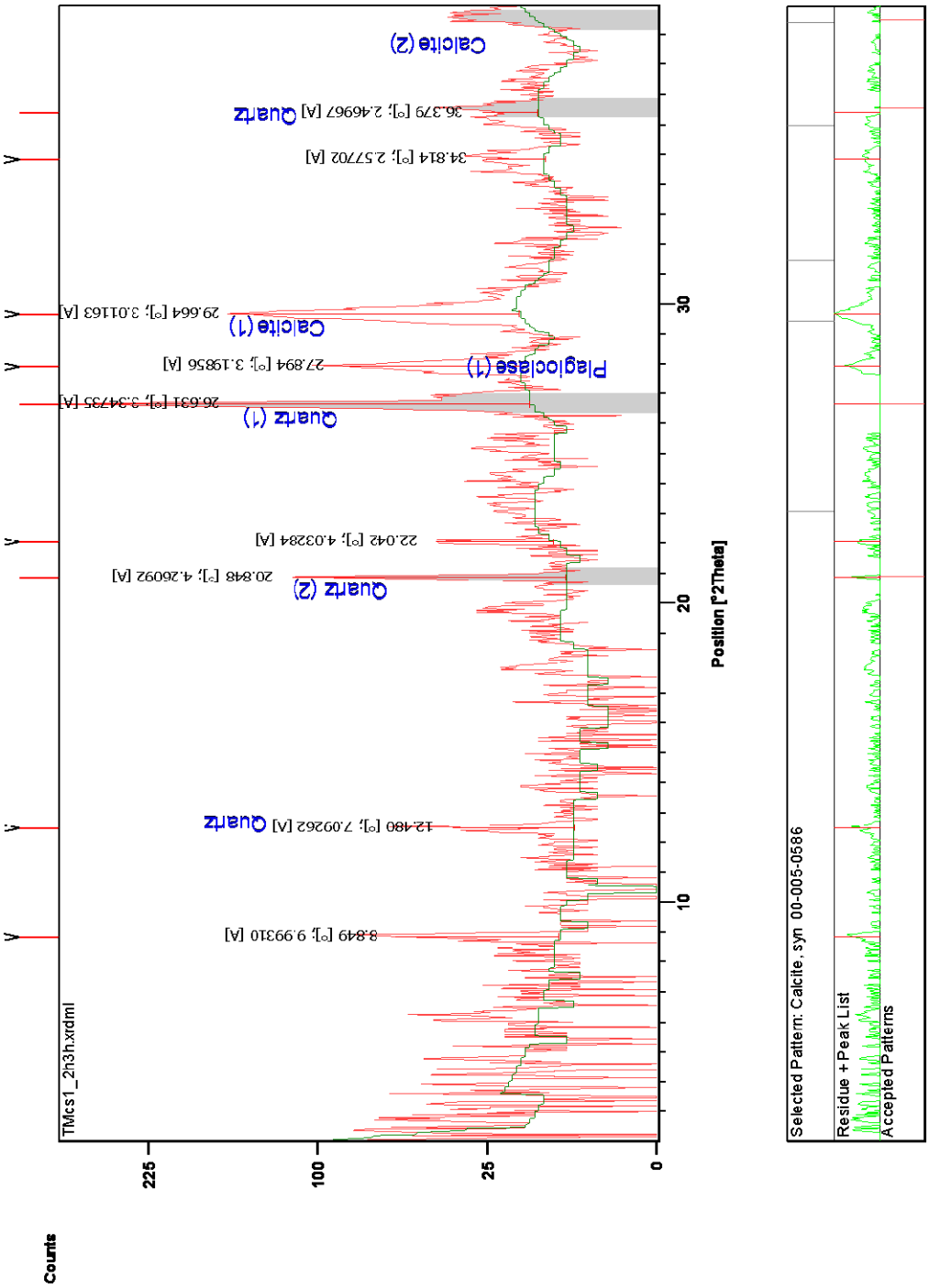
TMcs1_2h3h.xrdml
Counts
225
100
25
0
10
20
30
Position [°2Theta]
8.849 [°]; 9.99310 [Å]
Quartz
12.480 [°]; 7.09262 [Å]
Quartz (2)
20.848 [°]; 4.26092 [Å]
22.042 [°]; 4.03284 [Å]
Quartz (1)
26.631 [°]; 3.34735 [Å]
Plagioclase (1)
27.894 [°]; 3.19856 [Å]
Calcite (1)
29.664 [°]; 3.01163 [Å]
34.814 [°]; 2.57702 [Å]
Quartz
36.379 [°]; 2.46967 [Å]
Calcite (2)
Selected Pattern: Calcite, syn 00-005-0586
Residue + Peak List
Accepted Patterns

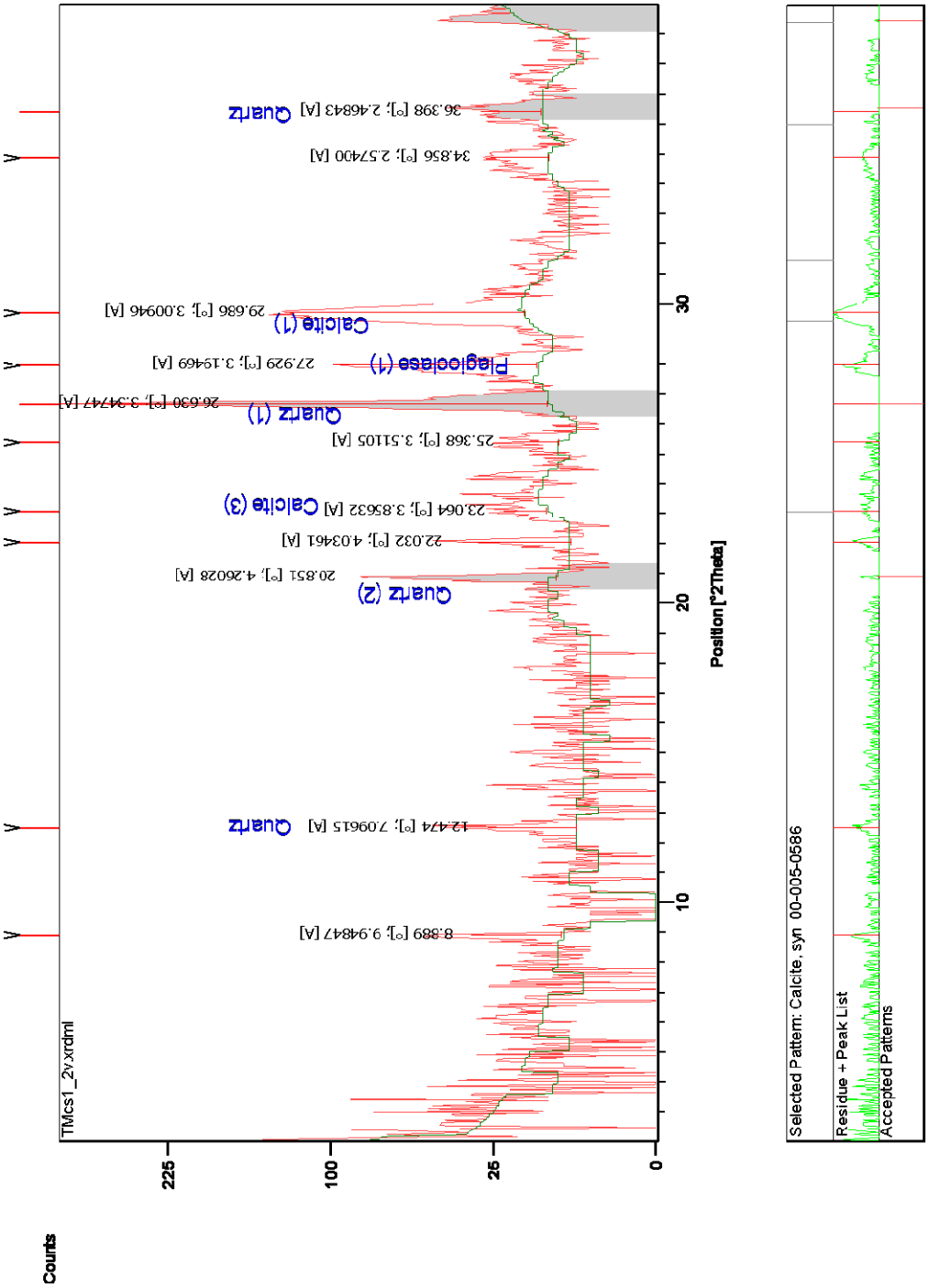
Counts
225
100
25
0
TMcs1_2θ.xrdml
8.889 [°]; 9.94847 [Å]
Quartz
12.474 [°]; 7.09615 [Å]
Quartz (2)
20.851 [°]; 4.26028 [Å]
22.032 [°]; 4.03461 [Å]
Calcite (3)
23.064 [°]; 3.85632 [Å]
25.368 [°]; 3.51105 [Å]
Quartz (1)
26.630 [°]; 3.34747 [Å]
Plagioclase (1)
27.929 [°]; 3.19469 [Å]
Calcite (1)
29.686 [°]; 3.00946 [Å]
34.856 [°]; 2.57400 [Å]
Quartz
36.398 [°]; 2.46843 [Å]
10
20
30
Position [°2Theta]
Selected Pattern: Calcite, syn 00-005-0586
Residue + Peak List
Accepted Patterns

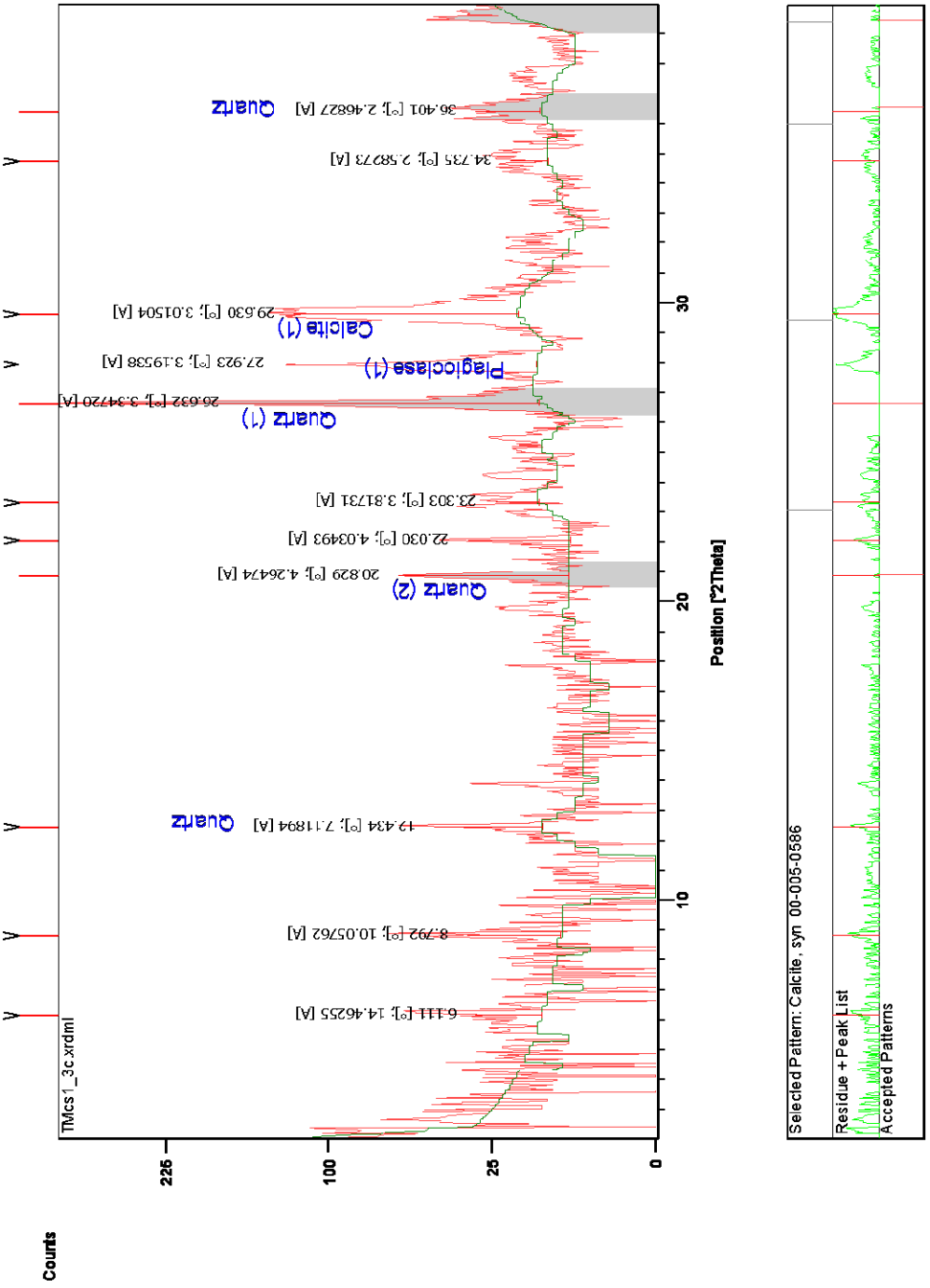
Counts
225
100
25
0
TMcs1_3c.xrdml
6.111 [°]; 14.46255 [A]
8.792 [°]; 10.05762 [A]
19.434 [°]; 7.11894 [A]
Quartz
20.829 [°]; 4.26474 [A]
Quartz (2)
22.030 [°]; 4.03493 [A]
23.303 [°]; 3.81731 [A]
26.632 [°]; 3.34720 [A]
Quartz (1)
27.923 [°]; 3.19538 [A]
Plagioclase (1)
29.630 [°]; 3.01504 [A]
Calcite (1)
34.735 [°]; 2.58273 [A]
36.401 [°]; 2.46827 [A]
Quartz
10
20
30
Position [°2Theta]
Selected Pattern: Calcite, syn 00-005-0586
Residue + Peak List
Accepted Patterns

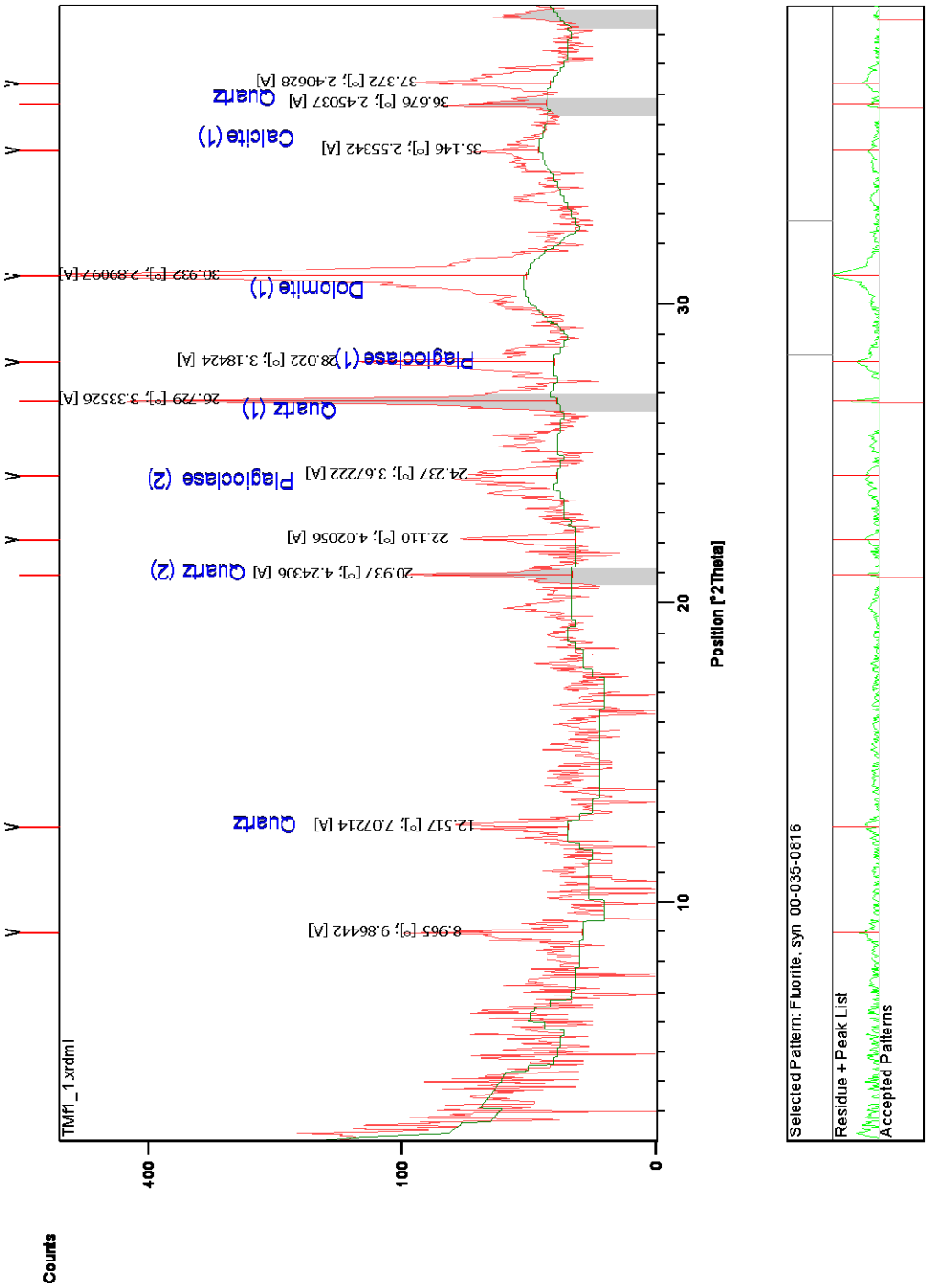
Counts
400
100
0
TMf1_1.xrdml
8.965 [°]; 9.86442 [Å]
Quartz
12.517 [°]; 7.07214 [Å]
Quartz (2)
20.937 [°]; 4.24306 [Å]
22.110 [°]; 4.02056 [Å]
Plagioclase (2)
24.237 [°]; 3.67222 [Å]
Quartz (1)
26.729 [°]; 3.33526 [Å]
Plagioclase (1)
28.022 [°]; 3.18424 [Å]
Dolomite (1)
30.932 [°]; 2.89097 [Å]
Calcite (1)
35.146 [°]; 2.55342 [Å]
Quartz
36.676 [°]; 2.45037 [Å]
37.372 [°]; 2.40628 [Å]
10
20
30
Position [°2Theta]
Selected Pattern: Fluorite, syn 00-035-0816
Residue + Peak List
Accepted Patterns

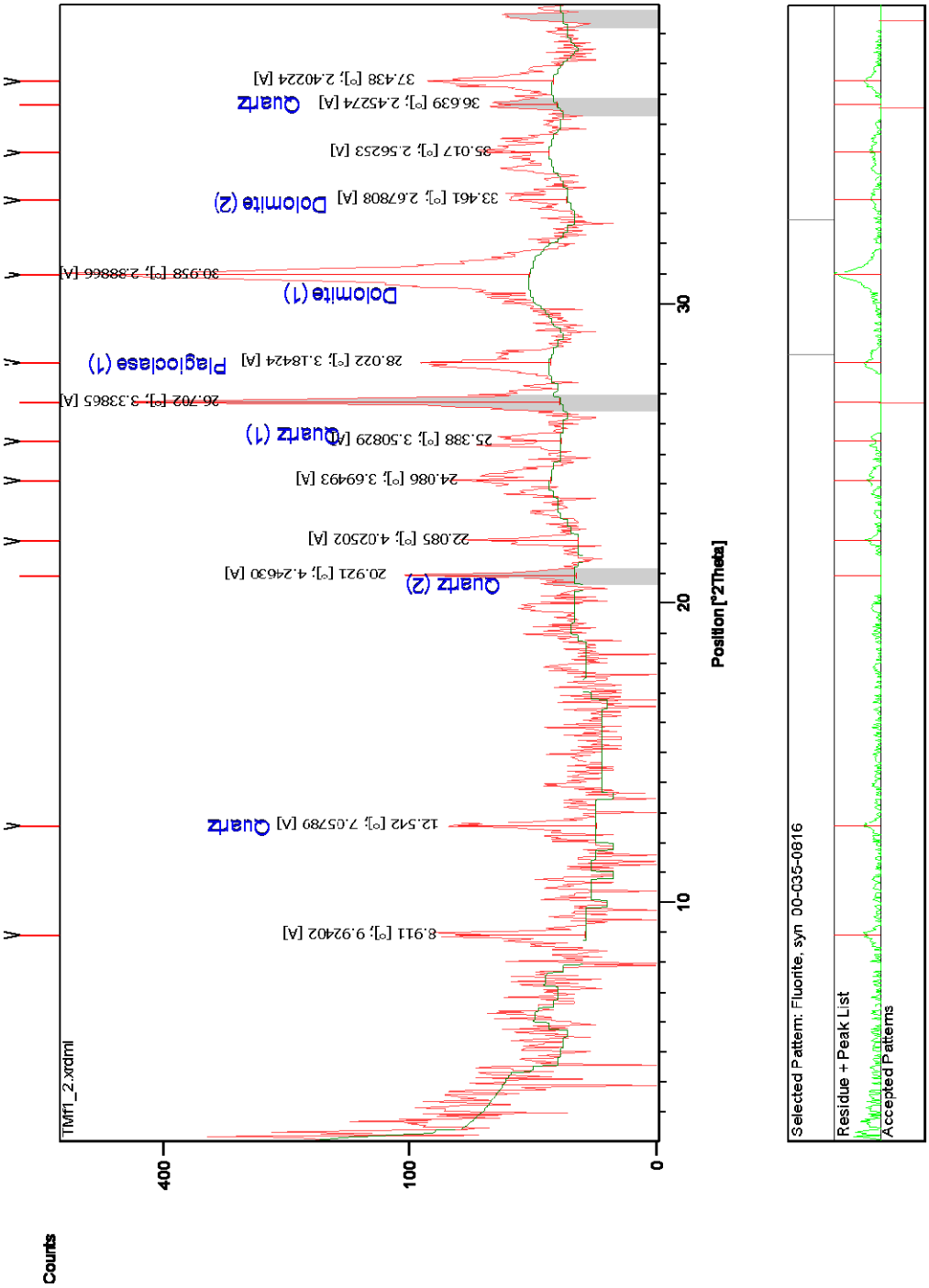
Counts
400
100
0
TMff1_2.xrdml
8.911 [°]; 9.92402 [Å]
12.542 [°]; 7.05789 [Å] Quartz
20.921 [°]; 4.24630 [Å]
Quartz (2)
22.085 [°]; 4.02502 [Å]
24.086 [°]; 3.69493 [Å]
25.388 [°]; 3.50829 [Å] Quartz (1)
26.702 [°]; 3.33865 [Å]
28.022 [°]; 3.18424 [Å] Plagioclase (1)
30.958 [°]; 2.88866 [Å]
Dolomite (1)
33.461 [°]; 2.67808 [Å] Dolomite (2)
35.017 [°]; 2.56253 [Å]
36.639 [°]; 2.45274 [Å] Quartz
37.438 [°]; 2.40224 [Å]
10
20
30
Position [°2Theta]
Selected Pattern: Fluorite, syn 00-035-0816
Residue + Peak List
Accepted Patterns

Counts
900
400
100
0
Thdf1_3.xrdml
12.570 [°]; 7.04222 [Å] Quartz
20.913 [°]; 4.24775 [Å] Quartz (2)
22.113 [°]; 4.01996 [Å]
24.160 [°]; 3.68385 [Å]
26.718 [°]; 3.33663 [Å] Quartz (1)
27.962 [°]; 3.19101 [Å] Plagioclase (1)
31.050 [°]; 2.88028 [Å] Dolomite (1)
33.622 [°]; 2.66563 [Å] Dolomite (2)
35.439 [°]; 2.53298 [Å]
37.457 [°]; 2.40106 [Å] Quartz
10
20
30
Position [°2Theta]
Selected Pattern: Fluorite, syn 00-035-0816
Residue + Peak List
Accepted Patterns

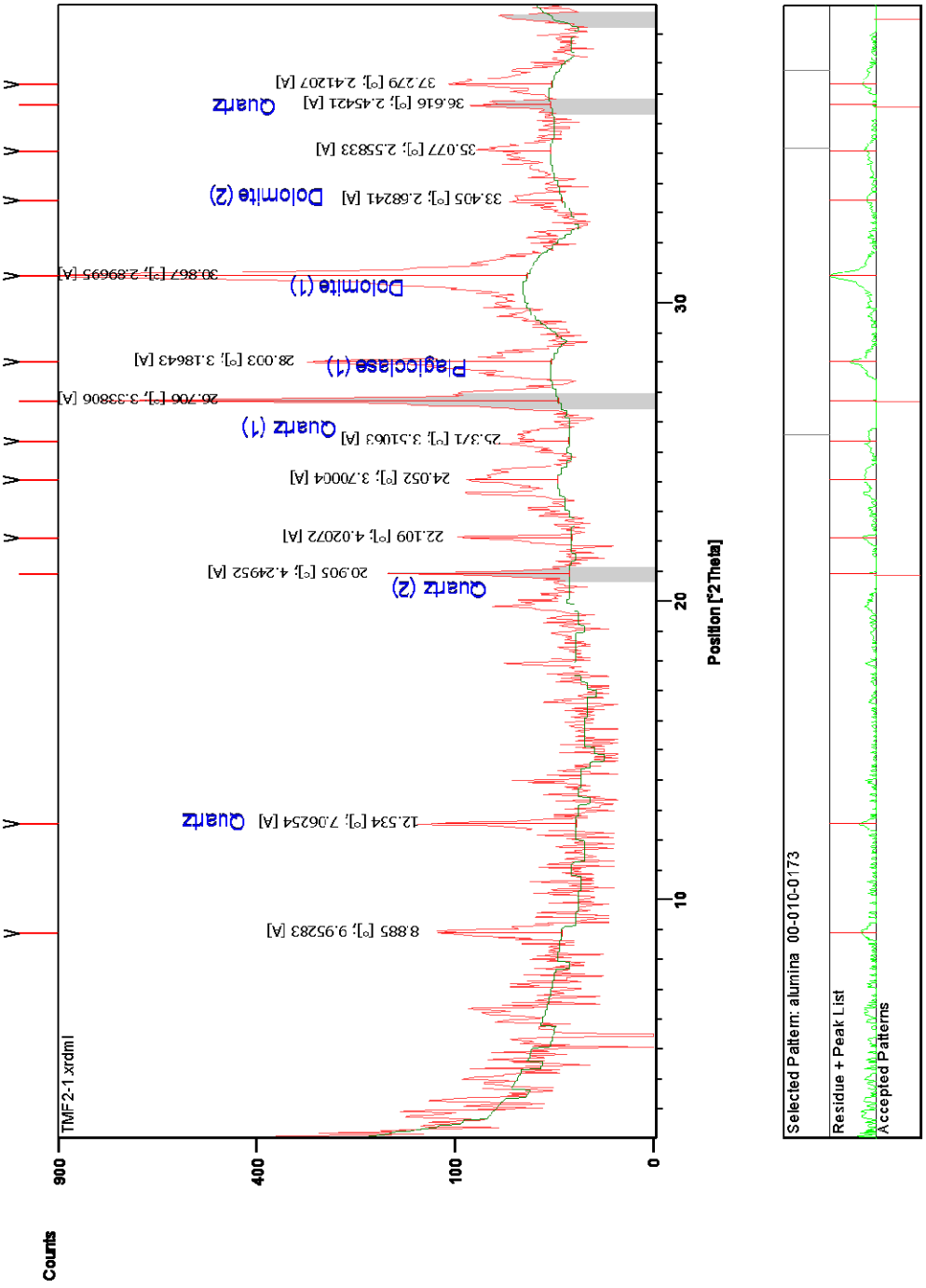
Counts
900
400
100
0
TMF2-1.xrdml
8.885 [°]; 9.95283 [Å]
Quartz
12.534 [°]; 7.06254 [Å]
Quartz (2)
20.905 [°]; 4.24952 [Å]
22.109 [°]; 4.02072 [Å]
24.052 [°]; 3.70004 [Å]
Quartz (1)
25.371 [°]; 3.51063 [Å]
26.706 [°]; 3.33806 [Å]
Plagioclase (1)
28.003 [°]; 3.18643 [Å]
Dolomite (1)
30.867 [°]; 2.89695 [Å]
Dolomite (2)
33.405 [°]; 2.68241 [Å]
35.077 [°]; 2.55833 [Å]
Quartz
36.616 [°]; 2.45421 [Å]
37.279 [°]; 2.41207 [Å]
10
20
30
Position [°2Theta]
Selected Pattern: alumina 00-010-0173
Residue + Peak List
Accepted Patterns

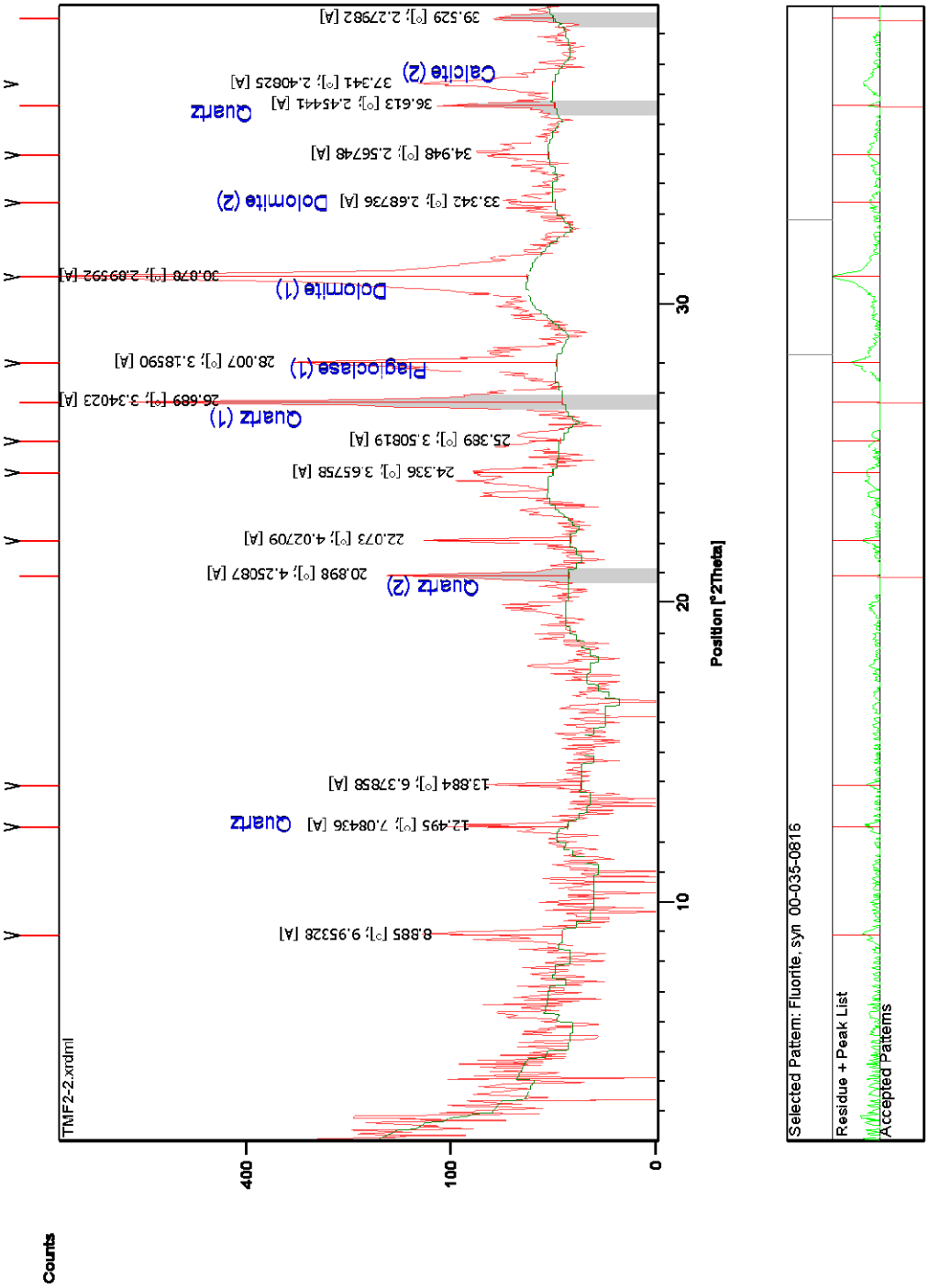
TMF2-2.xrdml
Counts
Position [°2Theta]
8.865 [°]; 9.95328 [A]
12.495 [°]; 7.08436 [A]
Quartz
13.884 [°]; 6.37858 [A]
20.898 [°]; 4.25087 [A]
Quartz (2)
22.073 [°]; 4.02709 [A]
24.336 [°]; 3.65758 [A]
25.389 [°]; 3.50819 [A]
26.689 [°]; 3.34023 [A]
Quartz (1)
28.007 [°]; 3.18590 [A]
Plagioclase (1)
30.879 [°]; 2.89592 [A]
Dolomite (1)
33.342 [°]; 2.68736 [A]
Dolomite (2)
34.948 [°]; 2.56748 [A]
36.613 [°]; 2.45441 [A]
Quartz
37.341 [°]; 2.40825 [A]
Calcite (2)
39.529 [°]; 2.27982 [A]
Selected Pattern: Fluorite, syn 00-035-0816
Residue + Peak List
Accepted Patterns

Counts
900
400
100
0
TMF2-3.xrdml
10
20
30
Position [°2Theta]
20.911 [°]; 4.24617 [Å]
Quartz (2)
22.051 [°]; 4.02933 [Å]
24.037 [°]; 3.70231 [Å]
26.686 [°]; 3.34051 [Å]
Quartz (1)
27.914 [°]; 3.19631 [Å]
Plagioclase (1)
30.944 [°]; 2.88991 [Å]
Dolomite (1)
33.499 [°]; 2.67512 [Å]
Dolomite (2)
35.287 [°]; 2.54359 [Å]
37.408 [°]; 2.40409 [Å]
Selected Pattern: alumina 00-010-0173
Residue + Peak List
Accepted Patterns

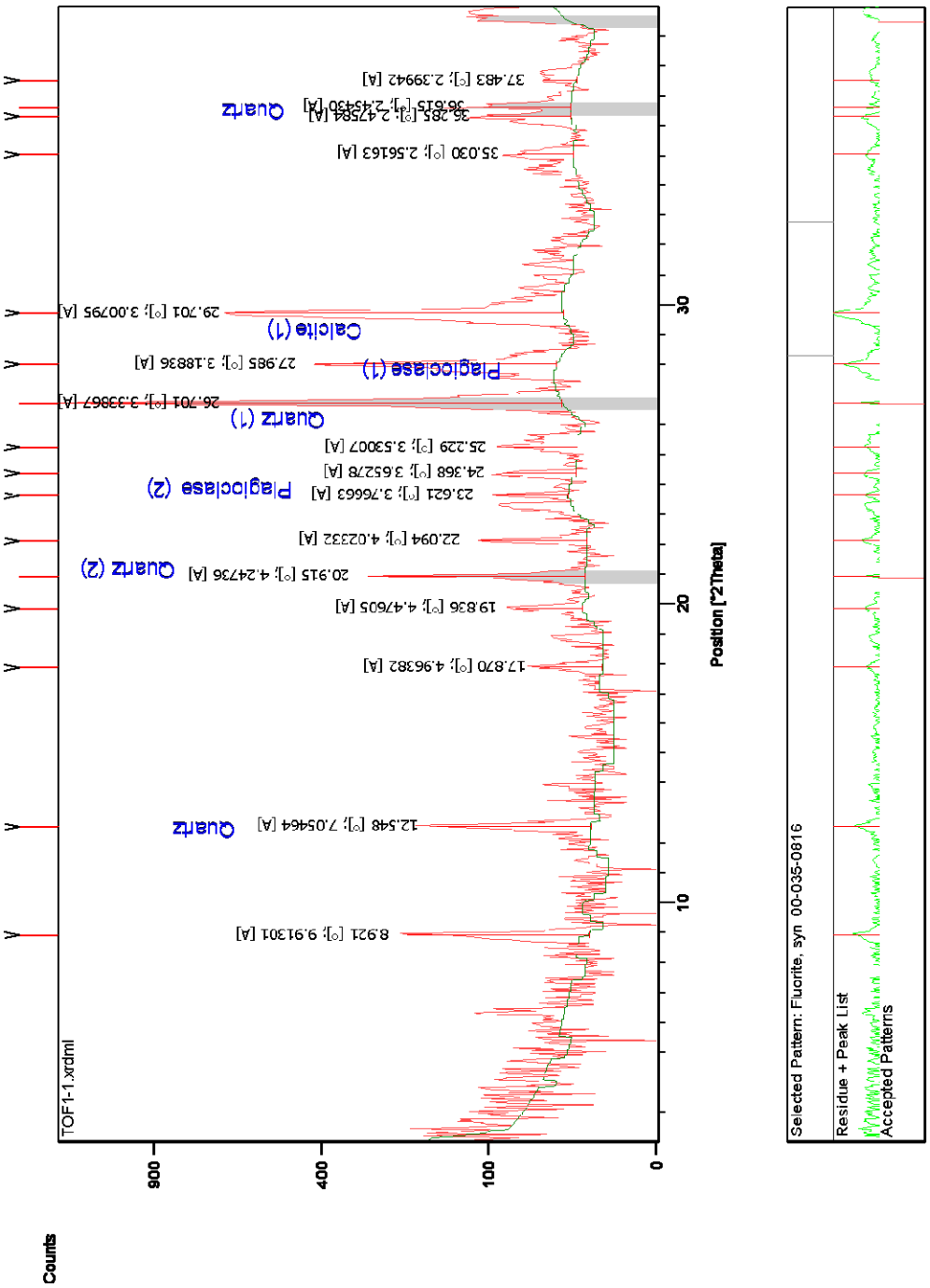
Counts
900
400
100
0
TOF1-1.xrdml
8.921 [°]; 9.91301 [A]
12.548 [°]; 7.05464 [A]
Quartz
17.870 [°]; 4.96382 [A]
19.836 [°]; 4.47605 [A]
20.915 [°]; 4.24736 [A]
Quartz (2)
22.094 [°]; 4.02332 [A]
23.621 [°]; 3.76663 [A]
24.368 [°]; 3.65278 [A]
Plagioclase (2)
25.229 [°]; 3.53007 [A]
26.701 [°]; 3.33867 [A]
Quartz (1)
27.985 [°]; 3.18836 [A]
Plagioclase (1)
29.701 [°]; 3.00795 [A]
Calcite (1)
35.030 [°]; 2.56163 [A]
36.285 [°]; 2.47584 [A]
36.515 [°]; 2.45450 [A]
Quartz
37.483 [°]; 2.39942 [A]
10
20
30
Position [°2Theta]
Selected Pattern: Fluorite, syn 00-035-0816
Residue + Peak List
Accepted Patterns

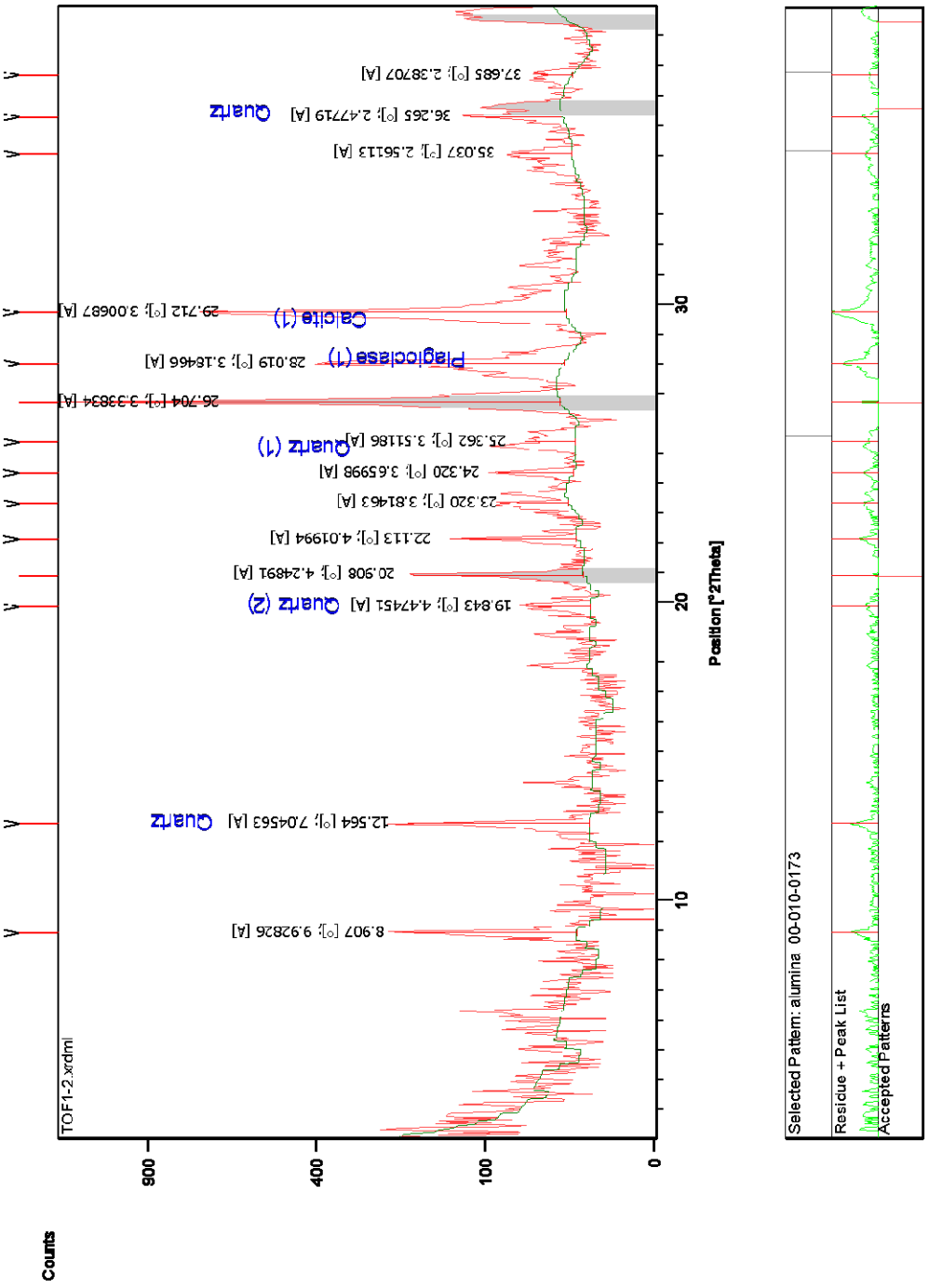
Counts
900
400
100
0
TOF1-2.xrdml
8.907 [°]; 9.92826 [Å]
12.564 [°]; 7.04563 [Å]
Quartz
19.843 [°]; 4.47451 [Å]
Quartz (2)
20.908 [°]; 4.24891 [Å]
22.113 [°]; 4.01994 [Å]
23.320 [°]; 3.81463 [Å]
24.320 [°]; 3.65998 [Å]
25.362 [°]; 3.51186 [Å]
Quartz (1)
26.704 [°]; 3.33834 [Å]
28.019 [°]; 3.18466 [Å]
Plagioclase (1)
29.712 [°]; 3.00687 [Å]
Calcite (1)
35.037 [°]; 2.56113 [Å]
36.265 [°]; 2.47719 [Å]
Quartz
37.685 [°]; 2.38707 [Å]
10
20
30
Position [°2Theta]
Selected Pattern: alumina 00-010-0173
Residue + Peak List
Accepted Patterns

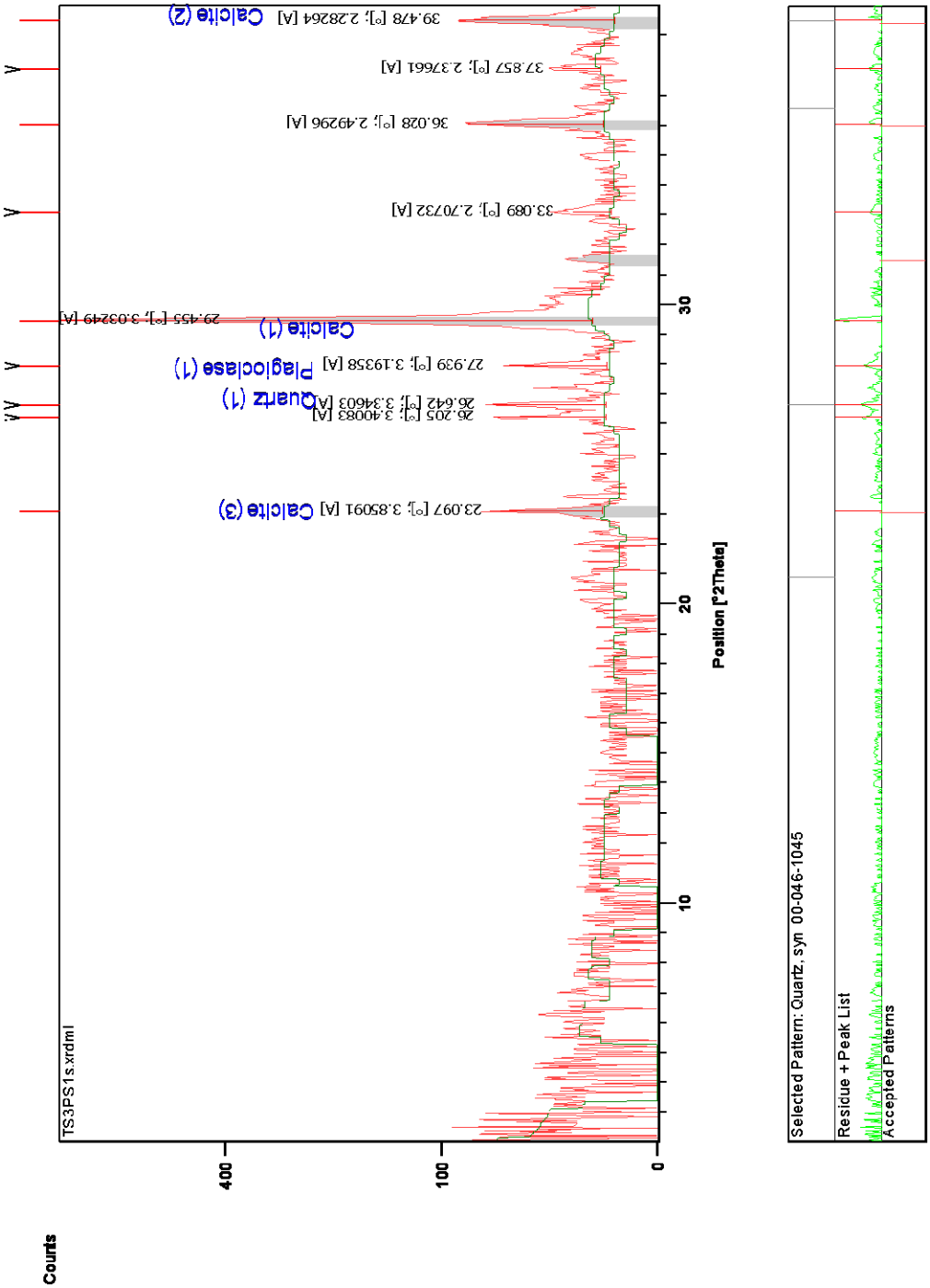
Counts
400
100
0
TS3PS1s.xrdml
10
20
30
Position [°2Theta]
39.478 [°]; 2.28264 [A]
Calcite (2)
37.857 [°]; 2.37661 [A]
36.028 [°]; 2.49296 [A]
33.089 [°]; 2.70732 [A]
29.455 [°]; 3.03249 [A]
Calcite (1)
27.939 [°]; 3.19358 [A]
Plagioclase (1)
26.642 [°]; 3.34603 [A]
26.205 [°]; 3.40083 [A]
Quartz (1)
23.097 [°]; 3.85091 [A]
Calcite (3)
Selected Pattern: Quartz. syn 00-046-1045
Residue + Peak List
Accepted Patterns

Counts
400
100
0
TWAF1-1.xrdml
8.922 [°]; 9.91130 [A]
12.543 [°]; 7.05706 [A] Quartz
19.846 [°]; 4.47375 [A]
20.932 [°]; 4.24406 [A]
Quartz (2)
22.116 [°]; 4.01950 [A]
23.416 [°]; 3.79908 [A] Orthoclase (1)
24.348 [°]; 3.65578 [A]
25.356 [°]; 3.51272 [A]
Quartz (1)
26.708 [°]; 3.33783 [A]
27.995 [°]; 3.18724 [A] Plagioclase (1)
29.706 [°]; 3.00747 [A]
Calcite (1)
32.015 [°]; 2.79564 [A]
Dolomite (1)
35.011 [°]; 2.56297 [A]
36.642 [°]; 2.45253 [A] Quartz
10
20
30
Position [°2Theta]
Selected Pattern: Fluorite, syn 00-035-0616
Residue + Peak List
Accepted Patterns

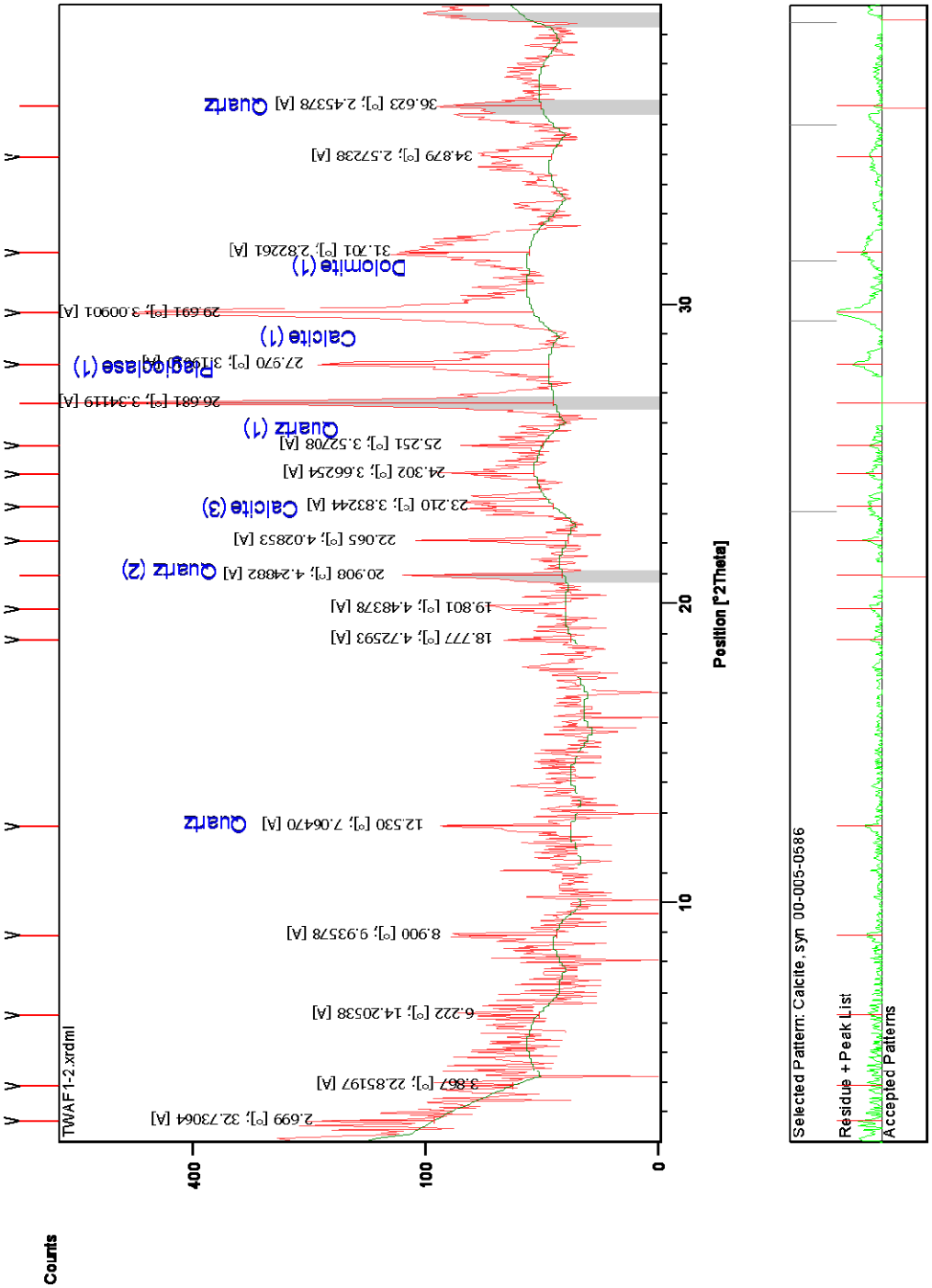
Counts
400
100
0
TWAF1-2.xrdml
2.699 [°]; 32.73064 [A]
3.867 [°]; 22.85197 [A]
6.222 [°]; 14.20538 [A]
8.900 [°]; 9.93578 [A]
12.530 [°]; 7.06470 [A] Quartz
18.777 [°]; 4.72593 [A]
19.801 [°]; 4.48378 [A]
20.908 [°]; 4.24882 [A] Quartz (2)
22.065 [°]; 4.02853 [A]
23.210 [°]; 3.83244 [A] Calcite (3)
24.302 [°]; 3.66254 [A]
25.251 [°]; 3.52708 [A]
Quartz (1)
26.681 [°]; 3.34119 [A]
Plagioclase (1)
27.970 [°]; 3.19
Calcite (1)
29.691 [°]; 3.00901 [A]
Dolomite (1)
31.701 [°]; 2.82261 [A]
34.879 [°]; 2.57238 [A]
36.623 [°]; 2.45378 [A] Quartz
10
20
30
Position [°2Theta]
Selected Pattern: Calcite, syn 00-005-0586
Residue + Peak List
Accepted Patterns

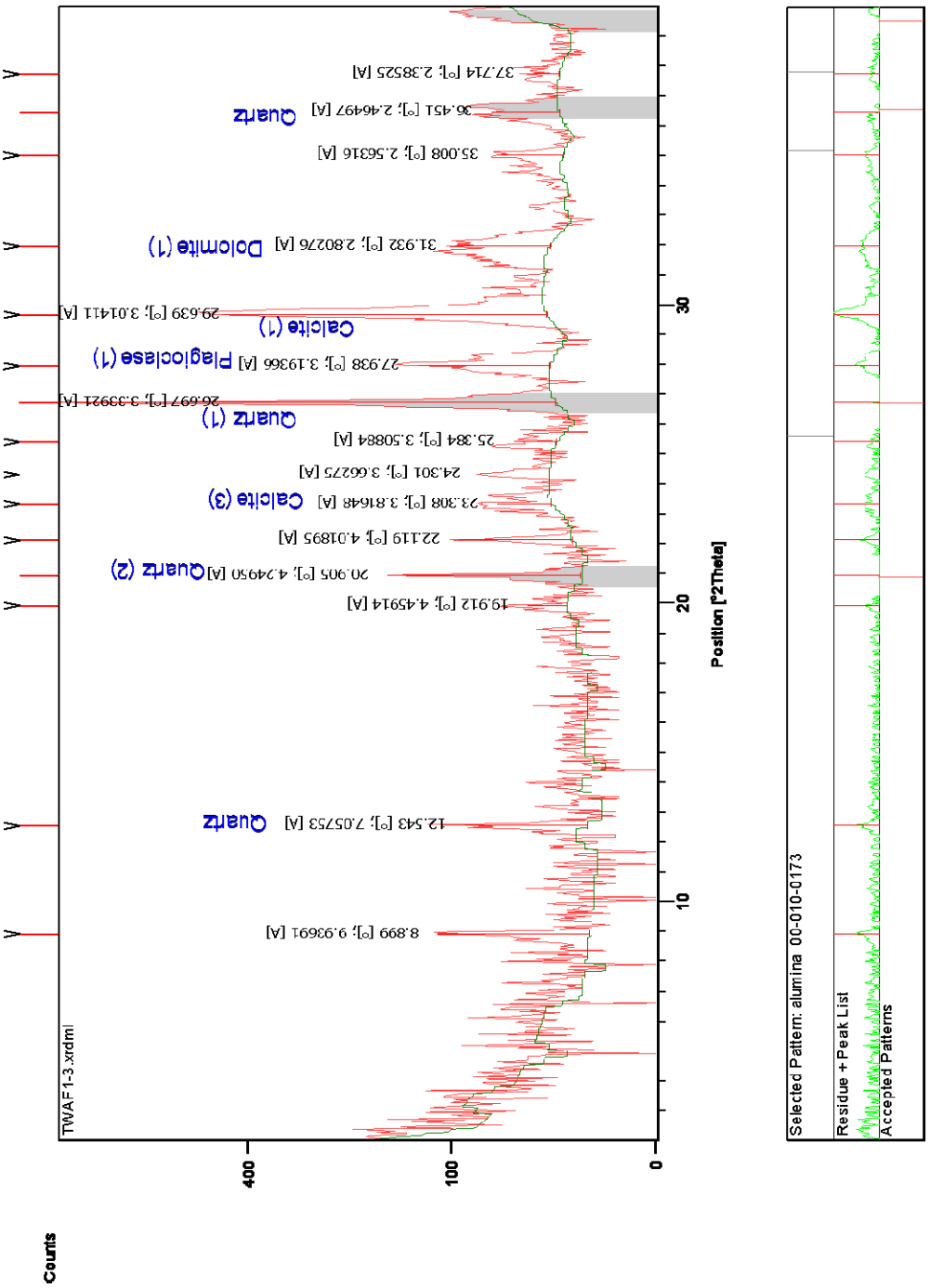
Counts
400
100
0
TWAF1-3.xrdml
8.899 [°]; 9.93691 [A]
12.543 [°]; 7.05753 [A] Quartz
19.912 [°]; 4.45914 [A]
20.905 [°]; 4.24950 [A] Quartz (2)
22.119 [°]; 4.01895 [A]
23.308 [°]; 3.81648 [A] Calcite (3)
24.301 [°]; 3.66275 [A]
25.384 [°]; 3.50884 [A]
26.697 [°]; 3.33921 [A] Quartz (1)
27.938 [°]; 3.19366 [A] Plagioclase (1)
29.439 [°]; 3.01411 [A] Calcite (1)
31.932 [°]; 2.80276 [A] Dolomite (1)
35.008 [°]; 2.56316 [A]
36.451 [°]; 2.46497 [A] Quartz
37.714 [°]; 2.38525 [A]
10
20
30
Position [°2Theta]
Selected Pattern: alumina 00-010-0173
Residue + Peak List
Accepted Patterns

7. SEM photographs and EDS graphs

Appendix Section 7 contains SEM photographs and EDS graphs that are characteristic of cement phases in the pipe and bulbous concretions.

9.1 SEM photographs of TMc1-3

The SEM images depict fine grained mudstone cemented by micritic carbonate. EDS analysis indicates the elemental composition is primarily calcium which corresponds to both calcite and plagioclase. Small amounts of iron, magnesium, aluminium, and silica are also present which corresponds to quartz and feldspars. The carbon peak is due to carbon coating of the sample during preparation.

SEM analysis of Taranaki samples did not reveal detailed information about the crystallography or composition of the mudstones and cement due to the fine grained nature of the components. The following photographs (Figs. A1.10 to A1.13) and EDS graphs are of TMc1-3 only. Further samples were investigated, however they were similar to TMc1-3.

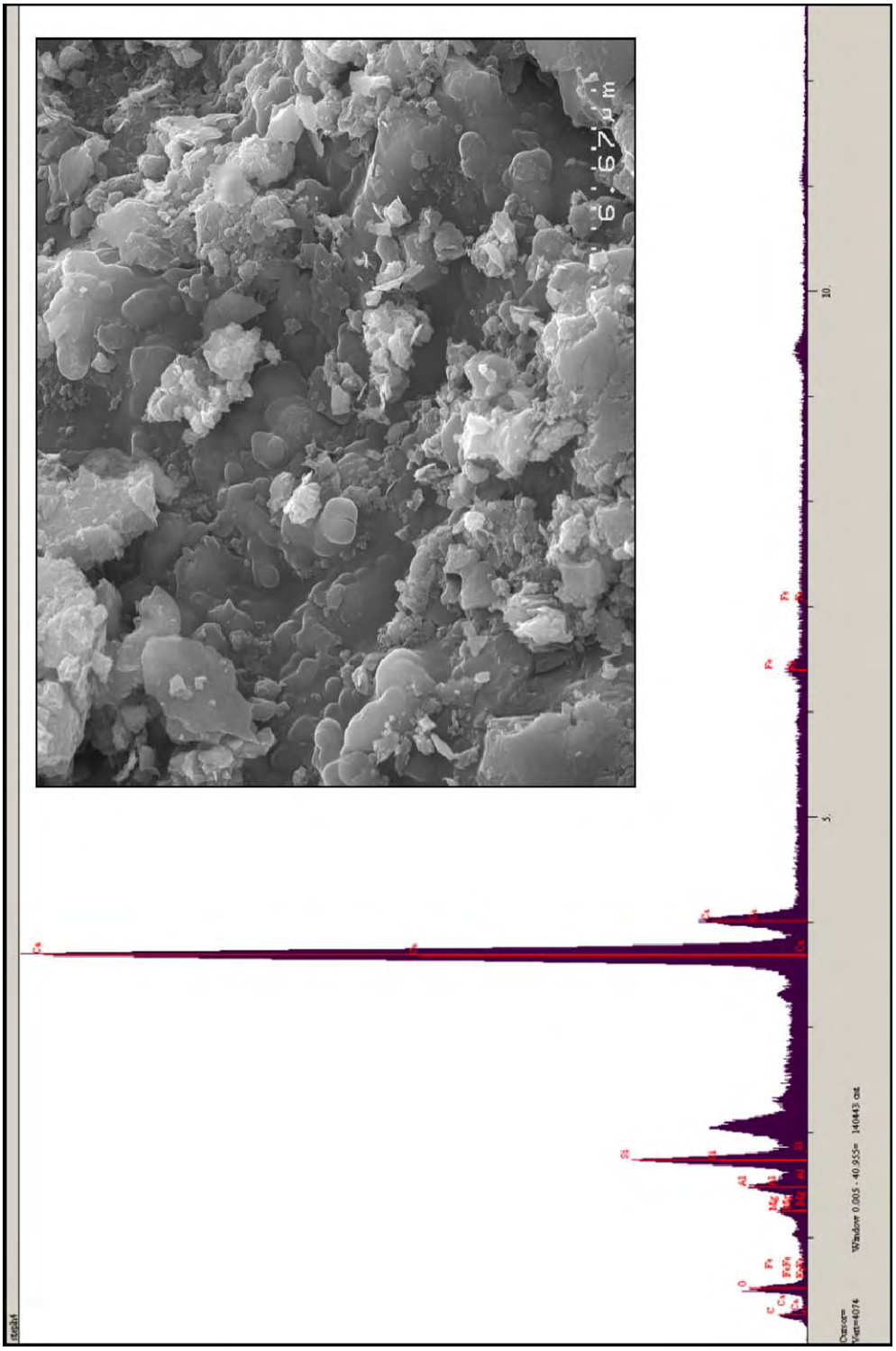

Figure A1.10. SEM image and EDS graph of micritic carbonate cement and siliciclastic sediment. EDS spectrum identifies the elemental composition is primarily calcium with lesser amounts of silica, aluminum, and magnesium, and traces of iron.

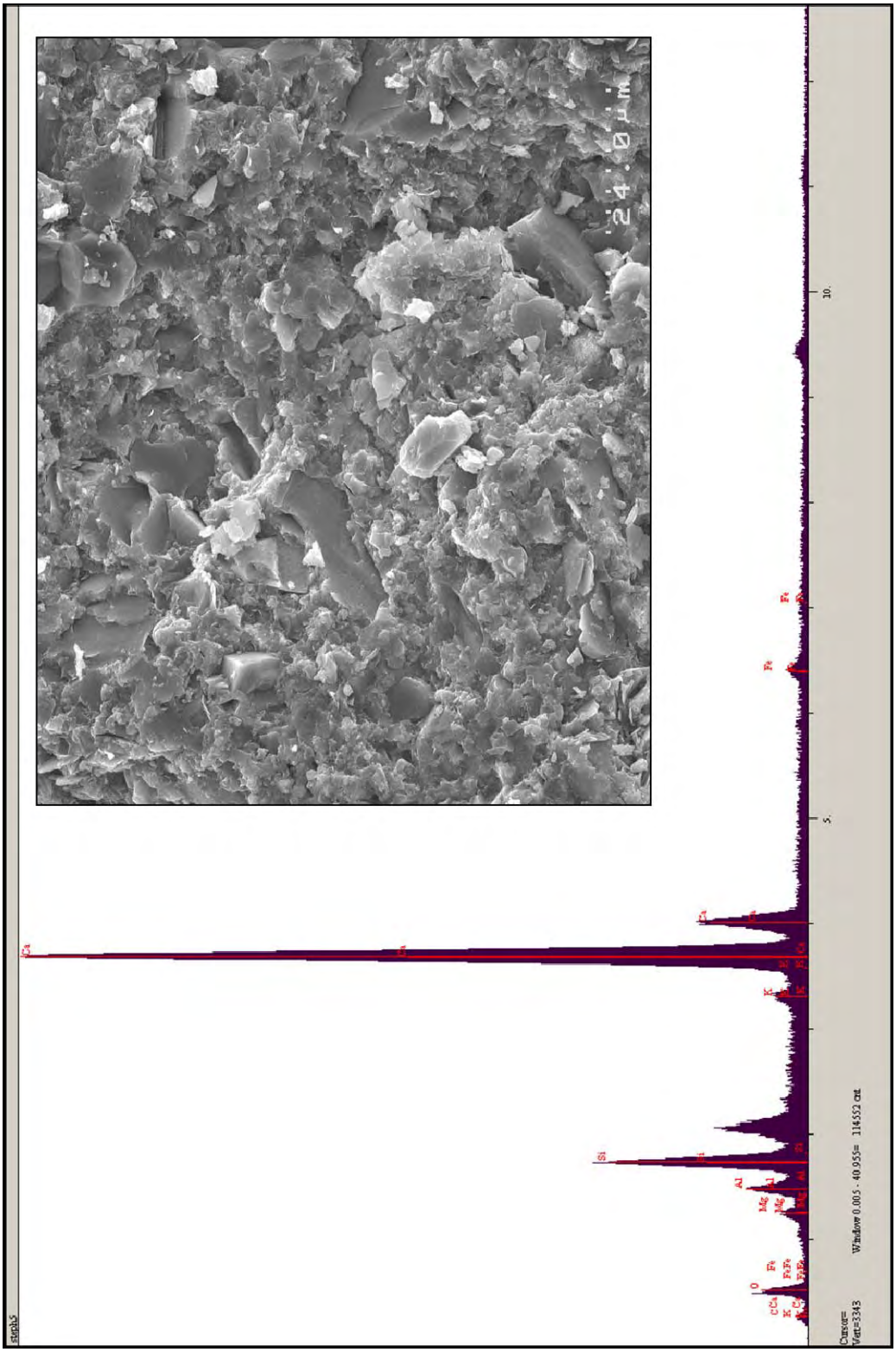

Figure A1.11. Lower magnification of Figure A1.10.

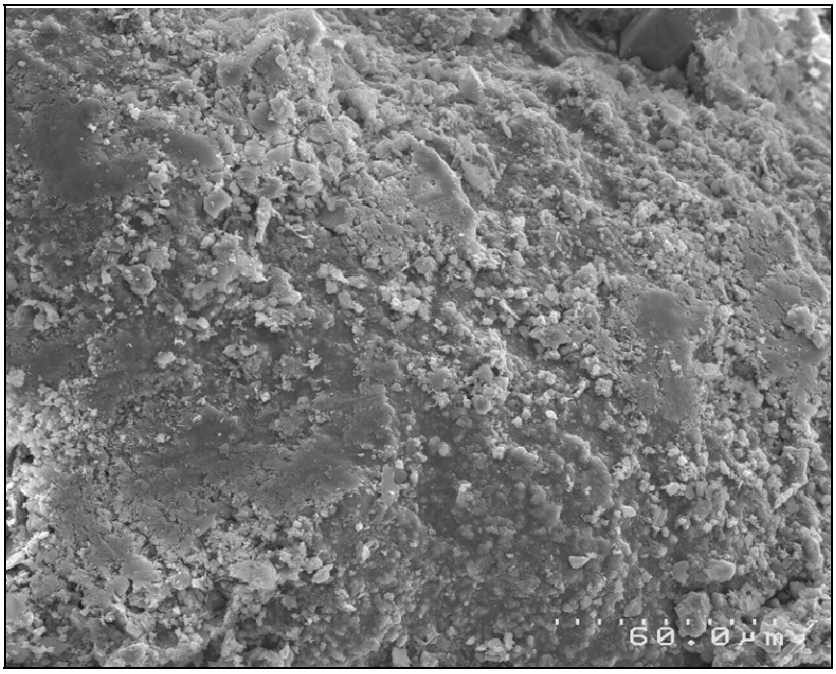

Figure A1.12. SEM image micritic carbonate cement and siliciclastic sediment.

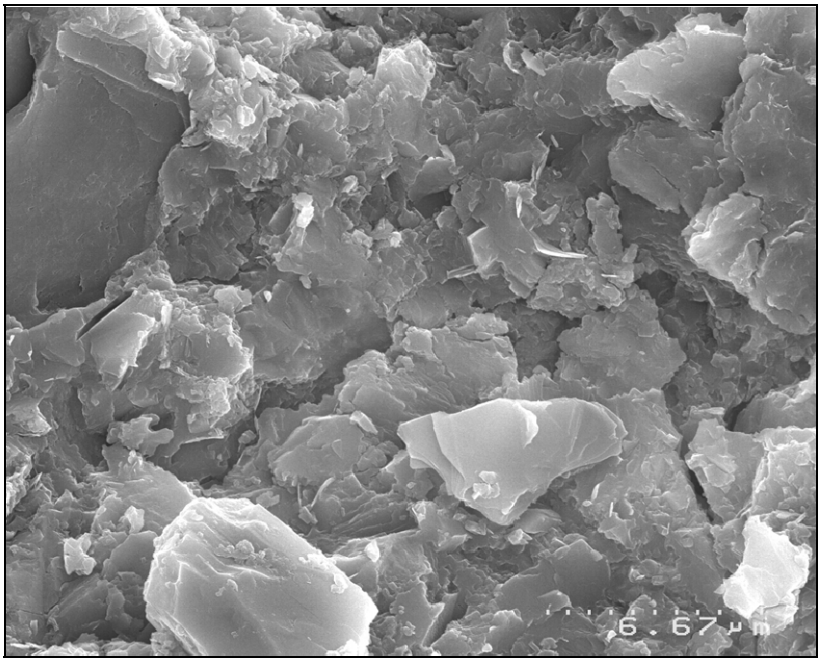

Figure A1.13. Higher magnification of Figure A1.13.

8. CO_3 determinations

Appendix Section 8 contains a table of some tubular concretions that were dissolved in solution to determine percentage of carbonate geochemically. Appendix 7, Section 7 contains the methodology for dissolution.

Table A1.8. Weight percent carbonate.

Sample name	Carbonate	Filter paper weight (g)	Residual sample + filter paper weight (g)	Residual sample weight (g)	Carbonate fraction weight (g)	Wt % Carbonate
TMc1-1	Calcite	1.205	1.219	0.014	0.026	65
TMc1-2	Calcite	1.201	1.213	0.012	0.028	70
TMc1-3	Calcite	1.204	1.213	0.009	0.031	77.5
T-01-07	Calcite	1.207	1.229	0.022	0.018	45
T-02-07	Calcite	1.203	1.238	0.035	0.005	12.5
T-04-07	Calcite	1.212	1.231	0.019	0.021	52.5
T-08-07	Calcite	1.18	1.216	0.036	0.004	10
T-09-07	Calcite	1.229	1.249	0.02	0.02	50
TMf1-1	Dolomite	1.213	1.218	0.005	0.035	87.5
TMf1-2	Dolomite	1.176	1.181	0.005	0.035	87.5
TMf1-3	Dolomite	1.195	1.198	0.003	0.037	92.5
TMf2-1	Dolomite	1.194	1.205	0.011	0.029	72.5
TMf2-2	Dolomite	1.183	1.188	0.005	0.035	87.5
TMf2-3	Dolomite	1.19	1.195	0.005	0.035	87.5
T-07-07	Dolomite	1.2	1.208	0.008	0.032	80

9. Isotope transects

Appendix Section 9 contains isotope transects for tubular concretions.

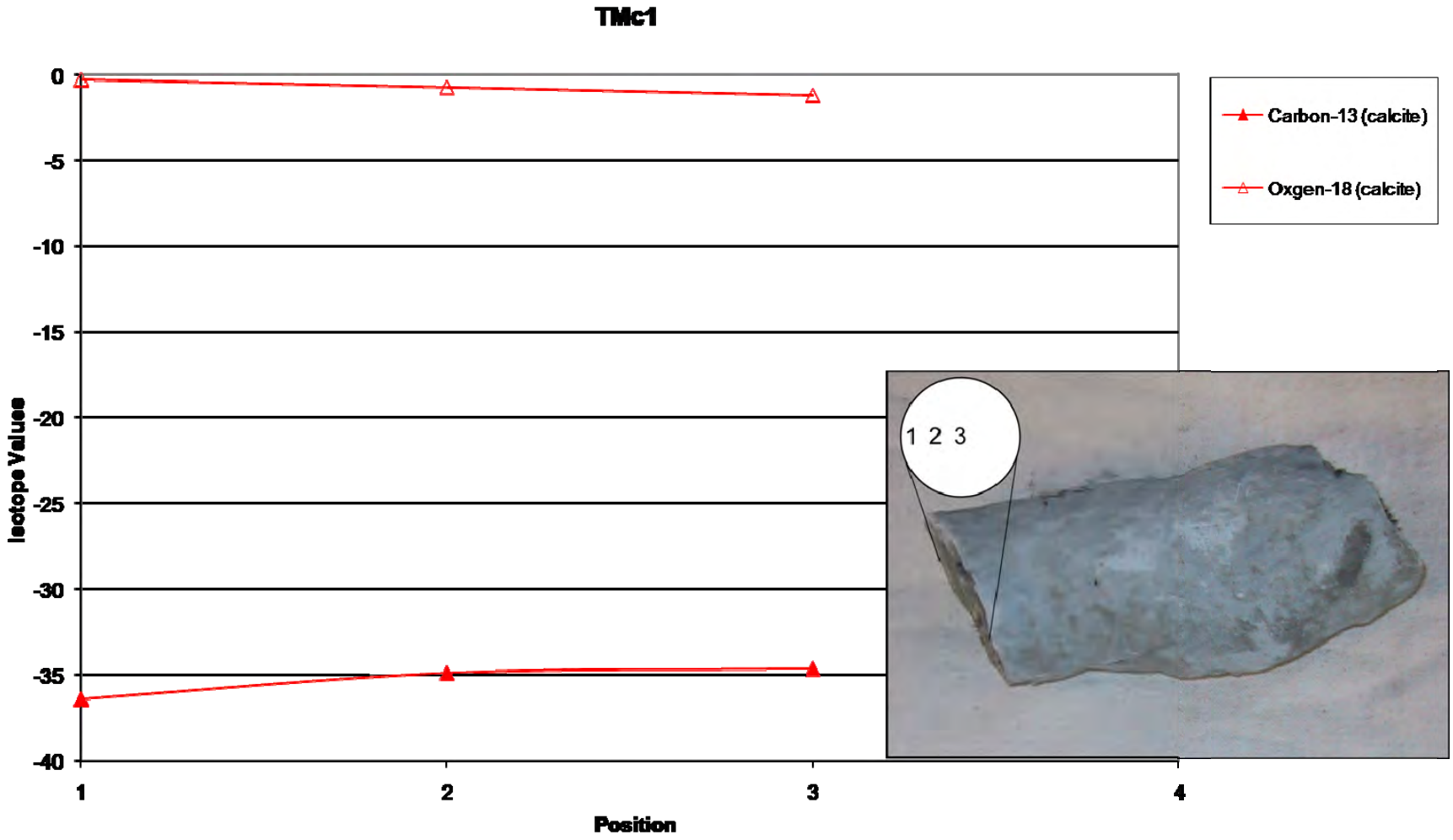
TMc1
0
-5
-10
-15
-20
-25
-30
-35
-40
Isotope Values
1
2
3
4
Position
Carbon-13 (calcite)
Oxgen-18 (calcite)
1 2 3

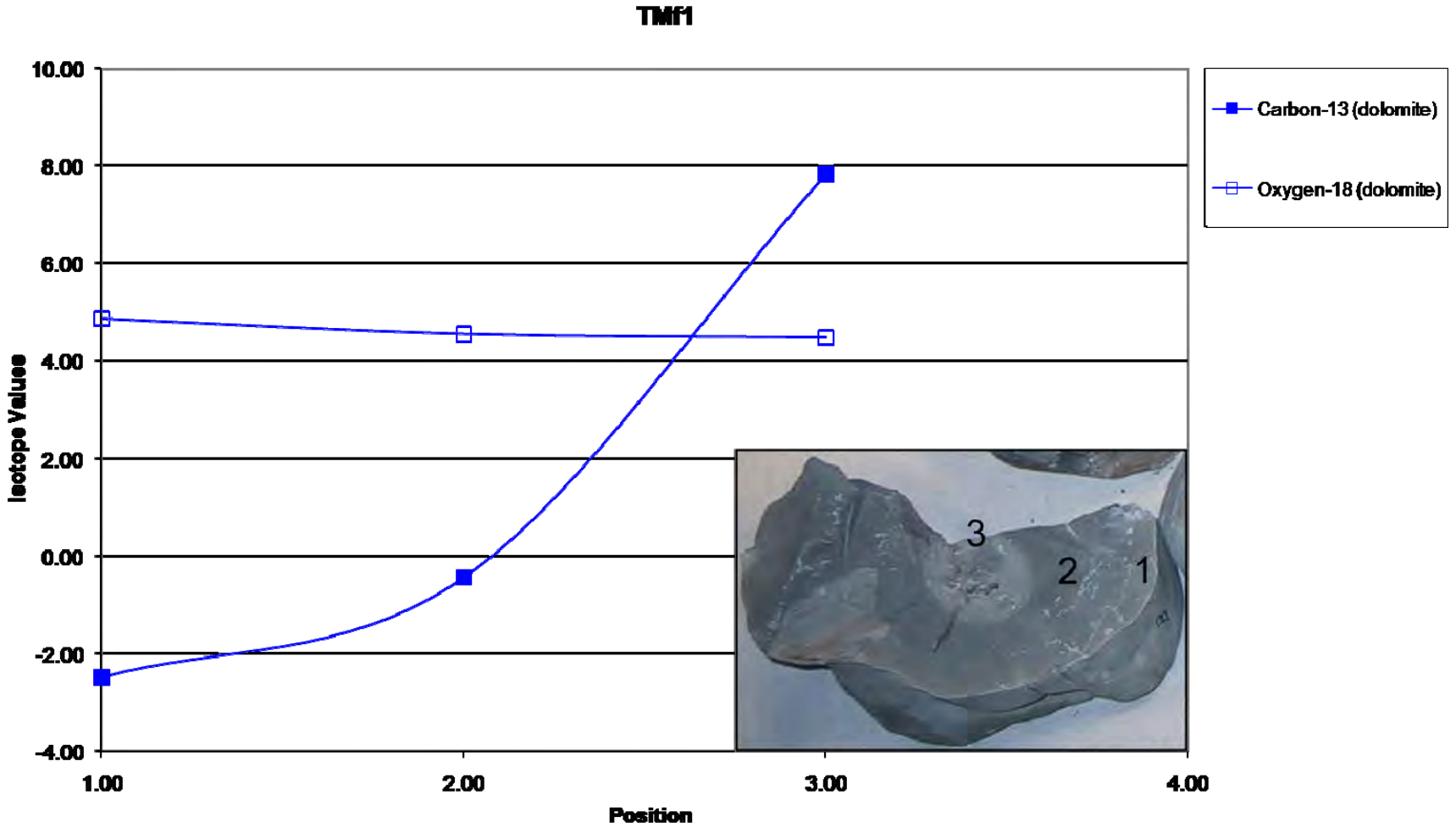
TMf1
10.00
8.00
6.00
4.00
2.00
0.00
-2.00
-4.00
Isotope Values
1.00
2.00
3.00
4.00
Position
Carbon-13 (dolomite)
Oxygen-18 (dolomite)
3
2
1

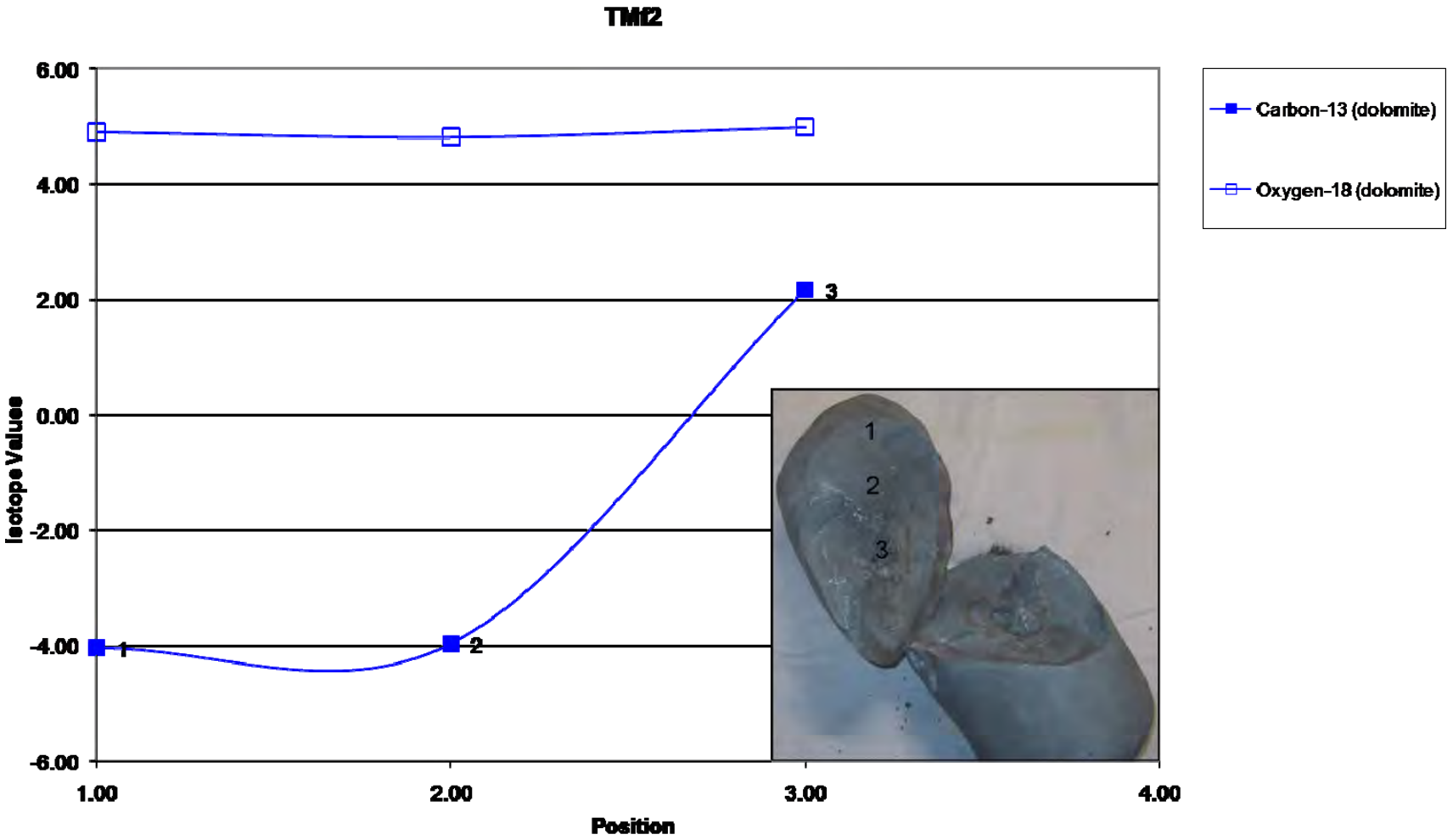
TMf2
6.00
4.00
2.00
0.00
-2.00
-4.00
-6.00
Isotope Values
1.00
2.00
3.00
4.00
Position
Carbon-13 (dolomite)
Oxygen-18 (dolomite)
1
2
3
1
2
3

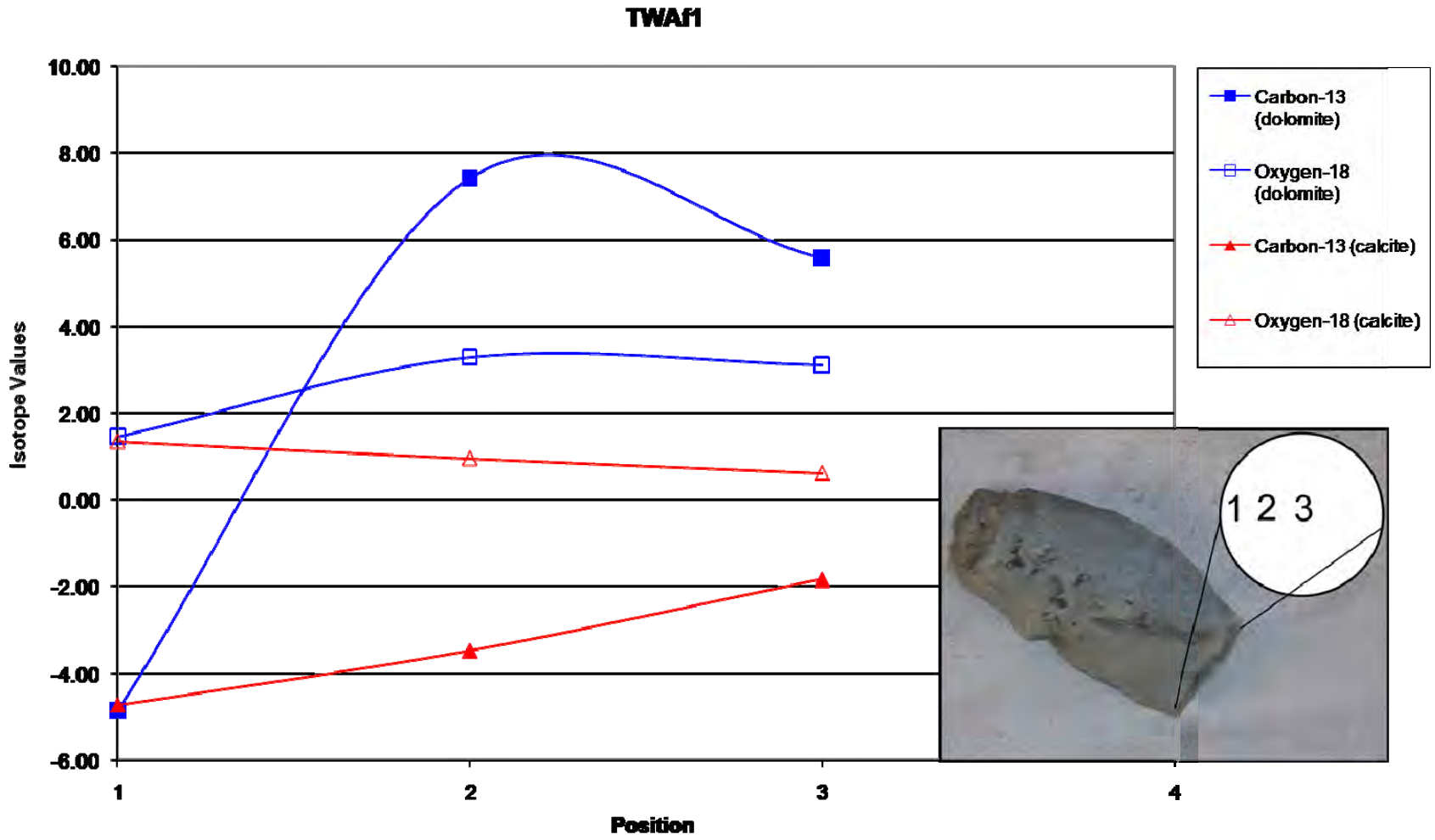
TWAf1
10.00
8.00
6.00
4.00
2.00
0.00
-2.00
-4.00
-6.00
Isotope Values
1
2
3
4
Position
Carbon-13 (dolomite)
Oxygen-18 (dolomite)
Carbon-13 (calcite)
Oxygen-18 (calcite)
1 2 3

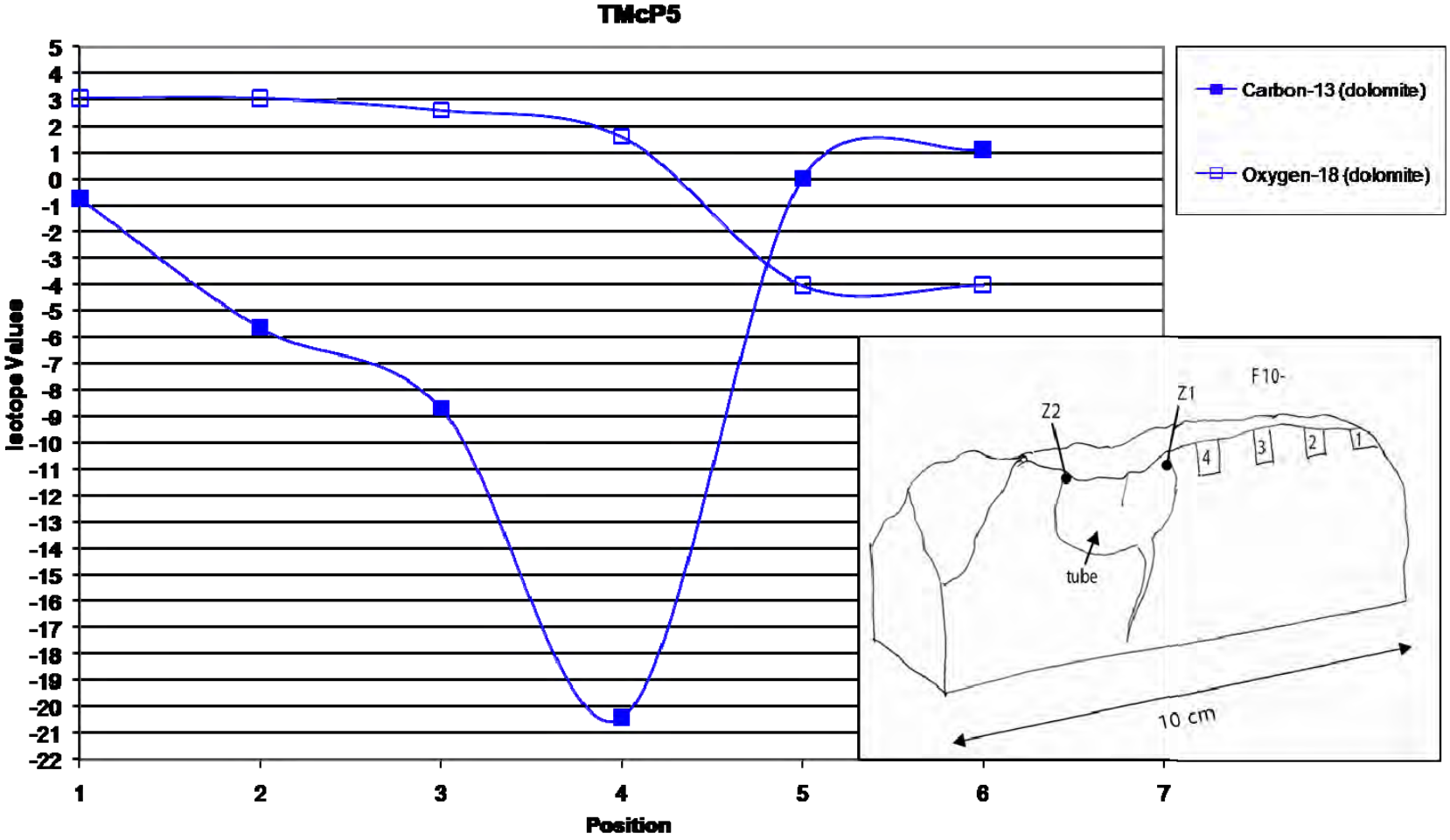
TMcP5
Carbon-13 (dolomite)
Oxygen-18 (dolomite)
Isotope Values
Position
5
4
3
2
1
0
-1
-2
-3
-4
-5
-6
-7
-8
-9
-10
-11
-12
-13
-14
-15
-16
-17
-18
-19
-20
-21
-22
1
2
3
4
5
6
7
F10-
Z1
Z2
4
3
2
1
tube
10 cm

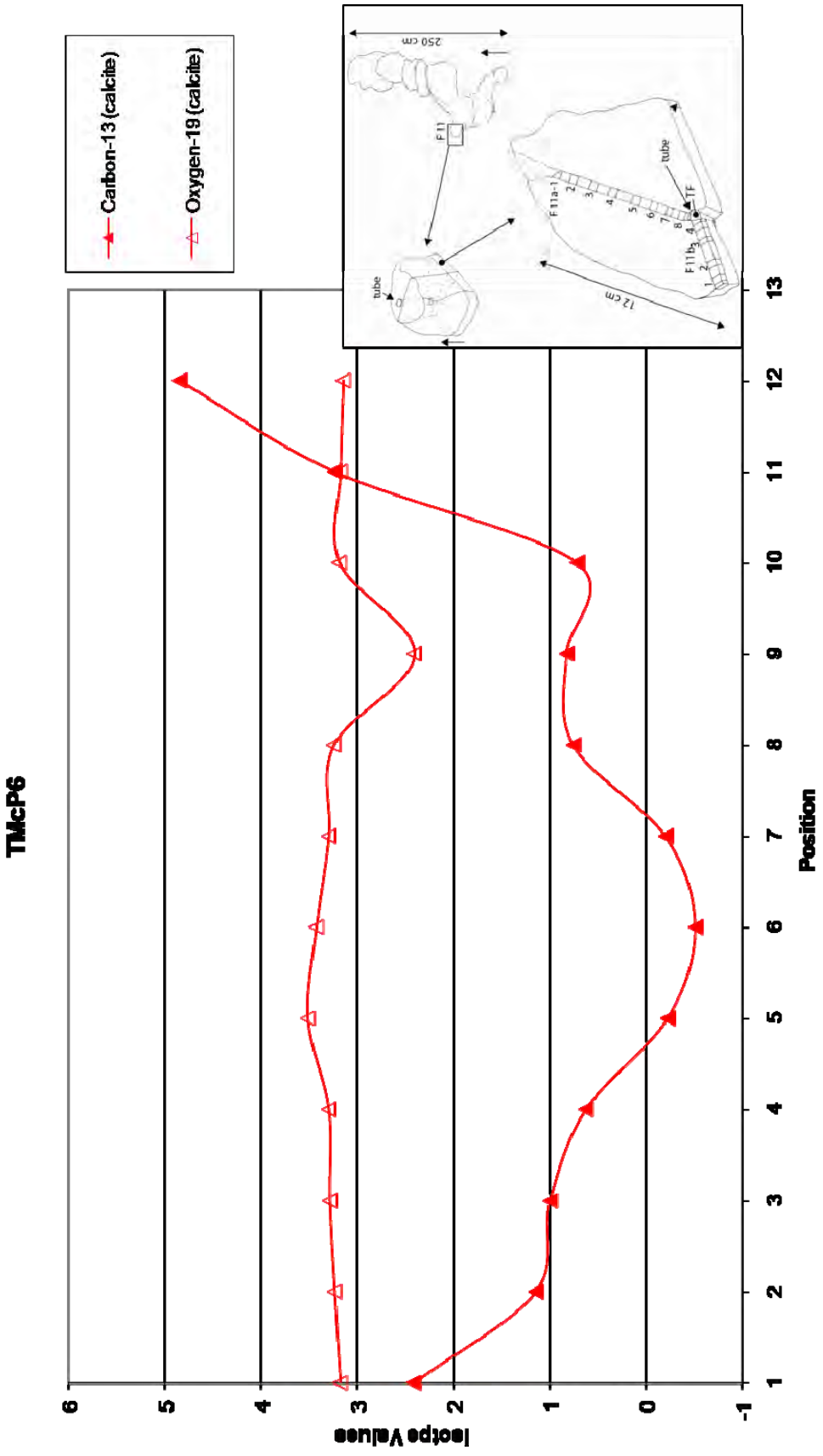
TMcP6
Carbon-13 (calcite)
Oxygen-19 (calcite)
Isotope Values
Position
250 cm
F11
tube
12 cm
F11a-1
F11b
TF

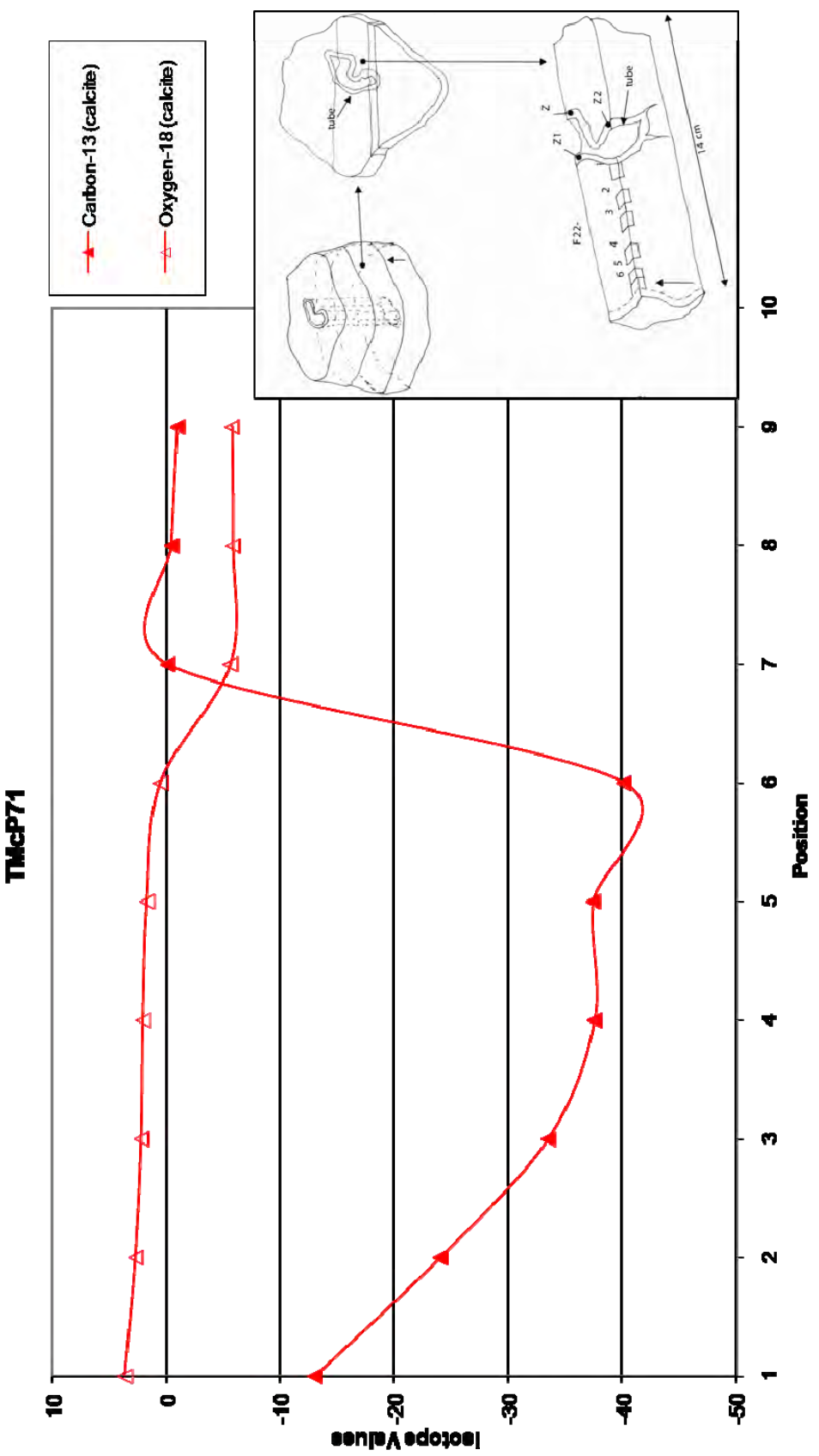
TMcP71
Carbon-13 (calcite)
Oxygen-18 (calcite)
Isotope Values
10
0
-10
-20
-30
-40
-50
Position
1
2
3
4
5
6
7
8
9
10
tube
Z
Z1
Z2
tube
14 cm
F22-
6 5 4 3 2

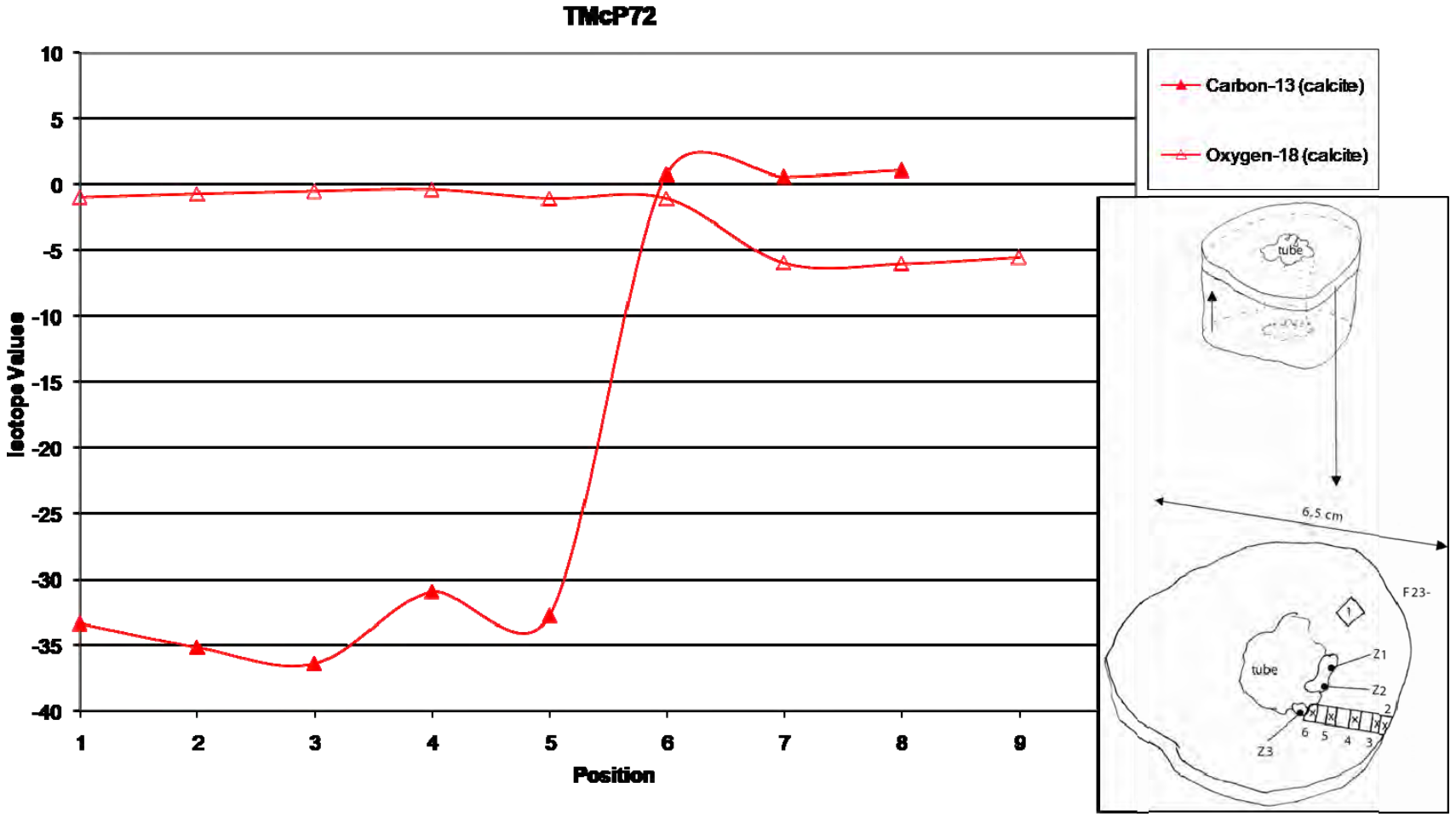
TMcP72
Carbon-13 (calcite)
Oxygen-18 (calcite)
Isotope Values
Position
10
5
0
-5
-10
-15
-20
-25
-30
-35
-40
1
2
3
4
5
6
7
8
9
tube
6,5 cm
F23-
tube
Z1
Z2
Z3
2
3
4
5
6

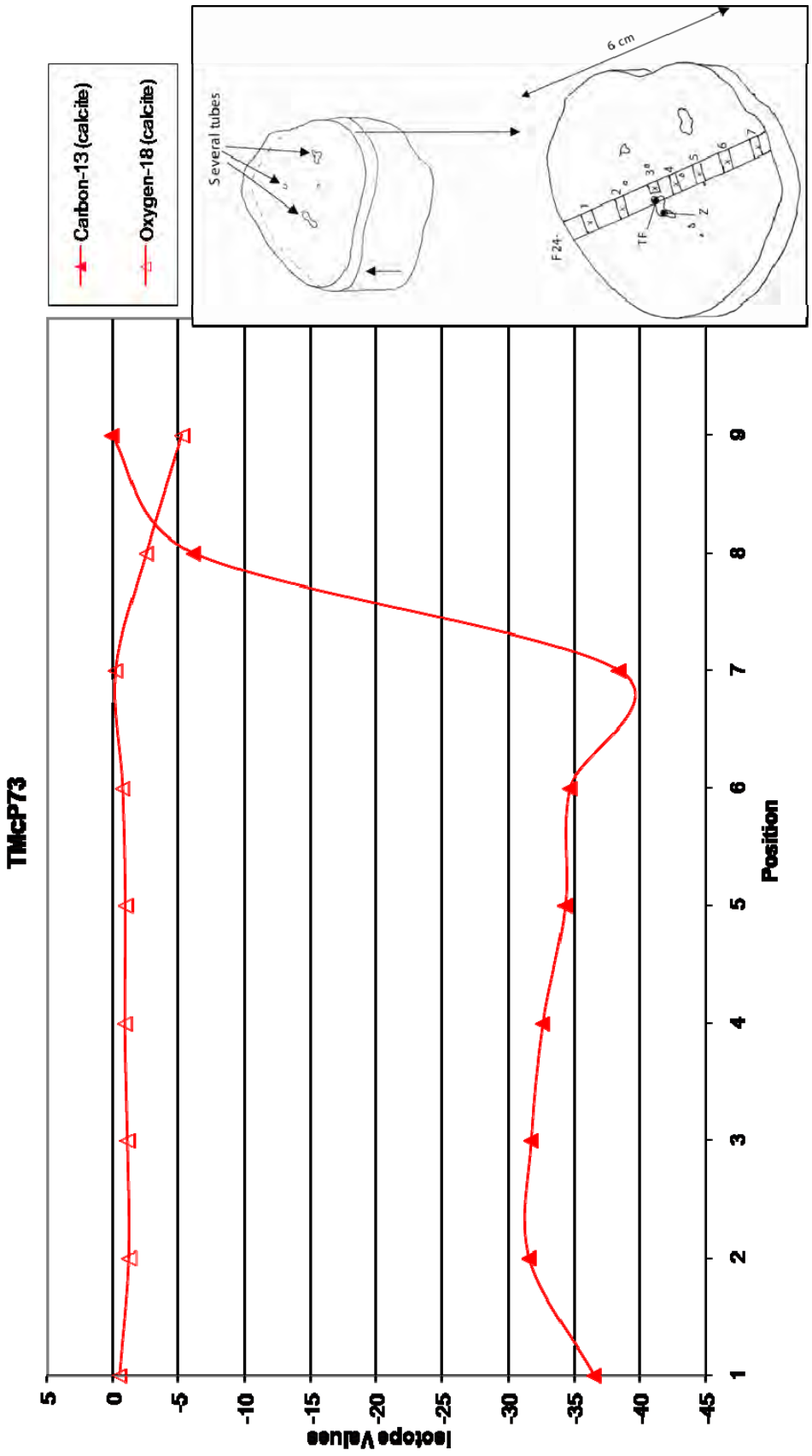
TMcP73
Carbon-13 (calcite)
Oxygen-18 (calcite)
Several tubes
6 cm
F24-
TF
Isotope Values
5
0
-5
-10
-15
-20
-25
-30
-35
-40
-45
Position
1
2
3
4
5
6
7
8
9

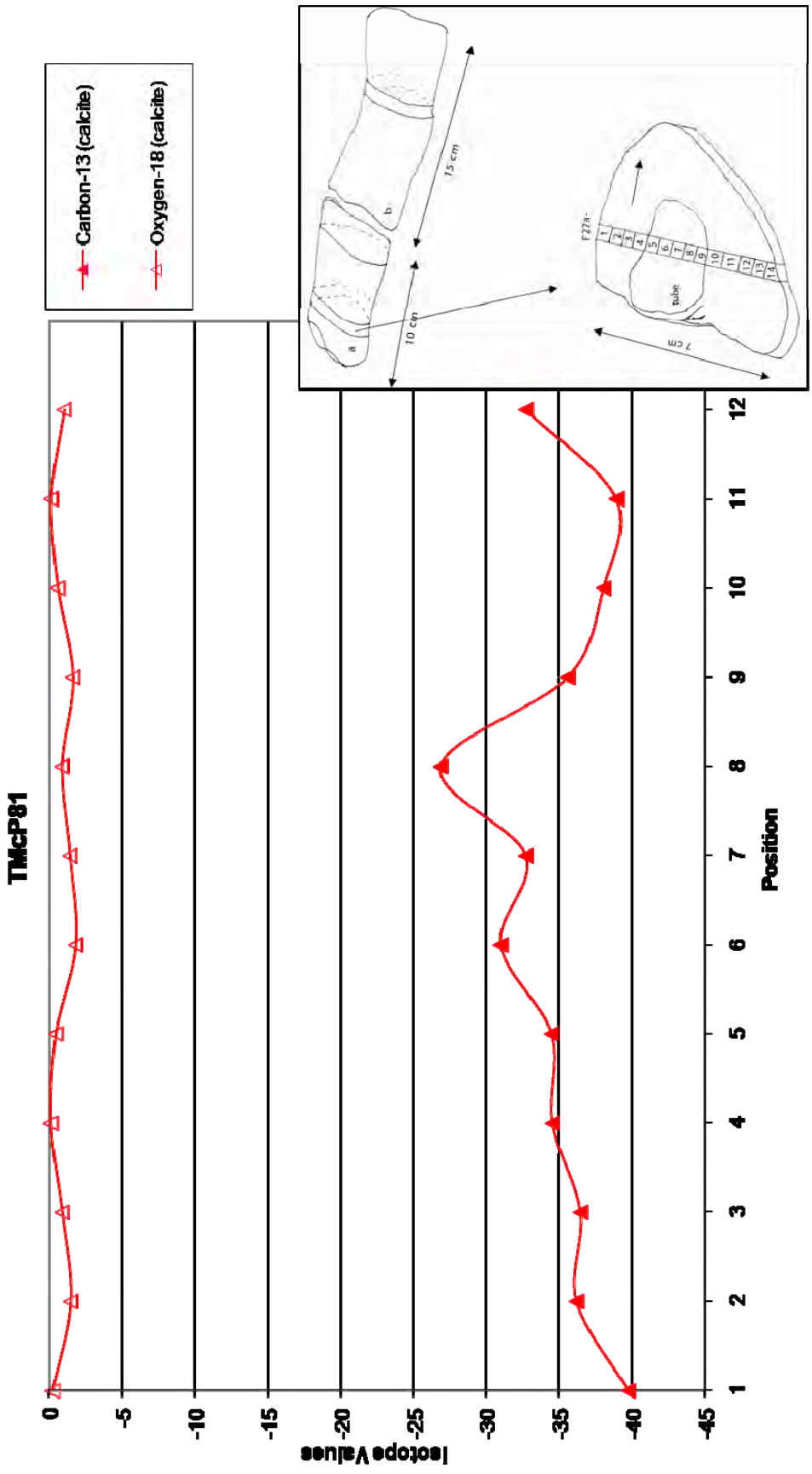
Carbon-13 (calcite)
Oxygen-18 (calcite)
TMcP81
Isotope Values
Position
0
-5
-10
-15
-20
-25
-30
-35
-40
-45
1
2
3
4
5
6
7
8
9
10
11
12
a
b
10 cm
15 cm
7 cm
tube
F27a

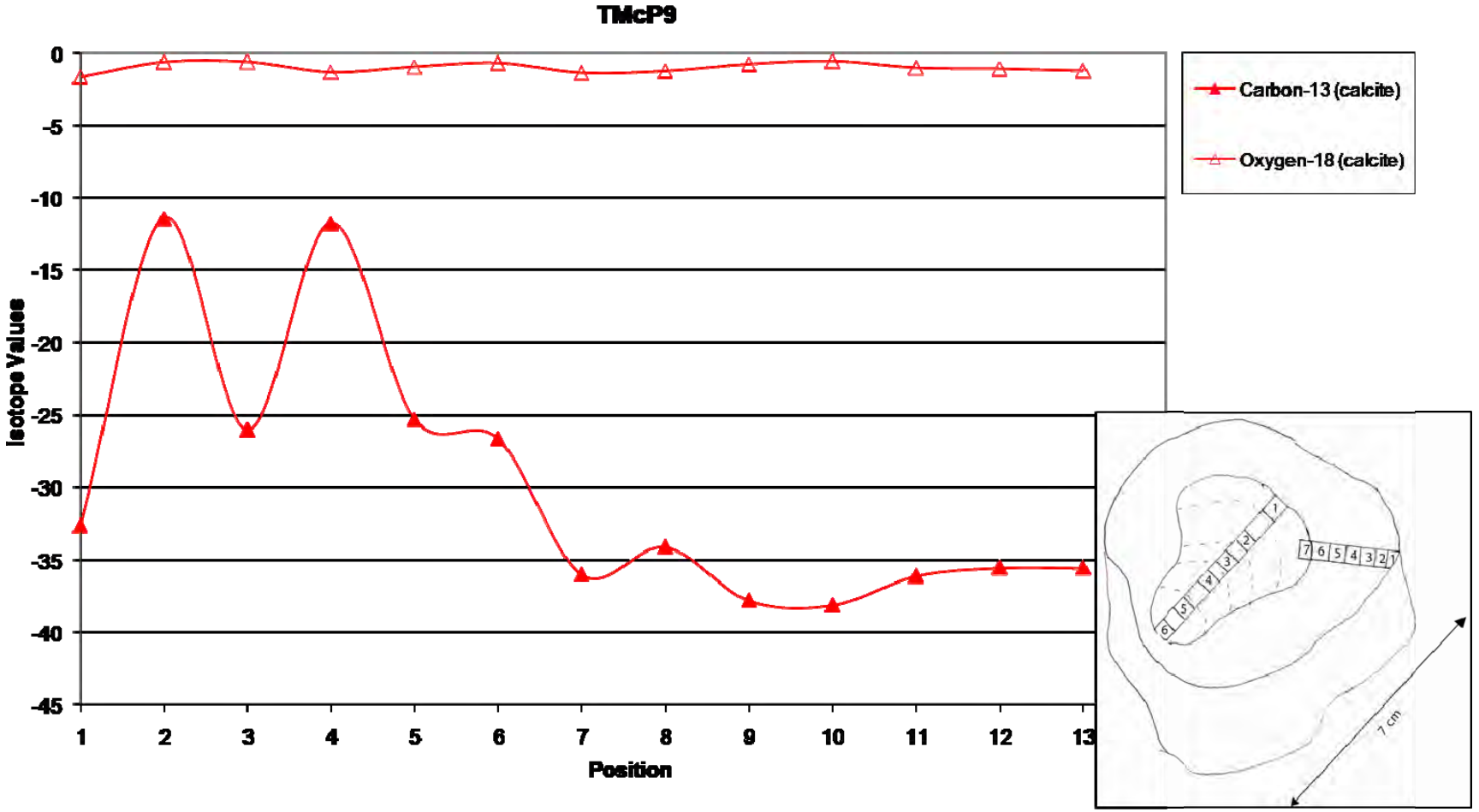
TMcP9
Carbon-13 (calcite)
Oxygen-18 (calcite)
Isotope Values
0
-5
-10
-15
-20
-25
-30
-35
-40
-45
1
2
3
4
5
6
7
8
9
10
11
12
13
Position
7 cm

10. XRF and ICPOEMS

This appendix contains Table A1.9 of XRF data and Table A1.10 ICP/MS data.

Table A1.9. XRD data.

Element	Dimension	TMH	Tmc1-1	Tmc1-2	Tmc1-3	Tmf1-1	Tmf1-2	Tmf1-3	Tmf2-1	Tmf2-2	Tmf2-3
Na	%	16.51	0.60	< 0.032	< 0.030	0.30	0.23	< 0.022	0.27	0.28	< 0.023
Mg	%	1.08	1.61	1.56	1.51	8.58	8.81	11.43	8.27	8.42	10.06
Al	%	4.89	4.84	3.60	2.90	4.13	4.05	2.80	4.19	4.18	2.79
Si	%	15.42	15.12	11.40	8.93	13.47	13.04	8.60	13.93	13.77	8.66
P	%	0.02	0.05	0.13	0.15	0.13	0.06	0.04	0.13	0.08	0.07
S	ppm	5972	2346	1788	1638	1433	1372	1171	1543	1945	1249
Cl	ppm	126700	3459	1461	469	879	123	144	318	271	136
K	%	2.07	1.44	1.05	0.83	1.21	1.17	0.75	1.19	1.15	0.74
Ca	%	1.67	20.40	26.08	28.92	14.60	14.64	17.18	14.61	14.89	17.90
Ti	%	0.37	0.23	0.17	0.13	0.19	0.19	0.12	0.20	0.19	0.12
V	ppm	103	70	58	53	54	48	35	56	54	38
Cr	ppm	63	36	20	12.2	25	31	18.9	29	27	19.3
Mn	%	0.05	0.14	0.17	0.17	0.14	0.09	0.06	0.10	0.10	0.06
Fe	%	3.48	2.34	1.94	1.73	2.50	2.10	1.51	2.12	2.11	1.56
Co	ppm	16.1	< 5.7	< 5.4	< 5.6	< 5.7	4.9	< 4.5	< 5.2	7.8	< 4.7
Ni	ppm	22.5	13.4	11.5	9.4	11.8	10.5	7.3	10.6	8.8	6.0
Cu	ppm	14.0	8.0	6.3	5.3	6.4	7.2	4.3	8.2	7.9	4.5
Zn	ppm	78	45	34	26	38	38	24	38	37	25
Ga	ppm	18.6	11.4	8.7	7.2	9.5	9.7	6.3	9.9	9.5	6.5
Ge	ppm	1.1	0.6	0.4	< 0.4	0.6	0.5	0.5	0.5	0.7	< 0.3
As	ppm	3.1	0.4	< 0.3	< 0.3	< 0.3	< 0.3	< 0.3	0.4	0.7	0.7
Se	ppm	< 0.3	0.5	0.6	0.2	0.2	0.3	< 0.2	0.3	0.4	0.3
Br	ppm	21	6.2	4.1	2.7	3.7	1.6	1.3	2.8	2.5	1.8
Rb	ppm	114	66	48	39	56	55	35	55	52	35
Sr	ppm	271	390	495	582	533	549	735	518	516	631
Y	ppm	22	22	18.2	12.9	13.8	11.1	8.2	11.9	11.1	7.4
Zr	ppm	194	108	87	60	92	88	56	100	94	57
Nb	ppm	10.0	6.7	5.7	5.1	5.9	5.6	4.2	5.8	5.6	4.1
Mo	ppm	1.2	4.1	8.0	11.9	0.9	2.2	3.5	1.2	1.8	3.9
Ag	ppm	< 0.4	< 0.4	< 0.4	< 0.4	< 0.4	< 0.4	< 0.4	< 0.4	< 0.4	< 0.4
Cd	ppm	< 0.5	< 0.5	< 0.5	< 0.5	< 0.5	< 0.5	< 0.5	< 0.5	< 0.5	< 0.5
In	ppm	< 0.7	< 0.7	< 0.7	< 0.7	< 0.7	< 0.7	< 0.7	< 0.7	< 0.7	< 0.7
Sn	ppm	1.6	0.5	< 0.7	< 0.7	1.3	0.8	0.5	< 0.7	1.0	< 0.7
Sb	ppm	< 0.9	< 0.9	< 0.9	0.5	< 0.9	< 0.9	< 0.9	< 0.9	< 0.9	< 0.9
Te	ppm	< 1.2	< 1.2	< 1.2	< 1.2	< 1.2	< 1.2	< 1.2	< 1.2	< 1.2	< 1.2
I	ppm	< 1.5	< 1.5	< 1.5	< 1.5	< 1.5	< 1.5	< 1.5	< 1.5	< 1.5	< 1.5
Cs	ppm	4.9	< 2.6	< 2.6	< 2.6	< 2.6	< 2.6	< 2.6	< 2.6	2.5	< 2.6
Ba	ppm	531	338	268	205	360	368	220	355	356	265
La	ppm	18.8	16.3	16.9	11.0	9.2	7.4	5.6	10.7	9.2	6.4
Ce	ppm	46	42	31	22	24	21	16.6	23	22	13.8
Pr	ppm	< 8.0	< 8.0	< 8.0	< 8.0	< 8.0	< 8.0	< 8.0	< 8.0	< 8.0	< 8.0
Nd	ppm	19.6	16.9	10.4	< 10	9.8	< 10	< 10	< 10	< 10	< 10
Hf	ppm	5.8	2.4	< 1.8	< 2.0	3.0	1.1	< 1.5	1.3	2.1	< 1.5
Ta	ppm	< 2.7	2.1	< 2.8	< 3.0	2.4	< 2.4	< 2.3	< 2.5	2.4	< 2.3
W	ppm	122	18.1	29	31	26	35	19.2	31	30	22
Hg	ppm	< 0.8	0.3	0.3	< 0.6	< 0.5	< 0.5	< 0.5	< 0.5	< 0.5	< 0.5
Tl	ppm	0.9	0.7	0.8	< 0.5	0.4	0.5	< 0.4	0.4	0.6	< 0.4
Pb	ppm	16.7	10.1	8.0	6.2	8.2	8.1	5.5	8.0	7.6	5.3
Bi	ppm	< 0.4	0.4	0.7	< 0.4	0.4	< 0.3	< 0.3	0.5	0.6	0.4
Th	ppm	14.3	11.3	9.4	8.5	9.0	8.7	7.2	8.6	7.9	7.1
U	ppm	5.0	10.1	14.5	16.4	2.8	2.9	9.2	3.2	3.7	5.2

Table A1.10. ICPMS data.

	Na 23	Mg 24	Al 27	K 39	Ca 43	Cr 52	Fe 54	Mn 55	Cu 65	Sr 88	Pb 206	Pb 207	Pb 208	U 235	U 238
Calibration blank															
merck XXI 50ppb +2% HNO3	40.15	50.00	50.00	50.00	39.80	50.00	45.29	50.00	50.00	50.00	50.00	50.00	50.00	50.00	50.00
merck IV 50ppb +2% HNO3	38.79	52.12	52.02	56.59	41.80	50.23	42.42	51.03	51.16	50.65	50.39	53.13	50.84	0.03	0.03
Merck 500ppb +2% HNO3	500.00	527.98	516.88	482.46	500.00	509.44	500.00	514.20	426.13	520.18	503.65	525.31	512.05	0.00	0.01
calibration blank	0.39	0.03	0.01	2.67	1.45	0.02	-2.08	0.01	0.01	0.01	0.01	0.01	0.01	0.00	0.00
flush blank	-1.32	0.01	0.00	2.61	2.25	-0.03	-9.67	-0.01	0.00	0.00	0.01	0.01	0.01	0.00	0.00
TMc1-1	653.33	1797.78	659.67	353.05	37026.65	3.52	931.70	315.63	53.09	99.66	21.11	21.18	21.01	3.16	1.48
TMc1-2	547.28	2536.87	651.50	375.76	51720.11	2.92	1285.12	491.27	17.03	167.44	12.32	12.36	12.25	7.32	3.27
TMc1-3	730.15	3045.96	540.56	386.94	60654.08	2.95	1468.24	504.56	17.64	226.73	6.49	6.55	6.38	10.27	4.64
T-01-07	1123.49	1413.85	899.35	526.71	22287.13	2.43	3108.67	601.44	18.47	98.50	10.44	10.60	10.38	0.56	0.26
T-02-07	716.59	1277.94	865.71	425.73	26030.00	2.38	2648.69	1027.78	17.31	59.40	5.61	5.54	5.55	0.65	0.26
T-04-07	598.83	22271.91	835.58	410.65	23785.21	3.56	2903.81	277.33	162.29	124.54	14.54	14.58	14.49	0.30	0.19
T-08-07	975.54	1066.65	821.94	583.29	29824.31	2.93	2167.98	888.57	14.43	60.16	9.45	9.52	9.29	0.54	0.25
T-09-07	1230.24	2842.18	824.79	426.16	25897.78	2.76	3075.79	707.60	10.88	94.97	5.71	5.76	5.72	0.51	0.26
flush	1.57	0.40	0.13	6.18	11.97	-0.09	-13.37	0.00	0.00	0.01	0.00	0.00	0.01	-0.02	0.00
TMf1-1	931.81	28462.41	1072.17	549.96	29750.70	3.93	3125.85	363.68	17.36	171.59	4.30	4.24	4.23	0.61	0.24
TMf1-2	1262.49	32362.44	1022.88	606.82	31854.74	4.16	1920.31	220.31	18.17	188.02	4.49	4.46	4.44	0.95	0.48
TMf1-3	1113.36	42347.02	1128.93	452.07	36673.67	3.89	1565.47	141.99	16.11	272.48	10.56	10.49	10.72	5.79	2.57
TMf2-1	914.12	26685.45	1180.89	472.43	29463.86	4.52	1916.72	236.90	17.62	162.12	3.88	3.88	3.87	0.62	0.32
TMf2-2	784.41	28770.85	1312.91	493.12	30226.39	4.10	1880.79	226.05	60.15	163.54	5.93	5.91	5.96	0.96	0.43
sample flush	4.88	3.45	0.25	20.53	17.96	0.02	-3.83	0.05	0.02	0.03	0.01	0.01	0.01	0.00	0.00
MerckXXI QC	74.87	70.11	62.10	72.92	71.07	50.82	50.37	46.24	54.18	49.65	52.62	53.31	52.03	50.33	54.60
Calibration blank															
merck XXI 50ppb +2% HNO3	68.02	50.00	50.00	50.00	62.72	50.00	51.48	50.00	50.00	50.00	50.00	50.00	50.00	50.00	50.00
merck IV 50ppb +2% HNO3	61.80	48.52	47.67	53.25	61.60	49.37	45.96	49.16	49.90	49.72	49.28	50.26	51.17	0.04	0.02
Merck 500ppb +2% HNO3	500.00	497.50	489.15	461.58	500.00	511.40	500.00	505.56	436.97	534.10	498.08	517.15	507.15	0.01	0.00
calibration blank	-0.13	0.05	0.01	1.65	1.69	0.09	6.19	0.01	0.00	0.01	0.01	0.01	0.02	0.01	0.00
TMf2-3	717.60	28737.57	828.68	335.98	34378.84	6.88	1577.26	153.79	6.94	249.18	5.16	5.05	5.20	2.73	1.05
T-07-07	658.23	23673.19	689.50	317.19	26583.38	3.57	4498.19	610.08	39.54	184.69	3.09	3.05	3.08	0.38	0.15

Appendix 2

Cape Turnagain

Cape Turnagain table of contents

1. Location

The Cape Turnagain occurrence has three locations (see Section 1.1). Only the Whangaehu (see Section 1.2) site was investigated in detail. This site is tide and weather dependent and can only be accessed 3 hours either side of low tide. However, large swells and strong easterly winds will shorten this timeframe. The first kilometre from the northern entry point is the most tide dependent. There are a few exit points along the section, and several safe areas if caught by an incoming tide. The second site at Herbertville (see Section 1.3) was discovered late in the project. It was visited, although no laboratory analysis was completed. This location is not tide dependent. Location three at Wimbledon had only a few tubular concretions (see Section 1.1). Two samples were collected and analysed for carbon and oxygen stable isotopes to determine any genetic relationship to the Whangaehu concretions. This site is in a forest with access through a muddy tree felled stream.

Coastal Section numbers on location maps (Fig. A2.2) correspond to the distribution of tubular concretions in outcrop (Chapter 4, Section 4.2).

1.1 Study locations

Table A2.1. Study locations and access information

Location	Topo map	GPS	Access (no permission needed)	Outcrop	Source information
Whangaehu Beach	V24	E2818450, S6083117 to E2817228, S6079328	Take Whangaehu Rd. from Porangahau. Beach entry at GPS E2818415, S6083117	Beach: late Miocene. Public access, tide and weather dependent.	Murry Baker
Herbertville	V24	E2814650, S6073200 to E2815000, S6073400	From Herbertville; Tautane Rd toward Cape. Gravel road to beach at GPS E2813200, S6073400	Note: gravel road to beach is public access, but must pass through an unlocked gate. Can be accessed anytime, regardless of tide.	Moore, 1981
Wimbledon	U24	E2790322, S6088060	Wainui River, Route 52, west of Wimbledon	Inland: Fossil record U24 f430; overturned unconformity, low dip 30-35^{o} below unconformity dark grey mudstone, occolith sandstone above paler mudstone; below contact.	Dave Francis

1.2 Regional map

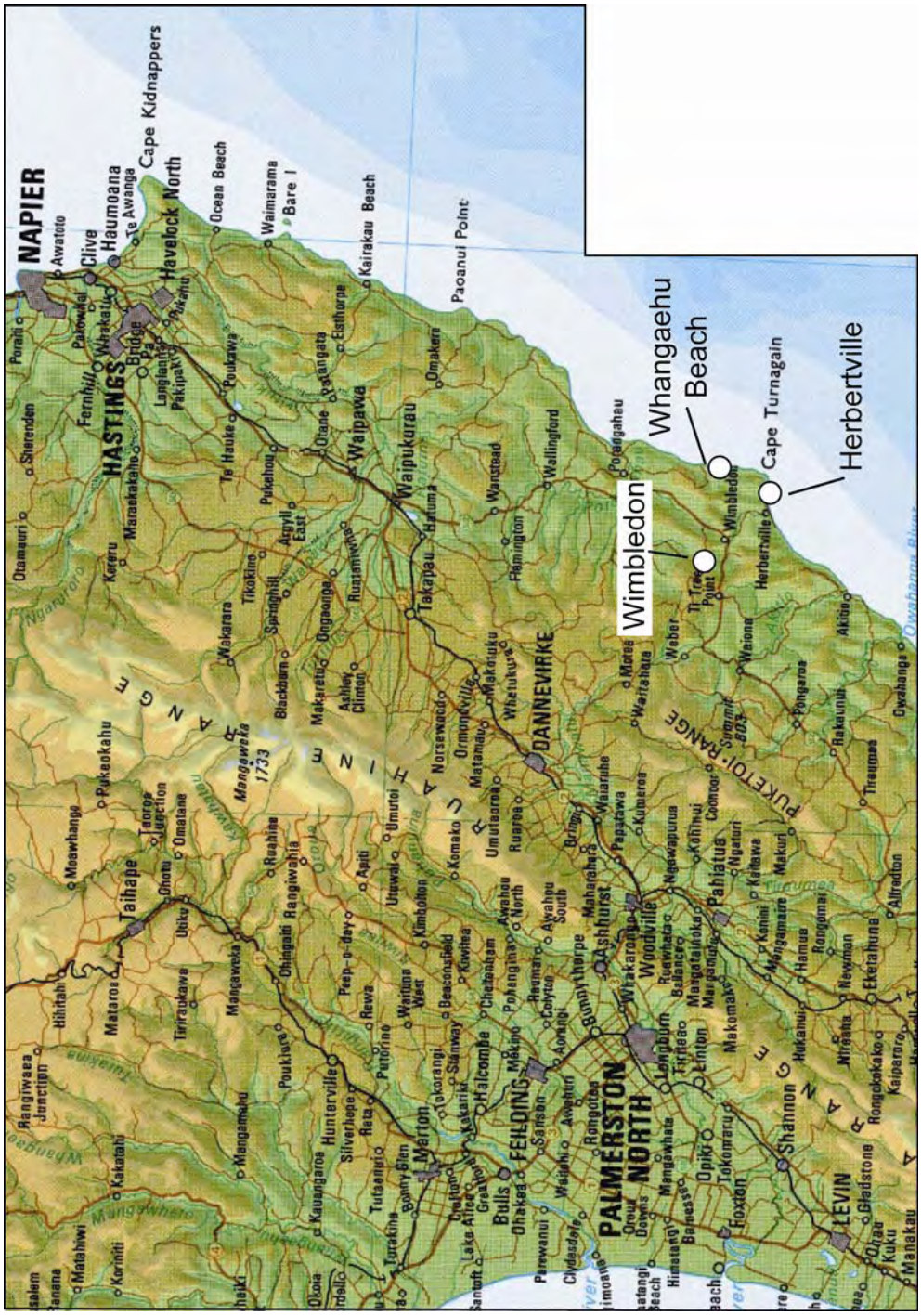

Figure A2.1. Regional map of Southern Hawkes Bay and study locations.

1.3 Map of Whangaehu outcrop

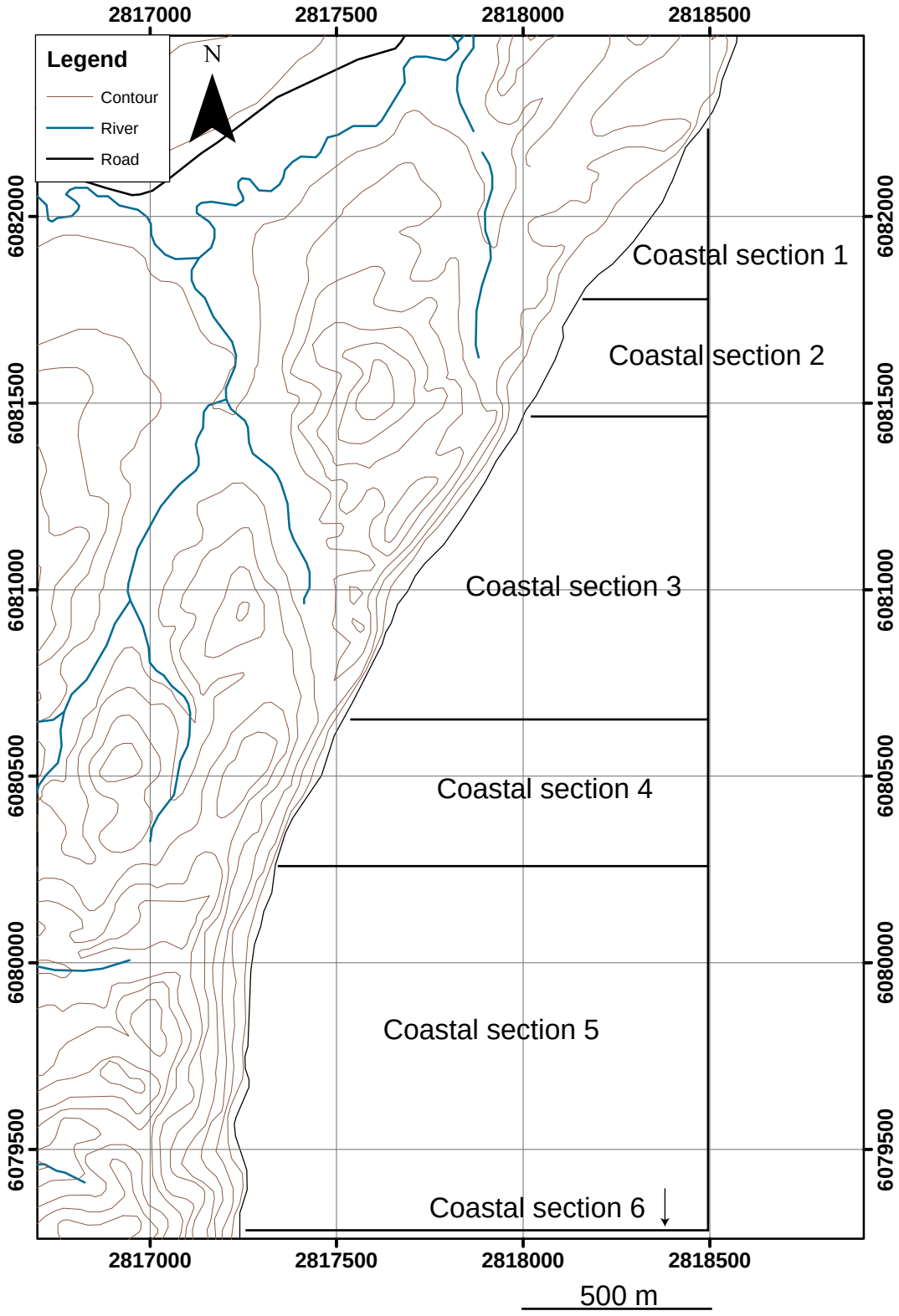

Figure A2.2. Map of coastal sections 1 to 5 of the Whangaehu outcrop.

1.3 Map of Whangaehu outcrop

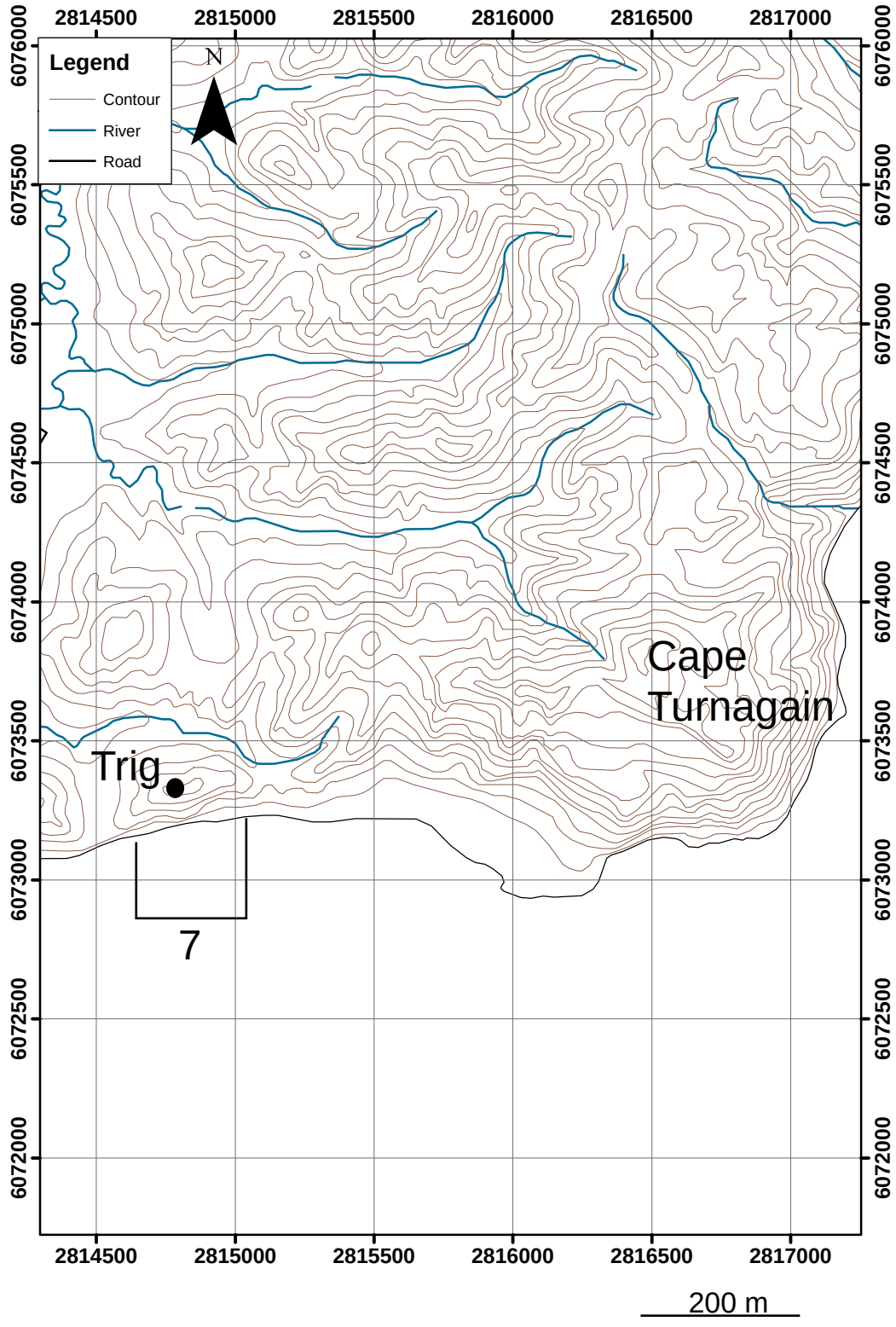

Figure A2.3. Map of coastal section 7, Herbertville outcrop.

2. Photomosaics

Photomosaics were constructed of the main Whangaehu outcrop (Coastal sections 1 to start of 5, Fig. A2-4). The photomosaic is not to scale due to distortion caused by focal length and angle, and scale bars are approximate. The cliff outcrop ranges from 10 to 30 m high. The relative abundance of tubular and spherical concretions (presented in Fig. 6 of Chapter 4) is superimposed below the photomosaic. Selected photographs of primary tubular concretion features are included and location indicated. Outcrop sections are indicated (and described in Chapter 4, Section 4.2). Additionally, Table A2.2 has captions for photographs of field examples (Fig. A2.5) and Table A2.3 is a detailed description of field GPS mapping (including photographs, Fig. A2.6). Each Table has a column which identifies the section of outcrop. Photomosaics were not constructed for the remaining coastal sections because the outcrops did not extend for much of a distance and only a few tubular concretions were present.

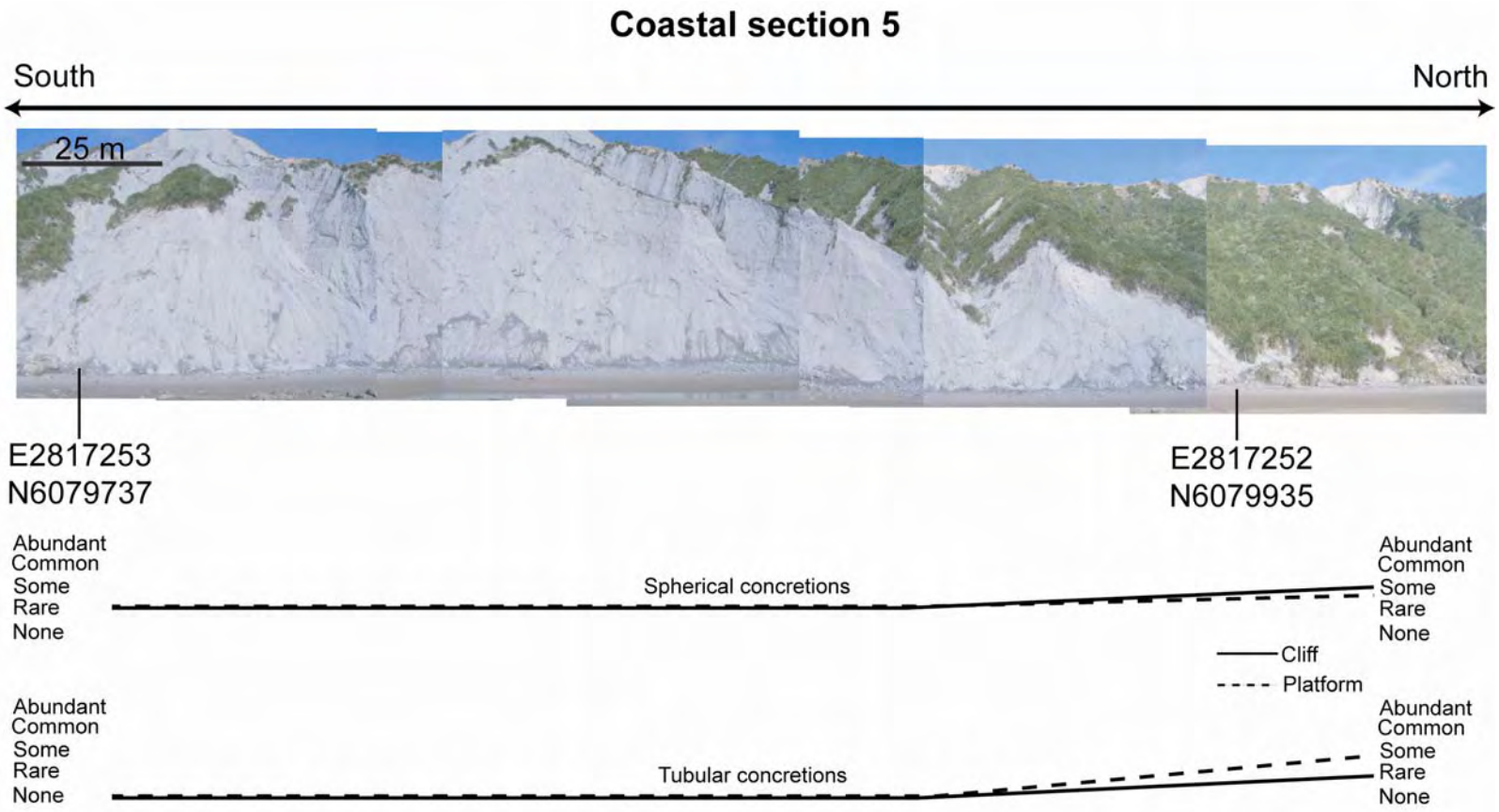

Figure A2.4a. Photomosaic of Whangaehu coastal section 5. See Figure A2.2 for location of coastal section. Right side of photomosaic lines up with the left side of photomosaic in Figure A2.4b.

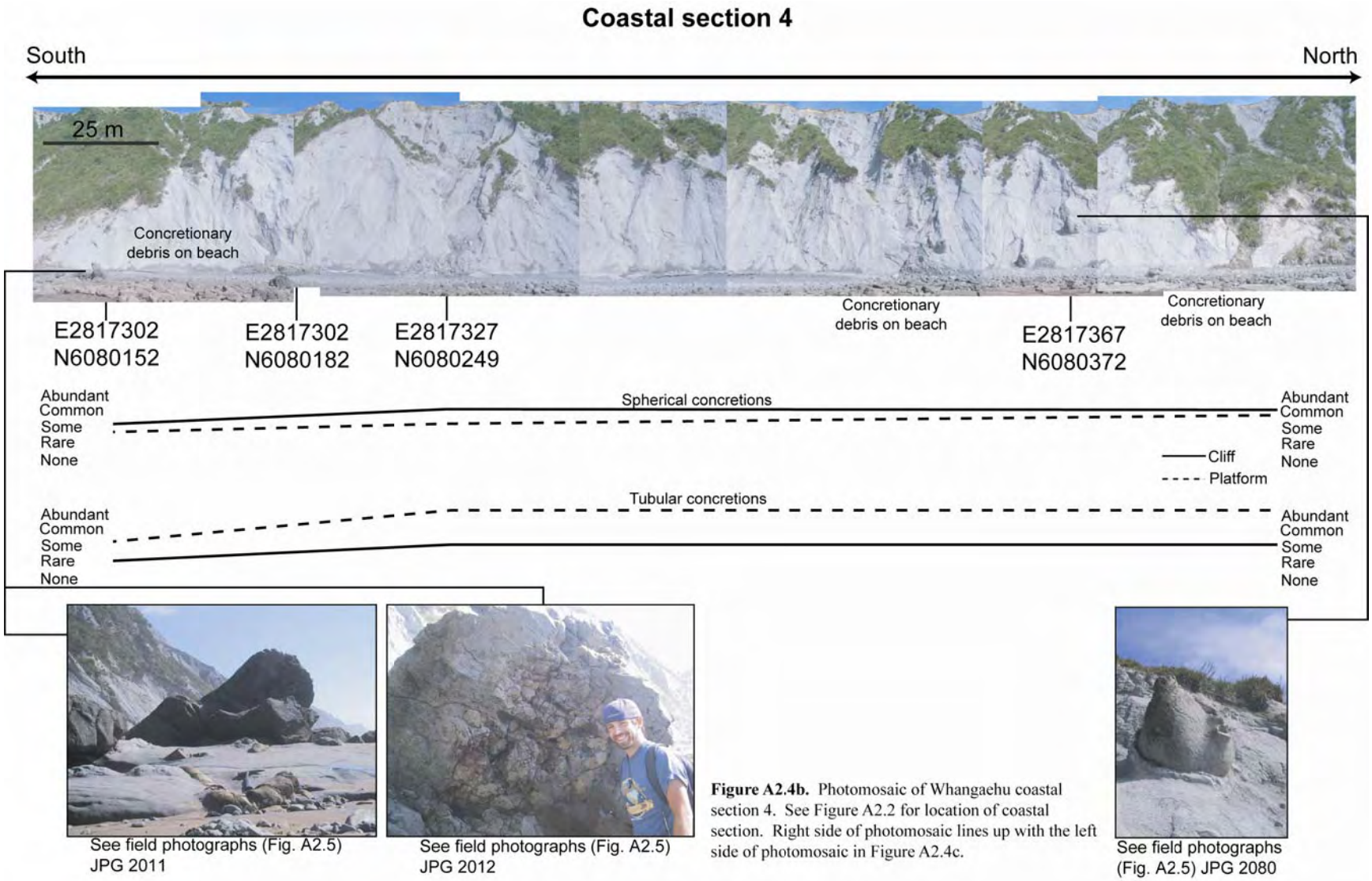

Figure A2.4b. Photomosaic of Whangaehu coastal section 4. See Figure A2.2 for location of coastal section. Right side of photomosaic lines up with the left side of photomosaic in Figure A2.4c.

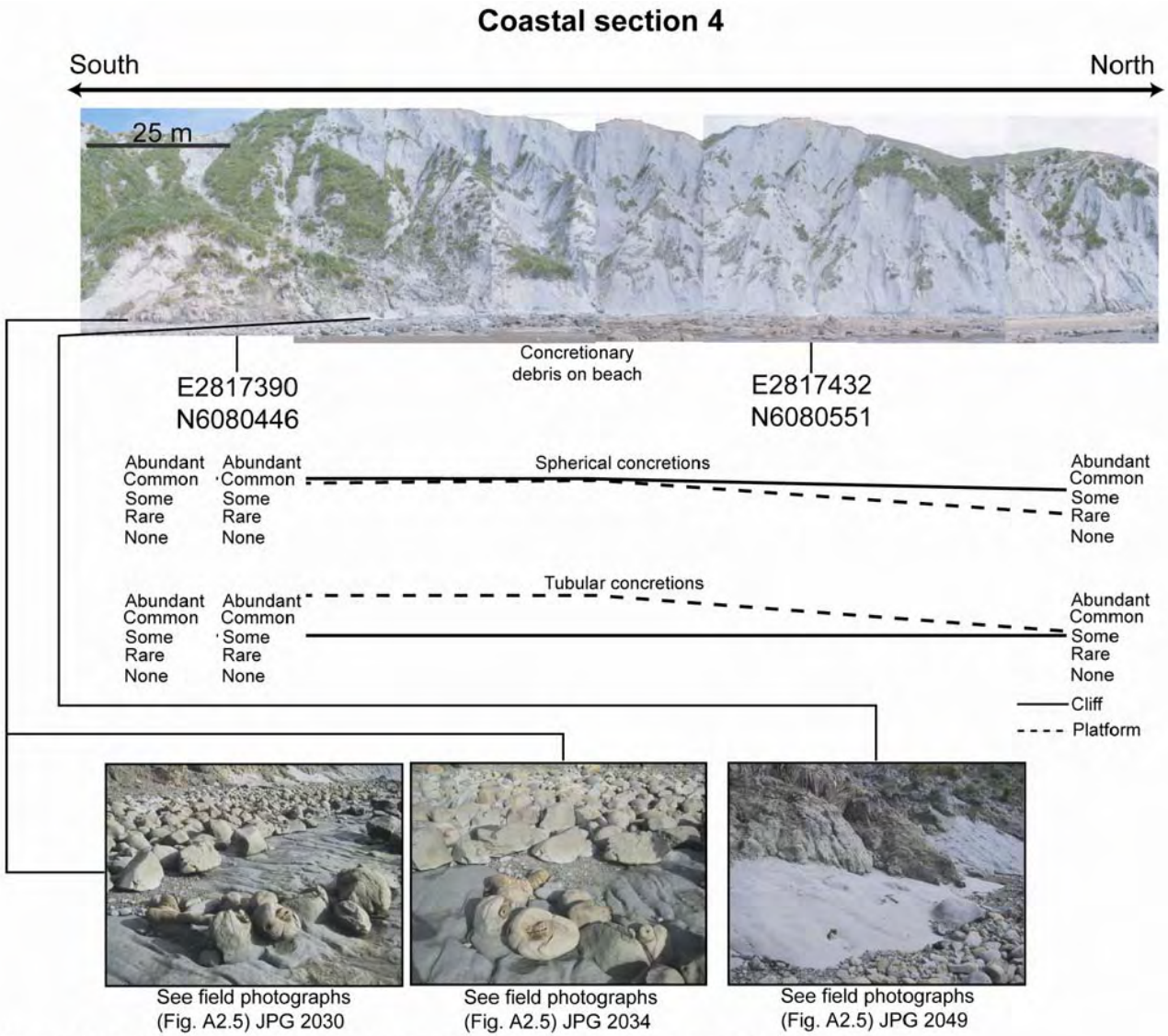

Figure A2.4c. Photomosaic of Whangaehu coastal section 4. See Figure A2.2 for location of coastal section. Right side of photomosaic lines up with the left side of photomosaic in Figure A2.4d.

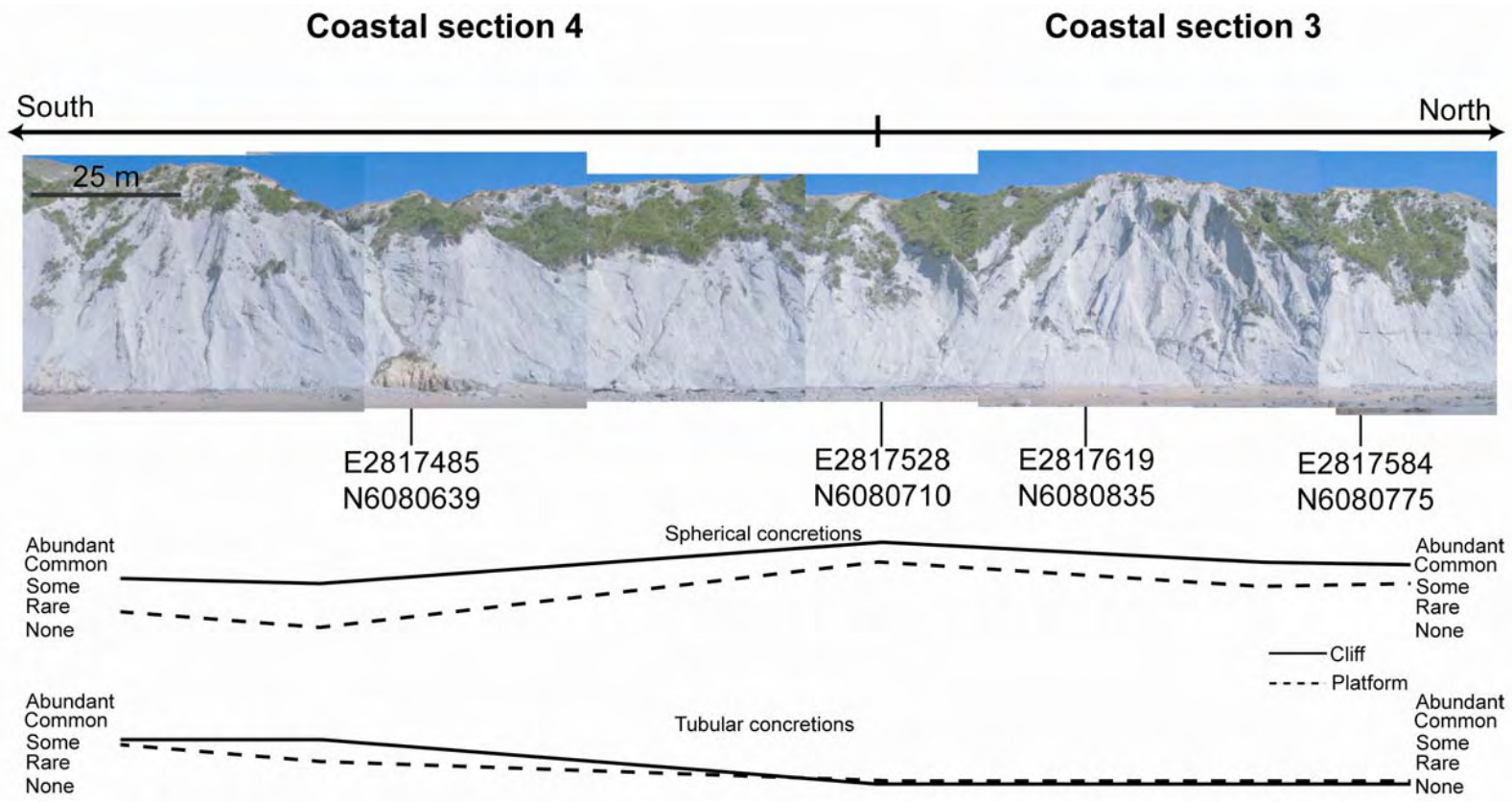

Figure A2.4d. Photomosaic of Whangaehu coastal sections 3 and 4. See Figure A2.2 for location of coastal section. Right side of photomosaic lines up with the left side of photomosaic in Figure A2.4e.

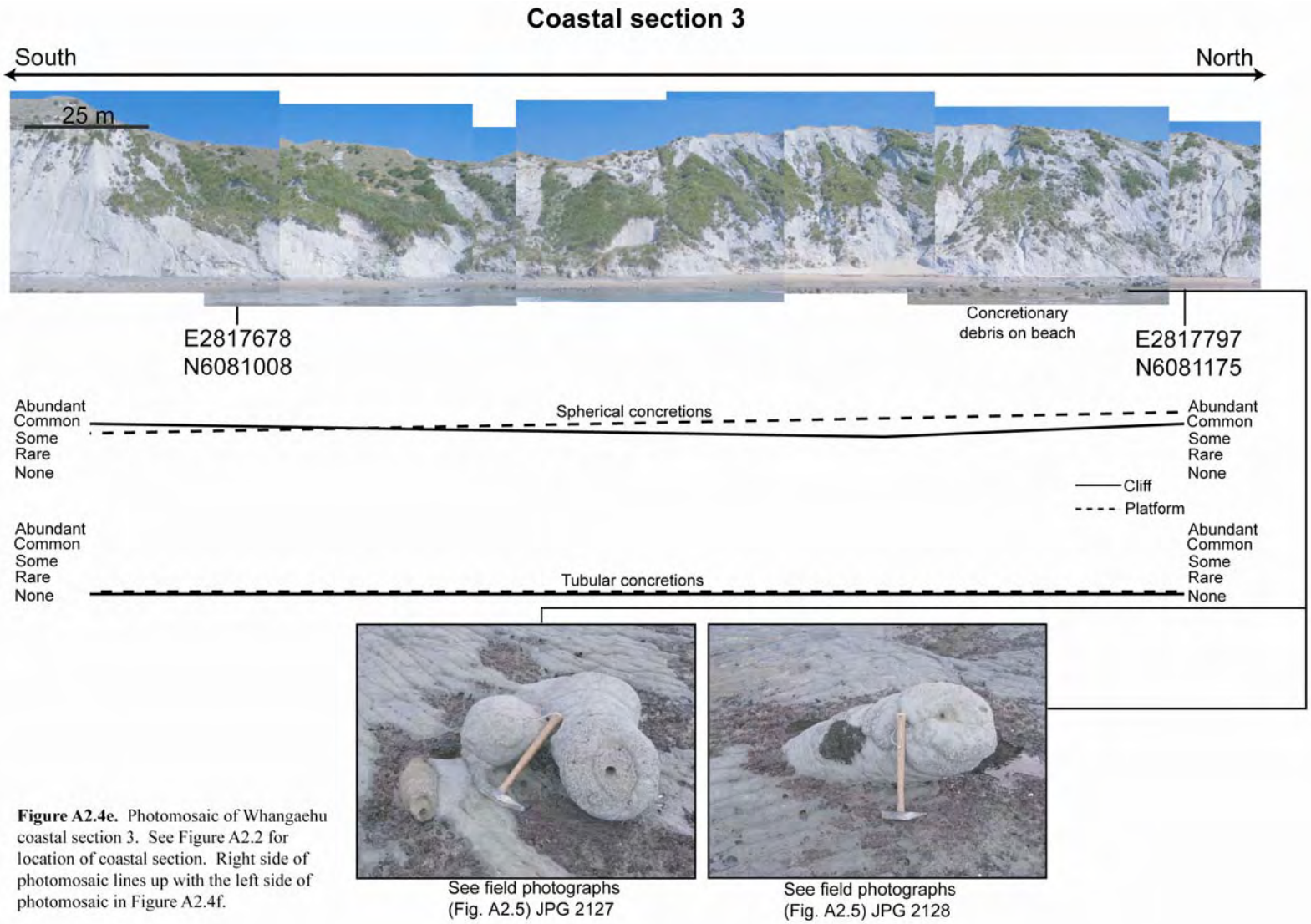

Figure A2.4e. Photomosaic of Whangaehu coastal section 3. See Figure A2.2 for location of coastal section. Right side of photomosaic lines up with the left side of photomosaic in Figure A2.4f.

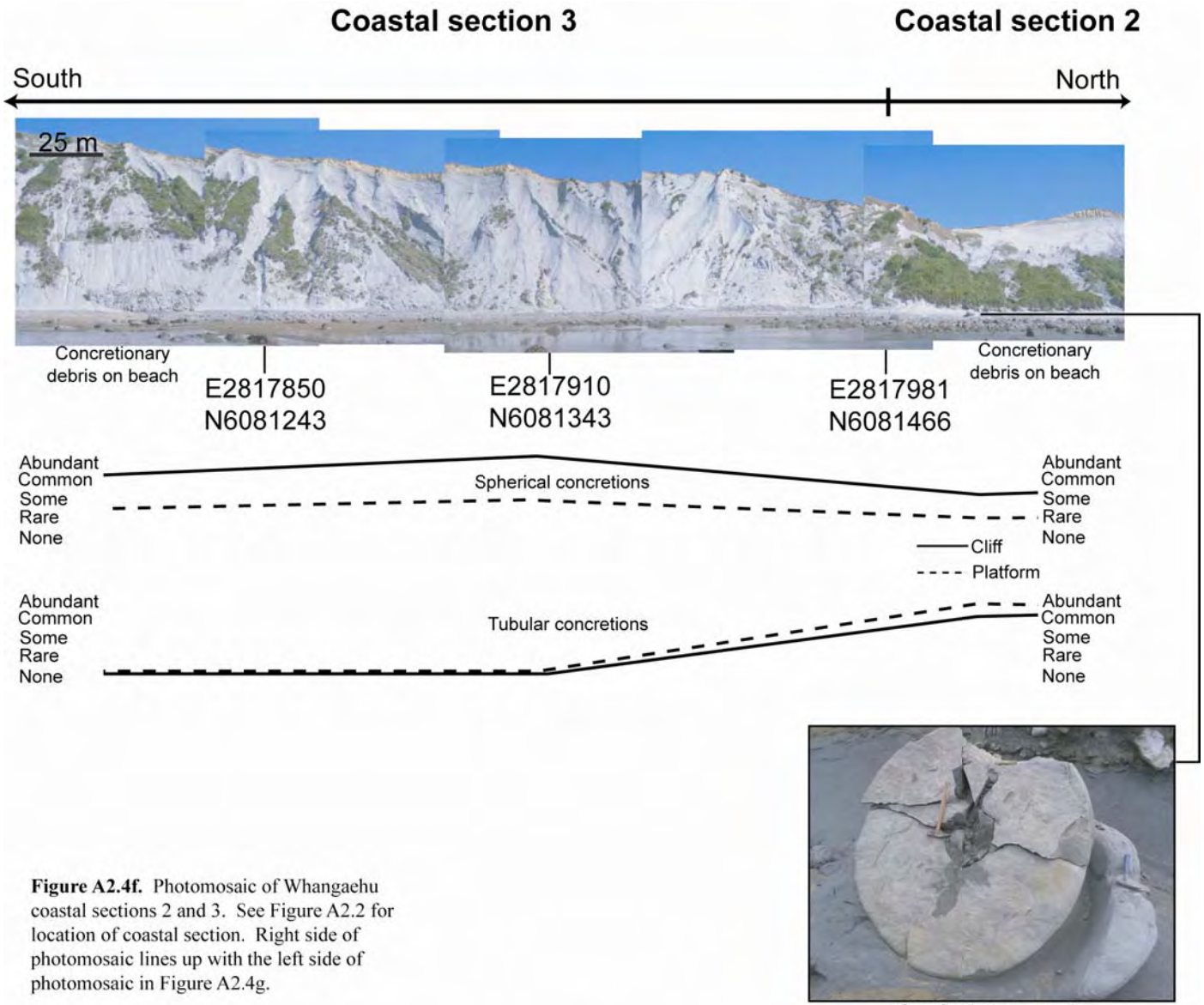

Figure A2.4f. Photomosaic of Whangaehu coastal sections 2 and 3. See Figure A2.2 for location of coastal section. Right side of photomosaic lines up with the left side of photomosaic in Figure A2.4g.

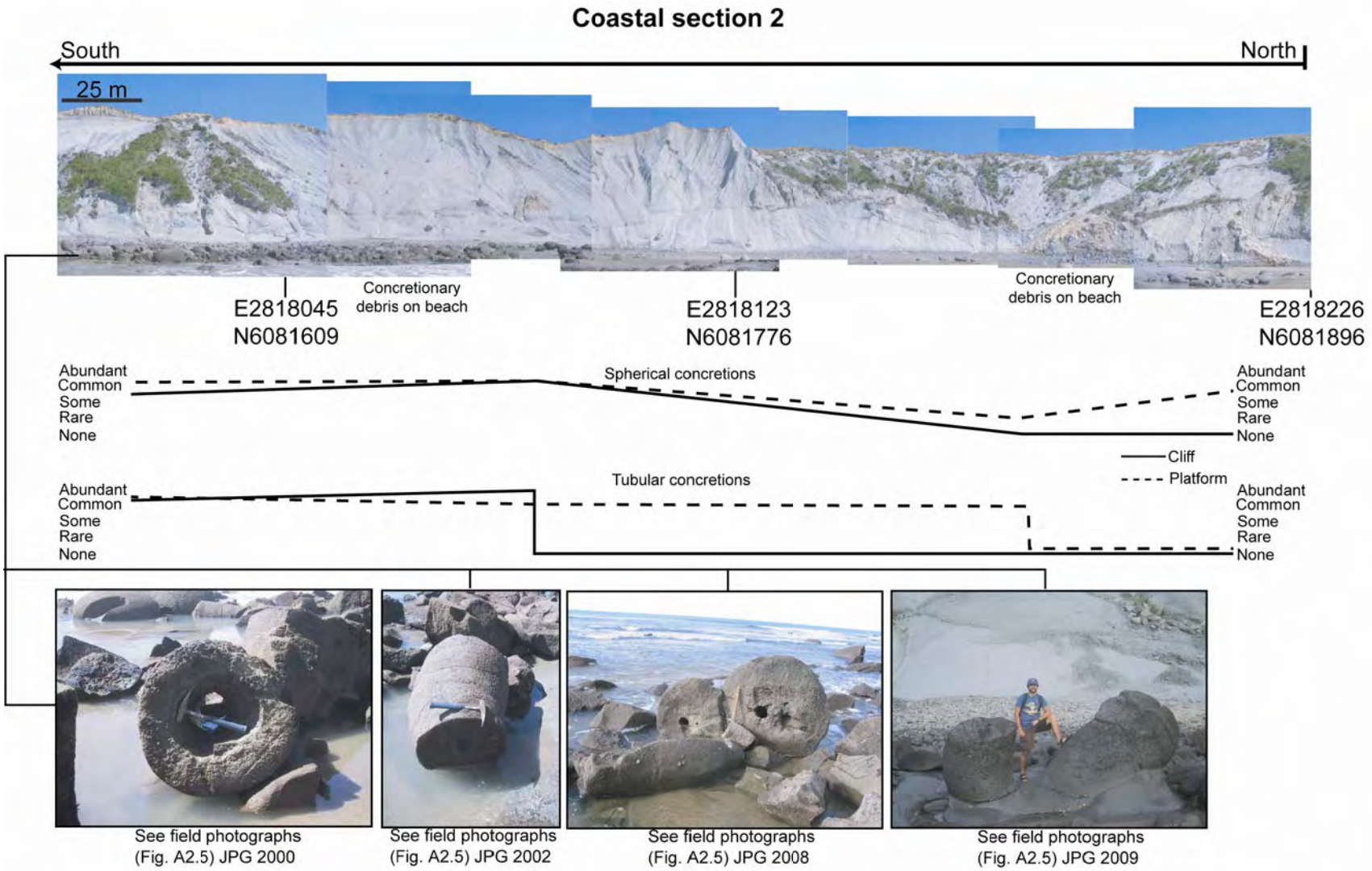

Figure A2.4g. Photomosaic of Whangaehu coastal section 2. See Figure A2.2 for location of coastal section. Right side of photomosaic lines up with the left side of photomosaic in Figure A2.4h.

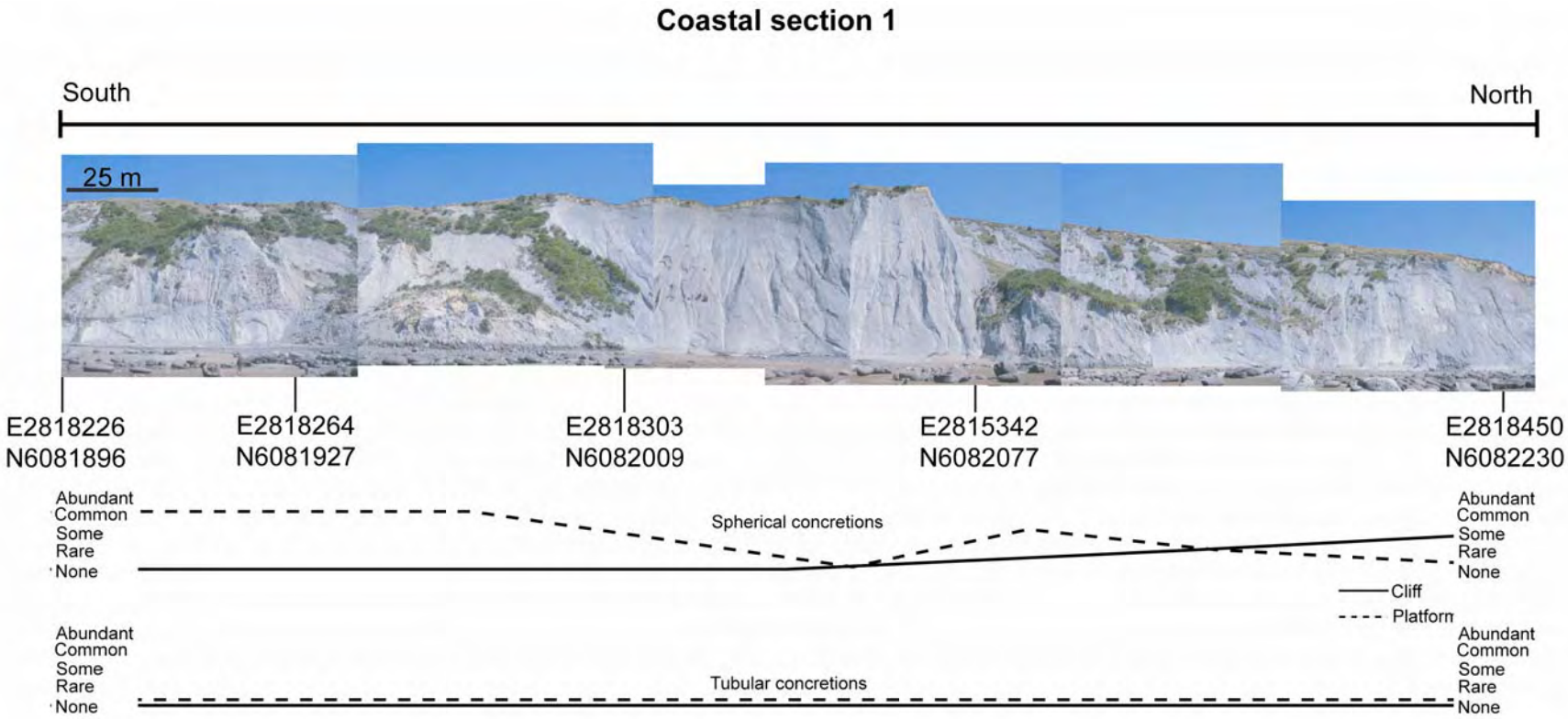

Figure A2.4h. Photomosaic of Whangaehu coastal section 1. See Figure A2.2 for location of coastal section.

3. Field photographs

Photographs of tubular concretions in the field (Fig. A2.5) are presented in this section along with brief descriptions in Tables A2.2-A2.3 (jpg number corresponds to that in Table). A DVD accompanies this volume, where the photographs can be viewed at a larger scale (Appendix\Whangaehu\FieldPhotos).

3.1 Table and photographs of tubular concretions in the field

Table A2.2. Descriptions of field photographs in Figure A2.5.

Photograph jpg no.	Outcrop section	Comment
2000	2	Thin outer pipe concretion with large open conduit
2001	2	Thick outer pipe concretion with small open conduit
2002	2	Thick outer pipe concretion with small open conduit
2003	2	Large pipe concretion fractured through its diameter
2004	2	Side view of 2003
2005	2	Large pipe concretion and conduit filled with ?modern debris
2006	2	Large pipe concretion with small conduit
2007		Concretion block with two semi-open conduits
2008	2	Branching pipe concretion, two conduits
2009	2	Branching pipe concretion, two conduits
2010	2	View of cliff behind 2009, note protruding pipes high in the cliff (upper left)
2011	4	Pipe with brecciated central conduit
2012	4	Close up of 2011
2013	2	Pipes eroding out of the cliff
2014		Pipe with small conduit lined with yellow calcite
2015	3	Small pipe eroding out of mudstone, based on the erosion pattern it appears the tube meanders
2016	3	Close up of 2015
2017	3	Tube with small cement filled conduit, concreted material in the background
2019	3	Small pipe eroding out of mudstone, based on the erosion pattern it appears the tube meanders
2020	3	Branching pipe with small conduit
2021	3	Small pipe with two pinhole conduits
2022	3	Small pipe with filled conduit
2023	3	Small tortuous pipe
2024	3	Small pipe eroding out of the mudstone
2025	3	Small pipe eroding out of the mudstone
2026	3	Small pipe eroding out of the mudstone with two small conduits
2027	3	Bulbous concretion with open conduit and futher to the left is a smaller bulbous concretion that may be connected
2028	3	Pipe protruding from the shore platform
2029	3	Bulbous concretions on the shore platform, small tubes littering the beach, and small pipes in cliff
2030	4	Tortuous pipe concretion with multiple branches and conduits
2031	4	Same concretion in 2030 from different angle
2032	4	Same concretion in 2030 from different angle

Table A2.2 continued

Photograph jpg no.	Outcrop section	Comment
2033	4	Same concretion in 2030 from different angle
2034	4	Same concretion in 2030 from different angle
2035	4	Sinuous pipe concretion (no apparent conduit)
2036	4	Sinuous pipe with pinhole conduit; note a second conduit connected and perpendicular to the main pipe and a third next to the rock hammer
2037	4	Curved (downward) pipe eroding out of the mudstone
2038	4	Note the 'humpback' shape of the curved pipe in the centre of the photograph, in the foreground is a 1/2 tube with thick conduit zone
2039	3	Sinuous tube
2040	3	Four tubes with pinhole conduits protruding from the shore platform
2041 - 2064	3	Many small tubes eroding out of the base of the cliff and shore platform. Some have small or pinhole open conduits, others are filled. Approximately 33 tubes are cropping out over 10 m. Many of these may be connected and branching from each other.
2044	3	Notice the curve in the pipe (also note above caption)
2049	3	The five protrusions in the mudstone are all tubes (also note 2041 caption)
2050	3	The discoloured areas in the mudstone (from foreground to background) are all tubes eroding out of the mudstone; also note that much of the debris supports open conduits (also note 2041 caption)
2065	3	Small pipe with yellowish-white calcite filling the conduit
2066	3	General photograph of the shore platform where many of the boulders contain conduits
2067	3	General photograph of the shore platform where many of the boulders contain conduits
2068	3	General photograph of the shore platform where many of the boulders contain conduits
2069	4	General photograph of the shore platform where many of the boulders contain conduits; note the large tubes eroding out of the cliff
2070	2	Tubes eroding out of the mudstone high up in the cliff
2071	2	Tubes eroding out of the mudstone high up in the cliff
2072	2	Tubes eroding out of the mudstone high up in the cliff
2073	2	Tubes eroding out of the mudstone high up in the cliff

Table A2.2 continued

Photograph jpg no.	Outcrop section	Comment
2074	2	Tubes eroding out of the mudstone high up in the cliff
2075	2	Tubes eroding out of the mudstone high up in the cliff
2076	2	Tubes eroding out of the mudstone high up in the cliff
2077	2	General photograph of the shore platform where many of the boulders contain conduits; note the large tubes
2078	4	Tubes eroding out of the mudstone
2079	4	Close up of tubes in 2069 eroding out of the cliff
2080	4	Close up of tube in 2069 eroding out of the cliff; note the fractures on the top of the left bulb
2081	2	Block with conduit
2082	2	Concretion eroding out of the cliff, pipe or spherical ?
2083		Typical concretionary debris on the shore platform, note many have conduits. See photomosaic annotations for locations at Whangaehu with clusters of debris.
2084	4	Close up of cobbles with conduits in 2083
2085	4	Close up of cobbles with conduits in 2083
2086	4	Close up of cobbles with conduits in 2083
2087	4	Close up of cobbles with conduits in 2083
2088	4	Small spherical concretions eroding out of cliff
2089	4	Large spherical concretion eroding out of cliff
2090	2	Large spherical concretions eroding out of the shore platform; a pipe is located in the background behind the spherical concretions (next photographs)
2091	2	See 2090
2092	2	See 2090
2093	1	Concretion layers jutting out to sea
2094	1	Part of a concretion layer which continues in the upper right of the photograph
2095	1	Cemented zones along joints in the cliff with small spherical concretions
2096	1	Cemented zones along joints in the cliff
2097	1	Bioturbation in the mudstone near the entrance to the Whangaehu section
2098	1	Bioturbation in the mudstone near the entrance to the Whangaehu section
2099	1	Bioturbation in the mudstone near the entrance to the Whangaehu section

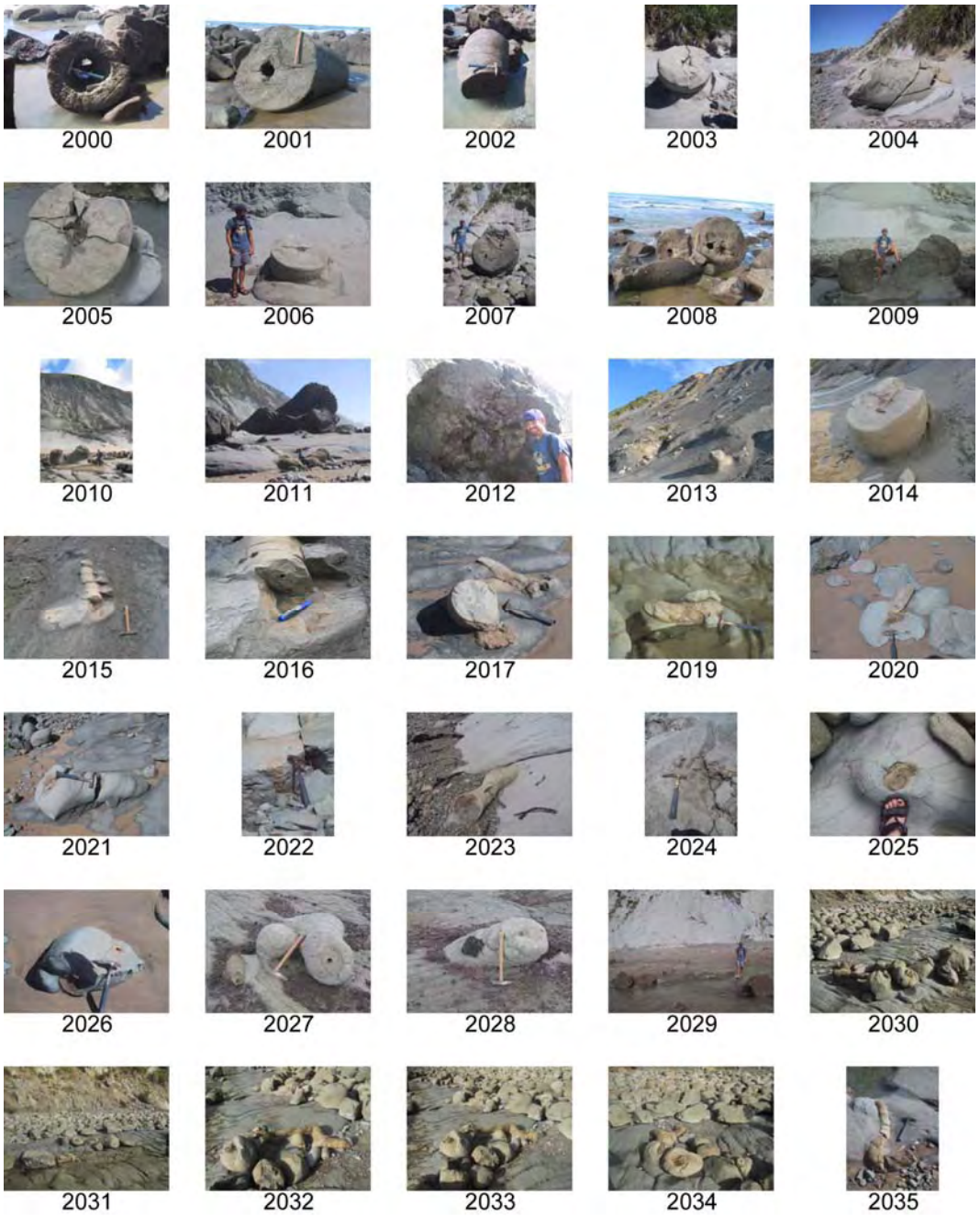

Figure A2.5. Photographs of tubular concretions from Whangaehu coastal sections. See Table A2.2 for descriptions.

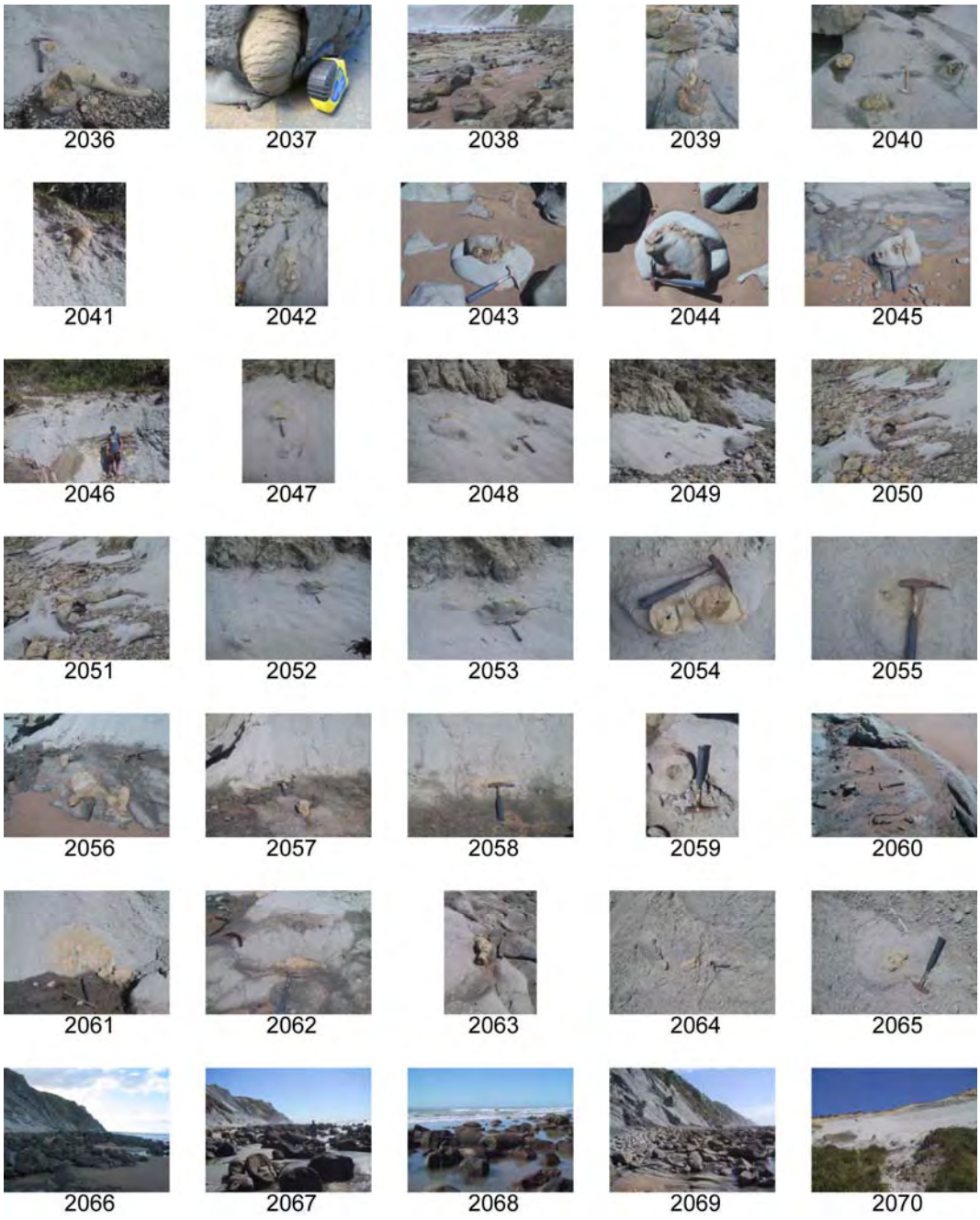

Figure A2.5 continued.

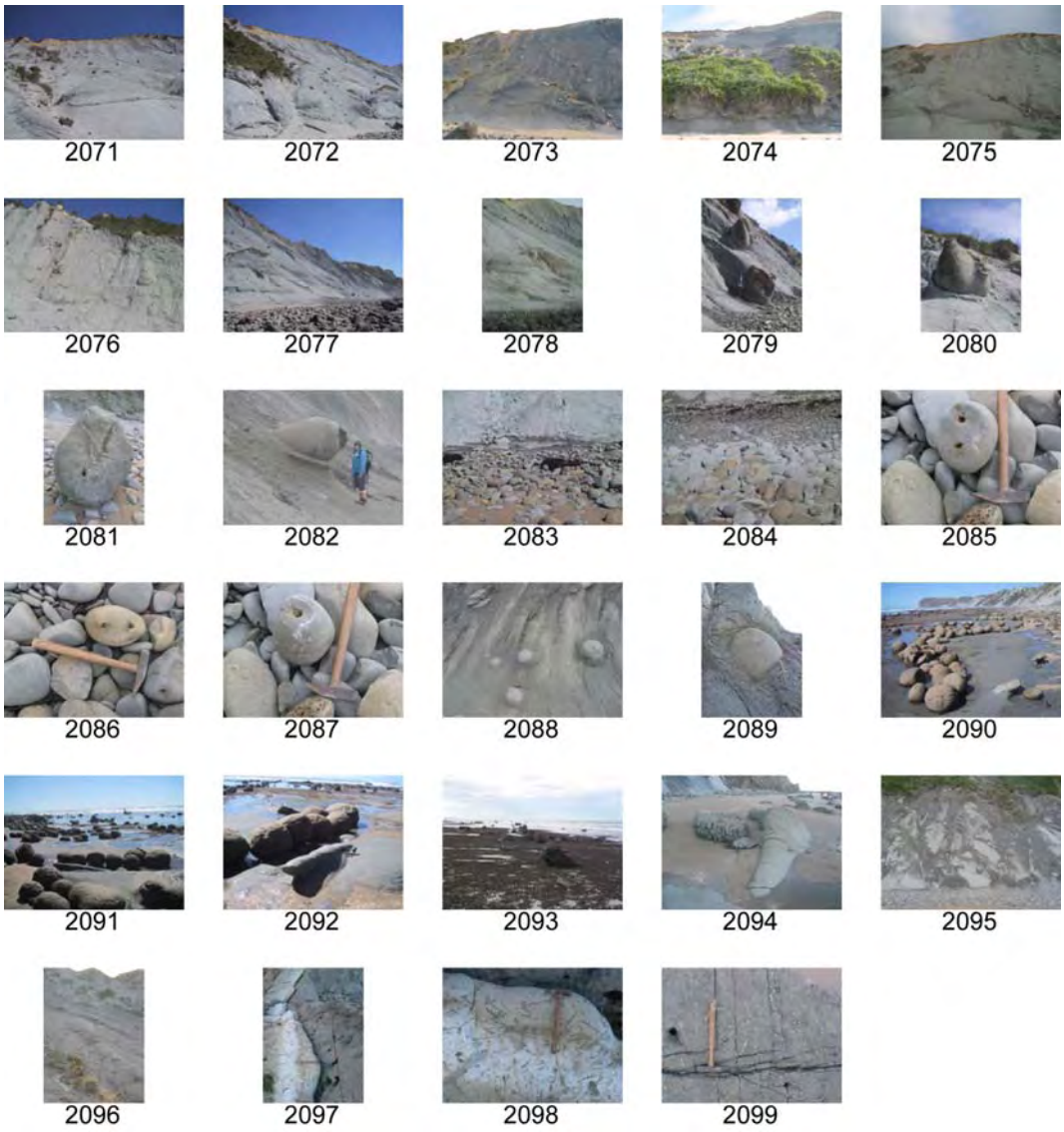

Figure A2.5 continued.

3.2 Table and photographs of GIS mapped concretion conduits

A DVD accompanies this volume, where the photographs can be viewed at a larger scale (Appendix\GIS mapping\FieldPhotos).

Table A2.3. Field data and GIS mapping of tubular concretions and conduits.

Outcrop section	Easting	Northing	Morphology	JPG numbers	Concretion	Concretion diameter (m)	Concretion length (m)	Conduit	Conduit diameter (m)	Comments
2	2817976	6081487	Pipe	839		1.6	1.6	Highly fractured	0.8	
2	2817992	6081487	Pipe	844-846		1.2	1.6	Micritic fill	0.1	Trace fossils; Scolicia
2	2817994	6081488	Boulder	847-849				Mement lined with micritic fill		
2	2817993	6081499	Pipe	852-853		0.44	0.75	Open	0.08	
2	2817992	6081500	Pipe	854-855		0.4	0.3		0.12	
2	2817988	6081499	Pipe	857-859	Sinuous	1.4	1.4	Center open, strong fracturing on conduit wall (radial?)	0.25	
2	2817992	6081509	Pipe	860-868	Highly fractured					
2	2817991	6081517	Pipe	869-872		0.3	0.3	Filled	0.06	From rubble
2	2817991	6081517	Pipe	869-872		0.4	0.4		0.15	From rubble
2	2817991	6081517	Pipe	869-872		0.35	0.35		0.1	From rubble
2	2817991	6081517	Pipe	869-872		0.3	0.3		0.08	From rubble
2	2818006	6081503	Pipe	873-874		0.57	1		0.2	
2	2818010	6081501	Pipe	875-883		1.5	1.5	Inside second conduit; conduit zoned with central more strongly cemented	0.3, 0.04	Conduit with in a conduit
2	2818017	6081499	Pipe	883-889	Coalesced pipes	1.14	1		0.18, 0.14, 0.1	Triple conduit/coalesced tube; 1 tube with 2 conduits (right side), with second apparent coalesced tube with 1 conduit (left side)
2	2818017	6081499	Pipe	890-892	Coalesced pipes	1.1	1.1		0.05	Back side of triple/coalesced tube; triple conduit joins to form one
2	2818010	6081534	Pipe	893-894		0.12	0.26	Open	0.03	Bioturbation
2	2818012	6081535	Pipe	895-896		0.35	0.45	Open	0.08	
2	2818022	6081526	Pipe	897-898		1	1.2	Appears to have zonation; centre open + harder	0.05, 0.3	
2	2818022	6081526	Pipe	899	Diameter is estimate	1.25		Two conduits	0.05, 0.05	Partially underwater, measurements approximate
2	2818016	6081541	Pipe	900-901		0.8			0.12	Conduit off centre, open centre, concretion harder, some fracturing

Table A2.3 continued.

Outcrop section	Easting	Northing	Morphology	JPG numbers	Concretion	Concretion diameter (m)	Concretion length (m)	Conduit	Conduit diameter (m)	Comments
2	2818025	6081547	Pipe	902-904		0.9		Zonation, open central	0.1, 0.45	
2	2818035	6081553	Block	905-908		0.01		Filled with harder material and pinhole conduit	0.01, 0.04, 0.3	
2	2818033	6081555	Pipe	909-911		0.75	1.6	Open	0.2	
2	2818019	6081578	Pipe	912		1.1	1	Open, some fracturing	0.15	Conduit approximate measurement (in cliff)
2	2818044	6081598	Pipe	913-914		1.1	0.8	Partially open, yellow calcite cement along fracture	0.01	
2	2818044	6081598	Pipe	915		0.4		Zoned; light outer rim, dark grey fill	0.1	
2	2818044	6081598	Pipe	915		0.4		Zoned; light outer rim, dark grey fill	0.1	
2	2818046	6081612	Pipe	916		0.22		Open lined with yellow calcite	0.02	
2	2818046	6081612	Pipe	916		0.22		Open lined with yellow calcite	0.02	
2	2818046	6081612	Pipe		Debris					Zonation with pin pricks, open with yellow calcite lining
2	2818052	6081605	Pipe	917-918	Sinuous	0.8	2	Filled	0.05	
2	2818052	6081605	Egg shaped	919		2.1		Open, odd oval	0.7, 0. 25	Oval conduit, conduit measurements length vs width
2	2818052	6081605	Pipe							Cliff exposure with many (10) tubes. Dense fog; number may be more
2	2818073	6081622	Pipe	923		1		Inner hard, outer harder than concretion	0.03	
2	2818073	6081622	Pipe	923		1		Inner hard, outer harder than concretion	0.03	
2	2818065	6081622	Pipe	924		1		Open	0.3	
2	2818062	6081623	Teardrop	925	Fractures	1		Filled (no fracturing)	0.1	
2	2818064	60816925	Sphere	926		1				Spherical concretion
2	2818069	6081626	Pipe	927-928		0.9	1.5	Open	0.12	
2	2818077	6081626	Pipe	929		1.35		No apparent conduit, internal differentiation		

Table A2.3 continued.

Outcrop section	Easting	Northing	Morphology	JPG numbers	Concretion	Concretion diameter (m)	Concretion length (m)	Conduit	Conduit diameter (m)	Comments
2	2818073	6081633	Pipe	930		0.35		Darker fill	0.18	
2	2818065	6081641	Pipe	931-934	Fractures	1.1, 1.0	2.5, 1.15	yellow calcite fill	0.28, 0.1	Branching pipes
2	2818072	6081648	Pipe	935-936		0.9	1.4	Open	0.15	
2	2818072	6081651	Block	937-938	Highly fractured	1.1		Open	0.2	
2	2818067	6081650	Pipe	939		0.6		Open	0.15	
2	2818068	6081656	Pipe	940-942		0.3		Semi-open; lining = cement	0.02	Zonation in conduit, debris field
2	2818057	6081664	Pipe	943		1.2	1.5			In cliff`
2	2818070	6081661	Block	944-946		1.5		Yellow calcite		Yellow calcite
2	2818092	6081699	Layer							Small concretion layer (cm in height above platform)
2	2808053	6081619	Pipe	947		0.4		Zoned fill, harder in centre	0.15, 0.01	
3	2818006	6081417	Pipe	948-949		1.37		Open all the way through	0.35	
2	2818008	6081485	Pipe	950-951		1.3	1.2		0.2	Vertical slice
2	2.8E+07	6081483	Pipe	952-953		1.2		Open conduit, hard rim	0.3, 0.5	
2	2817961	6081472	Pipe	954-955	Moderate fracturing	0.45	0.6	Pinhole	0.01	
5	2817286	6080128	Pipe	956-966	Pipe like/large block	1.8		Five conduits - filled and moderate fracturing	0.2 to 0.3	JPG- 963 front side, 966 back side
5	2817283	6080126	Pipe	967-969	Pipe like/large block	1		Four conduits - filled	0.15 to 0.1	
5	2817289	6080132	Block	970-971		1.2		One large filled and highly fractured	0.55	
5	2817302	6080157	Corkscrew	972-973	Sinuous	0.13	1.6	Small filled	0.03	Mostly buried
5	2817294	6080159	Pipe	974-975		0.18	0.35	Open pin hole with grey outer rim	0.01	
5	2817295	6080158	Pipe	976-980	Grey	2.3	4	Strongly fractured yellow	0.8 to 0.5	

Table A2.3 continued.

Outcrop section	Easting	Northing	Morphology	JPG numbers	Concretion	Concretion diameter (m)	Concretion length (m)	Conduit	Conduit diameter (m)	Comments
5	2817316	6080195	Pipe	981-984	Grey mudstone			Brownish yellow conduit network?	0.2, 0.01	Branching and anastomosing
5	2817310	6080205	Block	985-988	Fractured			May have multiple conduits, open and filled		
4	2817307	6080265	Pipe	989-999	With shear zone? And conjugate faults?				All through bedrock	Dip direction of conjugate faults? 120 & 70, covered in water, but appears to be conjugate faults, shear zone?
4	2817322	6080293	Pipe	1000-1004	No fracturing	2.2		Conduit zone, two small, strong fracturing	0.96, 0.14, 0.15	
4	2817366	6080360	Pipe	1005-1008	Strong fracturing			Harder cement		
4	2817361	6080370	Pipe	1009	No fracturing	0.08		No fracturing	0.04	
4	2817361	6080370	Pipe	1010	No fracturing	0.5		No fracturing	0.15	
4	2817361	6080370	Pipe	1011	No fracturing	0.1		Fracturing	0.01	
4	2817361	6080370	Pipe	1012-1013	Strong fracturing	0.2, 0.4	0.4	Strong fracturing (4 conduits, same measurements)	0.05	
4	2817361	6080370	Pipe	1014	Conc pipe with 5 conduits, strong fracturing	0.47		4 conduits, some open others filled and fracturediated	0.03	
4	2817361	6080370	Pipe	1015		0.26		Conduit difficult to discern	0.22	
4	2817361	6080370	Pipe	1016-1018		0.21	0.35	Cond only visable by slight color variation	0.14	JPG 1018 "whole field"
4	2817372	6080380	Pipe	1019-1025		2.7, 0.2	5.2, .09	Linear? Conduit fractured. back side, yellow calcite fill	1.1	JPG 1023-1025 back side, second measurements from back side
4	2817354	6080385	Pipe	1035		0.18			0.03	Beige to blue to rim of beige to brown to pinhole (0.01)
4	2817404	6080409	Pipe	1036-		0.2			0.01	

Table A2.3 continued.

Outcrop section	Easting	Northing	Morphology	JPG numbers	Concretion	Concretion diameter (m)	Concretion length (m)	Conduit	Conduit diameter (m)	Comments
4	2817412	6080413	Pipe	1038		0.11			0.02	
4	2817411	6080420	GPS Dip	1039-						Dip direction/ dip = 100/35
4	2817422	6080426	Pipe	1042		0.14		Open	0.3	
4	2817396	6080432	Pipe	1043		0.28		Open	0.04	Colour zonation, probably weathering
4	2817394	6080435	Pipe	1044		0.14		Open, yellow calcite	0.02	
4	2817394	6080435	Pipe	1045		0.15		Open	0.02	
4	2817389	6080437	Pipe	1046		0.04		Filled - cream color	0.01	
4	2817389	6080437	Pipe	1047		0.2		No apparent conduit	0	
4	2817388	6080443	Pipe	1048-		0.13			0.02	
4	2817393	6080446	Pipe	1050-1059		0.16		Pinhole		Pipes may interconnect along a more cemented zone of mud, some conduits open with zonation, others filled, very anastomosing
4	2817393	6080446	Pipe	1050-		0.16		Pinhole		"
4	2817393	6080446	Pipe	1050-		0.16		Pinhole		"
4	2817393	6080446	Pipe	1050-		0.16		Pinhole		"
4	2817393	6080446	Pipe	1050-		0.16		Pinhole		"
4	2817393	6080446	Pipe	1050-		0.16		Pinhole		"
4	2817393	6080446	Pipe	1050-		0.16		Pinhole		"
4	2817393	6080446	Pipe	1050-		0.16		Pinhole		"
4	2817393	6080446	Pipe	1050-		0.16		Pinhole		"
4	2817393	6080446	Pipe	1050-		0.16		Pinhole		"
4	2817393	6080446	Pipe	1050-		0.16		Pinhole		"
4	2817429	6080456	Pipe	1060-		0.15	0.2	Open	0.01	"
4	2817429	6080456	Pipe	1060-		0.12		Filled-dark grey micrite	0.04	Conduit has red brown rim
4	2817429	6080456	Pipe	1063-1064		0.15		Open or filled-dark grey micrite		Many of the pipes (14 pipes visible) may be interconnected
3	2817645	6080936	Bulbous	Photo quality poor due to fog conditions	Note: GPS only for one					Few small pipes in cliff, long bulbous like almost appearing corkscrew like; possibly a result of fracture pattern, at high angles to bedding. At least 7, some may continue out to sea, one has conduit.

Table A2.3 continued.

Outcrop	Easting	Northing	Morphology	JPG	Concretion	Concretion	Concretion	Conduit	Conduit	Comments
3	2817679	6080956								
3	2817679	6080956	Platform	1065-35						~ Five concretionary layers protruding from
3	2817973	6081456	Pipe		Some fractures	2.1		Open/filled	0.1, 0.13	
2	2818149	6081781								Dip direction/ dip = 120/30
1	2817342	6082041								Dip direction/ dip = 110/30, joint trend 130/50
1	2818108	6082086	Layer	1066_77	Layer 3	5 m to layer 2		Extent on beach 200-300 m		Dip direction/ dip = 105/30 seaward layer
1	2818441	6082145	Layer		Layer 2	30 m to layer 1		Extent on beach 200-300 m		Dip direction/ dip = 115/45, more resistant bed (other concretionary layers)
1	2818452	6082186	Layer		Layer 1			Extent on beach 200-300 m		Dip direction/ dip = 110/20
1	2818504	6082261	Layer		Layer 0					Dip direction/ dip = 110/35
1	2818547	6082365	Layer		Layer sub1					Dip direction/ dip = 115/30

Figure A2.6. Photographs of concretion conduits and samples measured and mapped with GIS. See Table A2.3 for descriptions.

Figure A2.6 continued.

Figure A2.6 continued.

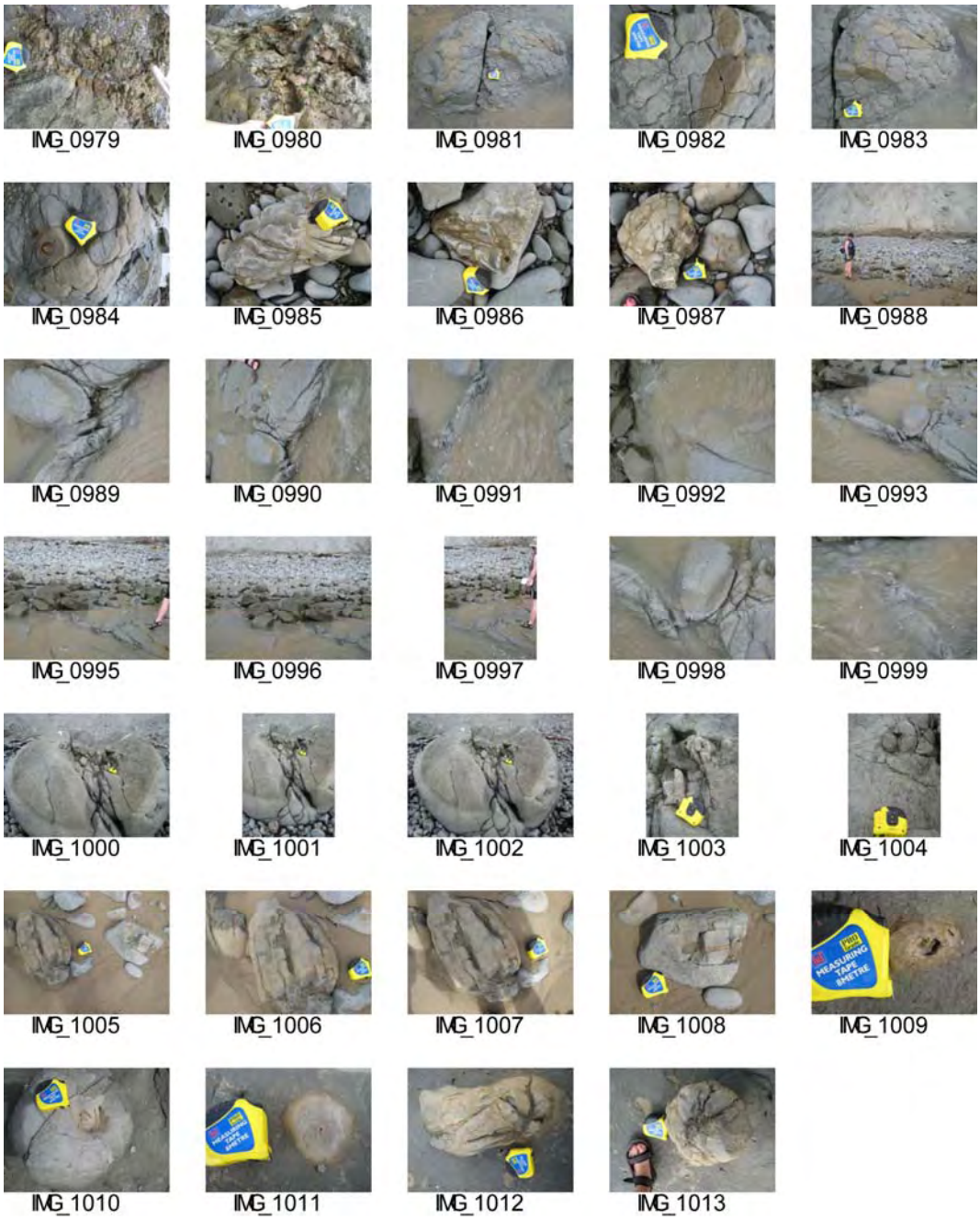

Figure A2.6 continued.

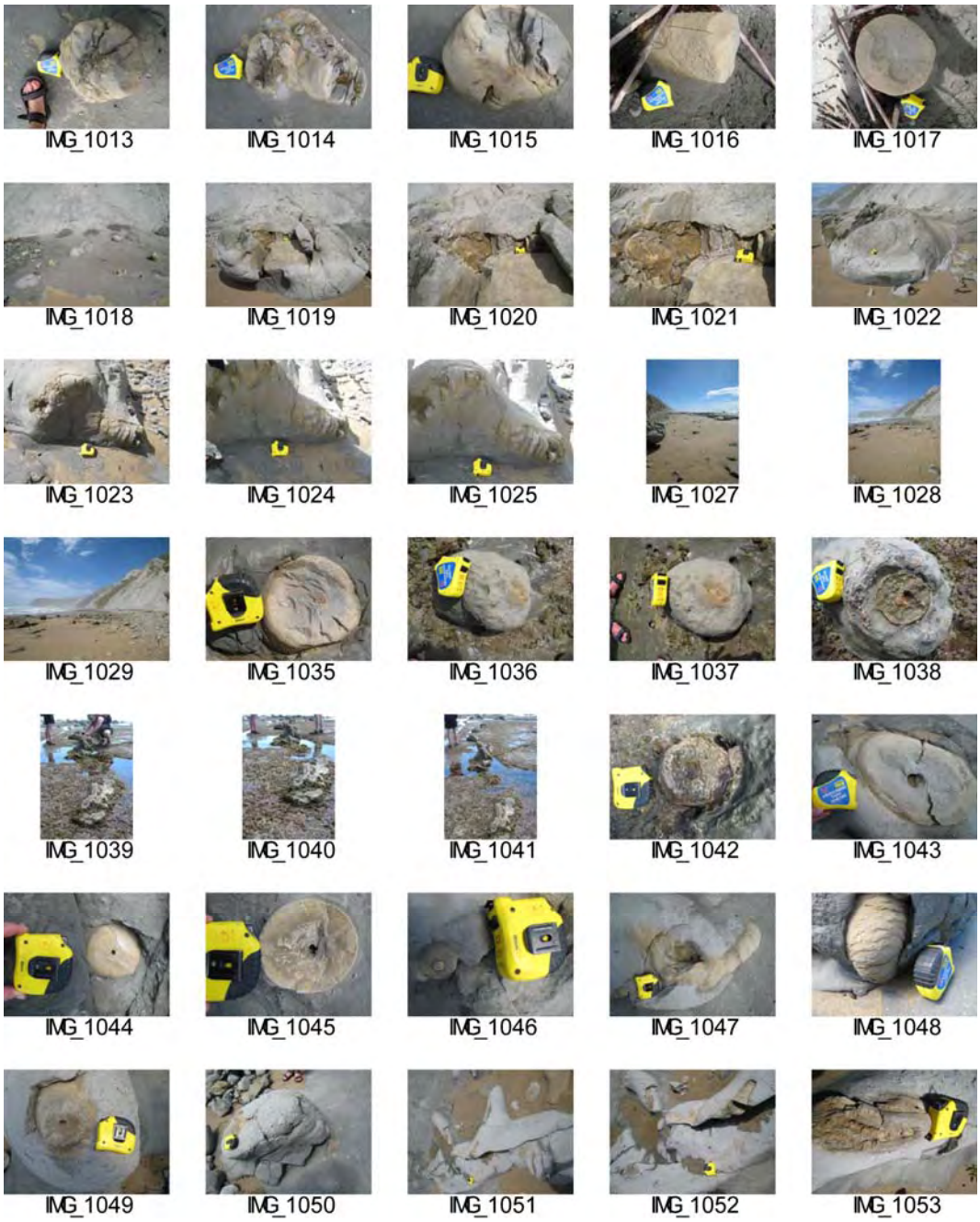

Figure A2.6 continued.

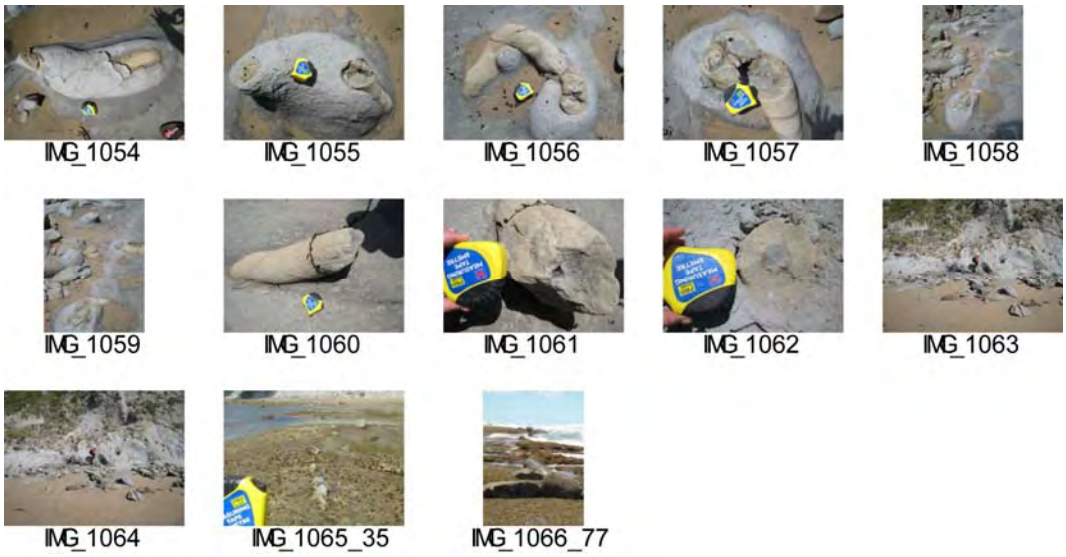

Figure A2.6 continued.

4. Samples

Photographs of tubular concretion samples (Fig. A2.7) are presented in this section along with brief descriptions in Table A2.4 (jpg number corresponds to that in Table). Sample names are followed by a hyphen. The number following the hyphen denotes a subsample along a cross-sectional transect (lower number = outer concretion, higher number = conduit/or adjacent to conduit if the conduit is open). The subsamples are treated as individual samples for petrographic and isotopic analyses. Subsample placement along the transect is shown in section 11 (Isotope transects). A DVD accompanies this volume, where the photographs can be viewed at a larger scale (Appendix\Whangaehu\Samples).

Table A2.4. Sample descriptions

UoW number	Sample (and JPG) number	Easting	Northing	Comment
20080236	124.10	2817748	6081124	Fracture fill, late phase
20080237	124.20	2817748	6081124	Cemented rock adjacent to 124.20
20080238	209.10	2818454	6082209	Concretion layer
20080239	352.10	2818516	6082352	Host mud near Whangehu Beach entry
20080240	372.10	2817441	6080372	Host mudstone from cliff (see Fig. 15B in Chapter 4)
20080241	489.10	2817979	6081489	Outer pipe concretion (see Fig. 15B in Chapter 4)
20080242	489.20	2817979	6081489	Middle pipe concretion (see Fig. 15B in Chapter 4)
20080243	489.30	2817979	6081489	Inner pipe concretion (see Fig. 15B in Chapter 4))
20080244	489.40	2817979	6081489	Outer, mudstone rim (see Fig. 15B in Chapter 4)
20080245	490.1a	2817979	6081489	Pipe concretion., small float
20080246	490.1b	2817979	6081489	Conduit of 490.1b
20080247	490.20	2817979	6081489	Small float sample with veined conduit
20080449	490.3			small float sample
20080450	490.40	2817979	6081489	Yellow calcite lining conduit
20080451	490.50	2817979	6081489	Zoned sediment filled conduit
20080452	530.10	2817441	6080530	Spherical
20080453	682.1a	2818073	6081682	Tube with mudstone jacket, float
20080454	682.2a; 682.2b	2818073	6081682	Pipe concretion (a), conduit (b)
20080455	682.2c	2818073	6081682	Mudstone surrounding 682.2
20080456	841.1a,b	2817600	6080841	Small tube, float
20080457	CTc1_1			Thin pipe outer
20080458	CTc1_2			Thin pipe mid
20080459	CTc1_3			Thin pipe conduit rim
20080460	CTc2_1			Pipe outer
20080461	CTc2_2			Pipe mid
20080462	CTc2_3			Pipe conduit fill
20080463	CTf3_1			Pipe outer
20080464	CTf3_2			Pipe mid
20080465	CTf3_3			Pipe conduit rim
20080466	CTf4_1			Pipe outer
20080467	CTf4_2			Pipe mid
20080468	CTf4_3			Pipe conduit rim

Figure A2.7. Photographs of samples. See Table A2.4 for descriptions.

5. Photomicrographs

Photomicrographs of tubular concretion samples (Fig. A2.8) are presented in this section along with brief descriptions in Table A2.5 (jpg number corresponds to that in Table). A DVD accompanies this volume, where the photomicrographs can be viewed at a larger scale (Appendix\Whangaehu\Petrography). A selection of subsamples were cut and mounted on glass slides for standard thin section analysis. No staining or impregnation was done on the thin sections. Further thin sections were not produced as the Turnagain samples were predominately micritic carbonate within fine grained siliciclastics.

Table A2.5. Descriptions of photomicrographs in Figure A2.8.

Sample	Photomicro-graph jpg no.	Comment
682.2	682-2a (PPL)	Main concretion body, fine grained siliciclastics (mud) cemented by micritic dolomite.
	682-2a (CL)	CL of 682-2a (PPL)
	682-2b (PPL)	Main concretion body near conduit, note the large open vug (bottom right, white) and smaller open vugs and veins to the left.
	682-b (CL)	CL of 682-2b (PPL); at least three cement phases can be identified, bright yellow clotted fabric (calcite, lower right), greenish-yellow adjacent to open vugs and veins (calcite), and bright orange between siliciclastics (dolomite).
	682-2c (PPL)	Main concretion body near conduit, note the large open vug (centre, white) and and varying cement fabrics.
	682-2c (CL)	CL of 682-2c (PPL); at least three cement phases can be identified, bright yellow clotted fabric (calcite, center), greenish-yellow a surrounding the large open vug (calcite), and bright orange in the upper portion of the image (dolomite). Notice the vein extending from the yellow clotted fabric towards the left side of the image. Compared to the previous photographs, there is much less siliciclastic grains present suggestive of a position nearer to the main conduit.
	682-2d (PPL)	Main concretion body near conduit, note the large open vug (upper left, white) with sand size siliciclastics compared to the mud sized fraction in the lower left and right side of the image. The sand grains are modern infill.
	682-2d (CL)	CL of 682-2d(PPL); CL again shows a gradation between three cement phases, repeating the pattern of the clotted fabric near the vug, followed by the greenish-yellow calcite, then the orange dolomite.
	682-2e (PPL)	Numerous open vugs (white) with three cement fabrics. Note the absence of siliciclastics within the light and medium grey cement.

Table A2.5 continued

Sample	Photomicro-graph jpg no.	Comment
	682-2e (CL)	CL of 682-2e(PPL); CL again shows a gradation between three cement phases, repeating the pattern of the clotted fabric near the vug (except in vug on lower right), followed by the greenish-yellow calcite, then the orange dolomite. Again, siliciclastics are absent from the bright yellow caclite cements.
	682-2f (PPL)	Thin section is dominated by the clotted cement fabric with few siliciclastic grains (concretion body near main conduit).
	682-2f (CL)	CL of 682-2f (PPL)
490.2	490_2a (PPL)	Note the more 'chaotic' cement patterns in this sample compared to the previous images. This image is from a strongly veined central conduit (lighter grey to white).
	490_2a (CL)	CL of 490_2a (PPL); siliciclastics cemented by orange dolomite from main concretion with darker areas (non-luminescent) cemented by a late phase cement (quartz) after methane migration.
490.5	490_5a (PPL)	Sediment filled conduit with fine grained siliciclastics (white to grey) cemented by carbonate, and pyrite (black).
	490_5a (CL)	CL of 490_5a (PPL); complex pattern of carbonate cementation (mixed calcite, yellow and dolomite, darker orange), note the pyrite (black).
	490_5b(PPL)	Close up of the pyrite framboids in the previous two images.

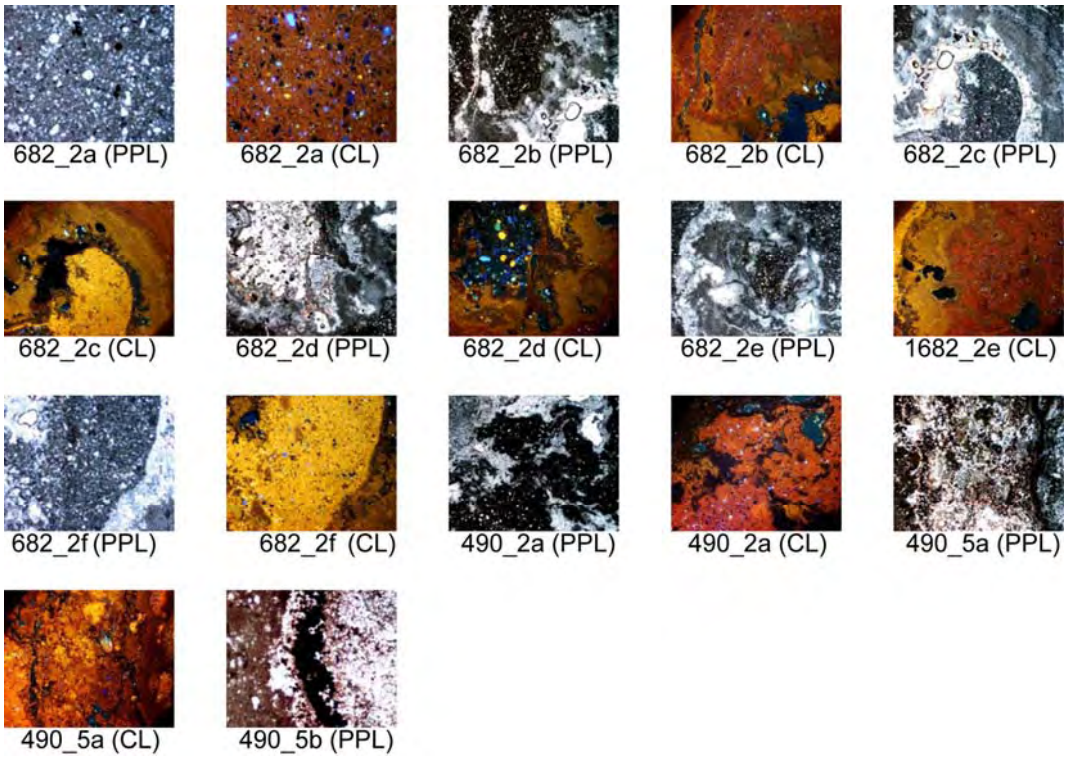

Figure A2.8. Photomicrographs of tubular concretions and conduits. See Table A2.5 for descriptions.

6. XRD graphs

Appendix Section 6 contains XRD graphs that are characteristic of pipe and bulbous concretions.

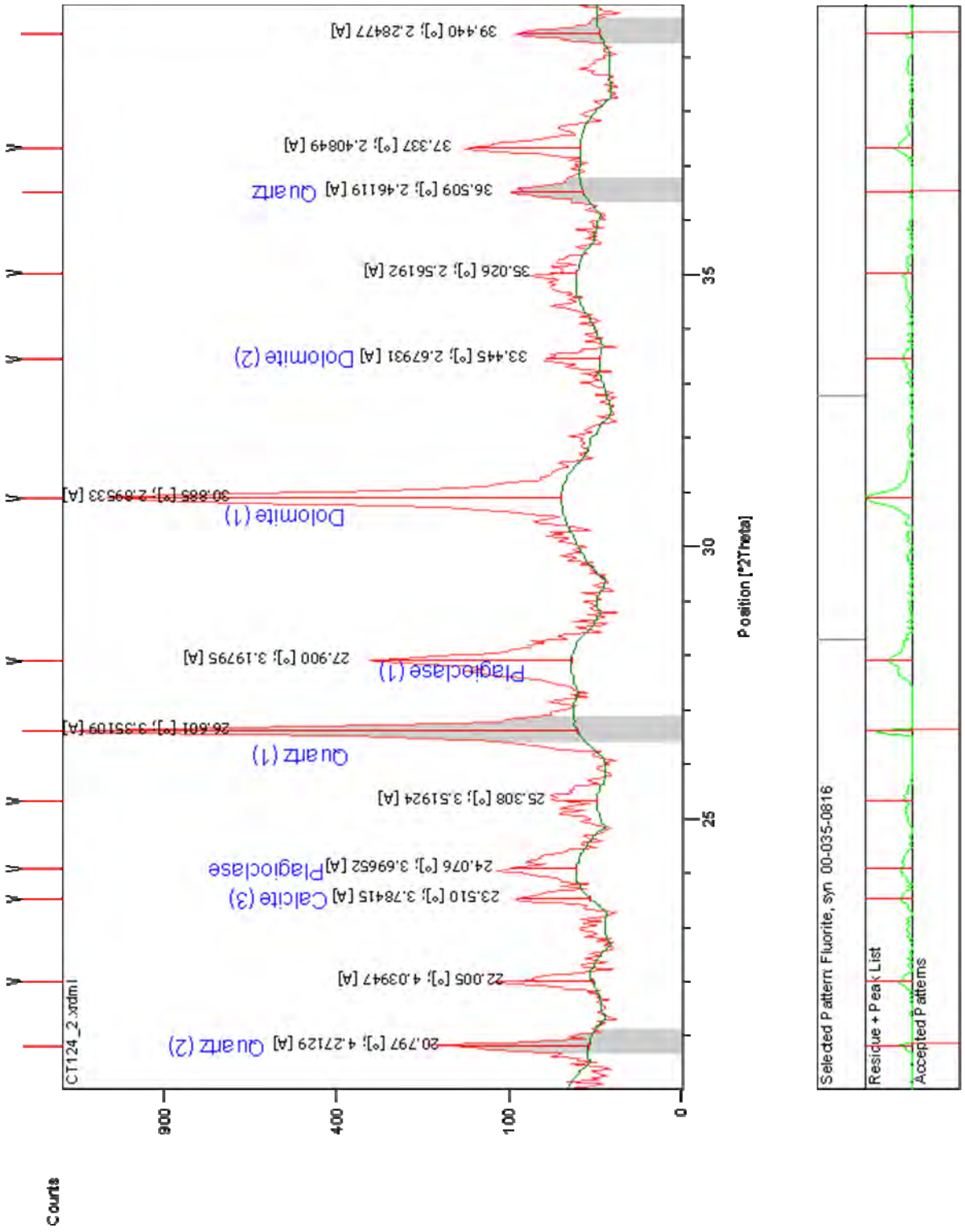
Counts
900
400
100
0
CT124_2.xdml
20.797 [°]; 4.27129 [A] Quartz (2)
22.005 [°]; 4.03947 [A]
23.510 [°]; 3.78415 [A] Calcite (3)
24.076 [°]; 3.69652 [A] Plagioclase
25.308 [°]; 3.51924 [A]
26.601 [°]; 3.35109 [A] Quartz (1)
27.900 [°]; 3.19795 [A] Plagioclase (1)
30.885 [°]; 2.89533 [A] Dolomite (1)
33.445 [°]; 2.67931 [A] Dolomite (2)
35.026 [°]; 2.56192 [A]
36.509 [°]; 2.46119 [A] Quartz
37.337 [°]; 2.40849 [A]
39.440 [°]; 2.28477 [A]
25
30
35
Position [°2Theta]
Selected Pattern: Fluorite, syn 00-035-0816
Residue + Peak List
Accepted Patterns

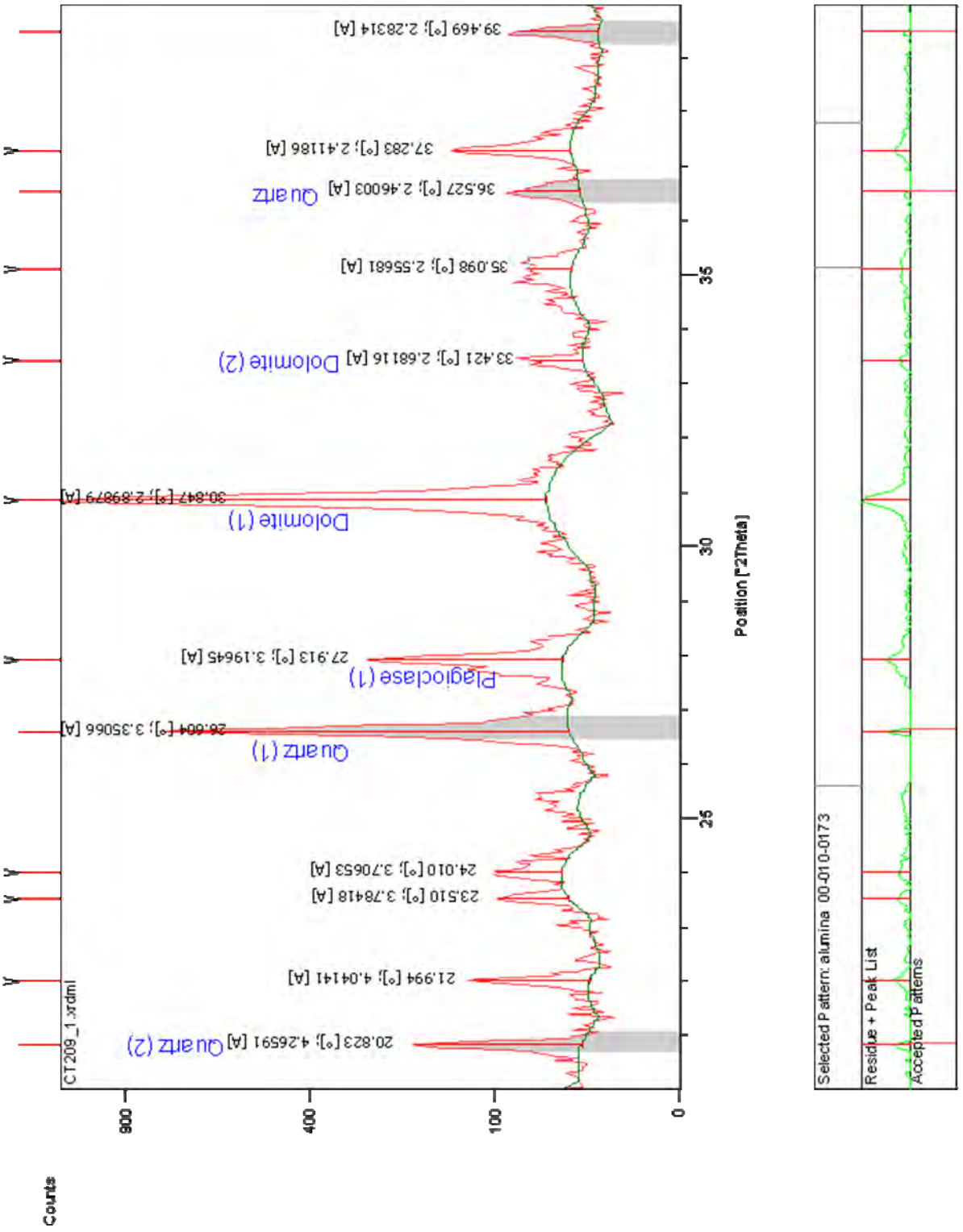
Counts
900
400
100
0
CT209_1.xrdml
20.823 [°]; 4.26591 [A]
Quartz (2)
21.994 [°]; 4.04141 [A]
23.510 [°]; 3.78418 [A]
24.010 [°]; 3.70653 [A]
26.604 [°]; 3.35066 [A]
Quartz (1)
27.913 [°]; 3.19645 [A]
Plagioclase (1)
30.847 [°]; 2.89879 [A]
Dolomite (1)
33.421 [°]; 2.68116 [A]
Dolomite (2)
35.098 [°]; 2.55681 [A]
36.527 [°]; 2.46003 [A]
Quartz
37.283 [°]; 2.41186 [A]
39.469 [°]; 2.28314 [A]
25
30
35
Position [°2Theta]
Selected Pattern: alumina 00-010-0173
Residue + Peak List
Accepted Patterns

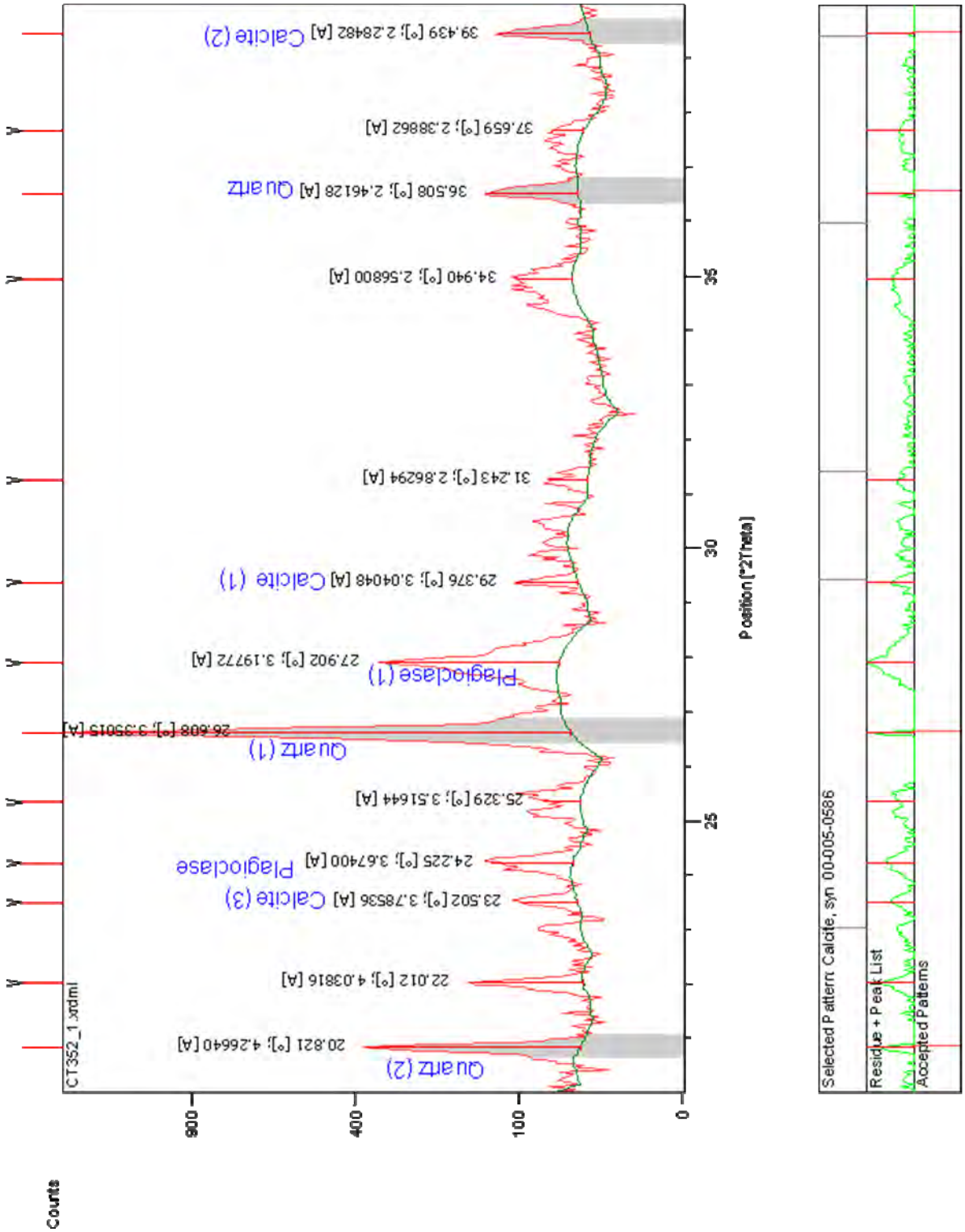
Counts
900
400
100
0
CT352_1.xrdml
Quartz (2)
20.821 [°]; 4.26640 [A]
22.012 [°]; 4.03816 [A]
Calcite (3)
23.502 [°]; 3.78536 [A]
Plagioclase
24.225 [°]; 3.67400 [A]
25.329 [°]; 3.51644 [A]
Quartz (1)
26.608 [°]; 3.35015 [A]
Plagioclase (1)
27.902 [°]; 3.19772 [A]
Calcite (1)
29.376 [°]; 3.04048 [A]
31.243 [°]; 2.86294 [A]
34.940 [°]; 2.56800 [A]
Quartz
36.508 [°]; 2.46128 [A]
37.659 [°]; 2.38862 [A]
Calcite (2)
39.439 [°]; 2.28482 [A]
25
30
35
Position [°2Theta]
Selected Pattern: Calcite, syn 00-005-0586
Residue + Peak List
Accepted Patterns

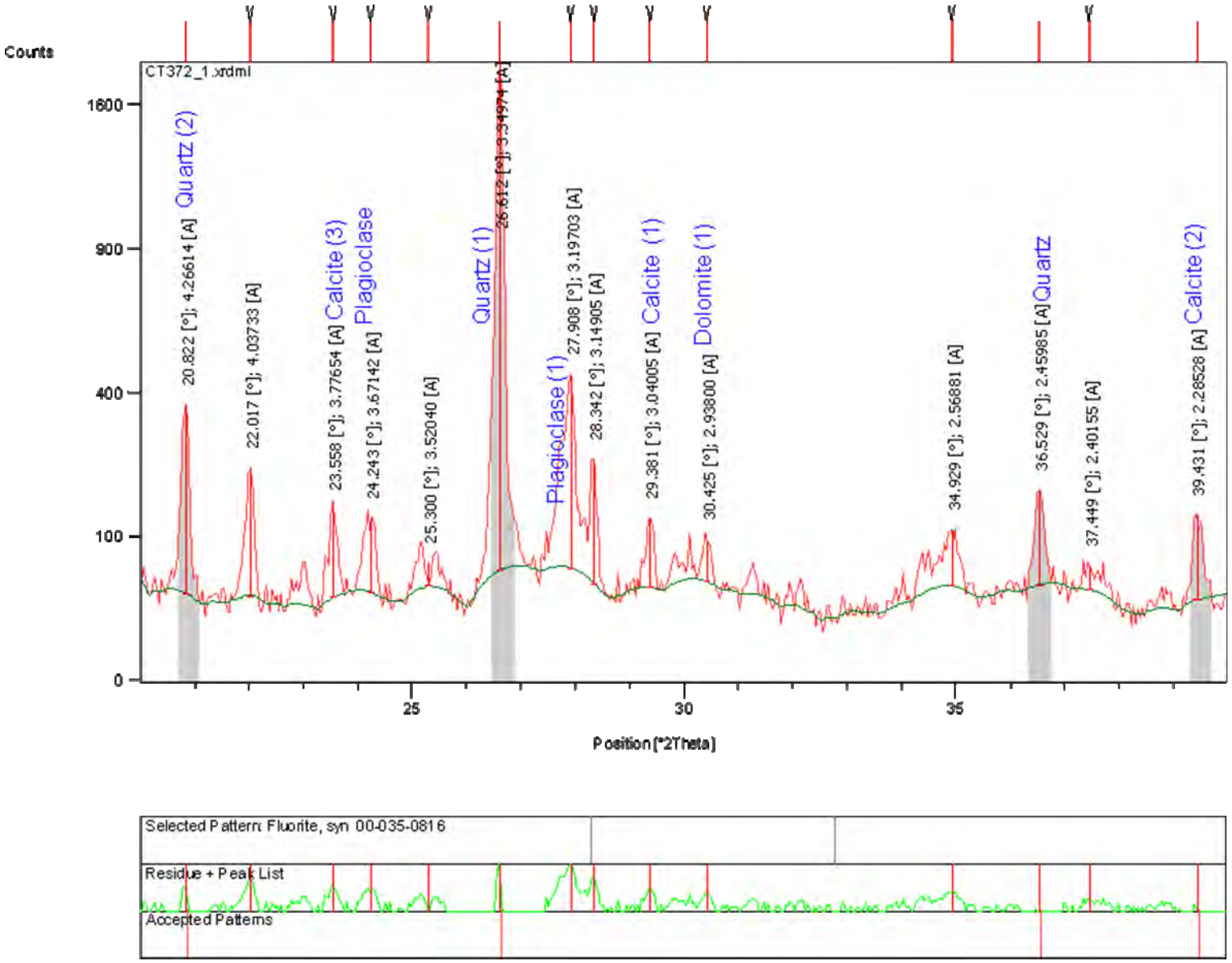
Counts
CT372_1.xrdml
1600
900
400
100
0
20.822 [°]; 4.26614 [A]
Quartz (2)
22.017 [°]; 4.03733 [A]
23.558 [°]; 3.77654 [A]
Calcite (3)
24.243 [°]; 3.67142 [A]
Plagioclase
25.300 [°]; 3.52040 [A]
26.612 [°]; 3.34974 [A]
Quartz (1)
27.908 [°]; 3.19703 [A]
Plagioclase (1)
28.342 [°]; 3.14905 [A]
29.381 [°]; 3.04005 [A]
Calcite (1)
30.425 [°]; 2.93800 [A]
Dolomite (1)
34.929 [°]; 2.56881 [A]
36.529 [°]; 2.45985 [A]
Quartz
37.449 [°]; 2.40155 [A]
39.431 [°]; 2.28528 [A]
Calcite (2)
25
30
35
Position [°2Theta]
Selected Pattern: Fluorite, syn 00-035-0816
Residue + Peak List
Accepted Patterns

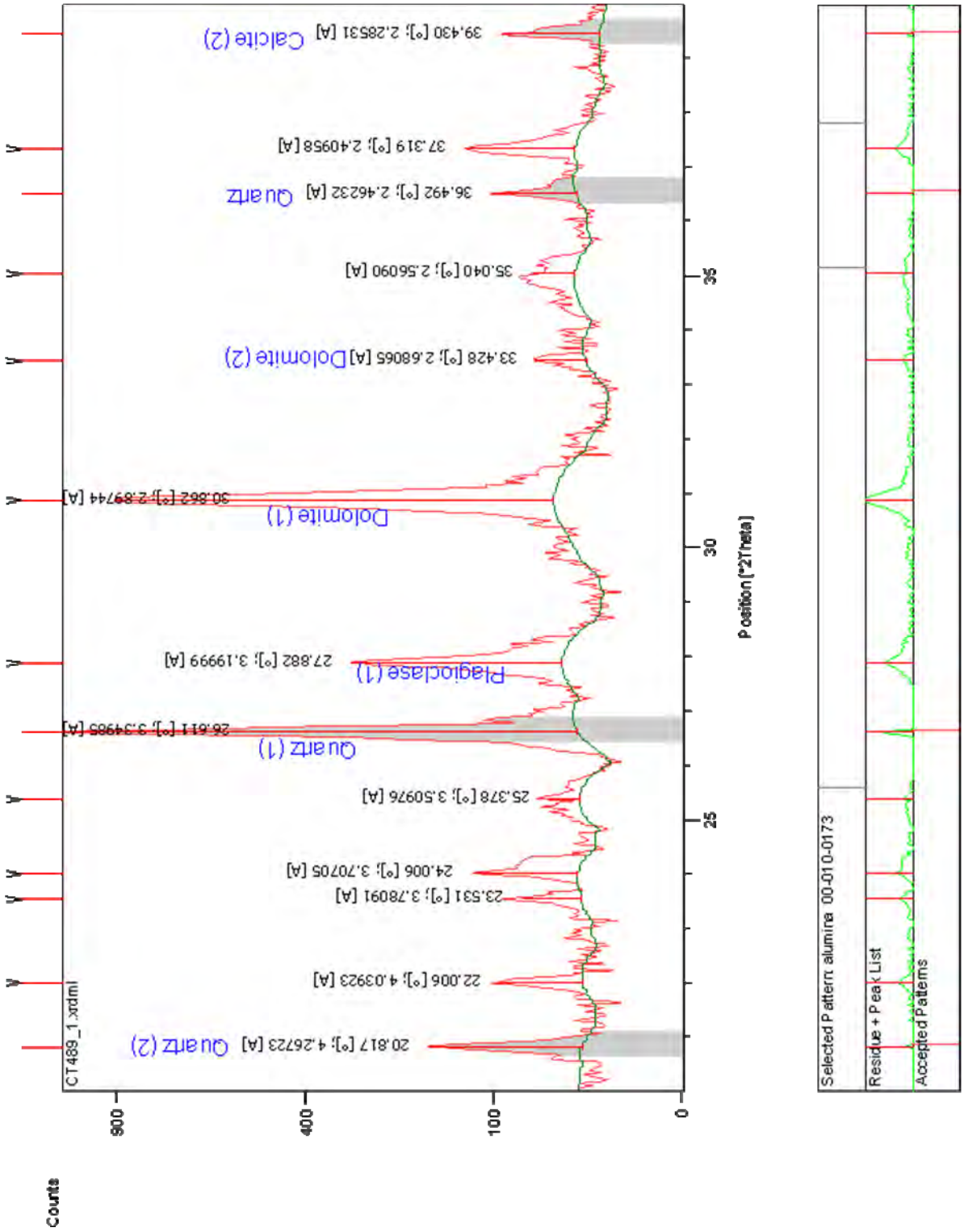
Counts
900
400
100
0
CT489_1.xrdml
Quartz (2)
20.817 [°]; 4.26723 [Å]
22.006 [°]; 4.03923 [Å]
23.531 [°]; 3.78091 [Å]
24.006 [°]; 3.70705 [Å]
25.378 [°]; 3.50976 [Å]
Quartz (1)
26.611 [°]; 3.34985 [Å]
Plagioclase (1)
27.882 [°]; 3.19999 [Å]
Dolomite (1)
30.862 [°]; 2.89744 [Å]
Dolomite (2)
33.428 [°]; 2.68065 [Å]
35.040 [°]; 2.56090 [Å]
Quartz
36.492 [°]; 2.46232 [Å]
37.319 [°]; 2.40958 [Å]
Calcite (2)
39.430 [°]; 2.28531 [Å]
25
30
35
Position [°2Theta]
Selected Pattern: alumina 00-010-0173
Residue + Peak List
Accepted Patterns

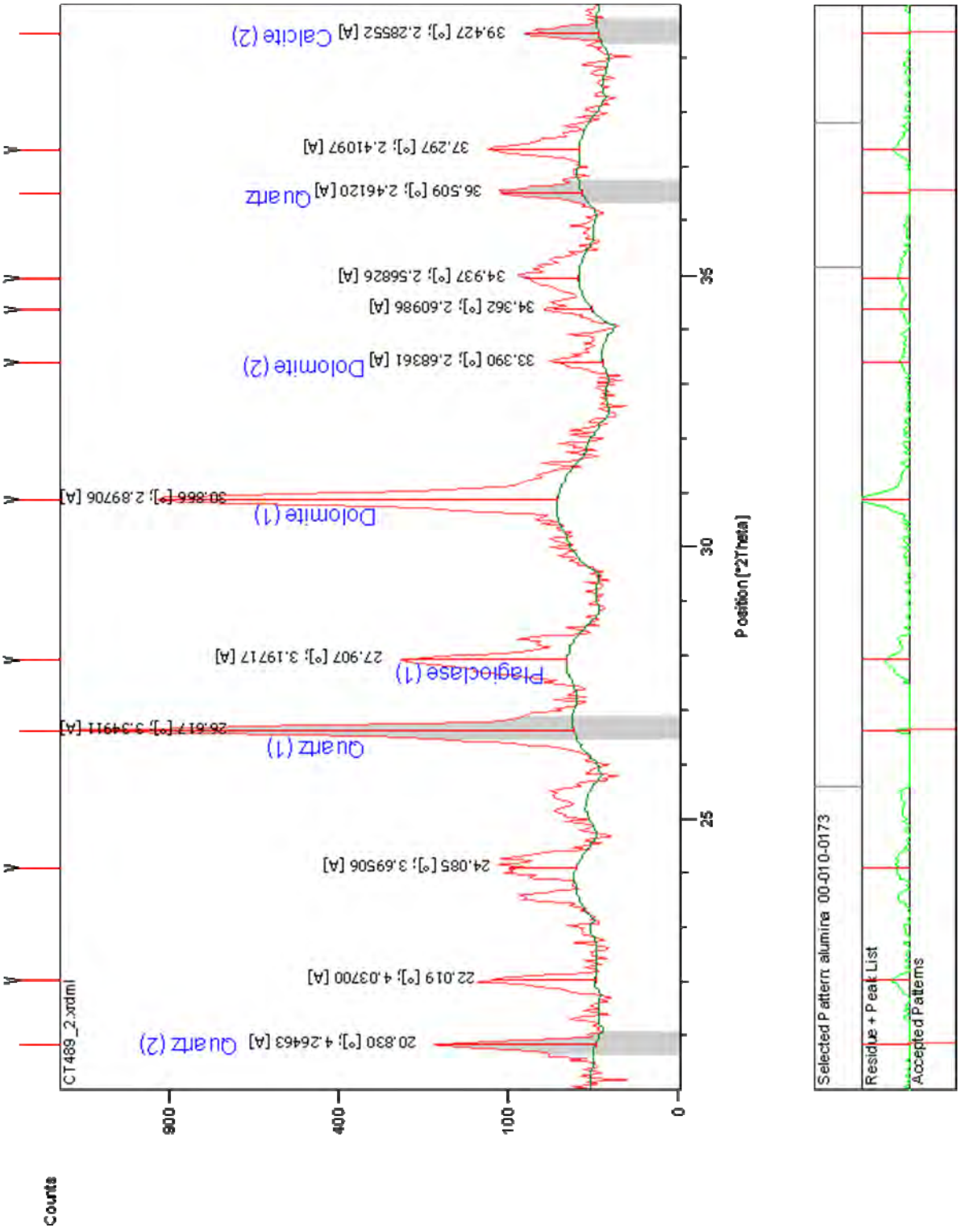
Counts
900
400
100
0
CT489_2.xrdml
Quartz (2) 20.830 [°]; 4.26463 [Å]
22.019 [°]; 4.03700 [Å]
24.085 [°]; 3.69506 [Å]
Quartz (1) 26.617 [°]; 3.34911 [Å]
Plagioclase (1) 27.907 [°]; 3.19717 [Å]
Dolomite (1) 30.866 [°]; 2.89706 [Å]
Dolomite (2) 33.390 [°]; 2.68361 [Å]
34.362 [°]; 2.60986 [Å]
34.937 [°]; 2.56826 [Å]
Quartz 36.509 [°]; 2.46120 [Å]
37.297 [°]; 2.41097 [Å]
Calcite (2) 39.427 [°]; 2.28552 [Å]
25
30
35
Position [°2Theta]
Selected Pattern alumina 00-010-0173
Residue + Peak List
Accepted Patterns

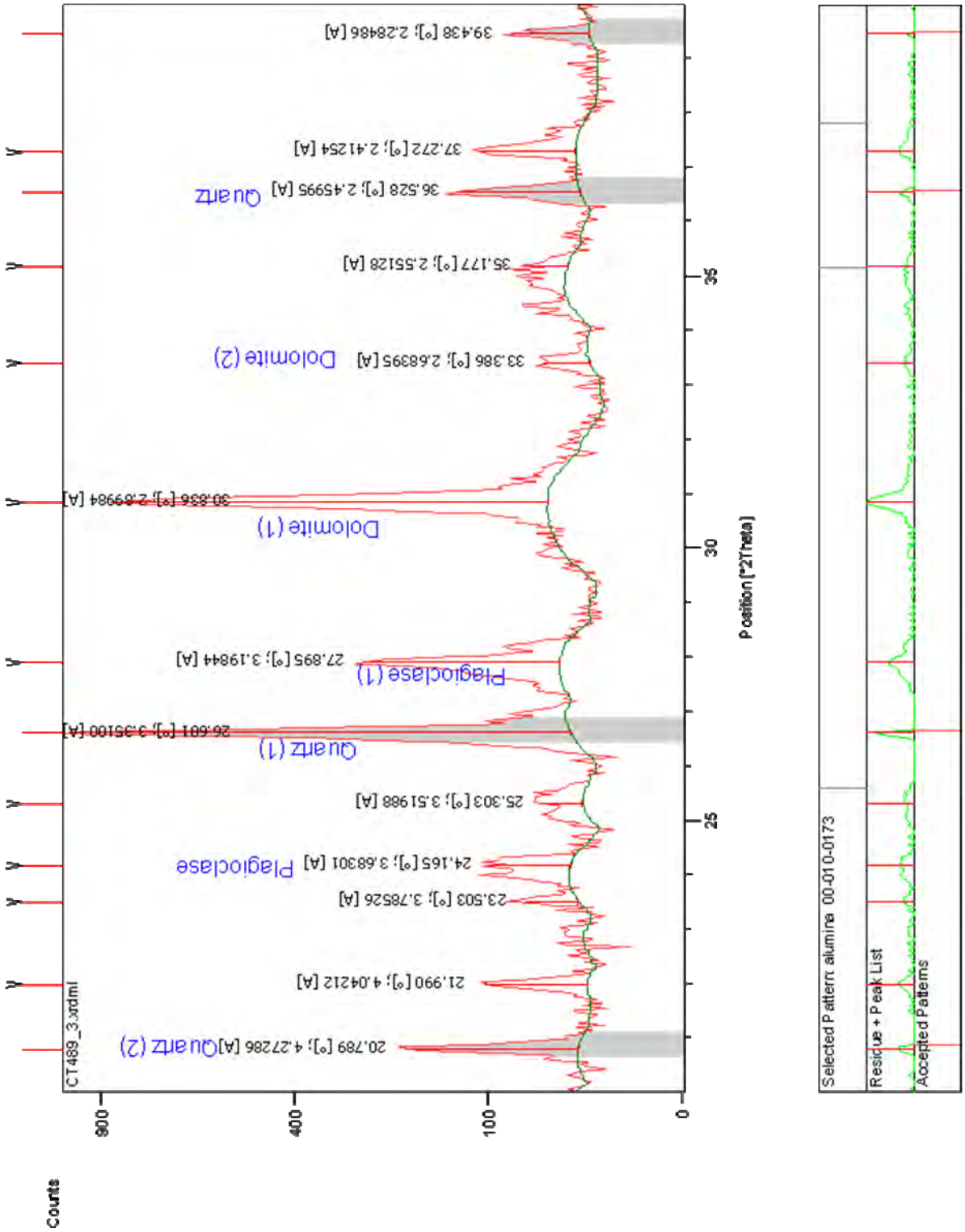
Counts
900
400
100
0
CT489_3.xrdml
20.789 [°]; 4.27286 [A]
Quartz (2)
21.990 [°]; 4.04212 [A]
23.503 [°]; 3.78526 [A]
24.165 [°]; 3.68301 [A]
Plagioclase
25.303 [°]; 3.51988 [A]
26.601 [°]; 3.35100 [A]
Quartz (1)
27.895 [°]; 3.19844 [A]
Plagioclase (1)
30.836 [°]; 2.89984 [A]
Dolomite (1)
33.386 [°]; 2.68395 [A]
Dolomite (2)
35.177 [°]; 2.55128 [A]
36.528 [°]; 2.45995 [A]
Quartz
37.272 [°]; 2.41254 [A]
39.438 [°]; 2.28486 [A]
25
30
35
Position [°2Theta]
Selected Pattern alumina 00-010-0173
Residue + Peak List
Accepted Patterns

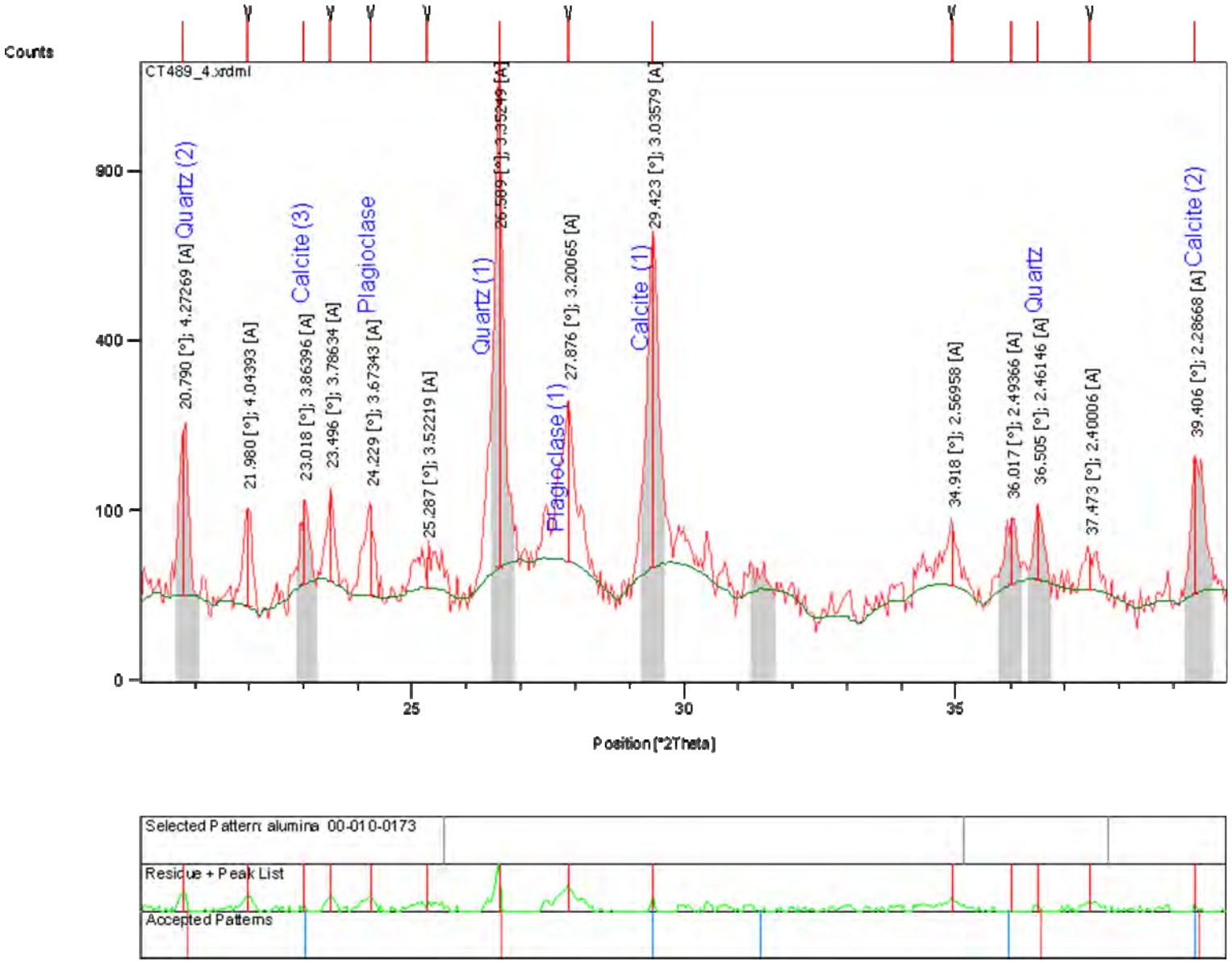
Counts
CT489_4.xrdml
900
400
100
0
20.790 [°]; 4.27269 [A] Quartz (2)
21.980 [°]; 4.04393 [A]
23.018 [°]; 3.86396 [A] Calcite (3)
23.496 [°]; 3.78634 [A]
24.229 [°]; 3.67343 [A] Plagioclase
25.287 [°]; 3.52219 [A]
26.589 [°]; 3.35249 [A] Quartz (1)
27.876 [°]; 3.20065 [A] Plagioclase (1)
29.423 [°]; 3.03579 [A] Calcite (1)
34.918 [°]; 2.56958 [A]
36.017 [°]; 2.49366 [A]
36.505 [°]; 2.46146 [A] Quartz
37.473 [°]; 2.40006 [A]
39.406 [°]; 2.28668 [A] Calcite (2)
25
30
35
Position [°2Theta]
Selected Pattern: alumina 00-010-0173
Residue + Peak List
Accepted Patterns

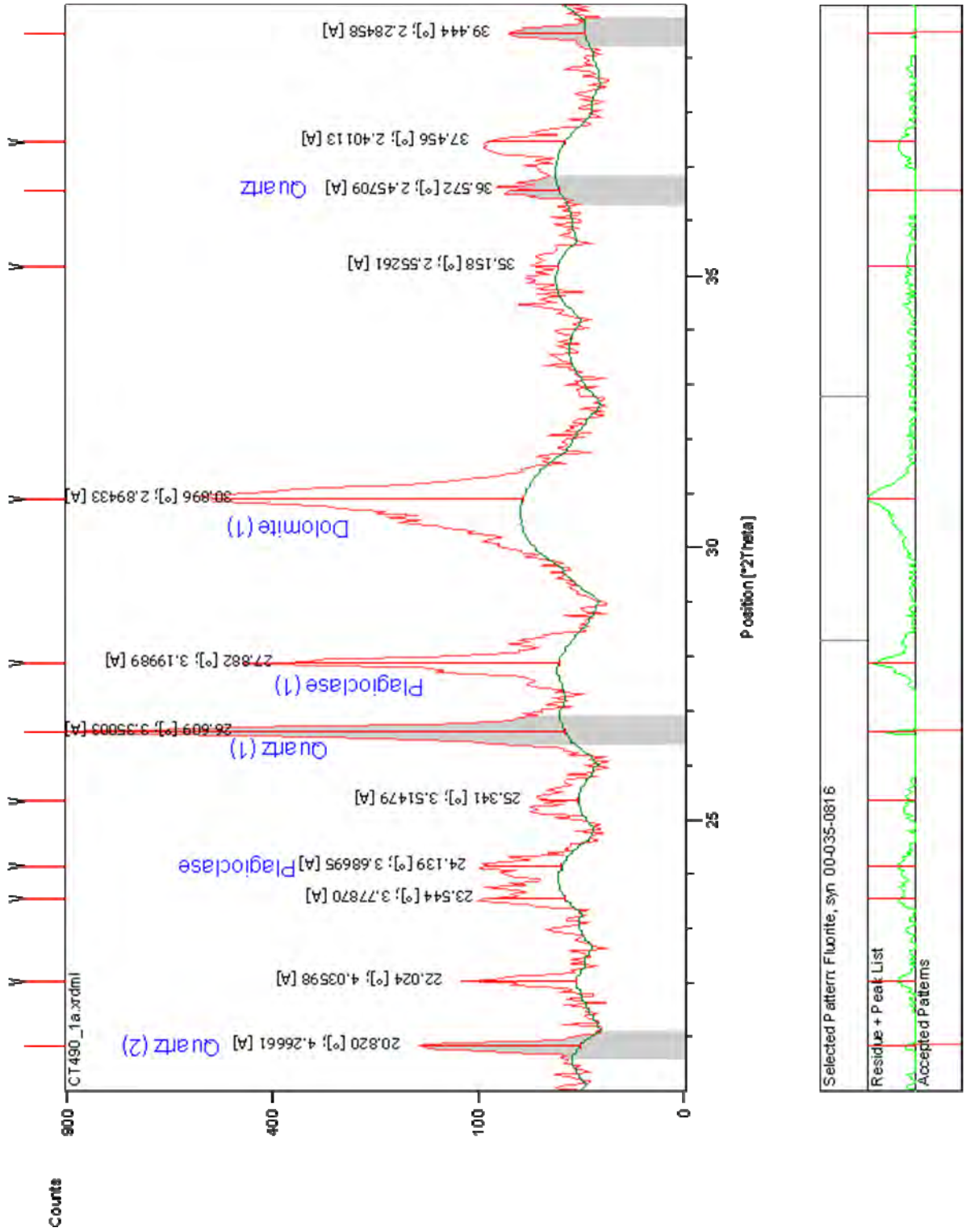
Counts
900
400
100
0
CT490_1a.xrdml
20.820 [°]; 4.26661 [A]
Quartz (2)
22.024 [°]; 4.03598 [A]
23.544 [°]; 3.77870 [A]
24.139 [°]; 3.68695 [A]
Plagioclase
25.341 [°]; 3.51479 [A]
26.609 [°]; 3.35003 [A]
Quartz (1)
27.882 [°]; 3.19989 [A]
Plagioclase (1)
30.896 [°]; 2.89433 [A]
Dolomite (1)
35.158 [°]; 2.55261 [A]
36.572 [°]; 2.45709 [A]
Quartz
37.456 [°]; 2.40113 [A]
39.444 [°]; 2.28458 [A]
25
30
35
Position [°2Theta]
Selected Pattern: Fluorite, syn 00-035-0816
Residue + Peak List
Accepted Patterns

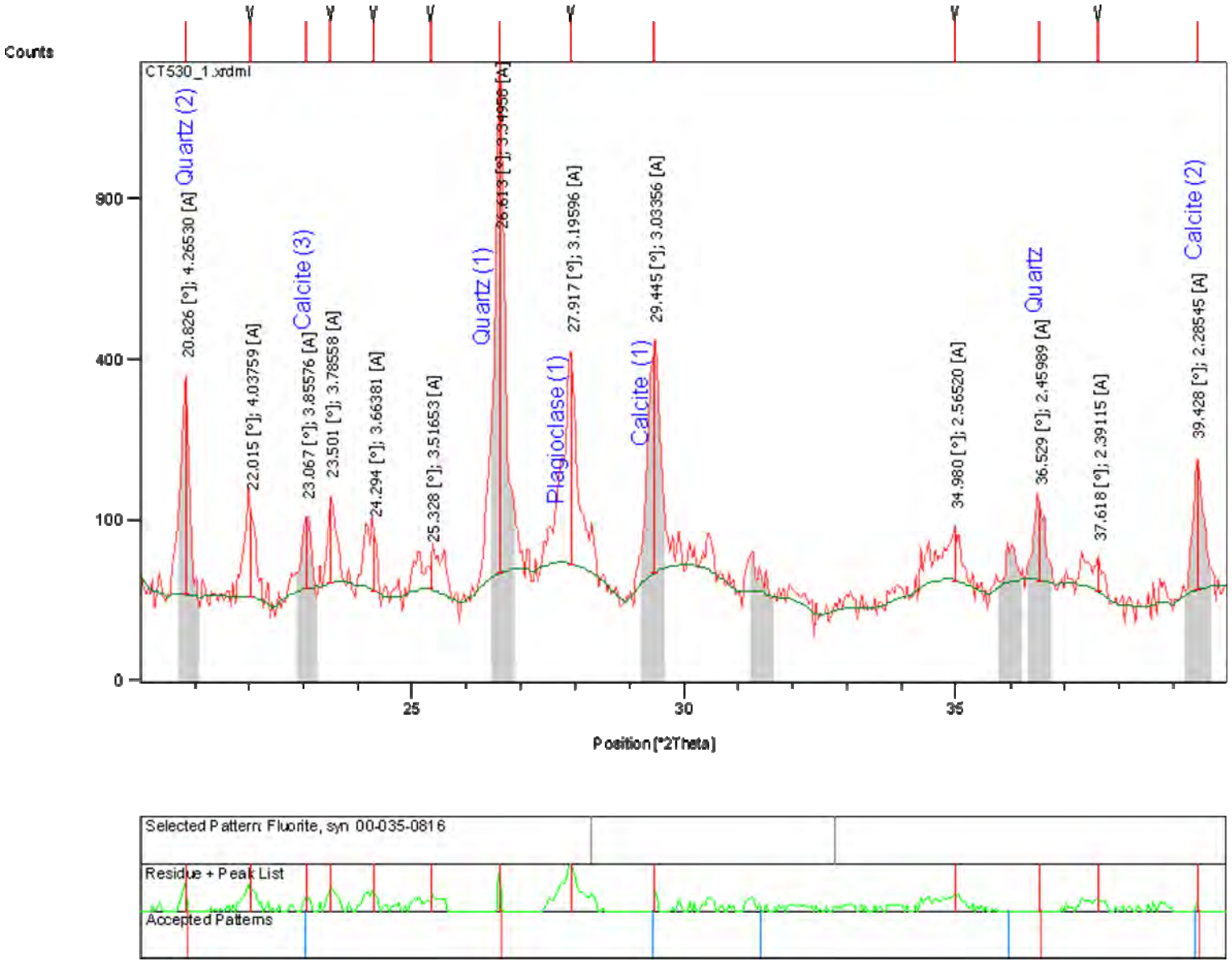
Counts
CT530_1.xrdml
900
400
100
0
Quartz (2)
20.826 [°]; 4.26530 [A]
22.015 [°]; 4.03759 [A]
Calcite (3)
23.067 [°]; 3.85576 [A]
23.501 [°]; 3.78558 [A]
24.294 [°]; 3.66381 [A]
25.328 [°]; 3.51653 [A]
Quartz (1)
26.613 [°]; 3.34986 [A]
Plagioclase (1)
27.917 [°]; 3.19596 [A]
Calcite (1)
29.445 [°]; 3.03356 [A]
34.980 [°]; 2.56520 [A]
Quartz
36.529 [°]; 2.45989 [A]
37.618 [°]; 2.39115 [A]
Calcite (2)
39.428 [°]; 2.28545 [A]
25
30
35
Position [°2Theta]
Selected Pattern: Fluorite, syn 00-035-0816
Residue + Peak List
Accepted Patterns

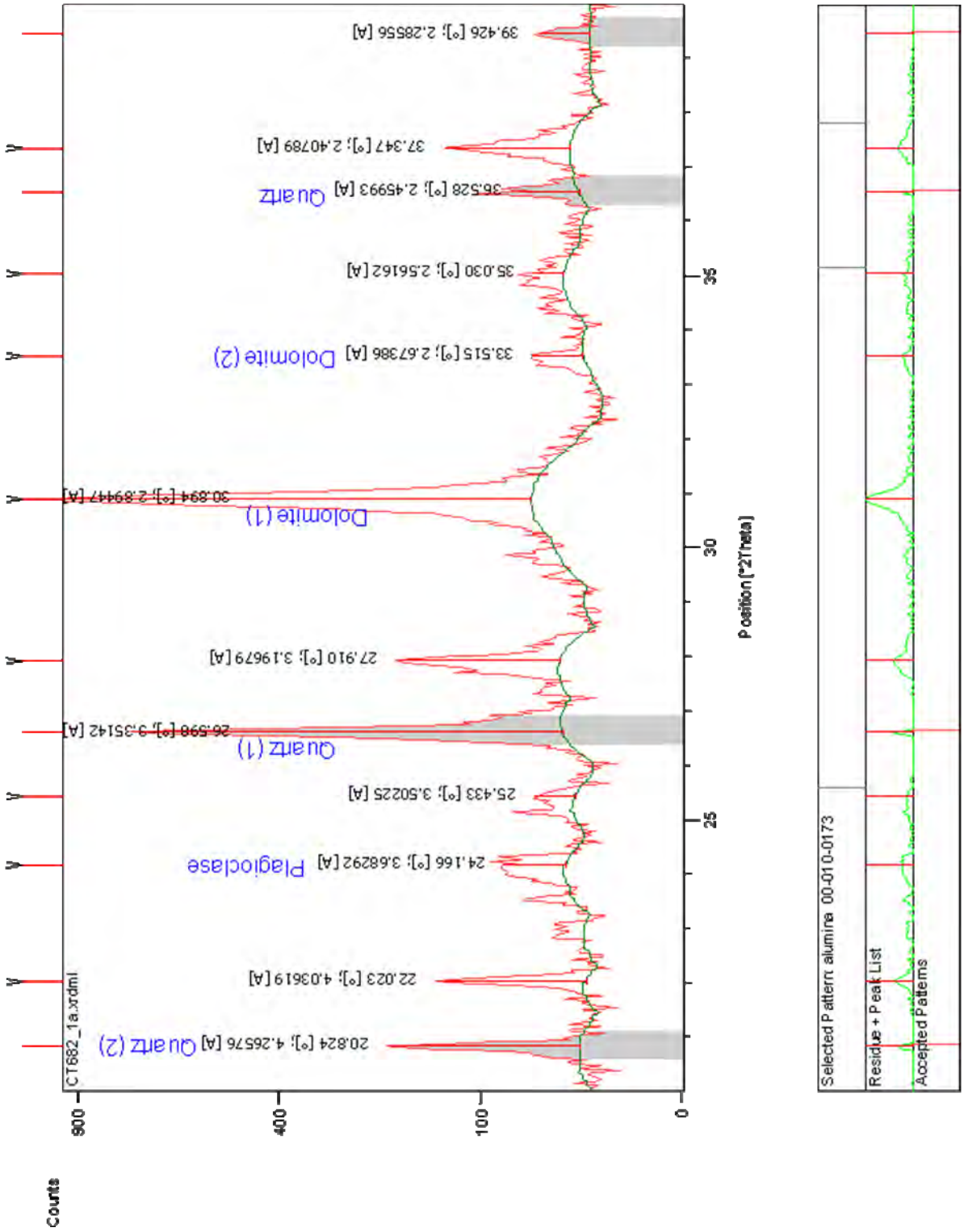
Counts
900
400
100
0
CT682_1a.xrdml
20.824 [°]; 4.26576 [A]
Quartz (2)
22.023 [°]; 4.03619 [A]
24.166 [°]; 3.68292 [A]
Plagioclase
25.433 [°]; 3.50225 [A]
26.598 [°]; 3.35142 [A]
Quartz (1)
27.910 [°]; 3.19679 [A]
30.894 [°]; 2.89947 [A]
Dolomite (1)
33.515 [°]; 2.67386 [A]
Dolomite (2)
35.030 [°]; 2.56162 [A]
36.528 [°]; 2.45993 [A]
Quartz
37.347 [°]; 2.40789 [A]
39.426 [°]; 2.28556 [A]
25
30
35
Position [°2Theta]
Selected Pattern: alumina 00-010-0173
Residue + Peak List
Accepted Patterns

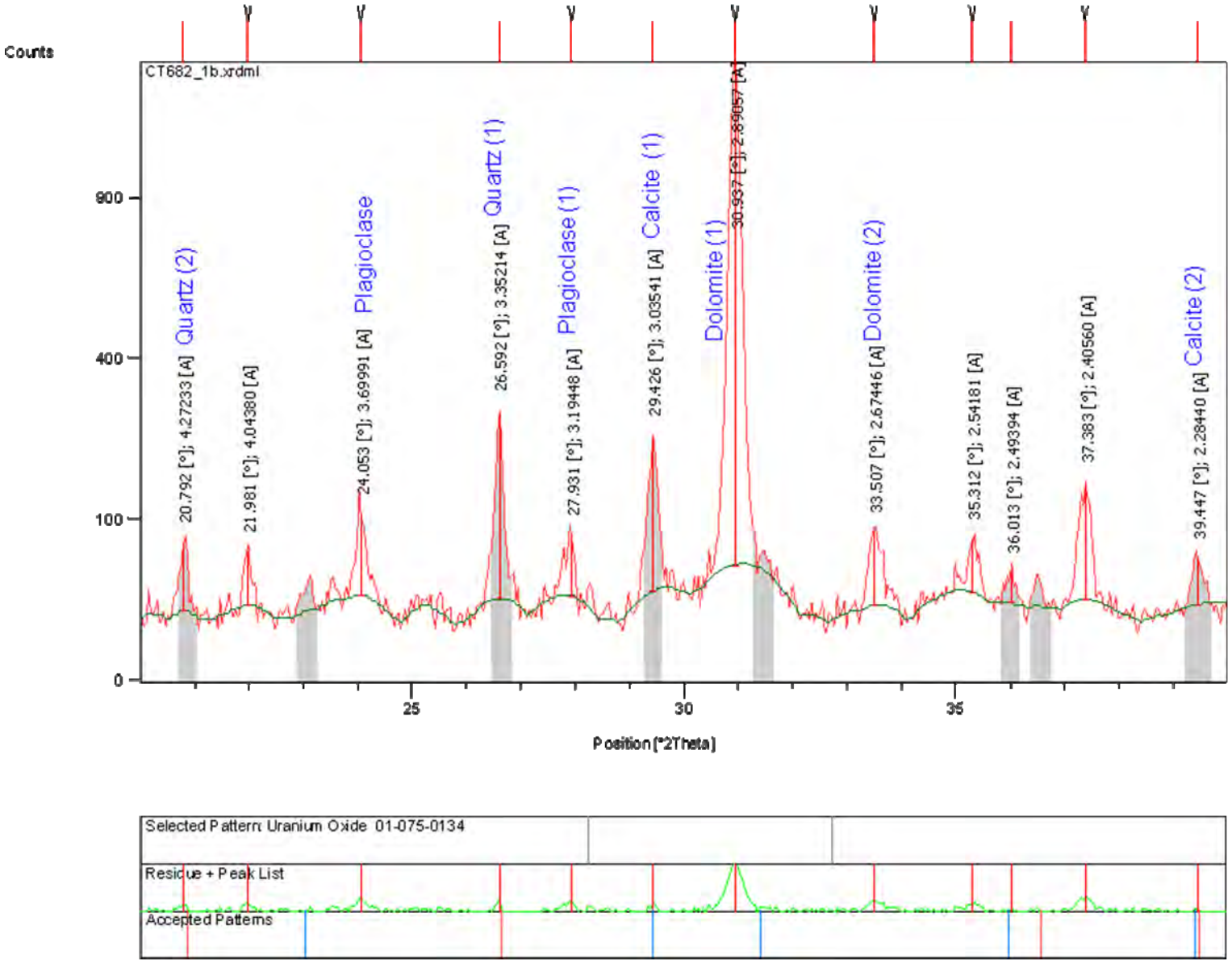
Counts
CT682_1b.xrdml
900
400
100
0
Quartz (2)
20.792 [°]; 4.27233 [A]
21.981 [°]; 4.04380 [A]
Plagioclase
24.053 [°]; 3.69991 [A]
Quartz (1)
26.592 [°]; 3.35214 [A]
Plagioclase (1)
27.931 [°]; 3.19448 [A]
Calcite (1)
29.426 [°]; 3.03541 [A]
Dolomite (1)
30.937 [°]; 2.89057 [A]
Dolomite (2)
33.507 [°]; 2.67446 [A]
35.312 [°]; 2.54181 [A]
36.013 [°]; 2.49394 [A]
37.383 [°]; 2.40560 [A]
Calcite (2)
39.447 [°]; 2.28440 [A]
25
30
35
Position [°2Theta]
Selected Pattern: Uranium Oxide 01-075-0134
Residue + Peak List
Accepted Patterns

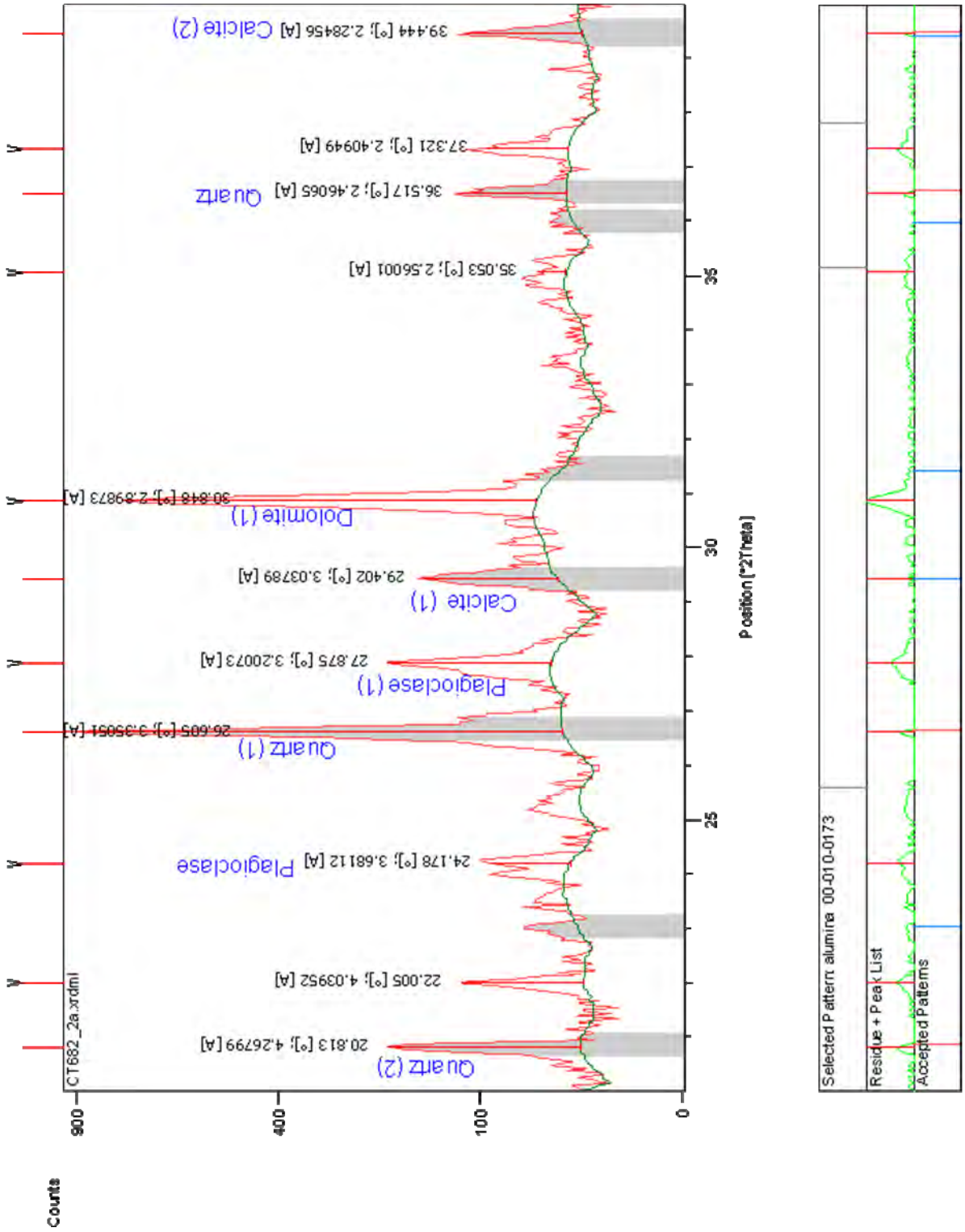
Counts
900
400
100
0
CT682_2a.xrdml
Quartz (2)
20.813 [°]; 4.26799 [Å]
22.005 [°]; 4.03952 [Å]
Plagioclase
24.178 [°]; 3.68112 [Å]
Quartz (1)
26.605 [°]; 3.35051 [Å]
Plagioclase (1)
27.875 [°]; 3.20073 [Å]
Calcite (1)
29.402 [°]; 3.03789 [Å]
Dolomite (1)
30.848 [°]; 2.89873 [Å]
35.053 [°]; 2.56001 [Å]
Quartz
36.517 [°]; 2.46065 [Å]
37.321 [°]; 2.40949 [Å]
Calcite (2)
39.444 [°]; 2.28456 [Å]
25
30
35
Position [°2Theta]
Selected Pattern: alumina 00-010-0173
Residue + Peak List
Accepted Patterns

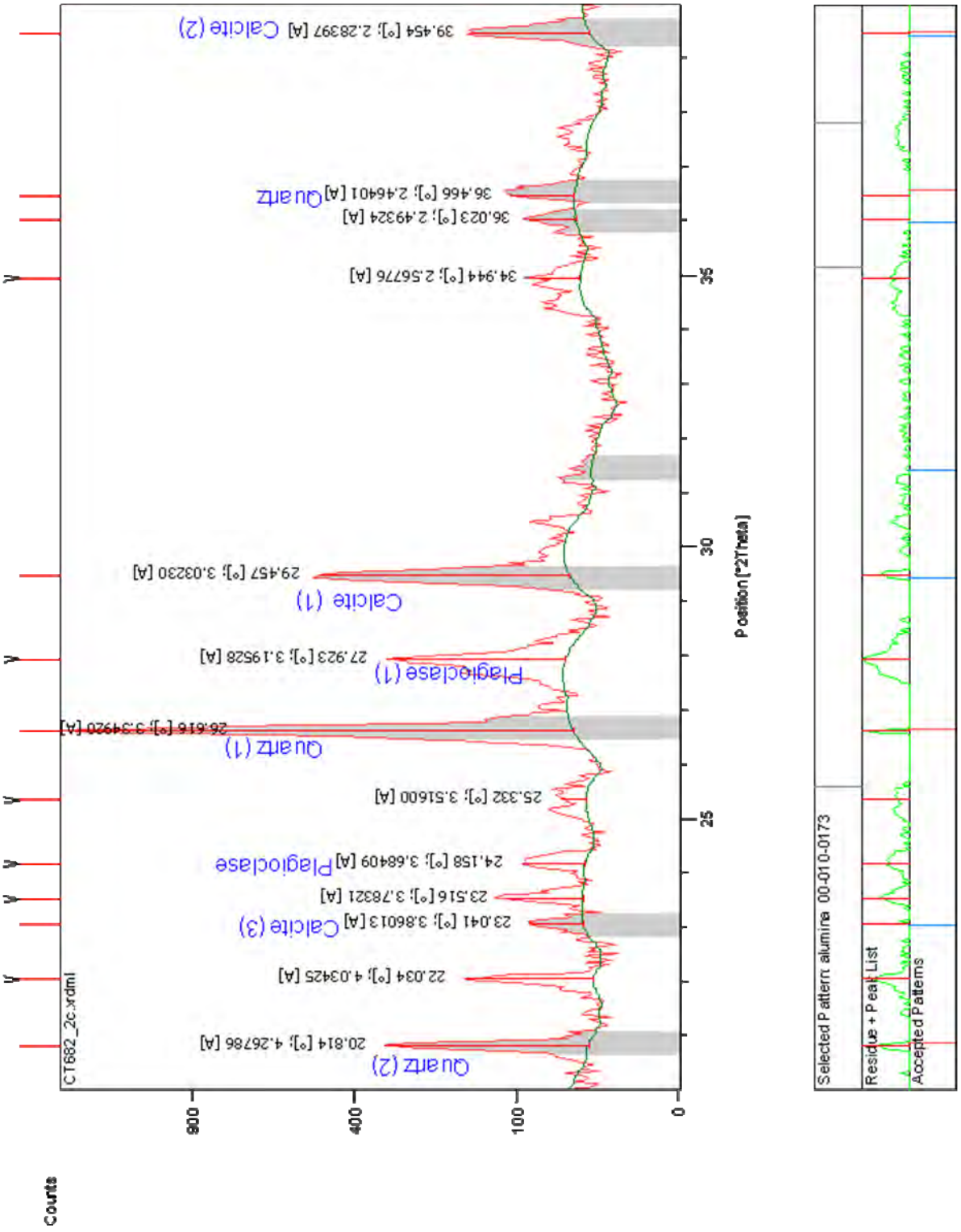
Counts
900
400
100
0
CT682_2c.xrdml
Quartz (2)
20.814 [°]; 4.26786 [A]
22.034 [°]; 4.03425 [A]
Calcite (3)
23.041 [°]; 3.86013 [A]
23.516 [°]; 3.78321 [A]
Plagioclase
24.158 [°]; 3.68409 [A]
25.332 [°]; 3.51600 [A]
Quartz (1)
26.616 [°]; 3.34920 [A]
Plagioclase (1)
27.923 [°]; 3.19528 [A]
Calcite (1)
29.457 [°]; 3.03230 [A]
34.944 [°]; 2.56776 [A]
Quartz
36.023 [°]; 2.49324 [A]
36.466 [°]; 2.46401 [A]
Calcite (2)
39.454 [°]; 2.28397 [A]
25
30
35
Position [°2Theta]
Selected Pattern: alumina 00-010-0173
Residue + Peak List
Accepted Patterns

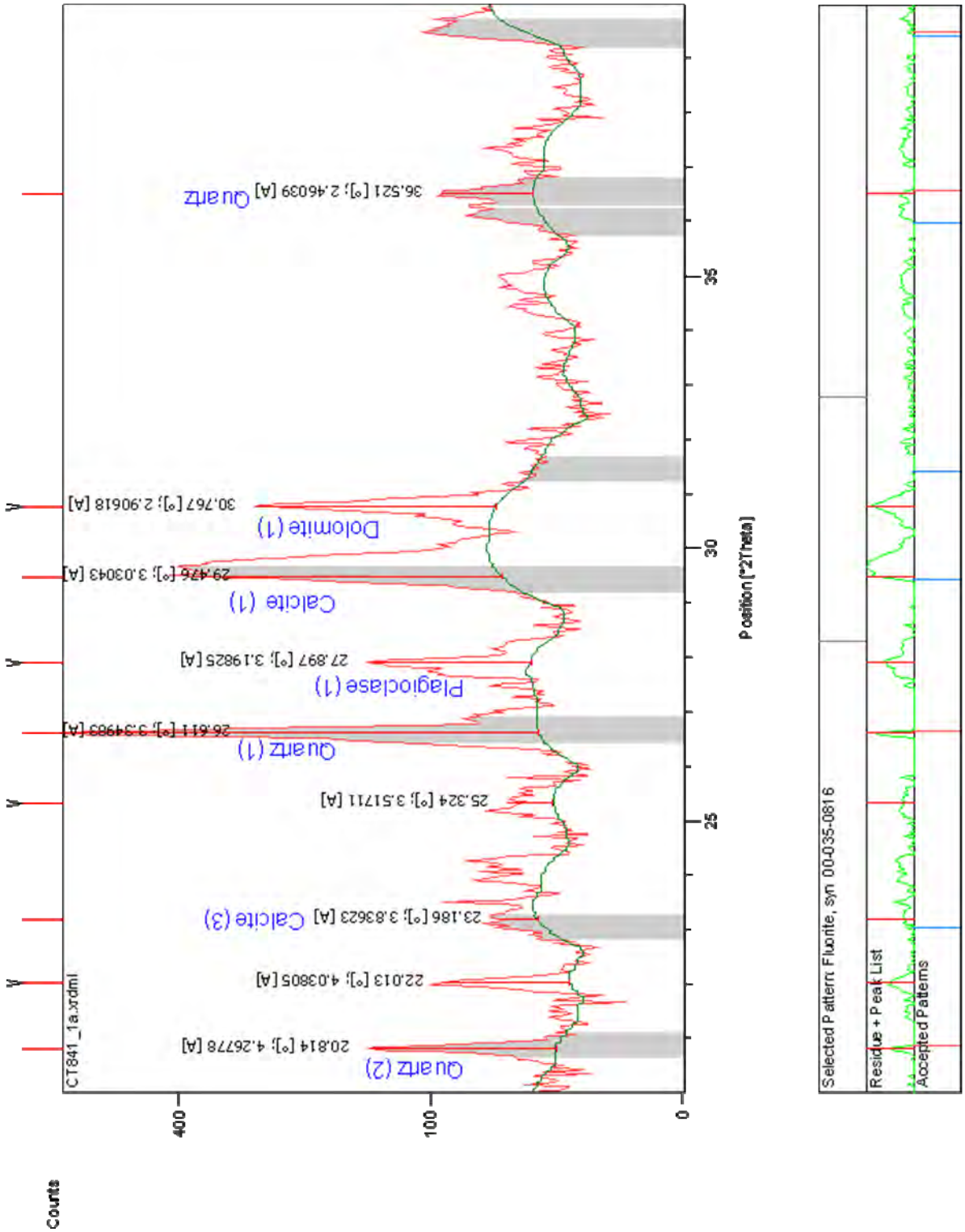
Counts
400
100
0
CT841_1a.xrdml
20.814 [°]; 4.26778 [A]
Quartz (2)
22.013 [°]; 4.03805 [A]
23.186 [°]; 3.83623 [A]
Calcite (3)
25.324 [°]; 3.51711 [A]
26.611 [°]; 3.34983 [A]
Quartz (1)
27.897 [°]; 3.19825 [A]
Plagioclase (1)
29.476 [°]; 3.03043 [A]
Calcite (1)
30.767 [°]; 2.90618 [A]
Dolomite (1)
36.521 [°]; 2.46039 [A]
Quartz
25
30
35
Position [°2Theta]
Selected Pattern: Fluorite, syn 00-035-0816
Residue + Peak List
Accepted Patterns

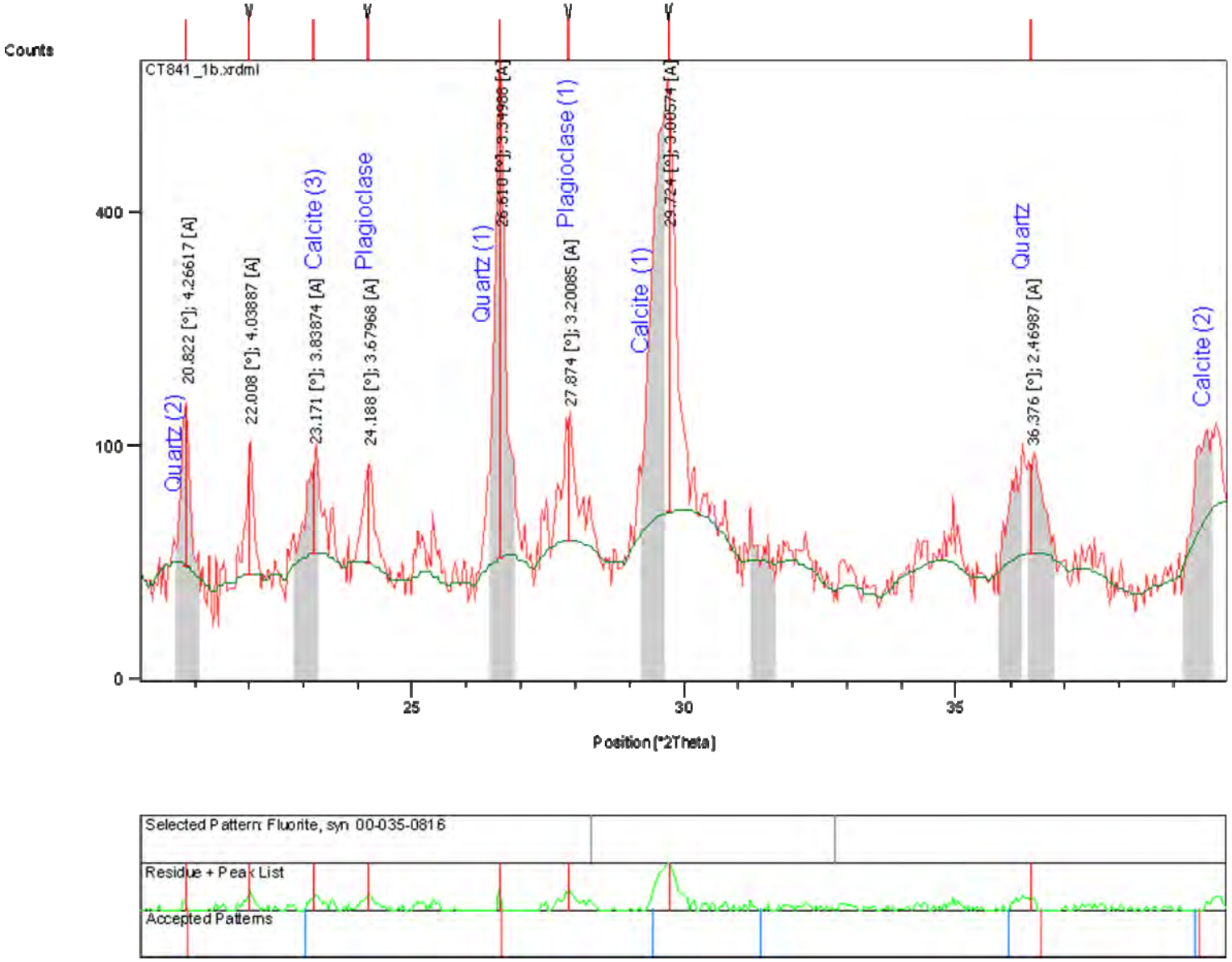
Counts
CT841_1b.xrdml
400
100
0
Quartz (2)
20.822 [°]; 4.26617 [A]
22.008 [°]; 4.03887 [A]
Calcite (3)
23.171 [°]; 3.83674 [A]
Plagioclase
24.188 [°]; 3.67968 [A]
Quartz (1)
26.610 [°]; 3.34988 [A]
Plagioclase (1)
27.874 [°]; 3.20085 [A]
Calcite (1)
29.724 [°]; 3.00574 [A]
Quartz
36.376 [°]; 2.46987 [A]
Calcite (2)
25
30
35
Position [°2Theta]
Selected Pattern: Fluorite, syn 00-035-0816
Residue + Peak List
Accepted Patterns

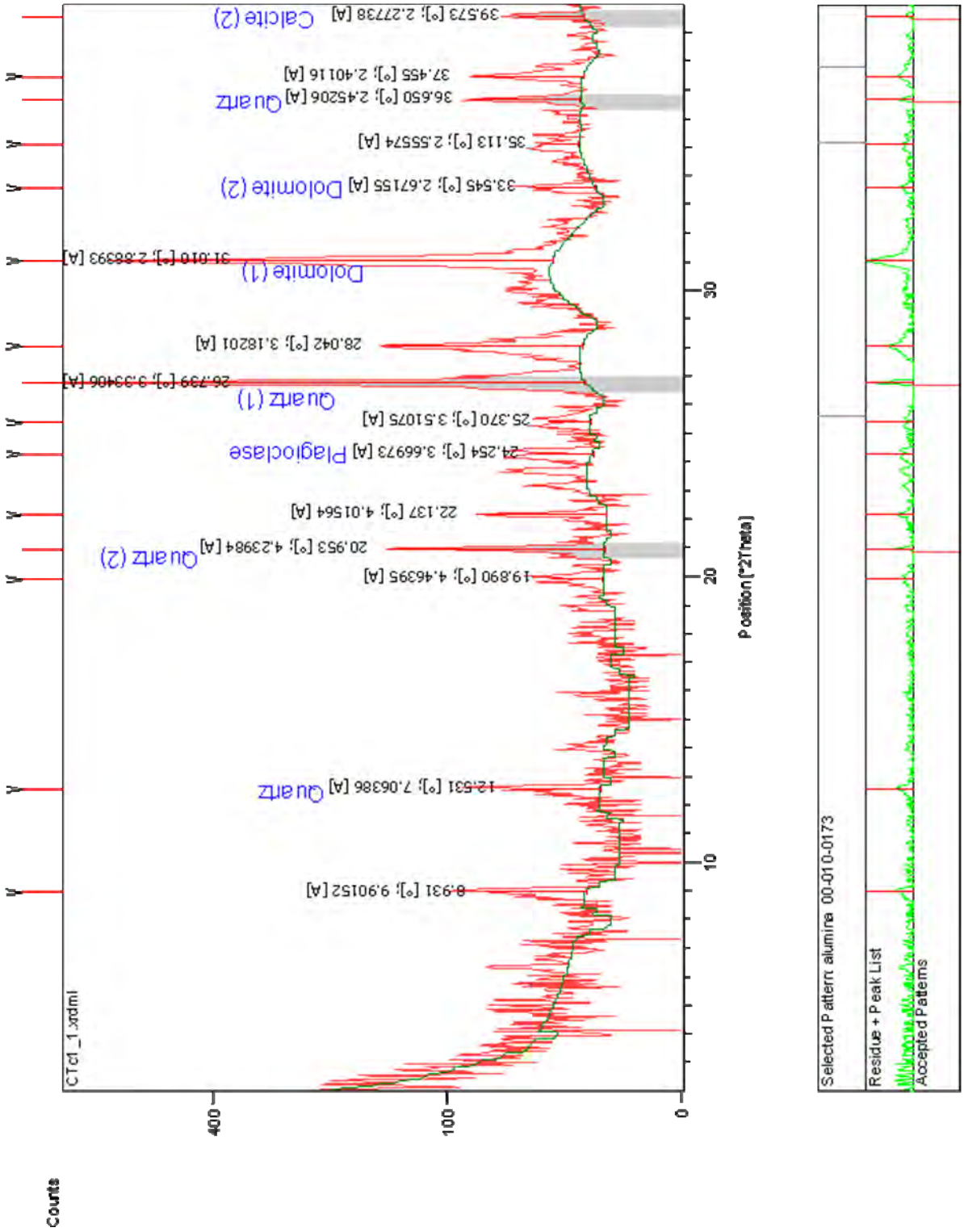
Counts
400
100
0
CTct_1.xrdml
8.931 [°]; 9.90152 [Å]
12.531 [°]; 7.06386 [Å]
Quartz
19.890 [°]; 4.46395 [Å]
20.953 [°]; 4.23984 [Å]
Quartz (2)
22.137 [°]; 4.01564 [Å]
24.254 [°]; 3.66973 [Å]
Plagioclase
25.370 [°]; 3.51075 [Å]
26.739 [°]; 3.33406 [Å]
Quartz (1)
28.042 [°]; 3.18201 [Å]
31.010 [°]; 2.88393 [Å]
Dolomite (1)
33.545 [°]; 2.67155 [Å]
Dolomite (2)
35.113 [°]; 2.55574 [Å]
36.550 [°]; 2.45206 [Å]
Quartz
37.455 [°]; 2.40116 [Å]
39.573 [°]; 2.27738 [Å]
Calcite (2)
10
20
30
Position [°2Theta]
Selected Pattern: alumina 00-010-0173
Residue + Peak List
Accepted Patterns

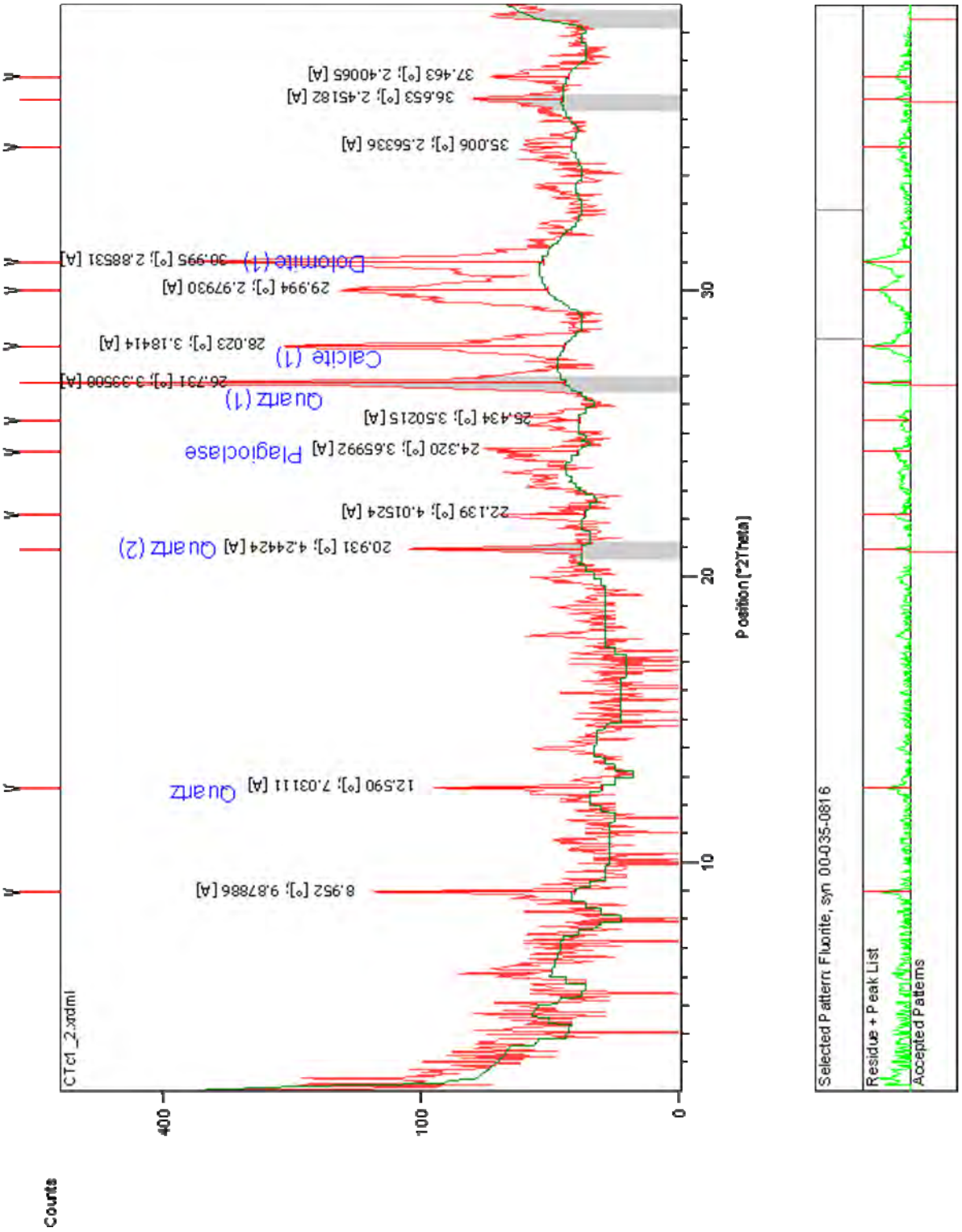
Counts
400
100
0
CTc1_2.xdml
8.952 [°]; 9.87886 [A]
Quartz
12.590 [°]; 7.03111 [A]
20.931 [°]; 4.24424 [A]
Quartz (2)
22.139 [°]; 4.01524 [A]
24.320 [°]; 3.65992 [A]
Plagioclase
26.434 [°]; 3.50215 [A]
26.731 [°]; 3.35506 [A]
Quartz (1)
28.023 [°]; 3.18414 [A]
Calcite (1)
29.994 [°]; 2.97930 [A]
30.995 [°]; 2.88531 [A]
Dolomite (1)
35.006 [°]; 2.56336 [A]
36.653 [°]; 2.45182 [A]
37.463 [°]; 2.40065 [A]
10
20
30
Position [°2Theta]
Selected Pattern: Fluorite, syn 00-035-0816
Residue + Peak List
Accepted Patterns

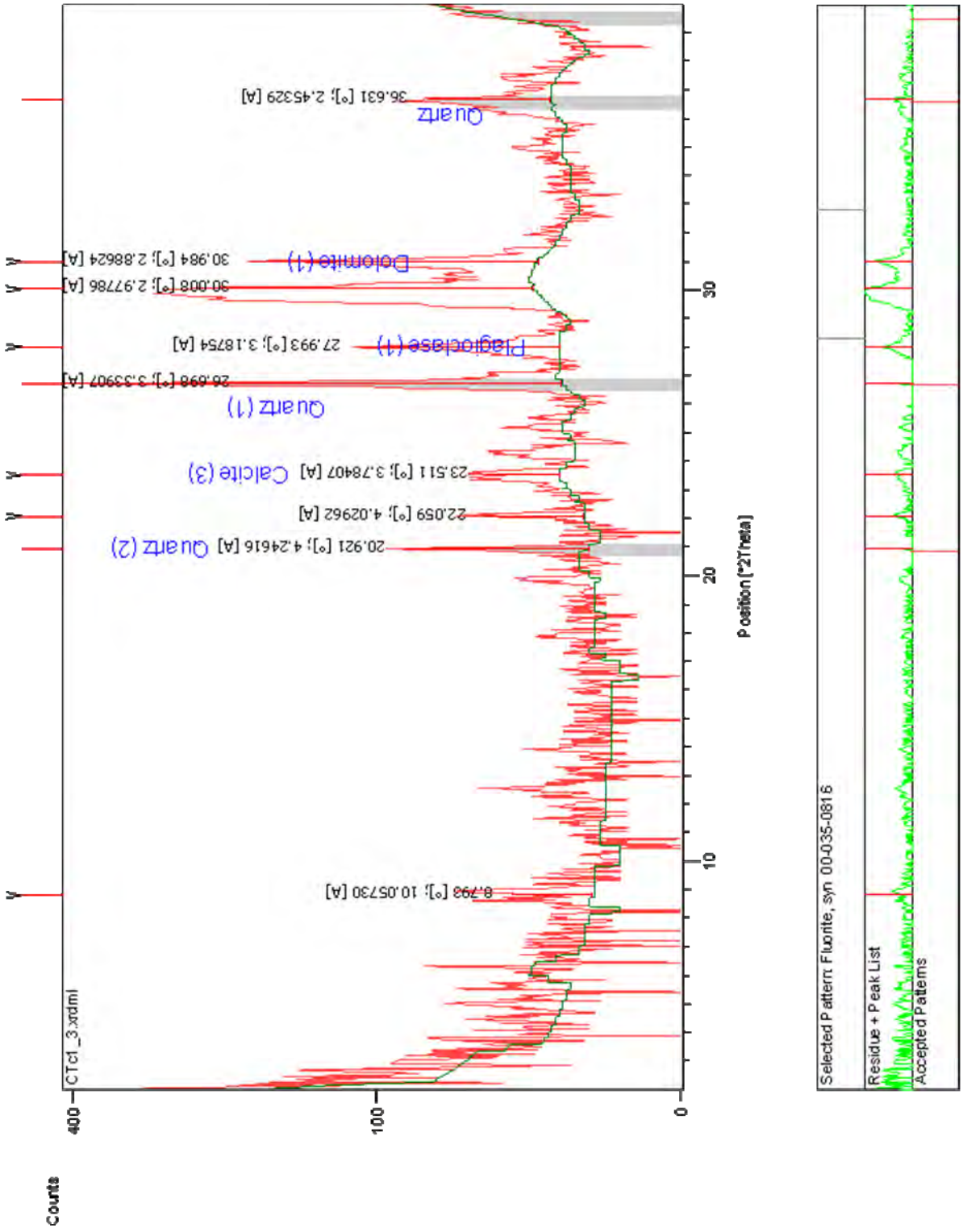
Counts
400
100
0
CTct_3.xrdml
8.792 [°]; 10.05730 [Å]
20.921 [°]; 4.24616 [Å]
Quartz (2)
22.059 [°]; 4.02962 [Å]
23.511 [°]; 3.78407 [Å]
Calcite (3)
26.698 [°]; 3.33907 [Å]
Quartz (1)
27.993 [°]; 3.18754 [Å]
Plagioclase (1)
30.008 [°]; 2.97786 [Å]
30.984 [°]; 2.88624 [Å]
Dolomite (1)
36.631 [°]; 2.45329 [Å]
Quartz
10
20
30
Position [°2Theta]
Selected Pattern: Fluorite, syn 00-035-0816
Residue + Peak List
Accepted Patterns

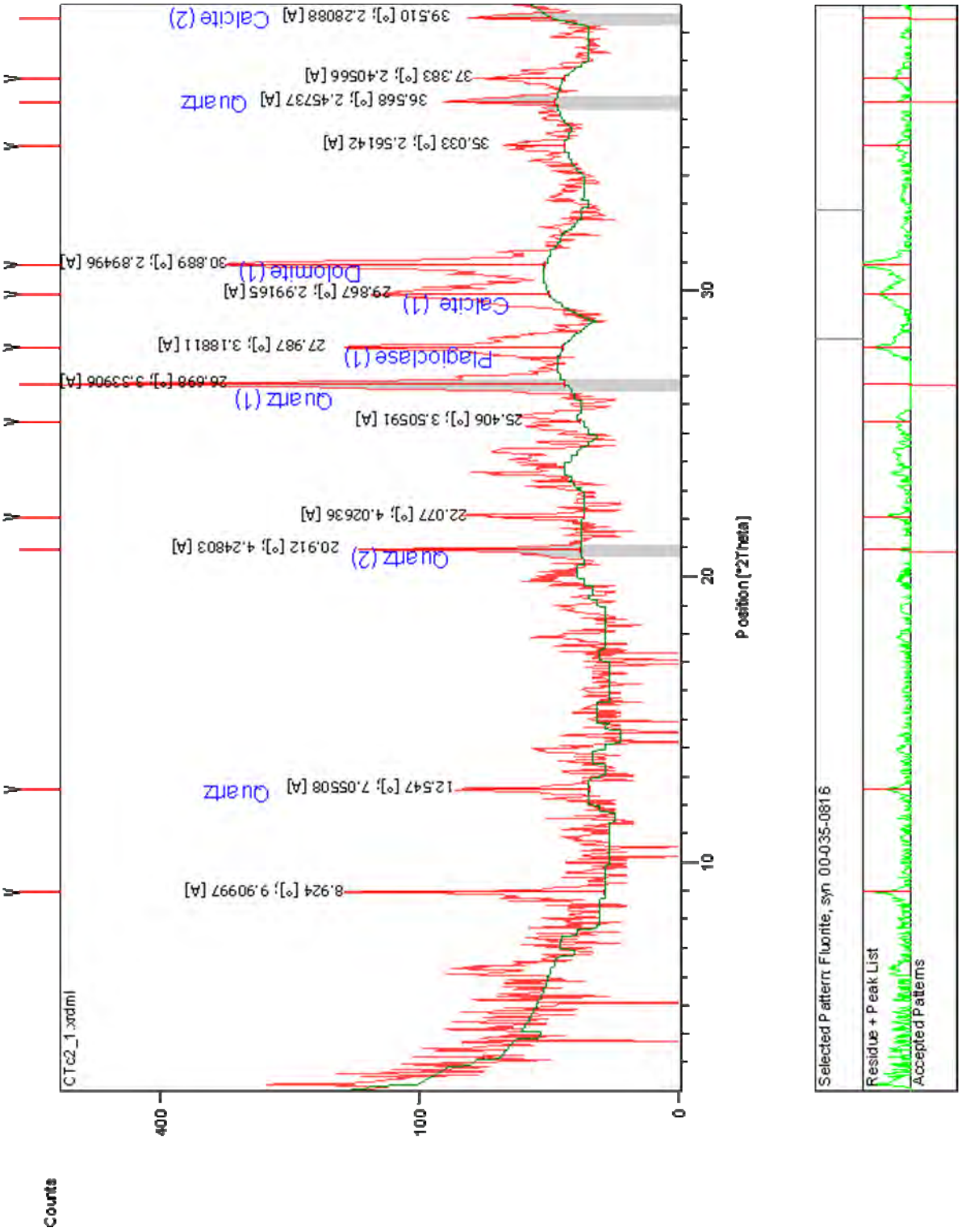
Counts
400
100
0
CTc2_1.xrdml
8.924 [°]; 9.90997 [A]
Quartz
12.547 [°]; 7.05508 [A]
Quartz (2)
20.912 [°]; 4.24803 [A]
22.077 [°]; 4.02636 [A]
25.406 [°]; 3.50591 [A]
Quartz (1)
26.698 [°]; 3.33906 [A]
Plagioclase (1)
27.987 [°]; 3.18811 [A]
Calcite (1)
29.867 [°]; 2.99165 [A]
Dolomite (1)
30.889 [°]; 2.89496 [A]
35.033 [°]; 2.56142 [A]
Quartz
36.568 [°]; 2.45737 [A]
37.383 [°]; 2.40566 [A]
Calcite (2)
39.510 [°]; 2.28088 [A]
10
20
30
Position [°2Theta]
Selected Pattern: Fluorite, syn 00-035-0816
Residue + Peak List
Accepted Patterns

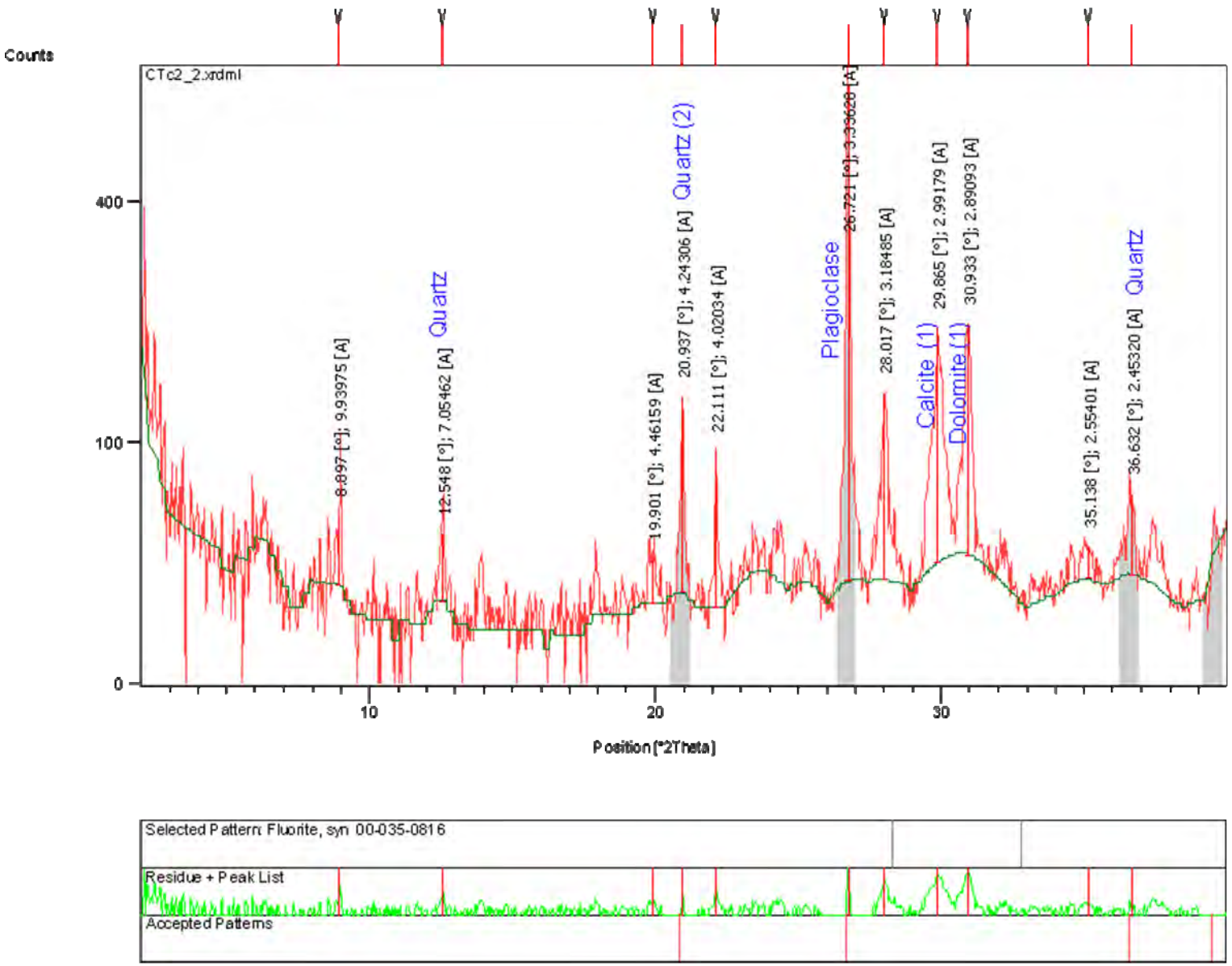
Counts
CTc2_2.xrdml
400
100
0
8.897 [°]; 9.93975 [A]
12.548 [°]; 7.05462 [A]
Quartz
19.901 [°]; 4.46159 [A]
20.937 [°]; 4.24306 [A]
Quartz (2)
22.111 [°]; 4.02034 [A]
Plagioclase
26.721 [°]; 3.33628 [A]
28.017 [°]; 3.18485 [A]
29.865 [°]; 2.99179 [A]
Calcite (1)
30.933 [°]; 2.89093 [A]
Dolomite (1)
35.138 [°]; 2.55401 [A]
36.632 [°]; 2.45320 [A]
Quartz
10
20
30
Position [°2Theta]
Selected Pattern: Fluorite, syn 00-035-0816
Residue + Peak List
Accepted Patterns

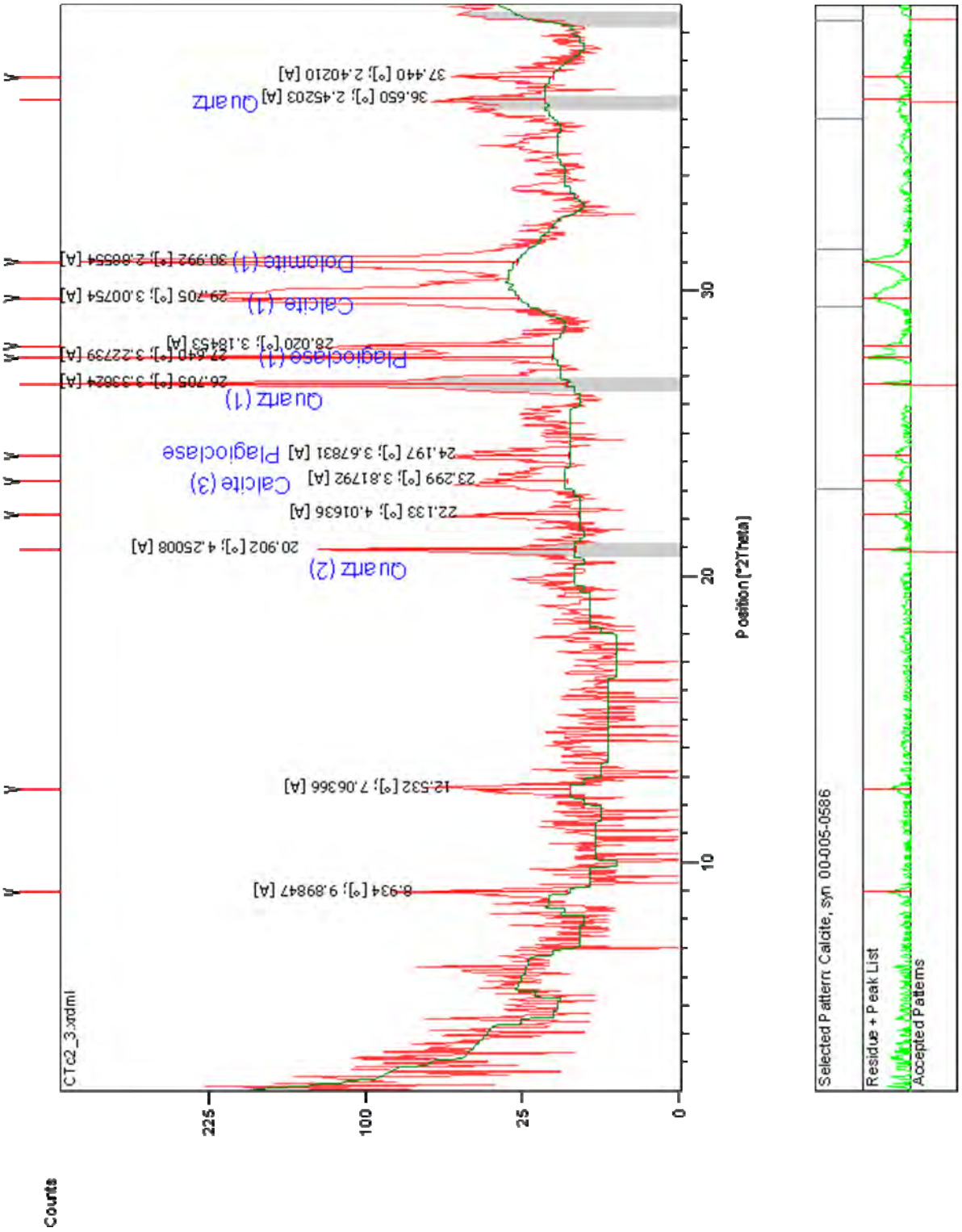
Counts
225
100
25
0
CTc2_3.xrdml
8.934 [°]; 9.89847 [Å]
12.532 [°]; 7.06366 [Å]
20.902 [°]; 4.25008 [Å]
Quartz (2)
22.133 [°]; 4.01636 [Å]
23.299 [°]; 3.81792 [Å]
Calcite (3)
24.197 [°]; 3.67831 [Å]
Plagioclase
26.705 [°]; 3.33624 [Å]
Quartz (1)
27.640 [°]; 3.22739 [Å]
28.020 [°]; 3.18453 [Å]
Plagioclase (1)
29.405 [°]; 3.00754 [Å]
Calcite (1)
30.992 [°]; 2.88554 [Å]
Dolomite (1)
36.650 [°]; 2.45203 [Å]
Quartz
37.440 [°]; 2.40210 [Å]
10
20
30
Position [°2Theta]
Selected Pattern: Calcite, syn 00-005-0586
Residue + Peak List
Accepted Patterns

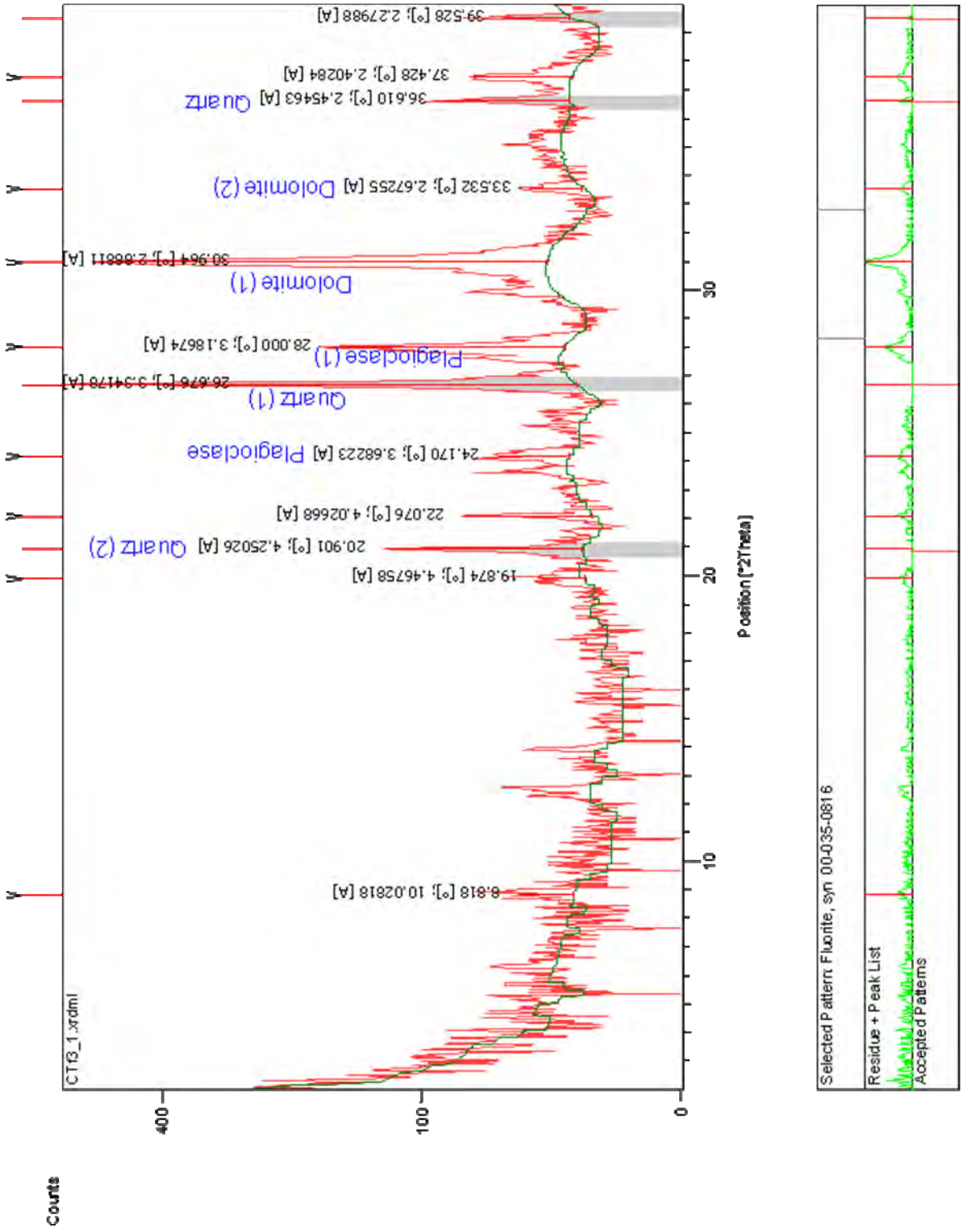
Counts
400
100
0
CT63_1.xrdml
8.818 [°]; 10.02818 [A]
19.874 [°]; 4.46758 [A]
20.901 [°]; 4.25026 [A]
Quartz (2)
22.076 [°]; 4.02668 [A]
24.170 [°]; 3.68223 [A]
Plagioclase
26.676 [°]; 3.34178 [A]
Quartz (1)
28.000 [°]; 3.18674 [A]
Plagioclase (1)
30.964 [°]; 2.88811 [A]
Dolomite (1)
33.532 [°]; 2.67255 [A]
Dolomite (2)
36.610 [°]; 2.45463 [A]
Quartz
37.428 [°]; 2.40284 [A]
39.528 [°]; 2.27988 [A]
10
20
30
Position [°2Theta]
Selected Pattern: Fluorite, syn 00-035-0816
Residue + Peak List
Accepted Patterns

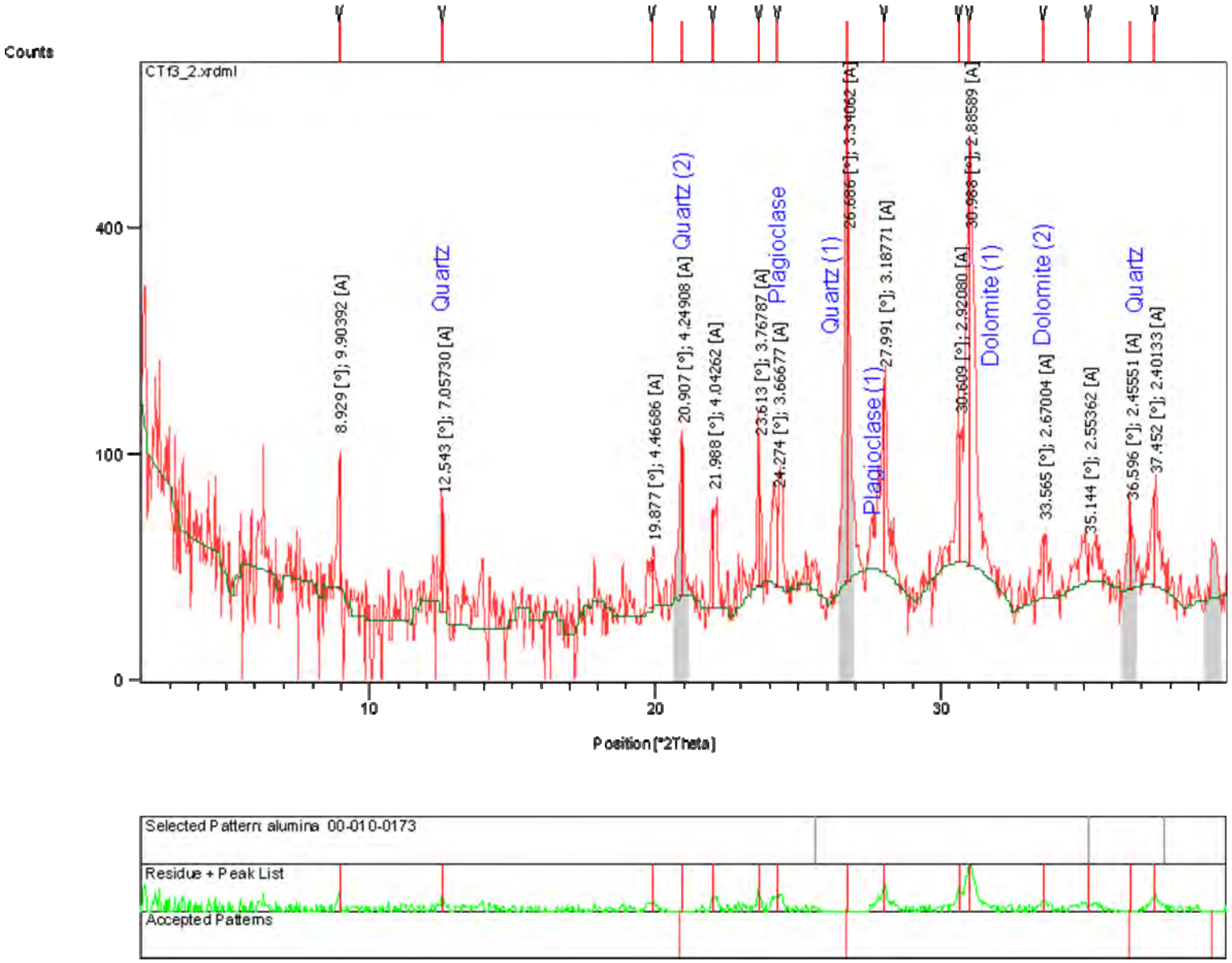
Counts
CTf3_2.xrdml
400
100
0
10
20
30
Position [°2Theta]
8.929 [°]; 9.90392 [A]
12.543 [°]; 7.05730 [A]
19.877 [°]; 4.46686 [A]
20.907 [°]; 4.24908 [A]
21.988 [°]; 4.04262 [A]
23.613 [°]; 3.76787 [A]
24.274 [°]; 3.66677 [A]
26.686 [°]; 3.34062 [A]
27.991 [°]; 3.18771 [A]
30.609 [°]; 2.92080 [A]
30.968 [°]; 2.88589 [A]
33.565 [°]; 2.67004 [A]
35.144 [°]; 2.55362 [A]
36.596 [°]; 2.45551 [A]
37.452 [°]; 2.40133 [A]
Quartz
Quartz (2)
Plagioclase
Quartz (1)
Plagioclase (1)
Dolomite (1)
Dolomite (2)
Quartz
Selected Pattern: alumina 00-010-0173
Residue + Peak List
Accepted Patterns

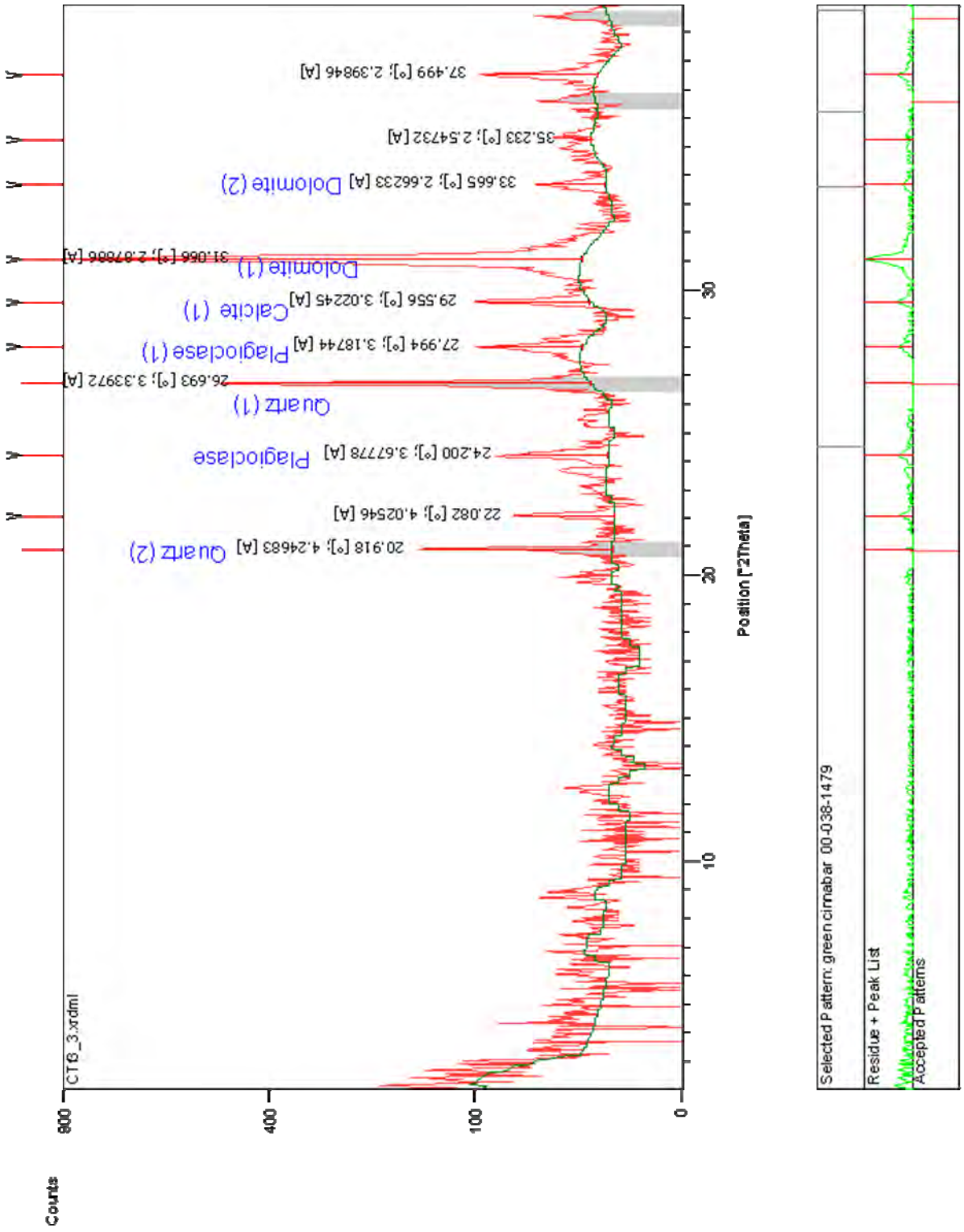
Counts
Position [°2Theta]
CT6_3.xrdml
Quartz (2)
Plagioclase
Quartz (1)
Plagioclase (1)
Calcite (1)
Dolomite (1)
Dolomite (2)
20.918 [°]; 4.24683 [A]
22.082 [°]; 4.02546 [A]
24.200 [°]; 3.67778 [A]
26.693 [°]; 3.33972 [A]
27.994 [°]; 3.18744 [A]
29.556 [°]; 3.02245 [A]
31.066 [°]; 2.87886 [A]
33.665 [°]; 2.66233 [A]
35.233 [°]; 2.54732 [A]
37.499 [°]; 2.39846 [A]
Selected Pattern: green cinnabar 00-038-1479
Residue + Peak List
Accepted Patterns

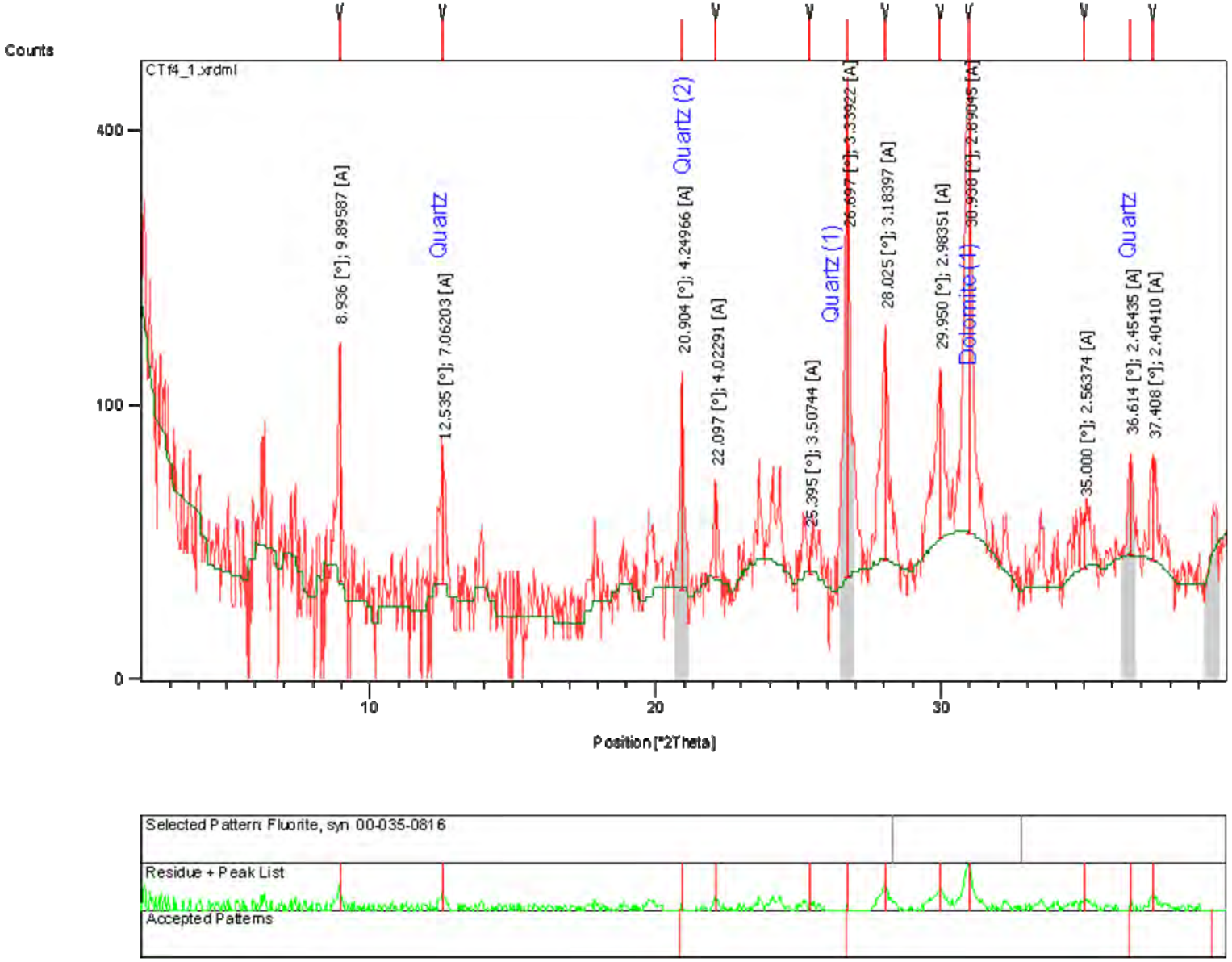
Counts
CTf4_1.xrdml
400
100
0
8.936 [°]; 9.89587 [A]
Quartz
12.535 [°]; 7.06203 [A]
Quartz (2)
20.904 [°]; 4.24966 [A]
22.097 [°]; 4.02291 [A]
25.395 [°]; 3.50744 [A]
Quartz (1)
26.697 [°]; 3.33922 [A]
28.025 [°]; 3.18397 [A]
29.950 [°]; 2.98351 [A]
Dolomite (1)
30.938 [°]; 2.89045 [A]
35.000 [°]; 2.56374 [A]
Quartz
36.614 [°]; 2.45435 [A]
37.408 [°]; 2.40410 [A]
10
20
30
Position [°2Theta]
Selected Pattern: Fluorite, syn 00-035-0816
Residue + Peak List
Accepted Patterns

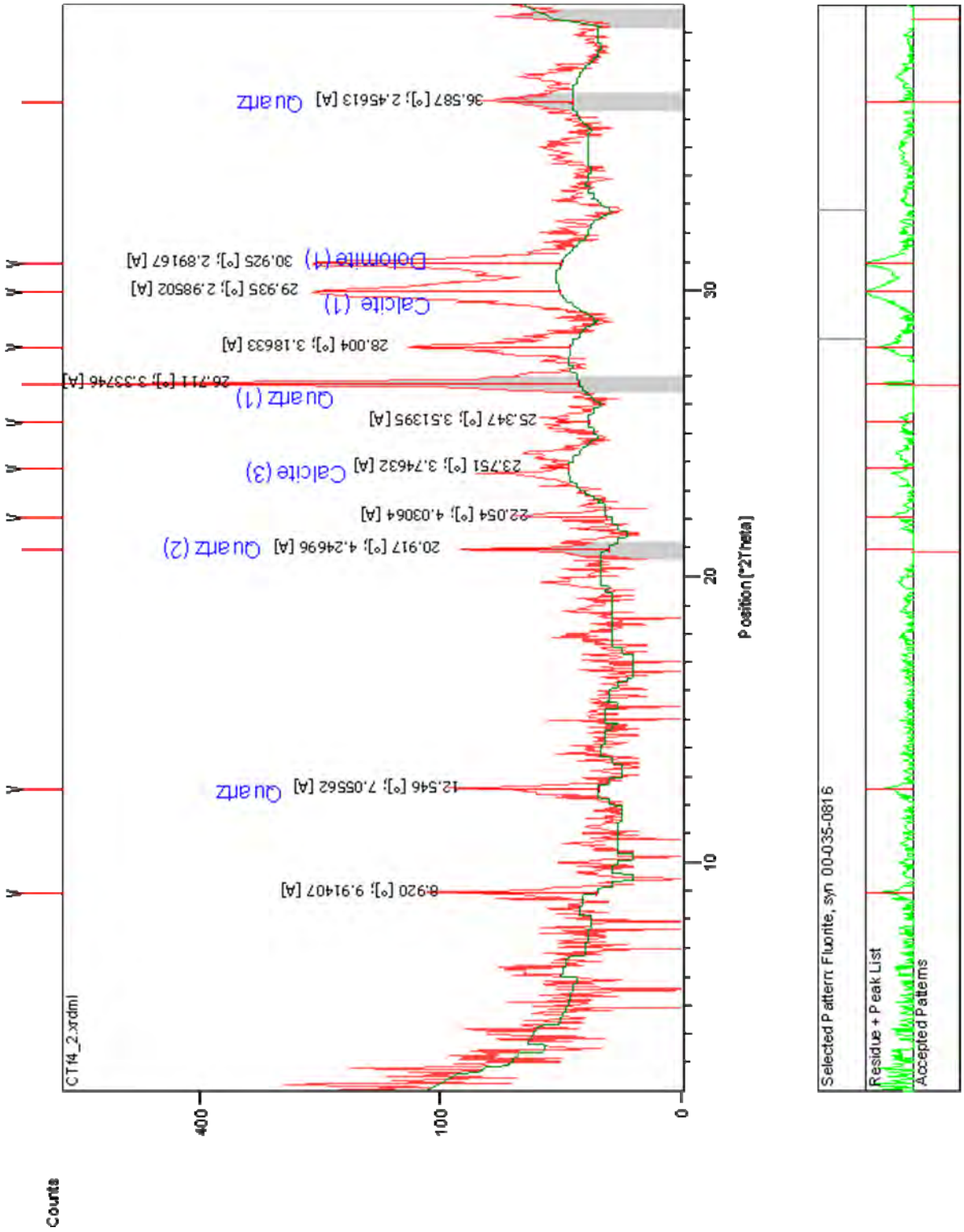
Counts
400
100
0
CT14_2.xrdml
8.920 [°]; 9.91407 [Å]
12.546 [°]; 7.05562 [Å]
Quartz
20.917 [°]; 4.24696 [Å]
Quartz (2)
22.054 [°]; 4.03064 [Å]
23.751 [°]; 3.74632 [Å]
Calcite (3)
25.347 [°]; 3.51395 [Å]
26.711 [°]; 3.33746 [Å]
Quartz (1)
28.004 [°]; 3.18633 [Å]
29.935 [°]; 2.98502 [Å]
Calcite (1)
30.925 [°]; 2.89167 [Å]
Dolomite (1)
36.587 [°]; 2.45613 [Å]
Quartz
10
20
30
Position [°2Theta]
Selected Pattern: Fluorite, syn 00-035-0816
Residue + Peak List
Accepted Patterns

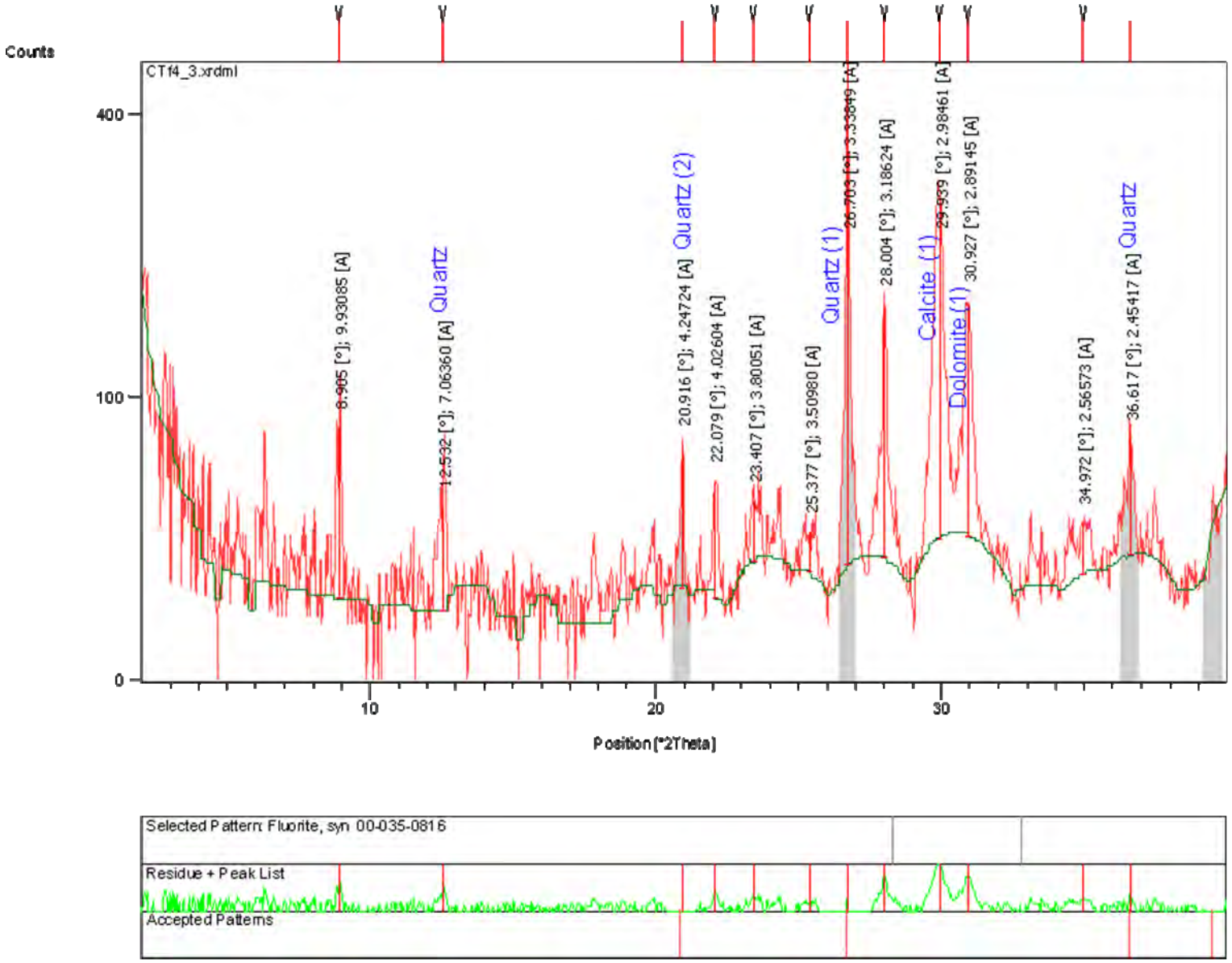
Counts
CT14_3.xrdml
400
100
0
10
20
30
Position [°2Theta]
8.985 [°]; 9.93085 [A]
Quartz
12.532 [°]; 7.06360 [A]
20.916 [°]; 4.24724 [A]
Quartz (2)
22.079 [°]; 4.02604 [A]
23.407 [°]; 3.80051 [A]
25.377 [°]; 3.50980 [A]
Quartz (1)
26.703 [°]; 3.33649 [A]
28.004 [°]; 3.18624 [A]
Calcite (1)
29.959 [°]; 2.98461 [A]
Dolomite (1)
30.927 [°]; 2.89145 [A]
34.972 [°]; 2.56573 [A]
36.617 [°]; 2.45417 [A]
Quartz
Selected Pattern: Fluorite, syn 00-035-0816
Residue + Peak List
Accepted Patterns

7. SEM photographs and EDS graphs

Appendix Section 7 contains SEM photographs and EDS graphs that are characteristic of cement phases in the pipe and bulbous concretions.

7.1 SEM photographs

The SEM images depict very fine grained mudstone that is cemented by micritic carbonate. EDS analysis indicates the elemental composition is primarily calcium which corresponds to both calcite and plagioclase. Small amounts of iron, magnesium, and silica are also present which corresponds to quartz and feldspars.

SEM analysis of Whangaehu samples did not reveal detailed information about the crystallography or composition of the mudstones and cement due to the fine grained nature of the components. SEM photograph in Figure A2.9 is of CTf3-2 (main concretion) and is characteristic of the tubular concretions at Whangaehu with fine grained siliciclastics cemented by micritic carbonate (dolomite or mixed calcite/dolomite). SEM and EDS images in Figure A2.10 are of CTc1-3 and from the main concretion, but adjacent to a pinhole conduit. Along with fine grained siliciclastics cemented by micrite, a second carbonate phase of blocky calcite is present. The EDS graph is from the bulk sample and is composed predominately of calcium, followed by magnesium, silica, and iron. SEM and EDS images of Figure A2.11 are a close up of Figure A2.10, focussing on the blocky calcite. Note the difference in the EDS spectrum, which is mostly calcium. Further samples were investigated, however most were identical to Figure A2.9; a few also contained blocky calcite as in Figures A2.10 and A2.11.

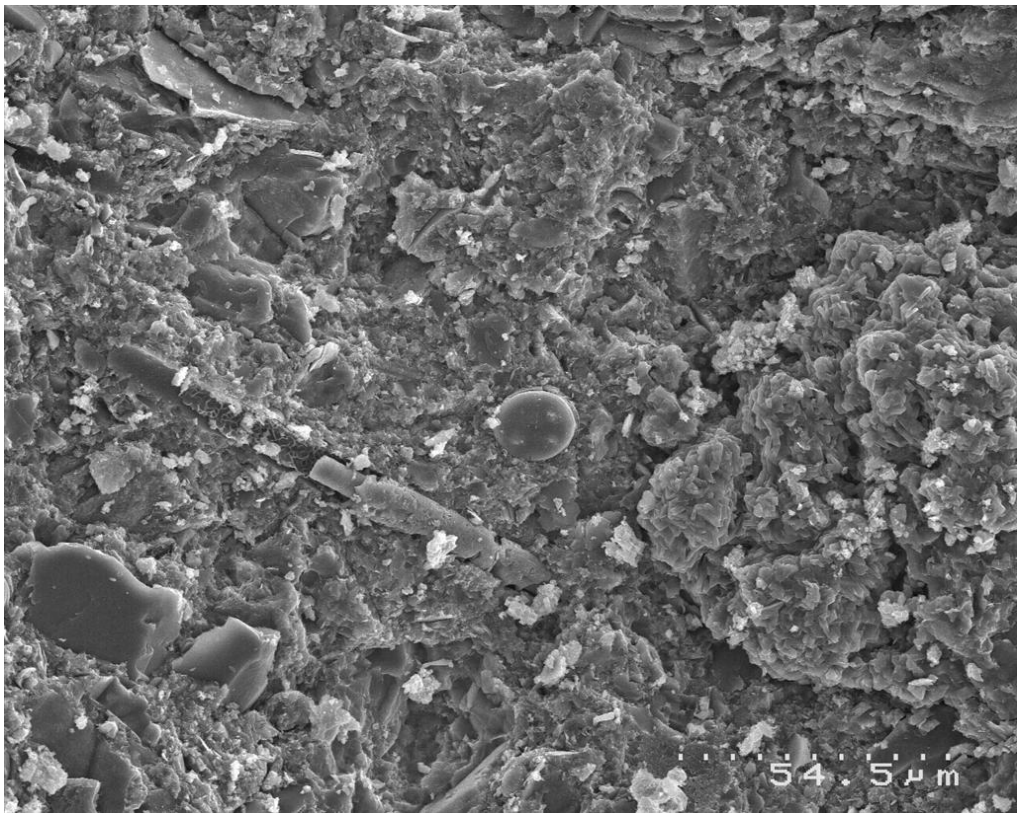

Figure A2.9

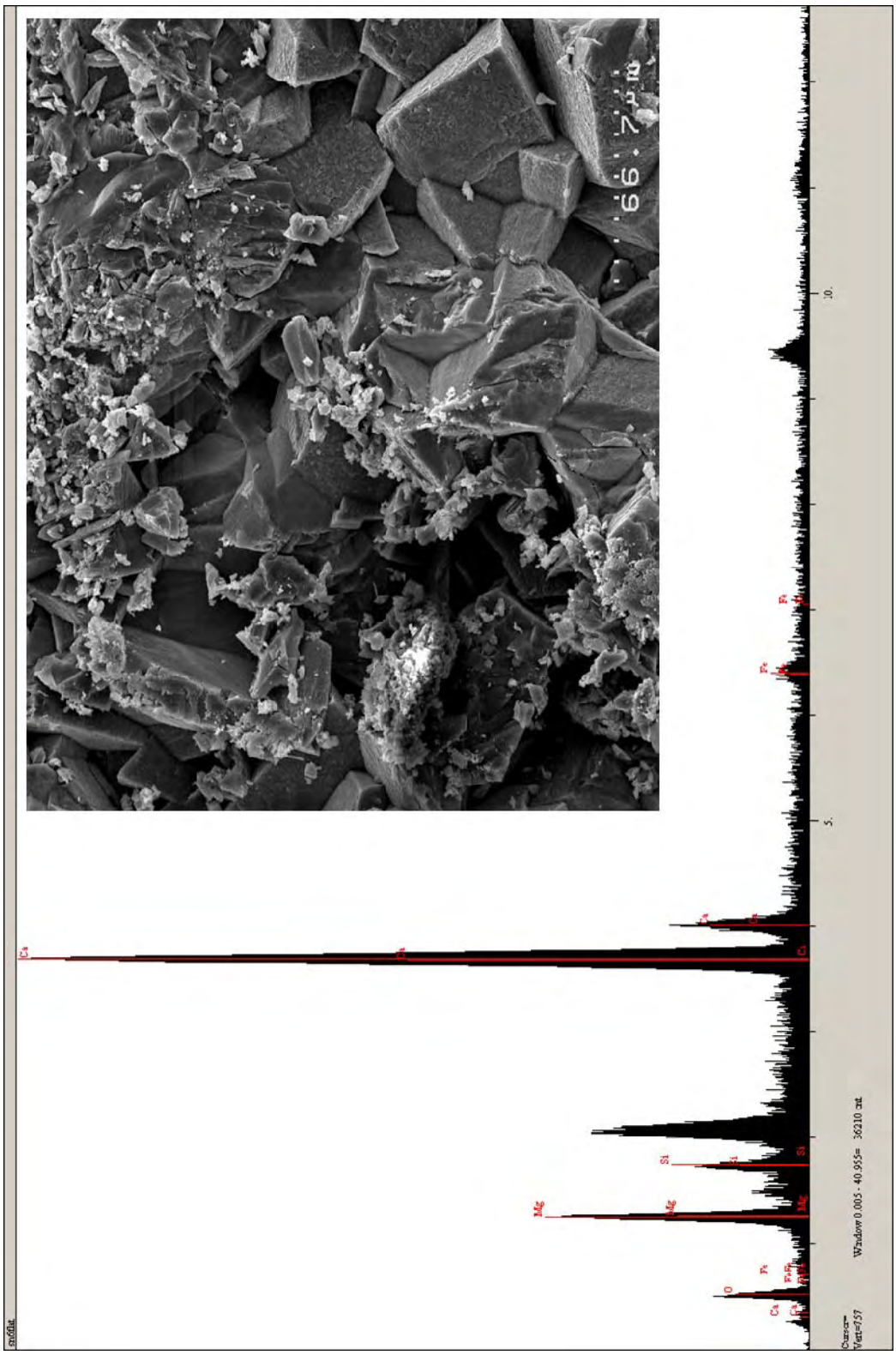

Figure A2.10

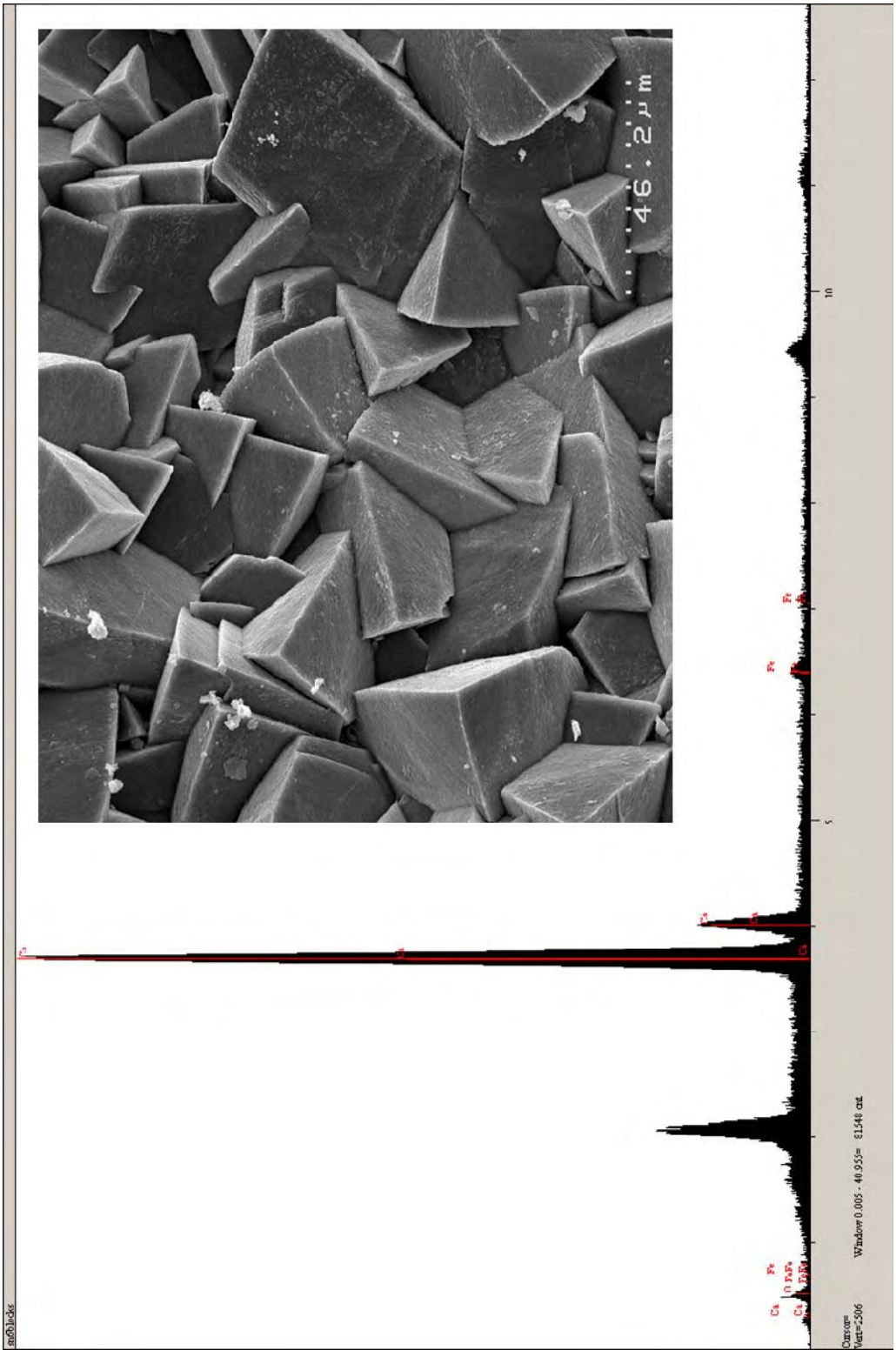

Figure A2.11

8. Isotope transects

Appendix Section 8 contains isotope transects for tubular concretions.

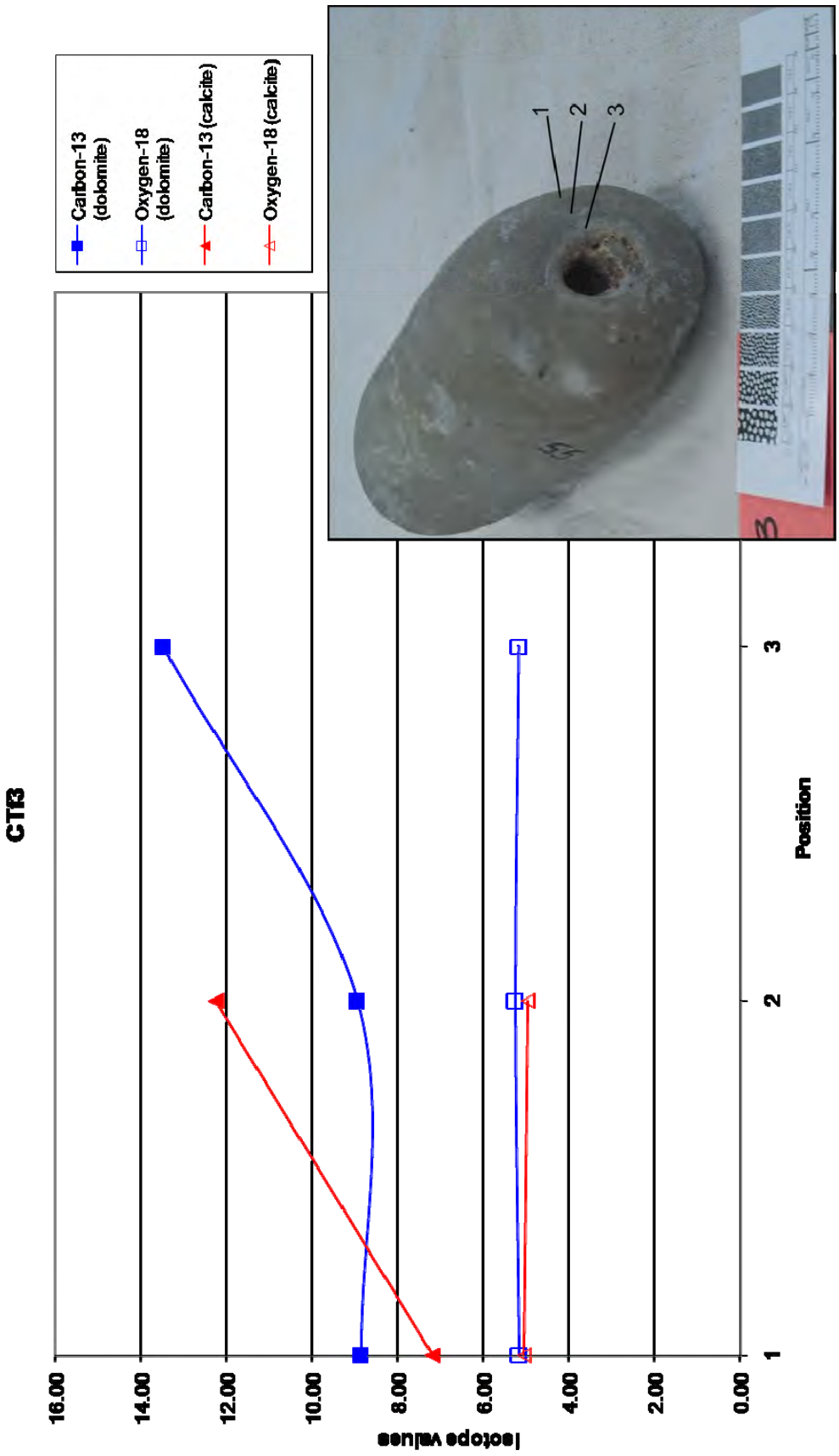
CT3
Carbon-13 (dolomite)
Oxygen-18 (dolomite)
Carbon-13 (calcite)
Oxygen-18 (calcite)
1
2
3
Isotope values
16.00
14.00
12.00
10.00
8.00
6.00
4.00
2.00
0.00
Position
1
2
3

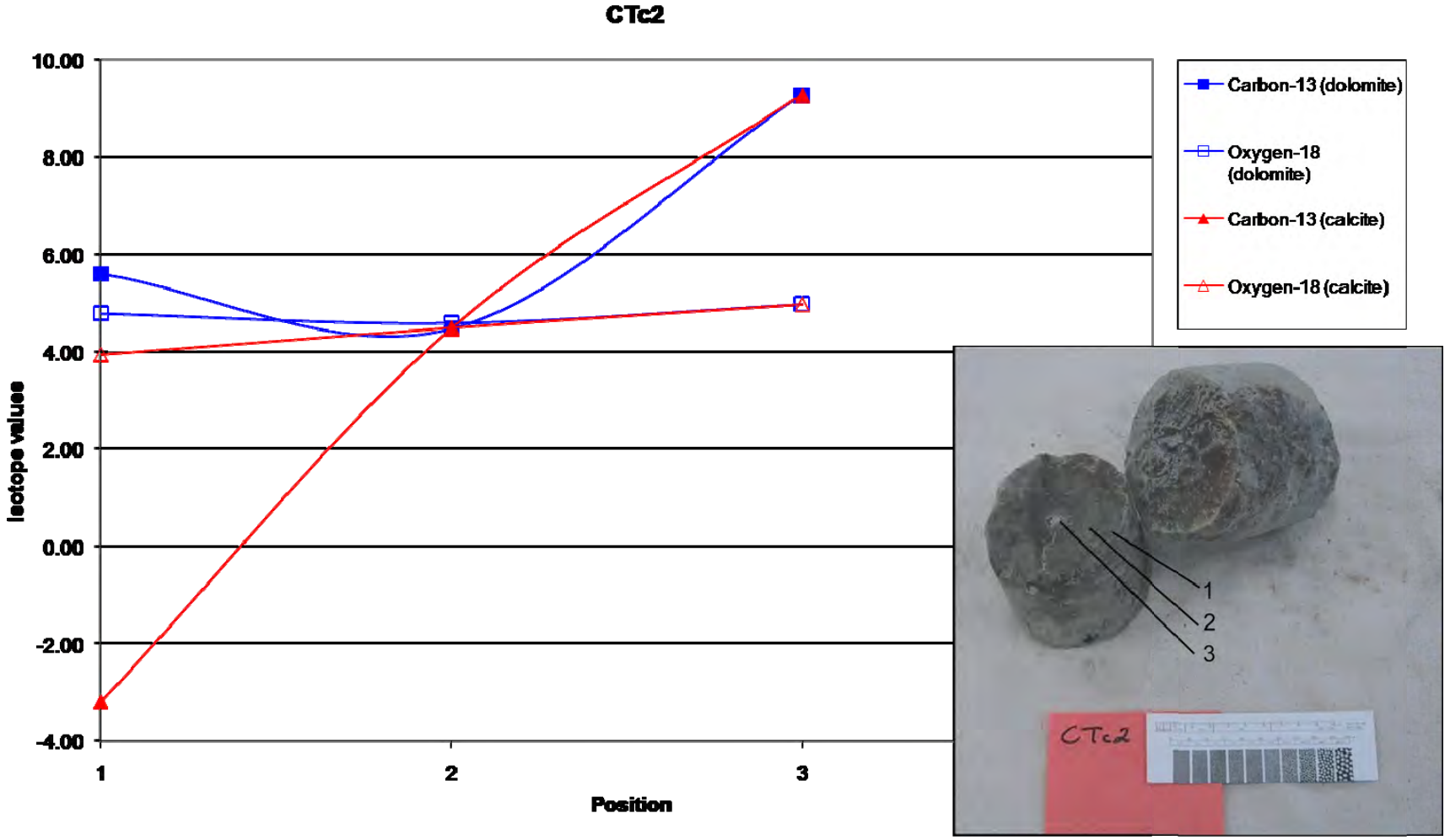
CTc2
10.00
8.00
6.00
4.00
2.00
0.00
-2.00
-4.00
Isotope values
1
2
3
Position
Carbon-13 (dolomite)
Oxygen-18 (dolomite)
Carbon-13 (calcite)
Oxygen-18 (calcite)
1
2
3
CTc2

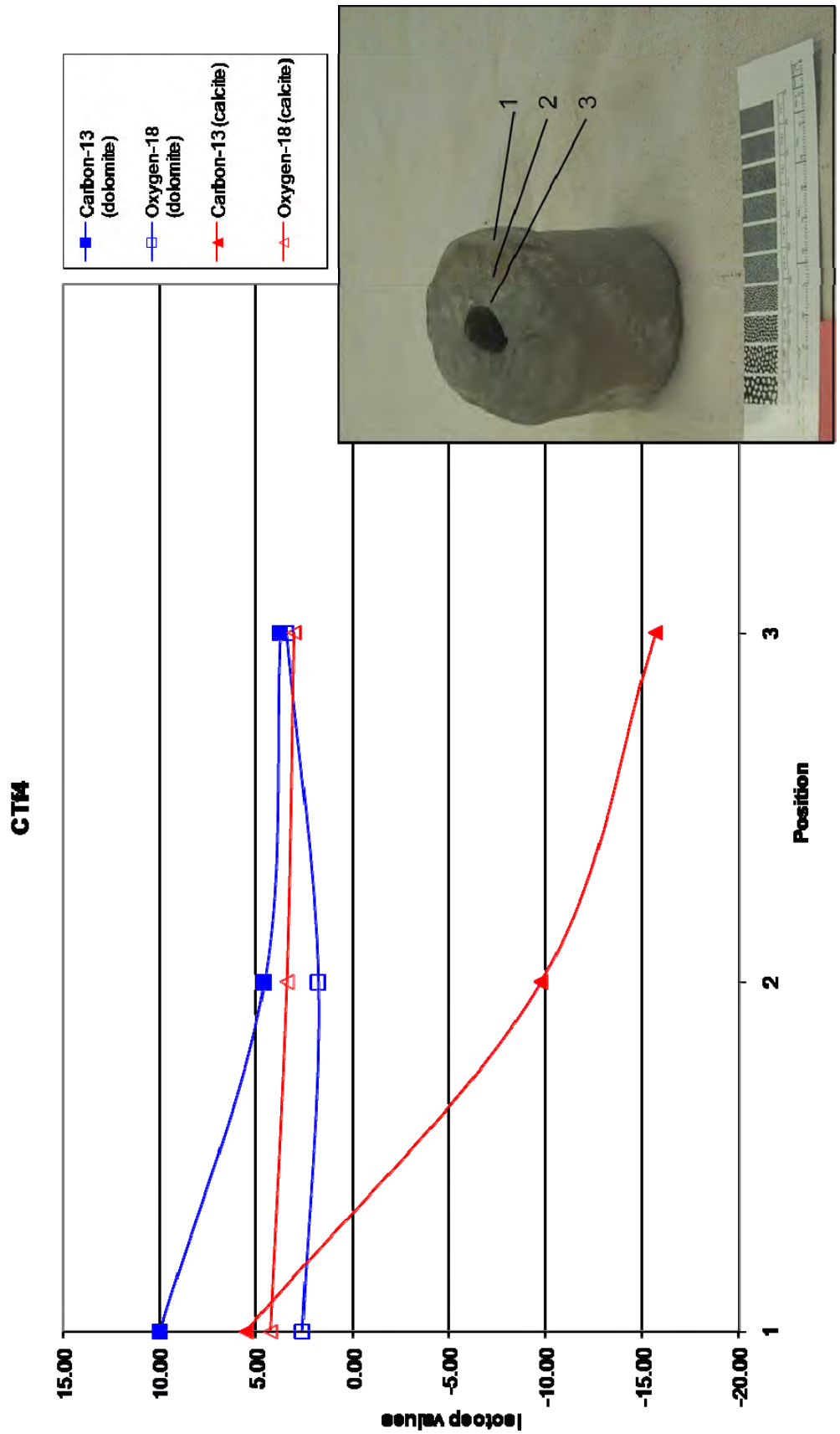
CT4
Carbon-13 (dolomite)
Oxygen-18 (dolomite)
Carbon-13 (calcite)
Oxygen-18 (calcite)
1
2
3
Isotope values
15.00
10.00
5.00
0.00
-5.00
-10.00
-15.00
-20.00
Position

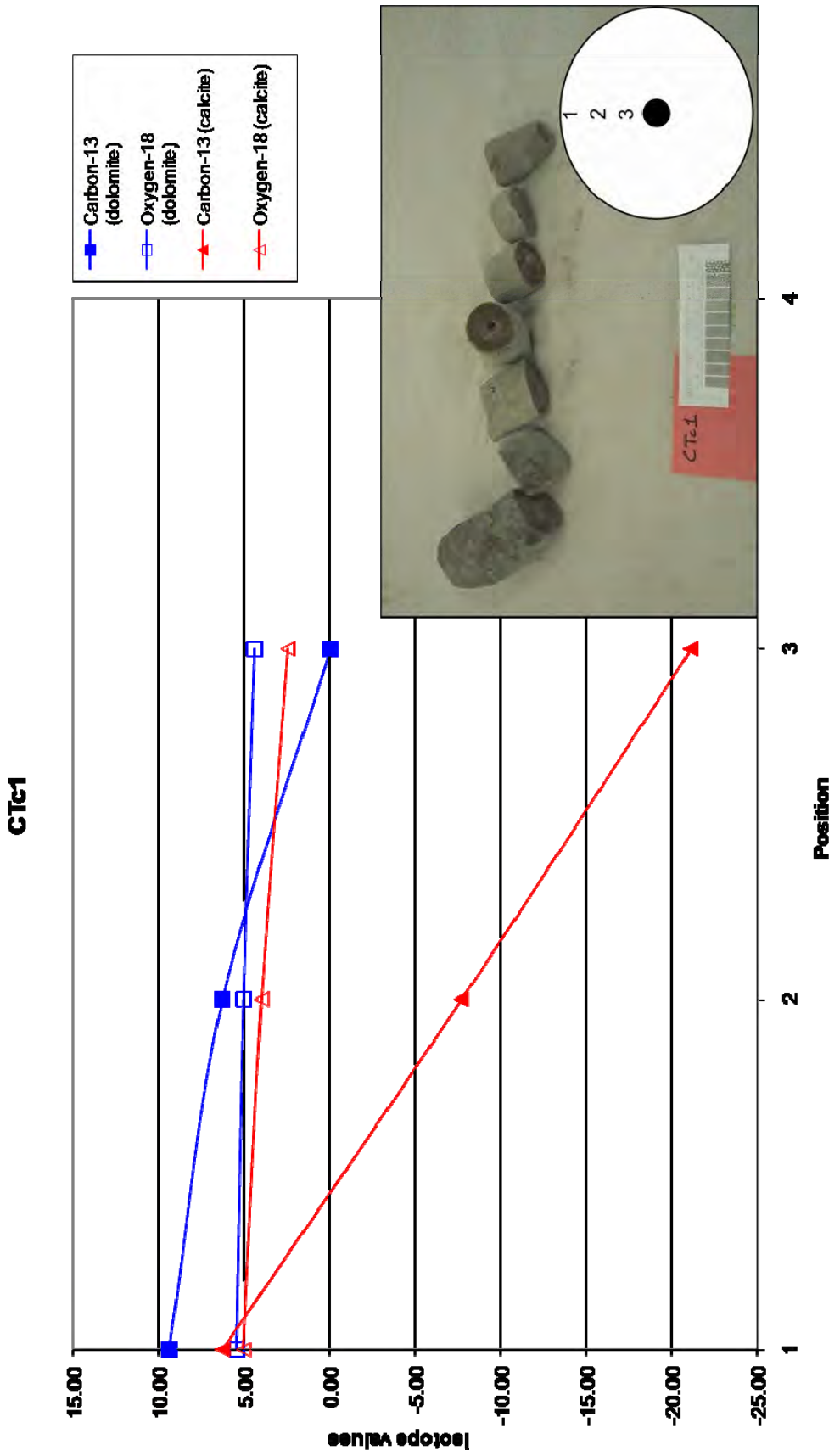
CTc1
Carbon-13 (dolomite)
Oxygen-18 (dolomite)
Carbon-13 (calcite)
Oxygen-18 (calcite)
Isotope values
15.00
10.00
5.00
0.00
-5.00
-10.00
-15.00
-20.00
-25.00
1
2
3
4
Position
CTc1

Appendix 3

East Cape

East Cape table of contents

1. Location

The East Cape occurrence involves three main outcrop sections from Te Araroa to East Cape. Table A3.1 and Figures A3.1 to A3.3 have detailed information for the sites locations. All access to outcrops is on public beaches. A majority of the concretions are exposed 3 to 4 hours either side of low tide, whereas a few are exposed only 1 hour either side of low tide. Tide hazards are not an issue at Hororera Point and Whararikí Point, however at Wharenaonao Point coastal cliffs leave few exit points.

Table A3.1. Field locations and descriptions

Location	Topo map	GIS	Access and comments	Outcrop	Source information
Horoera Point	Z14	E2992073, N6381198 to E2993044, N6381424	East side of short bridge after Dewes Road on East Cape Road	Best East Cape location, morphologies are dominated by doughnuts with some flower pots and pipes	Kathy Campbell and Murray Gregory
Wharenaonao Point	Z14	E2996651, N6377906 to E2995705, N6378770	Either side of point before lighthouse. Cape side is closer but crosses private property (owner unknown).	Mostly spherical concretions, potentially some tubular but highly weathered and unable to discern	Kathy Campbell and Murray Gregory
Whararikí Point	Z14	E2988880, N6382342 to E2987531, N6382641	East Cape Road, sandy beach north end before river	Scattered low volume of occurrences, but many pipes	Kathy Campbell and Murray Gregory
Awatere River	Z14	E2984529, N6382528	East Cape Road and Awatere River, north side of bridge	None *in situ* , but pieces found in river	Kathy Campbell and Murray Gregory
Tangakaka Stream	Z14	E2979730, N6373090 to E2980292, N6372709	E2980110, N6375310, bridge on Whakaangiangi Road	Many tubular concretions and 'stacked doughnuts' in stream	Martin Crundwell

1.2 Regional map

Figure A3.1. Regional map of Raukumara Peninsula and the four main study locations.

1.3 Local map of outcrops

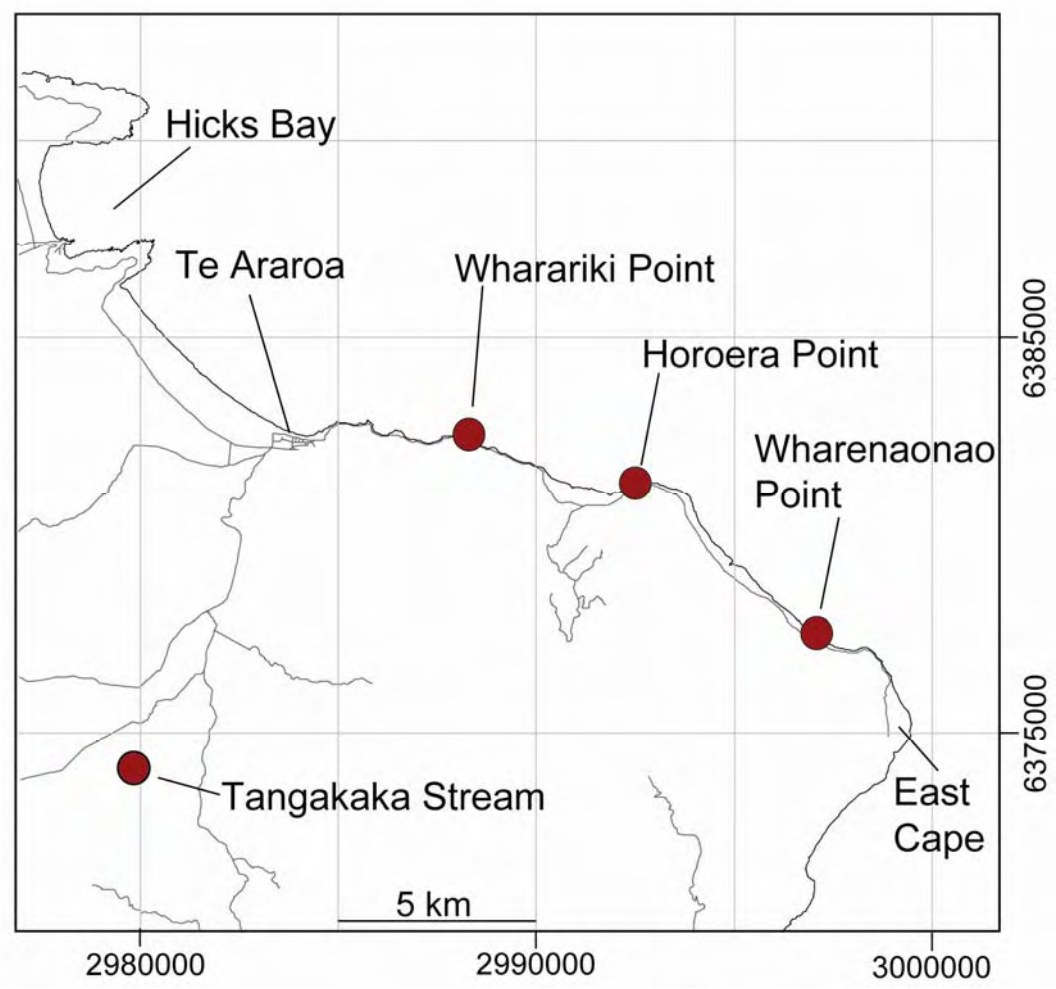

Figure A3.2. Local map of the four main outcrops.

1.4 Map of Horoera Point and concretion distribution

Figure A3.3. Map of Horoera Point and concretion distribution. This map corresponds to Table 1 and Figure 10 in Chapter 5. The letters on Figure A3.3 correspond to locations marked on aerial photographs in Section 2 (Figs. A3.4 to A3.11). Numbers 1 – 5 at the bottom of the map correspond to locations of photographs described Table A3.2.

2. Aerial Photographs

Aerial photographs were taken in a helicopter, piloted by John Campbell in 2007. The photographs document the distribution of concretions on the shore platform and their spatial relationship with faults. Figures A3.4 to A3.11 show a series of aerial photographs used to map the structural aspects of the outcrop. Letters on photographs correspond to locations on the distribution map in Figure A3.3. Table A3.2 is a catalogue of the remaining aerial photographs (Fig. A3.12) and includes brief descriptions. All photographs from Section 2 are on DVD (Appendix\EastCape\AerialPhoto).

Figure A3.4. Aerial photograph of Horoera Point. Letters correspond to Figure A3.3.

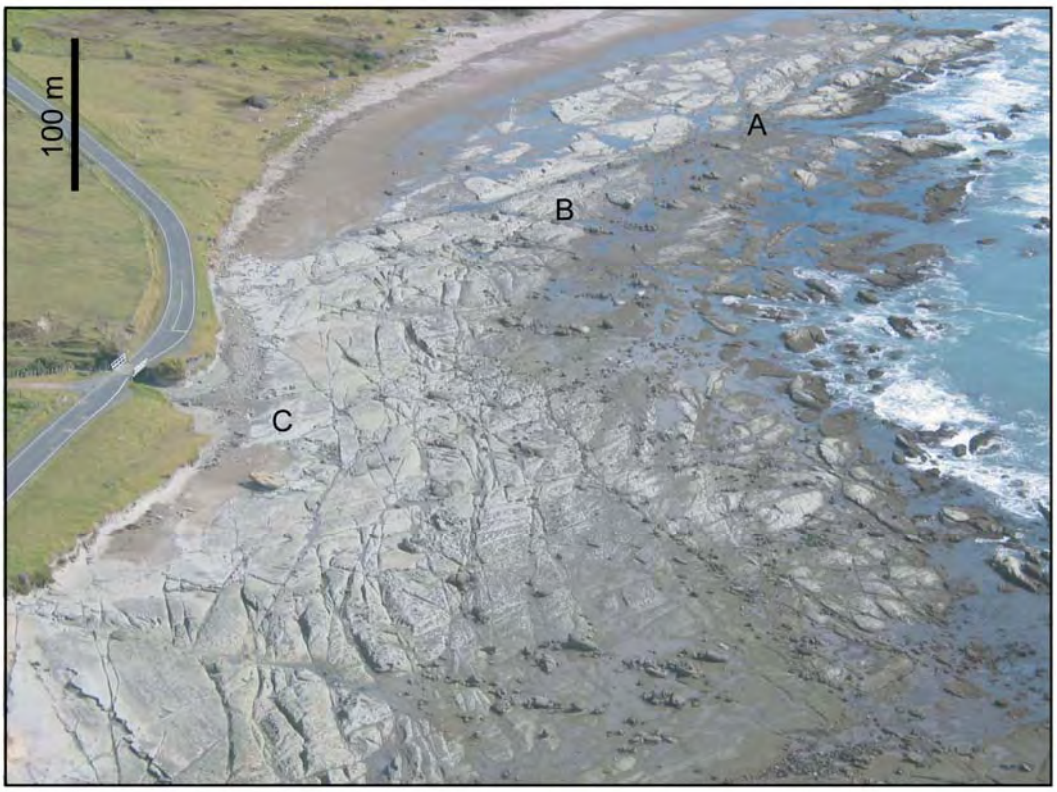

Figure A3.5. Aerial photograph of Horoera Point at location 1 and 2 (see Fig. A3.3 and Table A3.2). Letters correspond to locations in Figure A3.3.

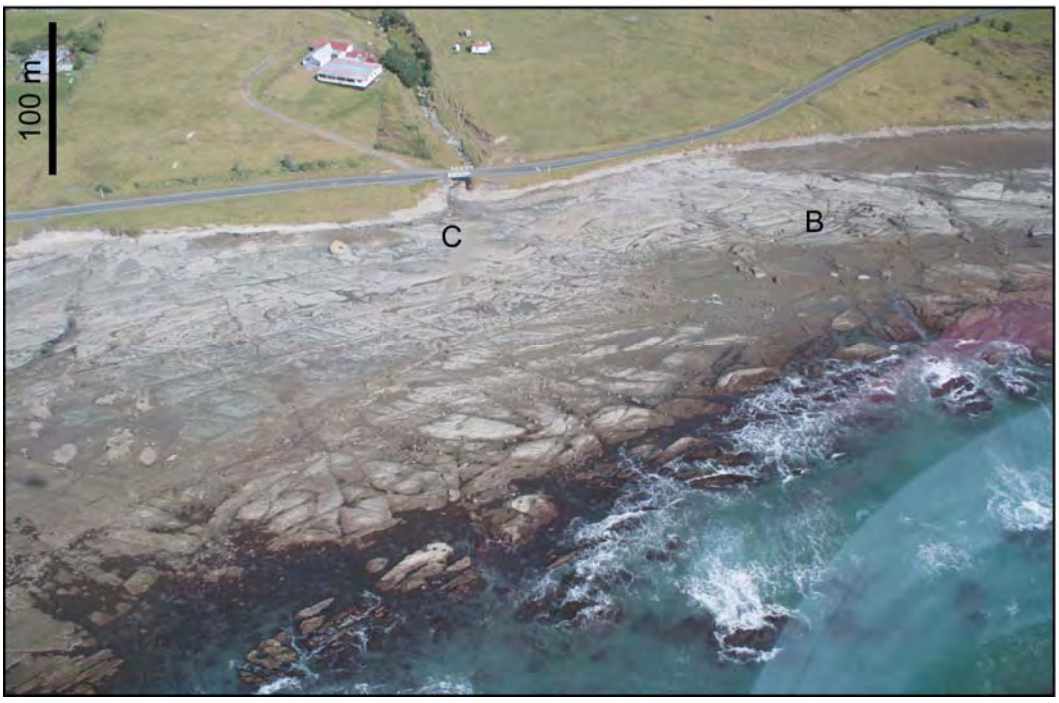

Figure A3.6. Aerial photograph of Horoera Point at location 2 (see Fig. A3.3 and Table A3.2). Letters correspond to locations in Figure A3.3.

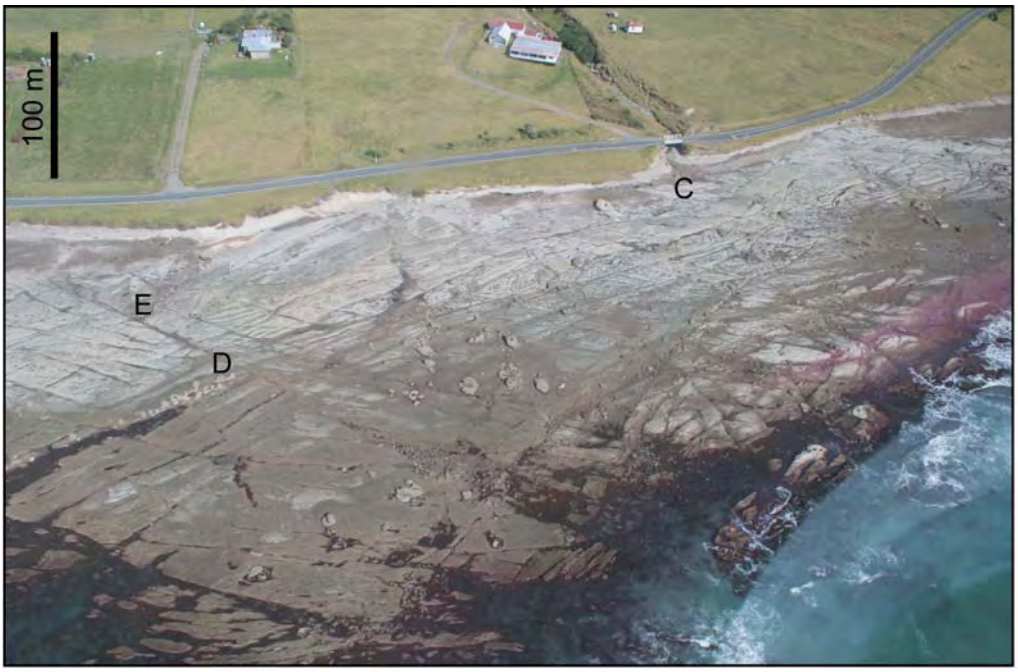

Figure A3.7. Aerial photograph of Horoera Point at location 2 and 3 (see Fig. A3.3 and Table A3.2). Letters correspond to locations in Figure A3.3.

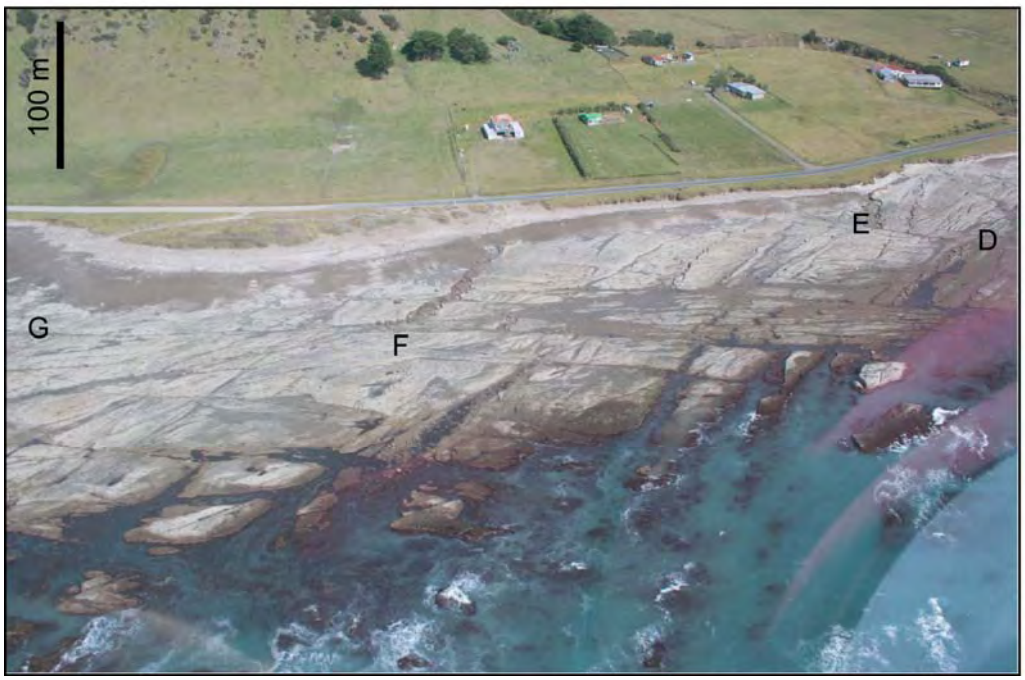

Figure A3.8. Aerial photograph of Horoera Point at location 3 and 4 (see Fig. A3.3 and Table A3.2). Letters correspond to locations in Figure A3.3.

Figure A3.9. Aerial photograph of Horoera Point at east end of location 3 (see Fig. A3.3 and Table A3.2). Letters correspond to locations in Figure A3.3.

Figure A3.10. Aerial photograph of Horoera Point at location 3 and 4 (see Fig. A3.3 and Table A3.2). Letters correspond to locations in Figure A3.3.

Figure A3.11. Aerial photograph of Horoera Point at the east end of location 3 to location 5 (see Fig. A3.3 and Table A3.2). Letters correspond to locations in Figure A3.3.

Table A3.2. Descriptions of aerial photographs in Figure A3.12.

Photograph jpg no.	Location (see Fig. A3.3)	Comment
3448	1	Main outcrop, examples of doughnuts aligned along a fault
3453	3-5	Overview of Horoera Point, view to the east
3454	2	B to C of distribution map
3455	2	Large doughnut visible to the left of bridge
3456	2-3	Note intersection of two major faults (bottom left); at least 13 doughnut concretions (debris) are present and highly fractured
3457	3	E to F of distribution map; both turbidites are visible
3458	3	E to F of distribution map; both turbidites are visible
3464	1-5	Overview of Horoera Point, view to the west; main outcrop is located in upper left
3465	1-5	View of conjugate faults in the eastern outcrop (I, bottom of photograph)
3466	1-5	View of conjugate faults in the eastern outcrop; the protruding rocks are all tubular concretions or concretion debris (unidentifiable due to extent of weathering)
3467	1-4	Largest example of a doughnut is partially exposed in the sand (lower left) and is estimated to be at least 8 m in diameter
3468	2-3	Close up of 3456
3469	2	Best doughnut example to the left of bridge
3470	1-2	Note the alignment of concretions along faults
3471	1	Further extent of 3448
3472	1	Further extent of 3448
3477	3	Turbidites and intersecting faults, this part of the outcrop is void of concretions
3480	4-5	Concretions in east side of outcrop are more weathered than the west side. Here, most are concretionary debris. Note the high concentration in left side of image
3497	3	Turbidite (E, upper right and F, middle)
3498	3	Futher extent of 3497
3506	2	Close up of main doughnut
3507	2	Note the deformed and fractured doughnut in upper right (C); deformed shape suggestive of partial formation during fault rupture

Table A3.2 continued.

Photograph jpg no.	Location (see Fig. A3.3)	Comment
3527		Photograph of Wharenaonao Point; this outcrop has less concretions, many undecipherable due to weathering
3554		Sets of conjugate faults east of Horoera Point
4997	3	Close up of faults east of the turbidites (F)
4998	3	Close up of faults adjacent to turbidite (E)
5000	2-3	Several fractured doughnuts in major fault intersection (3456); note from middle to upper right, 8 doughnuts are aligned
5001	2	From middle left to right, 3 doughnuts aligned
5003	1-2	The two most prominent tapered concretions (middle left and center)
5013	3-4	Turbidites in centre
5014	3-4	Turbidites in centre
5015	2	Westward view of main (partial) outcrop
5016	1-2	Concretionary debris to left and doughnuts to right
5017	1	B of distribution map
5018	1	Close up (left side of 3448)
5019	1	Close up (middle of 3448)
5020	1	Close up (right of 3448)
5029	1-3	Higher altitude photograph of western turbidite and main outcrop
5030	1-2	Higher altitude photograph of western turbidite and main outcrop
5031	1	Alternative view of 3448; note the doughnuts are progressively broken towards the left of the photograph
5032	3-4	Faults and turbidites
5033	3-4	Faults and turbidites
5034	3-4	Faults and turbidites
5035	1-3	View of turbidites, major fault intersection, and main outcrop
5036	1-3	View of major fault intersection and main outcrop
5037	1-3	View of major fault intersection and main outcrop
5043	1-3	View of turbidites, major fault intersection, and main outcrop
5044	1-3	View of major fault intersection and main outcrop

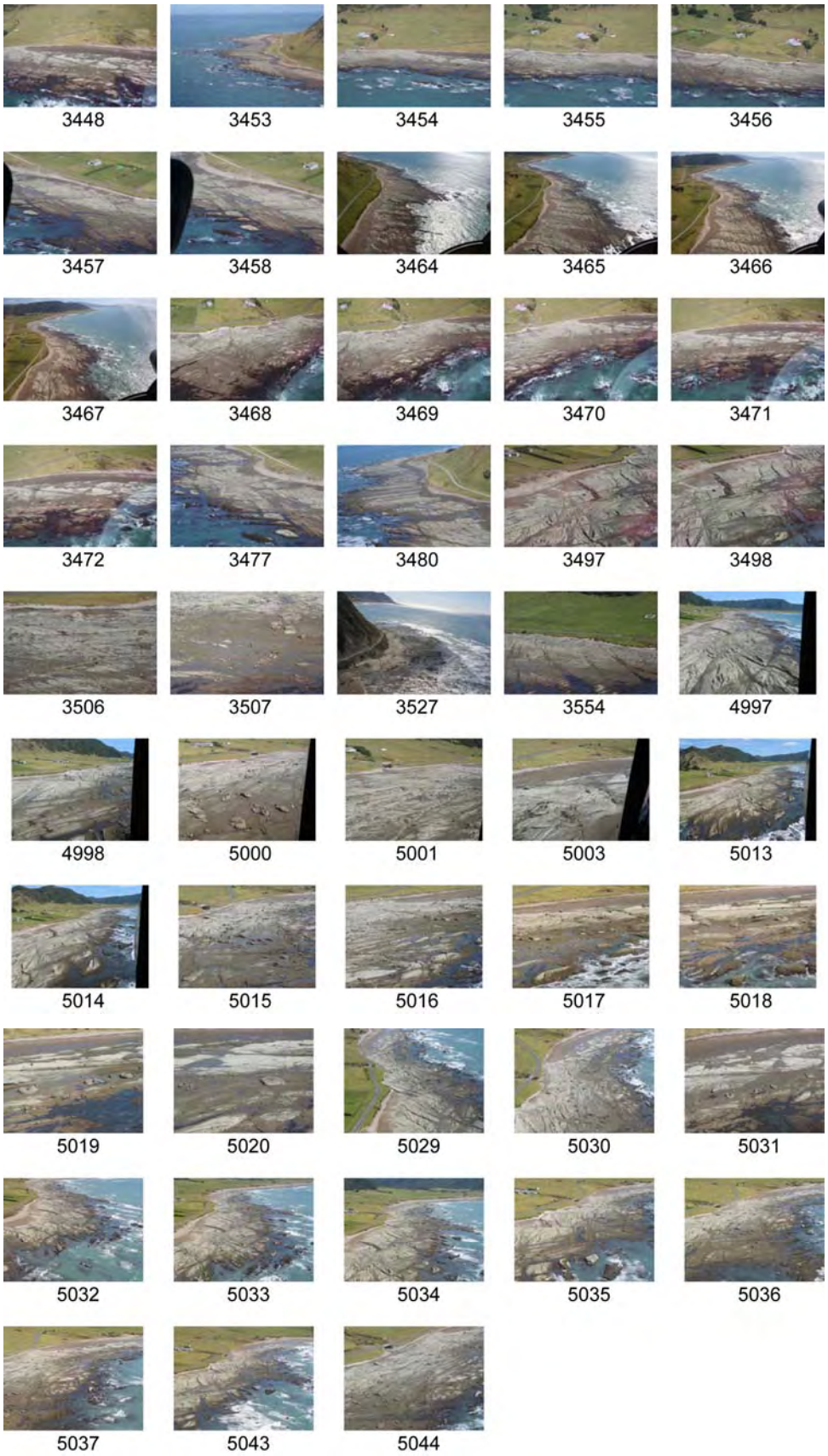

Figure A3.12. Aerial photograph catalogue. See Table A3.2 for descriptions.

3. Field photographs

Photographs of tubular concretions in the field are presented in this section along with brief descriptions in Tables A3.3 – A3.4 and Figures A3.13 and A3.14 (jpg number corresponds to that in Table). A DVD accompanies this volume, where the photographs can be viewed at a larger scale (Appendix\EastCape\ FieldPhotos).

Section 3.1 contains key field photographs from Horoera Point (Table A3.3, Fig. A3.13), Wharenaonao Point, Whararíki Point, and Tangakaka Stream (Table A3.4, Fig. A3.14). Section 3.2 contains photographs (Fig. A3.15) from GIS field mapping and corresponds to Chapter 5, Table 1 (DVD – Appendix \EastCape\GIS).

3.1 Tables and photographs of tubular concretions in the field

Table A3.3. Descriptions of field photographs

Photograph jpg no.	Location	Comment
7000	Horoera	Largest fully exposed doughnut (5 m diameter)
7001	Horoera	Side view of 7000
7002	Horoera	Conduit fill of 7000
7003	Horoera	Concial concretion
7004	Horoera	Close up of 7003, note the fracture pattern
7005	Horoera	View of inside 7003
7006	Horoera	Large pipe concretion, note the fracture pattern
7007	Horoera	View of the partially open conduit of 7006
7008	Horoera	Large doughnut with fractures in the same direction as nearby fault, note a 1/2 doughnut and doughnut (from 7000) in the background
7009	Horoera	Estimated to be the largest doughnut, at least 8 m in diameter
7010	Horoera	Close up view of inside 7005
7011	Horoera	Highly fractured partial doughnut
7012	Horoera	Large doughnut with two conduits on a fault, fracture orientation is the same as fault
7013	Horoera	Close up of 7012
7014	Horoera	Potentially a doughnut, but with a conduit located toward the outer margin instead of centrally
7015	Horoera	Bean shaped concretion with potentially a conduit in the centre
7016	Horoera	Linear concretion with multiple conduits along a fault (see Chapter 5, Fig. 18)
7017	Horoera	Additional view of 7016
7018	Horoera	Additional view of 7016
7019	Horoera	A partial dougnut extending from the end of the linear concretion in 7016; note 7015 in the background
7020	Horoera	Small concreted body adjacent to a fault
7021	Horoera	Broken doughnut, fractures oriented in same direction as fault, conduit not apparent
7022	Horoera	Small doughnut, note 7021 in background
7023	Horoera	Vertical pipe concretion with conduit
7024	Horoera	Another view of 7008
7025	Horoera	Small pipe with pinhole conduit
7026	Horoera	Conical concretion with large open conduit
7027	Horoera	Close up of 7026

Table A3.3 continued.

Photograph jpg no.	Location	Comment
7028	Horoera	Concretion with conduit, highly fractured
7029	Horoera	Rounded concretion with conduit
7030	Horoera	Pipe concretion with small conduit
7031	Horoera	Highly fractured smal dougnut with open conduit
7032	Horoera	Large rounded concretion with conduit
7033	Horoera	Open conduit of 7032
7034	Horoera	Pipe concretion with conduit on the side
7035	Horoera	Pipe concretion with open conduit
7036	Horoera	Pipe concretion with open conduit
7037	Horoera	Four pipes with open conduits
7038	Horoera	Pipe concretion with open conduit
7039	Horoera	Pipe-like concretion with two conduits
7040	Horoera	Pipe concretion with open conduit
7041	Horoera	7039 and 7040
7042	Horoera	Western turbidite
7043	Horoera	Western turbidite
7044	Horoera	Dip of western turbidite
7045	Horoera	Fault (normal) crossing turbidite
7046	Horoera	Fault (dip-slip) crossing turbidite, right-lateral, right side down thrown
7047	Horoera	View of lateral displacement in 7046
7048	Horoera	Doughnut along a fault shear zone
7049	Horoera	Concretions aligned along a fault
7050	Horoera	Deformed doughnut along a fault
7051	Horoera	Small conjugate fault sets
7052	Horoera	Small conjugate fault sets
7053	Horoera	Small conjugate fault sets
7054	Horoera	Doughnuts aligned along a fault
7055	Horoera	Additional view of 7054
7056	Horoera	Centimetre displacement of a doughnut
7057	Horoera	Additional view of 7056
7058	Horoera	Vertical displacement along a fault
7059	Horoera	Additional view of 7058
7060	Horoera	Additional view of 7058
7061	Horoera	Conjugate fault sets
7062	Horoera	Conjugate fault sets
7063	Horoera	Eastern limit of linear concretion along a fault; note large doughnut (7000) in background
7064	Horoera	Western limit of linear concretion along a fault
7065	Horoera	Small doughnut extending from the eastern limit of the linear concretion
7066	Horoera	Additional view of 7065

Figure A3.13. Photographs of tubular concretions at Horoera Point. See table A3.3 for descriptions.

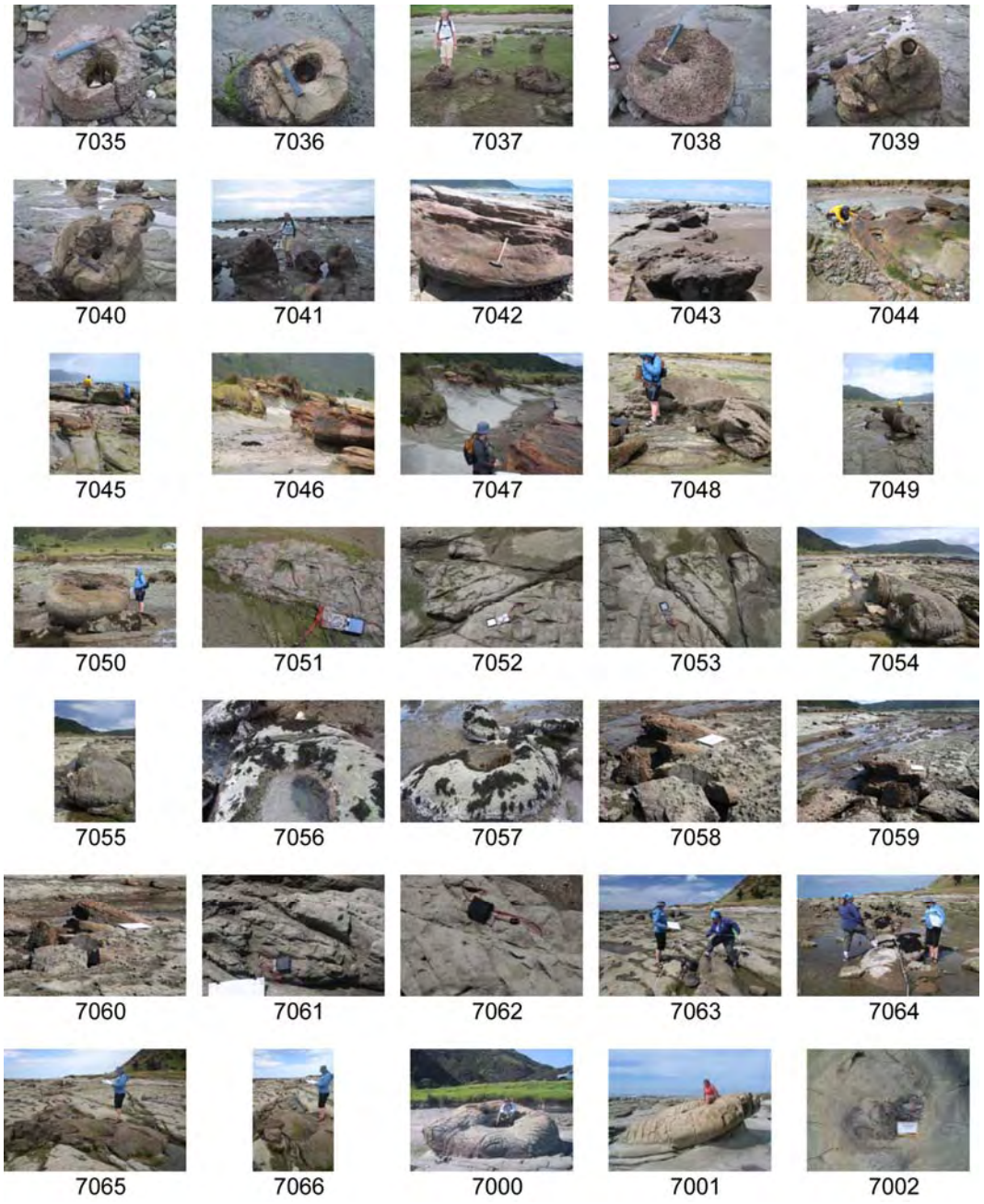

Figure A3.13 continued.

Table A3.4. Descriptions of field photographs.

Photograph jpg no.	Location	Comment
1331	Wharenaonao	Small pipe concretion with pinhole conduit
1332	Wharenaonao	Typical spherical concretion
1339	Wharenaonao	Spherical concretion with open centre, potentially a nucleation centre
1346	Wharenaonao	Concretion with small open conduit in centre and potentially a conduit exposed vertically in the front
1347	Wharenaonao	Pipe concretion with open conduit
1350	Wharenaonao	Pipe concretion with open conduit
1351	Wharenaonao	Pipe concretion with open conduit
1352	Wharenaonao	Small concretion along a fault with conduit
1355	Wharenaonao	Two pipe-like concretions potentially with conduits
1422	Whararíki	Small concretion with zonation
1423	Whararíki	View of 1422 along fault; note more concreted material further along fault
1424	Whararíki	Small pipe concretion with pinhole conduit
1426	Whararíki	Remains of a pipe concretion with open conduit
1427	Whararíki	Small pipe with cross section of conduit exposed
1428	Whararíki	Large roudned concretion with three conduits
1429	Whararíki	Curved concretion slab
1430	Whararíki	Concretion cross-cut by fault
1433	Whararíki	Rounded concretions with small conduits
1434	Whararíki	Small pipe with open conduit along a fault
1438	Whararíki	Small pipe with open conduit along a fault
1439	Whararíki	Small pipe with open conduit along a fault
1441	Whararíki	Large pipe concretion in background and small pipe with open conduit in foreground
1444	Whararíki	Additional view of 1441
1447	Whararíki	Highly fractured pipe with open conduit
1450	Whararíki	Concretion eroding out of the shore platform
1451	Whararíki	Concretion eroding out of the shore platform
1452	Whararíki	Small pipe with conduit
1453	Whararíki	Small curved slabby concretion
1454	Whararíki	Additional view of 1453
1455	Whararíki	Fractured, irregular shaped concretion
1456	Whararíki	Pipe concretion with open conduit
1457	Whararíki	Additional view of 1456, note intersections of faults

Table A3.4 continued.

Photograph	Location	Comment
1459	Whararikí	At least five concretions aligned along a fault, each a conduit
1460	Whararikí	Additional view of 1459
1461	Whararikí	Close up of conduit from 1459
1462	Whararikí	Linear concretion with protrusions nearby a fault
1464	Whararikí	Small pipe concretions with open conduits
1465	Whararikí	Large pipe concretion (notch next to person's hand is high tide mark)
6000	Tangakaka	Tubular shaped concretion with inter layers of finer grained mudstone; potentially stacked doughnut concretions
6001	Tangakaka	Additional view of 6000
6002	Tangakaka	Additional view of 6000
6003	Tangakaka	Additional view of 6000
6004	Tangakaka	Pipe concretion
6005	Tangakaka	Pipe concretion with central conduit composed of more resistant material
6006	Tangakaka	Doughnut concretion with open conduit, highly fractured
6007	Tangakaka	Concretion boulder
6008	Tangakaka	Concretion boulder with pinhole conduit
6009	Tangakaka	Highly fractured pipe concretion with conduit
6010	Tangakaka	Layers of concreted material in the exposed mudstone
6011	Tangakaka	Concretion eroding out of the stream bed
6012	Tangakaka	Concreted material eroding out of the stream bed, ?layers
6013	Tangakaka	Yellow calcite filling fractures in a concretion
6014	Tangakaka	Concretion containing yellow calcite in fractures (6013)
6015	Tangakaka	Small concretions protruding out of the mudstone
6016	Tangakaka	Concreted material eroding out of the stream bed, ?layers
6017	Tangakaka	Concreted material eroding out of the stream bed, ?layers
6018	Tangakaka	Concreted material eroding out of the stream bed, ?layers

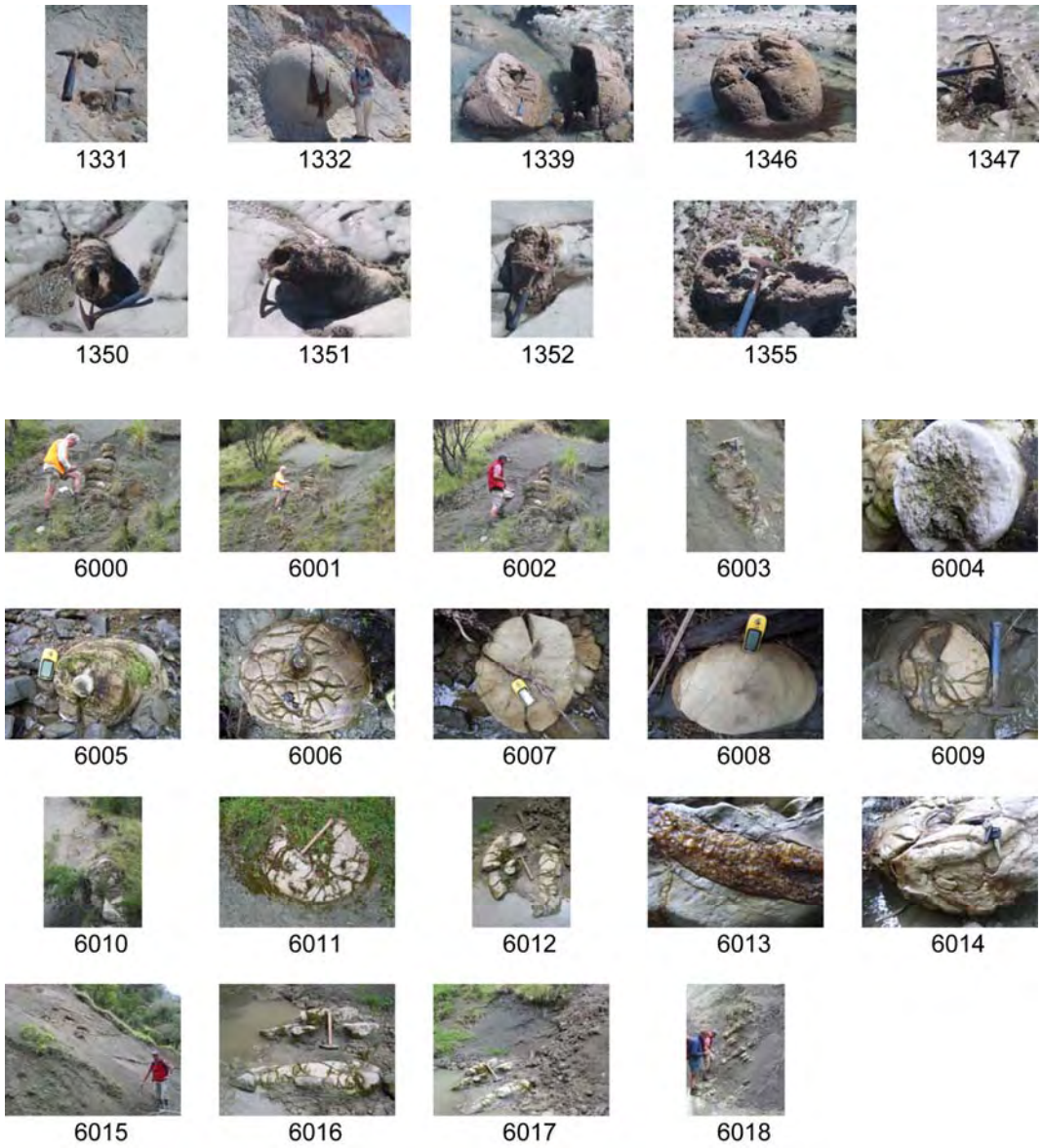

Figure A3.14. Field photographs from Whareanaro Point, Whararíki Point, and Tangakaka Stream. See table A3.4 for descriptions.

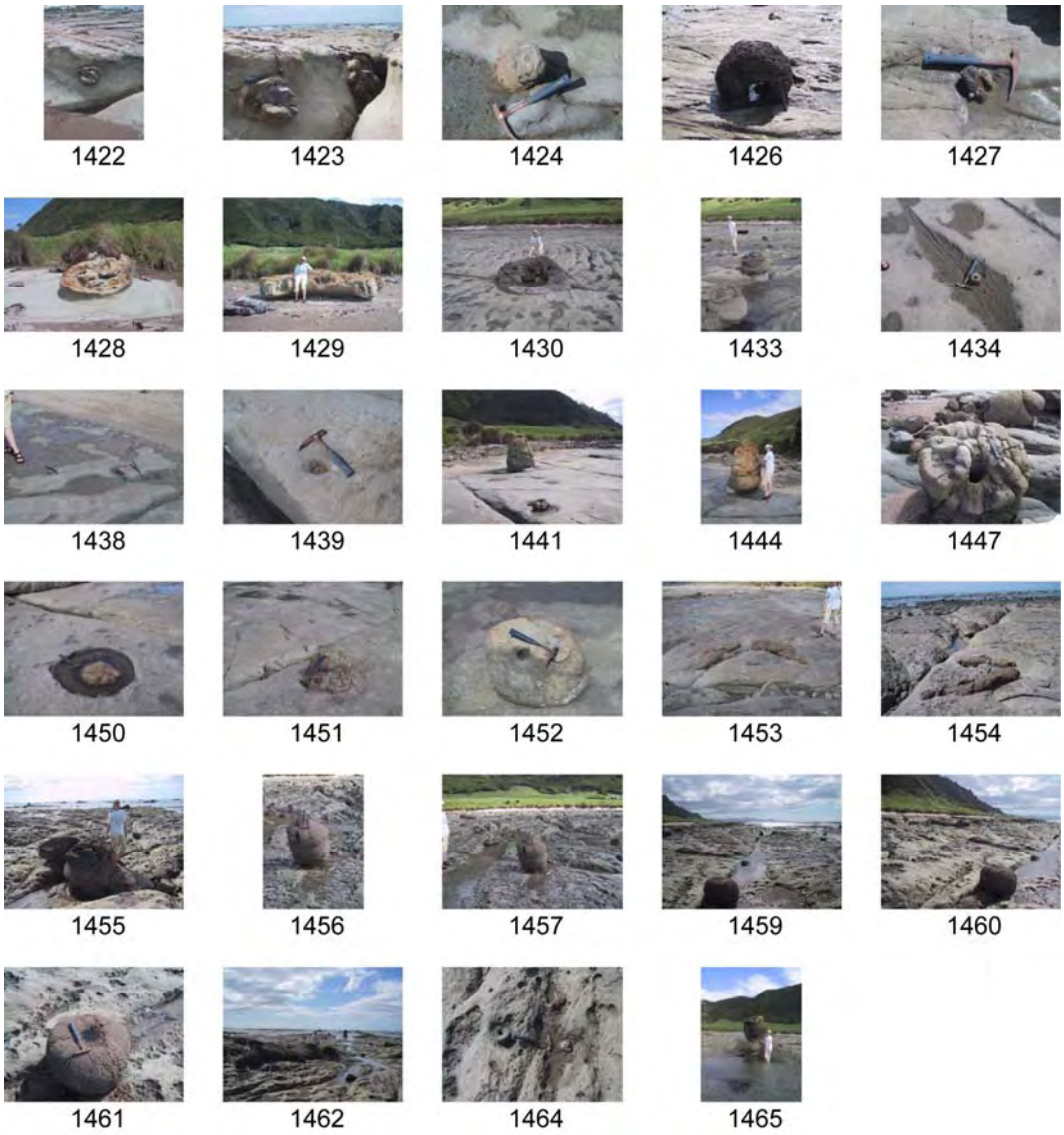

Figure A3.14 continued.

3.2 GIS mapping photographs

Figure A3.15. Field photographs from GIS mapping. See Chapter 5, Table 1 for descriptions of photographs.

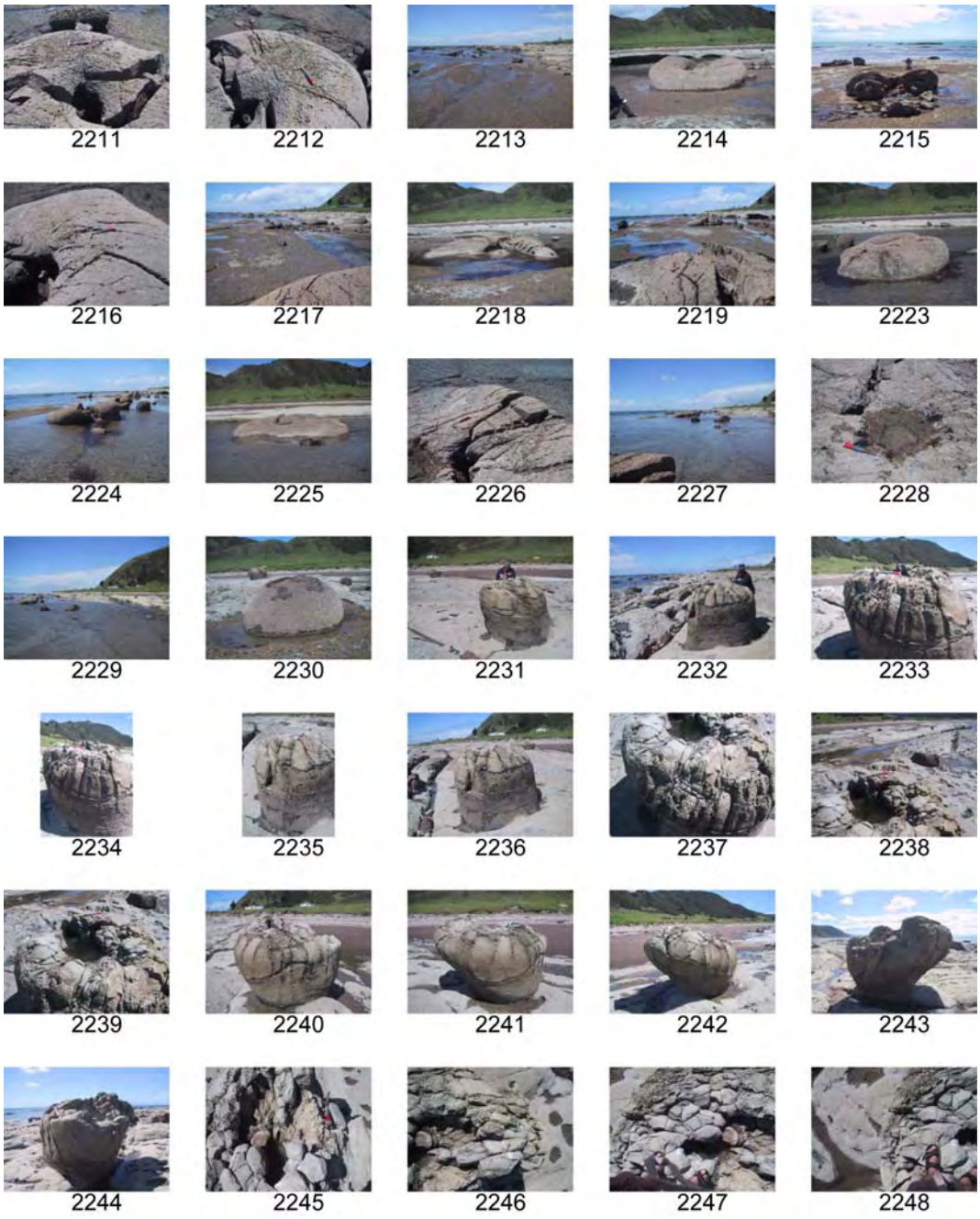

Figure A3.15 continued.

Figure A3.15 continued.

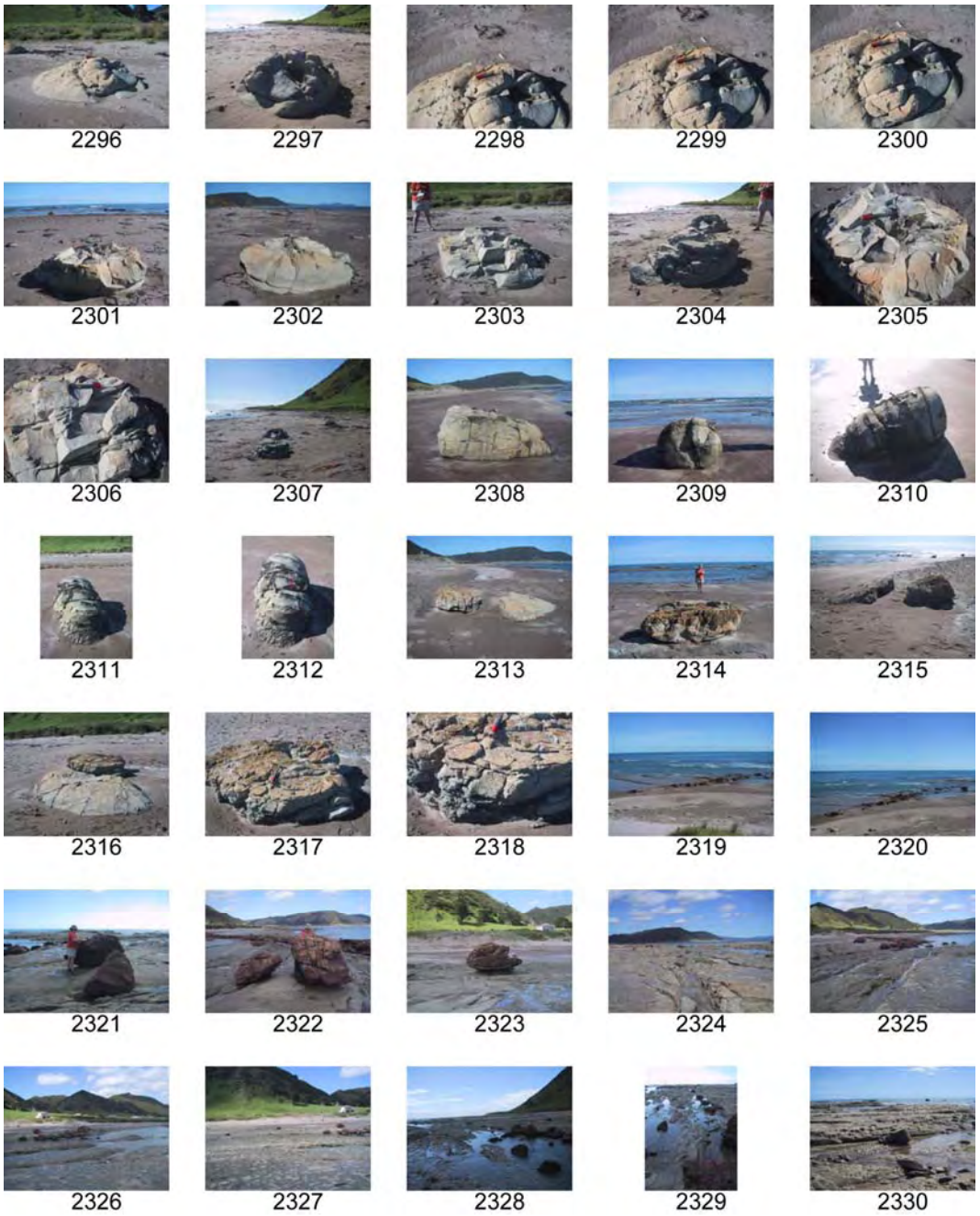

Figure A3.15 continued.

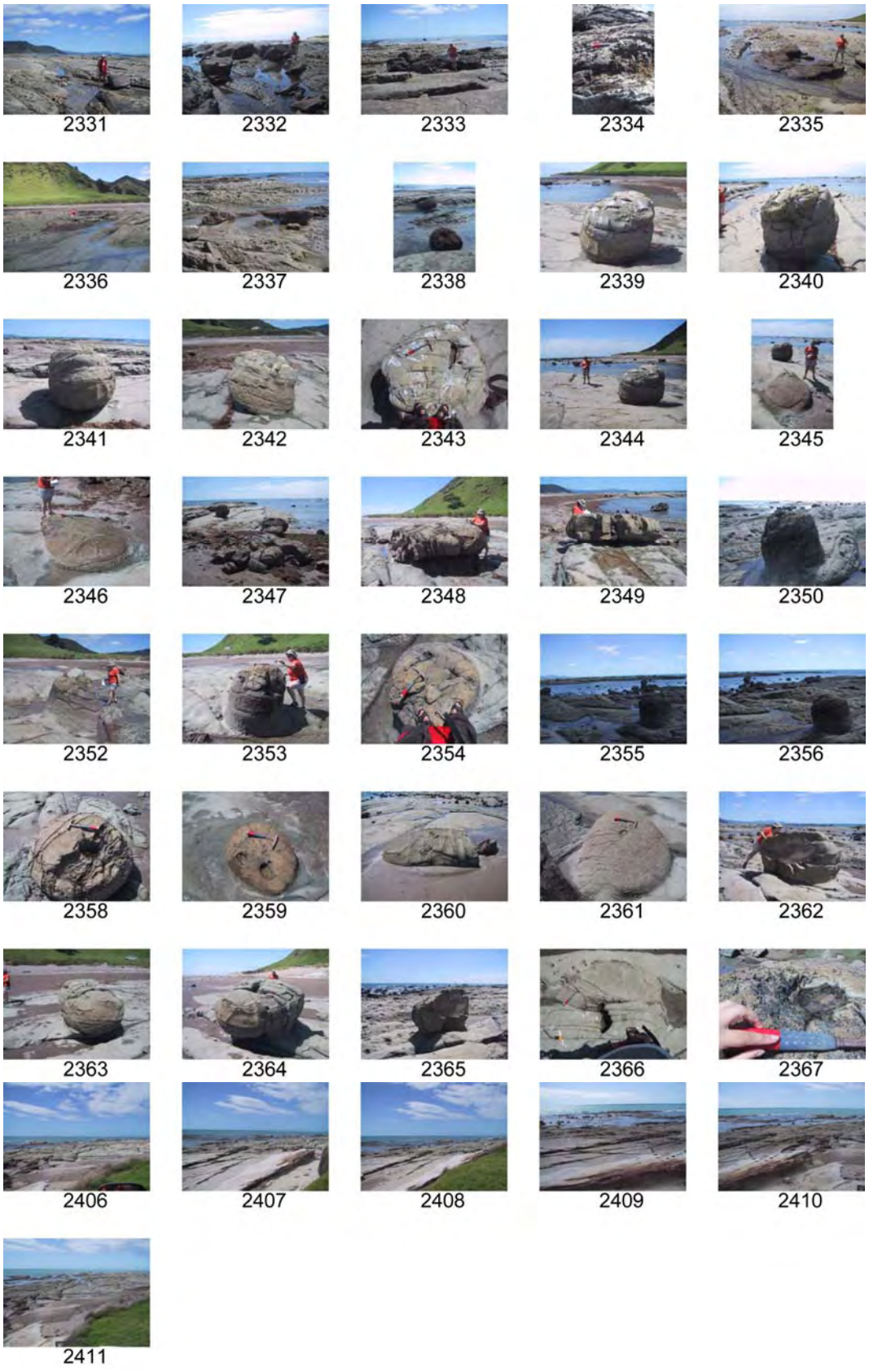

Figure A3.15 continued.

4. Samples

Tubular concretion samples are outlined in a Table A3.5. Sample names are followed by a hyphen. The number following the hyphen denotes a subsample along a cross-sectional transect (lower number = outer concretion, higher number = conduit/or adjacent to conduit if the conduit is open). The subsamples are treated as individual samples for petrographic and isotopic analyses. Subsample placement along the transect is shown in Appendix Section 9 (Isotope transects) accompanied by a photograph of the sample with transect location indicated.

Table A3.5. Sample list and descriptions. See Figure A3.3 for location.

UoW number	Sample number	Easting	Northing	Comment
20080267	ECD-1	2992360	6381281	Doughnut, outer (see JPG 7000 in Horoera field photographs)
20080268	ECD-2	2992360	6381281	Middle main concretion body
20080269	ECD-3	2992360	6381281	Middle main concretion body
20080270	ECD-4	2992360	6381281	Conduit/concretion border
20080271	ECD-5	2992360	6381281	Outer conduit
20080272	ECD-6	2992360	6381281	Conduit
20080273	FP1	2992208	6381195	Outer concretion
20080274	FP2	2992208	6381195	Mid structure, no clear
20080275	FP3	2992208	6381195	"conduit" but perhaps a large
20080276	FP4	2992208	6381195	conduit with thin concretionary
20080277	FP5	2992208	6381195	rim
20080278	FP6	2992208	6381195	Outer concretion
20080279	EC3-1	Horoera	Unknown GIS	Pipe outer
20080280	EC3-2	Horoera	Unknown GIS	Pipe mid
20080281	EC3-3	Horoera	Unknown GIS	Pipe conduit rim
20080282	EC2180-1	2992180	6381151	Newly exposed doughnut
20080283	EC2180-2	2992180	6381151	Newly exposed doughnut
20080284	EC2280-1	2992280	6381280	Linear pipe concretion along fault
20080285	EC2280-2	2992280	6381280	Linear pipe concretion along fault
20080286	EC2280-3	2992280	6381280	Linear pipe concretion along fault
20080287	EC2280-4	2992280	6381280	Linear pipe concretion along fault
20080288	EC2280-5	2992280	6381280	Linear pipe concretion along fault
20080289	EC2301-1	2992301	6381278	Doughnut at end of EC2280
20080290	EC2301-2	2992301	6381278	Doughnut at end of EC2280
20080291	EC2301-3	2992301	6381278	Host mudstone
20080292	EC2321-h	2992321	6381300	Host mudstone
20080293	EC2631-1	2992321	6381300	Conical concretion
20080294	EC2631-2	2992321	6381300	Conical concretion
20080295	EC2631-3	2992321	6381300	Conical concretion
20080296	EC2631-h	2992331	6381287	Host mst
20080297	EC2347-1h	2992347	6381297	Horizontal transect 1/2 doughnut
20080298	EC2347-2h	2992347	6381297	Horizontal transect 1/2 doughnut
20080299	EC2347-3h	2992347	6381297	Horizontal transect 1/2 doughnut

Table A3.5. Sample list and description.

UoW number	Sample number	Easting	Northing	Comment
20080300	EC2347-4h	2992347	6381297	Horizontal transect 1/2 doughnut
20080301	EC2347-5h	2992347	6381297	Horizontal transect 1/2 doughnut
20080302	EC2347-1v	2992347	6381297	Vertical transect 1/2 doughnut
20080303	EC2347-2v	2992347	6381297	Vertical transect 1/2 doughnut
20080304	EC2347-4v	2992347	6381297	Vertical transect 1/2 doughnut
20080305	EC2347-5v	2992347	6381297	Vertical transect 1/2 doughnut
20080306	EC2476-1	2992476	6381324	West turbidite
20080307	EC2476-2	2992476	6381324	West turbidite
20080308	EC2476-3	2992476	6381324	West turbidite
20080309	ECT			Eastward turbidite
20080310	EC2694-1	2992794	6381390	Host mudstone
20080311	EC2657-h	2992657	6381413	Host mudstone
20080312	EC2836-1	2992836	6381394	Conical concretion
20080313	EC2836-2	2992836	6381394	Conical concretion
20080314	EC2841-1	2992841	6381361	Conical concretion
20080315	EC2862-1	2992862	6381330	Largest doughnut
20080316	EC2862-2	2992862	6381330	Largest doughnut
20080317	EC2862-3	2992862	6381330	Largest doughnut
20080318	EC2862-4	2992862	6381330	Largest doughnut
20080319	EC2862-5	2992862	6381330	Largest doughnut
20080320	TK 1	2980210	6372680	Pipe
20080321	TK 2	2980177	6372685	Pipe
20080322	TK 3	2980177	6372685	Concreted material
20080323	TK 4	2980020	6372750	Bulbous with calcite healed veins
20080324	TK 5	2980008	6372770	Pipe with filled conduit
20080325	TK 6a	2979940	6372795	Conduit
20080326	TK 6b	2979940	6372795	Mudstone interlayer between concretion
20080327	TK 7a	2979797	6373009	Mudstone interlayer between concretion
20080328	TK 7b	2979797	6373009	Concretion
20080329	TK 7	2979797	6373009	Prismatic yellow calcite
20080330	TK 8	2979730	6373090	Unusual conduit fill
20080331	TK 9a	2975400	6373050	Concretion
20080332	TK 9b	2975400	6373050	Conduit
20080333	TK 10a	2975400	6373050	Concretion
20080334	TK 10b	2975400	6373050	Conduit

5. Photomicrographs

Photomicrographs of tubular concretions are presented in Figure A3.16 with brief descriptions in Table A3.6 and (jpg number corresponds to table). A DVD accompanies this volume, where the photomicrographs can be viewed at a larger scale (Appendix\EastCape\Petrography). A selection of subsamples were cut and mounted on glass slides for standard thin section analysis. No staining or impregnation was done on the thin sections. Further thin sections were not produced as the East Cape samples were predominately micritic carbonate within fine grained siliciclastics.

Table A3.6. Descriptions of photomicrographs. See Figure A3.16.

Sample	Photomicro-graph jpg no.	Comment
ECD-1	7100	Fine grained siliciclastic sediment and pyrite cemented by micritic dolomite (PPL) in the main concretion body of a doughnut (see Horoera field photographs JPG 7000)
ECD-1	7101	Cross polarized light of 7100
ECD-1	7102	Pyrite in between siliciclastic grains (PPL)
ECD-3	7104	Bioturbation in doughnut (7000) (PPL)
ECD-3	7110	Bioturbation of fine grained siliclastics in the conduit of a doughnut (PPL) (7000)
ECD-3	7111	Micritic dolomite cementing siliciclastics (CL of
ECD-3	7112	Fine grained siliciclastics in the conduit of a doughnut cemented by dolomite (PPL) (7000)
ECD-3	7113	Micritic dolomite cementing siliciclastics (CL of
ECD-3	7114	Bioturbation of fine grained siliclastics in the conduit of a doughnut (PPL) (7000)
ECD-3	7115	Micritic dolomite cementing siliciclastics (CL of
ECT	7124	Pristine quartz and feldspars in the western turbidite (PPL)
ECT	7125	Pristine quartz and feldspars in the western turbidite (XPL)

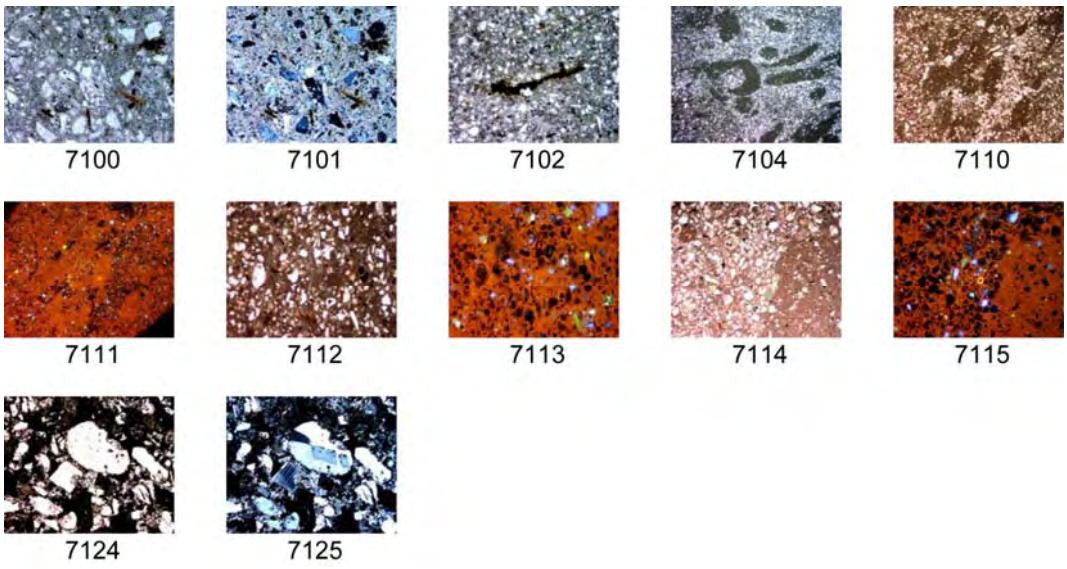

Figure A3.16. Photomicrographs of East Cape tubular concretions and conduits. See Table A3.6 for descriptions.

6. XRD graphs

Appendix Section 6 contains XRD graphs that are characteristic of pipe and bulbous concretions.

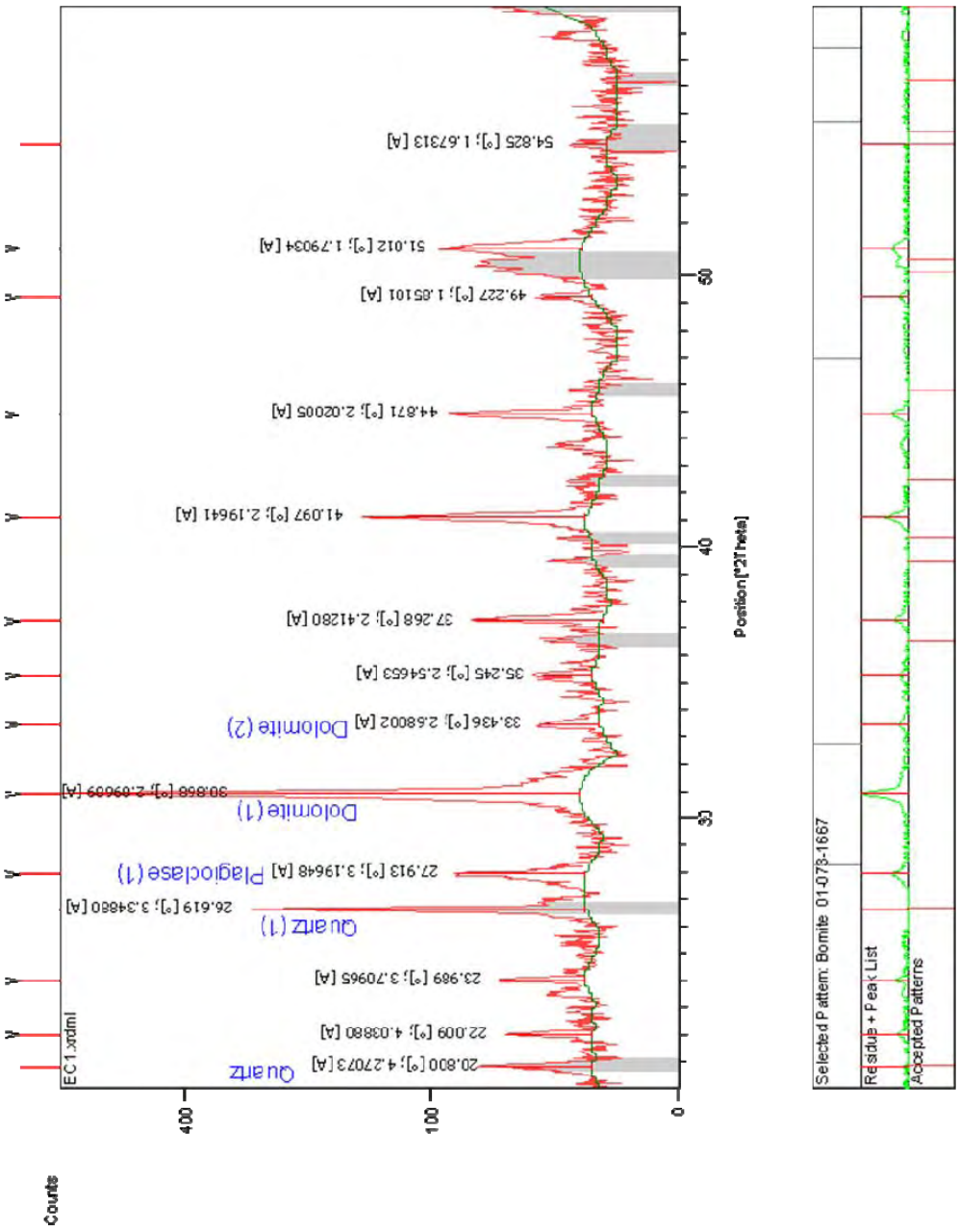
Counts
400
100
0
EC1.xrdml
Quartz
20.800 [°]; 4.27073 [Å]
22.009 [°]; 4.03880 [Å]
23.989 [°]; 3.70965 [Å]
Quartz (1)
26.619 [°]; 3.34880 [Å]
Plagioclase (1)
27.913 [°]; 3.19648 [Å]
Dolomite (1)
30.868 [°]; 2.89609 [Å]
Dolomite (2)
33.436 [°]; 2.68002 [Å]
35.245 [°]; 2.54653 [Å]
37.268 [°]; 2.41280 [Å]
41.097 [°]; 2.19641 [Å]
44.671 [°]; 2.02005 [Å]
49.227 [°]; 1.85101 [Å]
51.012 [°]; 1.79034 [Å]
54.825 [°]; 1.67313 [Å]
35
40
50
Position [°2Theta]
Selected Pattern: Bornite 01-078-1667
Residue + Peak List
Accepted Patterns

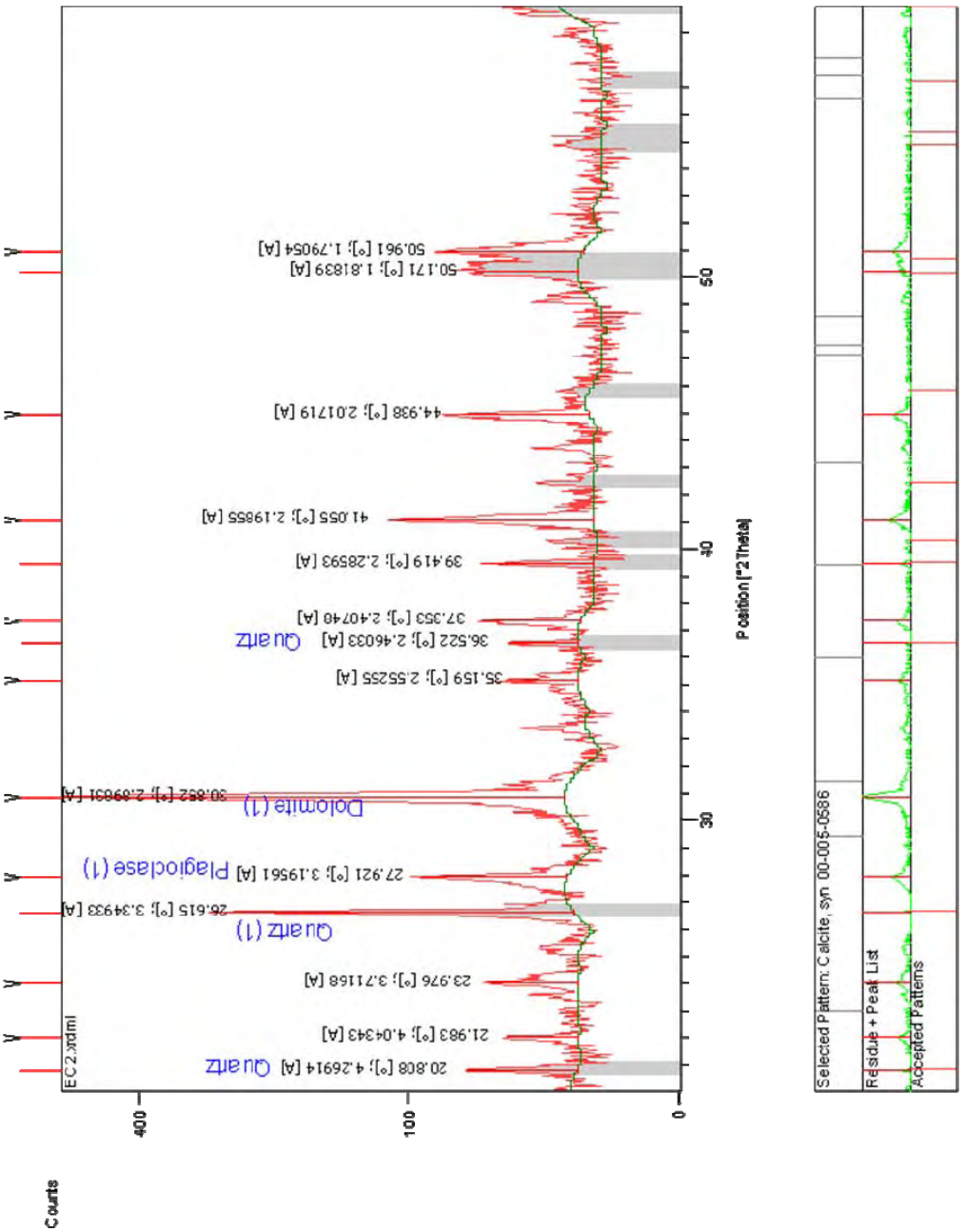
Counts
400
100
0
EC2.xrdml
20.808 [°]; 4.26914 [A] Quartz
21.983 [°]; 4.04343 [A]
23.976 [°]; 3.71168 [A]
26.615 [°]; 3.34933 [A] Quartz (1)
27.921 [°]; 3.19561 [A] Plagioclase (1)
30.852 [°]; 2.89831 [A] Dolomite (1)
35.159 [°]; 2.55255 [A]
36.522 [°]; 2.46033 [A] Quartz
37.353 [°]; 2.40746 [A]
39.419 [°]; 2.28593 [A]
41.055 [°]; 2.19855 [A]
44.938 [°]; 2.01719 [A]
50.171 [°]; 1.81839 [A]
50.961 [°]; 1.79054 [A]
30
40
50
Position [°2Theta]
Selected Pattern: Calcite, syn 00-005-0586
Residue + Peak List
Accepted Patterns

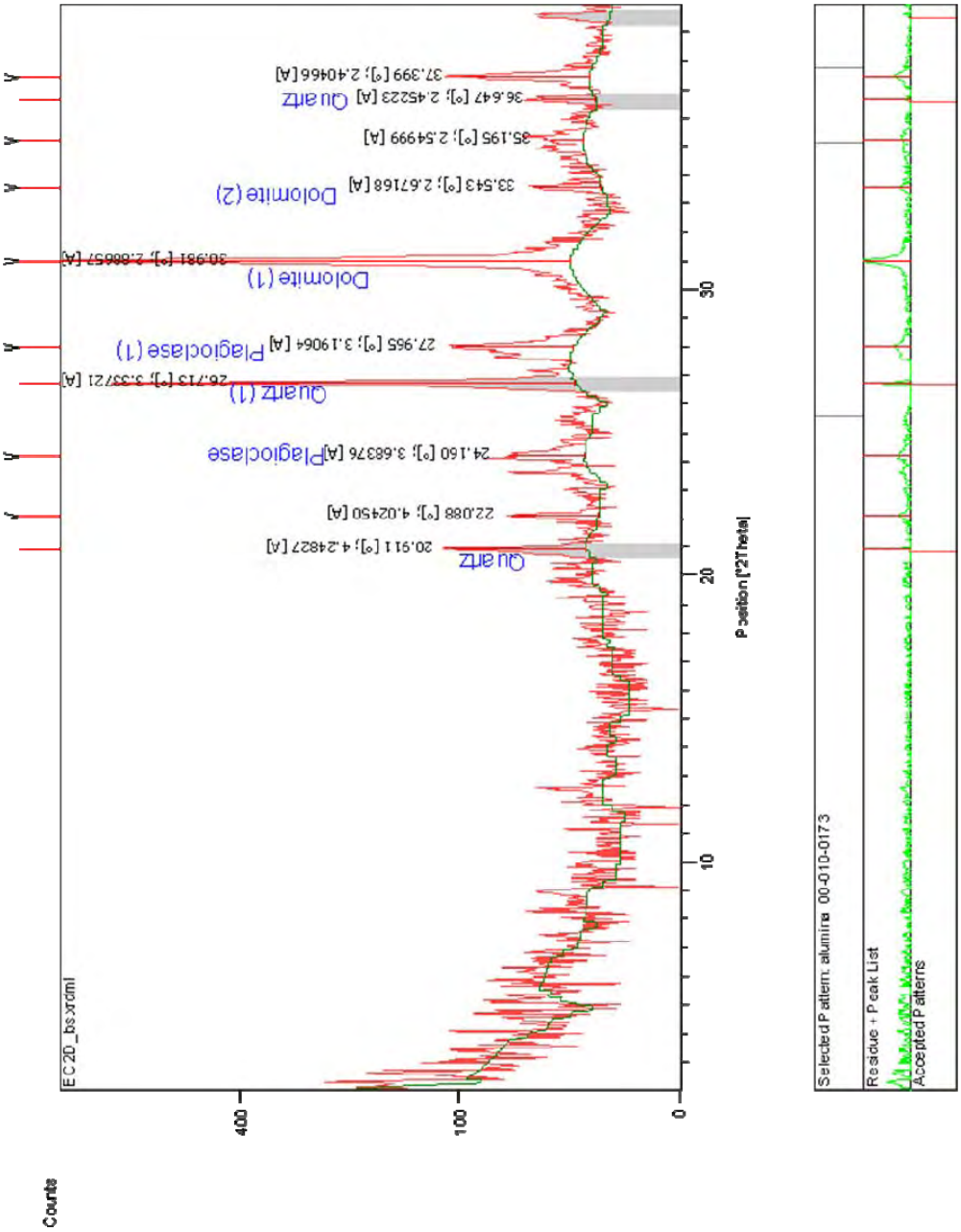
Counts
400
100
0
EC2D_bs.xrdml
10
20
30
Position [°2Theta]
20.911 [°]; 4.24827 [A]
Quartz
22.088 [°]; 4.02450 [A]
24.160 [°]; 3.68376 [A]
Plagioclase
26.713 [°]; 3.33721 [A]
Quartz (1)
27.965 [°]; 3.19064 [A]
Plagioclase (1)
30.981 [°]; 2.88657 [A]
Dolomite (1)
33.543 [°]; 2.67168 [A]
Dolomite (2)
35.195 [°]; 2.54999 [A]
36.647 [°]; 2.45223 [A]
Quartz
37.399 [°]; 2.40466 [A]
Selected Pattern: alumina 00-010-0173
Residue + Peak List
Accepted Patterns

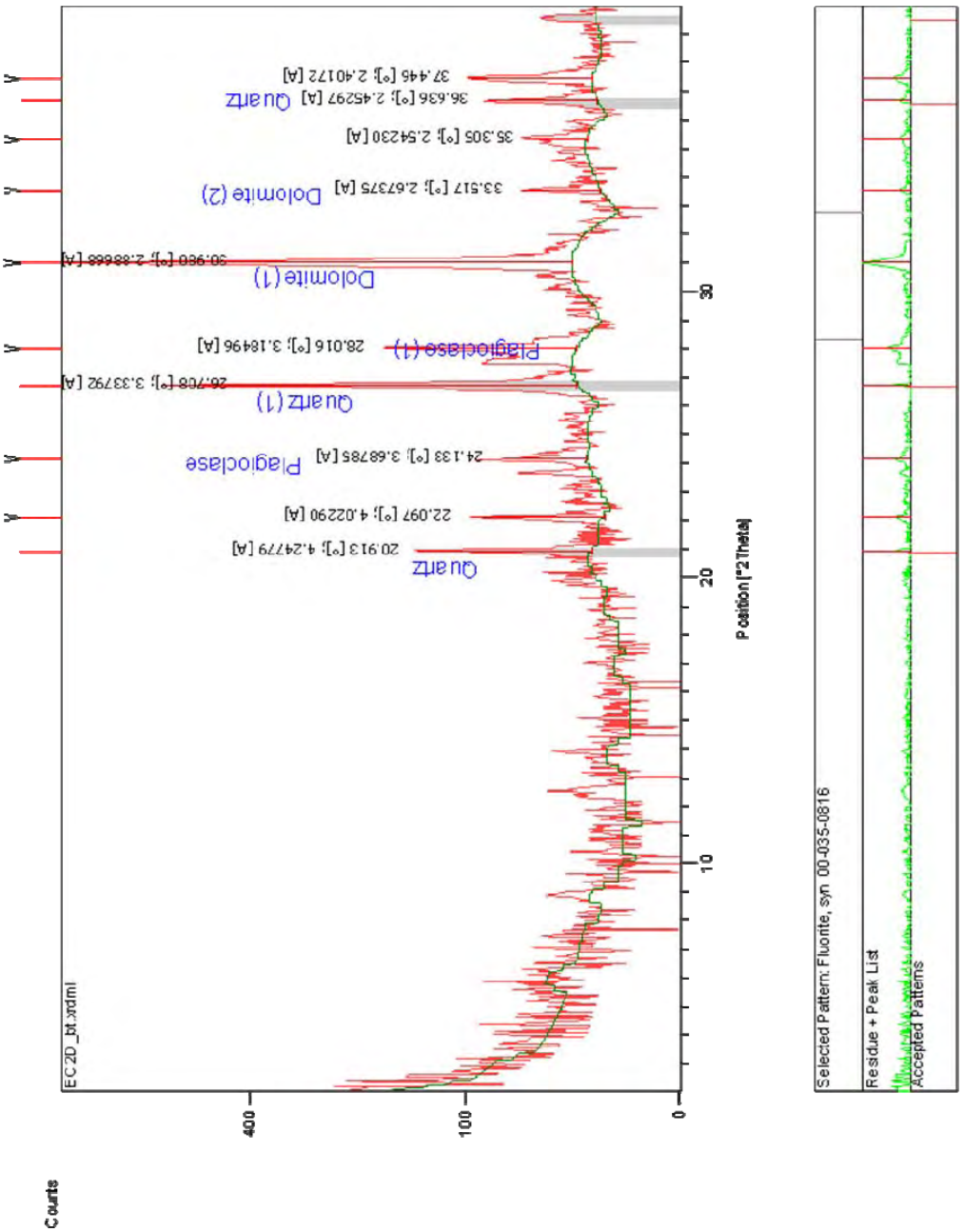
Counts
400
100
0
EC2D_bt.xrdml
10
20
30
Position [°2Theta]
Quartz
20.913 [°]; 4.24779 [A]
22.097 [°]; 4.02290 [A]
Plagioclase
24.133 [°]; 3.68785 [A]
Quartz (1)
26.768 [°]; 3.33792 [A]
Plagioclase (1)
28.016 [°]; 3.18496 [A]
Dolomite (1)
30.960 [°]; 2.88668 [A]
Dolomite (2)
33.517 [°]; 2.67375 [A]
35.305 [°]; 2.54230 [A]
Quartz
36.636 [°]; 2.45297 [A]
37.446 [°]; 2.40172 [A]
Selected Pattern: Fluorite, syn 00-035-0816
Residue + Peak List
Accepted Patterns

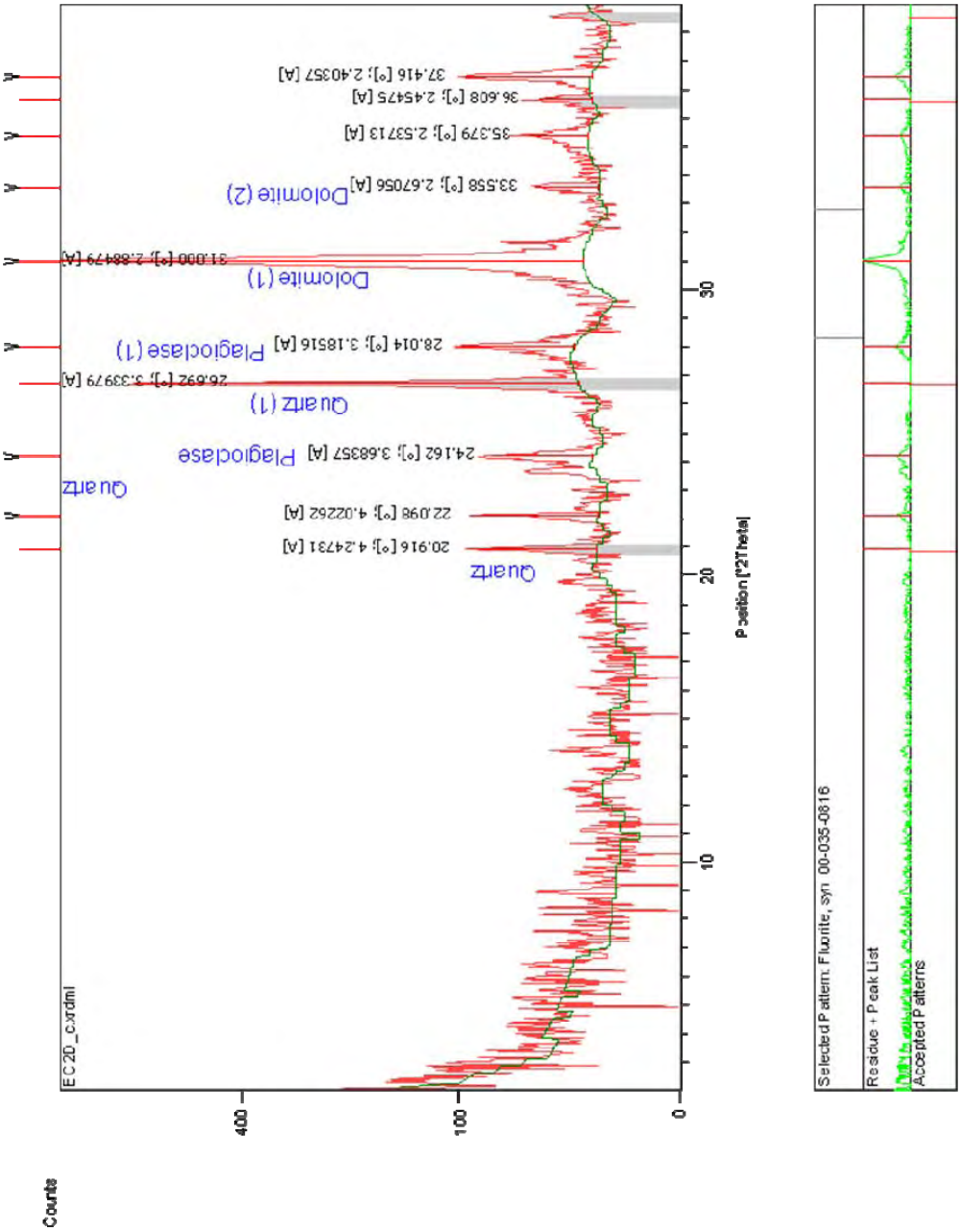
Counts
400
100
0
EC2D_c.xrdml
Quartz
20.916 [°]; 4.24731 [Å]
22.098 [°]; 4.02262 [Å]
Plagioclase
24.162 [°]; 3.68357 [Å]
Quartz (1)
26.692 [°]; 3.33979 [Å]
Plagioclase (1)
28.014 [°]; 3.18516 [Å]
Dolomite (1)
31.000 [°]; 2.88479 [Å]
Dolomite (2)
33.558 [°]; 2.67056 [Å]
35.379 [°]; 2.53713 [Å]
36.608 [°]; 2.45475 [Å]
37.416 [°]; 2.40357 [Å]
10
20
30
Position [°2Theta]
Selected Pattern: Fluorite, syn 00-035-0816
Residue + Peak List
Accepted Patterns

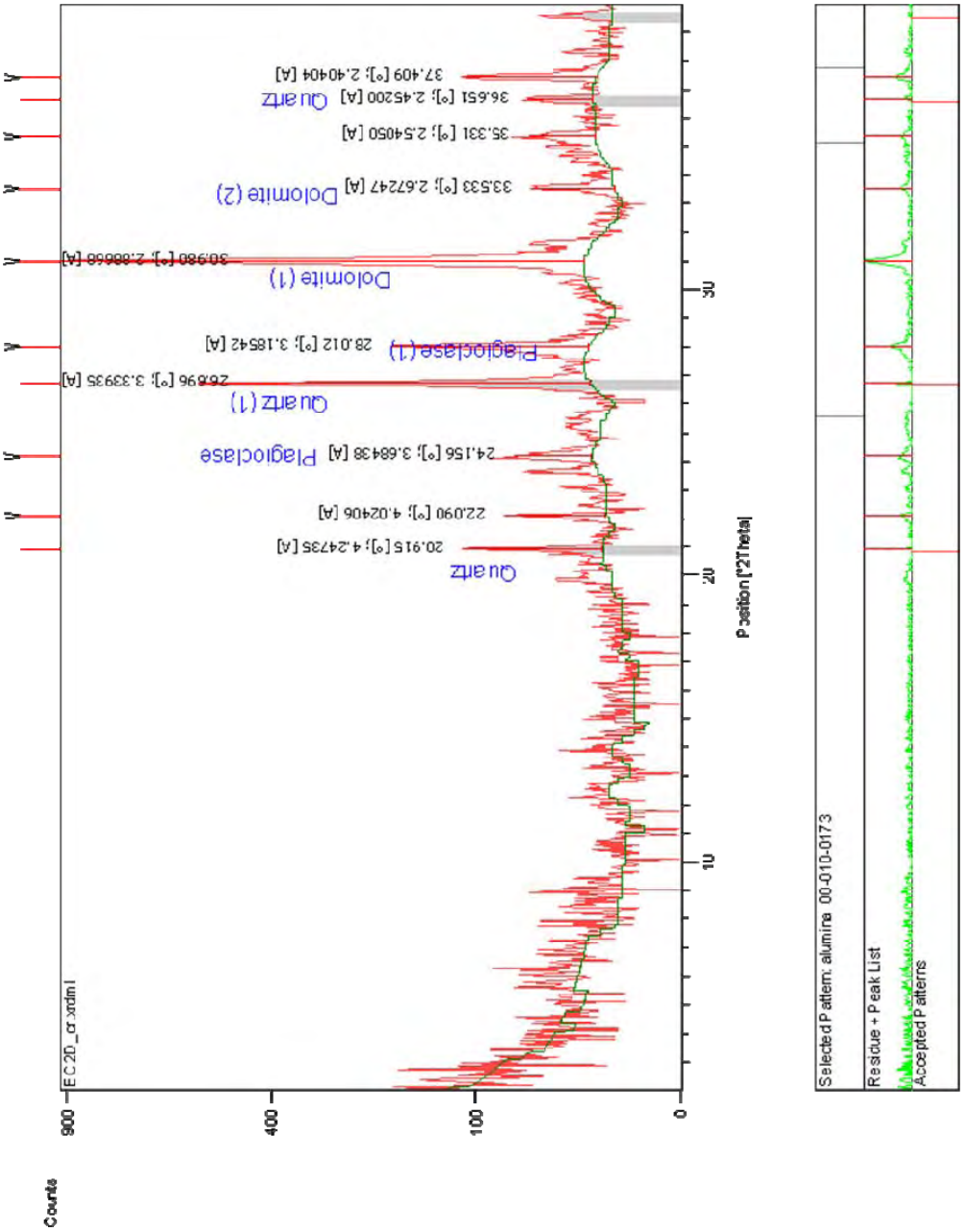
Counts
900
400
100
0
EC2D_cr.xdml
10
20
30
Position [°2Theta]
Quartz
20.915 [°]; 4.24735 [Å]
22.090 [°]; 4.02406 [Å]
Plagioclase
24.156 [°]; 3.68438 [Å]
Quartz (1)
26.696 [°]; 3.33935 [Å]
Plagioclase (1)
28.012 [°]; 3.18542 [Å]
Dolomite (1)
30.980 [°]; 2.88658 [Å]
Dolomite (2)
33.533 [°]; 2.67247 [Å]
35.331 [°]; 2.54050 [Å]
Quartz
36.651 [°]; 2.45200 [Å]
37.409 [°]; 2.40404 [Å]
Selected Pattern: alumina 00-010-0173
Residue + Peak List
Accepted Patterns

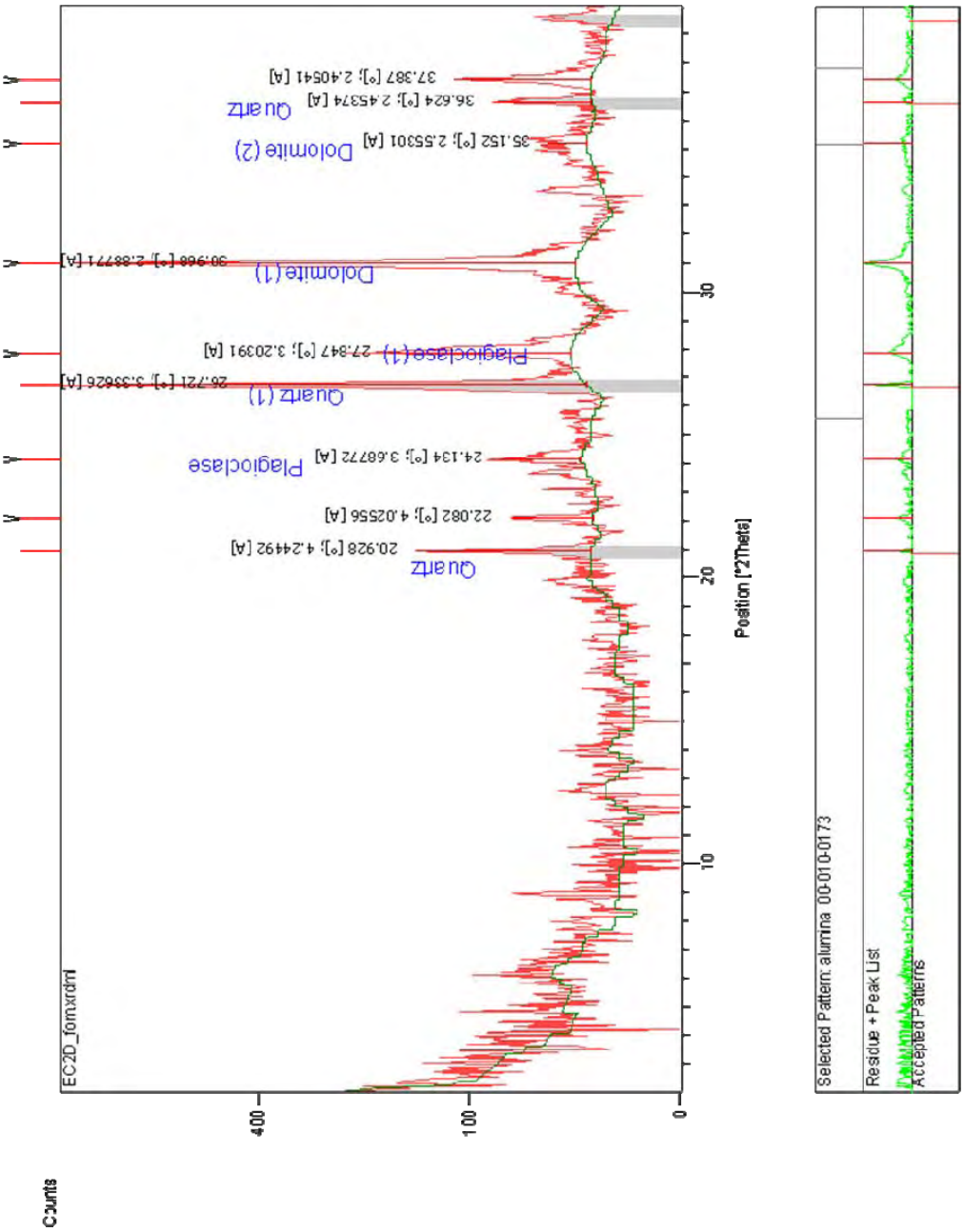
Counts
400
100
0
EC2D_fom.xrdml
Quartz
20.928 [°]; 4.24492 [Å]
22.082 [°]; 4.02556 [Å]
Plagioclase
24.134 [°]; 3.68772 [Å]
Quartz (1)
26.721 [°]; 3.33626 [Å]
Plagioclase (1)
27.847 [°]; 3.20391 [Å]
Dolomite (1)
30.968 [°]; 2.88771 [Å]
Dolomite (2)
35.152 [°]; 2.55301 [Å]
Quartz
36.624 [°]; 2.45374 [Å]
37.387 [°]; 2.40541 [Å]
10
20
30
Position [°2Theta]
Selected Pattern: alumina 00-010-0173
Residue + Peak List
Accepted Patterns

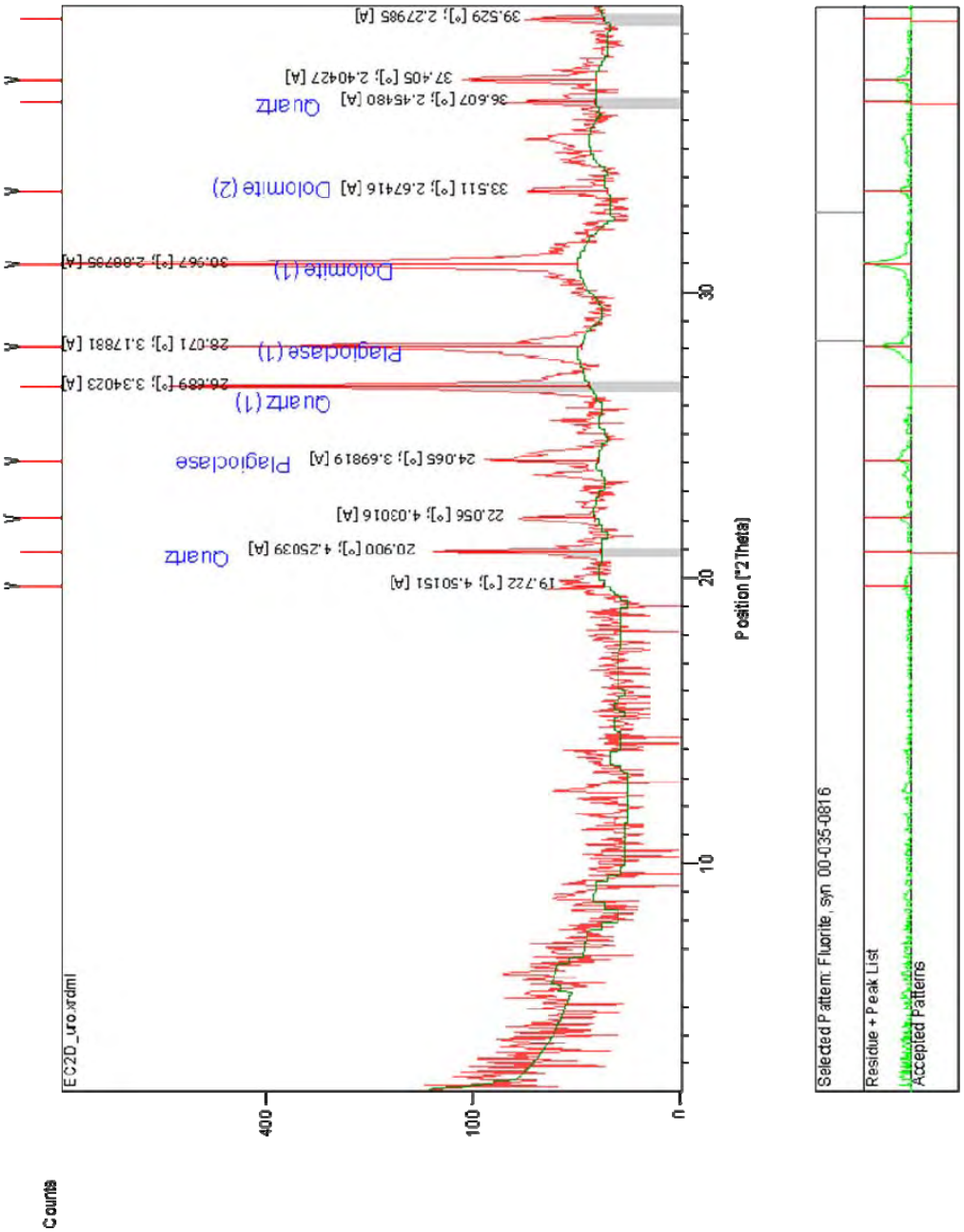
Counts
400
100
0
EC2D_uro.xrdml
10
20
30
Position [°2Theta]
19.722 [°]; 4.50151 [Å]
Quartz
20.900 [°]; 4.25039 [Å]
22.056 [°]; 4.03016 [Å]
Plagioclase
24.065 [°]; 3.69819 [Å]
Quartz (1)
26.689 [°]; 3.34023 [Å]
Plagioclase (1)
28.071 [°]; 3.17881 [Å]
Dolomite (1)
30.967 [°]; 2.88785 [Å]
Dolomite (2)
33.511 [°]; 2.67416 [Å]
Quartz
36.607 [°]; 2.45480 [Å]
37.405 [°]; 2.40427 [Å]
39.529 [°]; 2.27985 [Å]
Selected Pattern: Fluorite, syn 00-035-0816
Residue + Peak List
Accepted Patterns

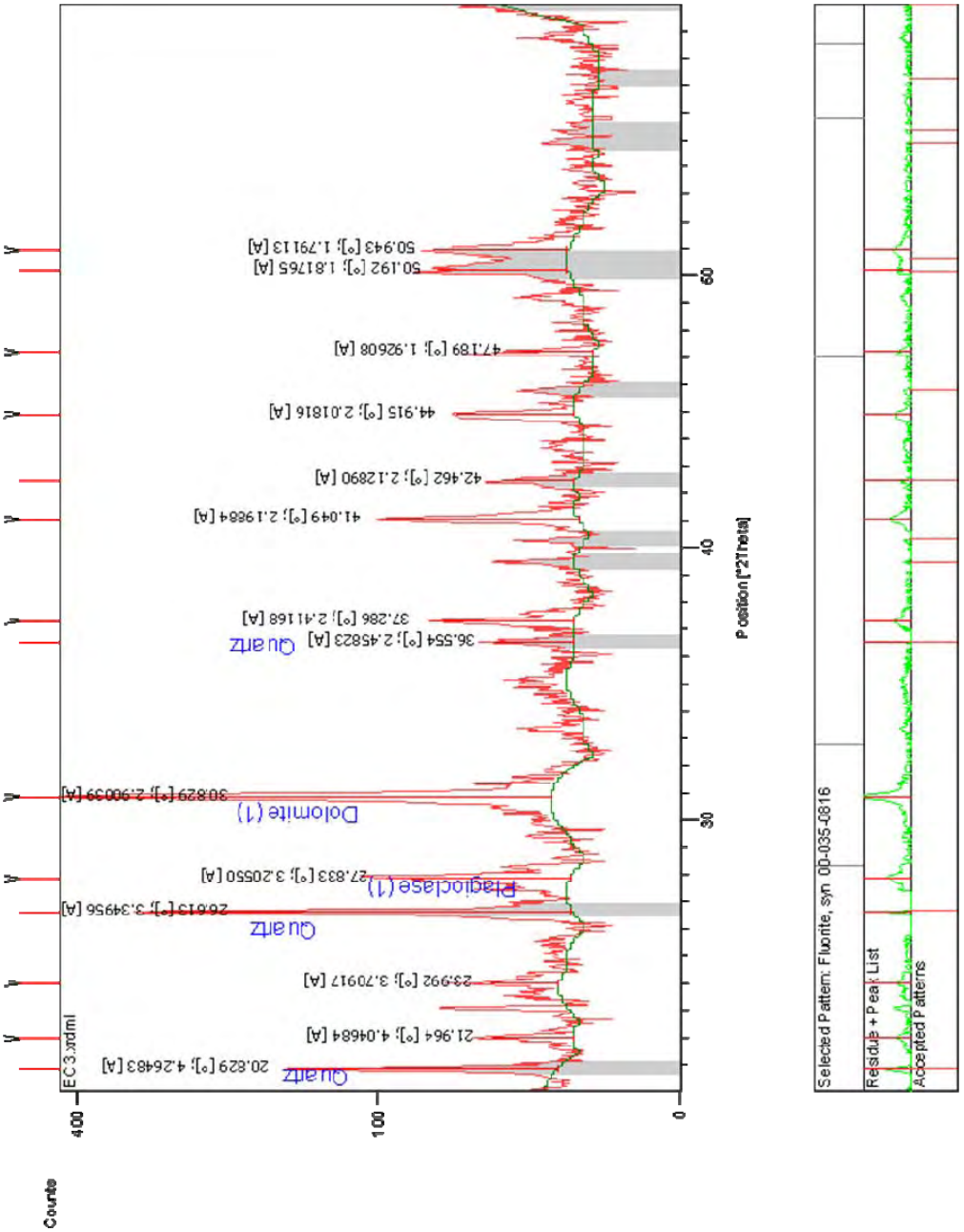
Counts
400
100
0
EC3.xrdml
20.629 [°]; 4.26483 [A]
Quartz
21.964 [°]; 4.04684 [A]
23.992 [°]; 3.70917 [A]
26.613 [°]; 3.34956 [A]
Quartz
27.833 [°]; 3.20550 [A]
Plagioclase (1)
30.829 [°]; 2.90039 [A]
Dolomite (1)
36.554 [°]; 2.45823 [A]
Quartz
37.286 [°]; 2.41168 [A]
41.049 [°]; 2.19684 [A]
42.462 [°]; 2.12890 [A]
44.915 [°]; 2.01816 [A]
47.189 [°]; 1.92608 [A]
50.192 [°]; 1.81765 [A]
50.943 [°]; 1.79113 [A]
30
40
50
60
Position [°2Theta]
Selected Pattern: Fluorite, syn 00-035-0816
Residue + Peak List
Accepted Patterns

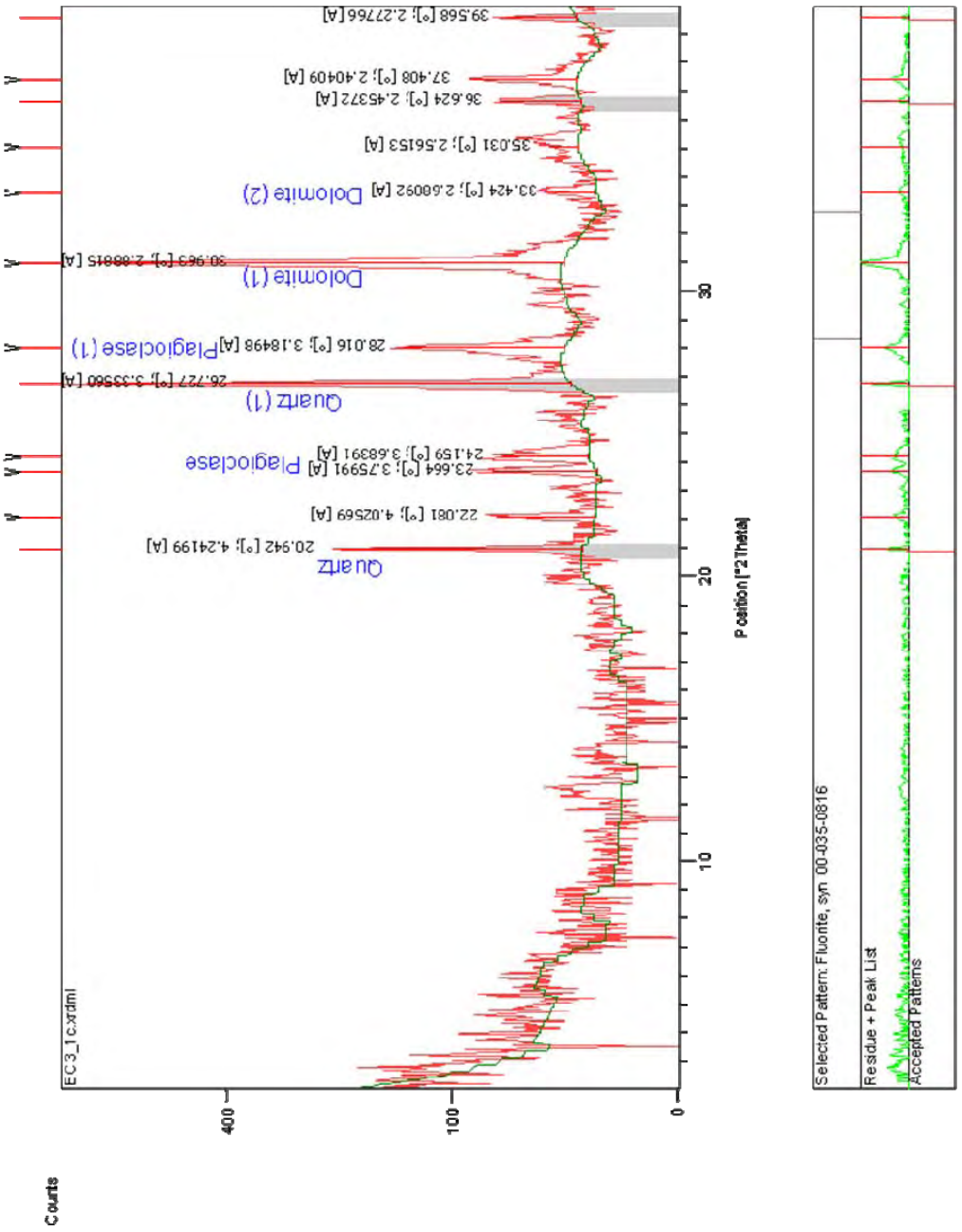
Counts
400
100
0
EC3_1c.xrdml
10
20
30
Position [°2Theta]
Quartz
20.942 [°]; 4.24199 [A]
22.081 [°]; 4.02569 [A]
23.664 [°]; 3.75991 [A]
24.159 [°]; 3.68391 [A]
Plagioclase
Quartz (1)
26.727 [°]; 3.33560 [A]
28.016 [°]; 3.18498 [A]
Plagioclase (1)
Dolomite (1)
30.963 [°]; 2.88815 [A]
33.424 [°]; 2.68092 [A]
Dolomite (2)
35.031 [°]; 2.56153 [A]
36.624 [°]; 2.45372 [A]
37.408 [°]; 2.40409 [A]
39.568 [°]; 2.27766 [A]
Selected Pattern: Fluorite, syn 00-035-0816
Residue + Peak List
Accepted Patterns

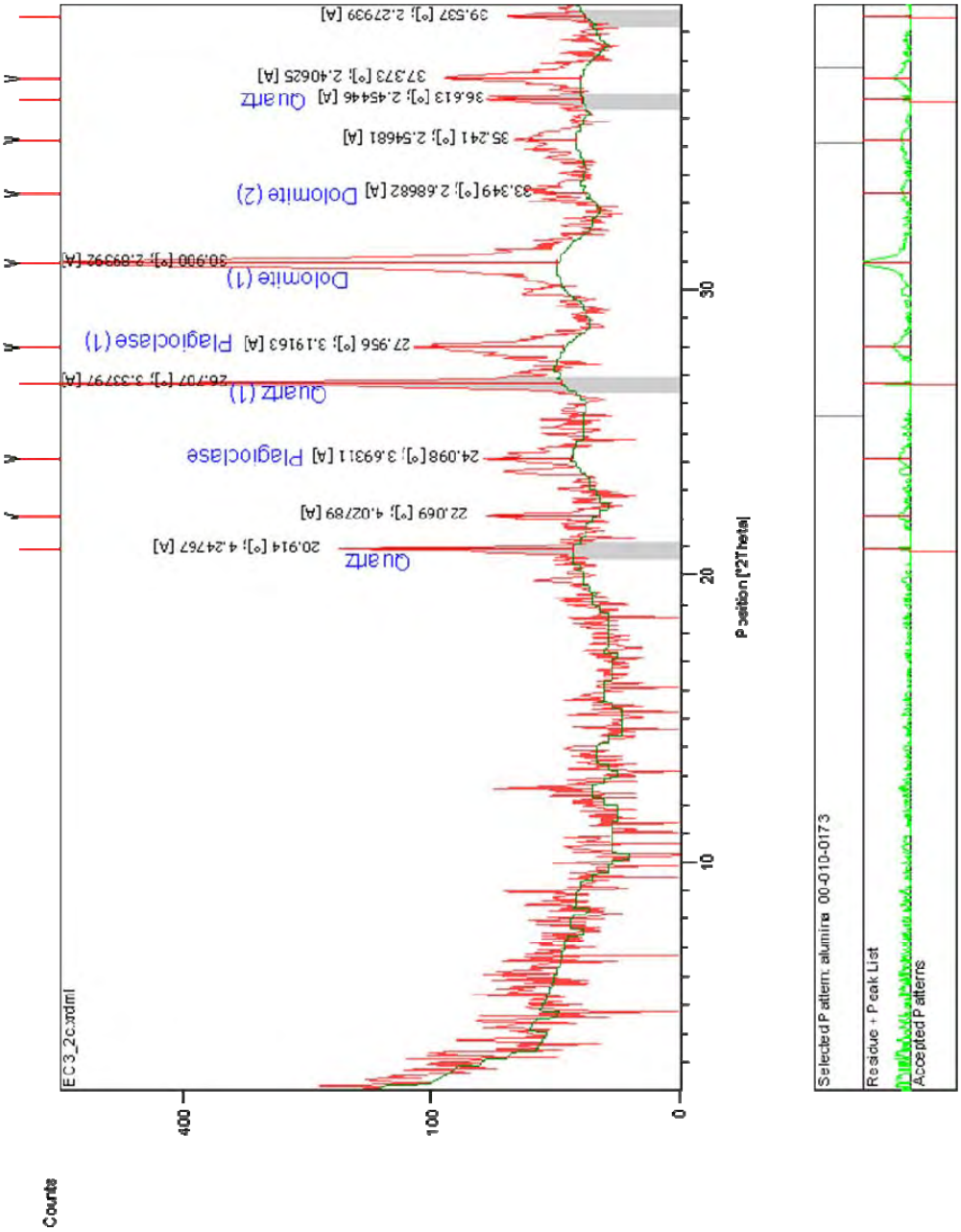
Counts
400
100
0
EC3_2c.xrdml
Quartz
20.914 [°]; 4.24767 [A]
22.069 [°]; 4.02789 [A]
Plagioclase
24.098 [°]; 3.69311 [A]
Quartz (1)
26.707 [°]; 3.33797 [A]
Plagioclase (1)
27.956 [°]; 3.19163 [A]
Dolomite (1)
30.900 [°]; 2.89392 [A]
Dolomite (2)
33.349 [°]; 2.68682 [A]
35.241 [°]; 2.54681 [A]
Quartz
36.613 [°]; 2.45446 [A]
37.373 [°]; 2.40625 [A]
39.537 [°]; 2.27939 [A]
10
20
30
Position [°2Theta]
Selected Pattern: alumina 00-010-0173
Residue + Peak List
Accepted Patterns

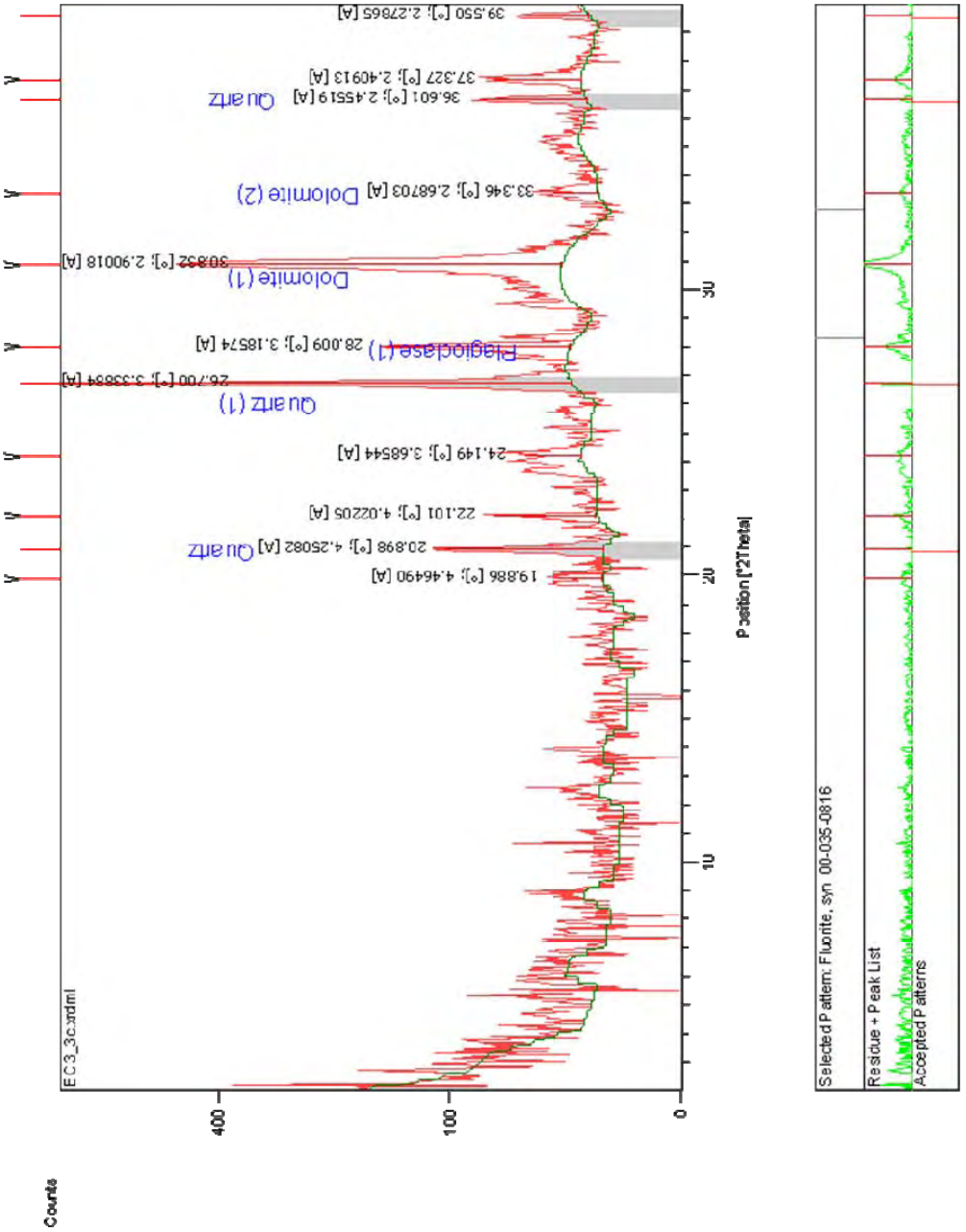
Counts
400
100
0
EC3_3c.xrdml
10
20
30
Position [°2Theta]
19.886 [°]; 4.46490 [A]
Quartz
20.898 [°]; 4.25082 [A]
22.101 [°]; 4.02205 [A]
24.149 [°]; 3.68544 [A]
Quartz (1)
26.700 [°]; 3.33589 [A]
Plagioclase (1)
28.009 [°]; 3.18574 [A]
Dolomite (1)
30.852 [°]; 2.90018 [A]
Dolomite (2)
33.346 [°]; 2.68703 [A]
Quartz
36.601 [°]; 2.45519 [A]
37.327 [°]; 2.40913 [A]
39.550 [°]; 2.27865 [A]
Selected Pattern: Fluorite, syn 00-035-0816
Residue + Peak List
Accepted Patterns

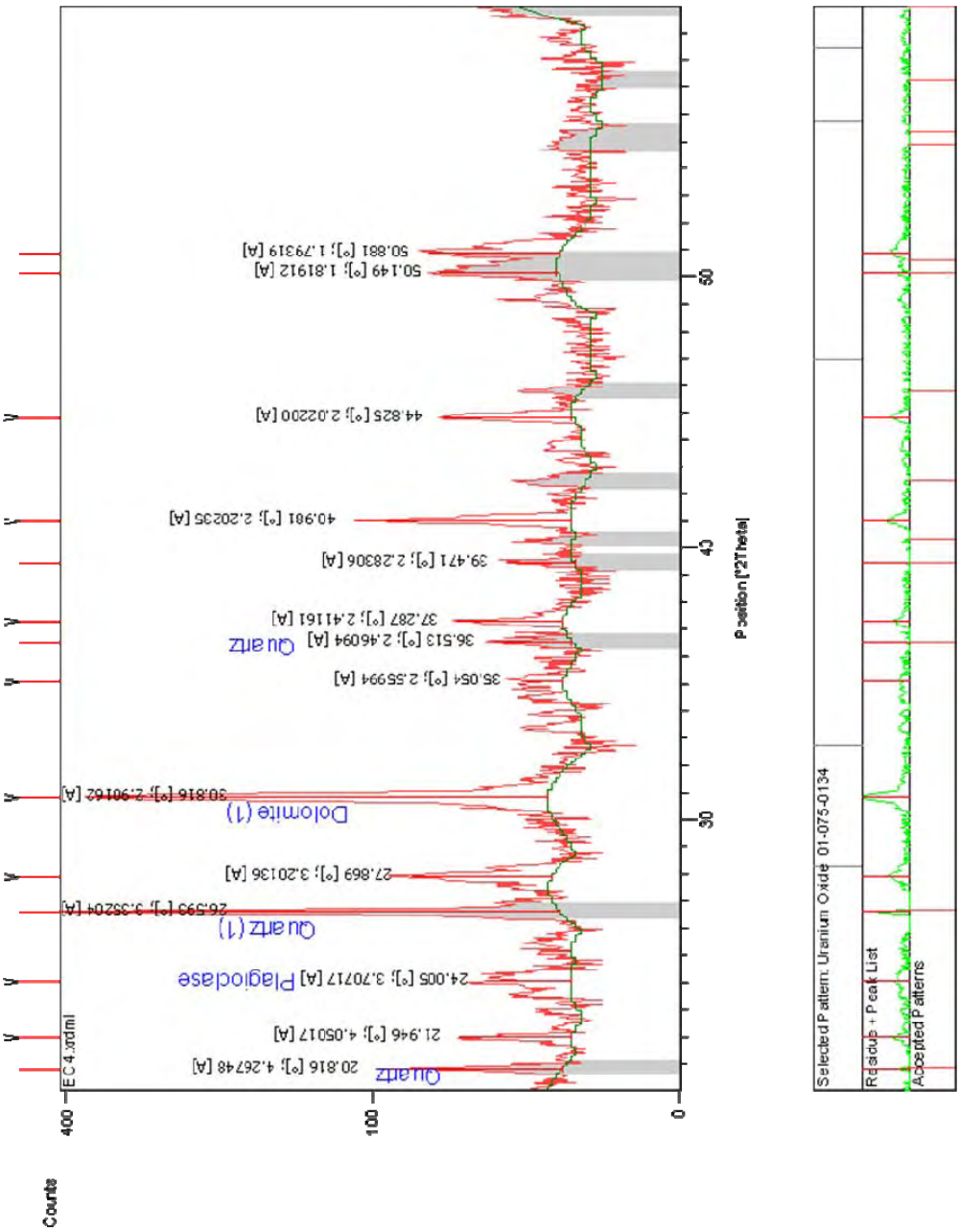
Counts
400
100
0
EC4.xrdml
Quartz
20.816 [°]; 4.26748 [A]
21.946 [°]; 4.05017 [A]
Plagioclase
24.005 [°]; 3.70717 [A]
Quartz (1)
26.593 [°]; 3.35204 [A]
27.869 [°]; 3.20136 [A]
Dolomite (1)
30.816 [°]; 2.90162 [A]
35.054 [°]; 2.55994 [A]
Quartz
36.513 [°]; 2.46094 [A]
37.287 [°]; 2.41161 [A]
39.471 [°]; 2.28306 [A]
40.901 [°]; 2.20235 [A]
44.825 [°]; 2.02200 [A]
50.149 [°]; 1.81912 [A]
50.881 [°]; 1.79319 [A]
30
40
50
Position [°2Theta]
Selected Pattern: Uranium Oxide 01-075-0134
Rdidup + Peak List
Accepted Patterns

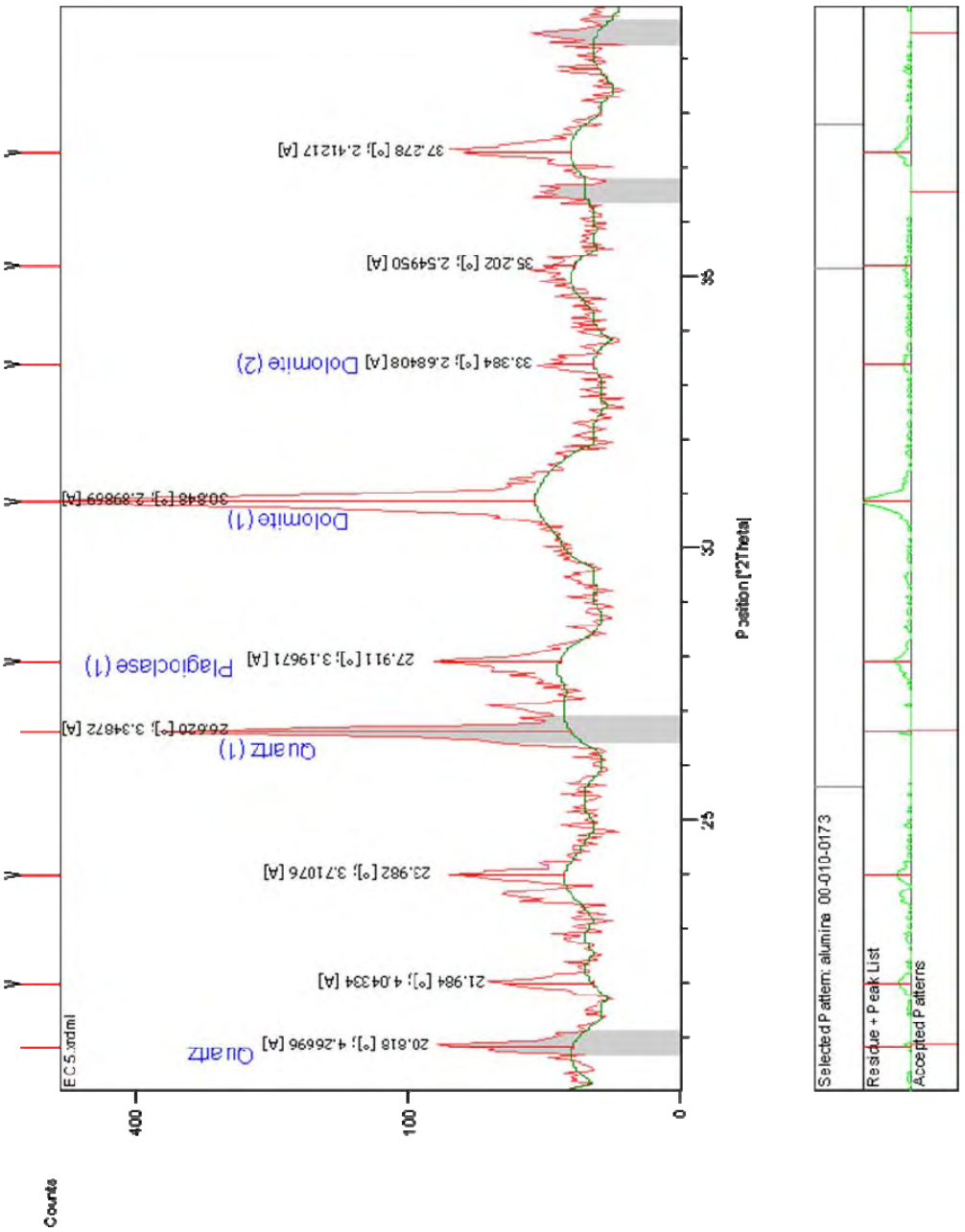
Counts
400
100
0
EC5.xrdml
Quartz
20.818 [°]; 4.26696 [A]
21.984 [°]; 4.04334 [A]
23.982 [°]; 3.71076 [A]
Quartz (1)
26.620 [°]; 3.3482 [A]
Plagioclase (1)
27.911 [°]; 3.19671 [A]
Dolomite (1)
30.848 [°]; 2.89869 [A]
Dolomite (2)
33.384 [°]; 2.68408 [A]
35.202 [°]; 2.54950 [A]
37.278 [°]; 2.41217 [A]
25
30
35
Position [°2Theta]
Selected Pattern: alumina 00-010-0173
Residue + Peak List
Accepted Patterns

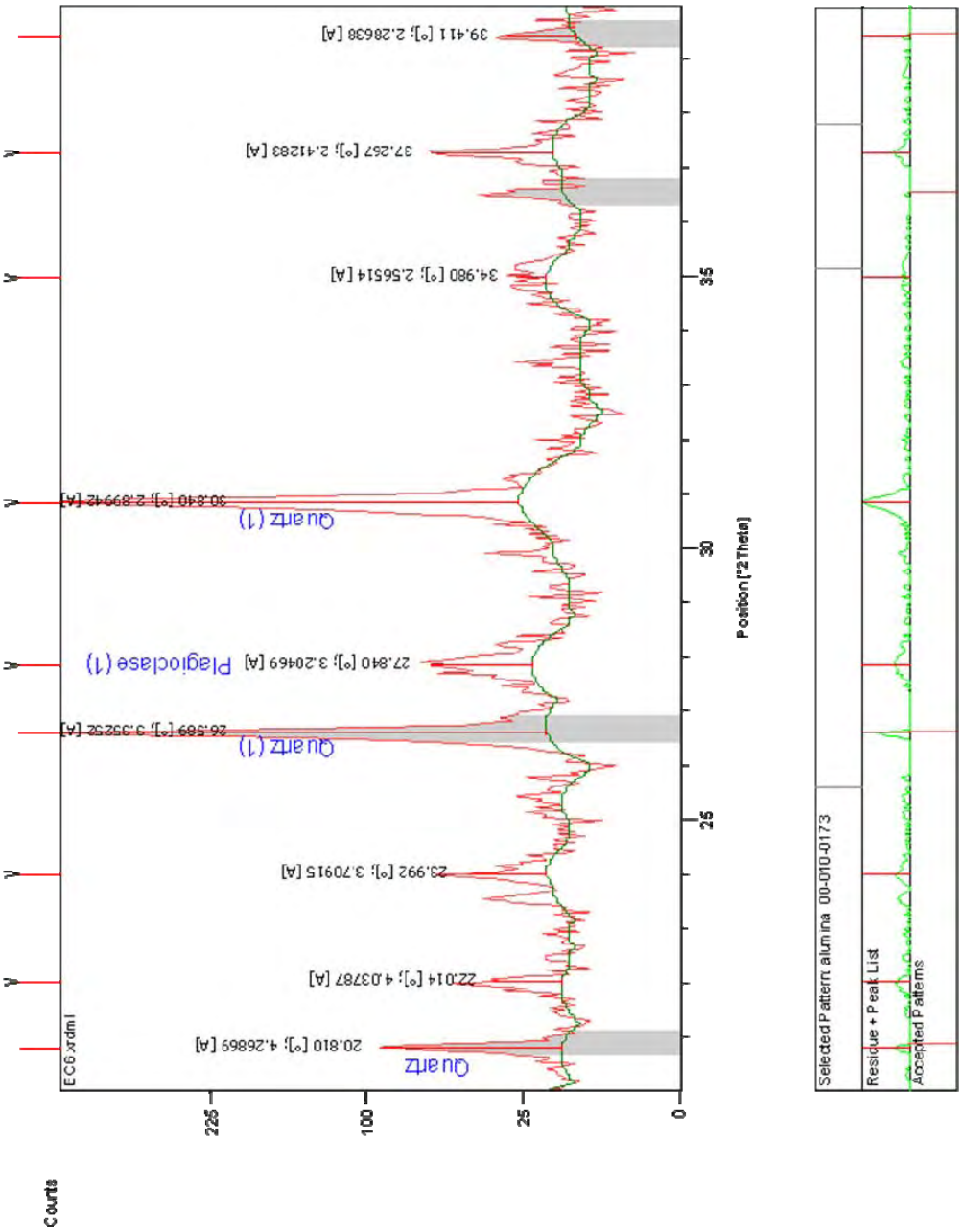
Counts
225
100
25
0
EC6.xrdml
Quartz
20.810 [°]; 4.26869 [A]
22.014 [°]; 4.03787 [A]
23.992 [°]; 3.70915 [A]
Quartz (1)
26.589 [°]; 3.35252 [A]
Plagioclase (1)
27.840 [°]; 3.20469 [A]
Quartz (1)
30.640 [°]; 2.89942 [A]
34.980 [°]; 2.56514 [A]
37.267 [°]; 2.41283 [A]
39.411 [°]; 2.28638 [A]
25
30
35
Position [°2Theta]
Selected Pattern: alumina 00-010-0173
Residue + Peak List
Accepted Patterns

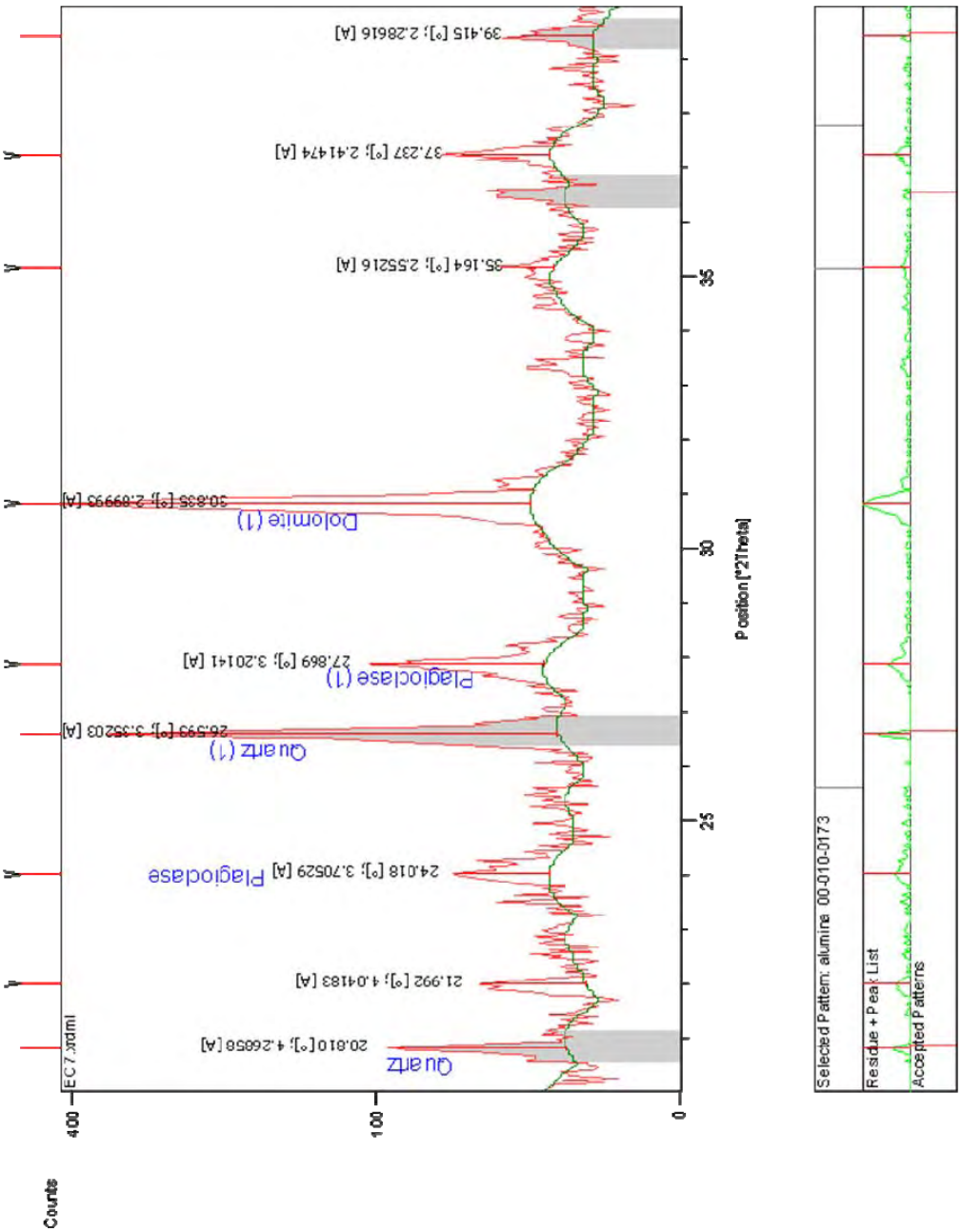
Counts
400
100
0
Position [°2Theta]
25
30
35
EC7.xrdml
Quartz
20.810 [°]; 4.26858 [A]
21.992 [°]; 4.04183 [A]
Plagioclase
24.018 [°]; 3.70529 [A]
Quartz (1)
26.599 [°]; 3.35203 [A]
Plagioclase (1)
27.869 [°]; 3.20141 [A]
Dolomite (1)
30.835 [°]; 2.89993 [A]
35.164 [°]; 2.55216 [A]
37.237 [°]; 2.41474 [A]
39.415 [°]; 2.28616 [A]
Selected Pattern: alumina 00-010-0173
Residue + Peak List
Accepted Patterns

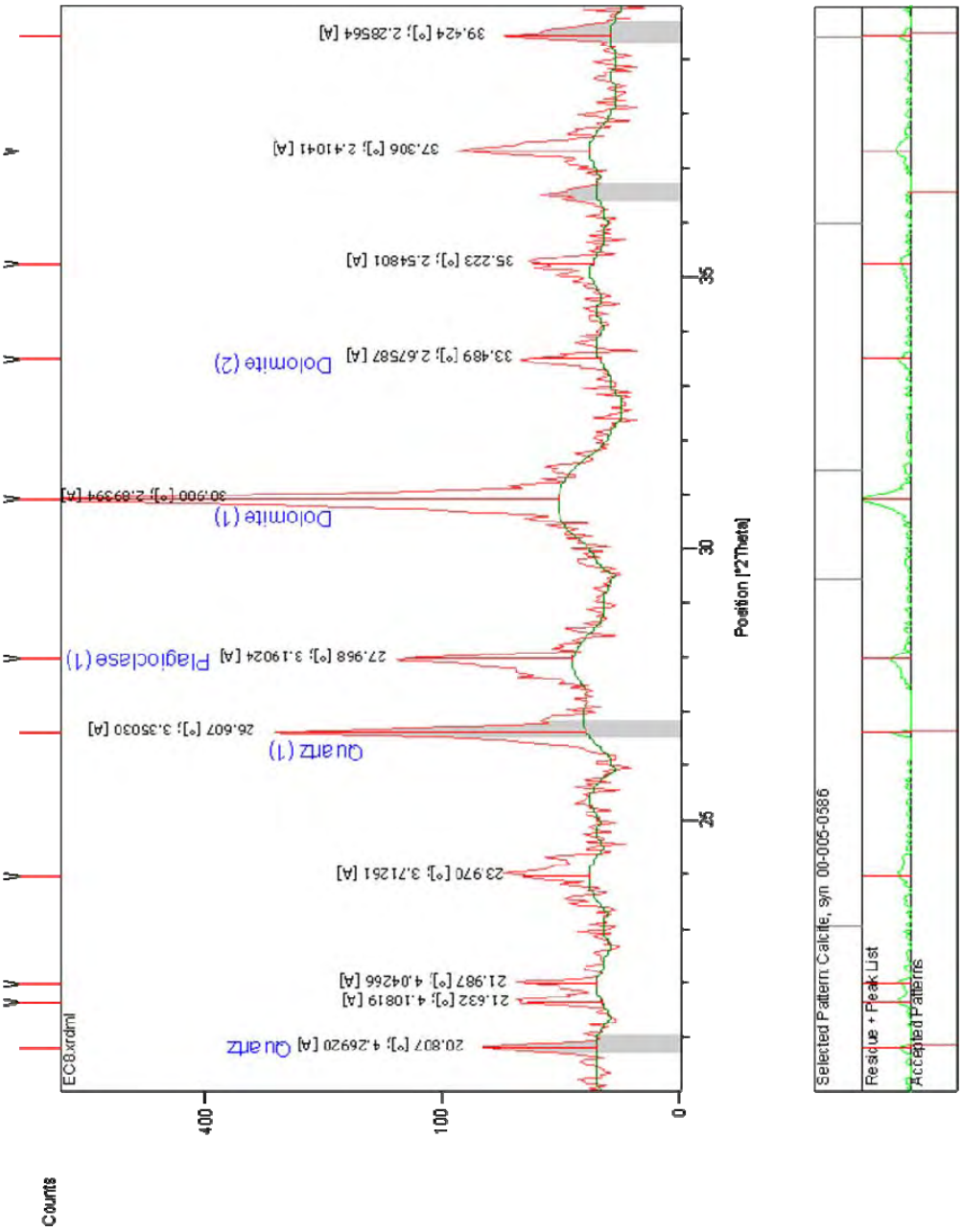
Counts
400
100
0
ECB.xrdml
Quartz
20.807 [°]; 4.26920 [A]
21.632 [°]; 4.10819 [A]
21.987 [°]; 4.04266 [A]
23.970 [°]; 3.71261 [A]
Quartz (1)
26.607 [°]; 3.35030 [A]
Plagioclase (1)
27.958 [°]; 3.19024 [A]
Dolomite (1)
30.500 [°]; 2.89394 [A]
Dolomite (2)
33.489 [°]; 2.67587 [A]
35.223 [°]; 2.54801 [A]
37.306 [°]; 2.41041 [A]
39.424 [°]; 2.28564 [A]
25
30
35
Position [°2Theta]
Selected Pattern Calcite, syn 00-005-0586
Residue + Peak List
Accepted Patterns

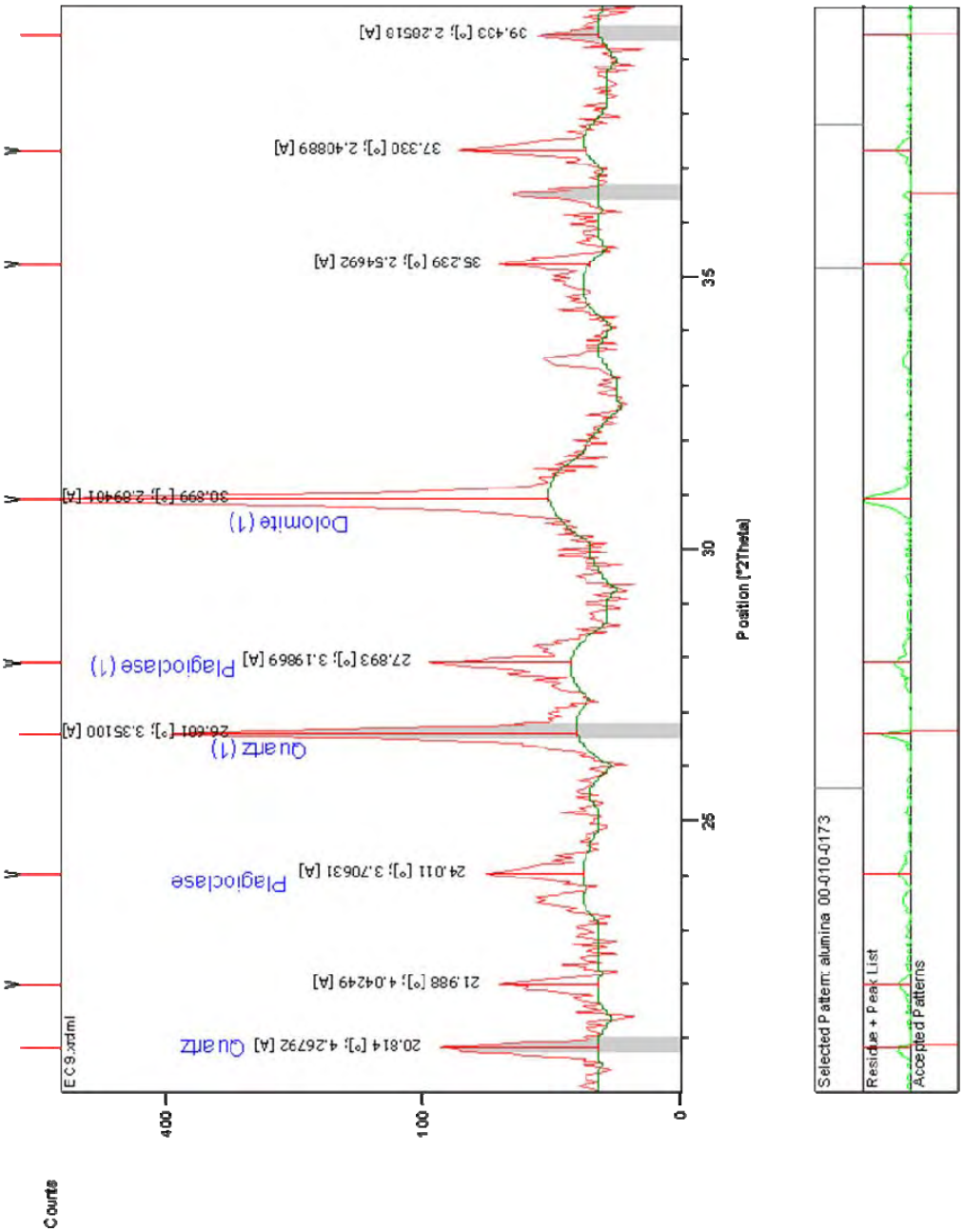
Counts
400
100
0
ECS.xrdml
20.814 [°]; 4.26792 [A]
Quartz
21.988 [°]; 4.04249 [A]
24.011 [°]; 3.70631 [A]
Plagioclase
26.661 [°]; 3.35100 [A]
Quartz (1)
27.893 [°]; 3.19869 [A]
Plagioclase (1)
30.899 [°]; 2.89401 [A]
Dolomite (1)
35.239 [°]; 2.54692 [A]
37.330 [°]; 2.40889 [A]
39.433 [°]; 2.28518 [A]
25
30
35
Position [°2Theta]
Selected Pattern: alumina 00-010-0173
Residue + Peak List
Accepted Patterns

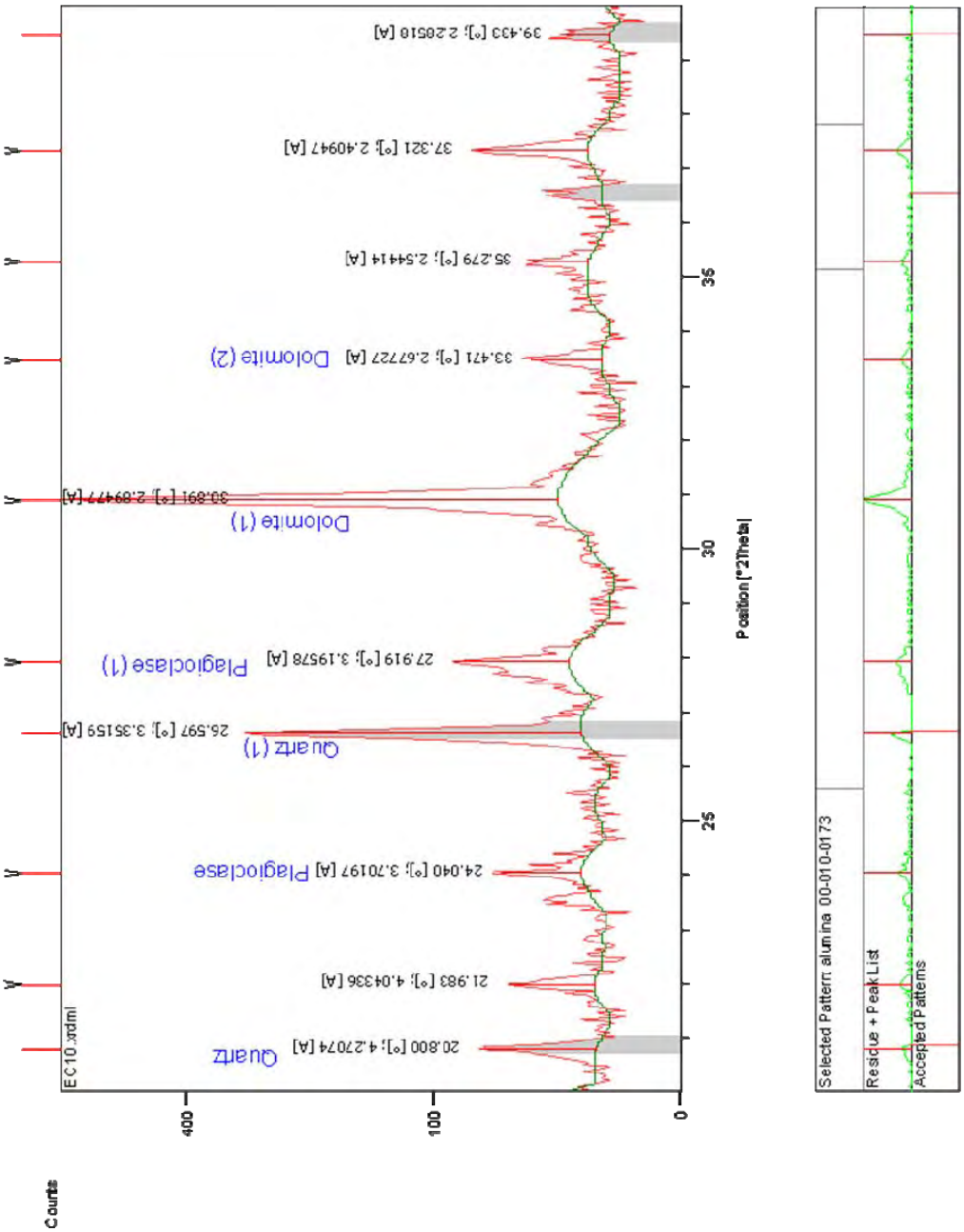
Counts
400
100
0
25
30
35
Position [°2Theta]
EC10.xrdml
Quartz
20.800 [°]; 4.27074 [A]
21.983 [°]; 4.04336 [A]
Plagioclase
24.040 [°]; 3.70197 [A]
Quartz (1)
26.597 [°]; 3.35159 [A]
Plagioclase (1)
27.919 [°]; 3.19578 [A]
Dolomite (1)
30.891 [°]; 2.89477 [A]
Dolomite (2)
33.471 [°]; 2.67727 [A]
35.279 [°]; 2.54414 [A]
37.321 [°]; 2.40947 [A]
39.433 [°]; 2.28518 [A]
Selected Pattern: alumina 00-010-0173
Residue + Peak List
Accepted Patterns

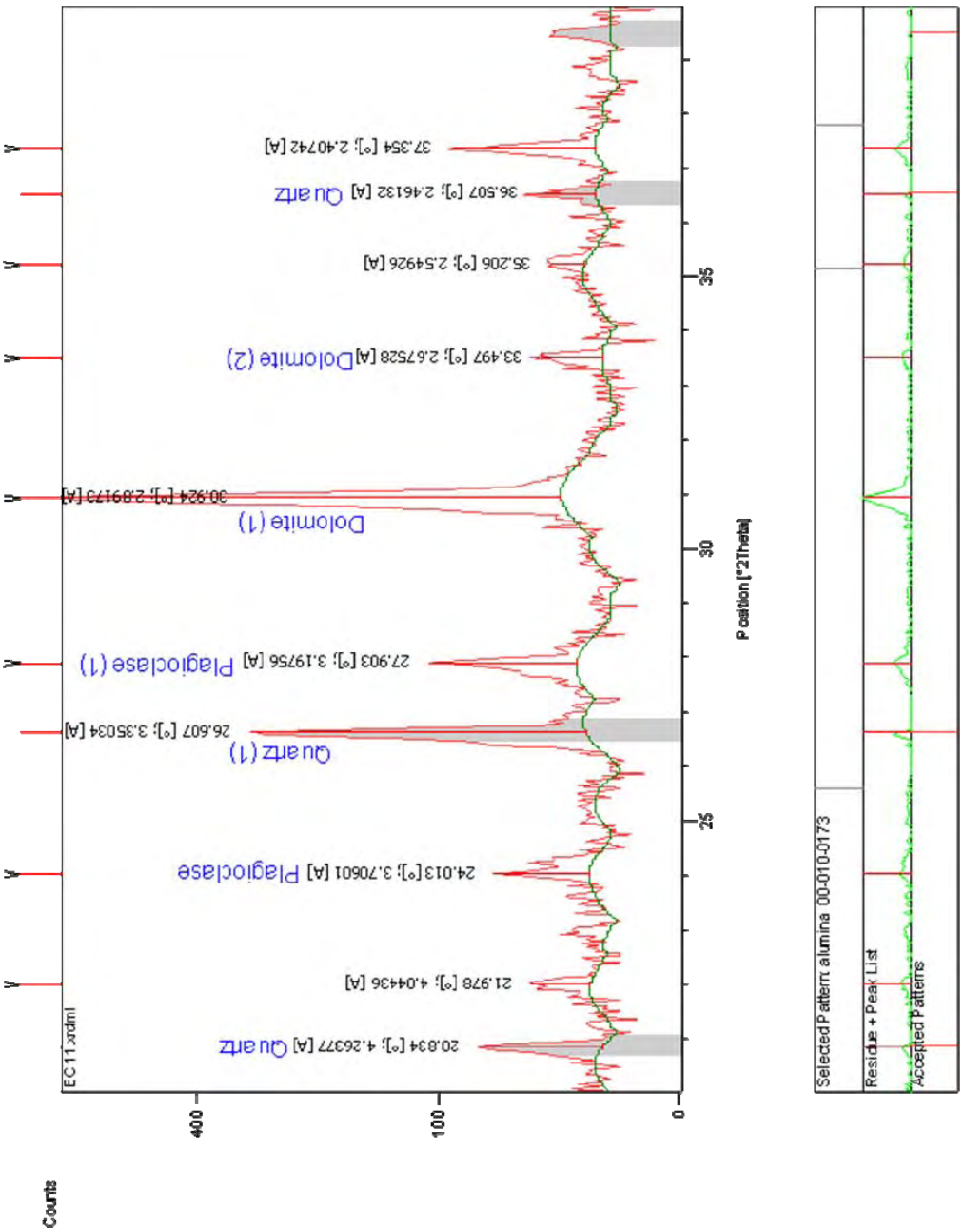
Counts
400
100
0
EC11.xrdml
20.034 [°]; 4.26377 [A] Quartz
21.978 [°]; 4.04436 [A]
24.013 [°]; 3.70601 [A] Plagioclase
26.607 [°]; 3.35034 [A] Quartz (1)
27.903 [°]; 3.19756 [A] Plagioclase (1)
30.924 [°]; 2.89173 [A] Dolomite (1)
33.497 [°]; 2.67528 [A] Dolomite (2)
35.206 [°]; 2.54926 [A]
36.507 [°]; 2.46132 [A] Quartz
37.354 [°]; 2.40742 [A]
25
30
35
Position [°2Theta]
Selected Pattern: alumina 00-010-0173
Residue + Peak List
Accepted Patterns

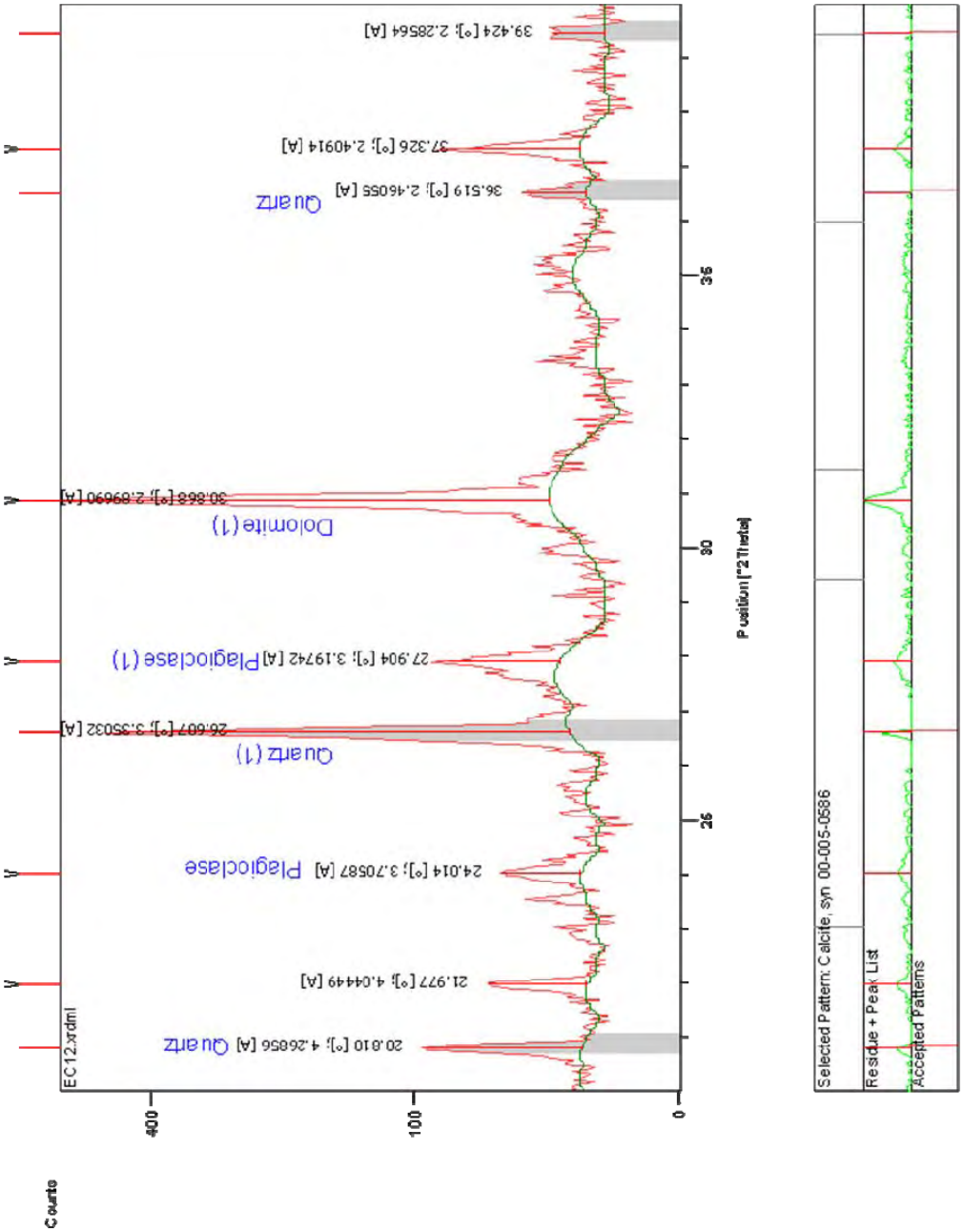
Counts
400
100
0
EC12.xrdml
20.810 [°]; 4.26856 [A] Quartz
21.977 [°]; 4.04449 [A]
24.014 [°]; 3.70587 [A] Plagioclase
26.607 [°]; 3.35032 [A] Quartz (1)
27.904 [°]; 3.19742 [A] Plagioclase (1)
30.868 [°]; 2.89690 [A] Dolomite (1)
36.519 [°]; 2.46055 [A] Quartz
37.326 [°]; 2.40914 [A]
39.424 [°]; 2.28564 [A]
26
30
35
Position [°2Theta]
Selected Pattern: Calcite, syn 00-005-0586
Residue + Peak List
Accepted Patterns

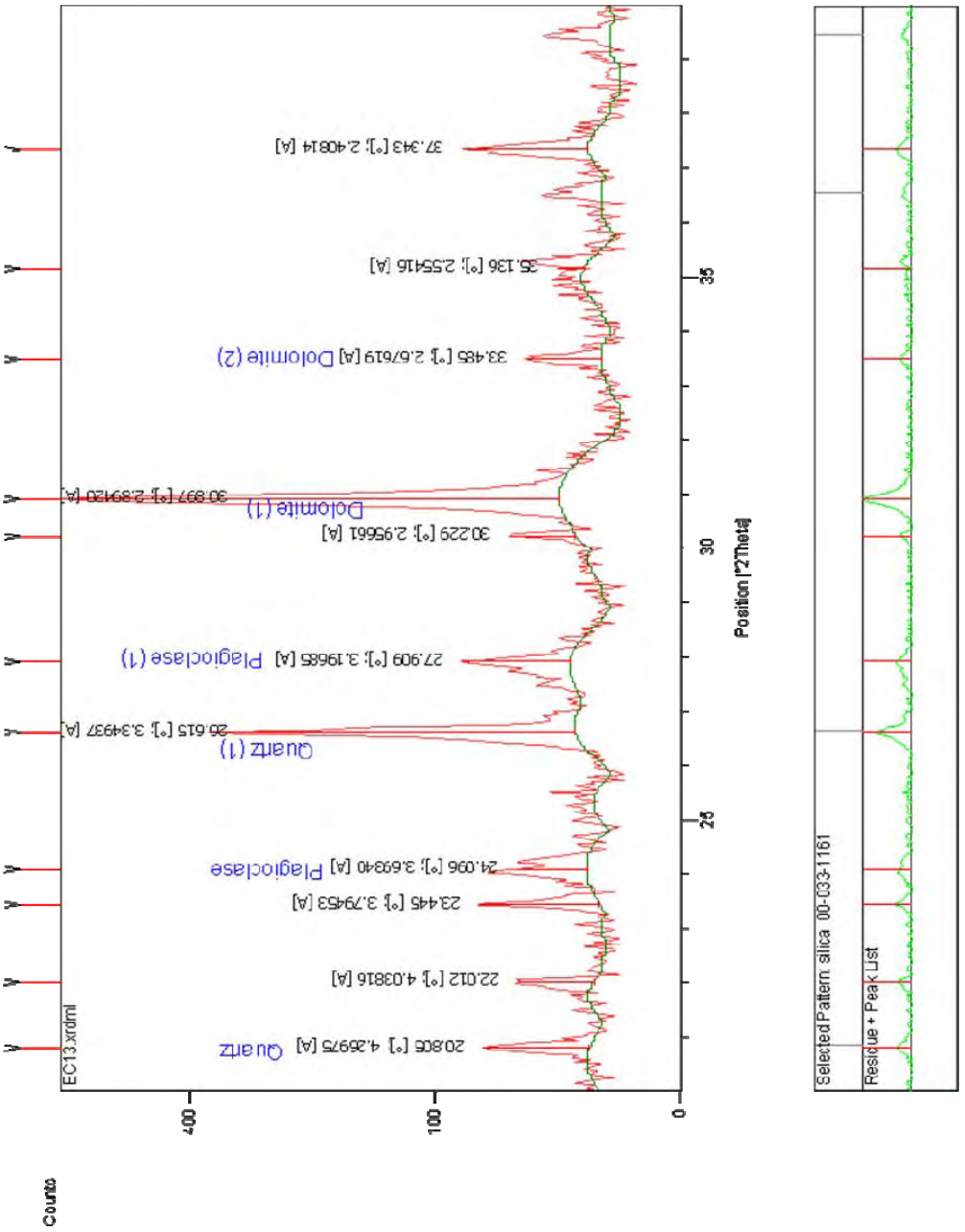
Counts
400
100
0
EC13.xrdml
Quartz
20.805 [°], 4.26975 [Å]
22.012 [°], 4.03816 [Å]
23.445 [°], 3.79453 [Å]
Plagioclase
24.096 [°], 3.69340 [Å]
Quartz (1)
26.615 [°], 3.34937 [Å]
Plagioclase (1)
27.909 [°], 3.19685 [Å]
30.229 [°], 2.95661 [Å]
Dolomite (1)
Dolomite (2)
33.485 [°], 2.67619 [Å]
35.136 [°], 2.55416 [Å]
37.343 [°], 2.40814 [Å]
20
30
35
Position [°2Theta]
Selected Pattern: silica 00-033-1161
Residue + Peak List

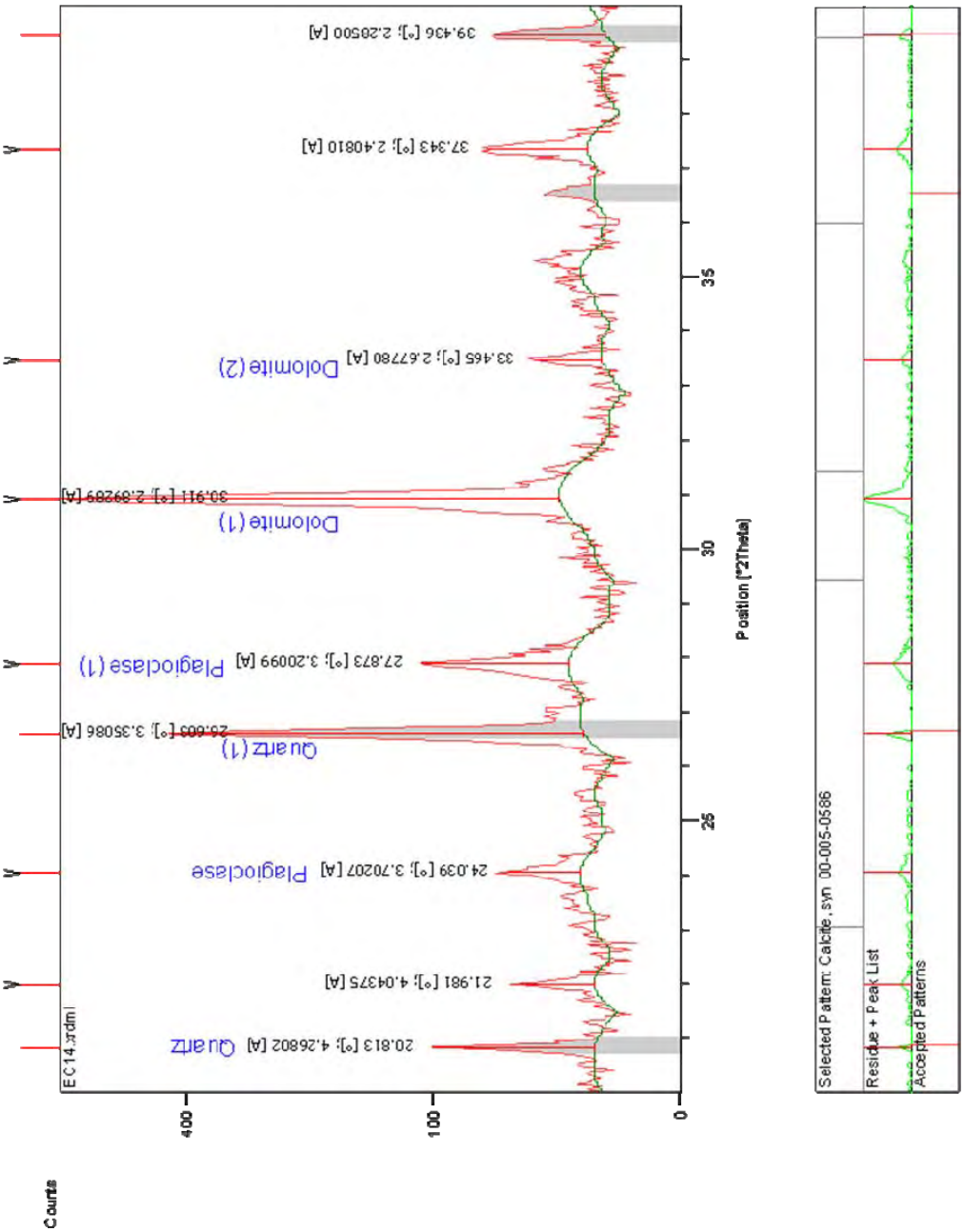
Counts
400
100
0
25
30
35
Position [°2Theta]
EC14.xrdml
Quartz
20.813 [°]; 4.26802 [A]
21.981 [°]; 4.04375 [A]
Plagioclase
24.039 [°]; 3.70207 [A]
Quartz (1)
26.603 [°]; 3.35086 [A]
Plagioclase (1)
27.873 [°]; 3.20099 [A]
Dolomite (1)
30.911 [°]; 2.89289 [A]
Dolomite (2)
33.465 [°]; 2.67780 [A]
37.343 [°]; 2.40810 [A]
39.436 [°]; 2.28500 [A]
Selected Pattern: Calcite, syn 00-005-0586
Residue + Peak List
Accepted Patterns

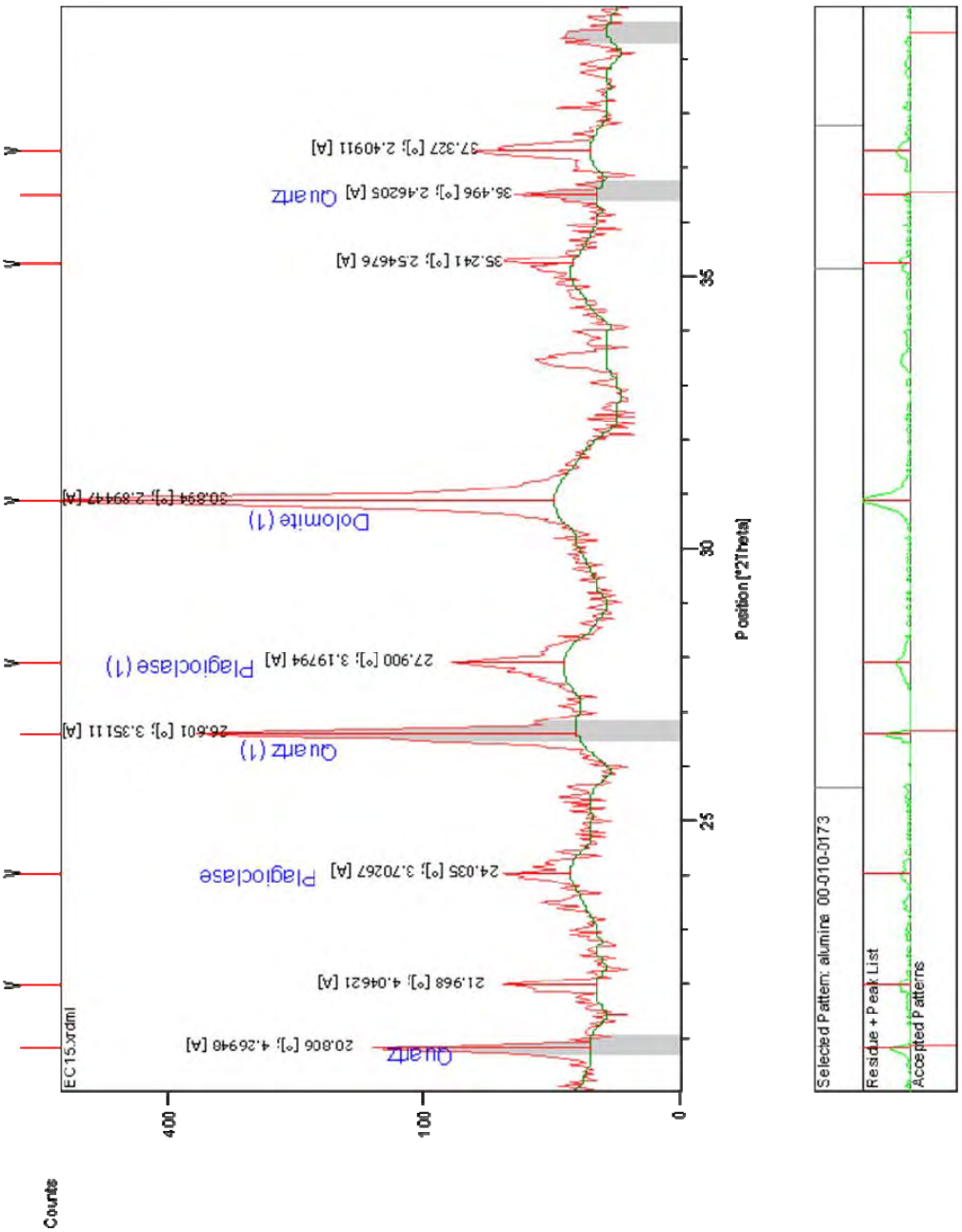
Counts
400
100
0
EC15.xrdml
Quartz
20.806 [°]; 4.26948 [A]
21.968 [°]; 4.04621 [A]
Plagioclase
24.035 [°]; 3.70267 [A]
Quartz (1)
26.601 [°]; 3.35111 [A]
Plagioclase (1)
27.900 [°]; 3.19794 [A]
Dolomite (1)
30.894 [°]; 2.89447 [A]
35.241 [°]; 2.54676 [A]
Quartz
36.496 [°]; 2.46205 [A]
37.327 [°]; 2.40911 [A]
25
30
35
Position [°2Theta]
Selected Pattern: alumina 00-010-0173
Residue + Peak List
Accepted Patterns

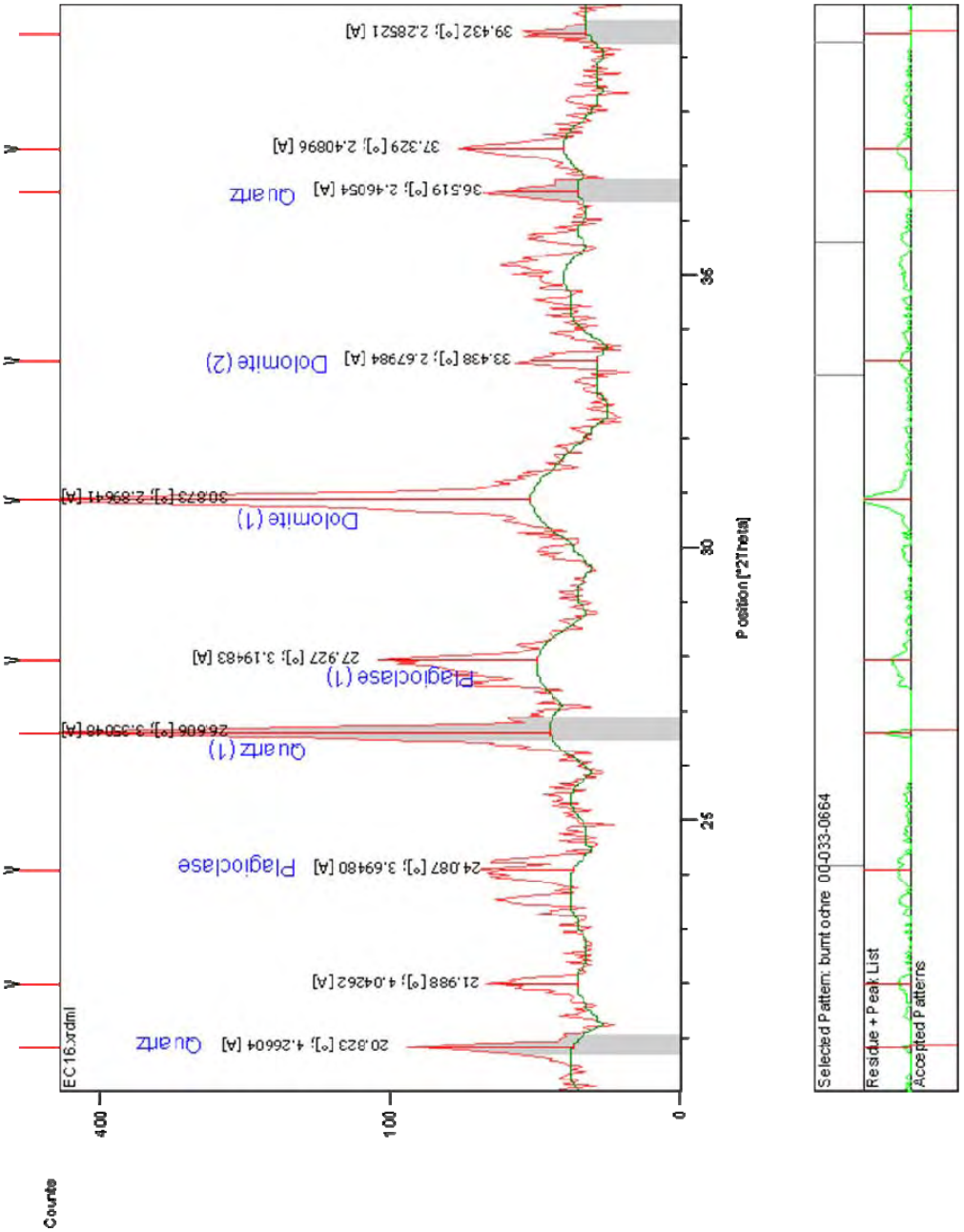
Counts
400
100
0
EC16.xrdml
Quartz
20.823 [°]; 4.26604 [A]
21.988 [°]; 4.04262 [A]
Plagioclase
24.087 [°]; 3.69480 [A]
Quartz (1)
26.606 [°]; 3.35046 [A]
Plagioclase (1)
27.927 [°]; 3.19483 [A]
Dolomite (1)
30.873 [°]; 2.89641 [A]
Dolomite (2)
33.438 [°]; 2.67984 [A]
Quartz
36.519 [°]; 2.46054 [A]
37.329 [°]; 2.40896 [A]
39.432 [°]; 2.28521 [A]
25
30
35
Position [°2Theta]
Selected Pattern: burnt ochre 00-033-0664
Residue + Peak List
Accepted Patterns

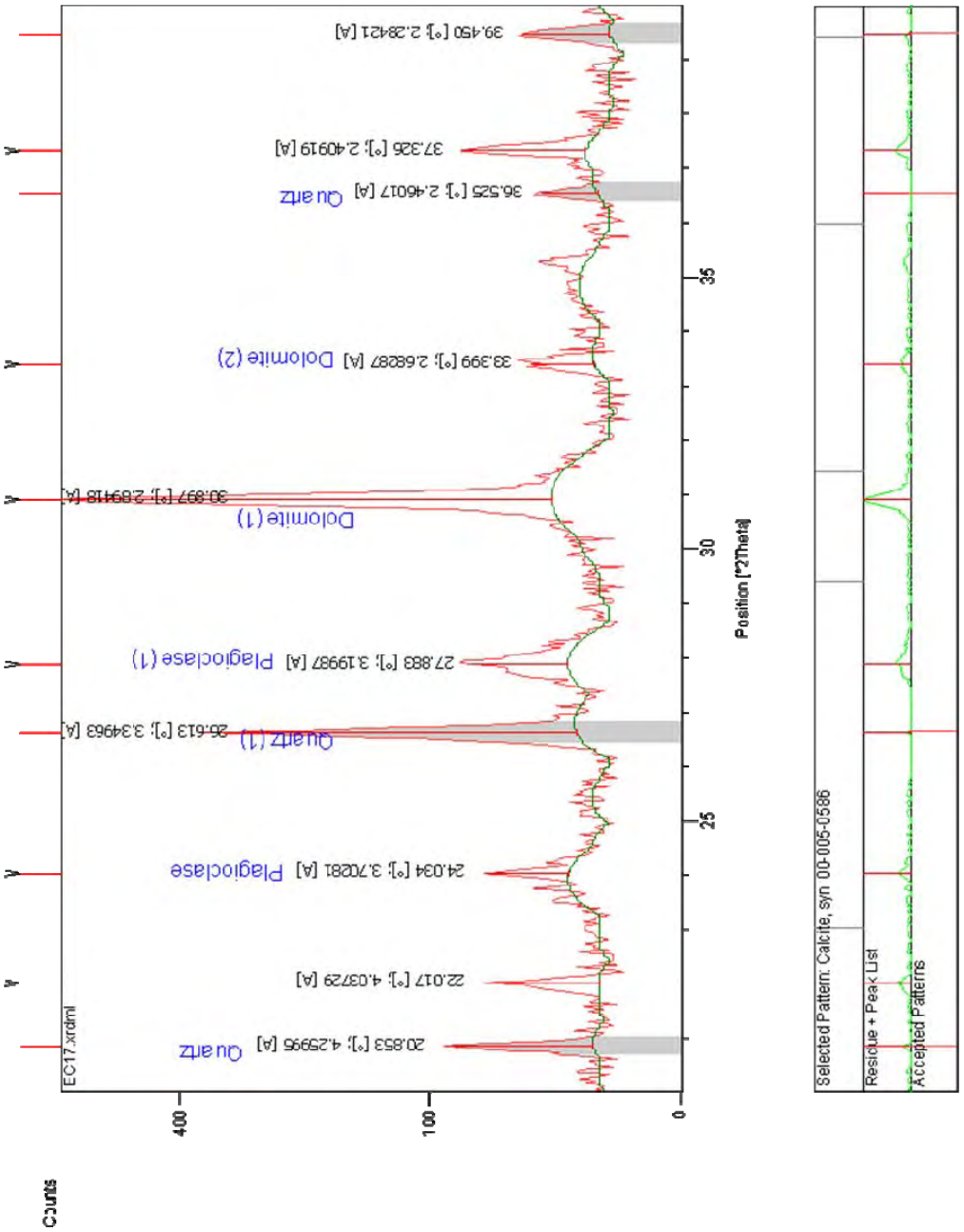
EC17.xrdml
Counts
Position [°2Theta]
Quartz
Plagioclase
Dolomite (1)
Dolomite (2)
Selected Pattern: Calcite, syn 00-005-0586
Residue + Peak List
Accepted Patterns

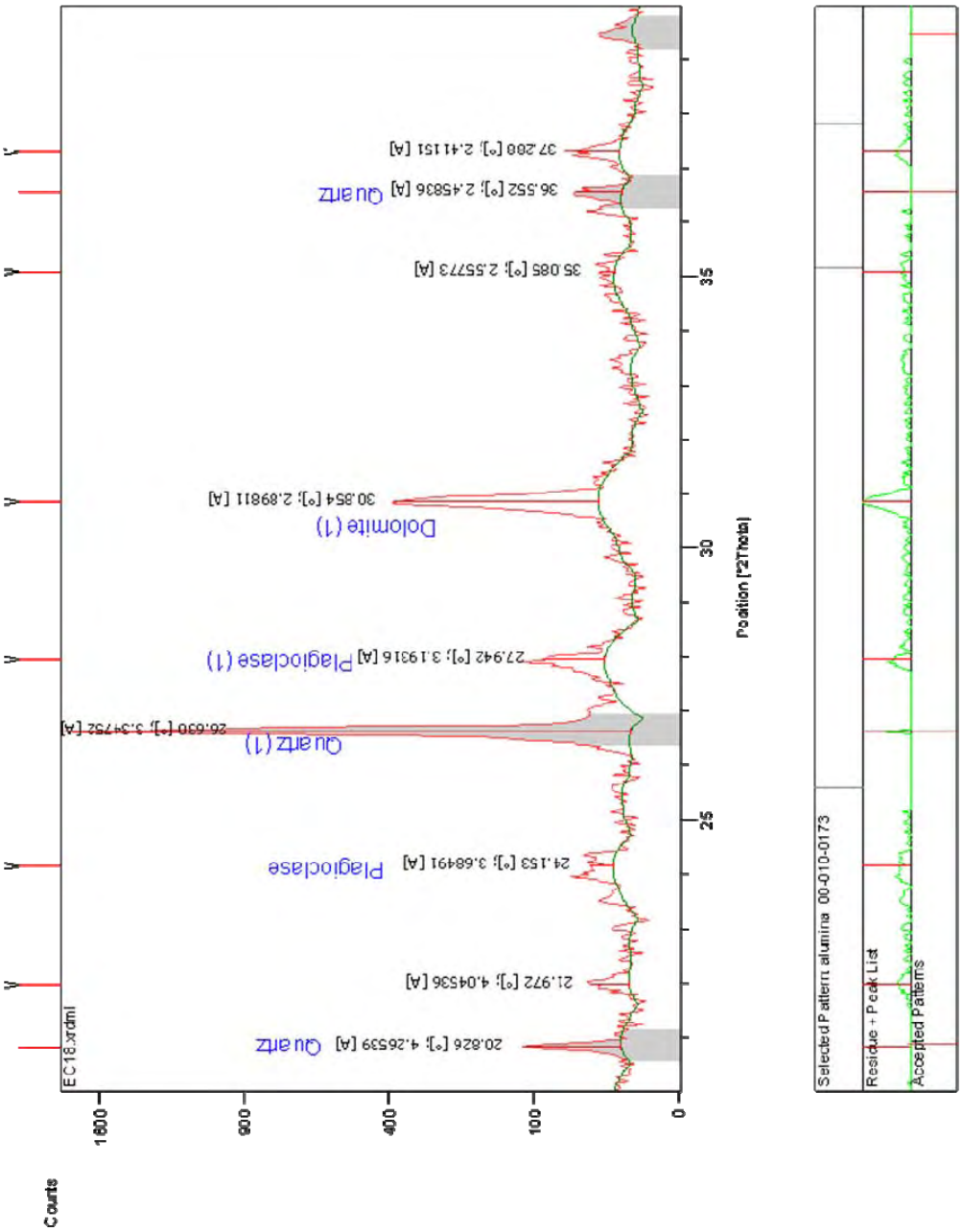
Counts
Position [°2Theta]
EC18.xrdml
Quartz
20.826 [°]; 4.26539 [Å]
21.972 [°]; 4.04536 [Å]
Plagioclase
24.153 [°]; 3.68491 [Å]
Quartz (1)
26.630 [°]; 3.3+752 [Å]
Plagioclase (1)
27.942 [°]; 3.19316 [Å]
Dolomite (1)
30.854 [°]; 2.89811 [Å]
35.085 [°]; 2.55773 [Å]
Quartz
36.552 [°]; 2.45836 [Å]
37.288 [°]; 2.41151 [Å]
Selected Pattern: alumina 00-010-0173
Residue + Peak List
Accepted Patterns

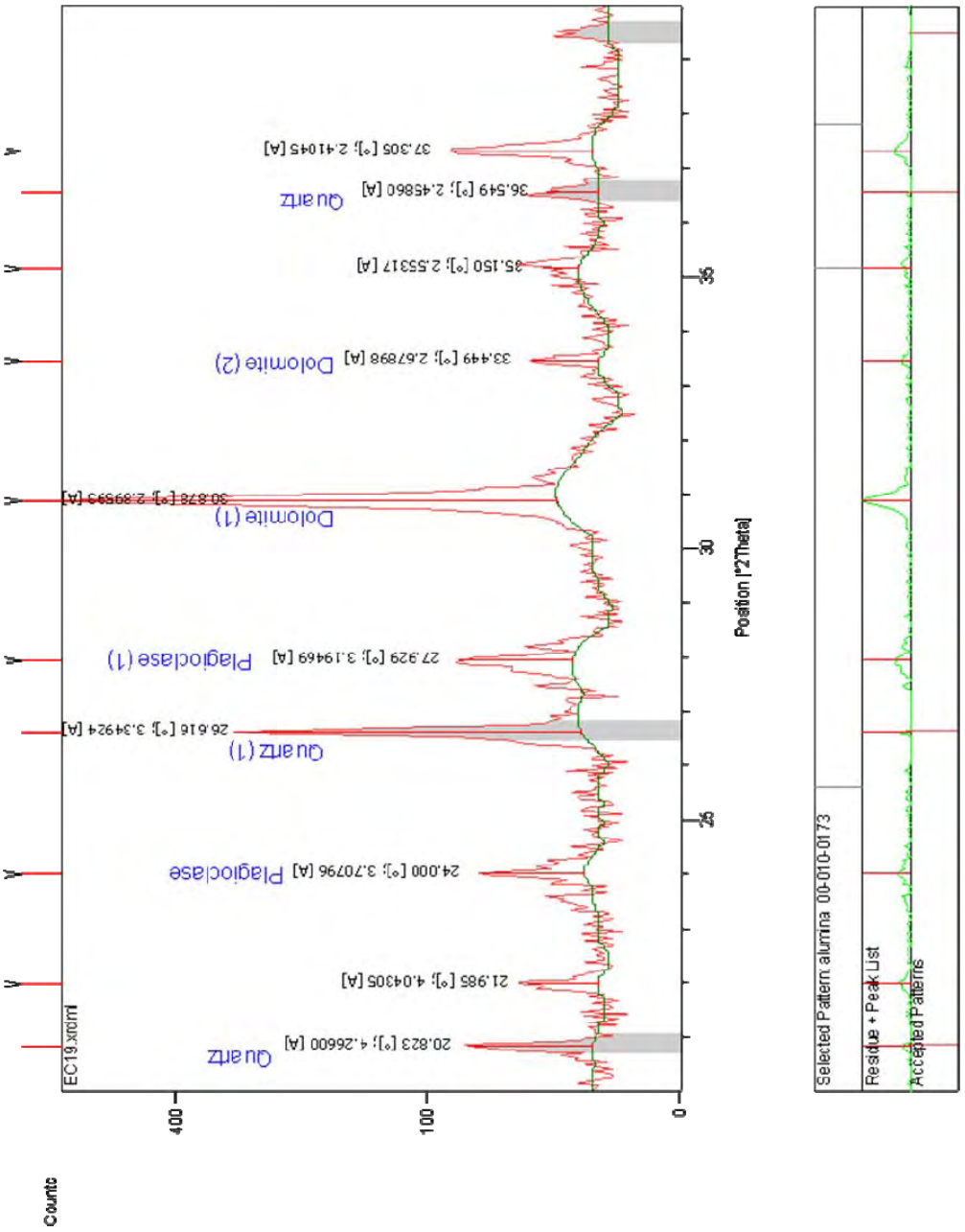
Counts
400
100
0
EC19.xrdml
Quartz
20.823 [°]; 4.26600 [Å]
21.985 [°]; 4.04305 [Å]
Plagioclase
24.000 [°]; 3.70796 [Å]
Quartz (1)
26.616 [°]; 3.34924 [Å]
Plagioclase (1)
27.929 [°]; 3.19469 [Å]
Dolomite (1)
30.878 [°]; 2.89593 [Å]
Dolomite (2)
33.449 [°]; 2.67898 [Å]
35.150 [°]; 2.55317 [Å]
Quartz
36.549 [°]; 2.45860 [Å]
37.305 [°]; 2.41045 [Å]
25
30
35
Position [°2Theta]
Selected Pattern alumina 00-010-0173
Residue + Peak List
Accepted Patterns

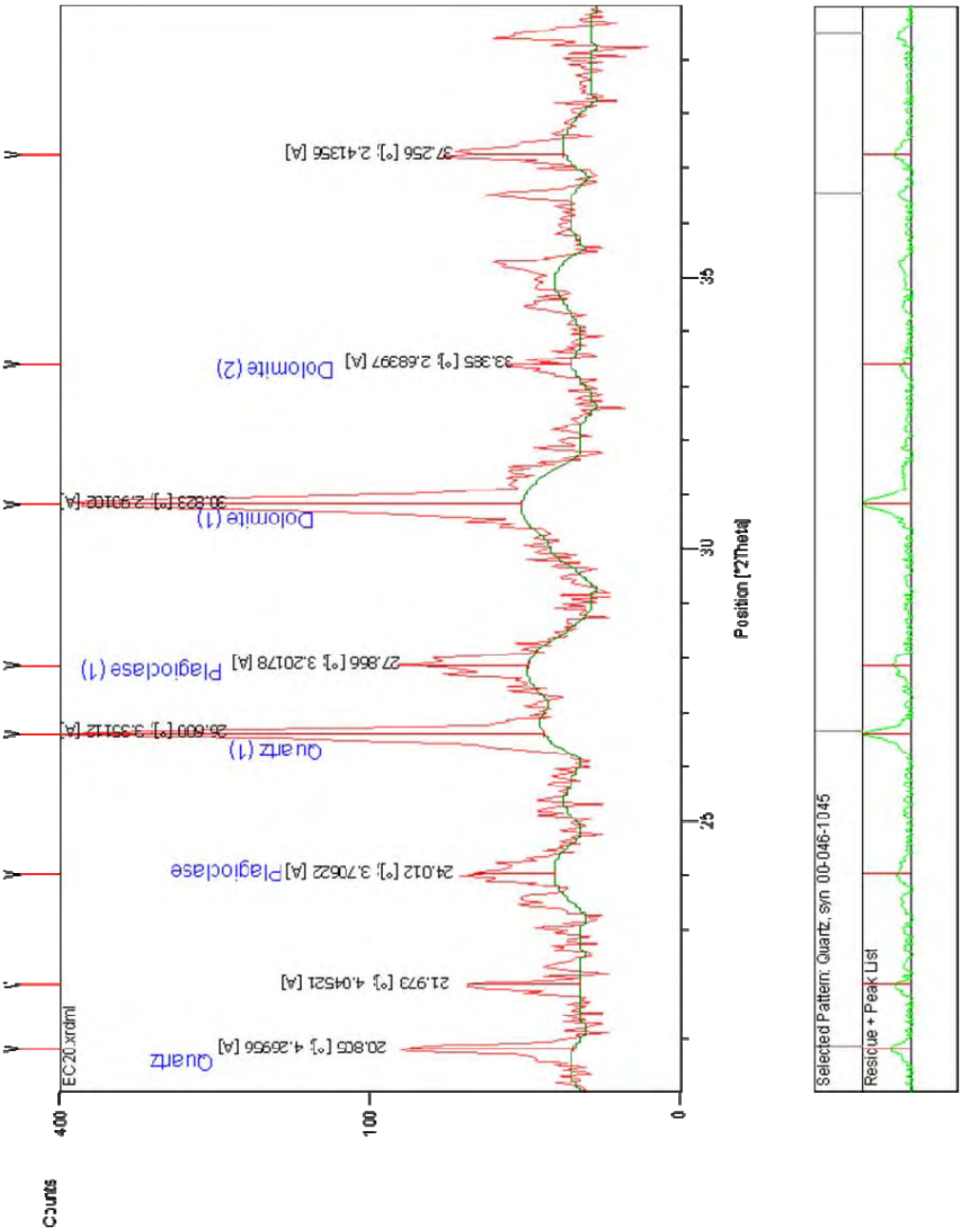
Counts
400
100
0
EC20.xrdml
Quartz
20.825 [°], 4.26956 [Å]
21.973 [°], 4.04521 [Å]
Plagioclase
24.012 [°], 3.70622 [Å]
Quartz (1)
26.600 [°], 3.35112 [Å]
Plagioclase (1)
27.866 [°], 3.20178 [Å]
Dolomite (1)
30.823 [°], 2.90102 [Å]
Dolomite (2)
33.365 [°], 2.68397 [Å]
37.256 [°], 2.41356 [Å]
25
30
35
Position [°2Theta]
Selected Pattern: Quartz, syn 00-046-1045
Residue + Peak List

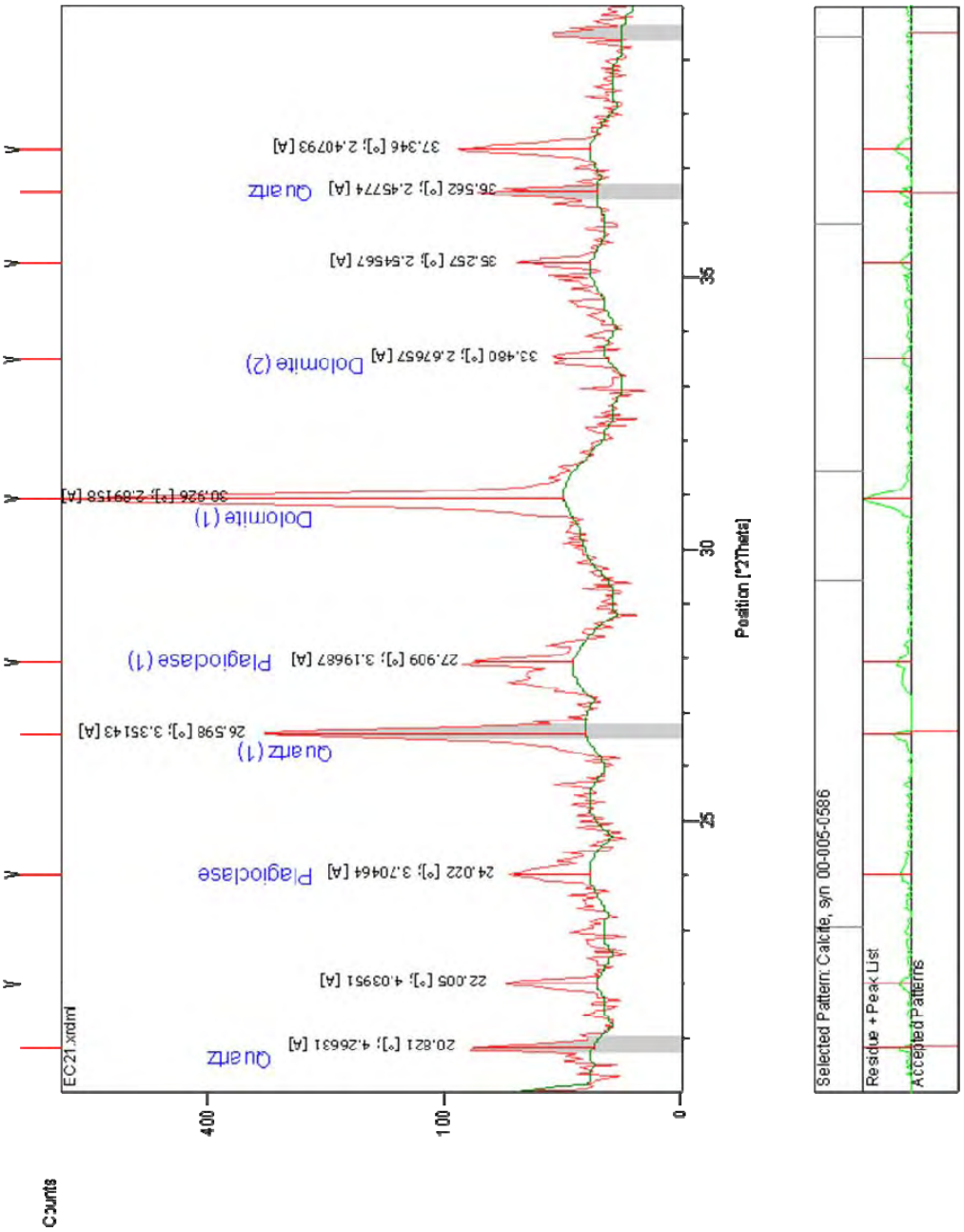
Counts
400
100
0
EC21.xrdml
Quartz
20.821 [°]; 4.26631 [Å]
22.005 [°]; 4.03951 [Å]
Plagioclase
24.022 [°]; 3.70464 [Å]
Quartz (1)
26.598 [°]; 3.35143 [Å]
Plagioclase (1)
27.909 [°]; 3.19687 [Å]
Dolomite (1)
30.926 [°]; 2.89158 [Å]
Dolomite (2)
33.460 [°]; 2.67657 [Å]
35.257 [°]; 2.54567 [Å]
Quartz
36.562 [°]; 2.45774 [Å]
37.346 [°]; 2.40793 [Å]
25
30
35
Position [°2Theta]
Selected Pattern: Calcite, syn 00-005-0586
Residue + Peak List
Accepted Patterns

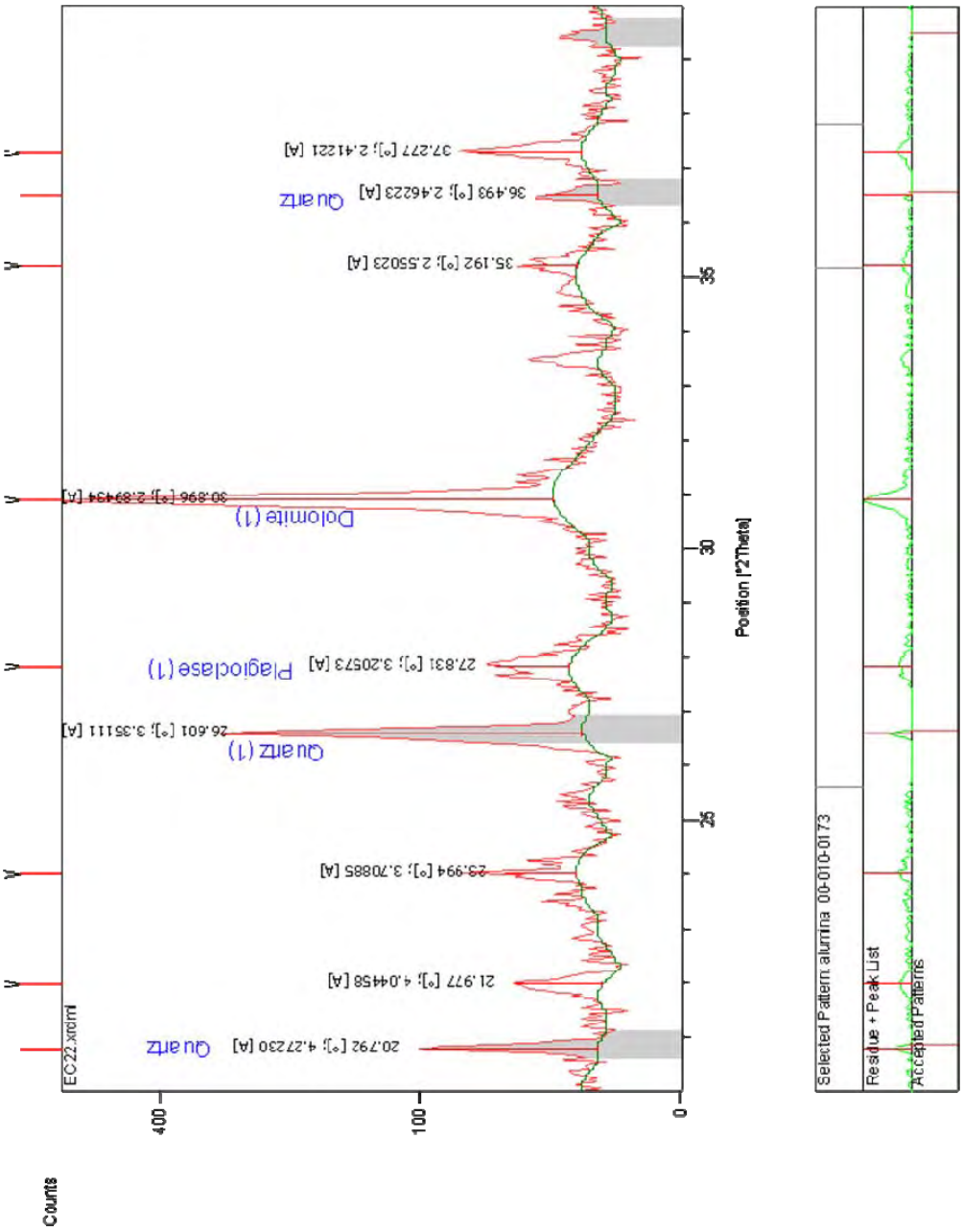
Counts
Position [°2Theta]
EC22.xrdml
Quartz
20.792 [°]; 4.27230 [Å]
21.977 [°]; 4.04458 [Å]
23.994 [°]; 3.70885 [Å]
Quartz (1)
26.601 [°]; 3.35111 [Å]
Plagioclase (1)
27.831 [°]; 3.20573 [Å]
Dolomite (1)
30.896 [°]; 2.89434 [Å]
35.192 [°]; 2.55023 [Å]
Quartz
36.493 [°]; 2.46223 [Å]
37.277 [°]; 2.41221 [Å]
Selected Pattern: alumina 00-010-0173
Residue + Peak List
Accepted Patterns

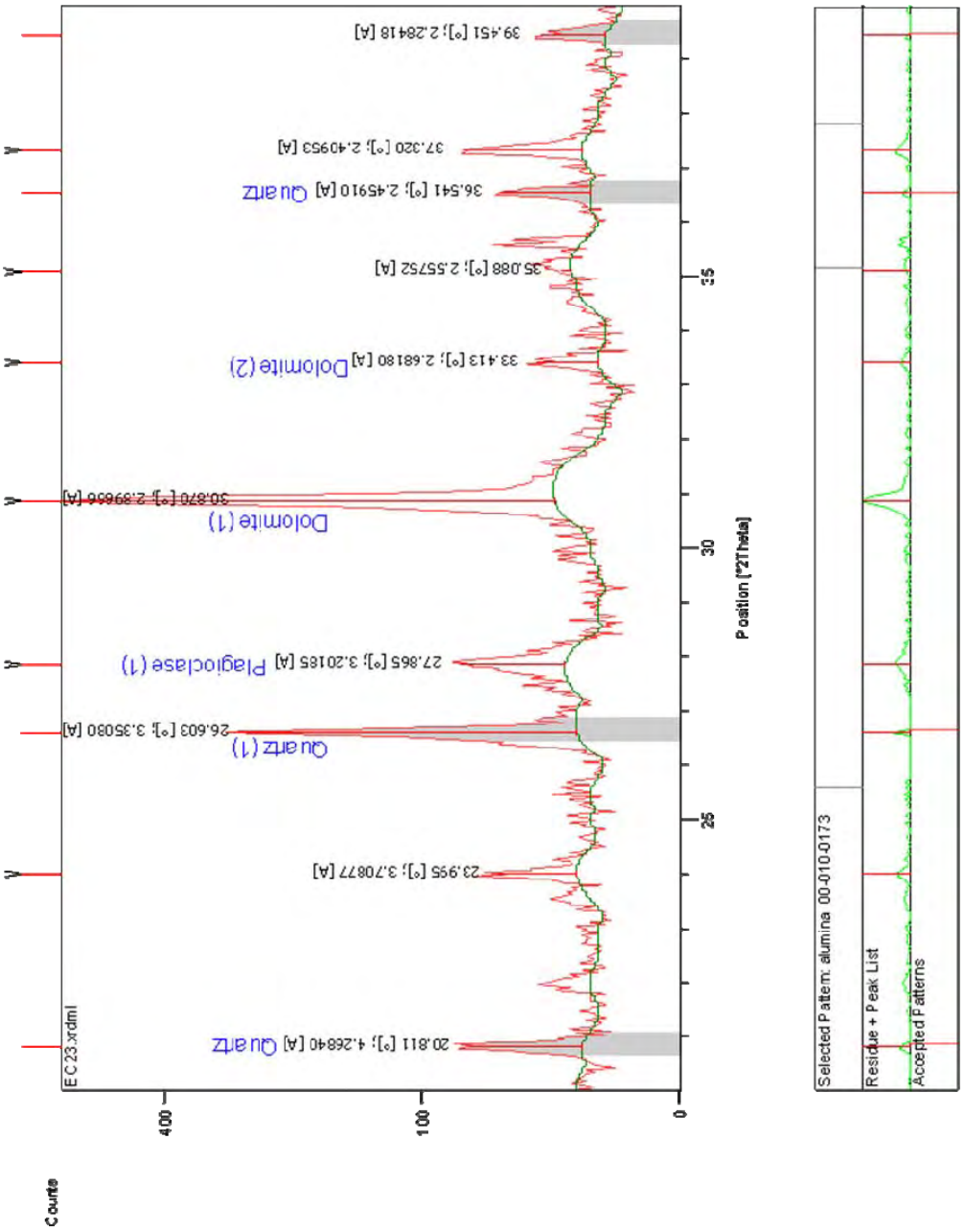
Counts
400
100
0
EC23.xrdml
20.811 [°]; 4.26840 [Å] Quartz
23.955 [°]; 3.70877 [Å]
26.603 [°]; 3.35080 [Å]
Quartz (1)
27.865 [°]; 3.20185 [Å] Plagioclase (1)
30.870 [°]; 2.89656 [Å]
Dolomite (1)
33.413 [°]; 2.68180 [Å] Dolomite (2)
35.088 [°]; 2.55752 [Å]
36.541 [°]; 2.45910 [Å] Quartz
37.320 [°]; 2.40953 [Å]
39.451 [°]; 2.28418 [Å]
25
30
35
Position [°2Theta]
Selected Pattern: alumina 00-010-0173
Residue + Peak List
Accepted Patterns

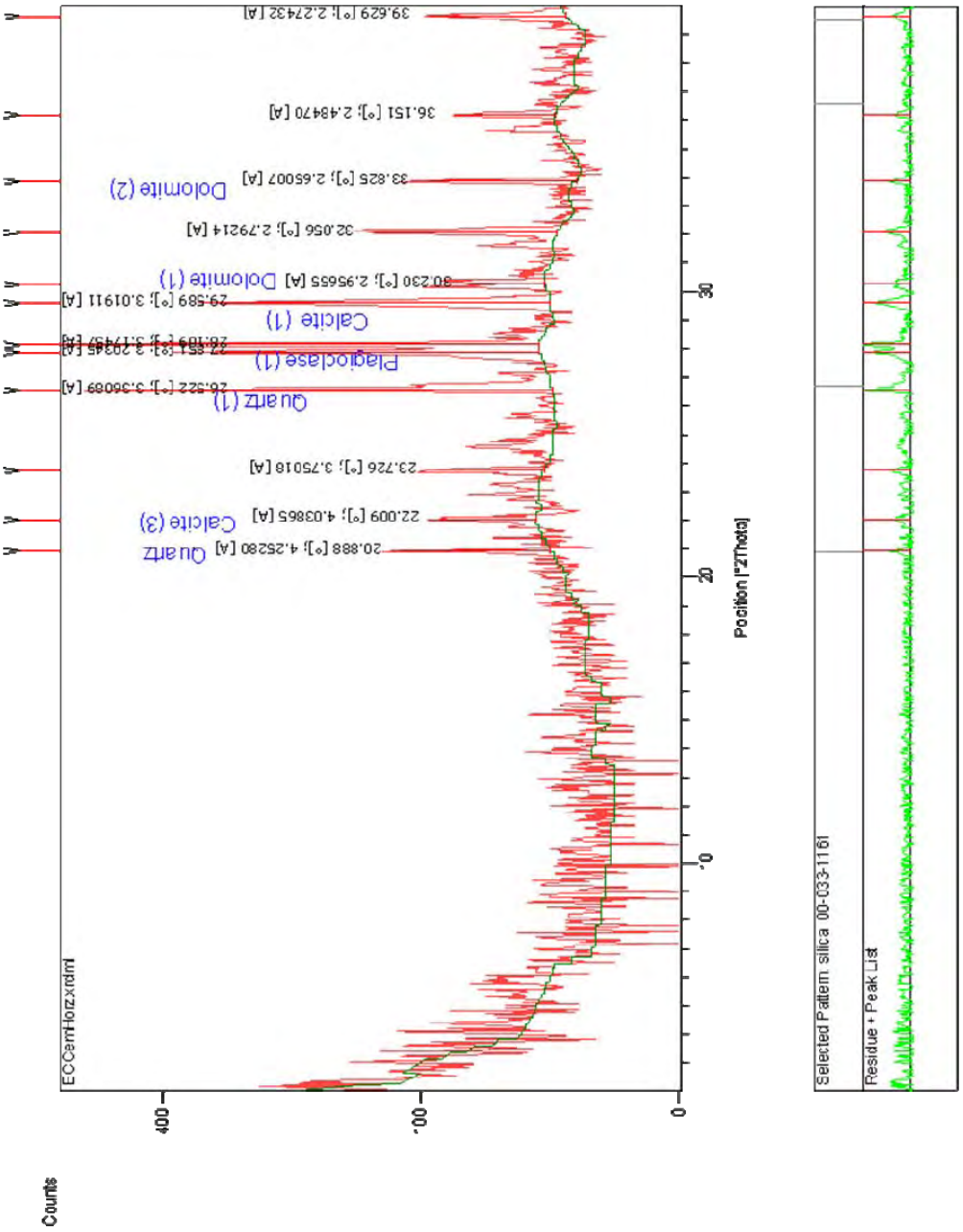
Counts
400
200
0
ECCamHorz.xrdml
Quartz
Calcite (3)
20.888 [°]; 4.25280 [Å]
22.009 [°]; 4.03865 [Å]
23.726 [°]; 3.75018 [Å]
Quartz (1)
26.622 [°]; 3.36089 [Å]
Plagioclase (1)
Calcite (1)
29.589 [°]; 3.01911 [Å]
Dolomite (1)
30.230 [°]; 2.95655 [Å]
32.056 [°]; 2.79214 [Å]
Dolomite (2)
33.825 [°]; 2.65007 [Å]
36.151 [°]; 2.48470 [Å]
39.629 [°]; 2.27432 [Å]
0
20
30
Position [°2Theta]
Selected Pattern silica 00-033-1161
Residue + Peak List

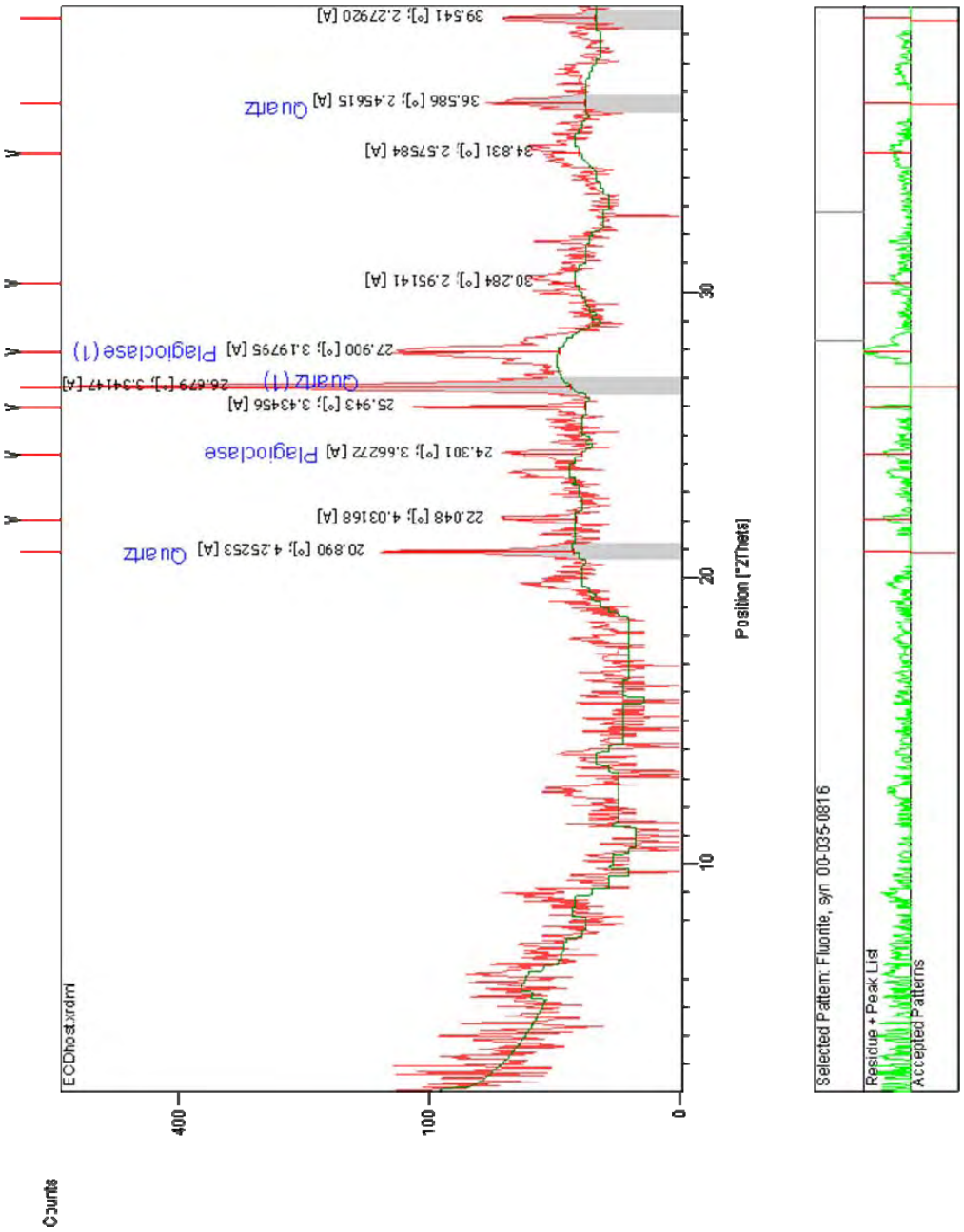
Counts
400
100
0
ECDhost.xrdml
10
20
30
Position [°2Theta]
39.541 [°]; 2.27920 [A]
Quartz
36.586 [°]; 2.45615 [A]
34.831 [°]; 2.57584 [A]
30.284 [°]; 2.95141 [A]
Plagioclase (1)
27.900 [°]; 3.19795 [A]
Quartz (1)
26.679 [°]; 3.34147 [A]
25.943 [°]; 3.43456 [A]
Plagioclase
24.301 [°]; 3.66272 [A]
22.048 [°]; 4.03168 [A]
Quartz
20.890 [°]; 4.25253 [A]
Selected Pattern: Fluorite, syn 00-035-0816
Residue + Peak List
Accepted Patterns

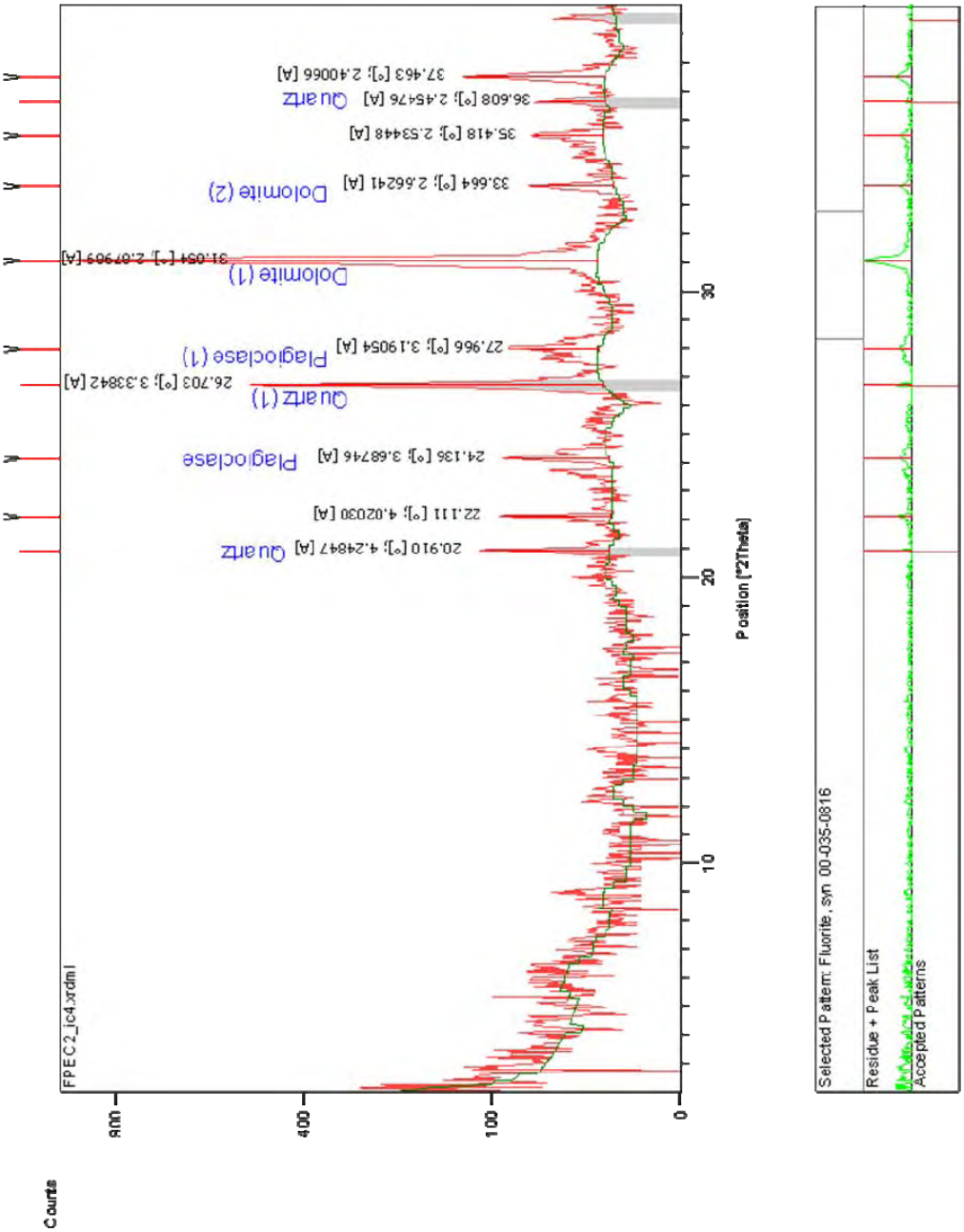
FPEC2_ic4.xrdml
Counts
Position [°2Theta]
Quartz
Plagioclase
Quartz (1)
Plagioclase (1)
Dolomite (1)
Dolomite (2)
Quartz
20.910 [°]; 4.24847 [A]
22.111 [°]; 4.02030 [A]
24.136 [°]; 3.68746 [A]
26.703 [°]; 3.33842 [A]
27.966 [°]; 3.19054 [A]
31.054 [°]; 2.87909 [A]
33.664 [°]; 2.66241 [A]
35.418 [°]; 2.53448 [A]
36.608 [°]; 2.45476 [A]
37.463 [°]; 2.40066 [A]
Selected Pattern: Fluorite, syn 00-035-0816
Residue + Peak List
Accepted Patterns

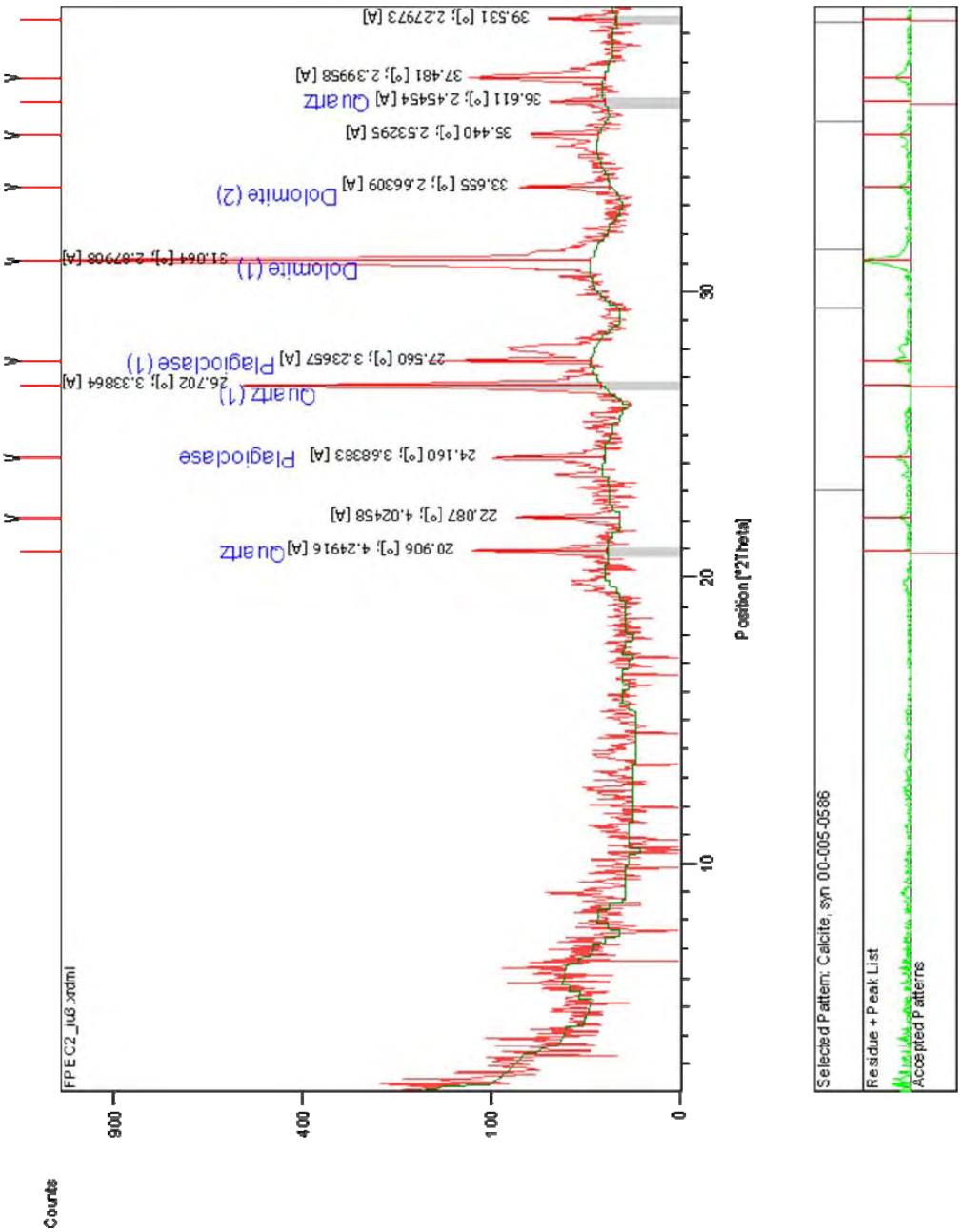
Counts
900
400
100
0
10
20
30
Position [°2Theta]
FPEC2_ju6.xrdml
Quartz
20.906 [°]; 4.24916 [A]
22.087 [°]; 4.02458 [A]
Plagioclase
24.160 [°]; 3.68383 [A]
Quartz (1)
26.702 [°]; 3.33864 [A]
Plagioclase (1)
27.560 [°]; 3.23657 [A]
Dolomite (1)
31.064 [°]; 2.87908 [A]
Dolomite (2)
33.655 [°]; 2.66309 [A]
35.440 [°]; 2.53295 [A]
Quartz
36.611 [°]; 2.45454 [A]
37.481 [°]; 2.39958 [A]
39.531 [°]; 2.27973 [A]
Selected Pattern: Calcite, syn 00-005-0586
Residue + Peak List
Accepted Patterns

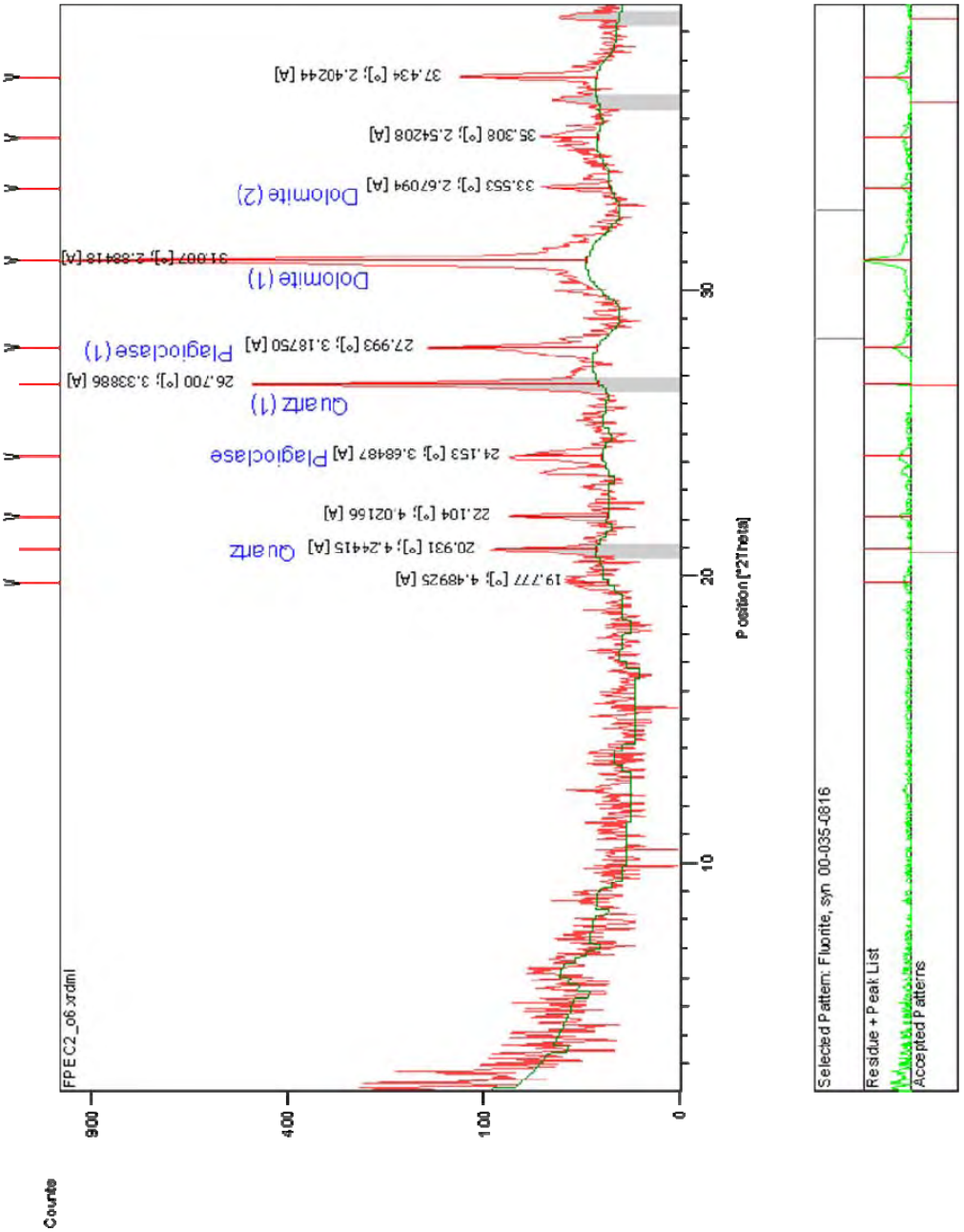
FPEC2_06.xrdml
Counts
900
400
100
0
10
20
30
Position [°2Theta]
19.777 [°]; 4.48925 [A]
Quartz
20.931 [°]; 4.24415 [A]
22.104 [°]; 4.02166 [A]
Plagioclase
24.153 [°]; 3.68487 [A]
Quartz (1)
26.700 [°]; 3.33886 [A]
Plagioclase (1)
27.993 [°]; 3.18750 [A]
Dolomite (1)
31.007 [°]; 2.88418 [A]
Dolomite (2)
33.553 [°]; 2.67094 [A]
35.308 [°]; 2.54208 [A]
37.434 [°]; 2.40244 [A]
Selected Pattern: Fluorite, syn 00-035-0816
Residue + Peak List
Accepted Patterns

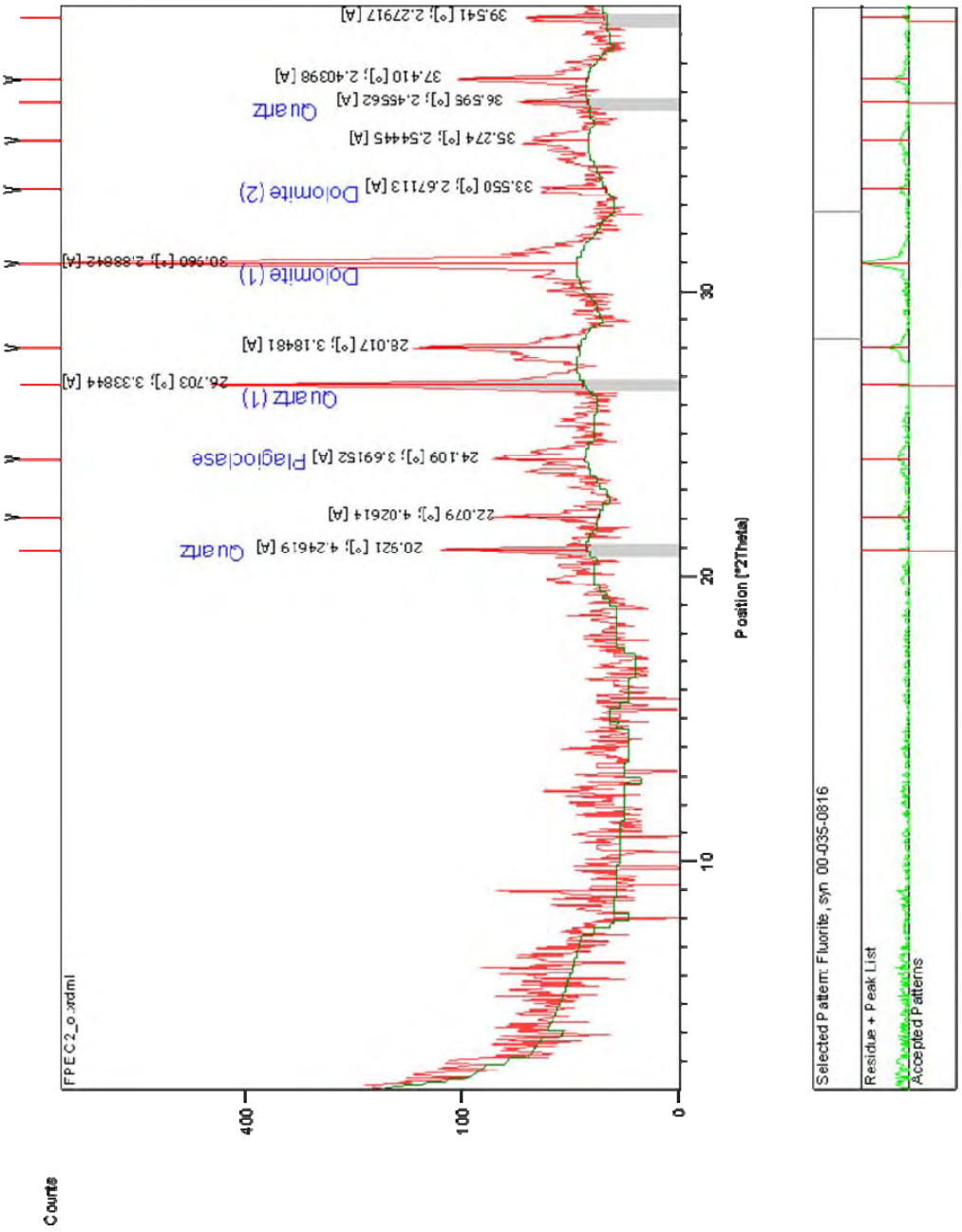
Counts
400
100
0
10
20
30
Position [°2Theta]
FPEC2_o.xrdml
20.921 [°]; 4.24619 [Å]
Quartz
22.079 [°]; 4.02614 [Å]
24.109 [°]; 3.69152 [Å]
Plagioclase
26.703 [°]; 3.33844 [Å]
Quartz (1)
28.017 [°]; 3.18481 [Å]
30.960 [°]; 2.88842 [Å]
Dolomite (1)
33.550 [°]; 2.67113 [Å]
Dolomite (2)
35.274 [°]; 2.54445 [Å]
36.595 [°]; 2.45562 [Å]
Quartz
37.410 [°]; 2.40398 [Å]
39.541 [°]; 2.27917 [Å]
Selected Pattern: Fluorite, syn 00-035-0816
Residue + Peak List
Accepted Patterns

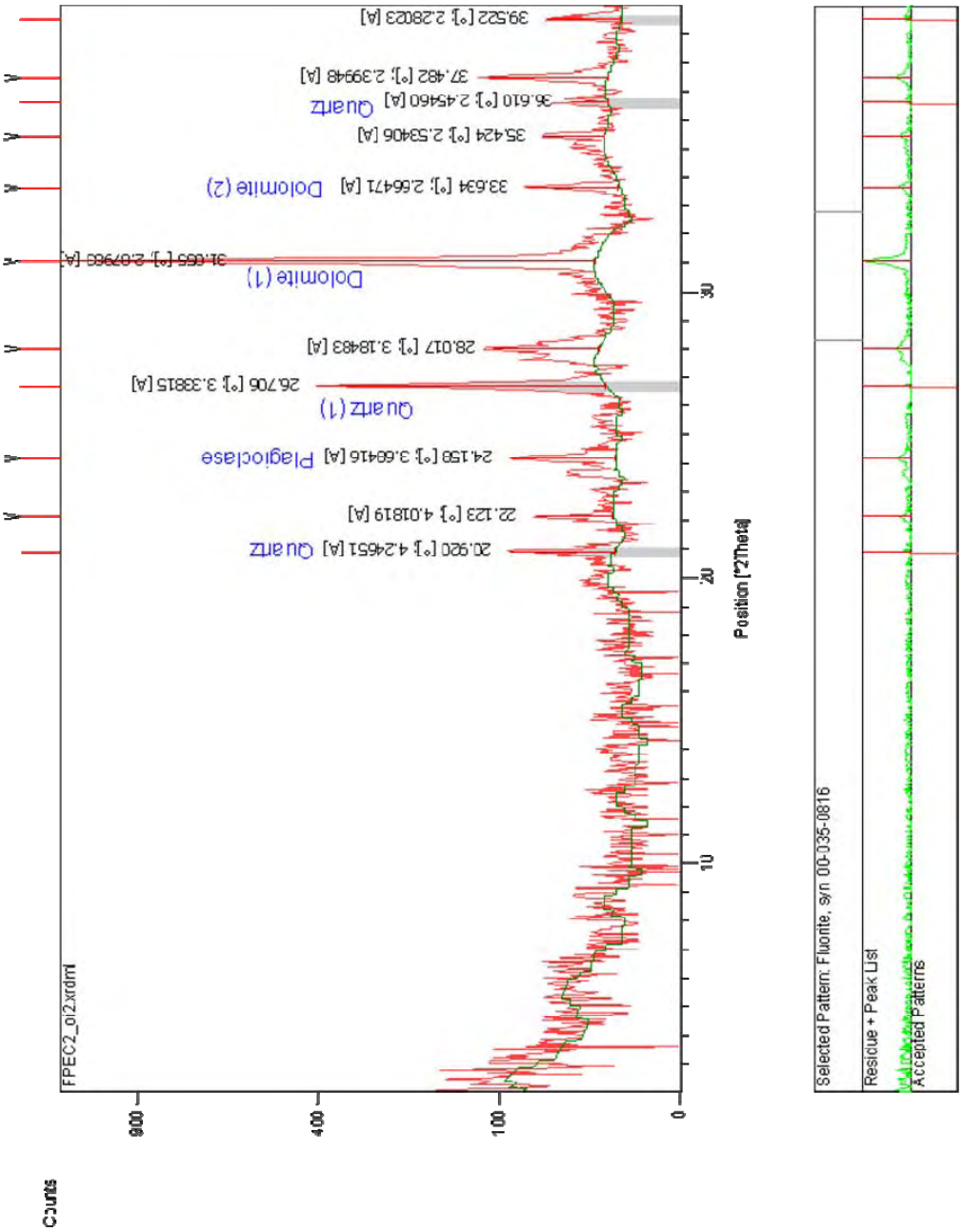
FPEC2_o12.xrdml
Counts
900
400
100
0
10
20
30
Position [°2Theta]
20.920 [°]; 4.24651 [A] Quartz
22.123 [°]; 4.01819 [A]
24.158 [°]; 3.68416 [A] Plagioclase
26.706 [°]; 3.33815 [A]
Quartz (1)
28.017 [°]; 3.18483 [A]
31.665 [°]; 2.82960 [A]
Dolomite (1)
33.634 [°]; 2.66471 [A] Dolomite (2)
35.424 [°]; 2.53406 [A]
36.610 [°]; 2.45460 [A] Quartz
37.482 [°]; 2.39948 [A]
39.522 [°]; 2.28023 [A]
Selected Pattern: Fluorite, syn 00-035-0816
Residue + Peak List
Accepted Patterns

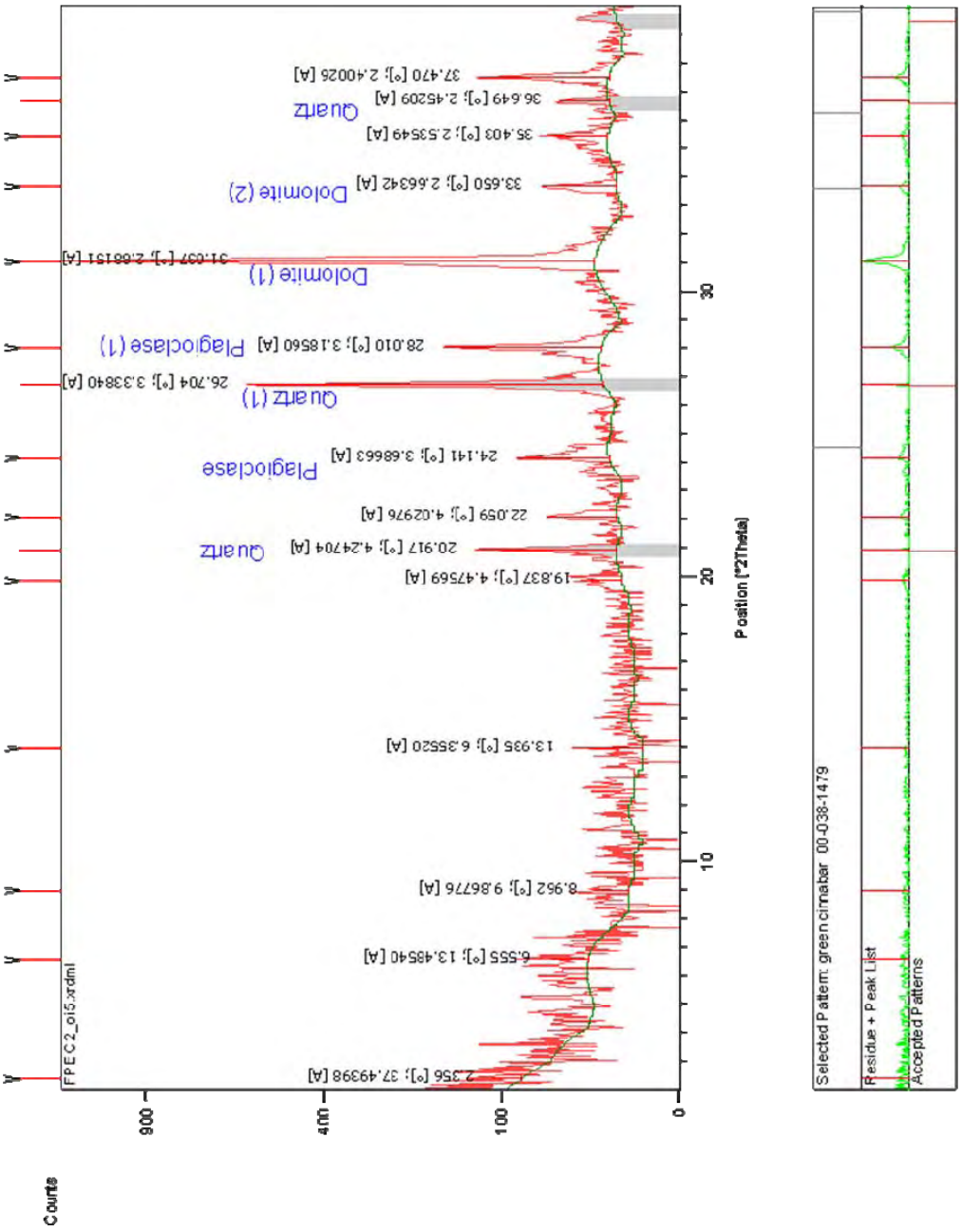
Counts
900
400
100
0
10
20
30
Position [°2Theta]
FPEC2_oi5.xrdml
2.356 [°]; 37.49398 [A]
6.555 [°]; 13.48540 [A]
8.962 [°]; 9.86776 [A]
13.935 [°]; 6.35520 [A]
19.837 [°]; 4.47569 [A]
20.917 [°]; 4.24704 [A]
Quartz
22.059 [°]; 4.02976 [A]
24.141 [°]; 3.68663 [A]
Plagioclase
26.704 [°]; 3.33840 [A]
Quartz (1)
28.010 [°]; 3.18560 [A]
Plagioclase (1)
31.037 [°]; 2.88151 [A]
Dolomite (1)
33.650 [°]; 2.66342 [A]
Dolomite (2)
35.403 [°]; 2.53549 [A]
36.649 [°]; 2.45209 [A]
Quartz
37.470 [°]; 2.40026 [A]
Selected Pattern: green cinnabar 00-038-1479
Residue + Peak List
Accepted Patterns

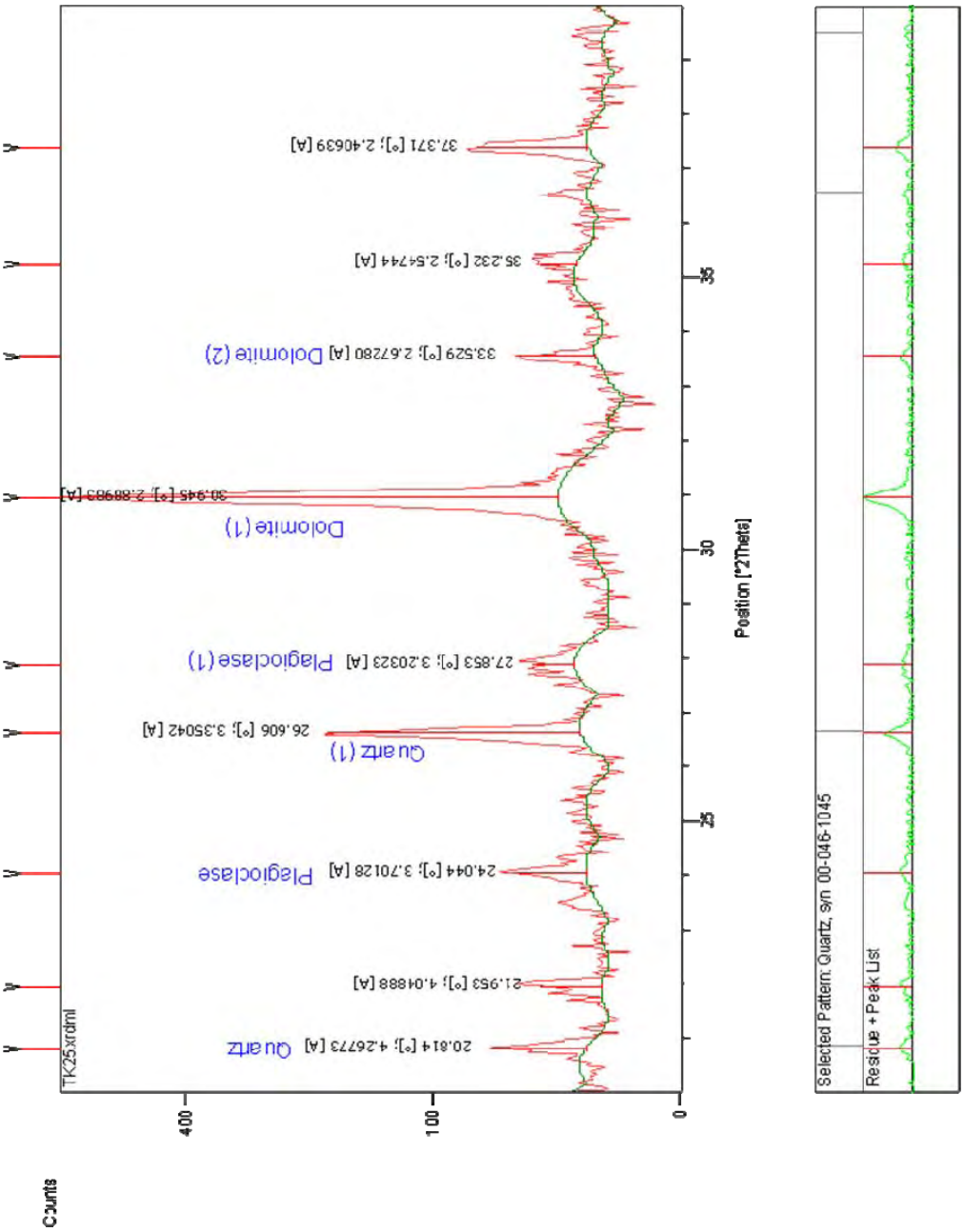
Counts
400
100
0
TK25.xrdml
Quartz
20.814 [°]; 4.26773 [Å]
21.953 [°]; 4.04888 [Å]
Plagioclase
24.044 [°]; 3.70128 [Å]
Quartz (1)
26.606 [°]; 3.35042 [Å]
Plagioclase (1)
27.853 [°]; 3.20323 [Å]
Dolomite (1)
30.945 [°]; 2.88983 [Å]
Dolomite (2)
33.529 [°]; 2.67280 [Å]
35.232 [°]; 2.54744 [Å]
37.371 [°]; 2.40639 [Å]
25
30
35
Position [°2Theta]
Selected Pattern: Quartz, syn 00-046-1045
Residue + Peak List

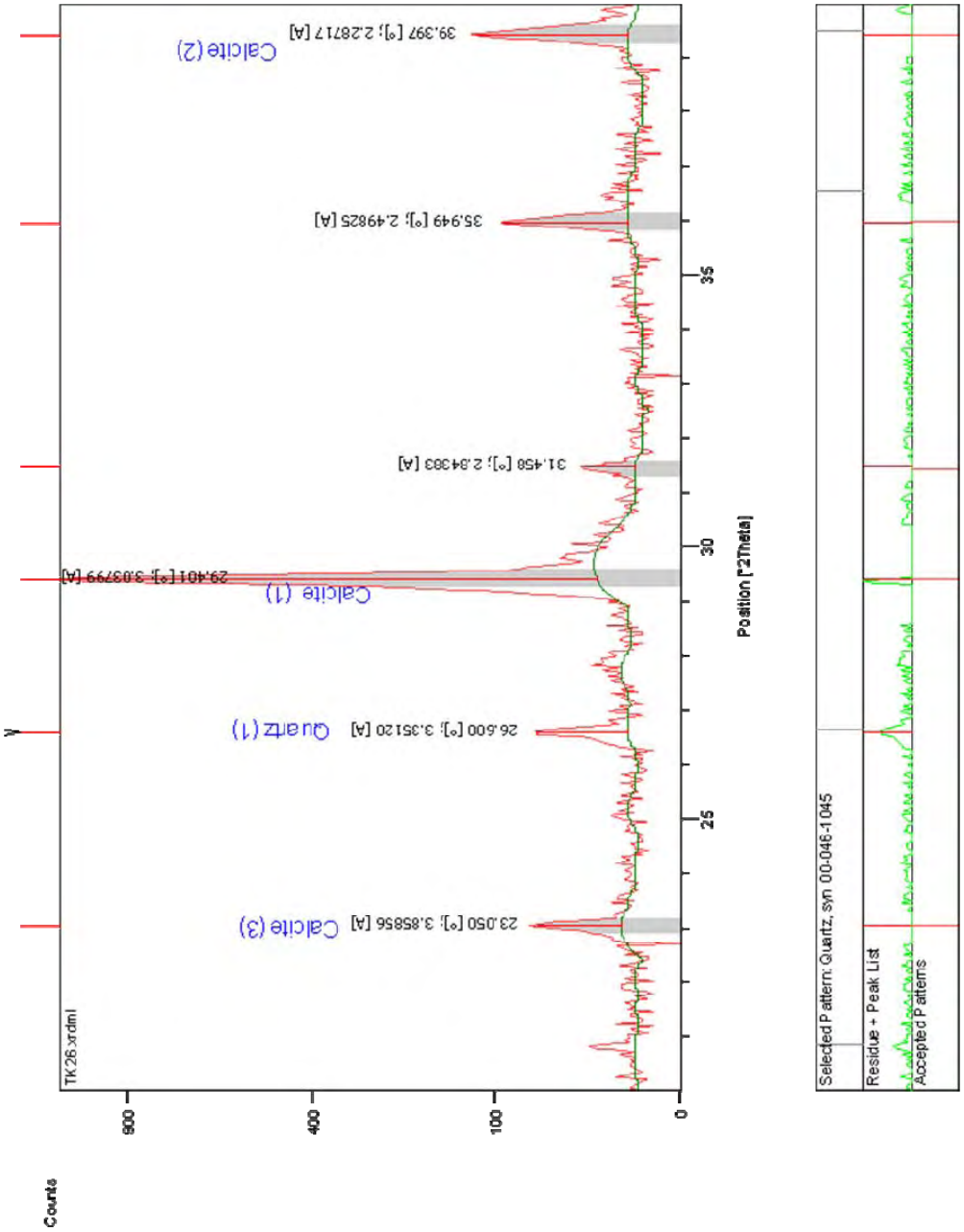
Counts
900
400
100
0
TK26.xrdml
Calcite (3)
23.050 [°]; 3.85856 [A]
Quartz (1)
26.600 [°]; 3.35120 [A]
Calcite (1)
29.401 [°]; 3.03799 [A]
31.458 [°]; 2.84383 [A]
35.949 [°]; 2.49825 [A]
Calcite (2)
39.397 [°]; 2.28717 [A]
25
30
35
Position [°2Theta]
Selected Pattern: Quartz, syn 00-046-1045
Residue + Peak List
Accepted Patterns

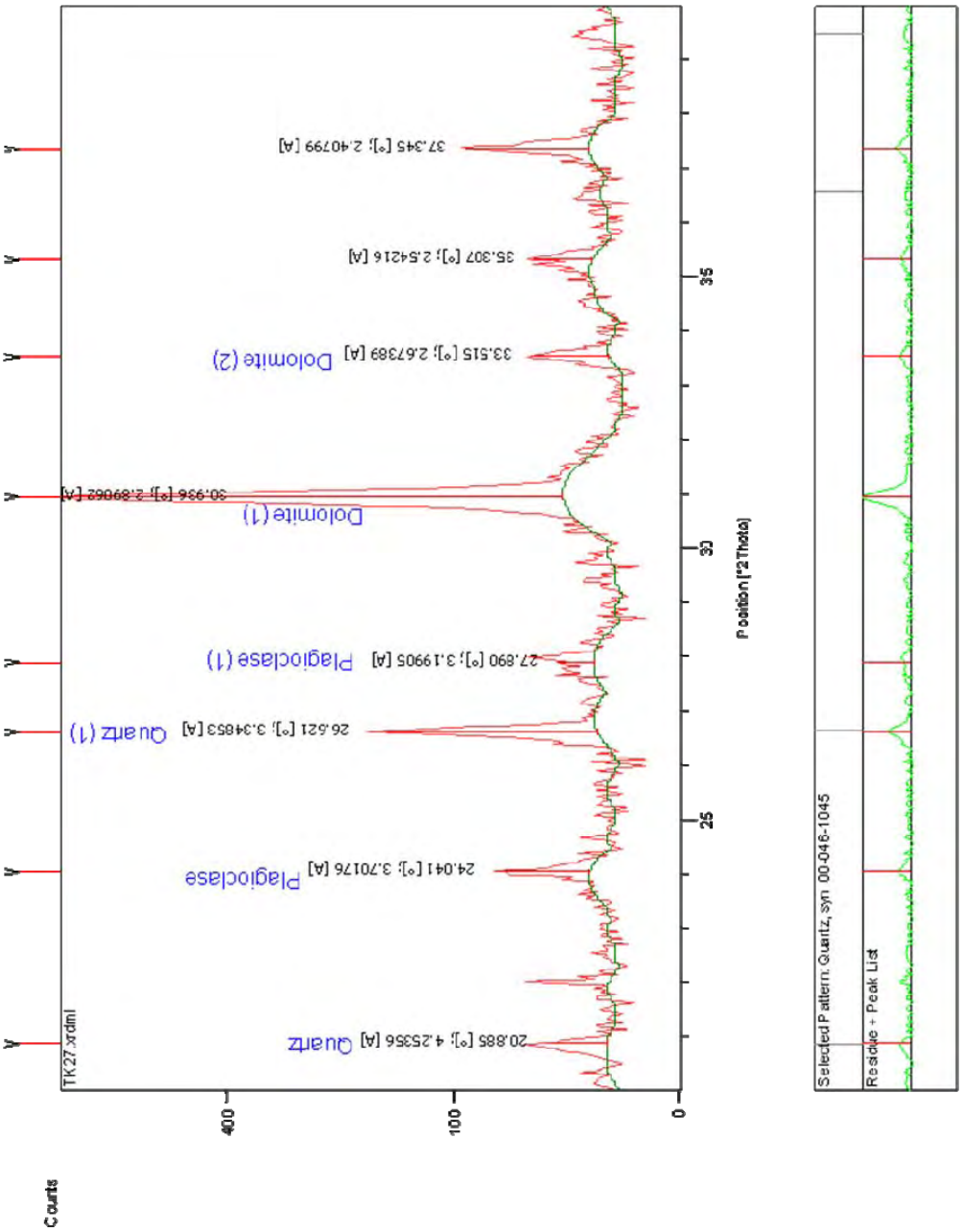
Counts
400
100
0
TK27.xrdml
Quartz
20.885 [°]; 4.25356 [Å]
Plagioclase
24.041 [°]; 3.70176 [Å]
Quartz (1)
26.621 [°]; 3.34853 [Å]
Plagioclase (1)
27.890 [°]; 3.19905 [Å]
Dolomite (1)
30.936 [°]; 2.89062 [Å]
Dolomite (2)
33.515 [°]; 2.67389 [Å]
35.307 [°]; 2.54216 [Å]
37.345 [°]; 2.40799 [Å]
25
30
35
Position [°2Theta]
Selected Pattern: Quartz, syn 00-046-1045
Residue + Peak List

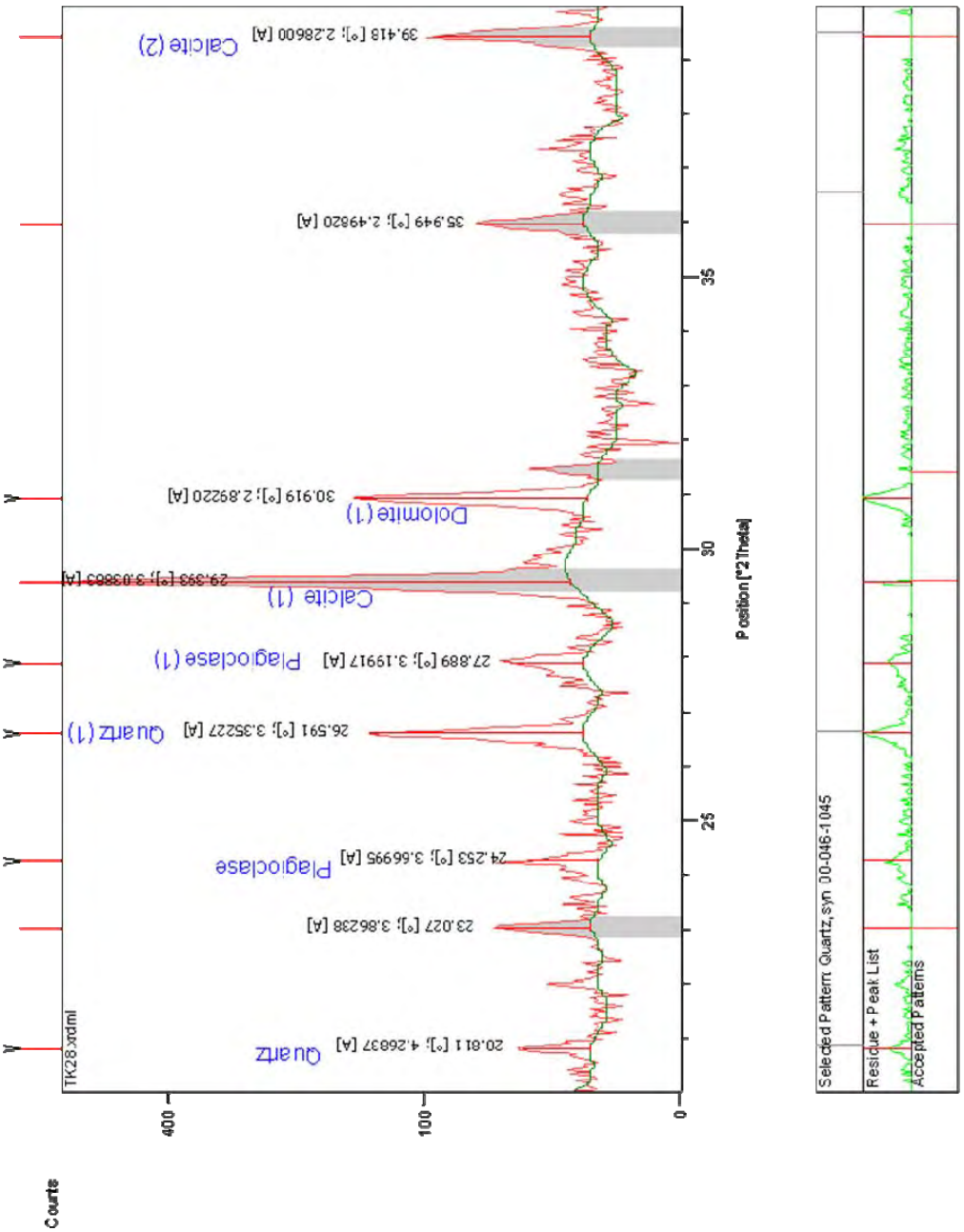
Counts
400
100
0
TK28.xrdml
Quartz
20.811 [°]; 4.26837 [Å]
23.027 [°]; 3.86238 [Å]
Plagioclase
24.253 [°]; 3.66995 [Å]
Quartz (1)
26.591 [°]; 3.35227 [Å]
Plagioclase (1)
27.889 [°]; 3.19917 [Å]
Calcite (1)
29.393 [°]; 3.03803 [Å]
Dolomite (1)
30.919 [°]; 2.89220 [Å]
35.949 [°]; 2.49820 [Å]
Calcite (2)
39.418 [°]; 2.28600 [Å]
25
30
35
Position [°2Theta]
Selected Pattern: Quartz, syn 00-046-1045
Residue + Peak List
Accepted Patterns

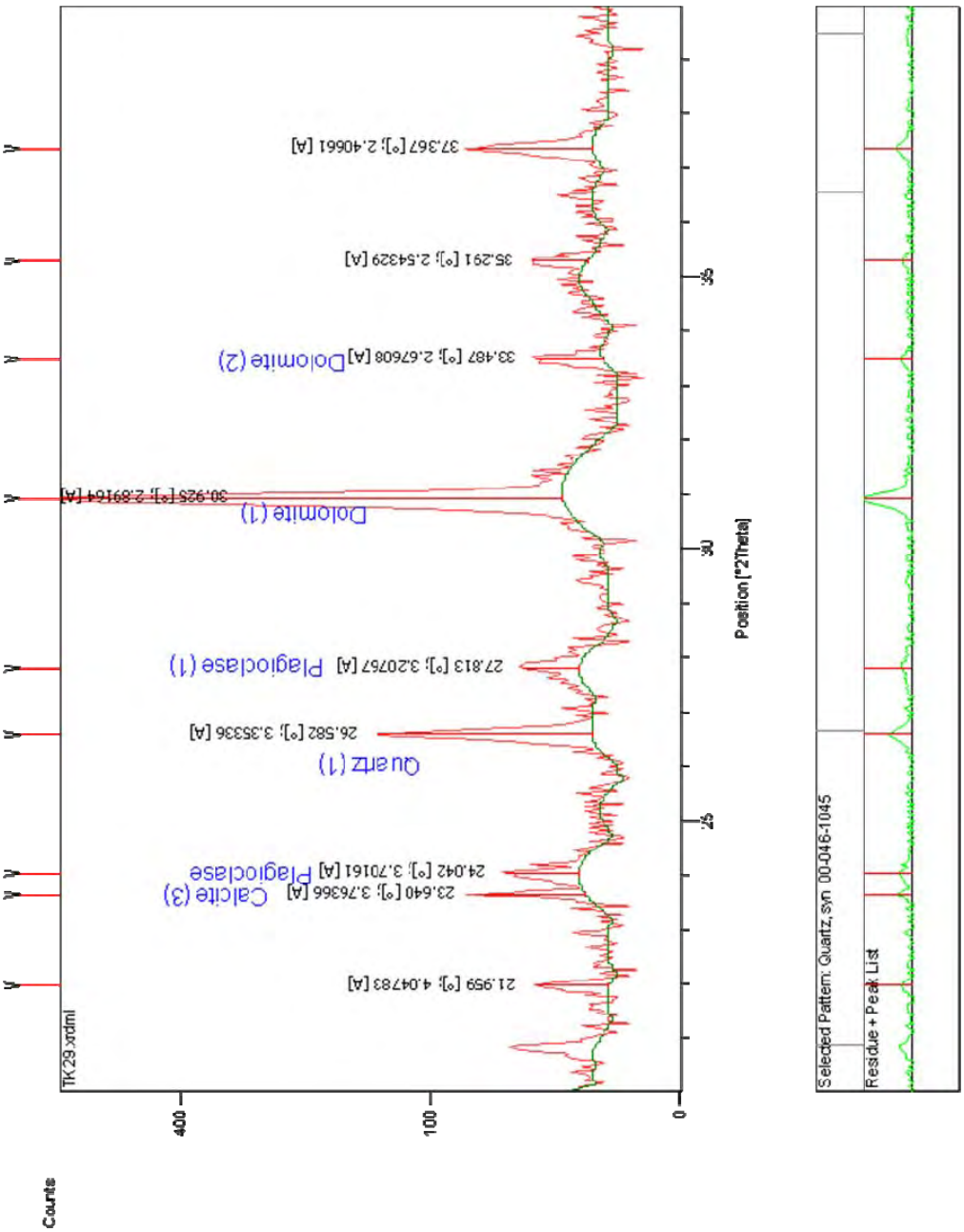
Counts
400
100
0
TK29.xrdml
21.959 [°]; 4.04783 [Å]
23.640 [°]; 3.76366 [Å]
Calcite (3)
24.042 [°]; 3.70161 [Å]
Plagioclase
Quartz (1)
26.582 [°]; 3.35336 [Å]
27.813 [°]; 3.20767 [Å]
Plagioclase (1)
30.925 [°]; 2.89164 [Å]
Dolomite (1)
33.487 [°]; 2.67608 [Å]
Dolomite (2)
35.291 [°]; 2.54329 [Å]
37.367 [°]; 2.40661 [Å]
25
30
35
Position [°2Theta]
Selected Pattern: Quartz, syn 00-046-1045
Residue + Peak List

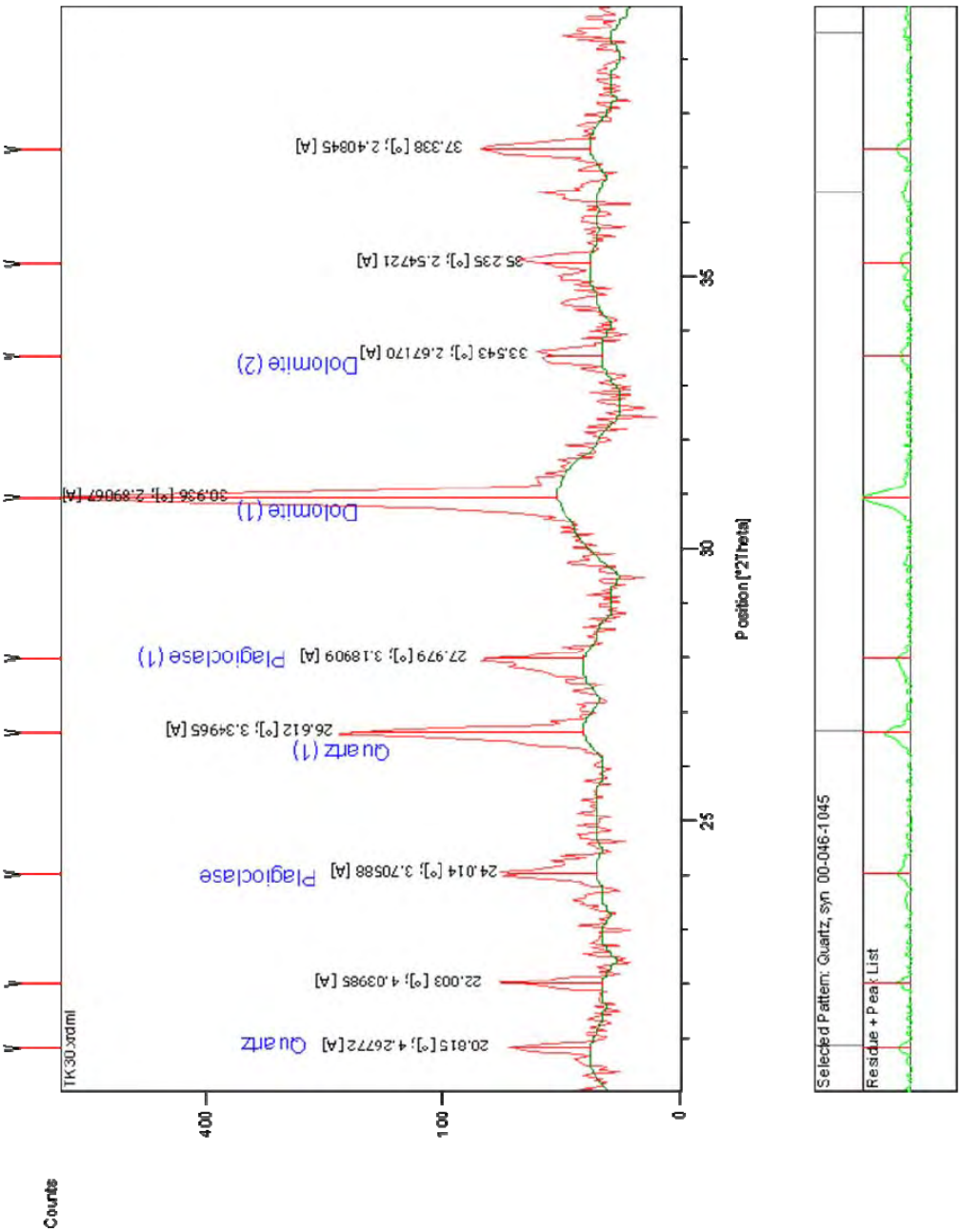
Counts
400
100
0
TK30.xrdml
20.815 [°]; 4.26772 [A]
Quartz
22.003 [°]; 4.03985 [A]
24.014 [°]; 3.70588 [A]
Plagioclase
26.612 [°]; 3.34965 [A]
Quartz (1)
27.979 [°]; 3.18909 [A]
Plagioclase (1)
30.936 [°]; 2.89067 [A]
Dolomite (1)
33.543 [°]; 2.67170 [A]
Dolomite (2)
35.235 [°]; 2.54721 [A]
37.338 [°]; 2.40845 [A]
25
30
35
Position [°2Theta]
Selected Pattern: Quartz, syn 00-046-1045
Residue + Peak List

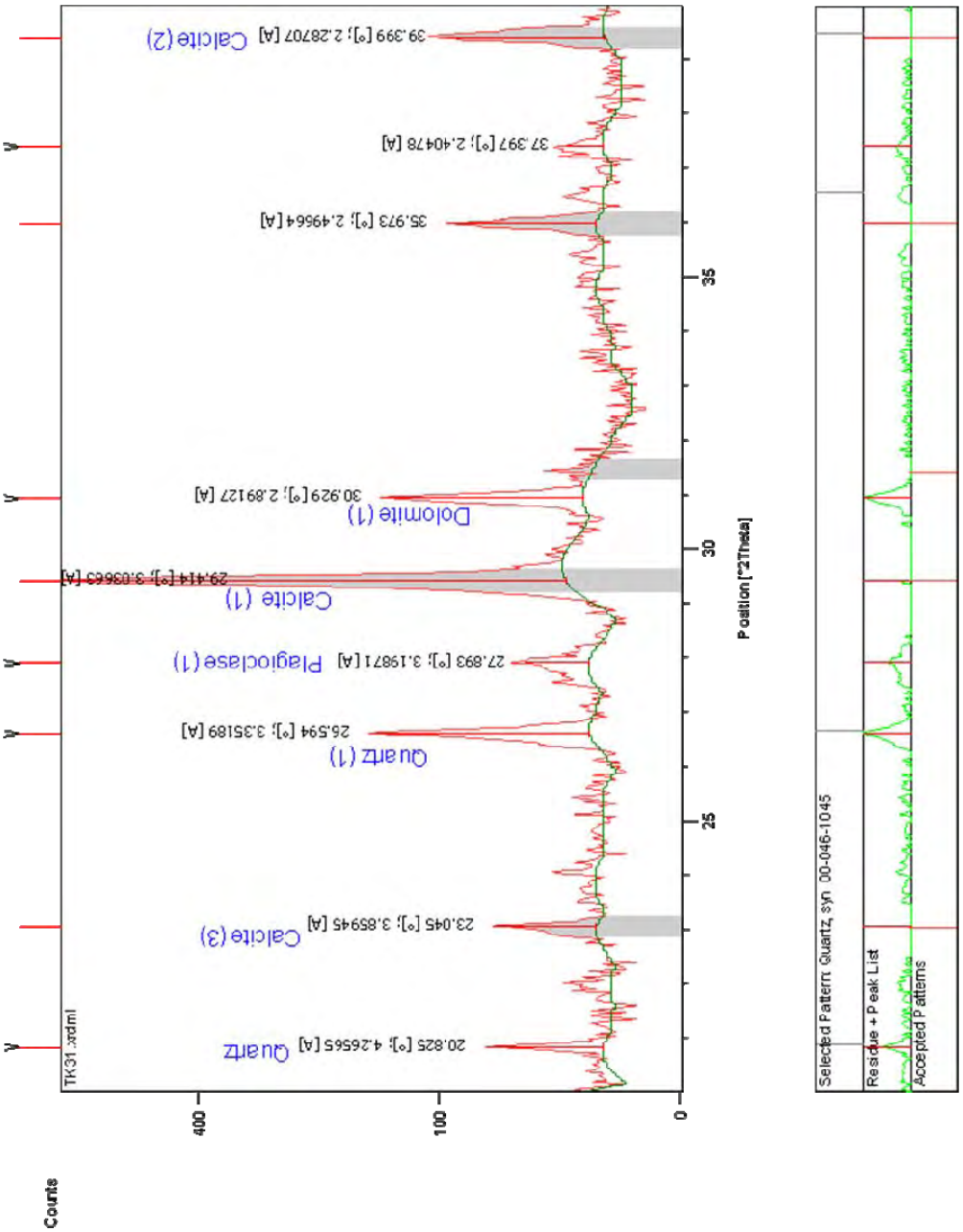
Counts
400
100
0
25
30
35
Position [°2Theta]
TK31.xrdml
Quartz
20.825 [°]; 4.26565 [A]
Calcite (3)
23.045 [°]; 3.85945 [A]
Quartz (1)
26.594 [°]; 3.35189 [A]
Plagioclase (1)
27.893 [°]; 3.19871 [A]
Calcite (1)
29.414 [°]; 3.03663 [A]
Dolomite (1)
30.929 [°]; 2.89127 [A]
35.973 [°]; 2.49664 [A]
37.397 [°]; 2.40478 [A]
Calcite (2)
39.399 [°]; 2.28707 [A]
Selected Pattern: Quartz, syn 00-046-1045
Residue + Peak List
Accepted Patterns

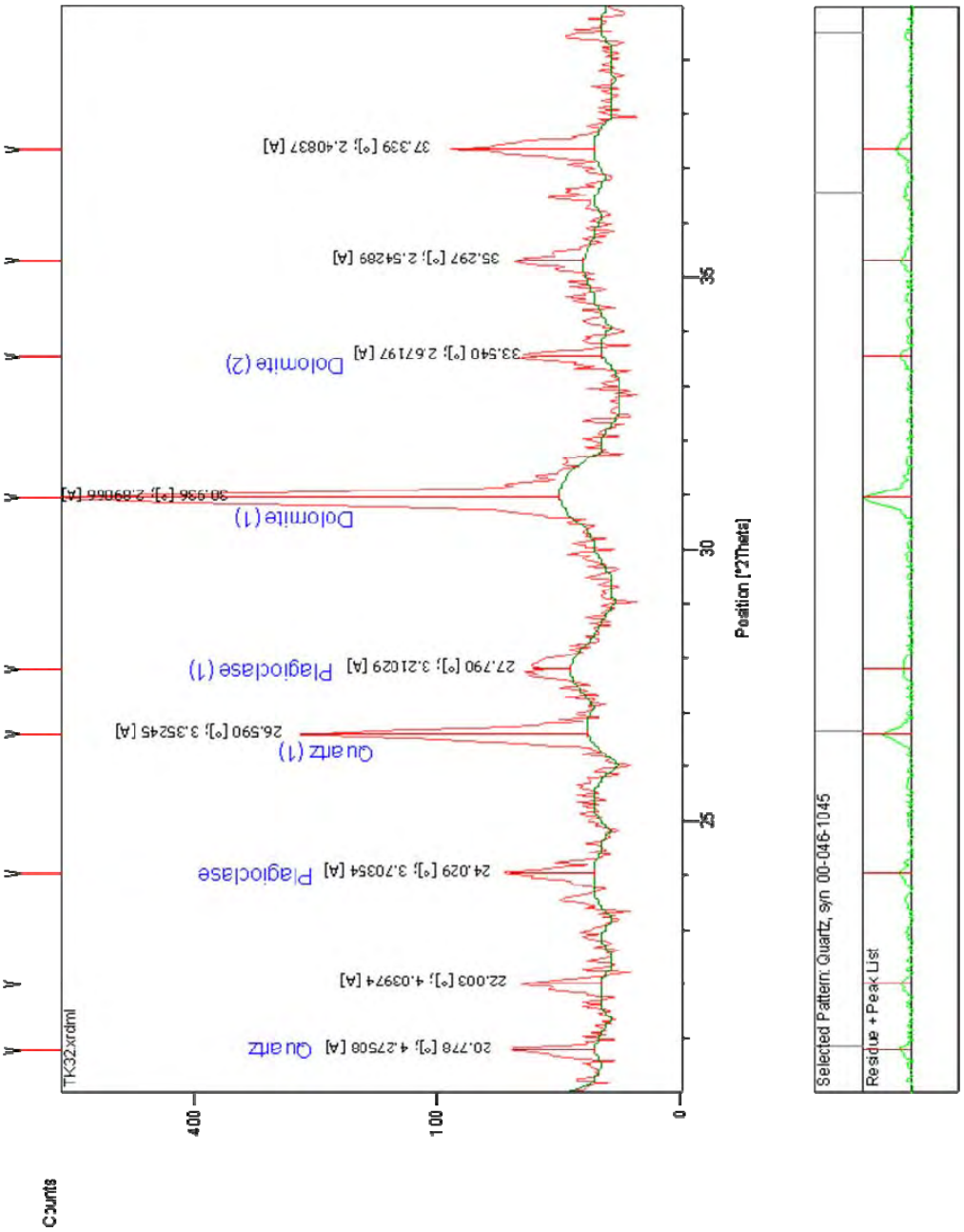
Counts
400
100
0
25
30
35
Position [°2Theta]
TK32.xrdml
Quartz
20.778 [°]; 4.27508 [A]
22.003 [°]; 4.03974 [A]
Plagioclase
24.029 [°]; 3.70354 [A]
Quartz (1)
26.590 [°]; 3.35245 [A]
Plagioclase (1)
27.790 [°]; 3.21029 [A]
Dolomite (1)
30.936 [°]; 2.89066 [A]
Dolomite (2)
33.540 [°]; 2.67197 [A]
35.297 [°]; 2.54289 [A]
37.339 [°]; 2.40837 [A]
Selected Pattern: Quartz, syn 00-046-1045
Residue + Peak List

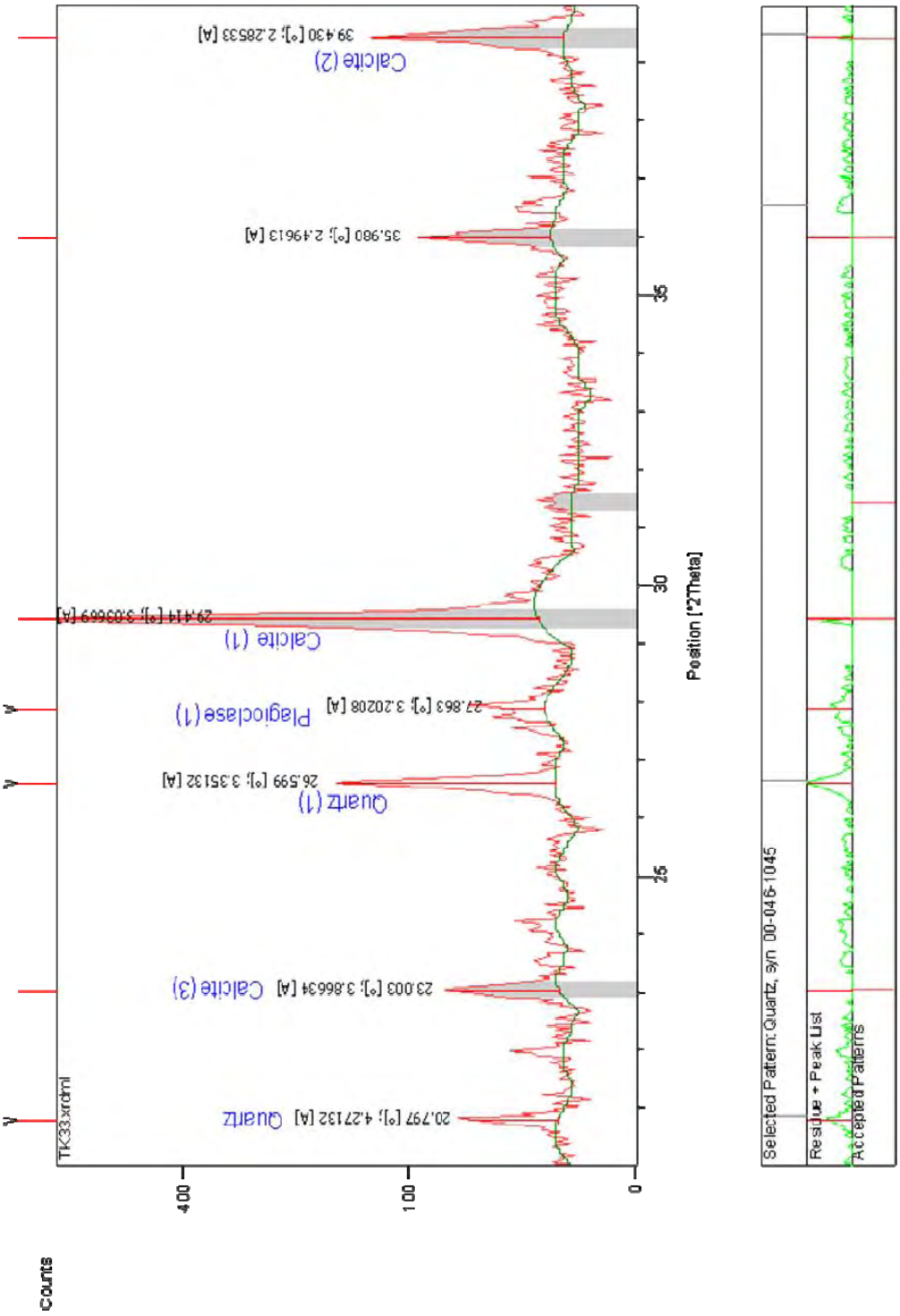
Counts
400
100
0
TK33.xrdml
Quartz
20.797 [°]; 4.27132 [A]
Calcite (3)
23.003 [°]; 3.86634 [A]
Quartz (1)
26.599 [°]; 3.35132 [A]
Plagioclase (1)
27.863 [°]; 3.20208 [A]
Calcite (1)
29.414 [°]; 3.03669 [A]
Calcite (2)
39.430 [°]; 2.28533 [A]
35.980 [°]; 2.49613 [A]
15
30
35
Position [°2Theta]
Selected Pattern: Quartz, syn 00-046-1045
Residue + Peak List
Accepted Patterns

7. SEM photographs and EDS graphs

Appendix Section 7 contains SEM photographs and EDS graphs that are characteristic of cement phases in the pipe and bulbous concretions.

7.1 SEM photographs

The SEM images depict very fine grained mudstone that is cemented by micritic carbonate. EDS analysis indicates the bulk composition is primarily calcium which corresponds to both calcite and plagioclase. Small amounts of iron, magnesium, and silica are also present which corresponds to quartz, feldspars and pyrite. SEM analysis of East Cape samples did not reveal detailed information about the crystallography or composition of the mudstones and cement due to the fine grained nature of the components.

Figure A3.17 is an SEM photograph of ECD-6 (conduit of large doughnut; see JPG 7000), and is characteristic of the tubular concretions at East Cape, composed of fine grained siliciclastics cemented by micritic carbonate (dolomite) and often containing sponge spicules. The EDS spectrum covers the field of view and shows peaks for calcium, silica, aluminium, magnesium, iron, and oxygen. Figure A3.18 is an SEM photograph and EDS spectrum of ECD-6 that shows framboidal pyrite in ECD-4 (main concretion body). The micritic dolomite, sponge spicules, and pyrite are found in all morphologies (doughnut, conical, and pipes) at East Cape.

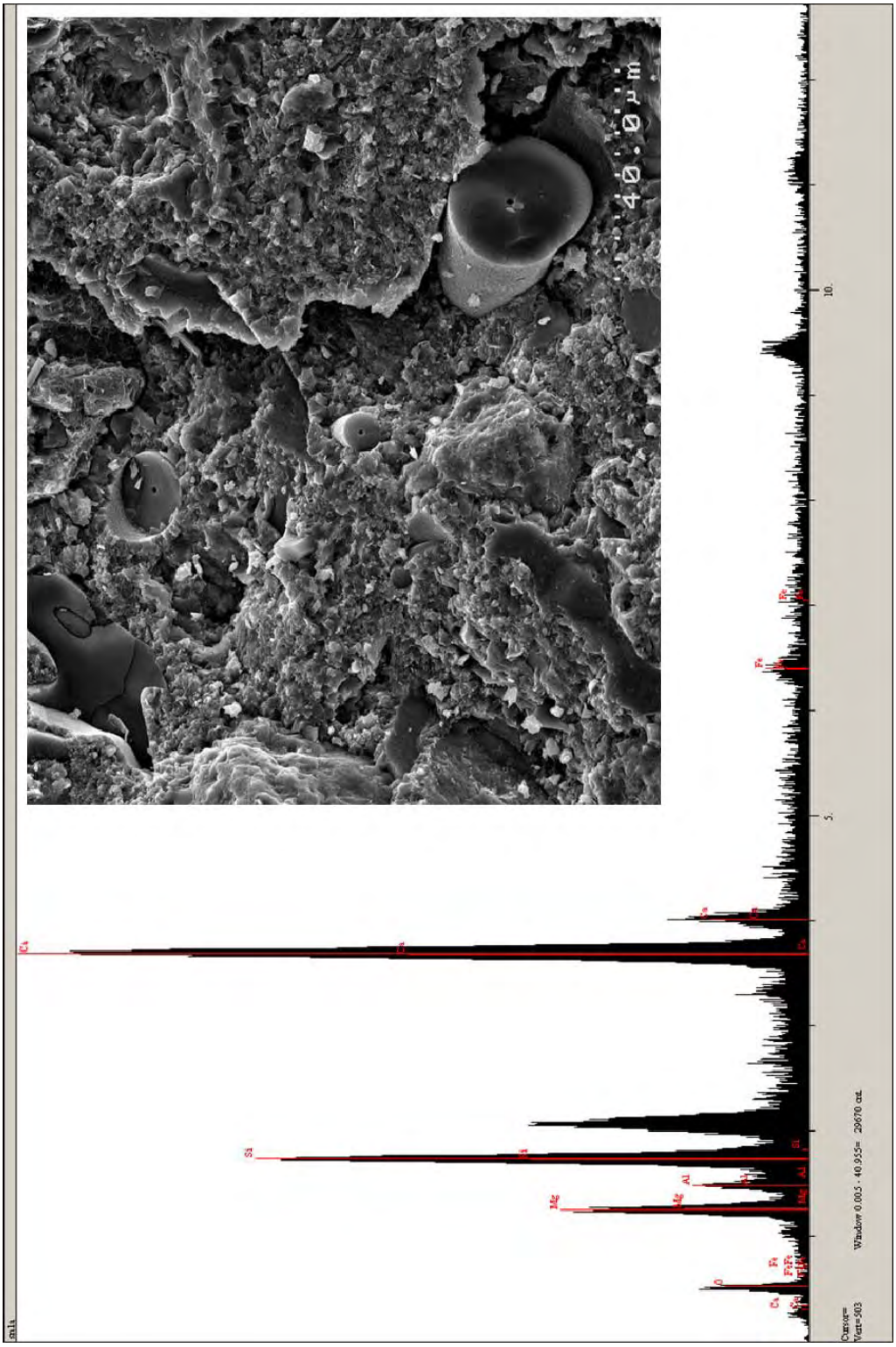

Figure A3.17. SEM photograph of a conduit in doughnut ECD-6 showing micritic dolomite, siliciclastic grains, and sponge spicules. EDS indicates elemental composition primarily of calcium, silica, magnesium, and aluminium.

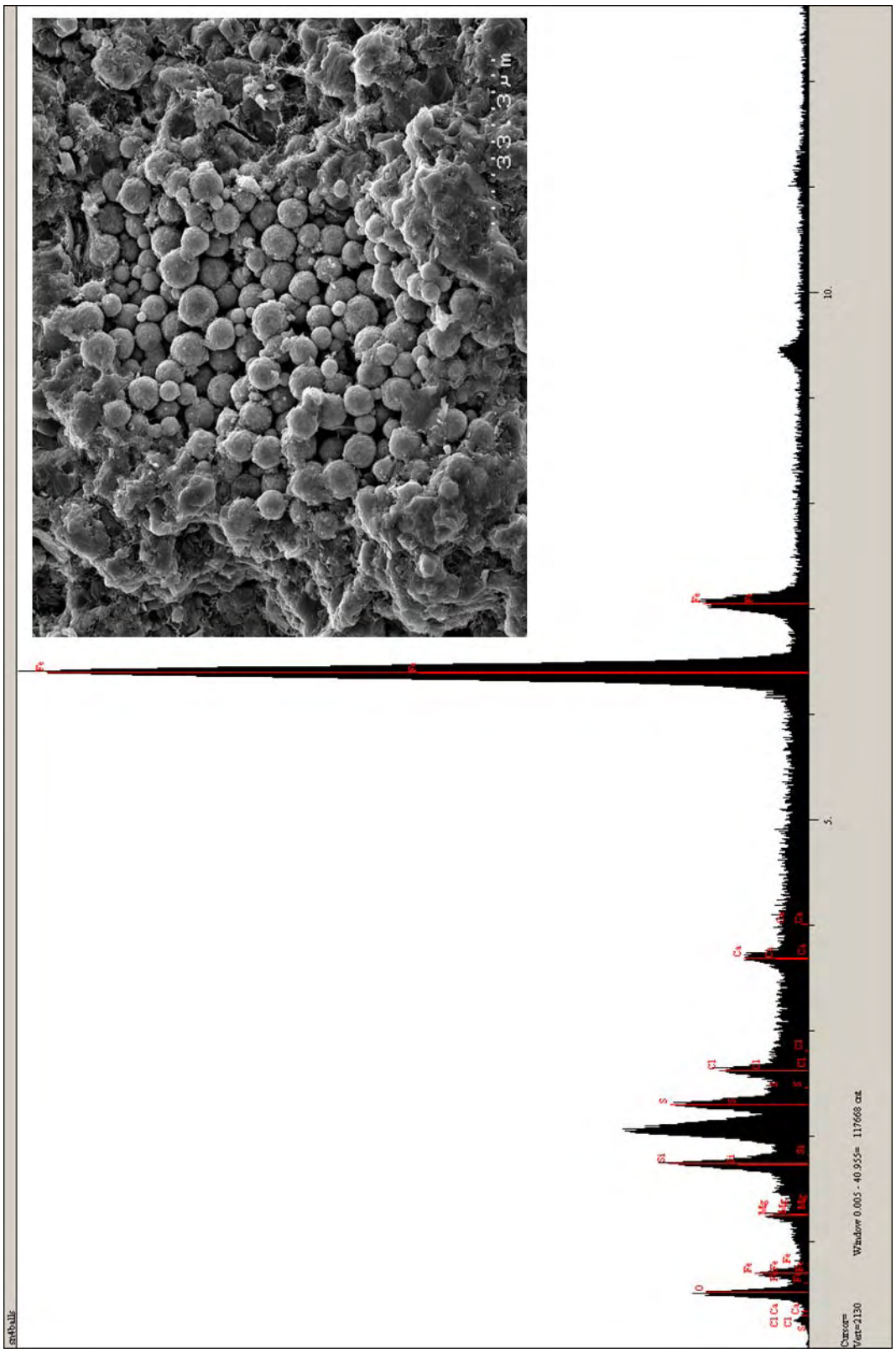

Figure A3.18. SEM photograph of pyrite framboids in the conduit of a doughnut (ECD-6). EDS indicates elemental composition primarily of iron.

8. CO_3 determinations

Appendix Section 8 contains a table of some tubular concretions that were dissolved in solution to determine percentage of carbonate geochemically.

Table A3.7. Weight percent carbonate in selected East Cape samples.

Sample name	Carbonate	Filter paper weight (g)	Residual Sample + filter paper weight (g)	Residual Sample weight (g)	Carbonate Fraction weight (g)	Wt % Carbonate
ECD-1	Dolomite	1.145	1.16	0.015	0.025	62.5
ECD-2	Dolomite	1.151	1.166	0.015	0.025	62.5
ECD-3	Dolomite	1.159	1.174	0.015	0.025	62.5
ECD-4	Dolomite	1.148	1.165	0.017	0.023	57.5
ECD-5	Dolomite	1.178	1.191	0.013	0.027	67.5
ECD-6	Dolomite	1.144	1.152	0.008	0.032	80
ECFP 1	Dolomite	1.159	1.174	0.015	0.025	62.5
ECFP 2	Dolomite	1.176	1.19	0.014	0.026	65
ECFP 3	Dolomite	1.171	1.179	0.008	0.032	80
ECFP 4	Dolomite	1.136	1.147	0.011	0.029	72.5
ECFP 5	Dolomite	1.167	1.179	0.012	0.028	70
ECFP 6	Dolomite	1.186	1.197	0.011	0.029	72.5
EC3-1c	Dolomite	1.136	1.151	0.015	0.025	62.5
EC3-2c	Dolomite	1.168	1.178	0.01	0.03	75
EC3-3c	Dolomite	1.192	1.206	0.014	0.026	65

9. Isotope transects

Appendix Section 9 contains isotope transects for tubular concretions.

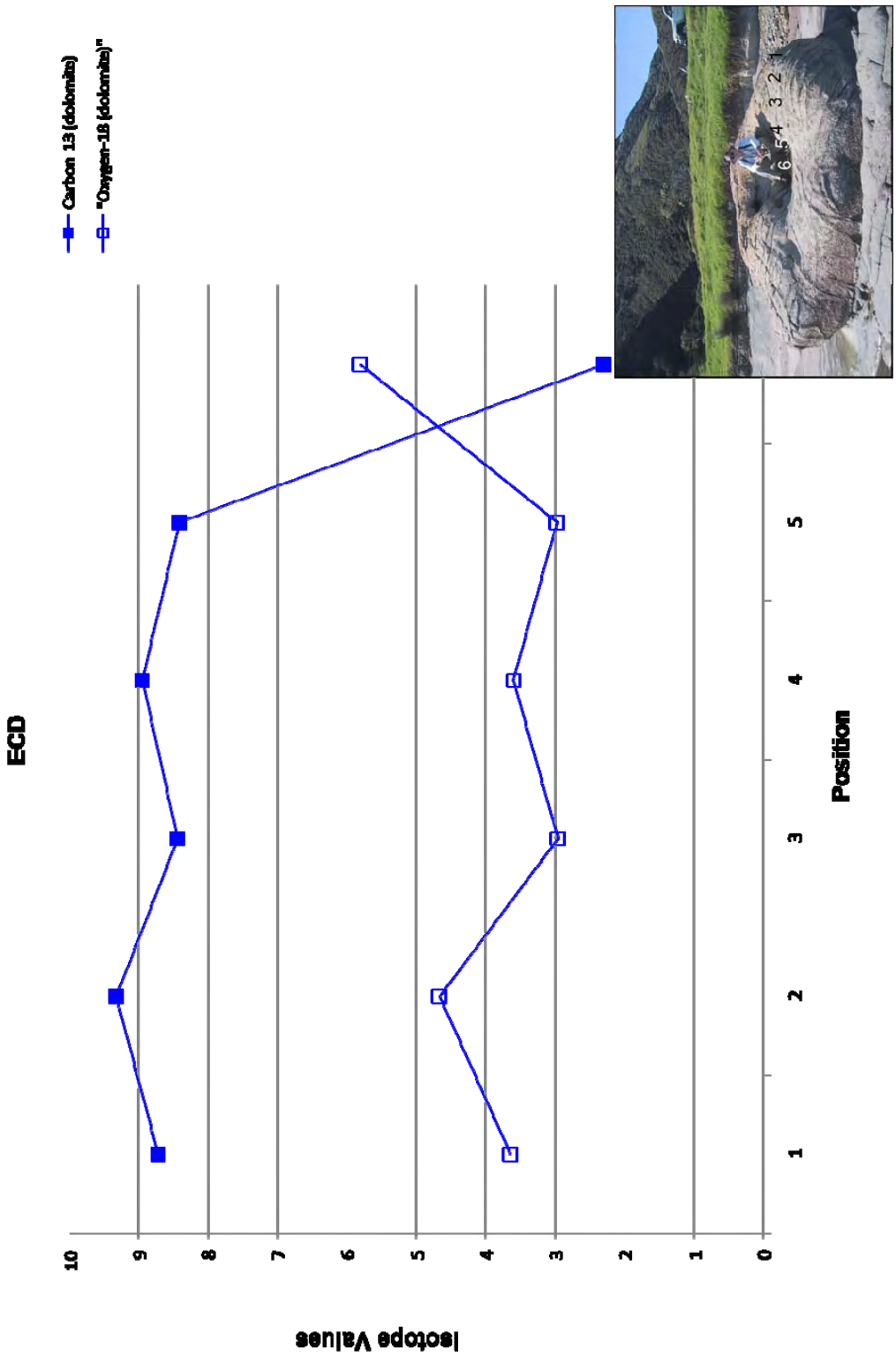
Carbon 13 (dolomite)
"Oxygen-18 (dolomite)"
ECD
Isotope Values
Position
10
9
8
7
6
5
4
3
2
1
0
1
2
3
4
5
6
5
4
3
2
1

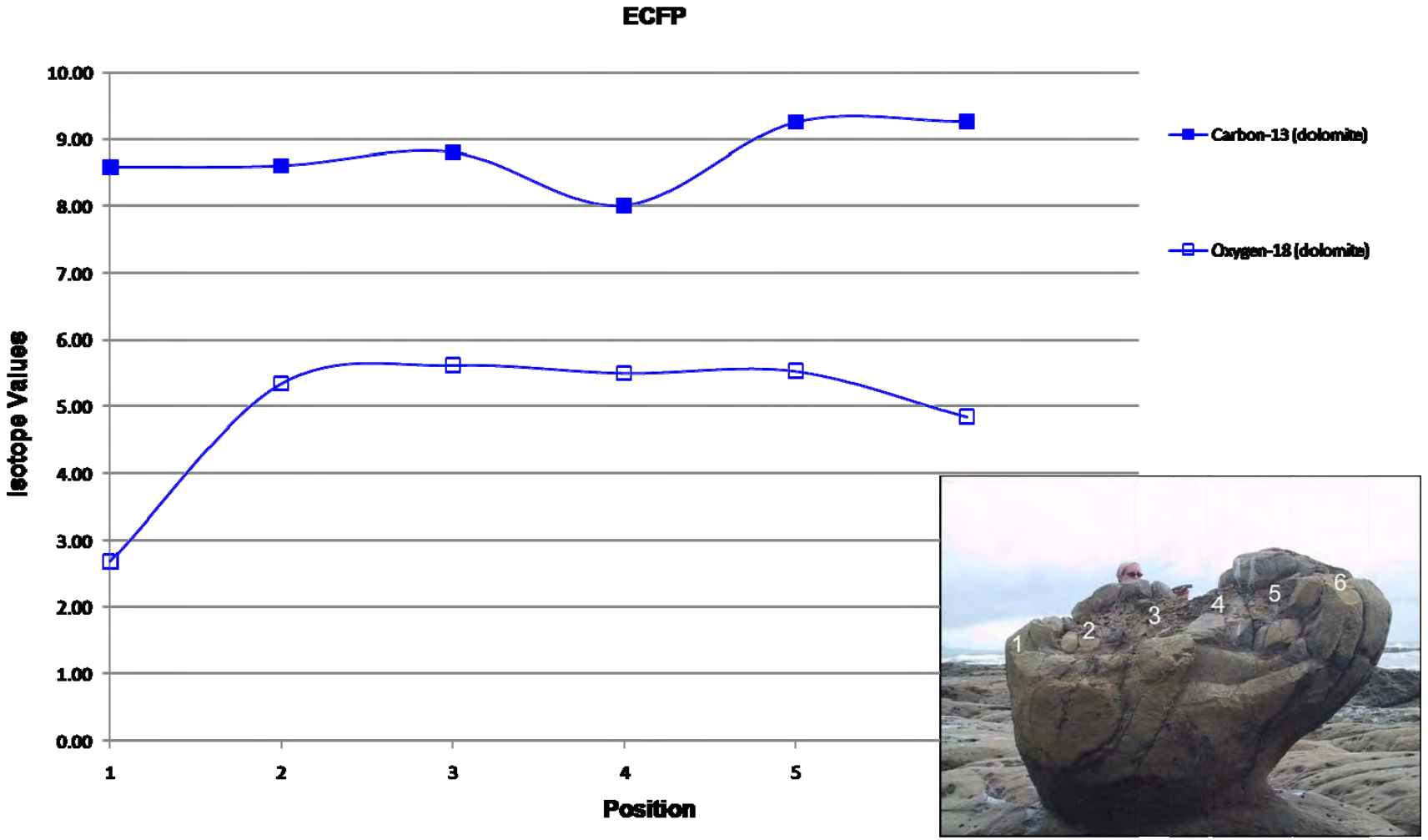
ECFP
10.00
9.00
8.00
7.00
6.00
5.00
4.00
3.00
2.00
1.00
0.00
Isotope Values
1
2
3
4
5
Position
Carbon-13 (dolomite)
Oxygen-18 (dolomite)
1
2
3
4
5
6

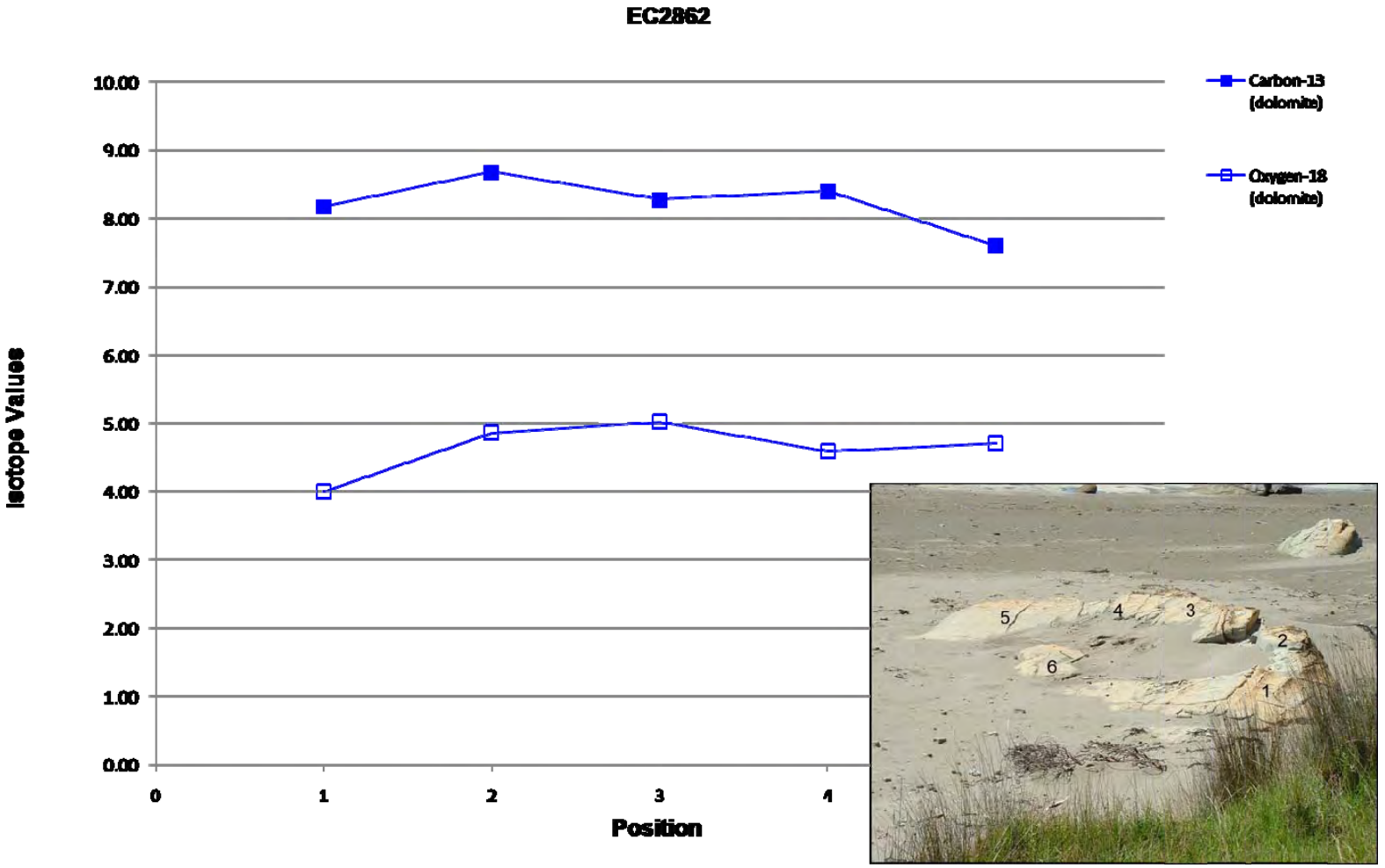
EC2862
Isotope Values
10.00
9.00
8.00
7.00
6.00
5.00
4.00
3.00
2.00
1.00
0.00
0
1
2
3
4
Position
Carbon-13 (dolomite)
Oxygen-18 (dolomite)
5
4
3
2
6
1

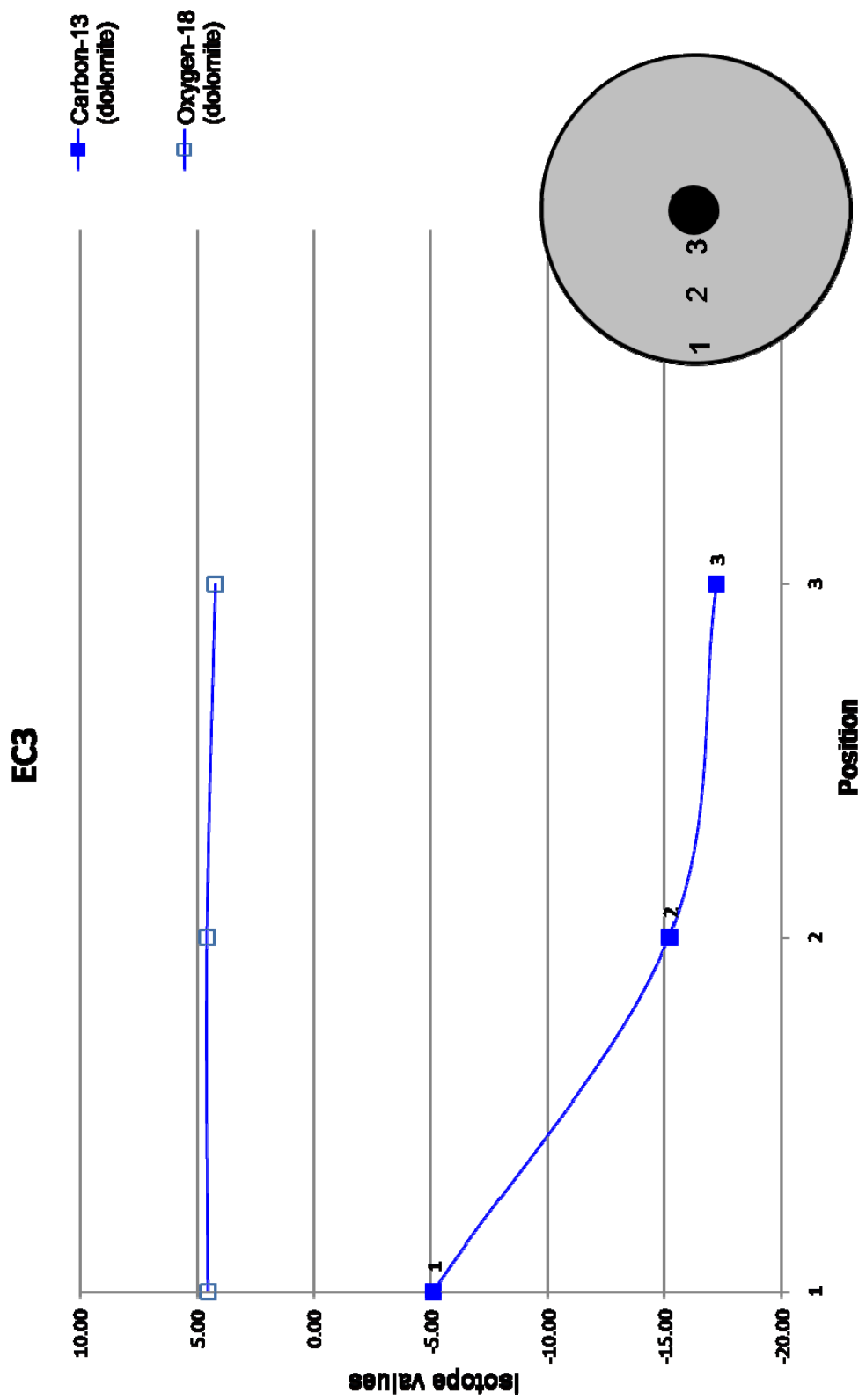
Carbon-13 (dolomite)
Oxygen-18 (dolomite)
EC3
Isotope values
10.00
5.00
0.00
-5.00
-10.00
-15.00
-20.00
Position
1
2
3
1
2
3

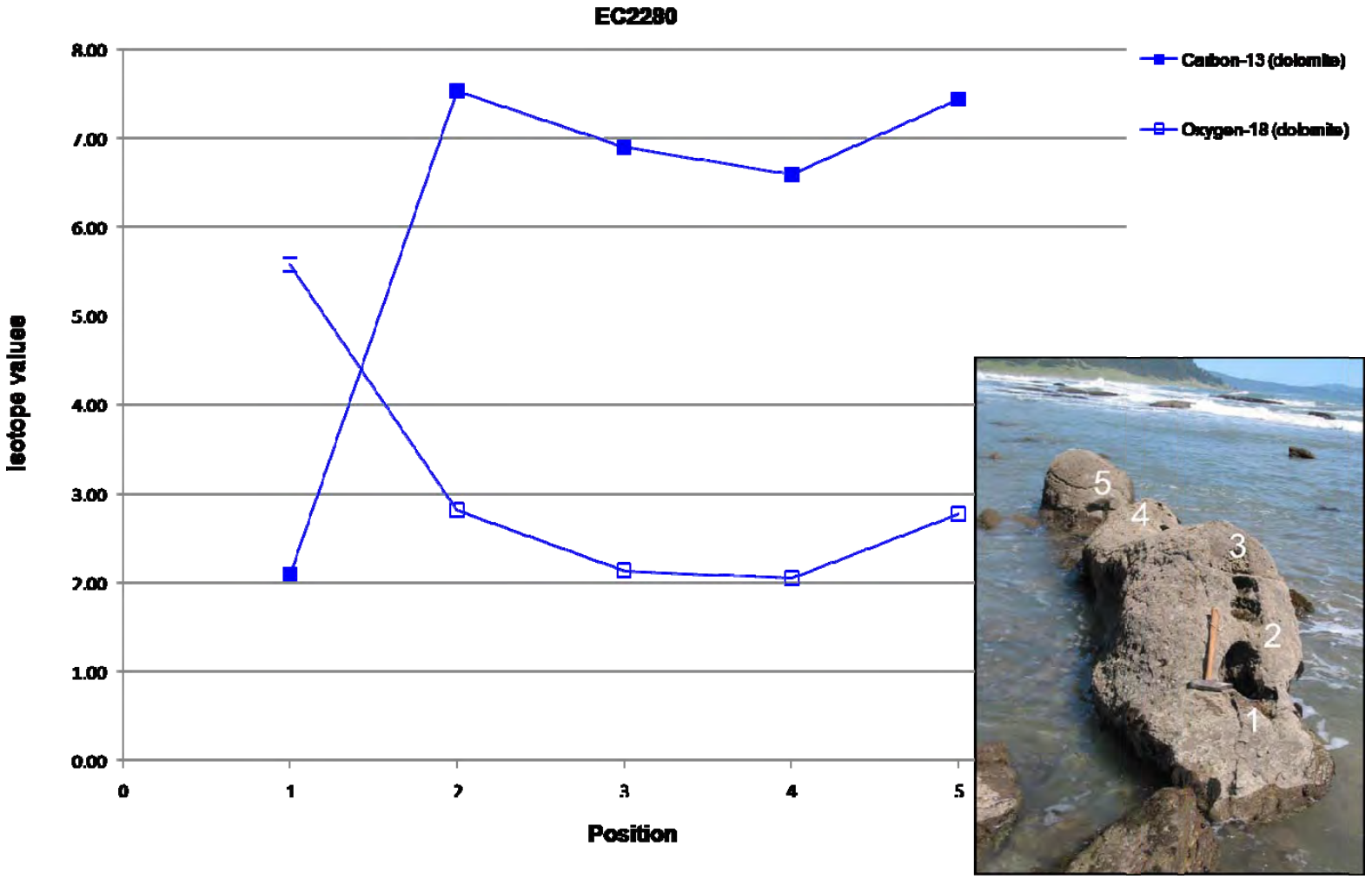
EC2280
Carbon-13 (dolomite)
Oxygen-18 (dolomite)
Isotope values
8.00
7.00
6.00
5.00
4.00
3.00
2.00
1.00
0.00
0
1
2
3
4
5
Position
5
4
3
2
1

10. XRF and ICPOEMS

Appendix Section 10 contains tables of XRF and ICP/MS data.

Table A3.8. XRF data

Element	Dimension	ECD-1	ECD-6	ECD-5	ECD-4	ECD-3	ECHost	FP1	FP2	FP3	FP4
Na	%	0.36	< 0.025	1.13	0.56	2.66	20.92	0.56	1.55	0.43	2.03
Mg	%	8.22	9.63	8.68	8.72	7.41	0.80	7.98	10.25	10.41	9.82
Al	%	3.69	2.75	3.40	3.75	3.73	2.84	3.86	2.85	3.09	2.84
Si	%	14.51	11.14	13.11	14.21	14.48	10.44	14.59	10.57	11.45	10.31
P	%	0.07	0.06	0.05	0.06	0.06	< 0.0018	0.05	0.03	0.04	0.03
S	ppm	2117	1225	1577	554	3432	3252	1467	2549	1882	2572
Cl	ppm	4145	746	13140	7122	26570	194600	5803	18020	6795	21310
K	%	0.99	0.73	0.91	0.99	1.07	1.28	1.01	0.74	0.77	0.73
Ca	%	12.56	15.27	13.30	13.06	11.20	0.73	12.81	14.89	14.86	14.75
Ti	%	0.17	0.12	0.16	0.18	0.18	0.24	0.18	0.13	0.14	0.13
V	ppm	47	31	41	51	51	68	49	40	43	40
Cr	ppm	32	30	31	35	40	55	34	29	30	28
Mn	%	0.05	0.02	0.04	0.04	0.05	0.03	0.04	0.02	0.02	0.02
Fe	%	2.72	1.51	2.32	2.64	2.91	2.34	2.77	1.65	1.71	1.50
Co	ppm	5.4	4.3	< 5.4	6.2	< 6.0	9.2	5.8	6.0	< 4.6	< 4.4
Ni	ppm	10.0	6.0	8.9	9.1	10.6	18.2	10.8	5.4	6.1	6.1
Cu	ppm	5.6	4.3	6.2	5.8	7.5	9.4	7.0	3.9	3.9	4.4
Zn	ppm	34	25	31	34	36	63	34	25	26	25
Ga	ppm	8.4	6.4	8.0	8.4	9.3	13.5	9.3	6.8	6.8	6.5
Ge	ppm	0.4	< 0.3	0.4	0.7	< 0.4	1.1	0.7	0.4	0.3	< 0.3
As	ppm	1.1	1.0	1.2	1.5	1.3	4.4	2.1	0.7	0.9	0.6
Se	ppm	< 0.2	0.4	0.2	0.3	0.4	0.7	0.5	0.3	0.2	0.2
Br	ppm	10.4	5.8	20	11.6	29	105	12.6	23	17.9	33
Rb	ppm	46	32	42	45	50	80	46	34	35	33
Sr	ppm	328	482	292	308	285	210	293	446	448	460
Y	ppm	9.5	7.1	9.1	9.8	10.4	19.3	9.3	7.6	7.5	7.4
Zr	ppm	111	83	102	109	120	196	111	87	95	83
Nb	ppm	4.7	3.6	4.5	4.5	4.9	7.2	4.5	3.7	3.9	3.9
Mo	ppm	0.7	2.3	0.6	0.5	1.0	1.7	0.7	< 1.0	0.5	< 1.0
Ag	ppm	< 0.4	< 0.4	< 0.4	< 0.4	< 0.4	< 0.4	< 0.4	< 0.4	< 0.4	< 0.4
Cd	ppm	< 0.5	< 0.5	< 0.5	< 0.5	< 0.5	< 0.5	< 0.5	< 0.5	< 0.5	< 0.5
In	ppm	< 0.7	< 0.7	< 0.7	< 0.7	< 0.7	< 0.7	< 0.7	< 0.7	< 0.7	< 0.7
Sn	ppm	0.9	< 0.7	0.9	< 0.7	< 0.7	1.0	0.4	< 0.7	< 0.7	< 0.7
Sb	ppm	< 0.9	< 0.9	< 0.9	< 0.9	< 0.9	< 0.9	< 0.9	< 0.9	< 0.9	< 0.9
Te	ppm	< 1.2	< 1.2	< 1.2	< 1.2	< 1.2	< 1.2	< 1.2	< 1.2	< 1.2	< 1.2
I	ppm	< 1.5	< 1.5	< 1.5	< 1.5	< 1.5	3.5	< 1.5	1.5	< 1.5	< 1.5
Cs	ppm	< 2.6	< 2.6	< 2.6	< 2.6	< 2.6	5.0	2.3	2.4	< 2.6	< 2.6
Ba	ppm	269	206	244	253	259	440	253	184	192	179
La	ppm	6.6	4.6	5.9	4.8	5.6	19.0	7.8	6.5	4.6	4.6
Ce	ppm	19.8	12.8	15.6	16.6	17.5	40	17.6	13.3	13.2	14.1
Pr	ppm	< 8.0	7.5	< 8.0	< 8.0	< 8.0	< 8.0	< 8.0	< 8.0	< 8.0	< 8.0
Nd	ppm	< 10	< 10	< 10	< 10	< 10	18.7	< 10	< 10	< 10	< 10
Hf	ppm	2.5	1.1	1.2	1.9	2.9	6.2	1.9	2.7	2.2	1.7
Ta	ppm	< 2.3	< 2.2	< 2.3	2.4	< 2.4	1.8	< 2.4	< 2.2	< 2.2	< 2.2
W	ppm	35	40	28	35	52	20.0	36	32	28	16.3
Hg	ppm	< 0.5	< 0.5	< 0.5	< 0.6	< 0.6	< 0.4	< 0.6	< 0.5	< 0.5	< 0.4
Tl	ppm	0.4	0.4	0.3	0.5	0.7	1.0	0.6	0.5	0.5	< 0.4
Pb	ppm	6.1	4.7	5.8	6.3	7.0	11.4	6.2	5.2	5.3	4.9
Bi	ppm	< 0.3	< 0.3	< 0.3	0.4	0.4	< 0.3	0.5	< 0.3	< 0.3	< 0.3
Th	ppm	7.8	5.9	7.0	7.6	7.6	10.4	7.4	6.2	6.1	6.5
U	ppm	4.1	2.8	3.6	3.2	3.4	4.8	3.3	2.5	2.4	2.7

Table A3.9. ICPMS data.

	Na 23	Mg 24	Al 27	K 39	Ca 43	Cr 52	Fe 54	Mn 55	Cu 65	Sr 88	Pb 206	Pb 207	Pb 208	Bi 209	U 235	U 238
Calibration blank																
merck XXI 50ppb +2% HNO3	40.15	50.00	50.00	50.00	39.80	50.00	45.29	50.00	50.00	50.00	50.00	50.00	50.00	50.00	50.00	50.00
merck IV 50ppb +2% HNO3	38.79	52.12	52.02	56.59	41.80	50.23	42.42	51.03	51.16	50.65	50.39	53.13	50.84	51.07	0.03	0.03
Merck 500ppb +2% HNO3	500.00	527.98	516.88	482.46	500.00	509.44	500.00	514.20	426.13	520.18	503.65	525.31	512.05	512.37	0.00	0.01
calibration blank	0.39	0.03	0.01	2.67	1.45	0.02	-2.08	0.01	0.01	0.01	0.01	0.01	0.01	0.05	0.00	0.00
flush blank	-1.32	0.01	0.00	2.61	2.25	-0.03	-9.67	-0.01	0.00	0.00	0.01	0.01	0.01	0.01	0.00	0.00
sample flush	4.88	3.45	0.25	20.53	17.96	0.02	-3.83	0.05	0.02	0.03	0.01	0.01	0.01	-0.01	0.00	0.00
MerckXXI QC	74.87	70.11	62.10	72.92	71.07	50.82	50.37	46.24	54.18	49.65	52.62	53.31	52.03	53.54	50.33	54.60
Calibration blank																
merck XXI 50ppb +2% HNO3	68.02	50.00	50.00	50.00	62.72	50.00	51.48	50.00	50.00	50.00	50.00	50.00	50.00	50.00	50.00	50.00
merck IV 50ppb +2% HNO3	61.80	48.52	47.67	53.25	61.60	49.37	45.96	49.16	49.90	49.72	49.28	50.26	51.17	51.56	0.04	0.02
Merck 500ppb +2% HNO3	500.00	497.50	489.15	461.58	500.00	511.40	500.00	505.56	436.97	534.10	498.08	517.15	507.15	520.68	0.01	0.00
calibration blank	-0.13	0.05	0.01	1.65	1.69	0.09	6.19	0.01	0.00	0.01	0.01	0.01	0.02	0.05	0.01	0.00
ECD-1	745.25	19567.02	839.41	445.16	21288.89	4.01	6289.47	161.35	6.97	83.40	5.35	5.24	5.38	0.53	0.70	0.24
ECD-2	833.11	19098.47	633.25	366.29	20543.10	3.47	4250.23	93.00	6.10	80.53	3.50	3.41	3.56	0.32	0.38	0.15
ECD-4	891.92	21266.85	906.04	434.78	22385.81	4.07	4442.91	94.98	6.79	83.81	5.10	5.01	5.07	0.31	0.35	0.21
ECD-5	1945.83	22497.36	881.82	462.97	23640.79	4.23	3987.35	81.96	7.45	76.76	6.37	6.12	6.42	0.31	0.51	0.22
ECD-6	911.30	28088.15	860.73	373.63	28318.10	4.77	1936.36	47.00	6.90	166.67	3.70	3.72	3.71	0.22	1.17	0.38
ECD-3	1373.86	18460.01	983.27	572.40	19696.80	4.08	5470.03	110.16	10.89	70.21	5.93	5.78	5.93	0.23	0.59	0.24
ECFP-1	1153.43	20595.29	742.48	437.93	21839.85	3.46	4845.01	96.13	6.98	77.56	10.22	10.21	10.31	0.22	0.47	0.21
ECFP-2	1325.42	29830.05	740.16	404.55	27266.29	4.63	2753.54	49.07	7.35	152.20	5.70	5.60	5.72	0.21	0.41	0.19
flush sample	-3.79	4.43	0.12	6.89	17.08	0.14	1.35	0.03	0.00	0.04	0.00	-0.01	0.00	-0.01	0.00	0.00
ECFP-3	1165.94	26871.72	795.54	406.86	25477.86	4.87	2671.83	49.99	45.54	144.58	18.17	17.95	18.39	0.16	0.39	0.16
ECFP-4	1610.78	28652.65	649.75	497.90	27024.16	6.58	2230.48	38.39	6.45	154.12	3.13	3.02	3.20	0.31	0.40	0.19
ECFP-5	1003.84	27168.14	737.46	356.73	25916.53	4.07	4233.20	98.84	5.37	129.45	3.82	3.76	3.89	0.17	0.34	0.16
ECFP-6	981.07	24372.47	763.01	408.00	24838.85	3.59	5698.38	119.89	7.43	104.47	4.41	4.28	4.50	0.24	0.57	0.20
EC3-1	1047.18	19663.14	1228.41	455.19	21861.80	4.08	2898.25	61.41	7.14	147.75	7.90	7.64	8.14	0.18	0.75	0.34
EC3-2	1107.28	22508.80	1076.72	451.87	24992.51	4.09	1797.48	40.83	7.18	160.77	7.94	7.84	7.98	0.20	1.01	0.41
EC3-3	1159.39	19893.15	914.62	390.71	25984.75	4.11	2477.63	64.18	7.19	167.66	5.93	5.82	5.99	0.13	2.30	0.88
flush blank	-2.26	2.53	0.62	6.09	21.09	0.22	5.39	0.03	0.01	0.02	-0.01	-0.02	0.00	-0.01	0.03	0.00
Merck XXI QC	46.30	46.60	44.78	47.77	61.75	51.71	55.83	49.59	52.33	50.50	47.68	46.74	48.59	49.12	49.87	51.12

Appendix 4

Rocky Knob

Rocky Knob table of contents

1. Location

Rocky Knob is located north of Gisborne in Moonlight Forest (NZ Map Series 260, 1:50000 scale, grid reference Y17, GIS E2941510, N6310525). Access is via HWY 2 and Whatatutu Road, past Whatatutu along Mangatu Road and Armstrong Road which leads to the forest entrance. Moonlight Forest is only accessible with permission from PF Olsen Forestry who can be contacted in Gisborne (Ph: 06-868-5426, 396 Childers Rd). PF Olsen will provide a key (bond necessary) and information as to the conditions of the forest, with detailed current maps. The forestry tracks are usually in good condition, however 4WD vehicles are recommended. Only in dry conditions is the Rocky Knob Track accessible by vehicle. The outcrop can be reached via Rocky Knob Track which ends at the bottom of the outcrop (seep plumbing carbonates), or Middle 2 Track which ends at the top of the outcrop (chemosynthesis-based fossils and seafloor seep carbonates). Figure A4.1 is a map of the 16 known ancient seep sites in North Island, New Zealand. Figure A4.2 and A4.3 are regional and local maps, respectively, identifying the location of Rocky Knob, and Figure A4.4 is a topographic map of the location with forestry tracks identified.

1.1 Map of ancient seep locations

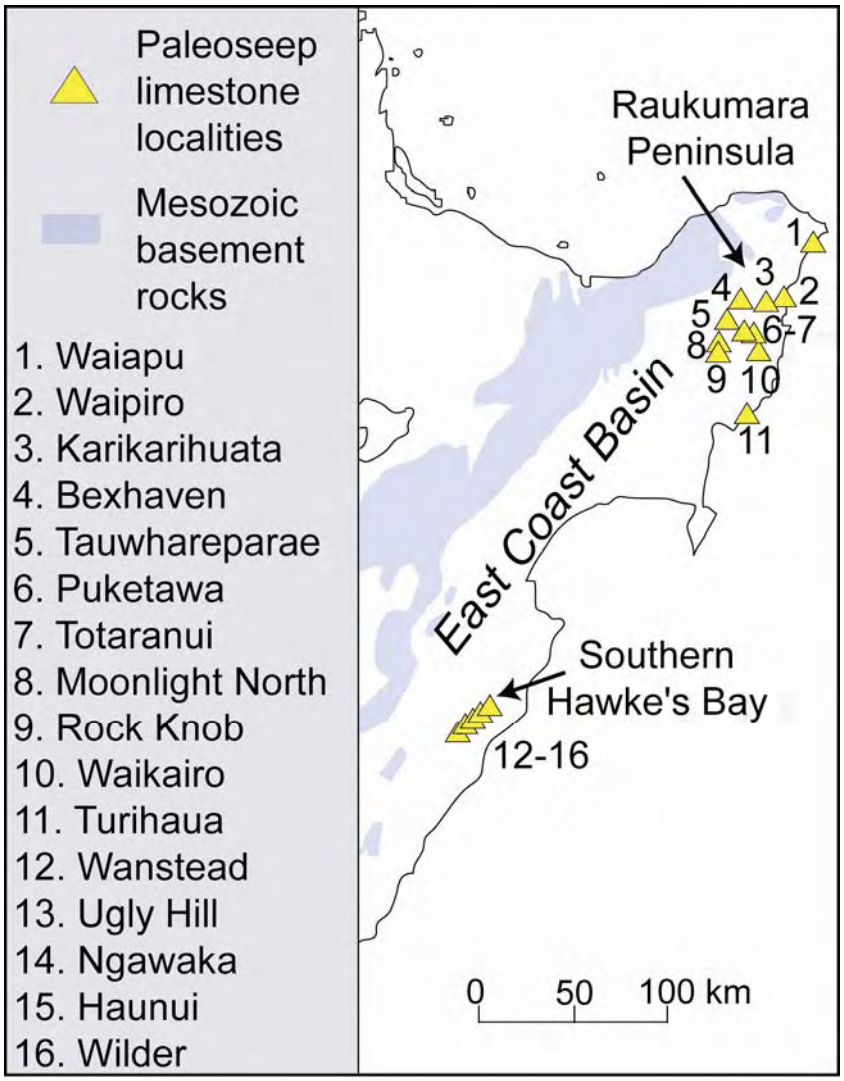

Figure A4.1. Map of the 16 known ancient seep locations in North Island, New Zealand.

1.2 Regional map

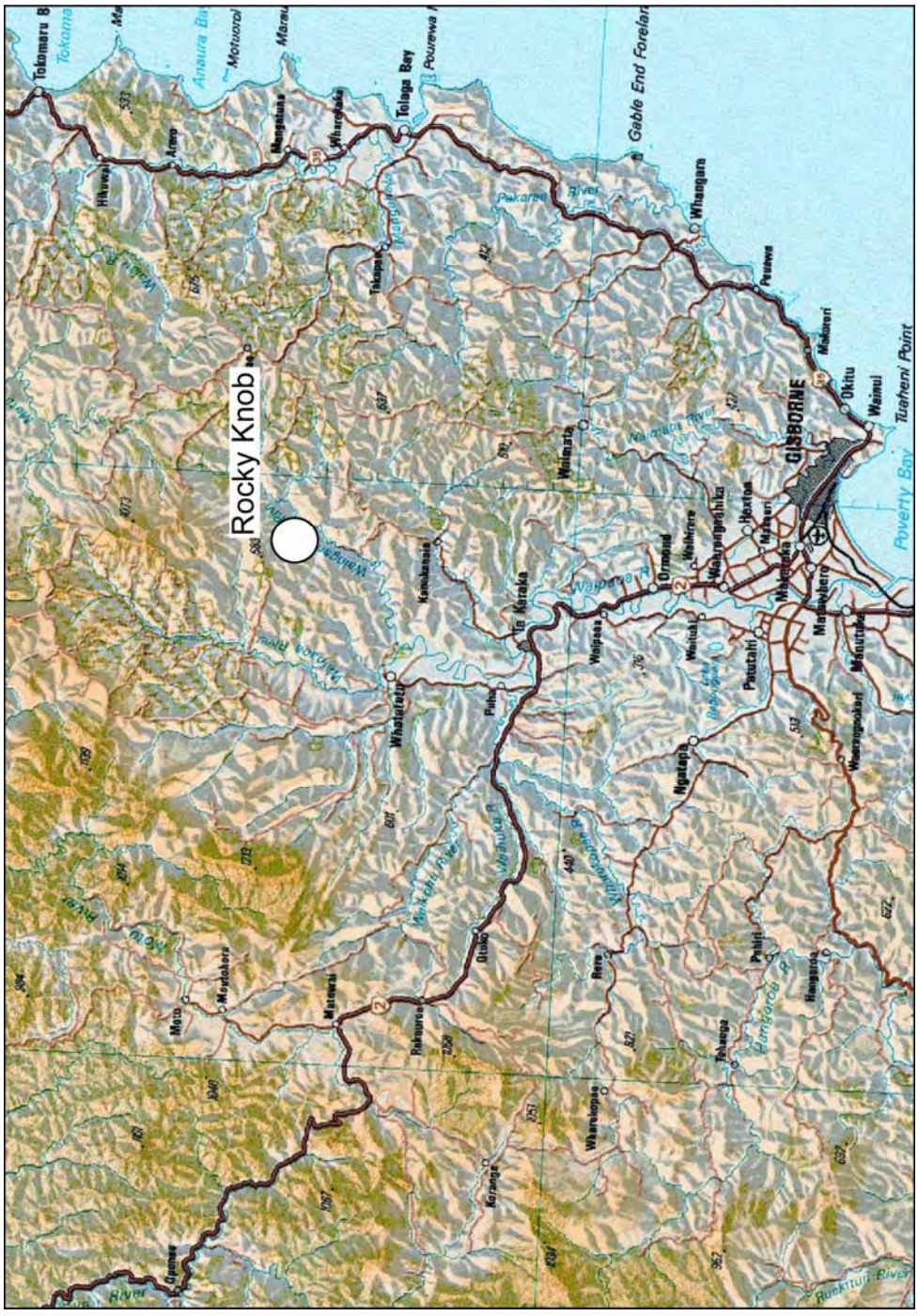

Figure A4.2. Map of Gisborne region and the location of Rocky Knob.

1.3 Local map

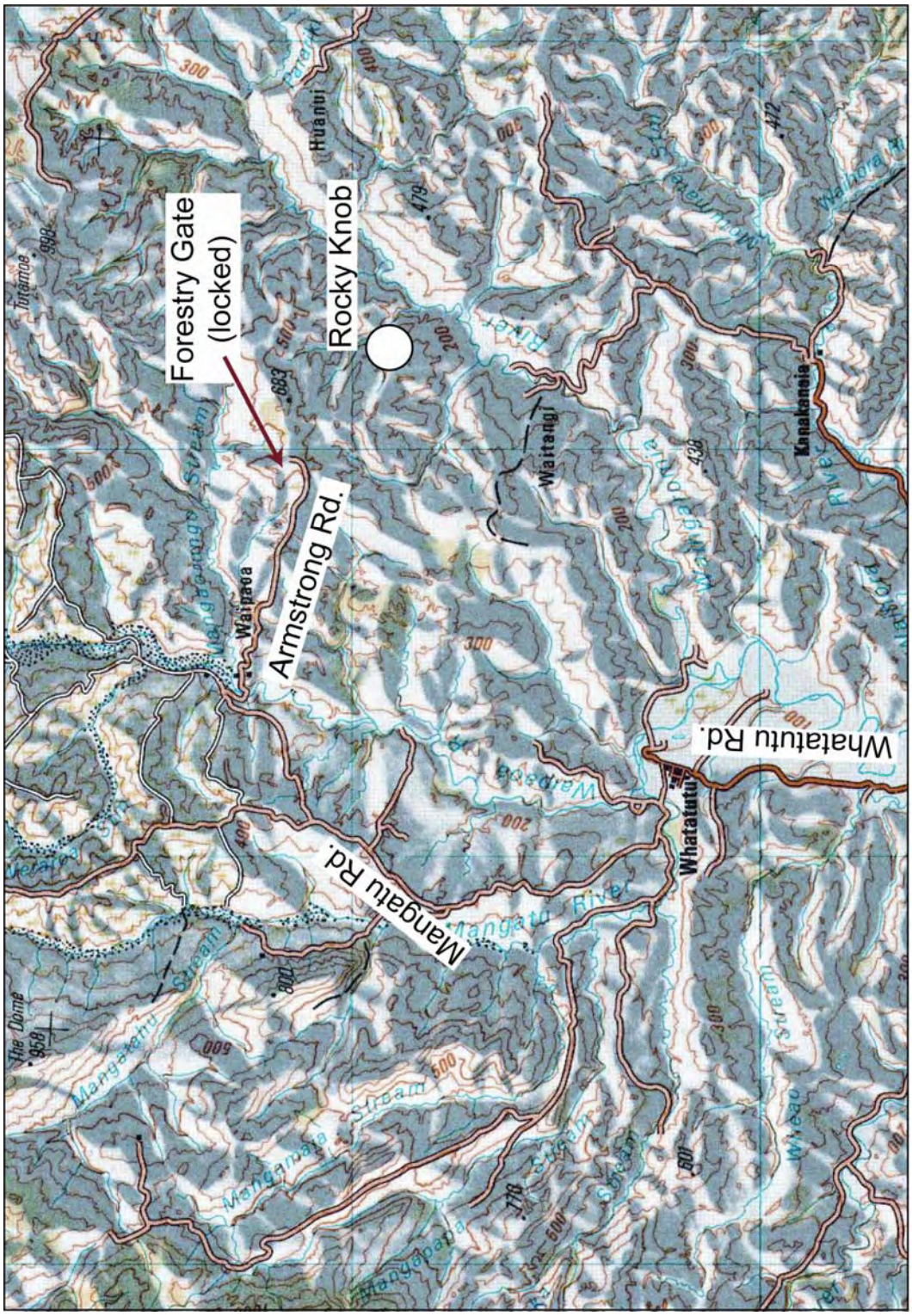

Figure A4.3. Local map of Whatatutu and location of Rocky Knob.

1.4 Map of forestry tracks

Figure A4.4. Map of forestry tracks and location of Rocky Knob.

2. Field photographs

Photographs of tubular concretions and seafloor seep carbonates (Fig. A4.5) at Rocky Knob are presented in this section along with brief descriptions in Table A4.1 (jpg number corresponds to table). A DVD accompanies this volume, where the photographs can be viewed at a larger scale (Appendix\RockyKnob\ FieldPhotos).

Table A4.1. Descriptions of field photographs in Figure A4.5.

Photograph	Location (see Ch. 6, Fig. 7)	Comment
8000	c	Base of Rocky Knob with exposed plumbing carbonate in the mudstone (facies 2), at the top of the scarp are float boulders of seafloor seep carbonates
8001	c	Tortuous, interconnected pipe concretions in facies 2, most pipes have filled conduits
8002	c	Tortuous, interconnected pipe concretions in facies 2, most pipes have filled conduits
8003	c	Tortuous, interconnected pipe concretions in facies 2 with an open conduit
8004	c	Tortuous, interconnected pipe concretions in facies 2, conduits are not apparent
8005	f	Base of the seafloor seep carbonate outcrop, a few tubular concretions were found in the mudstone directly below
8006	g	Base of the seafloor seep carbonate outcrop, a few tubular concretions were found in the mudstone directly below
8007	e	Seafloor seep carbonate mid way up the complex, and the first to contain significant amounts of fossils
8008	e	Thick fibrous aragonite veins in the seafloor seep carbonate
8009	d	Near the top of the seafloor seep carbonate
8010	d	Near the top of the seafloor seep carbonate
8011	d	Near the top of the seafloor seep carbonate
8012	f	Samples from the base of the seafloor seep carbonate outcrop, no fossils are present
8013	e	Chemosynthesis-based fossils (near 8008)
8014	e	Chemosynthesis-based fossils (near 8008)
8015	e	Chemosynthesis-based fossils (near 8008)
8016	e	Chemosynthesis-based fossils (near 8008)

Figure A4.5. Rocky Knob field photographs. See Table A4.1 for descriptions.

3. Samples

Tubular concretion samples are listed in Table A4.2. Sample numbers are followed by a lower case letter which denotes a subsample micro-drilled for isotope analysis (identified in photographs). JPG numbers correspond to the following photographs and a DVD accompanies this volume, where the photomicrographs can be viewed at a larger scale (Appendix\RockyKnob\ Samples).

Table A4.2. Sample descriptions (see Fig. A4.6 for photographs).

UoW number	Analysis sample number	Location (see Ch. 6, Fig. 5)	Comment	JPG
20080335	RK48	c	Host mud	
20080336	RK49	c	Nodular concretion	
20080337	RK50	In mudstone between c and f	Tubular concretion	
20080338	RK54a	c	Tubular concretion	8028
20080339	RK54b	c	Tubular concretion	8028
20080340	RK57a	In mudstone between c and b	Seep carbonate	8034
20080341	RK57b	In mudstone between c and b	Seep carbonate	8034
20080342	RK57c	In mudstone between c and b	Seep carbonate	8034
20080343	RK57d	In mudstone between c and b	Seep carbonate	8034
20080344	RK57e	In mudstone between c and b	Seep carbonate	8034
20080345	RK59a	Field sample	Seep carbonate with fossils	8032
20080346	RK59b	Field sample	Seep carbonate with fossils	8032
20080347	RK60a	g	Tubular concretion	8024-8025
20080348	RK60b	g	Tubular concretion	8024-8025
20080349	RK60c	g	Tubular concretion	8024-8025
20080350	RK60d	g	Tubular concretion	8024-8025
20080351	RK60e	g	Tubular concretion	8024-8025
20080352	RK60f	g	Tubular concretion	8024-8025
20080353	RK61a	g	Seep carbonate	8033
20080354	RK61c	g	Seep carbonate	8033
20080355	RK61d	g	Seep carbonate	8033
20080356	RK61f	g	Seep carbonate	8033
20080357	RK62a	a	Tubular concretion	8030
20080358	RK62b	a	Tubular concretion	8030
20080359	RK62c	a	Tubular concretion	8030
20080360	RK63a	a	Tubular concretion	8030
20080361	RK63b	a	Tubular concretion	8030
20080362	RK63c	a	Tubular concretion	8030
20080363	RK63d	a	Tubular concretion	8030
20080364	RK63e	a	Tubular concretion	8030
20080365	RK64a	a	Tubular concretion	8031
20080366	RK64b	a	Tubular concretion	8031
20080367	RK64c	a	Tubular concretion	8031

Table A4.2. continued.

UoW number	Analysis sample number	Location (see Ch. 6, Fig. 5)	Comment	JPG
20080368	RK65-1a	In mudstone between c and f	Tubular plumbing with triple conduit	8020-8021
20080369	RK65-1b	In mudstone between c and f	Tubular plumbing with triple conduit	8020-8021
20080370	RK65-1c	In mudstone between c and f	Tubular plumbing with triple conduit	8020-8021
20080371	RK65-2a	In mudstone between c and f	Tubular plumbing with triple conduit	8020-8021
20080372	RK65-2b	In mudstone between c and f	Tubular plumbing with triple conduit	8020-8021
20080373	RK65-2c	In mudstone between c and f	Tubular plumbing with triple conduit	8020-8021
20080374	RK65-3a	In mudstone between c and f	Tubular plumbing with triple conduit	8020-8021
20080375	RK65-3b	In mudstone between c and f	Tubular plumbing with triple conduit	8020-8021
20080376	RK65-3c	In mudstone between c and f	Tubular plumbing with triple conduit	8020-8021
20080377	RK65-4a	In mudstone between c and f	Tubular plumbing with triple conduit	8020-8021
20080378	RK65-4b	In mudstone between c and f	Tubular plumbing with triple conduit	8020-8021
20080379	RK65-4c	In mudstone between c and f	Tubular plumbing with triple conduit	8020-8021
20080380	RK65-5a	In mudstone between c and f	Tubular plumbing with triple conduit	8020-8021
20080381	RK65-5b	In mudstone between c and f	Tubular plumbing with triple conduit	8020-8021
20080382	RK65-6a	In mudstone between c and f	Tubular plumbing with triple conduit	8020-8021

Table A4.2. continued.

UoW number	Analysis sample number	Location (see Ch. 6, Fig. 5)	Comment	JPG
20080382	RK65-6b	In mudstone between c and f	Tubular plumbing with triple conduit	8020-8021
20080383	RK1-1	c	Tubular plumbing, outer pipe	
20080384	RK1-2	c	Tubular plumbing, middle pipe	
20080385	RK1-2	c	Tubular plumbing, conduit	
20080386	RK2-1	c	Tubular plumbing, outer pipe	
20080387	RK2-2	c	Tubular plumbing, middle pipe	
20080388	RK2-3	c	Tubular plumbing, conduit	
20080389	RK3	b	Seep carbonate	
20080390	RK66	RK-brachs	Brachipods	
20080391	RK67	b	Seep carbonate	
20080392	RK68	b	Seep carbonate	
20080393	RK69	Field sample number	Seep carbonate	
20080394	RK70	Field sample	Seep carbonate with fossils	
20080395	RK71	Field sample number	Misc. fossils	
20080396	RK72	d	Seep carbonate, lucinid	
20080397	RK73	b	Seep carbonate with breccia clasts	
20080398	RK74	g	Seep carbonate	
20080399	RK75	g	Seep carbonate	

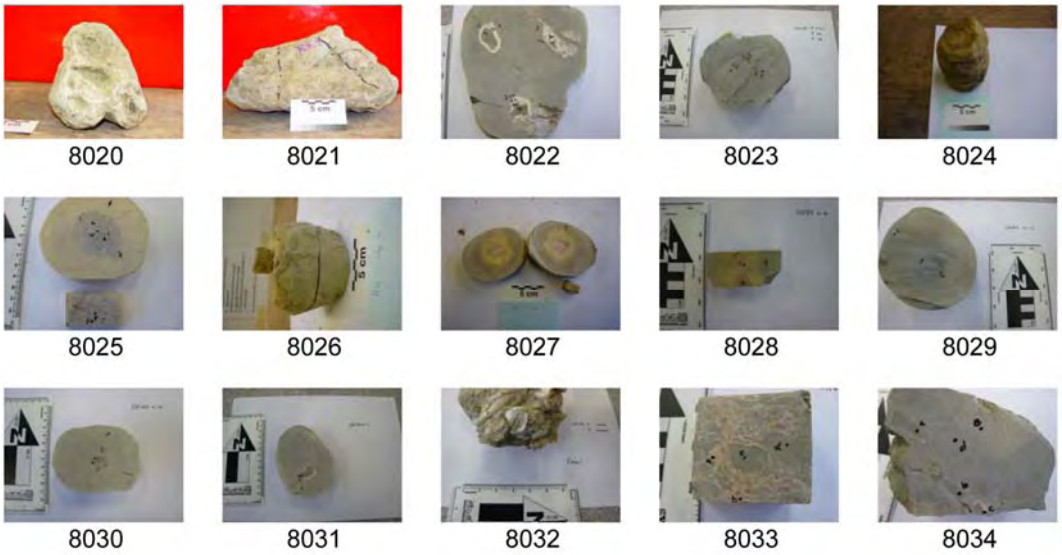

Figure A4.6. Rocky Knob sample photographs. See Table A4.2 for descriptions.

4. Photomicrographs

Photomicrographs of tubular concretions (Fig. A4.7) are presented with brief descriptions in Table A4.3 (jpg number corresponds to table). A DVD accompanies this volume, where the photomicrographs can be viewed at a larger scale (Appendix\RockyKnob\Petrography). A selection of samples were cut and mounted on glass slides for standard thin section analysis. Investigations from previous study locations determined that petrography of the concretionary body did not reveal significant information. Consequently, only tubular concretion conduits and seafloor seep carbonates were cut for thin section analysis. No staining or impregnation was done on the thin sections.

Table A4.3. Descriptions of photomicrographs in Figure A4.7.

Sample	Photomicro-graph jpg no.	Comment
RK 4	8040	Cross-cutting veins through micrite, note the low amount of siliciclastics (PPL)
RK 4	8041	CL of 8040
RK 4	8042	Fibrous aragonite, needles point towards a once open space now filled with micrite; note two micrite phases, the lighter is void of siliciclastics
RK 4	8043	CL of 8042
RK 4	8044	Vug filled with blocky cement (PPL)
RK 4	8045	CL of 8044, note the purple colour of the vug filling crystals, mineralogy indeterminable
RK 4	8046	Clotted calcite fabric filling a vug, boundaries of clotted calcite with the open vug appear to be corroded (PPL)
RK 4	8047	CL of 7047
RK 4	8048	Cross-cutting vein through siliciclastics (PPL)
RK 4	8049	CL of 7048, note the vein is non-luminescent which suggests it is not carbonate
RK 54	8050	Open and filled veins (PPL)
RK 54	8051	CL of 8050, open veins are dark, yellow veins are filled with calcite
RK 54	8052	At least four phases of micrite and very low amounts of siliciclastics (PPL)
RK 54	8053	CL of 8052
RK 54	8054	At least three phases of micrite and very low amounts of siliciclastics (PPL)
RK 54	8055	CL of 8054
RK 60	8056	Granular and blocky calcite filling veins which cut through micrite cemented siliciclastics (PPL)
RK 60	8057	CL of 8057
RK 60	8058	Granular and blocky calcite filling veins which cut through micrite cemented siliciclastics (PPL)
RK 60	8059	CL of 8058
RK 60	8060	Granular and blocky calcite filling veins which cut through micrite cemented siliciclastics (PPL)
RK 60	8061	CL of 8060
RK 60	8062	Blocky calcite cementing breccia clasts and an open vug (PPL)
RK 60	8063	Higher exposure time of 8062, note the corrosion surfaces surrounding the breccia (PPL)
RK 60	8064	CL of 8063, note the breccia comprises micrite cemented siliciclastics (from main concretion?) and the granular calcite is void of siliciclastics (the green colour in the vugs is interpreted to be an artifact)

Table A4.3 continued.

Sample	Photomicro-graph jpg no.	Comment
RK 60	8065	Blocky calcite lining micrite cemented siliciclastics and growing into an open vug (PPL)
RK 60	8066	CL of 8065
RK 60	8067	Granular calcite cementing two breccia clasts, note the corrosion features lining the breccia (PPL)
RK 60	8068	CL of 8067
RK 61	8069	Seafloor seep carbonate, note the cement pattern is more irregular compared to the tubular concretions, but the cement phases are the same (PPL)
RK 61	8070	CL of 8070; cross-cutting relationships indicate micrite cemented siliciclatics first (light orange), followed by aragonite (blue) and then granular calcite (darker orange)
RK 64	8071	Fibrous aragonite surrounded by granular and blocky calcite (PPL)
RK 64	8072	CL of 8071
RK 64	8073	Granular and blocky calcite with small open vugs, very little siliciclastics (PPL)
RK 64	8074	CL of 8073

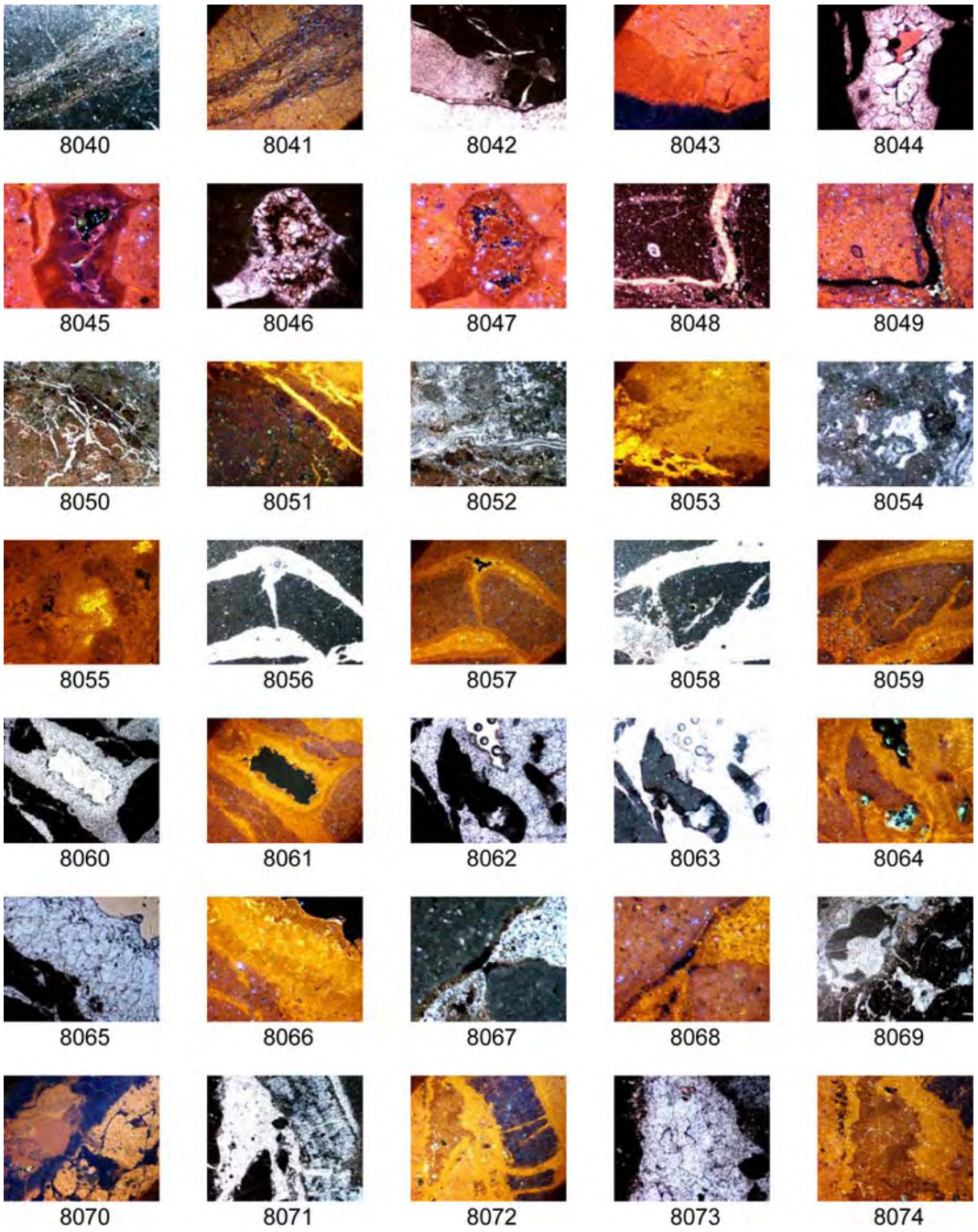

Figure A4.7. Rocky Knob photomicrographs. See Table A4.3 for descriptions.

5. XRD graphs

Appendix Section 5 contains XRD graphs that are characteristic of Rocky Knob tubular concretions and seafloor seep carbonates.

Counts
900
400
100
0
RK1_1hm_cx.raw
20.820 [°]; 4.26659 [A]
Quartz
21.998 [°]; 4.04079 [A]
Calcite (3)
23.520 [°]; 3.78250 [A]
24.198 [°]; 3.67812 [A]
Plagioclase
25.425 [°]; 3.50330 [A]
26.604 [°]; 3.35070 [A]
Quartz (1)
27.901 [°]; 3.19781 [A]
Plagioclase (1)
29.366 [°]; 3.04157 [A]
Calcite (1)
34.795 [°]; 2.57837 [A]
36.472 [°]; 2.46358 [A]
Quartz
37.666 [°]; 2.38820 [A]
39.387 [°]; 2.28772 [A]
25
30
35
Position [°2Theta]
Selected Pattern: Calcite, syn 00-005-0586
Residue + Peak List
Accepted Patterns

Counts
RK1_4tpa.xrdml
Quartz
20.825 [°]; 4.26559 [A]
Calcite (3)
23.064 [°]; 3.85637 [A]
Quartz (1)
26.617 [°]; 3.34912 [A]
Plagioclase (1)
27.832 [°]; 3.20558 [A]
Calcite (1)
29.420 [°]; 3.03606 [A]
34.738 [°]; 2.58249 [A]
36.035 [°]; 2.49247 [A]
39.415 [°]; 2.28615 [A]
Position [°2Theta]
Selected Pattern: silica 00-033-1161
Residue + Peak List
Accepted Patterns

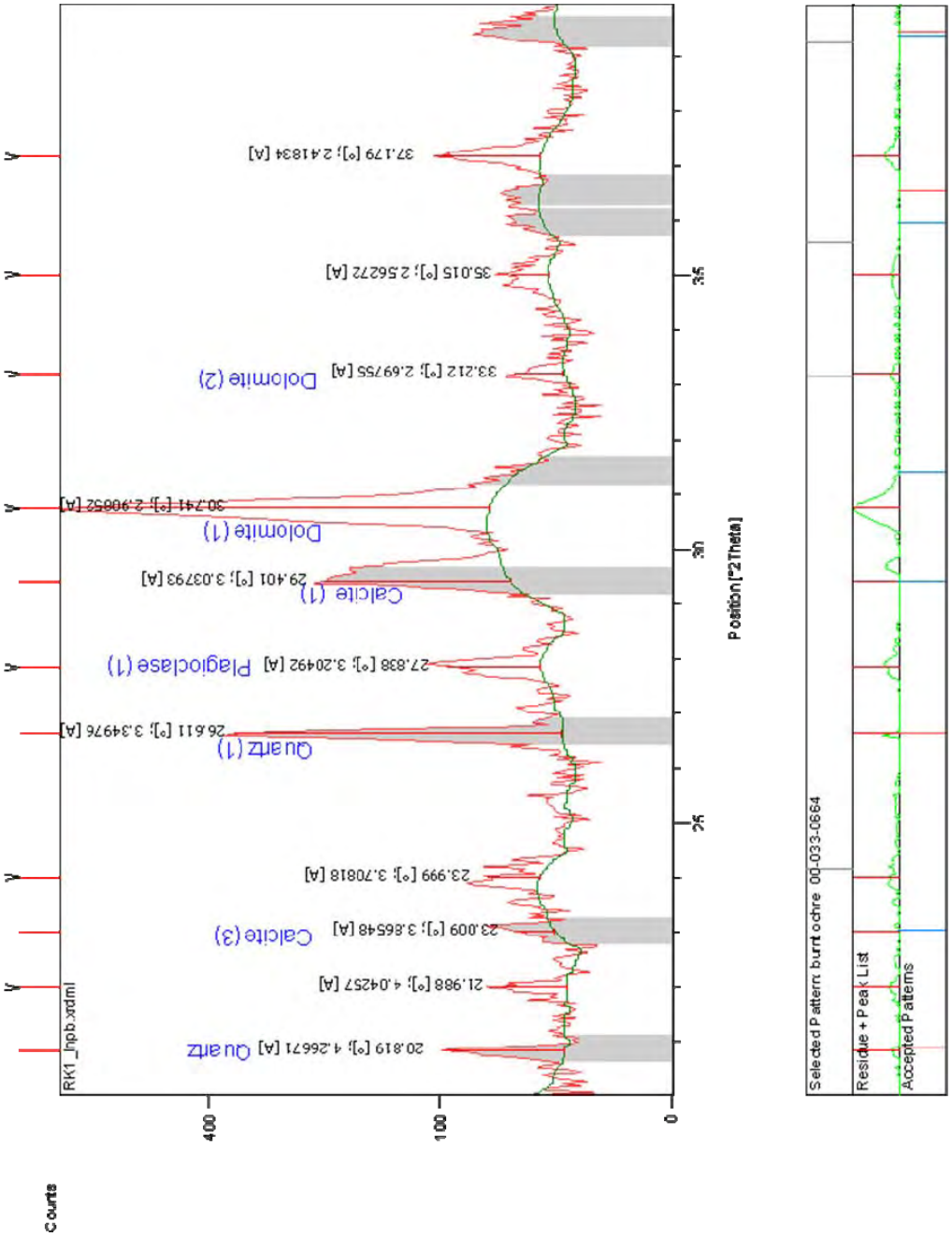
Counts
400
100
0
RK1_hpb.xrdml
Quartz
20.819 [°]; 4.26671 [Å]
21.988 [°]; 4.04257 [Å]
Calcite (3)
23.009 [°]; 3.86548 [Å]
23.999 [°]; 3.70818 [Å]
Quartz (1)
26.611 [°]; 3.34976 [Å]
Plagioclase (1)
27.838 [°]; 3.20492 [Å]
Calcite (1)
29.401 [°]; 3.03793 [Å]
Dolomite (1)
30.741 [°]; 2.90852 [Å]
Dolomite (2)
33.212 [°]; 2.69755 [Å]
35.015 [°]; 2.56272 [Å]
37.179 [°]; 2.41834 [Å]
Position [°2Theta]
Selected Pattern: burnt ochre 00-033-0664
Residue + Peak List
Accepted Patterns

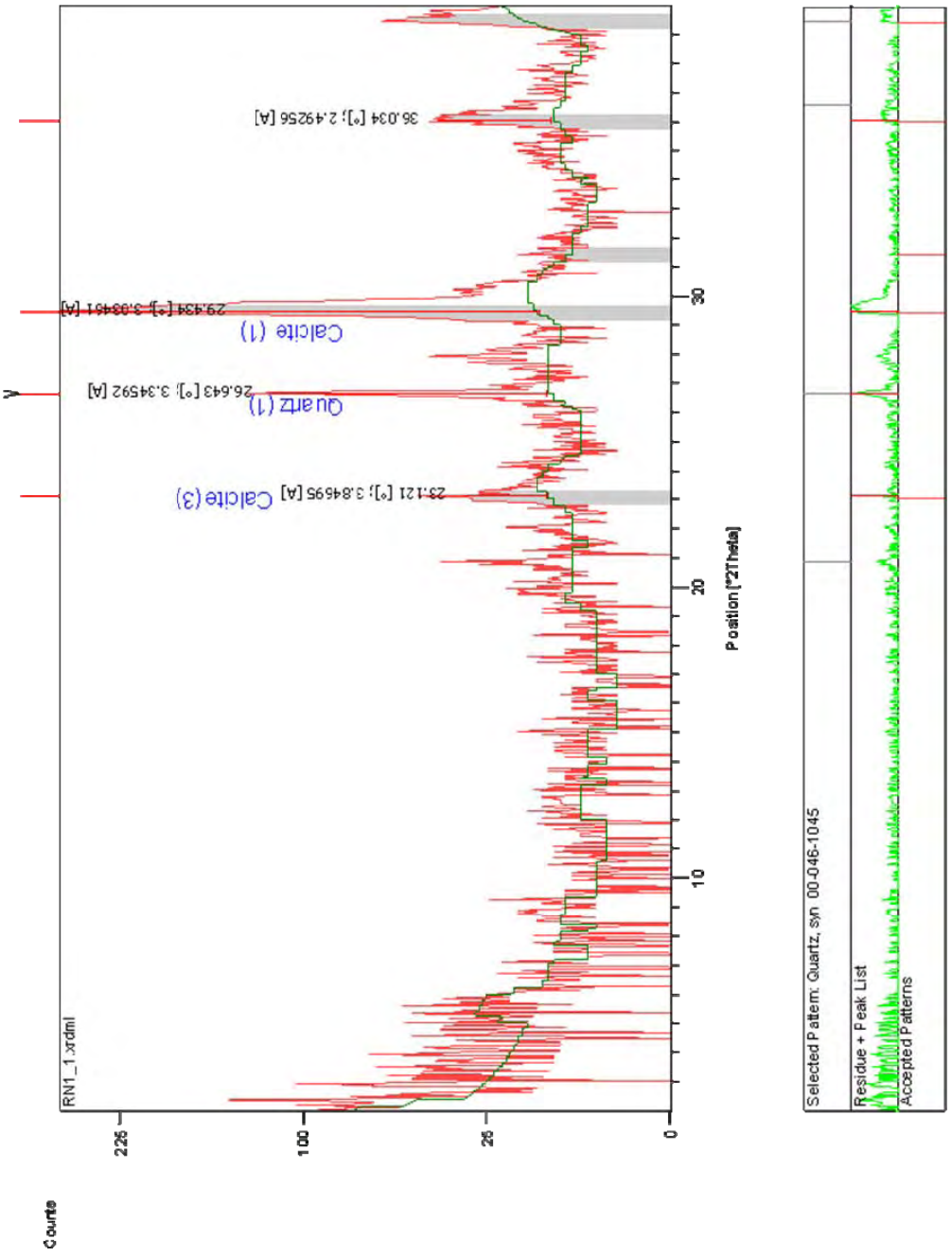
RN1_1.xrdml
Counts
226
100
26
0
10
20
30
Position [°2Theta]
Calcite (3)
23.121 [°]; 3.8469S [A]
Quartz (1)
26.643 [°]; 3.34592 [A]
Calcite (1)
29.434 [°]; 3.03491 [A]
36.034 [°]; 2.49256 [A]
Selected Pattern: Quartz, syn 00-046-1045
Residue + Peak List
Accepted Patterns

RN1_1bX.xrdml
5.012 [°]; 15.20597 [A]
20.852 [°]; 4.26004 [A]
Quartz
23.099 [°]; 3.85060 [A]
Calcite (3)
26.623 [°]; 3.34838 [A]
Quartz (1)
27.923 [°]; 3.19530 [A]
Plagioclase (1)
29.441 [°]; 3.03391 [A]
Calcite (1)
36.059 [°]; 2.49083 [A]
39.501 [°]; 2.28139 [A]
Counts
225
100
25
0
10
20
30
Position [°2Theta]
Selected Pattern: Quartz, syn 00-046-1045
Residue + Peak List
Accepted Patterns

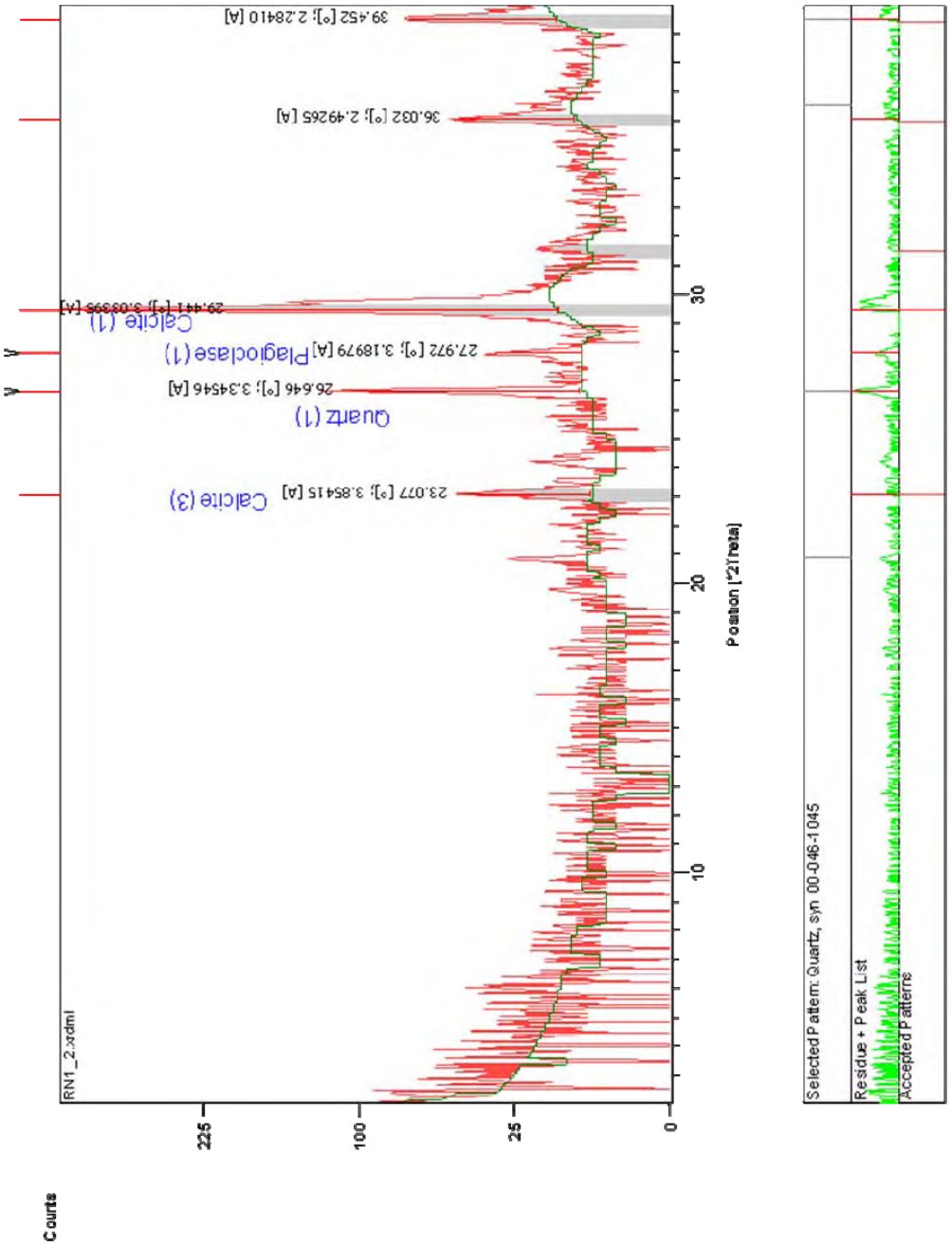
RN1_2.xdml
Counts
225
100
25
0
10
20
30
Position [°2Theta]
23.077 [°]; 3.85415 [A]
Calcite (3)
26.646 [°]; 3.34546 [A]
Quartz (1)
27.972 [°]; 3.18979 [A]
Plagioclase (1)
29.441 [°]; 3.03995 [A]
Calcite (1)
36.032 [°]; 2.49265 [A]
39.452 [°]; 2.28410 [A]
Selected Pattern: Quartz, syn 00-046-1045
Residue + Peak List
Accepted Patterns

Counts
400
100
0
RN1_3.xrdml
Position [°2Theta]
Calcite (3)
23.127 [°]; 3.84602 [Å]
Quartz (1)
26.649 [°]; 3.34507 [Å]
Calcite (1)
29.479 [°]; 3.03012 [Å]
36.051 [°]; 2.49142 [Å]
39.482 [°]; 2.28246 [Å]
Selected Pattern: Quartz, syn 00-046-1045
Residue + Peak List
Accepted Patterns

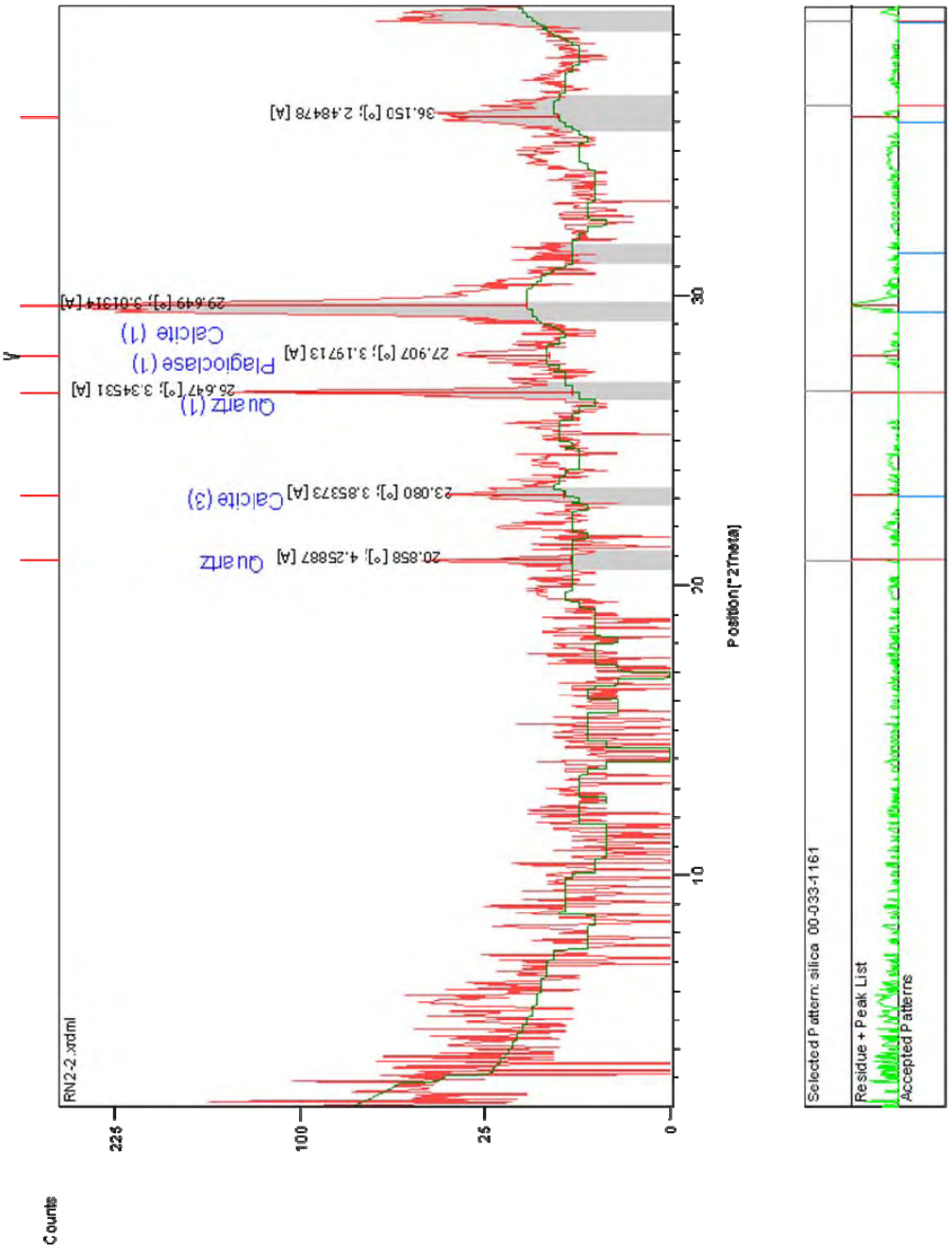
RN2-2.xrdml
Counts
225
100
25
0
10
20
30
Position [°2Theta]
Quartz
20.858 [°]; 4.25887 [A]
Calcite (3)
23.080 [°]; 3.85373 [A]
Quartz (1)
26.647 [°]; 3.34531 [A]
Plagioclase (1)
27.907 [°]; 3.19713 [A]
Calcite (1)
29.449 [°]; 3.01314 [A]
36.150 [°]; 2.48478 [A]
Selected Pattern: silica 00-033-1161
Residue + Peak List
Accepted Patterns

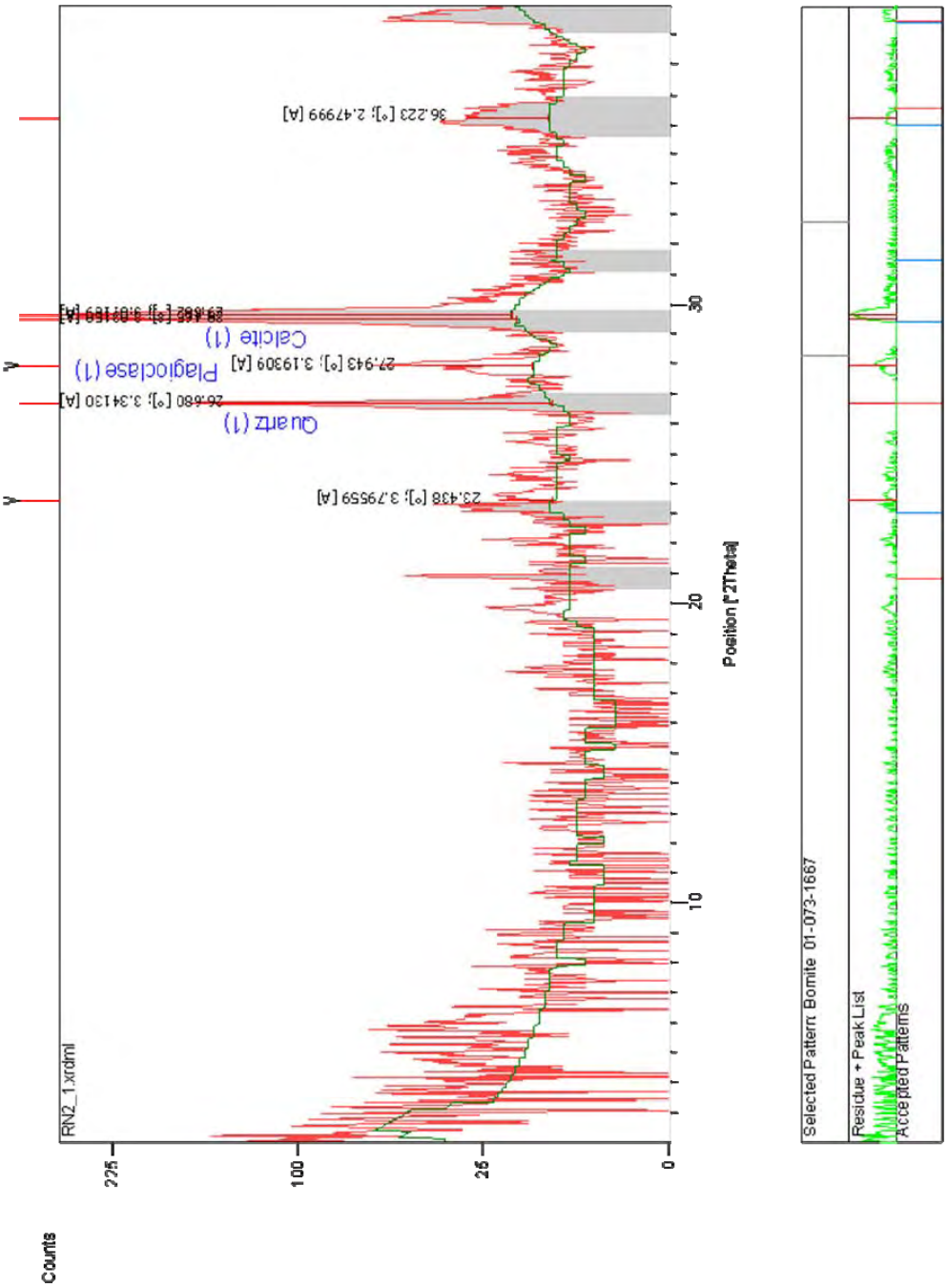
Counts
225
100
25
0
RN2_1.xrdml
10
20
30
Position [°2Theta]
23.438 [°]; 3.79559 [A]
Quartz (1)
26.680 [°]; 3.34130 [A]
27.943 [°]; 3.19309 [A]
Plagioclase (1)
Calcite (1)
36.223 [°]; 2.47999 [A]
Selected Pattern: Bomite 01-073-1667
Residue + Peak List
Accepted Patterns

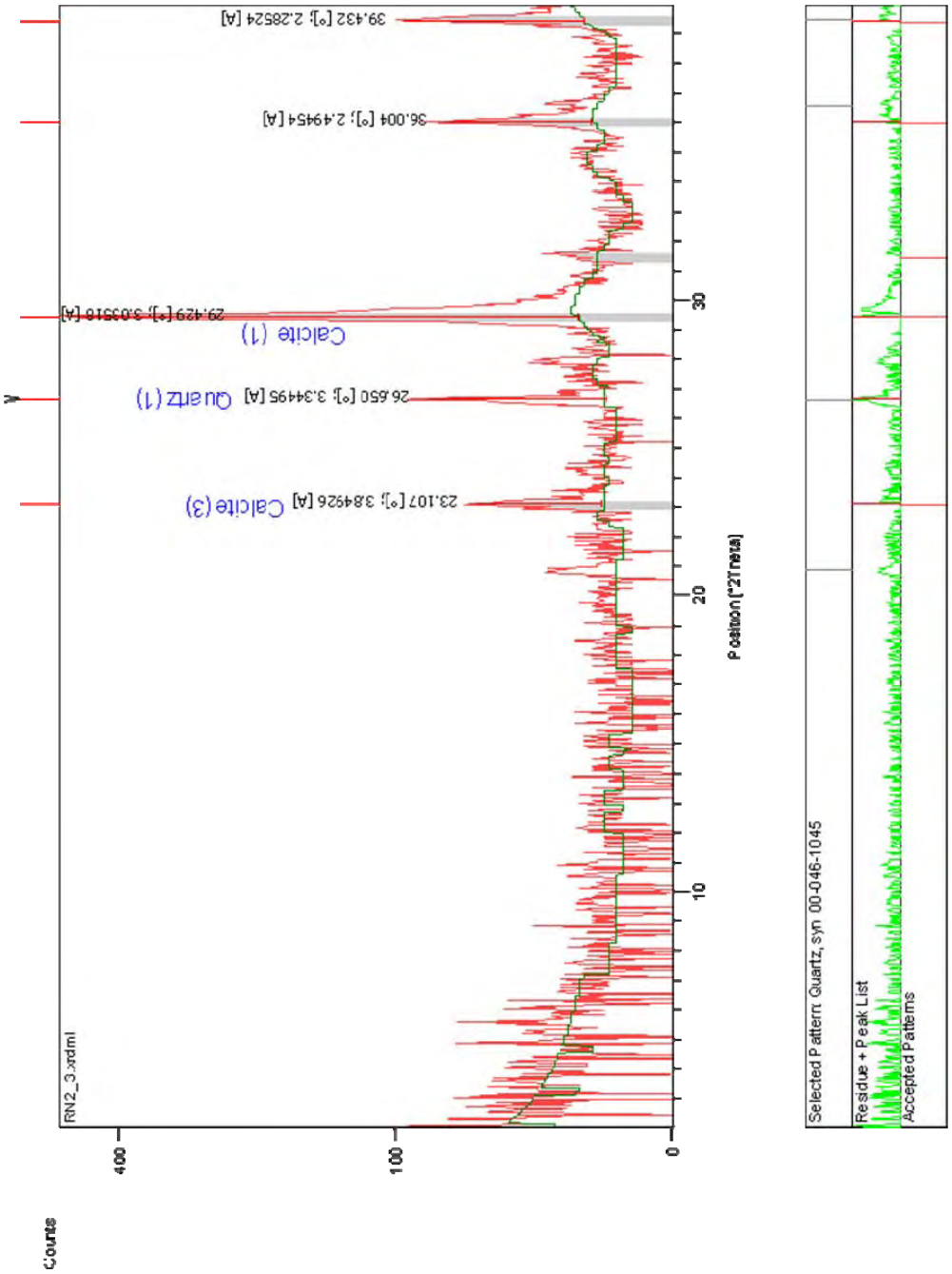
Counts
400
100
0
RN2_3.xdml
10
20
30
Position [°2Theta]
Calcite (3)
23.107 [°]; 3.84926 [A]
Quartz (1)
26.650 [°]; 3.34495 [A]
Calcite (1)
29.429 [°]; 3.03518 [A]
36.004 [°]; 2.49454 [A]
39.432 [°]; 2.28524 [A]
Selected Pattern: Quartz, syn 00-046-1045
Residue + Peak List
Accepted Patterns

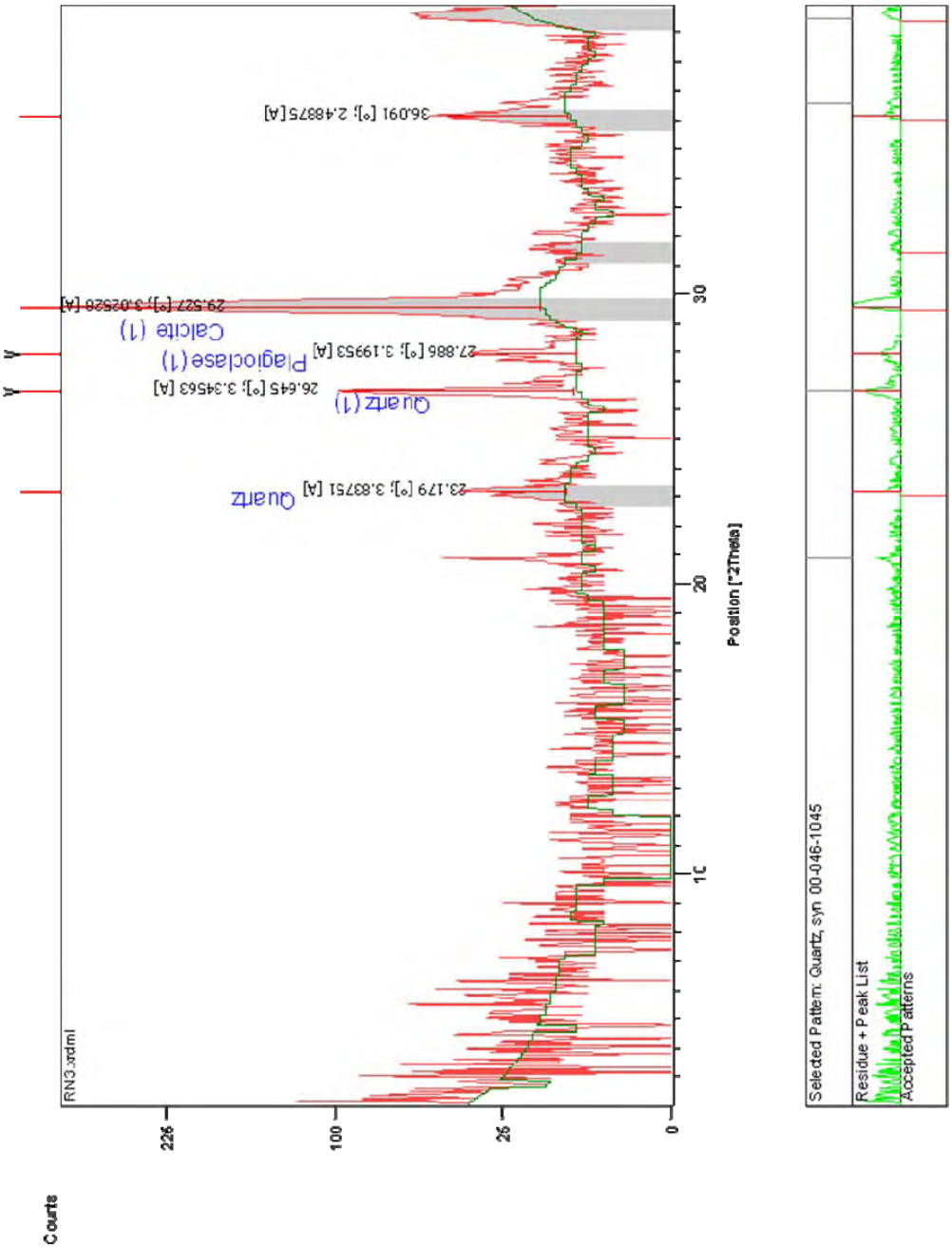
Counts
226
100
25
0
RN3.xrdml
10
20
30
Position [°2Theta]
23.179 [°]; 3.83751 [A]
Quartz
26.645 [°]; 3.34563 [A]
Quartz (1)
27.886 [°]; 3.19953 [A]
Plagioclase (1)
29.527 [°]; 3.02528 [A]
Calcite (1)
36.091 [°]; 2.48375 [A]
Selected Pattern: Quartz, syn 00-046-1045
Residue + Peak List
Accepted Patterns

6. SEM photographs and EDS graphs

Appendix Section 6 contains SEM photographs and EDS graphs that are characteristic of cement phases of the Rocky Knob tubular concretions.

7.1 SEM photographs

The SEM images depict very fine grained mudstone that is cemented by micritic carbonate and blocky calcite. EDS analysis indicates the elemental composition is primarily calcium which corresponds to both calcite and plagioclase. Small amounts of iron, magnesium, and silica are also present which corresponds to quartz, feldspars and pyrite.

The SEM photographs and EDS spectrum is of RK2-3 (conduit fill). SEM photograph and EDS spectrum (Fig. A4.7) show micrite cement. SEM images (Figs. A4.8 and A4.9) show micrite and blocky calcite in the conduit fill.

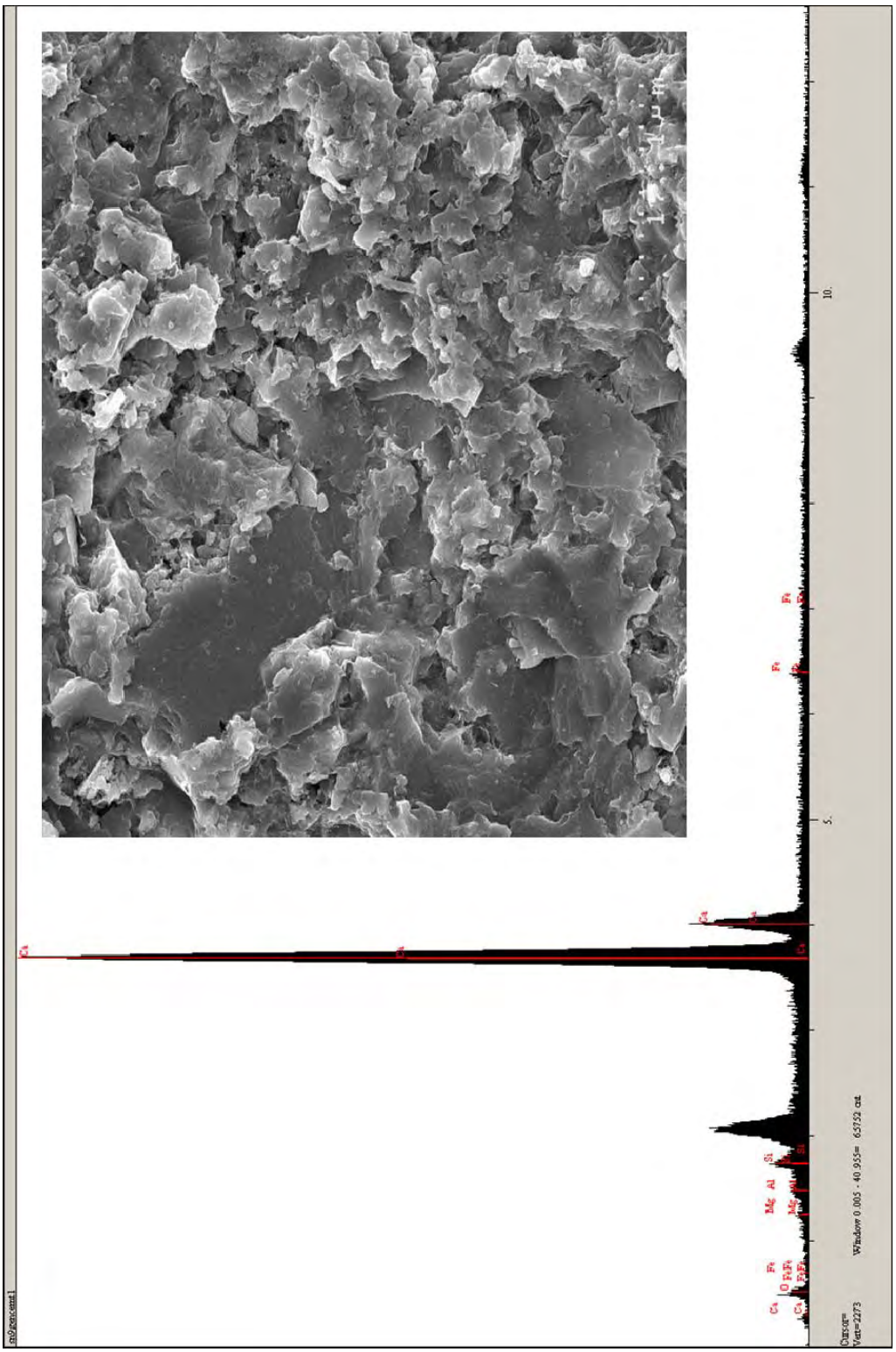

Figure A4.8. Sample RK2-3

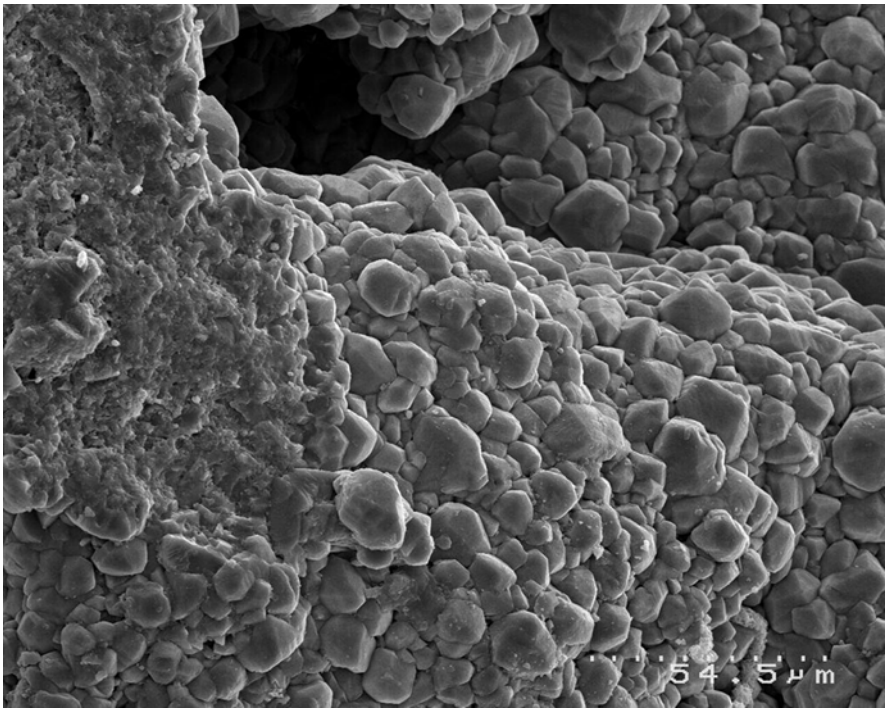

Figure A4.9. Sample RK2-3

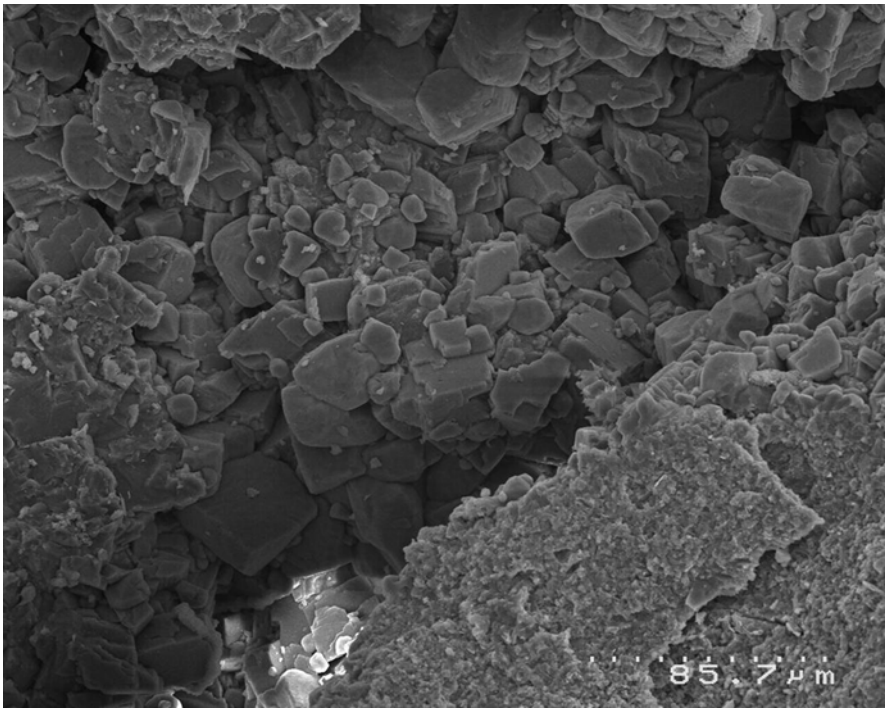

Figure A4.10. Sample RK2-3

7. CO_3 determinations

Appendix Section 7 contains Table A4-4 of some tubular concretions that were dissolved in solution to determine percentage of carbonate geochemically. Appendix 7, Section 7 contains the methodology for dissolution.

Table A4-4. Volume of carbonate in Rocky Knob samples

Sample name	Carbonate	Filter paper weight (g)	Residual sample + filter paper weight (g)	Residual sample weight (g)	Carbonate fraction weight (g)	Wt % carbonate
RN3	Calcite	1.196	1.208	0.012	0.028	70
RN2-1	Calcite	1.196	1.208	0.012	0.028	70
RN2-2	Calcite	1.223	1.234	0.011	0.029	72.5
RN2-3	Calcite	1.204	1.212	0.008	0.032	80
RN1-1	Calcite	1.206	1.22	0.014	0.026	65
RN1-2	Calcite	1.186	1.191	0.005	0.035	87.5
RN1-3	Calcite	1.208	1.21	0.002	0.038	95

8. Isotope transects

Appendix Section 8 contains isotope transects for tubular concretions. The lower case letters (or numbers) next to each data point correspond to the location of the subsample in the photograph to the bottom right. Sample RK65 has three conduits. Each conduit was subsampled as seen in the photographs (RK65-1 through RK65-3). A second cross-section of RK65 was subsampled also (RK65-4 through RK65-6).

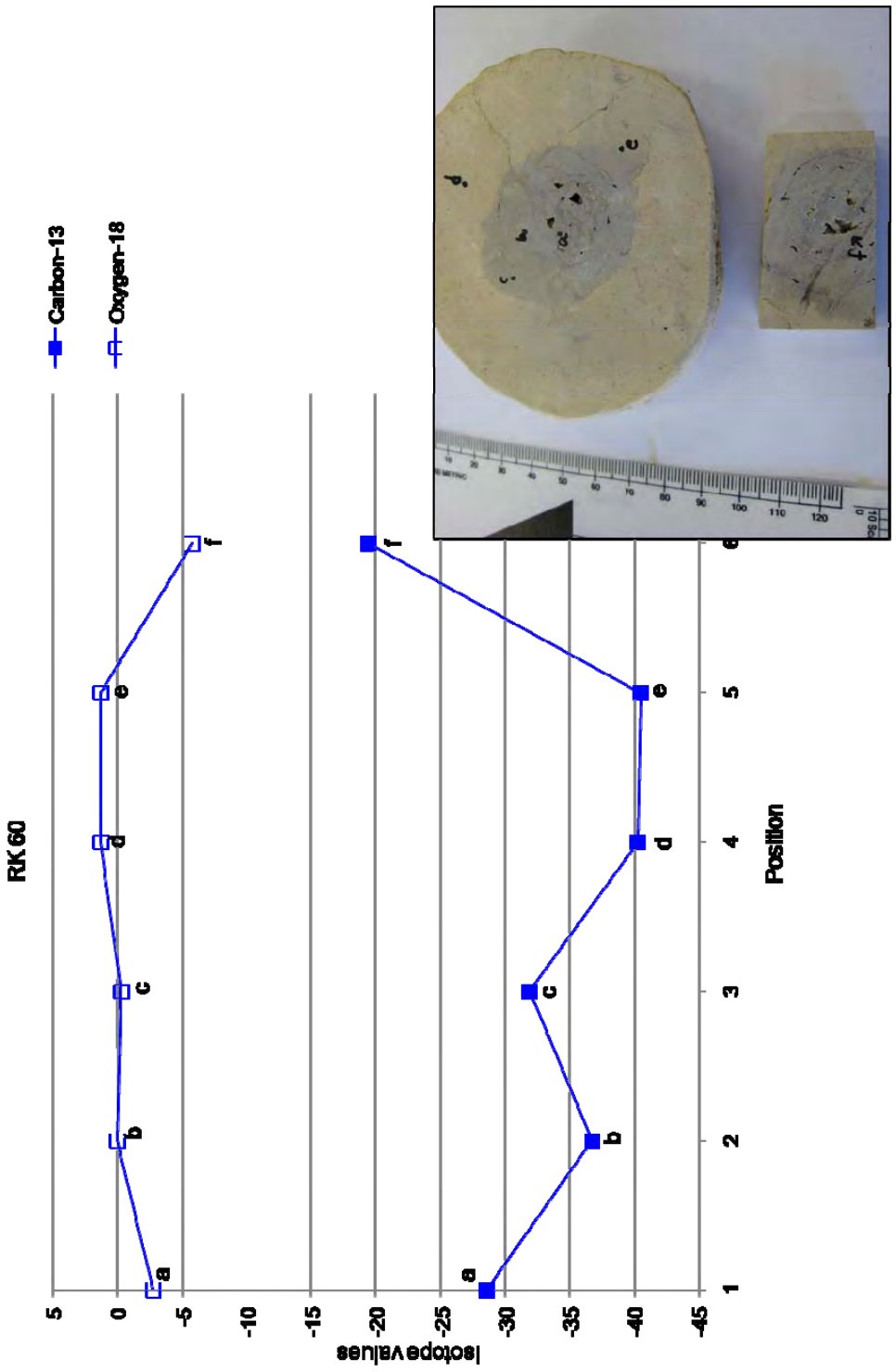
Carbon-13
Oxygen-18
RK 60
Isotope values
Position
5
0
-5
-10
-15
-20
-25
-30
-35
-40
-45
1
2
3
4
5
6
a
b
c
d
e
f

Carbon-13
Oxygen-18
RK62
Isotope values
Position
5
0
-5
-10
-15
-20
-25
-30
-35
-40
-45
-50
1
2
3
a
b
c
b
c
10 CM

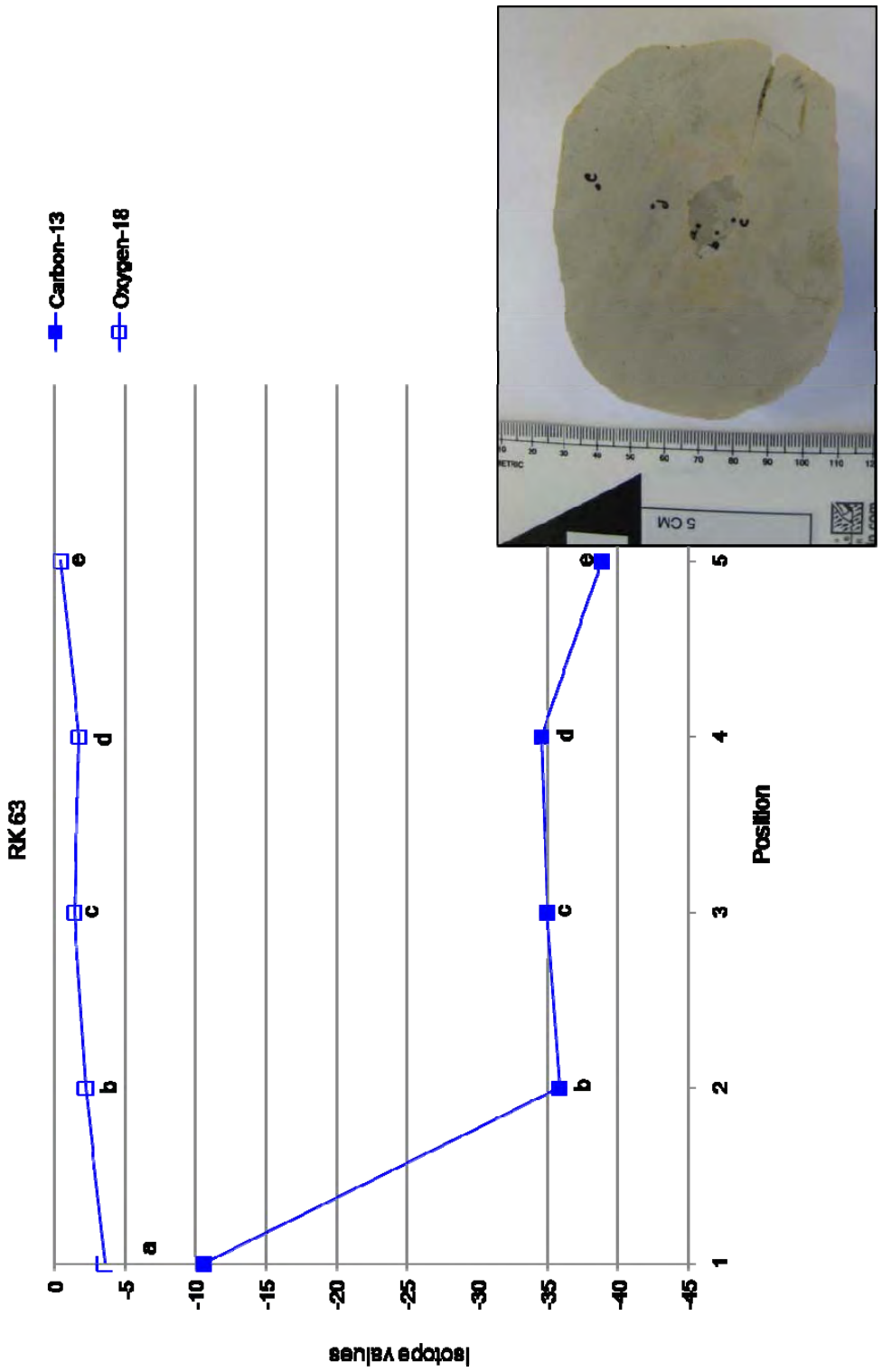
Carbon-13
Oxygen-18
RK 63
Isotope values
Position
0
-5
-10
-15
-20
-25
-30
-35
-40
-45
1
2
3
4
5
a
b
c
d
e
5 CM

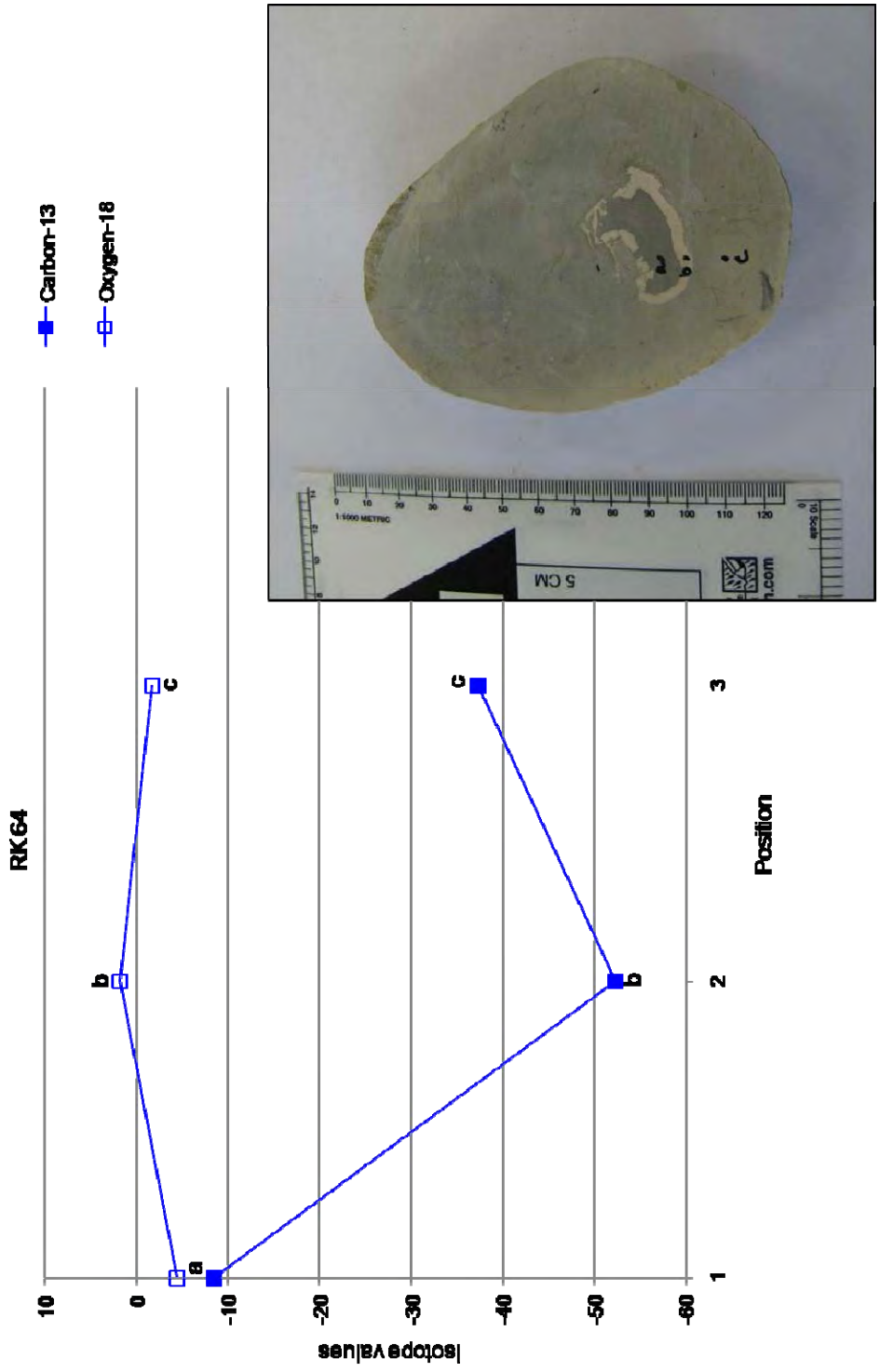
Carbon-13
Oxygen-18
RK64
Isotope values
Position
10
0
-10
-20
-30
-40
-50
-60
1
2
3
a
b
c
5 CM

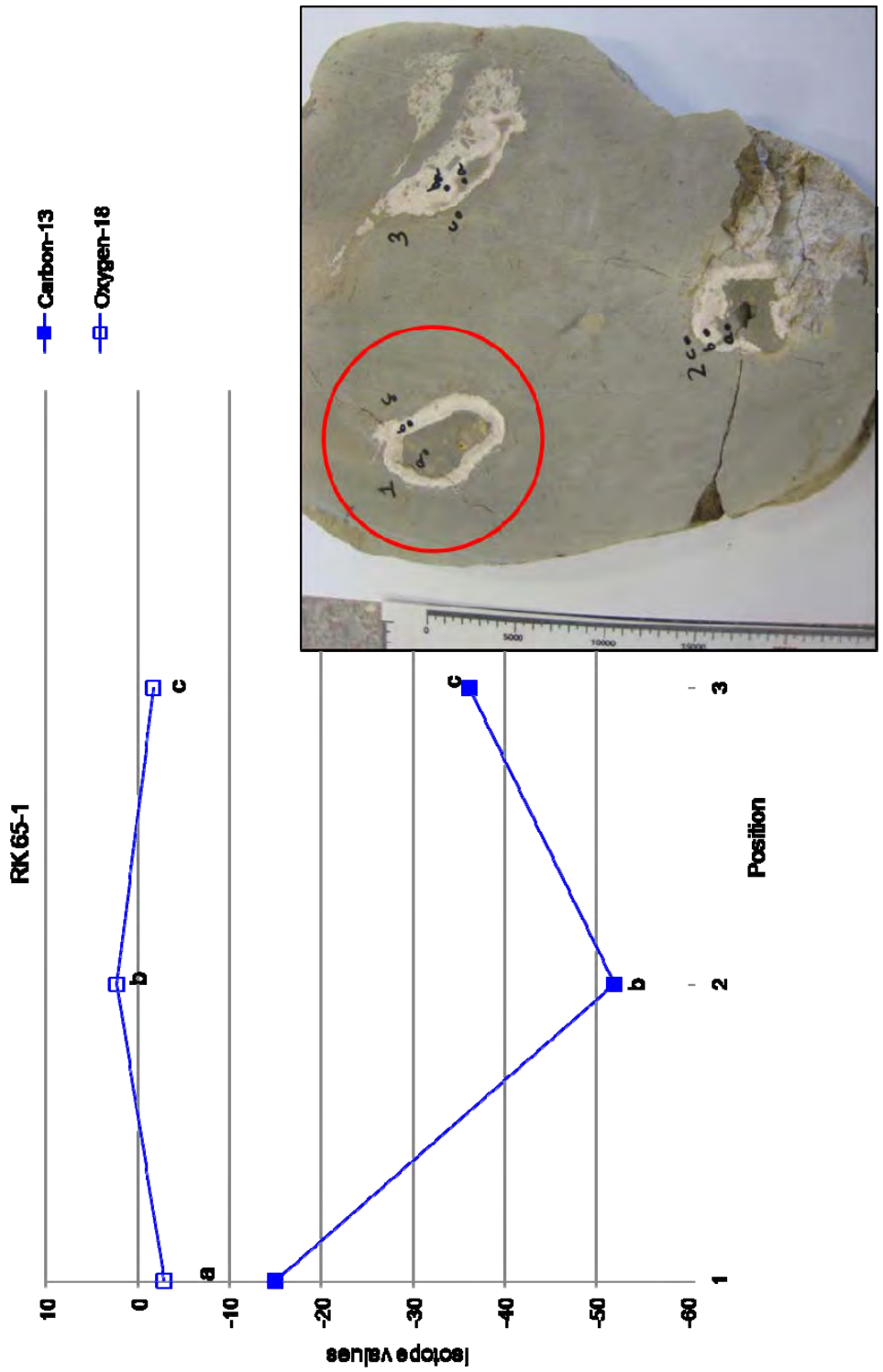
Carbon-13
Oxygen-18
RK65-1
Isotope values
Position
10
0
-10
-20
-30
-40
-50
-60
1
2
3
a
b
c

Carbon-13
Oxygen-18
RK65-2
Isotope values
Position
10
0
-10
-20
-30
-40
-50
-60
1
2
a
b
b
a

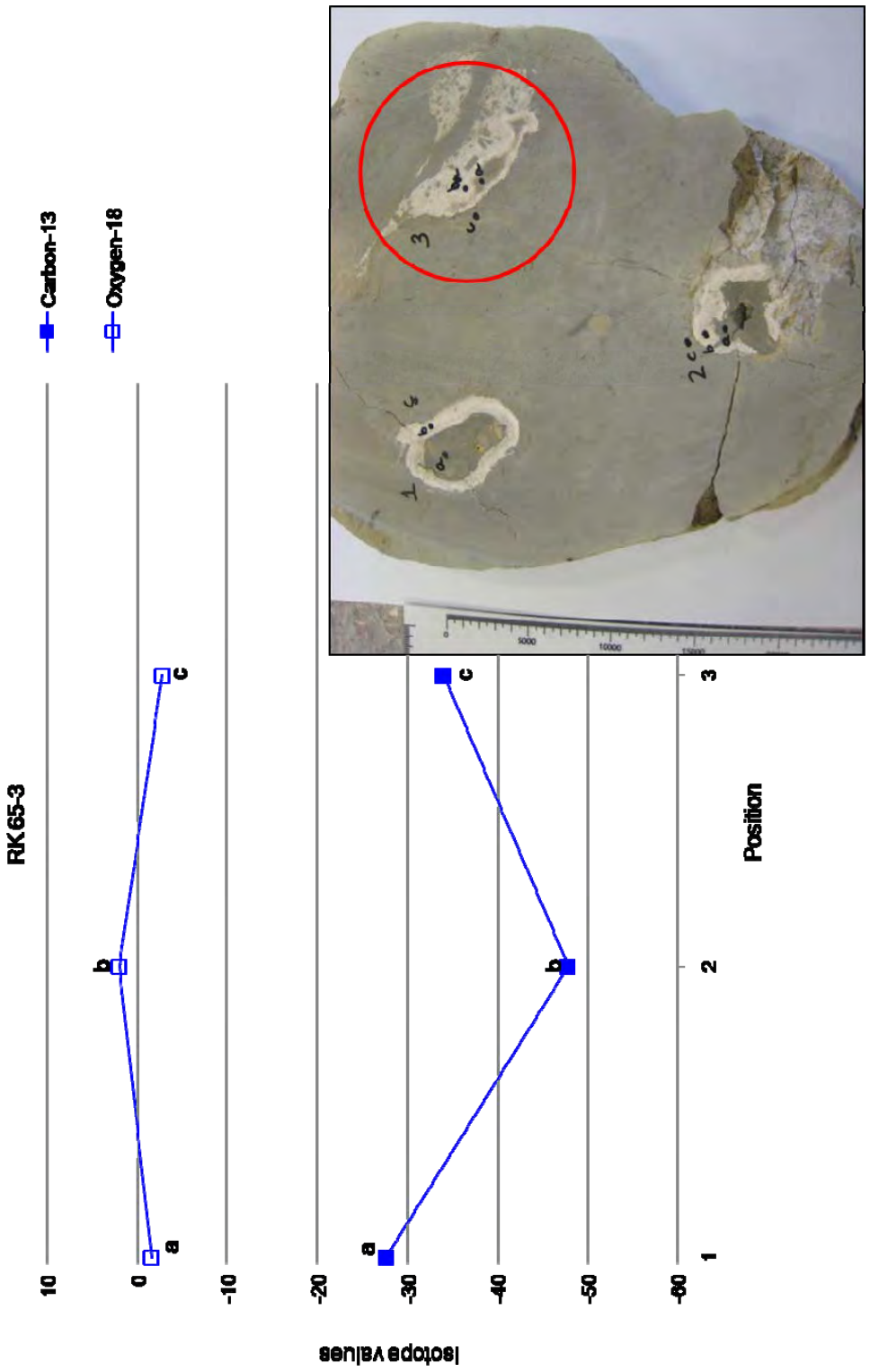
Carbon-13
Oxygen-18
RK 65-3
Isotope values
Position
10
0
-10
-20
-30
-40
-50
-60
1
2
3
a
b
c

Carbon-13
Oxygen-18
RK65-4
Position
Isotope values
5
0
-5
-10
-15
-20
-25
-30
-35
-40
-45
1
2
3
a
b
c
a
b
c

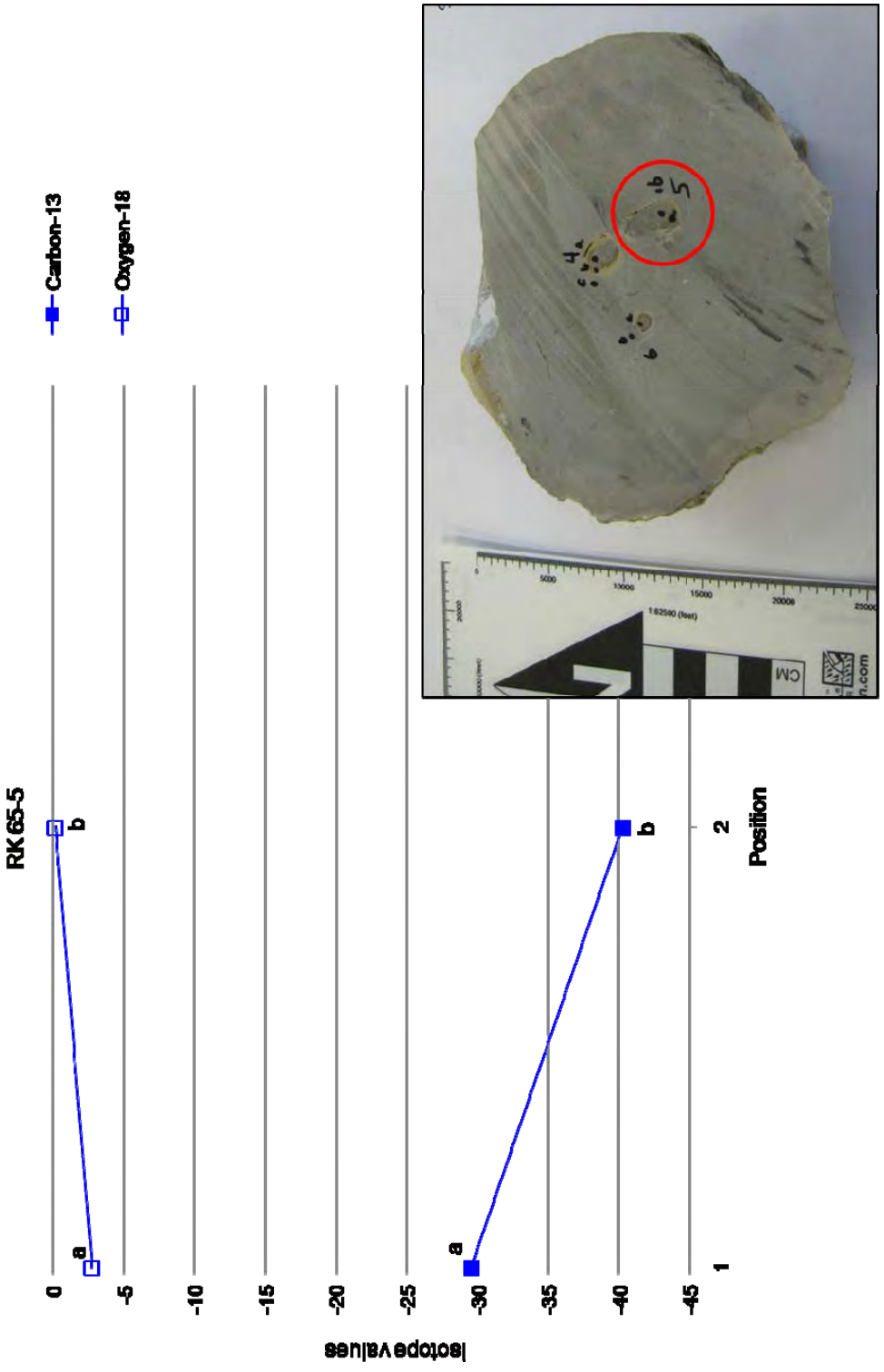
Carbon-13
Oxygen-18
RK 65-5
a
b
0
-5
-10
-15
-20
-25
-30
-35
-40
-45
Isotope values
1
2
Position

Carbon-13
Oxygen-18
RK 65-6
Isotope values
Position
5
0
-5
-10
-15
-20
-25
-30
-35
-40
-45
1
2
a
b
a
b

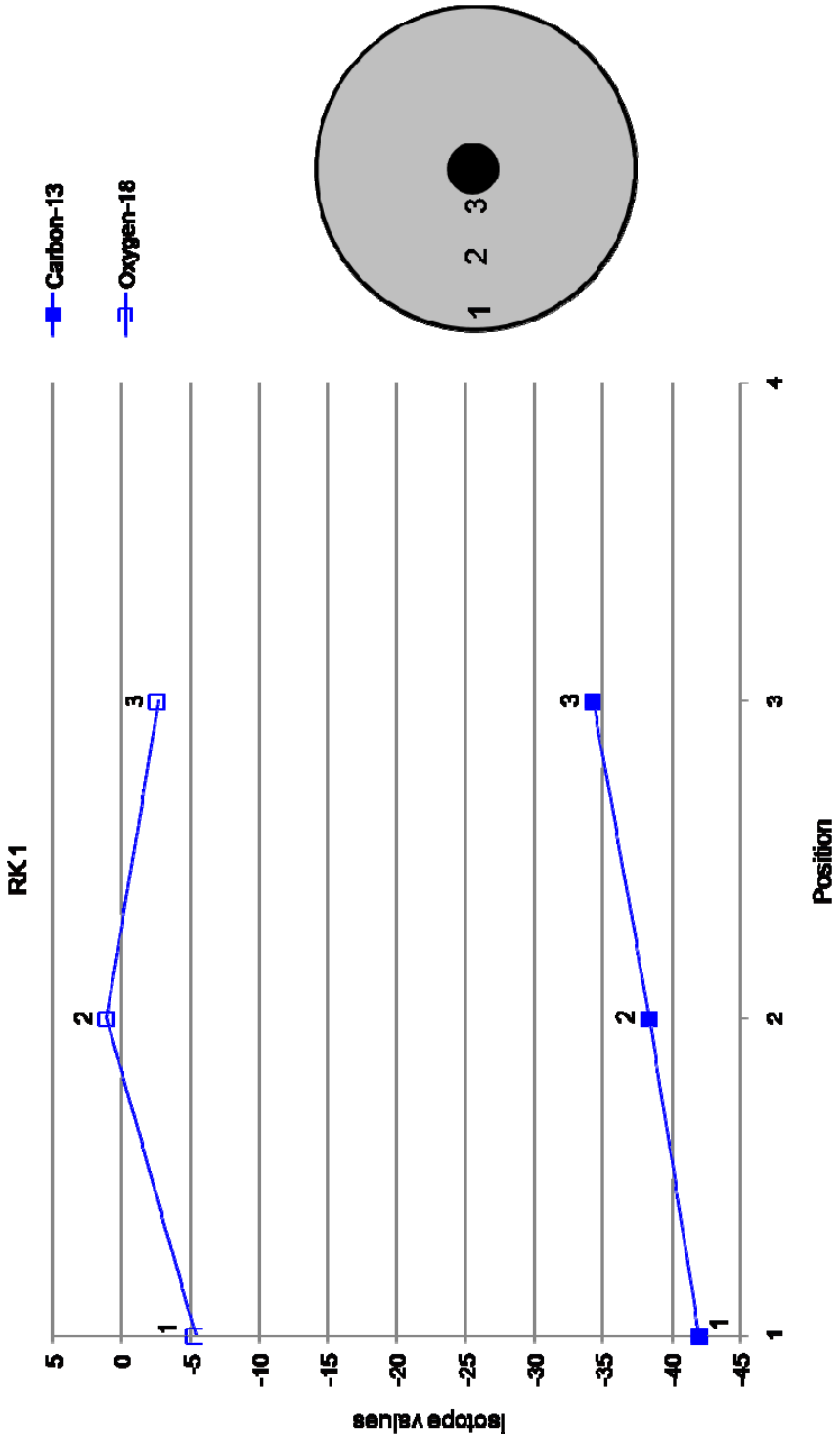
Carbon-13
Oxygen-18
1
2
3
RK 1
Position
Isotope values
5
0
-5
-10
-15
-20
-25
-30
-35
-40
-45
1
2
3
4

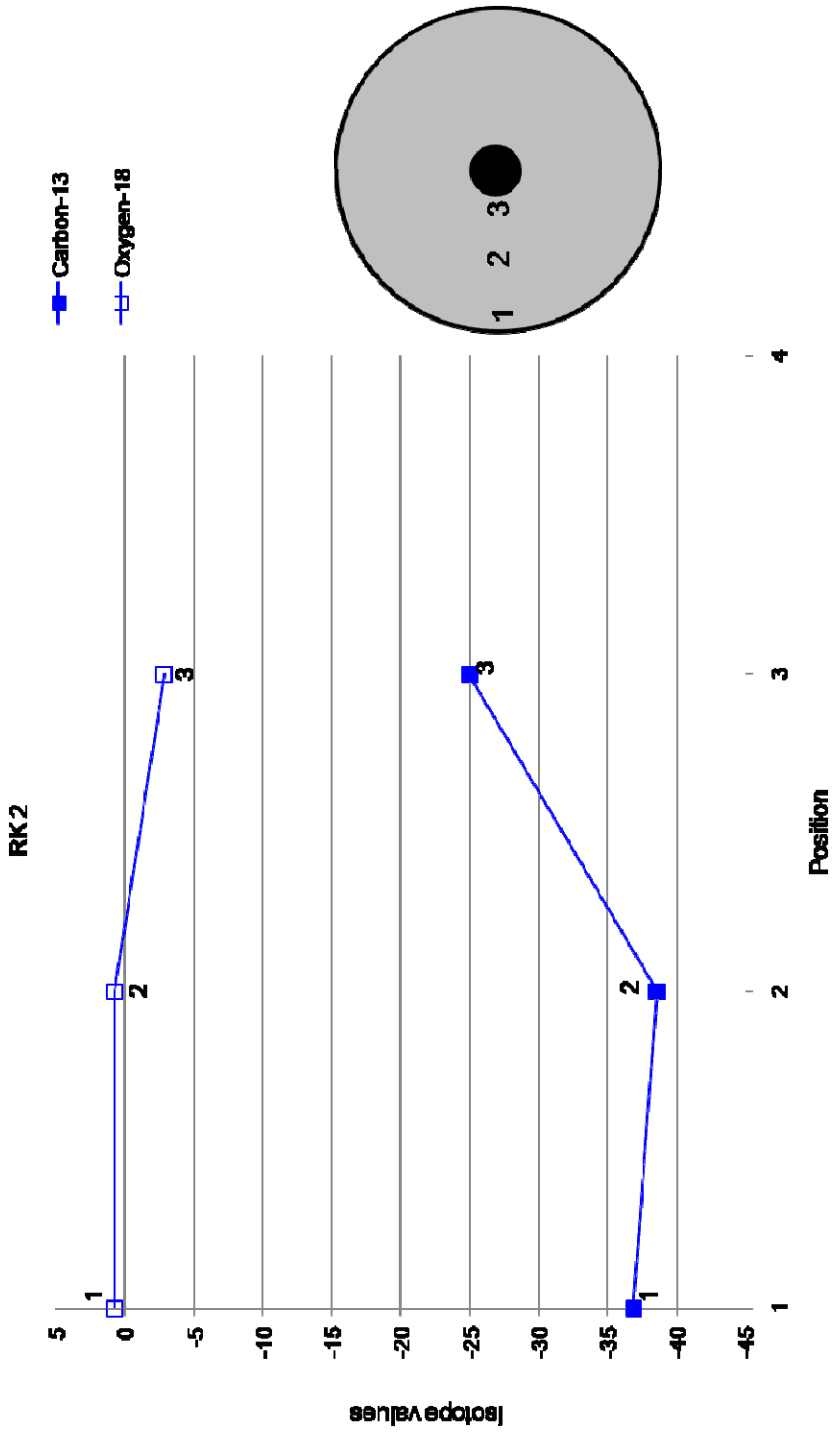
Carbon-13
Oxygen-18
RK 2
Position
Isotope values
5
0
-5
-10
-15
-20
-25
-30
-35
-40
-45
1
2
3
4

9. ICP/MS

Appendix Section 9 contains tables of ICP/MS data.

Table A4-5. ICPMS data

	Na 23	Mg 24	Al 27	K 39	Ca 43	Cr 52	Fe 54	Mn 55	Cu 65	Sr 88	Pb 206	Pb 207	Pb 208	U 235	U 238
Calibration blank															
merck XXI 50ppb +2% HNO3	40.15	50.00	50.00	50.00	39.80	50.00	45.29	50.00	50.00	50.00	50.00	50.00	50.00	50.00	50.00
merck IV 50ppb +2% HNO3	38.79	52.12	52.02	56.59	41.80	50.23	42.42	51.03	51.16	50.65	50.39	53.13	50.84	0.03	0.03
Merck 500ppb +2% HNO3	500.00	527.98	516.88	482.46	500.00	509.44	500.00	514.20	426.13	520.18	503.65	525.31	512.05	0.00	0.01
calibration blank	0.39	0.03	0.01	2.67	1.45	0.02	-2.08	0.01	0.01	0.01	0.01	0.01	0.01	0.00	0.00
flush blank	-1.32	0.01	0.00	2.61	2.25	-0.03	-9.67	-0.01	0.00	0.00	0.01	0.01	0.01	0.00	0.00
RN3	440.52	4222.68	780.28	253.48	59724.18	3.13	902.88	45.04	9.82	195.39	8.75	8.82	8.71	0.33	0.19
RN2-1	359.73	3504.26	746.88	235.76	47566.80	3.38	841.85	51.14	10.40	159.90	9.13	9.13	9.07	0.45	0.22
flush	1.57	0.40	0.13	6.18	11.97	-0.09	-13.37	0.00	0.00	0.01	0.00	0.00	0.01	-0.02	0.00
RN2-2	545.73	4333.91	781.33	234.78	54546.94	3.53	834.33	44.01	13.27	184.88	17.90	17.94	17.99	0.51	0.21
RN2-3	430.62	3056.24	515.37	183.17	85866.20	3.32	1165.44	172.04	8.36	228.96	4.37	4.37	4.36	0.82	0.35
RN1-1	655.13	3520.53	967.84	352.53	55755.50	3.47	1146.43	108.48	10.39	205.35	7.31	7.32	7.24	0.59	0.29
RN1-2	426.66	3868.89	638.16	221.30	65181.89	3.18	1075.32	103.12	8.80	334.47	4.33	4.28	4.32	1.40	0.60
RN1-3	546.57	3271.98	617.02	205.41	73668.03	3.66	1257.58	145.00	10.44	297.76	16.38	16.30	16.38	0.94	0.44
sample flush	4.88	3.45	0.25	20.53	17.96	0.02	-3.83	0.05	0.02	0.03	0.01	0.01	0.01	0.00	0.00
MerckXXI QC	74.87	70.11	62.10	72.92	71.07	50.82	50.37	46.24	54.18	49.65	52.62	53.31	52.03	50.33	54.60
Calibration blank															
merck XXI 50ppb +2% HNO3	68.02	50.00	50.00	50.00	62.72	50.00	51.48	50.00	50.00	50.00	50.00	50.00	50.00	50.00	50.00
merck IV 50ppb +2% HNO3	61.80	48.52	47.67	53.25	61.60	49.37	45.96	49.16	49.90	49.72	49.28	50.26	51.17	0.04	0.02
Merck 500ppb +2% HNO3	500.00	497.50	489.15	461.58	500.00	511.40	500.00	505.56	436.97	534.10	498.08	517.15	507.15	0.01	0.00
calibration blank	-0.13	0.05	0.01	1.65	1.69	0.09	6.19	0.01	0.00	0.01	0.01	0.01	0.02	0.01	0.00
flush sample	-3.79	4.43	0.12	6.89	17.08	0.14	1.35	0.03	0.00	0.04	0.00	-0.01	0.00	0.00	0.00
flush blank	-2.26	2.53	0.62	6.09	21.09	0.22	5.39	0.03	0.01	0.02	-0.01	-0.02	0.00	0.03	0.00
Merck XXI QC	46.30	46.60	44.78	47.77	61.75	51.71	55.83	49.59	52.33	50.50	47.68	46.74	48.59	49.87	51.12

Appendix 5

Additional Locations

Additional locations table of contents

1. Location

In North Island, New Zealand, a total of 23 additional tubular concretion locations are known. Fourteen of these sites were confirmed in this study, whereas the remaining 9 were not visited either due to access logistics, previous field notes indicating the exposure was minimal, or the site became known too late in the study. Four of the sites visited were sampled for isotope analysis to determine whether hydrocarbon sources were involved. However, these four sites were not investigated further as a decision was made to concentrate the study on the four main locations (Taranaki, Cape Turnagain, East Cape, and Rocky Knob) which provided a greater range of tubular concretion characteristics. Section 1.1 describes the locations with access information (Table A5.1). Section 1.2 is a regional map (Fig. A5.1) identifying the locations.

Table A5.1. Additional locations and access information. See Figure A5.1 for map of locations.

Location	Topo map	Grid Reference	Access and comments	Contacts / Permission	Outcrop	Source Information
Central North Island						
Gentle Annie	U20	984 974	Waikarokaro Stream		Mangatoro Formation, grey, moderately sorted, bioturbated, micaceous very fine and fine-grained muddy sandstone and sandy mudstone. Forams abundant, ostracods, molluscs (mostly gastropods), echinoid spines, bone fragments, fish teeth. Thin (<1cm) rhyolitic tuffs also present. Formation confined to Kuripapango area. A basal sedimentary contact is not exposed, and the formation is in fault contact with older formations. Formation as much as 1500 m thick.	Greg Browne
Tipohui	U18 or U19		Location not known		May have eroded away; on road between Taupo and Napier.	Greg Browne
Eastern Raukumara Peninsula						
Anauraiti Stream	Y16	637 255	Fernside Road		Inland: Huanui Forest; see Geologic Society Newsletter 1985, pg. 52, v. 68.	Mazengarb and Francis
Parariki Stream	Y16	510 115			Huanui Forest; [Dave Francis note: this is Tokomaru/Makomako Forest] see Geologic Society Newsletter 1985, pg. 52, v. 68.	Mazengarb and Francis

Table A5.1 continued.

Location	Topo map	Grid Reference	Access and comments	Contacts / Permission	Outcrop	Source Information
Tauwhareparae	Y16	558 103	Tauwhareparae Road		Inland: may have eroded away; on way from Tolaga; some mudstone, pale, calcareous, tuffaceous? Fossil sandstone beds 2-5cm often some 15-20 cm, rarely 30 cm.	Dave Francis
Waiau	Y16	581 188	Upper Waiau Stream		"Modiolus" limestone, lower Miocene, 3.5 m + thick, conglomerate with medium coarse sandstone matrix, appears very carbonaceous but probably clasts (angular) of Waipawa black shale. Large clasts dominantly hard concretions including tubular concretions.	Dave Francis
Loisel's Beach / Waihau Beach	Z17	724 927 711 902	Waihau Road and Waionanga Stream; maybe also Waihakeke Stream	Danny Angland Pakarae Station 06 862 2708 (Note:	Irregular concretion in muddy siltstone, bedding not seen, concretions up to 1 m generally 20-40 cm, shore platform 100-150 m wide, bedding not seen. Concretions 30 cm-1 m diameter, mudstone grain size, flinty, calcareous jointed if large irregular, some resemble tubular concretion 20 cm diameter. Good tubular concretions 40 cm diameter with 2 cm central spine; perpendicular to bedding, but some run along bedding up to 60 cm long. Most of occurences are further south near Maunupohatu Stream.	Dave Francis

Table A5.1 continued.

Location	Topo map	GPS	Access and comments	Contacts / Permission	Outcrop	Source Information
Pakarae Beach	Y17 and Z17	675 812 between 690 and 824	Pakarae Road		Miocene pelagic rich mudstone.	Dave Francis
Kamponui Stream	Z16	755 171	Nuhiti Road		Tubular concretions in dark siltstone below alluvial fan boulders; diameter 14 cm with 4 cm darker core.	Dave Francis
Anaura Bay / Nuhiti Beach	Z16	770 192	North end of beach on coast	Michael Ferris Nuhiti Station 06 862 6308 Anaura Bay	In silty mudstone, tubular concretions up to 15 cm diameter, run along bedding then turn up to be perpendicular to bedding.	Dave Francis
Anaura Bay / Nuhiti Beach	Z16	773 200	500 m north of Waihirere Stream, on coast	Michael Ferris Nuhiti Station 06 862 6308 Anaura Bay	Siltstone and thin sandstone beds, tubular concretions up to 20 cm diameter.	Dave Francis
Anaura Bay / Nuhiti Beach	Z16	768 193	Scar above track	Michael Ferris Nuhiti Station 06 862 6308 Anaura Bay	Mudstone, with up to 1.5 m spheroidal concretions plus tubular concretions 20-30 cm and up to 1 m long.	Dave Francis
Anaura Bay / Nuhiti Beach	Z16	772 204	Near track south of Karorotuau Stream	Michael Ferris Nuhiti Station 06 862 6308 Anaura Bay	Several sites tubular concretions in mudstone, tuff boulders nearby.	Dave Francis
Tokomaru Bay	Z16	793 301	East of Tokomaru Wharf		In dark grey silty mudstone, tubular concretions up to 50 cm diameter.	Dave Francis

Table A5.1 continued.

Location	Topo map	GPS	Access and comments	Contacts / Permission	Outcrop	Source Information
Karikarihuata Stream	Y16	657 351	Ernslaw Forestry		Difficult access, 4WD on forestry track, 2 km hike up tree felled stream. Some tubular concretion and seafloor seep limestone.	Kathy Campbell
Mahia Peninsula						
Waianiwaniwa Stream	Y19, X&Y20	342 097	Mahia East Coast Road and Wainuiorangi Road		Tunauni sandstone	Timbrell
Tawapata Stream	Y19, X&Y20	345 108	Mahia East Coast Road (south) and up beach 4WD needed		Tunauni sandstone	Timbrell
Haunui Stream	Y19, X&Y20	343 097	Mahia East Coast Road (south) and up beach 4WD needed		Tunauni sandstone	Timbrell
Black Reef	Y19, X&Y20	207 307	Mahia East Coast Road all the way south and 4WD needed		Beach: (south facing cliff of Black Reef) and in stream channel (north of Black Reef).	Dave Francis
Marlborough	P30	262 818	Through Bluff Station to Coverham, farmer can point out Sawpit Gully. Walk over the ridge to Sawpit Gully (do not follow streams, they are incorrectly mapped).	Bluff Station, Kekerengu Valley Road. Richard and Sue Murray, 03 575 8622.	Tubular concretions in mudstone just below a 2 m thick sandstone	James Crampton

1.2 Regional map

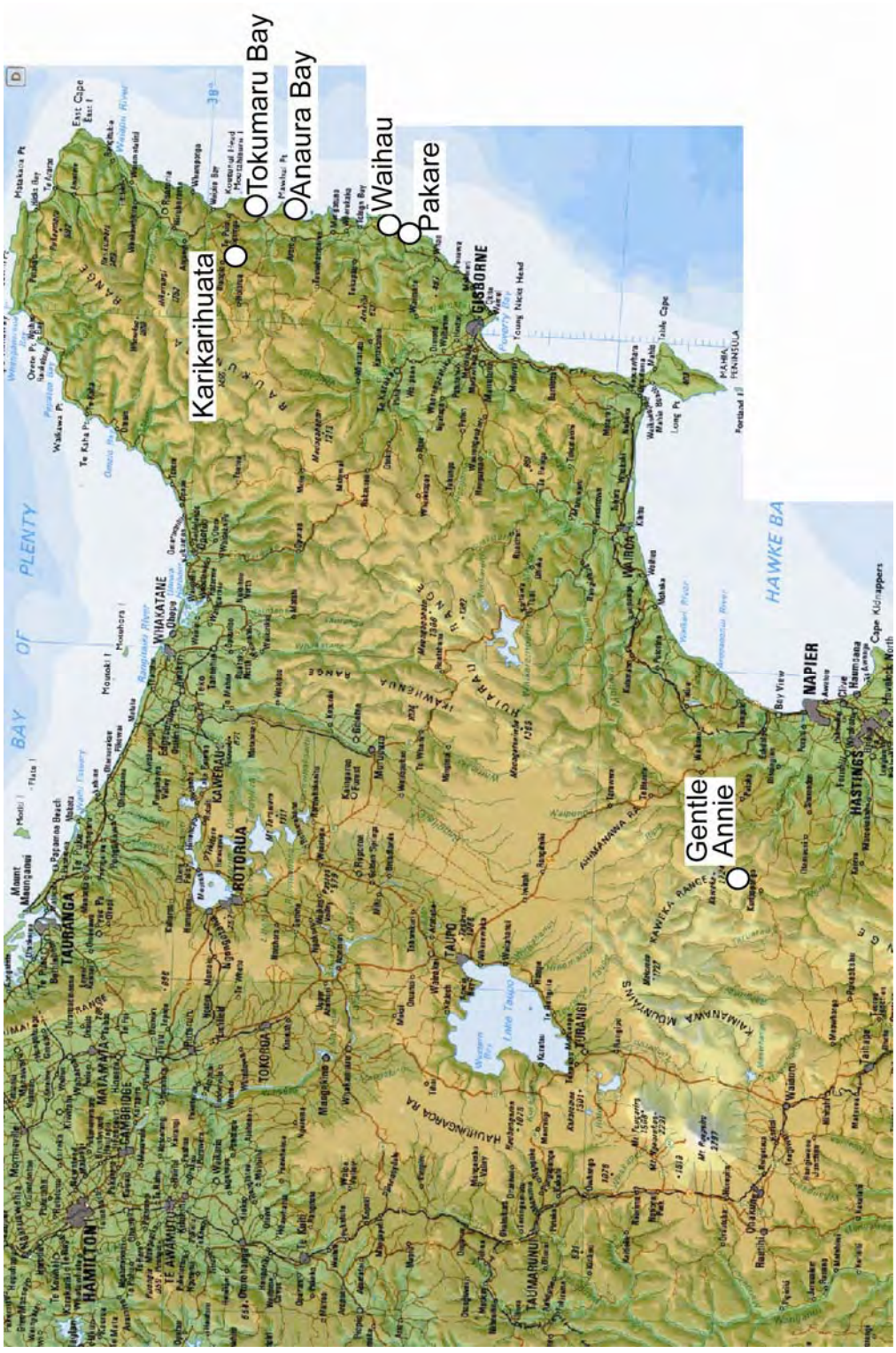

Figure A5.1. Regional map of the Gisborne region and Raukumara Peninsula identifying locations of the additional sites. See Table A5.1 for descriptions.

2. Field photographs

Photographs of tubular concretions (Fig. A5.2) in the field are presented in this section along with brief descriptions in Table A5.2 (jpg number corresponds to table). A DVD accompanies this volume, where the photographs can be viewed at a larger scale (Appendix\AdditionalLocations\FieldPhotos).

Table A5.2. Descriptions of photographs in Figure A5.2

Photograph jpg no.	Location	Comment
9000	Gentle Annie	Pipe concretions eroding out of mudstone
9001	Gentle Annie	Sinuous pipe concretions
9002	Gentle Annie	Sinuous pipe concretions
9003	Gentle Annie	Small pipe with conduit distinguishable only by colour differentiation
9004	Gentle Annie	Pipe concretions eroding out of mudstone (additional view of 9000)
9005	Gentle Annie	Two large pipes eroding out of the mudstone
9006	Gentle Annie	Bulbous-pipe
9007	Gentle Annie	Sinuous pipe concretion
9008	Gentle Annie	View of 9006 and 9007
9009	Gentle Annie	Pipe concretion
9010	Gentle Annie	Cross sections of tubular concretions in stream
9011	Gentle Annie	Cross sections of tubular concretions in stream
9012	Gentle Annie	Close up of 9011, note the pinhole
9013	Gentle Annie	Cross section of a pipe concretion with a filled conduit, note the large pipe on the left
9014	Gentle Annie	Cross section of small pipe
9015	Gentle Annie	Pipe concretion
9016	Gentle Annie	Additional view of 9014
9017	Gentle Annie	Sinuous pipe
9018	Gentle Annie	Bulbous concretions eroding out of the mudstone
9019	Gentle Annie	Bulbous concretions eroding out of the mudstone
9020	Gentle Annie	Concretionary layer
9021	Gentle Annie	Tubular concretions in the stream, note iron staining
9022	Gentle Annie	Bulbous concretion
9023	Gentle Annie	Bulbous to layered concretion, note bulbous concretions in the background
9024	Gentle Annie	Cross sections of tubular concretions in the stream
9025	Gentle Annie	Sinuous concretion
9026	Gentle Annie	Cross sections of tubular concretions in the stream, most have small pinhole conduits

Table A5.2 continued.

Photograph jpg no.	Location	Comment
9027	Gentle Annie	Close up of 9025
9028	Karikarihuata Stream	Mustone outcrop with 'stacked' doughnut concretions
9029	Karikarihuata Stream	Note the two stacked doughnuts in the middle of the photograph
9030	Karikarihuata Stream	Additional view of 9029
9031	Karikarihuata Stream	Close up of 9030
9032	Karikarihuata Stream	Close up of 9030
9033	Karikarihuata Stream	Close up of 9029 (concretion on right)
9034	Karikarihuata Stream	Additional view of 9029
9035	Karikarihuata Stream	Concretion debris in stream, note the 'stacked' appearance
9036	Karikarihuata Stream	Concretion with conduit, debris in stream
9037	Pakarae	Tubular concretion with open conduit
9038	Pakarae	Irregular concretionary body
9039	Pakarae	Additional view of 9038
9040	Pakarae	Additional view of 9038
9041	Pakarae	Additional view of 9038
9042	Pakarae	Additional view of 9038
9043	Pakarae	Additional view of 9038
9044	Pakarae	Irregular concretionary body nearby 9038
9045	Pakarae	"
9046	Pakarae	"
9047	Pakarae	"
9048	Pakarae	"
9049	Pakarae	View of entrance to Pakarae, note the rocks protruding out of the water in the centre of the photograph - location of 9038 - 9049
9050	Waihau	Concretion debris with open conduit
9051	Waihau	Pipe concretion with pinhole conduit
9052	Waihau	Pipe eroding out of the mudstone
9053	Waihau	Pipe with conduit discernable only by colour zonation
9054	Waihau	Pipe with large open conduit
9055	Waihau	Two pipes with filled conduits (harder material than the outer concretion)
9056	Waihau	Pipe concretion with open conduit

Table A5.2 continued.

Photograph jpg no.	Location	Comment
9057	Waihau	Concretionary material, potentially a tube in center
9058	Waihau	Pipe concretion with open conduit
9059	Waihau	Small pipe in bedrock with filled conduit
9060	Waihau	Pipe concretion with open conduit
9061	Waihau	Pipe concretion with open conduit
9062	Waihau	Pipe concretion debris on shoreface
9063	Waihau	Concretion debris on shoreface, many with conduits
9064	Waihau	Photograph of entrance to Waihau
9065	Waihau	Pipe concretion with open conduit and potentially an outer conduit
9066	Waihau	Concretion debris on shoreface, many with conduits
9067	Waihau	Concretion with potential conduit
9068	Waihau	Irregular concretion
9069	Waihau	Tube with open conduit
9070	Waihau	Tube with open conduit
9071	Waihau	Photograph of entrance to Waihau, where concretions first outcrop
9072	Anaura Bay	Photograph of entrance to Anaura Bay where concretions first outcrop
9073	Anaura Bay	Small pipe-like concretions with pinhole conduits
9074	Anaura Bay	Small pipe-like concretions with pinhole conduits
9075	Anaura Bay	Small pipe-like concretions with conduits filled with harder material than outer concretion
9076	Anaura Bay	Small pipe-like concretions with pinhole conduits
9077	Anaura Bay	Small pipe-like concretions with pinhole conduits
9078	Anaura Bay	Concretion with small conduit filled with harder material than surrounding concretion
9079	Anaura Bay	Concretion with small conduit filled with harder material than surrounding concretion

Table A5.2 continued.

Photograph jpg no.	Location	Comment
9080	Anaura Bay	Concretion with small conduit filled with harder material than surrounding concretion
9081	Anaura Bay	3D view of small pipe
9082	Anaura Bay	Cross sections of interconnected tubes
9083	Anaura Bay	Small tubes with pinhole conduits protruding out of the mudstone
9084	Anaura Bay	Small concretionary structure protruding out of the mudstone
9085	Anaura Bay	Small tubes with pinhole conduits protruding out of the mudstone
9086	Anaura Bay	Small concretionary structure protruding out of the mudstone
9087	Anaura Bay	Pipe-like concretion with large filled conduit
9088	Anaura Bay	Pipe-like concretion with large filled conduit
9089	Anaura Bay	Pipe-like concretion with filled conduit
9090	Anaura Bay	Cross sections of tubes with filled conduits
9091	Anaura Bay	Cross sections of tubes with filled conduits
9092	Anaura Bay	Cross sections of tubes with open
9093	Anaura Bay	Small pipe with pinhole conduit
9094	Tokomaru Bay	Tubular concretion protruding out of the mudstone
9095	Tokomaru Bay	Close up of 9095
9096	Tokomaru Bay	Bulbous-like concretion protruding out of the mudstone
9097	Tokomaru Bay	Strongly fractured concretionary material on shoreface
9098	Tokomaru Bay	Strongly fractured concretionary material on shoreface
9099	Tokomaru Bay	View of outcrop, person standing next to main exposure of tubes
9100	Tokomaru Bay	View of mudstone outcrop, note concretion layers in the lower middle of the photograph
9101	Matheson's Bay	Potential seafloor seep carbonate (strongly negative carbon isotope values)

Table A5.2 continued.

Photograph jpg no.	Location	Comment
9102	Matheson's Bay	Sandy sediments with small pipe-like concretions and open conduits,
9103	Matheson's Bay	Close up of pipe-like concretion cross section
9104	Matheson's Bay	Additional view of 9102
9105	Mahia	Large pipe concretions protruding out of the cliff outcrop (middle of photograph)
9106	Mahia	Large pipe concretions protruding out of the cliff outcrop
9107	Mahia	Large pipe-like concretion
9108	Mahia	View of 9105 and 9107
9109	Mahia	Additional view of 9105
9110	Mahia	Additional view of 9106
9111	Mahia	Additional view of 9105
9112	Mahia	Roadcut with concretionary features, some appear to have conduits
9113	Mahia	Large pipe-like protrusions in the upper outcrop
9114	Mahia	Close up of 9114
9115	Mahia	Large pipe-like protrusions in the outcrop
9116	Mahia	Close up of 9115
9117	Mahia	Close up of 9115
9118	Mahia	Potential tubes in the upper sections of the outcrop
9119	Mahia	Close up of 9118
9120	Mahia	Small pipe-like concretion protruding out of the mudstone
9121	Mahia	Small pipe-like concretion protruding out of the mudstone
9122	Mahia	Concreted layer with potential conduits
9123	Mahia	Concreted layer with large conduit
9124	Mahia	Additional view of 9123
9125	Mahia	View of main outcrop, many layers have conduits but rare tube like shapes

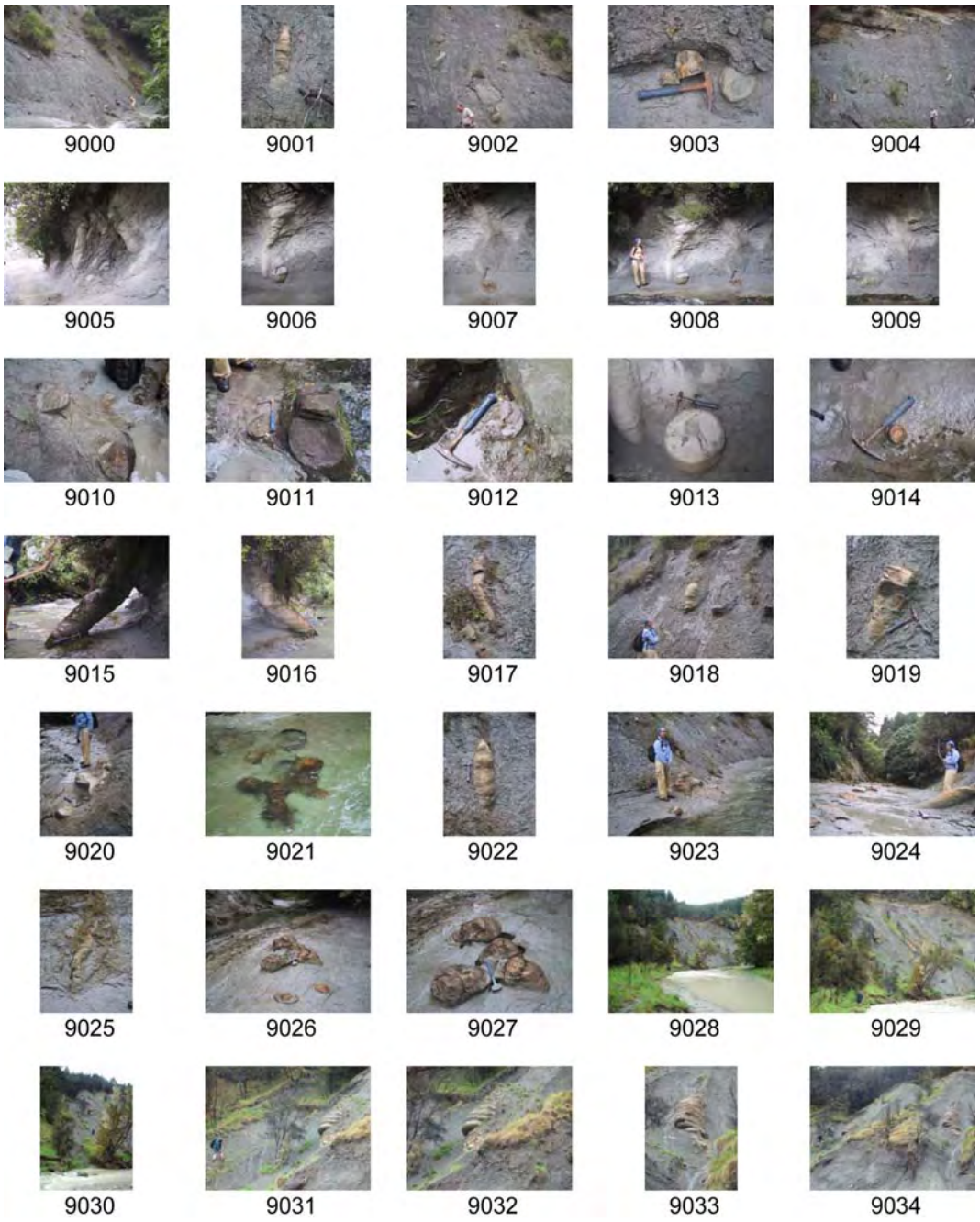

Figure A5.2. Field photographs of additional sites. See Table A5.2 for descriptions.

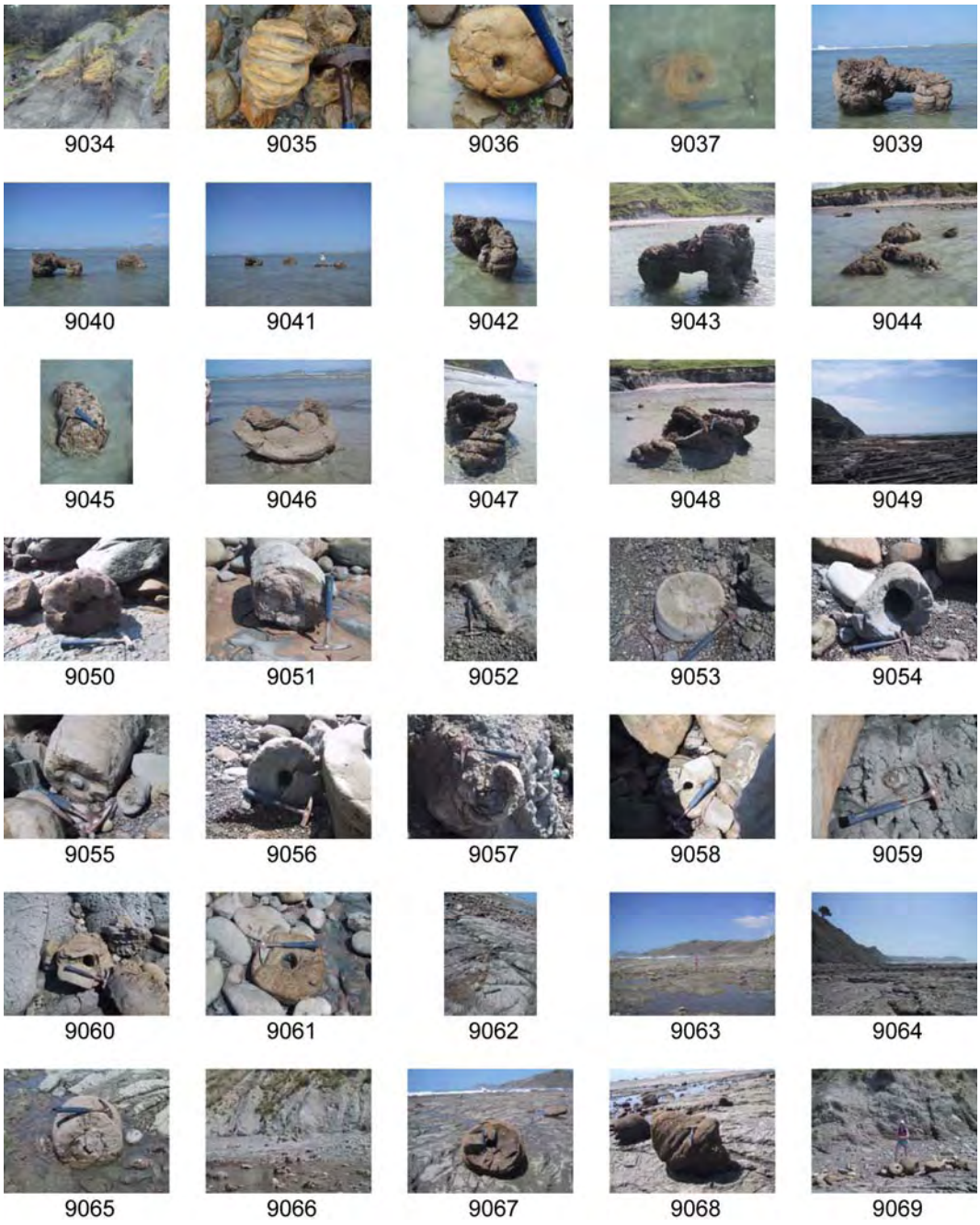

Figure A5.2 continued.

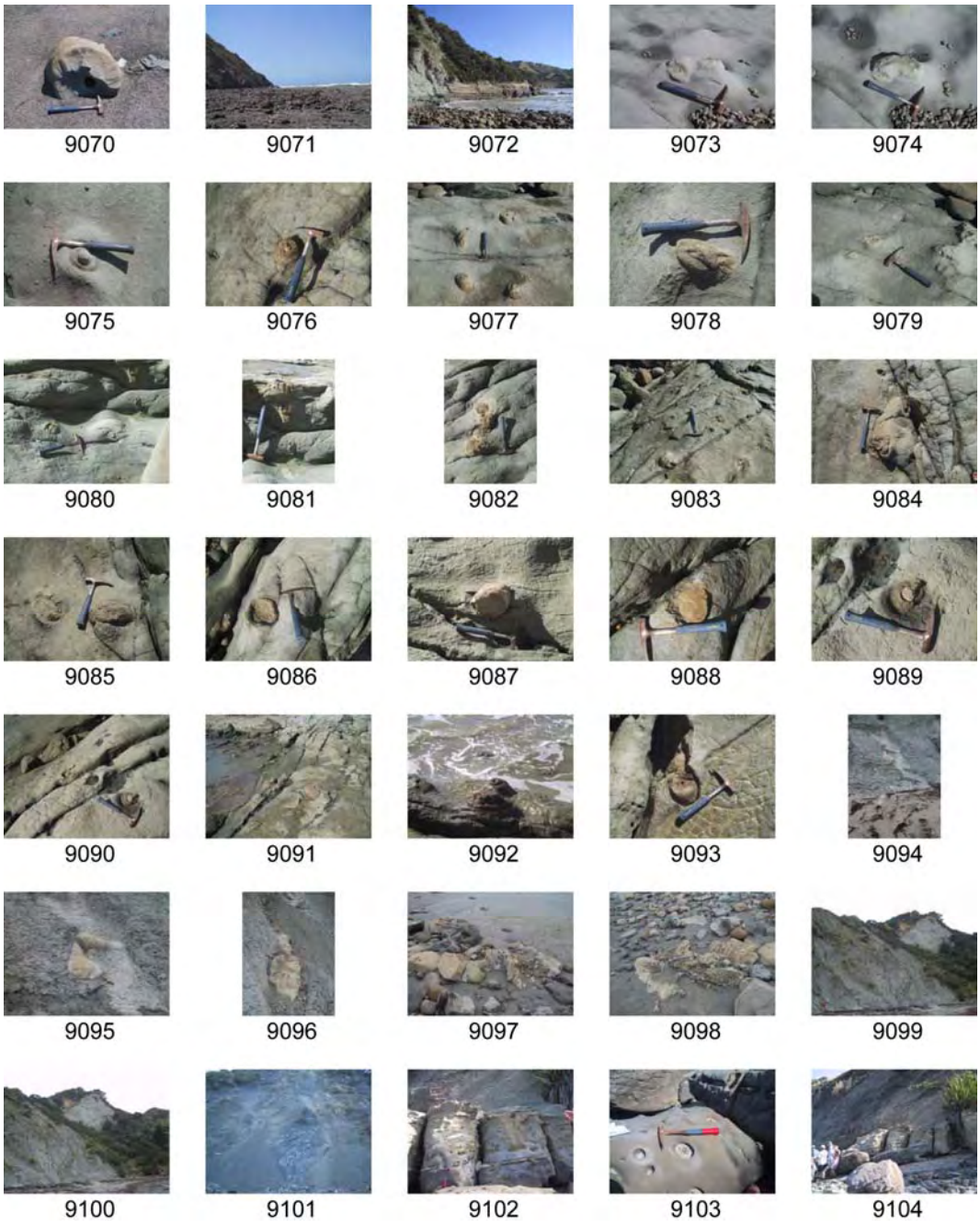

Figure A5.2 continued.

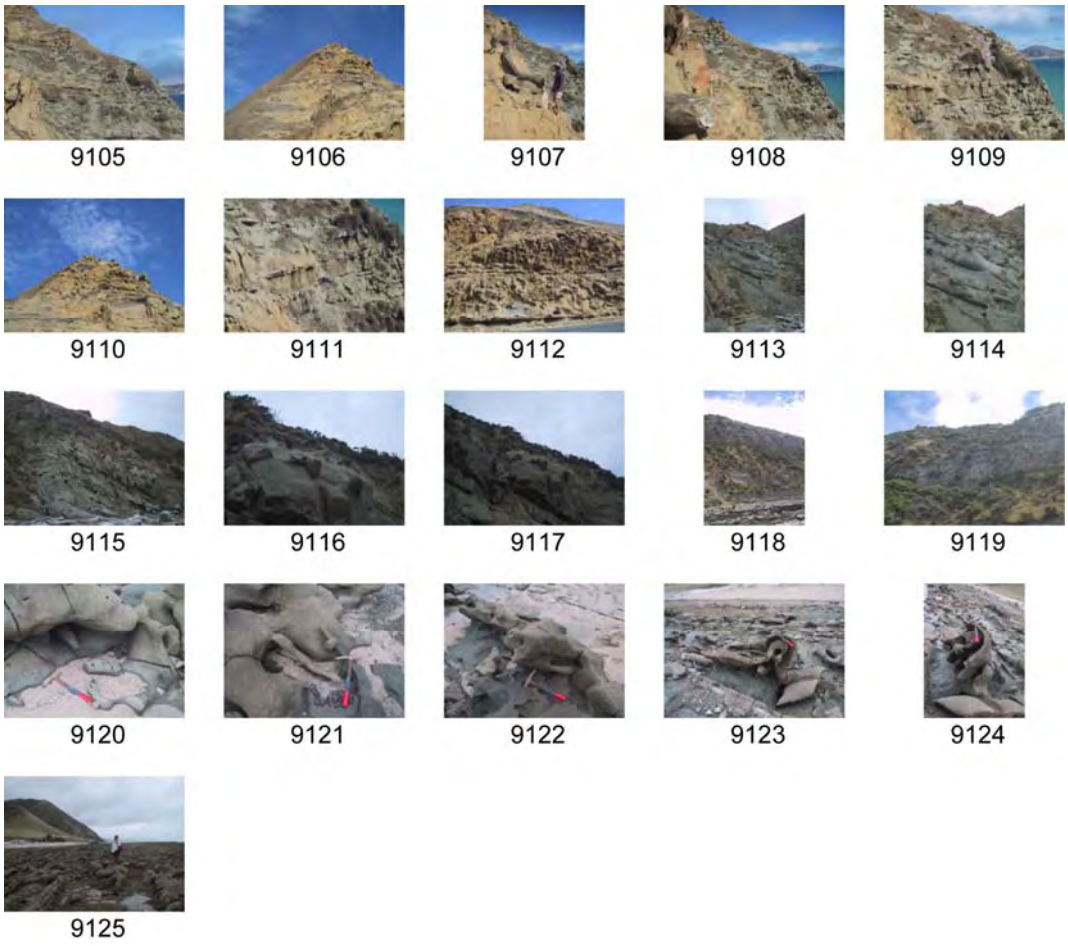

Figure A5.2 continued.

3. Samples

Tubular concretion samples are outlined in Table A5.3.

Table A5.3. Descriptions of additional samples

Waikato no.	Sample	Subsample	Location	Description
20080400	GAc1	GAc1-1	Gentle Annie	Pipe outer
20080401		GAc1-2	Gentle Annie	Pipe middle
20080402		GAc1-3	Gentle Annie	Pipe inner
20080403	GAc2	GAc3-1	Gentle Annie	Pipe outer
20080404		GAc3-2	Gentle Annie	Pipe middle
20080405		GAc3-3	Gentle Annie	Pipe inner
20080406	Dan1	Dan1-1	Waihau	Pipe outer
20080407		Dan1-2	Waihau	Pipe middle
20080408		Dan1-3	Waihau	Pipe inner (conduit fill)
20080409		PAK2-3	Pakare	Pipe middle
20080410	Mdi	Mdi-1	Mahia	Pipe middle
20080411		Mdi-2	Mahia	Pipe inner
20080412		Mdi-3	Mahia	Pipe outer
20080413	MBE1	MBE1-1	Mahia	Pipe outer
20080414		MBE1-1b	Mahia	Pipe outer (mirror side)
20080415		MBE1-2	Mahia	Pipe inner
20080416	MBE2	MBE2-1	Mahia	Pipe outer
20080417		MBE2-1b	Mahia	Pipe outer (mirror side)
20080418		MBE2-2	Mahia	Pipe inner
20080419	MBE3	MBE3-1	Mahia	Pipe outer
20080420		MBE3-2	Mahia	Pipe middle
20080421		MBE3-3	Mahia	Pipe inner
20080422	MBEA	MBEA-1	Mahia	Pipe outer
20080423		MBEA-2	Mahia	Pipe middle
20080424		MBEA-3b	Mahia	Pipe inner
20080425	MBc2	MBc2 1	Matheson's Bay	Pipe outer
20080426		MBc2 2	Matheson's Bay	Pipe middle
20080427		MBc2 3	Matheson's Bay	Pipe inner
20080428	MB Seep	MB_Seep	Matheson's Bay	Irregular carbonate deposite (seep carbonate?)
20080429	Kno#	Kno#-1	Modern samples	Dredged modern samples offshore New Zealand (fishing boats), location unknown.
20080430		Kno#-2	Modern samples	"
20080431		Kno#-3	Modern samples	"
20080432	KZ8314-2	KZ8314-1	Modern samples	"
20080433		KZ8314-2	Modern samples	"
20080434		KZ8314-3	Modern samples	"
20080435	T53P51g	T53P51g	Modern samples	"

4. XRD graphs

Appendix Section 4 contains XRD graphs that are characteristic of Rocky Knob tubular concretions and seafloor seep carbonates.

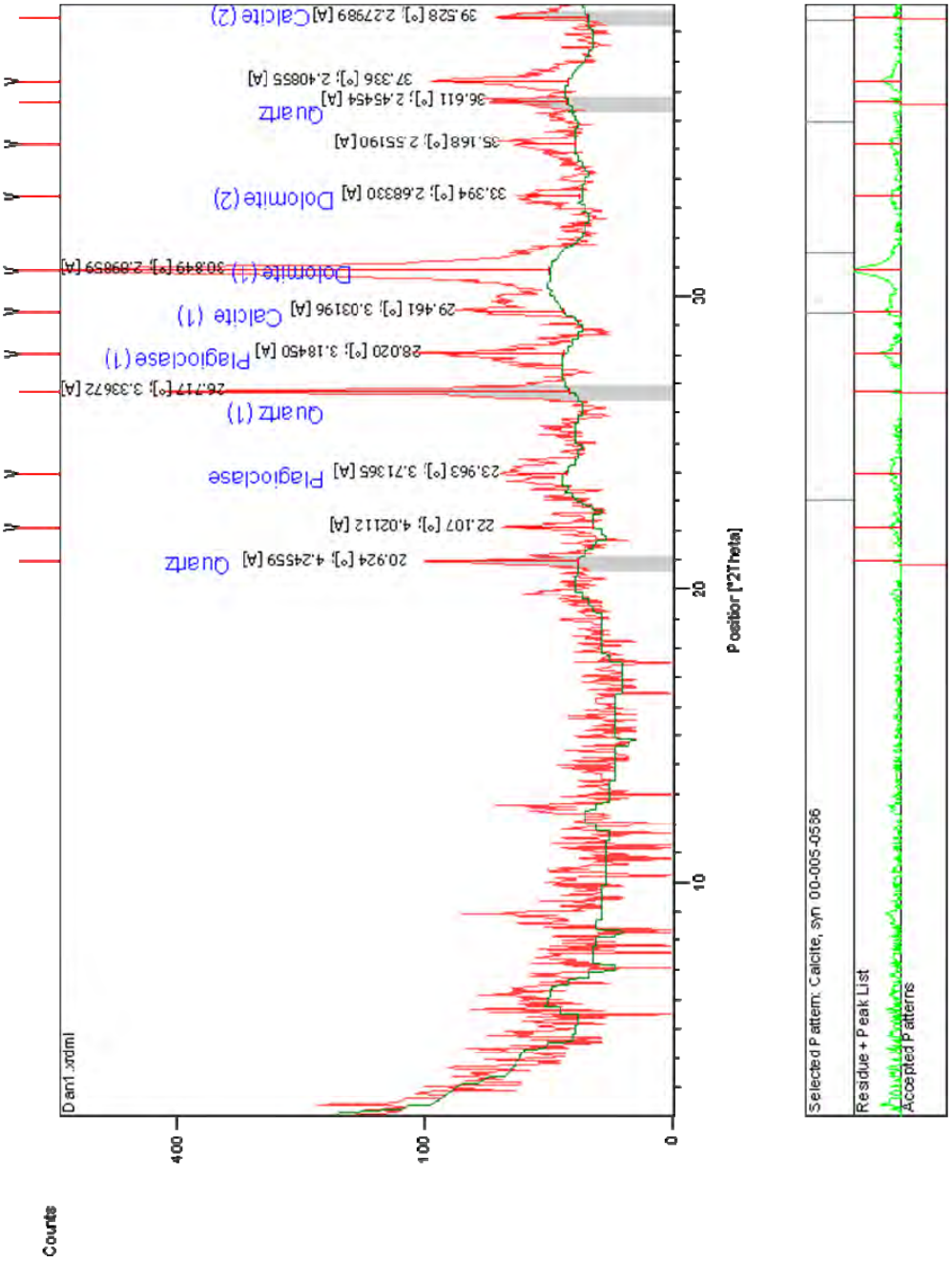
Counts
400
100
0
Dan1.xrdml
Quartz
20.924 [°]; 4.24559 [Å]
22.107 [°]; 4.02112 [Å]
Plagioclase
23.963 [°]; 3.71365 [Å]
Quartz (1)
26.717 [°]; 3.33672 [Å]
Plagioclase (1)
28.020 [°]; 3.18450 [Å]
Calcite (1)
29.461 [°]; 3.03196 [Å]
Dolomite (1)
30.849 [°]; 2.89859 [Å]
Dolomite (2)
33.394 [°]; 2.68330 [Å]
35.168 [°]; 2.55190 [Å]
Quartz
36.611 [°]; 2.45454 [Å]
37.336 [°]; 2.40855 [Å]
Calcite (2)
39.528 [°]; 2.27989 [Å]
10
20
30
Position [°2Theta]
Selected Pattern: Calcite, syn 00-005-0586
Residue + Peak List
Accepted Patterns

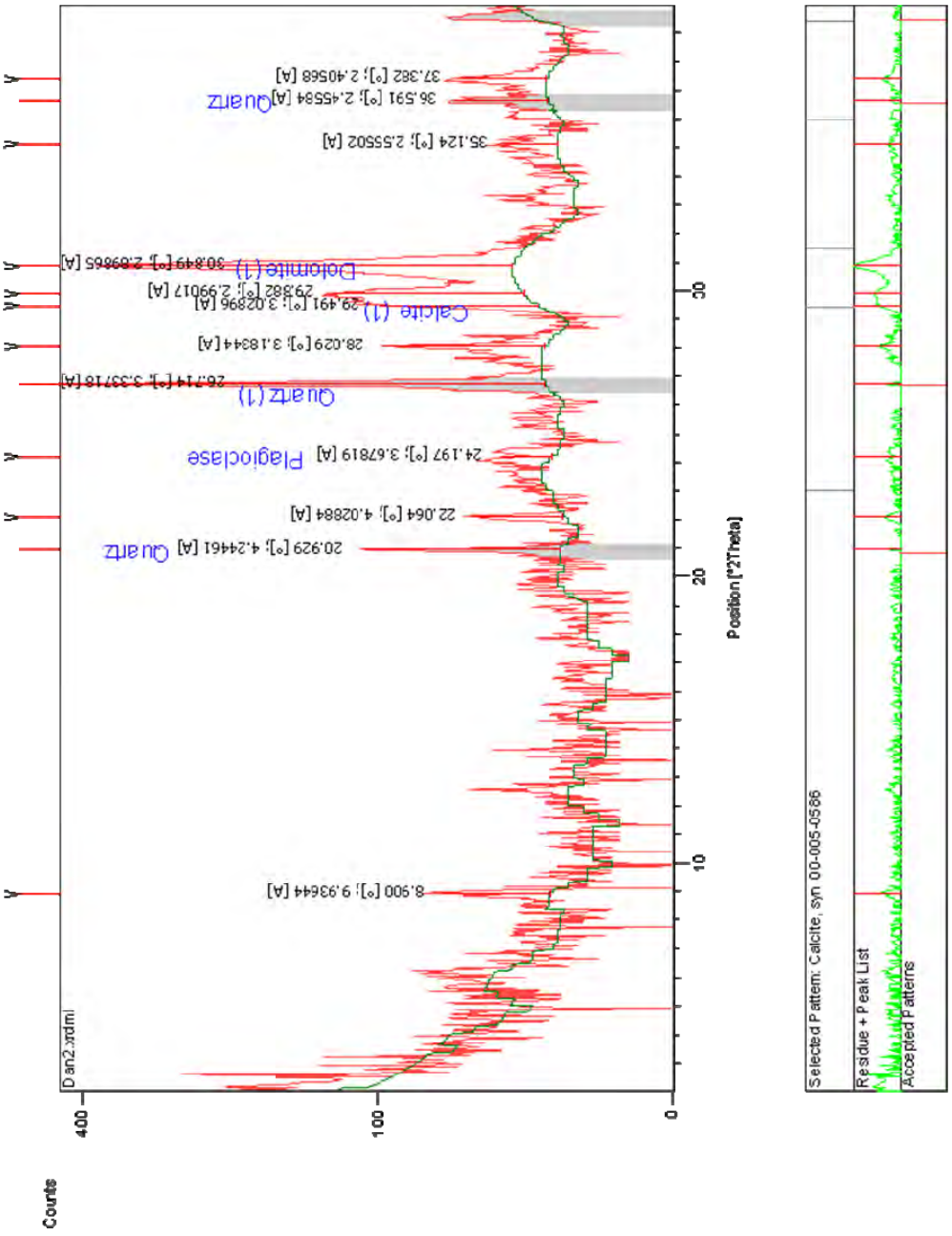
Counts
400
100
0
Dan2.xrdml
8.900 [°]; 9.93644 [A]
20.929 [°]; 4.24461 [A]
Quartz
22.064 [°]; 4.02884 [A]
24.197 [°]; 3.67819 [A]
Plagioclase
26.714 [°]; 3.33718 [A]
Quartz (1)
28.029 [°]; 3.18344 [A]
29.491 [°]; 3.02896 [A]
Calcite (1)
29.382 [°]; 2.99017 [A]
30.849 [°]; 2.89865 [A]
Dolomite (1)
35.124 [°]; 2.55502 [A]
36.591 [°]; 2.45584 [A]
Quartz
37.382 [°]; 2.40568 [A]
10
20
30
Position [°2Theta]
Selected Pattern: Calcite, syn 00-005-0586
Residue + Peak List
Accepted Patterns

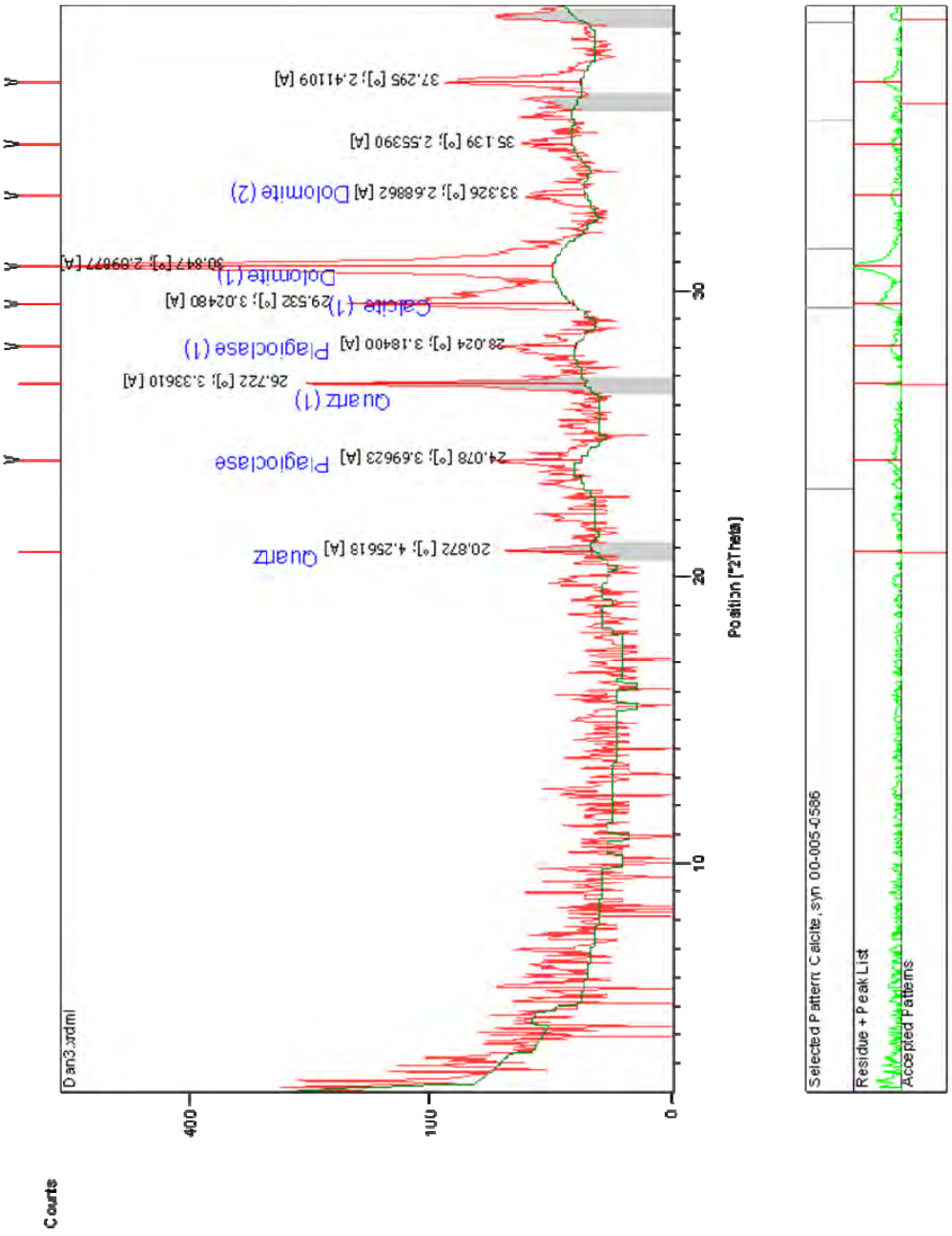
Counts
400
100
0
Dan3.xrdml
10
20
30
Position [°2Theta]
20.872 [°]; 4.25618 [A]
Quartz
24.078 [°]; 3.69623 [A]
Plagioclase
26.722 [°]; 3.33610 [A]
Quartz (1)
28.024 [°]; 3.18400 [A]
Plagioclase (1)
29.532 [°]; 3.02480 [A]
Calcite (1)
30.847 [°]; 2.89877 [A]
Dolomite (1)
33.326 [°]; 2.68862 [A]
Dolomite (2)
35.139 [°]; 2.55390 [A]
37.295 [°]; 2.41109 [A]
Selected Pattern: Calcite, syn 00-005-0586
Residue + Peak List
Accepted Patterns

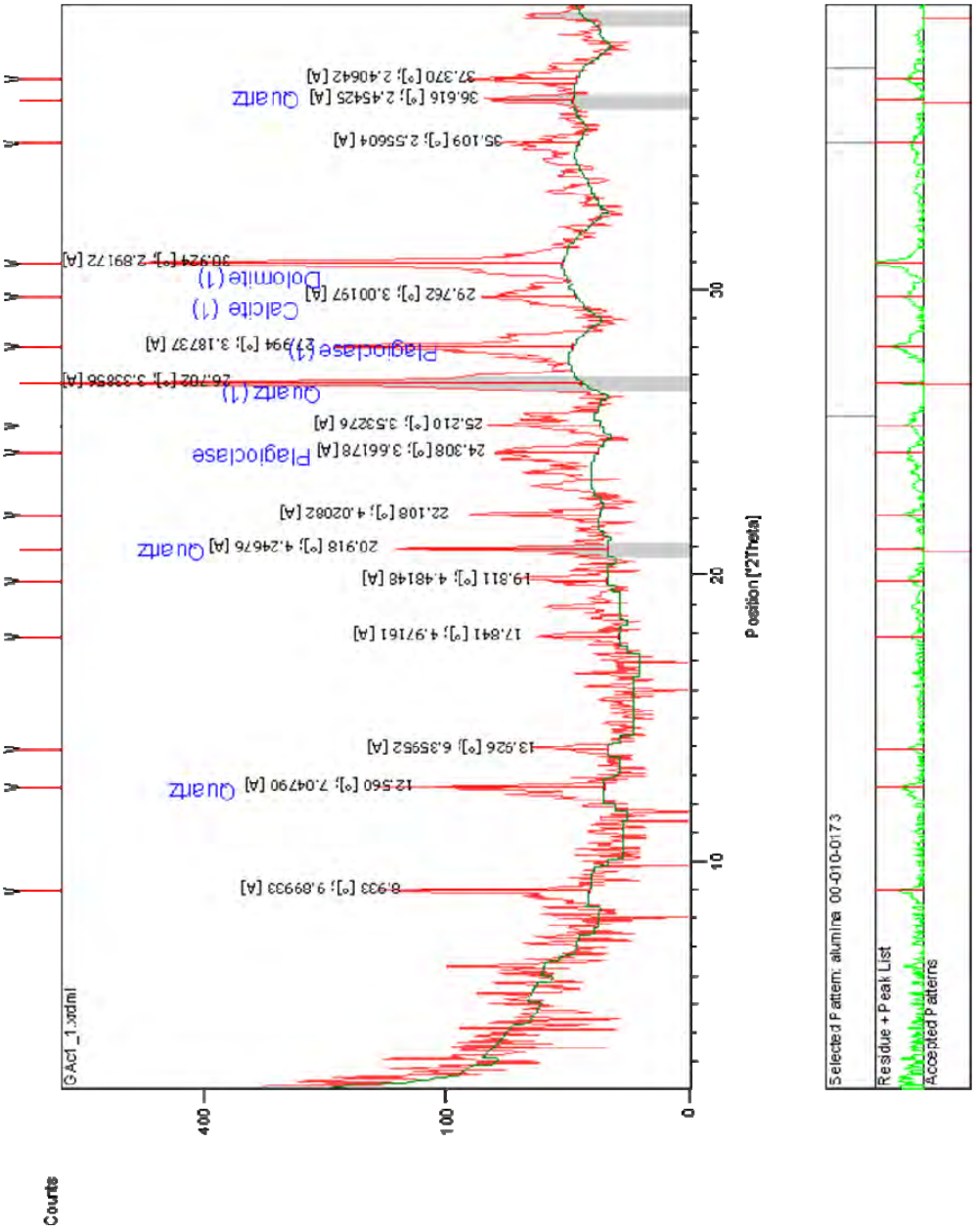
Counts
400
100
0
GAct1_1.xrdml
8.933 [°]; 9.89933 [A]
12.560 [°]; 7.04790 [A]
Quartz
13.926 [°]; 6.35952 [A]
17.841 [°]; 4.97161 [A]
19.311 [°]; 4.48148 [A]
20.918 [°]; 4.24676 [A]
Quartz
22.108 [°]; 4.02082 [A]
24.308 [°]; 3.66178 [A]
Plagioclase
25.210 [°]; 3.53276 [A]
26.702 [°]; 3.33856 [A]
Quartz (1)
27.994 [°]; 3.18737 [A]
Plagioclase (1)
29.762 [°]; 3.00197 [A]
Calcite (1)
Dolomite (1)
30.924 [°]; 2.89172 [A]
35.109 [°]; 2.55604 [A]
36.616 [°]; 2.45425 [A]
Quartz
37.370 [°]; 2.40642 [A]
10
20
30
Position [°2Theta]
Selected Pattern: alumina 00-010-0173
Residue + Peak List
Accepted Patterns

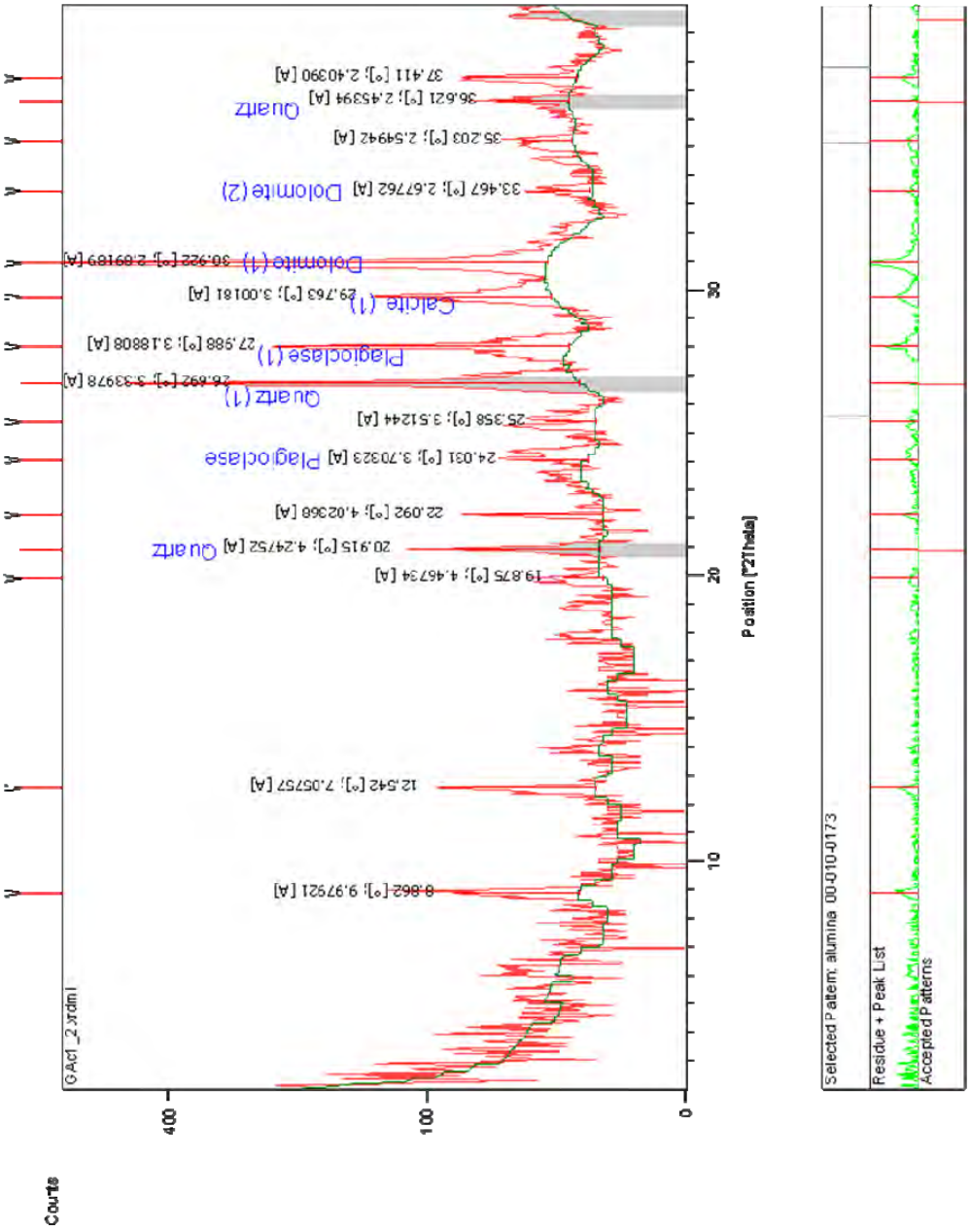
Counts
400
100
0
GAc1_2.xrdml
8.862 [°]; 9.97921 [A]
12.542 [°]; 7.05757 [A]
10
19.875 [°]; 4.46734 [A]
20.915 [°]; 4.24752 [A]
Quartz
22.092 [°]; 4.02368 [A]
24.031 [°]; 3.70323 [A]
Plagioclase
25.358 [°]; 3.51244 [A]
20
Position [°2Theta]
26.692 [°]; 3.33978 [A]
Quartz (1)
27.588 [°]; 3.18808 [A]
Plagioclase (1)
29.763 [°]; 3.00181 [A]
Calcite (1)
30.922 [°]; 2.89189 [A]
Dolomite (1)
33.467 [°]; 2.67762 [A]
Dolomite (2)
35.203 [°]; 2.54942 [A]
36.621 [°]; 2.45394 [A]
Quartz
37.411 [°]; 2.40390 [A]
30
Selected Pattern: alumina 00-010-0173
Residue + Peak List
Accepted Patterns

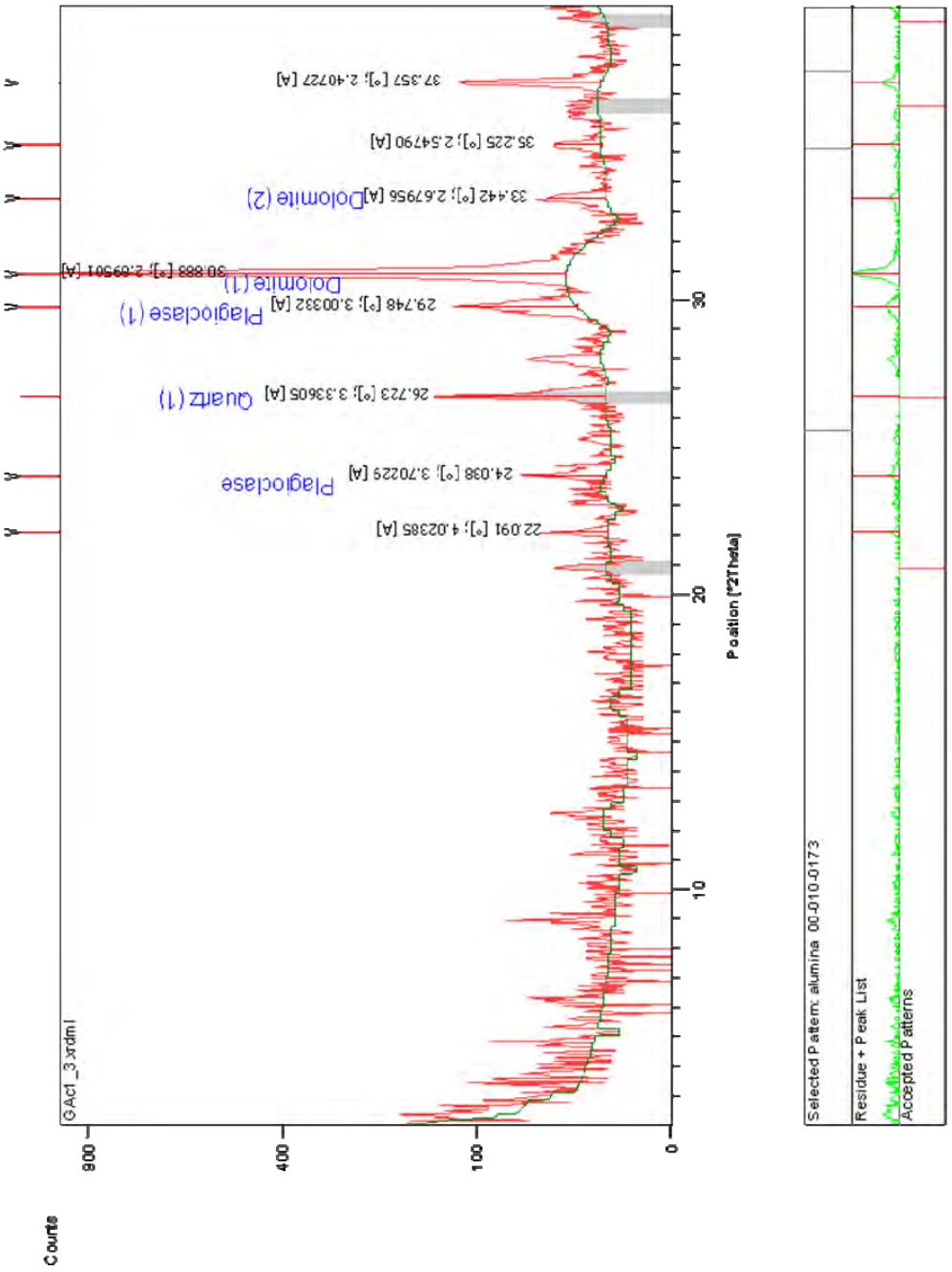
Counts
900
400
100
0
GAc1_3.xrdml
10
20
30
Position [°2Theta]
22.091 [°]; 4.02385 [A]
24.038 [°]; 3.70229 [A]
Plagioclase
26.723 [°]; 3.3605 [A]
Quartz (1)
29.748 [°]; 3.00332 [A]
Plagioclase (1)
30.888 [°]; 2.89501 [A]
Dolomite (1)
33.442 [°]; 2.67956 [A]
Dolomite (2)
35.225 [°]; 2.54790 [A]
37.357 [°]; 2.40727 [A]
Selected Pattern: alumina 00-010-0173
Residue + Peak List
Accepted Patterns

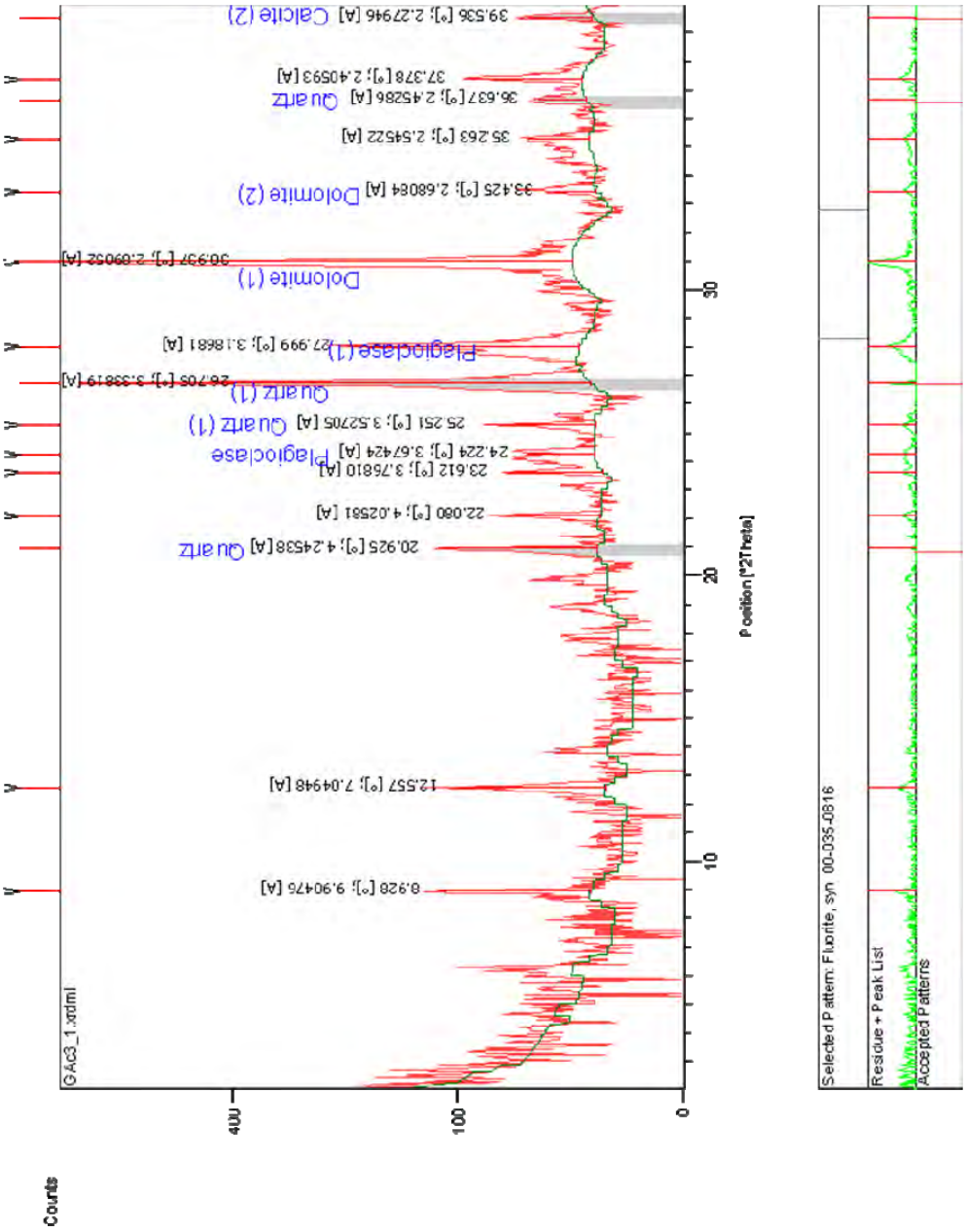
Counts
400
100
0
GAC3_1.xrdml
8.928 [°]; 9.90476 [A]
12.557 [°]; 7.04948 [A]
20.925 [°]; 4.24538 [A] Quartz
22.080 [°]; 4.02581 [A]
23.612 [°]; 3.76810 [A]
24.224 [°]; 3.67424 [A] Plagioclase
25.251 [°]; 3.52705 [A] Quartz (1)
26.705 [°]; 3.33819 [A] Quartz (1)
27.999 [°]; 3.18681 [A] Plagioclase (1)
30.937 [°]; 2.89052 [A] Dolomite (1)
33.425 [°]; 2.68084 [A] Dolomite (2)
35.263 [°]; 2.54522 [A]
36.637 [°]; 2.45286 [A] Quartz
37.378 [°]; 2.40593 [A]
39.536 [°]; 2.27946 [A] Calcite (2)
10
20
30
Position [°2Theta]
Selected Pattern: Fluorite, syn 00-035-0816
Residue + Peak List
Accepted Patterns

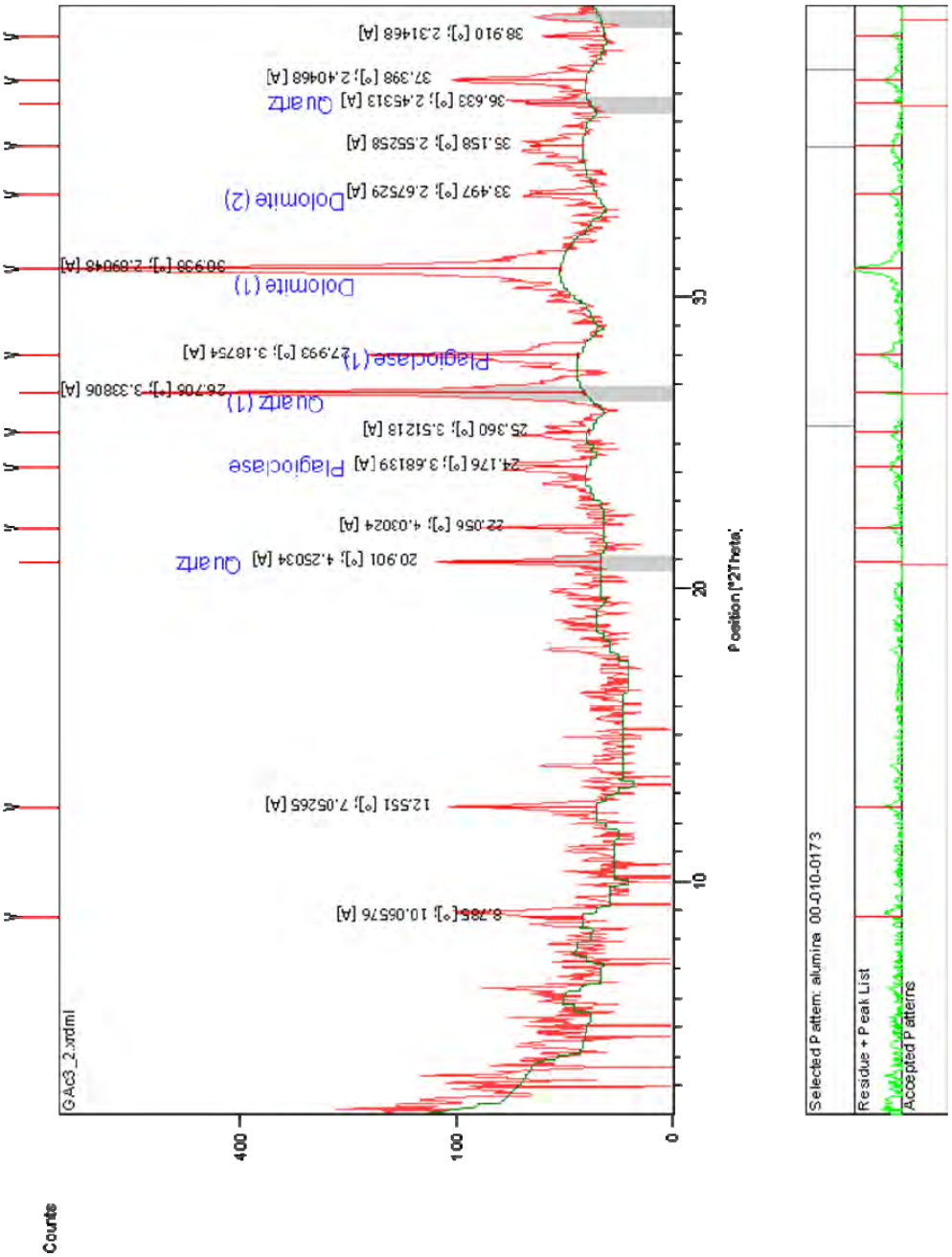
GAc3_2.xrdml
Counts
Position [°2Theta]
8.785 [°]; 10.05576 [A]
12.551 [°]; 7.05265 [A]
20.901 [°]; 4.25034 [A]
Quartz
22.056 [°]; 4.03024 [A]
24.176 [°]; 3.68139 [A]
Plagioclase
25.360 [°]; 3.51218 [A]
26.705 [°]; 3.33806 [A]
Quartz (1)
27.993 [°]; 3.18754 [A]
Plagioclase (1)
30.938 [°]; 2.89048 [A]
Dolomite (1)
33.497 [°]; 2.67529 [A]
Dolomite (2)
35.158 [°]; 2.55258 [A]
36.633 [°]; 2.45313 [A]
Quartz
37.398 [°]; 2.40468 [A]
38.910 [°]; 2.31468 [A]
Selected Pattern: alumina 00-010-0173
Residue = Peak List
Accepted Patterns

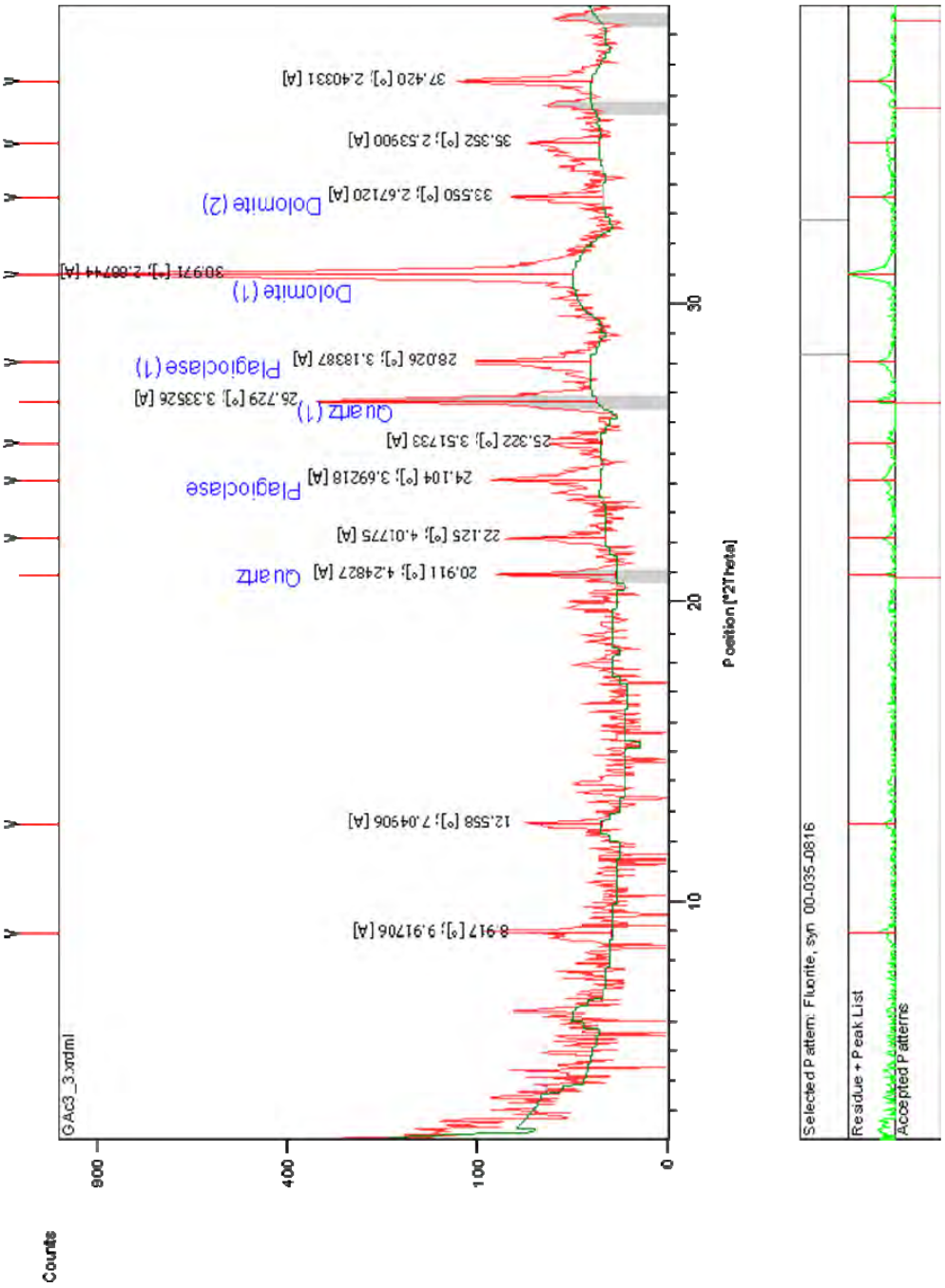
Counts
900
400
100
0
GAc3_3.xrdml
8.917 [°]; 9.91706 [Å]
12.558 [°]; 7.04906 [Å]
20.911 [°]; 4.24827 [Å]
Quartz
22.125 [°]; 4.01775 [Å]
24.104 [°]; 3.69218 [Å]
Plagioclase
25.322 [°]; 3.51733 [Å]
26.729 [°]; 3.33526 [Å]
Quartz (1)
28.026 [°]; 3.18387 [Å]
Plagioclase (1)
30.971 [°]; 2.88744 [Å]
Dolomite (1)
33.550 [°]; 2.67120 [Å]
Dolomite (2)
35.352 [°]; 2.53900 [Å]
37.420 [°]; 2.40331 [Å]
10
20
30
Position [°2Theta]
Selected Pattern: Fluorite, syn 00-035-0816
Residue + Peak List
Accepted Patterns

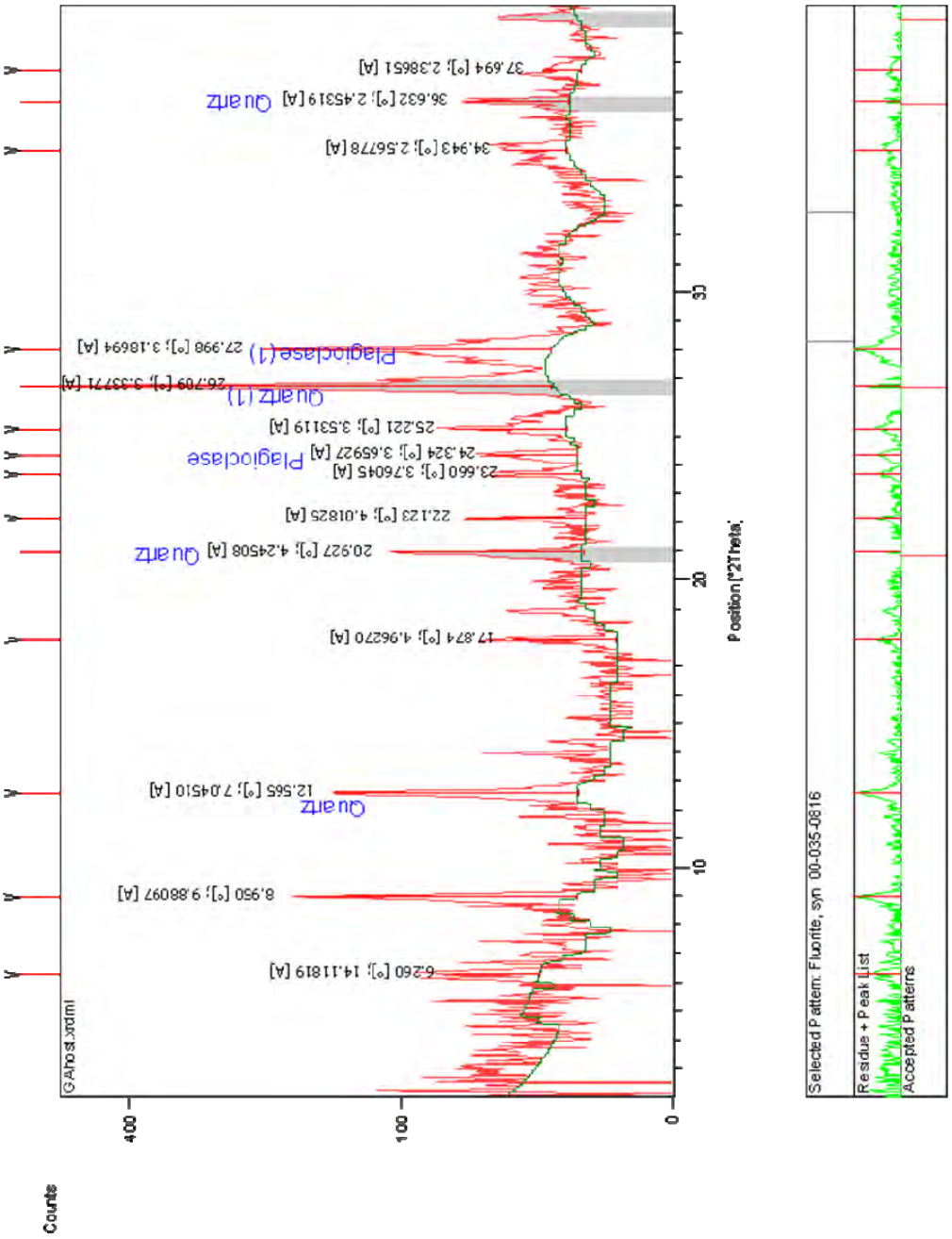
Counts
400
100
0
GAhost.ydml
6.260 [°]; 14.11819 [A]
8.950 [°]; 9.88097 [A]
12.565 [°]; 7.04510 [A]
Quartz
17.874 [°]; 4.96270 [A]
20.927 [°]; 4.24508 [A]
Quartz
22.123 [°]; 4.01825 [A]
23.660 [°]; 3.76045 [A]
24.324 [°]; 3.65927 [A]
Plagioclase
25.221 [°]; 3.53119 [A]
26.709 [°]; 3.33771 [A]
Quartz (1)
27.998 [°]; 3.18694 [A]
Plagioclase(1)
34.943 [°]; 2.56778 [A]
36.632 [°]; 2.45319 [A]
Quartz
37.694 [°]; 2.38651 [A]
10
20
30
Position [°2Theta]
Selected Pattern: Fluorite, syn 00-035-0616
Residue + Peak List
Accepted Patterns

Counts
900
400
100
0
10
20
30
Position [°2Theta]
k:\norium1.xrdml
Calcite (2)
39.532 [°]; 2.27966 [Å]
Quartz
36.131 [°]; 2.48609 [Å]
Calcite (1)
29.518 [°]; 3.02624 [Å]
Quartz (1)
26.641 [°]; 3.34612 [Å]
Calcite (3)
23.131 [°]; 3.84533 [Å]
Selected Pattern: Quartz, syn 00-046-1045
Residue + Peak List
Accepted Patterns

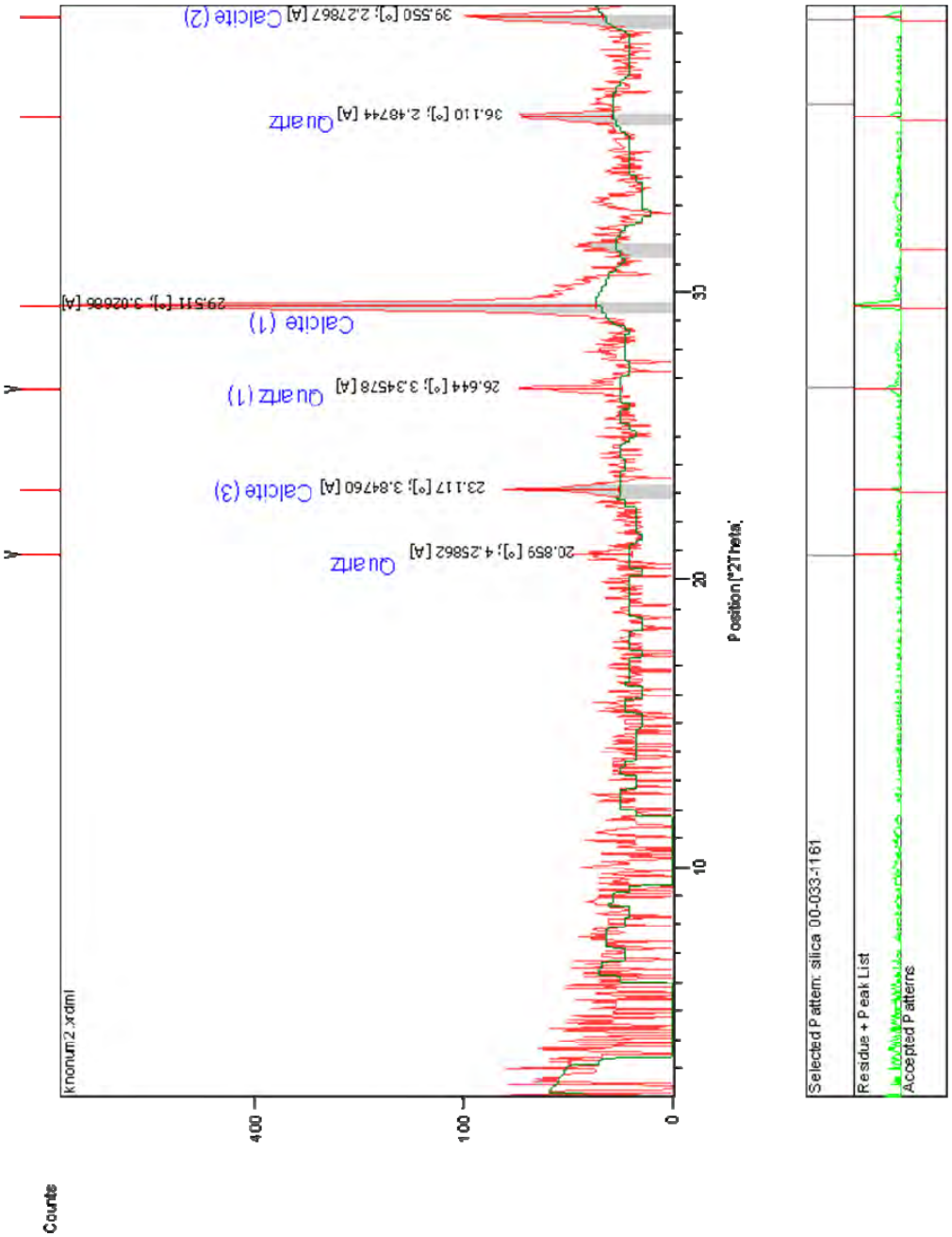
Counts
400
100
0
knonum2.xrdml
Quartz
20.859 [°]; 4.25862 [Å]
Calcite (3)
23.117 [°]; 3.84760 [Å]
Quartz (1)
26.644 [°]; 3.34578 [Å]
Calcite (1)
29.511 [°]; 3.02666 [Å]
Quartz
36.110 [°]; 2.48744 [Å]
Calcite (2)
39.550 [°]; 2.27867 [Å]
10
20
30
Position [°2Theta]
Selected Pattern: silica 00-033-1161
Residue + Peak List
Accepted Patterns

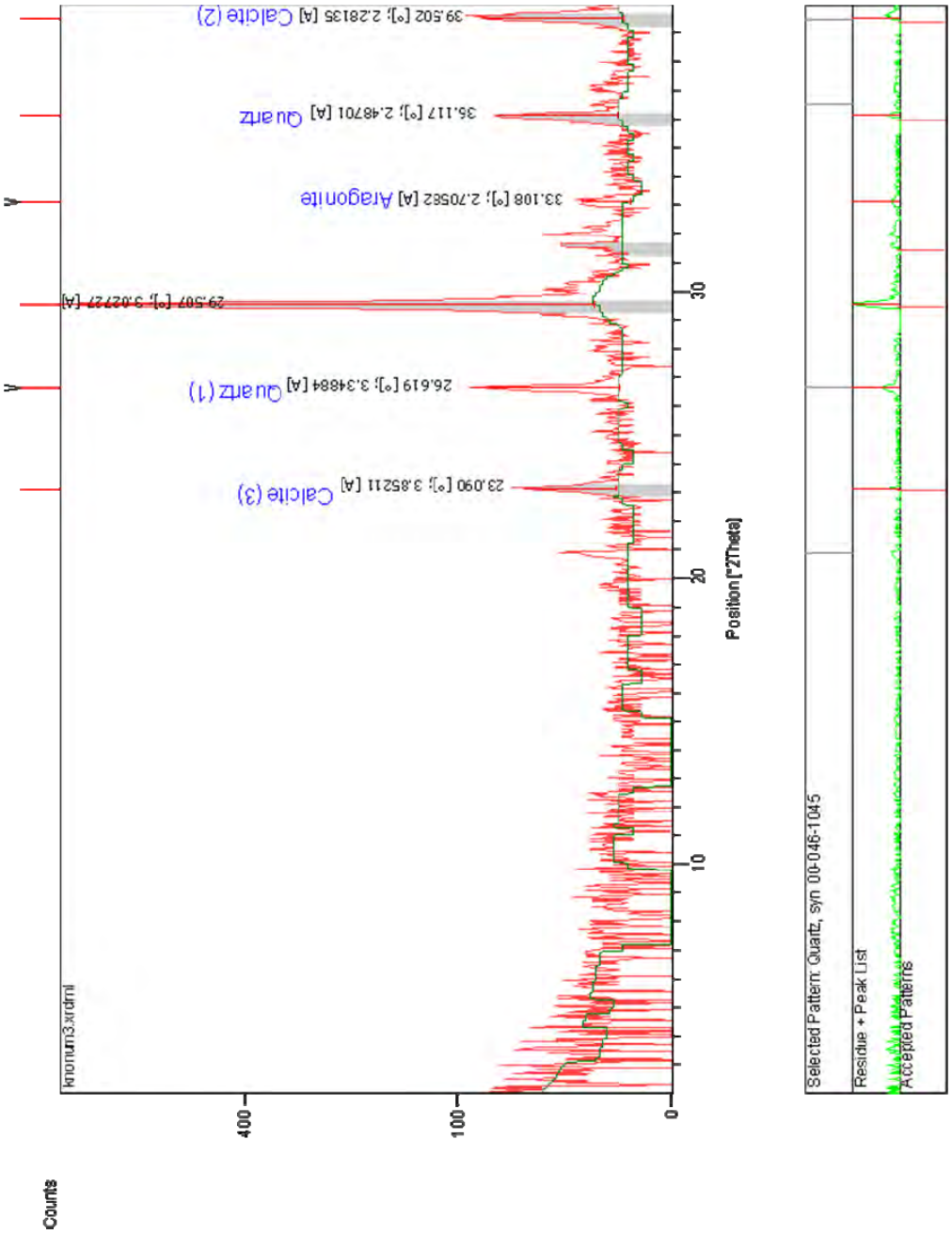
Counts
400
100
0
10
20
30
Position [°2Theta]
knonum3.xrdml
Calcite (3)
23.090 [°]; 3.85211 [Å]
Quartz (1)
26.619 [°]; 3.34884 [Å]
29.507 [°]; 3.02727 [Å]
Aragonite
33.108 [°]; 2.70562 [Å]
Quartz
36.117 [°]; 2.48701 [Å]
Calcite (2)
39.502 [°]; 2.28135 [Å]
Selected Pattern: Quartz, syn 00-046-1045
Residue + Peak List
Accepted Patterns

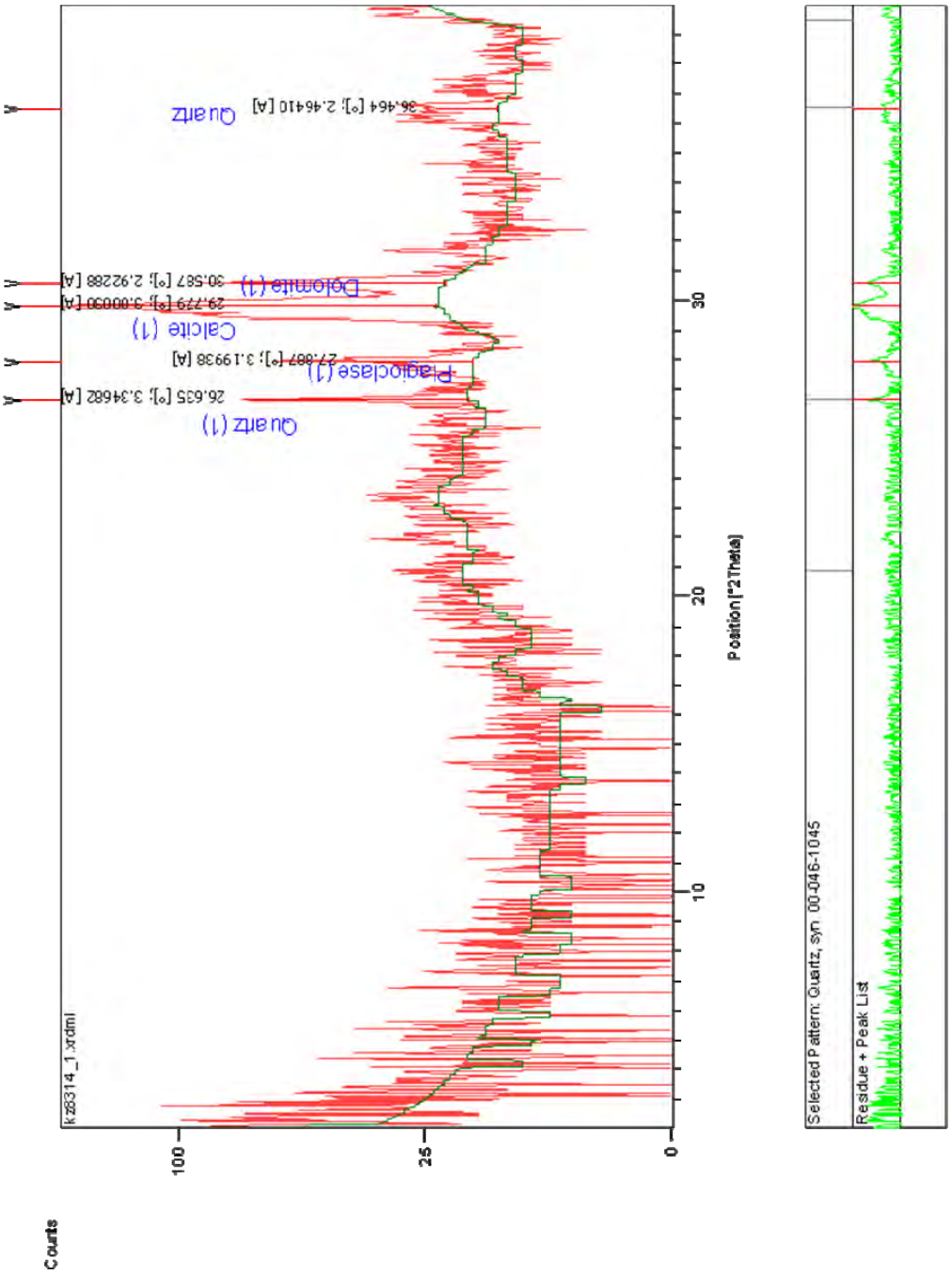
Counts
100
25
0
10
20
30
Position [°2Theta]
kz8314_1.xrdml
Quartz (1)
26.635 [°]; 3.34682 [A]
Plagioclase (1)
27.687 [°]; 3.19938 [A]
Calcite (1)
29.279 [°]; 3.05030 [A]
Dolomite (1)
30.587 [°]; 2.92288 [A]
Quartz
36.464 [°]; 2.46410 [A]
Selected Pattern: Quartz, syn 00-046-1045
Residue + Peak List

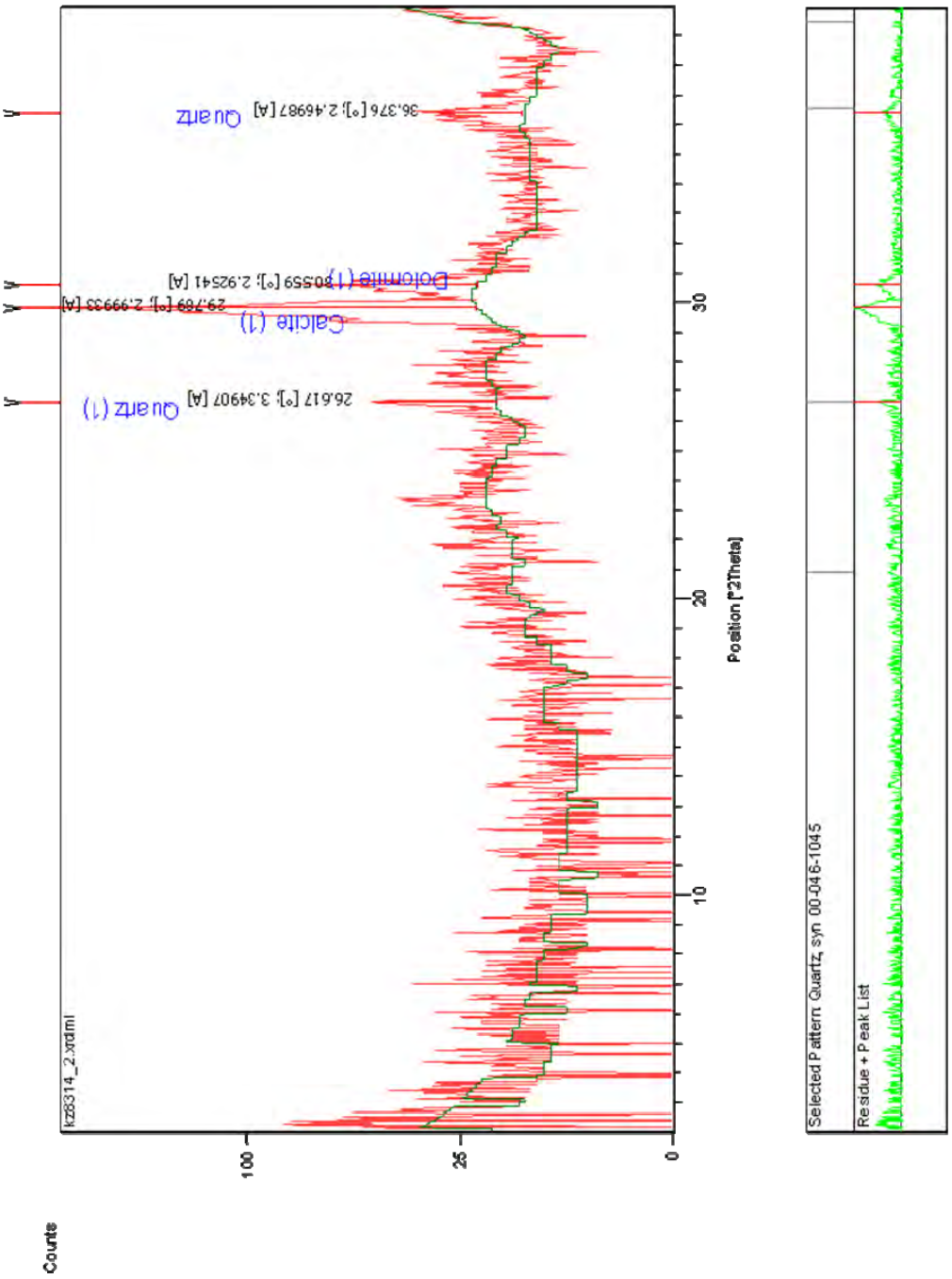
Counts
100
25
0
10
20
30
Position [°2Theta]
kz8314_2.xrdml
Quartz
36.376 [°]; 2.46987 [A]
Dolomite (1)
30.559 [°]; 2.92541 [A]
29.769 [°]; 2.99933 [A]
Calcite (1)
Quartz (1)
26.617 [°]; 3.34907 [A]
Selected Pattern: Quartz, syn 00-046-1045
Residue + Peak List

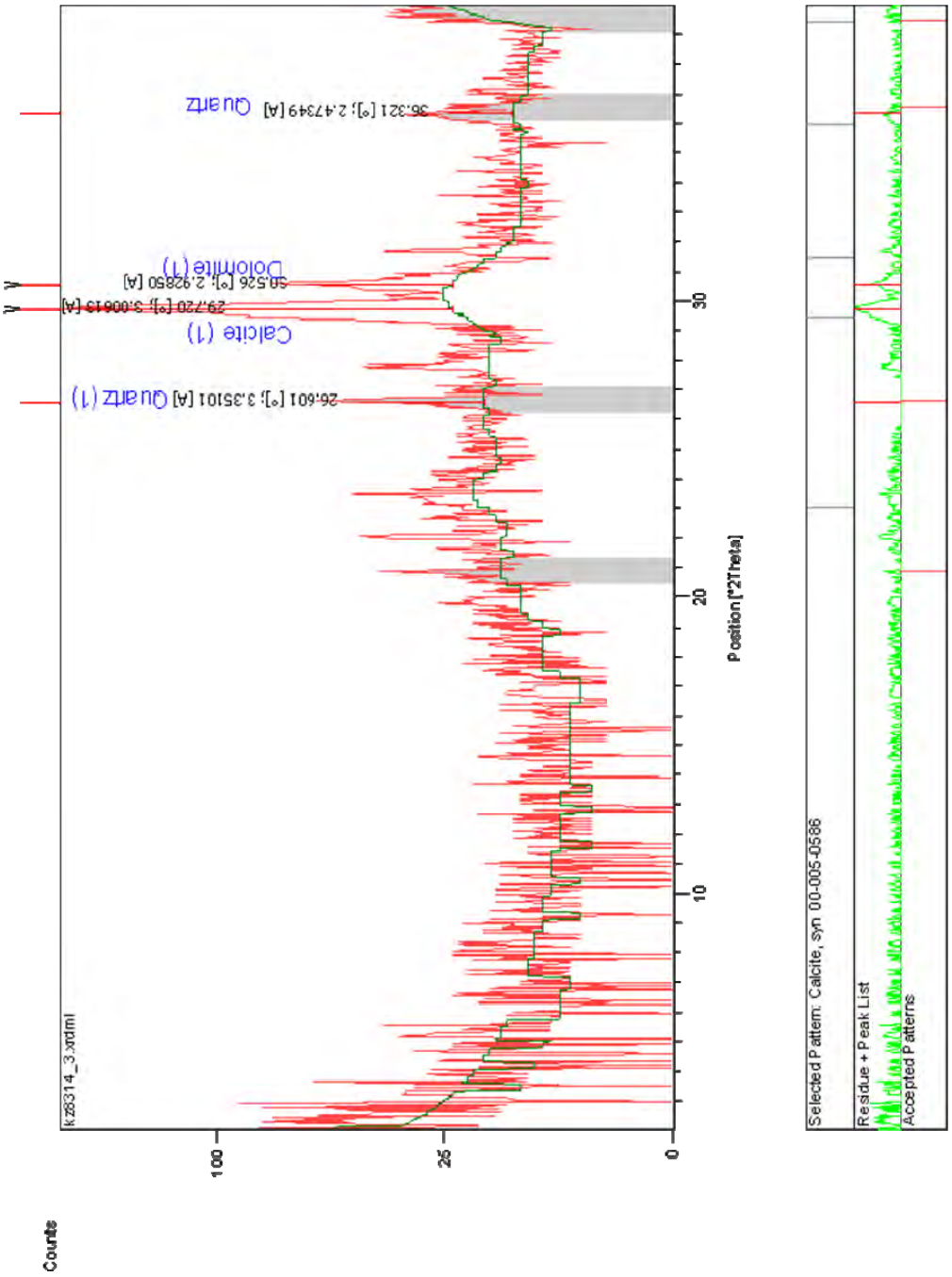
Counts
100
25
0
10
20
30
Position [°2Theta]
kz8314_3.xrdml
Quartz
36.321 [°]; 2.47349 [A]
Dolomite (1)
50.526 [°]; 2.92850 [A]
29.720 [°]; 3.00613 [A]
Calcite (1)
Quartz (1)
26.601 [°]; 3.35101 [A]
Selected Pattern: Calcite, syn 00-005-0586
Residue + Peak List
Accepted Patterns

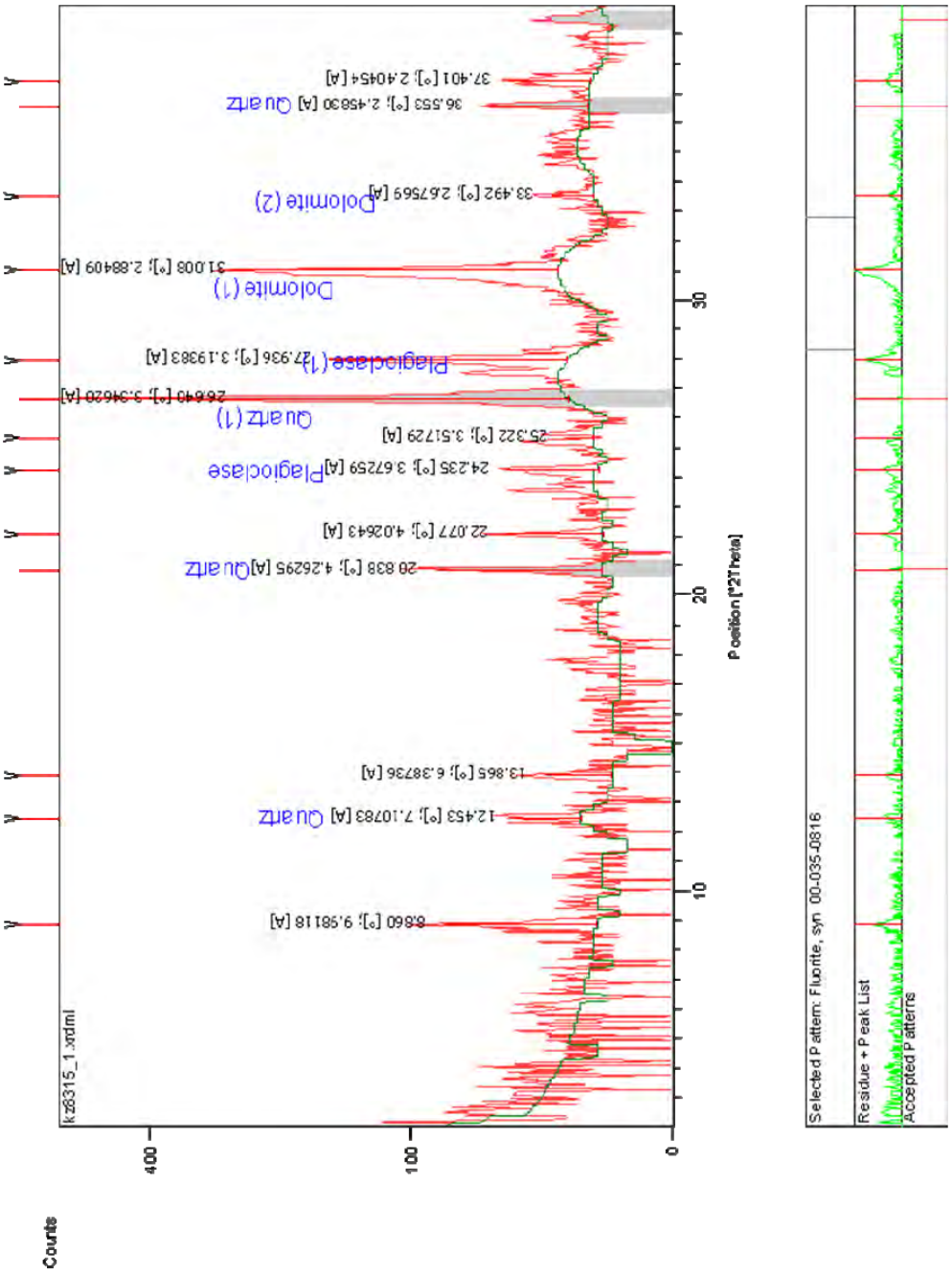
Counts
400
100
0
kz6315_1.xrdml
8.860 [°]; 9.98118 [A]
12.453 [°]; 7.10783 [A] Quartz
13.865 [°]; 6.38736 [A]
20.838 [°]; 4.26295 [A] Quartz
22.077 [°]; 4.02643 [A]
24.235 [°]; 3.67259 [A] Plagioclase
25.322 [°]; 3.51729 [A]
26.640 [°]; 3.34620 [A] Quartz (1)
27.936 [°]; 3.19383 [A] Plagioclase (1)
31.008 [°]; 2.88409 [A] Dolomite (1)
33.492 [°]; 2.67569 [A] Dolomite (2)
36.553 [°]; 2.45830 [A] Quartz
37.401 [°]; 2.40454 [A]
10
20
30
Position [°2Theta]
Selected Pattern: Fluorite, syn 00-035-0816
Residue + Peak List
Accepted Patterns

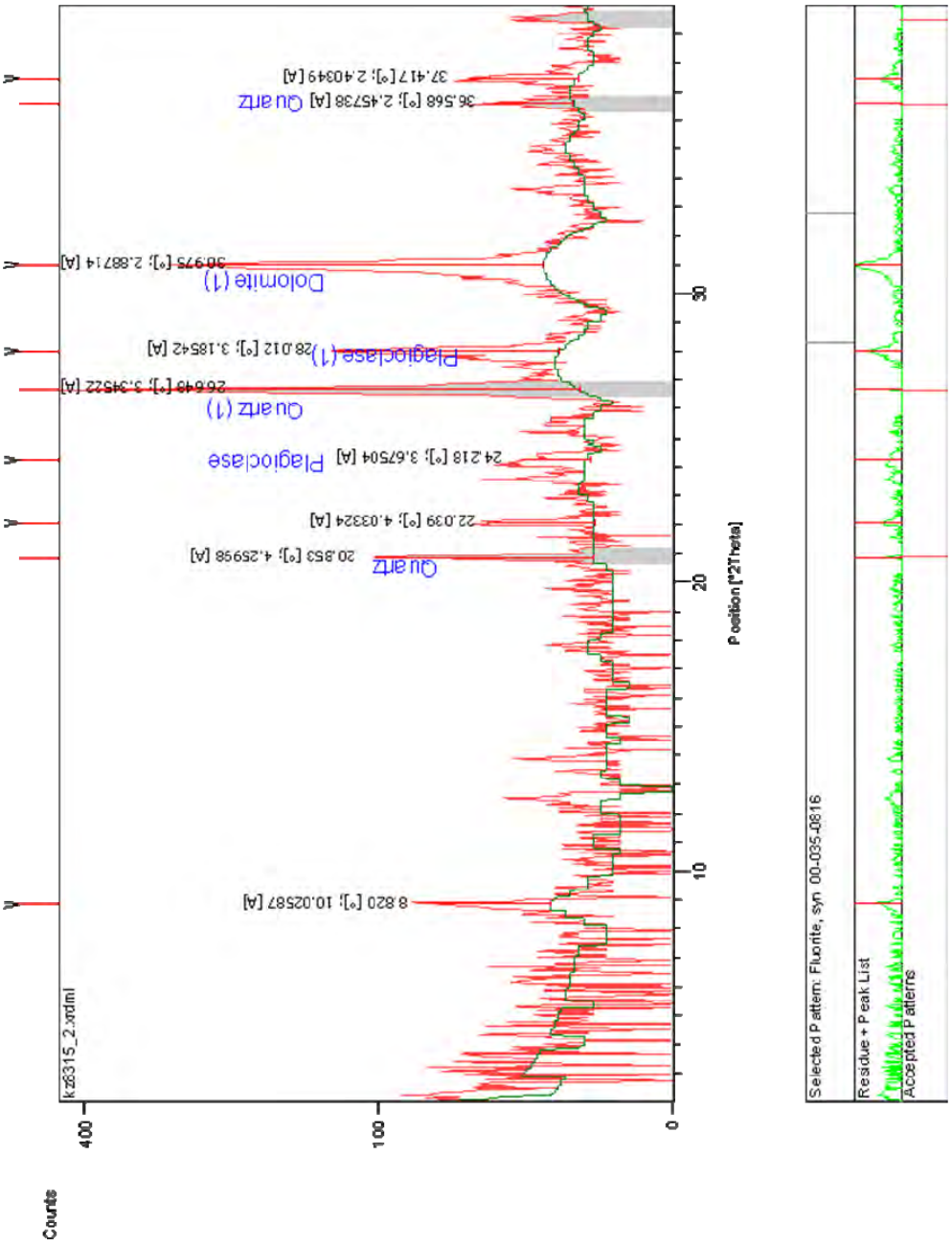
kz6315_2.xrdml
Counts
400
100
0
10
20
30
Position [°2Theta]
8.820 [°]; 10.02587 [A]
20.853 [°]; 4.25958 [A]
Qu artz
22.039 [°]; 4.03324 [A]
24.218 [°]; 3.67504 [A]
Plagioclase
26.649 [°]; 3.34522 [A]
Qu artz (1)
28.012 [°]; 3.18542 [A]
Plagioclase (1)
30.975 [°]; 2.88714 [A]
Dolomite (1)
36.568 [°]; 2.45738 [A]
Qu artz
37.417 [°]; 2.40349 [A]
Selected Pattern: Fluorite, syn 00-035-0816
Residue + Peak List
Accepted Patterns

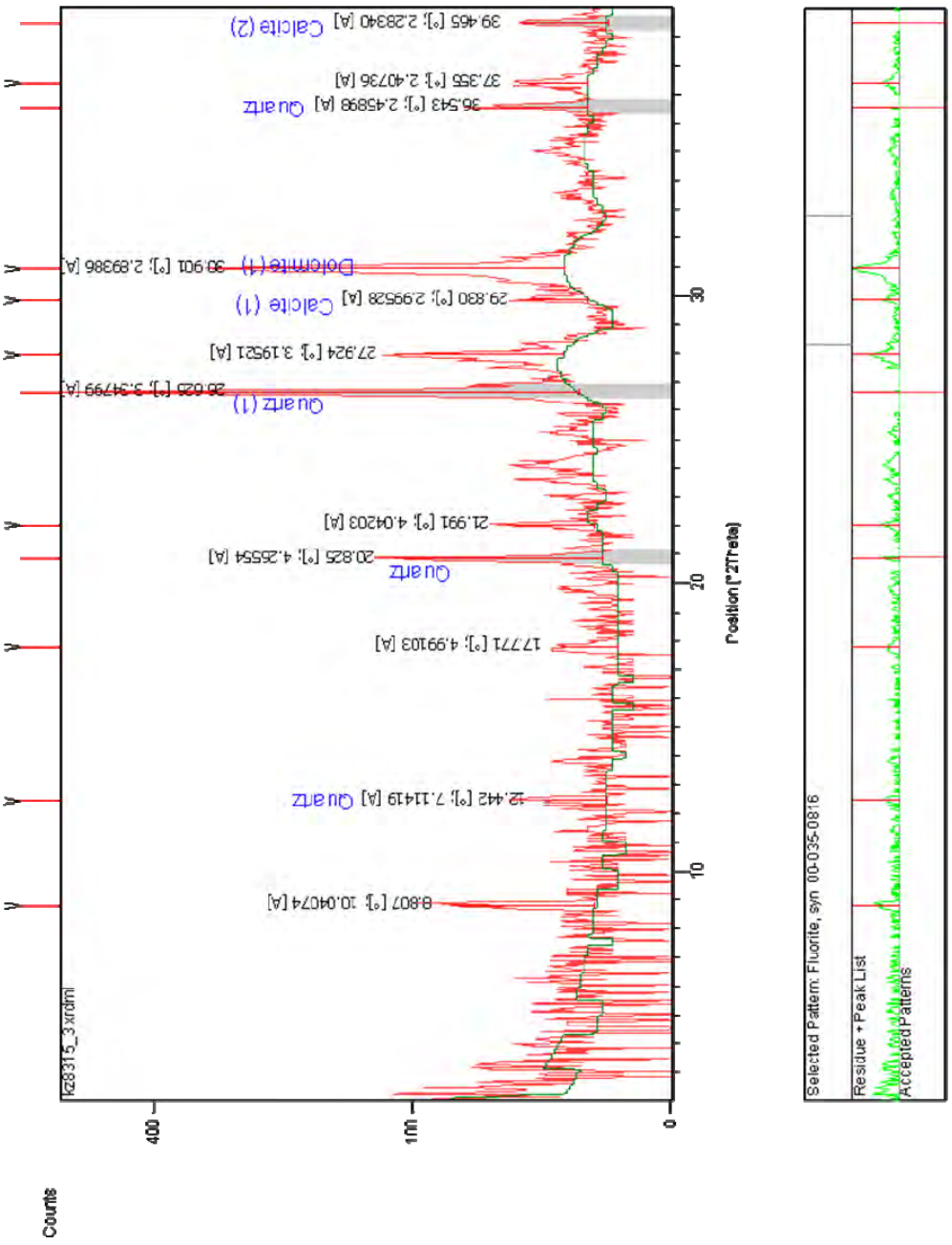
Counts
400
100
0
kz8315_3.xrdml
8.807 [°]; 10.04074 [A]
12.442 [°]; 7.11419 [A]
Quartz
17.771 [°]; 4.99103 [A]
20.825 [°]; 4.25554 [A]
Quartz
21.991 [°]; 4.04203 [A]
26.628 [°]; 3.34799 [A]
Quartz (1)
27.924 [°]; 3.19521 [A]
29.880 [°]; 2.99528 [A]
Calcite (1)
30.901 [°]; 2.89386 [A]
Dolomite (1)
36.543 [°]; 2.45898 [A]
Quartz
37.355 [°]; 2.40736 [A]
39.465 [°]; 2.28340 [A]
Calcite (2)
10
20
30
Position [°2Theta]
Selected Pattern: Fluorite, syn 00-035-0816
Residue + Peak List
Accepted Patterns

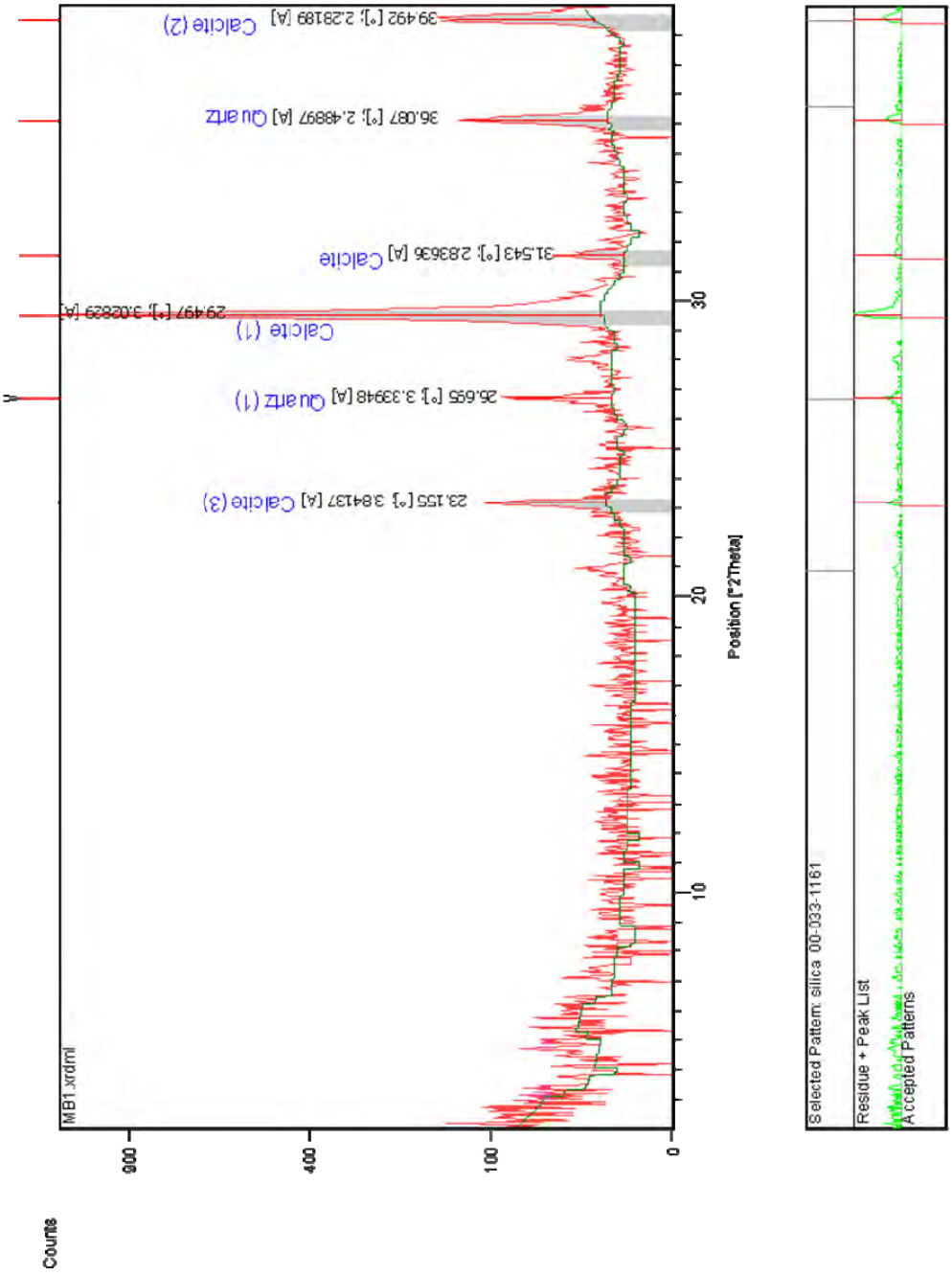
Counts
900
400
100
0
10
20
30
Position [°2Theta]
M-B1.xrdml
Calcite (2)
39.492 [°]; 2.28189 [Å]
Quartz
36.087 [°]; 2.48897 [Å]
Calcite
31.543 [°]; 2.83636 [Å]
Calcite (1)
29.497 [°]; 3.02829 [Å]
Quartz (1)
26.655 [°]; 3.33948 [Å]
Calcite (3)
23.155 [°]; 3.84137 [Å]
Selected Pattern: silica 00-033-1161
Residue + Peak List
Accepted Patterns

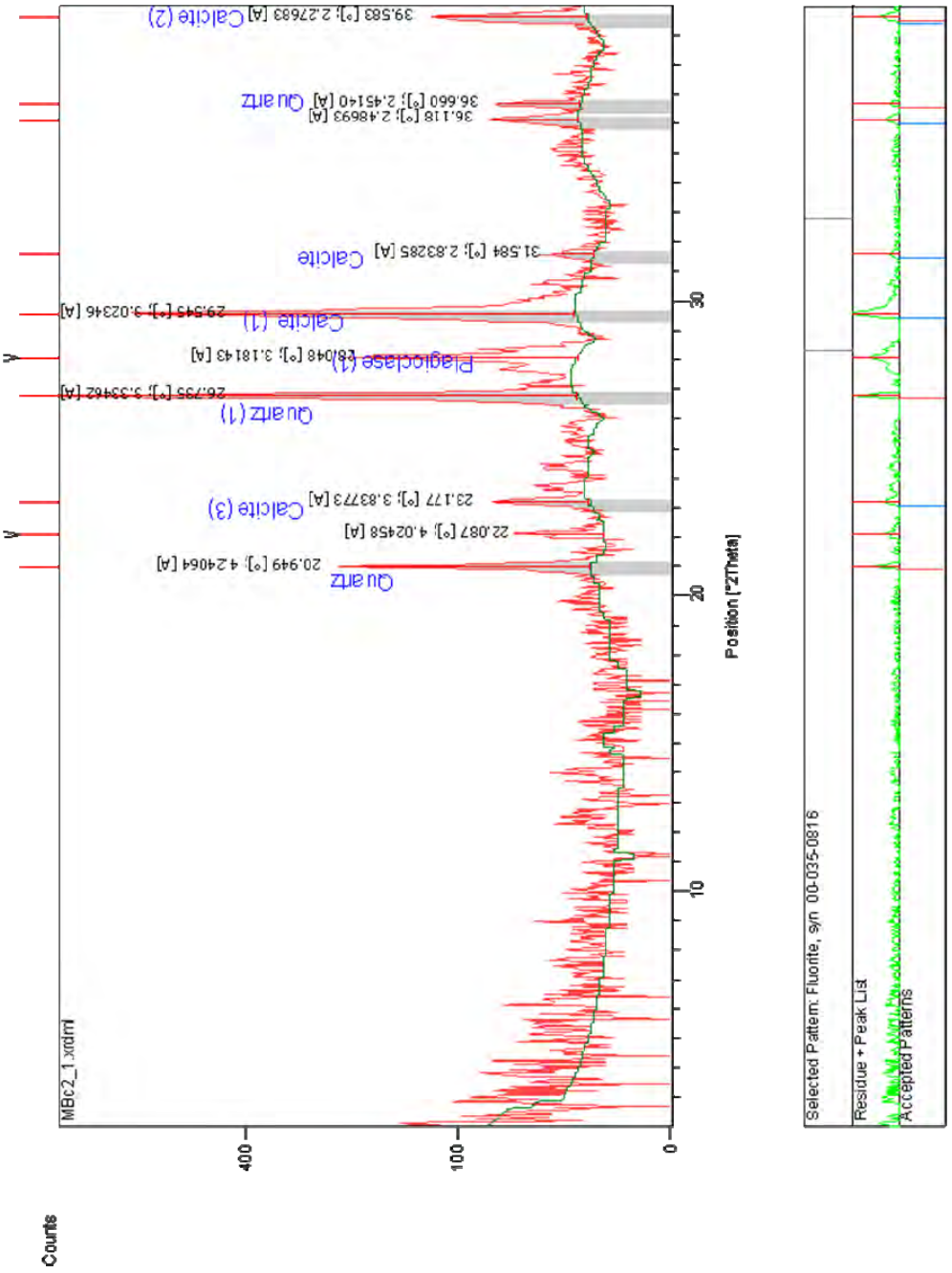
Counts
400
100
0
10
20
30
Position [°2Theta]
MBc2_1.xrdml
Quartz
20.949 [°]; 4.24064 [A]
22.087 [°]; 4.02458 [A]
Calcite (3)
23.177 [°]; 3.83773 [A]
Quartz (1)
26.735 [°]; 3.33462 [A]
Plagioclase (1)
28.048 [°]; 3.18143 [A]
Calcite (1)
29.343 [°]; 3.02346 [A]
Calcite
31.584 [°]; 2.83285 [A]
Quartz
36.118 [°]; 2.48693 [A]
36.660 [°]; 2.45140 [A]
Calcite (2)
39.583 [°]; 2.27683 [A]
Selected Pattern: Fluorite, syn 00-035-0816
Residue + Peak List
Accepted Patterns

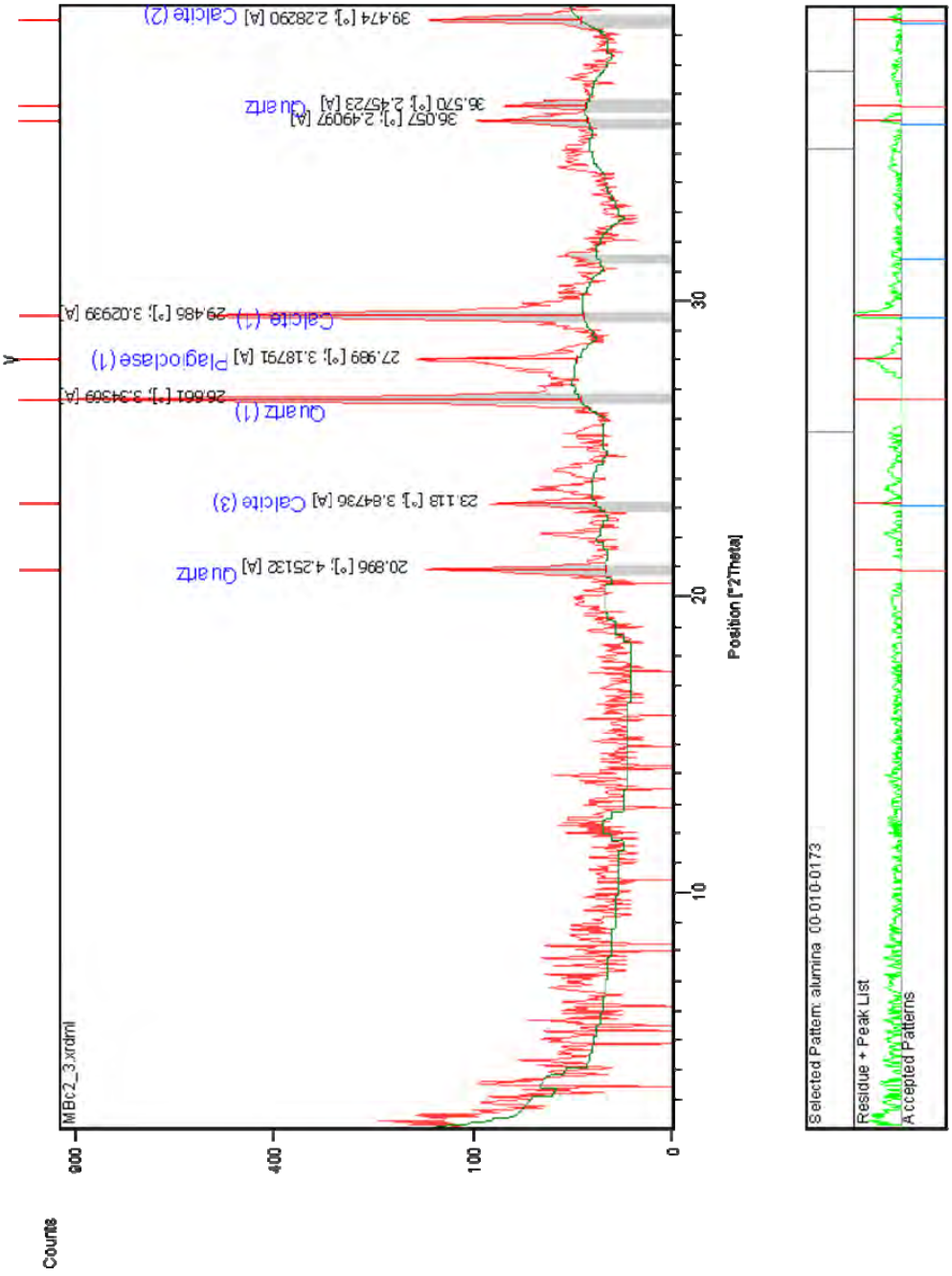
Counts
900
400
100
0
10
20
30
Position [°2Theta]
M:Bc2_3.xrdml
20.896 [°]; 4.25132 [Å] Quartz
23.118 [°]; 3.84736 [Å] Calcite (3)
26.661 [°]; 3.34369 [Å] Quartz (1)
27.989 [°]; 3.18791 [Å] Plagioclase (1)
29.485 [°]; 3.02939 [Å] Calcite (1)
36.057 [°]; 2.49097 [Å]
36.570 [°]; 2.45723 [Å] Quartz
39.474 [°]; 2.28290 [Å] Calcite (2)
Selected Pattern: alumina 00-010-0173
Residue + Peak List
Accepted Patterns

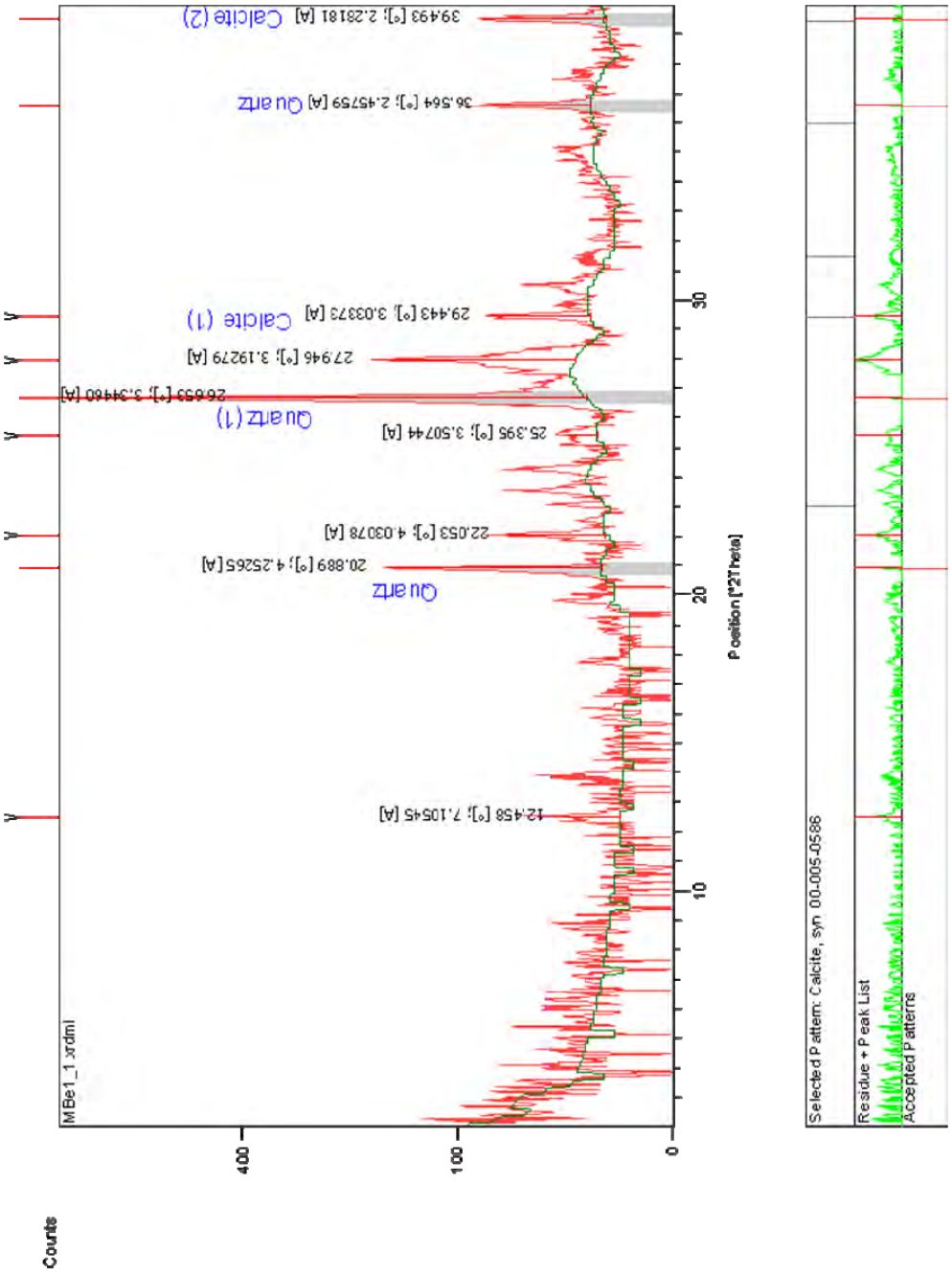
M:Be1_1.xrdml
Counts
Position [°2Theta]
Quartz
Quartz (1)
Calcite (1)
Quartz
Calcite (2)
20.889 [°]; 4.25265 [A]
22.053 [°]; 4.03078 [A]
25.395 [°]; 3.50744 [A]
26.653 [°]; 3.34460 [A]
27.946 [°]; 3.19279 [A]
29.443 [°]; 3.03373 [A]
36.564 [°]; 2.45759 [A]
39.493 [°]; 2.28181 [A]
12.458 [°]; 7.10545 [A]
Selected Pattern: Calcite, syn 00-005-0586
Residue + Peak List
Accepted Patterns

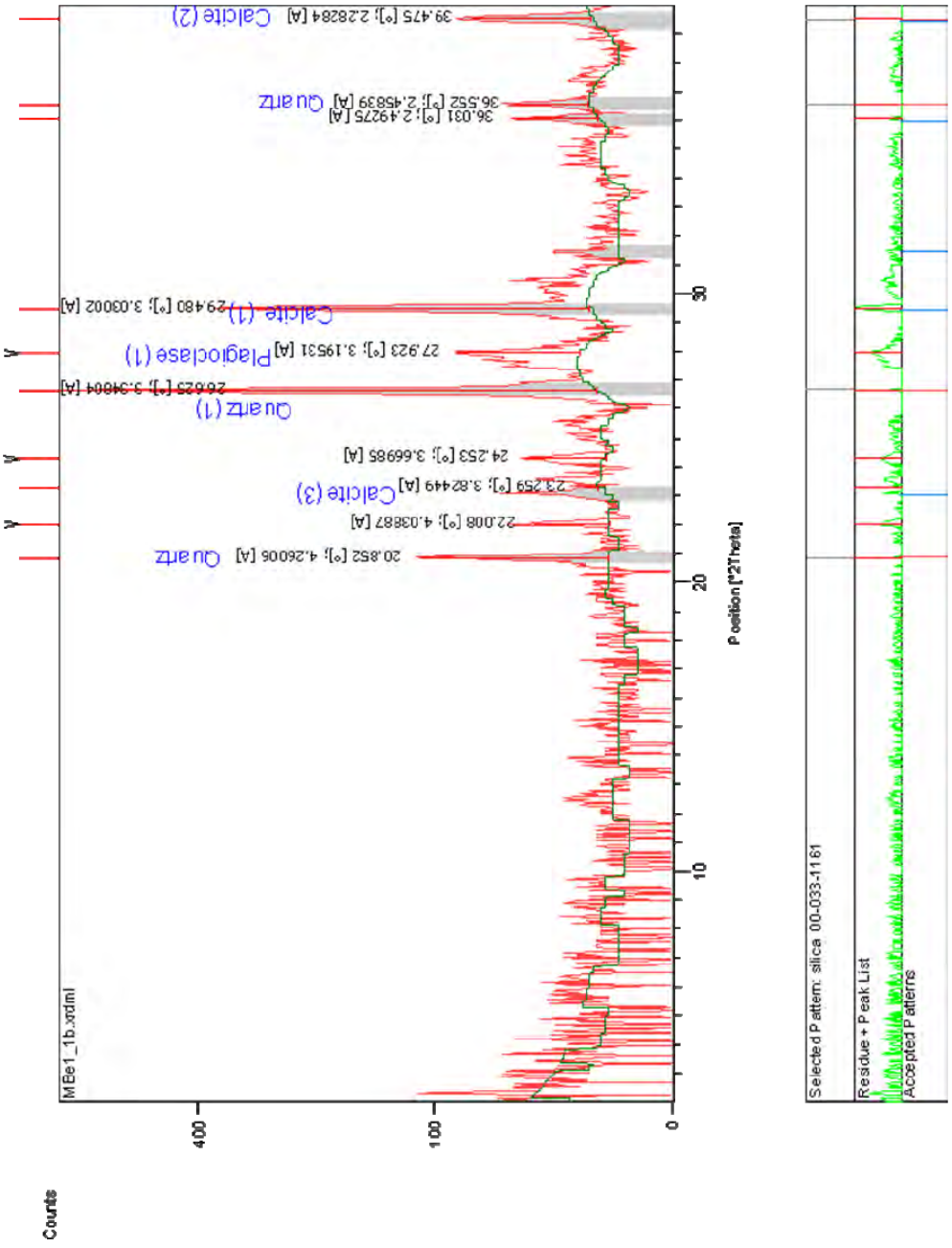
Counts
400
100
0
M:Be1_1b.xrdml
10
20
30
Position [°2Theta]
39.475 [°]; 2.2828 [A]
Calcite (2)
36.031 [°]; 2.49275 [A]
36.552 [°]; 2.45839 [A]
Quartz
29.480 [°]; 3.03002 [A]
Calcite (1)
27.923 [°]; 3.19531 [A]
Plagioclase (1)
26.629 [°]; 3.34604 [A]
Quartz (1)
24.253 [°]; 3.66985 [A]
23.259 [°]; 3.82449 [A]
Calcite (3)
22.008 [°]; 4.03887 [A]
20.852 [°]; 4.26006 [A]
Quartz
Selected Pattern: silica 00-033-1161
Residue + Peak List
Accepted Patterns

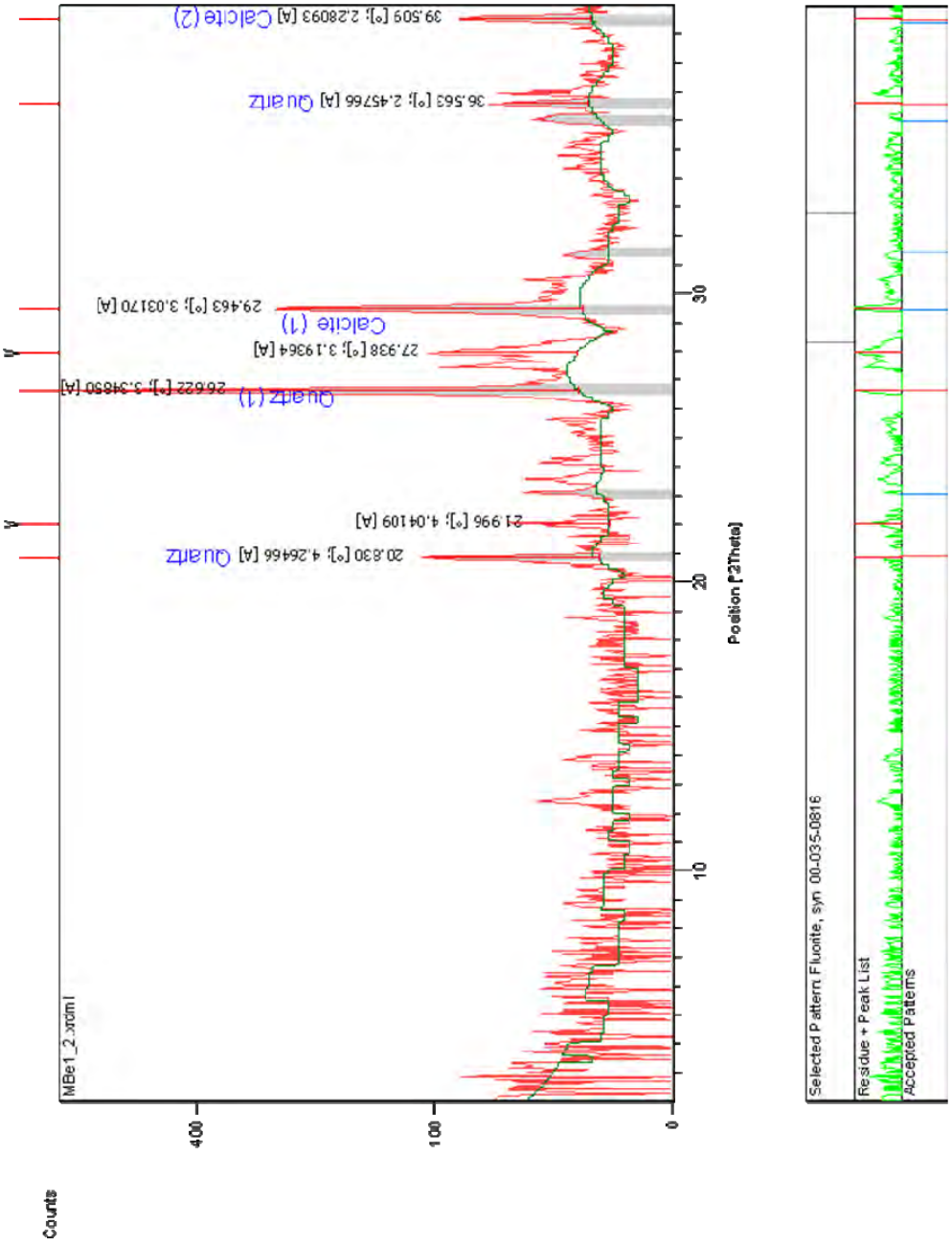
Counts
400
100
0
10
20
30
Position [°2Theta]
MBe1_2.xrdml
20.830 [°]; 4.26466 [A] Quartz
21.996 [°]; 4.04109 [A]
26.622 [°]; 3.34850 [A] Quartz (1)
27.938 [°]; 3.19364 [A]
Calcite (1)
29.463 [°]; 3.03170 [A]
36.563 [°]; 2.45766 [A] Quartz
39.509 [°]; 2.28093 [A] Calcite (2)
Selected Pattern: Fluorite, syn 00-035-0816
Residue + Peak List
Accepted Patterns

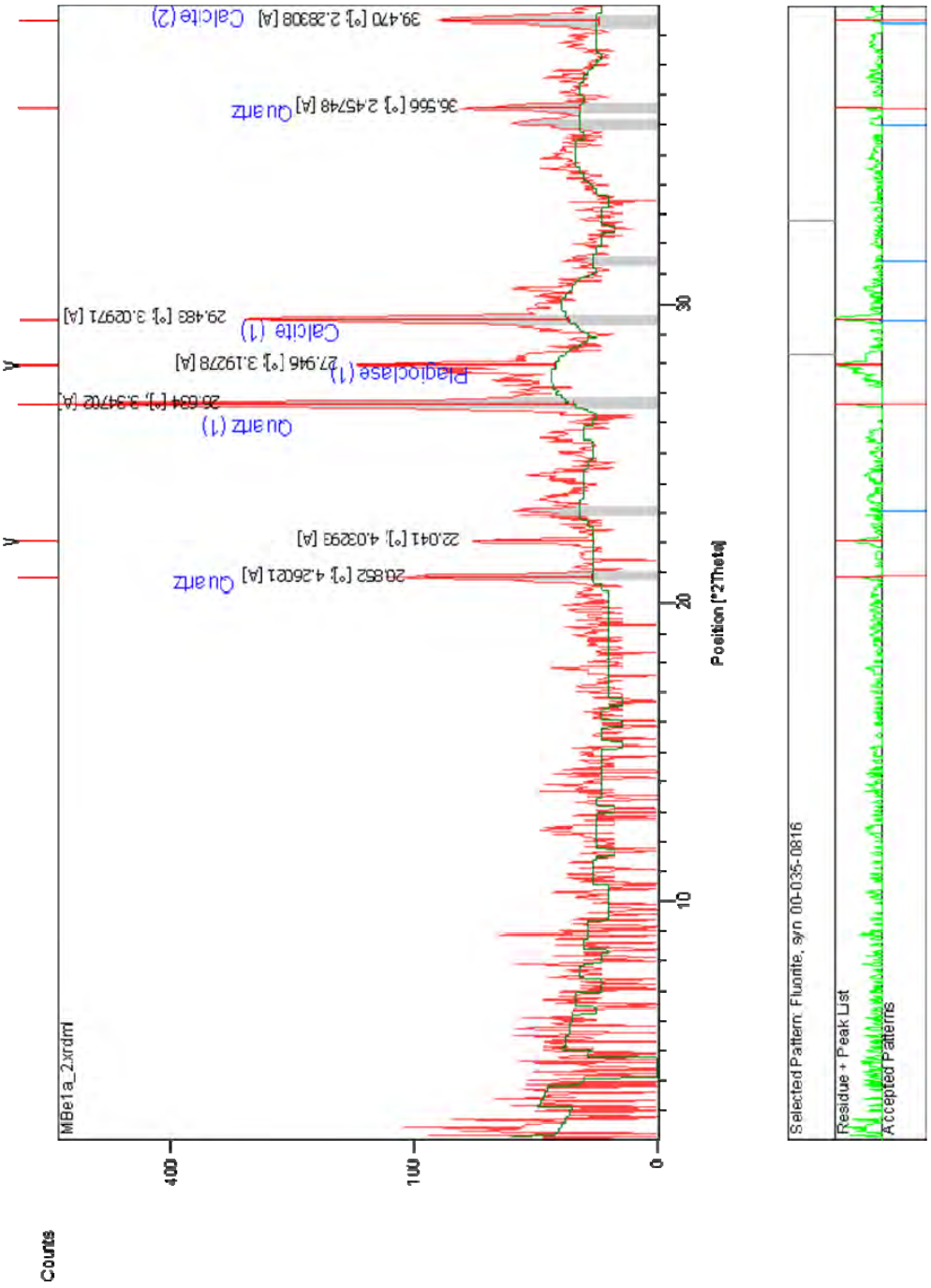
Counts
400
100
0
MBe1a_2.xrdml
Quartz
26.852 [°], 4.26021 [A]
22.041 [°], 4.03293 [A]
Quartz (1)
26.634 [°], 3.34702 [A]
Plagioclase (1)
27.946 [°], 3.19278 [A]
Calcite (1)
29.483 [°], 3.02971 [A]
Quartz
36.566 [°], 2.45748 [A]
Calcite (2)
39.470 [°], 2.28308 [A]
10
20
30
Position [°2Theta]
Selected Pattern: Fluorite, syn 00-035-0816
Residue + Peak List
Accepted Patterns

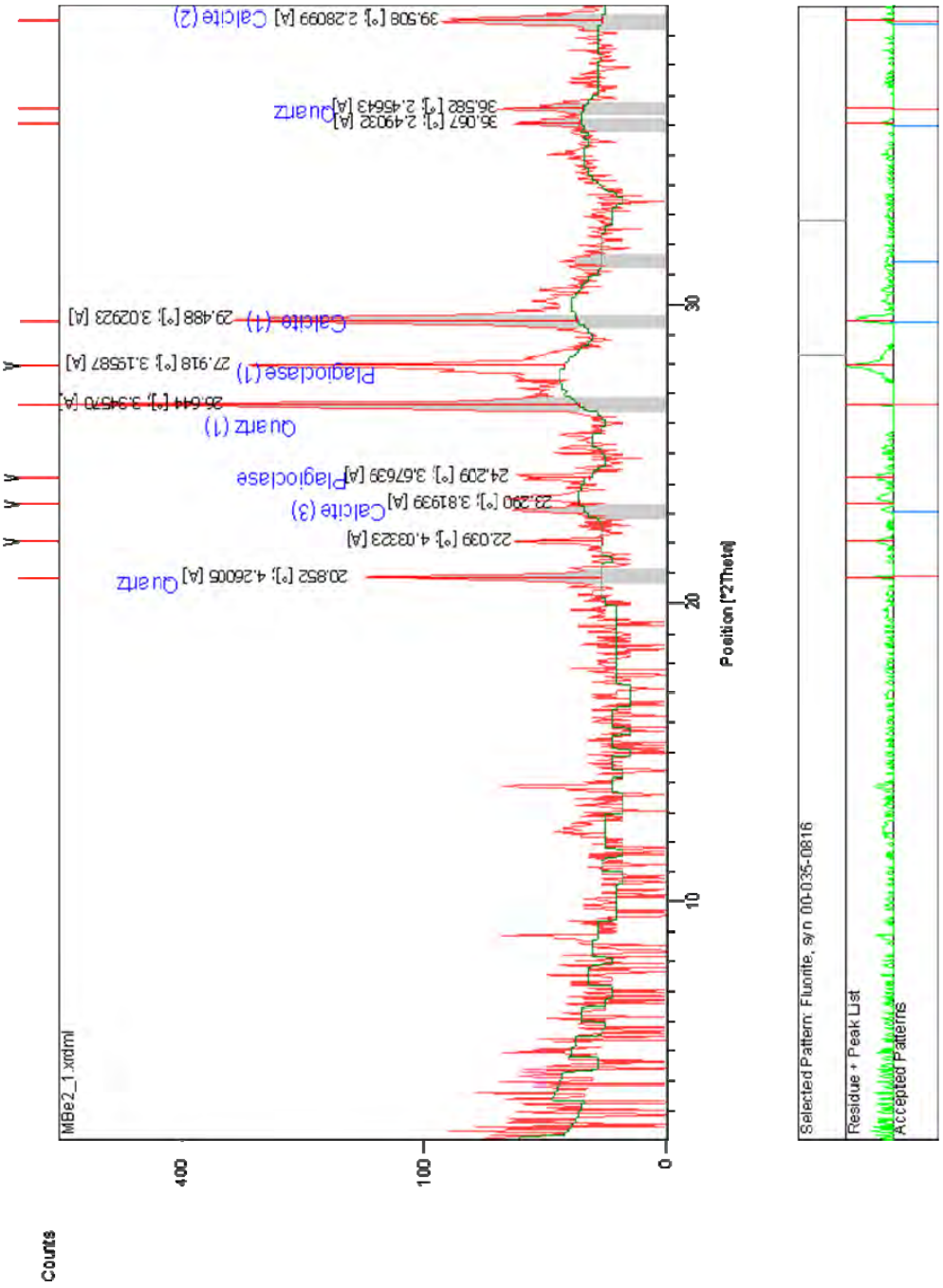
Counts
400
100
0
MBe2_1.xrdml
Quartz
20.852 [°]; 4.26005 [Å]
22.039 [°]; 4.03223 [Å]
Calcite (3)
23.290 [°]; 3.81939 [Å]
Plagioclase
24.209 [°]; 3.67539 [Å]
Quartz (1)
26.644 [°]; 3.34570 [Å]
Plagioclase (1)
27.918 [°]; 3.19587 [Å]
Calcite (1)
29.488 [°]; 3.02923 [Å]
Quartz
36.067 [°]; 2.49032 [Å]
36.582 [°]; 2.45643 [Å]
Calcite (2)
39.508 [°]; 2.28099 [Å]
10
20
30
Position [°2Theta]
Selected Pattern: Fluorite, syn 00-035-0816
Residue + Peak List
Accepted Patterns

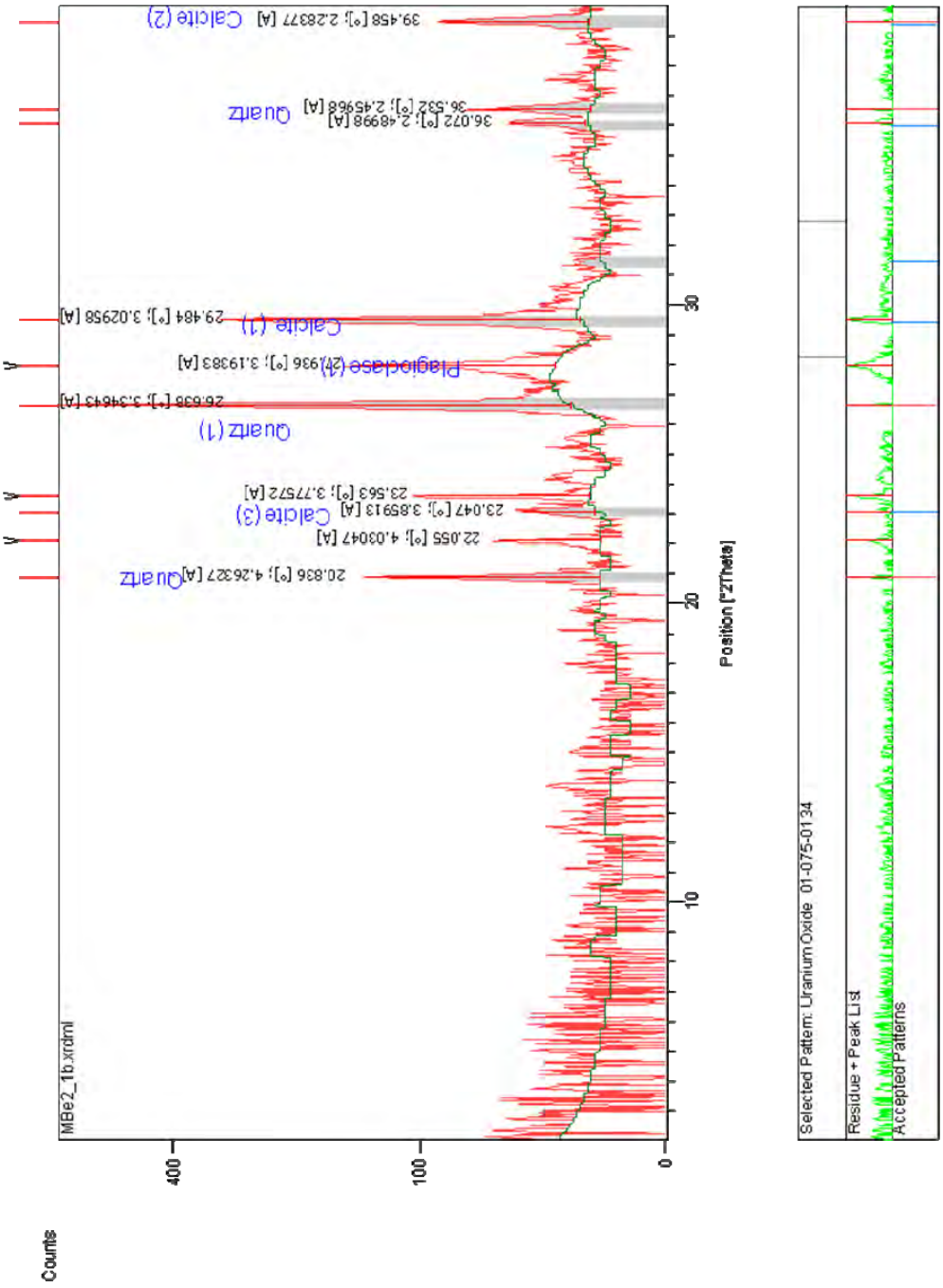
MBe2_1b.xrdml
Counts
Position [°2Theta]
Quartz (1)
Plagioclase (2)
Calcite (1)
Quartz
Calcite (3)
Quartz
Calcite (2)
Quartz
Selected Pattern: Uranium Oxide 01-075-0134
Residue + Peak List
Accepted Patterns

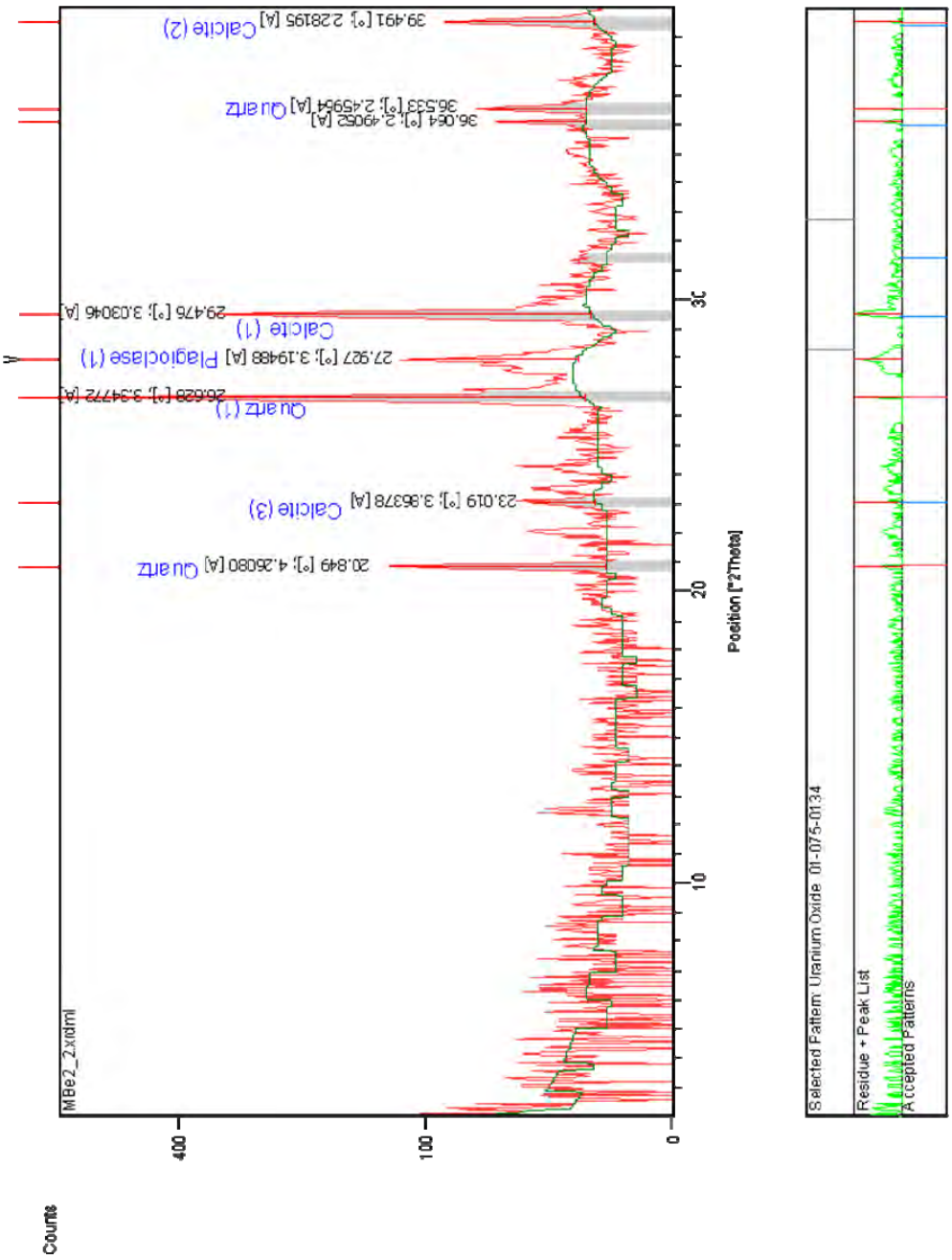
Counts
400
100
0
MBe2_2.xdml
20.849 [°]; 4.26080 [A] Quartz
23.019 [°]; 3.86378 [A] Calcite (3)
26.628 [°]; 3.34772 [A] Quartz (1)
27.927 [°]; 3.19488 [A] Plagioclase (1)
29.476 [°]; 3.03046 [A] Calcite (1)
36.064 [°]; 2.49052 [A]
36.533 [°]; 2.45964 [A] Quartz
39.491 [°]; 2.28195 [A] Calcite (2)
10
20
30
Position [°2Theta]
Selected Pattern: Uranium Oxide 01-075-0134
Residue + Peak List
Accepted Patterns

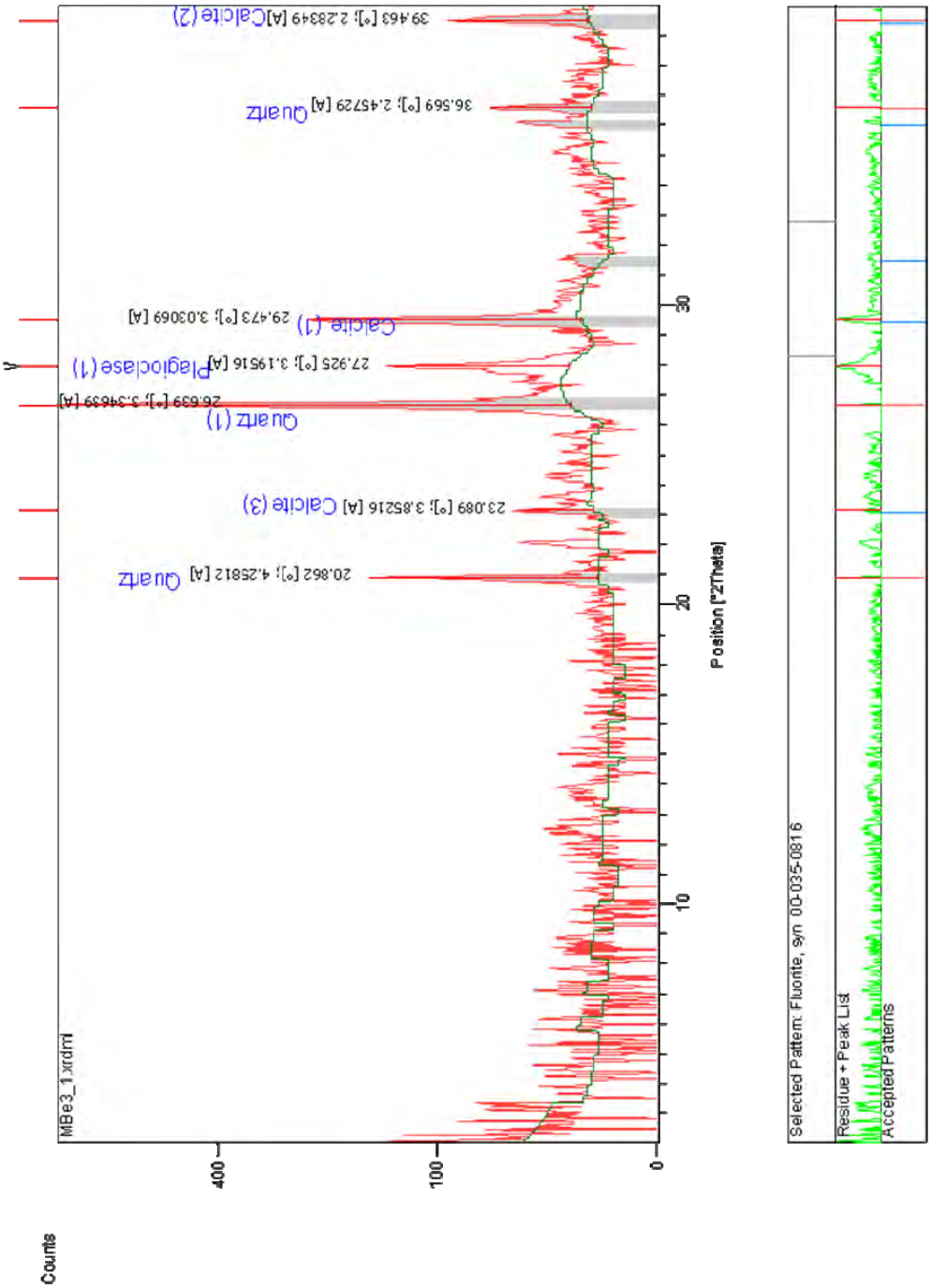
Counts
400
100
0
MBe3_1.xrdml
10
20
30
Position [°2Theta]
Quartz
20.862 [°]; 4.25812 [Å]
Calcite (3)
23.089 [°]; 3.85216 [Å]
Quartz (1)
26.639 [°]; 3.34639 [Å]
Plagioclase (1)
27.925 [°]; 3.19516 [Å]
Calcite (1)
29.473 [°]; 3.03069 [Å]
Quartz
36.569 [°]; 2.45729 [Å]
Calcite (2)
39.463 [°]; 2.28349 [Å]
Selected Pattern: Fluorite, syn 00-035-0816
Residue + Peak List
Accepted Patterns

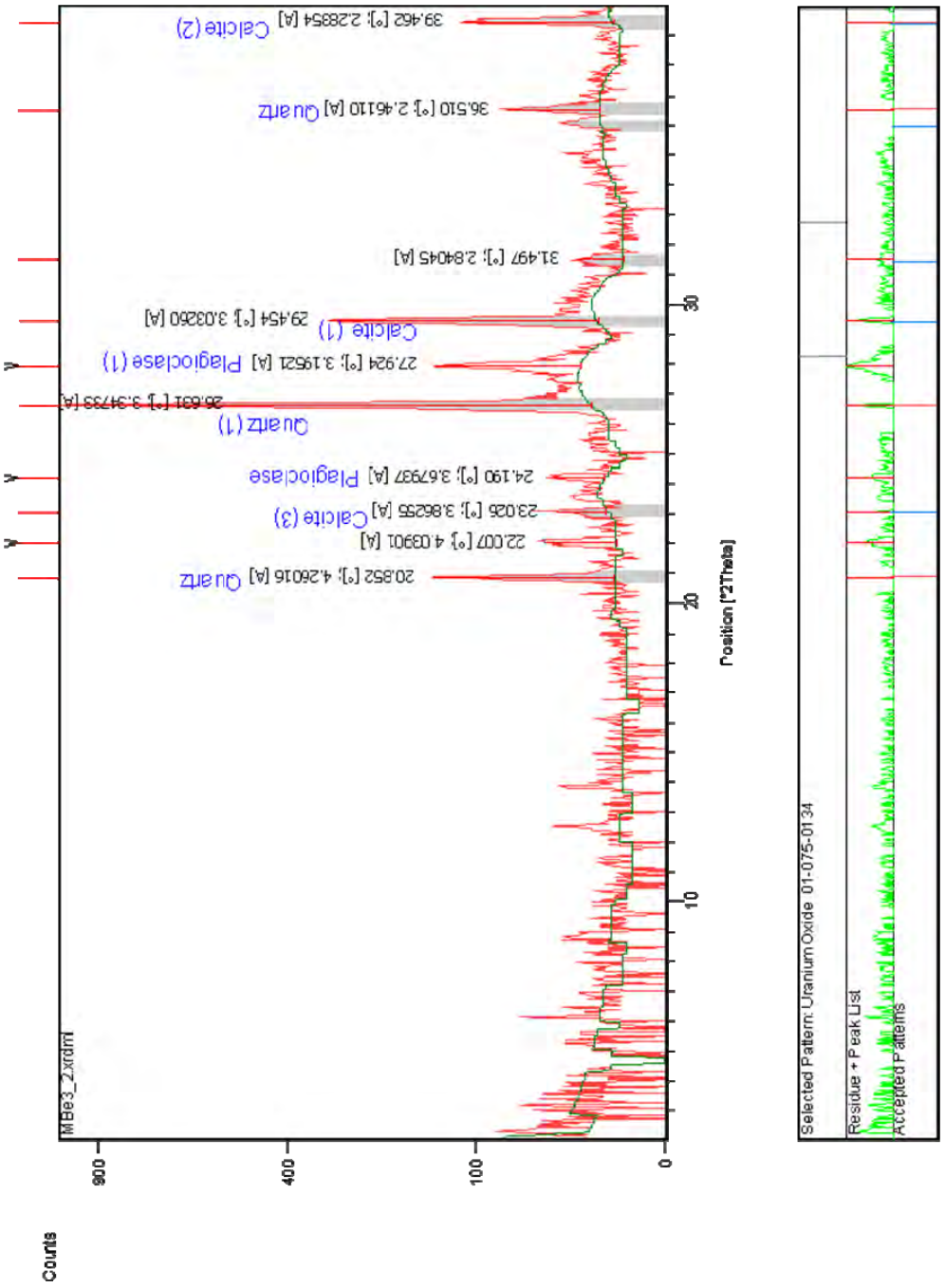
Counts
900
400
100
0
MBe3_2.xrdml
10
20
30
Position [°2Theta]
20.852 [°]; 4.26016 [A] Quartz
22.007 [°]; 4.03901 [A]
23.026 [°]; 3.86255 [A] Calcite (3)
24.190 [°]; 3.67937 [A] Plagioclase
26.631 [°]; 3.34733 [A] Quartz (1)
27.924 [°]; 3.19521 [A] Plagioclase (1)
29.454 [°]; 3.03260 [A] Calcite (1)
31.497 [°]; 2.84045 [A]
36.510 [°]; 2.46110 [A] Quartz
39.462 [°]; 2.28354 [A] Calcite (2)
Selected Pattern: Uranium Oxide 01-075-0134
Residue + Peak List
Accepted Patterns

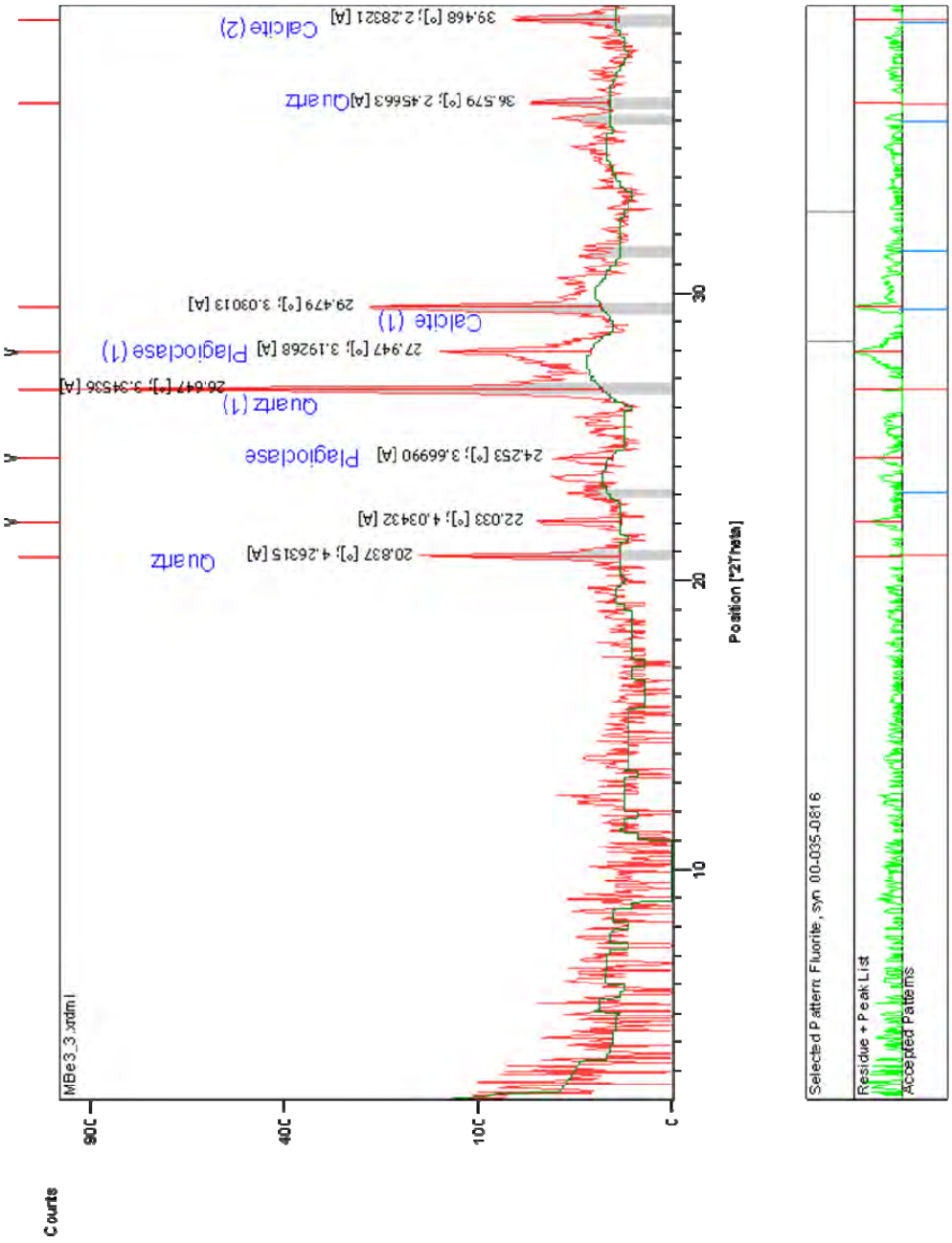
Counts
Position [°2Theta]
MBe3_3.xrdml
Quartz
20.837 [°]; 4.26315 [A]
22.033 [°]; 4.03432 [A]
Plagioclase
24.253 [°]; 3.66990 [A]
Quartz (1)
26.647 [°]; 3.34536 [A]
Plagioclase (1)
27.947 [°]; 3.19268 [A]
Calcite (1)
29.479 [°]; 3.03013 [A]
Quartz
36.579 [°]; 2.45663 [A]
Calcite (2)
39.468 [°]; 2.28321 [A]
Selected Pattern: Fluorite, syn 00-035-0816
Residue + Peak List
Accepted Patterns

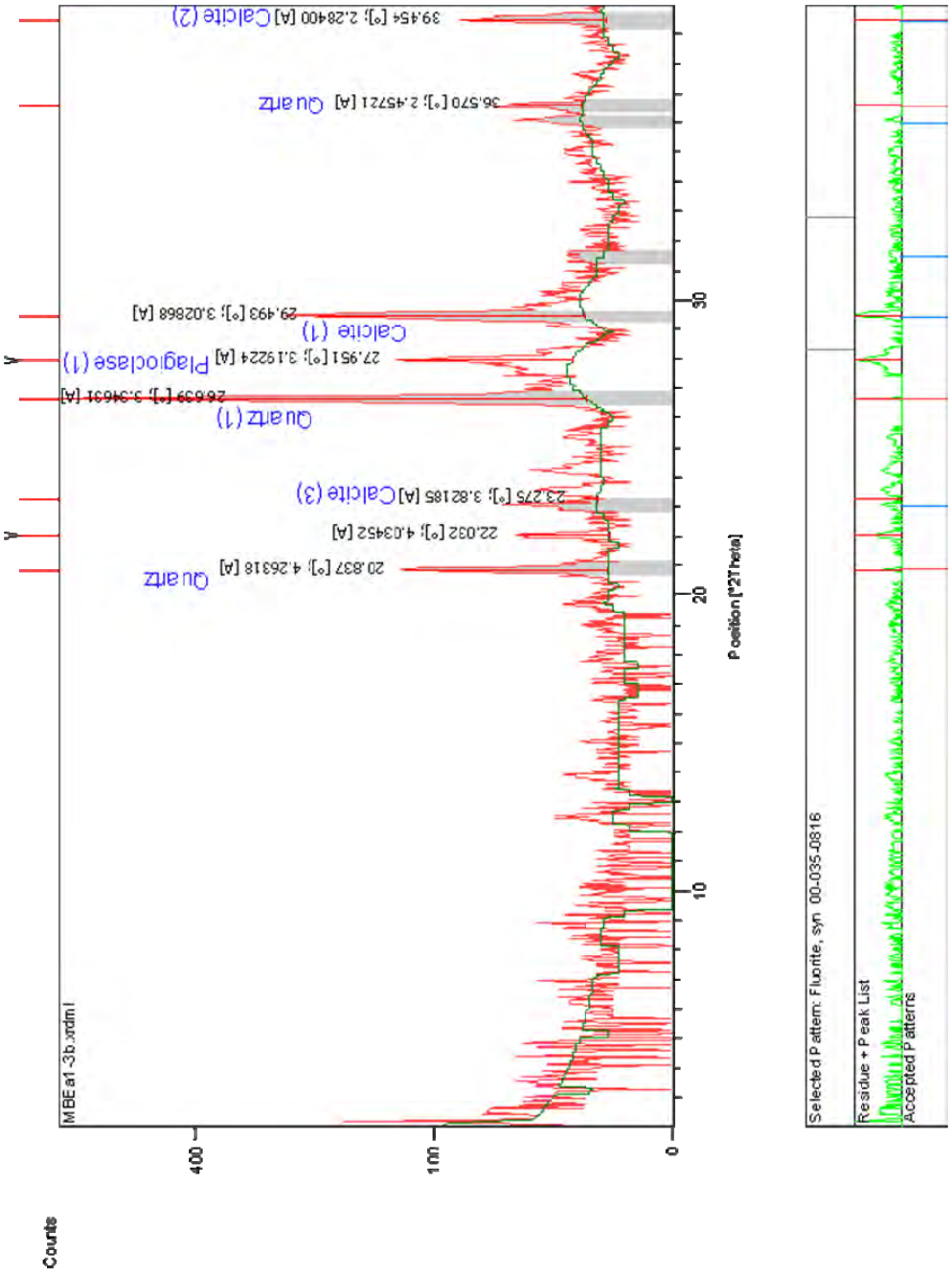
Counts
400
100
0
10
20
30
Position [°2Theta]
M BE a1 -3b.xrdml
Quartz
20.837 [°]; 4.26318 [A]
22.032 [°]; 4.03452 [A]
Calcite (3)
23.275 [°]; 3.82185 [A]
Quartz (1)
26.639 [°]; 3.34631 [A]
Plagioclase (1)
27.951 [°]; 3.19224 [A]
Calcite (1)
29.493 [°]; 3.02868 [A]
Quartz
36.570 [°]; 2.45721 [A]
Calcite (2)
39.454 [°]; 2.28400 [A]
Selected Pattern: Fluorite, syn 00-035-0816
Residue + Peak List
Accepted Patterns

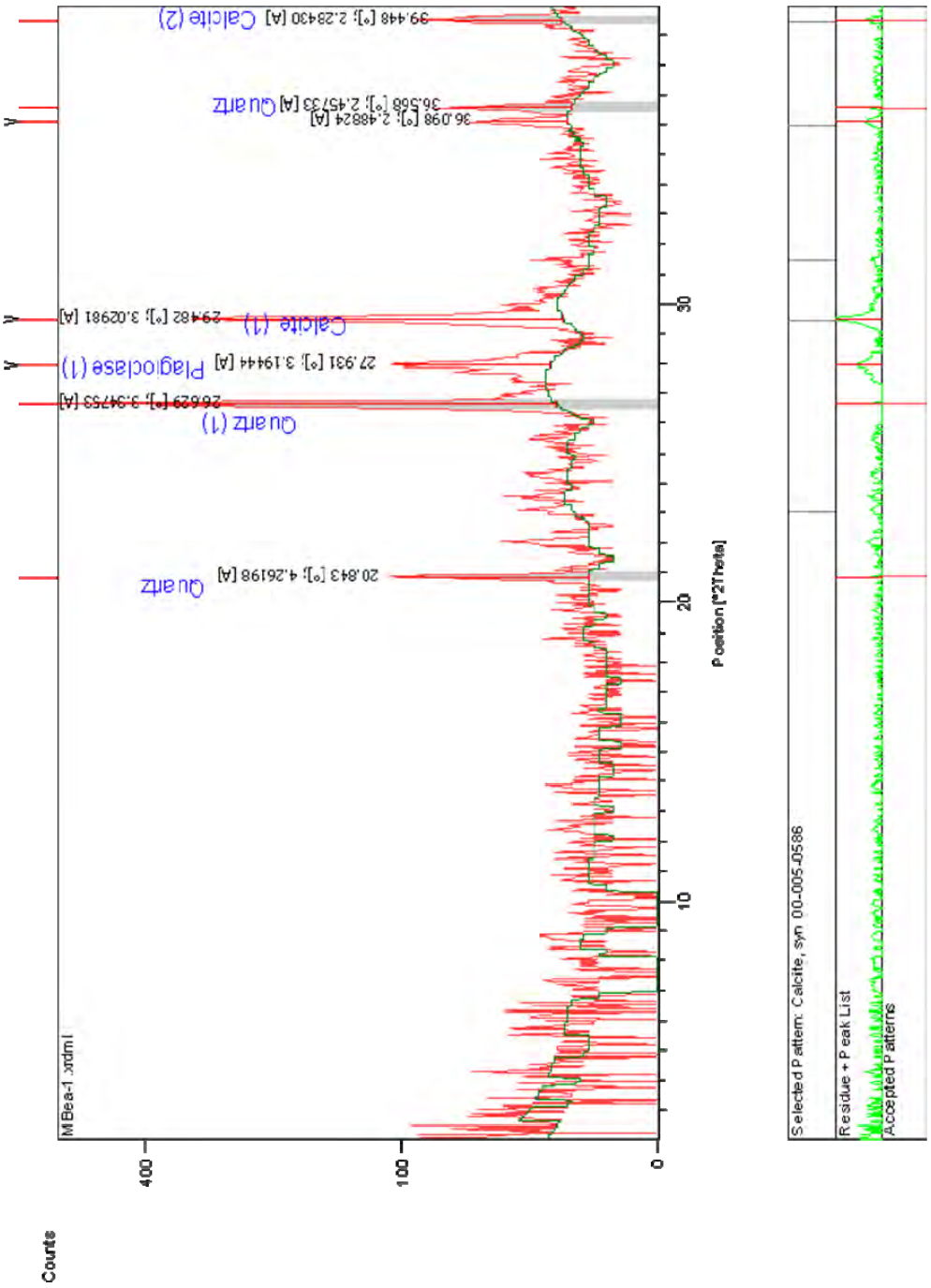
Counts
400
100
0
10
20
30
Position [°2Theta]
M Bea-1 .xrdml
Quartz
20.843 [°]; 4.26198 [A]
Quartz (1)
26.629 [°]; 3.34753 [A]
Plagioclase (1)
27.931 [°]; 3.19444 [A]
Calcite (1)
29.482 [°]; 3.02981 [A]
Quartz
36.098 [°]; 2.48824 [A]
36.568 [°]; 2.45733 [A]
Calcite (2)
39.448 [°]; 2.28430 [A]
Selected Pattern: Calcite, syn 00-005-0586
Residue + Peak List
Accepted Patterns

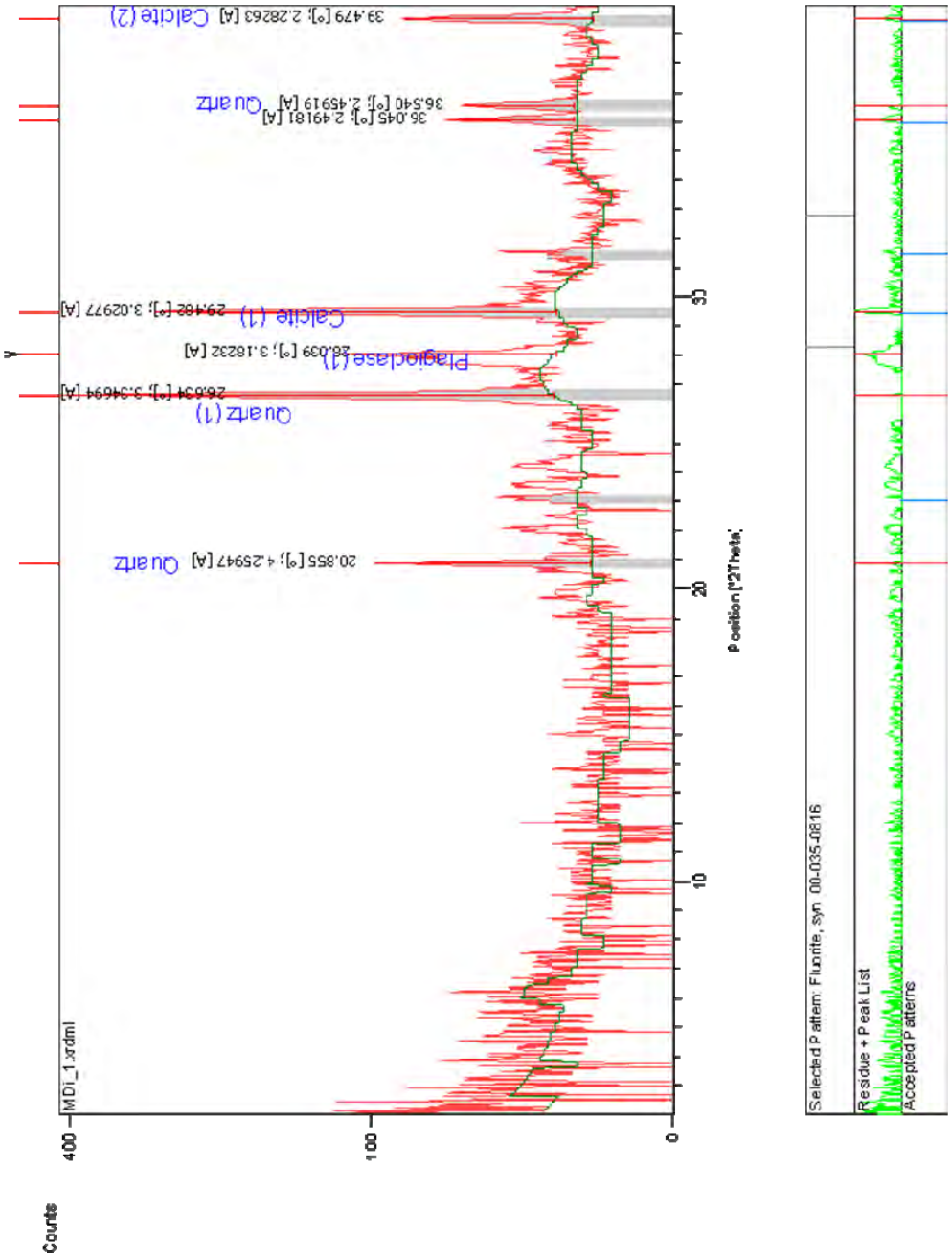
Counts
400
100
0
MDI_1.xrdml
Quartz
20.855 [°]; 4.25947 [Å]
Quartz (1)
26.634 [°]; 3.34694 [Å]
Plagioclase (1)
28.039 [°]; 3.18232 [Å]
Calcite (1)
29.462 [°]; 3.02977 [Å]
Quartz
36.045 [°]; 2.49181 [Å]
36.540 [°]; 2.45919 [Å]
Calcite (2)
39.479 [°]; 2.28263 [Å]
Y
10
20
30
Position [°2Theta]
Selected Pattern: Fluorite, syn 00-035-0816
Residue + Peak List
Accepted Patterns

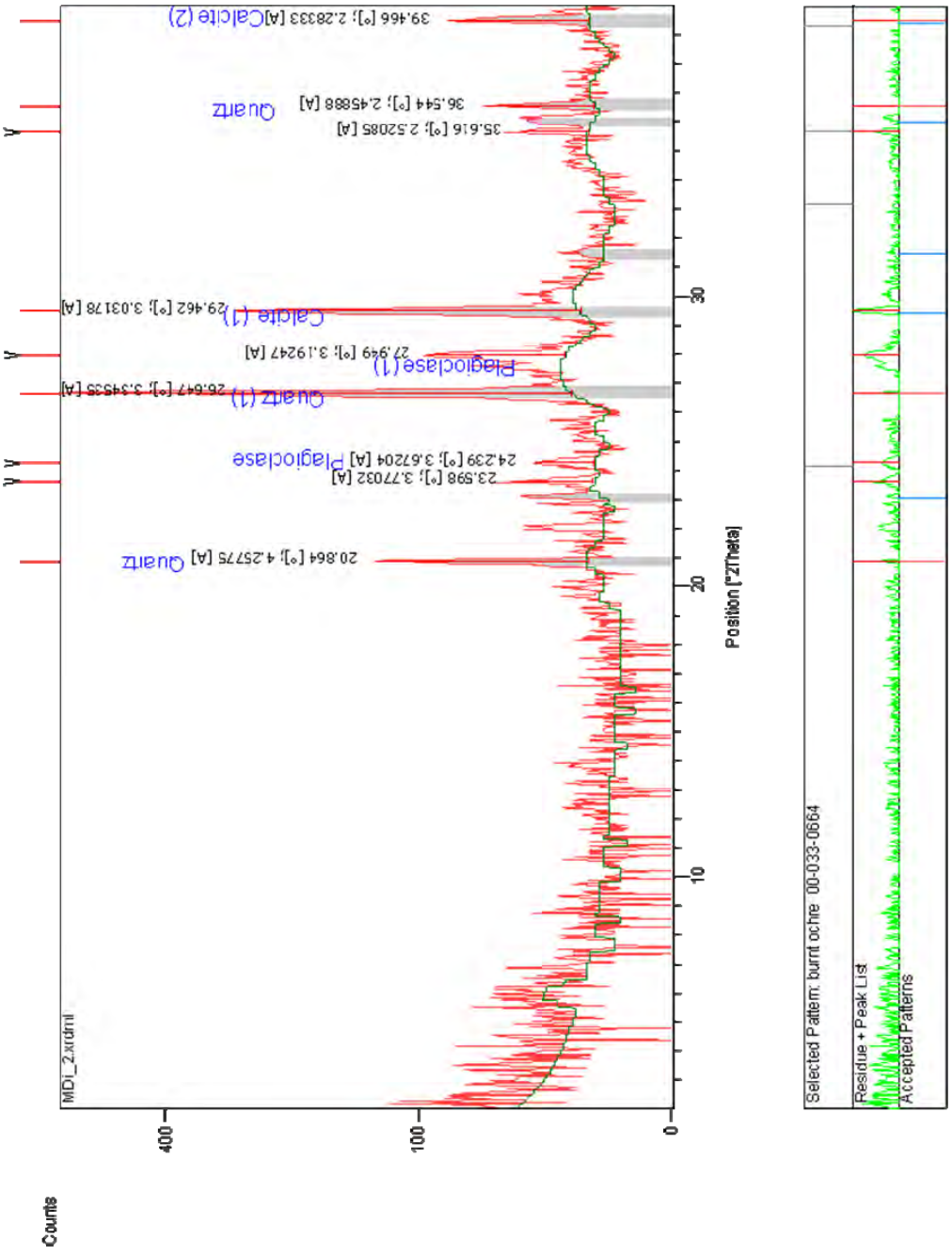
Counts
400
100
0
MDI_2.xrdml
10
20
30
Position [°2Theta]
20.864 [°]; 4.25775 [A] Quartz
23.598 [°]; 3.77032 [A]
24.239 [°]; 3.67204 [A] Plagioclase
26.647 [°]; 3.34535 [A] Quartz (1)
27.949 [°]; 3.19247 [A] Plagioclase (1)
29.462 [°]; 3.03178 [A] Calcite (1)
35.616 [°]; 2.52085 [A]
36.544 [°]; 2.45888 [A] Quartz
39.466 [°]; 2.28333 [A] Calcite (2)
Selected Pattern: burnt ochre 00-033-0664
Residue + Peak List
Accepted Patterns

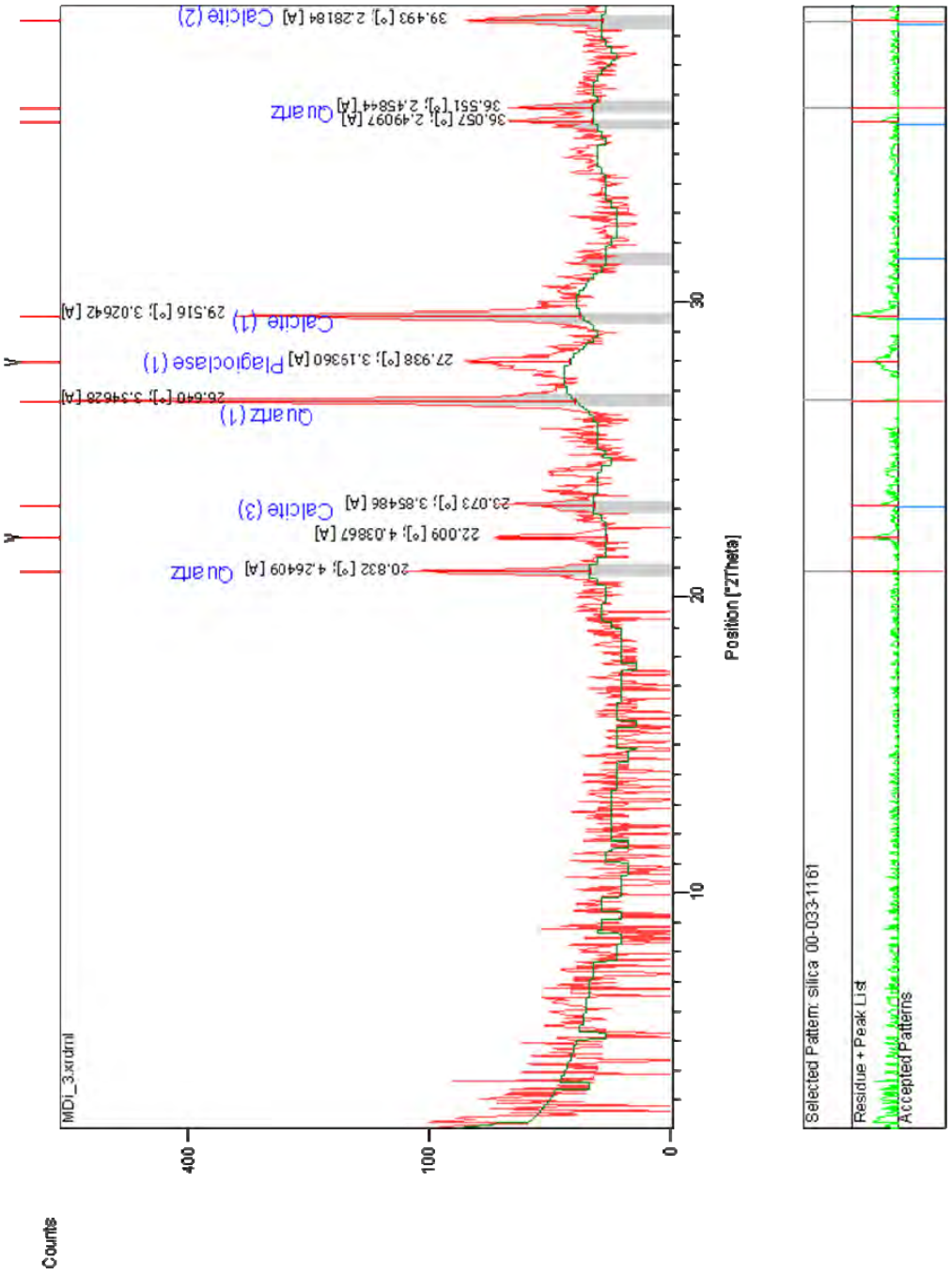
Counts
400
100
0
MDI_3.xrdml
10
20
30
Position [°2Theta]
39.493 [°]; 2.28184 [A]
Calcite (2)
36.057 [°]; 2.49097 [A]
36.551 [°]; 2.45844 [A]
Quartz
29.516 [°]; 3.02642 [A]
Calcite (1)
27.938 [°]; 3.19360 [A]
Plagioclase (1)
26.640 [°]; 3.34628 [A]
Quartz (1)
23.073 [°]; 3.85486 [A]
Calcite (3)
22.009 [°]; 4.03867 [A]
20.832 [°]; 4.26409 [A]
Quartz
Selected Pattern: silica 00-033-1161
Residue + Peak List
Accepted Patterns

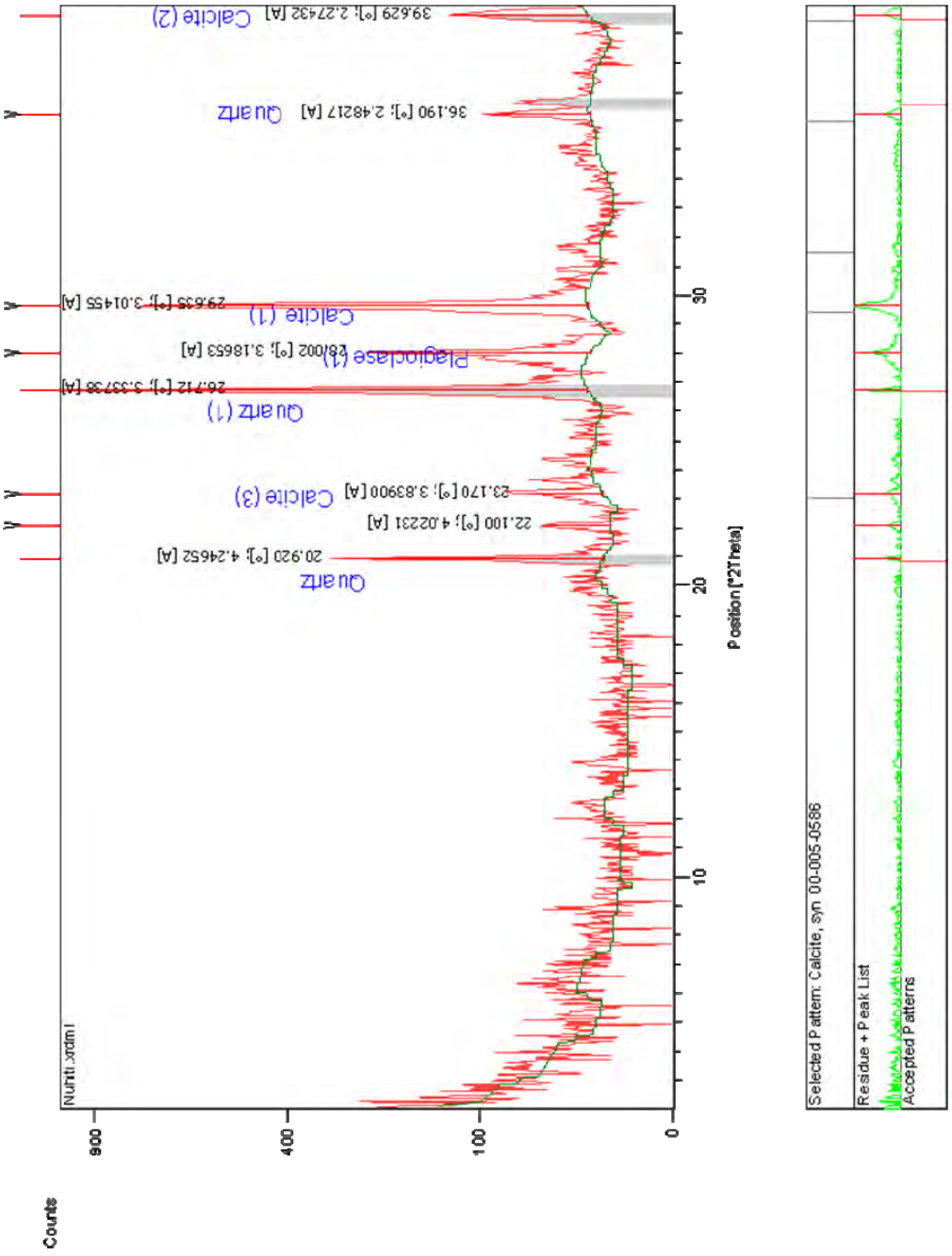
Counts
Position [°2Theta]
Quartz
20.920 [°]; 4.24652 [A]
22.100 [°]; 4.02231 [A]
Calcite (3)
23.170 [°]; 3.83900 [A]
Quartz (1)
26.712 [°]; 3.33738 [A]
Plagioclase (1)
28.002 [°]; 3.18653 [A]
Calcite (1)
29.435 [°]; 3.01455 [A]
Quartz
36.190 [°]; 2.48217 [A]
Calcite (2)
39.429 [°]; 2.27432 [A]
Selected Pattern: Calcite, syn 00-005-0586
Residue + Peak List
Accepted Patterns

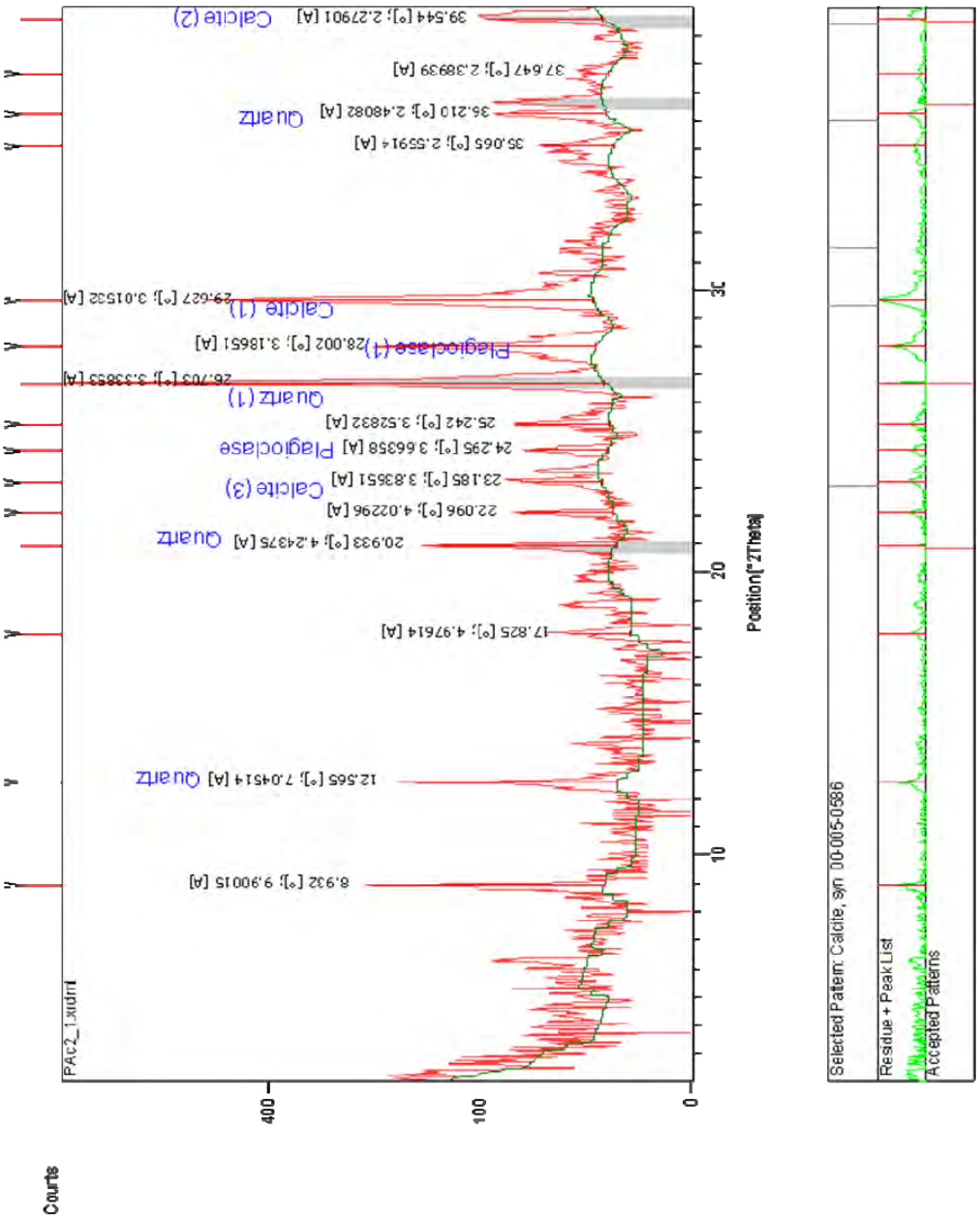
Counts
400
100
0
10
20
30
Position [°2Theta]
PAc2_1.xrdml
8.932 [°]; 9.90015 [A]
12.565 [°]; 7.04514 [A] Quartz
17.825 [°]; 4.97614 [A]
20.933 [°]; 4.24375 [A] Quartz
22.096 [°]; 4.02296 [A]
23.185 [°]; 3.83551 [A] Calcite (3)
24.295 [°]; 3.66358 [A] Plagioclase
25.242 [°]; 3.52832 [A]
26.703 [°]; 3.33853 [A] Quartz (1)
28.002 [°]; 3.18651 [A] Plagioclase (1)
29.427 [°]; 3.01532 [A] Calcite (1)
35.065 [°]; 2.55914 [A]
36.210 [°]; 2.48082 [A] Quartz
37.647 [°]; 2.38939 [A]
39.544 [°]; 2.27901 [A] Calcite (2)
Selected Pattern: Calcite, syn 00-005-0586
Residue + Peak List
Accepted Patterns

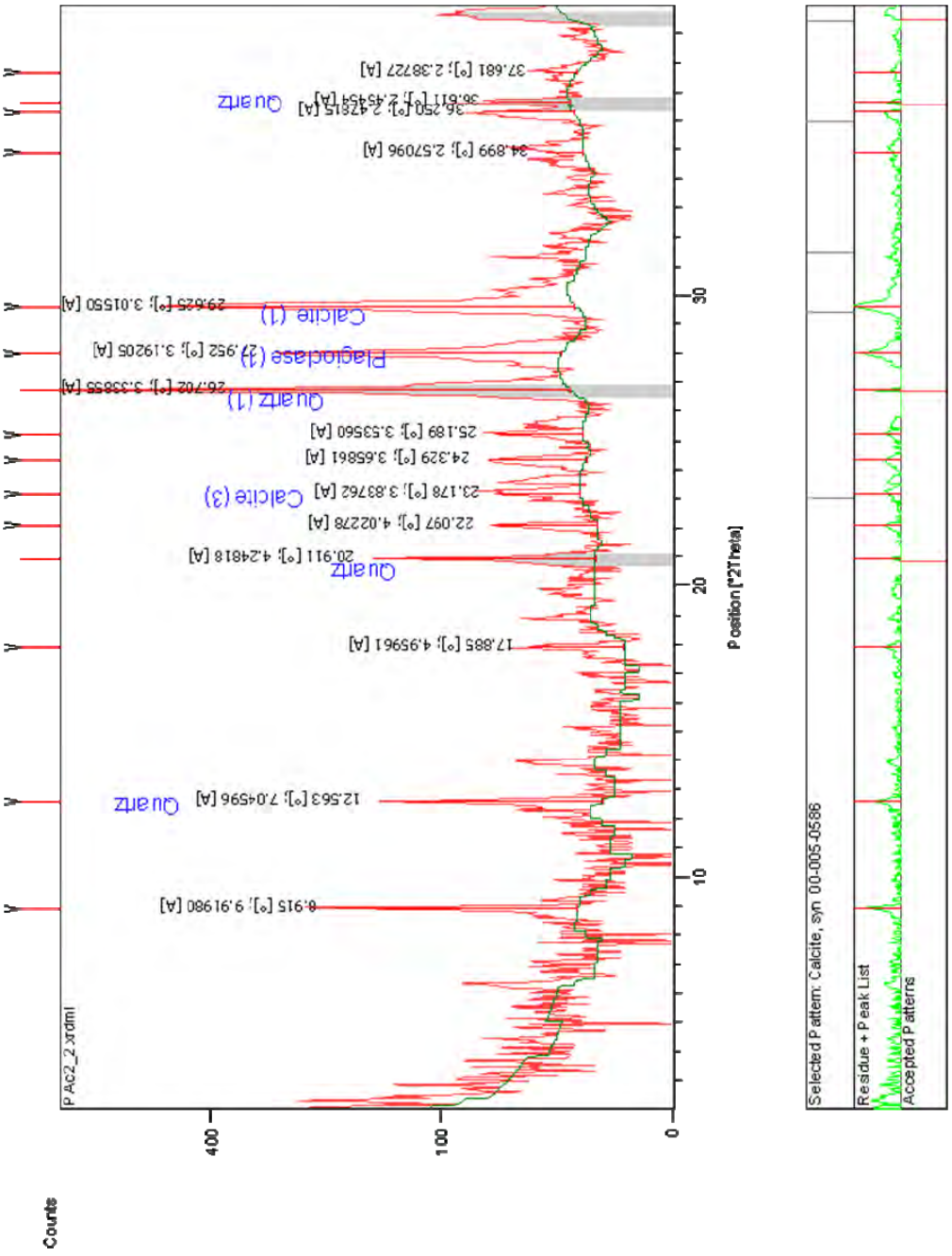
Counts
400
100
0
Position [°2Theta]
0
10
20
30
P Ac2_2.xrdml
8.915 [°]; 9.91980 [A]
12.563 [°]; 7.04596 [A]
Quartz
17.885 [°]; 4.95961 [A]
20.911 [°]; 4.24818 [A]
Quartz
22.097 [°]; 4.02278 [A]
23.178 [°]; 3.83762 [A]
Calcite (3)
24.329 [°]; 3.65861 [A]
25.189 [°]; 3.53560 [A]
26.702 [°]; 3.33855 [A]
Quartz (1)
27.952 [°]; 3.19205 [A]
Plagioclase (2)
29.625 [°]; 3.01550 [A]
Calcite (1)
34.899 [°]; 2.57096 [A]
36.250 [°]; 2.47815 [A]
Quartz
37.681 [°]; 2.38727 [A]
Selected Pattern: Calcite, syn 00-005-0586
Residue + Peak List
Accepted Patterns

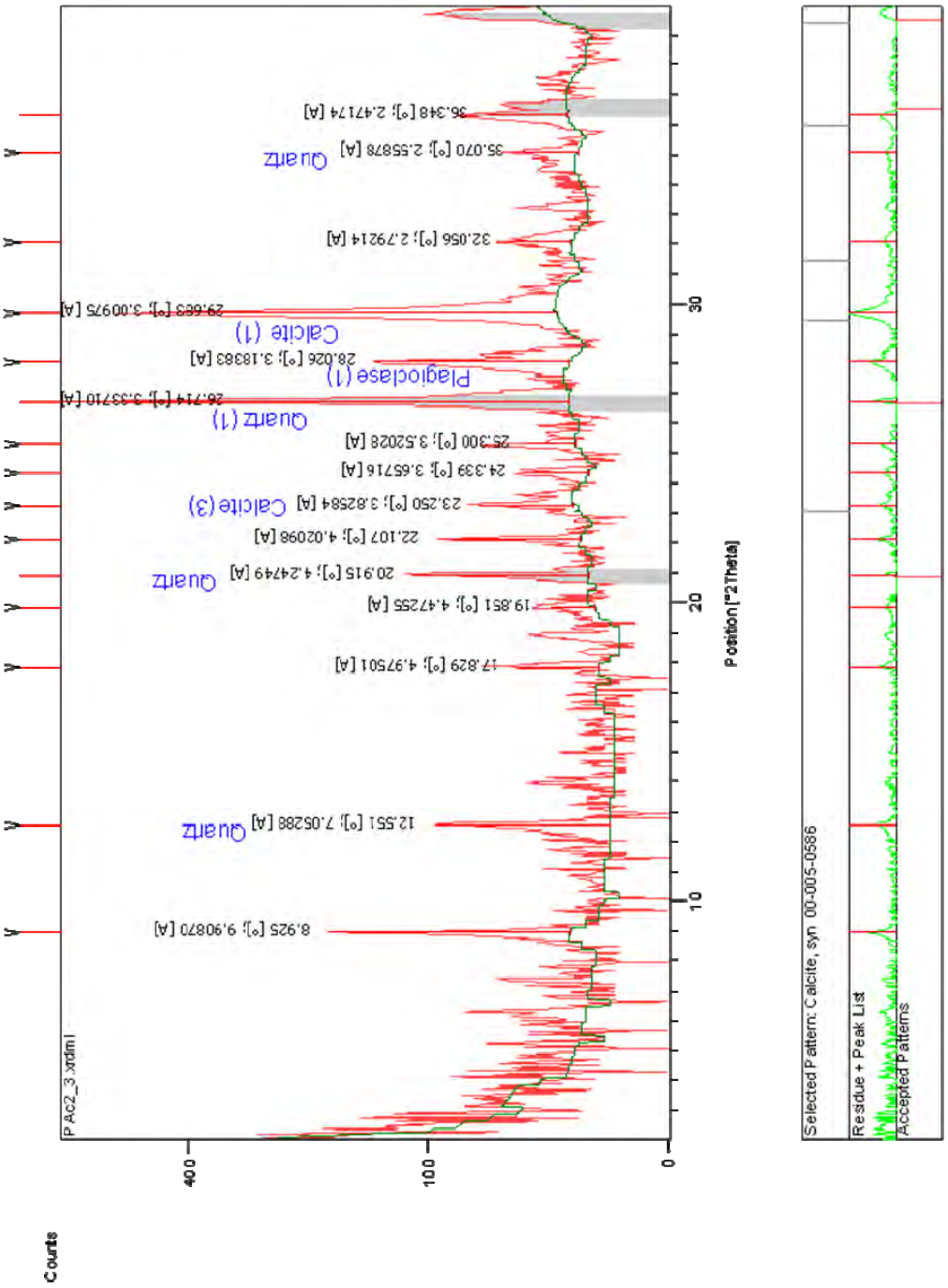
Counts
400
100
0
10
20
30
Position [°2Theta]
PAc2_3.xrdml
8.925 [°]; 9.90870 [Å]
12.551 [°]; 7.05288 [Å]
Quartz
17.829 [°]; 4.97501 [Å]
19.851 [°]; 4.47255 [Å]
20.915 [°]; 4.24749 [Å]
Quartz
22.107 [°]; 4.02098 [Å]
23.250 [°]; 3.82584 [Å]
Calcite (3)
24.339 [°]; 3.65716 [Å]
25.300 [°]; 3.52028 [Å]
26.714 [°]; 3.33710 [Å]
Quartz (1)
28.026 [°]; 3.18383 [Å]
Plagioclase (1)
29.463 [°]; 3.00975 [Å]
Calcite (1)
32.056 [°]; 2.79214 [Å]
35.070 [°]; 2.55878 [Å]
Quartz
36.348 [°]; 2.47174 [Å]
Selected Pattern: Calcite, syn 00-005-0586
Residue + Peak List
Accepted Patterns

Counts
400
100
0
PAc3_1.xrdml
8.925 [°]; 9.90884 [A]
12.552 [°]; 7.05221 [A]
Quartz
17.858 [°]; 4.96714 [A]
19.802 [°]; 4.48356 [A]
20.916 [°]; 4.24727 [A]
Quartz
22.101 [°]; 4.02217 [A]
23.176 [°]; 3.83786 [A]
Calcite (3)
24.367 [°]; 3.65305 [A]
Plagioclase
25.195 [°]; 3.53479 [A]
26.704 [°]; 3.33839 [A]
Quartz (1)
27.929 [°]; 3.19461 [A]
Plagioclase (1)
29.618 [°]; 3.01621 [A]
Calcite (1)
35.030 [°]; 2.56164 [A]
Quartz
36.241 [°]; 2.47878 [A]
10
20
30
Position [°2Theta]
Selected Pattern: Fluorite, syn 00-035-0816
Residue + Peak List
Accepted Patterns

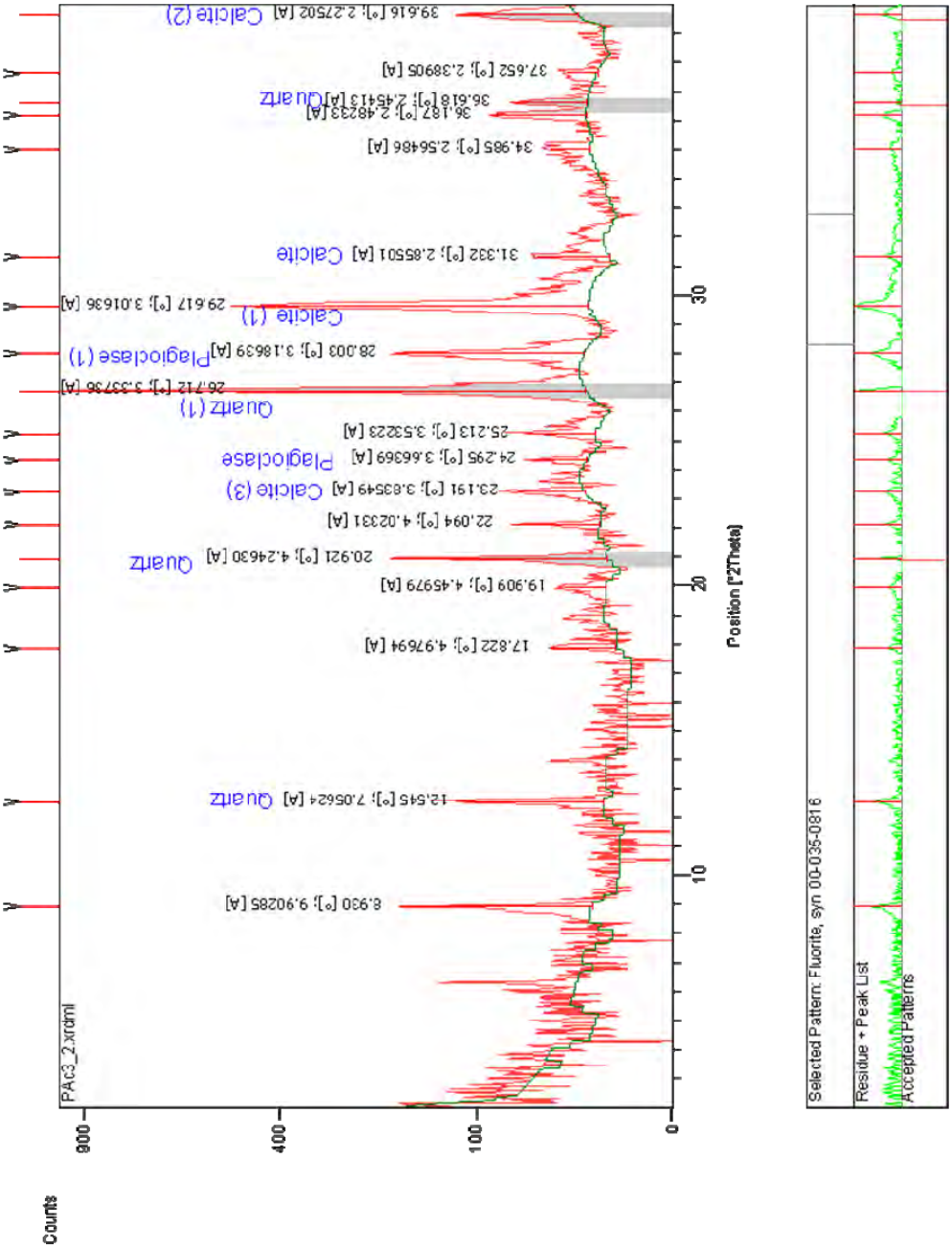
PAc3_2.xrdml
Counts
Position [°2Theta]
Quartz
Calcite (2)
Quartz
Calcite
Calcite (1)
Plagioclase (1)
Quartz (1)
Plagioclase
Calcite (3)
Quartz
Selected Pattern: Fluorite, syn 00-035-0816
Residue + Peak List
Accepted Patterns

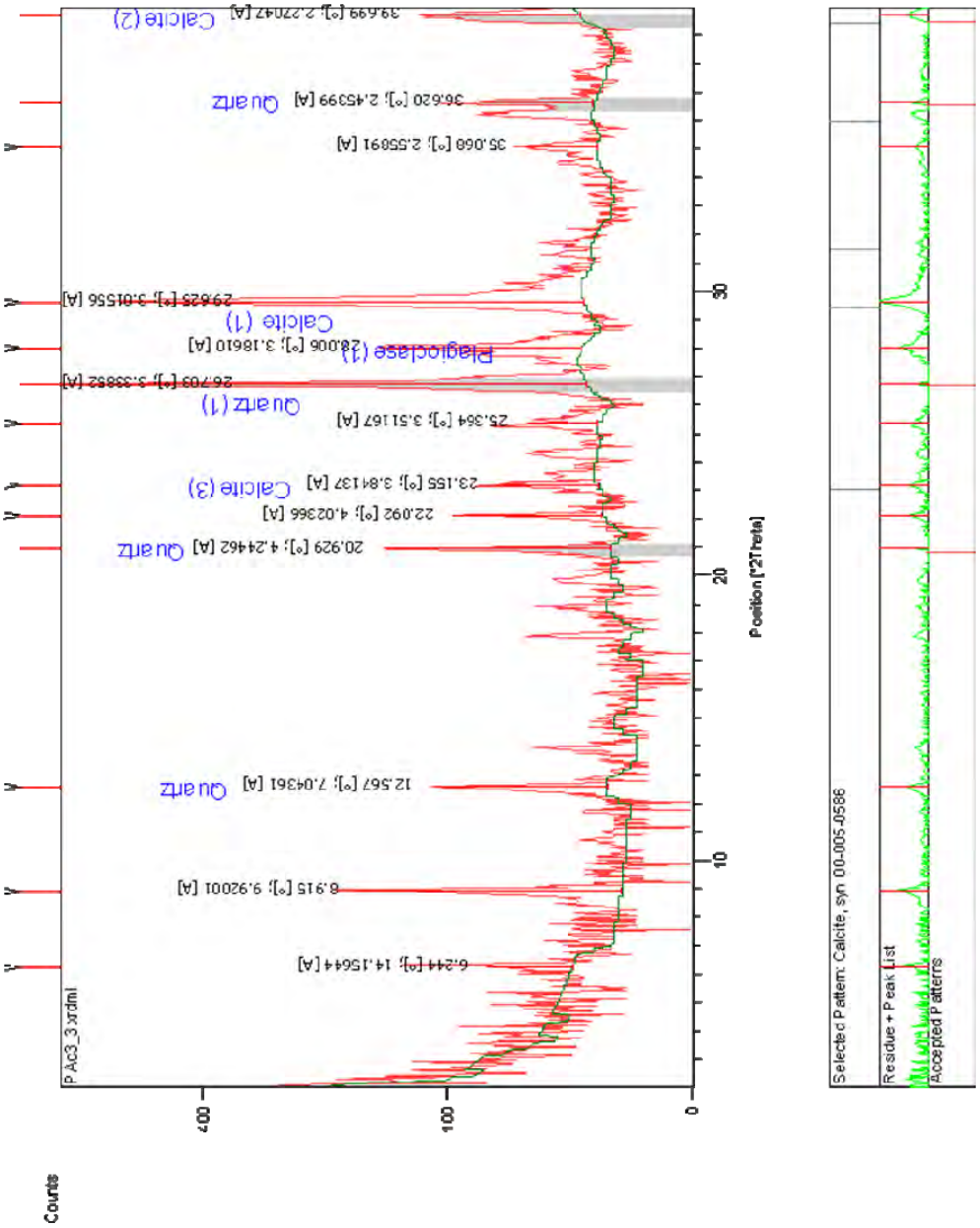
Counts
Position [°2Theta]
P Ac3_3.xrdml
Quartz
Calcite (2)
Quartz
Calcite (1)
Plagioclase (1)
Quartz (1)
Calcite (3)
Quartz
Quartz
Selected Pattern: Calcite, syn 00-005-0586
Residue + Peak List
Accepted Patterns

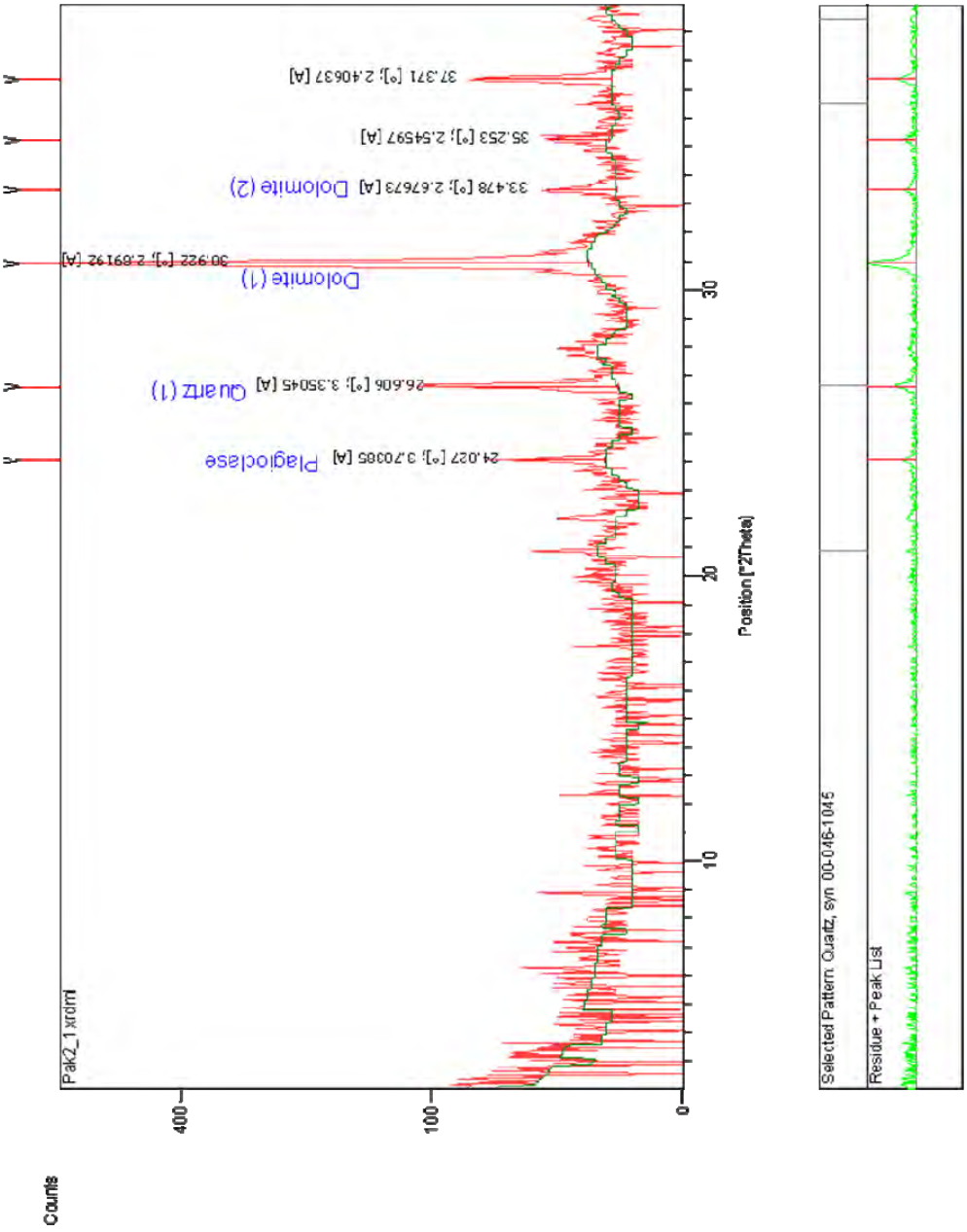
Counts
400
100
0
Pak2_1.xrdml
10
20
30
Position [°2Theta]
24.027 [°]; 3.70385 [Å]
Plagioclase
26.606 [°]; 3.35045 [Å]
Quartz (1)
30.922 [°]; 2.89192 [Å]
Dolomite (1)
33.478 [°]; 2.67673 [Å]
Dolomite (2)
35.253 [°]; 2.54597 [Å]
37.371 [°]; 2.40637 [Å]
Selected Pattern: Quartz, syn 00-046-1045
Residue + Peak List

Counts
400
100
0
Pak2_2.xrdml
24.027 [°]; 3.70384 [A] Plagioclase
26.674 [°]; 3.34210 [A] Quartz (1)
27.940 [°]; 3.19337 [A] Plagioclase (1)
30.939 [°]; 2.89059 [A] Dolomite (1)
33.547 [°]; 2.67143 [A] Dolomite (2)
35.290 [°]; 2.54334 [A]
37.339 [°]; 2.40837 [A]
10
20
30
Position [°2Theta]
Selected Pattern: Quartz, syn 00-046-1045
Residue + Peak List

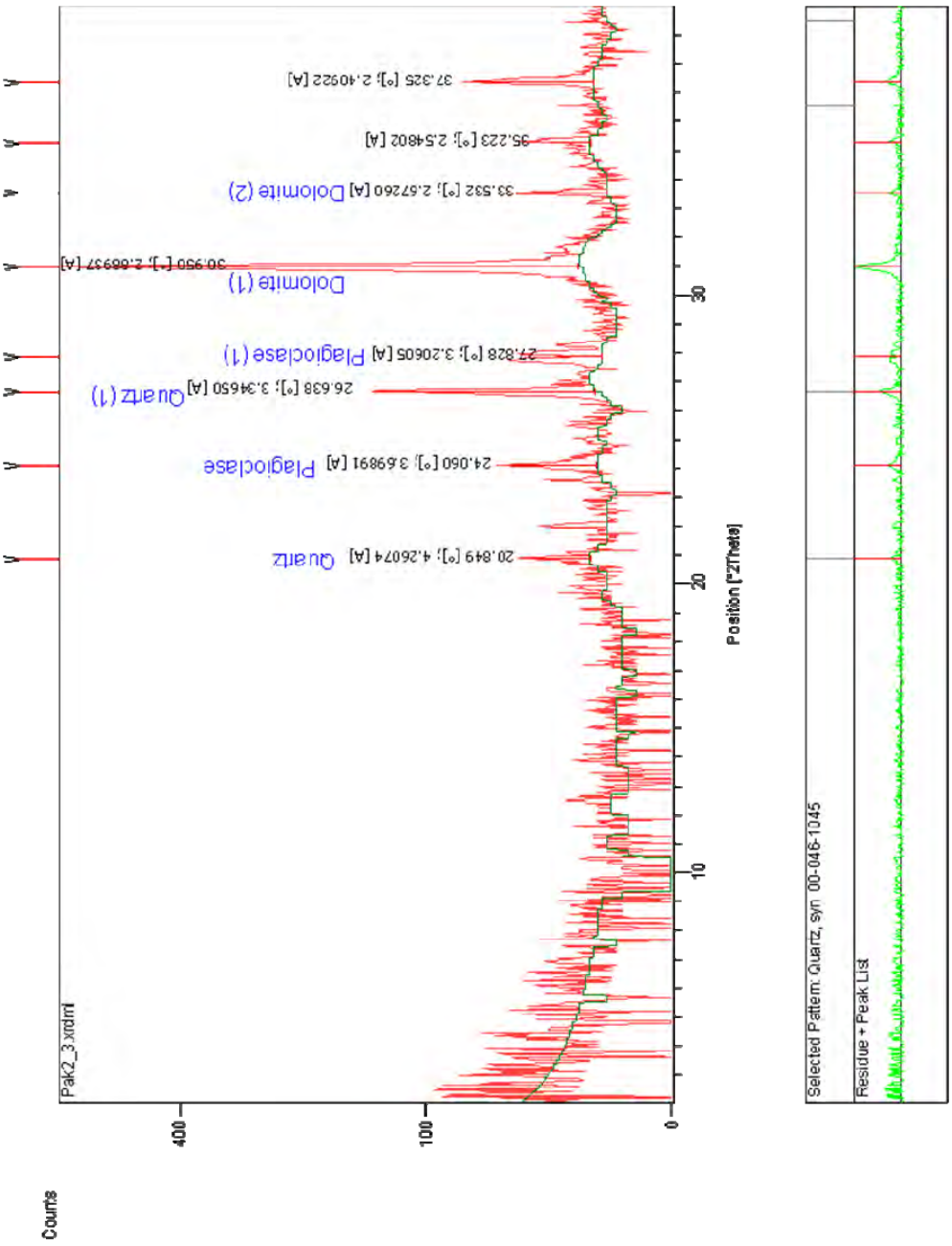
Counts
400
100
0
Pak2_3.xrdml
10
20
30
Position [°2Theta]
20.849 [°]; 4.26074 [A]
Quartz
24.060 [°]; 3.69891 [A]
Plagioclase
26.638 [°]; 3.34650 [A]
Quartz (1)
27.828 [°]; 3.20605 [A]
Plagioclase (1)
30.950 [°]; 2.88937 [A]
Dolomite (1)
33.532 [°]; 2.67260 [A]
Dolomite (2)
35.223 [°]; 2.54802 [A]
37.325 [°]; 2.40522 [A]
Selected Pattern: Quartz, syn 00-046-1045
Residue + Peak List

1. Isotope data

Appendix Section 5 contains isotope stable carbon and oxygen isotope data for the tubular concretions from additional locations (Table A5.4)

Table A5.4. Stable carbon and oxygen isotope data for additional samples

Sample	$\delta^{13}C$ ‰ PDB calcite	$\delta^{18}O$ ‰ PDB calcite	$\delta^{13}C$ ‰ PDB dolomite	$\delta^{18}O$ ‰ PDB dolomite	% dolomite	% calcite
GAc1-1	6.98	4.08	10.59	4.63	87	13
GAc1-2	5.01	4.57	10.11	5.28	80	20
GAc1-3	6.94	4.54	11.09	5.46	89	11
GAc3-1	10.12	5.05	9.95	5.12	95	5
GAc3-2			8.95	5.26	100	0
GAc3-3			9.1	5.36	100	0
Dan1-1	-9.70	4.89	-8.47	5.02	96	4
Dan1-2	-19.18	3.80	-12.26	4.58	73	27
Dan1-3	-10.83	3.64	-8.66	4.69	76	24
PAK2-3	7.66	4.54			0	100
Mdi-1	-0.055	-3.31			0	100
Mdi-2	0.41	-1.29			0	100
Mdi-3	-1.1	-4.28			0	100
MBE1-1	-1.1	-1.4			0	100
MBE1-1b	-0.32	-3.05			0	100
MBE1-2	-0.33	-3.13			0	100
MBE2-1	-0.47	-3.16			0	100
MBE2-1b	-0.2	-3.05			0	100
MBE2-2	-0.39	-3.24			0	100
MBE3-1	-0.19	-3.23			0	100
MBE3-2	-0.3	-4.13			0	100
MBE3-3	-0.23	-3.71			0	100
MBEA-1	-0.31	-3.17			0	100
MBEA-2	-0.52	-3.3			0	100
MBEA-3b	-0.55	-3.28			0	100
MBc2_1	-4.11	-6.69			0	100
MBc2_2	-4.26	-6.93			0	100
MBc2_3	-4.34	-6.88			0	100
MB_Seep	-36.56	-4.30			0	100
Kno#-1	-27.93	-1.06			0	100
Kno#-2	-25.8	-2.38			0	100
Kno#-3	-22.9	-4.27			0	100
KZ8314-1	-32.12	5.43			0	100
KZ8314-2	-32.78	5.39			0	100
KZ8314-3	-33.32	5.39			0	100
T53P51g	-42.41	-3.22			0	100

Appendix 6

Master sample list and analysis

1. The master sample list (Table A6.1) contains a list lab analysis for each sample.

Table A6.1. Laboratory analysis for samples

Location	Sample number	XRD	Isotopes	Petrography	ICPMS	XRF	Lipids
Taranaki							
	TMc1_1	X	X	X	X		X
	TMc1_2	X	X		X		X
	TMc1_3	X	X	X	X		X
	TMf1_1	X	X	X	X	X	
	TMf1_2	X	X		X	X	X
	TMf1_3	X	X	X	X	X	
	TMf2_1	X	X		X	X	
	TMf2_2	X	X		X	X	
	TMf2_3	X	X	X	X	X	
	TWAf1_1	X	X				
	TWAf1_2	X	X				
	TWAf1_3	X	X				
	TOf1_1	X	X				
	TOf1-2	X	X				
	Tmcs1-1v	X	X				
	Tmcs1-2v	X	X				X
	Tmcs1-2h3h	X	X				
	Tmcs1-3c	X	X				
	T1	X	X		X		
	T2	X	X		X		
	T3	X	X		X		
	T4	X	X		X		
	T5	X	X				X
	T6	X	X				
	T7	X	X		X		
	T8	X	X		X		
	T9	X	X		X		
	T10	X	X				
	T11	X	X				
	Tm-host	X	X				
	PAc2-1	X	X				
	PAc2-2	X	X				
	PAc2-3	X	X				
	PAc3-1	X	X				
	PAc3-2	X	X				
	PAc3-3	X	X				
Taranaki (Schellengberg, 2002 data)							
	TMcP71-z1		X				
	TMcP71-z2		X				
	TMcP71-z3		X				
	TMcP72-4-X		X				
	TMcP72-1		X				
	TMcP72-2		X				
	TMcP72-3		X				

Table A6.1 continued.

Location	Sample number	XRD	Isotopes	Petrography	ICPMS	XRF	Lipids
	TMcP72-4		X				
	TMcP72-5		X				
	TMcP72-z1		X				
	TMcP72-z2		X				
	TMcP72-z3		X				
	TMcP73-1		X				
	TMcP73-2		X				
	TMcP73-3		X				
	TMcP73-4		X				
	TMcP73-3b		X				
	TMcP73-2b		X				
	TMcP73-1b		X				
	TMcP73-z1		X				
	TMcP73-z2		X				
	TMcP81-2		X				
	TMcP81-3		X				
	TMcP81-4		X				
	TMcP81-z1		X				
	TMcP81-z2		X				
	TMcP81-z3		X				
	TMcP81-z4		X				
	TMcP81-z5		X				
	TMcP81-5b		X				
	TMcP81-3b		X				
	TMcP81-2b		X				
	TMcP81-1b		X				
	TMcP83_z1		X				
	TMcP83_z2		X				
	TMcP83_z3		X				
	TMcP9-1		X				
	TMcP9-2		X				
	TMcP9-3		X				
	TMcP9-4		X				
	TMcP9-5		X				
	TMcP9-6		X				
	TMcP9-7z		X				
	TMcP9-z1		X				
	TMcP9-z2		X				
	TMcP9-z3		X				
	TMcP9-z4		X				
	TMcP9-z5		X				
	TMcP9-z6		X				
	TMcP10-1		X				
	TMcP10-2		X				
	TMcP10-3		X				
	TMcP10-4		X				

Table A6.1 continued.

Location	Sample number	XRD	Isotopes	Petrography	ICPMS	XRF	Lipids
	TMcP10-5		X				
	TMcP10-5b		X				
	TMcP10-3b		X				
	TMcP10-1b		X				
	TMcP1-1		X				
	TMcP1-2		X				
	TMcP1-3		X				
	TMcP1-4		X				
	TMcP1-5		X				
	TMcP1-6		X				
	TMcP1-7		X				
	TMcP1-z1		X				
	TMcP1-z2		X				
	TMcP1-z3		X				
	TMcP3-1		X				
	TMcP3-2		X				
	TMcP3-3		X				
	TMcP3-4		X				
	TMcP3-5		X				
	TMcP3-6		X				
	TMcP3-7		X				
	TMcP3-9		X				
	TMcP3-10		X				
	TMcP3-11		X				
	TMcP5-1		X				
	TMcP5-2		X				
	TMcP5-3		X				
	TMcP5-4		X				
	TMcP5-z1		X				
	TMcP5-z2		X				
	TMcP6-1		X				
	TMcP6-2		X				
	TMcP6-3		X				
	TMcP6-4		X				
	TMcP6-5		X				
	TMcP6-6		X				
	TMcP6-7		X				
	TMcP6-8		X				
	TMcP6-4b		X				
Cape Turnagain							
	124.1	X	X				
	124.2	X	X				
	209.1	X	X				
	352.1	X	X				

Table A6.1 continued.

Location	Sample number	XRD	Isotopes	Petrography	ICPMS	XRF	Lipids
	372.1	X	X				
	489.1	X	X				
	489.2	X	X				
	489.3	X	X				
	489.4	X	X				
	490.1a	X	X				
	490.1b	X	X				
	490.2	X	X	X			
	490.4	X	X				
	490.5	X	X	X			
	530.1	X	X				X
	682.1a	X	X				
	682.2a; 682.2b	X	X	X			
	682.2c	X	X				
	841.1a,b	X	X				
	CTc1_1	X	X				
	CTc1_2	X	X				
	CTc1_3	X	X				
	CTc2_1	X	X				
	CTc2_2	X	X				
	CTc2_3	X	X				
	CTf3_1	X	X				X
	CTf3_2	X	X				X
	CTf3_3	X	X				X
	CTf4_1	X	X				X
	CTf4_2	X	X				X
	CTf4_3	X	X				X
East Cape							
	ECD-1	X	X	X	X	X	
	ECD-2	X	X		X		X
	ECD-3	X	X		X	X	
	ECD-4	X	X	X	X	X	
	ECD-5	X	X	X	X	X	
	ECD-6	X	X	X	X	X	X
	FP1	X	X	X	X	X	X
	FP2	X	X	X	X	X	X
	FP3	X	X		X	X	X
	FP4	X	X	X	X	X	
	FP5	X	X		X		X
	FP6	X	X		X		
	EC3-1	X	X		X		
	EC3-2	X	X		X		
	EC3-3	X	X		X		

Table A6.1 continued.

Location	Sample number	XRD	Isotopes	Petrography	ICPMS	XRF	Lipids
	EC2180-1	X	X				
	EC2180-2	X	X				
	EC2280-1	X	X				
	EC2280-2	X	X				
	EC2280-3	X	X				
	EC2280-4	X	X				
	EC2280-5	X	X				X
	EC2301-1	X	X				
	EC2301-2	X	X				
	EC2301-3	X	X				
	EC2321-h	X	X				
	EC2631-1	X	X				
	EC2631-2	X	X				
	EC2631-3	X	X				
	EC2631-h	X	X				
	EC2347-1h	X	X				
	EC2347-2h	X	X				
	EC2347-3h	X	X				
	EC2347-4h	X	X				
	EC2347-5h	X	X				
	EC2347-1v	X	X				
	EC2347-2v	X	X				
	EC2347-4v	X	X				
	EC2347-5v	X	X				
	EC2476-1	X	X				
	EC2476-2	X	X				
	EC2476-3	X	X				
	ECT	X	X	X			
	EC2694-1	X	X				
	EC2657-h	X	X				
	EC2836-1	X	X				
	EC2836-2	X	X				
	EC2841-1	X	X				
	EC2862-1	X	X				
	EC2862-2	X	X				
	EC2862-3	X	X				
	EC2862-4	X	X				
	EC2862-5	X	X				
	TK 1	X	X				
	TK 2	X	X				
	TK 3	X	X				
	TK 4	X	X				
	TK 5	X	X				
	TK 6a	X	X				
	TK 6b	X	X				

Table A6.1 continued.

Location	Sample number	XRD	Isotopes	Petrography	ICPMS	XRF	Lipids
	TK 7a	X	X				
	TK 7b	X	X				
	TK 7	X	X				
	TK 8	X	X				
	TK 9a	X	X				
	TK 9b	X	X				
	TK 10a	X	X				
	TK 10b	X	X				
Rocky Knob							
	RK48		X				
	RK49		X				
	RK50		X				
	RK54a		X	X			
	RK54b		X	X			
	RK57a		X	X			
	RK57b		X	X			
	RK57c		X	X			
	RK57d		X	X			
	RK57e		X	X			
	RK59a		X				
	RK59b		X				
	RK60a		X	X			
	RK60b		X	X			
	RK60c		X	X			
	RK60d		X	X			
	RK60e		X	X			
	RK60f		X	X			
	RK61a		X	X			
	RK61c		X	X			
	RK61d		X	X			
	RK61f		X	X			
	RK62a		X				
	RK62b		X				
	RK62c		X				
	RK63a		X				
	RK63b		X				
	RK63c		X				
	RK63d		X				
	RK63e		X				
	RK64a		X	X			
	RK64b		X	X			
	RK64c		X	X			
	RK65-1a		X	X			
	RK65-1b		X	X			

Table A6.1 continued.

Location	Sample number	XRD	Isotopes	Petrography	ICPMS	XRF	Lipids
	RK65-1c		X	X			
	RK65-2a		X				
	RK65-2b		X				
	RK65-2c		X				
	RK65-3a		X				
	RK65-3b		X				
	RK65-3c		X				
	RK65-4a		X	X			
	RK65-4b		X	X			
	RK65-4c		X	X			
	RK65-5a		X				
	RK65-5b		X				
	RK65-6a		X				
	RK65-6b		X				
	RK1-1	X	X		X		
	RK1-2	X	X		X		
	RK1-2	X	X		X		
	RK2-1	X	X		X		X
	RK2-2	X	X		X		X
	RK2-3	X	X		X		X
	RK3	X	X		X		X
	RK66		X				
	RK67		X				
	RK68		X				
	RK69		X				
	RK70		X				
	RK71		X				
	RK72		X				
	RK73		X				
	RK74		X				
	RK75		X				
Additional sites							
Gentle Annie	GAc1-1	X	X				
	GAc1-2	X	X				
	GAc1-2	X	X				
	GAc2-1	X	X				
	GAc2-2	X	X				
	GAc2-3	X	X				
Waihau	Dan1-1	X	X				
	Dan1-2	X	X				
	Dan1-3	X	X				
Mahia	Mdi-1	X	X				
	Mdi-2	X	X				
	Mdi-3	X	X				
	MBE1-1	X	X				

Table A6.1 continued.

Location	Sample number	XRD	Isotopes	Petrography	ICPMS	XRF	Lipids
	MBE1-2	X	X				
	MBE1-3	X	X				
	MBE2-1	X	X				
	MBE2-2	X	X				
	MBE2-3	X	X				
	MBE3-1	X	X				
	MBE3-2	X	X				
	MBE3-3	X	X				
	MBEA-1	X	X				
	MBEA-2	X	X				
	MBEA-3	X	X				
	MBc2-1	X	X				
	MBc2-2	X	X				
	MBc2-3	X	X				
	MB Seep	X	X				
Unknown	Kno#-1	X	X				
location	Kno#-2	X	X				
	Kno#-3	X	X				
	KZ8314-2	X	X				
		X	X				
		X	X				
	T53P51g	X	X				

Appendix 7

Methodology

Methodology table of contents

1. Photomicrographs

A selection of subsamples were cut and mounted on glass slides for standard thin section analysis. No staining or impregnation was done on the thin sections. Further thin sections were not produced as the samples were predominately micritic carbonate within fine grained siliciclastics.

2. Cathodoluminesence

Cathodoluminesence was conducted on a Cambridge Instrument Technologies Ltd. C1TL MK5-1. Typical CL operating conditions: current ~450 µA; voltage ~ 16 to 20 kV.

3. XRD

Powdered samples were run on a Philips X'Pert System. Quartz standards were run before each session. Initial samples were run from 0 to 40˚ 2θ. XRD analysis was undertaken to determine carbonate mineralogy for isotope analysis, and subsequent samples were run from 20 to 40˚ 2θ.

4. SEM

For SEM analysis, samples were broken into small (millimetre) sized fragments, mounted on a metal disk with carbon tape, and coated with platinum in a Hitachi E-1030 Ion sputter coater. The samples were analysed on a Hitachi S-4100 Field Emission scanning electron microscope with EDS capabilities.

5. Stable carbon and oxygen isotopes

5.1 Analysis at University of Waikato

Calcite and dolomite 'pure' samples (as determined by XRD) were reacted in a Europa CAPS (Carbonate Automatic Preparation System) using the individual acid dosing or 'drip' method, in which a small amount of acid is allowed to drip onto the sample, the product being frozen out.

The samples are loaded into individual reaction vessels, which in turn are placed in a 24-position carousel housed in an oven kept at 70ºC. Each sample is analysed sequentially. The vessel is evacuated and a predetermined dose of orthophosphoric acid is dispensed. While the sample is reacting the evolved CO_2 is frozen onto a dedicated cold finger, positioned close to the mass spectrometer inlet, to minimise sample transfer time. Water is removed during the reaction by passing the CO_2 through a loop that is maintained at -90°C.

After the reaction is completed (30 minutes for calcite and 2 hours for dolomite), the sample CO_2 is introduced to a Europa Geo 20-20, where gas pressures are balanced, and the sample gas run against an internal reference gas. This reference gas is calibrated daily by running an internal standard, WCS against it. WCS was calibrated against NBS-19, and cross-checked against NBS-20. External precision for replicate analyses of WCS is better than 0.05‰ for both carbon and oxygen.

Carbon 13 and oxygen 18 isotope values are presented in the usual delta (δ) notation, normalised, and expressed in per mille (‰), relative to Vienna Peedee belemnite, VPDB (Coplen, 1988, 1994).

In partially dolomitized rocks, calcite and dolomite are difficult to physically separate for stable isotope analysis. In this study, a variation of the differential phosphoric acid extraction method (Al-Aasm et al., 1990; Kyser et al., 2002) was used to derive values for calcite-CO_2 and dolomite-CO_2. The uncertainty of this method mainly comes from different degrees of cross mixing of gases derived from carbonate phases. Other uncertainties come from the time duration adopted

for acid extraction of calcite-CO_2 or dolomite-CO_2, as well as the grain size of the sample analyzed. These are often different in different studies (see summary in Yui and Gong, 2003), showing that explicit comparison among data sets is difficult.

As for the 'pure' samples above, all samples were reacted using the individual acid bath technique in a Europa CAPS, and the CO_2 produced was analysed in a Europa Geo 20-20. Samples were ground and placed in individual reaction vials. Calcite-CO_2 and dolomite-CO_2 were determined in two separate reactions (10 minutes for calcite, 2 hours for dolomite), due to restrictions on gas transfer rates induced by the geometry of the mass spectrometer inlet system. Replicate analyses using this technique are usually within 0.1 per mille for both $\delta^{13}C$ and $\delta^{18}O$. Standard corrections were applied, but no correction was applied for any differences in the fractionation of ^{18}O as a result of the dissolution of dolomite and calcite by phosphoric acid. Again, results are reported as per mille $\delta^{18}O$ and $\delta^{13}C$ relative to V-PDB. Comparisons of $\delta^{18}O$ to other studies where corrections for composition were made can be done by adding approximately 0.8 per mille (Vahrenkamp and Swart, 1994; Kyser et al., 2002), although Zheng (1999) calculates a difference of only 0.56 per mille.

References:

Al-Aasm IS, Taylor BE, South B, 1990. Selective stable isotope analysis of multiple carbonate samples using selective acid extraction. Chem. Geol., Isot. Geoscience Section, 80, 119-125.

Coplen, T B, 1988: Normalization of oxygen and hydrogen isotope data. Chemical Geology (Isotope Geoscience Section), 72, 293-297.

Coplen, T B, 1994: Reporting of stable hydrogen, carbon, and oxygen isotopic abundances. Pure Applied Chemistry, 66, 273-276.

Kyser TK, James NP, Bone Y, 2002. Shallow burial dolomitization and dedolomitization of Cenozoic cool-water limestones, southern Australia: geochemistry and origin. Journal of Sedimentary Research, 72, 146-157.

Vahrenkamp VC, Swart PK, 1994. Late Cenozoic dolomites of the Bahamas: metastable analogues for the genesis of ancient platform dolomites. In: Purser B, Tucker M, Zenger D (Eds.), Dolomites: A Volume in Honor of Dolomieu. International Association of Sedimentology Special Publication, 21, 133-153.

Yui T-F, Gong S-Y, 2003. Stoichiometry effect on stable isotope analysis of dolomite. Chemical Geology, 201, 359-368.

Zheng Y-H, 1999. Oxygen isotope fractionation in carbonate and sulphate minerals. Geochemistry Journal, 33, 109-126.

5.2 Analysis at Queen's University - Belfast

Depending on the % fraction of calcite or dolomite, a relevant amount was placed in a 6 mL round bottomed borosilicate vial and sealed with a lid and septum - both supplied by LabCo. If dealing with 100% calcite or dolomite these vials were placed in a temperature controlled tray at 50˚C and left for at least 2.5 hours. After this time, the vials were automatically flushed with helium through a needle for 1 minute and then 100% + H_3PO_4 was dripped onto the samples (manually injecting about 0.2 mL). Once acid injection was complete the samples were left overnight. The difference in protocol comes with calcite/dolomite mixes whereby a relevant amount of sample was placed into a vial depending on the fraction of each mineral. For calcite the samples were reacted for 30 minutes at room temperature and the vials then taken to the mass spec for measurement. For dolomite analysis, a separate vial was used and after 30 minutes of acid injection, the samples were re-injected with Helium to remove the CO_2 generated from the calcite fraction. The temperature of the tray was raised to 50˚C and left overnight for complete dolomite reaction. The next day the samples were removed from the tray and left to cool for at least 2.5 hours before analysis.

6. XRF

Trace element abundances were determined on pressed pellets using a polarizing energy dispersive X-Ray fluorescence (XRF) spectrometer (SPECTRO X-LAB 2000) at the University of Waikato.

7. ICP/MS

Selected samples were analysed for major and trace elements on an ICP/MS. Carbonate digestion and analysis was completed via the following method:

Apparatus:

50 ml beaker
100 ml vol. flask
Filter paper, Whatman No. 42 size 9 cm
Distilled and deionised water for ICP
100 ml plastic bottle for storage

Procedure:

1) Dry filter at 40°C and weigh
2) Weigh 0.04 g powdered sample into a 50 ml beaker, record weight of sample.
3) Add 8 ml of 8% v/v (1M HCl), swirl occasionally during digestion to mix solution and insoluable material.
4) Digest like this for approx 10-30 minutes, but no more than 30 minutes.
5) Carefully pour the contents of beaker through filter paper into a 100 ml volumetric flask, rinse beaker three times this way, until you are sure that all material has been washed out of the beaker. Use distilled deionised water for this.
6) Fill to 100 ml meniscus line, shake and transfer to storage flask.
7) Dry filter at 40°C again and reweigh to calculate insoluble fraction of carbonate material.

Standards:

The standards are to be made up using spectrosol standards, with the addition of 1M HCl to keep the same matrix as the samples.

Standard Range:

Ca	0 – 100 ppm
Fe	0 – 25 ppm
Mg	0 – 25 ppm
Mn	0 – 10 ppm
Na	0 – 50 ppm
Sr	0 – 10 ppm

Analysis:

The samples were analysed on an ICP/MS Elan 6100 DRCII made by Perkin Elmer Sciex. Samples were read on the ICP with a full range of standards, run a middle standard after every ten samples to check for drift, and include duplicates in every ten as well.

Appendix 8

New Zealand Geologic Timescale

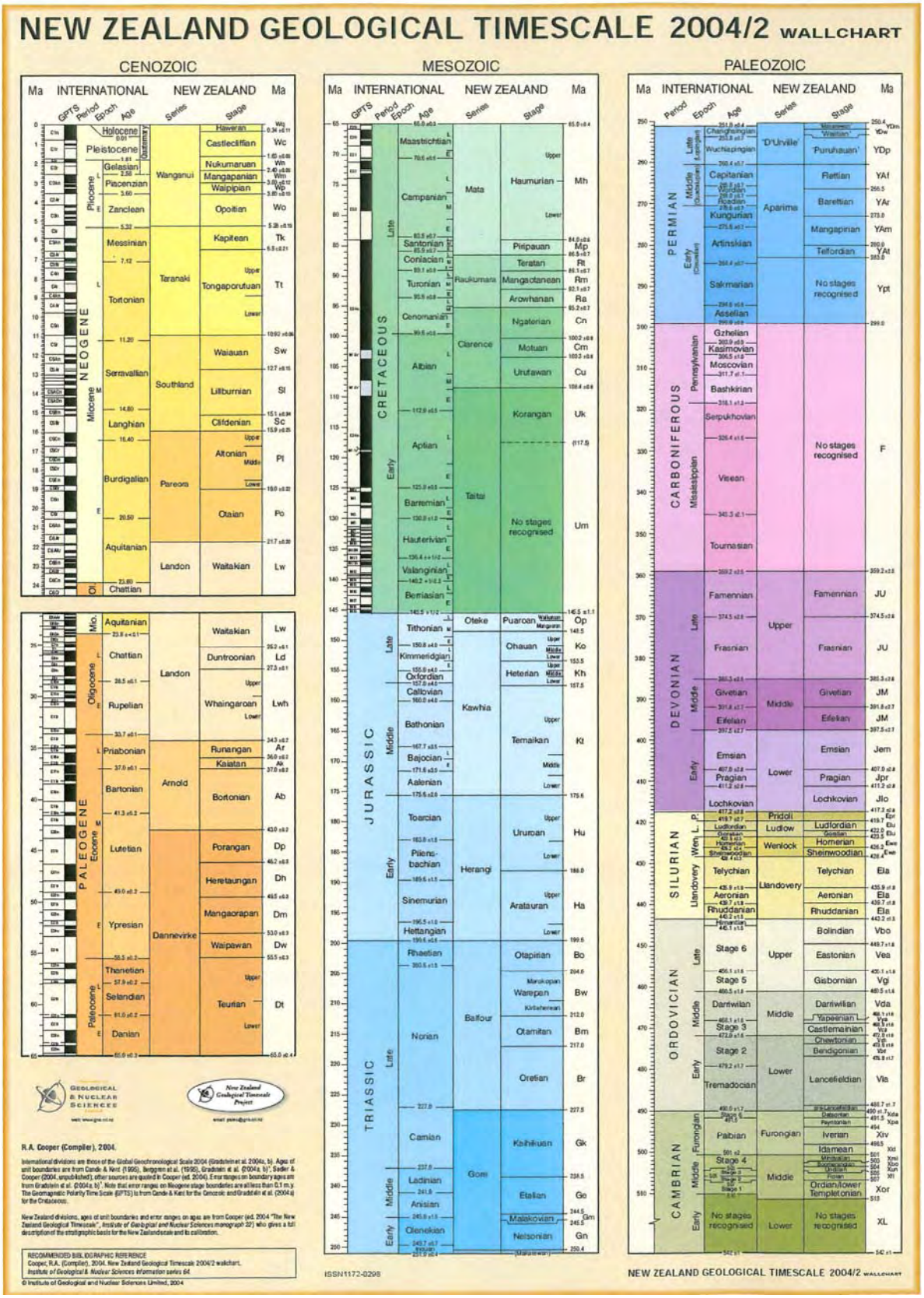
NEW ZEALAND GEOLOGICAL TIMESCALE 2004/2 WALLCHART
CENOZOIC
MESOZOIC
PALEOZOIC
Ma
INTERNATIONAL
NEW ZEALAND
GPTS
Period
Epoch
Age
Series
Stage
Ma
Holocene
Pleistocene
Gelasian
Piacenzian
Zanclean
Messinian
Tortonian
Serravallian
Langhian
Chattian
Aquitanian
Burdigalian
Waitakian
Duntroonian
Whaingaroan
Runangan
Kaiatan
Bortonian
Porangan
Heretaungan
Mangaorapan
Waipawan
Teurian
Haumurian
Piripauan
Mangaotanean
Arowhanan
Ngaterian
Motuan
Urutawan
Korangan
Taitai
No stages recognised
Tithonian
Kimmeridgian
Oxfordian
Callovian
Bathonian
Bajocian
Aalenian
Toarcian
Pliensbachian
Sinemurian
Hettangian
Rhaetian
Norian
Carnian
Ladinian
Anisian
Olenekian
Induan
Changhsingian
Wuchiapingian
Capitanian
Wordian
Roadian
Kungurian
Artinskian
Sakmarian
Asselian
Gzhelian
Kasimovian
Moscovian
Bashkirian
Serpukhovian
Visean
Tournasian
Famennian
Frasnian
Givetian
Eifelian
Emsian
Pragian
Lochkovian
Pridoli
Ludlow
Wenlock
Telychian
Aeronian
Rhuddanian
Hirnantian
Stage 6
Stage 5
Darriwilian
Stage 3
Stage 2
Tremadocian
Stage 4
Paibian
Furongian
Ordian/lower Templetonian
Lower
Middle
Upper
Permian
Carboniferous
Devonian
Silurian
Ordovician
Cambrian
Cretaceous
Jurassic
Triassic
Paleogene
Neogene
Quaternary
Wanganui
Taranaki
Southland
Landon
Arnold
Dannevirke
Mata
Raukumara
Clarence
Kawhia
Herangi
Ballour
Gore
Oteke
Waitakian
Otaian
Pareora
Aparima
D'Urville
Murihiku
Waipapa
Brook Street
Torlesse
Rakaia
Pahau
Haast
Rangitata
Pegasus
Bowen
Esk Head
Hikurangi
Wairarapa
Kaikoura
Marlborough
Median Batholith
Challenger
Reefton
Buller
Takaka
Lachlan
New England
Gondwana
Tuhua
Mayor Island
Coromandel
Whangarei
Northland
Chatham Rise
Campbell Plateau
Auckland
Challenger Plateau
Norfolk Ridge
Lord Howe Rise
Three Kings Ridge
Reinga Ridge
Colville Ridge
Hikurangi Plateau
Manihiki Plateau
Ontong Java Plateau
Louisville Ridge
Tonga-Kermadec Ridge
Lau Basin
Fiji Plateau
New Caledonia
Norfolk Ridge
Lord Howe Rise
Three Kings Ridge
Reinga Ridge
Colville Ridge
Hikurangi Plateau
Manihiki Plateau
Ontong Java Plateau
Louisville Ridge
Tonga-Kermadec Ridge
Lau Basin
Fiji Plateau
New Caledonia
GEOLOGICAL & NUCLEAR SCIENCES
New Zealand Geological Timescale Project
R.A. Cooper (Compiler), 2004.
RECOMMENDED BIBLIOGRAPHIC REFERENCE
Cooper, R.A. (Compiler), 2004. New Zealand Geological Timescale 2004/2 wallchart.
Institute of Geological & Nuclear Sciences Information series 64.
© Institute of Geological and Nuclear Sciences Limited, 2004
ISSN1172-0298
NEW ZEALAND GEOLOGICAL TIMESCALE 2004/2 WALLCHART

Appendix 9

Glossary of seep terminology

Glossary

The glossary defines seep related terms used in this study for clarification.

Bladed	Descriptive of a long narrow crystal with a knife shape.
Blocky	Equant to subequant crystals with subhedral form.
Cement	Intergranular precipitate binding grains together.
Concretion	Cemented body of rock within an otherwise uncemented host rock. See cement.
Dolomite	$CaMgCO_3$ with Mg content > 50 mol %. Most of the samples in this study have Mg contents < 50 mol % and therefore are protodolomites. However, all samples >40 mol % Mg are referred to as dolomites in the text for ease of discussion (clarified in petrographic Sections of the Chapters). See protodolomite.
Fibrous	Habit in which the crystals are shaped like threads.
HMC	High-Mg calcite (>12% mol $MgCO_3$).
Micrite	Microcrystalline (<0.004 mm) to cryptocrystalline calcite (or dolomite in this study) making up matrix or cement.
Minus cement porosity	(MCP) Volume of cement within the pore spaces of a rock which cements grains together. Equals the intergranular volume (IGV) minus the volume of cement. In this study, the cement is composed entirely of carbonate, therefore MCP equals the volume of carbonate cement.
Protodolomite	$CaMgCO_3$ with Mg content between 40 and 50 mol %. However, all samples >40 mol % Mg are referred to as dolomites in the text for ease of discussion (clarified in petrographic Sections of the Chapters). See dolomite.

Seep carbonate	Rock formed at the seafloor (or within centimetres of burial) from methane rich fluids. Composed of carbonate precipitates (primarily aragonite and calcite). The carbonate generally precipitates between the interparticle spaces of siliciclastic sediment as cement and therefore may be classified as a siliciclastic rock. However, carbonate volumes are greater than 50% (for most samples) and therefore may also be classified as a carbonate rock. This thesis does not favour either classification, but notes that the terminology may be confusing. Therefore, the term seep carbonate is used as opposed to limestone or calcareous mudstone to emphasise that these deposits are compositionally and texturally different than traditional definitions of siliciclastic and carbonate rocks.
Tubular concretion	Tubular shaped carbonate concretion (see concretion) with > 50% (generally) carbonate. The concretions are composed of carbonate cement between interparticle spaces of siliciclastic sediments, confirming subsurface formation within the encased siliciclastic sediments (mudstone in this study).

Appendix 10

References

Adams, J.H., 1910. The geology of the Whatatutu subdivision, Raukumara division, Poverty Bay. New Zealand Geological Survey Branch Bulletin 9 (new series), 1–48.

Aiello, I.W., Stakes, D.S., Kastner, M., Garrison, R.E., 1999. Carbonate vent structures in the Upper Miocene Santa Cruz Mudstone at Santa Cruz, California. In: Garrison, R.E., Aiello, I.W., Moore, J.C. (Eds.), Late Cenozoic Fluid Seeps and Tectonics Along the San Gregorio Fault Zone in the Monterey Bay Region, California. Pacific Section AAPG, v. GB-76, pp. 35-52.

Aiello, I.W., Garrison, R.E., Moore, J.C., Kastner, M., Stakes, D.S., 2001. Anatomy and origin of carbonate structures in a Miocene cold-seep field. Geology, 29, 1111-1114.

Aiello, I.W., 2005. Fossil seep structures of the Monterey Bay region and tectonic/structural controls on fluid flow in an active transform margin. Palaeogeography, Palaeoclimatology, Palaeoecology, 227, 124-142.

Al-Aasm, I.S., Taylor, B.E., South B., 1990. Selective stable isotope analysis of multiple carbonate samples using selective acid extraction. Chemical Geology, Isotope Geoscience Section, 80, 119-125.

Aloisi, G., Pierre, C., Rouchy, J.M., Foucher, J.P., Woodside, J., MEDINAUT Scientific Party, 2000. Methane-related authigenic carbonates of eastern Mediterranean Sea mud volcanoes and their possible relation to gas hydrate destabilisation. Earth and Planetary Science Letters, 184, 321-338.

Aloisi, G., Pierre, C., Rouchy, J., Faugères, J., 2002. Isotopic evidence of methane-related diagenesis in the mud volcanic sediments of the Barbados Accretionary Prism. Continental Shelf Research, 22, 2355-2372.

Ballance, P.F., Gregory, M.R., Gibson, G.W., Chaproniere, G.C.H., Kadar, A., Sameshima, T., 1984. A late Miocene to early Pliocene upper slope to shelf sequence in calcareous fine sediment from the Pacific margin of New Zealand. In: stow, D.A.V., Piper, D.J.P., (Eds.), Fine sediments: Deep Water Processes and Facies. Geological Society, London. Pp. 331-342.

Ballance, P.F., 1993. The New Zealand Neogene forearc basins. In: Ballance, P.F. (Ed.), South Pacific Sedimentary Basins: Sedimentary Basins of the World, 2. Amsterdam, Elsevier Publishers B.V. Pp. 93-110.

Barnes, P.M., Lamarche, G., Bialas, J., Henrys, S., Pecher, I. Netzeband, G.L., Greinert, J., Mountjoy, J.J., pedley, K., Crutchley, G., in review. Tectonic and geological framework for gas hydrates and cold seeps on the Hikurangi subduction Margin, New Zealand. Submitted to Marine Geology, special publication, methane seeps.

Barry, J.P., Greene, H.G., Ornage, D.L, Baxter, C.H., Robison, B.H., Kochevar, R.E., Nybakken, J.W., Reed, D.L., McHugh, C.M., 1996. Biologic and geologic characteristics of cold seeps in Monterey Bay, California. Deep Sea Research, 45, 1739-1762.

Belenkaia, I., 2000. Gas-derived carbonates: reviews in morphology, mineralogy, chemistry and isotopes (data collected during the TTR programme cruises during 1993-1999). In Abstracts of the Sixth International Conference on Gas in Marine Sediments. St. Petersburg, VNIOkeangeologia, pp. 9-10 (abstract).

Beu, A.G., Maxwell, P.A., 1990. Cenozoic mollusca of New Zealand. New Zealand Geological Survey Paleontological Bulletin, 58, 1–518.

Beu, A. G., 1995. Pliocene limestones and their scallops: lithostratigraphy, pectinid biostratigraphy and paleogeography of Eastern North Island late Neogene limestone. Institute of Geological and Nuclear Sciences monograph, 10, 243 pp.

Bjørlykke, K., 1998. Clay mineral diagenesis in sedimentary basins – a key to the prediction of rock properties. Examples from the North Sea Basin. Clay Minerals, 33, 15-34.

Boetius, A., Ravenschlag, K., Schubert, C.J., Rickert, D., Widdel, F., Giesecke, A., Amann, R., Joergensen, B.B., Witte, U., Pfannkuche, O., 2000. A marine microbial consortium apparently mediating anaerobic oxidation of methane. Nature, 407, 623-626.

Boetius, A., Suess, E., 2004. Hydrate Ridge: a natural laboratory for the study of microbial life fuelled by methane from near-surface gas hydrates. Chemical Geology, 205, 291-310.

Boggs, S., 1992. McConnin, R.A., (Ed.), Petrology of Sedimentary Rocks. Macmillian Publishing Company, New York. 707 pp.

Bohrmann, G., Greinert, J., Suess, E., Torres, M., 1998. Authigenic carbonates from the Cascadia subduction zone and their relation to gas hydrate stability. Geology, 26, 647-650.

Bouriak, S., Vanneste, M., Saoutkine, A., 2000. Inferred gas hydrates and clay diapirs near the Storegga Slide on the southern edge of the Vøring Plateau, offshore Norway. Marine Geology, 163, 125-148.

Bromley, R.G., Curran, H.A., Frey, R.W., Gutscheck, R.G., Suttner, L.J., 1975. Problems in interpreting unusually large burrows. In: Frey, R.W. (Ed.), The Study of Tracefossils. Springer-Verlag, New York., Pp. 351-376.

Campbell, K.A., Bottjer, D.J., 1993. Fossil cold seeps (Jurassic-Pliocene) along the convergent margin of western North America. National Geographic Research and Exploration, 9, 326-343.

Campbell, K.A., Farmer, J.D., Des Marais, D., 2002. Ancient hydrocarbon seeps from the Mesozoic convergent margin of California: carbonate geochemistry, fluids and palaeoenvironments. Geofluids, 2, 63-94.

Campbell, K.A., 2006. Hydrocarbon seep and hydrothermal vent paleoenvironments and paleontology: Past developments and future research directions. Palaeogeography, Palaeoclimatology, Palaeoecology, 232, 362-407.

Campbell, K.A., Francis, D.A., Collins, M., Gregory, M.R., Nelson, C.S., Greinert, J., Aharon, P., 2008. Hydrocarbon seep-carbonates of a Miocene forearc (East Coast Basin), North Island, New Zealand. Sedimentary Geology, 204, 83-105.

Campbell, K.A., Nelson, C.S., Alfaro, A.C., Boyd, S., Greinert, J., Nyman, S., Grosjean, E., Logan, G.A., Gregory, M.R., Cooke, S., Linke, P., Milloy, S., Wallis, I., in review. Geological imprint of methane seepage on the seabed

and biota of the convergent Hikurangi Margin, New Zealand: initial results from core and grab carbonates. Submitted to Marine Geology special publication: methane seeps.

Campbell, K.A., Nelson, C.S., Alfaro, A.C., Boyd, S., Greinert, J., Nyman, S., Grosjean, E., Logan, G.A., Gregory, M.R., Cooke, S., Linke, P., Milloy, S., Wallis, I., in review. Geological imprint of methane seepage on the seabed and biota of the convergent Hikurangi Margin, New Zealand: initial results from core and grab carbonates. Submitted to Marine Geology.

Cavagna, S., Clari, P., Martire, I., 1999. The role of bacteria in the formation of cold seep carbonates: geological evidence from Monferrato (Tertiary, NW Italy). Sedimentary Geology, 126, 253-270.

Chapman-Smith, M., Grant-Mackie, J.A., 1971. Geology of the Whangaparaoa area, eastern Bay of Plenty. New Zealand Journal of Geology and Geophysics, 14, 3-38.

Chaproniere, G.C.H., 1969. Geology of the Te Araroa area East Cape. Unpublished MSc. Thesis, University of Auckland.

Clari, P., Cavagna, S., Martire, L., Hunziker, J., 2004. A Miocene mud volcano and its plumbing system: A chaotic complex revisited (Monferrato, MW Italy). Journal of Sedimentary Research, 74, 662-676.

Clayton, C., 1992. Source volumetrics of biogenic gas generation. In Vially, R. (Ed.), Bacterial Gas. Paris, Editions Technip, pp. 191-204.

Cole, J.W., Lewis, K.B., 1981. Evolution of the Taupo-Hikurangi subduction system. Tectonophysics, 72, 1-21.

Coleman, D.D., Risatti, J.B., 1981. Fractionation of carbon and hydrogen isotopes by methane-oxidising bacteria. Geochimica et Cosmochimica Acta, 45, 1033-1037.

Collins, M., 1999. A biometric and taxonomic study of Miocene-age, hydrocarbon seep mussels from the East Coast of the North Island, New Zealand. MSc thesis, University of Auckland, Auckland, 67 pp.

Conti, S., Fontana, D., 1999. Chemosynthetic communities as fingerprints of submarine sliding-linking hydrocarbon seepage, Miocene deep-sea strata of

the Tuscan-Romagna Apennines, Italy. Palaeogeography, Palaeoclimatology, Palaeoecology, 227, 176-190.

Conti, S., Fontana, D., Gubertini, A., Sighinolfi, G., Tateo, F., Fioroni, C., Fregni, P., 2004. A multidisciplinary study of middle Miocene seep-carbonates from the northern Apennine foredeep (Italy). Sedimentary Geology, 169, 1-19.

Conti, S., Fontana, D., 2005. Anatomy of seep-carbonates: Ancient examples from the Miocene of the northern Apennines (Italy). Palaeogeography, Palaeoclimatology, Palaeoecology, 227, 156-175.

Cooke, P.J., Nelson, C.S., Crundwell, M.P., 2008. Miocene isotope zones, paleotemperatures, and carbon maxima events at intermediate water-depth, Site 593, Southwest Pacific. New Zealand Journal of Geology and Geophysics, 51, 1-22.

Corliss, J.B., Dymond, J.R., Gordon, L.I. et al., 1979. Submarine thermal springs on the Galapagos Rift. Science, 203, 1073-1083.

Cowen, J.P., Wen, X., Popp, B.N., 2002. Methane in aging hydrothermal plumes. Geochimica et Cosmochimica Acta, 66, 3563-3571.

Crutchley, G.J., Gorman, A.R., Fohrmann, M., 2007. Investigation of the role of gas hydrates in continental slope stability west of Fiordland, New Zealand. New Zealand Journal of Geology and Geophysics, 50, 357-364.

Curtis, C.D., 1978. Possible links between sandstone diagenesis and depth related geochemical reactions occurring in enclosing mudstones: Geological Society of London Journal, 135, 107-177.

Curtis, C.D., 1986. Mineralogic consequences of organic matter degradation in sediments: inorganic/organic diagenesis. In: Leggett, J.K., Zuffa, G.G., (Eds.), Marine Clastic Sedimentology. London, Graham and Trotman. Pp. 108-123.

Davidson, D. W., Leaist, D.J., Hesse, R., 1983. Oxygen-18 enrichment in water of a clathrate hydrate. Geochimica et Cosmochhimica Acta, 47, 2293-2295.

De Boever, E., Swennen, R., Dimitrov, L., 2006a. Lower Eocene carbonate cemented chimneys (Varna, NE Bulgaria): Formation mechanisms and the

(a)biological mediation of chimney growth? Sedimentary Geology, 185, 159-173.

De Boever, E., Swennen, R., Dimitrov, L., 2006b. Lower Eocene carbonate-cemented 'chimney' structures (Varna, Bulgaria) – Control of seepage rates on their formation and stable isotopic signature. Journal of Geochemical Exploration, 89, 78-82.

DeMets, C., Gordon, R.G., Argus, D.F., Stein, S., 1994. Effect of recent revisions to the geomagnetic reversal time scale on estimates of current plate motions. Geophysical Research Letters, 21, 2191-2194.

Díaz-del-Río, V., Somoza, L., Martínez-Frias, J., Mata, M.P., Delgado, A., Hernandez-Molina, F.J., Lunar, R., Martín-Rubí, J.A., Maestro, A., Fernández-Puga, M.C., León, R., Llave, E., Medialdea, T., Vázquez, J.T., 2003. Vast fields of hydrocarbon-derived carbonate chimneys related to the accretionary wedge/olistostrome of the Gulf of Cádiz. Marine Geology, 195, 177-200.

Dunham, R.J., 1962. Classification of carbonate rocks according to depositional texture. Ham, W.E., (Ed.), Classification of carbonate rocks. American Association of Petroleum Geologists Memoir, 1, pp. 108-121.

Falconbridge, J., 1994. Sedimentology, paleontology and petrology of the Urenui Formation, North Taranaki. Unpublished MSc Thesis, University of Auckland, New Zealand.

Faure, K., Greinert, J., Pecher, I.A., Graham, I.J., Massoth, G.J., De Ronde, C.E.J., Wright, I.C., Baker, E.T., Olson, E.J., 2006. Methane seepage and its relation to slumping and gas hydrate at the Hikurangi margin, New Zealand. New Zealand Journal of Geology and Geophysics, 49, 503-516.

Feary, D.A., Davies, P.J., Pigram, C.J., Symonds, P.A., 1991. Climatic evolution and control on carbonate deposition in northeast Australia. Palaeogeography, Palaeoclimatology, Palaeoecology, 89, 341-361.

Fergusson, L., 1985. The mineralogy, geochemistry and origin of lower Tertiary smectite-mudstones, East Coast Deformed Belt, New Zealand. Unpublished MSc thesis, University of Canterbury, Christchurch, New Zealand.

Field, B.D., Uruski, C.I., and others, 1997. Cretaceous-Cenozoic geology and petroleum systems of the East Coast Region, New Zealand. Institute of Geological and Nuclear Sciences monograph, 19, 301 pp.

Field, M.E., Barber, J.H.J., 1993. A submarine landslide associated with shallow seafloor gas and gas hydrates off Northern California. In: Schwab, W.C., Lee, H.J., Twichell, D.C. (Eds.), Submarine Landslides: Selected Studies in the U.S. Exclusive Economic Zone. U.S. Geological Survey Bulletin, 2002, 151-157.

Folk, R. L., 1962. Spectral subdivision of limestone types. Ham, W.E., (Ed.), Classification of carbonate rocks. American Association of Petroleum Geologists Memoir, 1, pp. 108-121.

Francis, D.F., 1997. Oil and Gas Generation in the East Coast Basin – an update. Petroleum Exploration in New Zealand News, volume 51, October 1997.

Francis, D.F., Bennett, D., Courteney, S., 2004. Advances in understanding of onshore East Coast Basin structure, stratigraphic thickness and hydrocarbon generation. 2004 New Zealand Petroleum Conference Proceedings, Auckland, 7-10 March 2004. 20pp. http://www.crownminerals.govt.nz/cms/ pdf-library/petroleum-conferences-1/2004/papers/Petroleum-23-04NZPC-Paper-ECBStructure.pdf.

Friedman, I., O'Neil, J.R., 1977. Compilation of stable isotope fractionation factors of geochemical interest, In Fleisher, M., (Ed.), U.S. Geological Survey Professional Paper, 440-kk.

Fritz, P., Smith, D.G.W., 1970. The isotopic composition of secondary dolomite. Geochimica et Cosmochimica Acta, 34, 1161-1173.

Fu, B., Aharon, P., Byerly, G.R., Roberts, H.H., 1994. Barite chimneys on the Gulf of Mexico slope: initial report on their petrography and geochemistry. Geo-Marine Letters, 14, 81-7.

Gautier D.L. and Claypool, G.E. (1984). Interpretation of methanic diagenesis in ancient sediments by analogy with processes in modern diagenetic environments. In: McDonald, D.A., Surdam, R.C. (Eds.), Clastic

Diagenesis. American Association of Petroleum Geologist Memoirs, 37, pp. 111-123.

Gay, A., Lopez, M., Cochonat, P., Séranne, M., Levaché, D., Sermondadaz, G., 2006a. Isolated seafloor pockmarks linked to BSRs, fluid chimneys, polygonal faults and stacked Oligocene-Miocene turbiditic palaeochannels in the Lower Congo Basin. Marine Geology, 226, 25-40.

Gay, A., Lopez, M., Ondreas, H., Charlou, J-L., Sermondadaz, G., Cochonat, P., 2006b. Seafloor facies related to upward methane flux within a Giant Pockmark of the Lower Congo Basin. Marine Geology, 226, 81-95.

Gieskes, J., Mahn, C., Day, S., Martin, J.B., Greinert, J., Rathburn, T., McAdoo, B., 2005. A study of the chemistry of pore fluids and authigenic carbonates in methane seep environments: Kodiak Trench, Hydrate Ridge, Monterey Bay, and Eel River Basin. Chemical Geology, 220, 329-345.

Goldsmith, J.R., Graf, D.L., Heard, H.C., 1961. Lattice constants of the calcium-magnesium carbonate. The American Mineralogist, 46, 453-457.

Grange, L.I., 1927. The geology of the Tongaporutu-Ohura subdivision, Taranki division. New Zealand Geological Survey Bulletin 31. Government Printer, Wellington.

Grauls, D. 2001. Gas hydrates: importance and applications in petroleum exploration. Marine and Petroleum Geology 18: 519-523.

Greinert, J., Bohrmann, G., Suess, E., 2001. Gas hydrate-associated carbonates and methane-venting at Hydrate Ridge: Classification, distribution, and origin of authigenic lithologies. In: Parnell, C.K., Dillon, K.P. (Eds.), Natural Gas Hydrates: Occurrence, Distribution and Detection. Geophysical Monograph, 124, 99-113.

Greinert, J., Bialas, J., Lewis, K., Suess, E., in review. Methane seeps and gas hydrates offshore New Zealand's North Island: Compiling results from three cruises in 2006 and 2007. Submitted to Marine Geology.

Henderson, J., Ongley, M., 1920. The geology of the Gisborne and Whatatutu Subdivisions, Raukumara Division. New Zealand Geological Survey Bulletin, 21, 1–88.

Hinrichs, K. U., Hayes, J.M., Sylva, S.P., Brewer, P.G., DeLong, E.F., 1999. Methane-consuming archaebacteria in marine sediments. Nature, 398, 802-805.

Hodell, D.A., Elmstrom, K.M., Kennett, J.P., 1986. Latest Miocene benthic $\delta^{18}O$ changes, global ice volume, sea level and the 'Messinian salinity crisis'. Nature, 320, 411-414.

Hollis, C., Manzano-Kareah, K., 2005. Source rock potential of the East Coast Basin. Open-file petroleum report 3179, Crown Minerals, Ministry of Commerce, Wellington.

Hovland, M., Svensen, H., Forsberg, C.F., Johansen, H., Fichler, C., Fosså, J.H., Jonsson, R., Rueslåtten, H., 2005. Complex pockmarks with carbonate-ridges off mid-Norway: Products of sediment degassing. Marine Geology, 218, 191-206.

Irwin, H., Curtis, C., Coleman, M., 1977. Isotopic evidence for source of diagenetic carbonates formed during burial of organic-rich sediments. Nature, 269, 209-213.

Iversen, N., Jørgensen, B.B., 1985. Anaerobic methane oxidation rates at the sulphate-methane transition in marine sediments from Kattegat and Skagerrak (Denmark). Limnology and Oceanography, 30, 944-955.

Jensen, P., Aagaard, I., Burke Jr. R.A., Dando, P.R., Jørgensen, N.O., Kuijpers, A., Laier, T., O'Hara, M.O., Schmaljohann, R., 1992. 'Bubbling reefs' in the Kattegat: submarine landscapes of carbonate-cemented rocks support a diverse ecosystem at methane seeps. Marine Ecology Progress Series, 83, 103-112.

Jørgensen, N.O., 1992. Methane-derived carbonate cementation of marine sediments from the Kattegat, Denmark: Geochemical and geological evidence. Marine Geology, 103, 1-13.

Judd, A.G. 2003. The global importance and context of methane escape from the seabed. Geo-Marine Letters, 23,147-154.

Judd, A.G., Hovland, M., 2007. Seabed fluid flow: The impact on geology, biology and the marine environment. Cambridge University Press, Cambridge, 475 pp.

Kamp, P.J.J., 1986. The mid-Cenozoic Challenger Rift system of western New Zealand and its implications for age of the Alpine Fault inception. Geological Society of America Bulletin, 97, 255-281.

Kamp, P.J.J., Nelson, C.S., 1988. Nature and occurrence of modern and Neogene active margin limestones in New Zealand. New Zealand Journal of Geology and Geophysics, 31, 1–20.

Kamp, P.J.J., Vonk, A.J., Bland, K.J., Griffin, A.G., Hayton, S., Hendy, A.J.W., McIntyre, A.P., Nelson, C.S., Naish, T., 2002. Measequence architecture of Taranaki, Wanganui, and King Country basins and Neogene progradation of two continental margin wedges across western New Zealand. 2002 New Zealand Petroleum Conference Proceedings, pp. 464-481.

Kamp, P.J.J, Vonk, A.J., Bland, K.J., Hansen, R.J., Hendy, A.J.W., McIntyre, A.P., Ngatai, M., Cartwright, S.J., Hayton, S., Nelson, C.S., 2004. Neogene stratigraphic architecture and tectonic evolution of Wanganui, King Country, and eastern Taranaki Basins, New Zealand. New Zealand. New Zealand Journal of Geology and Geophysics, 47, 625-644.

Kamp, P.J.J., Furlong, K.P., 2006. Neogene plate tectonic reconstructions and geodynamics of North Island sedimentary basins: Implications for the petroleum systems. 2006 New Zealand Petroleum Conference Proceedings, Auckland, 6-8 March 2006. 16 pp.

Kennicut, M.C., Brooks, J.M., Bidigare, R.R., et al., 1985. Vent type taxa in a hydrocarbon seep region on the Louisiana Slope. Nature, 317, 351-353.

Kenny, J.A., 1984. Stratigraphy, Sedimentology and structure of the Ihungia decollement, Raukumara Peninsula, North Island, New Zealand. New Zealand Journal of Geology and Geophysics, 27, 1-19.

King, P.R., Scott, G.H., Robinson, P.H., 1993. Description, correlation and depositional history of Miocene sediments outcropping along North

Taranaki coast. Institute of Geological and Nuclear Sciences Monograph 5. Institute of Geological and Nuclear Sciences Ltd, Lower Hutt.

King, P.R., Thrasher, G.P., 1996. Cretaceous-Cenozoic geology and petroleum systems of the Taranaki Basin, New Zealand. Institute of Geological and Nuclear Sciences Monograph 13. Institute of Geological and Nuclear Sciences Ltd, Lower Hutt.

King, P., Browne, G., 2002. Miocene slope to basin-floor sequences exposed in North Taranaki, New Zealand. 2002 New Zealand Petroleum Conference Proceedings, pp. 482-481.

King, P.R., Browne, G.H., Arnot, M.J., Crundwell, M.P., 2007. A 2-D oblique – dip outcrop transect through a third-order, progradational, deep-water clastic succession, Urenui-Mount Messenger Formations, New Zealand. In: Nilsen, T.H., Shew, R.D., Steffens, G.S., Studlick, J.R.J., (Eds.), Atlas of deep-water outcrops: AAPG Studies in Geology 56, CD-ROM, 42 pp.

Kukowski, N., Pecher, I., 1999. Thermo-hydraulics of the Peruvian accretionary complex at 12˚ S. Geodynamics, 27, 373-402.

Kulm, L.D., Suess, E. 1990. Relationship between carbonate deposits and fluid venting: Oregon accretionary prism. Journal of Geophysical Research, 95, 8899-8915.

Kyser, T.K., James, N.P., Bone Y., 2002. Shallow burial dolomitization and dedolomitization of Cenozoic cool-water limestones, southern Australia: geochemistry and origin. Journal of Sedimentary Research, 72, 146-157.

Laird, M.G., 1994. Geological aspects of the opening of the Tasman Sea. In: van der Lingen, G.J., Swanson, K.M., Muir, R.J. (Eds.). Evolution of the Tasman Sea Basin. A.A. Balkenma, Rotterdam. Pp. 1-17.

Lédesert, B., Buret, C., Chanier, F., Fèrriere, J., Recourt, P., 2003. Tubular structures of northern Wairarapa (New Zealand) as possible examples of ancient fluid expulsion in an accretionary prism: evidence from field and petrographical observations. Geological Society of London, Special Publication, 216, 95-107.

Lee, J.M., Begg, J.G., compilers, 2002. Geology of the Wairarapa Area. Institute of Geological and Nuclear Sciences Limited, Lower Hutt, N. Z., 66 pp.

Lewis, K.B., Pettinga, J.R., 1993. The emerging imbricate forntal wedge of the Hikurangi Margin. In: South Pacific Sedimentary Basins of the World, 2. Ballance, P.F. (Ed.), Elsevier Science Publishers B.V. Amsterdam. Pp. 225-250.

Lewis, K.B., Marshall, B.A., 1996. Seep faunas and other indicators of methane-rich dewatering on New Zealand convergent margins. New Zealand Journal of Geology and Geophysics, 39, 181-200.

Locat, J., 2001. Instabilities along ocean marine: a geomorphological and geotechnical perspective. Marine and Petroleum Geology, 18, 503-512.

Longstaffe, F.J., 1987. Stable isotope studies of diagenetic processes. In Kyser, T. (Ed.) Short Course in Stable Isotope Geochemistry of Low Temperature Processes. Mineralogical Society of Canada, Saskatoon, SK, pp. 187-257.

Lonsdale, P. Becker, K., 1985. Hydrothermal plumes, hot springs, and conductive heat flow in the Southern Trough of Guaymas Basin. Earth and Planetary Science Letters, 73, 211-225.

MacDonald, I.R., Reilly, J.F., Guinasso, N.L., Jr., et al., 1990. Chemosynthetic mussels at a brine-filled pockmark in the northern Gulf of Mexico. Science, 248, 1096-1099.

Martin, J.S., 1986. Paleoecology of East Cape upper Miocene strata. Unpublished MSc. Thesis, University of Auckland.

Mayer, L.A., Shor, A.N., Hughes Clark, J., Piper, D.J.W., 1988. Dense biological communities at 3850 m on the Laurentian Fan and their relationship to the deposits of the 1929 Grand Banks earthquake. Deep-Sea Research, 35, 1235-1246.

Mazengarb, C., Francis, D.A., Moore, P.R., 1991. Geological map of New Zealand, 1:50,000, Sheet Y16, Geology of the Tauwhareparae area. New Zealand Geological Survey, Wellington, New Zealand.

Mazzini, A., Duranti, D., Jonk, R., Parnell, J., Cronin, B.T., Hurst, A., Quine, M., 2003. Palaeo-carbonate seep structures above an oil reservoir, Gryphon Field, Tertiary, North Sea. Geo-Marine Letters, 23, 323-339.

McBride E.F., Milliken K.L., Cavazza W., Cibin U., Fontana D., Picard M.D. Zuffa G.G., 1995. Heterogeneous distribution of calcite cement at the outcrop scale in Tertiary sandstones, northern Apennines, Italy. American Association of Petroleum Geologists Bulletin, 79, 1044-1063.

McCrea, J.M., 1950. On the isotopic chemistry of carbonates and a paleotemperature scale. Journal of Chemical Physics, 18, 849-857.

McKay, A., 1877. On the geology of east Auckland and the northern district of Hawke's Bay. New Zealand Geological Survey, Reports of Geological Explorations during 1886–1887 (No. 18), pp. 183–219.

Middleton, H.A., Nelson, C.S., 1996. Origin and timing of siderite and calcite concretions in late Palaeogene non- to marginal-marine facies of the Te Kuiti Group, New Zealand, Sedimentary Geology, 103, 93-115.

Milkov, A.V., Sassen, R., 2002. Economic geology of offshore gas hydrate accumulations and provinces. Marine and Petroleum Geology, 19, 1-11.

Milkov, A.V., Vogt, P.R., Crane, K., Lein, A.Y., Sassen, R., and Cherkashev, G.A. 2004. Geological, geochemical, and microbial processes at the hydrate-bearing Hakon Mosby mud volcano: a review. Chemical Geology 205, 347-366.

Moore, J.C., 1981. Geology of the Late Tertiary section at Cape Turnagain. Journal of the Royal Society of New Zealand, 11, 223-230.

Moore, J.C., Vrolijk, P., 1992. Fluid in accretionary prisms. Reviews in Geophysics, 30, 113-135.

Mortimer, N., Herzer, R.H., Gans, P.B., Laporte-Magoni, C., Calvert, A.T., Bosch, D., 2007. Oligocene-Miocene tectonic evolution of the South Fiji basin and Northland Plateau, SW Pacific Ocean: evidence from petrology and dating of dredged rocks. Marine Geology, 237, 1-24.

Mörz, T., Karlik, E.A., Kreiter, S., Kopf, A., 2007. An experimental setup for fluid venting in unconsolidated sediments: New insights to fluid mechanics and structures. Sedimentary Geology, 196, 251-267.

Munnecke, A., Samtleben, C., 1996. The formation of micritic limestones and the development of limestone-marl alternations in the Silurian of Gotland, Sweden. Facies, 34, 159-176.

Neef, G., 1984. Late Cenozoic and Early Quaternary stratigraphy of the Eketahuna District (N153), New Zealand Geological Survey Bulletin, 96, 101 pp.

Nelson, C.S., Hume, T.M., 1977. Relative intensity of tectonic events revealed by the Tertiary sedimentary record in the North Wanganui Basin and adjacent areas, New Zealand. New Zealand Journal of Geology and Geophysics, 20, 369-392.

Nelson, C.S., Smith, A.M., 1996. Stable oxygen and carbon isotope compositional fields for skeletal and diagenetic components in New Zealand Cenozoic nontropical carbonate sediments and limestones: a synthesis and review. New Zealand Journal of Geology and Geophysics, 39, 93-107.

Nelson, C.S., Winefield, P.R., Hood, S.D., Caron, V., Pallentin, A., Kamp, P.J.J., 2003. Pliocene Te Aute limestones, New Zealand: expanding concepts for cool-water shelf carbonates. New Zealand Journal of Geology and Geophysics, 46, 407-424.

Nelson, C., Schellenberg, F., King, P., Ricketts, B., Kamp, P., Browne, G., Campbell, K., 2004. Note on paramoudra-like concretions in the Urenui Formation, North Taranaki: possible plumbing system for a Late Miocene methane seep field. 2004 New Zealand Petroleum Conference Proceedings, Auckland, 7-10 March 2004. 5 pp. [http://crownminerals.med.govt.nz/petroleum/publications/nzpconf/nzpconf-2004.html]

Nelson, C.S., Campbell, K.A., Nyman, S.L., Francis, D.A., Hood, S.D., Collins, M., Gregory, M.R., Greinert, J., Peckmann, J. Pearson, M.J., 2007. Miocene hydrocarbon seep-carbonate systems in North Island, New Zealand. 2007 GSA Denver Annual Meeting (28-31 October 2007), Geological Society of America, Abstracts with Programs, Vol. 39, No. 6, p. 147.

Nicol, A., Mazengarb, C., Chanier, F., Rait, G., Uruski, C., and Wallace, L., 2007, Tectonic evolution of the active Hikurangi subduction margin, New Zealand, since the Oligocene: Tectonics, 26, TC4002, doi:10.1029/ 2006TC002090.

Nyman, S.L., Nelson, C.S., Campbell, K.A., Schellenberg, F., Pearson, M.J., Kamp, P.J.J., Browne, G.H., King, P.R., 2006. Tubular carbonate concretions as hydrocarbon migration pathways? Examples from North Island New Zealand. 2006 New Zealand Petroleum Conference Proceedings, Auckland, 6-8 March 2006. 10 pp. [http://www.crownminerals.govt.nz/petroleum/ conference/papers/Poster_papers_21.pdf]

Nyman, S.L., Nelson, C.S., Campbell, K.A., in review. Possible late Miocene analogue for the subsurface plumbing of modern Hikurangi Margin cold seeps: Evidence from tubular concretions in southern Hawke's Bay. Submitted to Marine Geology special publication: methane seeps.

Olu, K., Lance, S., Sibuet, M., et al., 1997. Cold seep communities as indicators of fluid expulsion patterns through mud volcanoes seaward of the Barbados Accretionary Prism. Deep-Sea Research, 44, 811-841.

Orphan, V. J., Hinrichs, K.U., Ussler, III, W., Paull, C.K., Taylor, L.T., Sylva, S.P., Hayes, J.M., DeLong, E.F., 2001. Comparative analysis of methane-oxidizing archaea and sulphate-reducing bacteria in anoxic marine sediments. Applied and Environmental Microbiology, 67, 1922-1934.

Orpin, A. R., 1997. Dolomite chimneys as possible evidence of coastal fluid expulsion, uppermost Otago continental slope, southern New Zealand. Marine Geology, 138, 51-67.

Pancost, R.D., Damasté, J.S., De Lint, S., Van Der Maarel, M., Gottschal, J.C., Medinaut Shipboard Scientific Party, 2000. Biomarker evidence for widespread anaerobic methane oxidation in Mediterranean sediments by a consortium of methanogenic archaea and bacteria. Applied Environmental Microbiology, 66, 1126-1132.

Paull, C.K., Ussler, W., Dillon, W.P., 1991. Is the extent of glaciation limited by marine gas-hydrates? Geophysical Research Letters, 18, 432-434.

Pearce, A.R., Black, R.D., Nelson, C.S., 1981. Lithologic and weathering influences on slope form and process, eastern Raukumara Range, New Zealand. International Association of Hydrologic Science, 132, 95-122.

Pearson, M.J., Nelson, C.S., 2005. Organic geochemistry and stable isotope composition of New Zealand carbonate concretion and calcite fracture fills. New Zealand Journal of Geology and Geophysics, 48, 395-414.

Pearson, M.J., Grosjean, E., Nyman, S.L., Logan, G.A., Nelson, C.S., Hood, S.D., Campbell, K.A., 2008. Tubular concretions in New Zealand petroliferous basins: Lipid evidence for mineralization around proposed Miocene hydrocarbon seep conduits. 2008 New Zealand Petroleum Conference Proceedings, Auckland, 10-12 March 2008. 6 pp.

Pecher, I., Coffin, R., Henrys, S., et al., 2007. Tangaroa TAN0607 cruise report: gas hydrate exploration on the East Coast, North Island, New Zealand. Institute of Geological and Nuclear Sciences Ltd, Lower Hutt, New Zealand. GNS Science Report 2007/2. 112 pp.

Peckmann, J., Reimer, A., Luth, U., Luth, C., Hansen, B.T., Heinicke, C., Heofs, J., Reitner, J., 2001. Methane-derived carbonates and authigenic pyrite from the northwestern Black Sea. Marine Geology, 177, 129-150.

Peckmann, J., Goedert, J.L., Thiel, V., Michaelis, W., Reitners, J., 2002. A comprehensive approach to the study of methane-seep deposits from the Lincoln Creek Formation, western Washington State, USA. Sedimentology, 49, 855-873.

Pierre, C., Rouchy, J.-M., Blanc-Valleron, M.-M., 2002. Gas hydrate dissociation in the Lorca Basin (SE Spain) during the Mediterranean Messinian salinity crisis. Sedimentary Geology, 147, 247-252.

Pierre, C., Rouchy, J.-M., 2004. Isotopic compositions of diagenetic dolomites in the Tortonian marls of the western Mediterranean margins: evidence of past gas hydrate formation and dissociation. Chemical Geology, 205, 469-484.

Pierre, C. Foquat, Y., 2007. Authigenic carbonates from methane seeps of the Congo deep-sea fan. Geo-Marine Letters, 27, 249-257.

Popenoe, P., Schmuck, E.A., Dillon, W.P., 1993. The Cape Fear Landslide: slope failure associated with salt diapirism and gas hydrate decomposition. In: Schwab, W.C., Lee, H.J., Twichell, D.C. (Eds.), Submarine Landslides: Selected Studies in the U.S. Exclusive Economic Zone. U.S. Geological Survey Bulletin 2002, 40-53.

Pratson, L.F., 2001. A perspective on what is known and not known about seafloor instability in the context of continental margin evolution. Marine and Petroleum Geology, 18, 449-501.

Querellou, J., 2003. Biotechnology of marine extremophiles. Book of Abstracts, International Conference on the sustainable development of the Mediterranean and Black Sea environment, Thessaloniki, Greece, 28 May – 1 June (extended abstract).

Rait, G., Chanier, F., Waters, D.W., 1991. Landward- and seaward-directed thrusting accompanying the onset of subduction beneath New Zealand. Geology, 19, 230-233.

Reitner, J., Peckmann, J., Blumenberg, M., Michaelis, W., Reimer, A., Thiel, V., 2005. Concretionary methane-seep carbonates and associated microbial communities in Black Sea sediments. Palaeogeography, Palaeoclimatology, Palaeoclimatology, 227, 18-30.

Rice, D.D., 1992. Controls, habitat, and resource potential of ancient bacterial gas. In: Vially, R. (Ed.), Bacterial Gas. Paris, Editions Technip, 91-118.

Ridgway, N.M., 1969. Temperature and salinity of sea water at the ocean floor in the New Zealand region. New Zealand Journal of Marine Freshwater Research, 3, 57-72.

Roberts, H.H., Aharon, P., 1994. Hydrocarbon-derived carbonate buildups of the northern Gulf of Mexico continental slope: A review of submersible investigations. Geo-Marine Letters, 14, 135-148.

Rogers, K.M., Collen, J.D., Johnston, J.H., Elgar, N.E., 1999. A geochemical appraisal of oil seeps from East Coast Basin, New Zealand. Organic Geochemistry, 30, 593-605.

Safer, D.M., Bekins, B.A., 1998. Episodic fluid flow in the Nankai accretionary complex: timescale, geochemistry, flow rates, and fluid budget. Journal of Geophysical Research, 103, 30351-30370.

Schellenberg, F., 2002. The paramoudra concretions within the Urenui Formation, Taranaki Basin, West Coast of New Zealand: Fossil fluid conduits or giant trace fossils? Institute of Geology and Palaeontology, University of Tübingen, unpublished MSc Thesis.

Schwartz, H., Sample, J., Weberling, K.D., Minisini, D., Moore, J.C., 2003. An ancient linked fluid migration system: cold-seep deposits and sandstone intrusions in the Panoche Hills, California, USA. Geo-Marine Letters, 23, 340-350.

Sibson, R.H., 1992. Implications of fault-valve behaviour for rupture nucleation and recurrence. Tectonophysics, 211, 283-293.

Sibson, R.H., Rowland, J.V., 2003. Stress, fluid pressure, and structural permeability in seismogenic crust, North Island, New Zealand. Geophysical Journal International, 154, 584-594.

Sloan, E.D., 1988. Clathrate Hydrates of Natural Gas, 2nd Edn. New York, NY, Marcel Dekker.

Stagpoole, V., Nicol, A., 2008. Regional structure and kinematic history of a large subduction back thrust: Taranaki Fault, New Zealand. Journal of Geophysical Research, 113, B01403, doi:10.1029/2007JB005170.

Stakes, D., Orange, D., Paduan, J.B., Salamy, K.A., Maher, N., 1999. Cold-seeps and authigenic carbonate formation in Monterey Bay, California. Marine Geology, 159, 93-109.

Suess, E., Torres, M.E., Bohrmann, G., Collier, R.W., Greinert, J., Linke, P., Rehder, G., Trehu, A., Wallmann, K., Winckler, G., Zueger, E., 1999. Gas hydrate destabilization: enhanced dewatering, benthic material turnover and large methane plumes at the Cascadia convergent margin. Earth and Planetary Science Letters, 170, 1-15.

Taranaki GSNZ, 1994. *Paramoudra/Zoophycos* trace fossil association in the Miocene of the North Taranaki coast. Geological Society of New Zealand Miscellaneous Publication, 80A, 175.

Thiel, V., Peckmann, J., Richnow, H.-H., et al., 2001. Molecular signals for anaerobic methane oxidation in Black Sea seep carbonates and a microbial mat. Marine Chemistry, 73, 97-112.

Tonkin, N., 2003. Application of ichnofabric analysis and event stratigraphy to paleoenvironmental reconstruction in Late Miocene strata, East Cape – Te Araroa, New Zealand. Unpublished MSc thesis, University of Auckland.

Torres, M.E., Bohramann, G., Suess, E., 1996. Authigenic barites and fluxes of barium associated with fluid seeps in the Peru subduction zone. Earth and Planetary Science Letters, 144, 469-481.

Townend, J., 1997. Subducting a sponge: minimum estimates of the fluid budget of the Hikurangi Margin accretionary prism. Geological Society of New Zealand Newsletter, 112, 14-16.

Townsend, D., Vonk, A., Kamp, P.J.J., (compilers) 2008. Geology of the Taranaki area. Institute of Geological and Nuclear Sciences 1:250 000 geological map 7. 1 sheet + 79 p. Lower Hutt, New Zealand. GNS Science Limited, Lower Hutt, New Zealand, Department of Earth and Ocean Sciences, University of Waikato, Hamilton 2008.

Tucker, M.E. and Wright, V.P., 1990. Carbonate Sedimentology. Oxford, Blackwell Scientific. 482 pp.

Ussler III, W., Paull, C.K., 1995. Effects of ion exclusion and isotopic fractionation on pore water geochemistry during gas hydrate formation and decomposition. Geo-Marine Letters, 15, 37-44.

van der Lingen, G.J., Pettinga, J.R., 1980. The Makara Basin: a Miocene slope-basin along the New Zealand sector of the Australian-Pacific obliquely convergent plate boundary. In: Ballance, P.F., Reading, H.G. (Eds.), Sedimentation in Oblique Strike-slip Mobile Zones. Special Publication of the International Association of Sedimentologists, 191-215.

Vokes, H.E., 1955. Notes on Tertiary and Recent Solemyacidae. Journal of Paleontology, 29, 534-535.

Vonk, A.J., Kamp, P.J.J., 2008. The Late Miocene southern and central Taranaki inversion phase (SCTIP) and related sequence stratigraphy and paleogeography. 2008 New Zealand Petroleum Conference Proceedings, Auckland, 10-12 March 2008, 17 pp.

Whiticar, M.J., 1999. Carbon and hydrogen isotope systematics of bacterial formation and oxidation of methane. Chemical Geology, 161, 291-314.

Wiese, K., Kvenvolden, K.A., 1993. Introduction to microbial and thermal methane. In Howell, D.G. (Ed.), The Future of Energy Gases. United States Geological Survey Professional Paper, 1570, 13-20.

Wilkin, R.T., Barnes, H.L., 1997. Formation processes of framboidal pyrite. Geochimica et Cosmochimica Acta, 61, 323-339.